Reports of the Department of Mathematical Information Technology
Series A. Collections
No. A 1/2009

Proceedings of the 10th Finnish Mechanics Days
X Suomen Mekaniikkapäivät

Jyväskylän yliopisto
3.–4. joulukuuta 2009

Toimittajat
Raino Mäkinen
Pekka Neittaanmäki
Tero Tuovinen
Kati Valpe

University of Jyväskylä
Department of Mathematical Information Technology
P.O. Box 35 (Agora)
FI-40014 University of Jyväskylä
FINLAND

Phone +358 14 260 1211
Fax +358 14 260 2731
http://www.mit.jyu.fi/

ISBN 978-951-39-3738-6
ISSN 1456-4351

ESIPUHE

Suomen Mekaniikkapäivät järjestettiin kuluvana vuonna 2009 jo juhlallisen kymmenennen kerran. Mekaniikkapäiville kokoonnutaan joka kolmas vuosi tarkastelemaan mekaniikan tilannetta Suomessa ja kuuntelemaan mielenkiintoisia, usein nuorten tutkijoiden pitämiä, esitelmiä uusista tuloksista mekaniikan, siihen liittyvän matematiikan, tieteelliseen laskennan ja optimoinnin saralla.

Ensimmäiset mekaniikkapäivät järjestettiin Oulussa vuonna 1982. Siitä lähtien päivät on järjestetty Tampereella 1985, Otaniemessä 1988, Lappeenrannassa 1991, Jyväskylässä 1994, Oulussa 1997, Tampereella 2000, Otaniemessä 2003 ja Lappeenrannassa 2006. Tänä vuonna mekaniikkapäivien käytännön järjestelyvastuu oli Jyväskylän yliopistolla. Tapahtuma pidettiin 3.–4.12.2009 Mattilanniemen kampuksella Agora-rakennuksessa.

Mekaniikkapäivien kanssa järjestettiin rinnakkainen tapahtuma: "Integrated Multiphysics Simulation & Design Optimization: Database Workshop for Multiphysics Optimization Software Validation". Kutsutut esitelmät olivat yhteisiä molemmille tapahtumille. Kutsuttuina esitelmöijinä olivat professorit: *Tadeusz Burczynski*, Cracow University of Technology and Silesian University of Technology, *Jean-Antoine Désidéri*, INRIA Sophia-Antipolis, *Axel Klawonn*, Universität Duisburg-Essen, *Mohamed Masmoudi*, University of Toulouse ja *Kaisa Miettinen*, Jyväskylän yliopisto. Tämän lisäksi päivillä pidettiin muita esitelmiä yhteensä 53 kappaletta. Esitelmiin liittyvät artikkelit on koottu tähän konferenssijulkaisuun.

Haluamme lämpimästi kiittää kaikkia niitä, jotka ovat myötävaikuttaneet päivien onnistumiseen, osallistujia, artikkelien kirjoittajia ja esitelmöitsijöitä, tieteellistä neuvostoa ja ennen muuta kaikkia niitä henkilöitä, jotka ovat osallistuneet järjestelytyöhön paikan päällä.

Raino Mäkinen
Pekka Neittaanmäki
Tero Tuovinen
Kati Valpe

FOREWORD

The 10th Finnish Mechanics Days were held in Jyväskylä at the University of Jyväskylä December 3–4, 2009. The aim of the Finnish Mechanics Days is to bring together researchers, industrial specialists and doctoral students whose interest lies in mechanics, mathematics associated with it, scientific computing, and optimization.

The first Mechanics Days were held in Oulu 1982. Since then the days have taken place in Tampere 1985, Otaniemi 1988, Lappeenranta 1991, Jyväskylä 1994, Oulu 1997, Tampere 2000, Otaniemi 2003, and Lappeenranta 2006.

The 10th Mechanics Days was parallel event with "Integrated Multiphysics Simulation & Design Optimization: Database Workshop for Multiphysics Optimization Software Validation". Both events shared the invited speakers. Invited presentations were given by professors *Tadeusz Burczynski*, Cracow University of Technology and Silesian University of Technology, *Jean-Antoine Désidéri*, INRIA Sophia-Antipolis, *Axel Klawonn*, Universität Duisburg-Essen, *Mohamed Masmoudi*, University of Toulouse, and *Kaisa Miettinen*, University of Jyväskylä. In addition, 53 other presentations were given. The papers are included in these conference proceedings.

We express our warm gratitude to all of them who played roles in the success of the event, participants, speakers and authors, the scientific committee, and, first of all, the local organizers.

SISÄLLYS

Structural Mechanics I

Applications

Structural Mechanics II

Experimental Mechanics and Special Topics on Structural Mechanics

2. päivän esitelmät

Numerical Methods II

Optimization

Dynamics and Vibrations

Fluid Mechanics and Fluid Structure Interaction

Material and Fracture Mechanics

IMMUNE OPTIMIZATION

T. BURCZYNSKI[1,2], W. KUS[1], A. POTERALSKI[1] AND M. SZCZEPANIK[1]

[1] Department for Strength of Materials and Computational Mechanics
Silesian University of Technology, POLAND

[2] Institute of Computer Modelling
Cracow University of Technology, POLAND

ABSTRACT

Nature inspired computing has proved to be useful in various application areas. Evolutionary methods, neural networks, swarm intelligence and many other approaches have been applied to many technical and engineering problems, such as optimization, learning, data analysis, knowledge engineering and many others. Some of these methods perform better in the given application areas and some work better in others. However, it can hardly be assumed that there exists a problem domain in which nature inspired techniques are not employed, at least as a part of the proposed solution. After decades of development, biologically inspired methods are well established and appreciated tools. On the other hand, many novel approaches arise to solve problems in innovative ways, hopefully more effectively. One of such novel areas is the field of *Artificial Immune Systems (AIS)*. The question arises as to what AIS can offer as problem solving techniques and whether the paradigms proposed by AIS researchers are in fact novel. The aim of this paper is to provide a set of carefully selected problems connected with the current research directions of *Immune Computing*.

Immune system, especially this of vertebrates, is a very complicated system of interacting cells, organs and mechanisms, whose purpose is to protect the host body against any danger, either exterior or internal. To achieve that goal the immune system has to decide not only about what is not part of the host but also what can cause a damage. This is a very difficult task, as not all that comes from outside is dangerous. On the other hand, autoimmune diseases are examples of internal threats. To protect the host against all such dangers is not an easy task, especially in a changing environment. It is obvious that the immune system has to develop some sense of self, i.e., the sense of what is part of the host. How the immune system achieves this is hard to explain, as the host body changes its functioning and structure over time. Nonetheless, the immune system is able to perform its task effectively. To deal with such difficult task the immune system needs the ability to learn new threats, to remember previous experiences and to develop specialized responses to different pathogens. Taking a closer look at all these features one can state that the immune system can be considered as a cognitive system. For that reason the immune system gained an interest of computational sciences.

Given all the complexity of functioning of the immune system, it is necessary to extract higher level paradigms which could serve as the basis of constructing computational models and

algorithmic solutions. The most important paradigms in the filed of Artificial Immune Systems are *Clonal Selection* (CS), *Immune Network Theory* (IMT), *Negative Selection* (NS) and recently emerged *Danger Theory* (DT).

The question is whether AIS can offer anything really new and/or useful. Clonal Selection can seem to be another exemplification of evolutionary approach to problem solving. The fact of existing of immune networks in biological immune systems is questioned by biologists. Negative Selection appears to be truly novel approach, but one could ask whether it is enough to invest time and resources to develop AIS. In the first examinations of the immune ideas, the researchers developed several algorithmic solutions based on immune paradigms, often separately. Clonal Selection and Immune Network Theory have been applied to optimization, data analysis or clustering. Negative Selection has been applied to computer security, anomaly or fault detection. Many of the proposed algorithms have successfully dealt with the tasks appointed to them. However, their usefulness according to their robustness and scalability has been under dispute when compared to other well established computational methods.

The paper is devoted to applications of artificial immune systems to shape and topology optimizatiom of 2-D and 3-D structures. Grid-based artificial immune systems in optimization of mechanical systems are also presented. The paper contains detailed description of both serial and parallel versions of immune algorithms. Several numerical examples and engineering applications are presented.

NUMERICAL SIMULATION OF ARTERIAL WALL MODELS

AXEL KLAWONN

Faculty of Mathematics
University of Duisburg-Essen
Universitätsstr. 3
D-45117 Essen, GERMANY

Email: axel.klawonn@uni-duisburg-essen.de

ABSTRACT

The mechanical behavior of arterial walls in the physiological range can be described by anisotropic, hyperelastic elasticity models. Different models can be considered. Each of them is represented by a polyconvex strain energy function in order to guarantee the existence of minimizers. Discretization of these three dimensional models by the finite element method usually results in a large number of equations. Dual-primal FETI methods are among the most severely tested domain decomposition methods for the solution of partial differential equations on parallel computers. A computational framework using a Newton-Krylov-FETI approach for the solution of the discretized models will be discussed and applied to different material wall models and geometries.

This presentation is based on joint work with Oliver Rheinbach, Faculty of Mathematics, University of Duisburg-Essen, Dominik Brands and Jörg Schröder, Institute of Mechanics, Division of Civil Engineering, Faculty of Engineering, University of Duisburg-Essen and Dirk Böse and Raimund Erbel, West-German Heart Center and University Hospital, University of Duisburg-Essen.

EXTENDED ADJOINT APPROACH IN CFD

MOHAMED MASMOUDI

Institute of Mathematics of Toulouse (IMT)
University of Toulouse, FRANCE

Email: mohamed.masmoudi@math.univ-toulouse.fr

ABSTRACT

First and second order derivatives are classical tools for uncertainty quantification. It is well known that the adjoint approach is a powerful tool for first order sensitivity computation. But the efficient calculation of second order sensitivity is still an open problem.

We discovered that the second order variation of the solution could be split into smooth and oscillating parts. The regular behavior is taken into account by the adjoint approach and we don't need to calculate it. The high frequency part is very easy to compute using very local calculation.

For example, if we are dealing with shape parameters, we have just to modify the shape and to update the solution locally around the shape. The proposed solution is non invasive.

We obtained spectacular results in CFD, electromagnetism, and structural analysis.

A comparison of two approaches for ship collision simulations: dynamic calculations versus displacement controlled calculations

K. TABRI
Department of Applied Mechanics, Marine Technology
Teknillinen korkeakoulu
P.O.Box5300,
02015TKK, Finland
kristjan.tabri@tkk.fi

J. BROEKHUIJSEN
Damen Schelde Naval Shipbuilding
Glacisstraat 165, 4381 SE Vlissingen
The Netherlands
joep.broekhuijsen@damennaval.com

R. VILLAVICENCIO
Instituto Superior Técnico
Avenida Rovisco Pais
1049-001 Lisboa, Portugal
rvillavicencio@mar.ist.utl.pt

ABSTRACT

The paper presents two methods for numerical simulations of ship collisions: a displacement controlled approach at constant velocity and a dynamic approach using actual velocities in collision. In the displacement controlled method, the struck ship is kept motionless and the striking ship penetrates it along the direction of its initial velocity. In the dynamic approach the ships are allowed to move and the collision process considers the actual motions of the ships and thus, the collision is described more accurately. The paper discusses the advantages and disadvantages of both methods, such as the possibility of time scaling, duration and preciseness of simulations, etc. As a case study six collision scenarios of two river tankers are calculated with both methods and the deformation energy required to breach the inner hull of the struck ship is compared.

1. INTRODUCTION

Numerical simulations are often used to assess the crashworthiness of ship structures and to evaluate the outcomes of ship collisions. Such analysis is a demanding task and significant simplifications are required to achieve the outcomes in reasonable time. It is a common approach to decouple the analysis of structural deformations from the analysis of ship motions. There, the structural response is evaluated in so-called displacement controlled analysis – the struck ship is kept fixed and the striking ship collides with it at a constant velocity along a prescribed path, see for example Kitamura (2002). The analysis provides the contact force as a function of this prescribed penetration path. The actual extent of the penetration is obtained by comparing the area under the

force-penetration curve to the deformation energy evaluated with some calculation model that gives the deformation energy based on the conservation of momentum in collision (Pedersen and Zhang, 1998).

The accuracy of displacement controlled method depends on the level of precision on predicting the penetration path. This can be done rather precisely for symmetric collision, where the striking ship collides under a right angle at the amidships of the struck ship and only few motion components are excited. Statistical studies (Lützen, 2001; Tuovinen, 2005) have, however, indicated that the majority of collisions are non-symmetric in one way or another. Often the collision angle deviates from 90 deg or the contact point is not at the amidships. As in non-symmetric ship collisions more motion components are excited, the penetration path cannot be predefined with reasonable precision, but it should be evaluated in parallel with the ship motions. Pill and Tabri, 2009 presented a coupled numerical simulation procedure, where the ship motions and the structural deformations are evaluated in the same calculation run. This allows to evaluate the contact force and deformation energy based on the actual penetration and not based on the predictions made beforehand.

The paper gives a brief overview of both methods and discusses their advantages and disadvantages. Six non-symmetric collision scenarios are calculated with both approaches using explicit finite element (FE) code LS-Dyna. The deformation energy required to breach the inner hull of the struck ship is compared for both approaches. The paper does not present an extensive overview on the FE modelling techniques, which are elaborately presented elsewhere (see for example Ehlers et al, 2008), but concentrates fully on the dynamics and coupling aspects.

2. DISPLACEMENT CONTROLLED COLLISION SIMULATIONS

In displacement controlled simulations the striking ship collides with a struck ship, whose boundary nodes are constrained to prevent the ship from displacing from her initial position. Finite element model consists of partially modelled striking and struck ship as depicted in Figure 1. It is a recommended practise that the structures are modelled to extent where there are no plastic deformations at the boundaries. The striking ship is often modelled as a rigid body as the stiffness of the bow area is often superior to that of the side structure. The striking ship moves at constant velocity along the prescribed path and the contact between the ships does neither influence the speed nor the direction of the striking ship. Therefore, the rigid body motions of the colliding ships are excluded from the analysis and the emphasis is on the modelling of the structural response. Displacement controlled simulations are widely used in collision analyses due to their rather simple manner and fast simulation runs, see for example Kitamura (2002) or Ehlers et al (2008).

The method has several advantages and disadvantages. As the motion dynamics are not part of the simulation, some numerical manipulations can be made to shorten the duration of the simulation run. The main advantage is that the time step size can be increased using so-called mass-scaling in a certain range without significant loss of accuracy. In LS-Dyna the time step size is evaluated on the basis of the Courant stability criteria, which uses element dimensions, stiffness and density as input (Hallquist, 2007). The mass-scaling concept increases the density of the elements in which the Courant criterion is not met under the prescribed time step size minima. With reasonable selection of the step size the increase in mass and the ensuing dynamic effects remain insignificant and the mass scaling can be used. Furthermore, the speed of the striking ship often exceeds the typical speeds in collision. This, and the fact that the striking ship is not decelerating under the action of the contact force, significantly shortens the duration of the collision process and the simulation time required. Again, as the dynamics are of secondary importance, the error resulting from sometimes even unrealistically high collision speed is usually in acceptable range.

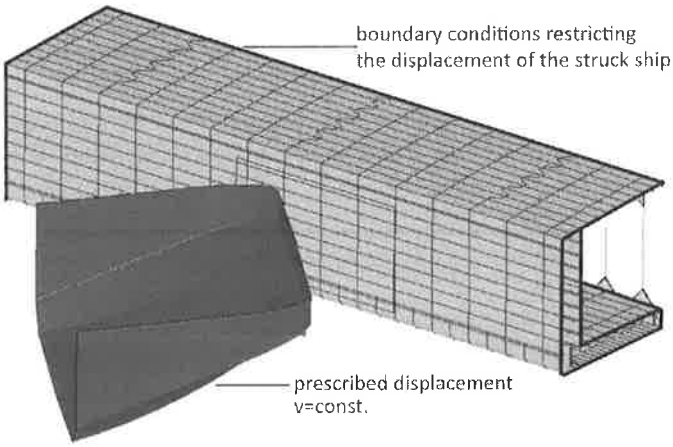

Figure 1. Displacement controlled calculations

The disadvantages of the displacement controlled method stem from the same aspects as its advantages – neglected collision dynamics. As the striking ship is moving at constant speed and the struck ship remains still throughout the collision, the dynamics of the collision, such as accelerations and velocities, are not physically correct. This means that some dynamic effects, such as strain rate effects in deforming structures, can not be properly included. Furthermore, under the prescribed displacement the collision process does not describe any actual collision scenario, but gives an assessment on the crashworthiness of the side structure.

3. DYNAMIC COLLISION SIMULATIONS

To properly simulate an actual collision scenario the analysis of structural response can not be decoupled from the ship motions. Mass, inertia and hydrodynamic properties of the ships have to be included in the FE model as the motion dynamics are part of the simulation. Pill and Tabri (2009) proposed a simplified method, which allows dynamics collision simulations. The ship motions were limited to the plane of water surface and thus the restoring forces were not included. Before proceeding to the overview of the simulation procedure, the forces acting on the colliding ships are discussed in brief.

3.1 Forces acting on colliding ships

When two ships collide, the contact force arises as a result of the penetration of structures, defined as a relative position between the striking and the struck ship. The contact force causes the ships to become displaced from their current position. At any time instant the force has to be in balance with the inertial and hydromechanical forces associated with this movement.

An accelerating or decelerating ship encounters a hydrodynamic radiation force induced by the relative acceleration between the hull and the water. The acceleration component $\mathbf{F}_{\mu}$ of this force is based on the constant added mass at an infinite frequency of motion multiplied by the ship's acceleration. In the presence of a free surface an additional force component – hydrodynamic damping $\mathbf{F}_K$ – arises. This is evaluated with the help of the convolution of the velocity and retardation function, which accounts for the memory effect of water (Cummins, 1962; Ogilvie, 1964). This approach requires the evaluation of the frequency-dependent added mass and the damping coefficients, which are calculated with the help of the strip theory (Journée, 1992). In time domain the hydrodynamic radiation force is evaluated as (Cummins, 1962)

$$\mathbf{F}_{\mu}(t)+\mathbf{F}_{K}(t)=-\left[\boldsymbol{a}_{\infty}\right]\begin{Bmatrix}\dot{\mathbf{u}}(t)\\ \dot{\boldsymbol{\Omega}}(t)\end{Bmatrix}-\int_{0}^{t}\left[\mathbf{K}_{b}(\tau)\right]\begin{Bmatrix}\mathbf{u}(t-\tau)\\ \boldsymbol{\Omega}(t-\tau)\end{Bmatrix}d\tau \tag{1}$$

where t denotes time, τ is a dummy variable, $\left[\boldsymbol{a}_{\infty}\right]$ is the matrix of added masses $a(\omega=\infty)$ at infinite frequency, and $[\mathbf{K}_b(\tau)]$ is a matrix of retardation functions, which account for the memory effects of water:

$$\left[\mathbf{K}_{b}(\tau)\right]=\frac{2}{\pi}\int_{0}^{\infty}\left[\mathbf{b}(\omega)\right]\cos(\omega\tau)\,d\omega \tag{2}$$

where $\left[\mathbf{b}(\omega)\right]$ is a matrix comprising of added damping terms $b(\omega)$. The retardation functions $K_b(\tau)$ are evaluated by Fast Fourier Transformation (Matusiak, 2001).

A ship moving in water also encounters frictional and residual resistance. Residual resistance is usually not included in the collision analyses because it is considered to be small compared to other phenomena. The friction force is proportional to the wetted surface and to the square of ships velocity.

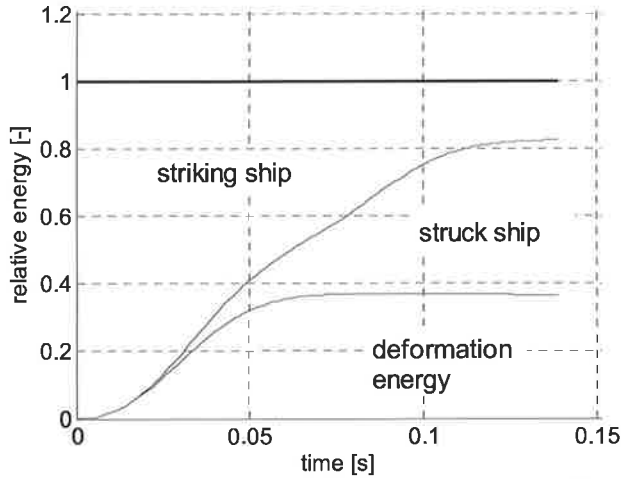

Figure 2. Division of relative energy components in collision

The importance of different forces and the corresponding energy components is presented based on the model-scale experiments conducted in Helsinki University of Technology (Tabri et al, 2008; Tabri et al, 2009). In Figure 2 the available energy in a model-scale collision experiment is divided into energy associated with the striking ship, energy associated with the struck ship and their difference, i.e. the deformation energy. Obviously, exact division depends on the collision parameters such as the masses of the participating ships, collision angle, location of the contact point etc, but for a general overview an analysis based on a single experiment serves it purpose. It should also be noticed, that when talking about the energy associated with a ship we exclude the deformation energy. We do so to separate the deformation process from other processes, which are mainly involved with the motion of a ship alone. What we refer to as energy associated with a ship consists of energies to overcome hydromechanic forces and the kinetic energy of moving ship structures.

Figure 3 presents a distribution of relative energy components other that the deformation energy. It can be seen that the kinetic energy involved with the motions of the ship structures and their added masses is clearly higher compared to the energy absorbed to overcome the friction and hydrodynamic damping.

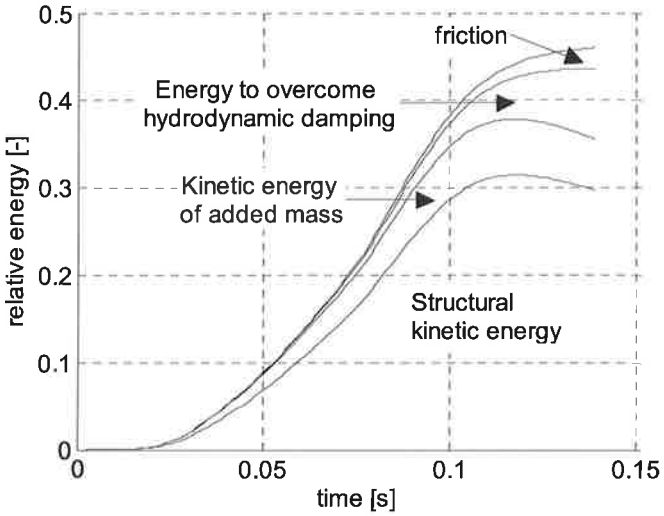

Figure 3. Division of relative energy components other than the contact force

3.2 Dynamic collision simulations

Previous chapter revealed that, in addition to the contact force, the inertial forces and the corresponding energies are the main components in collision. Linear effects associated with inertial forces can conveniently be included in FE simulations as they are proportional to the acceleration. The frictional force is proportional to the square of ships velocity and the hydrodynamic damping force requires the evaluation of convolution integral in the form of Eq. (1). Their inclusion in the simulations is not straight forward and as their share in the energy balance is relatively low, less than 10% of the total available energy in Figure 3, they are not yet included in the FE analysis.

The main challenge to include the inertia effects is to provide a proper description of the ship masses, inertias and added masses. These properties should be modelled with as few elements as possible in order to add little to the simulation time. Mass m and inertia about the vertical axis I_{zz} are the main properties of the ship when evaluating the planar motions under the external forces.

In a FE model, the masses and inertias of the colliding ships are modelled by using a small number of mass points. The principle of the modelling is presented in Figure 4. The striking ship consists of a modelled bow region and three mass points m_j. Correspondingly, the struck ship consists also of three mass points and a part of the side structure. If the mass of the modelled structure is m_{STR}, the total mass of the ship is obtained as

$$m = \sum_{j=1}^{3} m_j + m_{STR} \tag{3}$$

If one of the mass points is located at the COG of the ships, the distance $k_{zz,j}$ of the other two mass points from COG is evaluated from

$$I_{zz} + \mu_{66} = \sum_{j=1,3} m_j \cdot \left(k^*_{zz,j}\right)^2 + m_{STR} \cdot k^2_{STR} \tag{4}$$

where μ_{66} is the yaw added mass, $k^*_{zz,j}$ is the radius of gyration of the j-th mass element, which also takes into account the yaw added mass; and k_{STR} is the radius of gyration of the modelled structure about the centre of gravity (COG) of the ship. Therefore, the yaw added mass μ_{66} is included by calculating the suitable value for k^*_{ZZj}. Using three mass points enables to model the mass and inertia of the ship with respect to the vertical axis and to control the initial location of the COG. The mass points are constrained to move together with the boundary nodes of the modelled parts of the ship.

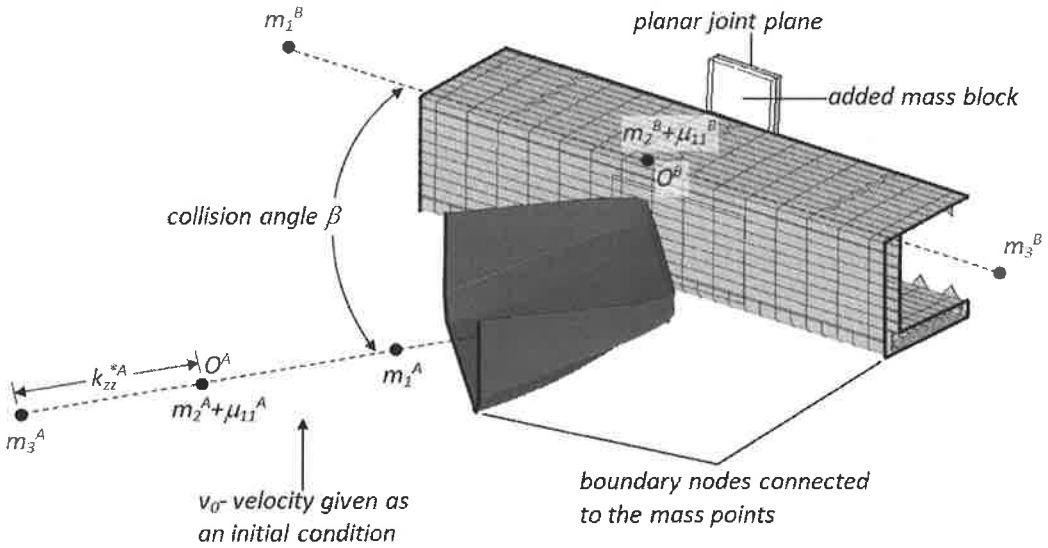

Figure 4. Calculation setup for dynamic collision simulations

As yaw is the only rotational motion component, its added mass is conveniently included by proper positioning of the mass points in the longitudinal direction of the ship. The added mass components associated with translational motions should be included in a certain directions only. The surge added masses of the striking and struck ships are marked as $\mu_{11}{}^A$ and $\mu_{11}{}^B$ in Figure 4. These added masses are positioned in the centres of gravity of the ships. The approach causes the surge added mass of to be included also in the sway direction. In the case of the striking ship the sway added mass is not properly modelled as her motions are predominantly in surge direction. Neglecting the sway added mass of the striking ship results in only minor error in the simulation results.

In the case of the struck ship the sway added mass can not be neglected and it is modelled as a single block of additional mass that is located on the side opposite to the side that is hit, see Figure 4. The mass of the sway added mass block is calculated by subtracting the surge added mass, already added to the node at the COG, from the sway added mass. The sway added mass of the struck ship is connected to a rigid support plate on the ship using a planar joint, which restricts

relative movement in one direction and allows the joined entities to move in the other directions with respect to each other. Therefore it is possible to take added masses into account in one direction only. In the case of surge motions, the sway added mass block remains in its initial position and is not included in the mass of the struck ship.

The side structure included in the FE model is connected through its boundary nodes to the mass points. Thus, any motion of the structure is transmitted to the mass nodes and the whole ship mass is included. Desired collision angle β and eccentricity are achieved by rotating the striking ship to the required angle and moving it to the proper location. The striking ship is given the initial velocity v_0.

The advantage of the dynamic simulations is that they simulate an actual collision event and no prescriptions other than initial conditions are required. The drawback is that the mass-scaling would lead to larger errors compared to displacement controlled simulations and is therefore not suggested. As both ships are moving, the whole contact process lasts longer as it takes longer time for the striking ship to penetrate deep enough into the struck ship to cause breaching of the inner hull. Therefore, the dynamic simulations require significantly longer computational time.

4. A CASE STUDY: COLLISIONS BETWEEN TWO RIVER TANKERS

4.1 Ship models and collision scenarios

As a case study six collisions between two river tankers are simulated. Both ships have the same mass of 2771 tons and the length of the ships is 110 m. The striking ship has a rather rectangular bow shape as seen from Figures 1 and 4. The struck ship has longitudinally stiffened double-hull with web-frame spacing of 1.65 m and the spacing of the corrugated bulkheads is 8.26 m, see Figures 5 and 6. The main dimensions are the same for both the striking and the struck ship and these are presented in Table 1.

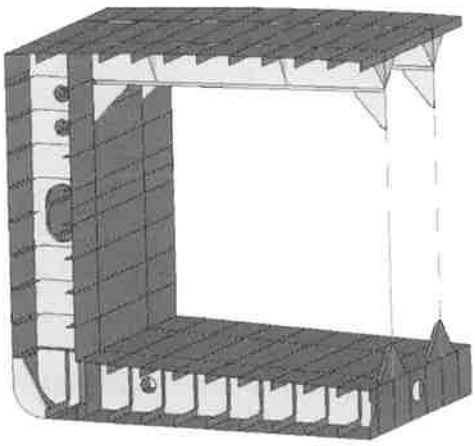

Figure 5. Side structure of a river tanker

The FE models of the striking bow and the side structure are the same for displacement controlled and dynamic simulations. While the bow structure is modelled as a rigid body, the side structure is allowed to undergo large deformations. Ships are assumed to be made of shipbuilding steel with yield strength of 284 MPa. Strain-rate sensitivity of the steel material is not considered. Length of the modelled side structure is 24.75 m, which is sufficient for the plastic deformations

not to occur at the boundaries. The fracturing of the structures is described by thru thickness failure criteria, which background and implementation is explained in Zhang et al (2004), Scharrer et al (2002) and Ehlers et al (2008). The thru thickness strain criterion in LS-DYNA erases an element if the through thickness strain reaches its critical limit. This approach requires rather fine mesh and therefore, in the contact area the prevailing element dimension is 30 x 30 mm. The inner hull is considered to be breached when at least four elements of the inner plating are erased.

Table 1. Main dimensions of the ships

Length, L	110	[m]
Beam, B	11.4	[m]
Draft, T	2.4	[m]
Displacement, Δ	2771	[ton]
Inertia with respect to vertical axis, I_{zz}	$2.1 \cdot 10^6$	[ton·m^2]
Surge added mass, μ_{11}	138.5	[ton]
Sway added mass, μ_{22}	593	[ton]
Yaw added mass, μ_{66}	$0.49 \cdot 10^6$	[ton·m^2]

Collisions to three different longitudinal locations along the side of the struck ship as depicted in Figure 6 are studied. Location 1 has eccentricity L_C of 4.5 m, location 2 has 8.6 m and location 3 has 28.9 m towards the aft of the midship section of the struck ship. In location 1 the contact point is exactly at the bulkhead while in other two locations it is between the bulkheads at web frame. The striking ship is at β=135 deg angle with respect to the struck ship. The collision velocity is either 3.5 or 5 m/s, except for location 1 where only 5 m/s is studied. In the displacement controlled simulations the striking ship is travelling at constant velocity of 5 m/s. The collision scenarios are summarized in Table 2, where also the initial kinetic energy E_0^A of the striking ship is presented.

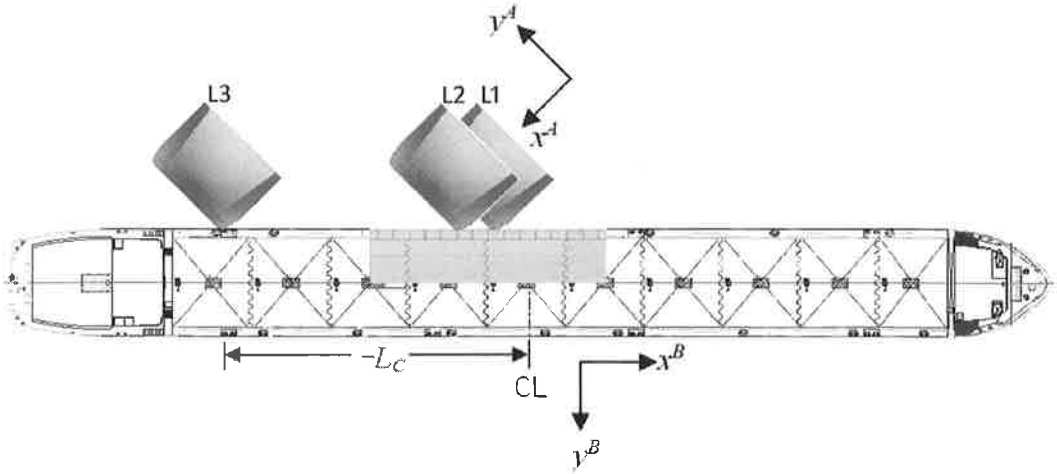

Figure 6. General arrangement of the struck ship and the collision locations.

Table 2. Collision scenarios

Location	v_0=3.5 m/s, β=135 deg		v_0=5 m/s, β=135 deg	
	L_C	E_0^A [MJ]*	L_C	E_0^A [MJ]
L1	-	-	-4.5	34.6
L2	-8.6	17.0	-8.6	34.6
L3	-28.9	17.0	-28.9	34.6

* E_0^A - initial kinetic energy of the striking ship without considering its added mass

4.2 Comparison between dynamic and displacement controlled simulations

Two approaches are compared by looking at the deformation energy at the time instant when the inner hull of the struck ship is breached. We refer to this energy as critical breaching energy. The time-histories of the deformation energies evaluated with the different approaches are presented in Figures 7 and 8. The energies are plotted until the critical breaching energy, which are also presented in Table 3 for different collision scenarios. The increase or decrease of critical breaching energy in the dynamic simulations with respect to that in displacement controlled simulations is presented in percentages.

Table 3. Critical breaching energy and its difference with respect to displacement controlled simulations as a function of collision position and velocity.

Loc.\Vel.	v=const=**5 m/s*** energy /diff. [MJ]/[%]	v_0=**3.5 m/s** energy /diff. [MJ]/[%]	v_0=**5 m/s** energy /diff. [MJ]/[%]
L1	2.88/-	-	3.16/9.9
L2	4.27/-	4.10/-4.0	4.70/9.9
L3	4.27/-	4.00**	4.75/11.1

*- displacement controlled calculation

**- inner hull not breached, but the penetration between the ships is already decreasing

The collisions with v_0=5 m/s are obviously more critical because of large initial kinetic energy of the striking ship. The inner hull of the struck ship is breached in all three scenarios. In dynamic simulations the critical breaching energy is about 10% higher compared to the displacement controlled simulations as revealed in Figure 7. The differences in the energy arise as the penetrations path of the striking ship becomes different due to the coupling of the ship motions and the contact force. Mainly due to the yawing of the ships the actual penetration path is different from the direction of the initial velocity as assumed the in displacement controlled simulations. Thus, the deformation is distributed to larger region and the energy absorption becomes higher.

Contrary, in the collisions with v_0=3.5 m/s the critical breaching energy in location 2 becomes 4% smaller in dynamic simulations, see Figure 8a. Even though the striking ship follows a slightly longer penetration path compared to the displacement controlled simulations, it heavily compresses the web frame causing it to fail faster compared to any other simulations.

In location 3 the inner hull of the struck ship is not breached. The striking ship penetrated until the inner hull, after which the velocity of the struck ship became roughly equal to that of the striking ship and the penetration in transverse direction with respect to the struck ship ceased to increase. The deformation energy still keeps on increasing to some extent as the side structure is still deformed during the separation of the ships. Even though the side structure has already absorbed more than 90% of the critical breaching energy obtained with the displacement controlled simulation, the inner hull is still far from being breached.

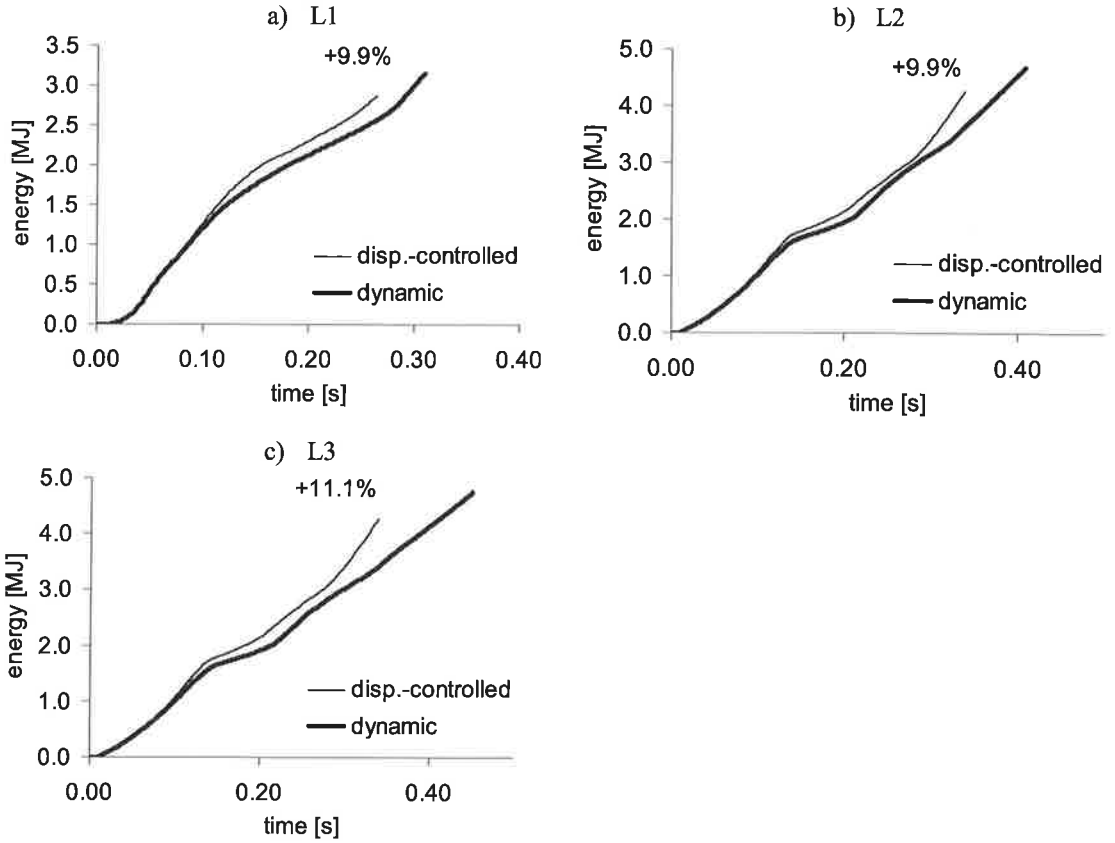

Figure 7. Energy absorption in the case of v_0=5 m/s

Energy plots also reveal that in dynamic simulations it takes longer time to reach the same energy level and to breach the inner hull. It is expected as the penetration and thus also the deformation energy increases less in the case of the decelerating striking ship and accelerating struck ship. In turn, this results in longer simulation runs.

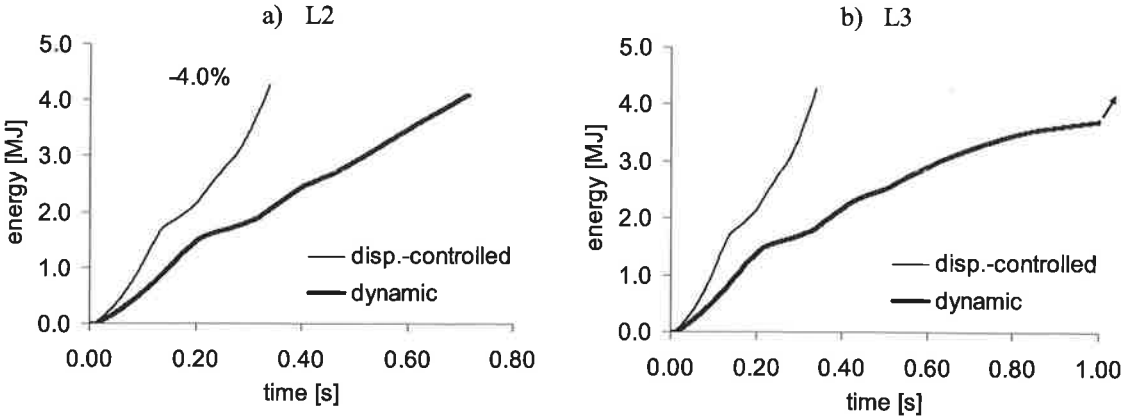

Figure 8. Energy absorption in the case of v_0=3.5 m/s

5. CONCLUSIONS

The paper compared two different approaches for ship collision simulations with FE method. In the displacement controlled method, the struck ship is kept motionless and the striking ship penetrates it along the direction of its initial velocity. The dynamic simulations consider the actual ship motions in collision and thus, the collision is described more accurately. The energy required to breach the inner hull of the struck ship was evaluated with both methods and compared.

In all the dynamic simulations the yaw motion of both ships were excited and the penetration paths became different from those of displacement controlled simulations. Thus, different portion of the side structure of the struck ship was engaged in energy absorption and the deformation energy became different. The difference in energy between the two approaches ranged from -4% to 11%. The exact difference to displacement controlled simulations depends on many aspects such as the masses of the ships, collision velocity, location, angle etc. In some cases, as in the collision at 3.5 m/s to location 2 for example, the structures can be deformed in an unfavourable way and the energy could become smaller despite the longer penetration path.

The dynamic simulations allow more precise analysis of collisions. The collision process itself last for a longer time because of physically correct collision dynamics. Also the increase of calculation time step based on mass scaling is not suggested as it would add artificial inertia to the system. Therefore, the dynamic simulations take significantly longer time, depending on the actual collision scenario the difference in simulation time could be 5-10 times.

It is expected that the structures with higher collision resistance and larger differences in ship masses could lead to a bigger scatter between the predictions of these two approaches. The same applies for the scenarios where the collision angle, structural solution and the shape of the bow region of the striking ship favours the sliding between the ships. The study on these aspects is left for future work.

6. ACKNOWLEDGEMENTS

This work has been performed in the scope of the project MARSTRUCT, Network of Excellence on Marine Structures (www.mar.ist.utl.pt/marstruct/), which has been financed by the European commission. This help is here kindly appreciated.

7. REFERENCES

Cummins, W.E., 1962. The Impulse Response Function and Ship Motions, Schifftechnik 9, No 47, pp.101-109.

Ehlers, S., Broekhuijsen, J., Alsos, H.S., Biehl, F., Tabri, K, 2008. Simulating the collision response of ship side structures: A failure criteria benchmark study. Int Ship Progress, vol. 55; pp.127-144.

Hallquist, J.O., 2007. LS-DYNA. Keyword User's Manual, Version 971. Livermore Software Technology Corporation.

Journée, J.M.J., 1992, Strip theory algorithms. Delft University of Technology; Report MEMT 24.

Kitamura, O., 2002. FEM approach to the simulation of collision and grounding damage, Marine Structures 15, pp 403-428

Lützen, M., 2001. Ship Collision Damage. Ph.D. Thesis, Technical University of Denmark.

Matusiak, J., 2001. Importance of memory effect for ship capsizing prediction. In: Proceedings of 5th International Workshop on Ship Stability, Trieste.

Ogilvie, T.F., 1964. Recent Progress Towards the Understanding and Prediction of Ship Motions, Fifth Symposium on Naval Hydrodynamics, Bergen, Norway, pp.3-128.

Pedersen, P.T., Zhang, S., 1998. On Impact Mechanics in Ship Collisions. Journal of Marine Structures, 1998. Vol. 11, pp. 429-449.

Pill, I. Tabri, K., 2009. Finite element simulations of ship collisions: A coupled approach to external dynamics and inner mechanics. In: Proceedings of MARSTRUCT 2009, The 2nd International Conference on Marine Structures, Lisbon, Portugal, 16-18 March 2009, pp. 103-109.

Scharrer, M., Zhang, L., Egge, E.D., 2002. Final report MTK0614, Collision calculations in naval design systems, Report Nr. ESS 2002.183, Version 1/2002-11-22, Germanischer Lloyd, Hamburg, p. 61.

Tabri, K., Määttänen, J., Ranta, J., 2008. Model-scale experiments of symmetric ship collisions, J Mar Sci Technol 13:71-84

Tabri, K., Varsta, P., Matusiak, J., 2009. Numerical and experimental motion simulations of non-symmetric ship collisions, Journal of Marine Science and Technology, accepted for publishing.

Tuovinen, J., 2005. Statistical Analysis of Ship Collisions. Master's Thesis, Helsinki University of Technology. p. 93.

Zhang, L., Egge, E.D., Bruhns, H., 2004. Approval Procedure Concept for Alternative Arrangements, Proceedings of the 3rd International Conference on Collision and Grounding of Ships (ICCGS), IZU, Japan, , pp. 87-96.

EPÄKONFORMINEN ELEMENTTIMENETELMÄ BRINKMANIN TEHTÄVÄLLE

JUHO KÖNNÖ JA ROLF STENBERG

Matematiikan ja systeemianalyysin laitos
Teknillinen korkeakoulu
PL 1100
02015 TKK
e-mail: juho.konno@tkk.fi

TIIVISTELMÄ

Brinkmanin tehtävä on parametririippuvainen tehtävä, jossa yhdistyvät sekä Darcyn että Stokesin tehtävät. Brinkmanin mallilla kuvataan viskoosin nesteen liikettä huokoisessa aineessa, tyypillisenä esimerkkinä maaperässä olevan öljyn mallintaminen. Esittelemme yhtälöille Darcyn tehtävälle kehitettyihin erikoiselementteihin perustuvan elementtimenetelmän, jota voidaan soveltaa kaikilla viskositeettiparametrin arvoilla. Oleellisena osana menetelmää on paineen jälkikäsittely, jonka avulla tehtävälle voidaan johtaa hyvin käyttäytyvä a posteriori -virhearvio.

1. JOHDANTO

Brinkmanin yhtälöllä kuvataan nesteen virtausta huokoisessa aineessa, jonka porositeetti on suuri. Tällöin myös nesteen viskositeetilla on vaikutusta virtaukseen. Tyypillisiä mallinnettavia aineita ovat esimerkiksi hiekka, erittäin huokoiset kivet sekä lämpöputkissa käytettävät metallihilat. Usein Brinkmanin mallia käytetään myös rajakerroksena huokoisen virtauksen ja vapaan nestevirtauksen välillä.

Artikkelissa tarkastellaan $H(\mathrm{div})$-konformisten elementtimenetelmien sovellusta Brinkmanin ongelmaan, joka johtaa epäkonformiseen elementtiapproksimaatioon. Konformisia menetelmiä Brinkamanin tehtävälle on käsitelty viitteessä [4]. Stabiilisuuden saavuttamiseksi käytämme Nitschen menetelmää [7, 3], jolloin bilineaarimuodosta tulee verkkoriippuva. $H(\mathrm{div})$-konformiset elementit ovat hyvin yleisiä teollisuussovelluksissa ratkaistaessa Darcyn yhtälöä, sillä niillä saavutetaan lokaali massan säilyvyys. Tavoitteena artikkelissa on laajentaa näiden elementtien käyttöaluetta Brinkmanin tehtävään.

2. BRINKMANIN MALLI

Merkitsemme $\boldsymbol{u}$:lla nesteen nopeuskenttää, p:llä huokoispainetta ja tarkastelemme aluetta $\Omega \subset \mathbb{R}^n$, missä $n = 2, 3$. Merkitsemällä nesteen efektiivistä viskositeettia parametrilla $t \geq 0$ Brinkmanin yhtälöt voidaan kirjoittaa muotoon [1, 5]

$$-t^2\Delta \boldsymbol{u} + \boldsymbol{u} - \nabla p = \boldsymbol{f}, \quad \Omega\text{: ssa}, \tag{1}$$
$$\operatorname{div} \boldsymbol{u} = g, \quad \Omega\text{: ssa}. \tag{2}$$

Kun $t > 0$, yhtälöt ovat rakenteeltaan samankaltaiset Stokesin ongelman kanssa ja vastaavat ratkaisuavaruudet ovat $(\boldsymbol{u}, p) \in \boldsymbol{V} \times Q = [H^1(\Omega)]^n \times L^2(\Omega)$. Parametrin arvolla $t = 0$ tehtävä palautuu Darcyn tehtäväksi, jolle ratkaisuavaruus on $\boldsymbol{V} \times Q = H(\operatorname{div}, \Omega) \times L^2(\Omega)$.

Määrittelemme seuraavat bilineaarimuodot

$$a(\boldsymbol{u}, \boldsymbol{v}) = t^2(\nabla \boldsymbol{u}, \nabla \boldsymbol{v}) + (\boldsymbol{u}, \boldsymbol{v}), \tag{3}$$
$$b(\boldsymbol{v}, p) = (\operatorname{div} \boldsymbol{v}, p) \tag{4}$$

ja

$$\mathcal{B}(\boldsymbol{u}, p; \boldsymbol{v}, q) = a(\boldsymbol{u}, \boldsymbol{v}) + b(\boldsymbol{v}, p) + b(\boldsymbol{u}, q). \tag{5}$$

Brinkmanin ongelman heikko muoto voidaan täten kirjoittaa: Etsi $(\boldsymbol{u}, p) \in \boldsymbol{V} \times Q$ jotka toteuttavat

$$\mathcal{B}(\boldsymbol{u}, p; \boldsymbol{v}, q) = (\boldsymbol{f}, \boldsymbol{v}) + (g, q), \quad \forall (\boldsymbol{v}, q) \in \boldsymbol{V} \times Q. \tag{6}$$

3. DISKRETAATIO ELEMENTTIMENETELMÄLLÄ

Verkkoriippuvat normit

Käytämme ongelman analysointiin seuraavia verkkoriippuvia normeja, jotka riippuvat myös parametristä t. Merkitsemme $\mathcal{K}_h$:lla alueen Ω kvasisäännöllistä kolmiointia, ja $\mathcal{E}_h$:lla kaikkien reunojen joukkoa. Funktion f hyppy kahden elementin K_1 ja K_2 reunalla E on $[\![f]\!] = f|_{K_1} - f|_{K_2}$, missä $E = \partial K_1 \bigcap \partial K_2$. Keskiarvo elementin reunalla on $\{f\} = \frac{1}{2}(f|_{K_1} + f|_{K_2})$. Nopeuskentän normi on

$$\|\boldsymbol{u}\|_{t,h}^2 = \|\boldsymbol{u}\|^2 + t^2 \left(\sum_{K \in \mathcal{K}_h} \|\nabla \boldsymbol{u}\|_{0,K}^2 + \sum_{E \in \mathcal{E}_h} \frac{1}{h_E} \|[\![\boldsymbol{u} \cdot \boldsymbol{\tau}]\!]\|_{0,E}^2 \right), \tag{7}$$

ja painekentän

$$|||p|||_{t,h}^2 = \sum_{K \in \mathcal{K}_h} \frac{h_K^2}{h_K^2 + t^2} \|\nabla p\|_{0,K}^2 + \sum_{E \in \mathcal{E}_h} \frac{h_E}{h_E^2 + t^2} \|[\![p]\!]\|_{0,E}^2. \tag{8}$$

Sekaelementtimenetelmä

Diskretaatioon käytetään joko Raviart-Thomas (RT) tai Brezzi-Douglas-Marini (BDM) elementtiavaruuksia. Stabiilisuustulosten todistamiseksi riittää tutkia ainoastaan RT tapausta, sillä $\boldsymbol{V}_h^{RT} \subset \boldsymbol{V}_h^{BDM}$ and $Q_h^{BDM} = Q_h^{RT}$. Approksimaatioavaruudet astetta k ovat [2]

$$\boldsymbol{V}_h^{RT} = \{\boldsymbol{v} \in H(\operatorname{div}, \Omega) \mid \boldsymbol{v}|_K \in [P_{k-1}(K)]^n \oplus \boldsymbol{x}\tilde{P}_{k-1}(K)\ \forall K \in \mathcal{K}_h\}, \tag{9}$$
$$\boldsymbol{V}_h^{BDM} = \{\boldsymbol{v} \in H(\operatorname{div}, \Omega) \mid \boldsymbol{v}|_K \in [P_k(K)]^n\ \forall K \in \mathcal{K}_h\}, \tag{10}$$
$$Q_h = \{q \in L^2(\Omega) \mid q|_K \in P_{k-1}(K)\ \forall K \in \mathcal{K}_h\}, \tag{11}$$

missä $\tilde{P}_{k-1}(K)$ ovat asteen $k-1$ homogeenipolynomit. Avaruudet on valittu siten, että seuraava tasapainotulos pätee:

$$\operatorname{div} \boldsymbol{V}_h \subset Q_h. \tag{12}$$

Jotta menetelmästä saataisiin stabiili, täytyy vapausasteet liimata kiinni tangentin suunnassa, sillä avaruus on luonnollisesti jatkuva ainoastaan normaalisuunnassa elementtien rajapinnoilla. Tähän käytetään Nitschen menetelmää, jossa α on sopivasti valittu stabilointiparametri [9, 7]. Määrittelemme seuraavan verkkoriippuvan bilineaarimuodon

$$\mathcal{B}_h(\boldsymbol{u}, p; \boldsymbol{v}, q) = a_h(\boldsymbol{u}, \boldsymbol{v}) + b(\boldsymbol{v}, p) + b(\boldsymbol{u}, q), \tag{13}$$

missä

$$a_h(\boldsymbol{u}, \boldsymbol{v}) = (\boldsymbol{u}, \boldsymbol{v}) + t^2 \Bigg[\sum_{K \in \mathcal{K}_h} (\nabla \boldsymbol{u}, \nabla \boldsymbol{v})_K + \sum_{E \in \mathcal{E}_h} \{ \frac{\alpha}{h_E} \langle [\![\boldsymbol{u}]\!], [\![\boldsymbol{v}]\!] \rangle_E - \langle \{ \frac{\partial \boldsymbol{u}}{\partial n} \}, [\![\boldsymbol{v}]\!] \rangle_E - \langle \{ \frac{\partial \boldsymbol{v}}{\partial n} \}, [\![\boldsymbol{u}]\!] \rangle_E \} \Bigg]. \tag{14}$$

Ongelman diskreetti formulaatio on täten: Etsi $\boldsymbol{u}_h \in \boldsymbol{V}_h$ ja $p_h \in Q_h$ siten, että

$$\mathcal{B}_h(\boldsymbol{u}_h, p_h; \boldsymbol{v}, q) = (\boldsymbol{f}, \boldsymbol{v}) + (g, q), \quad \forall (\boldsymbol{v}, q) \in \boldsymbol{V}_h \times Q_h. \tag{15}$$

Voidaan todistaa seuraava lause joka näyttää menetelmän konsistentiksi:

Lause 1. *Tarkalle ratkaisulle* $(\boldsymbol{u}, p) \in \boldsymbol{V} \times Q$ *pätee*

$$\mathcal{B}_h(\boldsymbol{u}, p; \boldsymbol{v}, q) = (\boldsymbol{f}, \boldsymbol{v}) + (g, q), \quad \forall (\boldsymbol{v}, q) \in \boldsymbol{V}_h \times Q_h. \tag{16}$$

Seuraavaksi osoitamme, että bilineaarimuoto $a_h(\cdot\,,\cdot)$ on stabiili verkkoriippuvassa normissa (7). Stabiiliustulos pätee ainoastaan diskreetissä avaruudessa $\boldsymbol{V}_h$, sillä todistuksessa tarvitaan käänteisepäyhtälöä. Estimoimalla allaolevan lausekkeen negatiivista termiä käyttäen Youngin epäyhtälöä, saamme tuloksen

$$a_h(\boldsymbol{v}, \boldsymbol{v}) = \|\boldsymbol{v}\|_0^2 + t^2 \sum_{K \in \mathcal{K}_h} \|\nabla \boldsymbol{v}\|_{0,E}^2 + t^2 \sum_{E \in \mathcal{E}_h} (\frac{\alpha}{h_E} \|[\![\boldsymbol{v}]\!]\|_{0,E}^2 - 2 \langle \frac{\partial \boldsymbol{v}}{\partial n}, [\![\boldsymbol{v}]\!] \rangle_E) \geq \min\{1 - \frac{C_I}{2\epsilon}, \alpha - \frac{\epsilon}{2}\} \|\boldsymbol{v}\|_{t,h}^2. \tag{17}$$

C_I on käänteisepäyhtälön vakio, ja ϵ sekä α ovat vapaita positiivisia parametreja. Valitsemalla $\epsilon > C_I/2$ ja $\alpha > \epsilon/2$ saadaan tulos

$$a_h(\boldsymbol{v}, \boldsymbol{v}) \geq \|\boldsymbol{v}\|_{t,h}^2, \quad \forall \boldsymbol{v} \in \boldsymbol{V}_h. \tag{18}$$

Menetelmä lisäksi toteuttaa diskreetin Brezzi-Babuska stabiilisuusehdon [2]. Todistus on perusrakenteeltaan samankaltainen kuin Darcyn tehtävälle esitetty vastaava tulos viitteessä [6].

Lemma 2. *Jollekin positiiviselle vakiolle* C *pätee*

$$\sup_{\boldsymbol{v} \in \boldsymbol{V}_h} \frac{b(\boldsymbol{v}, q)}{\|\boldsymbol{v}\|_{t,h}} \geq C |\!|\!| q |\!|\!|_{t,h}, \quad \forall q \in Q_h. \tag{19}$$

Yhdistämällä ylläolevat stabiiliustulokset $a_h(\cdot\,,\cdot\,)$:lle ja $b(\cdot\,,\cdot\,)$:lle saadaan seuraava stabiiliustulos koko tehtävälle:

Lemma 3. *Jollekin positiiviselle vakiolle C pätee*

$$\sup_{(\boldsymbol{v},q)\in \boldsymbol{V}_h\times Q_h} \frac{\mathcal{B}_h(\boldsymbol{r},s;\boldsymbol{v},q)}{\|\boldsymbol{v}\|_{t,h}+|||q|||_{t,h}} \geq C(\|\boldsymbol{r}\|_{t,h}+|||s|||_{t,h}), \quad \forall(\boldsymbol{r},s)\in \boldsymbol{V}_h\times Q_h. \tag{20}$$

Lisäksi tarvitsemme erityistä interpolaatio-operaattoria $\boldsymbol{R}_h : H(\mathrm{div},\Omega)\to \boldsymbol{V}_h$ [8, 2], joka toteuttaa

$$(\mathrm{div}\,(\boldsymbol{v}-\boldsymbol{R}_h\boldsymbol{v}),q)=0, \quad \forall q\in Q_h. \tag{21}$$

Olkoon $P_h : L^2(\Omega)\to Q_h$ standardi L^2-projektio. Tasapaino-ominaisuudesta (12) seuraa

$$(\mathrm{div}\,\boldsymbol{v}, q-P_hq)=0, \quad \forall \boldsymbol{v}\in \boldsymbol{V}_h. \tag{22}$$

Lisäksi interpolantti toteuttaa seuraavan kommutaatiodiagrammin:

$$\mathrm{div}\,\boldsymbol{R}_h = P_h\mathrm{div}. \tag{23}$$

Näiden työkalujen avulla voimme todistaa seuraavan konvergenssituloksen.

Lause 4. *Löytyy positiivinen vakio C jolle pätee*

$$\|\boldsymbol{u}-\boldsymbol{u}_h\|_{t,h}+|||P_hp-p_h|||_{t,h}\leq C\|\boldsymbol{u}-\boldsymbol{R}_h\boldsymbol{u}\|_{t,h}. \tag{24}$$

Todistus. Lemman 3 perusteella löytyy funktiot $(\boldsymbol{v},q)\in \boldsymbol{V}_h\times Q_h$ joille $\|\boldsymbol{v}\|_{t,h}+|||q|||_{t,h}\leq C$ siten, että

$$\begin{aligned}\|\boldsymbol{u}_h-\boldsymbol{R}_h\boldsymbol{u}\|_{t,h}+|||p_h-P_hp|||_{t,h} &\leq \mathcal{B}_h(\boldsymbol{u}_h-\boldsymbol{R}_h\boldsymbol{u},p_h-P_hp;\boldsymbol{v},q)\\ &= a_h(\boldsymbol{u}_h-\boldsymbol{R}_h\boldsymbol{u},\boldsymbol{v})+(\mathrm{div}\,\boldsymbol{v},p_h-P_hp)+(\mathrm{div}\,(\boldsymbol{u}_h-\boldsymbol{R}_h\boldsymbol{u}),q)\end{aligned} \tag{25}$$

Käyttämällä interpolantin ominaisuuksia (21) ja (22) sekä Lauseen 1 konsistenssitulosta, pätee

$$\|\boldsymbol{u}_h-\boldsymbol{R}_h\boldsymbol{u}\|_{t,h}+|||p_h-P_hp|||_{t,h}\leq a_h(\boldsymbol{u}-\boldsymbol{R}_h\boldsymbol{u},\boldsymbol{v})\leq C\|\boldsymbol{u}-\boldsymbol{R}_h\boldsymbol{u}\|_{t,h} \tag{26}$$

Lauseen tulos seuraa soveltamalla kolmioepäyhtälöä. □

Samoin kuin Darcyn tehtävälle, saadaan paineen virheelle $|||p_h-P_hp|||_{t,h}$ superkonvergenssitulos, jolloin paineratkaisua voidaan parantaa jälkikäsittelyllä. Mikäli oletetaan riittävä sileys tehtävälle, pätee

$$\|\boldsymbol{u}-\boldsymbol{u}_h\|_{t,h}+|||P_hp-p_h|||_{t,h}\leq \begin{cases} C(h^k+th^{k-1})\|\boldsymbol{u}\|_k, & \text{for RT},\\ C(h^{k+1}+th^k)\|\boldsymbol{u}\|_{k+1}, & \text{for BDM}.\end{cases} \tag{27}$$

4. JÄLKIKÄSITTELY PAINEELLE

Painekentän superkonvergenssituloksesta sekä virtauskentän hyvistä approksimaatio-ominaisuuksista johtuen voimme suorittaa paineelle jälkikäsittelyn elementeittäin mukaillen viitteessä [6] esitettyä

tekniikkaa Darcyn tehtävälle. Paineen approksimaatioavaruudeksi valitaan jälkikäsittelyssä $Q_h^* \supset Q_h$, joka määritellään seuraavasti.

$$Q_h^* = \begin{cases} \{q \in L^2(\Omega) \mid q|_K \in P_k(K)\ \forall K \in \mathcal{K}_h\}, & \text{RT elementeille,} \\ \{q \in L^2(\Omega) \mid q|_K \in P_{k+1}(K)\ \forall K \in \mathcal{K}_h\}, & \text{BDM elementeille.} \end{cases} \tag{28}$$

Jälkikäsittely määritellään seuraavien ehtojen avulla: Etsi $p_h^* \in Q_h^*$ joka toteuttaa

$$P_h p_h^* = p_h \tag{29}$$

$$(\nabla p_h^*, \nabla q)_K = (-t^2 \Delta \boldsymbol{u}_h + \boldsymbol{u}_h - \boldsymbol{f}, \nabla q)_K, \quad \forall q \in (I - P_h) Q_h^*|_K. \tag{30}$$

Jälkikäsittelymenettely voidaan upottaa osaksi koko tehtävän ratkaisua teoreettista tarkastelua varten. Määrittelemällä modifioitu bilineaarimuoto

$$\tilde{\mathcal{B}}_h(\boldsymbol{u}, p^*; \boldsymbol{v}, q^*) = \mathcal{B}_h(\boldsymbol{u}, p^*; \boldsymbol{v}, q^*) + \sum_{K \in \mathcal{K}_h} \frac{h_K^2}{h_K^2 + t^2} (-\nabla p^* + \boldsymbol{u} - t^2 \Delta \boldsymbol{u}, \nabla (I - P_h) q^*)_K \tag{31}$$

jälkikäsittelyn sisältävä tehtävä voidaan kirjoittaa muotoon: Etsi $(\boldsymbol{u}_h, p_h^*) \in \boldsymbol{V}_h \times Q_h^*$ siten, että jokaiselle $(\boldsymbol{v}, q^*) \in \boldsymbol{V}_h \times Q_h^*$ pätee

$$\tilde{\mathcal{B}}_h(\boldsymbol{u}_h, p_h^*; \boldsymbol{v}, q^*) = \mathcal{L}_h(\boldsymbol{f}, P_h g; \boldsymbol{v}, q^*), \tag{32}$$

missä

$$\mathcal{L}_h(\boldsymbol{f}, g; \boldsymbol{v}, q^*) = (\boldsymbol{f}, \boldsymbol{v}) + (g, q^*) + \sum_{K \in \mathcal{K}_h} \frac{h_K^2}{h_K^2 + t^2} (\boldsymbol{f}, \nabla (I - P_h) q^*)_K \tag{33}$$

Voimme todistaa seuraavan lauseen, joka kytkee alkuperäisen ja jälkikäsitellyn tehtävän toisiinsa.

Lause 5. *Olkoon $(\boldsymbol{u}_h, p_h^*) \in \boldsymbol{V}_h \times Q_h^*$ jälkikäsitellyn tehtävän* (32) *ratkaisu. Asettamalla $p_h = P_h p_h^*$ on $(\boldsymbol{u}_h, p_h) \in \boldsymbol{V}_h \times Q_h$ alkuperäisen tehtävän* (15) *ratkaisu. Toisaalta jos $(\boldsymbol{u}_h, p_h) \in \boldsymbol{V}_h \times Q_h$ on alkuperäisen ongelman* (15) *ratkaisu ja p_h^* on määritelty kuten yllä, on $(\boldsymbol{u}_h, p_h^*) \in \boldsymbol{V}_h \times Q_h^*$ ratkaisu tehtävään* (32).

Jälkikäsittelyn sisältävä bilineaarimuoto on lisäksi stabiili verkkoriippuvissa normeissa.

Lause 6. *Jollekin positiiviselle vakiolla $C > 0$ pätee kaikilla $(\boldsymbol{u}, p^*) \in \boldsymbol{V}_h \times Q_h^*$*

$$\sup_{(\boldsymbol{v}, q^*) \in \boldsymbol{V}_h \times Q_h^*} \frac{\tilde{\mathcal{B}}_h(\boldsymbol{u}, p^*; \boldsymbol{v}, q^*)}{\|\boldsymbol{v}\|_{t,h} + |||q^*|||_{t,h}} \geq C(\|\boldsymbol{u}\|_{t,h} + |||p^*|||_{t,h}). \tag{34}$$

Tämä antaa seuraavan a priori -tuloksen:

Lause 7. *Jälkikäsitellylle ratkaisulle pätee*

$$\begin{aligned} \|\boldsymbol{u} - \boldsymbol{u}_h\|_{t,h} + |||p - p_h|||_{t,h} \leq C \inf_{q^* \in Q_h^*} \{ & \|\boldsymbol{u} - R_h \boldsymbol{u}\|_{t,h} + |||p - q^*|||_{t,h} \\ & + \Big(\sum_{K \in \mathcal{K}_h} \frac{h_K^2}{h_K^2 + t^2} \| - \nabla q^* + R_h \boldsymbol{u} - t^2 \Delta R_h \boldsymbol{u} - \boldsymbol{f} \|_{0,K}^2 \Big)^{1/2} \} \end{aligned} \tag{35}$$

Todistus. Olkoon $q^* \in Q_h^*$. Lauseen 6 perusteella löytyy funktiot $(\boldsymbol{v}, r^*) \in \boldsymbol{V}_h \times Q_h^*$ joille $\|\boldsymbol{v}\|_{t,h} + |||r^*|||_{t,h} \leq C$ ja

$$\|\boldsymbol{u}_h - R_h\boldsymbol{u}\|_{t,h} + |||p_h^* - q^*|||_{t,h} \leq C\tilde{\mathcal{B}}_h(\boldsymbol{u}_h - R_h\boldsymbol{u}, p_h^* - q^*; \boldsymbol{v}, r^*)$$

Käyttämällä jälkikäsittelyn määritelmää sekä Lauseen 1 konsistenssiominaisuutta, saadaan tulos

$$\begin{aligned}\|\boldsymbol{u}_h - R_h\boldsymbol{u}\|_{t,h} + |||p_h^* - q^*|||_{t,h} &\leq C\tilde{\mathcal{B}}_h(\boldsymbol{u} - R_h\boldsymbol{u}, p - q^*; \boldsymbol{v}, r^*) - (g - P_h g, r^*) \\ &= a_h(\boldsymbol{u} - R_h\boldsymbol{u}, \boldsymbol{v}) + (\operatorname{div} \boldsymbol{v}, p - q^*) + (\operatorname{div}(\boldsymbol{u} - R_h\boldsymbol{u}), r^*) - (g - P_h g, r^*) \\ &\quad \sum_{K \in \mathcal{K}_h} \frac{h_K^2}{h_K^2 + t^2}(-\nabla(p - q^*) + (\boldsymbol{u} - R_h\boldsymbol{u}) + -t^2\Delta(\boldsymbol{u} - R_h\boldsymbol{u}), \nabla(I - P_h)r^*)_K\end{aligned}$$

Toisen rivin viimeiset termit kumoavat toisensa kommutaatiominaisuuden (23) perusteella. Sijoittamalla $\boldsymbol{f}$ viimeiseen lausekkeeseen käyttäen alkuperäisen tehtävän määritelmää saadaan

$$\begin{aligned}\|\boldsymbol{u}_h - R_h\boldsymbol{u}\|_{t,h} + |||p_h^* - q^*|||_{t,h} \leq C\{&\|\boldsymbol{u} - R_h\boldsymbol{u}\|_{t,h}\|\boldsymbol{v}\|_{t,h} + |||p - q^*|||_{t,h}\|\boldsymbol{v}\|_{t,h} \\ &+ (\sum_{K \in \mathcal{K}_h} \frac{h_K^2}{h_K^2 + t^2}\|\nabla q^* - R_h\boldsymbol{u} + t^2\Delta R_h\boldsymbol{u} + \boldsymbol{f}\|_{0,K}^2)^{1/2}|||r^*|||_{t,h}.\end{aligned}$$

□

Lause 7 osoittaa, että jälkikäsitelty paine suppenee kohti tarkkaa ratkaisua optimaalisella nopeudella. Täten epäkonformisella formulaatiolla saavutetaan hyvä tasapaino ratkaisun tarkkuuden ja ratkaistavan systeemin koon välillä. Jälkikäsittely suoritetaan elementeittäin, ja on täten laskennallisesti edullista, vaikka vapausasteiden määrä epäjatkuvalle paineapproksimaatiolle on varsin suuri.

5. YHTEENVETO

Näytimme, että $H(\mathrm{div})$-konformisia elementtejä voidaan käyttää Brinkmanin tehtävän ratkaisuun soveltamalla Nitschen menetelmää. Menetelmä on lisäksi stabiili kaikille viskositeettiparametrin arvoille $t \geq 0$. Lisäksi näytettiin, että Darcyn tehtävälle kehitetty jälkikäsittelymenettely voidaan laajentaa myös Brinkmanin tehtävään. Täten myös paineelle saadaan optimaalinen konvergenssinopeus. Jälkikäsittely on myös ensiarvoisen tärkeää luotettavan residuaalipohjaisen a posteriori indikaattorin löytämiseksi.

Kiitämme tutkimuksen tukemisesta KYT2010-tutkimusohjelmaa, sekä ensimmäinen kirjoittajan osalta Suomen kulttuurirahastoa.

VIITTEET

[1] T. Arbogast and H. L. Lehr. Homogenization of a Darcy-Stokes system modeling vuggy porous media. *Comput. Geosci.*, 10(3):291–302, 2006.

[2] F. Brezzi and M. Fortin. *Mixed and Hybrid Finite Element Methods*. Springer-Verlag, 1991.

[3] P. Hansbo and M Juntunen. Weakly imposed Dirichlet boundary conditions for the Brinkman model of porous media flow. *Applied Numerical Mathematics*, 59(6):1274–1289, 2009.

[4] M Juntunen and R Stenberg. Analysis of finite element methods for the brinkman problem. Research Report A 557, Institute of Mathematics, Helsinki University of Technology., 2009.

[5] T. Lévy. Loi de Darcy ou loi de Brinkman? *C. R. Acad. Sci. Paris Sér. II Méc. Phys. Chim. Sci. Univers Sci. Terre*, 292(12):871–874, Erratum (17):1239, 1981.

[6] Carlo Lovadina and Rolf Stenberg. Energy norm a posteriori error estimates for mixed finite element methods. *Math. Comp.*, 75(256):1659–1674 (electronic), 2006.

[7] J. Nitsche. Über ein Variationsprinzip zur Lösung von Dirichlet-Problemen bei Verwendung von Teilräumen, die keinen Randbedingungen unterworfen sind. *Abh. Math. Sem. Univ. Hamburg*, 36:9–15, 1971. Collection of articles dedicated to Lothar Collatz on his sixtieth birthday.

[8] J. Schöberl. Commuting quasi-interpolation operators for mixed finite elements. Preprint ISC-01-10-MATH, Institute for Scientific Computing, Texas AM University, 2001.

[9] R. Stenberg. On some techniques for approximating boundary conditions in the finite element method. *J. Comput. Appl. Math.*, 63(1-3):139–148, 1995.

A POSTERIORI ERROR ANALYSIS AND ADAPTIVE COMPUTATIONS FOR KIRCHHOFF–LOVE PLATE BENDING ELEMENTS

LOURENÇO BEIRÃO DA VEIGA[1], JARKKO NIIRANEN[2], ROLF STENBERG[3]

[1] Dipartimento di Matematica "Federigo Enriques"
Università degli Studi di Milano
via Saldini 50
20133 Milano, ITALY
e-mail: lourenco.beirao@unimi.it
[2] Department of Structural Engineering and Building Technology
Helsinki University of Technology
P.O. Box 2100
FIN-02015 TKK, FINLAND
e-mail: jarkko.niiranen@tkk.fi
[3] Department of Mathematics and Systems Analysis
Helsinki University of Technology
P.O. Box 1100
FIN-02015 TKK, FINLAND
e-mail: rolf.stenberg@tkk.fi

ABSTRACT

We present and compare the main results of a posteriori error analysis for two finite element methods for the Kirchhoff–Love plate bending model. The first method is the classical nonconforming Morley element which gives a discontinuous approximation for the deflection by second order piecewise polynomial basis functions. The second method is a family of stabilized finite elements which uses C^0-continuous approximations for both the deflection and the rotation, i.e., the same approach as typically used for the Reissner–Mindlin plate elements. For both methods, we present an a posteriori error estimator for adaptive mesh refinements. First, we recall the main results of the theoretical error analysis showing that the esimators are both reliable and efficient. Second, by benchmark computations, we illustrate and compare the robustness of the a posteriori error estimators in various types of problems with different kinds of boundary conditions.

INTRODUCTION

Thin structures can be regarded as the main building blocks in modern structural design. Beside the classical fields as civil engineering, the variety of applications for thin structures have strongly increased in many other fields as well: shells, plates, membranes and beams combined with new functional materials can be used in engineering design of smart electro-mechanical systems. These systems can be applied in different fields of science and technology: aeronautics, biomechanics,

surgical medicine and microelectronics, for instance. Accordingly, there is a need for advanced computer-aided design methodologies and for efficient and reliable computational methods for thin structures.

In this contribution, the focus will be in controlling the discretization error of finite element methods for Kirchhoff–Love plates, which is a key issue in both the theoretical analysis and applications. More precisely, we consider a posteriori error analysis and adaptive solution methods providing a cost efficient automated way to achieve a desired accuracy for approximate solutions. For Kirchhoff–Love plate elements, the variety of a posteriori error analysis is still quite limited [5, 11, 2, 1, 3, 4, 7]. Here we present and compare the main results of a posteriori error analysis for two finite element methods for the Kirchhoff–Love plate model: the classical nonconforming Morley element analyzed in [2, 4] and the stabilized C^0-family of [1, 3].

In the next sections, we first recall the Kirchhoff–Love plate bending model and then present the finite element formulations and a priori error estimates of the methods as well as the a posteriori error indicators and the corresponding reliability and efficiency results. In the final section, we confirm the theoretical results and the robustness of the estimators by benchmark computations.

KIRCHHOFF–LOVE PLATE BENDING PROBLEM

We consider the bending problem of an isotropic linearly elastic plate under the transverse loading g. The midsurface of the undeformed plate is described by a polygonal domain $\Omega \subset \mathbb{R}^2$. The plate is considered to be clamped on the part Γ_{C} of its boundary $\partial\Omega$, simply supported on the part $\Gamma_{\mathrm{S}} \subset \partial\Omega$ and free on $\Gamma_{\mathrm{F}} \subset \partial\Omega$. With $\mathcal{V}$ we indicate the collection of all the corner points in Γ_{F} corresponding to an angle of the free boundary.

Physical quantities and equilibrium equations

The material constants for the model, the bending stiffness and the shear modulus, respectively, are denoted by

$$\mathsf{D} = \frac{\mathsf{E}t^3}{12(1-\nu^2)} \quad \text{and} \quad \mathsf{G} = \frac{\mathsf{E}}{2(1+\nu)}, \tag{1}$$

with the Young modulus E and the Poisson ratio ν. The thickness of the plate is denoted by t. In what follows, we need the following differential operators: The strain tensor ε is defined as the symmetric tensor gradient

$$\varepsilon(\boldsymbol{\eta}) = \big(\nabla\boldsymbol{\eta} + (\nabla\boldsymbol{\eta})^T\big), \quad \nabla\boldsymbol{\eta} = \begin{pmatrix} \partial\eta_x/\partial x & \partial\eta_x/\partial y \\ \partial\eta_y/\partial x & \partial\eta_y/\partial y \end{pmatrix}. \tag{2}$$

The vector gradient ∇ and the vector divergence div are defined as usual, while the tensor divergence is defined as

$$\mathbf{div}\,\boldsymbol{\sigma} = \begin{pmatrix} \partial\sigma_{xx}/\partial x + \partial\sigma_{xy}/\partial y \\ \partial\sigma_{yx}/\partial x + \partial\sigma_{yy}/\partial y \end{pmatrix}. \tag{3}$$

With this notation, the stress resultants of the problem, the bending moment and shear force, respectively, are defined as

$$\boldsymbol{M}(\nabla w) = \mathsf{D}\big((1-\nu)\varepsilon(\nabla w) + \nu\,\mathrm{div}\,\nabla w\boldsymbol{I}\big), \tag{4}$$

$$\boldsymbol{Q}(\nabla w) = -\mathbf{div}\,\boldsymbol{M}(\nabla w), \tag{5}$$

where w denotes the deflection of the plate midsurface. The shear force satisfies the force equilibrium equation

$$-\operatorname{div} \boldsymbol{Q} = g\,. \tag{6}$$

Biharmonic and mixed formulations

Assuming that the loading g is sufficiently regular, the Kirchhoff–Love plate bending problem can be written as the well known biharmonic problem:

$$\mathsf{D}\Delta^2 w = g \qquad \text{in } \Omega\,, \tag{7}$$

with the boundary conditions

$$w = 0\,,\ \nabla w \cdot \boldsymbol{n} = 0 \qquad \text{on } \Gamma_{\mathrm{C}}\,, \tag{8}$$

$$w = 0\,,\ \boldsymbol{M}\boldsymbol{n} \cdot \boldsymbol{n} = 0 \qquad \text{on } \Gamma_{\mathrm{S}}\,, \tag{9}$$

$$\boldsymbol{M}\boldsymbol{n} \cdot \boldsymbol{n} = 0\,,\ \frac{\partial}{\partial \boldsymbol{s}}(\boldsymbol{M}\boldsymbol{n} \cdot \boldsymbol{s}) + (\operatorname{\mathbf{div}} \boldsymbol{M}) \cdot \boldsymbol{n} = 0 \qquad \text{on } \Gamma_{\mathrm{F}}\,, \tag{10}$$

$$(\boldsymbol{M}\boldsymbol{n}_1 \cdot \boldsymbol{s}_1)(c) = (\boldsymbol{M}\boldsymbol{n}_2 \cdot \boldsymbol{s}_2)(c) \qquad \forall c \in \mathcal{V}\,, \tag{11}$$

where $\boldsymbol{n}$ and $\boldsymbol{s}$, respectively, denote the unit outward normal and the unit counterclockwise tangent to the boundary. By the indices 1 and 2 we denote the sides of the boundary angle at a corner point c.

In order to interpret the Kirchhoff–Love model as the limit of the Reissner–Mindlin formulation, it is assumed, as usual, that the loading is scaled as $g = \mathsf{G}t^3 f$ with f fixed. Then the problem (7) becomes independent of the plate thickness:

$$\frac{1}{6(1-\nu)}\Delta^2 w = f \qquad \text{in } \Omega\,. \tag{12}$$

Then the corresponding scaled moment and shear force are defined, respectively, as

$$\boldsymbol{m}(\nabla w) = \frac{\boldsymbol{M}(\nabla w)}{\mathsf{G}t^3} \quad \text{and} \quad \boldsymbol{q}(\nabla w) = \frac{\boldsymbol{Q}(\nabla w)}{\mathsf{G}t^3}\,. \tag{13}$$

In the corresponding mixed formulation, the rotation and the scaled shear force, respectively, are taken as new unknowns:

$$\boldsymbol{\beta} = \nabla w \quad \text{and} \quad \boldsymbol{q} = -\operatorname{\mathbf{div}} \boldsymbol{m} = -\boldsymbol{L}\boldsymbol{\beta}\,, \tag{14}$$

where we have introduced a partial differential operator $\boldsymbol{L}$ by the scaled moment $\boldsymbol{m}$. Now the scaled mixed problem reads:

$$\operatorname{div} \boldsymbol{q} = f \qquad \text{in } \Omega\,, \tag{15}$$

$$\boldsymbol{L}\boldsymbol{\beta} + \boldsymbol{q} = \boldsymbol{0} \qquad \text{in } \Omega\,, \tag{16}$$

$$\nabla w - \boldsymbol{\beta} = \boldsymbol{0} \qquad \text{in } \Omega\,. \tag{17}$$

with the boundary conditions

$$w = 0\,,\ \boldsymbol{\beta} = \boldsymbol{0} \qquad \text{on } \Gamma_{\mathrm{C}}\,, \tag{18}$$

$$w = 0\,,\ \boldsymbol{\beta} \cdot \boldsymbol{s} = 0\,,\ \boldsymbol{m}(\boldsymbol{\beta})\boldsymbol{n} \cdot \boldsymbol{n} = 0 \qquad \text{on } \Gamma_{\mathrm{S}}\,, \tag{19}$$

$$(\nabla w - \boldsymbol{\beta}) \cdot \boldsymbol{s} = 0\,,\ \boldsymbol{m}(\boldsymbol{\beta})\boldsymbol{n} \cdot \boldsymbol{n} = 0\,,\ \frac{\partial}{\partial \boldsymbol{s}}(\boldsymbol{m}(\boldsymbol{\beta})\boldsymbol{n} \cdot \boldsymbol{s}) - \boldsymbol{q} \cdot \boldsymbol{n} = 0 \qquad \text{on } \Gamma_{\mathrm{F}}\,, \tag{20}$$

$$(\boldsymbol{m}(\boldsymbol{\beta})\boldsymbol{n}_1 \cdot \boldsymbol{s}_1)(c) = (\boldsymbol{m}(\boldsymbol{\beta})\boldsymbol{n}_2 \cdot \boldsymbol{s}_2)(c) \qquad \forall c \in \mathcal{V}\,. \tag{21}$$

FINITE ELEMENT FORMULATIONS AND A PRIORI ERROR ESTIMATES

In what follows, let a a regular family of triangulations $\mathcal{T}_h$ on Ω be given. We will indicate with h_K the diameter of each element $K \in \mathcal{T}_h$, while h will indicate the maximum size of all of the elements in the mesh. Furthermore, E denotes a general edge of the triangulation and h_E is the length of E. Next, let $\mathcal{E}_h$ represent the collection of all the edges of the triangulation, let $\mathcal{I}_h$ denote the collection of all the internal edges and let $\mathcal{C}_h$, $\mathcal{S}_h$ and $\mathcal{F}_h$ represent the collections of all the boundary edges in Γ_{C}, Γ_{S} and Γ_{F}, respectively,

Morley element

Let $[\![\cdot]\!]$ denote the jump operator which is assumed to be equal to the function value on boundary edges. The discrete Morley space [10] is introduced as

$$W_h = \left\{ v \in M_{2,h} \;\middle|\; \int_E [\![\nabla v \cdot \boldsymbol{n}_E]\!] = 0 \quad \forall E \in \mathcal{I}_h \cup \mathcal{C}_h \right\}, \tag{22}$$

where $M_{2,h}$ denotes the space of second order piecewise polynomial functions on $\mathcal{T}_h$ which are continuous at the vertices of all the internal triangles and zero at all the vertices of $\Gamma_{\mathrm{C}} \cup \Gamma_{\mathrm{S}}$. Then the finite element approximation of the Kirchhoff–Love problem with the Morley element reads [2]:

Method 1 *Find $w_h \in W_h$ such that*

$$a_h(w_h, v) = (f, v) \quad \forall v \in W_h\,, \tag{23}$$

where the bilinear form a_h is defined as

$$a_h(u, v) = \sum_{K \in \mathcal{T}_h} (\boldsymbol{m}(\nabla u), \boldsymbol{\varepsilon}(\nabla v))_K \quad \forall u, v \in W_h\,. \tag{24}$$

Introducing the discrete norm

$$|||v|||_h^2 := \sum_{K \in \mathcal{T}_h} |v|_{2,K}^2 + \sum_{E \in \mathcal{E}_h} h_E^{-3} \| [\![v]\!] \|_{0,E}^2 + \sum_{E \in \mathcal{E}_h} h_E^{-1} \| [\![\frac{\partial v}{\partial \boldsymbol{n}_E}]\!] \|_{0,E}^2 \tag{25}$$

the following a priori error estimate holds for the method [9]:

Proposition 1 *Let $w \in H^3(\Omega)$ and $f \in L^2(\Omega)$. Then there exists a positive constant C such that*

$$|||w - w_h|||_h \leq Ch \left(|w|_3 + h \|f\|_0 \right)\,. \tag{26}$$

Stabilized formulation

With integer values $k \geq 1$, we next define the discrete spaces for the stabilized C^0-element as

$$W_h = \{ v \in H^1(\Omega) \;|\; v_{|\Gamma_{\mathrm{C}} \cup \Gamma_{\mathrm{S}}} = 0, v_{|K} \in P_{k+1}(K) \;\; \forall K \in \mathcal{T}_h \}\,, \tag{27}$$

$$\boldsymbol{V}_h = \{ \boldsymbol{\eta} \in [H^1(\Omega)]^2 \;|\; \boldsymbol{\eta}_{|\Gamma_{\mathrm{C}}} = \boldsymbol{0}, \boldsymbol{\eta} \cdot \boldsymbol{s}_{|\Gamma_{\mathrm{S}}} = 0, \boldsymbol{\eta}_{|K} \in [P_k(K)]^2 \;\; \forall K \in \mathcal{T}_h \}\,, \tag{28}$$

for the approximations of the deflection and the rotation, respectively. Here $P_k(K)$ denotes the space of polynomials of degree k on K. In addition, let the positive stability constants α and γ be assigned. Now the stabilized C^0-continuous finite element method for the Kirchhoff–Love problem reads [1]:

Method 2 *Find* $(w_h, \boldsymbol{\beta}_h) \in W_h \times \boldsymbol{V}_h$ *such that*

$$\mathcal{A}_h(w_h, \boldsymbol{\beta}_h; v, \boldsymbol{\eta}) = (f, v) \quad \forall (v, \boldsymbol{\eta}) \in W_h \times \boldsymbol{V}_h\,, \tag{29}$$

where the bilinear form $\mathcal{A}_h$ *is defined with* $a(\boldsymbol{\phi}, \boldsymbol{\eta}) = (\boldsymbol{m}(\boldsymbol{\phi}), \boldsymbol{\varepsilon}(\boldsymbol{\eta}))$ *as*

$$\mathcal{A}_h(z, \boldsymbol{\phi}; v, \boldsymbol{\eta}) = \mathcal{B}_h(z, \boldsymbol{\phi}; v, \boldsymbol{\eta}) + \mathcal{D}_h(z, \boldsymbol{\phi}; v, \boldsymbol{\eta})\,, \tag{30}$$

$$\mathcal{B}_h(z, \boldsymbol{\phi}; v, \boldsymbol{\eta}) = a(\boldsymbol{\phi}, \boldsymbol{\eta}) - \sum_{K \in \mathcal{T}_h} \alpha h_K^2 (\boldsymbol{L}\boldsymbol{\phi}, \boldsymbol{L}\boldsymbol{\eta})_K \tag{31}$$

$$+ \sum_{K \in \mathcal{T}_h} \frac{1}{\alpha h_K^2} (\nabla z - \boldsymbol{\phi} - \alpha h_K^2 \boldsymbol{L}\boldsymbol{\phi}, \nabla v - \boldsymbol{\eta} - \alpha h_K^2 \boldsymbol{L}\boldsymbol{\eta})_K\,,$$

$$\mathcal{D}_h(z, \boldsymbol{\phi}; v, \boldsymbol{\eta}) = \sum_{E \in \mathcal{F}_h} \Big((m_{ns}(\boldsymbol{\phi}), (\nabla v - \boldsymbol{\eta}) \cdot \boldsymbol{s})_E \tag{32}$$

$$+ ((\nabla z - \boldsymbol{\phi}) \cdot \boldsymbol{s}, m_{ns}(\boldsymbol{\eta}))_E + \frac{\gamma}{h_E} ((\nabla z - \boldsymbol{\phi}) \cdot \boldsymbol{s}, (\nabla v - \boldsymbol{\eta}) \cdot \boldsymbol{s})_E \Big)$$

for all $(z, \boldsymbol{\phi})$, $(v, \boldsymbol{\eta}) \in W_h \times \boldsymbol{V}_h$, *with* $m_{ns} = \boldsymbol{m}\boldsymbol{n} \cdot \boldsymbol{s}$.

We next introduce the discrete norm for the deflection and the rotation as

$$|||(v, \boldsymbol{\eta})|||_h^2 := \sum_{K \in \mathcal{T}_h} |v|_{2,K}^2 + \|v\|_1^2 + \sum_{E \in \mathcal{I}_h} h_E^{-1} \| [\![\frac{\partial v}{\partial \boldsymbol{n}_E}]\!] \|_{0,E}^2 \tag{33}$$

$$+ \sum_{K \in \mathcal{T}_h} h_K^{-2} \|\nabla v - \boldsymbol{\eta}\|_{0,K}^2 + \|\boldsymbol{\eta}\|_1^2\,,$$

In addition, for the shear force, we introduce the following notation:

$$\boldsymbol{V}_* = \{\boldsymbol{\eta} \in [H^1(\Omega)]^2 \mid \boldsymbol{\eta} = \boldsymbol{0} \text{ on } \Gamma_{\mathrm{C}},\ \boldsymbol{\eta} \cdot \boldsymbol{s} = 0 \text{ on } \Gamma_{\mathrm{F}} \cup \Gamma_{\mathrm{S}}\}\,, \tag{34}$$

$$\|\boldsymbol{r}\|_{-1,*} = \sup_{\boldsymbol{\eta} \in \boldsymbol{V}_*} \frac{\langle \boldsymbol{r}, \boldsymbol{\eta} \rangle}{\|\boldsymbol{\eta}\|_1}\,, \tag{35}$$

$$\boldsymbol{q}_{h|K} = \frac{1}{\alpha h_K^2} (\nabla w_h - \boldsymbol{\beta}_h - \alpha h_K^2 \boldsymbol{L}\boldsymbol{\beta}_h)_{|K}\,. \tag{36}$$

Then the following a priori error estimate holds [1]:

Proposition 2 *Let* $0 < \alpha < C_I/4$, $\gamma > 2/C_I'$, *and* $w \in H^{s+2}(\Omega)$, *with* $1 \le s \le k$. *Then there exists a positive constant* C *such that*

$$|||(w - w_h, \boldsymbol{\beta} - \boldsymbol{\beta}_h)|||_h + \|\boldsymbol{q} - \boldsymbol{q}_h\|_{-1,*} \le C h^s \|w\|_{s+2}\,. \tag{37}$$

Finally, we note that the stabilized C^0-element, with 12 degrees of freedom for the lowest order element with $k = 1$, for instance, provides additional rotation degrees of freedom and exactly satisfied essential boundary conditions. The Morley element, instead, is a simple discontinuous method with 6 degrees of freedom. In addition, the essential boundary conditions are not satisfied exactly, which has direct implications to the a posteriori error estimator and analysis as well.

A POSTERIORI ERROR INDICATORS AND ERROR ESTIMATES

For a posteriori error indicators and estimates below, we indicate the Morley element by $(\mathcal{M})$ and the stabilized C^0-method by $(\mathcal{S})$.

The interior error indicators are defined for each element $K \in \mathcal{T}_h$ as

$$(\mathcal{M}) \quad \tilde{\eta}_K^2 = h_K^4 \|f\|_{0,K}^2 \,, \tag{38}$$

$$(\mathcal{S}) \quad \tilde{\eta}_K^2 = h_K^4 \|f + \operatorname{div} \boldsymbol{q}_h\|_{0,K}^2 + h_K^{-2} \|\nabla w_h - \boldsymbol{\beta}_h\|_{0,K}^2 \,, \tag{39}$$

and for internal edges $E \in \mathcal{I}_h$ as

$$(\mathcal{M}) \quad \eta_E^2 = h_E^{-3} \| [\![w_h]\!] \|_{0,E}^2 + h_E^{-1} \| [\![\frac{\partial w_h}{\partial \boldsymbol{n}_E}]\!] \|_{0,E}^2 \,, \tag{40}$$

$$(\mathcal{S}) \quad \eta_E^2 = h_E^3 \| [\![\boldsymbol{q}_h \cdot \boldsymbol{n}]\!] \|_{0,E}^2 + h_E \| [\![\boldsymbol{m}(\boldsymbol{\beta}_h) \boldsymbol{n}]\!] \|_{0,E}^2 \,. \tag{41}$$

Next, for the edges $E \in \mathcal{C}_h$ on the clamped boundary, the boundary indicator for the Morley element is defined as

$$(\mathcal{M}) \quad \eta_{E,C}^2 = h_E^{-3} \| [\![w_h]\!] \|_{0,E}^2 + h_E^{-1} \| [\![\frac{\partial w_h}{\partial \boldsymbol{n}_E}]\!] \|_{0,E}^2 \,. \tag{42}$$

For the stabilized C^0-element, the essential boundary conditions are satisfied on the clamped boundaries by (27) and (28), and hence no contribution for the estimator follows.

For the edges $E \in \mathcal{S}_h$ on the simply supported boundary, the boundary indicators are defined, with $m_{nn} = \boldsymbol{m}\boldsymbol{n} \cdot \boldsymbol{n}$, as

$$(\mathcal{M}) \quad \eta_{E,S}^2 = h_E^{-3} \| [\![w_h]\!] \|_{0,E}^2 \tag{43}$$

$$(\mathcal{S}) \quad \eta_{E,S}^2 = h_E \| m_{nn}(\boldsymbol{\beta}_h) \|_{0,E}^2 \,. \tag{44}$$

For the edges $E \in \mathcal{F}_h$ on the free boundary, the boundary indicator is defined for the stabilized C^0-element as

$$(\mathcal{S}) \quad \eta_{E,F}^2 = h_E \| m_{nn}(\boldsymbol{\beta}_h) \|_{0,E}^2 + h_E^3 \| \frac{\partial}{\partial s} m_{ns}(\boldsymbol{\beta}_h) - \boldsymbol{q}_h \cdot \boldsymbol{n} \|_{0,E}^2 \,. \tag{45}$$

For the Morley element, no contribution is present for free boundaries, cf. [4].

Finally, the local and global error indicators are defined as

$$\eta_K = \Big(\tilde{\eta}_K^2 + \frac{1}{2} \sum_{\substack{E \in \mathcal{I}_h \\ E \subset \partial K}} \eta_E^2 + \sum_{\substack{E \in \mathcal{C}_h \\ E \subset \partial K}} \eta_{E,C}^2 + \sum_{\substack{E \in \mathcal{S}_h \\ E \subset \partial K}} \eta_{E,S}^2 + \sum_{\substack{E \in \mathcal{F}_h \\ E \subset \partial K}} \eta_{E,F}^2 \Big)^{1/2} , \tag{46}$$

$$\eta = \Big(\sum_{K \in \mathcal{T}_h} \eta_K^2 \Big)^{1/2} . \tag{47}$$

We then have the following reliability and efficiency results [2, 1, 4]:

Theorem 1 *There exist positive constants C such that*

$$(\mathcal{M}) \quad |||w - w_h|||_h \le C\eta \,, \tag{48}$$

$$(\mathcal{S}) \quad |||(w - w_h, \boldsymbol{\beta} - \boldsymbol{\beta}_h)|||_h + \|\boldsymbol{q} - \boldsymbol{q}_h\|_{-1,*} \le C\eta \,. \tag{49}$$

Theorem 2 *There exist positive constants C such that*

$$(\mathcal{M}) \quad \eta_K \leq C\big(|||w - w_h|||_{h,K} + h_K^2 \|f - f_h\|_{0,K}\big)\,, \tag{50}$$

$$(\mathcal{S}) \quad \eta_K \leq C\big(|||(w - w_h, \boldsymbol{\beta} - \boldsymbol{\beta}_h)|||_{h,\omega_K} + h_K^2 \|f - f_h\|_{0,\omega_K} + \|\boldsymbol{q} - \boldsymbol{q}_h\|_{-1,*,\omega_K}\big)\,, \tag{51}$$

for each element $K \in \mathcal{T}_h$, with some approximation f_h of the load f. Here the domain ω_K denotes the set of all the triangles sharing an edge with K.

NUMERICAL RESULTS

In this section, we present some results on benchmark computations for a comparison of the numerical and theoretical results of the two methods proposed above. Regarding the stabilized C^0-element, we consider the lowest order element with $k = 1$ only. Hence, the rotation components are linear, while the deflection is quadratic, as the deflection of the Morley element.

Constants and adaptive solution strategy

In all of the test cases, we have used for the material and stability constants the following values: $\mathsf{E} = 1$, $\nu = 0.3$, $\alpha = 0.1$ and $\gamma = 100$. We have implemented the methods in the open-source finite element software Elmer [6] which utilizes local error indicators, and provides complete remeshing with Delaunay triangulations and error balancing strategy for adaptive refinements [3, 6].

Effectivity index — convex domains

In Fig. 1, the effectivity index for the adaptive error estimator, i.e., the ratio between the estimated and true error, is reported for three test problems with convex rectangular domains, cf. [3, 4]: In the first case, all the boundaries are clamped, while in the second case the boundaries are simply supported. In the third case, two opposite sides of the rectangle are simply supported, while the other two sides are free. The exact solution of each problem can be written as a trigonometric-hyperbolic series which we have used as a reference solution [3].

For the coarse meshes in Fig. 1, there is a decrease in the effectivity index, while for the finer meshes the effectivity index remains on a certain almost constant level uniformly in the mesh size for both methods. More precisely, for the Morley element the effectivity index finally remains in the range 0.4 ... 0.8, while for the stabilized method the index stays between 2 and 3. Hence, together with the theoretical results presented above, this gives a clear indication that the error estimators can be used as reliable and efficient error measures.

Robustness — non-convex domains

For a comparison of adaptive and uniform refinements, we consider a uniformly loaded non-convex domain with simply supported boundaries, as depicted in Figs. 3 and 4 for the example meshes of adaptive steps with error distributions for the estimator of the Morley element.

The convergence of the corresponding error estimator for uniformly (circles) and adaptively (triangles) refined meshes are shown in Fig. 2. The two upper graphs (solid lines) represent the global error estimator, while the lower ones (dashed lines) indicate the maximum local indicator. The convergence rates $\mathcal{O}(h^{1/5})$ and $\mathcal{O}(h)$ corresponding to the rates with and without the corner singularity

in the solution, respectively, have been plotted with solid and dashed straight lines without markers. Now, due to the singularity in the re-entrant V-corner, $w \in H^{11/5}(\Omega)$ [8], which implies the rate $\mathcal{O}(h^{1/5})$ for uniform refinements.

In Fig. 2, it can be seen that the convergence rate of the error estimator for the uniform refinements (circles) turns to follow the asymptotical convergence order $\mathcal{O}(h^{1/5})$. On the contrary, for the adaptive refinements (triangles), the method shows its robustness in finding the corner singularity of the solution and finally focuses the refinements locally near the V-corner. The accuracy reached with uniform refinements by more than 20000 elements is now achieved by circa 1800 elements.

For the stabilized C^0-element, the convergence results are very similar to the ones above for the Morley element, cf. [3]. However, for the stabilized element the refinements concentrate more clearly in the singular corner only, not along the other boundaries, since the essential boundary conditions are satisfied a priori by the finite element solution, as noted in the previous section.

REFERENCES

[1] L. Beirão da Veiga, J. Niiranen, and R. Stenberg. A family of C^0 finite elements for Kirchhoff plates I: Error analysis. *SIAM J. Num. Anal.*, 45:2047–2071, 2007.

[2] L. Beirão da Veiga, J. Niiranen, and R. Stenberg. A posteriori error estimates for the Morley plate bending element. *Numer. Math.*, 106:165–179, 2007.

[3] L. Beirão da Veiga, J. Niiranen, and R. Stenberg. A family of C^0 finite elements for Kirchhoff plates II: Numerical results. *Comp. Meths. Appl. Mech. Engrg.*, 197:1850–1864, 2008.

[4] L. Beirão da Veiga, J. Niiranen, and R. Stenberg. A posteriori error analysis for the Morley plate element with general boundary conditions. Research Reports A 556, Helsinki University of Technology, Institute of Mathematics, December 2008. `http://www.math.tkk.fi/reports`.

[5] A. Charbonneau, K. Dossou, and R. Pierre. A residual-based a posteriori error estimator for the Ciarlet–Raviart formulation of the first biharmonic problem. *Num. Meth. Part. Diff. Eq.*, 13:93–111, 1997.

[6] Elmer finite element software homepage. `http://www.csc.fi/elmer`.

[7] J. Hu and Z. Shi. A new a posteriori error estimate for the Morley element. *Numer. Math.*, 112:25–40, 2009.

[8] H. Melzer and R. Rannacher. Spannungskonzentrationen in Eckpunkten der vertikal belasteten Kirchhoffschen Platte. *Bauingenieur*, 55:181–189, 1980.

[9] W. Ming and J. Xu. The Morley element for fourth order elliptic equations in any dimensions. *Numer. Math.*, 103:155–169, 2006.

[10] L. S. D. Morley. The triangular equilibrium element in the solution of plate bending problems. *Aero. Quart.*, 19:149–169, 1968.

[11] P. Neittaanmäki and S. Repin. A posteriori error estimates for boundary value problems related to the biharmonic operator. *East–West J. Numer. Math.*, 9:157–178, 2001.

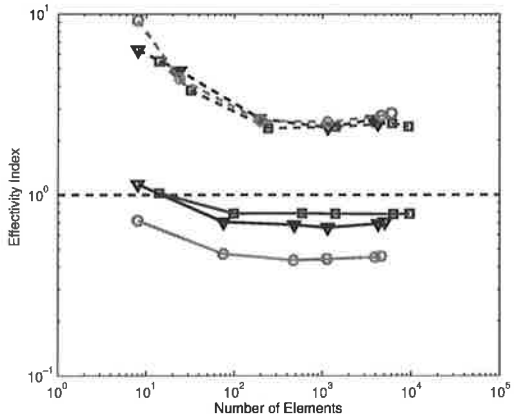

Figure 1: Uniformly loaded rectangular Kirchhoff–Love plates: Effectivity index for adaptive refinements; simply supported (circles), simply supported and free (triangles), clamped (squares) boundaries; Morley element (solid lines), stabilized C^0-element (dashed lines).

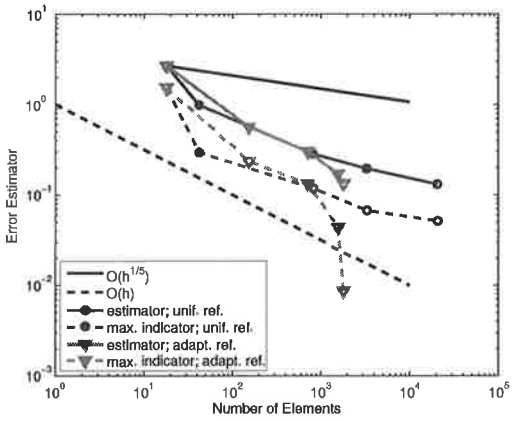

Figure 2: Uniformly loaded and simply supported non-convex Kirchhoff–Love plate: Convergence of the global estimator (solid lines) and the maximum local estimator (dashed lines); Circles for uniform refinements, triangles for adaptive refinements.

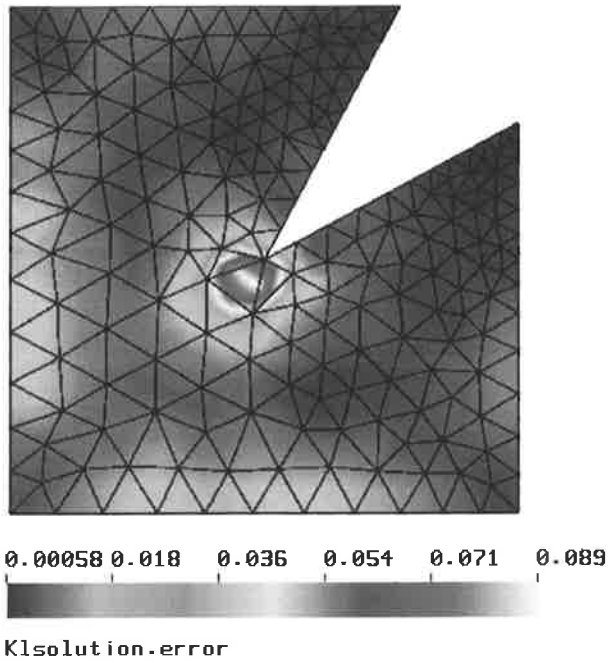

Figure 3: Uniformly loaded and simply supported non-convex Kirchhoff–Love plate with the Morley element: Distribution of the error estimator and the mesh for the step 3 of an adaptive process.

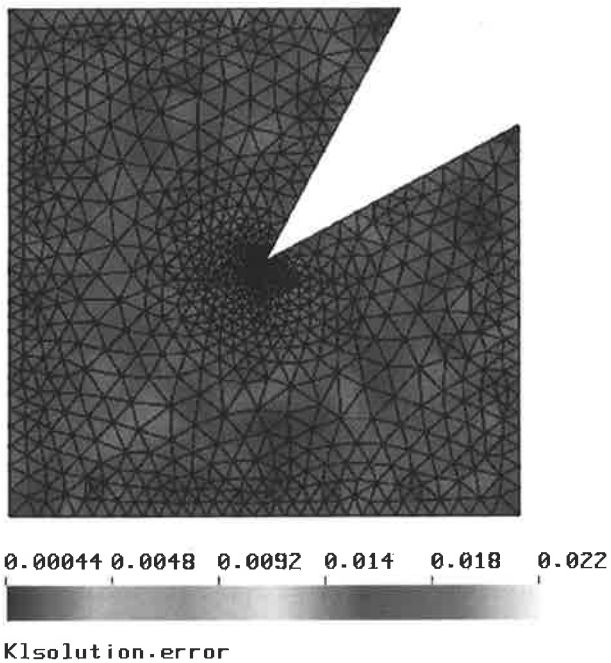

Figure 4: Uniformly loaded and simply supported non-convex Kirchhoff–Love plate with the Morley element: Distribution of the error estimator and the mesh for the step 8 of an adaptive process.

ELASTISTEN AALTOPULSSIEN MALLINTAMINEN

Timo Lähivaara[a,b,*], Tomi Huttunen[b], Heidi Niskanen[a]

[a]Fysiikan laitos, Kuopion yliopisto
PL 1627, FIN-70211 Kuopio
[b]Kuava Oy
PL 1188, FIN-70211 Kuopio
[*]timo.lahivaara@uku.fi

TIIVISTELMÄ

Työssä tutkittiin aikatason aalto-ongelmien (akustinen ja elastinen aaltoyhtälö) ratkaisuja kolmessa dimensiossa. Aaltoyhtälöiden paikkaderivaatat laskettiin käyttäen epäjatkuvaa Galerkinin (DG eng. *discontinuous Galerkin*) menetelmää ja aikaderivaatat laskettiin low-storage Runge-Kutta aikaintegrointimenetelmällä. Käytetyssä ratkaisijassa polynomikannan asteluku valittiin erikseen jokaiselle laskentahilan elementille.

Työssä tarkasteltiin kahta erityyppistä esimerkkiä, joista ensimmäinen on kirjallisuudessa paljon tutkittu elastisten aaltojen kulkua kuvaava mallinnusesimerkki. Toiseksi esimerkiksi valittiin mallinnuskohde, jossa tutkittiin suihkuturbiinin tuottaman äänen etenemistä virtaavassa väliaineessa. Jälkimmäisessä esimerkissä virtausmallinnusohjelmistolla mallinnettiin ensin virtausnopeuskenttä, jota käytettiin nesteen virtauskenttänä varsinaisessa akustisen partikkelinopeuden laskennassa. Yhteenvetona lasketuista ratkaisuista voidaan todeta, että DG-menetelmä yhdistettynä tehokkaaseen aika-askellusmenetelmään, on sovellettavissa hyvin aaltoilmiöiden tarkkaan mallintamiseen. Lisäksi approksimaatiomenetelmän epäjatkuvuus elementtirajapintojen yli mahdollistaa polynomikannan optimaalisen valinnan elementeittäin.

1. JOHDANTO

Useilla fysiikan ja tekniikan osa-alueilla on tärkeää simuloida värähtelypulssien etenemistä elastisessa tai akustisessa väliaineessa. Näitä tutkimuskohteita ovat esimerkiksi mekaaniset rakennevärähtelyt tai ultraäänellä tehtävä rakennetutkimus. Viime vuosikymmenten aikana useita numeerisia menetelmiä on esitetty edellä mainittujen ongelmien ratkaisemiseksi. Esimerkkeinä käytetyistä menetelmistä mainittakoon differenssi-, äärellisten elementtien- ja sädemenetelmät. Kuitenkin valitettavan usein, varsinkin korkeilla taajuuksilla ja monimutkaisissa geometrioissa, perinteiset lähestymistavat tuottavat liian epätarkkoja tai laskennallisesti liian raskaita ratkaisuja tutkittaville ongelmille.

Yksi lupaava lähestymistapa aaltoilmiöiden simulointiin elastisessa väliaineessa on epäjatkuva Galerkinin menetelmä. Menetelmän etuina ovat geometrinen joustavuus ja tehokas rinnakkaistuminen moniprosessoritietokoneille. Tässä tutkimuksessa DG-menetelmää sovelletaan aaltopulssien simulointiin elastisessa väliaineessa sekä virtaavassa nesteessä. Käytetyssä mallissa polynomikannan

asteluku valitaan erikseen jokaiselle laskentahilan elementille. Kantafunktioiden asteluvun valintakriteerin tavoitteena on tuottaa ratkaisulle vakiosuuruinen virhetaso riippumatta käytetystä hilasta, ja toisaalta, minimoida kunkin simulointitehtävän vaatima laskentakapasiteetti.

2. KYTKETTY ONGELMA

Tässä paperissa kytketyllä ongella tarkoitetaan tilannetta, jossa tutkitaan äänen etenemistä geometrioissa, jotka sisältävät kiinteän ja toisaalta myös liikkuvan nesteen (tai kaasun) komponentin. Yleisesti kirjallisuudessa puhutaan fluid-solid-ongelmista. Työssä tutkitut kytketyt ongelmat isotrooppiselle kiinteälle ja liikkuvalle neste-tyyppiselle väliaineelle voidaan kirjoittaa lineaarisena hyperbolisena systeeminä [1, 2, 3]

$$\frac{\partial \bar{\tau}}{\partial t} + \sum_{\ell=1}^{3} A_\ell \frac{\partial \bar{\tau}}{\partial x_\ell} = 0, \tag{1}$$

missä $\bar{\tau} = (\tau_{11}, \tau_{22}, \tau_{33}, \tau_{12}, \tau_{23}, \tau_{13}, u_1, u_2, u_3)^\top$ ($\top$ tarkoittaa transpoosia). Systeemissä (1) t on aika, x_ℓ paikka, τ_{11}, τ_{22} ja τ_{33} ovat jännityksen normaalikomponentit, τ_{12}, τ_{23} ja τ_{13} ovat jännityksen pinnansuuntaiset komponentit ja u_1, u_2 ja u_3 nopeuskomponentit.

Hyperbolisessa systeemissä (1) matriisit A_ℓ, $\ell = 1, 2, 3$ ovat kooltaan 9×9. Matriisit A_ℓ, $\ell = 1, 2, 3$ poikkeavat lähteissä [1, 2, 3] tarkastelluista, koska tässä paperissa tarkastellaan tilannetta, jossa neste voi liikkua. Liikkuvan nesteen nopeuskomponentit määritellään $v = (v_1, v_2, v_3)$. Esimerkkinä tarkastellaan matriisia A_1, joka voidaan kirjoittaa muodossa

$$A_1 = \begin{pmatrix} v_1 & 0 & 0 & 0 & 0 & 0 & -(\lambda+2\mu) & 0 & 0 \\ 0 & v_1 & 0 & 0 & 0 & 0 & -\lambda & 0 & 0 \\ 0 & 0 & v_1 & 0 & 0 & 0 & -\lambda & 0 & 0 \\ 0 & 0 & 0 & v_1 & 0 & 0 & 0 & 0 & 0 \\ 0 & 0 & 0 & 0 & v_1 & 0 & 0 & 0 & 0 \\ 0 & 0 & 0 & 0 & 0 & v_1 & 0 & 0 & 0 \\ -\frac{1}{\rho} & 0 & 0 & 0 & 0 & 0 & v_1 & 0 & 0 \\ 0 & 0 & 0 & -\frac{1}{\rho} & 0 & 0 & 0 & v_1 & 0 \\ 0 & 0 & 0 & 0 & 0 & -\frac{1}{\rho} & 0 & 0 & v_1 \end{pmatrix},$$

missä v_1 on nesteen nopeuden x_1-suuntainen komponentti, λ ja μ ovat Lamén vakioita ja ρ on väliaineen tiheys. Matriiseissa A_2 ja A_3 on samat nollasta poikkeavat arvot $-\lambda, -(\lambda+2\mu)$ ja $-1/\rho$, mutta eri paikoissa [1, 3]. Lisäksi matriiseissa A_2 ja A_3 on diagonaalilla eri nopeuskomponentit liikkuvalle nesteelle (vastaten suuntia x_2 ja x_3) [4]. Edelleen P- ja S- aaltojen nopeudet voidaan esittää Lamén vakioiden ja väliaineen tiheyden avulla seuraavasti

$$c_p = \sqrt{\frac{\lambda+2\mu}{\rho}} \quad \text{ja} \quad c_s = \sqrt{\frac{\mu}{\rho}}. \tag{2}$$

Elastiselle aaltoyhtälölle voidaan kirjoittaa laaja määrä erilaisia reunaehtoja ja edelleen reunaehdoille on lukuisia tulkintoja. Kattavampi yleiskatsaus aaltoilmiöistä elastisessa väliaineessa ja näiden ilmiöiden fysikaalisista ominaisuuksista on esitetty viitteessä [1]. Akustisen väliaineen yleisesti tunnettuja reunaehtoja ovat nk. Neumann- ja Dirichlet-tyyppiset reunaehdot sekä rajoittamattomien ongelmien katkaisuun käytetyt absorboivat reunaehdot. Akustisen väliaineen ilmiöitä ja edellä mainittujen reunaehtojen (Neumann, Dirichlet ja absorptio) fysikaalisia ominaisuuksia on tarkasteltu viitteessä [5].

Mallinnusongelmissa, joisssa tutkittava ongelma sisältää sekä akustisen että elastisen alueen, tulee näiden alueiden välille kirjoittaa jatkuvuusehdot. Käytettäessä epäjatkuvaa Galerkinin menetelmää, tulee jatkuvuusehto eri alueiden välille "automaattisesti" sillä menetelmän heikko muoto kirjoitetaan erikseen jokaiselle laskentahilan elementille ja kommunikointi elementtien välillä toteutetaan numeerisella vuolla (eng. *numerical flux*). Tässä työssä käytetty numeerinen vuo on esitelty tarkemmin viitteessä [4].

3. EPÄJATKUVA GALERKININ MENETELMÄ

Vuonna 1973 tutkijat Reed ja Hill julkaisivat epäjatkuvan Galerkinin menetelmän approksimoimaan neutronien kulkeutumista kuvaavaa yhtälöä [6]. Tämän jälkeen menetelmän matemaattista analyysiä ovat kehittäneet mm. LeSaint ja Raviart [7], Johnson ja Pitkäranta [8] ja Richter [9]. Viime vuosina DG-menetelmän käyttö on yleistynyt huomattavasti ja näin ollen sen käytöstä on olemassa useita satoja tieteellisiä julkaisuja. Nykyisin DG-lähestymistapaa on sovellettu useille fysiikan osa-alueille, joista esimerkkeinä mainittakoon sähkömagnetiikka [10, 11, 12], virtauslaskenta [13, 14], aaltoyhtälöt (elastinen ja akustinen) [3, 15] ja kytketyt ongelmat (akustinen ja elastinen aaltoyhtälö) [4].

DG-menetelmän käyttöön liittyy merkittäviä etuja perinteisiin laskentamalleihin verrattuna. Esimerkkeinä mainittakoon erityinen matriisirakenne, jonka johdosta muistin tarvetta aikatason mallinnuksessa on pystytty ratkaisevasti vähentämään. Toisaalta menetelmä on helppo rinnakkaistaa, joka on edellytys suurten ongelmien tehokkaassa mallinnuksessa. Hyvä lähdeteos DG-menetelmän analyysiin ja toisaalta myös sovelluspohjaiseen käyttöön on Hesthavenin ja Warburtonin vuonna 2007 kirjoittama kirja [16], joka on ollut merkittävässä roolissa myös tässä työssä käytettyjen koodien kehityksen taustalla.

4. NUMEERISET ESIMERKIT

Seuraavissa kappaleissa tarkastellaan kytkettyjen ongelmien (akustinen ja elastinen aaltoyhtälö) numeerisia ratkaisuja 3D ongelmissa. Tutkittavat esimerkit on valittu siten, että ensimmäinen on kirjallisuudessa paljon käytetty ja tutkittu ongelma. Toisessa esimerkissä tarkastellaan haastavampaa mallinnusgeometriaa, joka sisältää lentokoneen siiven ja siihen kiinnitetyn turbiinin. Esimerkkien tavoitteena on havainnollistaa käytetyn DG-menetelmän etuja matemaattisessa mallinnuksessa.

Työssä tarkastellaan ajansuhteen riippuvia ratkaisuja. Aika-askeleen pituus on kiinnitetty käyttäen Courant-Friedrichs-Lewy (CFL) -lukua [17]. CFL-luku voidaan kirjoittaa yhtälömuodossa seuraavasti:

$$\mathrm{CFL} = \frac{\delta_t c_{\max}}{h_{\min}}, \tag{3}$$

missä δ_t on aika-askeleen pituus, $c_{\max}$ on suurin esimerkissä käytetty aallonnopeus ja $h_{\min}$ on pienin etäisyys kahden solmun välillä laskentahilassa. Suurimalla aallonnopeudella tarkoitetaan P-aallon nopeutta (huomioiden nesteen virtauksen) $c_p + \|v\|$.

Kaikissa tutkittavissa ongelmissa CFL-luku asetetaan arvoon 0.02, jonka tavoitteena on minimoida aikaintegroinnista syntyvä virhe. Tässä työssä systeemissä (1) esitetyt aikaderivaatat ratkaistaan käyttäen eksplisiittistä low-storage Runge-Kutta (LSRK) -menetelmää [18].

Laskennassa käytetty DG-ratkaisija on kirjoitettu C++-ohjelmointikielellä ja rinnakkaistettu käyttäen MPI ympäristöä. Laskennan molemmat esimerkit on laskettu käyttäen perinteistä laskentaklusteria. Käytetty klusteri sisältää yhteensä 24 solmua (2.6 GHz Pentium 4) ja jokainen solmu yhteensä 4 GB keskusmuistia (RAM).

4.1 Palkin värähtely

Esimerkissä tarkastellaan värähtelyn etenemistä epähomogeenisessa väliaineessa. Kyseessä olevaa mallinnusongelmaa on tarkasteltu viitteessä [3]. Esimerkin geometria Ω koostuu kahdesta osasta (ks. kuva 1), jotka on määritelty seuraavasti:

$$\begin{aligned} \Omega_1 &= \left\{ \bar{x} \in \mathbb{R}^3 \mid |x_1| \leq 0.5,\ |x_2| + |x_3| \leq 0.1 \right\}, \\ \Omega_2 &= \left\{ \bar{x} \in \mathbb{R}^3 \mid |x_1| \leq 1.0,\ |x_2| + |x_3| \leq 0.5 \right\} \setminus \Omega_1. \end{aligned}$$

Elastisessa tapauksessa ongelman reunaehdot asetetaan siten, että pinta $x_1 = -1.0$ sisältää epähomogeenisen vapaatuentareunaehdon, pinnalle $x_1 = 1.0$ asetetaan absorboiva reunaehto ja kaikille muille geometrian ulkoreunoilla homogeeninen vapaatuentareunaehto. Vastaavasti kytketyssä ongelmassa, jossa alue Ω_1 on elastinen materiaali ja Ω_2 akustinen, asetetaan pinta $x_1 = -1.0$ epähomogeeniseksi värähteleväksi pinnaksi. Lisäksi pinnalle $x_1 = 1.0$ asetetaan absorboiva ehto ja muille homogeeninen Neumann-nollaehto (akustisesti kova pinta).

Lähdefunktiona epähomogeeniselle pinnalle sekä elastisessa että kytketyssä ongelmassa käytetään

$$\bar{g}(t) = \begin{cases} \sin(\omega t), & \text{jos } t \in \left[0, \frac{\pi}{\omega}\right], \\ 0, & \text{muulloin,} \end{cases} \tag{4}$$

missä kulmataajuus $\omega = 40\pi$. Elastisessa esimerkissä systeemin (1) fysikaaliset parametrit on asetettu seuraavasti: S-aallon nopeus $(c_{s_1}, c_{s_2}) = (10, 1)$, P-aallon nopeus $(c_{p_1}, c_{p_2}) = (20, 2)$ ja tiheys $(\rho_1, \rho_2) = (1, 1)$. Edelleen kytketyssä ongelmassa käytetään muuten samoja parametrivalintoja paitsi alueessa Ω_2 S-aallon nopeuskomponentti on nolla, joka tarkoittaa käytännössä, että Lamén vakio $\mu = 0$. Tutkittavassa esimerkissä oletetaan, että neste ei ole liikkeessä, jolloin $(v_1, v_2, v_3) = (0, 0, 0)$.

Kuvassa 1 on esitetty laskennassa käytetty tetraedriverkko. Kuvan värisävyjakauma näyttää kantafunktion asteluvun jokaiselle elementille. Hila sisältää 302358 elementtiä, 55175 solmua, $h_{\min} = 0.0162$ ja $h_{\max} = 0.0712$. Kantafunktioiden asteluku on valittu kiinnittäen virheen arvoon 1.0%. Kantafunktioiden asteluvun valintakriteeriä on tarkasteltu tarkemmin viitteessä [19] 3D-ongelmiin ja vastaavasti 2D-ongelmiin viitteessä [15].

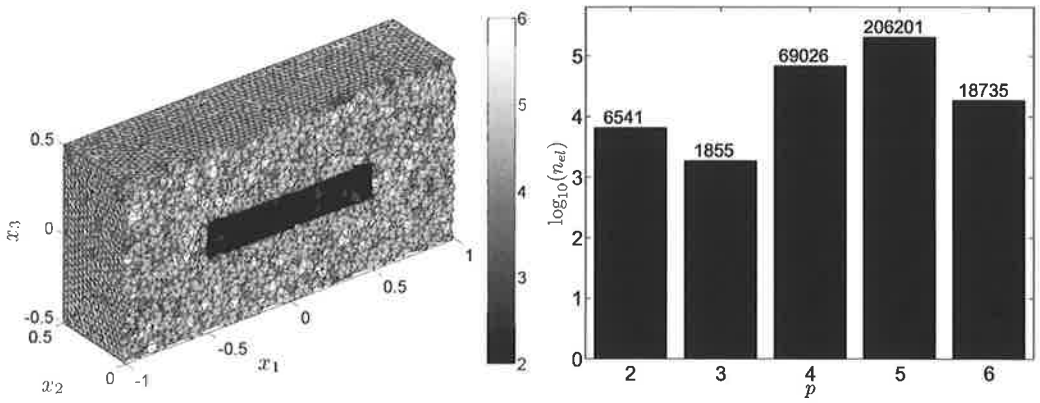

Kuva 1: Laskennassa käytetty tetraedriverkko (vasen) ja elementtien lukumäärä polynomikannan asteluvun funktiona (oikea).

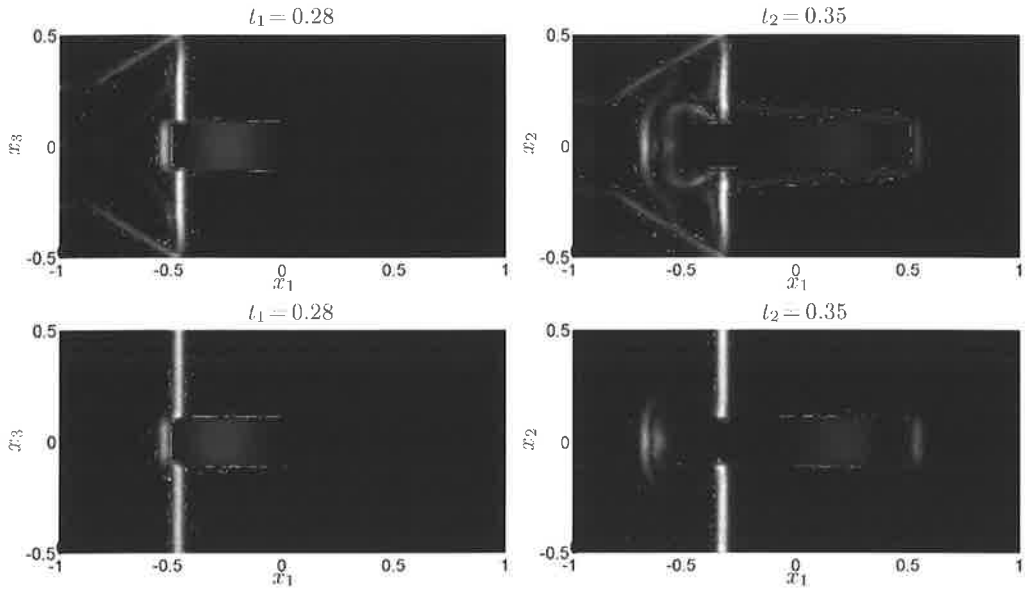

Kuva 2: Partikkelinopeuskomponentti $|u_1|$ kahdella ajanhetkellä $t_1 = 0.25$ (vasen) ja $t_2 = 0.35$ (oikea). Yllä elastisen ja alla kytketyn ongelman ratkaisu.

Kuvassa 2 on esitetty nopeuskomponentti $|u_1|$ kahdella ajanhetkellä $t_1 = 0.25$ ja $t_2 = 0.35$. Kuvassa on esitetty sekä elastisen (yllä) että kytketyn ongelman ratkaisu (alla). Ajanhetkistä ensimmäinen $t_1 = 0.25$ havainnollistaa tilannetta, jossa reunalta $x_1 = -1.0$ tuotettu lähde on edennyt värähtelevän palkin reunalle. Edelleen ajanhetki $t_2 = 0.35$ on valittu siten, että se havainnollistaa palkissa syntyviä värähtelyjä.

4.2 Turbiini

Esimerkissä tarkastellaan turbiinissa tuotetun äänen etenemistä homogeenisessa virtaavassa väliaineessa. Laskenta-alue on määritelty esimerkissä seuraavasti:

$$\Omega \quad = \quad \left\{ \bar{x} \in \mathbb{R}^3 \mid -2 \leq x_1 \leq 8,\ |x_2| + |x_3| \leq 2.5 \right\} \setminus \Omega_l, \tag{5}$$

missä Ω_l tarkoittaa lentokoneen siiven ja siihen kiinnitetyn turbiinin geometriaa (ks. kuva 3).

Ongelman reunaehdot asetetaan siten, että alueen ulkoreuna sisältää absorboivan reunaehdon. Turbiinin sisällä oleva pinta sisältää epähomogeenisen Neumann-reunaehdon. Kaikki muut lentokoneen siiven ja siihen liitetyn turbiinin reunaehdot asetetaan homogeeniseksi Neumann-nollaehdoksi (akustisesti kovia pintoja).

Mallinnusongelmassa lähdefunktioksi epähomogeeniselle reunaehdolle määritellään

$$\bar{g}(t) = \exp\left(-\alpha \left(t - t_0\right)^2\right) \sin\left(2\pi f \left(t - t_0\right)\right) \quad \forall\, t, \tag{6}$$

missä $\alpha = 1.5 \cdot 10^5$, $t_0 = 2$ ms ja $f = 1000$ Hz. Ongelman muut fysikaaliset parametrit valitaan siten, että $\mu = 0$, joten tarkastelemme vain akustista väliainetta. Tässä tapauksessa väliaineeksi valitaan ilma, joten $c_p = 343$ m/s ja tiheys $\rho = 1.21$ kg/m^3. Lisäksi esimerkissä lasketaan liikkuvan nesteen nopeus. Virtauslaskenta on selitetty myöhemmin tässä kappaleessa.

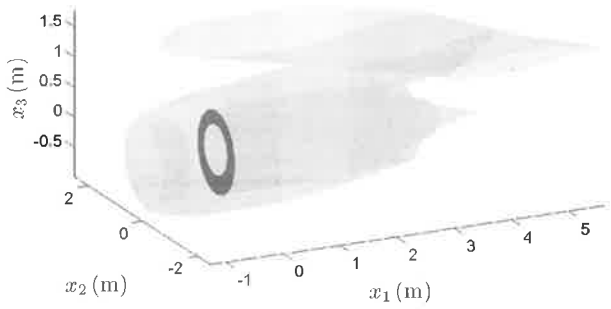

Kuva 3: Laskennassa käytetyn lentokoneen siiven ja siihen kiinnitetyn turbiinin geometria Ω_l. Kuvan musta rengas kuvaa aluetta, josta akustinen kenttä on tuotettu (epähomogeeninen Neumann-reunaehto).

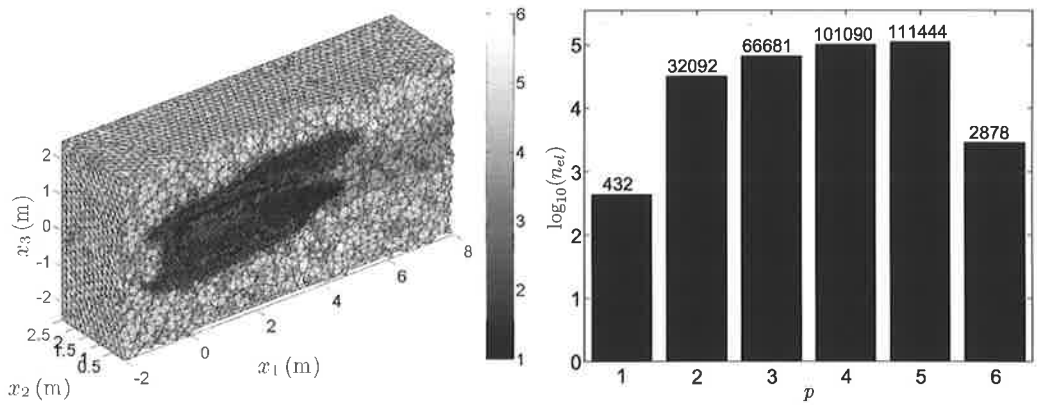

Kuva 4: Vasen: Laskennassa käytetty hila. Oikea: Tetraedrielementtien lukumäärä polynomikantafunktioiden asteluvun funktiona.

Kuvassa 3 on esitetty laskennassa käytetyn turbiinin geometria ja osa siipeä. Laskennassa käytetty geometria on osa Gambit-ohjelmiston mukana tullutta testigeometriaa. Lisäksi turbiiniin on lisätty sisäosa, joka ei ollut mukana alkuperäisessä mallissa.

Kuvassa 4 on esitetty laskennassa käytetty hila ja laskentaan käytetyt polynomikantojen asteluvut. Laskentahila sisältää yhteensä 314617 tetraedrielementtiä, 63009 solmupistettä, lyhin etäisyys kahden solmun välillä on $h_{\min} = 0.0103$ m ja vastaavasti pisin etäisyys $h_{\max} = 0.3926$ m. Polynomikantafunktioiden asteluvut kiinnitettiin käyttäen artikkelissa [19] esitettyjä tuloksia. Kyseisessä mallinnusesimerkissä virhetasoksi valittiin 1.0%. Kuvan jakaumasta kannattaa huomioida, että elementin kantafunktion asteluvun valitaan vaikuttaa myös elementissä oleva virtausnopeus. Kuvasta voidaan havaita, että turbiinin takana on tummempi alue, joka ulottuu pinnalle $x_1 = 8$ m asti ja joka sisältää korkeammat asteluvut kuin sitä ympäröivä alue. Tämä on suora seuraus siitä, että turbiinin takana oleva alue sisältää suuremman nesteen virtausnopeuden (kts. kuva 5).

Kuvassa 5 on esitetty virtauskenttä kahdessa tasossa. Ilmavirtaus turbiinissa ja sen ympäristössä mallinnettiin kaupallisella virtauslaskentaohjelmalla, Ansys CFX:n versiolla 11.0. Laskenta toteu-

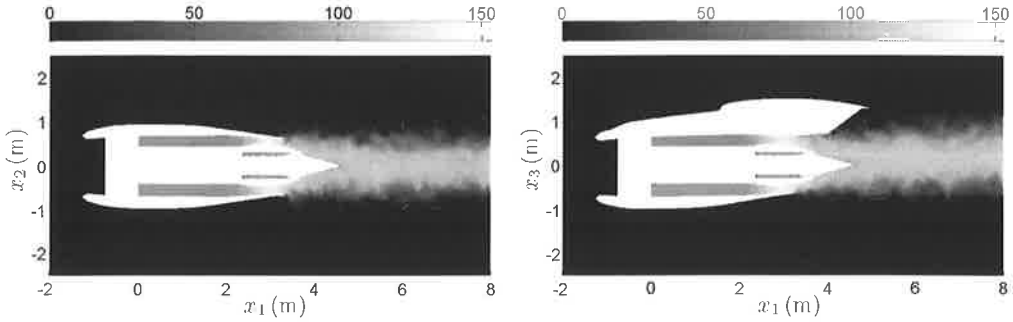

Kuva 5: CFX-ohjelmasta saatu virtauskenttä kahdessa eri tasossa kuvattuna. Värisävyjakauma kertoo virtausnopeuden $\|v\|$ arvon yksiköissä m/s.

tettiin ajasta riippumattomana käyttäen Reynoldsin jännitysmallia turbulenssin mallinnukseen. Valinta tehtiin, koska standardilla k-epsilon mallilla ei saavutettu riittävää konvergenssia ja mallin on todettu antavan virheellisiä tuloksia joissain tapauksissa. Tihentämällä verkkoa olisi saatu parempi konvergenssi, mutta käytettävissä olleen laskenta-ajan puitteissa valitulla verkolla saatiin sovelluksen kannalta riittävän hyvät tulokset. Ilman virtaus turbiinista on voimakkaasti turbulenttia, joten tilanteen mallinnus laminaarina ei olisi ollut mielekästä, koska tällöin olisi jouduttu muuttamaan aineen kuljetusominaisuuksia konvergenssin saavuttamiseksi, jolloin tilanne ei enää olisi ollut todellisuutta vastaava.

Varsinainen virtauskenttä laskettiin isommassa geometriassa kuin kappaleen alussa määritelty (ks. kaava (5)). Virtauskentän laskennassa käytettiin tilavuutta $[-2,\ 18] \times [-3,\ 3] \times [-3,\ 3]$ m^3, joka sisälsi yhteensä 4801928 elementtiä, 991357 solmua, $h_{\min} = 0.0021$ m ja $h_{\max} = 0.4028$ m. Lopuksi virtauslaskennasta saatu virtauskenttä interpoloitiin jokaisen akustisen kentän laskennassa käytetyn hilan (kts. kuva 4) elementin keskipisteeseen. Tällä tavoin jokainen elementti sisältää liikkuvalle nesteelle annetun nopeuden komponentit (v_1, v_2, v_3). Kuvassa 5 on esitetty interpoloitu nopeuskenttä $\|v\|$ kahdessa eri tasossa. Kuvan värisävyjakaumasta havaitaan, että virtausnopeus jakautuu välille $\approx [0,\ 155]$ m/s.

Kuvassa 6 on esitetty partikkelinopeus kahdella eri ajanhetkellä kahdessa eri tasossa. Tarkasteltavat ajanhetket ovat $t_1 = 0.82$ (ms) ja $t_2 = 1.12$ (ms). Ajanhetkistä ensimmäinen t_1 havainnollistaa tilannetta, jossa aaltopulssi on edennyt turbiinin kapeimpaan kohtaan. Tässä kohdassa nesteen virtausnopeus on voimakkain (kts. kuva 5). Toinen ajanhetki t_2 kuvaa tilannetta, jossa pulssi on edennyt turbiiniin taakse.

5. POHDINTA

Työssä tutkittiin elastisen aaltoyhtälön ja kytkettyjen ongelmien ratkaisuja 3D-ongelmissa sekä akustisen aaltopulssin mallintamista virtaavassa väliaineessa. Ensimmäisessä ongelmassa ratkaistiin elastinen aaltoyhtälö epähomogeenisessa väliaineessa. Testiongelma on haasteellinen, sillä kahden osa-alueen väliset materiaaliparametrierot ovat huomattavat. Tässä paperissa kyseinen mallinnusongelma ratkaistiin myös kytkettynä ongelmana.

Toisessa mallinnusesimerkissä tutkittiin lentokoneen turbiinilla tuotetun äänen etenemistä. Esimerkissä ratkaistiin aluksi virtauskenttä käyttäen kaupallista Ansys-CFX-ohjelmistoa, josta saatiin nesteen virtausnopeus akustisiin simulaatioihin. Tämän mallin osalta sekä virtaus että akustinen malli sisältävät huomattavan voimakkaita oletuksia (mm. virtauksen turbulenttisuudesta tai akustisista

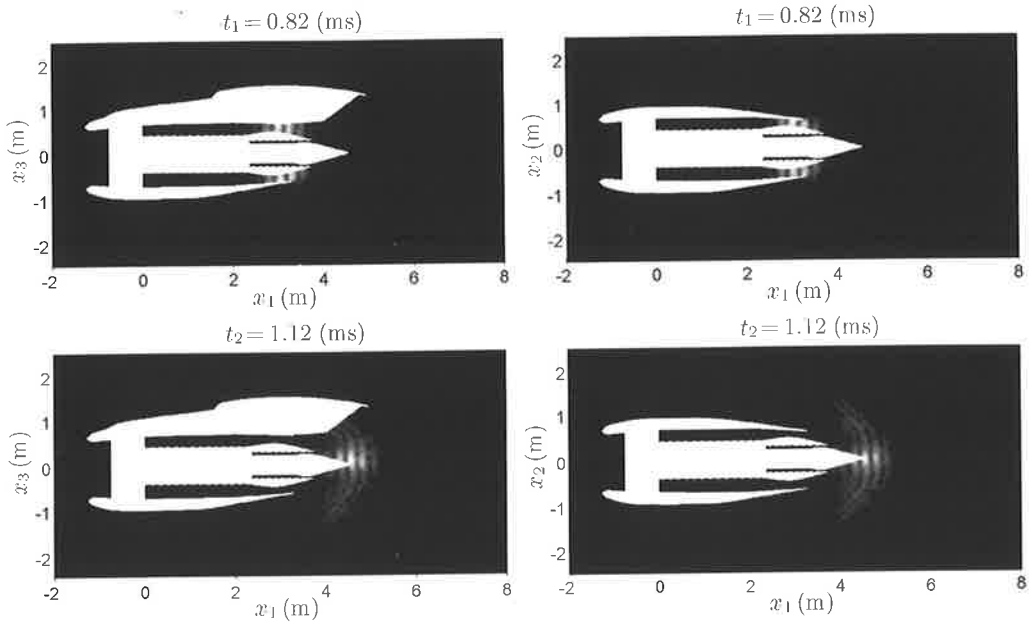

Kuva 6: Laskennasta saadun partikkelinopeuden $|u_1|$ arvot kahdessa tasossa kahdella eri ajanhetkellä. Tutkittava ajanhetki on esitetty kuvien otsikoissa.

reunaehdoista). Mallin tarkoituksena oli selvittää DG-menetelmän soveltuvuutta monimutkaisten virtausakustisten ongelmien simulointiin. Johtopäätöksenä voidaan todeta, että kyseisessä tapauksessa jo taustavirtauksen tarkkaa mallintamista voidaan pitää haasteellisena tehtävänä. Tällöin myös akustisen aallon kulkeutumismallia tulevat rajoittamaan virtausmallin epätarkkuudet.

VIITTEET

[1] R. J. Leveque, Finite Volume Methods for Hyperbolic Problems, Cambridge Texts in Applied Mathematics, 2002.

[2] M. Käser ja M. Dumbser, An arbitrary high-order discontinuous Galerkin method for elastic waves on unstructured meshes - I. The two-dimensional isotropic case with external source terms, Geophysical Journal International, **166**, 855–877, 2006.

[3] M. Dumbser ja M. Käser, An arbitrary high-order discontinuous Galerkin method for elastic waves on unstructured meshes - II. The three-dimensional isotropic case, Geophysical Journal International, **167**, 319–336, 2006.

[4] M. Käser, M. Dumbser, A highly accurate discontinuous Galerkin method for complex interfaces between solids ja moving fluids, Geophysics, **73**, 23–35, 2008.

[5] A.D. Pierce, Acoustics: An Introduction to Its Physical Principles and Applications, The Acoustical Society of America, 1981.

[6] W. Reed ja T. Hill, Triangular mesh methods for the neutron transport equation, Los Alamos National Laboratory, Los Alamos, New Mexico, USA, 1973.

[7] P. LeSaint ja P.A. Raviart, On a finite element method for solving the neutron transport equation, Mathematical Aspects of Finite Element Methods in Partial Differential Equations, Academic Press, New York, 89–123, 1974.

[8] C. Johnson ja J. Pitkäranta, An analysis of the discontinuous Galerkin method for a scalar hyperbolic equation, Mathematics of Computation, **46**, 1–26, 1986.

[9] G.R. Richter, An optimal-order error estimate for the discontinuous Galerkin method, Mathematics of Computations, **50**, 75–88, 1988.

[10] J. S. Hesthaven ja T. Warburton, Nodal high-order methods on unstructured grids I. Time-domain solution of Maxwell's equations, Journal of Computational Physics, **181**, 186–221, 2002.

[11] G. Cohen, X. Ferrieres ja P. Pernet, A spatial high-order hexahedral discontinuous Galerkin method to solve Maxwell's equations in time domain, Journal of Computational Physics, **217**, 340–363, 2006.

[12] B. Cockburn, F. Li ja C-W. Shu, Locally divergence-free discontinuous Galerkin methods for the Maxwell equations, Journal of Computational Physics, **194**, 588–610, 2004.

[13] C. M. Klaij, J. J. Q. van der Vegt ja H. van der Ven, Space-time discontinuous Galerkin method for the compressible Navier-Stokes equations, Journal of Computational Physics, **217**, 589–611, 2006.

[14] B. Cockburn, G. Kanschat ja D. Schötzau, A locally conservative LDG method for the incompressible Navier-Stokes equations, Mathematics of Computation, **74**, 1067–1095, 2005.

[15] T. Lähivaara ja T. Huttunen, A non-uniform basis order for the discontinuous Galerkin method of the acoustic ja elastic wave equations, Journal of Scientific Computing, *lähetetty*.

[16] J.S. Hesthaven ja T. Warburton, Nodal Discontinuous Galerkin Methods: Algorithms, Analysis, and Applications, Springer, 2007.

[17] R. Courant, K. Friedrichs ja H. Lewy, On the partial difference equations of mathematical physics, IBM Journal, 215–234, 1967.

[18] M.H. Carpenter ja C.A. Kennedy, Fourth-Order 2N-Storage Runge-Kutta Schemes, NASA-TM-109112, 1994.

[19] T. Lähivaara ja T. Huttunen, Optimal basis order for the discontinuous Galerkin method of the 3D dissipative wave equation with perfectly matched layer, Journal of Computational Physics, *lähetetty*.

MESH GENERATION OF HONEYCOMB MATERIAL

JOUNI FREUND

Department of Applied Mechanics
Helsinki University of Technology
P. O. Box 4300
FIN-02015 Espoo, FINLAND
e–mail: jouni.freund@tkk.fi

ABSTRACT

Simultaneous mesh and material property generation of a cellular texture in 2D domain is discussed. The description is based on a structural unit, a texture mapping, and an iteration giving a sheet of material. Solution domain and boundary condition colouring are obtained by clipping from the sheet. Implementation of the method makes use of a mesh tree data structure and simple insertion and deletion operations on the mesh tree. As an example, generation of a specimen for a numerical experiment on strength of heterogeneous material is discussed.

1. INTRODUCTION

Material and geometric modelling of the cell and growth ring structures [1] have significant roles in micromechanical simulations on wood. To mimic the heterogeneity of wood, a model may incorporate a statistical representation of geometrical and material parameters. As a consequence, simulation by the model gives answers to questions concerning the behaviour of population in statistical sense. As an example, the outcome can be a quantitative relationship between statistics of strength and that of the geometric features of the material.

A statistical study about material behaviour of wood, based purely on physical experiments, needs large sample sizes for reliable results. The experimental effort can be reduced, however, if simulations by a micromechanical model are first used to obtain a qualitative understanding of phenomena involved. This makes it possible to design clever experiments for verifying (or falsifying) hypotheses obtained from the predictions by the model. A virtual experiment on strength has design like a physical one: in order to study population characteristics –such as strength of a heterogeneous material–, experiment is repeated on a random sample from the population, and the population characteristics are estimated by using the results for the sample. The reliability of the estimate depends on the population characteristics and size of the sample. Control over the independent and dependent variables, loading, size and shape of the measuring domain etc. gives also additional freedom in design.

The aim of this work is to discuss generation of a material sample of virtual strength experiment. To be more specific, simultaneous mesh and material property generation of a wood-like material

having a hexagonal cell structure. Texture description of the material is adopted –with some modifications– from that of the regular and near-regular textures [2]. Without going into the details, a regular texture is something having a wallpaper-like, congruent appearance so that it can be generated by *mapping* from a single *structural unit* or a set of them. A near-regular texture has a similar appearance but with some statistical deviations in colour, shape, and size. If the variation of a physical property, like Young's modulus, is mapped to colour, the ideas of generating and analysing regular or near-regular textures find direct use in generating a honeycomb structure with a varying Young's modulus, say.

2. TEXTURE DESCRIPTION

The structural unit Δ of a planar texture description is here a triangle having attributes like colour, shape and size. Symbol Δ is used to indicate that the object contains, besides a geometrical information like vertex points defining shape and size, also non-geometrical information like colouring. The attributes are constants in a regular texture and follow some statistics in a near-regular texture. Subscript notation Δ_e will be used for an instance of triangle in the texture.

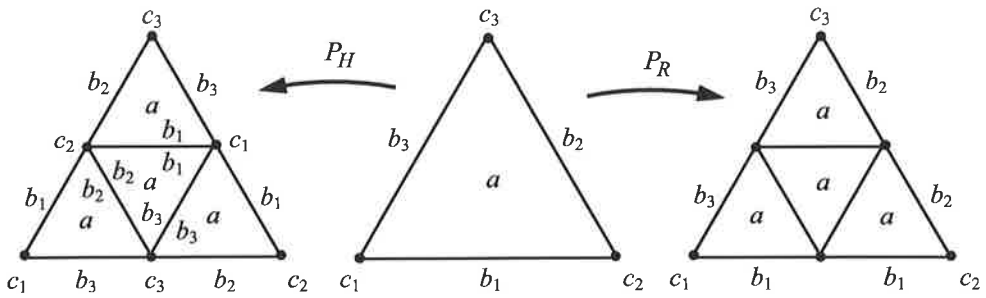

Figure 1: Examples of texture mappings: Refinement mapping P_R for preserving the texture and honeycomb mapping P_H for generating a hexagonal texture. A missing colour attribute is interpreted as transparency in graphical representations.

We discuss first mapping of the triangle colour a, the colours b_1, b_2, b_3 of the three edges, and colours c_1, c_2, c_3 of the vertex points (Fig.1). The vertex points of Δ are denoted by p_1, p_2, p_3, edges of Δ by $(p_1, p_2), (p_2, p_3), (p_3, p_1)$ and the triangle of Δ by (p_1, p_2, p_3). In the simultaneous texture and mesh generation for a finite element method, texture *mapping* ($n = 4$)

$$P : \Delta \rightarrow \{\Delta_1, \ldots, \Delta_n\} \tag{1}$$

is considered as a rule for generating the texture out of a single structural unit or a set of them by iteration: the first application of (1) gives a set 4 triangles, the second a set of 4^2 triangles, and so on, when applied to all the elements of the already generated set. Some examples of mappings, called honeycomb mapping P_H and refine mapping P_R, are illustrated in Fig.1. The former is used to generate hexagonal texture and the latter just to divide the triangles into smaller ones without affecting the texture itself. The mappings of Fig.1 are deterministic but one may as well use a stochastic mapping to produce near-regularity in colour. In what follows, a subscript is used to make difference between mappings of different properties.

The description above does not use any information about coordinates $p=(x,y)\in\mathbb{R}^2$ of the vertex points p_1, p_2, p_3. A separate coordinate mapping

$$X : p^3 \to p^6 \tag{2}$$

defines the coordinates of the points (Fig.1) and thereby geometrical attributes like size and shape. In the regular coordinate mapping $R(1/2)$, the positions of points p_1, p_2, p_3 are not changed, and points p_4, p_5, p_6 are placed at the midpoints of edges (p_1, p_2), (p_2, p_3), and (p_3, p_1), respectively. Hence shape is preserved but size is halved on application of $R(1/2)$. If the structural unit is triangle with the same length of all the edges, the outcome is a regular texture inside the initial triangle. The coordinate mapping is indicated by the second subscript of P. Hence, $P_{H,R(1/2)}$ denotes a honeycomb mapping with a regular position of the points.

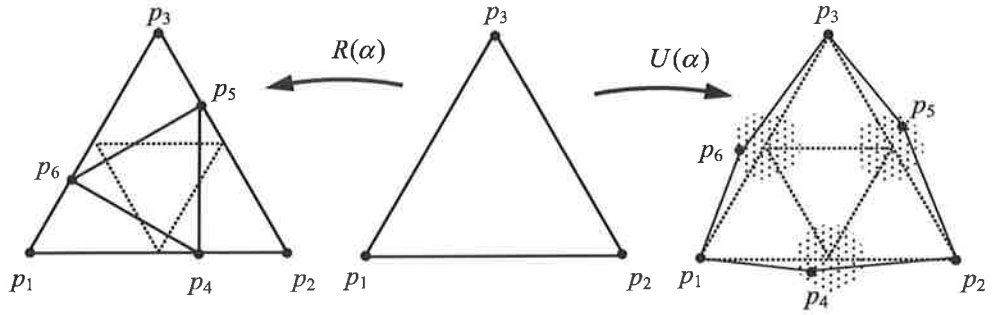

Figure 2: Examples of one-parameter coordinate mappings: $R(\alpha)$ $\alpha\in[0,1]$ interpolates the position between the end-points, $U(\alpha)$ $\alpha\in[0,1]$ produces a random offset from the regular positions.

Regular mapping $R(1/2)$ is a particular case of the one parameter mapping $R(\alpha)$ $\alpha\in[0,1]$

$$R(\alpha)=(p_1,\ p_2,\ p_3,\ \alpha p_1+(1-\alpha)p_2,\ \alpha p_2+(1-\alpha)p_3,\ \alpha p_3+(1-\alpha)p_1). \tag{3}$$

Although the mapping above gives a quite complicated texture whenever $\alpha\neq 1/2$, it is deterministic and application of the recipe in the texture generation gives always the same result. When the information about the texture is statistical, the mapping may use random sampling from some distribution. Repeated application of the recipe gives then near-regular textures which coincide in statistics. An example of a one-parameter mapping $U(\alpha)$ $\alpha\in[0,1]$ of stochastic type is

$$U(\alpha)=(p_1,\ p_2,\ p_3,\ \frac{p_1+p_2}{2}+\alpha p_{21},\ \frac{p_2+p_3}{2}+\alpha p_{32},\ \frac{p_3+p_1}{2}+\alpha p_{13}), \tag{4}$$

in which p_{ij} denotes a random offset from the uniform distribution on a circular domain of radius $|p_j-p_i|$. By a carefully chosen structural unit and mapping for colour, shape, and size– it is possible to generate textures showing close resemblance to those seen in wood cell structure.

A material region obtained by a restricted number of iterations on (1) is called as a material sheet. The sheet recipe consists of description of the initial sheet Δ or $\{\Delta_1,\ldots,\Delta_n\}$ and a sequence of

mappings used in generation of the texture. This makes it possible to specify the recipe of a sheet in a compact manner. Some sheets are shown in Fig.3 (only textural information). The highly regular texture $P_H^5\Delta$ is obtained by five iterations on the honeycomb mapping. The recipe $P_{H,R(2/5)}^5\Delta$ gives a deterministic texture with variations in size and shape. Texture $P_C P_H^5\Delta$ is regular in shape and size, but colouring of triangles follows the uniform distribution on the gray-scale. Finally, texture $P_{C,U(1/10)}P_{H,U(1/10)}^5\Delta$ is near-regular with respect to shape, size and colour. In all the cases, the structural unit Δ is a white triangle having one black and two white edges of the same length and transparent points.

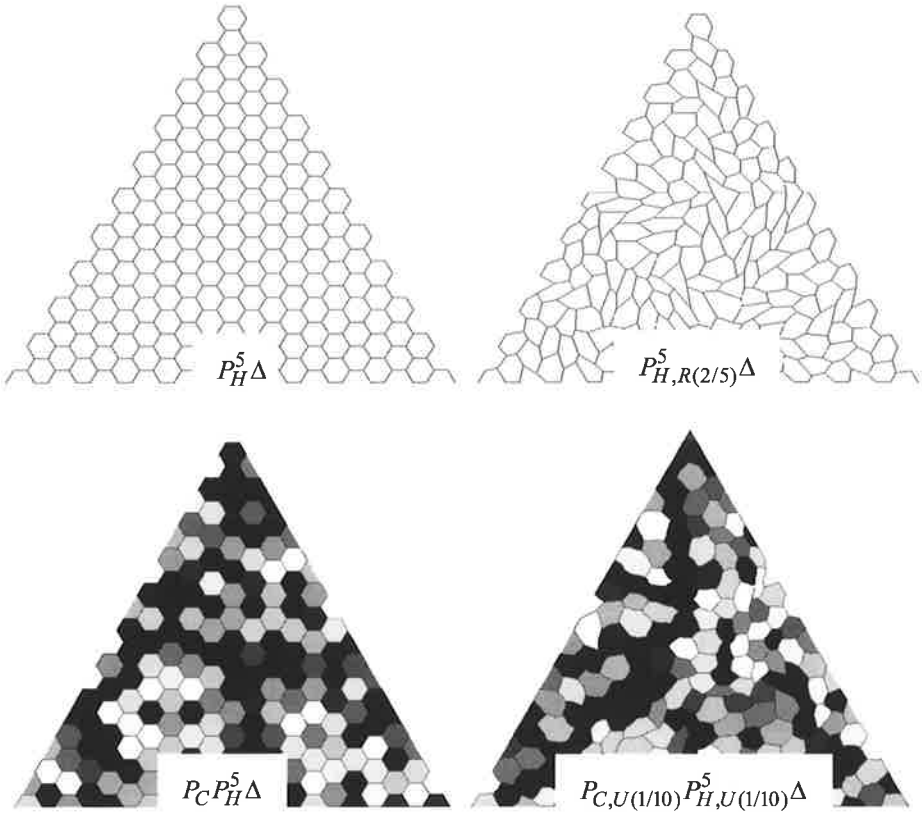

Figure 3: Examples of material sheets.

After the generation of texture, additional iterations on the refine mapping P_R produce smaller triangles without effect on the texture itself. Therefore, the mesh can be adopted to match e.g. a triangle size criterion. This is important in adaptive solution methods striving, say to more or less uniform distribution of error indicator of the numerical solution by the triangle size adaptation. Also generation of a solution domain may require the triangle size adaptation.

3. SOLUTION DOMAIN CLIPPING

Texture with it's attributes, interpreted as colours in a graphical representation, can be taken as a material description. Description of a boundary value problem means also specification of the

solution domain Ω and assignment of a problem dependent colouring to the parts $\partial\Omega_i$ having different boundary conditions (discussion of equations of the micromechanical model is outside the scope of this work). In what follows, the domains occupied by the material sheet and triangle Δ_e are denoted by Ω° and Ω_e, respectively.

The solution domain $\Omega \subset \Omega^\circ$ is obtained by removing all triangles outside the domain from the sheet. To be specific, triangle Δ_e is removed if $\Omega_e \subset \Omega^\circ - \Omega$ (set subtraction). In practice, the domain outside the solution domain is represented in the form

$$\Omega^\circ - \Omega = \Omega_1 \cup \Omega_2 \ldots \cup \Omega_n \tag{5}$$

and triangle Δ_e is removed whenever $\Omega_e \subset \Omega_i$. On removal, the colour of edges of the adjacent triangles (nearby triangles later) is changed to indicate a boundary condition associated with Ω_i.

As a sheet may contain triangles partly inside and partly outside the solution domain, iteration on refine mapping P_R, followed by the removal of descendants, is applied until wanted geometrical precision. Fig.4 shows a solution domain with boundary condition colouring generated in this manner. The clipping of the hole of radius R at (x_c, y_c) is performed with

$$\Omega_1 = \{(x,y) : (x-x_c)^2 + (y-y_c)^2 < R^2\}. \tag{6}$$

in equation (5). The red colour on $\partial\Omega_1$ indicates some, say zero-traction, boundary condition. Additional insertion with refine mapping P_R at the hole in Fig.4 (right) does not affect the texture, but generates smaller triangles and improves the geometrical precision.

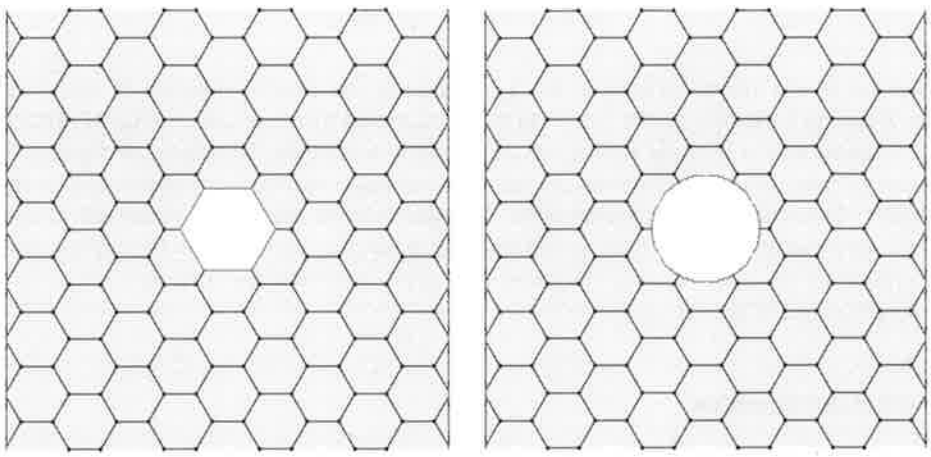

Figure 4: Solution domain with the boundary condition colouring. Clipping from a honeycomb sheet with (right) and without refinement (left).

4. MESH TREE STRUCTURE

An ordered tree is used for representing the texture and mesh structures [3]: The tree consists of triangles Δ_e and structuring information in the form of links. The triangles generated by $P\Delta_e$ are called (directs) *descendants* $S_e = \{\Delta_f, \ldots, \Delta_g\}$ of Δ_e. The first triangle of the mesh tree is called

the root and the triangles, having no *descendants*, leave triangles of the tree. The root does not have an *ancestor*. If the property of triangle Δ, called level, is given by l, the level of its direct descendant is l+1. A tree traversal is an operation on all triangles of the tree in some order called the visiting order. The algorithm for generating the material sheet and clipping of the solution domain is based on *insertion* and *deletion* tree traversal operations. The operations visit first root, then it's descendants following their ordering, and continue in the same manner.

Node insertion operation I is a tree traversal with the following main effects (the empty set will be denoted by $\{\}$ and subscripts e, f, g refer to generic triangles of the tree)

$$I\{\Delta_e \ldots \Delta_g\} = \{I\Delta_e \ldots I\Delta_g\}, \tag{7}$$

$$S_e \neq \{\}: \quad I\Delta_e = IS_e, \tag{8}$$

$$S_e = \{\}: \quad S_e = P\Delta_e. \tag{9}$$

If the starting point is root, texture mapping P is applied to all the leaves of the tree. The starting point of insertion can also be a set of triangles. Deletion operation D is also a tree traversal, with the following main effects

$$D\{\Delta_e \ldots \Delta_g\} = \{D\Delta_e \ldots D\Delta_g\}, \tag{10}$$

$$S_e \neq \{\}: \quad D\Delta_e = DS_e, \tag{11}$$

$$S_e = \{\}: \quad S_f = S_f - \Delta_e, \tag{12}$$

in which Δ_f is the (direct) ancestor of Δ_e. Omitting the details, deletion is the reverse to insertion. Deleting a triangle means that it cannot be accessed by a tree traversal i.e. it is not part of the tree. Therefore, if a triangle having no descendants is deleted, branching of the tree in that direction is no more possible. However, deletion of a triangle having descendants can be reverted by insertion. This feature is understandable through the tree metaphor. From the geometrical viewpoint, insertion at leave Δ_e means dividing the region Ω_e occupied by the triangle into four smaller regions in a regular manner. Deletion operates in the opposite direction and groups four small triangles into a single triangle.

4.1 Details of the algorithm

The set of nearby triangles $\{\Delta_k, \Delta_l, \Delta_m\}$ of Δ_e are those of the mesh tree having the minimum positive level distance to Δ_e and some edge or part of it in common (Fig.5). The point and nearby triangle update algorithm – needed on insertion – assumes a tree with the point and nearby triangle information prior to insertion, but does not require any information about coordinates of the points. As the mesh tree is the outcome of iteration on insertion operation, the point and nearby triangle information is generated during the build of the tree from the (trivial) information given at the root.

On insertion, the vertex points of Δ_e are inherited and the remaining points, if they exist, are chosen to coincide with those of the nearby triangles. In the example of Fig.5, nearby triangle Δ_l

has no descendants and therefore point p on edge (p_2, p_3) does not belong to any other triangle. Triangle Δ_k has descendants, and point p_4 on edge (p_1, p_2) is known to belong to some triangle already. The algorithm for finding the point is based on the edges of descendants of Δ_k. This set contains only one pair of type $\{(p_1, p), (p_2, p)\}$. Therefore, point p_4 on edge (p_1, p_2) is p. Descendants of Δ_e inherit first the nearby triangles as shown in Fig.5. As triangle Δ_l has no descendants, the nearby element of the descendant of Δ_e at edge (p_2, p_5) is Δ_l. As Δ_k has descendants, the positive level distance to descendants of Δ_e are not minimized by Δ_k. The algorithm for finding the right descendant of Δ_k is based on the identical point representations of the edges of nearby triangles having the same levels.

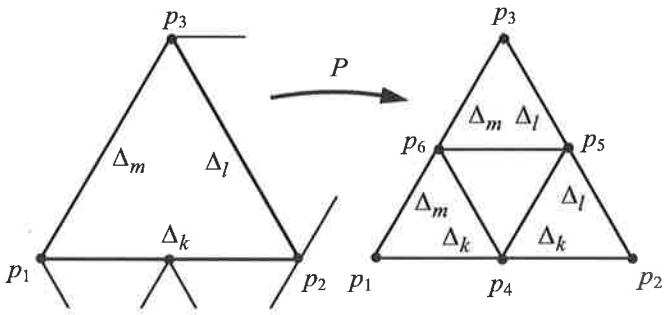

Figure 5: Nearby triangle update on insertion at Δ_e.

On deletion, leaves of the tree are not actually deleted but rather made invisible for a tree traversal operation. Insertion on the same node, assuming that the node is not a leave, makes then branch again visible. The mechanism allows fast adaptation of the mesh to match the needs of a numerical solution method.

5. EXAMPLE; MATERIAL ELEMENT OF STRENGTH EXPERIMENT

As the length to thickness ratio of wood-cells is large, the effect of heterogeneity on strength can be studied by using a 2D model. In a simple micromechanical model [4], the walls of the cells are taken as beams with some statistics on thickness, Young's modulus, length, and strength. In the texture representation, heterogeneity of the material produces near-regularity in colour, shape and size.

A two specimen sample of strength experiment is shown in Fig.6. The underlying population is characterized by constant values of material parameters and uniform distribution of the hexagonal cell shapes. The blue colour near the specimen edges indicates infinite strength. Otherwise the material properties of the blue and black beams are the same. This is quite essential as the constant loading acting on the edges tend to cause artefacts in stress distribution near the edges and thereby failure initiation whose location is not evenly distributed in the measuring domain. Zero traction condition seems not to be an exception in the rule. The computational mesh, consisting of triangles, is refined near the left and right edges without affecting the texture itself.

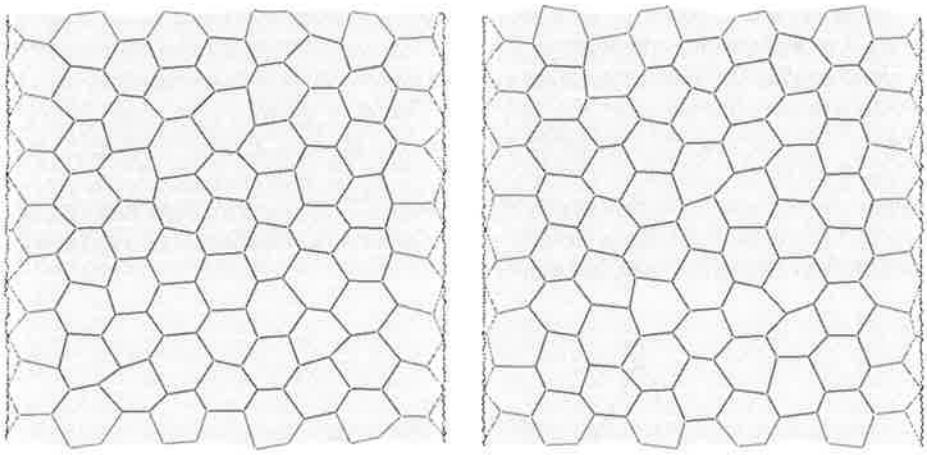

Figure 6: Examples of specimen chosen randomly from a population having uniform distribution in the shape of hexagons.

6. CONCLUDING REMARKS

In the texture and mesh generation of a honeycomb in plane, the structural unit was chosen to be triangle. The algorithm works also with lines, quadrilaterals, and tetrahedrons with minor modifications.

This work is part of the Virtual Wood task of E-wood – Energy Efficient Wood Processing and Machining – project. To aim of the task is to predict the strength statistics of wood by virtual experiments on a micromechanical model.

REFERENCES

[1] L. J. Gibson and M. F. Ashby, Cellular solids: Structure and properties, Pergamon Press, Oxford, Second edition, 1988.

[2] W. Lin and Y. Liu, IEEE Trans. Pattern Analysis and Machine Intelligence, 29, 777–792, 2007.

[3] N. Wirth, Algorithms + Data Structures = Programs, Prentice Hall, 1976.

[4] L. Mishnaevsky Jr. and H. Qing, Micromechanical modelling of mechanical behaviour and strength of wood: State-of-the-art review, Comp. Mater. Sci., 44, 363–370, 2008.

MULTI-FRACTURE OF 2D BEAMS MODELLED WITH COMBINED FINITE-DISCRETE ELEMENT METHOD

JANI PAAVILAINEN, JUKKA TUHKURI AND ARTTU POLOJÄRVI

Department of Applied Mechanics
Helsinki University of Technology
P. O. Box 4300
02015 TKK, FINLAND
e-mail: jani.paavilainen@tkk.fi

ABSTRACT

This paper presents a 2D combined finite-discrete element method to model the multi-fracture of beams and an application of the method to an ice-structure interaction problem. In the method, elastic beams and their fracture are modelled according to finite element method by using non-linear Timoshenko beam elements and cohesive crack model. Additionally, the beam elements are used to tie the discrete elements together. The contact forces between the colliding beams are calculated by using the discrete element method. The resulting equations are solved with explicit time integration. The presented method is applied to model the failure process of a floating ice beam against an inclined structure.

INTRODUCTION

A wide range of problems of mechanics involve multi-fracture phenomena. Such problems are characterized by transition from a continuous to a discontinuous media; a small number of continuous regions divide into a myriad of smaller regions through fracture processes to form a combination of continuous and discontinuous media. To be able to simulate such a process, both the continuous and the discontinuous phenomena must be modelled in addition to modelling of fracture. Examples of problems involving multi-fracture phenomena are concrete structural failure, rock blasting and ice-structure interaction.

Number of different methods are used for numerical modelling of continuous and discontinuous media. One way of modelling problems involving discontinuous media is the discrete element method (DEM). It is a technique for modelling the nonlinear dynamics of systems consisting of granular and particulate materials [1]. For modelling the continuous media, the finite element method (FEM) has proven to be advantageous. Thus, for modelling multi-fracturing solids it is beneficial to combine the finite and discrete element approaches as is previously done in [2, 3, 4], for instance.

This paper presents a 2D combined finite-discrete element method to model multi-fracture of beams and an application of the method to an ice-structure interaction problem. In the method, elastic beams and their fracture are modelled according to finite element method by using non-linear Timoshenko beam elements (see e.g. [5]) and cohesive crack model [6]. Additionally, the beam elements are used to tie the discrete elements together. The contact forces between the colliding beams

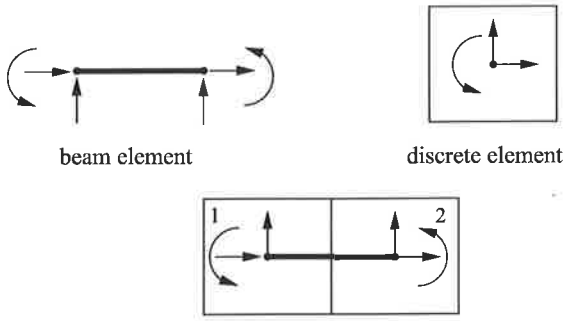

Figure 1: A beam element, a discrete element and their degrees of freedom. Combining two discrete elements with a beam element.

are calculated by using the discrete element method [1]. The resulting equations are solved with explicit time integration scheme. The method is applied to model the ice pile-up process against an inclined plate.

COMBINED FINITE-DISCRETE ELEMENT METHOD

The presented method can be divided into three main parts: i) continuum, ii) failure and iii) contact model. The forces obtained from these three parts are used in Newtons equations of motion, which are solved with explicit time integration scheme.

Here the three main parts are briefly presented. A more comprehensive presentation of the method can be found in [7].

Continuum and failure models

The continuum is modelled according to finite element method by using non-linear Timoshenko beam elements. A two dimensional beam element can be used to combine two adjacent discrete elements together as presented in Figure 1. A beam element node and the centroid of a discrete element have the same degrees of freedom, two displacements and a rotation. Furthermore, a beam element unite with a line connecting the centroids of two combined discrete elements. The internal forces of a beam element can therefore be superposed to the discrete element forces.

The basic kinematic assumption of the Timoshenko beam state that the cross sections remain plane but not necessarily normal to the mid surface during deformation. In addition, small strain assumption, large displacements and a viscous damping model are utilized in the model.

From the kinematic relations of the beam it follows that the only nonzero strains of the beam are the axial strain ϵ_{XX} and the shear strain $\epsilon_{XY} + \epsilon_{YX} = 2\epsilon_{XY}$. These are combined to a strain vector

$$\mathbf{e} = \begin{bmatrix} e_1 \\ e_2 \end{bmatrix} = \begin{bmatrix} \epsilon_{XX} \\ 2\epsilon_{XY} \end{bmatrix} = \begin{bmatrix} \varepsilon - Y\kappa \\ \gamma \end{bmatrix}, \tag{1}$$

where Y gives the distance form the neutral axis of the beam and the three strain quantities $\mathbf{h} = \begin{bmatrix} \varepsilon & \gamma & \kappa \end{bmatrix}^T$ characterize axial strains, shear strains and curvatures, respectively.

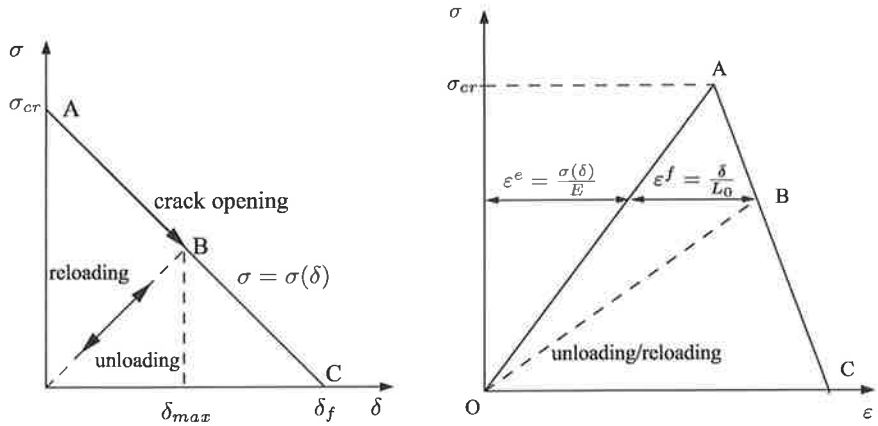

Figure 2: a) Linear softening function, $\sigma = \sigma(\delta)$ and the crack opening, unloading and reloading situations. b) Cohesive constitutive model with elastic ε^e and inelastic ε^f strains. In a) and b), the points A, B and C indicate the same phase in the fracturing process.

The material of the beam is assumed to be homogeneous and isotropic. Before fracture, the material behaves as linear elastic and the linear constitutive equation

$$\mathbf{s} = \begin{bmatrix} \sigma_x \\ \tau \end{bmatrix} = \begin{bmatrix} E & 0 \\ 0 & G \end{bmatrix} \begin{bmatrix} e_1 \\ e_2 \end{bmatrix} = \mathbf{Ce} \tag{2}$$

is used for defining the stresses. In Equation (2), E is the Young's modulus, G is the shear modulus and σ_x and τ are the normal and shear stresses. After fracture criterion $F = 0$ is met the above constitutive equation changes and the stresses are defined according to the cohesive crack model.

The main assumption of the cohesive crack model is that the stress transferred through the cohesive crack is a function of the crack opening displacement δ, i.e. $\sigma = \sigma(\delta)$. This softening function is considered as a material property. In the method presented, linear softening function, as shown in Figure 2a, is used. This function defines the stresses after the fracture initiation.

The use of the Timoshenko beam model enables an introduction of such a fracture criterion F that takes into account both normal and shear stresses. Adapting from Schreyer et al. [8], the fracture criterion is chosen to be

$$F(\sigma, \delta_{max}) = \sigma - \sigma_{cr}(1 - \frac{\delta_{max}}{\delta_f}) = 0\,. \tag{3}$$

where σ is the effective stress defined by

$$\sigma = \sigma_x + \frac{\sigma_{cr}}{\tau_{cr}^2}\tau^2\,, \tag{4}$$

δ_{max} is an increasing variable which keeps record of the maximum crack opening displacement reached, δ_f is the critical crack opening displacement, σ_{cr} is the critical normal stress and τ_{cr} is the critical shear stress. It should be noted that no compressive failure is included in the criterion.

The fracture criterion $F \leq 0$ indicates an admissible stress state. If $F < 0$, the material is intact or the crack is not propagating. The state $F = 0$ indicates the onset of fracture or unloading. The stress state in which $F > 0$ is not admissible. The fracture surface $F(\sigma, \delta_{max}) = 0$ is plotted with two different values of δ_{max} in Figure 3.

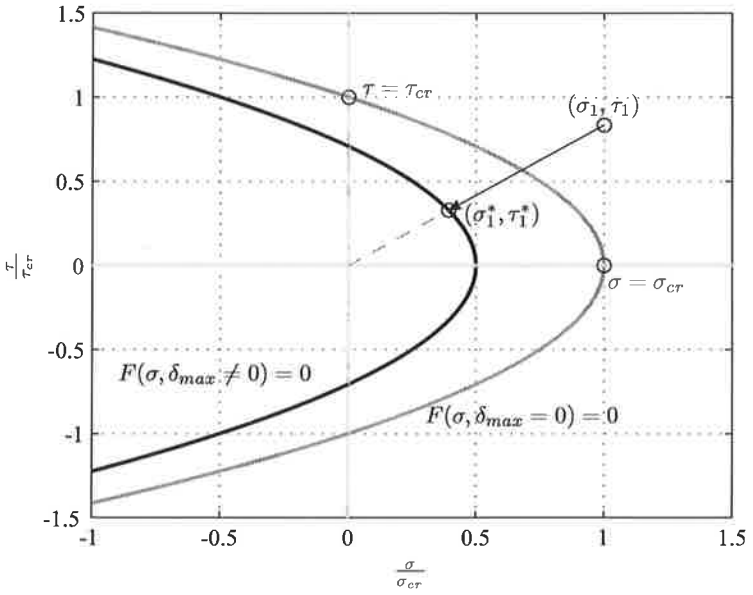

Figure 3: a) Fracture surface evolution when the crack is opening. Fracture criterion with different values of δ_{max} and a return mapping from point (σ_1, τ_1) to fracture surface $F(\sigma, \delta_{max} \neq 0) = 0$.

To determine weather the stress state is admissible or not, a trial stress state is computed. If the trial stress state is such that $F > 0$, a crack is propagating and a return mapping to the fracture surface $F = 0$ has to be made. This is illustrated in Figure 3. From a point (σ_1, τ_1) a return mapping is made to the new fracture surface $F(\sigma, \delta_{max} \neq 0) = 0$ to a point (σ_1^*, τ_1^*). The return mapping is done in such a way that the relation between the normal and shear stresses stays constant, i.e. $\frac{\sigma_1}{\tau_1} = \frac{\sigma_1^*}{\tau_1^*}$. A similar return-mapping procedure is presented in [9] for problems with plasticity.

To define the new fracture surface $F = 0$, the values for σ and δ_{max} has to be determined. To determine these values, the cohesive crack model is used. The crack is opening when moving between points A and C on the stress–strain curve of Figure 2b. Then the cohesive stress is defined by the softening function

$$\sigma = \sigma(\delta) = \sigma_{cr}(1 - \frac{\delta}{\delta_f}). \tag{5}$$

In the crack opening situation, the maximum reached crack opening displacement is equal to crack opening displacement i.e. $\delta_{max} = \delta$. Thus, in this situation the fracture criterion F in Equation (3) needs to be updated.

If a crack has formed and the stress state is such that $F < 0$ and $\sigma_x \geq 0$, the unloading or reloading case is active. This is shown in Figure 2b with a dashed line BO. In this case, the cohesive stress is defined by

$$\sigma(\delta) = \sigma_{cr}(\frac{\delta}{\delta_{max}} - \frac{\delta}{\delta_f}). \tag{6}$$

In this case δ_{max} has a constant value defined in the crack opening phase. In the case of crack closure, i.e. $F < 0$ and $\sigma_x < 0$, the stress σ is evaluated as if the material would be intact and the crack opening displacement is equal to zero, $\delta = 0$. Again, the δ_{max} has a constant value as in the cases of unloading and reloading. In summary, the value for δ_{max} changes only in the crack opening phase and it is an increasing function to make the failure process irreversible.

In process of defining the new fracture surface $F = 0$ as presented above, the stresses σ_x and τ are determined in the case of fracture. From stresses σ_x and τ, either defined by linear constitutive Equation (2) or by cohesive crack model, the stress resultants N, Q and M are obtained. They represent axial force, shear force and bending moment, respectively. The viscous forces N_d, Q_d and M_d that present axial damping, shear damping and damping moment are related to strain rates $\dot{\varepsilon}$, $\dot{\gamma}$ and $\dot{\kappa}$. The forces mentioned above are collected to the stress resultant vector

$$\mathbf{p}^T = [N + N_d \quad Q + Q_d \quad M + M_d]. \tag{7}$$

Variation of the strain energy, using the strain-displacement relation $\delta\mathbf{h} = \mathbf{B}\,\delta\mathbf{u}$ and the stress resultant vector, leads to the internal forces $\mathbf{f}_{int}$ for a beam element

$$\mathbf{f}_{int} = \int_{L_0} \mathbf{B}^T \mathbf{p}\, \mathrm{d}X \ , \tag{8}$$

where L_0 is the initial length of the beam element and $\mathbf{B}$ is the kinematic matrix. This expression for the internal forces is then used in the equations of motion.

Contact model and time stepping

Failure of beams results in creation of smaller beams which at later stages of the simulation can collide with other beams in the model. These interactions between discrete beams are simulated by using the discrete element method.

In addition to finite elements, interacting beams are also composed of one or more discrete elements. The contact detection and the calculation of the contact forces are handled by using these discrete elements. The contact detection is based on the algorithm presented by Munjiza and Andrews [10] and the forces between contacting discrete elements are calculated with an elastic-viscous-plastic normal force model and incremental Mohr-Coulomb tangential force model as described by Hopkins [11].

The elastic contact forces are based on the overlap area and the rate of change of the overlap area of contacting elements. Inelasticity is modelled by using a plastic limit for the material. The total normal force of the contact is determined by equation

$$\mathbf{f}_n = \min\{\mathbf{f}_{ne} + \mathbf{f}_{nv}, \mathbf{f}_p\} \ , \tag{9}$$

where $\mathbf{f}_{ne}$ is the elastic force, $\mathbf{f}_{nv}$ is the viscous force and $\mathbf{f}_p$ is the plastic limit force of the contact. The tangential force $\mathbf{f}_t$ is obtained from equation

$$\mathbf{f}_t = \min\{\mathbf{f}_{te},\ \mu\mathbf{f}_n\} \ , \tag{10}$$

where $\mathbf{f}_{te}$ is the incremental elastic tangential force of the contact and μ is the friction coefficient between the contacting elements. The upper limit for $\mathbf{f}_t$ is thus achieved by using Mohr-Coulomb model. The moment acting on each of the contacting elements is

$$\mathbf{m} = \mathbf{r} \times \mathbf{f}_{tot} \ , \tag{11}$$

where $\mathbf{r}$ is the vector pointing from the centroid of an element to the centroid of the overlap area and $\mathbf{f}_{tot}$ is the sum of tangential and normal forces of the contact. These forces and the moment are then used in the equations of motion.

For presenting the equations of motion, a vector notation $\mathbf{x}$ is introduced. It contains the positions x_i, y_i and rotations θ_i of all the N discrete elements in the system, ordered in the following manner

$$\mathbf{x} = \begin{bmatrix} x_1 & y_1 & \theta_1 & \dots & x_N & y_N & \theta_N \end{bmatrix}^T. \tag{12}$$

With the previous notation the equations of motion for the system can be presented in the form

$$\mathbf{M}\ddot{\mathbf{x}} = \mathbf{f}_{int} + \mathbf{f}_{col} + \mathbf{f}_{ext}, \tag{13}$$

where $\mathbf{M}$ is the diagonal mass matrix containing masses and moments of inertia of the discrete elements, $\mathbf{f}_{int}$ is defined by Equation (8), $\mathbf{f}_{col}$ is a vector containing forces and moments from the collisions and $\mathbf{f}_{ext}$ is a vector of external forces. The $\ddot{\mathbf{x}}$ denotes the second time derivative of $\mathbf{x}$.

In the proposed method, the equations of motion (13) are solved with explicit Newmark time-integration scheme with parameters $\beta = 0$ and $\gamma = \frac{1}{2}$. With these choices, the scheme is also known as the central difference method:

$$\mathbf{x}_{k+1} = \mathbf{x}_k + \Delta t \dot{\mathbf{x}}_k + \frac{\Delta t^2}{2}\ddot{\mathbf{x}}_k \tag{14}$$

$$\dot{\mathbf{x}}_{k+1} = \dot{\mathbf{x}}_k + \frac{\Delta t}{2}(\ddot{\mathbf{x}}_k + \ddot{\mathbf{x}}_{k+1}). \tag{15}$$

NUMERICAL EXAMPLE

The failure process of a floating ice sheet against an inclined structure was modelled. The process of ice sheet failure is described qualitatively based on snapshots of the simulation and quantitatively based on the force exerted on the structure by the ice sheet. In addition, comparison to laboratory scale experimental data and to an analytical model was done.

In the simulation, an ice beam was pushed at its left end with a constant velocity of 0.02 m/s against an infinitely rigid structure, as shown in Figure 4. Both ends of the structure were supported and the inclination angle was 50°. For the parameters used in the simulation see Table 1.

Figure 4 shows snapshots of the simulation and Figure 5 gives the horizontal force acting on the inclined structure as a function of the length of pushed ice L. Figure 5 shows also the force obtained in the laboratory experiments conducted by Saarinen [12]. For comparison of the forces and the stage of simulation, the subfigures of Figure 4 are pointed out in the $F(L)$ graph in Figure 5 with arrows.

Snapshots of the Figure 4 show the ice ridging process in short. Initially, the ice sheet failed against the inclined structure by bending (Figure 4a) and started to form a pile (Figure 4b) which grew both vertically and horizontally. After a pile was formed, the ice sheet either slided on top of the pile to the inclined structure and rode-up along the plate (Figure 4c) or failed against the pile (Figure 4e). Figures 4c and 4d illustrate a collapse of the pile. A collapse is a process where the pile fails under the load from the ice sheet ride-up or pile-up in front of the structure. Collapse resulted a movement of the pile down and left and a decrease of the horizontal force.

The cycle, growth of the pile against the plate and collapse of the pile, occurred several times during the simulation. In the simulation these collapses of the rubble pile caused the force to drop to zero as the contact between the sheet and the structure was lost. This is evident from the $F(L)$ graph. Another phenomenon observed in the simulations was a clockwise rotational motion of the rubble pile. Close the end of simulation, Figure 4f, the number of discrete elements was 683.

These qualitative results agree well with the results obtained in the laboratory tests conducted by Timco [13] and Saarinen [12]. Especially, Timco [13] has described the ridging process in his paper

Table 1: Parameters used in the simulation and parameters measured during the laboratory experiments [12].

	Parameter	Simulation	Experiments
Discrete elements	thickness [m], h	0.045	0.045 – 0.052
	width [m]	0.045	-
Intact ice	Young's modulus [MPa], E_i	70.0	14 – 90
	Poisson ratio, ν_i	0.3	-
	density [kg m^{-3}], ρ_i	930	930
	tensional strength [kPa], σ_{cr}	50.0	30 – 56
	shear strength [kPa], τ_{cr}	50.0	-
	critical crack opening disp. [mm], δ_f	0.725	-
	internal damping [kPa s], $c_{i,int}$	23.0	-
	ice sheet velocity [mm/s], v_i	20.0	10.9
DEM contact	normal stiffness [MPa], $k_{ne} = E_i$	70.0	14 – 90
	tangential stiffness [MPa], k_{te}	27.0	-
	viscous damping [kPa s], k_{nv}	23.0	-
	plastic limit [kPa], σ_p	50.0	15 – 40
	ice–ice friction coefficient, μ_i	0.5	0.32 – 0.36
	ice–ice friction coefficient (under water), μ_{is}	0.5	-
	ice–wall friction coefficient, μ_{iW}	0.07	0.07, 0.35
	ice–wall friction coefficient (under water), μ_{iWs}	0.07	-
Water	density [kg m^{-3}], ρ_w	1000	1000
Wall	inclination angle [°], α	50	50, 65, 80
	width [m]	-	4.6
Simulation	time step [s], Δt	$2.0 \cdot 10^{-5}$	-

as: "On several occasions, the ice would fail in a bending or flexural-type failure. The advancing ice sheet would usually ride up over the ice rubble and fail as it pushed against the sail of the rubble close to the structure." Further he writes: "Large-scale buckling was a frequent mode, especially in the early part of the test when there was little rubble in front of the structure. Ice crushing was also observed to occur, especially in small local crushing events." Timco also observed the rotational motion of the rubble pile during his experiments.

From the $F(L)$ graphs of Figure 5 it is noticed that the simulation is able to capture the force response of the pile-up and collapse cycle reasonably well. However, the simulated force drops to zero due to the loss of contact between the pile and the inclined structure after the collapse. This is assumed to be caused by the 2D nature of the simulations and is thus not observed during the experiments. Also the force peaks of the simulation are a bit higher. Nevertheless, the average forces of 310 and 370 N/m obtained from the $F(L)$ graphs of simulation and experiment, respectively, are in fair agreement.

The ice force obtained from the simulation can further be compared with results from analytical methods. A solution to the horizontal ice force F_h on a sloping-sided structure given by [14] divides the force into a bending failure force F_b and an ice ride-up F_r force

$$F_h = F_b + F_r = \sigma_b \left(\frac{\rho_w g h^5}{E}\right)^{1/4} \left(0.68 \frac{\sin\alpha + \mu_{iW}\cos\alpha}{\cos\alpha - \mu_{iW}\sin\alpha}\right) + z h \rho_i g \left(\sin\alpha + \mu_{iW}\cos\alpha\right) \left(\frac{\sin\alpha + \mu_{iW}\cos\alpha}{\cos\alpha - \mu_{iW}\sin\alpha} + \frac{\cos\alpha}{\sin\alpha}\right), \quad (16)$$

where z is the height of ride-up and the other symbols are as explained in Table 1. At the simulation

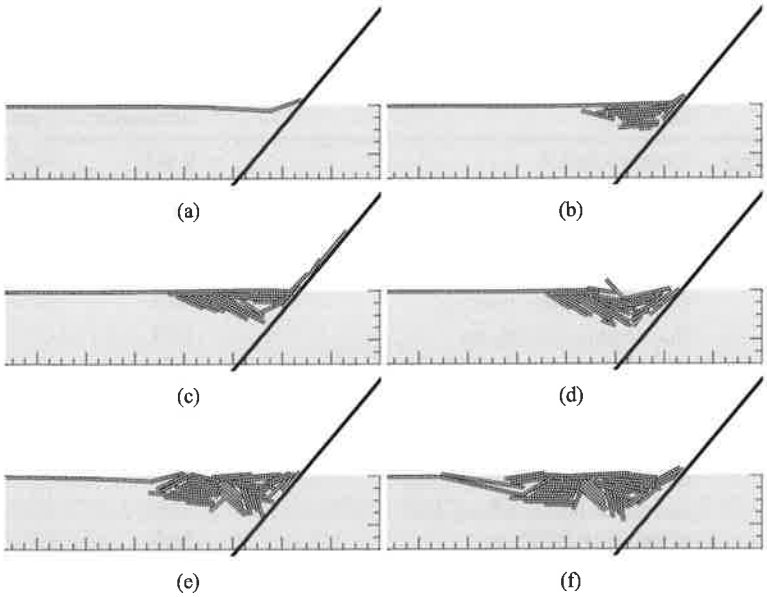

Figure 4: Snapshots of the ice-structure interaction simulation. Ice (white), water (gray) and structure (black).

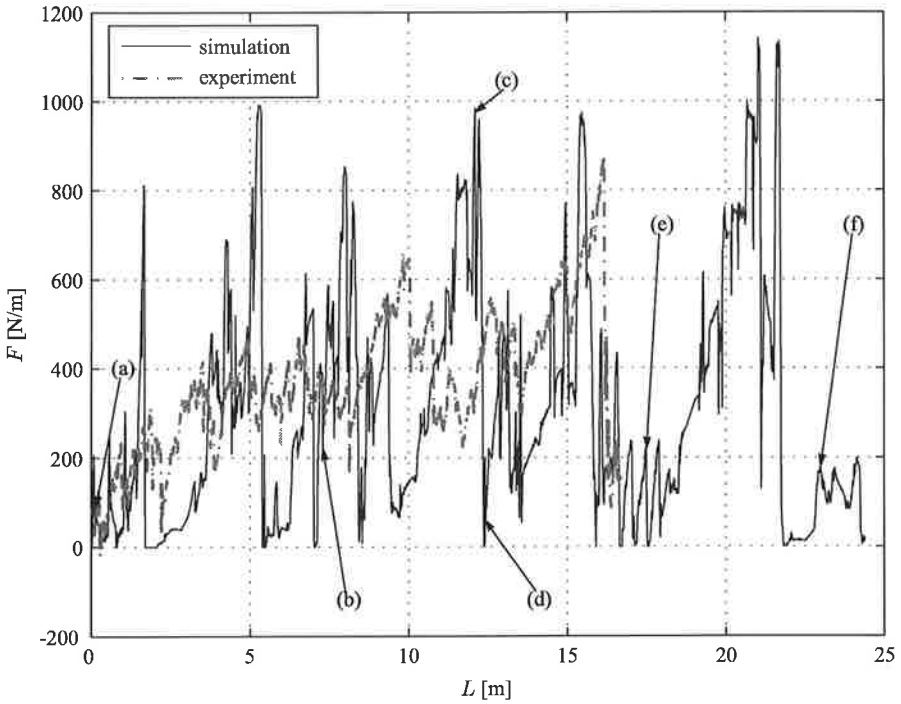

Figure 5: Horizontal force F acting on the structure as a function of the length of the pushed ice L as obtained from the simulation and experiment. The letters refer to Figure 4.

event shown in Figure 4c, $z = 1.0$ m and the simulated force was about 970 N/m. By using the values given in Table 1 and $z = 1.0$ m, a force $F_h = 843$ N/m is obtained by Equation (16).

CONCLUSIONS

A 2D combined finite-discrete element method for modelling the multi-fracture of beams was presented. In the method, elastic beams and their fracture was modelled according to finite element method by using non-linear Timoshenko beam elements and cohesive crack model. Furthermore, the beam elements tied discrete elements together. The contact forces between colliding beams were calculated with discrete elements using an elastic-viscous-plastic normal and incremental Mohr-Coulomb tangential force models. The resulting equations of motion were solved with central difference method.

The presented method was applied to model ice pile-up process. The process of ice sheet failure was described qualitatively based on the snapshot of the simulation and quantitatively as a force exerted on the structure from the ice. Based on the qualitative comparison of the experiments [13] and the simulation, a good agreement between the results was observed. Furthermore, the simulated force on the structure was shown to correlate well with force measured from the structure in the laboratory scale experiment done by Saarinen [12] as well as to the forces from the analytical model of Croasdale et al. [14].

ACKNOWLEDGEMENTS

The financial support from the Academy of Finland is gratefully acknowledged. Also the idea from Kari Kolari about using the cohesive crack model is appreciated.

References

[1] P.A. Cundall and O.D.L. Strack. A discrete numerical model for granular assemblies. *Géotechnique.*, 29:47–65, 1979.

[2] J.P. Morris, M.B. Rubin, G.I. Block, and M.P. Bonner. Simulations of fracture and fragmentation of geologic materials using combined fem/dem analysis. *International Journal of Impact Engineering.*, 33:463–473, 2006.

[3] E. Oñate and J. Rojek. Combination of discrete element and finite element method for dynamic analysis of geomechanics problems. *Comput. Methods Appl. Mech. Engrg.*, 193:3087–3128, 2004.

[4] A. Munjiza and K.R.F. Andrews. Penalty function method for combined finite-discrete element systems comprising large number of separate bodies. *Int. J. Numer. Meth. Engng.*, 49: 1377–1396, 2000.

[5] J.N. Reddy. *An Indroduction to Nonlinear Finite Element Analysis.* Oxford University Press Inc., New York., 2004. 463 p. ISBN 0-19-852529-X.

[6] A. Hillerborg, M. Modéer, and P-E. Petersson. Analysis of crack formation and crack growth in concrete by means of fracture mechanics and finite elements. *Cement and Concrete Research.*, 6:773–782, 1976.

[7] J. Paavilainen, J. Tuhkuri, and A. Polojärvi. 2d combined finite-discrete element method to model multi-fracture of beam structures. *Engineering Computations*, 26(6):578–598, 2009. doi: 10.1108/02644400910975397.

[8] H.L. Schreyer, D.L. Sulsky, L.B. Munday, M.D. Coon, and R. Kwok. Elastic-decohesive constitutive model for sea ice. *Journal of Geophysical Research.*, 111, 2006. doi: 10.1029/2005JC003334. C11S26.

[9] J.C. Simo and T.J.R. Hughes. *Computational Inelasticity*, volume 7 of *Interdisciplinary Applied Mathematics.* Springer-Verlag New York, Inc., 1998. 392 p. ISBN 0-387-97520-9.

[10] A. Munjiza and K.R.F. Andrews. Nbs contact detection algorithm for bodies of similar size. *Int. J. Numer. Meth. Engng.*, 43:131–149, 1998.

[11] M.A. Hopkins. Numerical simulation of systems of multitudinous polygonal blocks. Technical Report 92-22, Cold Regions Research and Engineering Laboratory, CRREL., 1992. 69 p.

[12] S. Saarinen. Description of the pile-up process of an ice sheet against an inclined plate. Master's thesis, Helsinki University of Technology, Department of Mechanical Engineering., 2000. 78 p.(In Finnish).

[13] G.W. Timco. The vertical pressure distribution on structures subjected to rubble-forming ice. In D.B. Muggeridge, D.B. Colbourne, and H.M. Muggeridge, editors, *11th International Conference on Port and Ocean Engineering under Arctic Conditions.*, volume I, pages 185–197, St. John's, Canada, September 24-28 1991.

[14] K.R. Croasdale, A.B. Cammaert, and M. Metge. A method for the calculation of sheet ice loads on sloping structures. In *IAHR 94 Proceedings of the 12th International Symposium on Ice*, volume 2, pages 874–885, aug 23-26 1994.

A MODEL FOR DETERMINING BUCKLING LIMITS OF IMPERFECT CYLINDRICAL COMPOSITE SHELLS

PETRI KERE[1] and MIKKO LYLY[2]

[1]Tampere University of Technology
Department of Mechanics and Design
P.O. Box 589, FI - 33101 Tampere, Finland
e-mail: petri.kere@tut.fi

[2]CSC - Scientific Computing Ltd.
P.O. Box 405, FI - 02101 Espoo, Finland
e-mail: mikko.lyly@csc.fi

ABSTRACT

Design of thin-walled cylindrical shells fabricated from composite materials leads to the requirement of validated procedures for the buckling simulation of realistic, geometrically imperfect shells. This work deals with the buckling simulation of imperfect cylindrical composite shells under axial compression. The buckling simulation is performed with a geometrically nonlinear analysis using Reissner-Mindlin-Von Kármán type shell facet model. A diamond shaped geometric imperfection pattern is applied in the computational model. Based on the simulation, limits of buckling loads are estimated for the imperfect cylindrical CFRP shells and compared to the test results from the literature.

1. INTRODUCTION

Many structural members made of composites have the form of thin-walled cylindrical shells. These kinds of members are the most common load-carrying systems in aeronautical, mechanical and civil engineering applications where high strength and stiffness, and low weight are of primary importance. Therefore, the accurate simulation of the stability behavior is of fundamental importance in the design of thin-walled cylindrical shell structures [1, 2, 4, 6, 7, 9, 11, 13, 14, 20].

Designing with the undisturbed shell geometry does not lead to the optimum with realistic, geometrically imperfect shells [6, 7, 9]. Particularly in buckling load maximization of cylindrical carbon fibre reinforced plastic (CFRP) shells, initial imperfection on the shell geometry should be taken into account to get realistic results in structural optimization. Besides the layer orientations used in the laminate, the laminate stacking sequence influence remarkably the buckling loads of the cylindrical shells. Bringing the initial imperfection on the shell geometry changes the order of buckling loads and thus the criticality of different stacking sequences.

Hühne *et al.* introduced a new deterministic approach for determining limits of buckling loads of thin-walled cylindrical composite shells [6, 7]. According to this approach, a single pre-buckle is

induced by a radial perturbation load before the axial loading starts. By varying amplitude and position of this perturbation a large amount of tests was realized and the new lower limit of buckling loads as well as the upper limit of buckling loads corresponding to the buckling load of an undisturbed shell geometry were derived.

The buckling simulation is performed with a geometrically nonlinear analysis using Reissner-Mindlin-Von Kármán type shell facet model. Typical postbuckling deformation pattern observed for the experimental test shells is used for modeling the geometric imperfection shape and amplitude [1, 2]. The shell facet model has been implemented in a grid computing platform [22] using the Elmer open-source computational tool [21] for multi-physics problems. Numerical results are compared to the experimental limits of buckling loads achieved for the geometrically imperfect cylindrical CFRP shells.

2. EXPERIMENTAL LIMITS OF CYLINDRICAL CFRP SHELL BUCKLING LOADS

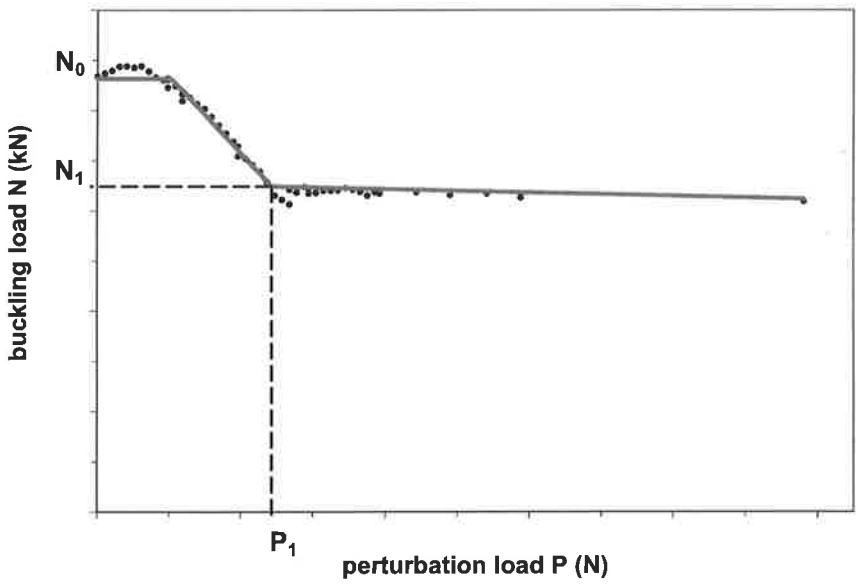

Figure 1: The relation of perturbation load and buckling load [6, 7].

A new deterministic approach for determining the lower bound of the buckling load of thin-walled cylindrical composite shells was introduced by Hühne *et al.* [6, 7]. According to this approach, a single pre-buckle is induced by a radial perturbation load before the axial loading starts. By varying amplitude and position of this perturbation a huge amount of tests was realized by using one test shell. The mechanical behaviour was investigated by employing a high-speed optical full-field measurement system.

The relation of perturbation load and buckling load are shown in Figure 1, whereas the run of the curve is idealized by three lines. For perturbation loads larger than P_1 the reduction of the buckling load is quite small. This means that the perturbation load P has to be increased very strongly in order to reduce the buckling load any further. For perturbation loads $P > P_1$ single buckles are clearly visible, can be detected by inspection and are therefore assumed to be unrealistic. Therefore the buckling load N_1 is defined as the new lower limit of buckling loads.

3. REISSNER-MINDLIN-VON KÁRMÁN TYPE SHELL FACET MODEL

The plate bending problem is formulated for a thin or moderately thick laminated composite plate which in its undeformed configuration occupies the region $\Omega \times (-t/2, t/2)$, where $\Omega \subset \mathbb{R}^2$ is the midsurface and $t > 0$ is the laminate thickness. The kinematical unknowns in the model are transverse deflection w, in-plane displacement $u = (u_x, u_y)$, rotation of the middle surface $\beta = (\beta_x, \beta_y)$, and drilling rotation ω. The plate is subjected to the in-plane load $f = (f_x, f_y)$ and the transverse pressure g.

We will use standard notation of tensor calculus. Dyadic and index notation with summation convention over repeated indices are used in parallel. Latin indices take their values in the set $\{1, 2, 3\}$ and Greek indices in the set $\{1, 2\}$.

3.1 Constitutive relation for a single layer

Let us denote by e_i and $\bar{e}_j$ the cartesian basis vectors for the so called 123-coordinate system of a single ply, and for the xyz-system of material coordinates common to all plies, respectively. In the material coordinate system, i.e., the laminate coordinate system, the layer system has been rotated by a positive counter clockwise angle θ about the z-axis. Hence, we define the transformation matrix between the two coordinate systems as $T = T_{ij} = e_i \cdot \bar{e}_j$, or

$$T = \begin{bmatrix} \cos\theta & \sin\theta & 0 \\ -\sin\theta & \cos\theta & 0 \\ 0 & 0 & 1 \end{bmatrix} \tag{1}$$

For linear orthotropic materials in plane stress state the constitutive relation for each ply has the form

$$\sigma = Q : \epsilon \tag{2}$$

where $\sigma = \sigma_{ij} = \sigma_{ji}$ is the second order stress tensor, $\epsilon = \epsilon_{ij} = \epsilon_{ji}$ is the strain tensor, and $Q = Q_{ijkl} = Q_{jikl} = Q_{ijlk} = Q_{klij}$ is the fourth order tensor of elastic stiffness coefficients. In the laminate coordinate system the constitutive equation is written as

$$\bar{\sigma} = \bar{Q} : \bar{\epsilon} \tag{3}$$

where $\bar{\sigma}_{ij} = T_{ip}T_{jq}\sigma_{pq}$ is the laminate stress, $\bar{\epsilon}_{ij} = T_{ip}T_{jq}\epsilon_{pq}$ is the laminate strain, and $\bar{Q}_{ijkl} = T_{ip}T_{jq}T_{kr}T_{ls}Q_{pqrs}$ is the tensor of stiffness coefficients in the laminate coordinate system.

The six independent non-zero components of Q are computed using the orthotropic material engineering constants $E_1, E_2, \nu_{12}, \nu_{21} = \nu_{12}E_2/E_1, G_{12}, G_{23}$, and G_{31} [8] as

$$\begin{gathered} Q_{1111} = E_1/(1 - \nu_{12}\nu_{21}),\ Q_{2222} = E_2/(1 - \nu_{12}\nu_{21}), \\ Q_{1122} = \nu_{12}E_2/(1 - \nu_{12}\nu_{21}), \\ Q_{1212} = G_{12},\ Q_{2323} = G_{23},\ Q_{3131} = G_{31} \end{gathered} \tag{4}$$

3.2 Kinematic relations for a laminate

The kinematic relations for a laminate are considered in the xyz-coordinate system. For notational simplicity, laminate stresses and strains in the xyz-coordinate system are in the following denoted without bar symbol.

Using the classical kinematic assumptions of Reissner, Mindlin, and Von Kármán the laminate strain is obtained from

$$\epsilon = \varepsilon(u) + \varphi(w) - z\varepsilon(\beta) \tag{5}$$

and

$$\epsilon_{3\alpha} = \gamma_\alpha(w, \beta), \quad \epsilon_{33} = 0 \tag{6}$$

where $z := x_3$, ε is the linear strain tensor, φ is the nonlinear membrane strain tensor, and γ the transverse shear strain vector, viz.

$$\varepsilon(u) = \frac{1}{2}(\nabla u + \nabla u^T) \tag{7}$$

$$\varphi(u, w) = \frac{1}{2}(\nabla u_x \otimes \nabla u_x + \nabla u_y \otimes \nabla u_y + \nabla w \otimes \nabla w) \tag{8}$$

$$\gamma(w, \beta) = \nabla w - \beta \tag{9}$$

3.3 Constitutive relations for a laminate

In plane-stress state, the laminate membrane stress resultants N (forces per unit length) and bending moment resultants M (moments per unit length) are obtained by integration of the stress resultants of all layers $z_{k-1} < z < z_k$, $k = 1, \ldots, n$, over the thickness of the laminate as

$$N = \int_{-t/2}^{t/2} \sigma dz = \sum_k \int_{z_{k-1}}^{z_k} \sigma dz \tag{10}$$

$$M = \int_{-t/2}^{t/2} \sigma z dz = \sum_k \int_{z_{k-1}}^{z_k} \sigma z dz \tag{11}$$

Furthermore, the resultant transvere shear forces S are obtained from

$$S = \int_{-t/2}^{t/2} \sigma_{3\alpha} dz = \sum_k \int_{z_{k-1}}^{z_k} \sigma_{3\alpha} dz \tag{12}$$

Using the constitutive equation and the kinematic relations of Reissner, Mindlin, and Von Kármán we get the following constitutive relations for the laminate

$$N(u, w, \beta) = A : [\varepsilon(u) + \varphi(w)] + B : \varepsilon(\beta) \tag{13}$$

$$M(u, w, \beta) = B : [\varepsilon(u) + \varphi(w)] + D : \varepsilon(\beta) \tag{14}$$

$$S(w, \beta) = A^\star \cdot \gamma(w, \beta) \tag{15}$$

The tensors A, B, D, and $A^\star$, are defined according to the Classical Lamination Theory (CLT) [8] as

$$A = \sum_k \int_{z_{k-1}}^{z_k} \bar{Q}\, dz = \sum_k (z_k - z_{k-1}) \bar{Q}^{(k)} \tag{16}$$

$$B = \sum_k \int_{z_{k-1}}^{z_k} \bar{Q} z \, dz = \frac{1}{2} \sum_k (z_k^2 - z_{k-1}^2) \bar{Q}^{(k)} \tag{17}$$

$$D = \sum_k \int_{z_{k-1}}^{z_k} \bar{Q} z^2 \, dz = \frac{1}{3} \sum_k (z_k^3 - z_{k-1}^3) \bar{Q}^{(k)} \tag{18}$$

$$A_{ij}^{\star} = \sum_k \int_{z_{k-1}}^{z_k} \bar{Q}_{3i3j} \, dz = \sum_k (z_k - z_{k-1}) \bar{Q}_{3i3j}^{(k)} \tag{19}$$

where $\bar{Q}^{(k)}$ defines the constitutive relation for linear orthotropic materials in plane stress state for layer k in the laminate coordinate system.

3.4 The shell facet model

The functions u, w, β, ω are determined from the condition that they minimize the potential energy of the plate. The energy is defined as

$$\begin{aligned} \Pi(u,w,\beta,\omega) &= \frac{1}{2} \int_\Omega N(u,w,\beta) : [\varepsilon(u) + \varphi(w)] \, d\Omega \\ &+ \frac{1}{2} \int_\Omega M(u,w,\beta) : \varepsilon(\beta) \, d\Omega + \frac{1}{2} \int_\Omega S(w,\beta) \cdot \gamma(w,\beta) \, d\Omega \\ &+ C \int_\Omega [\omega - rot(u)]^2 \, d\Omega - \int_\Omega f \cdot u \, d\Omega - \int_\Omega g w \, d\Omega \end{aligned} \tag{20}$$

where $C > 0$ is a penalty parameter for imposing the condition $\omega = rot(u)$ (see [5]), and

$$rot(u) = \frac{\partial u_x}{\partial y} - \frac{\partial u_y}{\partial x} \tag{21}$$

Substituting the constitutive equations in Eq. 20, we get

$$\begin{aligned} \Pi(u,w,\beta,\omega) &= \frac{1}{2} \int_\Omega \varepsilon(u) : A : \varepsilon(u) \, d\Omega + \int_\Omega \varepsilon(u) : B : \varepsilon(\beta) \, d\Omega \\ &+ \frac{1}{2} \int_\Omega \varepsilon(\beta) : D : \varepsilon(\beta) \, d\Omega + \frac{1}{2} \int_\Omega \gamma(w,\beta) \cdot A^{\star} \cdot \gamma(w,\beta) \, d\Omega \\ &+ C \int_\Omega [\omega - rot(u)]^2 \, d\Omega + \frac{1}{2} \int_\Omega \varphi(u,w) : A : \varphi(u,w) \, d\Omega \\ &+ \int_\Omega \varepsilon(u) : A : \varphi(u,w) \, d\Omega + \int_\Omega \varepsilon(\beta) : B : \varphi(u,w) \, d\Omega - \int_\Omega f \cdot u \, d\Omega - \int_\Omega g w \, d\Omega \end{aligned} \tag{22}$$

4. FE-IMPLEMENTATION

In the FE-implementation bilinear stabilized MITC plate elements [3, 16] are used. The shear energy term is modified as

$$\frac{1}{2} \frac{t^2}{t^2 + \alpha h^2} \int_\Omega \gamma_h(w,\beta) \cdot A^{\star} \cdot \gamma_h(w,\beta) \, d\Omega \tag{23}$$

where $\alpha > 0$ is a numerical stabilization parameter, h is the mesh parameter, i.e., the largest side length, and γ_h is the reduced shear strain [3, 16]. For the bilinear quadrilateral element used in the simulation, the reduced shear is defined locally such that

$$\gamma_h(w,\beta)_{|K} = \begin{bmatrix} a_K + c_K y \\ b_K + d_K x \end{bmatrix} \tag{24}$$

for every element K. The parameters a_K, b_K, c_K, and d_K are determined from the condition

$$\int_e [\gamma(w,\beta) - \gamma_h(w,\beta)] \cdot \tau \, ds = 0 \tag{25}$$

for every edge e of K. Here τ is the tangent to the edge. for every element K. The parameters a_K, b_K, c_K, and d_K are determined from the condition

$$\int_e [\gamma(w,\beta) - \gamma_h(w,\beta)] \cdot \tau \, ds = 0 \tag{26}$$

for every edge e of K. Here τ is the tangent to the edge. In the computation, the in-plane forces N and the bending moments M are obtained consistently from the constitutive equations. Shear forces are computed from

$$S(w,\beta) = \frac{t^2}{t^2 + \alpha h^2} A^\star \cdot \gamma_h(w,\beta) \tag{27}$$

To obtain the load-displacement curve and to sudy the stability behaviour, the nonlinear equations are solved iteratively by Riks' method with Crisfield's elliptical constraint for arc length [15, 17, 18, 19]. The differential equilibrium equations of the minimization problem are obtained using standard variational calculus and integration by parts. The linearized equations are then discretized by the finite element method. In the post-buckling region the algorithm follows the principal equilibrium path with the minimal stiffness.

In laminate failure prediction, a numerical method independent of the failure criterion internal formulation to obtain failure margins can be employed [10, 12].

5. MODELING THE IMPERFECT CYLINDRICAL CFRP SHELL

The FE-model used in the buckling simulation is based on specimens that were used in experimental tests by Hühne *et al.* [6, 7]. The specimens were characterised by an internal diameter and an overall length equipped with end plates to assure circular cross sections. The specimens were fabricated from CFRP unidirectional tape materials, for which the nominal ply properties are given in Table 1. Detailed description of the test specimens, equipment, and procedure is given by Hühne *et al.* [6, 7].

The model considers a complete cylinder with ply properties represented in Table 1 and geometric dimensions same of those of the real specimens used. The length of the FE-model is 510 mm, equal to the length of the specimen central part excluding the end plates at the top and bottom surfaces to assure circular cross sections. The top and bottom surfaces of the FE-model are constrained to remain plane and circular and to maintain the initial radius while the axial compression is transferred to nodal forces.

The midsurface of the cylinder is considered as the reference surface where the initial imperfections are given. A cylindrical coordinate system is employed and the nodal coordinate in the radial

CFRP	
E_1 [GPa]	123.550
E_2 [GPa]	8.708
G_{12} [GPa]	5.555
$\nu_{12} = \nu_{23}$	0.319
t_{ply} [mm]	0.125

Table 1: Mechanical properties of the CFRP plies used in the experimental tests and in the computational model.

direction is taken as $r = R + w^{\circ}$, where $R = 250$ mm is the nominal radius of the cylinder and w° is the amplitude of the imperfection shape.

The mesh sensitivity on the buckling load prediction by linear eigenvalue analysis was studied by Bisagni [1]. According to the study, the accuracy of the buckling load prediction depends highly on the FE-mesh resolution. Good convergence for critical loads was achieved with 220×52 quadrilateral elements, i.e., 220 elements in the circumferential direction and 52 elements in the axial direction, when compared to the analytical solutions. Hence, the FE-mesh with 11440 quadrilateral elements was employed in this work as well.

An analytical expression is used to define a diamond shape initial imperfection on the shell geometry for each shell as

$$w^{\circ}(z, \vartheta) = a \sin(m\pi z/L) \cos(n\vartheta) \tag{28}$$

where m is the number of axial semi-waves and n the number of circumferential waves, z is the axial coordinate, ϑ the circumferential coordinate, and L the cylinder length [1]. The analysis is performed using different values for the nondimensional imperfection amplitude defined as $\varepsilon = a/t$, where t is the shell thickness and $\varepsilon \in [0, 1]$.

All cylindrical shells considered are composed of unidirectional CFRP plies of Table 1. The shells differ only in their lay-up as shown in Table 2. The test shells Z07 and Z08 as well as the test shells Z10 and Z11 are nominally equal.

Shell	Lay-up	t [mm]
Z07	$[\pm 24/\pm 41]$	0.5
Z08	$[\pm 24/\pm 41]$	0.5
Z09	$[\pm 41/\pm 24]$	0.5
Z10	$[+24/+41]_{\text{AB}}$	0.5
Z11	$[+24/+41]_{\text{AB}}$	0.5
Z12	$[\pm 45/0/-79]$	0.5

Table 2: Laminate lay-ups for the cylindrical CFRP shell. AB denotes the antisymmetric balanced laminate structure.

6. RESULTS

Results of geometrically nonlinear analysis using the shell facet model implemented in Elmer Solver as described above are compared to the results represented by Hühne *et al.* [6, 7].

According to the experimental tests, several different postbuckling deformation patterns were observed. A typical post-buckling deformation pattern for the undisturbed shell include two half-waves in axial and twelve full-waves in circumferential directions, i.e., $m = 2, n = 12$. A corresponding diamond shaped initial imperfection pattern is illustrated in Figure 2.

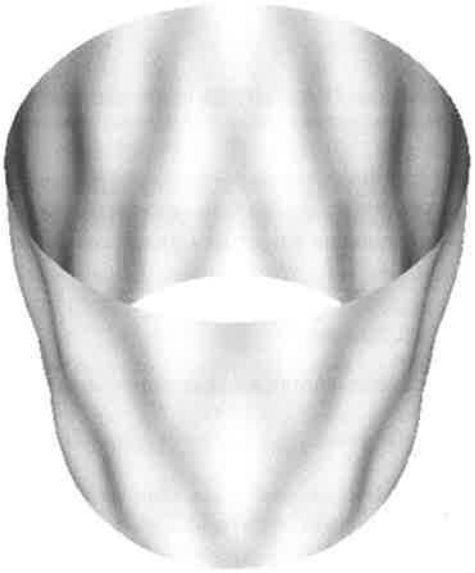

Figure 2: Visualization of the imperfection pattern, $m = 2, n = 12$.

In the geometrically nonlinear analysis, the critical load is determined by increasing gradually the applied load to search for the maximum of the load-displacement curve. The maximum of the load-displacement curve is called the critical load. In this work, arc length scale factor $c = 0.8$ and arc length weight $W = 0.1I$ are used in the nonlinear analysis. For the elements, drilling parameter $C = 0.2$ and stabilization parameter $\alpha = 0.2$ are used.

The effect of nondimensional imperfection amplitudes on the critical loads was investigated. Values as $\varepsilon = 0.0, 0.25, 0.5, 0.75, 1.0$ are involved for the different nondimensional imperfection amplitudes including the undisturbed shell geometry. When the initial imperfection on the shell geometry is added, the critical load for shell Z12 becomes clearly larger than that of Z07/Z08 [11]. The order of shell lay-ups with respect to the buckling loads is changed when imperfections occur.

Using the undisturbed shell geometry in the buckling simulation leads to unrealistic results [11]. Hence, a realistic initial imperfection pattern with small amplitude $\varepsilon = 0.25$ on the shell geometry is used to estimate the upper limit of the buckling loads corresponding to the undisturbed test case. The lower limit of the buckling loads, i.e., the worst case buckling load is estimated with large initial imperfection amplitude $\varepsilon = 1.00$ on the shell geometry. Results from the simulation are compared to the charasteristic loads N_0 and N_1 from the tests corresponding to the values of the undisturbed and worst case buckling loads, respectively [6, 7].

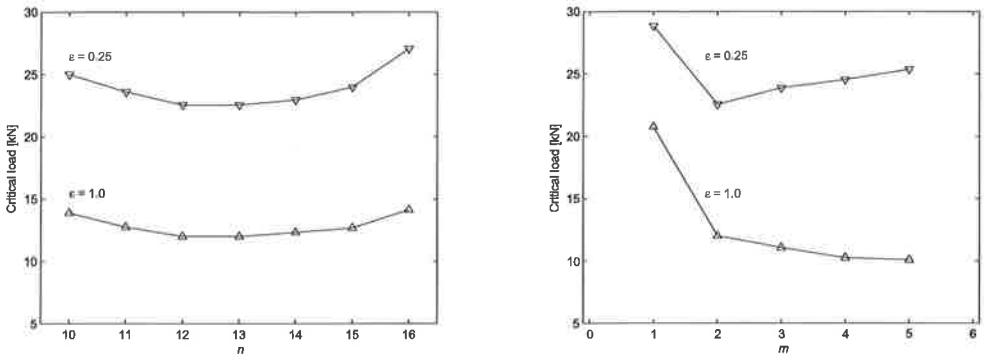

(a) $m = 2, n = 10, \ldots, 16$ (b) $m = 1, \ldots, 5, n = 12$

Figure 3: An example of critical load as a function of number of circumferential waves n and axial half-waves m predicted by Elmer nonlinear analysis for the test shell Z07 with the laminate $[\pm 24/\pm 41]$ lay-up.

Lay-up	N_0 [kN] Test [7]	N_1 [kN] Test [7]	$N_{\varepsilon=0.25}$ [kN] Elmer nonlin.	$N_{\varepsilon=1.00}$ [kN] Elmer nonlin.
$[\pm 24/\pm 41]$	21.8	16.2	22.5	12.0
$[\pm 24/\pm 41]$	21.9	17.1	22.5	12.0
$[\pm 41/\pm 24]$	15.7	14.4	18.5	12.6
$[+24/+41]_{\mathrm{AB}}$	15.7	13.1	18.5	9.2
$[+24/+41]_{\mathrm{AB}}$	16.7	13.0	18.5	9.2
$[\pm 45/0/-79]$	18.6	18.0	26.4	17.8

Table 3: Comparison among critical loads for the test shells [6, 7] and the Elmer model with initial diamond shape imperfection, $m = 2, n = 12$.

An example of the critical load as a function of number of circumferential waves n and axial half-waves m for the test shell Z07 predicted by Elmer nonlinear analysis is given in Figure 3. By varying the number of half-waves in the axial direction as $m = 1, \ldots, 5$ with the number of full-waves in the circumferential direction as $n = 12$ and small imperfection amplitude $\varepsilon = 0.25$, the minimum critical load is reached with $m = 2$ for shells Z07, Z09, Z10. For all other cases with imperfection amplitudes $\varepsilon = 0.25$ and $\varepsilon = 1.00$ the critical load tends to decrease as the number of axial half-waves is increased in the initial imperfection pattern on the shell geometry.

The effect of the number of full-waves in the circumferential direction as $n = 10, \ldots, 16$ on the critical load with $m = 2$ for the test shell Z07 is represented in Figure 3. The critical loads in each case is compared to the characteristic values N_0 and N_1 from the experimental tests [6, 7] as illustrated in Figure 4. The corresponding numerical results are shown in Table 3.

Both tests and the simulation results show that the critical load of undisturbed shell is higher than that with the initial imperfection pattern on the shell geometry. In all cases the experimental characteristic values N_0 and N_1 fall within the range of critical values $N_{\epsilon=0.25}$ and $N_{\epsilon=1.00}$ predicted by Elmer model with a diamond shaped initial imperfection pattern on the shell geometry. The results suggest that a diamond shaped initial imperfection on the shell geometry can be used in the buckling simulation to get realistic results and to to estimate the buckling limits of imperfect cylindrical shells.

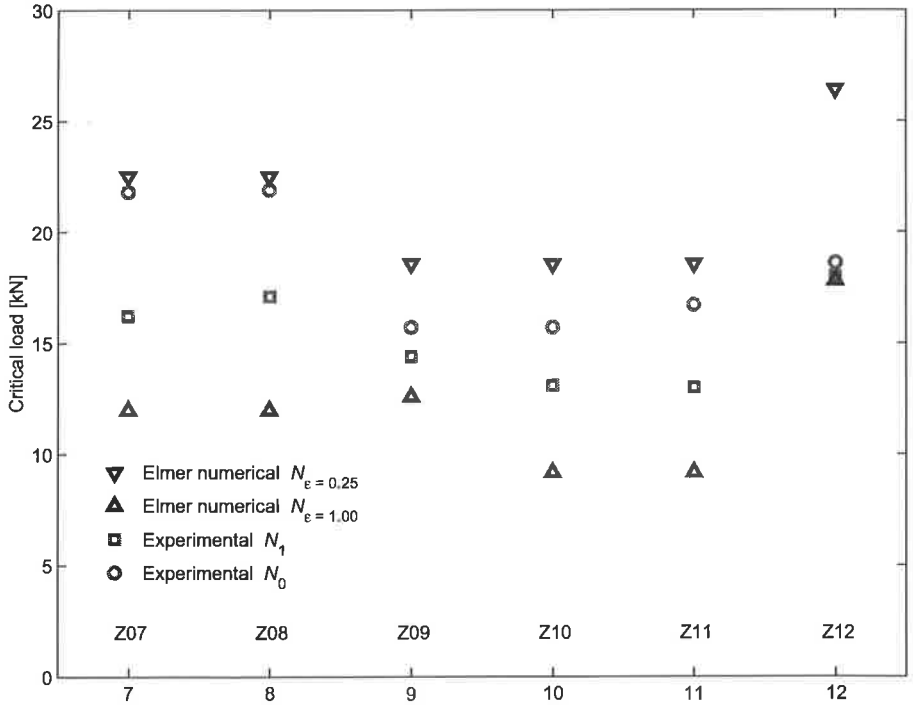

Figure 4: Critical load values from the test [6, 7] and predicted by Elmer using diamond shape initial imperfection on the shell geometry, $m = 2, n = 12$.

7. CONCLUSIONS

Both experimental tests and computational results show that an initial imperfection on the shell geometry should be taken into account in buckling simulation and structural optimization of CFRP cylindrical shells. Bringing the initial imperfection on the shell geometry changes the order of buckling loads and thus the criticality of different stacking sequences. Geometrically nonlinear analysis with Reissner-Mindlin-Von Kármán shell facet model and a diamond shaped initial imperfection on the shell geometry can be used to get realistic results in buckling simulation and to determine the buckling limits of imperfect cylindrical shells. The shell facet model is computationally efficient still providing accuracy for local failure prediction of the laminate. Implementation of the computational model in the Elmer open-source computational tool allows for the parallelization of the calculations over a grid platform and efficient solving of computationally expensive design optimization tasks.

ACKNOWLEDGMENTS

The first author is employed by National Board of Patents and Registration of Finland.

REFERENCES

[1] C. Bisagni, Numerical Analysis and Experimental Correlation of Composite Shell Buckling and Postbuckling. *Composites: Part B*, **31**, 655–667, 2000.

[2] C. Bisagni, P. Cordisco, An Experimental Investigation into the Buckling and Postbuckling of CFRP shells under combined axial and torsion loading. *Composite Structures*,**60**, 391–402, 2003.

[3] F. Brezzi, M. Fortin, R. Stenberg, Error analysis of mixed-interpolated elements for Reissner-Mindlin plates. *Math. Models Methods Appl. Sci.*, **1**, 125–151, 1991.

[4] M. Deml, W. Wunderlich, Direct evaluation of the 'worst' imperfection shape in shell buckling. *Computer Methods in Applied Mechanics and Engineering*, **149**, 201–222, 1997.

[5] T. J. R. Hughes, F. Brezzi, On drilling degrees of freedom. *Computer Methods in Applied Mechanics and Engineering*, **72**, 105–121, 1989.

[6] C. Hühne, *Robuster Entwurf beulgefährdeter, unversteifter Kreiszylinderschalen aus Faserverbundwerkstoff*. PhD Thesis, Braunschweig Technical University, Germany, 2005.

[7] C. Hühne, R. Rolfes, J. Tessmer, A new approach for robust design of composite cylindrical shells under axial compression. *Proc. European Conference on Spacecraft Structures, Materials and Mechanical Testing 2005*, 10-12 May, 2005, Noordwijk, The Netherlands. ESA SP-581 2005.

[8] R. M. Jones, *Mechanics of Composite Materials*. New York: Hemisphere Publishing Corporation, 1975.

[9] T. von Kármán, H. S. Tsien, The Buckling of Thin Cylindrical Shells under Axial Compression. *Journal of the Aeronautical Sciences*, **8**, 303–312, 1941.

[10] P. Kere, M. Lyly, Reissner-Mindlin-Von Kármán type plate model for nonlinear analysis of laminated composite structures. *Composite Structures*, **71**, 289–292, 2005.

[11] P. Kere, C. Hühne, M. Lyly, Geometrically Nonlinear Analysis of Imperfect Cylindrical Composite Shells Using Reissner-Mindlin-Von Kármán Type Shell Facet Model. *Proc. 6th International Conference on Composite Science and Technology (ICCST/6)*. 22-24 January, 2007, Durban, South Africa.

[12] P. Kere, J. Lento, M. Lyly, A. Teräs, A Structural Design Optimization System Exploiting Distributed Grid Resources. *Proc. 47th AIAA/ASME/ASCE/AHS/ASC Structures, Structural Dynamics and Materials Conference*, 1-4 May, 2006, Newport, RI, USA. Paper AIAA-2006-1626.

[13] P. Kere, M. Lyly, On Post-Buckling Analysis and Experimental Correlation of Cylindrical Composite Shells with Reissner-Mindlin-Von Kármán Type Facet Model. *Computers & Structures*, **86**, 1006–1013, 2008.

[14] P. Kere, M. Lyly, Buckling Simulation of Imperfect Cylindrical Composite Shells Using Reissner-Mindlin-Von Kármán Type Shell Facet Model. *Proc. XXII International Congress of Theoretical and Applied Mechanics (ICTAM 2008)*. 24-29 August, 2008, Adelaide, Australia. Paper 10341.

[15] R. Kouhia, On the Solution of Non-linear Finite Element Equations. *Computers & Structures*, **44**, 243–254, 1992.

[16] M. Lyly, On the connection between some linear triangular Reissner-Mindlin plate bending elements. *Numer. Math.*, **85**, 77–107, 2000.

[17] E. Ramm, *Strategies for Tracing the Nonlinear Response Near Limit Points*. Nonlinear Finite Element Analysis in structural Mechanics. Bochum: Springer Verlag, 1981.

[18] W. C. Rheinboldt, *Numerical Analysis of Parametrized Nonlinear Equations*. New York: Wiley, 1986.

[19] E. Riks, The Application of Newton's Method to The Problem of Elastic Stability. *Journal of Applied Mechanics*, **39**, 1060–1065, 1972.

[20] T. Winterstetter, H. Schmidt, Stability of Circular Cylindrical Steel Shells Under Combined Loading. *Thin-Walled Structures*, **40**, 893-909, 2002.

[21] Elmer Models Manual, CSC - Scientific Computing Ltd., 2007. Elmer web site www.csc.fi/elmer.

[22] NorduGrid Middleware, the Advanced Resource Connector, Release 0.6.1, The NorduGrid Collaboration, 2007. NorduGrid web site www.nordugrid.org.

Bending Response of Laser-Welded Web-core Sandwich Deck Structures under Lateral Loads

J. Romanoff, P. Varsta
Department of Applied Mechanics / Marine technology
Helsinki University of Technology
P.O. Box 4100
FIN-02015 TKK, Finland

ABSTRACT

Steel sandwich panels are considered as a potential candidate to replace the traditional stiffened plates in ship structures. These types of sandwich panels are mainly used as deck structures in ships and often they are supported by the girder system. Present paper investigates bending response of laser-welded web-core sandwich panels supported by the girder system.

1 INTRODUCTION

Demand for lighter, safer and modular structures has stimulated the need to study new materials and new structural configurations in civil and mechanical engineering. Laser-welded sandwich panels are considered a very interesting alternative when the traditional industries using steel as their main material are concerned. In ship-building these panels have been used for example in naval and commercial vessels; see for example Refs. [1], [2].

These panels are composed of steel faces which are connected by steel profiles, such as corrugations, vertical webs, C-profiles etc. The connection between the faces and the core elements is done by stake laser-welding, i.e. outside the closed structure. Due to this fact the welds can have smaller thickness than the structural members that is joining. This is especially the problem on commercially widely used web-core sandwich panels where the thickness of the laser weld is between 1.0 mm and 1.5 mm while the thickness of the faces and webs is 2.5 mm and 4.0 mm respectively. For details of this kind of structure see Figure 1. This can cause significant decrease in panel shear stiffness [3] in the weaker direction, i.e. opposite to the web plate direction. If equivalent single layer (ESL) plate theories are applied, the low shear stiffness can in turn result into cases where the First-order Shear Deformation Theory (FSDT) is not valid [4]. This is due to the fact that the normal strains are not anymore linear across the plate thickness, but can have zigzag distribution. The other problem with ESL is that the panel needs to be homogenized. Since in practice the size of a unit cell is not infinitely small when compared to the plate dimensions, the homogenization can lead to averaging of quantities that should not be averaged [5]. This is especially a problem in shear-induced local bending moment opposite to the web plate direction. This local bending moment vanishes in averaging as presented in Ref. [5] causing significant under estimation in normal stresses, see [4], [5], [6]. Therefore, enhanced plate bending model was developed to tackle these weaknesses, see Ref. [4]. However, the plate bending model has been validated only for simple plate boundary conditions, i.e. simply supported or clamped around its all four edges. In reality these boundary conditions very seldom occur and the support is flexible as in the case of girder system.

In case of ships this surrounding structure is grillage made from T-beams. In traditional, single-plated, ship structures the T-beams are designed by considering the effective breadth of the

plate it is supporting. The plate is often assumed to act as membrane and only part of it is considered when the moment of inertia for the beam is determined, [7]. However, in case of steel sandwich panels there will be two plates contributing to the effective breadth and the panel will have bending stiffness of its own. Therefore, the traditionally made assumption that the plate acts like a membrane needs to be reconsidered. Thus, the coupled action between sandwich and grillage has to be considered when the panel strength assessment is carried out. In Ref. [8] analytical approach was applied for this, but the accuracy was found to be insufficient for design purposes. The alternative for the strength assessment is to use full 3D FE analysis as presented in Refs. [8], [9]. However, there the influence of the laser weld was excluded and thus the plates can be considered too stiff. As presented in Ref. [6] the full 3D model including the laser-weld becomes too large for practical design work due to differences of scale of the ship (150m-350m), the sandwich plate (1m-10m) and the laser weld (1mm-1.5mm).

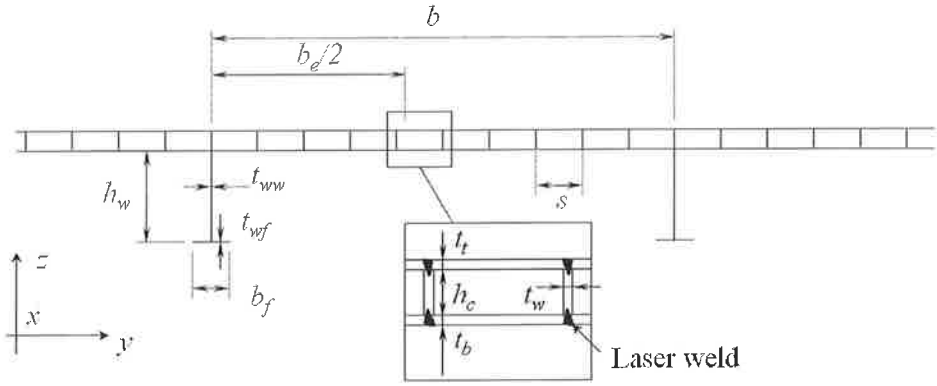

Figure 1. Web-core sandwich panel with the supporting girder system.

The purpose of the present paper is to study the influence of the interaction between the sandwich panels and grillage using simplified FE modeling with equivalent plate and beam elements. The investigation is limited to sandwich panels under lateral, i.e. out-of plane loading. This means that the influence of hull-girder bending is excluded from the stress analysis. The method is demonstrated through case study on accommodation deck.

2 DEFINITIONS

The web-core sandwich plate consists of web and face plates, which are connected by laser welds. The web plates are parallel to the xz-plane and have the thickness t_w and the height h_c; see Figure 1. The web plate spacing is s. The top and bottom face plates are parallel to the xy-plane and have the thicknesses t_t and t_b respectively. The sandwich plate has the length L, the breadth B, and the total height $h = h_c + t_t + t_b$, and the neutral planes of the face plates have the distance $d = h_c + (t_t + t_b)/2$. The T-joint consists of the laser weld and parts of the face and web plates connected to it, and it is modeled by a rotation spring with the stiffness k_θ. The girders have web and flange thickness t_{ww} and t_{wf} respectively. Similarly the web height and flange breadth are denoted with h_w and b_f respectively. The web frame spacing is denoted with b and the length of the sandwich panels with l. The effective breadth is denoted with b_e. The notation q is used for external distributed loads. Young's modulus is denoted with E and Poisson's ratio with ν. The sub- and superscripts t, b, and w are used to denote the top face, the bottom face, and the web plates, respectively.

3 STRUCTURAL ANALYSIS

3.1 Sandwich Plate Bending Model

The details of the derivation of the sandwich plate equations can be found from Ref. [4]. The main features are repeated here to underline the specifics of the plate bending problem when the interaction between the sandwich plate and the girder are considered. The displacements in the sandwich plate are assumed to have following form [4]

$$\begin{aligned} u_i &= u_0(x,y) - d_i\theta_x(x,y) - z_i\theta_x^i(x,y) \\ v_i &= v_0(x,y) - d_i\theta_y(x,y) - z_i\theta_y^i(x,y) \\ w_i &= w_g(x,y) + w_l^i(x,y) \end{aligned} \quad (1)$$

where the x-direction of the sandwich plate is taken parallel to the web plate orientation while z-direction is normal to the plane of the sandwich. The x-, y- and z-displacements are denoted by u, v and w, respectively. Subscript 0 denotes the displacements at geometrical mid-plane of the sandwich plate. Subscripts g and l are used to denote the global and local deflection, respectively. Sub- and superscript i is used to denote the structural element in question, i.e. face or web plates. The slopes θ with subscripts x and y describes the rotation around axis y and x, respectively. For details of the kinematics and stress resultants for equivalent single layer plate see Figure 2.

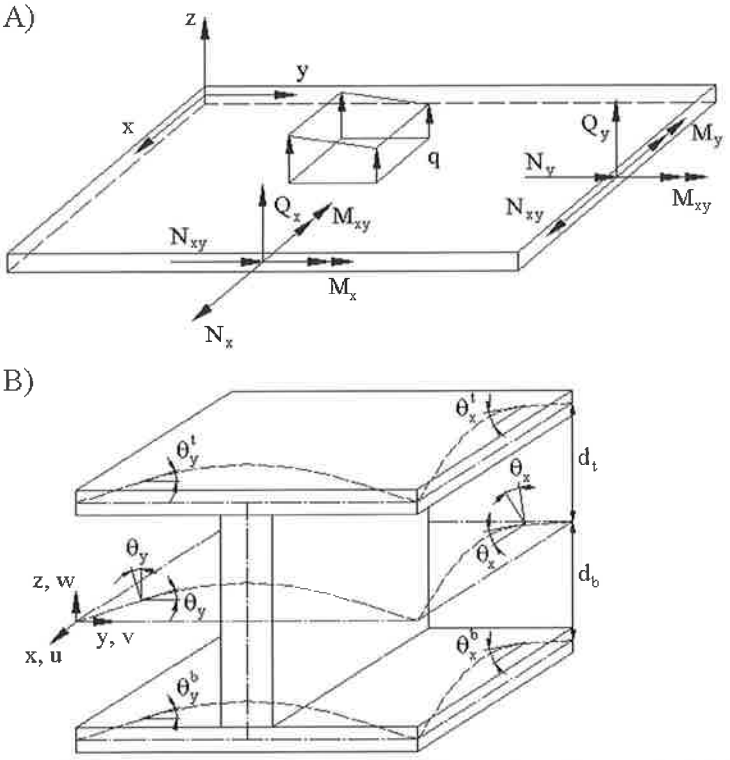

Figure 2. A) The load and stress resultants and B) the kinematics of the sandwich plate.

The local deflection of the face plate can be divided into three parts as

$$w_l = w_Q + w_{tf} + w_q, \quad (2)$$

where w_Q corresponds the shear deflection, w_{tf} the thick face plates effect and the w_q the local deflection due to the pressure load applied on the face plate. Based on the assumed kinematics and carrying out homogenization leads to six differential equations

$$
\begin{aligned}
&A_{11}u_{0,xx} + A_{33}u_{0,yy} + (A_{12} + A_{33})v_{0,xy} - B_{11}\theta_{x,xx} - B_{33}\theta_{x,yy} - (B_{12} + B_{33})\theta_{y,xy} = 0 \\
&A_{22}v_{0,yy} + A_{33}v_{0,xx} + (A_{12} + A_{33})u_{0,xy} - B_{22}\theta_{y,yy} - B_{33}\theta_{y,xx} - (B_{12} + B_{33})\theta_{x,xy} = 0 \\
&D_{Qx}(w_{RM,xx} - \theta_{x,x}) + D_{Qy}(w_{RM,yy} - \theta_{y,y}) + q_{RM} = 0 \\
&B_{11}u_{0,xx} + B_{33}u_{0,yy} + (B_{12} + B_{33})v_{0,xy} - D_{11}\theta_{x,xx} - D_{33}\theta_{x,yy} - (D_{12} + D_{33})\theta_{y,xy} - D_{Qx}(w_{RM,x} - \theta_x) = 0 \\
&B_{22}v_{0,yy} + B_{33}v_{0,xx} + (B_{12} + B_{33})u_{0,xy} - D_{22}\theta_{y,yy} - D_{33}\theta_{y,xx} - (D_{12} + D_{33})\theta_{x,xy} - D_{Qy}(w_{RM,x} - \theta_y) = 0 \\
&D_f(w_{tf,xxxx} + 2w_{tf,xxyy} + w_{tf,yyyy}) = q_{tf}
\end{aligned}
\tag{3}
$$

where the equivalent stiffness properties A_{ij}, B_{ij}, D_{ij} and $D_{Q,i}$ are given in Ref. [4] together with detailed derivation; these are summarized in Appendix 1. The problem is solved using two FE meshes, so that the five first equations of Eq. (3) are modeled with one set of Reissner-Mindlin type shell elements and the sixth equations with another set. These two meshes are connected with deflection constraint, i.e. $w_{RM} = w_{tf}$ at all coincident nodes.

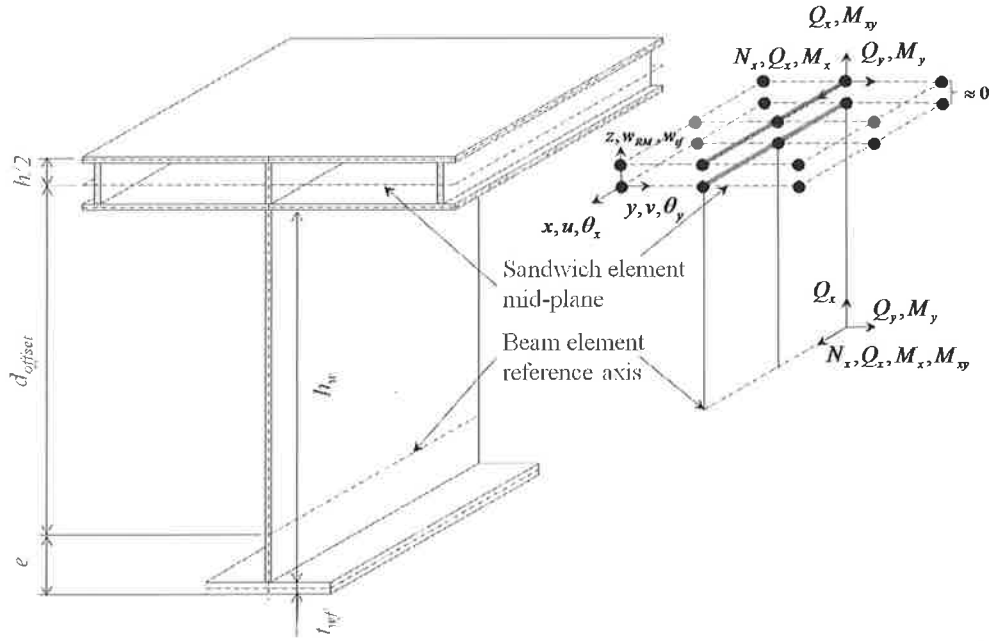

Figure 3. Modeling of the sandwich grillage interaction with equivalent beam and shell elements.

3.2 *Interaction between the Sandwich Plate and the Girder*

For ship building applications the girders are always positioned on one side of the panel, so that one surface remains flat. Thus, there is an offset between the sandwich panel and the girder neutral axis, see Figure 3. In FEM only the geometry of the geometrical mid-plane of the sandwich plate is modeled. Therefore, the offset is defined as

$$d_{offset} = \frac{h}{2} + (h_w + t_{wf} - e), \tag{4}$$

where h is the sandwich height and h_w, t_{wf} and e the web height, the flange thickness and the position of the neutral axis of the girder respectively. The degrees of freedom in the elements are displacements in x-, y- and z-direction and rotations induced by bending; thus drilling degree of freedom is excluded. Timoshenko beam element is used and the stiffness properties for it are calculated according to basic beam theory.

3.3 *Stress calculation in the Sandwich Plate*

The finite element solution gives stress resultants $\{N\}$, $\{M\}$ and $\{Q\}$ for the homogenized plate. Since the size of unit cell is fairly large the actual periodic structure should be considered in stress calculations. This is done using the relation for strains and curvatures of the mid-plane [4]

$$\begin{Bmatrix} \varepsilon \\ -\kappa \end{Bmatrix} = \begin{bmatrix} A & B \\ B & D_0 \end{bmatrix}^{-1} \left(\begin{Bmatrix} N \\ M \end{Bmatrix}_{RM} - \begin{Bmatrix} 0 \\ M_Q \end{Bmatrix} \right), \tag{5}$$

where $\begin{bmatrix} ABD_0 \end{bmatrix}$ is the stiffness matrix and $\begin{Bmatrix} N & M \end{Bmatrix}_{RM}^T$ is obtained as the solution of differential equations Eq. (3). The moments for $\{M_Q\}$ are determined from [4]

$$M_{Q,x}^i(y_l) = \nu M_{Q,y}^i$$

$$M_{Q,y}^i(y_l) = \int Q_{Q,y}^i(y_l) dy_l - \left[\iint \frac{Q_{Q,y}^i(y_l)}{s} dy_l dy_l \right]_{yl=s}$$

$$M_{Q,xy}^i = 0 \,,$$

where $Q_{Q,y}^i$ is the shear force distribution obtained from the FE solution and the moment is evaluated locally at the unit cell. Then the in-plane strains and curvatures can be calculated from Eq. (5). From these strains and curvatures the periodic stresses for the face plates and webs can be calculated as presented in Ref. [4].

3.4 *Stress Calculation in the Girder*

The Finite Element solution of the beam elements gives the stress resultants N, $\{M\}$ and $\{Q\}$ with respect to beam reference axis, see Figure 3. From these quantities the normal stress in the beam can be calculated as

$$\sigma = \frac{N}{A} + \frac{M_x z}{I_x} + \frac{M_z y}{I_z}, \tag{7}$$

where the area A, and the moments of inertia I_x and I_z are considered without the effective breadth of the plating. Due to the interaction between the girder and the sandwich plate the shear stresses become more difficult to define if only beam element stress resultants are considered. The engineering approach to define shear stress is to assume simply that the shear is carried out by the continuous part in the direction of the acting shear force, e.g. height of web in xz-direction. Thus, we get the simple relation

$$\tau_{xz} = \frac{Q_x}{A_{xz}} = \frac{Q_x}{t_{ww}\left(h_w + t_{wf}\right)}$$
$$\tau_{xy} = \frac{Q_y}{A_{xy}} = \frac{Q_y}{t_{wf} b_f} \quad . \tag{8}$$

However, this gives average shear stress on the web. This can underestimate the shear stress at the neutral axis and be over conservative at the intersections of the web and flange of the web frame or web and sandwich plate. In order to get more accurate shear stress distribution following relation has to be used

$$\tau = \frac{QS}{I^* b} \quad . \tag{9}$$

where Q is the shear force, b the breadth of beam in considered location, S is the first moment of area calculated from flange tip and I^*, is the second moment of area of both the sandwich plate and the T-girder. The problem with Eq. (9) is that both the first and second moments of the area, S and I^* depend on the interaction between the sandwich and the T-girder. This problem is solved by considering effective breadth of the different layers of the sandwich, i.e. top face, core and bottom face.

3.5 Effective Breadth

The idea of the effective breadth is to take into account the shear lag in wide flange of the beam by considering the following relation [7]

$$b_e = \frac{\int_{-b/2}^{b/2} \sigma_x dy}{\sigma_{x,\max}} \quad . \tag{10}$$

where $\sigma_x = \sigma_x(y)$ is the normal stress presented as a function of y and $\sigma_{x,\max}$ is the maximum value of the normal stress at the intersection of the sandwich plate and the girder. Often the effective breadth is presented in terms of effectiveness parameter, which is written as

$$C = \frac{b_e}{b} \quad . \tag{11}$$

4 CASE STUDIES

4.1 Validation of the Interaction between Sandwich and Girder

The kinematics presented in Figure 3 are validated with case study of standard I-core produced at Meyer Werft shipyard in Germany. The sandwich panel has face plate thickness $t_f = t_b = 2.5$ mm, core height $h_c = 40$ mm, web plate thickness $t_w = 4.0$ mm and web plate spacing s=120 mm. It is supported by girder having web height $h_{web} = 450$ mm, flange breadth $b_f = 200$ mm, web thickness $h_{web} = 4.0$ mm and flange thickness $t_f = 12$ mm. The length of the structure is L=8 m and the breadth is B=3.12 m. Material is steel with Young's modulus E=206 GPa and Poisson's ratio ν=0.3. The load on girder is -50 kN/m in z-direction and the entire structure is constrained from the support end by setting $u_y = u_z = \theta_x = 0$ at mid-plane of the sandwich. Half symmetry is considered by setting $u_x = \theta_y = \theta_z = 0$ over all nodes at $x = L/2$. The 3D topology is modeled using 21680 eight node shell element, while the model consisting of shells and beams with equivalent stiffness properties has 5040 elements. Figure 4 presents a comparison of the x-direction normal stresses at

the mid-span $x=L/2$ of the structure for min-planes of the top and bottom face of the sandwich and girder flange. It also presents the effective breadth for the top and bottom face of the sandwich determined from the normal stress in x-direction according to Eq. (10). Figure 5 shows the effective breadth presented in the form of Eq. (11), while Figure 6 shows the comparison of the shear stresses from Eqs. (8) and (9).

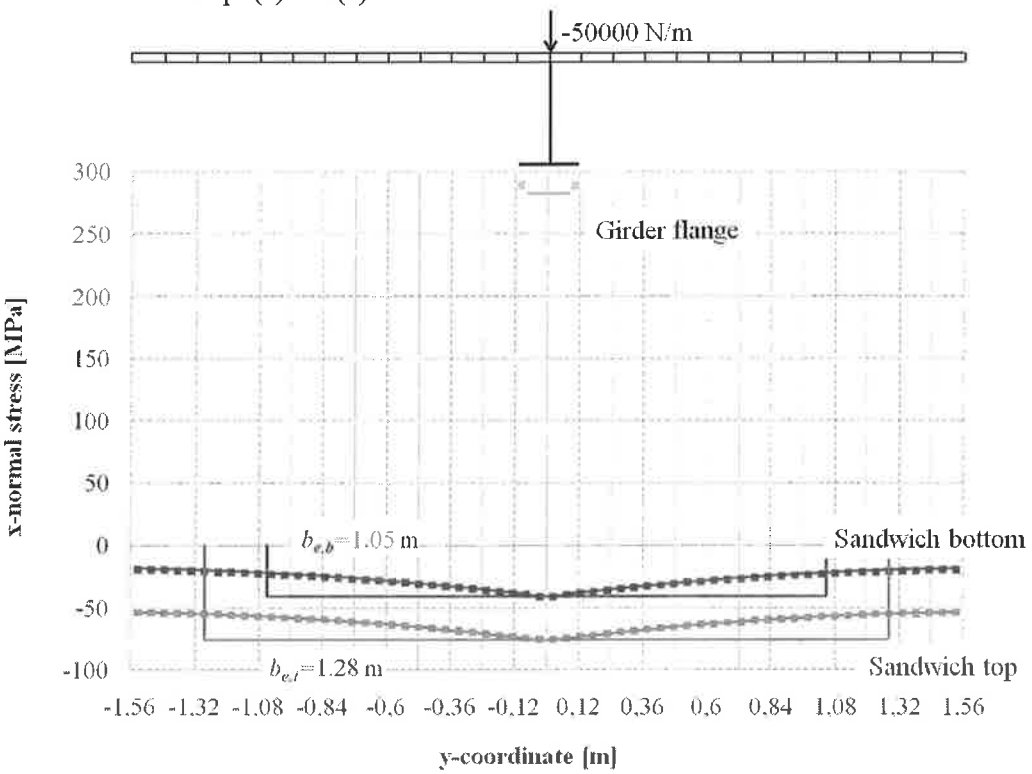

Figure 4. Comparison of the x-direction normal stresses at x=L/2. Dots denote the present model with equivalent plates and beams, while the solid line is for the 3D FEM based on shell elements.

The deflections of the 3D-FEM and the present model are 26.7 mm and 26.5 mm for the 50 kN/m load; thus maximum deflection has less than 1% difference. Figure 4 shows, that the maximum x-direction normal stress in the girder flange is 283 MPa and 289 MPa for the 3D-FEM and present model respectively. For sandwich bottom face the corresponding values are 41.1 MPa and 41.2 MPa, while for top face of sandwich this figures are 75.8 MPa and 75.6 MPa. So in case of stresses the maximum error of 2% is found on girder flange. Figure 4 also clearly shows that the effective breadth is 22% higher in the top face of the sandwich than in the bottom.

Figure 5 shows that the effective breadth of the top and bottom faces of the sandwich have different values along the span of the beam, but also that these two values differ from each other. At the mid-span the effective breadth of the sandwich top face is 82% of the total breadth, while for the bottom face the value is 67%. At the girder ends the corresponding values are 53% and 39%.

Figure 6 present that constant shear stress assumption leads to considerable overestimation of the shear stresses at the intersection of the web plate and flange of the web frame. When the parabolic distribution is considered, these two locations become more precisely defined, but the value at the neutral axis becomes too small by 4%.

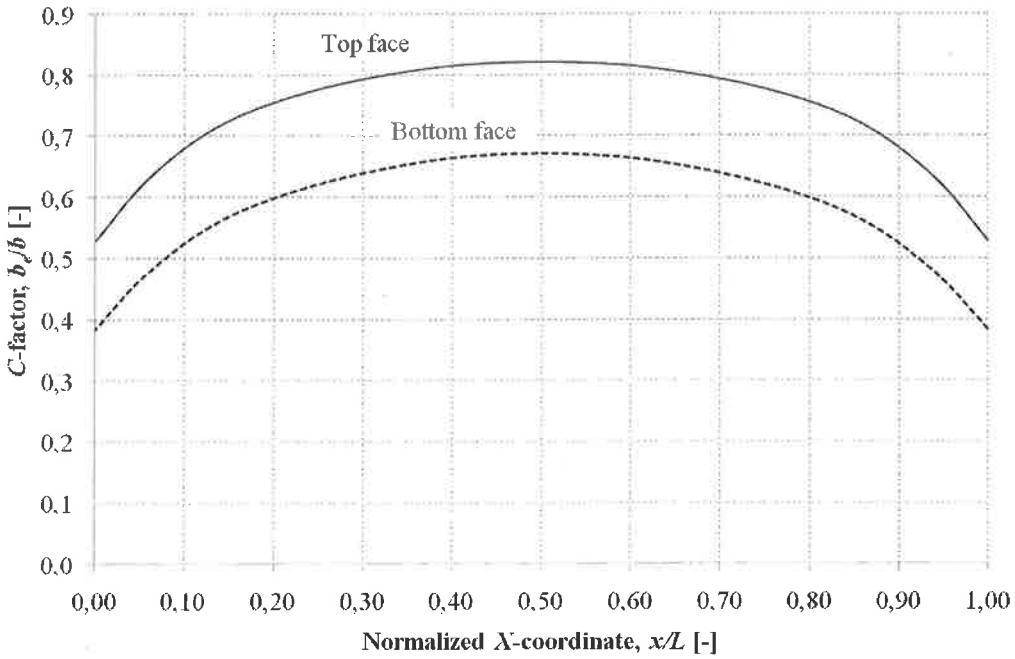

Figure 5. Effective breadth as a function of normalized X-coordinate. Simply supported beam.

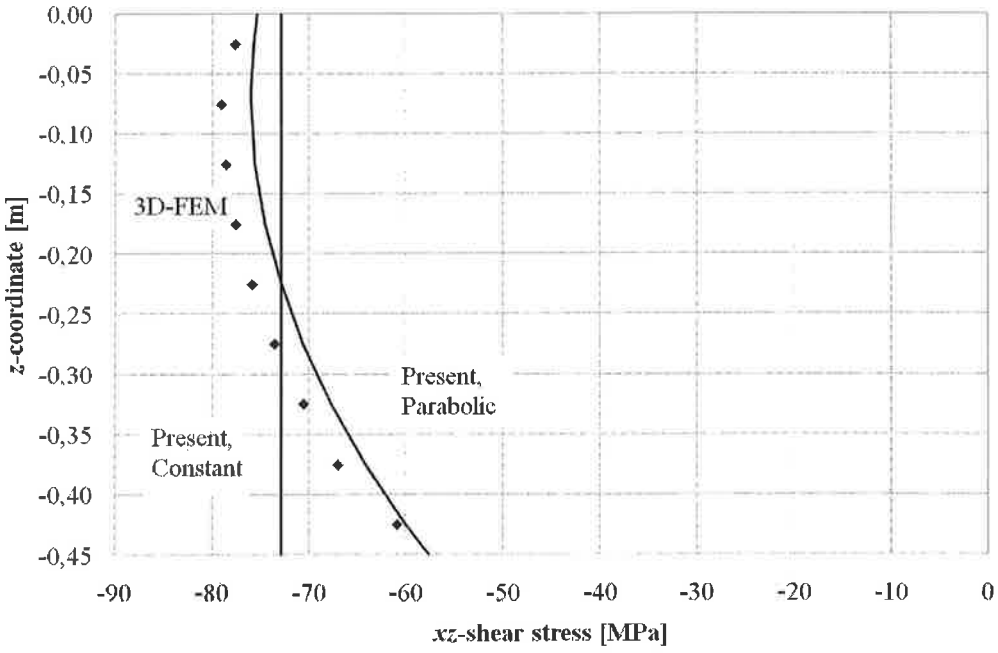

Figure 6. Comparison of the xz-shear stresses at x=2.85m.

4.2 Accommodation Deck

In reality the ship structure is not as simple as the one presented in the validation case study. Usually, for example the accommodation decks extend from across the whole ship breadth and the length can be equal to so-called fire zone (max length 40m or max area 1600m^2). So, the present

case study considers a deck with length 39.2 m and breadth 38.6 m. The web frame spacing is 2.8 m on longitudinal girders have spacing of 8.0 m, 7.48 m and 7.82 m. Every second web frame will have pillars in the intersection with longitudinal girders. The other dimensions are as in previous example, except the T-girder has web height and thickness h_w=488 mm and t_{ww}=7 mm, and flange breadth and thickness b_f=200 mm and t_f =12 mm. The applied load is 2.5 kPa applied on the sandwich plate. The FE mesh of the structure is presented in Figure 7.

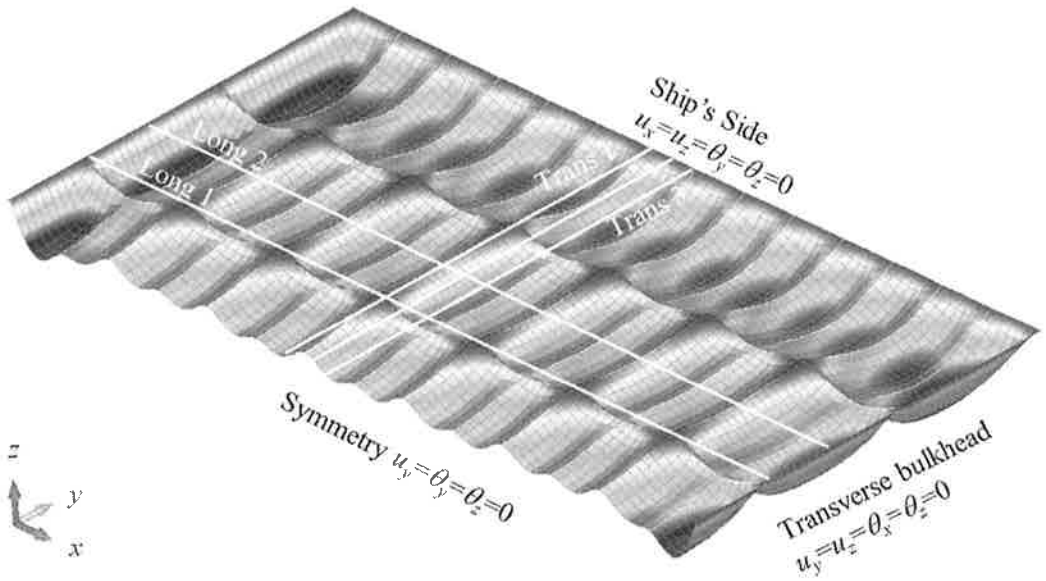

Figure 7. FE-mesh of the accommodation deck. Positioning of the grillage and pillars can be identified from the hungry-horse shape.

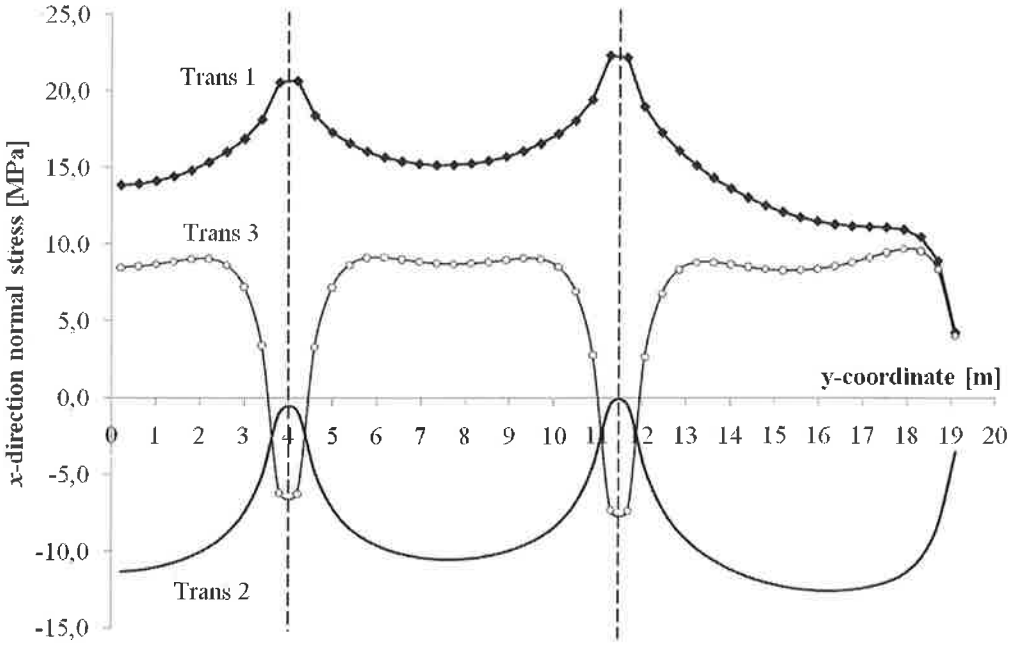

Figure 8. x-direction normal stress in the sandwich plate top face plate along different transverse paths.

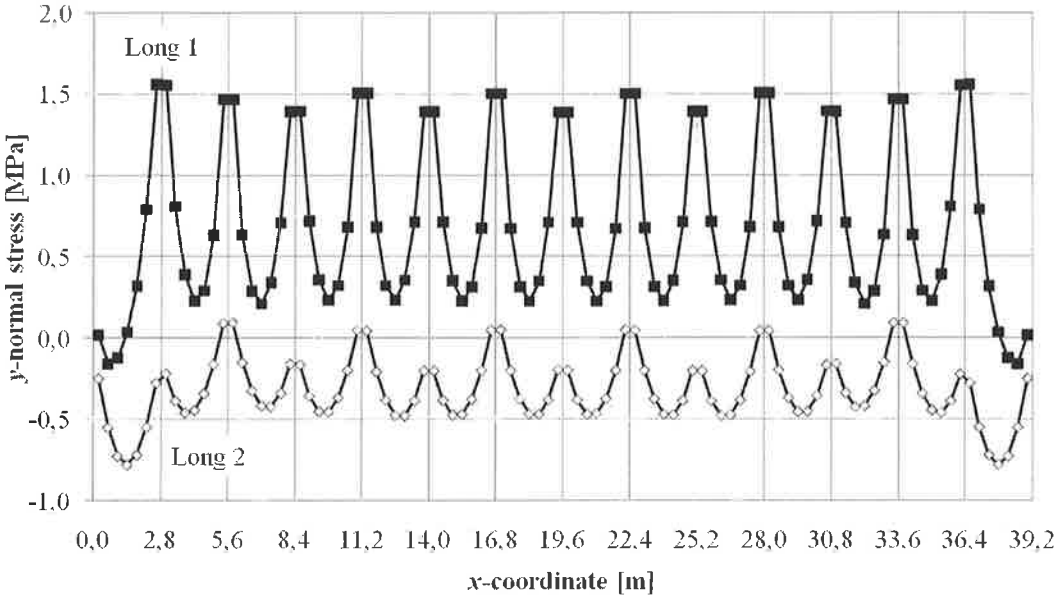

Figure 9. y-direction normal stress in the sandwich plate top face plate along different longitudinal paths.

The stress response in the sandwich plate top face plate is evaluated along different paths in transverse and longitudinal directions, see Figure 7. The results are presented for transverse paths in Figure 8, while the corresponding paths in longitudinal direction are given in Figure 9. Figure 8 and Figure 9 that the girders induce significant peaks to the stresses along girder direction. Figure 8 shows that the highest stress values occur in the line Trans 1 which is just next to the web frame with pillars. Figure 9 shows similar behavior. However, there it is more clearly seen that at the location of the web frame without the pillar supports the stress peaks induced by the web frames are much smaller than those at stiff web frames.

5 CONCLUSIONS AND DISCUSSION

The aim of this paper was to investigate the interaction between the web-core sandwich plate and the supporting girder system. First, the equivalent plate bending model was presented. Then, this model was connected to standard beam element using element offset. The accuracy of this type of modeling was checked using 3D FE models based on shell elements.

The validation of the equivalent modeling was proved to be accurate when normal stresses in the sandwich plates and in the girder are concerned. This indicates that the theory developed in Ref. [4] for plates can be extended to more complex structural assemblies. However, there seems to be slight differences in the shear stresses of the girder web, thus this need to be further investigated. The validation case showed that the effective breadth has different values at the top and bottom face of the sandwich. This is in line with the findings of [8]. It was also found out that this the ratio of these two values depends on the location across the length of the girder.

The case study on realistic ship structure was carried out on accommodation deck having size 39.2 m x 38.6 m. This investigation shows that the interaction between the girder system and the sandwich is indeed significant. The girder bending induces significant stress peaks on the sandwich which cannot be ignored in the stress analysis.

The case studies carried out in this paper consider typical grillage and web-core sandwich used nowadays in industry. The numerical values obtained indicate that some of the structural members are far from being optimal and significant weight savings could be obtained with optimization. However, this is left for future work.

6 ACKNOWLEDGEMENTS

This work was initiated out in EU-funded research project DE-Light Transport. The work was finished in Post Doctoral research project of Helsinki University of Technology. This financial support is gratefully acknowledged.

7 REFERENCES

[1] Marsico, T.A., Denney, P. and Furio, A., "Laser-Welding of Lightweight Structural Steel Panels", Proceedings of Laser Materials Processing Conference ICALEO 1993, pp. 444-451.

[2] Roland, F. and Reinert, T., "Laser Welded Sandwich Panels for the Shipbuilding Industry", Lightweight Construction – Latest Developments, February 24-25, 2000, London, SW1, pp. 1-12.

[3] Romanoff, J., Remes, H., Socha, G., Jutila, M. and Varsta, P., "The Stiffness of Laser Stake Welded T-joints in Web-core Sandwich Structures", Thin- Walled Structures, Vol. 45, No. 4, 2007, pp. 453-462.

[4] Romanoff, J. and Varsta, P., "Bending response of web-core sandwich plates", Composite Structures, Vol. 81, No. 2, 2007, pp. 292-302.

[5] Romanoff, J., Varsta, P. and Klanac, A., "Stress Analysis of Homogenized Web-Core Sandwich Beams", Composite Structures, Vol. 79, No. 3, 2007, pp. 411-422.

[6] Romanoff, J., Varsta, P. And Remes, H., "Laser-Welded Web-Core Sandwich Plates under Patch-Loading", Marine Structures, Vol. 20, No. 1-2, 2007, pp. 25–48.

[7] Scahde, H.A., "The Effective Breadth of Stiffened Plating under Bending Loads", The Society of Naval Architects and Marine Engineers, 1951, pp. 403-430.

[8] Klanac, A. "Optimal design of cardeck applying sand-wich panels", Master Thesis, Tehnički fakultet, Rijeka, 2002. (In Croatian)

[9] Kalnins, K., Skukis, E. and Auzins, J. "Metamodels for I-core and V-core Sandwich Panel Optimization", Proceedings of 8th International Conference on Shell Structures: Theory and Applications, SSTA-05, Jurata, October 12th – 14th 2005, pp. 569-572.

APPENDIX 1 –STIFFNESS PROPERTIES FOR BEAMS AND SANDWICH PLATES

The in-plane, coupling, and bending stiffness values are:

$$[A]=\int_{-h/2}^{h/2}[E]_i\,dz,\quad [B]=\int_{-h/2}^{h/2}[E]_i\,d_i\,dz,\quad [D_0]=\int_{-h/2}^{h/2}[E]_i\,d_i\,z\,dz,\quad i=t,c,b\,, \tag{A 1}$$

and the local bending stiffness of the face plates are

$$[D]_t=\frac{t_t^3}{12}[E]_t,\quad [D]_b=\frac{t_b^3}{12}[E]_b\,, \tag{A 2}$$

where

$$d_t=\frac{h}{2}-\frac{t_t}{2},\quad d_c=z,\quad d_b=-\frac{h}{2}+\frac{t_b}{2}, \tag{A 3}$$

and the elasticity matrix $[E]$ of the face plates i is

$$[E] = \frac{1}{1-\nu_i^2}\begin{bmatrix} E_i & \nu_i E_i & 0 \\ \nu_i E_i & E_i & 0 \\ 0 & 0 & G_i\left(1-\nu_i^2\right) \end{bmatrix}, \quad i = t, b. \tag{A 4}$$

The core has the elasticity matrix $[E]$

$$[E]_c = \frac{E_w t_w}{s}\begin{bmatrix} 1 & 0 & 0 \\ 0 & 0 & 0 \\ 0 & 0 & 0 \end{bmatrix}. \tag{A 5}$$

Similarly, the shear stiffness values are

$$D_{Qx} = k_{11}^2 \cdot \left(G_t t_t + G_b t_b + \frac{t_w}{s} G_w h_c \right), \quad D_{Qy} = \frac{12 D_w}{s^2\left(k_Q\left(\frac{D_w}{D_b} + 6\frac{d}{s} \right) + 12\frac{D_w}{k_\theta^b s} - 2\frac{d}{s} \right)}, \tag{A 6}$$

where

$$D_{Qx} = k_{11}^2 \cdot \left(G_t t_t + G_b t_b + \frac{t_w}{s} G_w h_c \right), \quad D_{Qy} = \frac{12 D_w}{s^2\left(k_Q\left(\frac{D_w}{D_b} + 6\frac{d}{s} \right) + 12\frac{D_w}{k_\theta^b s} - 2\frac{d}{s} \right)}, \tag{A 7}$$

and

$$k_{11} = \sqrt{\frac{1}{A\left(\sum_i \int \left(\frac{\tau_i}{Q_{Q,x} s} \right)^2 t_i ds_i \right)}}, \quad i = t, c, b, \qquad k_Q = \frac{1 + 12\frac{D_t}{s}\left(\frac{1}{k_\theta^t} - \frac{1}{k_\theta^b} \right) + 6\frac{D_t}{D_w}\frac{d}{s}}{1 + 12\frac{D_t}{D_w}\frac{d}{s} + \frac{D_t}{D_b}}, \tag{A 8}$$

$$k_\theta^i = Q_{Q,y} s / \theta_c^i, \qquad k_1^t = 1 - k_Q, \; k_1^b = k_Q, \; k_2^t = 2 - 3k_Q, \; k_2^b = 3k_Q - 1$$

The beam areas for normal force and shear forces and the moments of inertia are given as

$$A = h_w t_{ww} + b_f t_{wf}, \qquad A_{xz} = \left(h_w + t_{wf}\right) t_{ww}, \qquad A_{yz} = b_f t_{wf}$$
$$I_x = \frac{t_{wf} b_f^3 + h_w t_{ww}^3}{12} \qquad I_y = \frac{b_f e_1^3 - \left(b_f - t_{ww}\right)\left(e_1 - t_{ww}\right)^3 + t_{ww} e_2^3}{3}, \qquad J = \frac{t_{ww}^3 h_w + b_f t_{wf}^3}{3}, \tag{A 9}$$

where

$$e_1 = \frac{1}{2}\frac{t_{ww}\left(h_w + t_{wf}\right)^2 + \left(b_f - t_{ww}\right) t_{wf}^2}{t_{ww}\left(h_w + t_{wf}\right) + \left(b_f - t_{ww}\right) t_{wf}}. \tag{A 10}$$
$$e_2 = h_w + t_{wf} - e_1$$

OPTIMISATION FOR CRASHWORTHINESS

S. EHLERS
Marine Technology
Helsinki University of Technology
P.O.Box 5300
FIN-02015 TKK, FINLAND

ABSTRACT

Structural crashworthiness can be assessed with the non-linear finite element method. Thereby the structural energy is calculated until a certain penetration or fracture limit is reached. As a result a stiffened plate is optimized for indentation loading. The commonly used power material relation and a constant strain failure criterion serve to treat the non-linear material behaviour. The utilization of a parametric finite element model allows the structural elements to be varied automatically. A particle swarm algorithm is used to identify the crashworthy concept.

1. INTRODUCTION

Designing structures for the increase of crashworthiness is a complex task. Crashworthiness, described here as a capacity to absorb energy prior to rupture, depends on structural scantlings and topology, and this dependence is neither linear nor monotonous. Simple principle of adding steel to make a structure more crashworthy might only insignificantly raise crashworthiness, and it will definitely lead to irrational increase in mass. Several studies (Klanac et al 2005, Ehlers et al 2007, Klanac et al 2008) clearly presented this conclusion on both local panel level and on large structural level, and also fostered structural optimization as a rational principle behind design for crashworthiness.

The main objective in design of crashworthy structures is to distribute the available material rationally, i.e. to increase the energy absorption capability of the structure with least added mass. A crashworthy structure is presently designed according to best practice and verified through numerical simulations. The question then remains weather such a structure presents a rational design.

To make structural optimization for crashworthiness operable, two major conditions need to be met. Firstly, crashworthiness needs to be computed rapidly, and secondly, the optimization method should be capable to optimize different objectives and handle different discrete variables and nonlinear constraints. Literature shows that crashworthiness can be estimated through the numerical collision simulations that predominantly utilize nonlinear finite element method (FEM) (Ehlers et al 2008).

This paper presents the basis of a parametric model and extends its capability to automatically model any type of steel structure consisting of various stiffened plates. It includes a changing number of stiffeners and stiffener types and plate thickness. Therefore this paper seeks to define a procedure to combine LS-DYNA with automatic finite element modelling of ANSYS language. In this procedure, all parameters of a finite element model can be treated as variables. In other words, thicknesses, stiffener dimensions and amount can be varied and optimized. As a result, a rational crashworthy structure is obtained through a formal procedure, absorbing more

energy with least increase in mass over the initial structure. Additionally the procedure gives a rational insight into the sensitivity of design parameters. To demonstrate the procedure, paper presents crashworthiness optimization of a stiffened panel.

2. THE PARAMETRIC FINITE ELEMENT MODEL

The parametric finite element model is built based on the assumption that the structural cross section can be split into a discrete number of strakes, i.e. plate with stiffening, bounded by 'hard-points', i.e. connections of strong structural elements. As an example a ship cross-section is given in Figure 1 adopting the strake definition principle. Figure 2 presents a single strake between hard points. In this paper, strakes are assumed to be longitudinally stiffened between frames, the hard-points are marked as *P1* and *P2*, the thickness of the plate is t and the frame spacing s. Other strake variables are: the number of stiffeners and their type, and the web-frame spacing S.

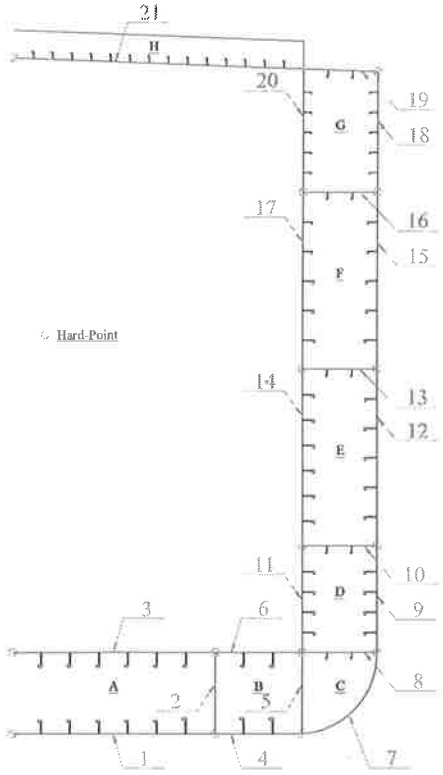

Figure 1: Example ship cross section split into 21 strakes

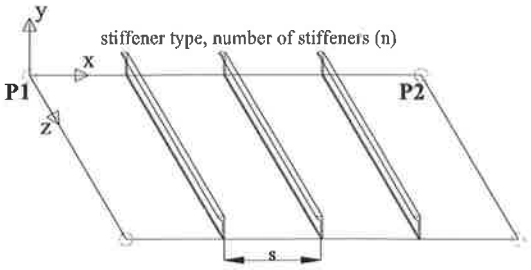

Figure 2: Strake variables

The parametric finite element model adopts the steps given in the flowchart presented in Figure 3. The detailed ANSYS parametric design language code is given in the Appendix of this paper.

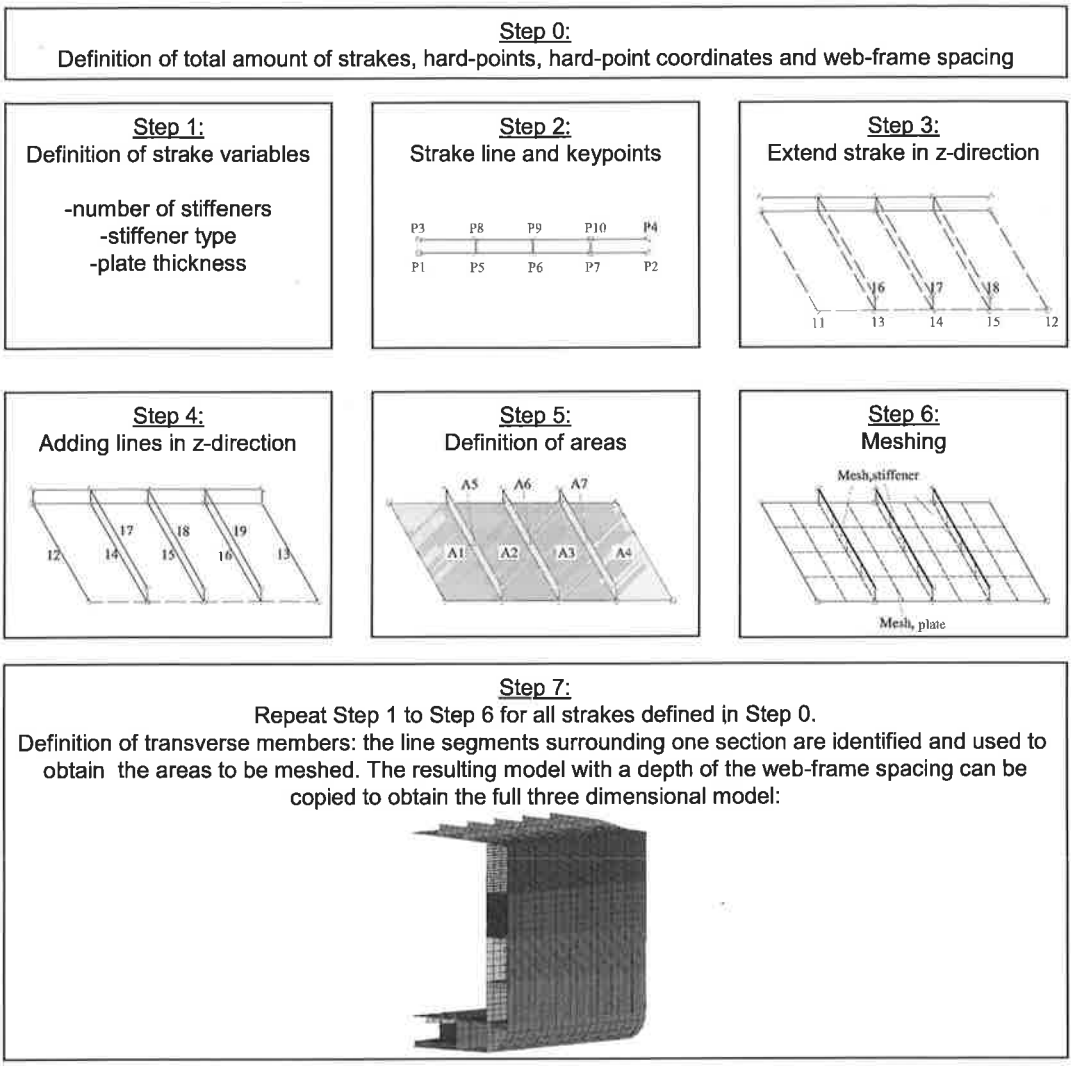

Figure 3: Steps of the parametric finite element model

3. OPTIMISATION FOR CRASHWORTHINESS

To demonstrate how to combine the presented FE modelling procedure with optimization, a single stiffened plate is designed to maximize the ratio between the capacity to absorb energy in collision with a rigid spherical indenter and the mass of the structure, see Figure 4. The geometry of the stiffened plate is of similar type as shown in Figure 2. The plate and stiffener thicknesses range from 1 to 10 mm. The stiffeners are flat bars, with an overall varying height between 50 to 200 mm. The number of stiffeners ranges from 2 to 19. Therefore the effective variable length becomes non-constant, because each stiffener can have a different thickness. The variables are changed in discrete steps of 1 for the stiffeners, or 1 mm for the thicknesses. The overall dimensions of the plate are 3m x 4.5m, having the short edges fixed and long edges freed. The displacement-controlled rigid sphere indents the plate in the centre.

3.1 The finite element model

The collision simulations are carried out with LS-DYNA version 971, see Hallquist (2005). The stiffened plate is modelled using four nodded quadrilateral Belytschko-Lin-Tsay shell elements with 5 integration points through their thickness. The common engineering tensile test formed the basic material information for the applied failure criterion used in these simulations. The engineering stress-strain curve was constructed from the load elongation measurements. LS-DYNA requires for an input the true stress versus strain curve, where the stress and strain becomes non-linear as a function of the true cross-sectional area of the specimen. The true stress-strain curve was obtained as presented by Peschmann (2001) and by reverse engineering resulting in the following power law form

$$\sigma = K \cdot \varepsilon^n \tag{1}$$

where the strength coefficient K is equal to 730 and the strain hardening index n is equal to 0.2. The experimental yield stress is found to be 284 MPa, see Figure 10. The Young's Modulus is equal to 206 GPa, Poisson ratio equals 0.3 and the steel density is 7850 kg/m³. The simulation terminates ones the plate ruptures, namely when the critical through thickness strain according to Zhang *et al.* (2004) is reached

$$\varepsilon_f(l_e) = \varepsilon_g + \varepsilon_e \cdot \frac{t}{l_e} \tag{2}$$

where ε_g is the uniform strain and ε_e is the necking strain, t is the plate thickness and l_e is the individual element length. It is commonly recommended that the ratio l_e / t is not less than 5 for shell elements. The values of the uniform and necking strain are achieved from thickness measurements related to the calculated stress states given by Zhang *et al.* (2004) are 0.056 for the uniform strain and 0.54 for the necking strain in the case of shell elements.

Implementation of those values is performed for material model 123 of LS-DYNA. Material 123 is a modified piecewise linear plasticity model using the stress versus strain curve defined in Figure 5. This material model allows fracture based on plastic thinning. The pre-calculated critical strain values are input for the material definition. The critical strain values are a function of the actual shell thickness and the prescribed element size. The prescribed element size in this example is set to 50 mm. For further details on the crashworthiness simulation and optimization procedure see Ehlers *et al.* (2007) and Ehlers *et al.* (2008) and Klanac *et al.* (2008).

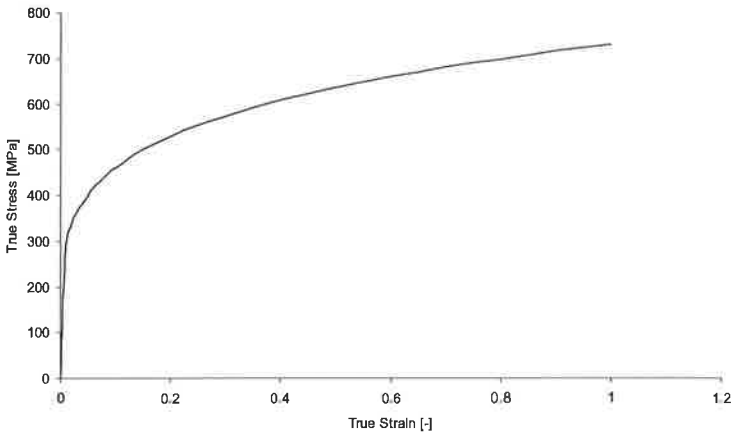

Figure 5: True stress versus strain relation

3.2 The optimization procedure

The crashworthiness optimization is unconstrained, and it is performed with Particle Swarm Optimization (PSO) algorithm (Eberhart and Kennedy 1995). MATLAB is utilized as a shell program managing the process and communication between LS-DYNA and PSO. The particle swarm size is set to 20 with 40 calculation rounds. Inertia in PSO is at start 1.4, the dynamic inertia reduction factor is 0.8 and the number of rounds to improve the solutions before the inertia is reduced is 4. Optimization is initiated with a random population. All together 800 alternatives are generated. Each structural alternative is indented with the rigid sphere until the plate ruptures. To treat the non-constant effective variable length, namely the changing amount of stiffeners and their individual thicknesses, a set of dummy variables is introduced. Thereby the total amount of variables passed by the PSO remains constant and is equal to 21. The resulting energy versus penetration curve is stored for comparison. Furthermore, the maximum energy value divided by the specific mass ob the structural alternatives, namely the Energy-per-Mass ratio (E/M), serves as the optimisation objective. The choice of this optimality criterion arises from the fact that it combines these two conflicting criteria into one single criterion. Therefore, a rational structure with an optimal E/M ratio can be achieved.

3.3 The crashworthiness optimization results

After 40 calculation rounds PSO converges to a solution, see Figure 6. All together 800 alternatives are generated. Their energy vs. penetration plots are seen in Figure 7. From the same figure it is also possible to see that this simple example of a stiffened plate can produce a significant scatter in the capacity to absorbed energy until the plate ruptures. In such a sensitive system, finding a good design is difficult. Therefore, using presented optimization-based approach to identify rational solutions is well justified. The alternative with the highest energy capacity per mass ratio has 11 stiffeners with the stiffener thicknesses as given in Figure 4. This panel weighs 695 kg (51.5 kg/m^2) and absorbs 11.9 kJ until rupture. To indicate significance of these values, the panel with the minimum plate thickness and 11 stiffeners weighs 144 kg (10.6 kg/m^2) and absorbs 0.9 kJ and the panel with the maximum plate thickness and 11 stiffeners weighs 1448 kg (107.2 kg/m^2) and absorbs 15.4 kJ.

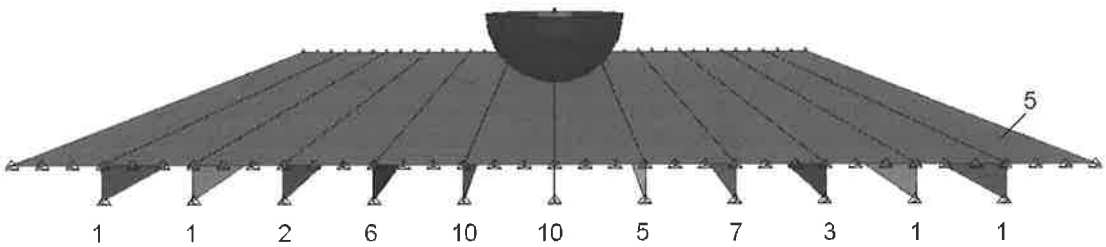

Figure 4: Finite element model of the optimal stiffened plate with indicated plate thicknesses in mm

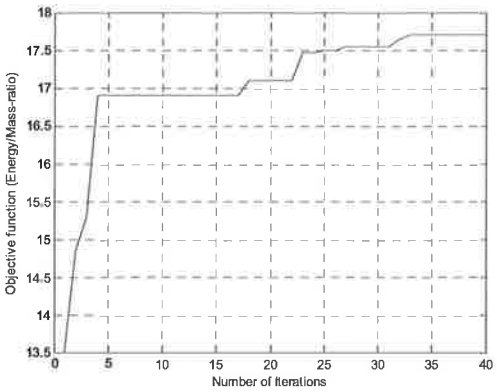

Figure 6: Convergence of objective function

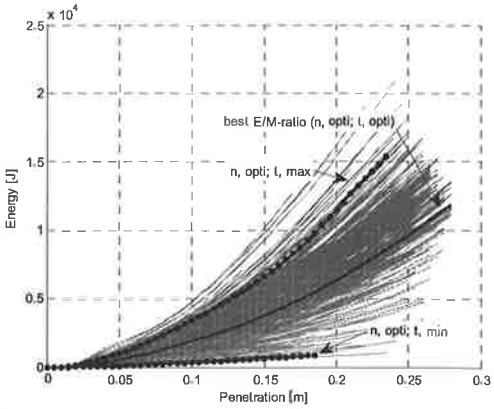

Figure 7: Energy versus penetration curves

4. SUMMARY AND CONCLUSIONS

A parametric FE modelling procedure has been presented to build structural models suitable for optimization for crashworthiness. This strake based approach handles the parameters of each strake as variables. This procedure allows a rational design for impact loading if coupled with an optimization algorithm, as presented in the case study. The case study unveiled that the panel with the best energy per mass ratio absorbs 77% of the Energy of the panel with the same amount of stiffeners at maximum thickness with only 48% of the weight. Furthermore, the PSO served as a robust tool to identify the structure with the highest E/M-ratio and it is, together with the parametric finite element model, capable to identify the optimum.

ACKNOWLEDGEMENT

The study presented in this paper is partial financial supported by the Finnish national project FIMECC/Light Research Program and is thankfully acknowledged.

REFERENCES

Eberhart, R. C. and Kennedy, J. A new optimizer using particle swarm theory. Proceedings of the Sixth International Symposium on Micromachine and Human Science, Nagoya, Japan. pp. 39-43, 1995

Ehlers S, Broekhuijsen J, Alsos HS, Biehl F, Tabri K. Simulating the collision response of ship side structures: A failure criteria benchmark study. Int Ship Progress 2008;55:127-144

Ehlers S, Klanac A, Tabri K. Increased safety of a tanker and a RO-PAX vessel by implementing a novel sandwich structure. In: Proc Fourth Int Conf Collision and Grounding of Ships. Germany, 2007. p. 109-115

Ehlers S, Tabri K, Schillo N, Ranta J. Implementation of a novel ship side structure into a tanker and a ropax vessel for increased crashworthiness. 6th European LS-DYNA Users' Conference, Gothenburg, Sweden, 2007. p 4.111-4.120

Hallquist J.O. LS-DYNA Theory Manual. Livermore Software Technology Corporation. 2005.
Klanac, A, Ehlers, S, Jelovica, J. Rational increase of safety of tankers in collision: Structural optimization for crashworthiness. Submitted for publication in Marine Structures.

Klanac, A., Ehlers, S., Tabri, K., Rudan, S., Broekhuijsen, J. Qualitative design assessment of crashworthy structures, Proceedings of International Maritime Association of Mediterranean - IMAM, Lisboa 2005, p. 461-9.

Zhang, L., Egge, E.D., Bruhns, H. Approval procedure concept for alternative arrangements, in: Proceedings of the 3rd International Conference on Collision and Grounding of Ships (ICCGS), IZU, Japan, 2004, pp. 87-96.

APPENDIX

The following step by step procedure builds a strake model using the parametric design language of ANSYS. Once a single strake is modelled, this procedure is looped over the total number of strakes to build the full parametric finite element model. The procedure is initiated with the definition of all hard-points, strake thicknesses, stiffener types and material grades in a format suitable for ANSYS. This initial data set will be used by the following strake modelling procedure.

Step 1: Definition of strake variables

xy	x- and y-coordinates of strake hard-points (P1 and P2)
n	number of stiffeners
type	stiffener type defining the height if the stiffener, *h*
t	plate thickness
S	webframe spacing
n_str	number of strakes in the model

Step 2: Strake line and keypoints

```
a=1                                  ! Initial counter for keypoint and line numbering
nr1=0                                ! Counting variable
count=0                              ! Counting variable
nr=-1                                ! Counting variable
*do,i,1,n_str,1                      ! Do loop from 1 to n_str
count=count+1                        ! Increases counter count by one
nr1=nr1+1                            ! Counting variable is increased by one per loop
k,,xy(1,nr1),xy(3,nr1)               ! Creates P1
k,,xy(2,nr1),xy(4,nr1)               ! Ccreates P2
WPLANE,,xy(1,nr1),xy(3,nr1),,xy(2,nr1),xy(4,nr1)        ! Creates workplane in P1
CSYS,4                               ! Places local coordinate system in P1
lstr,a,a+1                           ! Creates strake line between P1 and P2
num=n(count)                         ! Reads the correct stiffener number
htype=h(ht(nr1))                     ! Reads the stiffener height from predefined table
ldiv,a,,,num+1                       ! Divides strake line into num+1 lines
lstr,a+2,a+3                         ! Creates line between P3 and P4
ldiv,a+num+1,,,num+1                 ! Divides line between P3 and P4
u=a+3                                ! Creates counter u
e=a+num+3                            ! Creates counter e
*do,j,1,num                          ! Do loop to create stiffener lines
u=u+1                                ! Increases counter u by one
e=e+1                                ! Increases counter e by one
lstr,u,e                             ! Creates line between new points
*enddo                               ! Closes the do loop
*endif                               ! Closes the if loop
```

Strake do loop continues...

Step 3: Extend of the strake in z-direction

```
kgen,2,a,a+1,1,,,S,,0                  ! Generates P11 and P12 in z-direction
*if,num,gt,0,then                      ! Initiates if loop
kgen,2,a+4,a+3+num,1,,,S,,0            ! Copies P5 to P7 in z-direction
kgen,2,a+4+num,a+3+2*num,1,,,S,,0      ! Copies P8 to P10 in z-direction
*endif                                 ! Closes the if loop
a=a+100                                ! Sets counter a for next strake
numstr,kp,a                            ! Sets keypoint number to counter a
CSYS,0                                 ! Places coordinate system in origin
*enddo                                 ! Closes the global do loop
```

Step 4: Adding lines in z-direction

```
numstr,line,0                          ! sets starting points for lines
a=1                                    ! Initial counter for keypoint and line numbering
count=0                                ! Counting variable
*do,i,1,n_str,1                        ! Do loop from 1 to n_str
count=count+1                          ! Increases counter count by one
num=n(count)                           ! Reads the correct stiffener number
*if,num,gt,0,then                      ! If number of stiffeners is >0, than 12 to 19 are generated
f=2*(num+2)+a                          ! Creates counter f
*else                                  ! Otherwise lines 12 to 19
f=a+2                                  ! Increases counter f
*endif                                 ! Closes the if loop
lstr,a,f                               ! Creates line 12
lstr,a+1,f+1                           ! Creates line 13
*if,num,gt,0,then                      ! If number of stiffeners is >0 lines are created
f=f+1                                  ! Increases counter f by one
e=a+3                                  ! Creates counter e
*do,g,1,2*num                          ! Start do loop
f=f+1                                  ! Increases counter f by one
e=e+1                                  ! Increases counter e by one
lstr,e,f                               ! Creates lines
*enddo                                 ! Closes the do loop
*endif                                 ! Closes the if loop
a=a+100                                ! Sets counter a for next strake
numstr,line,a                          ! Sets line number to counter a
*enddo                                 ! Closes the global do loop
```

Step 5: Defining areas

```
numstr,line,0                          ! Sets starting points for lines
a=1                                    ! Initial counter for keypoint and line numbering
count=0                                ! Counting variable
*do,i,1,n_str,1                        ! Do loop from 1 to n_str
count=count+1                          ! Increases counter count by one
num=n(count)                           ! Reads the correct stiffener number
*if,num,gt,0,then                      ! If number of stiffeners is >0 areas are created
e=a-1                                  ! Creates counter e
f=a+3*num+1                            ! Creates counter f
k=a+3*num+3                            ! Creates counter k
c=a+3*num+3                            ! Creates counter c
b=a+2*num+1                            ! Creates counter b
count2=0                               ! Creates counter count2
```

```
*do,i,1,2*num+1                          ! Starts do loop
count2=count2+1                          ! Increases counter count2 by one
e=e+1                                    ! Increases counter e by one
*if,count2,eq,1,then                     ! Starts if loop
f=f+1                                    ! Increases counter f by one
adrag,e,,,,,,f                           ! Creates area A1
*endif                                   ! Closes if loop
*if,count2,gt,1,and,count2,le,num+1,then ! Starts if loop
k=k+1                                    ! Increases counter k by one
adrag,e,,,,,,k                           ! Creates area A2 to A4
*endif                                   ! Closes if loop
*if,count2,gt,num+1,then                 ! Starts if loop
c=c+1                                    ! Increases counter c by one
b=b+1                                    ! Increases counter b by one
adrag,b,,,,,,c                           ! Creates areas A5 to A7
*endif                                   ! Closes if loop
*enddo                                   ! Closes do loop
*else                                    ! Starts else loop in the case of zero stiffeners
adrag,a,,,,,,a+1                         ! Creates areas A1 to A4
*endif                                   ! Closes else loop
a=a+100                                  ! Sets counter a for next strake
numstr,area,a                            ! Sets area number to counter a
*enddo                                   ! Closes global do loop
```

Step 6: Meshing

```
lsize,all,meshsize                       ! Applies predefined meshsize to all lines
type,1                                   ! Shell element type for plates
mat,m1                                   ! Material for strake plate according to initial table
real,1                                   ! Real constant defining the plate thickness
amesh,A1,A2,A3,A4                        ! Meshes the plate areas of the strake
mat,m2                                   ! Material for stiffeners
real,2                                   ! Real constant defining the stiffener thickness
amesh,A5,A6,A7                           ! Meshes the stiffener areas of the strake
type,2                                   ! Beam element type for stiffeners
real,3                                   ! Real constant set for beam cross-section
latt,m2,3,2,,KB,                         ! Creates orientation of the unmeshed lines
lmesh,17,19                              ! Meshes lines 17 to 19
```

The iterative nature of step 6 can be achieved by adopting the procedures presented in the previous steps.

SHEAR BUCKLING OF STEEL PLATES AT ELEVATED TEMPERATURES

M. SALMINEN, M. HEINISUO, A. AALTO
Department of Structural Engineering
Tampere University of Technology
P.O.Box 600
FIN-33101 Tampere, FINLAND
mikko.a.salminen@tut.fi, markku.heinisuo@tut.fi, ari.aalto@tut.fi

ABSTRACT

This study presents a design method to predict the shear buckling load of a rectilinear simply supported steel plate when temperature distribution across the height of the plate is non-uniform. The proposal is based on the results of finite-element method and search of solutions applying different averaging schema and taking the most promising to use. The basic idea is to use equations and reduction factors given in the Eurocodes. Only the shear buckling is considered in this paper. Post-critical phase including tension field resistance and yielding of the flanges will be considered in the forthcoming papers.

1. INTRODUCTION

Shear buckling of steel plates at elevated temperatures occurs in many applications when considering the resistance of steel structures. Webs of all metal sandwich panels in fire, webs of pipelines for hot gases, webs of WQ-beams in buildings in fire etc, are examples of the applications.

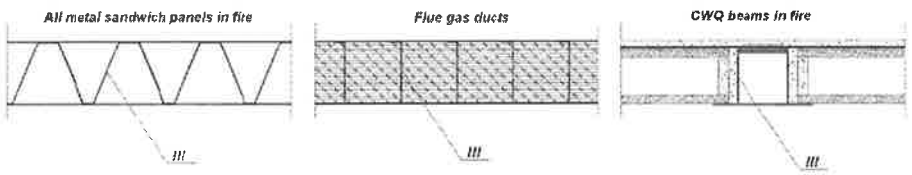

Figure 1. Webs at elevated temperatures.

If the temperature is high and uniform across the entire web, then test results and theories are available for shear resistance [1-4]. If the temperature is non-uniform across the entire height of the web, no test results or theories could be found for this case. Numerical investigations have been done for steel members under high, non-uniform temperature field concerning the axial strength of cold-formed steel channels and torsional buckling of I-beams [5,6], but not for shear. The safe solution is always to use the maximum temperature of the web.

In elevated temperatures there are two properties that should be reduced following the Eurocode equations: elastic modulus E_w and yield strength f_{yw}. It is extremely difficult to search for the solution for two reductions at one search, so the task is divided into two stages.

The goal of this part of the study is to develop a method to reduce the elastic modulus E_w with only one value for the whole plate in the case where the temperature distribution is non-uniform across the height of the plate. The method should be practical to use and it should give results that are conservative compared to FE-calculation.

The goal of the next study would then be to develop a method to reduce the yield strength f_{yw} of the plate with one value so that the ultimate shear resistance of the plate could be practically calculated in a case where the temperature distribution is non-uniform.

2. SHEAR BUCKLING OF STEEL PLATES AT ROOM TEMPERATURE

Consider the rectangular web of the steel beam, which is simply supported by the top and bottom flanges of the beam and by the vertical stiffeners. When the shear loading is increasing, the behavior of the web can be divided into three stages:

- web, before elastic shear buckling
- web resistance including post-buckling resistance with the tension field
- collapse stage leading to yielding of the flanges

These three stages are illustrated in the figure 2.

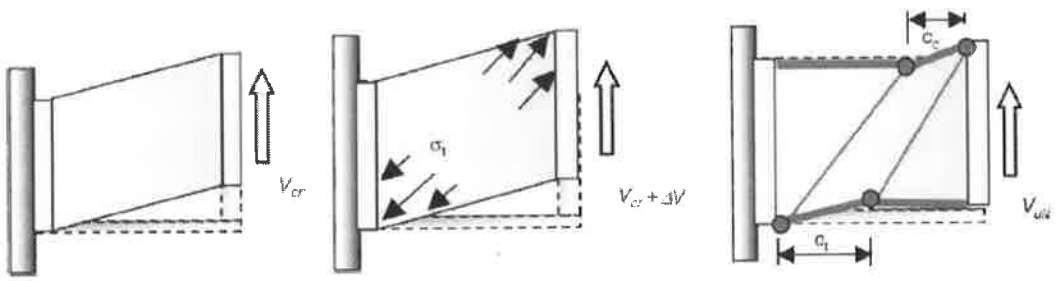

Figure 2. Three stages of web towards the collapse [1]

These parts can be written as follows:

$$V_{b,Rd} = V_{cr} + V_{\text{tension field}} + V_{bf,Rd} \quad (1)$$

Where $V_{b,Rd}$ represents the ultimate shear resistance
V_{cr} represents the elastic shear buckling load for simply supported plate,
$V_{\text{tension field}}$ represents the tension field resistance and
$V_{bf,Rd}$ represents the yield of flanges at the ultimate collapse stage

Only the elastic shear buckling is considered in this study. The buckling modes and corresponding eigenvalues for simply supported plates can be solved from von Karman's equations applying the double sinus Fourier series, known as Navier's solution. The result, the eigenvalue of the system, is

$$V_{cr} = h_w\, t_w\, \tau_{cr} \tag{2}$$

where h_w is the height of the web,
t_w is the thickness of the web and
τ_{cr} is the critical shear stress

The critical shear stress can be determined from classical stability theory for plates [7].

$$\tau_{cr} = k_\tau \frac{\pi^2 E_w}{12 \cdot (1-\nu)} \cdot \left(\frac{t_w}{h_w}\right)^2 \tag{3}$$

where E_w is the elastic modulus of the web material (E_w = 210000 MPa for steel),
ν is the Poisson ratio of the web material (ν = 0,3 for steel) and
the buckling coefficient k_τ is obtained from

$$k_\tau = 5{,}34 + 4 \cdot \left(\frac{h_w}{a}\right)^2 \quad \text{for } a \geq h_w$$

$$k_\tau = 5{,}34 \cdot \left(\frac{h_w}{a}\right)^2 + 4 \quad \text{for } a \leq h_w,$$

where a is the distance between stiffeners of the web.

In the Eurocodes [8] the design resistance of the web for shear is given as follows:

$$V_{b,Rd} = V_{bw,Rd} + V_{bf,Rd} \leq \frac{\eta f_{yw} h_w t}{\sqrt{3}\gamma_{M1}} \tag{4}$$

where $V_{bw,Rd}$ represents the contribution of the web including post-buckling
$V_{bf,Rd}$ represents the contribution from the flanges (ignored in this study)
η = 1,2 when T $\leq$ 400 °C and 1,0 when T > 400 °C [9]
γ_{M1} = 1,0 (material factor)

From the eq. (4) can be seen that in the Eurocodes the parts of the ultimate shear resistance V_{cr} and $V_{tension\ field}$ shown in eq. (1) are not calculated separately. Equation (3) can still be found from the Eurocodes and it is used when calculating the slenderness parameter $\bar{\lambda}_w = 0{,}76\sqrt{\frac{f_{yw}}{\tau_{cr}}}$.

In fig. 3 are shown the maximum shear stress of the web according to the Eurocodes (for non-rigid end post, flanges ignored) and the critical shear stress τ_{cr} using eq. (3). Both stresses are divided by the yield strength of the plate τ_{yw} and they are presented as a function of the Eurocode slenderness parameter. From the fig. 3 can be seen that the post-buckling resistance of the web is very significant part of the ultimate shear resistance especially in the case of slender web.

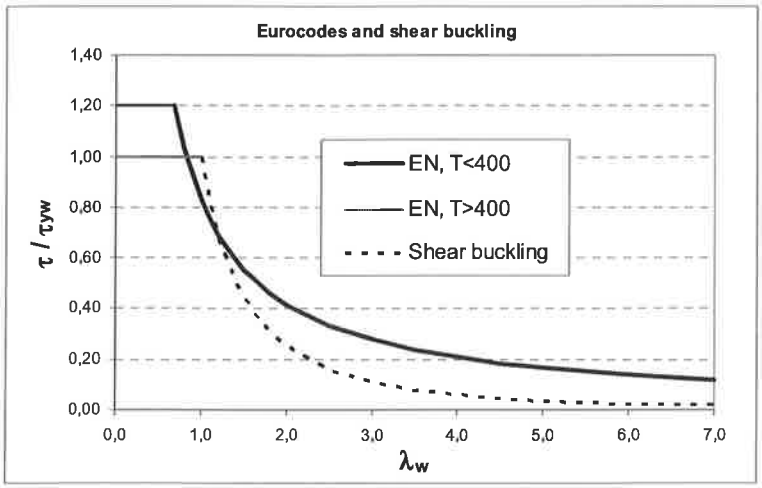

Figure 3. Critical shear stress and Eurocode maximum shear stress

3. SHEAR BUCKLING OF STEEL PLATES AT ELEVATED TEMPERATURES

Uniform temperature distribution across the web height

For this case there are test results available. In table 1 are shown properties of webs of the girders that were loaded primarily in shear at ambient and elevated temperature. In the table 2 are shown the tested shear buckling loads compared to the Eurocode resistances. Eurocode resistances are calculated using formulas (2) and (3). Elastic modulus E_w in formula (3) is reduced according to EN 1993-1-2 [10]. From the formula (3) can be seen that the critical shear stress is dependent only on the elastic modulus. Reduction for the yield strength is then not needed. The test results are originating from the reference [1]. It should be noted that in the test TG4 there were some problems during the execution.

Table 1. Properties of webs of tested girders [1]

	Web details				
Test panel	*b* (mm)	*d* (mm)	*t* (mm)	*b/d*	*d/t*
TG1	139	139	6.1	1	22.8
TG2	181	181	8	1	22.6
TG3	305	305	2	1	152.5
TG4	305	305	2.7	1	112.9
TG5	305	305	1.5	1	203.3

Table 2. Comparison between the test results [1] and the Eurocodes

Test	T [°C]	$V_{cr,Test}$ [kN]	$V_{cr,calculated}$ [kN]	$V_{cr,Test}$ / $V_{cr,calc.}$	Test	T [°C]	$V_{cr,Test}$ [kN]	$V_{cr,calculated}$ [kN]	$V_{cr,Test}$ / $V_{cr,calc.}$
TG1-1	20	172,2	167,4	1,03	TG4-1	20	101,4	109,0	0,93
TG1-2	550	79,85	104,6	0,76	TG4-2	400	58,9	76,3	0,77
TG2-1	20	270,3	277,6	0,97	TG4-3	550	24,54	49,6	0,49
TG2-2	400	260	277,6	0,94	TG4-4	700	10,59	14,2	0,75
TG2-3	550	183,6	173,5	1,06	TG5-1	20	21,05	18,7	1,13
TG2-4	700	62,4	63,8	0,98	TG5-2	400	17,63	13,1	1,35
TG3-1	20	53,35	44,3	1,20	TG5-3	550	13	8,5	1,53
TG3-2	400	30,08	31,0	0,97	TG5-4	700	4,5	2,4	1,88
TG3-3	565	19,87	18,2	1,09					
TG3-4	690	7,05	6,6	1,07					

Non-uniform temperature distribution across the web height

The problem in this case is to find the correct temperature for the reduction of the elastic modulus E_w and for the yield strength f_{yw} (not in this study).

Due to lack of the test results, the eigenvalue solutions are the controls for the search of solutions for the design methods. Critical shear stresses were calculated using FE-software *COMSOL Multiphysics* [11,12]. The plate was modeled in 3D using the following properties:

E_w = 210 000 MPa (room temperature)
ν = 0,3
t_w = 6 and 10 mm
h_w = 1000 mm
a = 1000, 2000 and 3000 mm

The plate was supported at all the edges at the perpendicular direction against the web plane and the rigid body motion was supported. The finite elements were solid quadratic elements. The plate was divided in 20 horizontal sections, which all had different values for elastic modulus E_w depending on the distribution of the temperature. The boundary conditions, applied shear stress and the element mesh used are shown in fig. 4. First the calculations were performed in room temperature to compare the results to classical theory and to get the reference value for elevated temperatures. In room temperature the difference to the classical theory (equations (2) and (3)) was in every case less than 3,5 %.

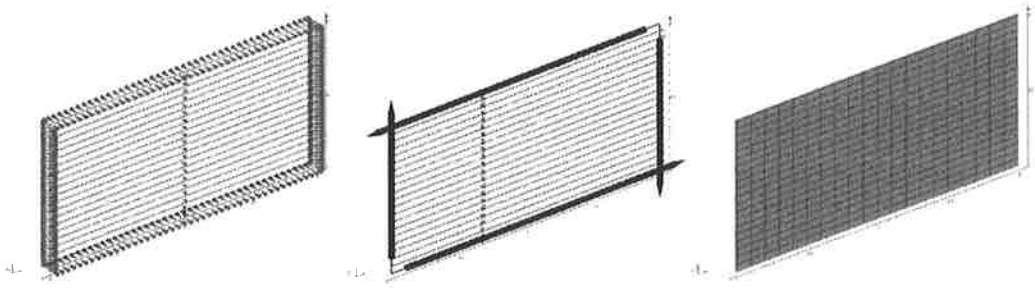

Figure 4. Modeling of the plate 1000 x 2000 x 10 mm^3

In fig. 5 are shown the lowest buckling modes for the plate 1000 x 2000 x 10 mm^3 in four different cases. First one on the left is in room temperature and the next temperature distributions are linear 100-500, 100-700 and 100-900 °C applied so that the hottest temperature affects on the lower edge of the plate.

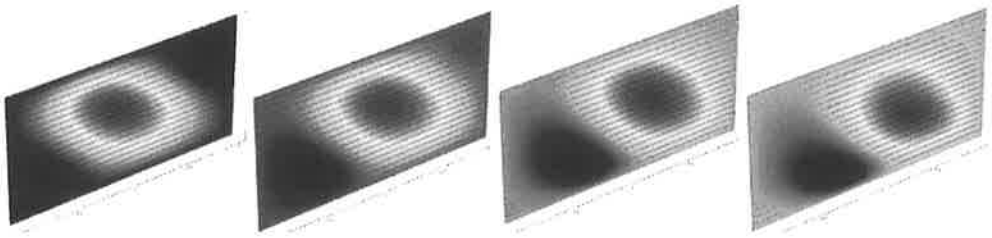

Figure 5. Buckling modes of the plate 1000 x 2000 x 10 mm^3 in different temperature distributions (room temperature, 100-500, 100-700 and 100-900 °C)

There may exist many ways how the temperature may vary across the plate height in fire situation and in this study the used temperature distributions across the web height are: 100-300, 100-500, 100-700, 100-900, 200-500, 300-600, 400-700, 500-800 and 600-900 degrees of Celsius. All these distributions are considered as a linear and non-linear (3.rd order polynomial) so that the hottest temperature affects on the lower edge of the plate in every case. In fig. 6 are shown all these used distributions and examples of the temperature distributions measured in the fire tests [13] of a typical hat beam of the slim floor.

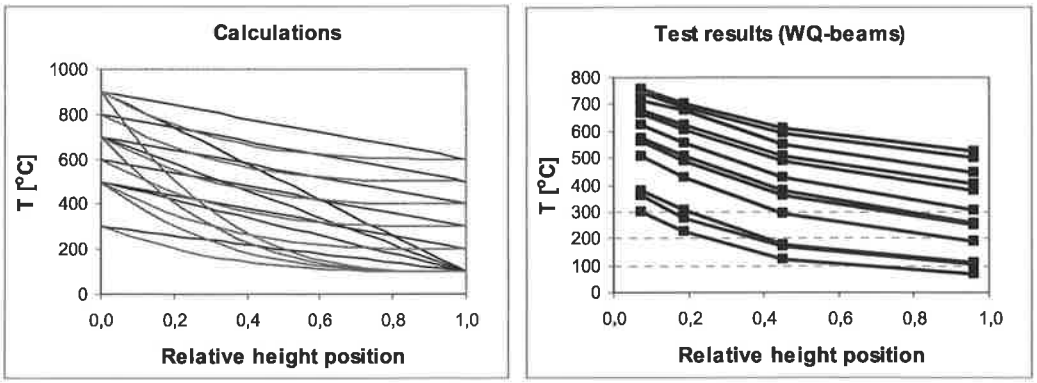

Figure 6. Temperature distributions used in calculations and from the test results [13].

Critical shear stresses were calculated also using *ABAQUS* [14] program in cases where the temperature distributions were linear 100-300, 100-500, 100-700 and 100-900 °C. The difference between the results that these two used softwares gave was in average 1,8 %.

The search space for the reduction of the elastic modulus

The search space for the reduction of the elastic modulus E_w is done by trying 6 different methods (a-f), which are described in the following.

Methods a-d are very simply to use. In the method a reduction of the elastic modulus E_w is based only on the temperature that the web has in the middle of its height. In the methods b, c and d also the hottest and the coldest temperature of the web are used to calculate the reduction factor $k_{E,\theta}$. Web temperatures needed in these methods are shown in figure 7.

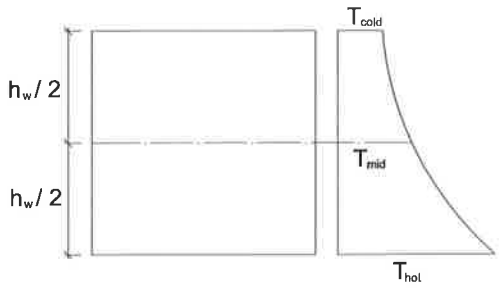

Figure 7. Web temperatures needed in methods a-d

The reduction factors $k_{E,\theta}$ in methods a - d are calculated as follows:

Method a: $k_{E,\theta,a} = k_{E,\theta}(T_{mid})$
Method b: $k_{E,\theta,b} = [k_{E,\theta}(T_{cold}) + k_{E,\theta}(T_{mid}) + k_{E,\theta}(T_{hot})] / 3$
Method c: $k_{E,\theta,c} = [k_{E,\theta}(T_{cold}) + 1{,}1k_{E,\theta}(T_{mid}) + 1{,}2k_{E,\theta}(T_{hot})] / 3{,}3$
Method d: $k_{E,\theta,d} = [k_{E,\theta}(T_{cold}) \times k_{E,\theta}(T_{mid}) \times k_{E,\theta}(T_{hot})]\text{^}(1/3)$

The idea in method e is to leave the hottest part (T>500 °C) out of the calculations and use the temperature in the middle of the cold part. This means that also the height of the web is reduced in this method. Therefore this method is more complicated to use than the previous ones. The strategy is shown in figure 8.

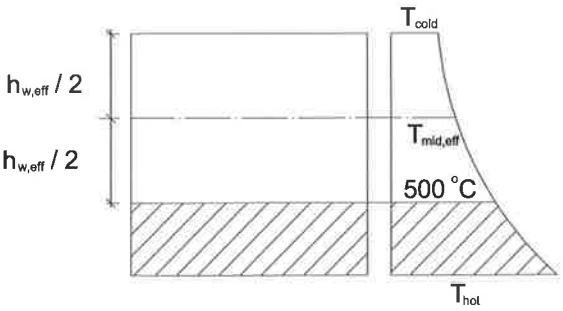

Figure 8. Method e

The reduction factor according to method e is calculated as follows:

Method e: $k_{E,\theta,e} = (h_{w,eff} / h_w)\ k_{E,\theta}(T_{mid,eff})$

If the maximum temperature of the web is less than 500 °C, then the method e becomes the same as method a. When the minimum temperature of the web is more than 500 °C the reduction factor becomes zero. Another problem when using this method is that the shape of the effective plate is not the same as the shape of the original plate. That means that the buckling coefficient k_τ changes also. In the calculations that has not been considered.

Method f is a graphical way to solve the problem. It is based on the reduction factor curve for elastic modulus given in EN 1993-1-2. The temperatures needed in this method are shown in figure 9.

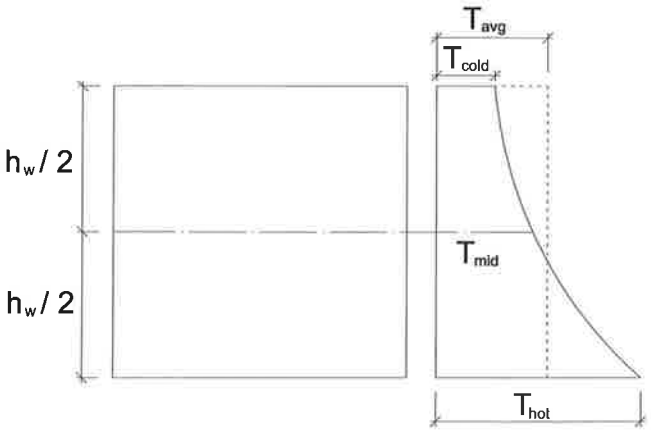

Figure 9. Temperatures needed in method f

In the method f the idea is to draw a line between points (T_{mid}, $k_{E,\theta}(T_{hot})$) and ($2T_{avg}$ - T_{cold}, $k_{E,\theta}(T_{cold})$). The crossing point of this curve and the Eurocode reduction curve shows the temperature and the reduction factor to use. The use of method f is shown in figure 10.

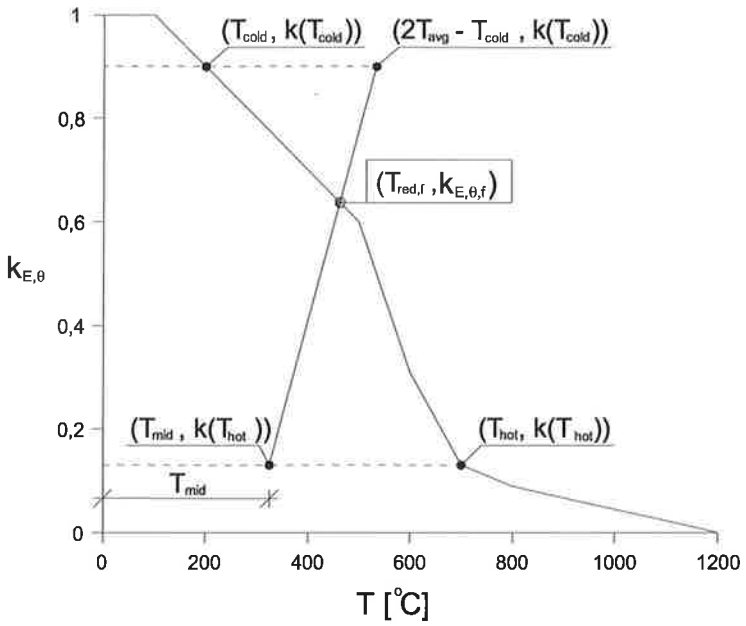

Figure 10. Method f

If the line drawn is vertical it gives the same result as method a, but now its angle between vertical line depends on the distribution of the temperature. The advantage of the method f is that it takes effectively into account the shape of the reduction curve. Method f can also be presented

analytically as a formula by calculating the crossing points of the elastic modulus' reduction factor curve and the line shown in figure 10. Since the reduction factor curve is defined in parts, this is an iterative process, which may contain few steps.

4. RESULTS

The methods were compared to finite-element method results with 18 different temperature distributions (9 linear and 9 third order polynomial). The result from the FE-calculation ($V_{cr,fire}/V_{cr,room}$) and the calculated reduction factors according to each method are shown in table 3. In the last column is shown the reduction factor of the design strength $k_{0.2p,\theta}$ calculated using the average temperature of the plate (EN 1993-1-2 [10] method). It should be noted that factor $k_{0.2p,\theta}$ is used to calculate the ultimate shear resistance (not shear buckling resistance) for class 4 steel sections, therefore the comparison to other methods is complicated.
FE-calculation was performed for each temperature distribution six times (three different lengths and two different thicknesses of the plate). The minimum value for reduction factor is used. In each case the minimum value for the reduction factor is got from the square plate 1000 x1000 mm^2.

Table 3. Comparison of the methods and FEM-calculations

	Reduction factor $k_{E,\theta}$							
Temperature distribution	FE_{min}	a	b	c	d	e	f	$k_{0.2p,\theta}$
1. 100-300 °C linear	0,897	0,900	0,900	0,894	0,896	0,900	0,867	0,890
2. 100-500 °C linear	0,788	0,800	0,800	0,788	0,783	0,800	0,733	0,780
3. 100-700 °C linear	0,566	0,700	0,610	0,584	0,450	0,533	0,510	0,650
4. 100-900 °C linear	0,288	0,600	0,556	0,528	0,344	0,425	0,306	0,530
5. 200-500 °C linear	0,746	0,750	0,751	0,741	0,740	0,750	0,700	0,715
6. 300-600 °C linear	0,607	0,650	0,587	0,572	0,544	0,467	0,540	0,590
7. 400-700 °C linear	0,377	0,455	0,428	0,411	0,346	0,217	0,314	0,415
8. 500-800 °C linear	0,192	0,220	0,303	0,288	0,228	-	0,175	0,215
9. 600-900 °C linear	0,112	0,110	0,163	0,155	0,132	-	0,102	0,100
10. 100-300 °C non-linear	0,953	0,975	0,925	0,919	0,921	0,975	0,927	0,945
11. 100-500 °C non-linear	0,901	0,950	0,850	0,838	0,829	0,950	0,855	0,890
12. 100-700 °C non-linear	0,811	0,923	0,684	0,658	0,493	0,829	0,761	0,835
13. 100-900 °C non-linear	0,640	0,899	0,656	0,691	0,394	0,753	0,697	0,780
14. 200-500 °C non-linear	0,830	0,862	0,787	0,778	0,775	0,862	0,791	0,808
15. 300-600 °C non-linear	0,718	0,762	0,624	0,609	0,574	0,677	0,678	0,683
16. 400-700 °C non-linear	0,562	0,662	0,497	0,480	0,392	0,476	0,544	0,560
17. 500-800 °C non-linear	0,351	0,490	0,393	0,378	0,298	-	0,334	0,358
18. 600-900 °C non-linear	0,182	0,242	0,207	0,199	0,172	-	0,163	0,173

Method e doesn't give a result for the distribution where $T_{cold} > 500$ °C even though the reduction factor may still be in some cases about 0,35 according to FE-results.

In figure 11 are shown the minimum-, average- and maximum value of the ratio $k_{E,\theta,FE} / k_{E,\theta,method}$ for each presented method. If the value of the ratio is more than 1, the result that the method gives is conservative compared to the FE-result.

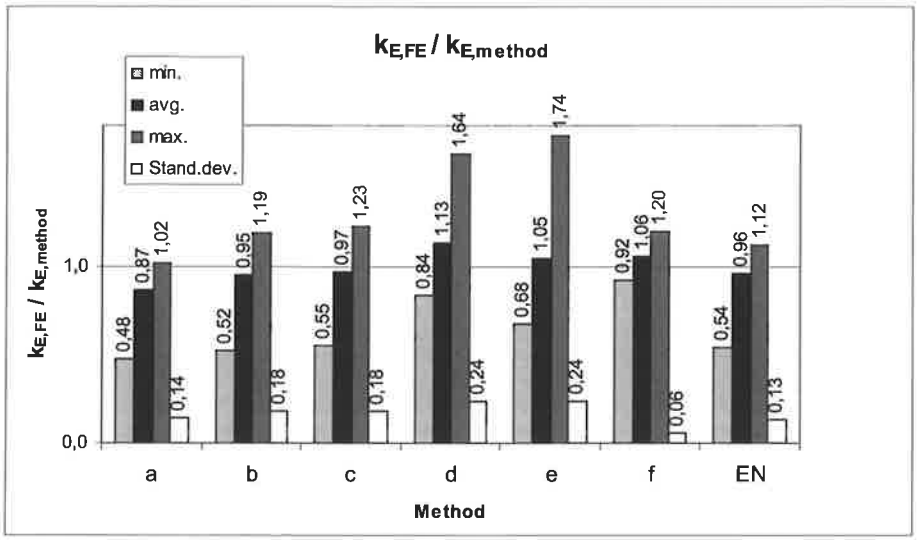

Figure 11. Comparison of the methods

5. CONCLUSIONS

Based on table 3 and figure 11 it can be said that method f gives the best results compared to the results from FE-calculation. Unfortunately there are no test results available.

In figure 12 is shown a comparison between FE-results, method f results and the upper and lower limits for the reduction factor $k_{E,\theta}$. Upper limit for the reduction factor means that the reduction is done using the coldest temperature and lower limit that the reduction is done using the hottest temperature of the plate.

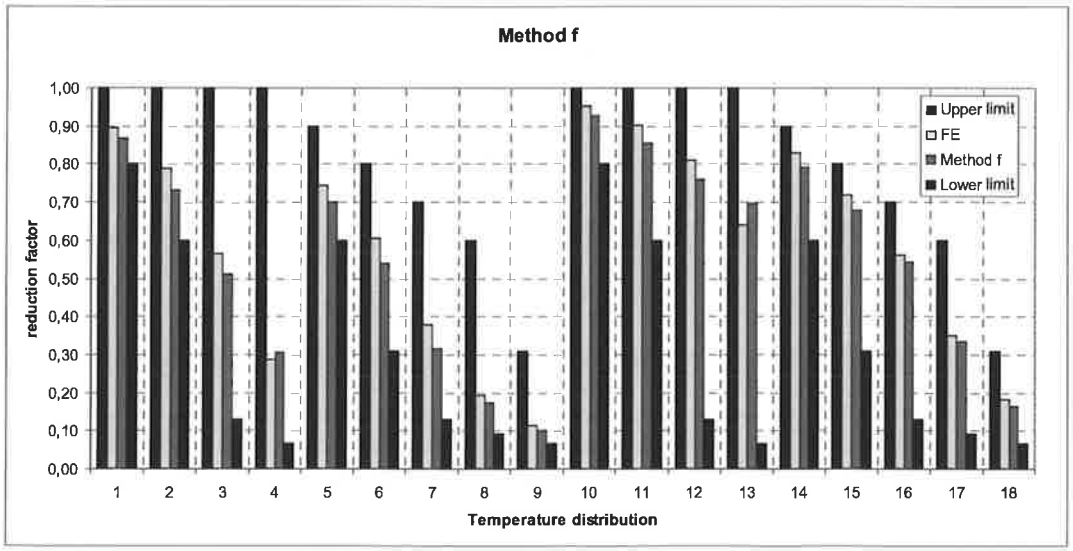

Figure 12. Comparison between method f and FE-calculation

The proposed method seems to be simple way to check the shear buckling resistance in fire. In the forthcoming studies the post-buckling resistances of the webs will be considered. The test results are badly needed to verify the theories.

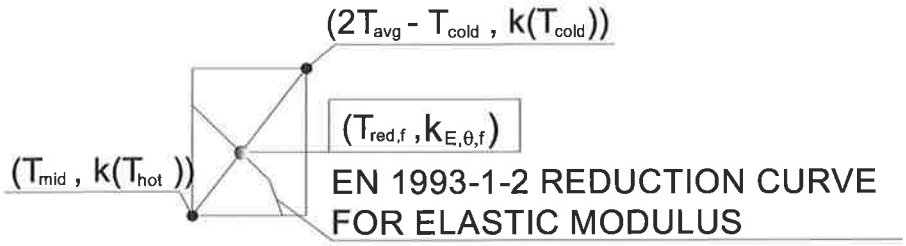

Figure 13. Graphical expression for the proposed design method (see also figures 9 and 10).

In following is shown the analytical way to find the reference temperature T_{ref}, which can be used for the whole web in case where the temperature distribution is non-uniform.

$$T_{ref,1} = \frac{1{,}1 + \phi T_{mid} - k_{E,\theta,hot}}{\phi + 0{,}001} \Rightarrow T_{ref,1} \le 500^\circ C \Rightarrow T_{ref} = T_{ref,1}$$

$$T_{ref,1} > 500^\circ C$$

$$T_{ref,2} = \frac{2{,}05 + \phi T_{mid} - k_{E,\theta,hot}}{\phi + 0{,}0029} \Rightarrow 500^\circ C < T_{ref,2} \le 600^\circ C \Rightarrow T_{ref} = T_{ref,2}$$

$$T_{ref,2} > 600^\circ C$$

$$T_{ref,3} = \frac{1{,}39 + \phi T_{mid} - k_{E,\theta,hot}}{\phi + 0{,}0018} \Rightarrow 600^\circ C < T_{ref,3} \le 700^\circ C \Rightarrow T_{ref} = T_{ref,3}$$

$$T_{ref,3} > 700^\circ C$$

$$T_{ref,4} = \frac{0{,}41 + \phi T_{mid} - k_{E,\theta,hot}}{\phi + 0{,}0004} \Rightarrow 700^\circ C < T_{ref,4} \le 800^\circ C \Rightarrow T_{ref} = T_{ref,4}$$

$$T_{ref,4} > 800^\circ C$$

$$T_{ref,5} = \frac{0{,}27 + \phi T_{mid} - k_{E,\theta,hot}}{\phi + 0{,}000225} \Rightarrow 800^\circ C < T_{ref,5} \Rightarrow T_{ref} = T_{ref,5}$$

Where $\phi = \dfrac{\Delta k}{2T_{avg} - T_{cold} - T_{mid}}$

$\Delta k_{E,\theta} = k_{E,\theta,cold} - k_{E,\theta,hot}$

$k_{E,\theta,cold}$,$k_{E,\theta,hot}$ are reduction factors according to EN 1993-1-2

T_{cold}, T_{mid} and T_{avg} are shown in fig. 9

REFERENCES

[1] Vimonsatit V., Tan K.H., Qian Z.H., Testing of plate girder web panel loaded in shear, Journal of structural Engineering, ASCE, 2007

[2] Vimonsatit V., Tan K.H., Ting S.K., Shear strength of plate girder web panel at elevated temperature, Journal of Constructional Steel Research 63, 2007, pp. 1442-1451

[3] Tan K.H., Qian Z.H., Experimental behaviour of a thermally restrained plate girder loaded in shear at elevated temperature, Journal of Constructional Steel Research 64, 2008, pp. 596-606

[4] Kaitila O., Finite element modeling of cold-formed steel members at high temperatures, Helsinki University of Technology, Laboratory of Steel Structures, Publications TKK-TER-24, Otamedia, Espoo, 2002

[5] Feng M., Wang Y.C., Davies J.M., Axial strength of cold-formed thin-walled steel channels under non-uniform temperatures in fire, Fire Safety Journal 38, 2003, pp. 679-707

[6] Yin Y.Z., Wang Y.C., Numerical simulations of the effects of non-uniform temperature distributions on lateral torsional buckling resistance of steel I-beams, Journal of Constructional Steel Research 59, 2003, pp. 1009-1033

[7] Timoshenko S.P., Gere J.M., Theory of elastic stability, International Student Edition, Second Edition, McGraw-Hill Book Company Inc., 1961

[8] EN 1993-1-5, Eurocode 3: Design of steel structures, Part 1-5: Plated structural elements, CEN, Brussels, 2005

[9] Kansallinen liite standardiin SFS-EN 1993-1-5 Eurokoodi 3: Teräsrakenteiden suunnittelu. Osa 1-5: Tasomaiset levyrakenteet (In Finnish), Ympäristöministeriö, Helsinki, 2008

[10] EN 1993-1-2, Eurocode 3: Design of steel structures, Part 1-2: Structural fire design, CEN, Brussels, 2005

[11] COMSOL Multiphysics User's Guide, Version 3.5a COMSOL AB, 2008

[12] Structural Mechanics Module User's Guide, Version 3.5a COMSOL AB, 2008

[13] Teräsnormikortti N:o 21/2009, WQ-palkin poikkileikkauksen mitoitus normaali- ja palotilanteessa (In Finnish), TRY, 2009

[14] ABAQUS/Standard, User's Manual, Volume II, Version 6.2, Hibbitt, Karlsson & Sorensen, Inc. 2001

Poranterän kuormittuminen väännön ja puristuksen sekä rotaation alaisena

Matti A Ranta
Teknillinen korkeakoulu, Informaatio- ja luonnontieteiden tiedekunta,
Matematiikan ja systeemianalyysin laitos,
PL 1100, 02015 Espoo
matti.ranta@tkk.fi

TIIVISTELMÄ

Porattaessa reikää kappaleeseen tulee vääntömomentin ja syöttävän voiman sekä poranterän pyörimisnopeuden olla sopivan suuruiset, jotta vältetään terän katkeaminen.

Yksinkertaistetaan pora istukasta lähteväksi tasapaksuksi ympyräpoikkipintaiseksi ulokepalkiksi, jota väännetään momentilla M_t ja syötetään eli puristetaan voimalla N. Myöhemmin kuormitukseen lisätään vielä rotaatiosta ω johtuva keskipakoisvoima.

Liikeyhtälöt johdetaan olettaen deformaatiot pieniksi ja aikariippuvuus harmoniseksi. Tällöin päädytään 4. kertaluvun lineaariseen differentiaaliyhtälöön ns. stabiiliusyhtälöön. Se voidaan ratkaista koeratkaisua käyttäen. Tällöin saadaan 4. asteen algebrallinen yhtälö, jolla on kompleksiset juuret. Ratkaisu muodostuu trigonometrisistä ja hyperbolisista sini- ja kosini-funktioista. Yleisessä tapauksessa saadaan *vääntö-puristus-rotaationurjahduksen* transkendenttinen ns. karakteristinen VPR-funktio, jonka juuret antavat kriittiset kuormitustilat. Näistä voidaan päätellä poran katkeamisvaara.

Tavallisimmat reunaehdot johtuvat poran keskityksen virheistä ja siitä että porauskohdassa terä vetää sivuun. Virheiden otaksutaan esiintyvän poran alkukäyristyksen tasossa, jolloin niiden vaikutus on suurimmillaan.
Reunaehdot kiinteässä istukkapäässä ovat siis asennusvirheet: lineaarinen sivuttaissiirtymä ja kaltevuus.
Poran lastuavassa päässä voidaan ajatella kolmea erilaista reunaehtoa:
Tapaus 1. Poran pää on *vapaa* ja pyörii tasaisella nopeudella.
Tapaus 2. Kun poran kärki on tunkeutumassa porattavaan kappaleeseen, voidaan olettaa että taivutusmomentti häviää ja että kärki on vakioetäisyydellä pystyakselista. Tämä vastaa *nivelkiinnitystä.*
Tapaus 3. Kun poraus on pidemmälle edennyt, voidaan reunaehdon katsoa vastaavan *jäykkää kiinnitystä,* jossa pora tunkeutuu tietyllä etäisyydellä pystyakselista materiaaliin vakiokulmassa.

Kirjallisuudesta tunnetut stabiliteetin menettämistapaukset saadaan tämän yleisen VPR-funktion erikoistapauksina.

Johdanto

Matemaattisen mallin johtamisessa viitataan lähinnä lähteen [1] kappaleisiin 16-21, missä perusteet on esitetty. Erityisen tärkeä on kappale 21 ja sen tehtävät 1,2,3 ja 5, joissa puristus ja vääntö on käsitelty erikseen.

Koordinaatiston valinta

Ortogonaalinen kanta **tnb** (tangentin t=dr/ds , päänormaalin ja sivunormaalin suuntaiset yksikkövektorit) liikkuu pitkin palkin neutraaliakselia kaarenpituuden s muuttuessa. Kiinteässä päässä on $s=0$ ja leikkaavassa päässä on $s=l$. Siirtymän **ds** jälkeen kanta **tnb** on kiertynyt kulman $d\Phi$ verran. Suure $\Omega = d\Phi/ds$ kuvaa koordinaatiston kiertymisen voimakkuutta. Kiertymisvektorin komponenttiesitys on ([1] k. (18.4))

$$\Omega = \mathrm{t}\Omega_t + \mathrm{n}0 + \mathrm{b}\Omega_b \qquad (1)$$

Tässä komponenteilla on seuraava merkitys

$\Omega_t = d\varphi/ds = 1/T$ kierevyys (torsion) $\qquad \Omega_b = d\alpha/ds = 1/R$ käyristys (curvature)

Näissä φ on kiertymiskulma tangentin ympäri ja α on tangentin kaltevuuskulma oskuloivassa **tn**-tasossa. T on kierevyyssäde ja R kaarevuussäde (katso [2] sivut 30-32).
Koska minkä hyvänsä vektorin **A** absoluuttisen dA ja relatiivisen muutoksen δA erotus johtuu koordinaatiston kierrosta, saadaan absoluuttisen ja relatiivisen derivaatan välille yhteys

$$dA/ds = \delta A/\delta s + \Omega \times A \qquad (2)$$

Voimat ja momentit sekä tasapainoyhtälöt

Palkin sisäisiä suureita ovat momenttivektori **M** ja voimavektori **F**, joiden komponenttiesitykset ovat ([1] k. (19.7))

$\mathrm{M} = \mathrm{t}M_t + \mathrm{n}0 + \mathrm{b}M_b$ ja $\mathrm{F} = \mathrm{t}F_t + \mathrm{n}F_n + \mathrm{b}F_b$

Poraan vaikuttaa ulkoisena kuormituksena hitausvoimajakautuma $ds\mathrm{K}$, jossa

$$\mathrm{K} = -\mathrm{t}\rho A l\, d^2u/dt^2 - \mathrm{n}\rho A\, d^2v/dt^2 + \rho A\omega^2\left(\mathrm{j}y + \mathrm{k}z\right)$$

Kertomalla skalaarisesti vuoronperää yksikkövektoreilla **n** ja **b** saadaan

$$K_n = \mathrm{K}\cdot\mathrm{n} = -\rho A\, d^2v/dt^2 + \rho A\omega^2\left(\mathrm{j}\cdot\mathrm{n}y + \mathrm{k}\cdot\mathrm{n}z\right) \approx -\rho A\, d^2v/dt^2 + \rho A\omega^2 y = \rho A\, d^2la/dt^2 + \rho A\omega^2 la$$
$$K_b = \mathrm{K}\cdot\mathrm{b} = \rho A\omega^2\left(\mathrm{j}\cdot\mathrm{b}y + \mathrm{k}\cdot\mathrm{b}z\right) \approx \rho A\omega^2 z \approx 0$$

Tässä on otettu käytäntöön dimensioton yksinkertaistettu amplitudifunktio

$$a = a(\varsigma) = \int_0^{\varsigma=s/l} \alpha(\zeta)d\zeta \qquad (3)$$

Lisäksi poraan vaikuttaa rotaatiohitaudesta aiheutuva momenttijakautuma dsm

$$\mathrm{m}=-\mathrm{t}\rho I_t\, d^2\psi/dt^2 - \mathrm{b}\rho I_b\, d^2\alpha/dt^2 \qquad (4)$$

Poran materiaalin tiheys on ρ. Poikkipinnan ala on A sekä sen tavallinen hitausmomentti neutraaliakselin suhteen on $I_n = I_b = I$ että hitausmomentti vääntöakselin suhteen on $I_t = I_n + I_b = 2I$. Poran alkion pituusakselin suuntainen siirtymä on lu. Poran vääntökulma on ψ, joka ei ole sama kuin sen kiertymiskulma φ. Poran rotaationopeus on ω, jolloin keskipakoistermi on $\rho A\omega^2 la$.

Tasapainoyhtälöt saadaan tarkastelemalla infinitesimaalisen lyhyttä irtileikatuksi ajateltua pätkää, johon sisäiset suureet **M** ja **F** pienine lisäyksineen on merkitty ulkoisiksi suureiksi ([1]). Lisäksi sovelletaan derivointikaavaa (2).

$$\delta\mathrm{F}/\delta\mathrm{s} + \Omega\times\mathrm{F} + \mathrm{K}=0 \qquad \text{ja} \qquad \delta M/\delta\mathrm{s} + \Omega\times M + \mathrm{t}\times\mathrm{F}+\mathrm{m}=0$$

Puretaan nämä komponenttiyhtälöiksi ja koska skalaareille on voimassa $d/ds \equiv \delta/\delta s$, siirrytään takaisin tavallisiin derivaattamerkintöihin

Voimayhtälöt

$$dF_t/ds \quad -\Omega_b F_n - \rho Al\, d^2u/dt^2 = 0 \qquad (5)$$

$$dF_n/ds + \Omega_b F_t - \Omega_t F_b - \rho Al\, d^2a/dt^2 = -\rho Al\omega^2 a \qquad (6)$$

$$dF_b/ds + \Omega_t F_n = 0 \qquad (7)$$

Momenttiyhtälöt

$$dM_t/ds \quad -\rho I_t\, d^2\psi/dt^2 = 0 \qquad (8)$$

$$\Omega_b M_t - \Omega_t M_b - F_b = 0 \qquad (9)$$

$$dM_b/ds \quad +F_n - \rho I_b\, d^2\alpha/dt^2 = 0 \qquad (10)$$

Tasapainoyhtälöitä on 6 kpl, mutta tuntemattomia on 9 kpl. Tarvittavat lisäyhtälöt saadaan lujuusopista.

Lujuusopillisia kaavoja

Lujuusopista tiedetään:

Puristusvoima

$$F_t = EAl\, du/ds \quad (= EA\varepsilon) \qquad (11)$$

Vääntömomentti

$$M_t = GI_t\, d\psi/ds \qquad (12)$$

Taivutusmomentti

$$M_b = EI\left(d\alpha/ds - d\alpha_0/ds\right) \qquad (13)$$

Näissä kaavoissa G on liukumoduuli, joka kytkeytyy Poissonin luvun ν ja kaavan $E/G = 2(1+\nu)$ välityksellä kimmokertoimeen E. Poran alkukäyristys on $d\alpha_0/ds$. Nyt on yhtälöitäkin 9kpl.

Dimensioton esitysmuoto

Aikaisemmin kaavassa (3) on jo otettu käyttöön amplitudifunktio. Siinä referoitiin pituuskoordinaatti s poran pituuteen l dimensiottoman muuttujan $\varsigma = s/l$ avulla. Merkitään derivaattaa ς :n suhteen pilkulla eli

$$d(\ )/ds = d(\ )/d\varsigma : l = (\ )'/l$$

Sijoitetaan puristuksen, kierevyyden ja käyristyksen lausekkeisiin $\varepsilon = u'$, $\Omega_t = \varphi'/l$ ja $\Omega_b = \alpha'/l$. Lisäksi on syytä huomata, että $\alpha = a'$. Lujuusopin kaavat (11), (12) ja (13) kuuluvat

$F_t = EAu'$, $M_t = GI_t\psi'/l$ ja $M_b = EI(\alpha' - \alpha_0')/l$

Otetaan käyttöön dimensioton *rotaatioparametri* Γ ja dimensioton voima f kaikilla indekseillä:

$\Gamma = \rho A l^4 \omega^2/EI$ ja $f = Fl^2/EI$ (14)

On syytä huomata, että ehjälle d säteiselle ympyräpoikkipinnalle saadaan suhde $\kappa = I/Al^2 = (d/l)^2/16$.

Voima- ja momenttiyhtälöt (5)-(10) voidaan kirjoittaa dimensiottomassa muodossa

$$(u'' - \ddot{u})/\kappa - \alpha' f_n = 0 \quad (15)$$

$$f_n' + \alpha' u'/\kappa - \varphi' f_b - \ddot{a}/\kappa + \Gamma a = 0 \quad (16)$$

$$f_b' + \varphi' f_n = 0 \quad (17)$$

$$\psi''/(1+\nu) - 2\ddot{\psi} = 0 \quad (18)$$

$$\alpha'\psi'/(1+\nu) - \varphi'(\alpha' - \alpha_0') - f_b = 0 \quad (19)$$

$$\alpha'' - \alpha_0'' - \ddot{\alpha} + f_n = 0 \quad (20)$$

Väännön, puristuksen, kierevyyden ja taipuman välinen yhteys

Ensimmäinen momenttiyhtälö (18) on tunnettu vääntövärähtelyjen osittaisdifferentiaaliyhtälö. Sen analyyttinen ratkaisu fysikaalisissa koordinaateissa on D'Alembertin mukaan *vääntökulma*

$$\psi(t,s) = M\left(t\sqrt{G/\rho l^2} + s/l\right) + N\left(t\sqrt{G/\rho l^2} - s/l\right)$$

Funktiot M ja N määrittyvät alku- ja reunaehdoista, jotka saattavat riippua muista suureista. Asiaa ei tarkastella tässä enempää.

Yhtälöstä (15) eliminoidaan f_n yhtälön (20) avulla jolloin saadaan *puristus-taipumayhtälö*

$$(u'' - \ddot{u})/\kappa + a''(a''' - a_0''' - \ddot{a}') = 0 \quad (21)$$

Derivoidaan yhtälö (19) pituuskoordinaatin suhteen ja käytetään hyväksi yhtälöitä (17) ja (20). Saadaan *vääntö-kierevyys-taipumayhtälö*

$$\left[a''\psi'/(1+\nu)\right]' - (a'' - a_0'')\varphi'' - 2(a''' - a_0''')\varphi' + \ddot{a}'\varphi' = 0 \quad (22)$$

Derivoidaan yhtälö (20) pituuskoordinaatin suhteen ja käytetään hyväksi yhtälöitä (16) ja (19).

Saadaan *puristus-vääntö-kierevyys-taipumayhtälö*

$$a''' - a_0''' - \ddot{a}'' + \ddot{a}/\kappa - \Gamma a - a'' u'/\kappa + \left[a'' \psi'/(1+\nu) - (a'' - a_0'')\varphi'\right]\varphi' = 0 \qquad (23)$$

Poran sisäiset rasitukset

Poran sisäisiä rasituksia tarkasteltaessa otetaan käyttöön kuormitusparametrit k_N (24) ja k_M (25).

Dimensioton puristusvoima

$$f_t = u'/\kappa \quad \left(= F_t l^2/EI = -k_N^2\right) \qquad (24)$$

Miinusmerkki johtuu siitä, että $f_t < 0$.

Dimensiottomat leikkausvoimat:

$$f_n = \ddot{a}' - (a''' - a_0''') \qquad \left(= F_n l^2/EI\right)$$

$$f_b = a'' \psi'/(1+\nu) - \varphi'(a'' - a_0'') \quad \left(= F_b l^2/EI\right)$$

Dimensiottomat momentit:

Vääntömomentti

$$m_t = \psi'/(1+\nu) \quad \left(= M_t l/EI = 2k_M\right) \qquad (25)$$

Taivutusmomentti

$$m_b = a'' - a_0'' \quad \left(= M_b l/EI\right)$$

Stationaarinen tila

Jos värähtelyt ovat vähäisiä, voidaan otaksua poran dynaamisen tilan olevan stationaarisen, jolloin kaikki aikaderivaatat häviävät. Puristukseen, vääntöön, kierevyyteen ja taipumaan liittyvät yhtälöt (21), (22) ja (23) voidaan kirjoittaa muotoon:

Puristus-taipumayhtälö

$$\left[u'/\kappa + \tfrac{1}{2}(a'')^2\right]' - a'' a_0''' = 0 \qquad (26)$$

Vääntö-kierevyys-taipumayhtälö

$$a'''\left[\psi'/(1+\nu) - 2\varphi'\right] - a''\varphi'' + a_0''\varphi'' + 2a_0'''\varphi' = 0 \qquad (27)$$

Puristus-vääntö-kierevyys-taipumayhtälö

$$a''' + \left[-u'/\kappa + \left(\psi'/(1+\nu) - \varphi'\right)\varphi'\right]a'' - \Gamma a + a_0'''' + (\varphi')^2 a_0'' = 0 \qquad (28)$$

Näissä kaavoissa $\psi'/(1+\nu) = 2k_M$ on vakio, koska $\psi''/(1+\nu) = 2\ddot{\psi} \equiv 0$

Alkujaan tasaisesti käyrä pora

Pora on tasaisesti käyrä, jos $a_0'' = \alpha_0'$ on vakio eli korkeammat derivaatat häviävät. Koska (25):n mukaan

$$\psi'/(1+\nu) = 2k_M \qquad (29)$$

vääntö-kierevyys-taipumayhtälöstä (27) seuraa ensin $(a'' - a_0'')\varphi'' + 2a'''(\varphi' - k_M) = 0$. Tästä seuraa edelleen, koska k_M ja a_0'' ovat vakioita, differentiaaliyhtälö

$$(\varphi' - k_M)'/(\varphi' - k_M) = -2(a'' - a_0'')'/(a'' - a_0'').$$

Sen ratkaisu on $\varphi' = k_M + vakio/\left(a'' - a_0''\right)^2$. Se johtaa äärettömään kierevyyteen kohdassa, jossa $m_b = a'' - a_0'' = 0$. Vakion täytyy siis olla nolla, joten kierevyys on vakio

$$\varphi' = k_M \tag{30}$$

Sijoitetaan puristus (24) ja kierevyys (30) yhtälöön (28) sekä merkitään puristus-vääntökuormitusparametri

$$k^2 = k_N^2 + k_M^2 \tag{31}$$

Yhtälöstä (28) seuraa nyt sovellutusten kannalta tärkeä lineaarinen differentiaaliyhtälö

$$a'''' + k^2 a'' - \Gamma a = -k_M^2 a_0'' \tag{32}$$

poran kriittisten kuormitustapausten määrittämiseksi.

Poran taipuman amplitudifunktio

Dimensiottomalle amplitudifunktiolle on saatu tavallinen epähomogeeninen differentiaaliyhtälö (32), jonka yksityisratkaisu on $k_M^2 \alpha_0' / \Gamma$. Homogeenisen yhtälön $a'''' + k^2 a'' - \Gamma a = 0$ koeratkaisu $a(\varsigma) = Ae^{r\varsigma}$ johtaa deterministiseen polynomiin

$r^4 + k^2 r^2 - \Gamma = 0$.

Sen juuret ovat $r_i = \pm\sqrt{-k^2 \pm \sqrt{k^4 + 4\Gamma}}/\sqrt{2}$. Merkitään

$$\gamma = \sqrt{-k^2 + \sqrt{k^4 + 4\Gamma}}/\sqrt{2} \text{ ja } \lambda = \sqrt{+k^2 + \sqrt{k^4 + 4\Gamma}}/\sqrt{2} \tag{33}$$

jolloin juuret voidaan kirjoittaa lyhyesti $r_{1,2} = \pm\gamma$ ja $r_{3,4} = \pm i\lambda$.
Amplitudifunktio on tarkoituksenmukaisinta kirjoittaa muotoon (34)

$$a(\varsigma) = A(\cosh\gamma\varsigma - \cos\lambda\varsigma) + B\gamma(\sinh\gamma\varsigma/\gamma - \sin\lambda\varsigma/\lambda) + C(\cosh\gamma\varsigma + \cos\lambda\varsigma) + D\gamma(\sinh\gamma\varsigma/\gamma + \sin\lambda\varsigma/\lambda) + k_M^2\alpha_0'/\Gamma$$

Tästä seuraa derivoimalla kaltevuuskulma (35)

$$\alpha(\varsigma) = A(\gamma\sinh\gamma\varsigma + \lambda\sin\lambda\varsigma) + B\gamma(\cosh\gamma\varsigma - \cos\lambda\varsigma) + C(\gamma\sinh\gamma\varsigma - \lambda\sin\lambda\varsigma) + D\gamma(\cosh\gamma\varsigma + \cos\lambda\varsigma)$$

ja edelleen käyristys (36)

$$\alpha'(\varsigma) = A(\gamma^2\cosh\gamma\varsigma + \lambda^2\cos\lambda\varsigma) + B\gamma(\gamma\sinh\gamma\varsigma + \lambda\sin\lambda\varsigma) + C(\gamma^2\cosh\gamma\varsigma - \lambda^2\cos\lambda\varsigma) + D\gamma(\gamma\sinh\gamma\varsigma - \lambda\sin\lambda\varsigma)$$

ja käyristyksenderivaatta (37)

$$\alpha''(\varsigma) = A(\gamma^3\sinh\gamma\varsigma - \lambda^3\sin\lambda\varsigma) + B\gamma(\gamma^2\cosh\gamma\varsigma + \lambda^2\cos\lambda\varsigma) + C(\gamma^3\sinh\gamma\varsigma + \lambda^3\sin\lambda\varsigma) + D\gamma(\gamma^2\cosh\gamma\varsigma - \lambda^2\cos\lambda\varsigma)$$

Poran kiinnityspään reunaehdot

Poran tulisi olla keskellä istukkaa ja suorassa. Todellisuudessa syntyy kuitenkin pieni kaltevuusvirhe $\alpha 0$ ja keskitysvirhe δ . Kun kaavoihin (35) ja (34) sijoitetaan $\varsigma = s/l = 0$, saadaan $\alpha(0) = D\gamma 2 = \alpha 0$ ja $a(0) = 2C + k_M^2\,\alpha_0'/\Gamma = \delta/l$. Näistä ratkaistaan integroimisvakiot $C = \frac{1}{2}\left(\delta/l - k_M^2\alpha_0'/\Gamma\right)$ ja $D\gamma = \frac{1}{2}\alpha 0$

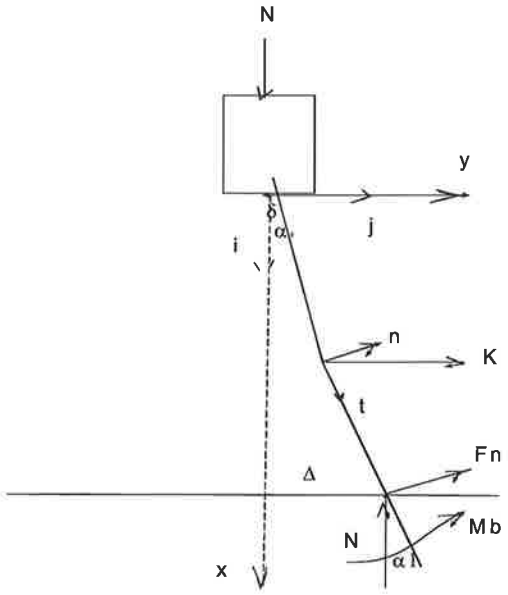

Kuva 1. Poran reunaehdot

Lastuavan pään reunaehdot

Integroimisvakiot A ja B määrittyvät lastuavan pään reunaehdoista. Koska stabiliteetin menetyksen kriteeri saadaan reunaehdon kertoimien A ja B kerroindeterminantin oleellisen osan nollakohdista, reunaehtolausekkeita ei tarvitse kirjoittaa täydellisinä esiin.

Poran lastuavan pään $\varsigma = s/l = 1$ reunaehdot voivat olla kolmenlaiset:

Tapaus 1. Leikkaava pää on vapaa $k_M = k_N = 0$, sillä sekä momentti että syöttövoima häviävät

$M_b(1) = 0 \;\Rightarrow\; \alpha'(1) - \alpha_0' = 0$

$F_n(1) = 0 \;\Rightarrow\; \alpha''(1) - \alpha_0'' = 0 \;\Rightarrow\; \alpha''(1) = 0$

$F_b(1) = 0 \;\Rightarrow\; k_M\left[\alpha'(1) + \alpha_0'\right] \xrightarrow[k_M \to 0]{} 0$

Sijoitetaan reunaehdot kaavoihin (36) ja (37) jolloin tulee

$A\left(\gamma^2 \cosh\gamma + \lambda^2 \cos\lambda\right) + B\gamma\left(\gamma \sinh\gamma + \lambda \sin\lambda\right) = vakio$

$A\left(\gamma^3 \sinh\gamma - \lambda^3 \sin\lambda\right) + B\gamma\left(\gamma^2 \cosh\gamma + \lambda^2 \cos\lambda\right) = vakio$

Tämän kerroindeterminantti antaa karakteristisen funktion

$f(k,\Gamma) = \gamma^4 + \lambda^4 - \gamma\lambda\left(\gamma^2 - \lambda^2\right)\sinh\gamma \sin\lambda + 2\gamma^2\lambda^2 \cosh\gamma \cos\lambda$

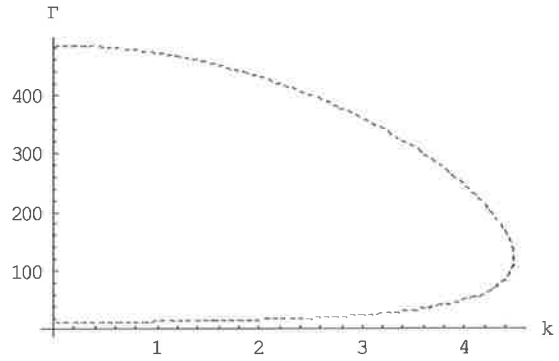

Kuva 2. Vapaan poran karakteristinen funktio eli $f(k,\Gamma)=0$ fiktiiviset ratkaisuparit

Koska pora pyörii vapaasti ilmassa, ei sillä ole varsinaista kuormitusta vaan $k=0$. Yhtälöllä $f(0,\Gamma)=0$ on kaksi katkaisua $\Gamma=12{,}3624$ ja $\Gamma=485{,}519$, joista jälkimmäinen tuskin tulee kysymykseen.

Kun $k=0$, kaavoista (33) seuraa juuret $\gamma=\lambda=\sqrt[4]{\Gamma}$ ja karakteristinen yhtälö kuuluu

$$f(\Gamma)=1+\cosh\sqrt[4]{\Gamma}\cos\sqrt[4]{\Gamma}=0 \qquad (38)$$

Tämän ensimmäiset juuret ovat (katso [6] Ch IV.5:d p31) $\sqrt[4]{\Gamma}=1{,}8751$ ja $7{,}8548$. Näistä seuraa

$$\Gamma=12{,}3624 \text{ ja } 3806{,}5463 \qquad (39)$$

Tapaus 2. Kun poran kärki on tunkeutumassa porattavaan kappaleeseen, voidaan olettaa että kärki on x-akselista etäisyydellä Δ ja että taivutusmomentti M_b häviää. Se vastaa nivelkiinnitystä eli

$$M_b(1)=0 \;\Rightarrow\; \alpha'(1)-\alpha_0'=0 \quad \text{ja} \quad a(1)=\Delta/l$$

Sijoitetaan kaavoihin (34) ja (36) jolloin tulee

$$A(\cosh\gamma-\cos\lambda)+B\gamma(\sinh\gamma/\gamma-\sin\lambda/\lambda)=vakio$$

$$A(\gamma^2\cosh\gamma+\lambda^2\cos\lambda)+B\gamma(\gamma\sinh\gamma+\lambda\sin\lambda)=vakio$$

Tämän kerroindeterminantti antaa karakteristisen VPR-funktion oleellisen osan

$$f(k,\Gamma)=\cos\lambda\sinh\gamma/\gamma-\cosh\gamma\sin\lambda/\lambda \qquad (40)$$

Vääntö-puristus-rotaationurjahdus. Eräät arvoparit k ja Γ, jotka toteuttavat stabiliteettiehdon eli ovat yhtälön (40) $f(k,\Gamma)=0$ juuria, on esitetty taulukossa 1.

Γ	0	1	3	4	5	10	20	50	100	200	237,72
k	4,49	4,48	4,47	4,46	4,45	4,40	4,31	4,00	3,44	1,81	0,00

Taulukko 1. Vääntö-puristus-rotaationurjahduksen ominaisarvopareja.

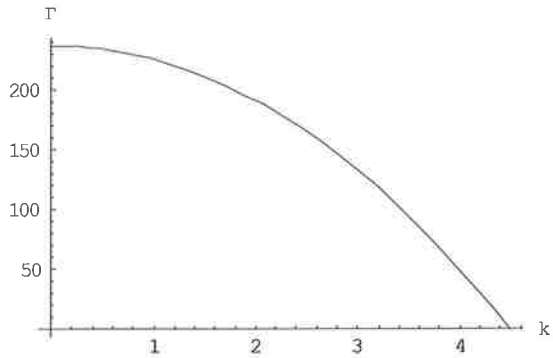

Kuva 3. Vääntö-puristus- rotaationurjahduksen karakteristinen funktio

Vääntö-puristusnurjahdus. Jos ei ole rotaatiota $\Gamma \to 0$ niin silloin $\lambda \to k$ ja $\gamma \to 0$ jolloin $\gamma^{-1}\sinh\gamma \to 1$. Tällöin rajalla ehdoksi tulee

$$\tan k - k = 0 \tag{41}$$

Sen ensimmäiset nollasta poikkeavat juuret ovat (katso [6] Gh IV.1. p 30).

$$k = 4,4934 \text{ ja } 7,7253 \tag{42}$$

kuten tiedetään (katso [1] ja/tai [4])

Rotaationurjahdus. Jos $k = 0$ seuraa siitä, että $\gamma = \lambda = \sqrt[4]{\Gamma}$ ja karakteristinen yhtälö kuuluu

$$\tan\sqrt[4]{\Gamma} - \tanh\sqrt[4]{\Gamma} = 0 \tag{43}$$

Tämän ensimmäiset nollasta poikkeavat juuret ovat (katso [6] ChIV.5.c) p31)

$\sqrt[4]{\Gamma} = 3,9266$ ja $7,0686$, josta edelleen seuraa

$$\Gamma = 237,7211 \text{ ja } 2496,4874 \tag{44}$$

Tapaus 3. Kun poraus on on edennyt, voidaan kiinnityksen porattavaan kappaleeseen katsoa olevan jäykän ja pora tunkeutuu x-akselista etäisyydellä Δ materiaaliin kulmassa $\alpha 1$. Reunaehdot ovat $a(1) = \Delta/l$ ja $\alpha(1) = \alpha 1$. Sijoitetaan kaavoihin (34) ja (35) jolloin tulee

$$A(\cosh\gamma - \cos\lambda) + B\gamma(\sinh\gamma/\gamma - \sin\lambda/\lambda) = vakio$$

$$A(\sinh\gamma + \sin\lambda) + B\gamma(\cosh\gamma - \cos\lambda) = vakio$$

Tämän kerroindeterminantti antaa karakteristisen VPR-funktion oleellisen osan

$$f(k,\Gamma) = 1 - \cosh\gamma\cos\lambda - \tfrac{1}{2}\lambda\left(1 - \gamma^2/\lambda^2\right)\sin\lambda\sin\gamma/\gamma \tag{45}$$

Eräät arvoparit k ja Γ, jotka toteuttavat stabiliteettiehdon eli ovat yhtälön (45) $f(k,\Gamma) = 0$ juuria, on esitetty taulukossa 2.

Γ	0	1	5	10	50	100	200	300	400	500	500,57
k	2π	6,28	6,25	6,22	5,85	5,01	3,84	3,06	2,15	0,16	0

Taulukko 2. Vääntö-puristus-rotaationurjahduksen ominaisarvopareja.

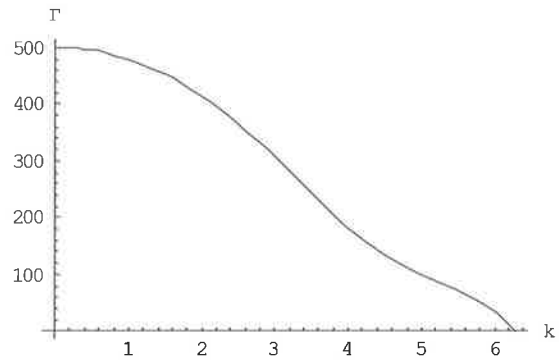

Kuva 4. Vääntö-puristus- rotaationurjahduksen karakteristinen funktio

Vääntö-puristusnurjahdus. Jos ei ole rotaatiota $\Gamma \to 0$ niin silloin $\lambda \to k$ ja $\gamma \to 0$ jolloin $\gamma^{-1} \sinh \gamma \to 1$. Tällöin rajalla ehdoksi tulee

$$1 - \cos k - \tfrac{1}{2} k \sin k = 0 \qquad (46)$$

Sen ensimmäiset nollasta poikkeavat juuret ovat

$$k = 2\pi = 6,2832 \text{ ja } 8,9868 \qquad (47)$$

kuten tiedetään (katso [1] ja/tai [4]).

Rotaationurjahdus. Jos $k = 0$ seuraa siitä, että $\gamma = \lambda = \sqrt[4]{\Gamma}$ ja karakteristinen yhtälö kuuluu

$$1 - \cosh \sqrt[4]{\Gamma} \cos \sqrt[4]{\Gamma} = 0 \qquad (48)$$

Tämän ensimmäiset nollasta poikkeavat juuret ovat $\sqrt[4]{\Gamma} = 4,7300$ ja $10,9956$ josta seuraa

$$\Gamma = 500,5639 \text{ ja } 14617,6301 \qquad (49)$$

Maksimaalisten kulmanopeuksien suhde

Maksimaalisten, $k = 0$, rotaatioparametrien suhde eri reunaehtotapauksissa on

$$\Gamma_1 : \Gamma_2 : \Gamma_3 = 12,3624 : 237,7211 : 500,5639 = 1 : 19,2294 : 40,4910$$

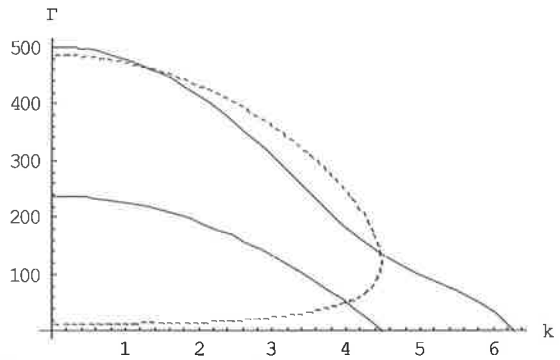

Kuva 5. Tapaukset 1, 2 ja 3 samassa kuvassa

Vastaavien kulmanopeuksien suhde on Γ -suhteiden neliöjuuri

$$\omega_1 : \omega_2 : \omega_3 = 1 : 4,3851 : 6,333 \approx 1 : 4 : 6$$

Vääntö-puristus-rotaatiokuormitus

Kun vääntö-puristuskuormitusparametri kaavoista (24) ja (25) sekä rotaatioparametri kaavasta (14) on määritetty, saadaan auki kirjoitettuna

$$k = \sqrt{k_M^2 + k_N^2} = \sqrt{\left(\frac{M_t}{2EI}\right)^2 + \left(\sqrt{\frac{Nl^2}{EI}}\right)^2} \qquad \Gamma = \frac{\rho A l^4 \omega^2}{EI}$$

Nyt voidaan vääntö-puristus-rotaatiokuormituksen stabiilius todeta taulukoista 1 ja 2. Näiden taulukoiden avulla voidaan myös määrittää joko rotaatioparametrin Γ tai vääntö-puristus-parametrin k maksimiarvo, kun toisen arvo tunnetaan. Nämä kuormitusparametrit eivät ole täysin toisistaan riippumattomia, sillä puristusvoiman lisääminen lisää lastun paksuutta, joka taas vaatii lisää vääntömomenttia.
Kaavoista (29) ja (30) saadaan poranterän vääntökulma ja kierevyys

$\psi' = 2(1+\nu)k_M$ ja $\varphi' = k_M$

Olisi mahdollista laskea myös poranterän jännityksiä, mutta lähellä stabiiliuden menettämistä laskelmat eivät enää pidä paikkaansa.

Lähteet

[1] Landau L. D. and Lifshitz E. M., *Theory of Elasticity*, Pergamon Press, Oxford 1970
[2] Väisälä Kalle, Vektorianalyysi, Porvoo, 1954.
[3] Ylinen Arvo, *Kimmo- ja lujuusoppi* osat I ja II, WSOY, Porvoo, 1948 ja 1950.
[4] Timoshenko Stephen. & Gere James M., *Theory of Elastic Stability*, McGraw-Hill, 1961.
[5] Lindelöf Ernst, *Differentiaali- ja integraalilasku ja sen sovellutukset* III.1 Tavalliset differentiaaliyhtälöt, Mercatorin Kirjapaino, 1935.
[6] Janhnke E. and Emde F., *Tables of Functions*, Chapter IV. Elementary transcendental equations, pp 30 and 31, Dover Publications, New York, 1945.

TYKIN AMMUKSEN JA TULIPUTKEN VUOROVAIKUTUKSEN NUMEERINEN LASKENTA

H. KEINÄNEN
VTT
PL 1000
02044 VTT
heikki.keinanen@vtt.fi

S. MOILANEN
Patria Land & Armament Oy
Weapon System Engineering
PL 18
38201 SASTAMALA
seppo.moilanen@patria.fi

TIIVISTELMÄ

Tykin tuliputken ja ammuksen vuorovaikutuksen numeerinen laskenta on suoritettu yksinkertaistetulla mallilla käyttäen kaupallista Abaqus Explicit ohjelmaa. Tuliputki on oletettu sileäksi eli rihlan geometriaa ei ole huomioitu. Kuormituksena on sisäballistiikan simuloinnilla määritetty paine-aikahistoria ammuksen perässä. Laskennassa on otettu huomioon materiaalin plastisoituminen sekä ammuksen ja tuliputken välinen kontakti ja kitka. Mallinnuksen yksinkertaistuksista huolimatta laskennallisesti saatiin tuloksia, jotka vahvistavat kirjallisuustutkimusten ja mittaustulosten perusteella tehtyjä päätelmiä. Artikkelissa esitetään lyhyesti laskennallisissa tarkasteluissa käytetyt mallinnusperiaatteet, esimerkkituloksia sekä vertailuja koeammuntojen mittaustuloksiin. Lopuksi tarkastellaan tulosten merkitystä tuliputken käyttöiän kannalta.

1 JOHDANTO

Tykin ammuksen johtorengas varmentaa ammuksen latauskiinnittyvyyden latausvaiheen jälkeen. Sisäballistisen vaiheen alussa johtorenkaan muovautumisen tuliputken rihlaukseen ylimenokartion alueella tulee antaa panoksen hallitun syttymisen kannalta sopiva vastusvoima sekä uutta että paljon ammuttua, kulunutta tuliputkea käytettäessä. Lisäksi johtorengas välittää ammukselle putken rihlauksen kiertovaikutuksen ja se toimii tiivistyselimenä ammuksen ja tuliputken välissä estäen ruutikaasujen ohivirtauksen (Kuva 1). Suurikaliiperisilla, rihlatuilla tuliputkilla varustetuilla tykistöaseilla ammuttavien ammusten johtorengasmateriaalina käytetään pehmeitä metalliseoksia, tavallisimmin kuparia tai kuparipohjaisia seoksia, joiden on todettu antavan sopivan mekaanisten ominaisuuksien yhdistelmän sekä tuliputken kulumisen ja kestävyyden että ammuksen halutun liiketilan aikaansaamisen kannalta.

Kirjallisuustutkimuksin [1, 2, 3, 9] on todettu ja koeammuntamittauksin on vahvistettu, että johtorenkaan aiheuttama kuormitus saattaa aiheuttaa ennakoimattoman suuria tuliputken rasituksia suhteessa ruutikaasun painekuormaan joillakin ammus-johtorengasrakenteilla. Rasitukset saattavat olla erityisen suuria matalilla painetasoilla ja pienillä lähtönopeuksilla ammuttaessa tuliputken

suupäässä. Perinteisesti tuliputken mitoitus on perustunut ruutikaasun painekuormitukseen [7, 8]. Paine on suurimmillaan tuliputken panoskammiossa ja rihlauksen alkuosalla suurilla panoksilla ja lähtönopeuksilla ammuttaessa ja paine pienenee tuliputken suuta kohden mentäessä. Tuliputken seinämä on paksuimmillaan panoskammion ja ylimenokartion, jossa johtorengas muovautuu putken rihloihin, alueilla ja seinämä ohenee ja jäykkyys pienenee tuliputken suulle päin edettäessä.

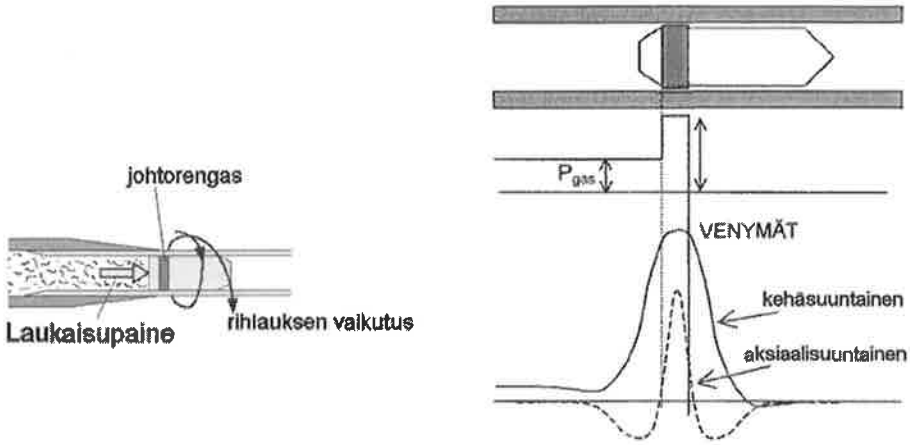

Kuva 1. Johtorengas estää kaasun ohivirtauksen ja välittää rihlauksen kiertovaikutuksen sisäballistisessa vaiheessa. Oikealla on esitetty tuliputken ulkopinnan venymien periaatteellinen muoto.

Laskennallisesti simuloitiin ammuksen ja tuliputken vuorovaikutusta sisäballistisessa vaiheessa. Tavoitteena on ollut tutkia ammus-johtorengaskonstruktion muutoksien vaikutusta tuliputken rasituksiin sekä tuliputken staattisen lujuuden että väsymiskeston kannalta.

2 MALLINNUSPERIAATE

2.1 Yleistä

Numeerinen laskenta suoritettiin käyttäen kaupallista Abaqus Explicit ohjelmistoa [10]. Laskenta perustuu explisiittiseen aikaintegroinnin ja elementtien diagonaalisen massamatriisin käyttöön. Käytettäessä explisiittistä proseduuria ei iteraatioita eikä tangentiaalista jäykkyysmatriisia tarvita ja integrointi tapahtuu käyttäen lukuisia pieniä aika-askelia. Laskenta on ehdollisesti stabiili. Aika-askeleen stabiiliusehto voidaan esittää muodossa (ilman vaimennusta) suurimman ominaisarvon (ω_{max}) avulla

$$\Delta t \leq \frac{2}{\omega_{max}}. \tag{1}$$

Korkeataajuuksisten värähdysten kontrolloimiseksi käytetään pientä vaimennusta, jolloin stabiiliusehto voidaan esittää muodossa

$$\Delta t \leq \frac{2}{\omega_{max}}\left(\sqrt{1+\xi^2}-\xi\right), \tag{2}$$

missä ζ on kriittisen vaimennuksen osuus korkeimman ominaistaajuuden tapauksessa. Jokaiselle elementille lasketaan aika-askel arvio käyttäen yhtälöä

$$\Delta t \leq \frac{2}{\omega_{\max}^{element}}, \tag{3}$$

missä $\omega^{element}_{max}$ on elementin suurin ominaisarvo. Konservatiivinen arvio aika-askeleelle saadaan määrittämällä yhtälön (3) minimi kaikkien elementtien suhteen, jolloin saadaan [10]

$$\Delta t \leq \min\left(\frac{L_e}{c_d}\right), \tag{4}$$

missä L_e on karakteristinen elementin suuruus ja c_d on materiaalissa etenevän ääniaallon nopeus. On siis huomattava, että mallin elementtien pienin koko vaikuttaa aika-askeleeseen ja sitä kautta myös ratkaisuaikaan.

2.2 Mallin geometria, reunaehdot ja kuormitus

Tuliputken pituudesta mallinnettiin noin 1600 mm pituinen alkuosa, joka sisälsi osan panoskammiota, ylimenokartion ja alkuosan tuliputken rihlatusta työlierioistä. Rihloja ei mallinnettu, vaan putken sisähalkaisija määritettiin putken rihlauksen pinta-alojen (rihlan uran ja harjan) painotetun keskiarvon perusteella. Tällöin sisähalkaisijan arvoksi saatiin n. 156,52 mm. Koko rakenteesta mallinnettiin kehäsuunnassa yhden asteen suuruinen osa.

Laskentamallin reunaehdot on esitetty kuvassa 2. Mallin panoskammion katkaisupinta kiinnitettiin putken aksiaalisuunnassa. Mallin toisen pään katkaisupinnan oletettiin pysyvän tasomaisena. Ammuskuoren lähinnä putken akselia olevat solmut oletettiin radiaalisesti kiinnitetyiksi. Siivumallin sivuille oletettiin symmetriareunaehdot. Laskentamallin osa on esitetty kuvassa 3.

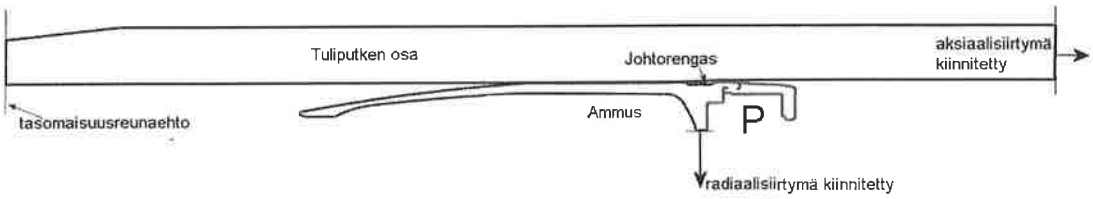

Kuva 2. Laskentamallin reunaehdot.

Kaikille vapaille pinnoille määritettiin yleiset kontaktiehdot (Abaqus [10]). Kitkakertoimen oletettiin riippuvan kontaktipaineesta Taulukon 1 mukaisesti. Esimerkiksi lähteessä [5] on käytetty kitkakertoimelle arvoa 0,01, koska johtorengasmateriaalin ohut pintakerros saattaa jopa sulaa kitkan, liukunopeuden ja kontaktipaineen vaikutuksesta.

Taulukko 1. Kontaktipaineesta riippuvan kitkakertoimen arvot.

Kitkakerroin	Kontaktipaine (MPa)
0,35	0
0,25	300
0,15	350
0,10	400
0,01	500

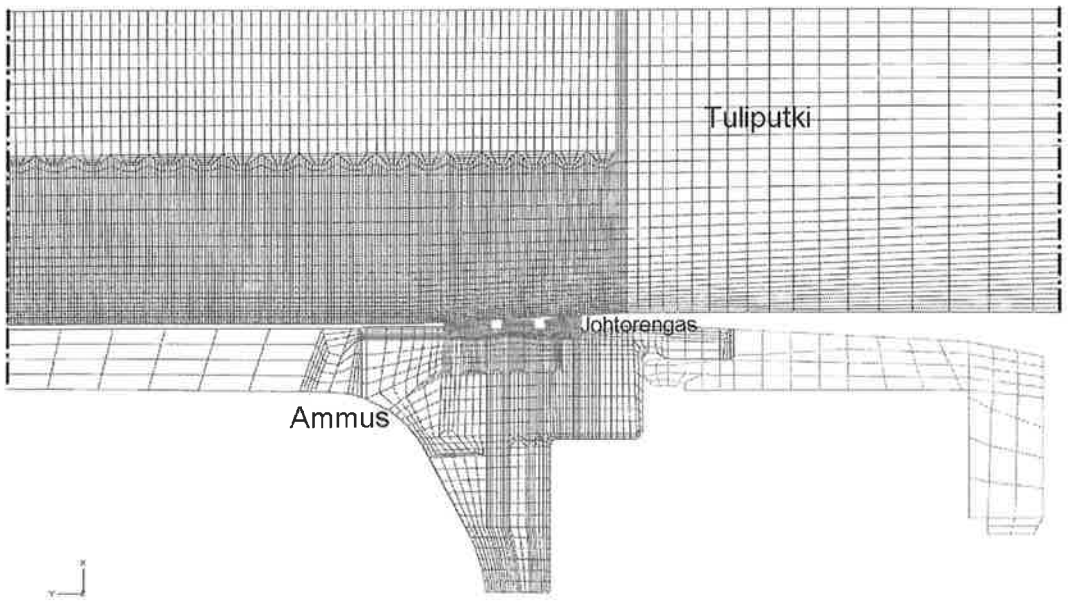

Kuva 3. Laskentamallin osa alkutilanteessa, jossa ammuksen johtorengas on tuliputken ylimenokartion kohdalla.

Kuormitus annettiin ajasta riippuvana ammuksen peräosaan kohdistuvana paineena. Painekäyrä (Kuva 4) perustuu sisäballistiseen simulointiin, joka on tehty käyttäen FNGUN ohjelmaa [11]. FEM-laskennassa paine skaalattiin siten, että yhtä suuri paineresultanttivoima vaikutti jokaisen laskentamallin tapauksessa riippumatta johtorenkaan alkuperäisestä ulkohalkaisijasta. Koeammunnoissa on käytetty kolmea eri nopeus- ja painealueen panostyyppiä, joista ammuksen ja tuliputken vuorovaikutuksen FEM-laskentaan kuormitukseksi valittiin yli 900 m/s lähtönopeuden antavaa laukausyhdistelmää likimain vastaava sisäballistisen simuloinnin ammuspaine.

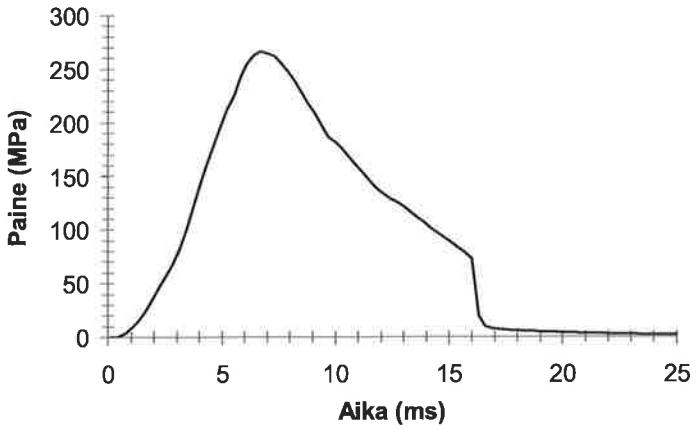

Kuva 4. Kuormituksena käytetty paine-aika historia.

Ammusten ID2, ID3 ja ID5 johtorengas on hitsattu ja rakenne oletettiin jatkuvaksi. Ammusten ID1, ID6 ja ID17 johtorengas on valmistettu puristamalla, josta aiheutuva johtorenkaan jäännöspuristus mallinnettiin käyttäen hyväksi lämpölaajenemista. Johtorengasmateriaalin lämpölaajenemis-

kertoimeksi oletettiin $\alpha = 20{,}0 \cdot 10^{-6}$ 1/°C (muiden materiaalien osalta $\alpha = 0$) ja koko rakenteelle oletettiin 300 °C lämpötilannousu. Johtorenkaan ja ammuksen välille mallinnettiin kontaktiehdot.

Taulukossa 2 on esitetty ammusten tunnusnumerointi ja johtorengaskonstruktioiden likimääräinen luokitus. Kuvassa 5 on esitetty periaatteellisesti erityyppisiä johtorengasrakenteita ja johtorenkaan deformoituneen tilan nimitykset.

Taulukko 2. Ammusten tunnus ja johtorengaskonstruktioiden likimääräinen luokitus.

Tunnus ID	Johtorengas					Ammuskuoren jäykkyys
	geom.	mat.	valm.men.	vahvuus	urakoko	
1	K	CuZn	Puristettu	Paksu	Suuri	Keskimäär.
2	K	CuZn	Hitsattu	Ohut	Pieni	Suuri
3	Sk	CuZn	Hitsattu	Ohut	Pieni	Suuri
5	Sk	CuZn	Hitsattu	Mod.	Pieni	Suuri
6	Sk	CuZn	Puristettu	Paksu	Pieni	Suuri
17	Sk	Luja	Puristettu	Paksu	Pieni	Keskimäär.
Esimerkki	Esimerkki, ei todellinen rakenne					

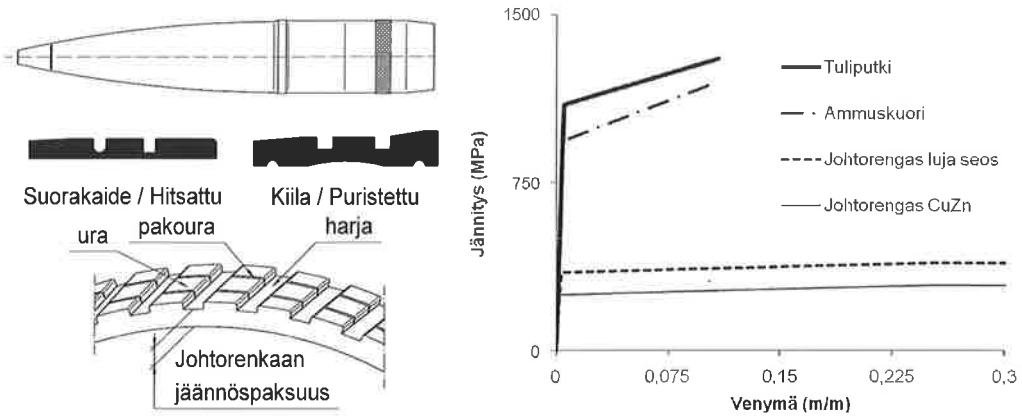

Kuva 5. Ammus ja johtorengasrakenteiden periaatteelliset muodot sekä johtorenkaan deformoituneen tilan nimitykset perustuen tuliputken rihlamuotoon, vasen kuva. Tuliputken, ammuskuoren ja johtorenkaan materiaalien jännitys-venymäkäyrät σ-ε, oikea kuva.

2.3 Materiaaliominaisuudet

Materiaaliominaisuudet mallinnettiin elastis-plastisena olettaen lujittuminen isotrooppiseksi. Muodonmuutosnopeuden vaikutusta materiaalien myötölujuuteen ei otettu huomioon. Materiaalien periaatteelliset jännitys-venymäkäyrät on esitetty kuvassa (Kuva 5).

Muut laskennassa käytetyt materiaaliominaisuudet olivat Poissonin vakio 0,3 sekä kimmomoduli teräsosille 207 GPa ja johtorengasmateriaalille 100 GPa.

Ammuksen sisällä oleva räjähdysainetäytön massa otettiin huomioon kasvattamalla ammuksen kuorimateriaalin tiheyttä siten, että ammuksen tavoitepaino (n. 45 kg) saavutettiin. Todellisuudessa räjähdysaineen massa vaikuttaa myös hitausvoimien kautta ammuksen kuoren

jännitystilaan ja sitä kautta mahdolliseen ammuskuoren plastisoitumiseen. Koska rihlausta ja ammuksen pyörimistä ei mallinnettu, voivat tulokset tältä osin olla todellisuudesta poikkeavia.

Kaasunpaineen vaikutusta tuliputken sisäpinnalla ei tässä raportoidussa laskennassa otettu vielä huomioon, koska tavoitteena oli erilaisten johtorengaskonstruktioiden keskinäinen vertailu. Lämpövaikutuksia ja esimerkiksi ammuksen pyörimistä ei myöskään otettu huomioon. Laskentamallin koon ajateltiin olevan riittävä lyhytaikaisten dynaamisten ilmiöiden tarkasteluun.

3 LASKENTATULOKSIA

Kuvassa (Kuva 6) on esitetty laskettu ammuksen kulkema matka ajan funktiona. Vertailun vuoksi on kuvassa esitetty myös sisäballistisen ratkaisun tulos. Käyrien hajonta ja poikkeama sisäballistisesta ratkaisusta ajan ollessa > 6 ms aiheutuu todennäköisesti ammuksen kussakin tapauksessa mallinnetusta painosta, mikä oli suurempi kuin ammuksen paino sisäballistisessa ratkaisussa. Joka tapauksessa käyrät ovat kohtuullisen hyvin samankaltaisia, mikä vahvistaa sen, että ammuksen liikettä vastustava voima on sekä numeerisessa että sisäballistisessa laskennassa lähes samansuuruinen.

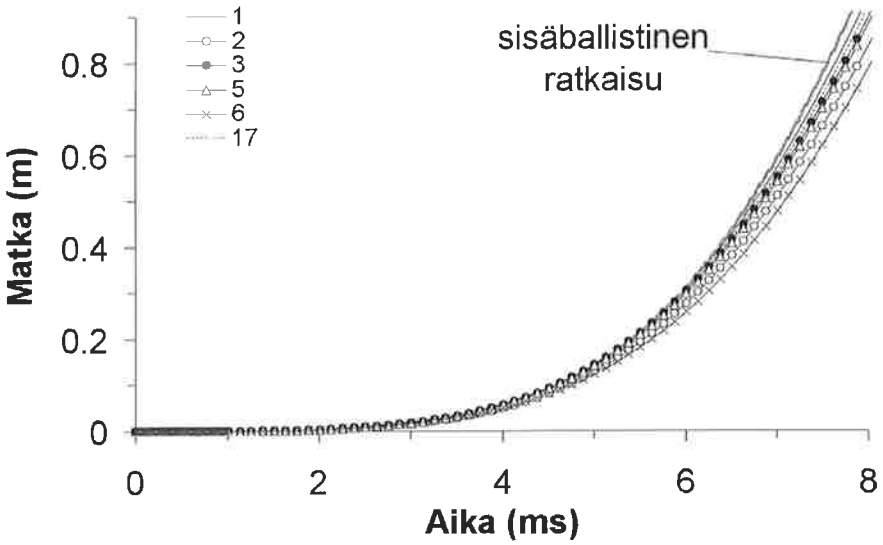

Kuva 6. Ammuksen kulkema matka ajan funktiona. Numeerisen laskennan (FEM) tulokset ammustyypeittäin sekä sisäballistisen ratkaisun tulos.

Kuvassa (Kuva 7) on esitetty radiaalijännityksen jakauma esimerkkilaskennan tapauksessa ajanhetkellä 1,25 ms, jolloin ammus on kulkenut noin 0,1 m matkan. Putken radiaalijännityksen minimi on arviolta (-750…-800) MPa, jota voidaan pitää johtorenkaan aiheuttaman kontaktipaineen likiarvona. Kuvassa (Kuva 8) on esitetty ekvivalenttinen plastinen venymä johtorenkaan muovautuessa tuliputken mittaan.

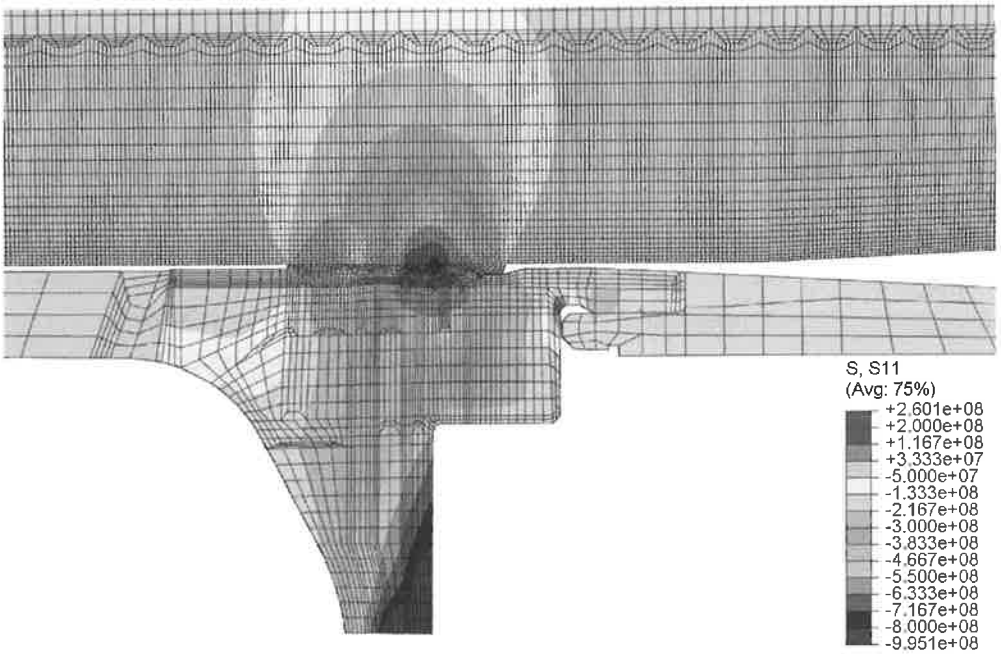

Kuva 7. Laskettu radiaalijännitys esimerkkitapaukselle, kun ammus on kulkenut arviolta 0,1 m matkan. Putken minimi radiaalijännitys on noin (-750…-800) MPa.

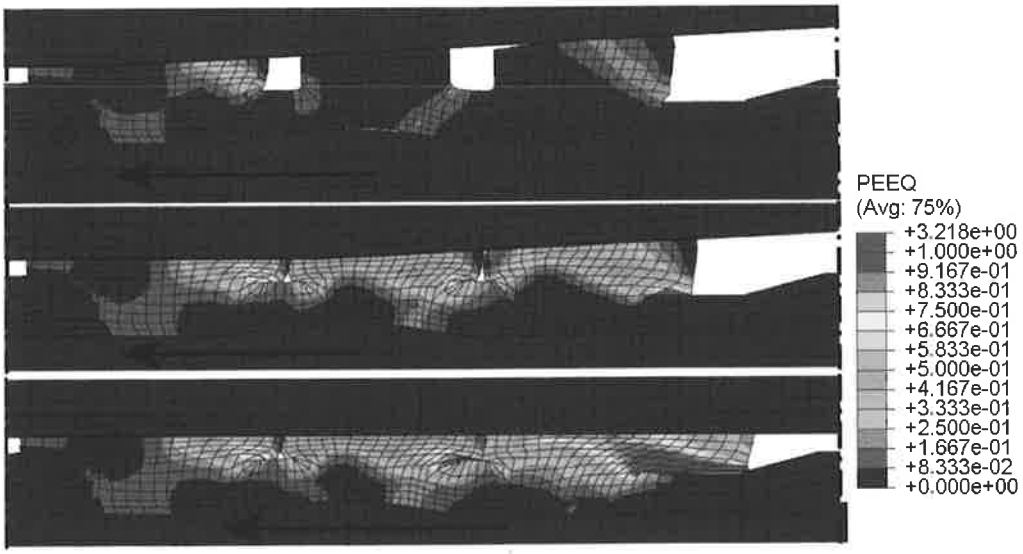

Kuva 8. Ekvivalentti plastinen venymä johtorenkaan muovautuessa tuliputken mittaan. Plastisen venymän maksimi on noin 322 %.

Kuvassa (Kuva 9) on esitetty ammustyypeittäin laskettu kehä- ja aksiaalivenymä putken ulkopinnalla ajan funktiona hieman tuliputken täyden rihlauksen alkamiskohdan jälkeen.

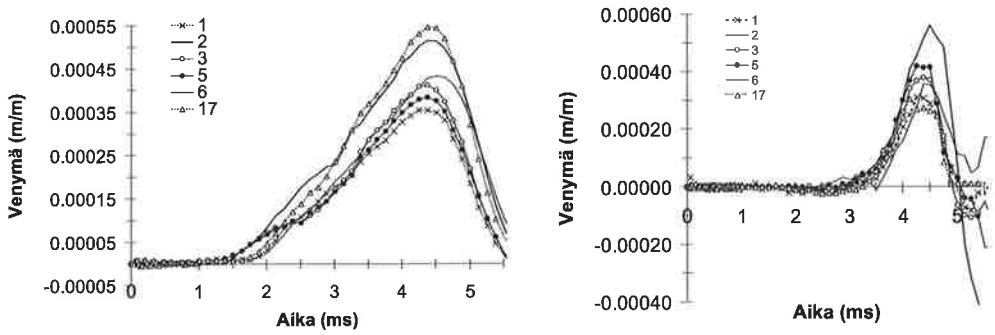

Kuva 9. Laskettu kehävenymä $\varepsilon_\Theta(t)$ (vasen kuva) ja aksiaalivenymä $\varepsilon_x(t)$ (oikea kuva) putken ulkopinnalla ajan funktiona noin 51 mm etäisyydellä täyden rihlauksen alkukohdasta. Johtorengas ohittaa kohdan likimäärin ajanhetkellä 4,3 ms.

Kehä- ja aksiaalivenymän avulla laskettiin ns. vertailupaine p_C yhtälöllä

$$p_C = \frac{\omega^2 - 1}{2} \cdot \frac{E}{1-\nu}\left(\varepsilon_\Theta + \nu\varepsilon_x\right), \tag{5}$$

missä

$$\omega = \frac{D}{d}$$

ja d on putken sisähalkaisija, D on putken ulkohalkaisija, E on kimmomoduli, ν on Poissonin luku, ε_Θ on kehävenymä, ja ε_x on aksiaalivenymä. Yhtälö (5) perustuu pitkän paksuseinämäisen putken, joka on päistään avoin, sisäisen paineen ja putken ulkopinnan venymien keskinäiseen riippuvuuteen [4].

Kuvassa (Kuva 10) on esitetty venymien avulla laskettu vertailupaine p_C eri ammustyypeille ajan funktiona noin 51 mm etäisyydellä putken täyden rihlauksen alkamiskohdasta. Laskennallisesti kuormitukset putoavat lähelle nollaa ammuksen ohitettua tarkastelukohdan, koska tuliputken sisäpintaan ammuksen ohituksen jälkeen vaikuttavaa painetta ei mallinnettu.

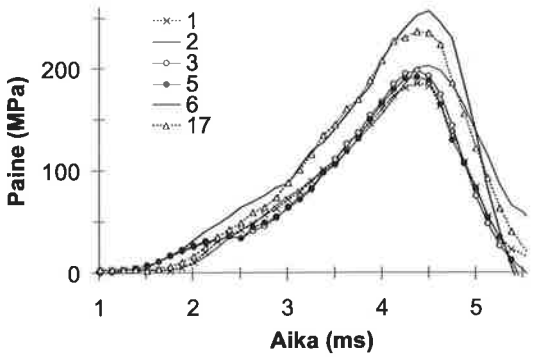

Kuva 10. Venymien avulla laskettu vertailupaine $p_C(\varepsilon_\Theta, \varepsilon_x)$ (Kaava 5) ajan funktiona noin 51 mm etäisyydellä putken täyden rihlauksen alkukohdasta. Vrt. venymät Kuva 9.

Kuvassa (Kuva 11) on esitetty laskennallinen kontaktipainejakauma ja kontaktipaineen keskimääräinen arvo johtorenkaan pituudella ajanhetkellä 1,25 ms, jolloin ammus on kulkenut noin 0,1 m matkan. Kuvan (Kuva 4) mukaan tarkasteluhetkellä ruutikaasun paine ammuksen perässä on luokka $p_1 = 20$ MPa ja suurimmillaankin se on max $p_1 \sim 300$ MPa, joten laskennallisesti tiivistys on taattu. Ammustyypin ID2 laskennallinen kontaktipaine on ehkä tarpeettomankin korkea.

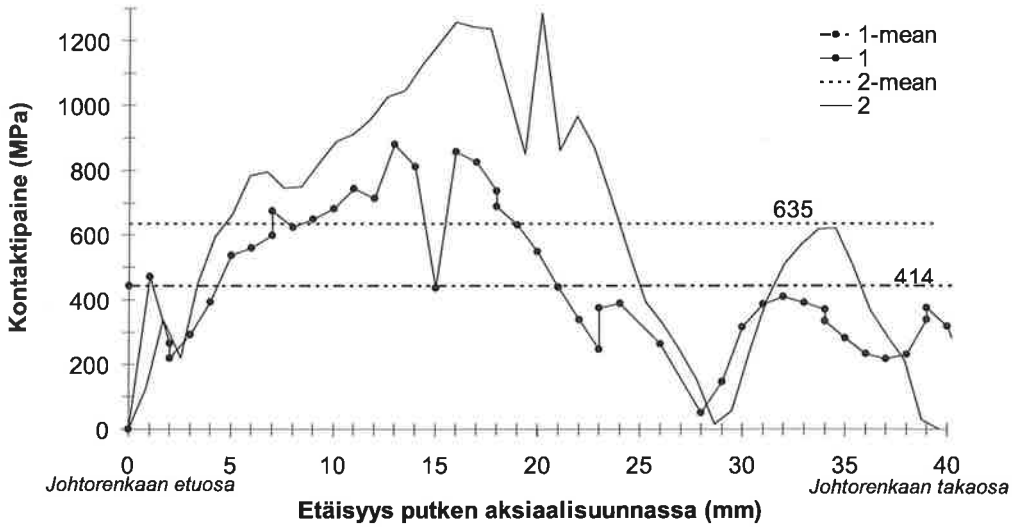

Kuva 11. Laskettu kontaktipainejakauma ja sen keskimääräinen arvo johtorenkaan pituudella ajanhetkellä 1,25 ms, jolloin ammus on kulkenut noin 0,1 m matkan. Ammustyypit ID1 ja ID2.

Laskennalliset vertailupaine- ja venymätulokset osoittavat ammusten ja johtorenkaiden rakenteista aiheutuvat tuliputken rasituserot sisäballistisen vaiheen alussa, ylimenokartion jälkeen.

4 LASKENNALLISTEN JA MITATTUJEN TULOSTEN VERTAILU

Kuvissa (Kuva 12 ja Kuva 13) on esitetty tuliputken ulkopinnan laskettujen ja mitattujen aksiaali- ja kehävenymien vertailu ammusten ID1 ja ID3 tapauksessa välittömästi johtorenkaan muovauduttua tuliputken rihlaukseen. Venymätulosten vastaavuus on hyvä, varsinkin, kun laskentamallin yksinkertaistukset ja putken painekuorman puuttuminen otetaan huomioon.

Laskennallisten ja mitattujen vertailupaineen maksimien suhteellinen vertailu ammustyypeittäin on esitetty kuvassa (Kuva 14). Kuvan perusteella mittaustulokset ja laskennalliset tulokset ovat likipitäen samat ainakin suhteellisella tasolla ja molemmista tuloksista on nähtävissä ammustyyppien aiheuttamien putkirasituksien erot sisäballistisen vaiheen alussa.

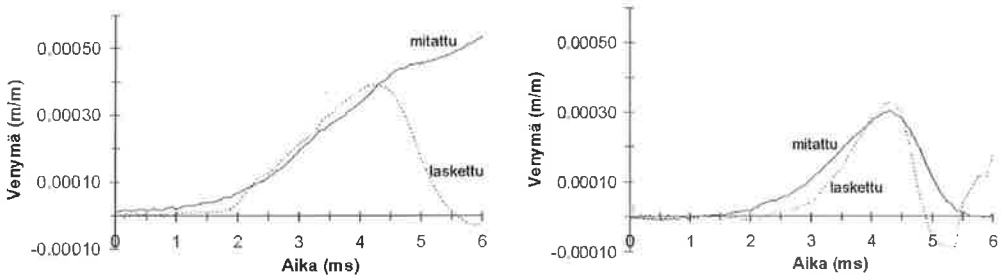

Kuva 12. Laskettu ja koeammunnassa mitattu tuliputken kehävenymä (vasen kuva) sekä aksiaalivenymä (oikea kuva) välittömästi ylimenokartion jälkeen, ammus ID1.

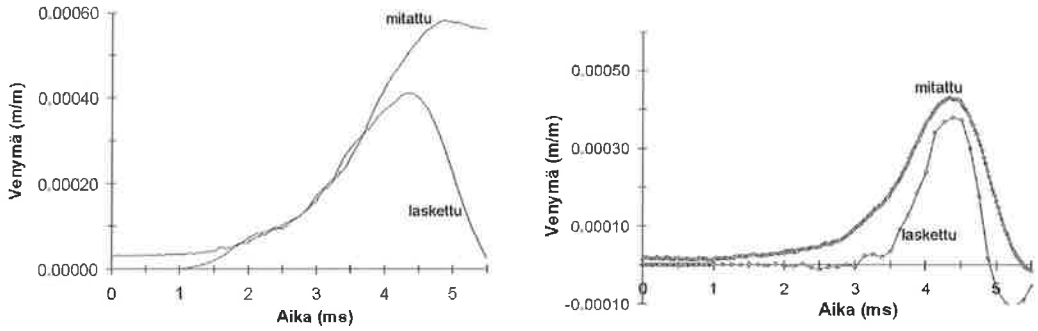

Kuva 13. Laskettu ja mitattu kehävenymä ε_Θ (vasen kuva) ja aksiaalivenymä ε_x (oikea kuva) välittömästi ylimenokartion jälkeen, ammus ID3.

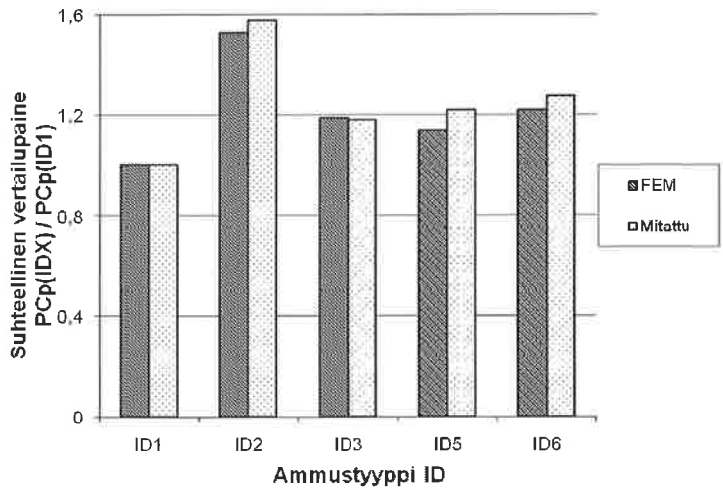

Kuva 14. Laskennallinen (FEM) ja koeammunnoissa mitattu vertailupaineen p_C suhteellinen maksimi ammustyypeittäin johtorenkaan muovautumisen jälkeen, putkivaiheen alussa.

5 TUTKIMUKSEN JATKO

Työtä on jatkettu siten, että putken sisäpuolinen paine ammuksen takana on otettu huomioon putkikuormituksena ja geometriamallia on pidennetty siten, että tuliputken koko rihlattu pituus on mallinnettu. Tällöin laskettuja venymiä voidaan paremmin verrata mitattuihin venymiin ja johtorenkaan aiheuttamia rasituksia voidaan tarkastella myös tuliputken muissa osissa. Laskennallisesti on tarkoitus mallintaa myös matalamman lähtönopeuden ja paineen antavan laukausyhdistelmän putkirasitukset, joita tarvitaan erityisesti putken suuosan väsymiskeston laskennalliseen arviointiin.

Tavoitteena on määrittää särön kasvunopeus lasketuilla kuormituksilla putken eri osissa ja sitä kautta putken laskennallinen käyttöikä käyttäen apuna aiemmin määritettyjä materiaaliominaisuuksia [8].

6 YHTEENVETO JA PÄÄTELMÄT

Tutkimuksen ensi vaiheen tarkoituksena oli selvittää tuliputkeen kohdistuvan johtorengasrasituksen vaikutusta putken laukaus- ja väsymiskestävyyteen sekä johtorengas- ja ammusrakenteiden vaikutuksia putken kuormituksiin laskennallisesti. Vaikka käytetty laskentamenetelmä oli yksinkertainen todelliseen tilanteeseen nähden, saatiin laskennallisesti mittaustuloksien kanssa yhteneviä tuloksia. Laskennalliset johtorengaspaineen ja plastisen venymän arviot olivat kirjallisuusviitteissä [2, 3, 9] raportoitujen laskennallisten tulosten suuruusluokkaa ollen niissä esitettyjen ääriarvojen välissä. Johtorengaspaine- ja venymäarvojen erojen arvioitiin olleen seurausta mallinnustapojen, johtorengasmateriaalin parametriarvojen ja geometrian eroavaisuuksista.

Laskentatulokset osoittivat, että johtorengas- ja ammuskonstruktioilla on selkeä vaikutus tuliputken laukausrasituksiin. Säteensuunnassa jäykkään ammuskuoreen hitsattu ohut, suuri ulkohalkaisijainen ja pienet pakourat omaava johtorengas-ammuskonstruktio aiheuttaa suuret laskennalliset putkirasitukset. Sama päätelmä on todennettu myös koeammuntamittauksin. Jatkotutkimuksen keskeinen aihe on havaittujen johtorengaskuormituksien kriittisyyden arviointi tuliputken staattisen lujuuden ja väsymiskeston kannalta ts. miten johtorengaskuormitukset tulisi huomioida tuliputken lujuusteknisessä mitoituksessa tai miten uusien ampumatarvikkeiden yhteensopivuus olemassa olevien asejärjestelmien kanssa voidaan varmentaa. Molemmissa ongelmissa voidaan esitetyllä yksinkertaistetulla numeerisella laskennalla vähentää mittauskoeammuntojen määrää ja siten saavuttaa merkittäviä kustannussäästöjä ampumatarvikkeiden ja etenkin johtorengasrakenteiden suunnittelu- ja testausvaiheessa.

KIITOKSET

Kirjoitelman laatijat esittävät kiitoksensa artikkelin julkaisuluvasta Maavoimien Materiaalilaitoksen Esikunnan Järjestelmäosastolle.

VIITTEET

1. Andrews T.D. *Projectile Driving Band Interactions with Gun Barrels.* In: Gun Tubes 2005 Conference. GT2005. Conference Proceedings. 10th to 13th April 2005. Keble College Oxford. Paper S7/P28. RMCS, Shrivenham. 2005. (Also in: Journal of Pressure Vessel Technology. Vol 128, May 2006. pp. 273 - 278.)

2. Chen, P.C.T. *Analysis of Engraving and Wear in a Projectile Rotating Band.* In: Kathe, L.C. (ed.) *Proceedings of the Ninth U.S. Army Symposium on Gun Dynamics.* Report ARCCB-SP-99015. Benet Laboratories. Watervliet, N.Y. 2000. pp. 2-1 - 2-12.

3. Chen, P.C.T. & Leach, M. *Modeling of Barrel/Projectile Interaction in a Rotating Band.* Technical Report ARCCB-TR-01011. Benet Laboratories. Watervliet, N.Y. 2001. 13 p.

4. Flynn, P.D. *Strain-gage Instrumentation for Ammunition Testing.* In: Experimental Mechanics. May 1975. pp. 192 - 200.

5. Montgomery, R.S. *Surface melting of rotating bands.* Technical Report WVT-TR-75060. Benet Weapons Laboratory. Watervliet, N.Y. 1975. 24 p.

6. Montgomery, R.S. *Evidence for the melt-lubrication of projectile bands.* Report ARLCB-TR-83031. Benet Weapons Laboratories. Watervliet, NY. 1983.

7. Peter, H. *Mechanical Engineering. Principles of Armament Design.* Trafford Publishing, Victoria. 2004. 373 p.

8. Planman, T. & Keinänen, H. *Tykinputken mutumismekaniikkaan perustuva lujuustarkastelu. Projektin loppuraportti: Tykinputken käyttöiän arviointi.* Luottamuksellinen ja julkaisematon tutkimusraportti VTT VAL64-023483. 10.6.2002. Espoo. 19 s. + 4 liites.

9. Viljoen, G.G. *Driving Band Design Considerations.* In: Mayseless, M. & Bodner, S.R. (eds.). *15th International Symposium on Ballistics. Jerusalem, Israel, 21-24, May, 1995. Proceedings.* IB20. Vol 3. International Ballistics Committee. 1995. pp. 153 - 158.

10. *Abaqus/Explicit User's Manual, version 6.7-1.* Abaqus Inc. Pawtucket, Rhode Island. 2007.

11. *FNGUN User Manual.* Frasher-Nash Consultancy Ltd. Dorking, UK.

KARKAISTUN LASIN VISUAALISEN LAADUN PARANTAMINEN

ANTTI ARONEN, REIJO KARVINEN
Energia- ja prosessitekniikan laitos
Tampereen teknillinen yliopisto
PL 589
FIN-33101 Tampere, FINLAND
s-posti: antti.aronen@tut.fi,
reijo.karvinen@tut.fi

TIIVISTELMÄ

Hyvä visuaalinen laatu on tärkeää lasin karkaisussa. Tela-aallot ja muut muodonmuutokset muodostuvat helposti karkaisuprosessin aikana. Muodonmuutosten muodostumisen ymmärtämiseen tarvitaan teoreettista mallia, jonka avulla voidaan tutkia lämmönsiirron, telojen ja prosessiparametrien, kuten nopeuden tai lämmityksen aikaisen oskilloinnin vaikutusta. Tässä artikkelissa esitetään esimerkkejä lasin käyttäytymisestä lämmitysjakson aikana. Esimerkeistä nähdään lämpötilan ja ajan suuri merkitys visuaaliseen laatuun.

JOHDANTO

Karkaistu lasi on hyvin yleinen rakennusmateriaali. Monet julkisivut tai ikkunat on tehty karkaistusta lasista, sen hyvän kestävyyden vuoksi. Yleensä kyseiset lasit sijoitetaan näkyvälle paikalle ja asiakkaat haluavat tämän johdosta hyvää laatua lasilta. Karkaisulaatu, eli lasin kestävyys ja murukoko, on standardisoitu ja yleensä korkea. Karkaisulaadun lisäksi myös visuaaliset kysymykset tulevat koko ajan tärkeämmäksi, vaikka jännitykset ovat edelleen tärkein tekijä lasin laatua tarkasteltaessa. Lasissa voi olla erilaisia visuaalisia virheitä. Muutamia esimerkkejä on esitetty kuvassa 1. Osa kyseisistä virheistä voidaan välttää oikealla lämmönsiirron hallinnalla. Tässä artikkelissa keskitytään tela-aaltojen muodostumiseen.

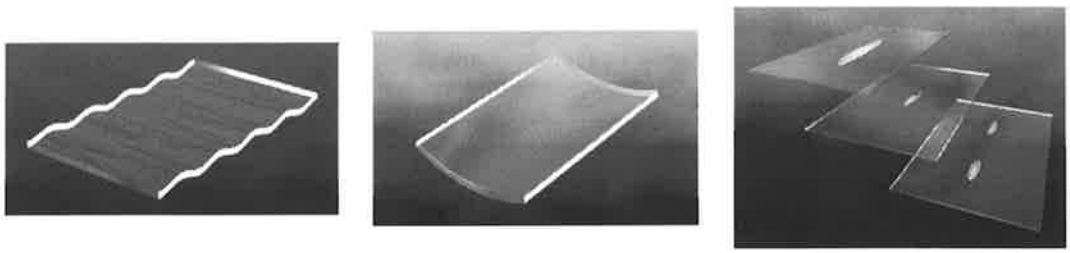

Kuva 1. Tela-aallot, taipuminen ja juovat.

Lasin karkaisu-uunissa lasilevyn lämpötila on yli 600 °C lämmitysjakson lopussa. Koska relaksoitumisaika aika on lyhyt, syntyy plastisia muodonmuutoksia, jotka eivät ole palautuvia. Jos muodonmuutokset ovat tarpeeksi suuria, on mahdollista nähdä eritavoin heijastuvia kohtia lasin pinnassa. Kuvassa 2 on esitetty taustalla pystyssä olevan ruudukon heijastus lasin pinnasta. Lasista

huomataan tällöin syntyneet tela-aallot. Erityisesti heijastuman poikkeama voidaan nähdä lasin päädyissä, jos lasi on ollut kuumana samassa kohdassa pitkän aikaa. Oskilloinnin aikana lasin liike pysähtyy hetkeksi monta kertaa. Plastisia muodonmuutoksia muodostuu kuumaan lasiin tänä aikana, jos lasin ei ole täysin tuettu. Kaikki muutokset lasissa näkyvät poikkeamina.

Kuva 2. Tela-aalloista johtuva lasin pinnan heijastuman vääristymä.

Lasin karkaisusta ja karkaisujännitysten teoreettisista perusteista on julkaistu useita papereita [1-4]. Karkaistun lasin muodonmuutoksista ja kokeellisista mittauksista on myös julkaistu [5], mutta tela-aaltojen teoreettista taustaa ei ole tutkittu.

Tämän artikkelin tarkoituksena on esittää teoreettinen tausta karkaistun lasin muodonmuutoksille. Artikkelissa otetaan esille myös mitä tapahtuu karkaisuprosessin aikana ja miksi muodonmuutokset syntyvät. Lämmönsiirto on jätetty tästä artikkelista, koska esimerkit on tehty vakiolämpötilassa. Lasin lämmönsiirrosta löytyy kirjallisuutta [6-8].

MUODONMUUTOSTEN TEOREETTINEN TAUSTA

Lasinkarkaisuprosessissa venymät syntyvät lämpötilakentän muutoksen ja tilavuusvoimien vaikutuksesta. Kun lasin lämpötila on korkea, lasi on viskoosi materiaali ja syntyy virumisilmiö. Viruminen muodostaa pysyviä plastisia muodonmuutoksia lasiin.

Ottamalla lämpötilan muutoksen huomioon, lämpövenymä ε_{th} saadaan

$$\left(\varepsilon_{th}\right)_{ii} = \alpha \Delta T \tag{1}$$

Tilavuusvoima on riippuvainen lasin tiheydestä ρ ja maanvetovoiman kiihtyvyydestä g

$$b = \rho g \tag{2}$$

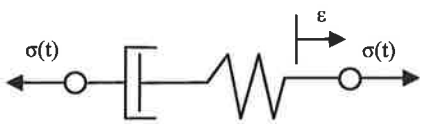

Kuva 3. Maxwellin malli.

Lasi on viskoelastinen materiaali. Matalissa lämpötiloissa lasin käyttäytyminen on elastista, koska viskoosi vaikutus on hyvin hidas. Kun lämpötila ylittää transitiolämpötilan, viskoosin käyttäytymisen vaikutus kasvaa. Viskoelastista käyttäytymistä voidaan kuvata Maxwellin mallin avulla, jossa jousi ja vaimennin ovat sarjassa, kuten esitetty kuvassa 3. Mallissa jousi kuvaa kiinteän aineen käyttäytymistä ja vaimennin viskoosia käyttäytymistä. Yleinen konstitutiivinen yhtälö Maxwellin mallille on [9]

$$\dot{\varepsilon} = \frac{\dot{\sigma}}{E} + \frac{\sigma}{\eta} \tag{3}$$

Käyttämällä yhtälöä (3) yhteys jännitysten ja venymien välillä on

$$\sigma(t) = E \exp\left(-\frac{E}{\eta} t\right) \varepsilon \tag{4}$$

Tässä yhtälössä venymän kerroin on relaksaatiofunktio *G(t)*, joka kuvaa jännityksen muutosta ajan funktiona vakio venymällä ε. Koska venymät voivat muuttua ja relaksoituminen on aika ja lämpötila riippuva, tulee jännitystä laskettaessa koko historia ottaa huomioon

$$\sigma = \int_0^t G(t-t') \frac{\partial \varepsilon}{\partial t'} dt' \tag{5}$$

Muodostuneet venymät voidaan jakaa deviaattoriseen ja hydrostaatiseen osaan [10]

$$\varepsilon_{ij} = e_{ij} + \delta_{ij} \overline{\varepsilon} \tag{6}$$

Analogisesti jännitykset voidaan jakaa leikkaus- ja normaalijännityksiin

$$\sigma_{ij} = s_{ij} + \delta_{ij} \overline{\sigma} \tag{7}$$

Kun jännitykset on jaettu yhtälön (7) mukaan, voidaan jännitysten ja venymien yhteys esittää seuraavasti

$$s = \int_0^t G_1(t-t') \frac{\partial e}{\partial t'} dt' \tag{8}$$

$$\overline{\sigma} = \int_0^t G_2(t-t') \frac{\partial \overline{\varepsilon}}{\partial t'} dt' \tag{9}$$

Relaksoitumisen aikariippuvuus yleistetyn Maxwellin mallin mukaan liukukertoimelle $G_1(t)$ ja puristuskertoimelle $G_2(t)$ voidaan kuvata Pronyn sarjan avulla

$$G_1(t) = 2G_0 \sum_{i=1}^{n} w_{1i} \exp\left(-\frac{t}{\tau_{1i}}\right) \tag{10}$$

$$G_2(t) = 3K_\infty + (3K_0 - 3K_\infty)\sum_{i=1}^{n} w_{2i} \exp\left(-\frac{t}{\tau_{2i}}\right) \tag{11}$$

Yllä olevissa yhtälöissä G_0 on alkutilan liukukerroin, K_0 alkutilan puristuskerroin and K_∞ lopputilan puristuskerroin. Edellä esitetyt kertoimet voidaan kuvata kimmokertoimen E ja Poissonin luvun ν avulla.

$$G_0 = \frac{E}{2(1+\nu)}, \quad K_0 = \frac{E}{3(1-2\nu)} \tag{12}$$

Termit τ_{1i} ja τ_{2i} ovat relaksoitumisaikoja jokaiselle liukukertoimen ja puristuskertoimen Pronyn tekijälle sekä w_{1i} ja w_{2i} ovat painokertoimia. Relaksoitumisajat määritellään [10]

$$\tau_{1i} = \frac{\eta_i}{w_{1i} G_0}, \quad \tau_{2i} = \frac{\eta_i}{w_{2i} K_0} \tag{13}$$

, jossa η_i on viskositeetti.

Lasin viskoosit ominaisuudet riippuvat lämpötilasta. Jos relaksoitumisfunktion kertoimet tiedetään referenssilämpötilassa T_{ref}, voidaan relaksoitumisajat toisessa lämpötilassa laskea siirtofunktion $a(T)$ avulla. Stabiloidulle lasille siirtofunktio voidaan esittää [10]

$$a(T) = \frac{\tau_{ref}}{\tau(T)} \tag{14}$$

, jossa τ_{ref} kuvaa yhtälössä (13) esitettyä relaksoitumisaikaa referenssilämpötilassa T_{ref}. Siirtofunktio saadaan yhtälöstä

$$\ln a(T) = \frac{H}{R}\left(\frac{1}{T_{ref}} - \frac{1}{T}\right) \tag{15}$$

, jossa H on aktivointienergia ja R yleinen kaasuvakio.

Lasi käyttäytyy eri tavoin eri lämpötiloissa viskoelastisesta käyttäytymisestä johtuen. Matalassa lämpötilassa lasi on kiinteän aineen kaltainen materiaali, kun taas korkeassa lämpötilassa lasi käyttäytyy enemmän nesteen kaltaisesti. Tällöin tulee huomioida rakenteellisen relaksoitumisen avulla poikkeama tasapainotilasta. Rakenteellinen relaksoituminen voidaan kuvata ominaisuuden muutoksena lämpötilan muutoksesta johtuen. Vastefunktio $M_p(t)$ mille tahansa ominaisuudelle $p(t)$ esitetään

$$M_p(t) = \frac{p(t) - p_2(\infty)}{p_2(0) - p_2(\infty)} = \frac{T_f(t) - T_2}{T_1 - T_2} \tag{16}$$

Fiktiivinen lämpötila T_f voidaan laskea yhtälöstä (16) ja se kuvaa poikkeamaa tasapainotilasta. Fiktiivisen lämpötilan laskennassa tulee ottaa huomioon koko lämpötilahistoria.

$$T_f(t) = T(t) - \int_0^t M_p(t-t')\frac{dT(t)}{dt'}dt' \tag{17}$$

Vastefunktio $M_p(t)$ voidaan kuvata analogisesti viskoosin relaksoitumisen kanssa

$$M_p(t) = \sum_{i=1}^{n} C_i \exp\left(-\frac{t}{\lambda_i}\right) \tag{18}$$

Rakenteellinen relaksoitumisaika λ_i on lämpötilariippuva ja on analoginen jännitysten relaksoitumisen kanssa (13). Kun lasi ei ole stabiilissa tilassa, relaksoitumisajan siirtofunktio riippuu todellisesta lämpötilasta sekä fiktiivisestä lämpötilasta.

$$\ln a(T) = \frac{H}{R}\left(\frac{1}{T_{ref}} - \frac{x}{T} - \frac{(1-x)}{T_f}\right) \tag{19}$$

Siirtofunktiota (19) tulee käyttää karkaisun aikana sekä jännitysten että rakenteellista relaksoitumista tarkasteltaessa. Yhtälössä (19) termi x on vakio, joka riippuu materiaalista.

TULOKSIA

Taulukko 1. Materiaali ominaisuuksia.

Kimmokerroin E = 70 GPa
Poisson vakio ν = 0.22
Lämpöpitenemiskerroin kiinteälle lasille $\alpha_s = 9\cdot10^{-6}$ 1/K
Lämpöpitenemiskerroin nestemäiselle lasille $\alpha_l = 25\cdot10^{-6}$ 1/K
Lämmönjohtuminen $k = 0.975 + 8.58\cdot10^{-4}$ T W/mK, jossa T [°C]
Ominaislämpö nestemäiselle lasille ($T>T_g$ = 850 K) $c_{p,l} = 1433 + 6.5\cdot10^{-3}$ T J/kgK, jossa T [K]
Ominaislämpö kiinteälle lasille ($T\leq T_g$ = 850 K) $c_{p,s} = 893 + 0.4$ T $- 1.8\cdot10^{-7}/T^2$ J/kgK, jossa T [K]
Suhde H/R = 55000 K
Vakio x = 0.5
Tiheys ρ = 2530 kg/m^3

Taulukko 2. Materiaalivakiot liuku- ja puristuskertoimille sekä rakenteellisen relaksoitumisen vastefunktiolle (T_{ref} = 869 K).

Liukukerroin		Puristuskerroin ($K_\infty/K_0 = 0.3$)		Rakenteellinen osa	
w_{1i}	τ_{1i}	w_{2i}	τ_{2i}	C_i	λ_i
0.0552	$6.658\cdot10^{-5}$	0.0222	$5.009\cdot10^{-5}$	0.05523	$5.965\cdot10^{-5}$
0.0821	$1.197\cdot10^{-3}$	0.0224	$9.945\cdot10^{-4}$	0.08205	$1.077\cdot10^{-2}$
0.1215	$1.514\cdot10^{-2}$	0.0286	$2.022\cdot10^{-3}$	0.1215	0.1362
0.2286	0.1672	0.2137	$1.925\cdot10^{-2}$	0.2286	1.505
0.286	0.7497	0.394	0.1199	0.2860	6.747
0.2266	3.292	0.3191	2.033	0.2265	29.63

Elementtimenetelmä-laskentaohjelmaa, ANSYStä, on käytetty jännitysten ja muodonmuutosten laskentaan. Referenssiarvot materiaaliominaisuuksille ja niiden lämpötilariippuvuudelle on esitetty taulukossa 1. Vakiot lasin jännitysten ja rakenteellisen relaksaation käyrille referenssilämpötilassa (T_{ref} = 869 K) on annettu taulukossa 2. Nämä sooda-kalkki lasin arvot ovat Daudevillen ja Carrén artikkelista [1].

Suurin vaikutus lasin muodonmuutoksiin on korkea lämpötila. Lasin relaksoitumisaika lyhenee lasin lämpötilan noustessa yli transitiolämpötilan (noin 550 °C). Samaan aikaan virumisnopeus kasvaa. Kuvassa 5. on esitetty lasin lämpötilan vaikutus vapaasti tuetun ulokepalkin (kuva 4.) taipumaan yhden sekunnin jälkeen.

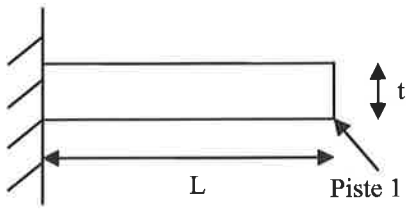

Kuva 4. Ulokepalkki, L = 10 cm, t = 4 mm.

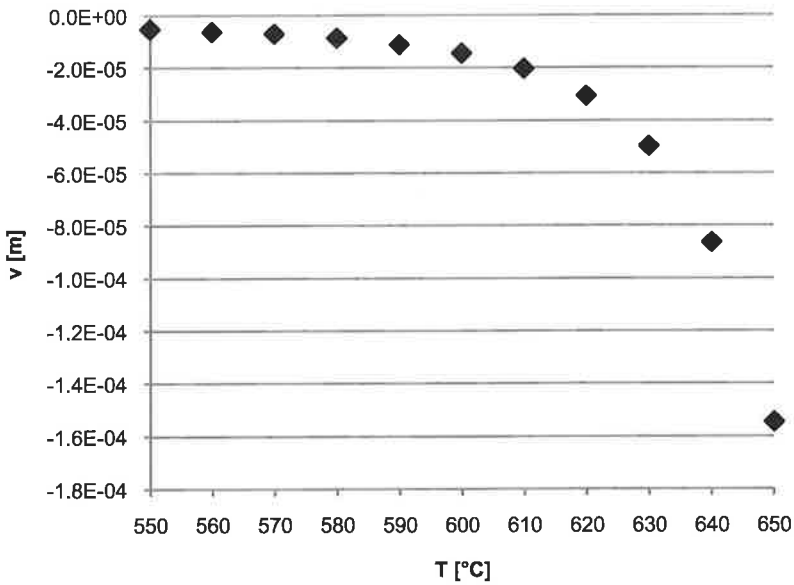

Kuva 5. Lämpötilan vaikutus pisteen 1 siirtymään ulokepalkilla.

Mitä pidempään lasi on korkeassa lämpötilassa sitä enemmän se viruu. Telatuetun lasin tapaus on esitetty kuvassa 6.

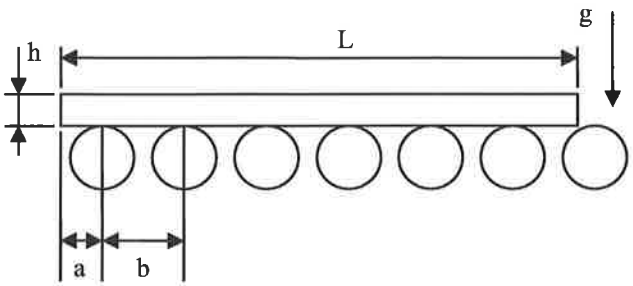

Kuva 6. Telatuettu lasi.

Tapauksessa, jossa kuuma lasi on telojen päällä, muodonmuutokset telojen välissä ja vapaiden reunojen välillä on erilainen, lasin tuennasta johtuen. Vapaa reuna taipuu yleensä enemmän kuin muu osa lasista. Lasin taipuman suuruus riippuu vapaan pään pituudesta. Jos vapaa pää on lyhyt, sen vieressä olevalla telavälillä on suurempi vaikutus ja vapaa pää nousee ylös. Yleensä vapaan pään muodonmuutoksilla on hallitseva vaikutus koko lasilevyn taipumille. Telojen päällä paikallaan olevan lasi levyn muodonmuutokset on esitetty kuvassa 7. Tapauksen lasilevyn paksuus on 4 mm, pituus 1 m, lasin lämpötila 630 °C, telaväli (b) 120 mm ja etäisyys lasin reunan ja ensimmäisen telan välillä (a) 60 mm. Alkutilassa lasilla on ainoastaan elastiset muodonmuutokset ja tämän jälkeen lasi viruu alun elastisesta tilasta lähtien. Vapaan pään vaikutus nähdään molemmista päistä. Jos vapaapää on pidempi, levy taipuu paljon enemmän. Tässä tapauksessa vasemman pään vapaan osan pituus on 60 mm ja oikean pään 100 mm. Samalla kun vapaa pää laskee, lasi nousee viereisessä telavälissä, vapaan pään vaikutuksesta. Vapaalla päällä on pienempi vaikutus lasilevyn keskiosalla.

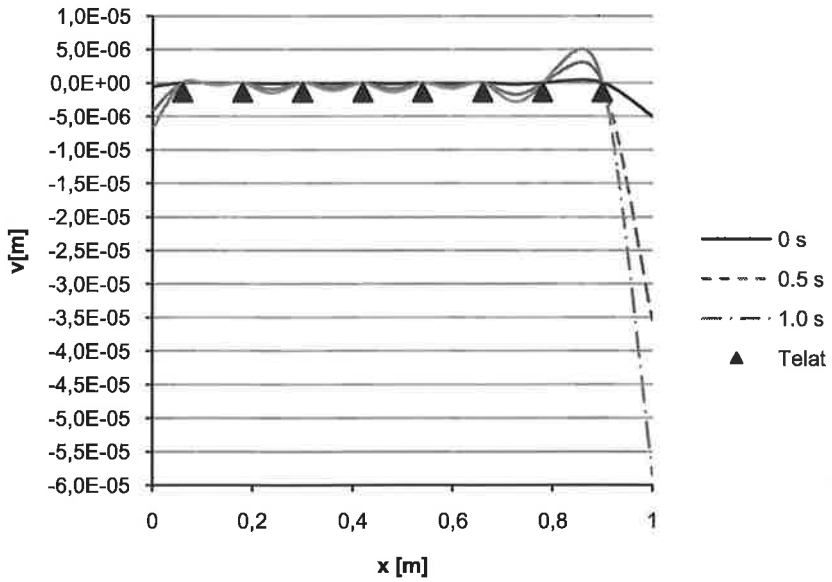

Kuva 7. Paikallaan, telojen päällä olevan lasilevyn muodonmuutokset. Lasin paksuus 4 mm, pituus 1 m, lämpötila 630 °C.

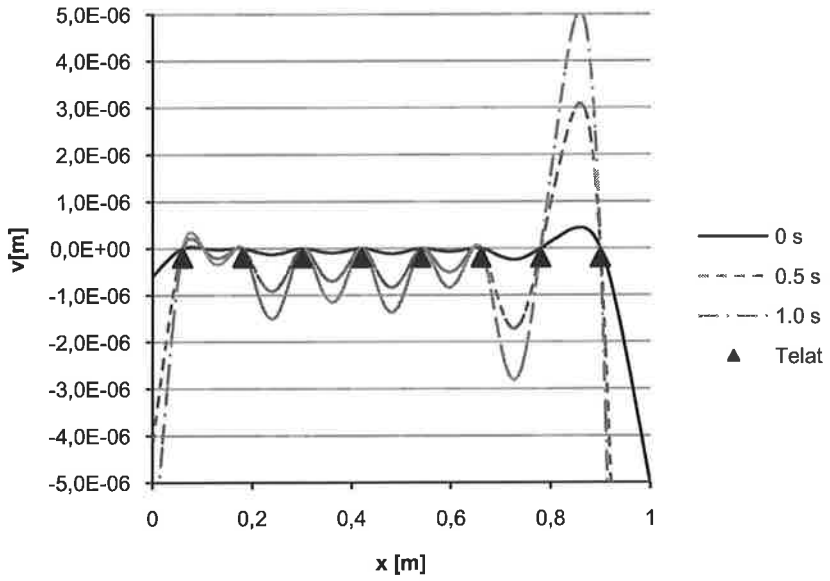

Kuva 8. Paikallaan telojen päällä olevan lasilevyn muodonmuutokset. Tarkempi kuvaaja kuvasta 7. telojen välisten muodonmuutosten näkemiseksi.

Yleensä karkaisuprosessin aikana lasilevy on liikkeessä. Tällöin vapaiden päiden pituudet vaihtelevat ajan mukana ja vaikuttavat eritavoin loppuun osaan lasista. Lasin muodonmuutosten muuttuminen ajan mukana on esitetty kuvassa 9. Tässä esimerkissä lasin paksuus on 4 mm, pituus 0,75 m, lämpötila 630 °C etäisyys telojen välillä (b) 120 mm ja etäisyys lasin reunan ja ensimmäisen telan välillä (a) alkutilassa 20 mm. Lasin nopeus on 500 mm/s. Ajan hetkellä 0 s lasissa on ainoastaan elastiset muodonmuutokset. Liikkeen aikana lasi muuttaa muotoaan. Kuuden sekunnin kuluttua lasi on teloihin nähden samalla paikalla ja ero alkutilan ja uuden tilan (alun elastinen muodonmuutos ja viruminen) välillä nähdään.

Tuloksia edellä esitetystä tapauksessa esitetään myös kuvassa 10. Kyseisessä kuvassa esitetään mitä tapahtuu, kun lasi kulkee yhden telavälin yli. Liikkeen aikana vapaan reunan pituus ja taipuma muuttuvat ajan mukaan. Reunalle muodostuu epäjatkuvuuskohta, kun lasi nousee telalle tai tippuu telalta pois. Kun lasi on liikkunut jonkin aikaa, nähdään lasin taipuvan koko ajan alaspäin. Tuloksista nähdään, että aallonpituuden ja amplitudin ennustaminen on hankalaa.

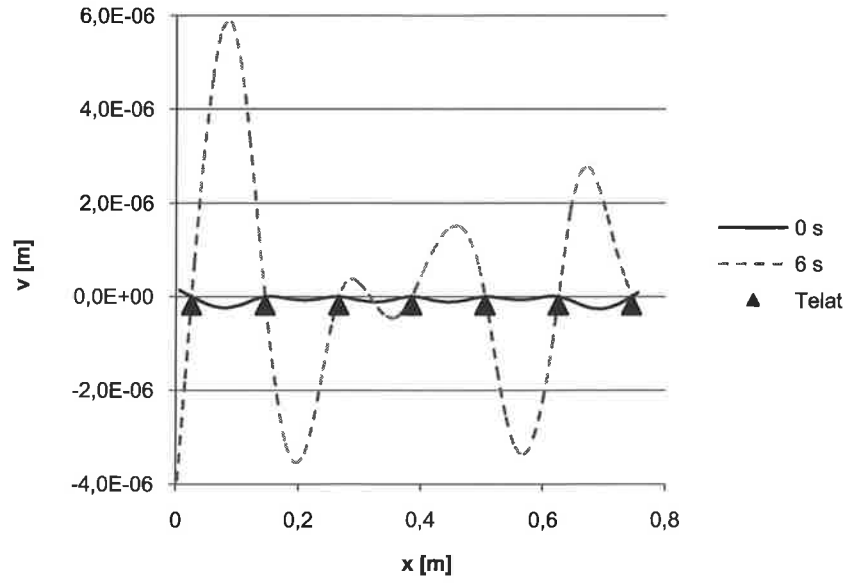

Kuva 9. Elastiset muodonmuutokset (aika 0 s) ja lasin muodonmuutokset 6 s kuluttua.

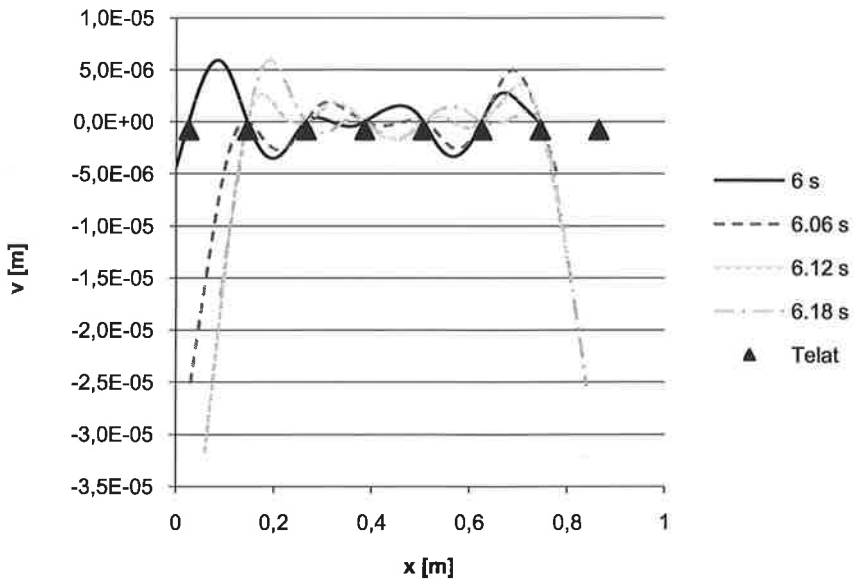

Kuva 10. Lasin muodonmuutokset telavälin matkalla.

YHTEENVETO

Lasinkarkaisuprosessia muodonmuutokset muodostuvat lasin massasta ja teloista johtuen. Kuuma lasi on viskoosi materiaali ja jännitysten relaksoitumista esiintyy. Mitä kuumempi lasi on, sitä viskoosimpi se on. Kuumempi lasi tekee karkaisulaadun paremmaksi, mutta samalla

muodonmuutokset lasissa kasvavat ja visuaalinen laatu kärsii. Jos lasin lämpötila on alle transitiolämpötilan, plastisia muodonmuutoksia ei synny ja mekaaninen karkaisu on mahdotonta.

Korkeassa lämpötilassa oleva lasi viruu liikkeen aikana. Lasin muodonmuutokset riippuvat nopeus-aika jakaumasta. Oskillointi ja nopeuden muutokset vaikuttavat muodonmuutoksiin, kuten myös telojen välinen etäisyys. Lasin tulisi olla mahdollisimman vähän aikaa kuumana. Symmetrisellä lasin jäähdytyksellä ei ole suurta vaikutusta lasin muodonmuutoksiin. Epäsymmetrinen jäähdytys taas aiheuttaa kulhomuodon lasille. Lasin jäähdytystehoa kasvattamalla voidaan karkaisulämpötilaa hieman laskea, mutta jos jäähdytyksen voimakkuus on liian suuri, pinnan vetojännitys rikkoo lasin.

Numeerista simulointia voidaan käyttää hyödyksi lasin muodonmuutosten syntyyn vaikuttavien tekijöiden tutkimisessa. Karkaistun lasin muodonmuutokset voidaan mitata, mutta se mitä tapahtuu lämmityksen ja jäähdytyksen aikana liikkeen ja lämpötilan muuttumisen vaikutuksesta, ei voida mitata. Tähän numeerinen simulointi tuo apua. Numeeriseen ratkaisuun telat tuovat ongelmia. Kun lasin reuna nousee telan päälle tai tippuu telalta, muodostuu epäjatkuvuus lasin reunan siirtymälle.

Vaikka kirjallisuudesta löytyy teoria lasin viskoelastiselle käyttäytymiselle, materiaaliominaisuuksien ja muiden parametrien mittaaminen on hankalaa. Näin ollen ainoastaan simulointiparametrien, kuten nopeuden ja telavälin, vaikutusta tuloksiin voidaan tutkia.

Tekijät haluavat kiittää Glaston R&D osastoa neuvoista ja kuvista. Lisäksi kiitos CSC:lle mahdollisuudesta ANSYS ohjelman käyttöön tutkimuksessa.

LÄHTEET

[1] Daudeville L., Carré H. Thermal Tempering Simulation of Glass Plates: Inner and Edge Residual Stresses, Journal of Thermal Stresses, 21, 1998, s. 667-689.
[2] Narayanaswamy, O. S., Stress and Structural Relaxation in Tempering Glass, Journal of the American Ceramic Society, 61: 3-4, 1978, s. 146-152.
[3] Gardon. R. The Tempering of Flat Glass by Forced Convection, Proceedings VIIth International Congress on Glass, Bryssel, Belgium, 1965.
[4] Aronen, A., Karvinen, R. How to Affect Residual Stresses in Glass Tempering, Bos, F. et al. (eds.). Challenging Glass, Conference on Architectural and Structural Applications of Glass, May 2008, Delft University of Technology, the Netherlands, s. 303-312.
[5] Abbott M., Madocks J., Roller Wave Distortion - Definition, Causes and a Novel Approach to Accurate, On-line Measurement, Proceedings of Glass Processing Days 2001, 18-21 June 2001, Tampere, Finland, s. 226-230.
[6] Karvinen, R., Rantala, M., Pesonen, T., Heat Transfer in Glass Tempering and Forming Process, Advanced in Heat Transfer Engineering, ed. by B. Sunden and J. Vilemas, 4th Baltic Heat Transfer Conference 2003, s. 217-225.
[7] Rantala, M., Karvinen, R., Heat Transfer Under an Impinging Jet at Long Nozzle-to-Surface Distances, Proceedings of 13th International Heat Transfer Conference, August 2006, Sydney Australia, 12 s.
[8] Jalkanen, E., The High Performance Low-E Tempering Process, Proceedings of Glass Performance Days 2007, June 2007, Tampere, Finland, s. 675-678.
[9] Ottosen, N.S., Ristinmaa, M., The Mechanics of Constitutive Modeling, Elsevier, Amsterdam, 2005.
[10] Scherer, G. Relaxation in Glass and Composites, John Wiley & Sons, Inc., USA, 1986.

HIERREJAUHIMEN VIRTAUSMALLINNUS JA OPTIMOINTI

M. LINDSTEDT, J.-P. HUHTANEN, R. KARVINEN
Energia- ja prosessitekniikan laitos
Tampereen Teknillinen Yliopisto
PL 589
FI-33101 Tampere, Finland
s-posti: matti.lindstedt@tut.fi, juha-pekka.huhtanen@tut.fi, reijo.karvinen@tut.fi

TIIVISTELMÄ/ABSTRACT

Hierrejauhimella valmistetaan kuitumassaa hakepaloista ja vedestä pyörivien kuvioitujen kiekkojen välissä. Työssämme sen toimintaa simuloidaan epänewtoniseen virtausdynamiikkaan perustuvalla mallilla, jossa käytämme apuna pumpputeoriaa. Mitattu ja simuloitu lämpötilajakauma vastaavat toisiaan hyvällä tarkkuudella. Jauhatuksen kolme tärkeintä kriteeriä ovat: kustannukset, laatu ja tuotantomäärä. Jauhimessa pyritään minimoimaan energiankulutus tuotantomäärä kohti ja samalla maksimoimaan laadun kuvaamiseen käytettyä ominaisintensiteettiä, jolla on tietty yhteys massan Freeness-arvoon. Monitavoiteoptimointitehtävä ratkaistaan omalla MOPSO-algoritmin muunnoksella. Tulokset osoittavat, että sekä kustannuskriteeriä että laatukriteeriä voidaan parantaa samanaikaisesti teollisuudessa käytössä olevaan vertailujauhimeen verrattuna. Geometrian optimoinnilla voidaan vaikuttaa jauhatuksen tehokkuuteen enemmän kuin ajoarvojen optimoinnilla.

JOHDANTO

Mekaaninen massanvalmistus perustuu puun kuituja yhdessä pitävän ligniinin pehmentämiseen värähtelevien mekaanisten voimien ja korkean lämpötilan avulla. Kuumahierreprosessissa (TMP) kosteiden hakepalojen ja veden muodostama suspensio ohjataan syöttöruuvilla ja keskuslevyllä kulkemaan vastakkain asetettujen kuvioitujen levyjen väliin, joista vähintään toinen pyörii. Tuotteen laadusta riippuen jauhinlinjassa on yksi jauhin tai kaksi jauhinta sarjassa ja tyypillisen kaksivaiheisen TMP-linjan jauhimet kuluttavat noin 20 MW sähköä. TMP-massaa käytetään pääasiallisesti sanomalehtipaperissa sekä SC- ja LWC-laaduissa ja kartongissa. [1]

Hierrejauhimen terävälissä olevan sakean (kuiva-ainepitoisuus 30–50 %) suspension kitka, hakepalojen murskaaminen ja kuitujen käsittely muuttavat suurimman osan roottorin akseliin tuodusta mekaanisesta energiasta lämmöksi. Osa suspension vedestä höyrystyy synnyttäen vaikeasti mallinnettavan höyry-vesi-kuitususpension, jossa höyry virtaa muita faaseja nopeammin. Veden kyllästyslämpötilaan vaikuttava painetaso ja muu virtauskenttä voidaan laskea virtausdynamiikkaan perustuvalla mallilla riittävän tarkasti, jotta niistä voidaan laskea arvio jauhatuksen lopputuotteen laadulle [2]. Tällöin hierrejauhimen toimintaa voidaan myös systemaattisesti optimoida kustannusten ja laadun suhteen monitavoiteoptimointiin soveltuvilla algoritmeilla [3]. Tässä työssä esitellään parannettu versio aiemmasta virtauslaskentamallista [4,5] ja optimoidaan omalla MOPSO-algoritmin muunnoksella taso- ja kartio-osista koostuvaa CD-jauhinta, jonka poikkileikkaus ja roottorin teräpakka on esitetty kuvassa 1.

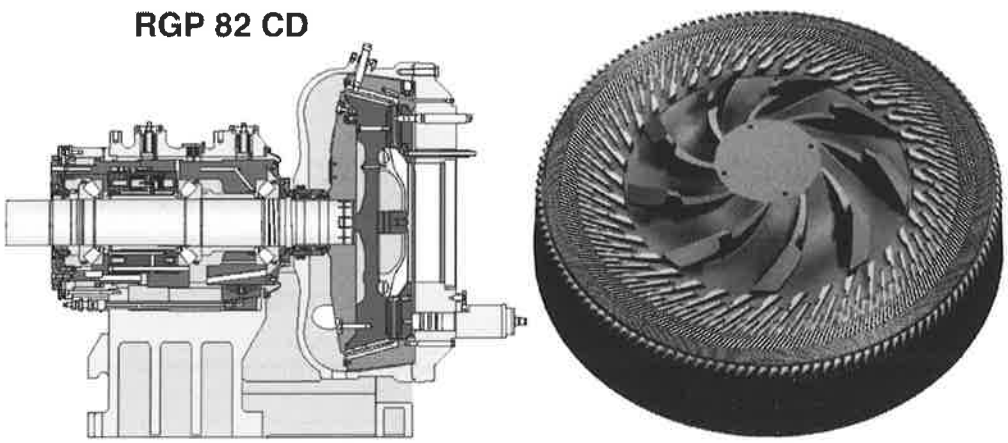

Kuva 1. Vasemmalla Metso RGP 82 CD-jauhimen poikkileikkaus ja oikealla tyypillinen Turbine Segments™ teknologian mukainen roottorin teräpakka.

HALLITSEVAT YHTÄLÖT

Hierrejauhimessa virtaavan suspension virtausta hallitsee massan, liikemäärän ja energian säilymislait. Kun oletetaan painovoiman vaikutus merkityksettömäksi ja virtaus ajasta riippumattomaksi, voidaan massan (1) ja liikemäärän (2,3,4) säilymisyhtälöt eli Navier-Stokes-yhtälöt ja energian säilymisyhtälö (5) kirjoittaa $r\omega z$ -sylinterikoordinaatistossa seuraavasti [6,7]

$$\frac{1}{r}\frac{\partial(\rho v_r)}{\partial r}+\frac{1}{r}\frac{\partial(\rho v_\theta)}{\partial \theta}+\frac{\partial(\rho v_z)}{\partial z}=0, \tag{1}$$

$$v_r\frac{\partial v_r}{\partial r}+\frac{v_\theta}{r}\frac{\partial v_r}{\partial \theta}-\frac{v_\theta^2}{r}+v_z\frac{\partial v_r}{\partial z}=-\frac{\partial p}{\rho\partial r}-\frac{1}{\rho}\left(\frac{\partial r\tau_{rr}}{r\partial r}+\frac{\partial r\tau_{\theta r}}{r\partial\theta}-\frac{\tau_{\theta\theta}}{r}+\frac{\partial\tau_{zr}}{\partial z}\right), \tag{2}$$

$$v_r\frac{\partial v_\theta}{\partial r}+\frac{v_\theta}{r}\frac{\partial v_\theta}{\partial \theta}+\frac{v_r v_\theta}{r}+v_z\frac{\partial v_\theta}{\partial z}=-\frac{\partial p}{\rho r\partial\theta}-\frac{1}{\rho}\left(\frac{\partial r^2\tau_{r\theta}}{r^2\partial r}+\frac{\partial\tau_{\theta\theta}}{r\partial\theta}+\frac{\partial\tau_{z\theta}}{\partial z}\right), \tag{3}$$

$$v_r\frac{\partial v_z}{\partial r}+\frac{v_\theta}{r}\frac{\partial v_z}{\partial \theta}+v_z\frac{\partial v_z}{\partial z}=-\frac{\partial p}{\rho\partial\theta}-\frac{1}{\rho}\left(\frac{\partial r\tau_{rz}}{r\partial r}+\frac{\partial\tau_{\theta z}}{r\partial\theta}+\frac{\partial\tau_{zz}}{\partial z}\right), \tag{4}$$

$$\begin{aligned}\rho\left(v_r\frac{\partial h}{\partial r}+\frac{v_\theta}{r}\frac{\partial h}{\partial\theta}+v_z\frac{\partial h}{\partial z}\right)&=\left(v_r\frac{\partial p}{\partial r}+\frac{v_\theta}{r}\frac{\partial p}{\partial\theta}+v_z\frac{\partial p}{\partial z}\right)\\ &+\left\{\frac{1}{r}\frac{\partial}{\partial r}\left(rk\frac{\partial T}{\partial r}\right)+\frac{1}{r^2}\frac{\partial}{\partial\theta}\left(k\frac{\partial T}{\partial\theta}\right)+\frac{\partial}{\partial z}\left(k\frac{\partial T}{\partial z}\right)\right\}-\left\{\tau_{rr}\frac{\partial v_r}{\partial r}+\frac{\tau_{\theta\theta}}{r}\left(\frac{\partial v_\theta}{\partial\theta}+v_r\right)+\tau_{zz}\frac{\partial v_z}{\partial z}\right\}\\ &-\left\{\tau_{r\theta}\left[r\frac{\partial}{\partial r}\left(\frac{v_\theta}{r}\right)+\frac{1}{r}\frac{\partial v_r}{\partial\theta}\right]+\tau_{rz}\left(\frac{\partial v_z}{\partial r}+\frac{\partial v_r}{\partial z}\right)+\tau_{\theta z}\left(\frac{1}{r}\frac{\partial v_z}{\partial\theta}+\frac{\partial v_\theta}{\partial z}\right)\right\}+\dot{q}'''\end{aligned} \tag{5}$$

missä h on fluidin ominaisentalpia, p on paine ja $\dot{q}'''$ on lähdetermi. Energiayhtälön yksikkö on tehoa tilavuutta kohti. Liikeyhtälöiden sulkemiseksi tarvitaan materiaalimalli eli fluidiin kohdistuvan kuormituksen ja sen aiheuttaman muodonmuutoksen nopeuden välinen yhteys. Hierrejauhimessa virtaavalle vesi-kuitususpensiolle on valittu materiaalimalliksi Ostwald-de Waele- eli Power-law-malli

$$\tau = K\left|\frac{\partial v}{\partial x}\right|^{n-1}\left(\frac{\partial v}{\partial x}\right), \tag{6}$$

missä K on suspension sakeudesta riippuva konsistenssiarvo ja n on Power-law-indeksi [8]. Mallin vakioille on reologisten mittausten [4] perusteella määritetty hierrejauhimen vesi-kuitususpensiota vastaavat arvot. Vesi-kuitususpension virtaus on todellisuudessa erittäin monimutkainen ilmiö [9], mutta Power-law-mallin käyttö on olennainen yksinkertaistus tulosten saamiseksi.

JAUHIMEN MALLINNUS

Hierrejauhin on virtauskone, jonka roottorissa ja staattorissa on useita avonaisia, kapeita ja syviä uria. Kapeat urat ja suuri virtausnopeus aiheuttavat suuren kitkahäviön ja täten pienen hydraulisen hyötysuhteen, mutta keskipakopumpuille tyypillinen pyörimisestä johtuva siipien paine- ja imupuolien nopeusero ei ole merkittävä häviöiden lähde. Staattorissa voi tapahtua takaisinvirtausta tilavuusvoiman puuttumisen ja positiivisen painegradientin vuoksi, mistä johtuu jauhimien huomattavan pieni volumetrinen hyötysuhde. Jauhimen tapauksessa Navier-Stokes- ja energiayhtälöistä voidaan supistaa termejä suuruusluokkatarkastelun ja muiden oletusten avulla. Lopputuloksena saadaan r-suuntaisen virtauksen yksiulotteisen teorian kaavat, joita sekä Huhtanen [4], että Hahtokari [5] käyttivät simulointiohjelmissaan. Hierrejauhimia yksinkertaisempien matalasakeusjauhimien virtausta on yritetty laskea myös kaupallisella virtauslaskentaohjelmalla [10], mutta jopa tässäkin on ongelmana monimutkaisen virtauksen ja geometrian vaatima suuri laskentateho.

Termien supistaminen sylinterikoordinaatistossa esitetyistä hallitsevista yhtälöistä ei ole suoraviivaista, koska urat eivät ole säteen suuntaisia ja virtaus on olennaisesti urien suuntaista. Tällöin on tarkoituksenmukaisempaa tarkastella pyörivässä koordinaatistossa tapahtuvaa monifaasivirtausta poikkileikkaukseltaan vähitellen muuttuvassa, näennäisesti yksiulotteista kanavassa. Liikeyhtälön mukaan kanavan kontrollitilavuuteen vaikuttavien voimien summa aiheuttaa kontrollitilavuuden reunojen ylittävien liikemäärävirtojen muutoksen. Tämä on esitetty kuvassa 2.

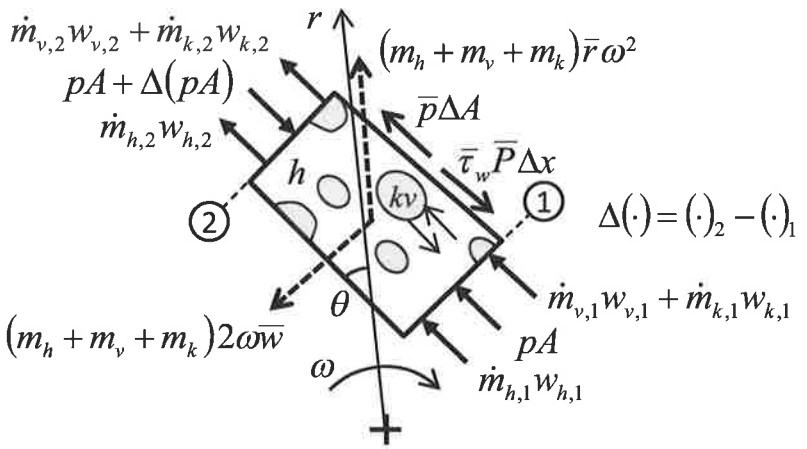

Kuva 2. Kontrollitilavuuteen tulevat liikemäärävirrat ja siihen vaikuttavat voimat. Koordinaatiston pyörimisen aiheuttamat kuvitteelliset hitausvoimat on merkitty katkoviivalla. h on höyry-, v on vesi- ja k on kuitufaasi. ω on jauhimen kulmanopeus ja θ on hammaskulma. Yläviiva tarkoittaa suureen keskimääräistä arvoa kontrollitilavuudessa.

Hierrejauhimen höyry-vesi-kuitu-kolmifaasivirtaus käsitellään siten, että vesi-kuitususpensio muodostaa yhden faasin, ja höyry toisen. Liikemäärävirtoja laskettaessa oletetaan, että faasit kulkevat samalla nopeudella $w = w_h = w_v = w_k$ jolloin faasien väliset kitkavoimat kumoutuvat liikeyhtälössä. Kuitupitoisuus on niin suuri, että vesi-kuitususpension virtaus on tulppamainen eli nopeudella on tasajakauma. Kun mukana on höyryä, on virtaus lähes aina voimakkaan turbulenttinen, jolloin nopeusjakauma on edelleen lähellä tasajakaumaa. Tämän takia liikemäärävirta voidaan kaikkialla jauhimessa laskea käyttäen virtauksen keskinopeutta eikä korjauskerrointa tarvita.

Crowe et. al. antavat [11] liikeyhtälön edellä kuvatulle kanavavirtaukselle. Yhtälössä esiintyy putouskiihtyvyyden kanavan suuntainen komponentti, joka jauhimen tapauksessa korvataan koordinaatiston pyörimisen synnyttämien kuviteltujen lisäkiihtyvyystermien uran suuntaisten komponenttien summalla $r\omega^2 \cos\theta$. Corioliskiihtyvyys on kohtisuorassa nopeutta vastaan, joten se ei vaikuta uran suuntaiseen komponenttiin. Käyttämällä derivoinnin laskusääntöä tähän termiin, voidaan ratkaista staattisen paineen muutos laskentapisteiden välillä

$$\Delta p = \bar{\rho}_{sus}\Delta\left(\frac{r^2\omega^2}{2}\right) - \frac{1}{\bar{A}}\Delta(\dot{m}_{tot}w) - \frac{1}{2}\left(\bar{\alpha}_{kv}\frac{\bar{\xi}_{kv}}{4}\bar{\rho}_{kv} + \bar{\alpha}_h\frac{\bar{\xi}_h}{4}\bar{\rho}_h\right)\overline{w|w|}\frac{\bar{P}}{\bar{A}}\Delta x, \tag{7}$$

missä viimeinen termi on faasien tilavuusosuuksilla α painotettu kitkan aiheuttama painehäviö ja P on kanavan märkäpiiri. Vesi-kuitususpensiolle käytetään Power-law-mallia noudattavan fluidin laminaarin kanavavirtauksen Darcy-kitkakerrointa [12]

$$\xi_{kv} = \frac{8K}{\rho_{kv}V^{2-n}D_h^n}\left(6+\frac{2}{n}\right)^n, \tag{8}$$

missä D_h on kanavan hydraulinen halkaisija ja V virtauksen keskinopeus. Höyry käsitellään newtonisena aineena, jolloin $n=1$ ja K korvataan viskositeetilla μ_h, mutta sen kitkakerroin määritetään turbulentille kanavavirtaukselle Blasiuksen kaavalla

$$\begin{aligned} \xi_h &= 0.3164Re^{-1/4}, \\ Re &= VD_h\rho_h / \mu_h, \end{aligned} \tag{9}$$

jonka tarkkuus on hyvä, kun Reynoldsin luku $Re_h < 10^5$ [6].

Tehonkulutuksen ja intensiteetin laskenta

Jauhimeen syötetty teho kulutetaan suspension pumppaamiseen sekä staattorin ja roottorin hampaiden välissä olevan terävälin leikkausjännityksen ylläpitämiseen eli jauhatukseen. Eulerin yhtälön mukaan pumppauksessa tarvittava teho lasketaan kaavalla [13]

$$P_{12} = \frac{\dot{m}_{tot}}{\eta_{vol}}\omega\Delta(rc_u), \tag{10}$$

missä η_{vol} on jauhimen volumetrinen hyötysuhde. Volumetrinen hyötysuhde on keskimääräisen tilavuusvirran ja takaisinvirtauksen tai vuotojen takia roottorissa kulkevan suuremman tilavuusvirran suhde. Sen laskentaa ei esitellä tässä työssä. c_u on suspension absoluuttisen virtausnopeuden kehän suuntainen komponentti. Roottorin pyöriminen tuo terävälin leikkausjännityksen, hakepalojen hajottamisen ja kuitujen muokkaamisen takia suspensioon suuren jauhatustehon Φ, mikä

näkyy energiayhtälössä (5) dissipaatioterminä $\tau_{z\theta}(\partial u_\theta / \partial z)$. Tilavuus, johon dissipaatio kohdistuu, on terävälin suuruuden d_g, laskentavälin pituuden Δr ja tehokkaan kehäpituuden eli ominaisjauhatuspinta-alan A' tulo. Ominaisjauhatuspinta-ala on vastakkain olevien staattorin ja roottorin hampaiden kehää pitkin mitatun yhteispituuden keskiarvo roottorin pyörähtäessä täyden kierroksen.

$$A' = \frac{\int_0^{2\pi} A'_r \cap A'_s d\theta}{\int_0^{2\pi} d\theta} = 2\pi r a_s a_r , \tag{11}$$

missä a_s ja a_r ovat staattorin ja roottorin hampaiden pintojen peittämän pinta-alan prosentuaalinen osuus koko kehän pituudesta. Kun terävälin leikkausjännitys lasketaan Power-law mallilla (6), saadaan laskentapisteiden välille tuotu jauhatusteho integroimalla dissipaatiotermin ja terävälin keskimääräisen poikkipinta-alan tulo laskentavälin yli

$$\Phi_{12} = \int_{r_1}^{r_2} \tau_{\theta z}\left(\frac{\partial u_\theta}{\partial z}\right) d_g A' \frac{dr}{\sin\varphi} = \int_{r_1}^{r_2} A' K \frac{(\omega r)^{n+1}}{d_g^n} \frac{dr}{\sin\varphi}, \tag{12}$$

missä φ on jauhimen kartiokulma.

Crowe et. al. antavat [11] virtauksen termisen energiayhtälön vastaavalle tilanteelle kuin liikeyhtälön (7). Kun ei huomioida lämmönjohtumisesta ja säteilystä johtuvia energiavirtoja, voidaan kontrollitilavuuden energiatase laskentapisteiden 1 ja 2 välillä kirjoittaa

$$\Phi_{12} - \Delta\left[\dot{m}_h h_h(T) + \dot{m}_v h_v(T) + \dot{m}_k h_k(T)\right] - \Delta(\dot{m}_h) h_L(\overline{T}) = 0. \tag{13}$$

Ominaisentalpioiden $h(T)$ ja höyrystymislämmön $h_L(T)$ arvot määritetään kylläisen veden ja vesihöyryn aineominaisuustaulukoista tehdyillä sovitteilla. Alikylläisen veden ominaisentalpia muuttuu hyvin vähän paineen funktiona, minkä takia se lasketaan samalla sovitteella kuin kylläinen vesi.

Jauhin jaetaan säteittäisessä suunnassa tasavälisiin laskentapisteisiin, joissa massan, liikemäärän ja energian taseyhtälöt toteutetaan iteroimalla halutulla tarkkuudella. Koko jauhimen kuluttama teho lasketaan summana laskentapisteiden välisistä jauhatus- ja pumppaustehoista.

$$P_{tot} = \sum P_{12} + \Phi_{12} \tag{14}$$

Jauhatuksen intensiteetti on kuitukäsittelyn tehokkuuden mitta. Huhtanen esitti [2] sille yksinkertaisen lausekkeen

$$I = \frac{60 P_{tot}}{N n_b t_r} \tag{15}$$

missä N on pyörimisnopeus, n_b on staattorin hampaiden lukumäärä ja t_r on suspension viipymäaika. Hän totesi simulointien ja kokeellisten mittausten avulla, että näin määriteltyä intensiteettiä voi käyttää ennustamaan jauhimen Freeness-pudotusta hyvällä tarkkuudella.

JAUHIMEN TOIMINNAN OPTIMOINTI

Jauhatuksen tehokkuuden kolme tärkeintä kriteeriä ovat kustannukset, laatu ja määrä. Uuden tiettyyn prosessiin sopivan segmentin geometrian suunnittelussa tai ajoarvojen säädössä pyritään tällöin saavuttamaan kolme ristiriitaista tavoitetta: 1. matala tehonkulutus, 2. korkea laatu ja 3. korkea tuotantomäärä. Optimointitehtävää voidaan yksinkertaistaa yhdistämällä kaksi kriteeriä yhdeksi. Koska kustannusten ja laadun optimointia ei voida tehdä tuotantomäärän kustannuksella, käytetään minimoitavana kohdefunktiona energian ominaiskulutusta

$$EOK = \frac{P_{tot}}{\dot{m}_k}, \tag{16}$$

jolloin energiankulutusta minimoidaan ja tuotantomäärää maksimoidaan samanaikaisesti. Jauhatuksen laatua voidaan kuvata useilla kuitumassasta mitattavilla suureilla, joita ovat esimerkiksi kuitujen kokojakauma, Freeness sekä lopputuotteen optiset ja lujuusominaisuudet. Laadun kuvaamiseen on valittu Freeness-arvo, jota edustaa kaavalla (15) laskettu intensiteetti jaettuna tuotantomäärällä eli ominaisintensiteetti

$$I_{omin} = \frac{I}{\dot{m}_k} \tag{17}$$

Ominaisintensiteettiä yritetään maksimoida. Tarkasteltavassa prosessissa on järkevää asettaa rajoitusehdoksi massan optisten ominaisuuksien kannalta riittävän alhainen maksimilämpötila $T_{\max}$. Koska tavoitteena on parantaa molempia kriteerejä vertailujauhimeen nähden, vaaditaan lisäksi, että EOK:n arvon on oltava pienempi kuin vertailujauhimen arvon EOK_{vert} ja I_{omin}:n arvon on oltava suurempi kuin vertailujauhimen arvon $I_{omin,vert}$.

Tässä työssä esitetyn optimointialgoritmin ja simulointiohjelman aiempia versioita on sovellettu kuuden ajoparametrin optimointiin [3] ja nyt mukaan otetaan geometrian optimointi. Esimerkkiajossa E1 etsitään optimaaliset ajoarvot jauhimelle, jonka segmenttien geometria on annettu ja esimerkkiajossa E2 etsitään annettuihin prosessin ajoarvoihin optimaalinen segmenttien geometria. Geometrian optimoinnissa suunnittelumuuttujat ovat segmenttien geometrian kuvaamiseen käytettyjen muotofunktioiden parametreja. Testiajoissa on havaittu, että geometrian likimääräisen kuvaamisen aiheuttama virhe simulointien tuloksiin on pieni.

Taulukko 1. Optimoitavat ajoparametrit ja geometriset suureet. n on suureeseen liittyvien muuttujien lukumäärä. Muuttujien tyyppi T on joko jatkuva (j) tai diskreetti (d).

E1 - Ajoparametrit	**n**	**T**	**E2 - Geometriaparametrit**	**n**	**T**
Terävälin säätö Δd_g (taso & kartio)	2	j	Terävälin profiili $\boldsymbol{d_g}$	3	j
Tuotantomäärä $\dot{m}_k$	1	j	Hammaskulma $\boldsymbol{\beta}$	8	j
Sakeus C	1	j	Uran syvyys $\boldsymbol{b}$	10	j
Ulostulon paine p_{out}	1	j	Hampaita kehällä $\boldsymbol{z}$	15	d
Laimennusveden massavirta $\dot{m}_d$	1	j	Hampaiden leveys $\boldsymbol{s}$	14	j
Laimennusveden lämpötila T_d	1	j			

Kehällä olevien hampaiden lukumäärät ovat segmenttien lukumäärällä jaollisia kokonaislukuja. On huomattava, että CD-jauhimessa taso- ja kartio-osien staattorilla ja roottorilla on kaikilla erilainen geometria ja ajossa E2 optimoitavat 50 geometriaparametria kattavat kaikkien neljän segmenttityypin optimoinnin. Geometrian täydelliseen optimointiin tarvittaisiin yli 100 muuttujaa, mutta

tehtävän yksinkertaistamiseksi vain tärkeimmät parametrit on valittu suunnittelumuuttujiksi. Tehtävän monimutkaisuuden sekä segmenttien valmistuksen ja teräkokeiden kalleuden takia on selvää, että pelkästään kokeilemalla ei voida saavuttaa huomattavia parannuksia vanhoihin jauhimiin nähden, vaan on käytettävä sopivia monitavoiteoptimointimenetelmiä virtausmallinnuksen tukena.

Vertailujauhimen ajoparametrit ja geometria ovat lähtökohta optimoinnin suunnittelumuuttujille, joista jokaiselle asetetaan ala- ja ylärajat vertailujauhimen vastaavien arvojen ympärille sopivalle etäisyydelle. Optimointia varten jokaisen jatkuvan suunnittelumuuttujan sallittu vaihteluväli diskretoidaan siten, että muuttuja j, joka on alun perin jatkuva, voi saada vain $x_j^u = 1001$ kappaletta arvoja tasavälein ala- ja ylärajan väliltä. Alun perin diskreeteillä muuttujilla on kullakin oma mahdollisten arvojen lukumääränsä x_j^u. Optimointialgoritmissa käsitellään alkuperäisten jatkuvien ja diskreettien muuttujien arvojen X_j sijaan niiden arvoihin viittaavia indeksejä $x_j = 1,2,..., x_j^u$. Jatkuvien muuttujien diskretointi on hyväksyttävää, koska tavoite ei ole matemaattisesti oikean ratkaisun löytäminen vaan merkittävä parannus vertailujauhimeen nähden. Täten jauhatuksen monitavoitteinen optimointiongelma voidaan asetella seuraavasti

$$\begin{aligned} &\min_{\boldsymbol{x}\in\Omega} \boldsymbol{f}(\boldsymbol{x}) = \left[-I_{omin},\, EOK\right]^T, \\ &\Omega = \{\boldsymbol{x} \in \mathrm{N}^m \mid 1 \le x_j \le x_j^u, \\ &\qquad g_1(\boldsymbol{x}) = T_{\max} - T_{sall} \le 0, \\ &\qquad g_2(\boldsymbol{x}) = I_{omin,vert} - I_{omin} \le 0, \\ &\qquad g_3(\boldsymbol{x}) = EOK - EOK_{vert} \le 0\}, \end{aligned} \tag{18}$$

missä N on luonnollisten lukujen joukko ja m on suunnittelumuuttujien lukumäärä. Rajoitusehtoja rikkovat ratkaisut hylätään kokonaan, koska käypien ratkaisuiden löytäminen ei ole ongelma. Vertailujauhin on tunnettu piste ja sitä käytetään optimoinnin lähtökohtana.

Monitavoiteoptimointitehtävän matemaattinen ratkaisu on Pareto-optimaalinen joukko. Suunnitteluavaruuden piste on Pareto-optimaalinen, jos mitään kriteeriä ei voida parantaa huonontamatta vähintään yhtä muuta kriteeriä [14]. Vastaavaa kriteeriavaruuden pistettä kutsutaan minimaaliseksi pisteeksi. Pisteen $\boldsymbol{z}$ sanotaan dominoivan pistettä $\boldsymbol{y}$, jos pisteen $\boldsymbol{z}$ kaikki kriteerit ovat parempia tai yhtä suuria kuin pisteellä $\boldsymbol{y}$, mutta kyseessä ei ole sama piste.

Optimoinnin konvergoitumista tarkastellaan kullakin iteraatiokierroksella minimaalisista pisteistä lasketuilla painotetuilla minmax-arvoilla

$$f_w^k = \min_{\boldsymbol{x}\in REP^k} \left(\max \left((1-w) \frac{I_{omin,\max} - I_{omin}(\boldsymbol{x})}{I_{omin,\max} - I_{omin,\min}}, w \frac{EOK(\boldsymbol{x}) - EOK_{\min}}{EOK_{\max} - EOK_{\min}} \right) \right), \tag{19}$$

missä $w \in [0,1]$ on painokerroin ja REP^k on minimaalisten pisteiden joukko iteraatiokierroksen k jälkeen. $EOK_{\min}$ ja $EOK_{\max}$ ovat optimoinnin jälkeen pienin ja suurin minimaaliseen joukkoon kuuluva EOK:n arvo. $I_{omin,\min}$ ja $I_{omin,\max}$ määritellään vastaavasti.

PSO- ja MOPSO-algoritmit

Parveilualgoritmi (Particle Swarm Optimization, PSO) on epälineaarisiin yksitavoiteoptimoinnin tehtäviin soveltuva heuristinen, populaatiopohjainen menetelmä. Algoritmi perustuu suunnitteluavaruuden pisteiden eli potentiaalisten ratkaisujen muodostamaan parveen, jonka yksilöiden lentoa ohjaa kaksi houkutinta; jokaisen yksilön henkilökohtaisesti löytämä paras ratkaisu sekä koko parven löytämä paras ratkaisu. [15] PSO voidaan laajentaa useamman kohdefunktion käsittelyyn muuttamalla yksilöiden houkuttimia. Ensimmäisessä MOPSO-algoritmissa (Multi-Objective PSO) [16] yksilöillä on kaksi houkutinta, koko parven löytämien Pareto-optimaalisten ratkaisujen varaston yksi ratkaisu $REP[h]$, sekä yksilön i itsensä löytämien ratkaisujen historiasta riippuva ratkaisu $PBESTS[i]$. Sijainnin $REP[h]$valinnassa painotetaan sellaisia suunnitteluavaruuden pisteitä joita vastaavat kriteeriavaruuden pisteet ovat harvassa. Houkuttimien avulla lasketaan kaavalla (20) iterointikierroksen $k+1$ haun suunta ja suuruus eli nopeusvektori $\boldsymbol{v}_{i,k+1}$ jokaiselle yksilölle i. Uudet sijainnit lasketaan kuten PSO:ssa lisäämällä edellisen kierroksen k sijainteihin $\boldsymbol{x}_{i,k}$ nopeusvektorit $\boldsymbol{v}_{i,k+1}$.

$$\begin{aligned} \boldsymbol{v}_{i,k+1} &= w\boldsymbol{v}_{i,k} + c_1 r_1\left(REP[h] - \boldsymbol{x}_{i,k}\right) + c_2 r_2\left(PBESTS[i] - \boldsymbol{x}_{i,k}\right), \\ \boldsymbol{x}_{i,k+1} &= \boldsymbol{x}_{i,k} + \boldsymbol{v}_{i,k+1}, \end{aligned} \tag{20}$$

missä w on inertiakerroin, c_1 ja c_2 ovat kognitiivinen ja sosiaalinen oppimiskerroin sekä $r_1, r_1 \in [0,1]$ ovat satunnaislukuja. Kriteerien arvojen määrittämisen jälkeen yksilöiden tuntemat parhaat sijainnit *PBESTS* ja Pareto-optimaalinen joukko *REP* päivitetään. *PBESTS* sisältää jokaista yksilöä i kohden yhden ratkaisun, joka päivitetään jos yksilön uusi sijainti dominoi vanhaa $PBESTS[i]$ arvoa. Jos kumpikaan ei dominoi toista, uusi $PBESTS[i]$ valitaan satunnaisesti uudesta ja vanhasta sijainnista.

Reyes-Sierra ja Coello Coello esittelevät katsauksessaan [17] tunnetuimmat MOPSO:n muunnokset. Minimaalisten ratkaisujen tasainen jakautuminen pyritään varmistamaan muun muassa adaptiivisilla inertiakertoimilla ja satunnaisnopeustermeillä sekä rajoittamalla Pareto-optimaalisten ratkaisujen varaston kokoa ja asettamalla kriteereitä varastosta pudottamiseen. Lisäksi voidaan käyttää relaksoitua dominanssin määritelmää, joka harventaa joukkoa, josta globaali houkutin valitaan. Parveen voidaan myös määritellä naapurustoja tai rakenteita, jotka voivat välittää tietoa parhaista sijainneista vain keskenään, millä yritetään estää liian nopea lokaaliin minimiin johtava konvergoituminen.

Oma MOPSO:n muunnos

Omassa MOPSO:n muunnoksessamme $REP[h]$ on yksilöä toiseksi lähin Pareto-optimaalinen suunnitteluavaruuden sijainti euklidisella normilla mitattuna. Alun perin jatkuvien ja diskreettien suunnittelumuuttujien arvoina käytetään niitä edustavien diskreettien arvojen indeksejä x_j. Etäisyyden laskennassa muuttujien arvot suhteutetaan niiden mahdollisten arvojen lukumäärään, jotta kaikki muuttujat olisivat mahdollisimman tasa-arvoisia etäisyyden laskennassa. Yksilön i etäisyys varaston REP alkioon h on siis

$$d_{i,h} = \sqrt{\sum_{j=1}^{N}\left[\frac{REP[h]_j - x_{i,j}}{x_j^u - 1}\right]^2}, \tag{21}$$

Kun $REP[h]$ on valittu, uudet nopeudet partikkeleille lasketaan kuten edellä, mutta ne pyöristetään lähimpään kokonaislukuun *NINT* -funktiolla, jotta ne voidaan tulkita diskretoitujen muuttujien indekseiksi.

$$\begin{aligned} \boldsymbol{v}_{i,k+1} = NINT(w\boldsymbol{v}_{i,k} + c_1 r_1(REP[h] - \boldsymbol{x}_{i,k}) + c_2 r_2(PBESTS[i] - \boldsymbol{x}_{i,k}) \\ + (\boldsymbol{r}_3 < p_r \boldsymbol{I}) * SIGN\left(\boldsymbol{r}_3 \frac{p_r}{2} - \boldsymbol{I}\right) * INT(c_3 \boldsymbol{x}^u * \boldsymbol{r}_3 + \boldsymbol{I})), \end{aligned} \tag{22}$$

Viimeinen termi on turbulenssi- eli satunnaisnopeustermi, jolla estetään ratkaisujen juuttuminen suunnitteluavaruuden reunalle, kun todellinen optimi on sitä lähellä. $\boldsymbol{r}_3$ on satunnaislukuja väliltä [0,1] sisältävä vektori, jolloin turbulenssitermi lisää erikseen jokaiseen nopeuskomponenttiin väliltä $[-c_3 x_j^u, c_3 x_j^u]$ satunnaisesti valitun luvun todennäköisyydellä p_r. Operaattorilla * tarkoitetaan vektoreiden kertolaskua alkioittain, ja vertailuoperaattori antaa tuloksen -1, kun ehto on tosi ja 0 kun se on epätosi. Optimoinnissa käytetään arvoja $c_1 = 2$, $c_2 = 2$, $c_3 = 0.1$ ja $p_r = 0.8$. Iteraatiokierroksen suurin sallittu nopeus määritellään indeksien avulla kaavalla

$$\boldsymbol{v}_{\max} = NINT(0{,}3(\boldsymbol{x}^u - \boldsymbol{I}) + \boldsymbol{I}), \tag{23}$$

missä $\boldsymbol{x}^u$ sisältää jokaisen muuttujan mahdollisten arvojen lukumäärät. Tällöin kaikki alun perin diskreetit muuttujat on mahdollista saavuttaa niiden lukumäärästä ja arvoista riippumatta. Inertiakerrointa w vähennetään dynaamisesti arvosta 1.4 arvoon 0.3, siten, että aina viiden iterointikierroksen jälkeen sen arvo kerrotaan 0.9:llä. Näin varmistetaan hakuavaruuden kattava haku alussa ja nopeampi konvergoituminen lopussa.

TULOKSET

Laskentamalli validoidaan testiajolla, jossa verrataan jauhimen simuloitua lämpötilajakaumaa kuvan 1 poikkileikkauksessa näkyvistä taso- ja kartio-osien TDC-antureilla (termoelementeillä) mitattuihin arvoihin. Kuvassa 3 on esitetty simuloinnin tuloksena saadut jauhimen lämpötila- ja tehojakaumat ja mitatut lämpötilan arvot.

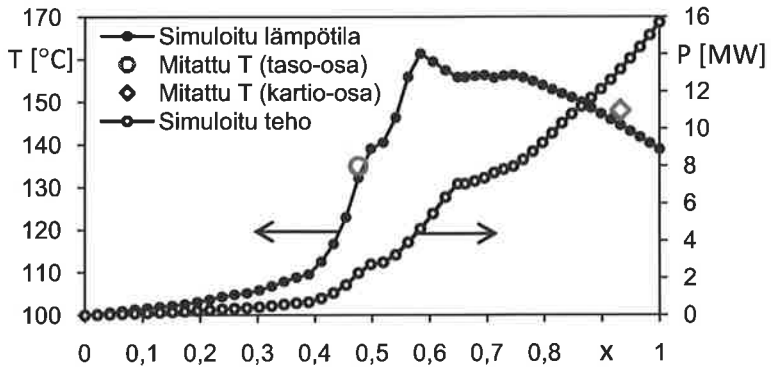

Kuva 3. Simuloidut ja mitatut lämpötila- ja tehojakaumat. x on dimensioton etäisyys sisääntulosta ulostuloon.

Lämpötila- ja tehojakauma seuraavat taso-osalla toisiaan. Jauhimen taso-osan alussa tehon tuotto on vähäistä, mutta se kääntyy nousuun jauhimen hampaiden määrän kasvaessa taso-osan ulkokehällä. Kun vettä ja höyryä esiintyy samanaikaisesti, on lämpötila paineen määräämä kyllästysläm-

pötila. Jauhimen kartio-osalla paine ja lämpötila laskevat höyryn kitkan aiheuttaman painehäviön takia, suuresta lämmöntuotosta huolimatta.

Optimointi suoritettiin omalla MOPSO-algoritmin muunnoksella. Kuvassa 4 on esitetty ajojen E1 ja E2 kaikki ratkaistut pisteet, optimaaliset pisteet ja lisäksi vertailujauhimen kriteerien arvot. Ajossa E1 populaation koko on 30 ja iteraatiokierrosten lukumäärä on 100, ajossa E2 ne ovat vastaavasti 40 ja 200.

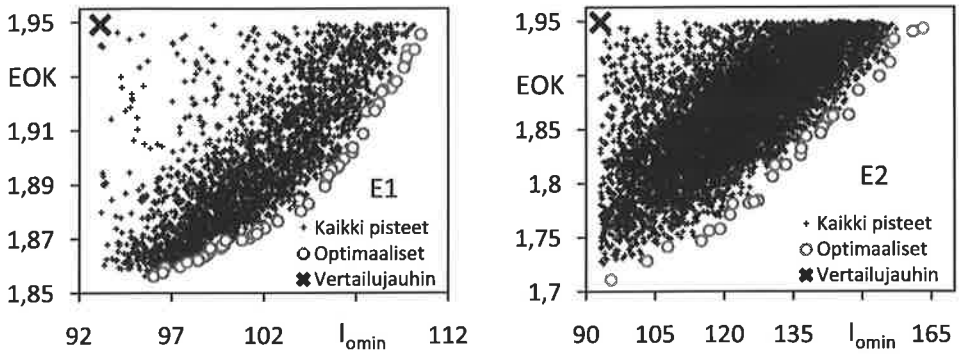

Kuva 4. Ajojen E1 ja E2 ratkaisut. EOK [MJ/kg] yritetään minimoida ja I_{omin} [kJ/kg/isku] maksimoida.

Kuvan 4 tuloksista nähdään, että kumpaakin jauhatuksen kriteeriä on mahdollista parantaa samanaikaisesti vertailujauhimeen nähden ja saavutetut optimaaliset pisteet ovat jakautuneet tasaisesti. Kuvassa 5a on esitetty kaavalla (19) laskettujen painotettujen minmax-arvojen kehitys ajossa E1. Sadan iterointikierroksen jälkeen optimoinnin jatkaminen ei enää tuota merkittävää parannusta vertailujauhimeen nähden, ja kaikki muutokset ovat simulointiohjelman tarkkuuden ulottumattomissa. Ajossa E2 konvergoituminen on huomattavasti hitaampaa johtuen suunnittelumuuttujien määrästä, ja painotetut minmax-arvot muuttuvat merkittävästi vielä 150 kierroksen kohdalla. Kuvaan 5b on vertailun vuoksi piirretty ajojen E1 ja E2 optimaaliset pisteet vierekkäin.

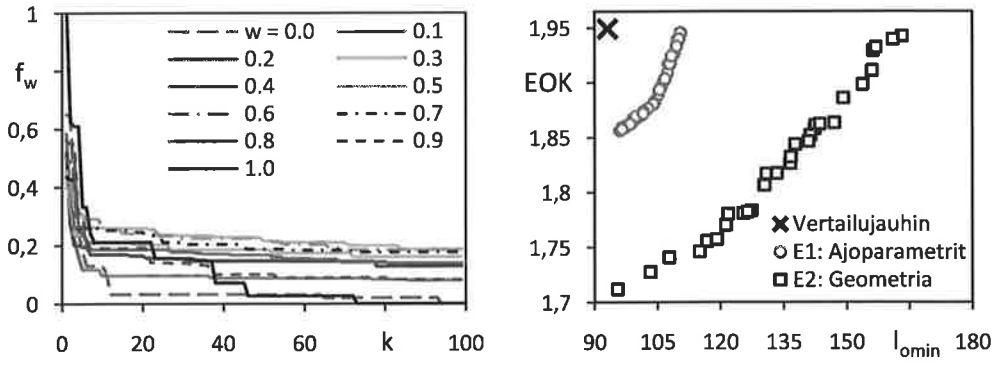

Kuva 5. a) Ajon E1 konvergoituminen. Painokertoimen arvo on annettu selitteessä. b) Ajojen E1 ja E2 optimaaliset pisteet, EOK [MJ/kg] yritetään minimoida ja I_{omin} [kJ/kg/isku] maksimoida.

Kuvasta 5b nähdään, että pidettäessä laatutaso samana, geometrian optimoinnilla voidaan saavuttaa yli kaksinkertainen *EOK* :n pudotus ajoparametrien optimointiin verrattuna.

Tämä tutkimus on jatkoa pitkälle kehitystyölle hierrejauhatuksen energiatehokkuuden parantamiseksi. Vuonna 1999 alkanut Joutsenon BCTMP-tehtaan energian ominaiskulutuksen lasku on esitetty kuvassa 6.

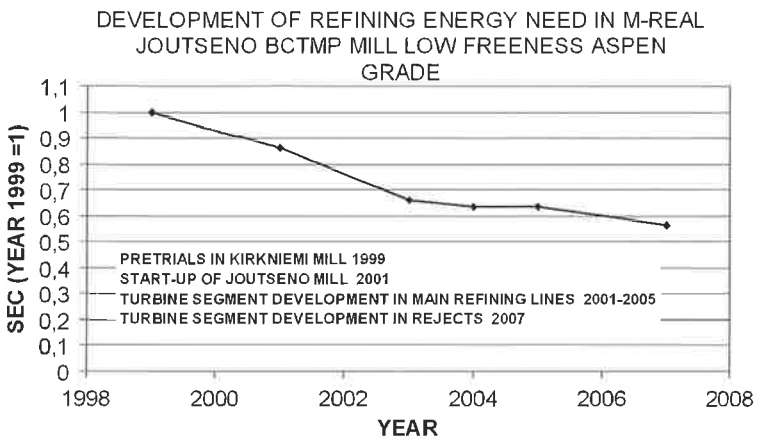

Kuva 6. Energiankulutuksen kehitys Joutsenon BCTMP-tehtaan linjalla. Kehitys on suhteutettu vuoden 1999 SEC :n eli EOK :n arvoon. [18]

Energian ominaiskulutus on jo pudonnut 40 % verrattuna vuoden 1999 tasoon. Työmme tulosten perusteella voidaan arvioida, että käyttämällä optimoituja segmenttejä, viimeisimmän kehitysvaiheen jauhimien energian ominaiskulutusta olisi mahdollista alentaa nykyisestä vielä noin 10 % laatutason pysyessä samana.

JOHTOPÄÄTÖKSET

Jauhimessa virtaavan suspension liikeyhtälö muodostetaan pyörivässä koordinaatistossa olevalle näennäisesti yksiulotteiselle kanavalle. Jauhimen tehonkulutus muodostuu terävälin kitkan voittamisen ja suspension pumppauksen vaatimasta tehosta ja tehokas jauhatuspinta-ala lasketaan paikallisesti yhden roottorin kierroksen keskiarvona. Jauhatuksen intensiteetti (energia/isku/aika) määrää lopputuotteen laadun. Simuloitu lämpötilajakauma vastaa hyvin tarkasti lämpötilamittausten arvoja lähellä segmenttien ulkokehää olevien TDC-anturien kohdalla.

Teollisuudessa käytössä olevan jauhimen ajoarvot, geometria ja tehokkuus asetettiin vertailukohdaksi optimointiin. Jauhatuksen tehokkuuden monitavoitteisessa optimoinnissa tavoiteltiin pientä tehonkulutusta tuotantomäärää kohti ja suurta Freeness-pudotusta, jota kuvattiin ominaisintensiteetillä. Omaa MOPSO-algoritmin muunnosta sovellettiin simulointiohjelmaan kahdessa eri esimerkissä. Tulosten mukaan jauhatuksen tehokkuutta voidaan parantaa samanaikaisesti kustannusten ja laadun suhteen. Geometrian muuttamisella voidaan saavuttaa suurempi parannus kumpaankin kriteeriin kuin säätämällä ajoarvoja. Löydetyistä minimaalisista pisteistä nähdään, että tämän hetken parhaiden jauhinten tehonkulutusta voidaan vähentää arviolta 10 % huonontamatta laatua. Jauhinprojektin aikana on jo saatu energian ominaiskulutus pienenemään 40 % (kuva 6).

KIITOKSET

Tekijät kiittävät Metso Paperia ja M-Realia rahoituksesta. Lisäksi kiitämme Petteri Vuoriota (Metso Paper Valkeakoski) yhteistyöstä ja Juhani Koskea TTY:n Teknillisen Mekaniikan ja Optimoinnin laitokselta työhön liittyvistä keskusteluista.

LÄHTEET

[1] J. Sundholm, Papermaking Science and Technology. Book 5: Mechanical Pulping, Fapet Oy, Helsinki, 1999.

[2] J.-P. Huhtanen, R. Karvinen, K. Vikman & P. Vuorio, Determination of Freeness Reduction by Refining Intensity Definition Based on Fluid Dynamical Model, Proceedings, IMPC 2009. Sundsvall, 2009.

[3] M. Lindstedt, J.-P. Huhtanen & R. Karvinen, Optimization of Pulp Refiner Performance. CD-Rom Proceedings, Papermaking Research Symposium 2009, Kuopio, 2009.

[4] J.-P. Huhtanen, Modeling of Fiber Suspension Flows in Refiner and Other Papermaking Processes by Combining Non-newtonian Fluid Dynamics and Turbulence, Väitöskirja, Tampereen Teknillinen Yliopisto, 2004.

[5] J. Hahtokari, Puukuitupohjaisen jauhatuksen laskentamallin verifiointi (Verification of the Calculation Model for Refining), Diplomityö, Tampereen Teknillinen yliopisto, 2004.

[6] H. Schlichting, Boundary-Layer Theory. McGraw-Hill Series in mechanical engineering, McGraw-Hill Book Company, New York, 1979.

[7] V. N. Constantinescu, Laminar Viscous Flow, Mechanical Engineering Series, Springer Verlag, New York, 1995.

[8] R. I. Tanner, Engineering Rheology, Oxford Engineering Science Series, 2. Painos, Oxford University Press Inc., New York, 2000.

[9] A. Jäsberg, Flow behaviour of fibre suspensions in straight pipes: new experimental techniques and multiphase modeling, Väitöskirja, Jyväskylän Yliopisto, 2007.

[10] D. Asendrych & G. Kondora, CFD Study of Refining Hydraulics, SIG 43 "Fibre Suspension Flows", 1st Workshop, Jyväskylä, 2009.

[11] C. Crowe, M. Sommerfeld & Y. Tsuji, Multiphase Flows with Droplets and Particles, CRC Press LLC, Boca Raton, 1998.

[12] G. W. Govier & K. Aziz, The Flow of Complex Mixtures in Pipes, Van Nostrand Reinhold Ltd, New York, 1972.

[13] S. Łazarkiewicz & A. T. Troskolański, Impeller Pumps, Pergamon Press Ltd, London, 1965.

[14] V. Pareto, Course d'economic politique, Lausanne, Rouge, 1896.

[15] Y. Shi & R. Eberhart, A modified particle swarm optimizer, IEEE World Congress on Computational Intelligence, Evolutionary Computation Proceedings, 69-73, 1998.

[16] C. A. C. Coello Coello & M. S. Lechuga, MOPSO: A Proposal for Multiple Objective Particle Swarm Optimization, Proceedings of the 2002 Congress on Evolutionary Computation, **2** Honolulu, 2002.

[17] M. Reyes-Sierra & C. A. Coello Coello, Multi-Objective Particle Swarm Optimizers: A Survey of the State-of-the-Art, International Journal of Computational Intelligence Research, **2**(3), 287-308, 2006.

[18] J.-P. Huhtanen, M. Koivikko & R. Karvinen, Means to Reduce Energy Consumption in Paper and Board Production, CD-Rom Proceedings, Papermaking Research Symposium 2009, Kuopio, 2009.

VISCOELASTIC ROLLING CONTACT MODEL FOR A PAPER MACHINE PRESS NIP

MIKA LAITINEN[1], PETTER HONKALAMPI[2]

[1] Corresponding author. Numerola Oy, Jyväskylä, Finland. E-mail: mika.laitinen@numerola.fi
[2] Metso Paper, Inc., Jyväskylä, Finland. E-mail: petter.honkalampi@metso.com

ABSTRACT

In a paper machine press nip the pressure pulse needed to squeeze water out of the paper web generates also shear stresses, energy dissipation and surface slippages which cause wear of the press fabrics, shoe press belts and press roll covers. To study the effect of different paper machine press nip configurations on wear, we model the press nip as a two dimensional rolling contact problem with viscoelastic fabrics, elastic roll covers and elastic belts. The frictions on contact surfaces are modelled by Coulomb law. The numerical problem is solved by finite element method.

1 INTRODUCTION

Press section is a part of the paper machine where water is removed from the paper and the structure of the paper is processed such that it is compatible in following processes of the paper making line, see Figures 1 and 2. Press section consists of rolling rolls and fabrics which are designed to deform the paper web at up to five pressing points.

The motivation to this study is to increase the understanding of the effects of pressing to the pressing fabrics, belts, roll covers and the paper web in the press nips at the press section of the paper machine. The press nip consists of the pair of the roll or the roll and the shoe which are compressed against to each other. There are also compressible media between the pressing surfaces, such as paper web, pressing fabrics (felts and belts) or roll covers. All these together with running conditions define the effect of the press nip to these media. It is known fact that the media in the press nips will wear, so they will compress and loose some of the thickness because of the viscoplasticity of the media. The media will also wear such that the amount of the material in will be lost and the strength properties will be decreased. This is an important characteristic to know in order to reach the best production efficiency.

Practice at the paper machine has been taught the fabric manufactures to make good enough fabrics and has been taught the paper makers the way to run the machine in order to maximize the lifetime of the fabrics and also the machine builders have learned the way to take into account the lifetime in machine designs. Nevertheless all these factors interacts to each other. However, even though this plays very important role in paper making, there are still only a few published reports or articles, and the problem has been mostly studied through aging tests, see [5], [4]. Hence, here we introduce the model that describes the impact of the pressing to the wearing phenomenon of the pressing media and will glance its application possibilities.

The press section of a paper machine has been modelled by several authors without taking into account shear forces or frictional surface contacts, see [8] for example. Tervonen [10] modelled a press nip as a frictional rolling contact problem with linearly viscoelastic rolls and parallel viscoelastic springs to model the sheet. Babat et al. [1] developed a nonlinear viscoelastic model for rubber-covered rolls. However, as far as the authors know, general nonlinear viscoelastic model for a press nip including shear forces and frictional contacts has not been reported before. The generality of our model allows us to study also shoe press nips, which are nowadays of importance in the paper machine industry. The modelling of a shoe press nip seems to be almost devoid of research.

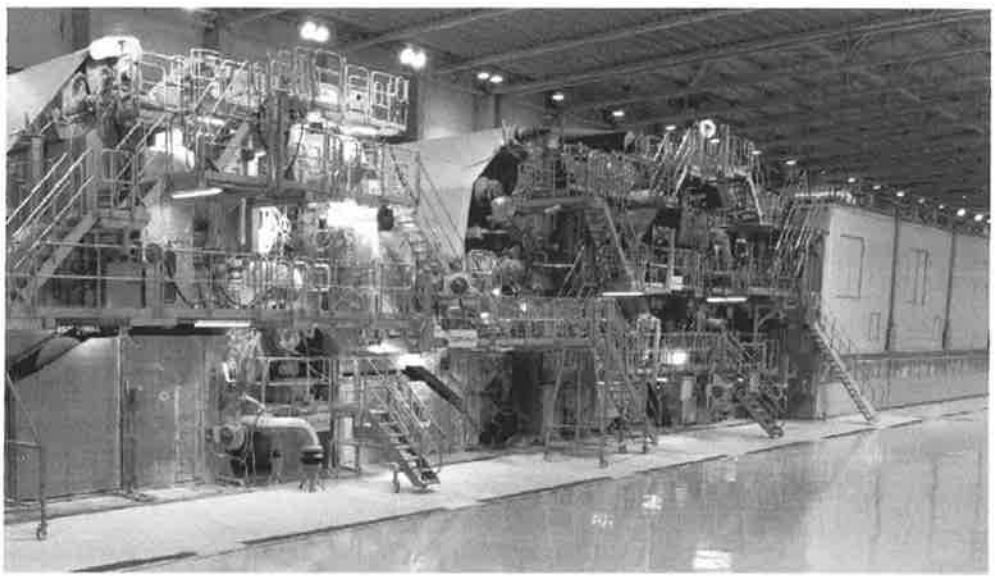

Figure 1: Paper machine.

2 MODEL OF A PRESS NIP

The sketch of a roll press nip is presented in Figure 3. We assume that the nip is driven by the lower roll while the upper roll revolves along with some power loss (P_0) due to rolling friction. The rolls are covered by a layer of deformable material. The rolls compress one or more fabrics and the paper web with a given linear load. Each fabric has a given tension and due to shear forces, the tension before the nip (T_i) is usually greater than the tension after the nip (T_o). Our model contains the following phenomena:

1. Viscoelastic large deformation model for the fabrics and the paper web.
2. Elastic large deformation model for the roll covers.
3. Frictional contact model for material interfaces.
4. Tension balance in the machine direction for each fabric.
5. Angular momentum balance for the roll with no drive.
6. Equation forcing the given linear load.

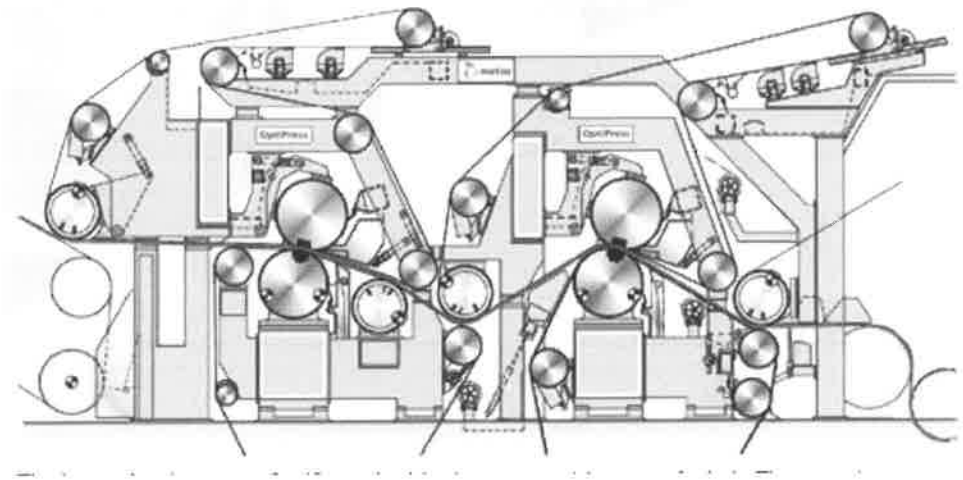

Figure 2: Press section of a paper machine.

Since we are interested mainly in stresses and strains in a press nip we ignore the effect of water flow and temperature effects and concentrate on mechanical aspects of a press nip. The large deformation models are needed since fabrics and the paper web can be compressed up to 50 %. Viscoelasticity is essential part of the model because it is clearly observed in the stress-strain measurements of fabrics (see [7]), and on the other hand, internal friction and wear of material is by nature related to viscoelastic energy dissipation. The viscoelasticity of the rolls could be also included in the model, but since temperature effects play an important role in the viscoelastic behavior of the rolls, we chose to use standard elastic model for the rolls. The surface wear of fabrics and roll covers is proportional to velocity differences of the surfaces which are taken into account by frictional contact models. The solution variables of this model are displacements in the fabrics, in the roll covers and in the paper web, viscoelastic strain in the fabrics, normal and tangential stresses at the material interfaces, average speeds of the fabrics, the rolls and the paper web as well as the relative position of the roll centers.

The input parameters of the model are material parameters of the fabrics, the roll covers and the paper web, friction coefficients of the material interfaces, tensions of the fabrics, roll radiuses, machine velocity, linear load and the the power loss of the roll with no drive.

2.1 Momentum balance

We assume that inertial effects in the momentum equations are negligible, so that the momentum balance equation within the fabric can be written as

$$\nabla \cdot \sigma = 0 \tag{1}$$

where σ is the stress tensor. First we introduce some notation typical for nonlinear solid mechanics, see [2], [6], [12]: We denote by $\mathbf{x}$ the coordinate in the deformed geometry while $\mathbf{X}$ stands for the coordinate in the undeformed reference geometry. $\mathbf{F} = \partial \mathbf{x}/\partial \mathbf{X}$ denotes the deformation gradient, $J = \det(\mathbf{F})$ and $\mathbf{C} = \mathbf{F}^T\mathbf{F}$ is the right Caychy-Green tensor. The constitutive law will be formulated in the reference geometry using the second Piola-Kirchoff tensor defined by

$$S = J\mathbf{F}^{-1}\sigma\mathbf{F}^{-T}, \tag{2}$$

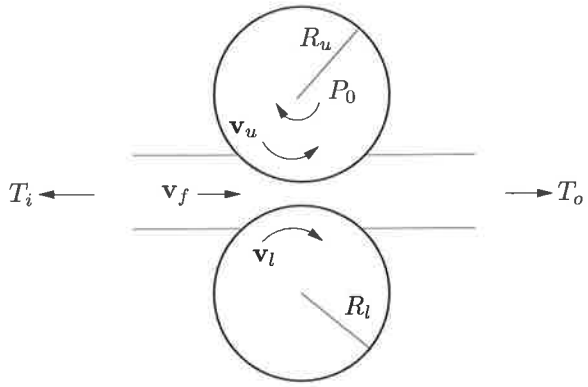

Figure 3: Roll press nip geometry.

To meet the compression, tension and shear measurements, we compose the second Piola-Kirchoff tensor S from five components

$$\mathbf{S} = \mathbf{S}_1 + \mathbf{S}_2 + \mathbf{S}_3 + \mathbf{S}_4 + \mathbf{S}_5 \tag{3}$$

where $\mathbf{S}_1$ describes the material response under compression, $\mathbf{S}_2$ hardens the fabric under tension and $\mathbf{S}_3$ hardens the material under higher shear strain. $\mathbf{S}_4$ is the standard elastic neo-Hookean term which couples the compression, tension and shear stresses. $\mathbf{S}_5$ accounts for viscoelastic behavior. In the next section we discuss how the tensors given below are fitted to measurements.

To describe these tensors in more detail, we denote by $\mathbf{a}_0$ the fabric fiber orientation vector (which in our case points to machine direction, $\mathbf{a}_0 = (1, 0, 0)$), by I_1 the first invariant $I_1 = \sum_i C_{ii}$ and by I_4 the fourth invariant $I_4 = \mathbf{a}_0 \cdot \mathbf{C}\mathbf{a}_0$. We choose

$$\mathbf{S}_1 = \frac{E_1 J}{s_0 - (1.0 - J)}\mathbf{C}^{-1}, \tag{4}$$

$$\mathbf{S}_2 = E_2\, I_4\, \mathbf{a}_0 \otimes \mathbf{a}_0, \tag{5}$$

$$\mathbf{S}_3 = E_3(I_1 - 3)\mathbf{I}, \tag{6}$$

$$\mathbf{S}_4 = E_4(\mathbf{I} - \mathbf{C}^{-1}) \tag{7}$$

$$\tag{8}$$

Here E_1, E_2, E_3, E_4 are elasticity coefficients and s_0 is a parameter describing the maximum compression of a fabric. The viscoelastic stress is modelled using internal viscoelastic variables and formalism of le Tallec [9]. We use a Kelvin type viscoelastic model which leads to stress

$$\mathbf{S}_5 = 2k_1\mathbf{A} - 2k_1 J^2\mathbf{C}^{-1}, \tag{9}$$

where k_1 is an elasticity coefficient and $\mathbf{A}$ is $\mathbf{A}$ is a viscoelastic tensor variable which is solved from equation

$$\nu\dot{\mathbf{A}}^{-1} - q\mathbf{A}^{-1} - k_1\mathbf{C} = 0, \tag{10}$$

$$\det \mathbf{A} = 1, \tag{11}$$

where $\dot{\mathbf{A}}^{-1}$ is the time derivative of $\mathbf{A}^{-1}$, q is a Lagrange multiplier (a variable to be solved) corresponding to the constraint $\det \mathbf{A} = 1$ and ν is the viscosity coefficient. Since momentum

balance is formulated using stationary equations, the time derivative consists merely of convective derivative

$$\dot{\mathbf{A}}^{-1} = \mathbf{V} \cdot \nabla \mathbf{A}^{-1}, \tag{12}$$

where V is the average fabric velocity.

In the rolls covers we use standard Neo-Hookean large deformation model

$$\mathbf{S} = \mu(\mathbf{I} - \mathbf{C}^{-1}) + \frac{\lambda}{2}(J^2 - 1)\mathbf{C}^{-1}, \tag{13}$$

where μ and λ are the Lamé coefficients of the roll cover.

2.2 Frictional Contact Model

Since we solve our model as frictional rolling contact problem, we need normal and tangential contact conditions on contact surfaces, see [11]. Denoting by g_N the normal gap between the surfaces and by σ_N the normal stress, the contact conditions read as

$$g_N \geq 0, \quad \sigma_N \leq 0, \quad g_N \sigma_N = 0. \tag{14}$$

so that $g_N = 0$ and $\sigma_N < 0$, when the surfaces are actually in contact. To define the tangential contact law, we denote by $\dot{\mathbf{g}}_T$ the relative velocity difference of the surfaces, by σ_T the tangential stress and by μ the sliding friction coefficient of the surfaces. Now, for tangential contacts we use Coulomb law

$$\text{if } \dot{\mathbf{g}}_T = 0 \quad \text{then } |\sigma_T| < \mu\,|\sigma_N|, \tag{15}$$

$$\text{if } \dot{\mathbf{g}}_T \neq 0 \quad \text{then } \sigma_T \mathbf{t} = -\mu\,|\sigma_N| \frac{\dot{\mathbf{g}}_T}{\|\dot{\mathbf{g}}_T\|}. \tag{16}$$

When computing the surface velocities $\mathbf{v}$ to obtain the relative velocity difference, one has to take into account the average velocity $\mathbf{V}$ as well as the velocity due to deformation

$$\mathbf{v}(x) = \mathbf{V} + \mathbf{V} \cdot \nabla \mathbf{u}(x). \tag{17}$$

where $\mathbf{u}$ is the displacement.

2.3 Constraint Equations

To complete our model we derive next constraint equations for linear load, tension balance and angular momentum balance. By definition of linear load, the integral of the normal stress σ_N over the compressed surface γ should be equal to the given linear load L

$$\int_\gamma \sigma_N \, ds = L. \tag{18}$$

For each fabric we have the force balance in the machine direction (see [10])

$$T_i = \int_{\gamma_u} \sigma_T \, ds + \int_{\gamma_l} \sigma_T \, ds + T_o \tag{19}$$

where T_i, T_o are the given fabric tensions before and after the nip respectively, and γ_u, γ_l are the upper and lower surfaces of the fabric. On the upper roll which has no drive, we have the balance of the angular momentum (see [10])

$$P_0 = v_u \int_{\gamma_u} \sigma_T \, ds - \frac{v_u}{R_u} \int_{\gamma_u} \sigma_N \, x_1 \, ds \tag{20}$$

where P_0 is the power loss due to rolling friction and v_u, R_u are the speed and the radius of the upper roll, respectively. On the lower roll which has a drive we do not need to enforce the angular momentum balance, since we can simply set the roll speed to machine speed.

3 MEASUREMENTS

The coefficients of the constitutive laws (4)–(7) were fitted to compression and shear force measurements. Fitting to tensile measurements is planned in near future. The static compression measurements were performed at the Department of Physics in the University of Jyväskylä. Dynamic shear force measurements were performed by Hakala et al. at the Institute of Fibre Materials Science at the Tampere University of Technology, see [3]. Applicable shear force measurement technique for fabrics were not found from literature and hence new measurement technique had to be developed. The measurement were done using Testometric 500 device and standards SFS-EN 12090 and SFS-ISO 1922.

Figure 4 shows a typical stress-strain behavior for a fabric under shear stress. The constitutive laws (4)–(7) were fitted to measurements by simulating numerically the measurements and optimizing the form and the coefficients of the constitutive laws by hand. The topmost stress-strain curve was ignored from the fit since it is apparently caused by straightening of the yarns within the fabric in the beginning of the measurement and thus irrelevant to the modelling of a tensioned fabric. These curves highlight very well the nonlinear viscoelastic nature of the fabrics.

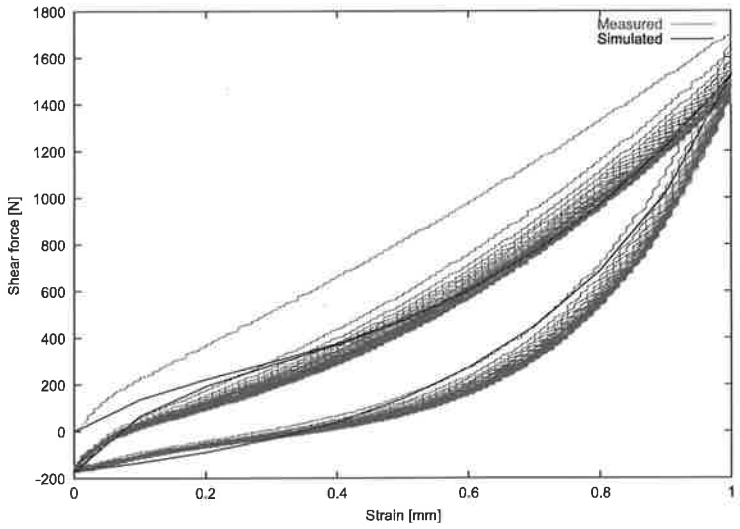

Figure 4: Stress-strain curves for fabric under shear stress.

4 SIMULATED TEST CASE

To illustrate the use of model, we simulated a roll nip with a linear load 130 kN/m. The both rolls have diameter of 1 m and the roll covers are hard (steel). The pressed media between rolls consists of one fabric, the paper web is ignored. The bottom roll has a drive with speed 1200 m/min and the upper roll revolves along with no rolling friction power losses. As typical for roll nips, the fabric tension is set to 30 % higher value before the nip compared to the tension after the nip. The

model was implemented using finite element method and Numerrin software package developed at Numerola Oy. In the following figures, the rolling direction is from left to right.

Figure 5 shows the deformation of the fabric in the press nip. Bottom side of the fabric is stretched because the driven roll is located on the bottom side and the loading force between the rolls will compress the fabric (normal stress).

Figure 5: Displacements in the fabric. The fabric thickness and displacements are magnified for illustrative purposes.

Figure 6 shows the normal stress (also called a nip pressure) on fabric surfaces. It depends on the loading force between top and bottom surface (rolls), geometry of pressing area (roll diameter or shoe press geometry), and compressible properties of materials (felts, fabrics, and covers) with rheological behavior of compressible media.

Figure 7 shows the tangential stress which describes the surface frictions determined by Coulomb law (15)-(16). The tangent direction is chosen here as the rolling direction, pointing to the right. On the bottom side, in the beginning of the nip, the fabric adheres relatively quickly to the roll. However, at the end part of a nip the friction force on the bottom side starts to increase (tangential stress decreases) and finally the bottom roll slides on the surface of the fabric. At that point the speed of the fabric is lower that roll and the elongation of the fabric starts to decrease. The sliding continues until normal stress goes to zero and the fabric separates from the roll. On the top side the fabric will settle on the roll already in the beginning because the speed of the fabric is higher compared to the roll and the fabric keeps its contact on the roll through the nip.

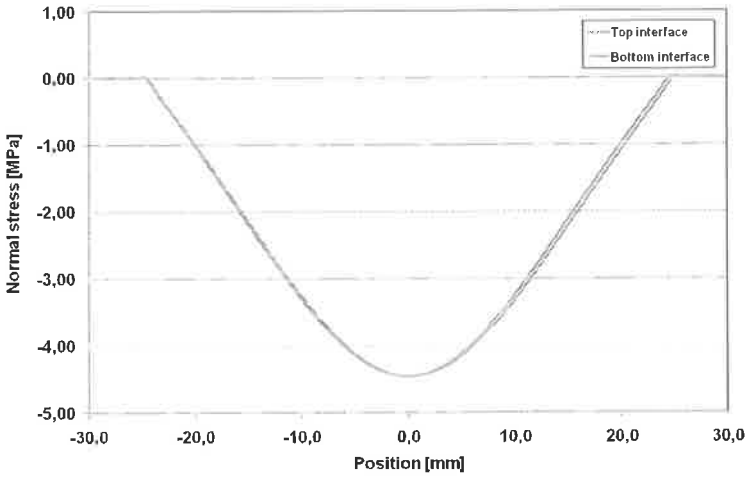

Figure 6: Normal stresses on top and bottom surfaces of the fabric.

Figure 8 shows the relative stretch of the fabric surfaces. The relative stretch is defined as a length in

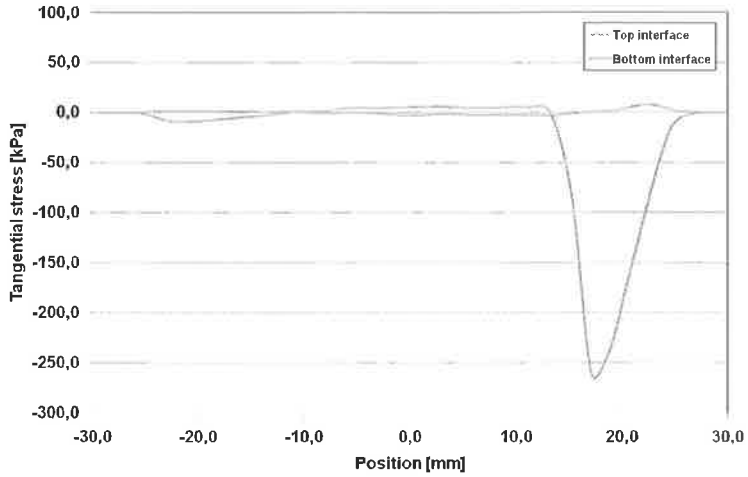

Figure 7: Tangential stresses on surfaces of the fabric.

proportion to length at the tension before nip. The driven roll on the bottom side creates a stretching-shrinking phenomenon. On bottom side the stretching will increase as long as the friction will keep the fabric on contact to roll. At the end part of the nip the fabric starts to slide and shrink. On top surface, the stretch will decrease all the time because top roll will move slowly compared to bottom roll. The final stretch depends on boundary conditions like tensions before and after the nip. In this example the tension before press nip is higher compared to tension after the nip. In this case the maximum stretch is about 0.7 % and shrinking about -1.0 % which are rather significant values especially considering that this happens within 0.5 ms.

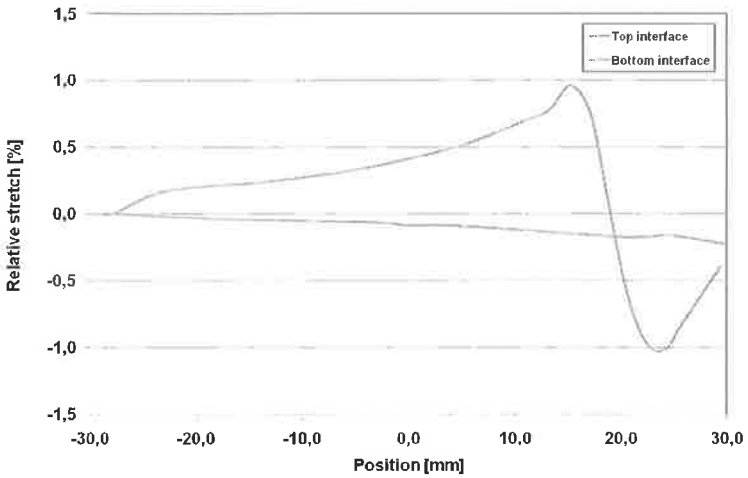

Figure 8: Relative stretch of the fabric surfaces.

The surface speeds in Figure 9 are determined by the driven bottom roll. When computing these speeds, the effect of surface deformations are taken into account, see (17). Since deformations are taken into account the stretching and shrinking of the surfaces due to tension differences give

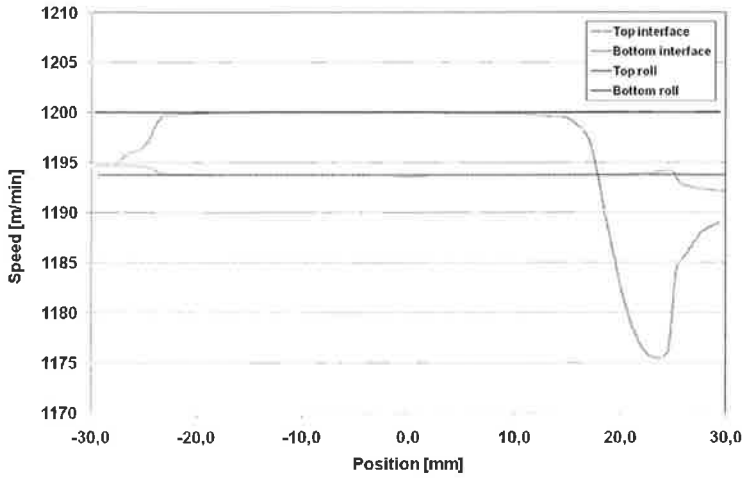

Figure 9: Speed at the fabric and roll surfaces.

the fabric surfaces speeds differing from the constant mean velocity. On a point where tangential stress at bottom surface goes to negative, the speed of the bottom surface start to decrease which means that the friction force between the fabric and roll increases to its maximum value. The speed differences of the contact surfaces are surely important when monitoring the wear of the surfaces.

The figure 10 shows the internal viscoelastic energy dissipation within the fabric. The viscous energy loss is the biggest at the point where the shrinking reaches the maximum value (cf. Figure 8). Since internal friction within the fabric is related to viscous energy dissipation, this term can illustrate the effect of the press nip to the wearing of medium.

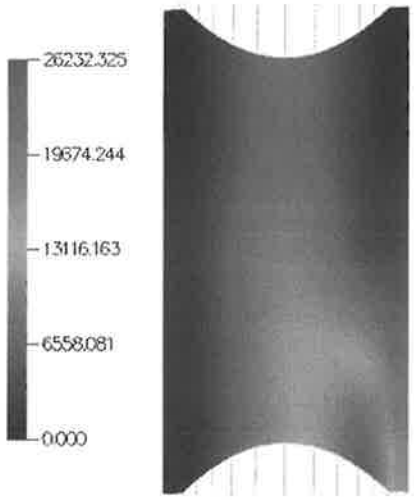

Figure 10: Viscoelastic energy dissipation within the fabric (in Joules).

The shear stress in figure 11 has the biggest effect on the driven roll side where also the deformation of the fabric has the biggest variation (see figure 8). On the topside the fabric will shrink through

the nip which means that at the end the shear stress reach the maximum value. On the bottom of the fabric the shear stress increases while the fabric is stretching. When the fabric starts to slide and shrink the shear force changes from positive to negative.

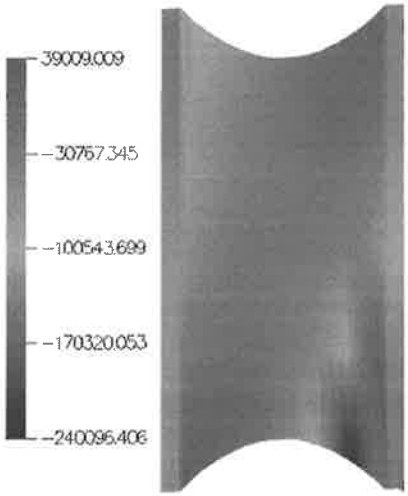

Figure 11: Shear stress within the fabric (in Pascals).

5 CONCLUSIONS

Here, we introduced the viscoelastic pressing model to study the pressing phenomena at the press section of the paper machine. The focus was to find out factors related to the wearing of the fabrics by using the viscoelastic model including also shear forces and frictional surface contacts. We found out that pressing causes the internal stress and deformation to fabric in normal and tangential directions but also friction forces in roll contacts. The model can be applied to press section design such that the performance of the fabrics and covers, by means of lifetime, can be optimized to specific press. Naturally, it also enables possibilities to develop new characteristics to fabrics and covers to reach better performance over the lifetime at the press section.

REFERENCES

[1] Bapat, C.N., Batra, R.C.: Finite plane strain deformations of nonlinear viscoelastic rubber-covered rolls. Int. J. for numerical methods in engineering **20**, 1911–1927 (1984)

[2] Bonet, J., Wood, R.: Nonlinear Continuum Mechanics for Finite Element Analysis, 2nd edn. Cambridge University Press (2008)

[3] Hakala, T., Harlin, A.: A case study of the out-of-plane shear strength measurement of paper machine clothing. Submitted to Textile Research Journal

[4] Hakala, T., Harlin, A.: Simulation of a rapid nip pressure strike and its effect on press felt samples. AUTEX Research Journal **8**(3), 84–91 (2008)

[5] Hakala, T., Wilenius, T., Harlin, A.: Laboratory ageing test device for press-felt clothes of paper machine. AUTEX Research Journal **7**(1), 70–79 (2007)

[6] Holzapfel, G.: Nonlinear solid mechanics: a Continuum Approach for Engineering. Wiley (2000)

[7] HU, J.: Structure and Mechanics of Woven fabrics. Woodhead Publishing – CRC Press (2004)

[8] Kataja, M., Hiltunen, K., Timonen, J.: Flow of water and air in a compressible porous medium. a model of wet pressing of paper. J. Phys. D: Appl. Phys **25**, 1053–1063 (1992)

[9] le Tallec, P.: Numerical Methods for Nonlinear Three-dimensional Elasticity. North Holland (1994)

[10] Tervonen, M.: Numerical models for plane viscoelastic rolling contact of covered cylinders and a deforming sheet. Ph.D. thesis, University of Oulu (1997)

[11] Wriggers, P.: Computational Contact Mechanics. Springer-Verlag (2006)

[12] Zienkiewicz, O., Taylor, R.: The Finite Element Method. Butterworth-Heinemann (2000)

PHOTOPLETHYSMOGRAPHIC TECHNIQUES FOR ARTERIAL STIFFNESS MEASUREMENTS AND PULSE WAVE DECOMPOSITIONS WITH MEANS OF A PHYSICAL MODEL

MATTI HUOTARI

Department of Electrical and Information Engineering

Microelectronics and Materials Physics Laboratories, UNIVERSITY OF OULU, POBox 4500, FIN-90014 OULU UNIVERSITY, FINLAND, email matti.huotari@ee.oulu.fi

ABSTRACT

Photoplethysmography (PPG) is an optoelectronic technique and when combined with pulse wave analysis it becomes an information-rich and non-invasive diagnosis method. In pulse wave analysis, PPG is widely used to calculate arterial stiffness. However, its clinical experience is not developed. The main aim of this study is an easy-to-use point-of-care device for arterial stiffness measurement and analysis for early diagnosis and periodic monitoring of the patient's arterial stiffness. A core component of the measurement system is a noiseless optoelectronic amplifier with the finger and toe tip sensors, and ECG and PCG (phonocardiography) measurement devices for the corresponding signal capture. The PPG device captures the arterial pulse waves, the ECG device the ECG, and the PCG device the phonocardiogram simultaneously for the off-line analysis. The analysis device is capable of seamlessly analysis the all signals for the calculations of cross-, auto-, and coherence spectra for qualification and classification of the measured signals. The further pulse wave analysis is done by a PC based software which produces the separated primary waves. Using the same software it is possible to calculate the second derivative of the PPG recording called SDPPG. The pulse wave components clearly show the characteristics of the young and elderly persons. The pulse wave analysis works very well on the data of the young subjects, and the SDPPG on the data of the older subjects. The method could be hopefully applied to diagnosis purposes of arterial stiffness.

1. Introduction

For this research a new constructed biomedical device was developed which can record pulse waveforms by a photonic sensor from finger and toe, and with a physics-based model we mathematically decompose the PPG waveforms into their four primaries. Based on these divided pulse waves is possible to estimate vessel elasticity which is called ***arterial stiffness***. The pulse wave decomposition produces four primary waveforms which are named according to physical basis in the pulse wave analysis.

Pulse wave analysis

In order to explore a potential mechanism by which arterial stiffness influences on arterial walls, especially causing hypertension, pulse wave analysis can be undertaken in healthy persons. Arterial stiffness is manifest as an increase in pulse wave velocity (PWV) and also in pulse

waveform, which can be measured non-invasively by an optoelectronic device for the determination of pulse wave velocity in the finger and toe arteries, namely radial arteries. The original arterial pulse wave is generated by left ventricular ejection. It later adds with waves travelling along arterial tree and a reflected wave from the periphery. As arterial stiffness increases, transmission velocity of the both waves increase, resulting in the reflected wave arriving earlier in the central aorta and causing higher pressure during the cardiac cycle. PPG measurement recording takes typically 5 min. In pulse wave analysis (PWA) measurements are typically taken in a quiet temperature controlled room (22 C) using the arterial stiffness measurement system after a period of at least 5 min of rest. Persons are fasted overnight and are asked to refrain from smoking or drinking caffeine containing drinks. In analysis, acceptable pulse waves are checked by visual inspection for including in the analysis.

As we have seen PWV is a measure of regional arterial stiffness of the arterial tree between the two measurement sites. This parameter is related to the elastic modulus (E) of the arterial wall. It represents the intrinsic stiffness of the arterial wall. Thickness h and radius r represent the arterial geometry with momentum transfer caused by blood density (ρ). During the end of the 19th century, Moens and Korteweg derived a relationship (1) for that as follows

$$PWV = \sqrt{\frac{E \cdot h}{2 \cdot r \cdot \rho}} \tag{1}$$

Bramwell and Hill applied the Moens-Korteweg equation to arterial physiology and described the relationship (2) in terms of relative change in volume (ΔV/V) and pressure (ΔP) during ex vivo experiments:

$$PWV^2 = \frac{\Delta PV}{\Delta V \rho} \tag{2}$$

It is to be noticed that PWV is a direct measurement of arterial stiffness since it is the square value of 1/distensibility. Distensibility reflects the extent of developed arteriosclerosis and also vascular tone mediated by vasomotor nerves. In this aspect, it differentiates itself from indirect methods not considered here. The assessment of PWV involves measurement of two quantities: transit time of the arterial pulse along the analyzed arterial segment and distance on the skin between both recording sites, or decomposing the pulse wave into primary waves and calculating the time differences between the waves.

In PWV measurements four devices are leading the market. One of the arterial measurement devices is the Complior System (Artech, Les Lilas, France), which allows to simultaneously record both the arterial wave pulses through mechanotransducer probes and the other is the SphygmoCor system (ArtCor, Sydney, Australia) that has been used in large clinical trials and population survey in Europe. This device uses a large band piezoelectric probe and allows the arterial pulse recording in succession (carotid then femoral), both signals being synchronized with the same time basis (ECG R wave) which impose to accurately check. The most recent device is the PulsePen device (Diatecne, Milano, Italy) which uses the successive recordings of arterial pulse waves with the ECG as a time basis. Each instrument is already in clinical use.

Although the PWV measurements provided by the techniques which are correlated with gold standard techniques, they remain proxies for the most direct measures of arterial stiffness. A Japanese device (Omron, Japan) based on the brachiale-ankle pulse wave velocity (baPWV). It is based on oscillometric pressure in cuff placed on the brachial artery and calf, the time delay

between both signals is determined. This approach contains uncertainties about path, it includes highly heterogeneous length such as the aorta, lower and upper peripheral circulation. In Arteriograph device (TensionMed, Hungary), the measurement is based on the enhancement of the reflected wave signal on oscillometric tracings, during suprasystolic cuff occlusion. Based on assumptions about wave travel path, it is possible to derive pulse wave velocity from single spot cuff measurements. However, no optoelectronic system yet measures PWV in the market.

After the measurements, the original wave analysis is done in a digital signal analyzer either in the time domain: to calculate auto- and cross correlations, or in the frequency domain: to calculate auto-, and cross spectra and coherence function to be sure of the signal quality. In the further time domain analysis, each single pulse wave is analyzed by PC software as follows. The analysis software is capable of seamlessly analysis the all signals for the calculations of selected equation or combination of equations for classification and qualification of the measured signals. Then we used the PC based software which produces the separated primary waves. These primary waves have the sound physical bases for calculation of the pulse wave characteristics. The pulse wave can become aware of momentum transfer, because no mass or concentration can travel so fast as pulse wave.

In the all living objects, the blood circulatory system (BCS) is a pipeline, a vascular network, with descending arterial diameters from the aorta, arteries, arterioles, and to the capillaries being the smallest. These small organs are measured with photoplethysmographic (PPG) technique. However, this technique gives rise different questions to be answered. While PPG waveform closely resembles the volume flow, PPG does not measure the pressure or flow itself, but the momentum transfer experienced by the blood and arterial walls. In the young BCS, the pulse wave travels slower velocity then in the elderly. In every case, BCS serve the purpose of supplying all parts of tissue during the aging period with blood at physiologically necessary ranges of pressures and flows. The pulse wave propagation is one of the important features of hemodynamic models of the BCS. The purpose of this study is, if it is possible to measure and apply the multi-lognormal mathematical model for determination of ***arterial stiffness.***

2. Instrumentation and methodical procedure

A new photoplethysmographic (PPG) device was developed which is applied to find an effective reproduction of the PPG waves. The pulse waves can be measured by PPG device in the radial artery, in the index finger and the second toe by applying both red LED or IR LED lights. The developed instrument is based on the phase sensitive detection (PSD) used as measurement principle. The PSD method allows simultaneous real time measurement of a object by one or more different optical wavelengths. In this instrument two different wavelengths 660 nm (red) and 940 nm (near infrared) are used. The PSD method is noise immune detection method which allows using a low power light sources by efficiently optimizing the signal to noise ratio. An optical component of this kind is a light emitting diode (LED), which is a low cost, small size and due to low power absolutely safe for the human eye. The system consists of two optical measurement heads, an electronics unit and a laptop computer which collects measurement results and later analyzes them. Each of two optical measurement heads one installed on a finger and second on a toe in the actual measurement setup. The measurement head consists of two LEDs and one large area semiconductor photo detector which efficiently collects light emitted by the LEDs through finger or toe tips. The measurement heads are connected to the electronic unit by means of wires. The electronic unit contains electronics for driving the LEDs, two preamplifiers for signals from the photodiodes, four PSD channels for two wavelengths from the finger and toe, an A/D-converter for digitizing the signals and an USB-interface to transfer the digitized results to the laptop computer.

In the analysis, each pulse wave is solved by separating its content into multi-lognormal functions. These waveforms are compared visually to the original wave by the residual error curve in addition to chi-square variable as goodness of fit. The multi-lognormal functions have their basis on vascular network with many asymmetric double-branching at each bifurcating point that gives rise to an asymptotic lognormal flow distribution. In addition to this, the capillary lengths have lognormal distribution [1]. These properties give us the opportunity to determine whether the peaks and the areas which are determined by the arterial PPG pulse waves, that they have lognormal distribution. In pulse wave dynamics, constructive and deconstructive pulse wave reflections are important to take an account. The pulse wave is composed by either constructive or deconstructive wave interaction depending on arterial wall elasticity.

In the young persons, the radial artery wave is easy to analyze, whereas in the elderly persons, it is very difficult to be analyzed completely satisfactory. We were educated with pulse wave analysis of the young persons. When studying wave reflections, it is possible to decompose the measured PPG waveform into the percussion wave, which is during the beginning of systole caused by ejection of blood from the left ventricle. The four reflected components are the tidal wave, which is during the late systole caused by the returning pulse wave from upper body, the dichrotic wave which is during the beginning of diastole caused by closure of the aortic valve, and the peripheral reflection wave is at the end of diastole and the pulse wave caused by the pulse which is reflected from lower body. For fully characterizing the time and real nature of wave reflection and also allowing accurate determination of the time of arrival of the reflected waves we firstly educated ourselves by a trial and error procedure both in the frequency and time domain. We selected the time domain analysis which can be done with means of general optimization principles. This technique has its pros and cons, but the final fitting result based on the residual error is a very good method. All of the fitted pulse waves were checked to guarantee a reasonable good fit based on inspection to the residual error curve. There have been also other attempts at obtaining stiffness indices from waveform analysis of single peripheral pulse wave [2], [3].

In the BCS, the arterial pulse wave reflection depends on the arterial wall stiffness. For example, it is also amplified in young persons, if their vessel walls are harder than normal, which indicates early global pathology in the BCS and it could be detected by PPG technique. In elderly persons, their arterial walls are harder because of aging process which has very obvious effects on the arterial waveforms at different locations of the BCS. This is easy to determine by PPG method. If their arterial walls are harder than normal age-matched persons, the persons need closer medical inspection focused into their arterial system. Namely, with advancing age, arterial stiffness and wave reflections increase causing higher blood pressure, both systolic and pulse pressures. That's why arterial stiffness could be the primary measurement goal than the higher blood pressure before causing hypertension.

PPG waveforms were recorded from volunteer subjects in the morning before no coffee intake. Each measurement took for about five minutes from which sequential 10 to 20 pulse waves were selected. The optimization algorithm is implemented in Origin 7.5 (OriginLab). To decompose PPG waves into the individual physiological components, waveform analysis for decomposition can be adopted. The use of waveform decomposition techniques can also enhance the baseline restoration, in particular the artifact introduced by the fluctuation in the finger or toe with the PPG sensor. One potential technique for waveform decomposition is Levenberg-Marquardt optimization algorithm (LMO) for non-linear fitting. Preliminary trial of the LMO technique is performed on a PPG data recorded from the elderly and young subjects in supine position.

3. Results and discussion

In Figures 1 a there is pictured the measurement setup and in Figure 1 b the PPG waves, ECG, and phonocardiogram (PCG). The two PPGs are for finger with its P, T, and D (PPG1wave) and for toe (PPG2), the ECG amplifier records the corresponding ECG with its P,Q, R, S, and T wave, the PCG with its P1 and P2 sounds is recorded by a stethoscope microphone all of which were connected to the labtop. In the Figure 2a it is shown the actual PPG record and in the Figure 2b it is baseline removed and absolute value taken. In the Figures 2c and d we can see two PPG pulse waves analyzed from the Figure 2b. The black line is the measured PPG wave, the green is the percussion, the blue is the tidal, the magneta is the dichrotic, and the navy is the peripheral reflections wave.

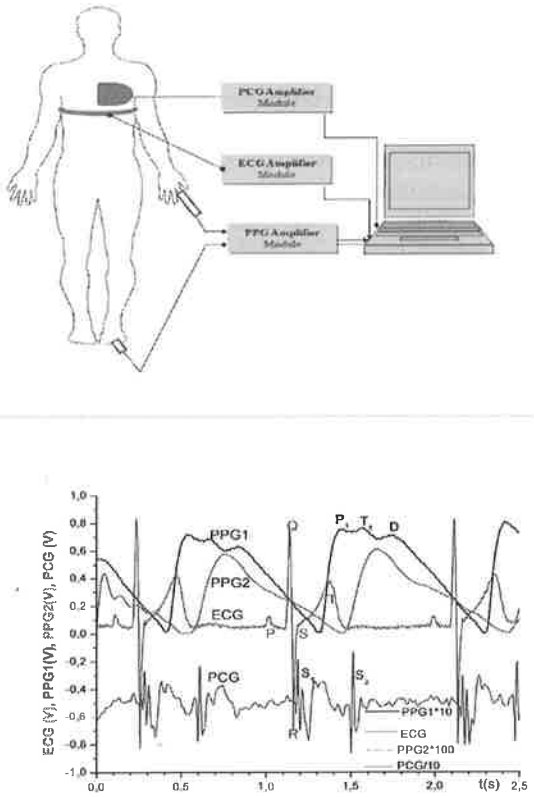

Figure 1a) The measurement setup (up), the PPG waves from the finger and toe, ECG, and phonocardiogram (PCG) with their characteristic letters (low).

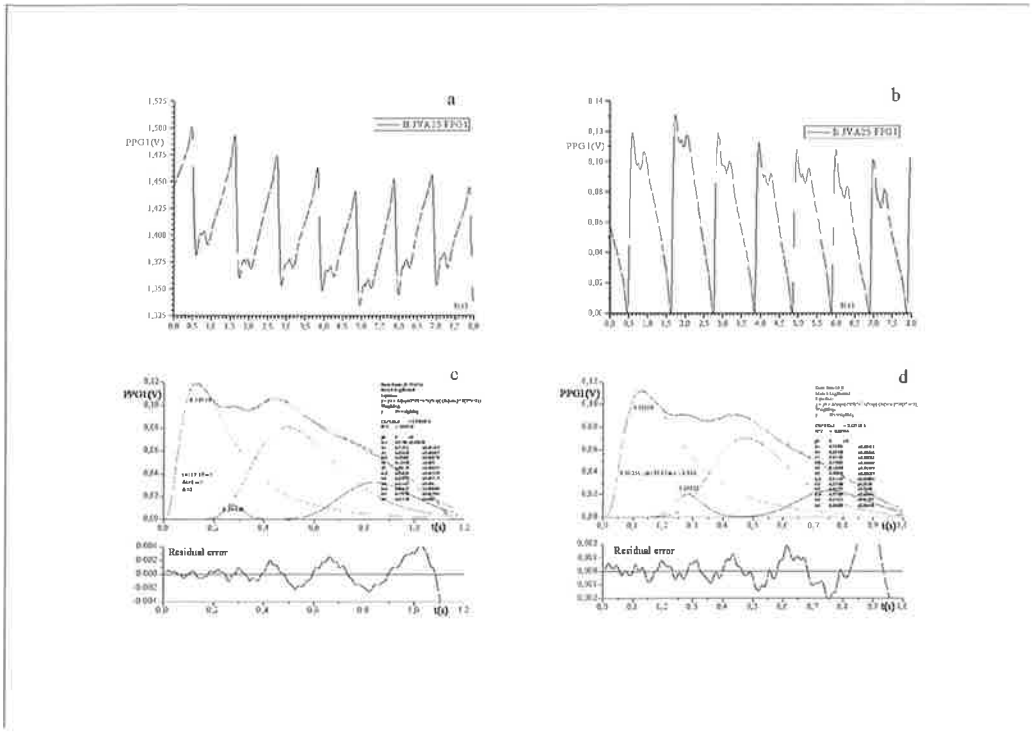

Figure 2 a) The actual PPG record, b) PPG with the baseline removed and absolute value taken, c) and d) two pulse waves analyzed from the Figure 2b. The black line is the measured PPG wave, the green is the percussion, the blue is the tidal, the magneta is the dichrotic, and the navy is the peripheral reflections wave.

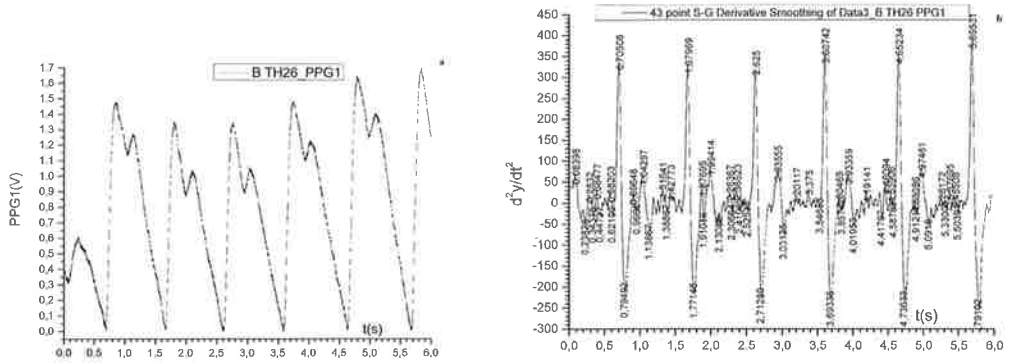

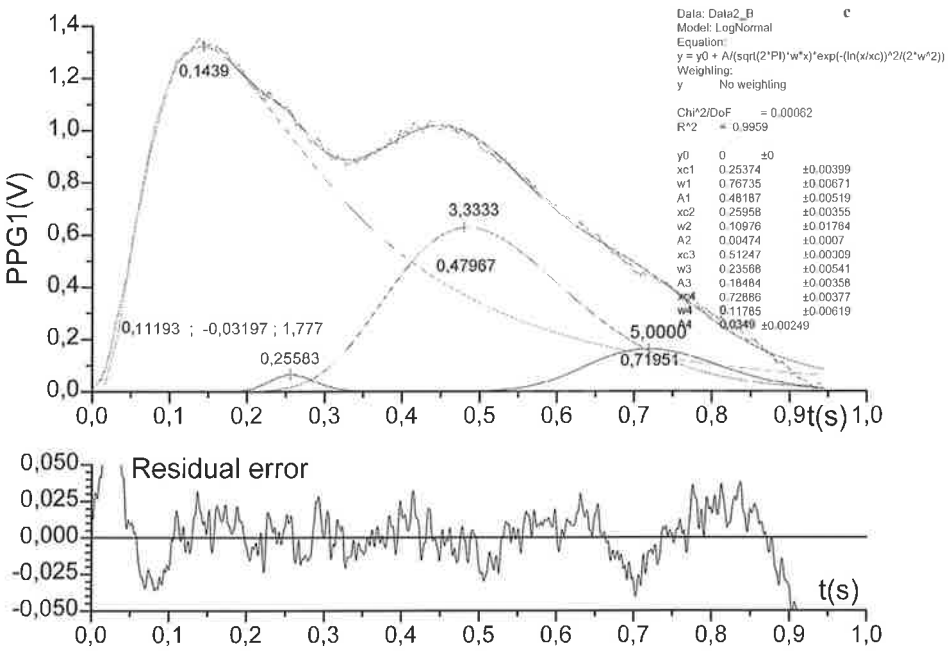

Figure 3 a) An other PPG with the baseline removed and absolute value taken, b) the corresponding SDPPG with the characteristic values marked, and c) the first pulse wave of (a) analyzed. The black line is the measured PPG wave, the green is the percussion, the blue is the tidal, the magneta is the dichrotic, and the navy is the peripheral reflections wave.

In the young subjects, e.g., radial wave is easy for analysis purposes, whereas in the elderly, it is very difficult to be analyzed completely by the LMO. When studying wave reflections, it is possible to decompose the measured PPG waveform into the percussion wave and the four reflected components, e.g., the tidal wave, the dichrotic wave, the peripheral reflection wave, and sometimes the pre-ejection wave. For fully characterizing the time and real nature of wave reflection and also allowing accurate determination of the time of arrival of the reflected waves we realized a trial and error procedure at first. This analysis can be done in the time domain using the principle of general optimization procedures. This technique has its pros and cons, but the final fitting result based on the residual error is a very good method. However, it is supported by the SDPPG method.

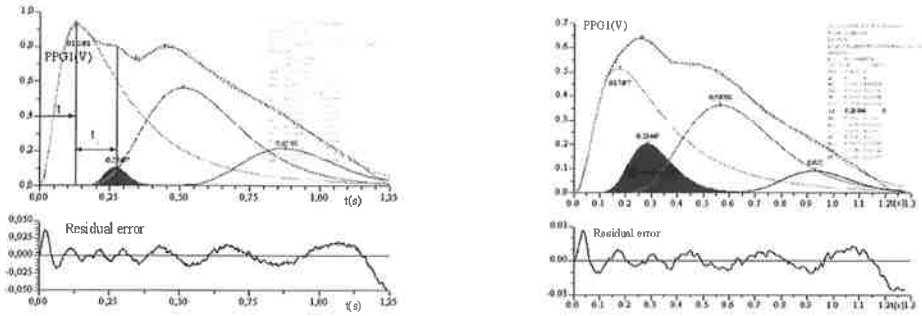

Figure 3 The analyzed PPG of a young person (38 y, left) and pulse wave times marked by the arrows. On the right side, the analyzed PPG of an elderly person (58 y). The tidal wave marked.

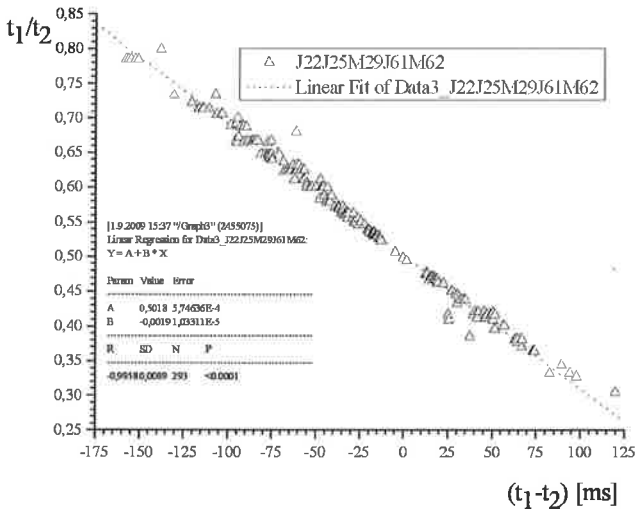

Figure 4 Values t_1/t_2 as a function of t_1-t_2.

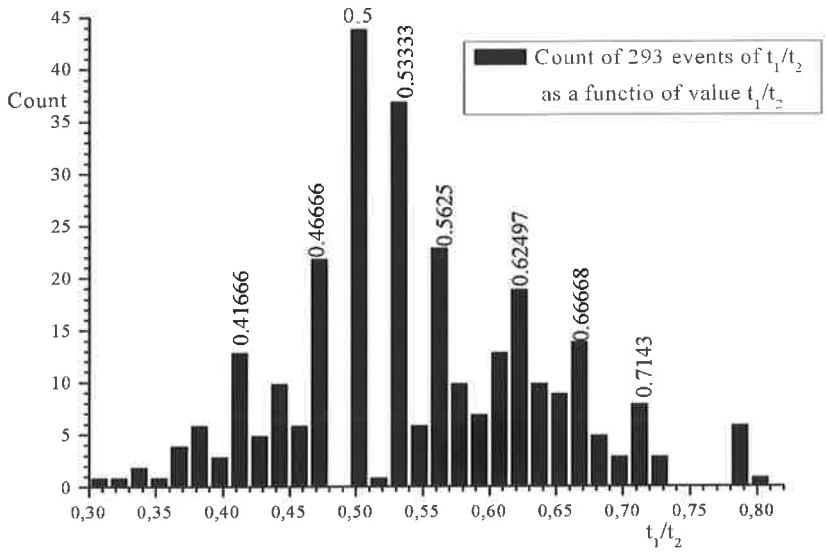

Figure 5 Count of t_1/t_2 values as a function of t_1/t_2

Figure 3 shows the analyzed PPG waves of a young (38 y) and an elderly (58 y) person. We can see clearly the difference between the PPG pulse wave of the young person and the elderly. Figure 4 shows the value t_1/t_2 as a function of t_1-t_2. This indicates simply the correlation between two variables. Figure 5 shows the counts of t_1/t_2. This indicates that the intervals are centered at value 0.5, but lagging some values around the value 0.5, e.g., from 0.480 to 0.495, and from 0.510 to 0.525.

When analysis the elderly tidal wave we can see that in the younger persons the width of the tidal wave is within the limits under the value of 0.2 and that is the limit, whereas in the case of the elderly persons the width of the tidal wave must be fixed to 0.2 but it has a snowball effect. The method is under clinical trial and analysis of the data from the elder individuals, the tidal wave of the PPG is challenging and decomposition by the current software is under the further analysis.

References

[1] H Qian, J B Bassingthwaighte (2000) A Class of Flow Bifurcation Models with Lognormal Distribution and Fractal Dispersion, Journal of theoretical Biology 205, 261-268.

[2] A G Scandurra, G J Meschino, L I Passoni, A L Dai Pra, A R Introzzi and F M Clara (2007) Optimization of arterial age prediction models based in pulse wave, Journal of Physics: Conference Series **90** 012080.

[3] A Qasem, A Avolio (2008) Determination of aortic pulse wave velocity from waveform decomposition of the central aortic pressure pulse, Hypertension 51;188-195.

Muistimetallitoimilaitteiden mallinnus ja suunnittelu tarkkuusmekaniikkaan

JUHA-PEKKA TEERIAHO[1], JARI AHOLA[2], KALERVO NEVALA[1,2]

[1]Oulun yliopisto, Mekatroniikan ja konediagnostiikan laboratorio

PL 4200, 90014 Oulun yliopisto

s-posti: juha-pekka.teeriaho@oulu.fi

[2]VTT, Verkottuneet järjestelmät

PL 1100, 90571 Oulu

TIIVISTELMÄ

Muistimetallista (SMA) valmistetusta toimilaitteesta on mahdollista tehdä rakenteeltaan yksinkertainen, halpa sekä kompakti. Muistimetallin monimutkaisen termomekaanisen käyttäytymisen vuoksi materiaalin antamia mahdollisuuksia ei ole vielä täysimittaisesti hyödynnetty. Tutkimuksen tavoitteena oli hankkia käytännön tietoa SMA-toimilaitteen suunnittelusta tarkkuusmekaniikkasovellutuksiin. Tavoitteena oli myös selvittää SMA-pohjaisten toimilaitteiden suunnitteluun käytettävissä olevia elementtimenetelmä (FE) -työkaluja. Käytännön suunnittelutiedon hankkimiseksi tutkimuksen aikana suunniteltiin muistimetallitoimilaite tarkkuusmekaniikan sovelluskohteeseen. Suunniteltu toimilaite valmistettiin, jolla käytännön läheisesti osoitettiin SMA-rakenteilla saavutettavia hyötyjä. Muistimetallien FE-simulointiin sopivia malleja on niukasti saatavilla, mutta niillä pystytään suunnittelutyötä merkittävästi helpottamaan sekä optimoimaan toimilaitteiden rakennetta. Suunnittelutyön tuloksena syntyi resistiivisesti kuumennettava antagonistinen muistimetallilevystä valmistettava toimilaite.

1. JOHDANTO

Perinteiset muistimetallit ovat metalliseoksia, joilla on yleensä kaksi kiinteän tilan stabiilia faasia: symmetrisen kiderakenteen omaava austeniittinen faasi ja epäsymmetrinen martensiittinen faasi. Seoksien kiderakenne on historiariippuva lämpötila-jännitys -avaruudessa. Kiderakenteen muuttumisesta johtuen seosten mekaaniset ja sähköiset ominaisuudet muuttuvat muodonmuutoksen mukana austeniittisen ja martensiittisen faasin ominaisuuksien välillä. Muistimetalliseokset voivat palautua jopa 8 % muodonmuutoksesta, kun martensiittinen materiaali lämmitetään austeniittiseksi. Tätä ilmiötä kutsutaan muisti-ilmiöksi, josta myös nimitys muistimetalli tulee. Tietyllä lämpötila-alueella materiaaleilla on myös kyky kokea suuri dissipatiivinen ja palautuva muodonmuutos, joka on nimetty superelastisuus tai pseudoelastisuusilmiöksi. [6,8]

Ensimmäinen laajasti kaupallisesti hyödynnetty muistimetalliseos Nitinol löydettiin 1960-luvulla Buehler ym. kehittäessä materiaalia avaruusaluksen lämpökilpeen [3]. Tämän jälkeen on löydetty useita muistimetalliseoksia. Materiaalitutkimus on myös kartuttanut tietoa SMA:n ominaisuuksien takana olevista ilmiöstä sekä materiaalien seossuhteiden, lämpökäsittelyiden ja lisäaineiden vaikutuksista seosten ominaisuuksiin. Tällä hetkellä useita SMA-seoksia on saatavilla hyllytavarana niitä valmistavilta yrityksiltä hintaan, joka tekee niiden käytön houkuttelevaksi useisiin sovelluskohteisiin. [6]

Muistimetalleja käsittelevissä julkaisuissa [6,8] materiaalien sovellutuskohteeksi ilmoitetaan huomattavia määriä sovelluksia esimerkiksi ilmailuun, lääketieteeseen, ajoneuvotekniikkaan sekä pienempiin aloihin kuten urheiluun ja öljynporaustekniikkaan. Ensimmäiset onnistuneet sovellukset ovat usein tuoneet materiaalin kyseisen alan suunnittelijoiden tietoisuuteen ja sitä kautta synnyttäneet voimakkaasti uusia tekniikkaan perustuvia innovaatiota.

Tutkimuksessa suunniteltiin muistimetallipohjainen sovellus yhteen Oulun VTT:n kanssa valittuun tarkkuusmekaniikan ongelmaan. Tavoitteena oli tuottaa samantyyppisiin sovellutuskohteisiin jatkossa uusia rakenneratkaisuja. Tutkimuksen tavoitteena oli myös tuottaa käytännön tietoa SMA-toimilaitteen suunnittelusta erityisesti tarkkuusmekaniikka sovellutuksiin sekä selvittää SMA-pohjaisten toimilaitteiden suunnitteluun käytettävissä olevia elementtimenetelmätyökaluja.

2. SUUNNITTELUTAVOITTEET

Yhteistyössä Oulun VTT:n optomekaniikan asiantuntijoiden kanssa tarkkuusmekaniikan alueelta valittiin esimerkkitapaus ongelmasta, joita tarkkuusmekaniikan suunnittelijat voisivat muistimetallitoimilaitteen avulla ratkaista. Tutkimuksen tavoitteena oli löytää tähän ongelmaan ratkaisu. Sovelluslähtöisellä tutkimuksella pyrittiin tuottamaan käytännön suunnittelutietoa sekä kartoittamaan olemassa olevia FE-työkaluja, joilla suunnittelutyötä voitaisiin avustaa. Konkreettisella sovelluksella pyrittiin yksinkertaisella tavalla kuvaamaan materiaalilla saavutettavia etuja sekä luomaan demonstraatiolaite, joka rohkaisisi uusien SMA:lla toteutettavien toimilaitteiden kehittämistä.

Sovelluskohde oli optiikan säätösovellus, jolla pyrittiin pienentämään optisten laitteiden valmistuskustannuksia sekä vähentämään laaduntarkastuksessa hylättävien laitteiden määrää. Muistimetallitoimilaitteella oli tarkoitus kompensoida linssien taittovirheitä tai optiikan komponenttien asennusvirheitä. Tutkimuksen aikaan ei ollut sopivaa teknologiaa komponenttien asennusvirheiden tai linssien taittovirheiden kompensoimiseen kokoonpanon jälkeen. Muistimetallitoimilaitteen suunnittelutavoitteet määriteltiin seuraaviksi:

1. toimilaitteen oli tuotettava yhden akselin suuntaisia tarkkoja portaattomia tasoliikkeitä, liikealue vähintään ±0,1mm, mutta tarvetta löytyy aina ±1mm liikealueeseen

2. toimilaite tuli olla edullinen valmistaa, sarjavalmisteisena hinta alle 10€/kpl.

3. toimilaitteen oli kokonsa puolesta sovelluttava käytettäväksi optisen laitteen sisällä, pienempi kuin 20 mm * 20 mm * 1mm

4. toimilaitteen liike oli pystyttävä lukitsemaan ultraviolettivalolla kovetettavalla liimalla

3. SUUNNITTELUMENETELMÄT

Useimmat SMA-toimilaitteet on suunniteltu ja rakennettu ilman modernien suunnittelu ja analyysityökalujen käyttöä. SMA-toimilaitteet ovat syntyneet suunnittele-valmista-testaa – iteroinnin tuloksena. Yksi syy tähän on ollut se että suunnittelijoiden käytössä ei ole ollut materiaalimallia, joka luotettavasti kuvaisi SMA:n termomekaanista käyttäytymistä. Menetelmä on tehnyt erityisesti moniulotteisten muistimetallitoimilaitteiden suunnittelusta haastavaa ja hidasta. [6]

Suunnittelutyötä helpottamaan on kehitetty jo usean vuosikymmenen ajan SMA:n ominaisuuksia kuvaavia malleja. Osa malleista perustuu materiaalin mikromekaanisesta käyttäytymisestä johdettuihin malleihin [3]. Toiset mallit perustuvat ilmiöpohjaiseen tarkasteluun, joista yhteenveto Lagoudas ym. kirjassa [6]. Vaikkakin muistimetallin mallinnuksen teorioita on esitetty runsaasti, suunnitteluun soveltuvia implementoituja malleja löydettiin suunnitteluun vain muutamia:

IRLOOP

IRLOOP on tsekkiläisen IT ASCR yliopiston kehittämä Matlab-pohjainen SMA:n yksiuloitteinen malli. IRLOOP on ilmiöpohjainen malli, joka pyrkii kuvaamaan sekä superelastisuutta että muisti-ilmiötä. Mallin pohjana oleva teoria on selostettu lähteessä[4]. Suomessa Merja Sippola on VTT:llä implementoinut mallia Abaqukseen [10]. IRLOOP:n pohjana olevan RLOOP:n koodeja on saatavilla kehittäjä yliopiston verkkosivuilta [12].

Abaquksen ja Ansyksen SMA-materiaalivalinnat

Ansys ja Abaqus FE-ohjelmistot sisältävät muistimetallimateriaalivalinnan, joka kuvaa materiaalin superelastisuusilmiötä. Ansys ohjelman malli perustuu Auricchio:n teoriaan ja Abaqus ohjelman malli Auricchio -Taylorin teoriaan. Lisää tietoa mallien ominaisuuksista ja rajoitteista on ohjelmistojen manuaaleissa [1,2].

Lagoudaksen ym. termomekaaninen 3D-materiaalimalli

Lagoudas, Bo ja Qidwai ovat esittäneet 3D-teorian SMA:n superelastisuuden ja muisti-ilmiöiden kuvaamiseen käyttämällä pienten siirtymien teoriaa [7]. Malli on implementoitu Abaqus-ohjelmistoon. Ohjeet mallin käyttöön sekä lähdekoodi on saatavilla Lagoudasin ym. kirjassa [6] esitetyltä verkkosivuilta [11].

3.1. KÄYTETTY SUUNNITTELUMENETELMÄ

Tutkimuksessa suunnittelu eteni kuvan 1 mukaisesti. Toimilaitteen geometriaa suunniteltiin Autodesk Inventor 2009 3D-mallinnusohjelmistolla. CAD -ohjelmalla suunniteltujen toimilaitteiden toiminnallisuutta analysoitiin FE -mallien avulla ja analyysin tuloksien perusteella tehtiin muutoksia toimilaitteen geometriaan. Kun toimilaitteen geometria todettiin toimivaksi FE -analyysin perusteella, valmistettiin siitä fyysinen prototyyppi. Suunnittelemalla toimilaite mahdollisimman pitkälle virtuaalisuunnittelun työkaluilla, saavutettiin säästöjä valmistuskustannuksissa ja ajankäytössä.

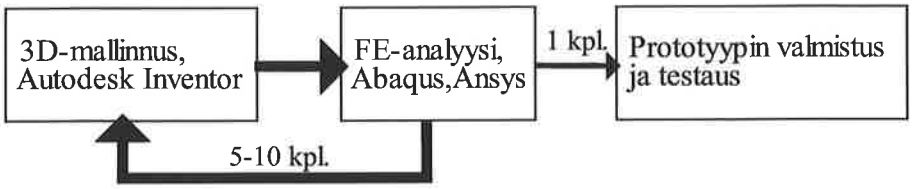

Kuva 1. Demostraatiotoimilaitteen suunnittelun eteneminen.

3.1.1. FE-analyysi

Suunnitellut toimilaitteet toimivat kuvan 2 mukaisella muistimetalli levystä leikatulla antagonistisella toimintaperiaatteella. Toimilaite asetetaan käyttökuntoon venyttämällä sitä kiinnityspisteistä, jotka sen jälkeen lukitaan paikoilleen. Liike saavutetaan kun osa SMA:n muodonmuutoksesta palautetaan lämmittämällä resistiivisesti rakennetta.

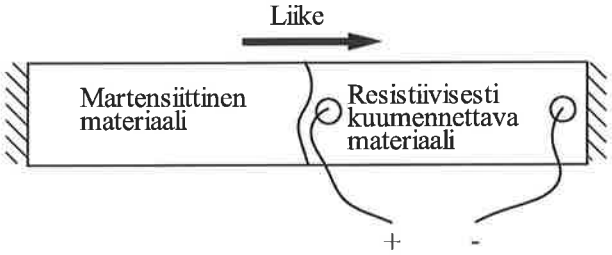

Kuva 2. Resistiivisesti kuumennettavan antagonistisen SMA-toimilaitteen toimintaperiaate.

FE-analyysilla helpotettiin toimilaitteen toiminnan kannalta oleellisten muodonmuutosalueiden etsintää, toimilaitteen muodon suunnittelua ja optimoimista sekä pyrittiin arviomaan toimilaitteen liikealueita. Lagoudasin 3D SMA-mallia ei ollut käytettävissä suunnitteluvaiheessa, joten FE-mallinnus toteutettiin Abaqus- ja Ansys -mallien sisältämien materiaalivalintojen avulla. Analyysi toteutettiin mallintamalla toimilaitteen jännityksiä ja muodonmuutoksia sekä lämpötilan kehittymistä erillisillä malleilla. Malleissa käytetty materiaalikuvaus on esitetty kappaleissa 3.1.1.1 ja 3.1.1.2.

3.1.1.1. Jännitysten ja siirtymien analysoinnin materiaalimallit

Resistiivisesti kuumennettava osa

Kuumennettavan SMA-osan materiaalin käyttäytymisen kuvaamiseen käytettiin sekä kimmoista mallia että Ansys-ohjelmassa löytyvää muistimetallin superelastisuusmallia. Kimmoinen materiaalimalli vastaa tilannetta, jossa muistimetallin lämpötila on noussut niin korkealle, että se käyttäytyy kuormituksenkin alaisena kimmoisesti. Alemmissa lämpötiloissa materiaalin käyttäytymisen kuvaamiseen käytettiin Ansys -ohjelmistosta materiaalivalintana löytyvää superelastisuusmallia.

Martensiittisessa tilassa oleva osa

Itsesovitteinen kaksostunut martensiittinen (twinned martensite) SMA käyttäytyy yksiulotteisessa vetokokeessa vakio lämpötilassa karkeasti kuvan 3.a. mukaisesti[1]. Materiaalin 3D-käyttäytymistä arvioitiin Ansys v. 11 ohjelmiston multilineaarisella isotrooppisesti lujittuvalla materiaalivalinnalla. Mallissa käytetään von Mises tyyppistä myötöehtoa assoasitiivisella myötösäännöllä. Myötöehdon muokkauslujittumista kuvaava lujittumisfunktio kuvattiin paloittain lineaarisella funktiolla kuvan 3.b. mukaisesti. Kun jälkimmäisen lineaarisen osuuden kulmakerrointa kasvatetaan suureksi, eli vakiolla n on pieni arvo ja vakiolla m suuri arvo saadaan plastisen 3D-mallin yksiulotteisen vetotestin ja martensiittisen SMA:n vetotestin kuvaajat vastaamaan toisiaan.

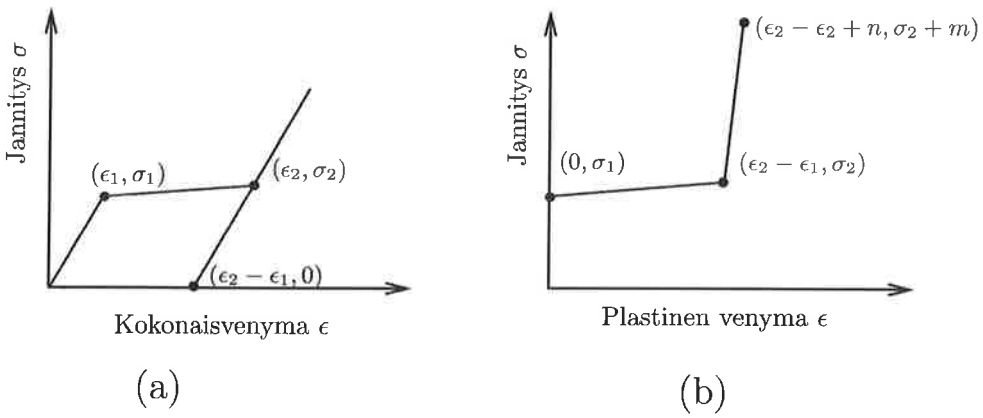

Kuva 3. Martensiitin yksiylotteisen käyttäytymisen kuvaamiseen käytetty (a) jännitys-kokonaisvenymä kuvaaja sekä (b) palottain lineaarinen lujittumisfunktio. Jännityssuureena on käytetty Cauchy-jännitystä ja venymäsuureena logaritmista venymää.

3.1.1.2. Resistiivisen kuumennuksen analyysissä käytetty materiaalimalli

Tavoitteet huomioiden resistiivisessä kuumennuksessa käytettiin karkeata yksinkertaistusta SMA-materiaalin käyttäytymisestä kuumennustilanteessa: analyysissä käytettiin martensiittisen tilan arvoja ja resistiivisyys oletettiin isotrooppiseksi eikä faasimuutoksen vaikutusta huomioitu. Kuumennustilanteessa faasimuutos martensiitista austeniittiin on endoterminen ja jäähdytystilanteessa faasimuutos austeniitista martensiittiin eksoterminen reaktio. Eri faaseilla on myös voimakkaasti erilaiset resistiiviset ominaisuudet johtuen niiden erilaisesta kiderakenteesta [9]. Myöskään muodonmuuttumisen vaikutusta ei huomioitu. Resistiivistä kuumennusta analysoitiin Abaqus-ohjelmiston kytketyllä lämpö-sähkökenttä transientilla analyysillä (Coupled thermal-electrical analysis).

[1] Vetokokeesta tyypillisesti saatava voima-insinöörivenymä-kuvaaja on muutettu Cauchy-logaritminenvenymä-kuvaajaksi käyttämällä kokoonpuristumattomuusoletusta. Esitetty Ansys-ohjelman manuaalissa [2].

4. SUUNNITELTUN TOIMILAITTEEN VALMISTUS, RAKENNE JA KOKEELLINEN TESTAUS

4.1. Toimilaitteen rakenne ja toimintaperiaate

SMA:n termomekaanisista ominaisuuksista johtuen materiaalin työstäminen on hankalaa. Leikkaavissa menetelmissä kuten poraus ja jyrsintä tarvitaan korkeita leikkausnopeuksia. Vesileikkausta ja kipinätyöstöön perustuvia menetelmiä (EDM, electrical discharge machining) on myös käytetty SMA:n työstämiseen. [6]

Tutkimuksessa suunniteltu levytoimilaite valmistettiin kipinätyöstöön perustuvalla lankasahauksella (Charmilles Robofill 440cc) 0,54 mm paksusta Memory metalle Gmbh valmistamasta luokituksen M NiTi–levystä. Käytettäessä ohuinta valmistajan lankapaksuutta 0,1 mm langan todettiin katkeavan niin herkästi että useamman toimilaitteen valmistus olisi ollut liian työlästä. Paksummalla langalla ongelmaa ei esiintynyt. Vahvemman langan käyttö vaati kuitenkin leikkuu-urien suurentamisen 0,35 mm:stä 0,45 mm:iin ja siten kahta hieman geometrialtaan poikkeavaa toimilaitetta. Kuvassa 4 esitetyn toimilaiteen pituus on 15,7 mm ja leveys 20 mm.

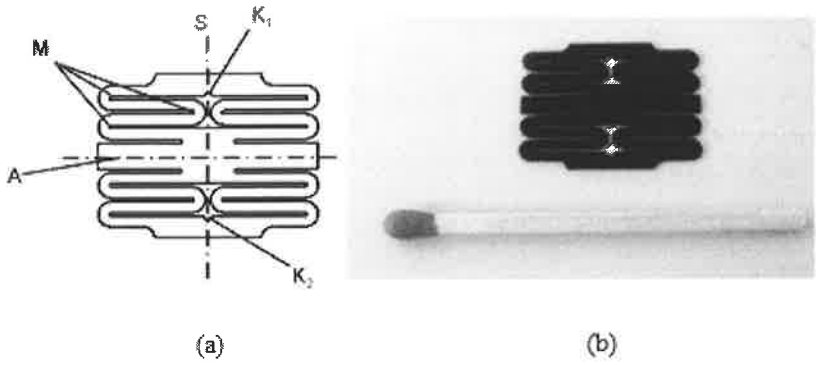

Kuva 4. Toimilaitteen geometria (a) valmistettu toimilaite (b).

Toimilaite tuottaa yhden akselin suuntaisen lineaariliikkeen. Liike syntyy, kun suuntautuneita, kaksostuneita ja martensiittisia levyn alueita kuumennetaan. Liikkeen suuruus määräytyy esivenytyksen suuruudesta ja resistiivisen kuumennuksen voimakkuudesta. Kuvan 4.a. mukaisessa toteutuksessa muodonmuutosalueet on merkitty M-kirjaimella. Kiinnityspisteet on merkitty kirjaimilla K1 ja K2. Toimilaite asetetaan käyttökuntoon venyttämällä toimilaitetta kiinnityspisteistä, jotka lukitaan paikoilleen. Toimilaitteen liike saavutetaan syöttämällä sähkövirtaa keskusosan (A) ja kiinnityspisteen K1 tai K2 välille. Sähkövirta nostaa muodonmuutosalueiden lämpötilaa, jotka palautuvat ja aiheuttavat keskusosan lineaariliikkeen. Keskusosan kiertyminen on estetty tekemällä toimilaitteesta symmetrinen keskilinjan (S) suhteen.

Sähköjohtimien kiinnittämiseen levytoimilaitteeseen kokeiltiin tinausta, mutta johtimia ei saatu tarttumaan NiTi:n pintaan. Sähköjohteet kiinnittyivät kuitenkin helposti sähköä johtavalla epoksi liimalla (Chemtronics CW2400).

4.2. Liikealuetestit

Toimilaitteen liikealueet mitattiin optisesti työkalumikroskoopilla, jonka mittaustarkkuus on 0,01mm. Liikkeet olivat portaattomia ja niitä pystyttiin helposti hallitsemaan käyttötarkoitukseen

nähden karkealla virtalähteellä[2]. Toimilaitteita valmistettiin kaikkiaan kolme kappaletta. Kahdessa jälkimmäisessä toimilaitteessa leikkuu-urien väli oli valmistusteknisistä syistä hieman suurempi. Taulukossa 1. on esitetty mittauksista saadut tulokset. Mittauksissa toimilaitetta ajettiin liikealueen päästä päähän jatkamalla resistiivistä kuumennusta niin kauan, että löydettiin toimilaitteen liikealueen ääriarvot. Osa toimilaitteen tuottamasta liikkeestä palautui resistiivisesti kuumennetun alueen jäähtyessä. Hyödynnettävissä olevalla liikkeellä tarkoitetaan toimilaitteen liikealueen suuruutta vähennettynä palautuvan liikkeen suuruudella.

Taulukko 1. Levytoimilaitteiden liikealueiden mittaustulokset.

Toimilaite	Esivenytys	Hyödynnettävissä olevan liikkeen keskiarvo	Palautuman keskiarvo
1	5,2mm	1,3mm	0.23mm
	6,2mm	1,6mm	0,39mm
	7,1mm	1,9mm	0,43mm
2	5,9mm	2,1mm	0,48mm
3	5,8mm	2,0mm	0,44mm

Toimilaitteen liikealueen havaittiin pienenevän aavistuksen verran ajokertojen lisääntyessä. Kokeellisissa tutkimuksissa on osoitettu, että levytoimilaitteen liikkeen tuottavat kiderakenteen muutokset indusoivat aluksi myös plastisuusmekanismilla tapahtuvia muodonmuutoksia, mikä johtaa pysyvään muodonmuutokseen. Toistojen lisääntyessä tämä ilmiö pienenee, kunnes häviää olemattomiin materiaalin stabiloituessa [9]. Suunnitellussa käyttökohteessa näillä ilmiöillä ei katsottu olevan merkitystä. Toimilaitetta ajetaan vain muutamia kertoja halutun aseman saavuttamiseksi, minkä jälkeen liikealue lukitaan aseman pitämiseksi.

5. JOHTOPÄÄTÖKSET

Tutkimuksen aikana onnistuttiin suunnittelemaan tutkimustavoitteet erinomaisesti täyttävä demonstraatiotoimilaite Oulun VTT:n optomekaniikan asiantuntijoiden kanssa määriteltyyn tarkkuusmekaniikan ongelmaan. Vastaavanlaista toimilaitetta ei kyseiseen ongelmaan ole aikaisemmin kehitetty ja sen kaupallista hyödynnettävyyttä selvitellään Oulun VTT:llä.

Muistimetallin monimutkainen termomekaaninen käyttäytyminen käytännössä edellyttää FEA-työkalujen hyödyntämistä suunniteltaessa lankasovellutuksia monimutkaisempia SMA-elementtejä. Ansys- ja Abaqus-ohjelmistojen olemassa olevia malleja pystytään tehokkaasti käyttämään ainoastaan superelastisuutta hyödyntävien toimilaitteiden suunnitteluun. Tutkimuksessa suunniteltujen resistiivisellä kuumennuksella aktivoitavien toimilaitteiden analysoinnissa joudutaan tekemään huomattavasti yksinkertaistuksia ja rajoittumaan vain tiettyihin toimilaitteiden ajonaikana esiintyviin kuormitustilanteisiin. Käytetty FE-analyysi toimi suunnittelussa karkeana työkaluna, jolla helpotettiin toimilaitteen toiminnan kannalta oleellisten muodonmuutosalueiden etsintää, toimilaitteen muodon suunnittelua ja optimoimista sekä pyrittiin arviomaan toimilaitteen liikealueita.

[2] DC- teholähde (30V/ 5A), malli: DF 1731SB, valmistaja:Ningbo Jinyuan (G.S) Electricity Co., LTD

Tutkimuksen aikana ei ehditty testata käytetyn SMA-materiaalin materiaaliarvoja. FE-malleissa käytettiin aikaisemmissa tutkimuksissa samantyyppiselle materiaalille tehtyjen materiaalitestien testaustuloksia. Tämä ei mahdollistanut mallien tarkkuuden arvioimista valmistetusta rakenteesta saataviin mittaustuloksiin vertaamalla.

6. KIITOKSET

Tutkimusta on ollut osittain rahoittamassa Suomen Akatemia sekä Valtion teknillinen tutkimuskeskus (VTT). Saimme tutkimuksessa käytetyt FE-ohjelmistot käyttöömme Tieteen tietotekniikan keskuksen (CSC) kautta.

LÄHTEET

[1] ABAQUS, Version 6.8 Documentation. Dassault Systemes Simulia Corp. USA.

[2] ANSYS, Version 11 Documentation. ANSYS, Inc. USA.

[3] Bhattacharya, K. 2003. Microstructure of Martensite:Why it Forms and How it Gives Rise to the Shape-Memory Effect. Oxford University Press, Oxford.

[4] Frost, Miroslav. 2007. Elastic properties of blood veins with a scaffold. Diplomityö. Mathematical Institute of Charles University.

[5] Kauffman, G.B., Mayo, I. 1997. The story of Nitinol: The serendipitous discovery of the memory metal and its applications. The Chemical Educator. 2, s. 1-21.

[6] Lagoudas, D. C. 2008 Shape Memory Alloys: Modeling and Engineering Applications (New York: Springer)

[7] Lagoudas, D. C., Bo, Z., Qidwai, M. A. 1996. A unified thermodynamic constitutive model for SMA and finite element analysis of active metal matrixcomposites. Mechanics of Composite Materials and Structures. 3, 153–179.

[8] Otsuka, K., Wayman, C.M. 1998. Shape Memory Materials. Cambridge University Press, Cambridge, UK.

[9] Patoor, E., Lagoudas, D. 2006. Shape memory alloys, Part 1: General properties and modeling of single crystals. Mechanics of materials. 38.

[10] Sippola, Merja, Lindroos, Tomi. Modelling and testing of a load-limiting sandwich structure.September 7-11, 2009. ESOMAT 2009 - 8th European Symposium on Martensitic Transformations, Prague, Czech Republic,

[11] SMARTLAB:n kotivisut, http://smart.tamu.edu/SMAText/,_14.10.2009.

[12] Tsekkiläisen IP ASCR yliopiston Martensitic Transformations ja SMA GROUP:n kotisivut, http://www.fzu.cz/departments/metals/sma/index.php?file=./home.html, 14.10.2009.

SEISMIC HAZARD EVALUATION FOR NEW NPP SITES IN FINLAND USING DIFFERENT SCALING PARAMETERS

P. VARPASUO
Fortum Nuclear Services Ltd.
P.O.Box 10, 00048 FORTUM,
FINLAND

ABSTRACT

This paper reports the seismic hazard evaluation for two prospective nuclear plant sites in Finland: Simo and Pyhajoki. The Simo site is located in the northern extremity of the Bothnian gulf near the city of Kemi and the Pyhajoki site is located near the city of Raahe. The assignment for this task was given by Finnish Radiation Protection Center (STUK) in the beginning of the year 2009 for the consortium whose members are: 1) AF-consult as a leader and providing the expertise in the source area delineation; 2)The Institute of Seismology of the Helsinki University as a partner providing the information about earthquake catalogs and seismic source mechanisms in the investigated area and Fortum Nuclear Services Ltd as an expert partner providing the experience from prior seismic hazard studies in Finland. The final report for the STUK will be submitted by the end of October 2009. According to the preliminary results the Simo site differs from the Pyhajoki site in the shape of the ground response spectrum as well as in the magnitude of the peak ground acceleration (PGA) to be expected at the site. Because of that difference it was decided to develop the seismic hazard of these to two prospective sites also in terms cumulative absolute velocity (CAV) values parallel with the peak ground acceleration formulation. This comparison will clarify if the difference between these two sites can be attributed to the choice of the scaling parameter or is the difference to be attributed to the inherent variability of seismic sources in the vicinity of these two sites.

I. INTRODUCTION

This paper deals with the task of the Determination of Seismic Hazard and of the ground response spectrum for Finland land area south of Polar circle. The preparation of input data for the task has been organized as follows. The Helsinki University Faculty of Seismology is responsible for the input material of the seismicity in the investigated area. The input material will be collected for the area (15-40°E)x(55-75°N). The Helsinki University Faculty of Seismology delivers the epicentral map of earthquakes and the structural information (the biggest asperities and faults etc.) which is related to them inside the investigated area. The epicentral maps are compiled separately for the magnitude classes, M>1.5, M>3.0, M>3.5 and M>4.0. Historical earthquakes and instrumentally located earthquakes are denoted with different symbols depending on detection accuracy. The all input material is delivered for subsequent hazard quantification as a file which is suitable to the Excel format or in the format (for example text) which is easily converted into it.

The hazard quantificator (AF-consult Ltd) delineates the seismic source areas based on delivered the input material. Inside the source ares the Gutenberg-Richter (Gutenberg and Richter, 1944) source parameters (the values b) are determined as well as the maximum magnitudes. Fortum

Nuclear Services Ltd. is responsible for formulating the input data files for hazard curve and uniform hazard ground response spectra computations on the basis of this information of the source area and attenuation information. The hazard quantification calculations are carried out with the aid of SEISRISK III (Bender & Perkins 1987). By the end of October 2009 all supplementary calculations (among others PGA contour curves for the whole investigated area for median annual exceedance frequency of 10^{-5}) will be carried out.

2. EARHQUAKE CATALOG AND EPICENTRAL MAP FOR FENNOSCANDIA

The regional data were taken from the Fennoscandian earthquake catalogue (FENCAT, Figure 1), which is compiled and maintained by the Institute of Seismology of University of Helsinki (http://www.seismo.helsinki.fi/english/bulletins). The catalogue contains a well-quantified and homogenous data base, with spatial distribution of the epicenters being as complete as possible. The first version of the catalogue was compiled by Ahjos and Uski in 1992. The original FENCAT catalogue included both macroseismically and instrumentally located events until the year 1990. Since 1992 the catalogue has been continuously updated by the Institute of Seismology of University of Helsinki. New data is added from the annual earthquake bulletins published by the Insitute of Seismology as well as from the new studies of earthquakes in Fennoscandia.

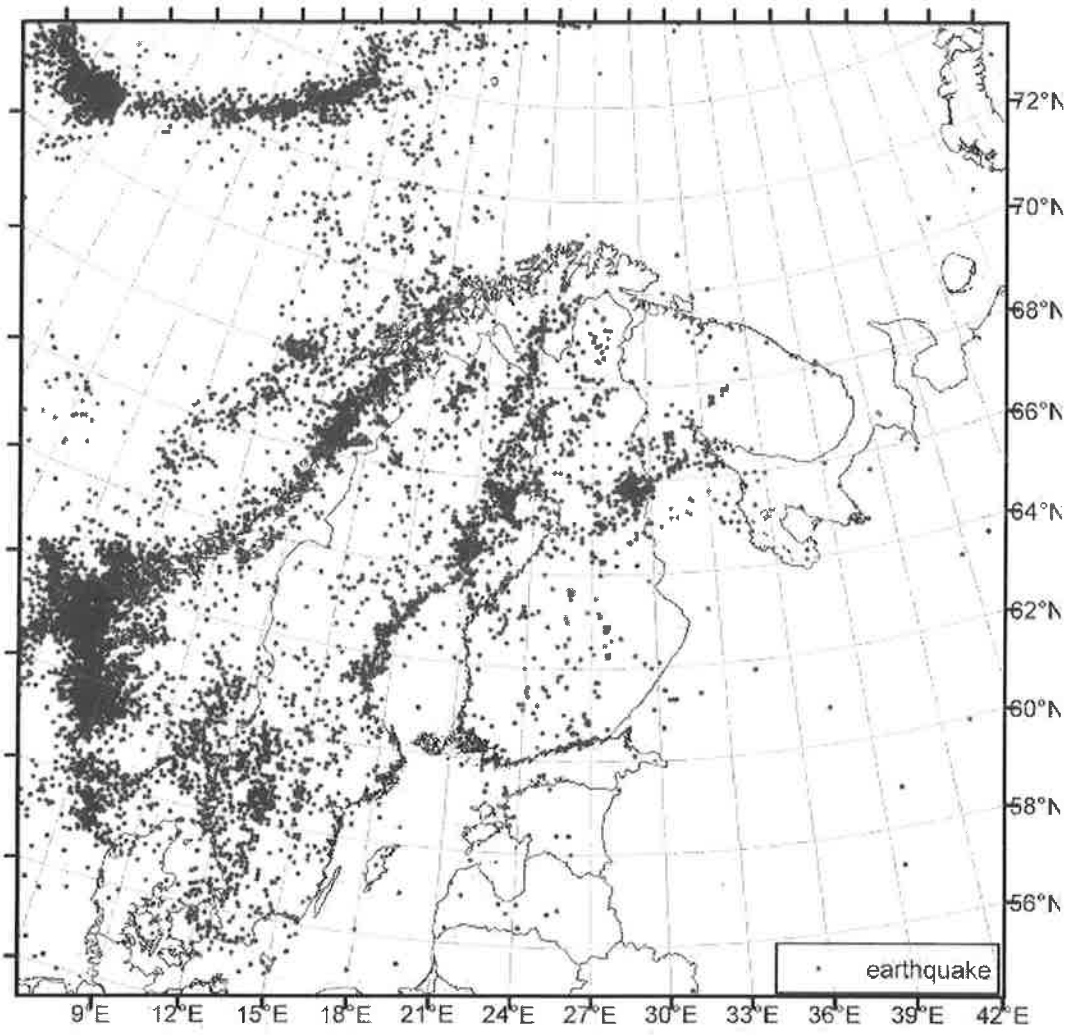

Figure 1 Locations of all earthquakes (red dots) in Fennoscandia and adjacent areas according to FENCAT, 1375- 30.10.2008 (ref. [1]).

3. REGIONAL SEISMICITY IN NORTHERN FINLAND

The study utilises similar subsets of FENCAT for the potential nuclear power plant sites Pyhäjoki and Simo. The subsets include earthquake data within 500 km of Pyhäjoki and Simo respectively (Figure 2). The seismic characteristics of Finland and examinations of attenuation (Varpasuo et al 2000) suggest that areas within a distance of 500 km from the nuclear power plant site is considered large enough to include all significant seismic events.

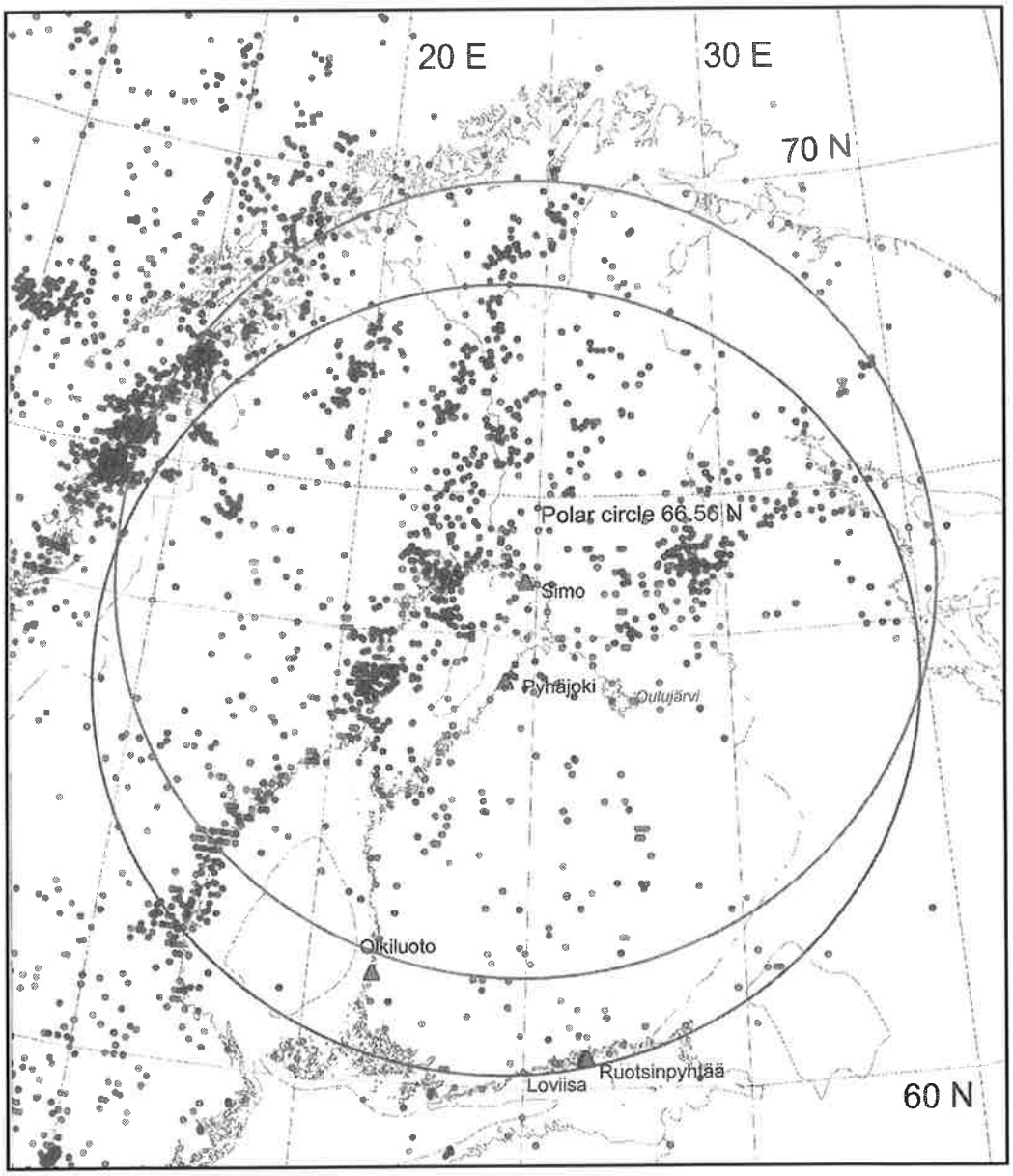

Figure 2 Pyhäjoki region (blue circle) and Simo region (red circle). Earthquakes 1375-30.10.2008 (M>1.4). Macroseismically located earthquakes are presented by light blue circles and instrumentally located by dark blue circles (ref. [1]).

The Finnish earthquake data has been considered to be satisfactory after 1880, when systematic studies of earthquakes started. That can be seen as increased number of seismic in Figure 2. Second increase of observations is related to beginning of systematic instrumental monitoring. That is shown clearly in magnitudes smaller than 3. The third increase is related to magnitudes less than 2 during the last 20-25 years.

The number of earthquakes as a function of magnitude for a specific region often conforms to the equation (Gutenberg & Richter 1944):

$$\text{Log } N = a - b*M \quad (1)$$

N is the number of earthquakes whose magnitude is > M occurring in a specified time interval and a and b are constants. Parameters of this equation are used in SEISRISK III to describe seismicity of regional subsets and seismic zones.

4. ATTENUATION RELATIONSHIP FOR PEAK GROUND ACCELERATION

The Dahle regression model (Dahle et al. 1990) represents a intra-plate strong-motion model, applicable to areas where the lack of local strong motion recordings prevents the use of appropriate region specific strong ground motion models. Development of Dahle model is based on data set that consists of 87 recordings from 56 different earthquakes, out of which the Tangshan earthquake of July 28, 1976, and several smaller aftershocks comprise a significant part. The Friuli earthquakes, also occurring in 1976, comprise a second large subset. Of particular importance for Dahle model are the many recordings achieved from the November 25, 1988, Saguenay earthquake in Quebec, Canada, with many good recordings at large distances. The remaining data emerge from various regions in eastern North America, Canada, Australia and Europe.The Dahle attenuation function form with minor modifications is adopted for the attenuation relationship used in this work. The Dahle attenuation equation can be written as

$$\begin{aligned} \ln(y) &= c_1 + c_2 M + c_3 \ln R^{-1} + c_4 R \quad \text{for } R<R_0 \\ \ln(y) &= c_1 + c_2 M + c_3 \ln R + c_4 R \quad \text{for } R>R_0 \end{aligned} \quad (2)$$

where c_1, c_2, c_3, c_4, R_0 are coefficients to be determined. Coefficients c_1,c_2 c3, c_4, and R_0 have been estimated with the aid of non-linear regression. on the basis of the data compiled data set for the geometric spreading model described in Equation 2, with R_0 = 100 km. The units of ground motion were selected in terms of meters and seconds. In this study, the ground acceleration registrations used for evaluating coefficients c1, c2, c3, c4, and R_0 were selected from those geological and tectonic regions that were judged to be similar to the investigated area. The second principle for choosing these areas was the availability of registrations. By use this procedure strong motion recordings the Saguenay region from Eastern Canada (13 sites) and the Newcastle region from Australia (5 sites) were chosen. These are both moderate seismicity, intra-plate regions and the registrations were observed on the bedrock. In case of Saguenay, the bedrock was of Precambrian formations, similar to Fennoscandia, but in case of Newcastle the rock formations were sedimentary rocks.

5. RESULTS FOR PEAK GROUND ACCELERARTION HAZARD (MEDIAN VALUE FOR RETURN PERIOD OF 100 000 YEARS) AND CUMULATIVE ABSOLUTE VELOCITY HAZARD FOR SIMO AND PYHAJOKI SITES

For handling the uncertainties in the analysis so called Decision tree approach was chosen. The code basis for the ground motion estimation in probabilistic seismic hazard studies stipulates the median spectra for mean return period of 100 000 years [Draft. Reg. Guide DG-1015, 1992].

The decision three is used in the treatment of uncertainties input data. Each branch end node in decision tree characterizes the credible alternative inputs to probabilistic seismic hazard analysis and their likelihoods. The end node likelihood can be calculated by multiplying the branch

likelihoods leading to end node. The sum of end node likelihoods as well as branch likelihoods at each level must be one.

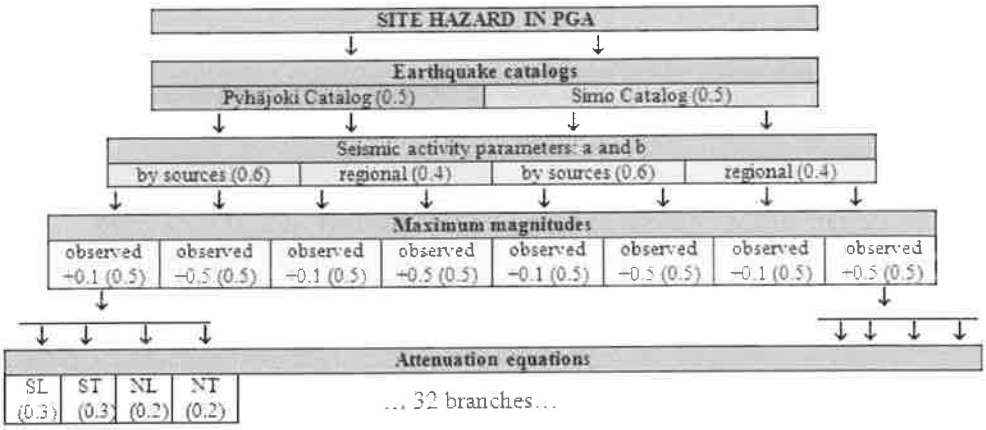

Figure 3 Decision tree structure for treating uncertainties (ref. [1]).

The peak ground acceleration median, 5% fractile, and 95% fractile hazard curves for Pyhajoki and Simo sites are depicted in Figures 4 and 5.

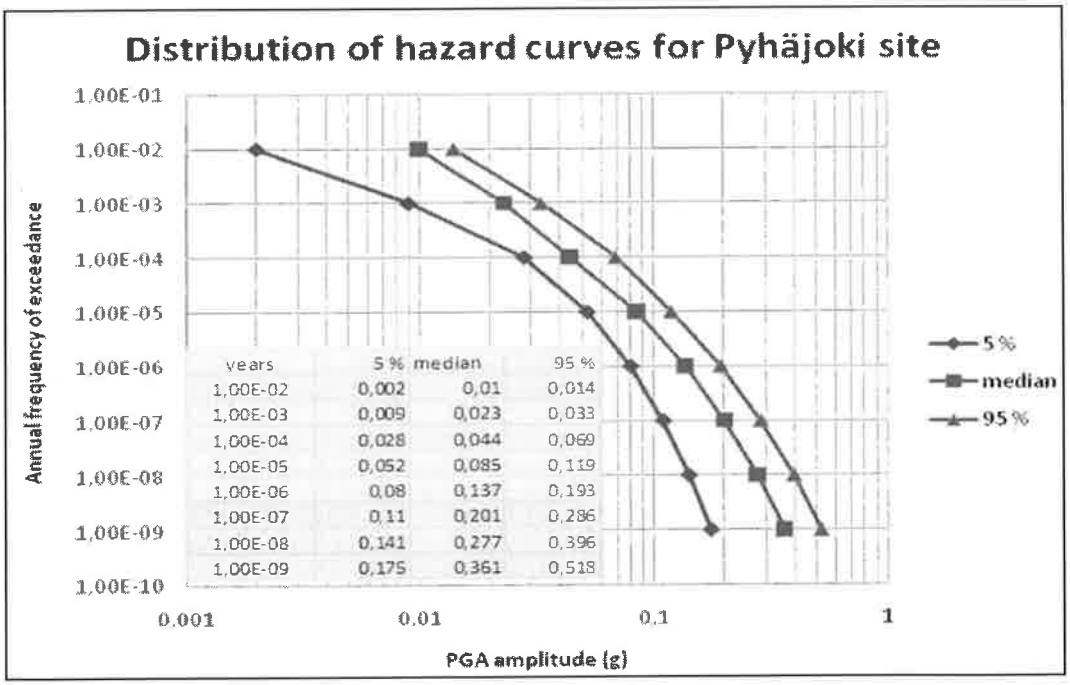

Figure 4 Peak ground acceleration hazard for Pyhajoki site (ref. [1]).

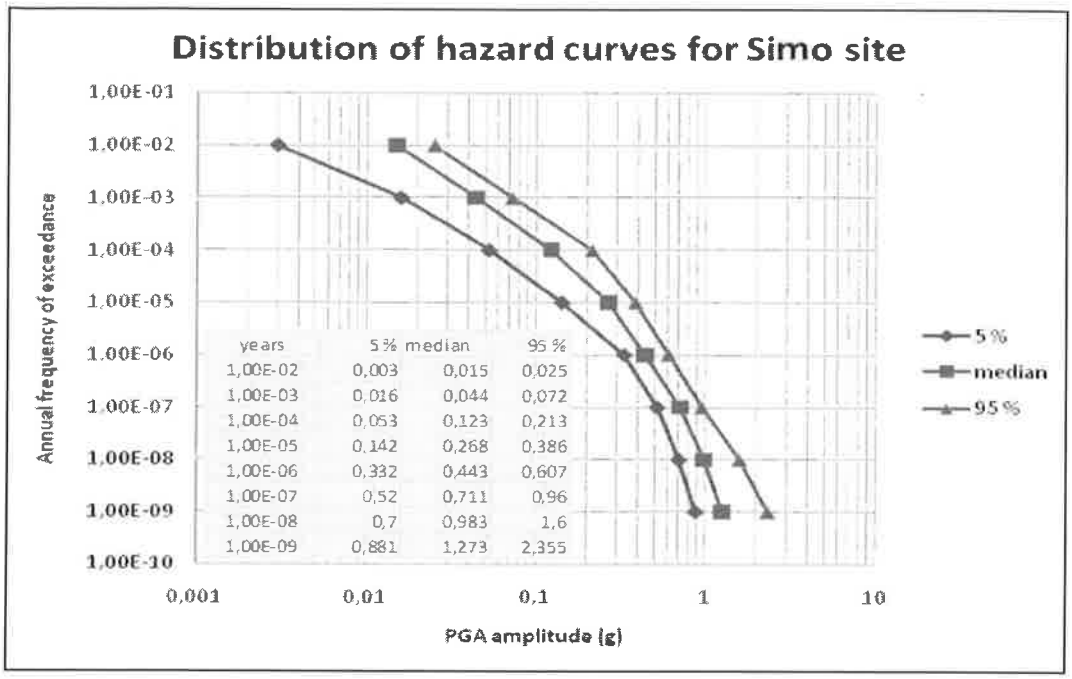

Figure 5 Peak ground acceleration hazard for Simo site (ref. [1]).

In the following section the Simo and Pyhajoki site hazards are estimated in terms Cumulative Absolute Velocity. The Cumulative Absolute Velocity (CAV) is defined as follows:

$$CAV(t_n) = CAV(t_{n-1}) + \int a(t)dt \quad (3)$$

The limits of the integral of the Equation 3 in the definition formula of the CAV are: lower limit is t_{n-1} and the upper limit is t_n. For the attenuation definition in the CAV hazard analysis so called Campbell-Bozorgnia attenuation is used. (Campbell and Bozorgnia, 2009). The Campbell-Bozorgnia attenuation used in this study is defined with the following equation

$$LN(CAV) = C_0 + C_1 * M + C_2 * LN(R^2 + C_3^2) \quad (4)$$

The unknown coefficients in the Equation 4 are determined on the basis of Saguenay-Newcastle data similarly as in case of peak ground acceleration attenuation for Dahle attenuation. The Campbell -Bozorgnia CAV attenuation for Saguenay longitudinal data subset is given in Figure 6 and the Pyhajoki and Simo CAV hazard curves in Figures 7 and 8.

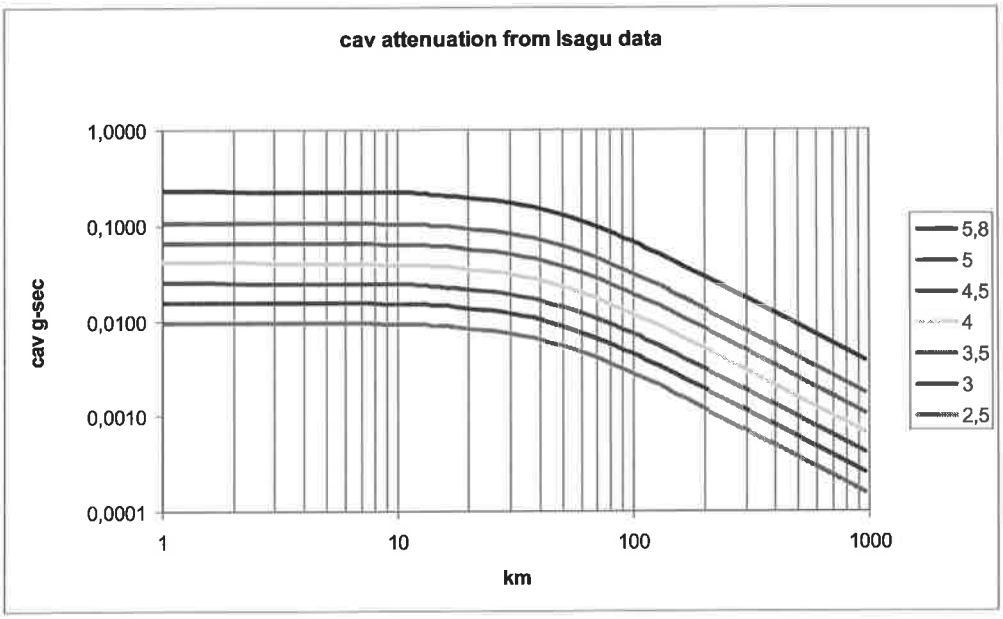

Figure 6 The Campbell -Bozorgnia CAV attenuation for Saguenay longitudinal data subset

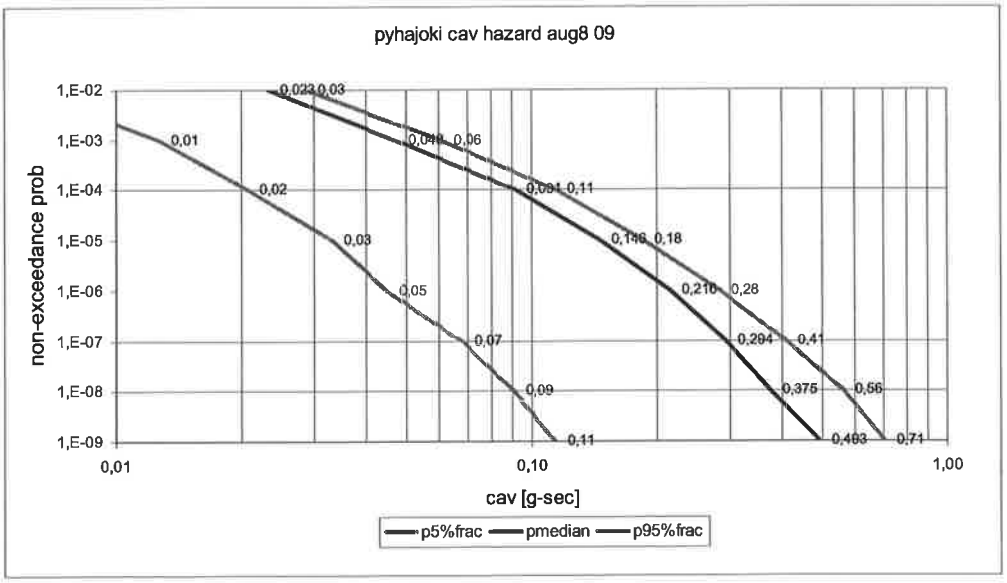

Figure 7 CAV hazard for Pyhajoki site

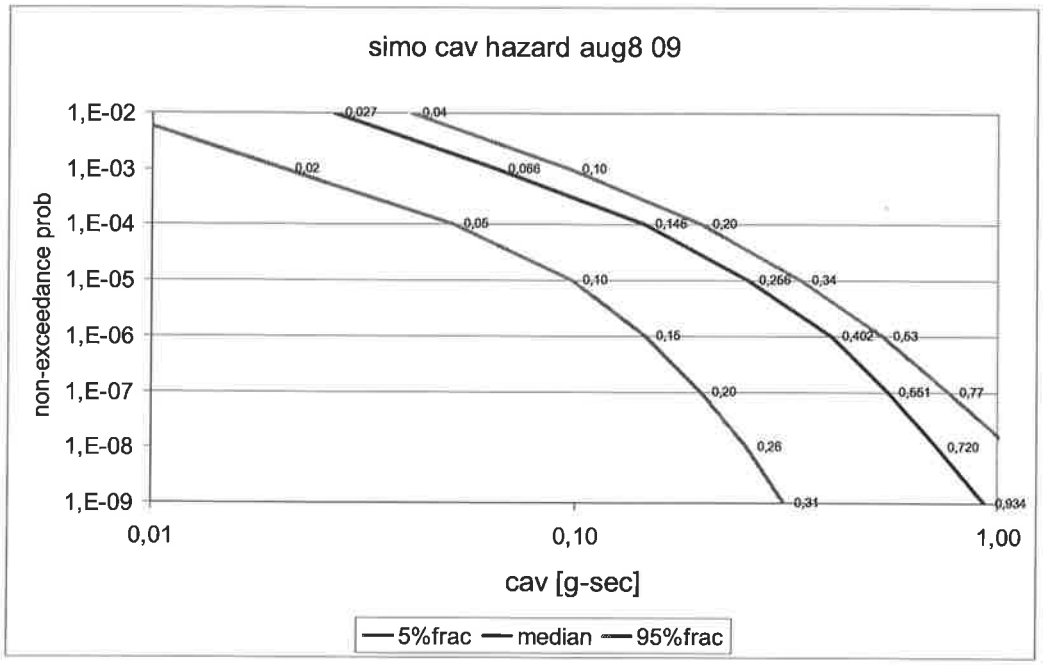

Figure 8 CAV hazard for Simo site

6. CONCLUSION

Seismic Hazard and the design spectral shape in the prospective sites is site dependent. There can be no generic seismic hazard definition or the design spectral shape that coul be applicable for entire Finland. Difference in pga hazard between Simo and Pyhajoki sites is threefold whereas it is 60 % in CAV hazard.

7. REFERENCES

J. Saari (Ed.) , P. Heikkinen, P. Varpasuo, M. Malm, E. Turunen, K. Karkkulainen, O. Valtonen and M. Uski "ESTIMATION OF SEISMIC HAZARD IN TERRITORY OF FINLAND", Report Number EXP-500, (draft text) AF-Consult, October 2009.

Gutenberg, B. & Richter, C.F. 1944. Frequency of earthquakes in California. Bull. Seism. Soc. Am., 34, 185-188

Bender B. & Perkins D. M. 1987. SEISRISK III: A Computer Program for Seismic Hazard Estimation, U. S. Geological Survey Bulletin 1772, United States Governement Printing Office; Washington.

Ahjos, T. & Uski, M. 1992. Earthquakes in northern Europe in 1375-1989. Tectonophysics, 207:1-23.

Dahle A., Bungum H., Kvamme L. B., Attenuation Models inferred from Intraplate Earthquake Recordings, Earthquake Engineering and Structural Dynamics, vol 19, 1125-1141(1990).

Draft Regulatory Guide DG-1015, Identification and Characterization of Seismic sources, Deterministic Source Earthquakes, and Ground Motion, U.S. Nuclear Regulatory Commission Office of Nuclear Regulatory Research, November 1992.

Kenneth W. Campbell,ABS Consulting (EQECAT), Beaverton, Oregon, USA., Yousef Bozorgnia, Pacific Earthquake Engineering Research Center (PEER),University of California, Berkeley, California, USA, " Relationships Between Cumulative Absolute Velocity (CAV) and JMA Instrumental Intensity (IJMA) and Attenuation Relationships for CAV and IJMA Using the NGA Database", IAEA CS on Alternative Ground Motion Scaling in Attenuation Relationships: Progress and Planning in the USA, Progress Report #2, May 18, 2009

ON THE DIRECT COMPUTATION OF CRITICAL EQUILIBRIUM STATES IN SOLID AND STRUCTURAL MECHANICS

ALEXIS FEDOROFF[1], REIJO KOUHIA[1], HEIKKI MARJAMÄKI[2] and JARI MÄKINEN[2]

[1] Department of Structural Engineering and Building Technology
Helsinki University of Technology, P.O. Box 2100, FI-02015 TKK, Finland
[2] Department of Mechanics and Design,
Tampere University of Technology, P.O. Box 589, FI-33101 Tampere, Finland

ABSTRACT

Determination of critical points along an equilibrium path of a structure is a non-linear eigenvalue problem. If the external load is parametrized by a single parameter such an eigenvalue problem consist of solving the critical state variables, the eigenmode and the critical load parameter from the equation system consisting of the equilibrium equations, the criticality condition and some auxiliary conditions depending what kind of a critical point is in question. The non-linear eigenvalue problem can be solved by using the Newton's method. To obtain the Jacobian of the augmented equation system, second order derivatives of the residual vector with respect to the state variables need to be evaluated. Since correct computation of the critical points require geometrically exact kinematics, such derivatives are tedious to obtain. In this paper, explicit formulas for those second order derivatives of a 3D geometrically exact beam element based on the Reissner's model are presented. Additionally, some alternative iterative schemes which avoid the formation of the second order derivatives are presented and compared to the full Newton's method.

1 INTRODUCTION

An important task in computational structural analysis is the determination of the critical loads. If the pre-buckling displacements are small, it is usually sufficient to solve the linearized eigenvalue problem, where the linearization is performed with respect to the undeformed configuration. However, in many cases the pre-buckling deflections have considerable effect on the buckling behaviour and cannot be neglected.

One way to compute the critical points is to use a path-following method to solve the non-linear equilibrium equations and as a byproduct detect the change in stability properties along the traced path. Such an an indirect method is considered e.g. in [1, 2, 3, 4]. Also solving a polynomial eigenvalue problem at a certain equilibrium state is an appealing approach, [5, 6].

A direct method to compute the critical point is so constituted that the equilibrium equations are augmented with a criticality condition. The criticality condition has in some sense to state the vanishing stiffness of the stucture and can be either a scalar equation [7, 8] or an eigenvalue problem [10, 9, 11, 13, 20]

The idea of augmenting the equilibrium equations with the criticality condition appears to be due to Keener and Keller [10], presented as early as in 1973. Most papers found in literature deal only with simple critical points, and the extension to multiple bifurcations, see Keener [14], will not be considered in this paper.

Direct solution of the critical points along the equilibrium path requires complete kinematical description of the underlying mechanical model. In particular, for dimensionally reduced models, like beam- and shell models, the description has to be capable to handle large rotations. Development of a geometrically exact model with large rotations is not a trivial task [21, 22, 23].

2 DETERMINATION OF CRITICAL POINTS

2.1 Non-linear eigenvalue problem

A critical point along an equilibrium path can be determined by solving the non-linear eigenvalue problem: find the critical value of $\mathbf{q}$, λ and the corresponding eigenvector $\mathbf{v}$ such that

$$\left\{ \begin{array}{rcl} \mathbf{f}(\mathbf{q},\lambda) & = & \mathbf{0} \\ \mathbf{f}'(\mathbf{q},\lambda)\boldsymbol{\phi} & = & \mathbf{0} \end{array} \right. \tag{1}$$

where $\mathbf{f}$ is the vector of unbalanced forces and $\mathbf{f}'$ denotes the Gateaux derivative (Jacobian matrix) with respect to the state variables $\mathbf{q}$. Equation $(1)_1$ is the equilibrium equation, which has to be satisfied at the critical point, and equation $(1)_2$ states the zero stiffness in the direction of the critical eigenmode $\boldsymbol{\phi}$, which is the actual criticality condition. Such a system is considered in Refs. [9], [12], [20]. Abbot [7] considers a different extended system where the criticality is identified by means of the determinant of the tangent stiffness matrix. The drawback of this procedure is that the directional derivative of the determinant is difficult to compute.

The equilibrium equation $(1)_1$ constitutes the balance of internal forces $\mathbf{r}$ and external loads $\mathbf{p}$, which is usually parametrized by a single variable λ, the load parameter, defining the intensity of the load vector:

$$\mathbf{f}(\mathbf{q},\lambda) \equiv \mathbf{r}(\mathbf{q}) - \lambda \mathbf{p}_{\mathrm{r}}(\mathbf{q}). \tag{2}$$

If the loads does not dependent on deformations, like in dead-weight loading, the reference load vector $\mathbf{p}_{\mathrm{r}}$ is independent of the displacement field $\mathbf{q}$.

The system (1) consists of $2N+1$ unknowns, the displacement vector $\mathbf{q}$, the eigenmode $\mathbf{v}$ and the load parameter value λ at the critical state. Since the eigenvector $\mathbf{v}$ is defined uniquely up to a constant, the normalizing condition can be added to the system (1):

$$\mathbf{g}(\mathbf{q},\boldsymbol{\phi},\lambda) = \left\{ \begin{array}{c} \mathbf{f}(\mathbf{q},\lambda) \\ \mathbf{f}'(\mathbf{q},\lambda)\boldsymbol{\phi} \\ N(\boldsymbol{\phi},\lambda) \end{array} \right\} = \mathbf{0}, \tag{3}$$

where the Jacobian matrix $\mathbf{f}' = \partial \mathbf{f}/\partial \mathbf{q}$ is usually denoted by $\mathbf{K}$ in structural applications, and $N(\boldsymbol{\phi})$ defines some normalizing condition to the eigenvector. The Jacobian matrix of the extended system (3) has the form

$$\mathbf{J} = \left[\begin{array}{ccc} \mathbf{K} & \mathbf{0} & -\mathbf{p}_r \\ \mathbf{Z} & \mathbf{K} & \mathbf{z} \\ \mathbf{0}^{\mathrm{T}} & \mathbf{n}^{\mathrm{T}} & a \end{array} \right], \tag{4}$$

where

$$\mathbf{Z} = \left[\mathbf{f}'\boldsymbol{\phi}\right]', \quad \mathbf{z} = \partial(\mathbf{f}'\boldsymbol{\phi})/\partial\lambda, \quad \mathbf{n}^{\mathrm{T}} = \partial N/\partial\boldsymbol{\phi}, \quad \text{and } a = \partial N \partial\lambda. \tag{5}$$

One problem in using Newton's method to the system (3) is the computation of the matrix $\mathbf{Z}$ and vector $\mathbf{z}$. Finite difference approximations are usually used [15, 16, 8, 17, 18, 19, 20].

In order to obtain asymptotically quadratic convergence for the Newton's iteration, the Jacobian should be non-singular at the solution point. For Jacobian of the form (4) this is true only Therefore the use of system (3) is efficient for the computation of limit points only [12]. However, it has been used also to compute bifurcation points in Refs. [9].

Wriggers and Simo [20] regularized the system (3) with penalty terms by appending the constraint $\mathbf{e}_i^T\mathbf{q} = \mu$ to it

$$\mathbf{g}(\mathbf{q},\phi,\lambda,\mu) = \left\{ \begin{array}{c} \mathbf{f}(\mathbf{q},\lambda) + \gamma(\mathbf{e}_i^{\mathrm{T}}\mathbf{q} - \mu)\mathbf{e}_i \\ \mathbf{f}'(\mathbf{q},\lambda)\phi + \gamma(\mathbf{e}_i^{\mathrm{T}}\phi - \phi_0)\mathbf{e}_i \\ \mathbf{e}_i^{\mathrm{T}}\phi - \phi_0 \\ \mathbf{e}_i^{\mathrm{T}}\mathbf{q} - \mu \end{array} \right\} = \mathbf{0}, \tag{6}$$

where γ is the non-negative regularizing penalty parameter and $\mathbf{e}_i$ is a unit vector having the unit value at position i corresponding to the smallest diagonal entry of the factorized tangent stiffness matrix.

2.2 Polynomial eigenvalue problem

Assuming an equilibrium state $(\mathbf{q}_*, \lambda_*)$ with a regular tangent matrix, a Taylor expansion of the non-linear eigenvalue problem (1) with respect to the load parameter λ has the form

$$\mathbf{q} = \mathbf{q}_* + \Delta\lambda\mathbf{q}_1 + \tfrac{1}{2}(\Delta\lambda)^2\mathbf{q}_2 + \cdots, \tag{7}$$

$$\mathbf{f} = \mathbf{f}_* + \Delta\lambda\frac{\mathrm{d}\mathbf{f}}{\mathrm{d}\lambda}\bigg|_* + \frac{1}{2}(\Delta\lambda)^2\frac{\mathrm{d}^2\mathbf{f}}{\mathrm{d}\lambda^2}\bigg|_* + \cdots = \mathbf{0} \tag{8}$$

$$\left(\mathbf{f}'_* + \Delta\lambda\frac{\mathrm{d}\mathbf{f}'}{\mathrm{d}\lambda}\bigg|_* + \frac{1}{2}(\Delta\lambda)^2\frac{\mathrm{d}^2\mathbf{f}'}{\mathrm{d}\lambda^2}\bigg|_* + \cdots\right)\phi = \mathbf{0} \tag{9}$$

where $\Delta\lambda = \lambda - \lambda_*$. Expressions for the derivatives are [1]

$$\frac{\mathrm{d}\mathbf{f}}{\mathrm{d}\lambda} = \frac{\partial\mathbf{f}}{\partial\mathbf{q}}\frac{\partial\mathbf{q}}{\partial\lambda} + \frac{\partial\mathbf{f}}{\partial\lambda} = \mathbf{f}'\dot{\mathbf{q}} + \dot{\mathbf{f}}, \tag{10}$$

$$\frac{\mathrm{d}^2\mathbf{f}}{\mathrm{d}\lambda^2} = \mathbf{f}'\ddot{\mathbf{q}} + \mathbf{f}''\dot{\mathbf{q}}\dot{\mathbf{q}} + 2\dot{\mathbf{f}}'\dot{\mathbf{q}} + \ddot{\mathbf{f}}, \tag{11}$$

$$\frac{\mathrm{d}\mathbf{f}'}{\mathrm{d}\lambda} = \mathbf{f}''\dot{\mathbf{q}} + \dot{\mathbf{f}}', \tag{12}$$

$$\frac{\mathrm{d}^2\mathbf{f}'}{\mathrm{d}\lambda^2} = \mathbf{f}''\ddot{\mathbf{q}} + \mathbf{f}'''\dot{\mathbf{q}}\dot{\mathbf{q}} + 2\dot{\mathbf{f}}''\dot{\mathbf{q}} + \ddot{\mathbf{f}}'. \tag{13}$$

Evaluating these quantities at the equilibrium state $(\mathbf{q}_*, \lambda_*)$, gives

$$\dot{\mathbf{q}}_* = \mathbf{q}_1, \quad \text{and} \quad \ddot{\mathbf{q}}_* = \mathbf{q}_2, \quad \text{etc..} \tag{14}$$

and the expressions (10)-(13) result in

$$\frac{\mathrm{d}\mathbf{f}}{\mathrm{d}\lambda}\bigg|_* = \mathbf{f}'_*\mathbf{q}_1 + \dot{\mathbf{f}}_*, \qquad \frac{\mathrm{d}\mathbf{f}'}{\mathrm{d}\lambda}\bigg|_* = \mathbf{f}''_*\mathbf{q}_1 + \dot{\mathbf{f}}'_*, \tag{15}$$

$$\frac{\mathrm{d}^2\mathbf{f}}{\mathrm{d}\lambda^2}\bigg|_* = \mathbf{f}'_*\mathbf{q}_2 + \mathbf{f}''_*\mathbf{q}_1\mathbf{q}_1 + 2\dot{\mathbf{f}}'_*\mathbf{q}_1 + \ddot{\mathbf{f}}_*, \qquad \frac{\mathrm{d}^2\mathbf{f}'}{\mathrm{d}\lambda^2}\bigg|_* = \mathbf{f}''_*\mathbf{q}_2 + \mathbf{f}'''_*\mathbf{q}_1\mathbf{q}_1 + 2\dot{\mathbf{f}}''_*\mathbf{q}_1 + \ddot{\mathbf{f}}'_*, \tag{16}$$

[1] Notice the difference between derivatives $\mathrm{d}\mathbf{f}/\mathrm{d}\lambda$ and $\dot{\mathbf{f}} = \partial\mathbf{f}/\partial\lambda$, i.e. $\mathrm{d}\mathbf{f}/\mathrm{d}\lambda = \mathbf{f}'(\partial\mathbf{q}/\partial\lambda) + \partial\mathbf{f}/\partial\lambda$.

where $\mathbf{f}_* = \mathbf{f}(\mathbf{q}_*, \lambda_*)$ etc. In the expansion of the equilibrium equations (8) all terms $\mathrm{d}^p\mathbf{f}/\mathrm{d}\lambda^p, p = 1, 2, \ldots$ has to vanish, thus giving the equation to solve the fields $\mathbf{q}_i$

$$\mathbf{f}'_*\mathbf{q}_1 = -\dot{\mathbf{f}}_*, \qquad \mathbf{f}'_*\mathbf{q}_2 = -\left[\mathbf{f}''_*\mathbf{q}_1\mathbf{q}_1 + 2\dot{\mathbf{f}}'_*\mathbf{q}_1 + \ddot{\mathbf{f}}_*\right], \ldots \quad \text{etc.} \tag{17}$$

It is worthwhile to notice that the coefficent matrix to solve $\mathbf{q}_1, \mathbf{q}_2 \ldots$ is the same for all cases. In structural mechanics, the symbol $\mathbf{K}$ is usually used to denote the stiffness matrix, thus the matrices in (9) can be written as

$$\mathbf{K}_{0|*} = \mathbf{f}'_*, \qquad \mathbf{K}_{1|*} = \left.\frac{\mathrm{d}\mathbf{f}}{\mathrm{d}\lambda}\right|_* = \mathbf{f}''_*\mathbf{q}_1 + \dot{\mathbf{f}}'_*, \tag{18}$$

$$\mathbf{K}_{2|*} = \left.\frac{\mathrm{d}^2\mathbf{f}}{\mathrm{d}\lambda^2}\right|_* = \mathbf{f}''_*\mathbf{q}_2 + \mathbf{f}'''_*\mathbf{q}_1\mathbf{q}_1 + 2\dot{\mathbf{f}}''_*\mathbf{q}_1 + \ddot{\mathbf{f}}'_*, \tag{19}$$

and the polynomial eigenvalue problem can be written as

$$\left(\mathbf{K}_{0|*} + \Delta\lambda\mathbf{K}_{1|*} + \tfrac{1}{2}(\Delta\lambda)^2\mathbf{K}_{2|*} + \cdots\right)\phi = \mathbf{0}, \tag{20}$$

In the classical linear stability analysis the reference state is the undeformed stress free configuration. Assuming also dead weight loading, i.e. $\dot{\mathbf{f}}' \equiv \mathbf{0}$, the matrices for the linear stability eigenvalue problem are simply the following:

$$\mathbf{K}_{0|0} = \mathbf{f}'(\mathbf{0}, 0) \tag{21}$$

$$\mathbf{K}_{1|0} = \mathbf{f}''(\mathbf{0}, 0)\mathbf{q}_1, \tag{22}$$

where $\mathbf{K}_{0|0}\mathbf{q}_1 = \mathbf{p}_r$. Therefore the strains are linear functions of the displacements $\mathbf{q}_1$ and the geometric stiffness matrix $\mathbf{K}_{1|0}$ is a linear function of the displacements $\mathbf{q}_1$.

It is seen from the definition of the $\mathbf{K}_{1|0}$ matrix that the "initial stress" state to the linear eigenvalue problem has to be linear with respect to the load parameter change. This is not true if the linear stability eigenvalue problem is solved from

$$\left(\mathbf{K}_{0|*} + s(\mathbf{K}_{0|*} - \mathbf{K}_{0|**})\right)\phi = \mathbf{0}, \tag{23}$$

where $\mathbf{K}_{0|*}$ and $\mathbf{K}_{0|**}$ are the tangent stiffness matrices from two consecutive equilibrium states. It will be a correct approximation to the linear eigenvalue problem only if the load increment $\Delta\lambda = \lambda_* - \lambda_{**}$ is small, i.e. $\mathbf{K}_{1|*} \approx (\Delta\lambda)^{-1}(\mathbf{K}_{0|*} - \mathbf{K}_{0|**})$.

2.3 Some computational issues

One bottleneck in applying the Newton's method to the extended system (3) or (6) is the need to compute the matrix $\mathbf{Z}$ or the vector $\mathbf{z}$ which requires evaluation of the second derivatives of the residual vector with respect to the state variables. If the iteration is started at the undeformed configuration, i.e. at $(\mathbf{q} = \mathbf{0}, \lambda = 0)$ the $\mathbf{Z}$ matrix is simply the initial stress or geometric stiffness matrix formed from the linearized stresses evaluated from a displacement field which is the initial guess of the eigenvector ϕ. This can be seen by comparing equations (5) and (22). A modified Newton scheme, where the $\mathbf{Z}$ matrix is not updated will completely avoid the evaluation of the second derivative terms. However, the rate of convergence can be slow. The vector $\mathbf{z}$ is simply the load stiffness matrix multiplied with the eigenmode approximation.

If direct solvers for the solution of the linearized system is used, a block elimination scheme is a feasible choise. Denoting the extended system (3) as

$$\begin{cases} \mathbf{f}(\mathbf{q},\lambda) = \mathbf{0} \\ \mathbf{h}(\mathbf{q},\boldsymbol{\phi},\lambda) \equiv \mathbf{f}'(\mathbf{q},\lambda)\boldsymbol{\phi} = \mathbf{0} \\ N(\boldsymbol{\phi},\lambda) = 0, \end{cases} \tag{24}$$

the Newton step can be written as

$$\begin{cases} \mathbf{K}\delta\mathbf{q} - \mathbf{p}_{\mathrm{r}}\delta\lambda = -\mathbf{f} \\ \mathbf{Z}\delta\mathbf{q} + \mathbf{K}\delta\boldsymbol{\phi} + \mathbf{z}\delta\lambda = -\mathbf{h} \\ \mathbf{n}^{\mathrm{T}}\delta\boldsymbol{\phi} + a\delta\lambda = -N. \end{cases} \tag{25}$$

Partitioning the iterative steps $\delta\mathbf{q}$ and $\delta\boldsymbol{\phi}$ as

$$\delta\mathbf{q} = \mathbf{q}_f + \mathbf{q}_p\delta\lambda, \quad \delta\boldsymbol{\phi} = \boldsymbol{\phi}_h + \boldsymbol{\phi}_z\delta\lambda, \tag{26}$$

where the vectors $\mathbf{q}_f, \mathbf{q}_p, \boldsymbol{\phi}_h$ and $\boldsymbol{\phi}_z$ can be solved from equations

$$\mathbf{K}\mathbf{q}_f = -\mathbf{f}, \quad \mathbf{K}\mathbf{q}_p = \mathbf{p}_{\mathrm{r}}, \quad \mathbf{K}\boldsymbol{\phi}_h = -\mathbf{h} - \mathbf{Z}\mathbf{q}_f, \quad \mathbf{K}\boldsymbol{\phi}_z = -\mathbf{z} - \mathbf{Z}\mathbf{q}_p. \tag{27}$$

The iterative change in the load parameter can be solved from the normalizing condition resulting in

$$\delta\lambda = -\frac{N + \mathbf{n}^{\mathrm{T}}\boldsymbol{\phi}_h}{a + \mathbf{n}^{\mathrm{T}}\boldsymbol{\phi}_z}. \tag{28}$$

3 GEOMETRICALLY EXACT BEAM MODEL

3.1 Description of rotation

A rotation motion can be represented by rotation operators $\mathbf{R}$ forming a special noncommutative Lie-group of the proper orthogonal linear transformations, which is defined as

$$SO(3) := \left\{ \mathbf{R} : \mathsf{E}^3 \to \mathsf{E}^3 \,\middle|\, \mathbf{R}^{\mathrm{T}}\mathbf{R} = \mathbf{I}, \ \det\mathbf{R} = +1 \right\}, \tag{29}$$

where E^3 denotes the 3-dimensional Euclidean vector space. The rotation tensor can be represented minimally by three parameters, which parametrize rotation tensor only locally. It is well known that there exist no a single three-parametric global presentation of rotation tensor because the rotation group is a compact group. The rotation operator $\mathbf{R}$ can be written in terms of the rotation vector that is defined by $\boldsymbol{\Psi} := \psi\mathbf{n}$, $\mathbf{n} \in \mathsf{E}^3, \psi \in \mathsf{R}_+$. This yields the expression of the rotation operator

$$\mathbf{R} := \mathbf{I} + \frac{\sin\psi}{\psi}\tilde{\boldsymbol{\Psi}} + \frac{1-\cos\psi}{\psi^2}\tilde{\boldsymbol{\Psi}}^2 = \exp(\tilde{\boldsymbol{\Psi}}), \quad \psi = \|\boldsymbol{\Psi}\|, \tag{30}$$

where the skew-symmetric rotation tensor $\tilde{\boldsymbol{\Psi}}$, is defined formally $\tilde{\boldsymbol{\Psi}} := \tilde{\boldsymbol{\Psi}}\times$. Compound rotation can be defined by two different, nevertheless, equivalent ways: the material description, and the spatial description. The material description of a compound rotation is defined as

$$\mathbf{R}\mathbf{R}_{\mathrm{inc}}^{\mathrm{mat}} = \mathbf{R}\exp(\tilde{\boldsymbol{\Theta}}) \quad \mathbf{R}_{\mathrm{inc}}^{\mathrm{mat}}, \mathbf{R} \in SO(3), \tag{31}$$

where $\mathbf{R}_{\mathrm{inc}}^{\mathrm{mat}}$ is an incremental material rotation operator, and $\boldsymbol{\Theta}$ is an incremental material rotation vector with respect to the base point $\mathbf{R} \in SO(3)$. This description is called material, since the

incremental rotation operator acts on a material vector space. Differentiating the material expression of the compound rotation $\mathbf{R}\exp(\eta\,\tilde{\boldsymbol{\Theta}})$ with respect to the parameter η and setting $\eta = 0$, yields the material tangent space at the base point $\mathbf{R} \in SO(3)$, defined as

$$ {}_{\mathrm{mat}}T_{\mathbf{R}}SO(3) := \{\tilde{\boldsymbol{\Theta}}_{\mathbf{R}} := (\mathbf{R}, \tilde{\boldsymbol{\Theta}}) \mid \text{for any } \tilde{\boldsymbol{\Theta}} \in so(3)\}, \tag{32} $$

where the skew-symmetric tensor $\tilde{\boldsymbol{\Theta}}_{\mathbf{R}} \in {}_{\mathrm{mat}}T_{\mathbf{R}}SO(3)$ is an element of the material tangent space. The notation $(\mathbf{R},\ \tilde{\boldsymbol{\Theta}})$, the pair of the rotation operator $\mathbf{R}$ and the skew-symmetric tensor $\tilde{\boldsymbol{\Theta}}$, represents the material skew-symmetric tensor at the base point $\mathbf{R} \in SO(3)$. Considering the material form of a compound rotation (31), with the aid of η-parametrized exponential mappings

$$ \exp(\tilde{\boldsymbol{\Psi}} + \eta\,\delta\tilde{\boldsymbol{\Psi}}) = \exp(\tilde{\boldsymbol{\Theta}})\exp(\eta\,\delta\tilde{\boldsymbol{\Theta}}_{\mathbf{R}}) \tag{33} $$

where we are finding an incremental rotation tensor, the virtual rotation tensor$\delta\tilde{\boldsymbol{\Psi}}$, such that it belongs to the same tangent space as the rotation tensor $\tilde{\boldsymbol{\Psi}}$, i.e. such that $\delta\tilde{\boldsymbol{\Psi}}, \tilde{\boldsymbol{\Psi}} \in {}_{\mathrm{mat}}T_{\mathbf{I}}SO(3)$ with the identity as a base point omitted for simplicity. Taking the derivative of (33) with respect to the parameter η at $\eta = 0$ gives

$$ \delta\tilde{\boldsymbol{\Theta}}_{\mathbf{R}} = \mathbf{T}\cdot\delta\tilde{\boldsymbol{\Theta}} \tag{34} $$

$$ \mathbf{T} := \frac{\sin\psi}{\psi}\mathbf{I} - \frac{1-\cos\psi}{\psi^2}\tilde{\boldsymbol{\Psi}} + \frac{\psi-\sin\psi}{\psi^3}\tilde{\boldsymbol{\Psi}}\otimes\tilde{\boldsymbol{\Psi}} \tag{35} $$

$$ \psi := \|\tilde{\boldsymbol{\Psi}}\|, \quad \mathbf{R} = \exp(\tilde{\boldsymbol{\Psi}}), \quad \lim_{\tilde{\boldsymbol{\Psi}}\to\mathbf{0}} \mathbf{T}(\tilde{\boldsymbol{\Psi}}) = \mathbf{I} \tag{36} $$

where the material tangential transformation $\mathbf{T} = \mathbf{T}(\boldsymbol{\Psi})$ is a linear mapping between the virtual material tangent spaces: ${}_{\mathrm{mat}}T_{\mathbf{I}}SO(3) \rightarrow {}_{\mathrm{mat}}T_{\mathbf{R}}SO(3)$. The virtual incremental rotation vector $\delta\boldsymbol{\Theta}_{\mathbf{R}}$ and the virtual total rotation vector $\delta\boldsymbol{\Psi}$ belong to different vector spaces on the manifold, since the tangential transformation $\mathbf{T}$ is equal to the identity only at $\boldsymbol{\Psi} = \mathbf{0}$. Note that the transformation $\mathbf{T}$ has an effect on the base points, changing the base point $\mathbf{I}$ into $\mathbf{R}$. For convenience, a material vector space on the rotation manifold at any point $\mathbf{R}$ is defined as

$$ {}_{\mathrm{mat}}T_{\mathbf{R}} := \left\{ \boldsymbol{\Theta}_{\mathbf{R}} \in \mathsf{E}^3 \;\middle|\; \tilde{\boldsymbol{\Theta}}_{\mathbf{R}} \in {}_{\mathrm{mat}}T_{\mathbf{R}}SO(3) \right\} \tag{37} $$

where an element of the material vector space is $\boldsymbol{\Theta}_{\mathbf{R}} \in {}_{\mathrm{mat}}T_{\mathbf{R}}$, which is an affine space with the rotation vector $\boldsymbol{\Psi}$ as a base point and the incremental rotation vector $\boldsymbol{\Theta}$ as a tangent vector, then $\mathbf{T} : {}_{\mathrm{mat}}T_{\mathbf{I}} \rightarrow {}_{\mathrm{mat}}T_{\mathbf{R}}$. Definition (37) gives a practical notation for sorting rotation vectors in different tangent spaces.

3.2 Virtual work expression for the Reissner's beam model

In the material representation, the internal virtual work expression for the Reissner's beam model is

$$ \delta W_{\mathrm{int}} = \int_L (\delta\boldsymbol{\Gamma}\cdot\mathbf{N} + \delta\mathbf{K}_{\mathbf{R}}\cdot\mathbf{M}_{\mathbf{R}})\,\mathrm{d}s, \tag{38} $$

where the material curvature tensor is defined by $\tilde{\mathbf{K}}_{\mathbf{R}} := \mathbf{R}^{\mathrm{T}}\mathbf{R}'$, and the prime denotes derivative with respect to the coordinate s along the beam's axis. The material internal force vector $\mathbf{N}$ and the material internal moment vector $\mathbf{M}_{\mathbf{R}}$ are related to the material strain and curvature vectors by a linear constitutive law

$$ \mathbf{N} = \mathbf{C}_{\mathrm{N}}\boldsymbol{\Gamma}, \quad \mathbf{M}_{\mathbf{R}} = \mathbf{C}_{\mathrm{M}}\mathbf{K}_{\mathbf{R}}. \tag{39} $$

The work conjugate of the material vector $\mathbf{N}$ is the variation of the material strain vector $\mathbf{\Gamma}$, defined by the formula and its variation:

$$\mathbf{\Gamma} := \mathbf{R}^{\mathrm{T}}\mathbf{x}'_{\mathrm{c}} - \mathbf{E}_1, \quad \delta\mathbf{\Gamma} = \mathbf{R}^{\mathrm{T}}\delta\mathbf{x}'_{\mathrm{c}} - \delta\tilde{\mathbf{\Theta}}\mathbf{R}^{\mathrm{T}}\mathbf{x}'_{\mathrm{c}}. \tag{40}$$

In the total Lagrangian formulation, the virtual work expression has to be written in terms of the total material rotation vector $\mathbf{\Psi}$ and its virtual counterpart $\delta\mathbf{\Psi}$. The virtual work of the internal forces (38) has the form

$$\delta W_{\mathrm{int}} = \int_L (\delta\mathbf{x}'_{\mathrm{c}} \cdot \mathbf{R}\mathbf{N})\,\mathrm{d}s + \int_L (\delta\mathbf{\Psi} \cdot (-\mathbf{T}^{\mathrm{T}}\widetilde{\mathbf{R}^{\mathrm{T}}\mathbf{x}'_{\mathrm{c}}}\mathbf{N} + \mathbf{C}_1^{\mathrm{T}}(\mathbf{\Psi}', \mathbf{\Psi})\,\mathbf{M}_{\mathbf{R}}) + \delta\mathbf{\Psi}' \cdot \mathbf{T}^{\mathrm{T}}\mathbf{M}_{\mathbf{R}})\,\mathrm{d}s, \tag{41}$$

where the tensor $\mathbf{C}_1$ is given in the Appendix. The internal virtual work can be written compactly as

$$\delta W_{\mathrm{int}} = \int_L \delta\hat{\mathbf{q}} \cdot \mathbf{B}^{\mathrm{T}}\mathbf{F}_{\mathrm{int}}\,\mathrm{d}s, \tag{42}$$

where $\delta\hat{\mathbf{q}} := (\delta\mathbf{x}'_{\mathrm{c}}, \delta\mathbf{\Psi}', \delta\mathbf{\Psi})$. The generalized internal force field $\mathbf{F}_{\mathrm{int}}$ and the kinematic tensor $\mathbf{B}$ are

$$\mathbf{F}_{\mathrm{int}} := \begin{pmatrix} \mathbf{N} \\ \mathbf{M}_{\mathbf{R}} \end{pmatrix}, \quad \mathbf{B} := \begin{pmatrix} \mathbf{R}^{\mathrm{T}} & \mathbf{O} & \widetilde{\mathbf{R}^{\mathrm{T}}\mathbf{x}'_{\mathrm{c}}}\mathbf{T} \\ \mathbf{O} & \mathbf{T} & \mathbf{C}_1(\mathbf{\Psi}', \mathbf{\Psi}) \end{pmatrix}. \tag{43}$$

Moreover, the field $\mathbf{F}_{\mathrm{int}}$ can be given in the term of the material strain and curvature vectors with the aid of the constitutive relations (39). Linearizing the internal work form δW_{int} at the point $\mathbf{q}_0^{\mathrm{T}} = (\mathbf{d}_0^{\mathrm{T}}, \mathbf{\Psi}_0^{\mathrm{T}})$ in the vector direction $\Delta\hat{\mathbf{q}}^{\mathrm{T}} = (\Delta\mathbf{x}'^{\mathrm{T}}_{\mathrm{c}}, \Delta\mathbf{\Psi}'^{\mathrm{T}}, \Delta\mathbf{\Psi}^{\mathrm{T}})$ will result in the equation

$$\mathrm{Lin}\,(\delta W_{\mathrm{int}}(\mathbf{q}; \delta\hat{\mathbf{q}})) = \delta W_{\mathrm{int}}(\mathbf{q}_0; \delta\hat{\mathbf{q}}) + \mathrm{D}_{\mathbf{q}}\delta W_{\mathrm{ext}}(\mathbf{q}_0, \delta\hat{\mathbf{q}}) \cdot \Delta\hat{\mathbf{q}}, \tag{44}$$

where the linear form $\mathrm{D}_{\hat{\mathbf{q}}}\delta W_{\mathrm{int}} \cdot \Delta\hat{\mathbf{q}}$ can be written using the material stiffness tensor $\mathbf{K}_{\mathrm{mat}}$ and the geometric stiffness tensor $\mathbf{K}_\sigma$ as

$$\mathrm{D}_{\hat{\mathbf{q}}}\delta W_{\mathrm{int}} \cdot \Delta\hat{\mathbf{q}} = \int_L (\mathbf{K}_{\mathrm{mat}} + \mathbf{K}_\sigma) : (\delta\hat{\mathbf{q}} \otimes \Delta\hat{\mathbf{q}})\,\mathrm{d}s, \quad \mathbf{K}_{\mathrm{mat}} := \mathbf{B}_0^{\mathrm{T}}\mathbf{C}_{\mathrm{NM}}\mathbf{B}_0, \tag{45}$$

$$\mathbf{K}_\sigma := \begin{pmatrix} \mathbf{O} & \mathbf{O} & -\mathbf{R}\tilde{\mathbf{N}}\mathbf{T} \\ \mathbf{O} & \mathbf{O} & \mathbf{C}_2(\mathbf{M}_{\mathbf{R}}, \mathbf{\Psi}_0) \\ \mathbf{T}^{\mathrm{T}}\tilde{\mathbf{N}}\mathbf{R}^{\mathrm{T}} & \mathbf{C}_2^{\mathrm{T}}(\mathbf{M}_{\mathbf{R}}, \mathbf{\Psi}_0) & \mathbf{K}_{\sigma 33} \end{pmatrix}, \quad \text{where}$$

$$\mathbf{K}_{\sigma 33} = \mathbf{C}_3(\mathbf{M}_{\mathbf{R}}, \mathbf{\Psi}'_0, \mathbf{\Psi}_0) + \mathbf{C}_2(\tilde{\mathbf{N}}\mathbf{R}^{\mathrm{T}}\mathbf{x}'_{\mathrm{c}}, \mathbf{\Psi}_0) + \mathbf{T}^{\mathrm{T}}\tilde{\mathbf{N}}\widetilde{\mathbf{R}^{\mathrm{T}}\mathbf{x}'_{\mathrm{c}}}\mathbf{T}. \tag{46}$$

The material stiffness tensor $\mathbf{K}_{\mathrm{mat}}$ arises from the linearization of the vector $\mathbf{F}_{\mathrm{int}}$ with the aid of kinematic relation, and the geometric stiffness tensor $\mathbf{K}_\sigma$ arises from the linearization of the kinematic operator $\mathbf{B}$. The tensors $\mathbf{C}_2$ and $\mathbf{C}_3$ are given in the Appendix. Note that the material stiffness tensor $\mathbf{K}_{\mathrm{mat}}$ is symmetric due to the symmetry of the elasticity tensor $\mathbf{C}_{\mathrm{NM}}$. In addition, the geometric stiffness $\mathbf{K}_\sigma$ is also a symmetric tensor. This symmetry of the stiffness tensor is due to the local parametrization of the rotation operator.

The $\mathbf{Z}$-matrix, needed in the Jacobian (4) of the extended system (3) can be divided as

$$\mathbf{Z} = \mathbf{Z}_{\mathrm{mat}} + \mathbf{Z}_\sigma, \tag{47}$$

where the matrices can be defined as

$$\int_L \mathbf{Z}_{\mathrm{mat}}\,\mathrm{d}s := \int_L \mathrm{D}_{\hat{\mathbf{q}}}\mathbf{K}_{\mathrm{mat}}\hat{\boldsymbol{\phi}}\,\mathrm{d}s = \int_L \mathrm{D}_{\hat{\mathbf{q}}}\mathbf{B}^{\mathrm{T}}\mathbf{C}\mathbf{B}\hat{\boldsymbol{\phi}}\,\mathrm{d}s, \quad \int_L \mathbf{Z}_\sigma\,\mathrm{d}s := \int_L \mathrm{D}_{\hat{\mathbf{q}}}\mathbf{K}_\sigma\hat{\boldsymbol{\phi}}\,\mathrm{d}s. \tag{48}$$

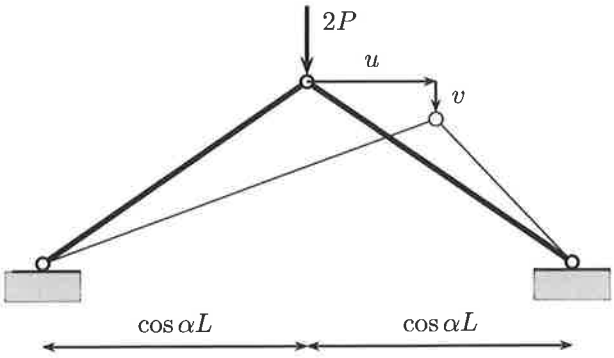

Figure 1: Von Mises truss.

Partitioning the eigenvector $\hat{\phi}$ similarly as the displacement vector $\hat{\mathbf{q}}$: $\hat{\boldsymbol{\phi}}^{\mathrm{T}} := [\boldsymbol{\phi}_1^{\mathrm{T}}, \boldsymbol{\phi}_2^{\mathrm{T}}, \boldsymbol{\phi}_3^{\mathrm{T}}] \sim \hat{\mathbf{q}}^{\mathrm{T}} := [\mathbf{x}'^{\mathrm{T}}_{\mathrm{c}}, \boldsymbol{\Psi}'^{\mathrm{T}}, \boldsymbol{\Psi}^{\mathrm{T}}]$, the matrices $\mathbf{Z}_{\mathrm{mat}}$ and $\mathbf{Z}_\sigma$ have expressions

$$\mathbf{Z}_{\mathrm{mat}} = \mathbf{K}_\sigma(\mathbf{C}_{\mathrm{NM}}\mathbf{B}\hat{\boldsymbol{\phi}}) + \\ + \mathbf{B}^{\mathrm{T}}\mathbf{C}_{\mathrm{NM}} \begin{bmatrix} -\widetilde{\mathbf{T}\boldsymbol{\phi}_3}\mathbf{R}^{\mathrm{T}} & \mathbf{O} & \widetilde{\mathbf{R}^{\mathrm{T}}\boldsymbol{\phi}_1}\mathbf{T} + \widetilde{\mathbf{R}^{\mathrm{T}}\mathbf{x}'_{\mathrm{c}}}\mathbf{C}_1(\boldsymbol{\phi}_3, \boldsymbol{\Psi}) - \widetilde{\mathbf{T}\boldsymbol{\phi}_3}\widetilde{\mathbf{R}^{\mathrm{T}}\mathbf{x}'_{\mathrm{c}}}\mathbf{T} \\ \mathbf{O} & \dot{\mathbf{T}}(\boldsymbol{\phi}_3, \boldsymbol{\Psi}) & \mathbf{C}_1(\boldsymbol{\phi}_2, \boldsymbol{\Psi}) + \mathbf{C}_8(\boldsymbol{\phi}_3, \boldsymbol{\Psi}', \boldsymbol{\Psi}) \end{bmatrix}, \tag{49}$$

and

$$\mathbf{Z}_\sigma = \begin{bmatrix} \mathbf{O} & \mathbf{O} & \widetilde{\mathbf{R}\tilde{\mathbf{N}}\mathbf{T}\boldsymbol{\phi}_3}\mathbf{T} - \mathbf{R}\tilde{\mathbf{N}}\mathbf{C}_1(\boldsymbol{\phi}_3, \boldsymbol{\Psi}) \\ \mathbf{O} & \mathbf{O} & \mathbf{C}_7(\boldsymbol{\phi}_3, \mathbf{M}, \boldsymbol{\Psi}) \\ \dot{\mathbf{T}}^{\mathrm{T}}(\boldsymbol{\phi}_3, \boldsymbol{\Psi})\tilde{\mathbf{N}}\mathbf{R}^{\mathrm{T}} & \mathbf{C}_9(\boldsymbol{\phi}_3, \mathbf{M}, \boldsymbol{\Psi}) & \mathbf{Z}_{\sigma 33} \end{bmatrix} + \mathbf{Z}_{\mathrm{NM}}, \tag{50}$$

where

$$\mathbf{Z}_{\sigma 33} = \mathbf{T}^{\mathrm{T}}\tilde{\mathbf{N}}\widetilde{\mathbf{R}^{\mathrm{T}}\boldsymbol{\phi}_1}\mathbf{T} + \mathbf{C}_1(\tilde{\mathbf{N}}\widetilde{\mathbf{R}^{\mathrm{T}}\boldsymbol{\phi}_1}, \boldsymbol{\Psi}) + \mathbf{C}_3(\mathbf{M}, \boldsymbol{\phi}_2, \boldsymbol{\Psi}) + \mathbf{C}_{10}(\boldsymbol{\phi}_3, \mathbf{M}, \boldsymbol{\Psi}', \boldsymbol{\Psi}) + \dot{\mathbf{T}}^{\mathrm{T}}(\boldsymbol{\phi}_3, \boldsymbol{\Psi})\tilde{\mathbf{N}}\widetilde{\mathbf{R}^{\mathrm{T}}\mathbf{x}'_{\mathrm{c}}}\mathbf{T} + \\ + \mathbf{C}_7(\boldsymbol{\phi}_3, \tilde{\mathbf{N}}\mathbf{R}^{\mathrm{T}}\mathbf{x}'_{\mathrm{c}}, \boldsymbol{\Psi}) + \mathbf{C}_2(\tilde{\mathbf{N}}\widetilde{\mathbf{R}^{\mathrm{T}}\mathbf{x}'_{\mathrm{c}}}\mathbf{T}\boldsymbol{\phi}_3, \boldsymbol{\Psi}) - \mathbf{T}^{\mathrm{T}}\tilde{\mathbf{N}}\widetilde{\mathbf{T}\boldsymbol{\phi}_3}\widetilde{\mathbf{R}^{\mathrm{T}}\mathbf{x}'_{\mathrm{c}}}\mathbf{T} + \mathbf{T}^{\mathrm{T}}\tilde{\mathbf{N}}\widetilde{\mathbf{R}^{\mathrm{T}}\mathbf{x}'_{\mathrm{c}}}\mathbf{C}_1(\boldsymbol{\phi}_3, \boldsymbol{\Psi}) \tag{51}$$

and

$$\mathbf{Z}_{\mathrm{NM}} = \begin{bmatrix} \widetilde{\mathbf{R}\mathbf{T}\boldsymbol{\phi}_3} & \mathbf{O} \\ \mathbf{O} & \dot{\mathbf{T}}^{\mathrm{T}}(\boldsymbol{\phi}_3, \boldsymbol{\Psi}) \\ \mathbf{Z}_{\mathrm{NM}31} & \dot{\mathbf{T}}^{\mathrm{T}}(\boldsymbol{\phi}_2, \boldsymbol{\Psi}) + \dot{\mathbf{C}}_1^{\mathrm{T}}(\boldsymbol{\phi}_3, \boldsymbol{\Psi}', \boldsymbol{\Psi}) \end{bmatrix} \mathbf{C}_{\mathrm{NM}}\mathbf{B}, \tag{52}$$

where

$$\mathbf{Z}_{\mathrm{NM}31} = -\mathbf{T}^{\mathrm{T}}\widetilde{\mathbf{R}^{\mathrm{T}}\boldsymbol{\phi}_1} - \dot{\mathbf{T}}^{\mathrm{T}}(\boldsymbol{\phi}_3, \boldsymbol{\Psi})\widetilde{\mathbf{R}^{\mathrm{T}}\mathbf{x}'_{\mathrm{c}}} - \mathbf{T}^{\mathrm{T}}\mathrm{skew}(\widetilde{\mathbf{R}^{\mathrm{T}}\mathbf{x}'_{\mathrm{c}}}\mathbf{T}\boldsymbol{\phi}_3). \tag{53}$$

4 NUMERICAL EXAMPLE

To demonstrate the behaviour of different scemes, a two bar truss, von Mises truss, is analysed, see fig. 1. Length and the initial angle of the bars at the initial state are L and α, respectively, the axial stiffness equals to EA, and the bars are assumed to be absolutely rigid in bending.

Using the Green-Lagrange definition for the strain and assuming linear relation between the axial force and the strain, $N_i = EA\epsilon_i$, the equilibrium equations take the form

$$\mathbf{f}(\mathbf{q}) = \begin{cases} f_1 = 2c^2q_1 + q_1^3 - 2sq_1q_2 + q_1q_2^2 & = 0 \\ f_2 = -sq_1^2 + q_1^2q_2 + 2s^2q_2 - 3sq_2^2 + q_2^3 - 2\lambda & = 0 \end{cases}, \tag{54}$$

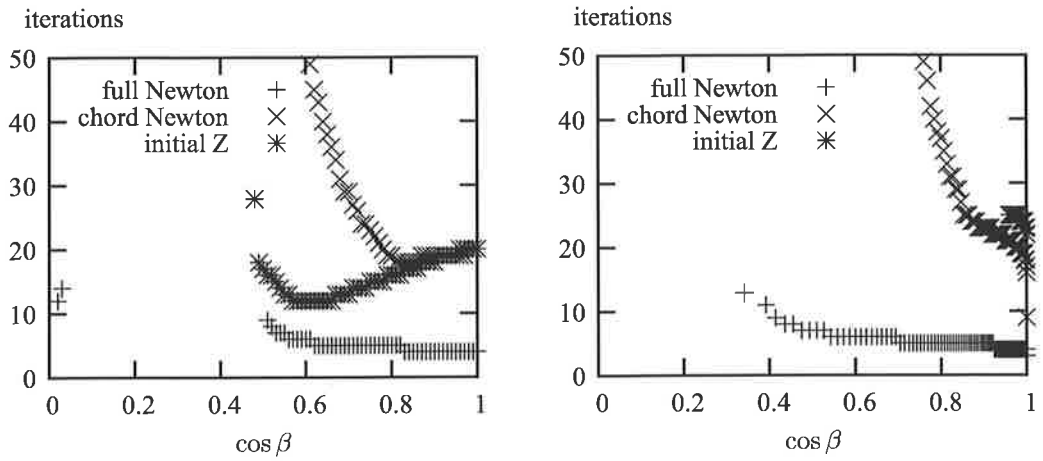

Figure 2: Number of iterations needed for convergence of the three iteration schemes with different intial values of the eigenvector: $\alpha = 30°$ limit point (l.h.s.) and $\alpha = 70°$ bifurcation.

where $\lambda = P/EA$ and the non-dimensional state variables are $q_1 = u/L, q_2 = v/L$ and $s = \sin\alpha$ and $c = \cos\alpha$. If the angle α is less than $\arctan\sqrt{2} \approx 54.75°$, the equilibrium path has a limit point at the load value $\lambda_{\mathrm{cr}} = \frac{1}{9}\sqrt{3}\sin^3\alpha$.

The effect of the initial value for the eigenvector on the convergence is shown in fig. 2. Simple vector norm condition, $N := \|\phi\| - 1 = 0$ is used in the extended system (3). The angle between the initial eigenvector approximation and the converged eigenvector is denoted by β. It should be noted that in the chord Newton the stiffness matrix has to be evaluated at every iteration step due to the criticality condition. The strategy with constant $\mathbf{Z}$-matrix do not work properly for the bifurcation point ($\alpha = 70°$, in fig. 2).

APPENDIX

The tensors $\mathbf{C}_i, i = 1, 2, 3$ are defined by directional derivatives

$$\mathbf{C}_1(\mathbf{V}, \boldsymbol{\Psi}) \cdot \Delta\boldsymbol{\Psi} := \mathrm{D}_{\boldsymbol{\Psi}}(\mathbf{T} \cdot \mathbf{V}) \cdot \Delta\boldsymbol{\Psi}, \tag{55}$$

$$\mathbf{C}_2(\mathbf{V}, \boldsymbol{\Psi}) \cdot \Delta\boldsymbol{\Psi} := \mathrm{D}_{\boldsymbol{\Psi}}(\mathbf{T}^{\mathrm{T}} \cdot \mathbf{V}) \cdot \Delta\boldsymbol{\Psi}, \tag{56}$$

$$\mathbf{C}_3(\mathbf{V}, \boldsymbol{\Psi}', \boldsymbol{\Psi}) \cdot \Delta\boldsymbol{\Psi} := \mathrm{D}_{\boldsymbol{\Psi}}(\mathbf{C}_1^{\mathrm{T}}(\boldsymbol{\Psi}', \boldsymbol{\Psi}) \cdot \mathbf{V}) \cdot \Delta\boldsymbol{\Psi}, \quad \forall \mathbf{V} \in E^3, \tag{57}$$

and have the following explicit expressions

$$\mathbf{C}_1(\mathbf{V}, \boldsymbol{\Psi}) = c_1 \mathbf{V} \otimes \boldsymbol{\Psi} - c_2(\tilde{\boldsymbol{\Psi}}\mathbf{V}) \otimes \boldsymbol{\Psi} + c_3(\boldsymbol{\Psi} \cdot \mathbf{V})\boldsymbol{\Psi} \otimes \boldsymbol{\Psi} - c_4\tilde{\mathbf{V}} + c_5\left((\boldsymbol{\Psi} \cdot \mathbf{V})\mathbf{I} + \boldsymbol{\Psi} \otimes \mathbf{V}\right),$$

$$\mathbf{C}_2(\mathbf{V}, \boldsymbol{\Psi}) = c_1 \mathbf{V} \otimes \boldsymbol{\Psi} + c_2(\tilde{\boldsymbol{\Psi}}\mathbf{V}) \otimes \boldsymbol{\Psi} + c_3\left(\boldsymbol{\Psi} \cdot \mathbf{V}\right)\boldsymbol{\Psi} \otimes \boldsymbol{\Psi} + c_4\tilde{\mathbf{V}} + c_5\left((\boldsymbol{\Psi} \cdot \mathbf{V})\mathbf{I} + \boldsymbol{\Psi} \otimes \mathbf{V}\right),$$

$$\mathbf{C}_3(\mathbf{V}, \boldsymbol{\Psi}', \boldsymbol{\Psi}) = \Big(c_1\left(\boldsymbol{\Psi}' \cdot \mathbf{V}\right) + c_2(\boldsymbol{\Psi} \cdot \tilde{\mathbf{V}}\boldsymbol{\Psi}') + c_3(\boldsymbol{\Psi} \cdot \boldsymbol{\Psi}')(\mathbf{V} \cdot \boldsymbol{\Psi})\Big)\,\mathbf{I} + c_2(\boldsymbol{\Psi} \underset{\mathrm{S}}{\otimes} \tilde{\mathbf{V}}\boldsymbol{\Psi}') +$$

$$+ c_3(\boldsymbol{\Psi} \cdot \boldsymbol{\Psi}')\left(\boldsymbol{\Psi} \underset{\mathrm{S}}{\otimes} \mathbf{V}\right) + \frac{1}{\psi}\Big(c_1'\left(\boldsymbol{\Psi}' \cdot \mathbf{V}\right) + c_2'(\boldsymbol{\Psi} \cdot \tilde{\mathbf{V}}\boldsymbol{\Psi}') + c_3'(\boldsymbol{\Psi} \cdot \boldsymbol{\Psi}')(\mathbf{V} \cdot \boldsymbol{\Psi})\Big)\left(\boldsymbol{\Psi} \otimes \boldsymbol{\Psi}\right) +$$

$$+ c_3(\mathbf{V} \cdot \boldsymbol{\Psi})\left(\boldsymbol{\Psi} \underset{\mathrm{S}}{\otimes} \boldsymbol{\Psi}'\right) + c_5(\boldsymbol{\Psi}' \underset{\mathrm{S}}{\otimes} \mathbf{V}),$$

where $\underset{S}{\otimes}$ denotes the symmetric tensor product $(\mathbf{a} \underset{S}{\otimes} \mathbf{b}) := (\mathbf{a} \otimes \mathbf{b}) + (\mathbf{b} \otimes \mathbf{a}), \quad \forall \mathbf{a}, \mathbf{b} \in E^3$.
The coefficients c_i and their derivatives are given by

$$\begin{aligned} c_1 &:= (\psi \cos\psi - \sin\psi)\psi^{-3}, & c_2 &:= (\psi \sin\psi + 2\cos\psi - 2)\psi^{-4}, \\ c_3 &:= (3\sin\psi - 2\psi - \psi\cos\psi)\psi^{-5}, & c_4 &:= (\cos\psi - 1)\psi^{-2}, \\ c_5 &:= (\psi - \sin\psi)\psi^{-3}, \end{aligned} \tag{58}$$

$$\begin{aligned} c_1' &= (3\sin\psi - \psi^2\sin\psi - 3\psi\cos\psi)\psi^{-4}, \\ c_2' &= (\psi^2\cos\psi - 5\psi\sin\psi - 8\cos\psi + 8)\psi^{-5}, \\ c_3' &= (7\psi\cos\psi + 8\psi + \psi^2\sin\psi - 15\sin\psi)\psi^{-6}, \end{aligned} \tag{59}$$

$$\begin{aligned} c_1'' &= (-\psi^3\cos\psi + 5\psi^2\sin\psi + 12\psi\cos\psi - 12\sin\psi)\psi^{-5}, \\ c_2'' &= -(\psi^3\sin\psi + 8\psi^2\cos\psi - 28\psi\sin\psi - 40\cos\psi + 40)\psi^{-6}, \\ c_3'' &= (\psi^3\cos\psi - 11\psi^2\sin\psi - 50\psi\cos\psi - 40\psi + 90\sin\psi)\psi^{-7}. \end{aligned} \tag{60}$$

The limit processes for the tensors $\mathbf{C}_i$ give

$$\lim_{\boldsymbol{\Psi}\to\mathbf{0}} \mathbf{C}_1(\mathbf{V}, \boldsymbol{\Psi}) = \tfrac{1}{2}\tilde{\mathbf{V}}, \qquad \lim_{\boldsymbol{\Psi}\to\mathbf{0}} \mathbf{C}_2(\mathbf{V}, \boldsymbol{\Psi}) = -\tfrac{1}{2}\tilde{\mathbf{V}}, \tag{61}$$

$$\lim_{\boldsymbol{\Psi}\to\mathbf{0}} \mathbf{C}_3(\mathbf{V}, \boldsymbol{\Psi}', \boldsymbol{\Psi}) = -\tfrac{1}{3}(\boldsymbol{\Psi}' \cdot \mathbf{V})\mathbf{I} + \tfrac{1}{6}(\boldsymbol{\Psi}' \underset{S}{\otimes} \mathbf{V}) \tag{62}$$

The time derivative of the transformation $\mathbf{T}$ is

$$\begin{aligned} &\dot{\mathbf{T}}(\dot{\boldsymbol{\Psi}}, \boldsymbol{\Psi}) = \\ &c_1\left(\boldsymbol{\Psi}\cdot\dot{\boldsymbol{\Psi}}\right)\mathbf{I} - c_2\left(\boldsymbol{\Psi}\cdot\dot{\boldsymbol{\Psi}}\right)\tilde{\boldsymbol{\Psi}} + c_3\left(\boldsymbol{\Psi}\cdot\dot{\boldsymbol{\Psi}}\right)\boldsymbol{\Psi}\otimes\boldsymbol{\Psi} + c_4\dot{\tilde{\boldsymbol{\Psi}}} + c_5\left(\dot{\boldsymbol{\Psi}}\otimes\boldsymbol{\Psi} + \boldsymbol{\Psi}\otimes\dot{\boldsymbol{\Psi}}\right), \end{aligned} \tag{63}$$

where the coefficients are given in (58). The limit value of the tensor $\dot{\mathbf{T}}$ is

$$\lim_{\boldsymbol{\Psi}\to\mathbf{0}} \dot{\mathbf{T}}(\dot{\boldsymbol{\Psi}}, \boldsymbol{\Psi}) = -\tfrac{1}{2}\dot{\tilde{\boldsymbol{\Psi}}}. \tag{64}$$

The tensors $\mathbf{C}_i, i = 7, \ldots, 10$ are defined by directional derivatives

$$\mathbf{C}_7(\mathbf{W}, \mathbf{V}, \boldsymbol{\Psi})\cdot\Delta\boldsymbol{\Psi} := \mathrm{D}_{\boldsymbol{\Psi}}\left(\mathbf{C}_2(\mathbf{V}, \boldsymbol{\Psi})\cdot\mathbf{W}\right)\cdot\Delta\boldsymbol{\Psi}, \tag{65}$$

$$\mathbf{C}_8(\mathbf{W}, \mathbf{V}, \boldsymbol{\Psi})\cdot\Delta\boldsymbol{\Psi} := \mathrm{D}_{\boldsymbol{\Psi}}\left(\mathbf{C}_1(\mathbf{V}, \boldsymbol{\Psi})\cdot\mathbf{W}\right)\cdot\Delta\boldsymbol{\Psi}, \tag{66}$$

$$\mathbf{C}_9(\mathbf{X}, \mathbf{W}, \boldsymbol{\Psi})\cdot\Delta\mathbf{V} := \mathrm{D}_{\mathbf{V}}\left(\mathbf{C}_3(\mathbf{W}, \mathbf{V}, \boldsymbol{\Psi})\cdot\mathbf{X}\right)\cdot\Delta\mathbf{V}, \tag{67}$$

$$\mathbf{C}_{10}(\mathbf{X}, \mathbf{W}, \mathbf{V}, \boldsymbol{\Psi})\cdot\Delta\boldsymbol{\Psi} := \mathrm{D}_{\boldsymbol{\Psi}}\left(\mathbf{C}_3(\mathbf{W}, \mathbf{V}, \boldsymbol{\Psi})\cdot\mathbf{X}\right)\cdot\Delta\boldsymbol{\Psi}, \tag{68}$$

$$\mathrm{D}_{\mathbf{W}}\left(\mathbf{C}_3(\mathbf{W}, \mathbf{V}, \boldsymbol{\Psi})\cdot\mathbf{X}\right) = \dot{\mathbf{C}}_1^{\mathrm{T}}(\mathbf{X}, \mathbf{V}, \boldsymbol{\Psi}), \tag{69}$$

$$\mathrm{D}_{\mathbf{V}}\left(\mathbf{C}_1(\mathbf{V}, \boldsymbol{\Psi})\cdot\mathbf{W}\right) = \dot{\mathbf{T}}(\mathbf{W}, \boldsymbol{\Psi}), \tag{70}$$

$$\mathrm{D}_{\mathbf{V}}\left(\mathbf{C}_2(\mathbf{V}, \boldsymbol{\Psi})\cdot\mathbf{W}\right) = \dot{\mathbf{T}}^{\mathrm{T}}(\mathbf{W}, \boldsymbol{\Psi}), \quad \forall \mathbf{V}, \mathbf{W}, \mathbf{X} \in E^3, \tag{71}$$

and have the following explicit expressions

$$\begin{aligned} \mathbf{C}_7(\mathbf{W}, \mathbf{V}, \boldsymbol{\Psi}) &= c_1\mathbf{V}\otimes\mathbf{W} - c_2(\boldsymbol{\Psi}\cdot\mathbf{W})\tilde{\mathbf{V}} + c_2\tilde{\boldsymbol{\Psi}}\mathbf{V}\otimes\mathbf{W} + c_3(\boldsymbol{\Psi}\cdot\mathbf{W})\boldsymbol{\Psi}\otimes\mathbf{V} + c_3(\boldsymbol{\Psi}\cdot\mathbf{V})\boldsymbol{\Psi}\otimes\mathbf{W} + \\ &+ \left(c_3(\boldsymbol{\Psi}\cdot\mathbf{W})(\boldsymbol{\Psi}\cdot\mathbf{V}) + c_5(\mathbf{W}\cdot\mathbf{V})\right)\mathbf{I} + c_5\mathbf{W}\otimes\mathbf{V} + \frac{c_1'}{\psi}(\boldsymbol{\Psi}\cdot\mathbf{W})\mathbf{V}\otimes\boldsymbol{\Psi} + \frac{c_2'}{\psi}(\boldsymbol{\Psi}\cdot\mathbf{W})\tilde{\boldsymbol{\Psi}}\mathbf{V}\otimes\boldsymbol{\Psi} + \\ &+ \left(\frac{c_3'}{\psi}(\boldsymbol{\Psi}\cdot\mathbf{V})(\boldsymbol{\Psi}\cdot\mathbf{W}) + c_3(\mathbf{W}\cdot\mathbf{V})\right)\boldsymbol{\Psi}\otimes\boldsymbol{\Psi} - c_2\tilde{\mathbf{V}}\mathbf{W}\otimes\boldsymbol{\Psi} + c_3(\boldsymbol{\Psi}\cdot\mathbf{V})\mathbf{W}\otimes\boldsymbol{\Psi} \end{aligned} \tag{72}$$

$$\mathbf{C}_8(\mathbf{W},\mathbf{V},\boldsymbol{\Psi}) = c_1\mathbf{V}\otimes\mathbf{W} + c_2(\boldsymbol{\Psi}\cdot\mathbf{W})\tilde{\mathbf{V}} - c_2\tilde{\boldsymbol{\Psi}}\mathbf{V}\otimes\mathbf{W} + c_3(\boldsymbol{\Psi}\cdot\mathbf{W})\boldsymbol{\Psi}\otimes\mathbf{V} + c_3(\boldsymbol{\Psi}\cdot\mathbf{V})\boldsymbol{\Psi}\otimes\mathbf{W} +$$
$$+ \left(c_3(\boldsymbol{\Psi}\cdot\mathbf{W})(\boldsymbol{\Psi}\cdot\mathbf{V}) + c_5(\mathbf{W}\cdot\mathbf{V})\right)\mathbf{I} + c_5\mathbf{W}\otimes\mathbf{V} + \frac{c_1'}{\psi}(\boldsymbol{\Psi}\cdot\mathbf{W})\mathbf{V}\otimes\boldsymbol{\Psi} - \frac{c_2'}{\psi}(\boldsymbol{\Psi}\cdot\mathbf{W})\tilde{\boldsymbol{\Psi}}\mathbf{V}\otimes\boldsymbol{\Psi} +$$
$$+ \left(\frac{c_3'}{\psi}(\boldsymbol{\Psi}\cdot\mathbf{V})(\boldsymbol{\Psi}\cdot\mathbf{W}) + c_3(\mathbf{W}\cdot\mathbf{V})\right)\boldsymbol{\Psi}\otimes\boldsymbol{\Psi} + c_2\tilde{\mathbf{V}}\mathbf{W}\otimes\boldsymbol{\Psi} + c_3(\boldsymbol{\Psi}\cdot\mathbf{V})\mathbf{W}\otimes\boldsymbol{\Psi} \tag{73}$$

$$\mathbf{C}_9(\mathbf{X},\mathbf{W},\boldsymbol{\Psi}) = c_1\mathbf{X}\otimes\mathbf{W} + c_2\boldsymbol{\Psi}\otimes\tilde{\boldsymbol{\Psi}}\mathbf{W} + c_2\mathbf{X}\otimes\tilde{\boldsymbol{\Psi}}\mathbf{W} + \left(c_3(\mathbf{X}\cdot\mathbf{W}) + \frac{c_3'}{\psi}(\boldsymbol{\Psi}\cdot\mathbf{X})(\boldsymbol{\Psi}\cdot\mathbf{W})\right)\boldsymbol{\Psi}\otimes\boldsymbol{\Psi} +$$
$$+ c_3(\boldsymbol{\Psi}\cdot\mathbf{W})\mathbf{X}\otimes\boldsymbol{\Psi} + c_3(\boldsymbol{\Psi}\cdot\mathbf{W})\boldsymbol{\Psi}\otimes\mathbf{X} + c_5\mathbf{W}\otimes\mathbf{X} + (c_5(\mathbf{W}\cdot\mathbf{X}) + c_3(\boldsymbol{\Psi}\cdot\mathbf{X})(\boldsymbol{\Psi}\cdot\mathbf{W}))\mathbf{I} +$$
$$+ \frac{c_1'}{\psi}(\boldsymbol{\Psi}\cdot\mathbf{X})\boldsymbol{\Psi}\otimes\mathbf{W} + \frac{c_2'}{\psi}(\boldsymbol{\Psi}\cdot\mathbf{X})\boldsymbol{\Psi}\otimes\tilde{\boldsymbol{\Psi}}\mathbf{W} + c_2(\boldsymbol{\Psi}\cdot\mathbf{X})\tilde{\mathbf{W}} + c_3(\boldsymbol{\Psi}\cdot\mathbf{X})\mathbf{W}\otimes\boldsymbol{\Psi} \tag{74}$$

$$\mathbf{C}_{10}(\mathbf{X},\mathbf{V},\boldsymbol{\Psi}',\boldsymbol{\Psi}) = \left(c_2(\tilde{\mathbf{V}}\boldsymbol{\Psi}'\cdot\mathbf{X}) + c_3(\boldsymbol{\Psi}\cdot\boldsymbol{\Psi}')(\mathbf{V}\cdot\mathbf{X}) + c_3(\boldsymbol{\Psi}\cdot\mathbf{V})(\boldsymbol{\Psi}'\cdot\mathbf{V})\right)\mathbf{I} +$$
$$+ \frac{1}{\psi^2}\left(c_1''(\boldsymbol{\Psi}'\cdot\mathbf{V}) + c_2''(\boldsymbol{\Psi}\cdot\tilde{\mathbf{V}}\boldsymbol{\Psi}') + c_3''(\boldsymbol{\Psi}\cdot\boldsymbol{\Psi}')(\mathbf{V}\cdot\boldsymbol{\Psi})\right)(\boldsymbol{\Psi}\cdot\mathbf{X})\boldsymbol{\Psi}\otimes\boldsymbol{\Psi} +$$
$$+ \frac{1}{\psi}\left(c_3'(\mathbf{V}\cdot\boldsymbol{\Psi})(\boldsymbol{\Psi}'\cdot\mathbf{X}) + c_3'(\boldsymbol{\Psi}'\cdot\boldsymbol{\Psi})(\mathbf{V}\cdot\mathbf{X}) + c_2'(\tilde{\mathbf{V}}\boldsymbol{\Psi}'\cdot\mathbf{X})\right)\boldsymbol{\Psi}\otimes\boldsymbol{\Psi} +$$
$$+ \frac{1}{\psi}\left(c_1'(\boldsymbol{\Psi}'\cdot\mathbf{V}) + c_2'(\boldsymbol{\Psi}\cdot\tilde{\mathbf{V}}\boldsymbol{\Psi}') + c_3'(\boldsymbol{\Psi}\cdot\boldsymbol{\Psi}')(\mathbf{V}\cdot\boldsymbol{\Psi})\right)(\boldsymbol{\Psi}\cdot\mathbf{X})(\mathbf{I} - \frac{1}{\psi^2}\boldsymbol{\Psi}\otimes\boldsymbol{\Psi}) + c_2\mathbf{X}\underset{\mathrm{S}}{\otimes}\tilde{\mathbf{V}}\boldsymbol{\Psi}' +$$
$$+ \left(c_3(\mathbf{V}\cdot\mathbf{X}) + \frac{c_3'}{\psi}(\boldsymbol{\Psi}\cdot\mathbf{X})(\mathbf{V}\cdot\boldsymbol{\Psi})\right)\boldsymbol{\Psi}\underset{\mathrm{S}}{\otimes}\boldsymbol{\Psi}' + c_3(\mathbf{V}\cdot\boldsymbol{\Psi})\mathbf{X}\underset{\mathrm{S}}{\otimes}\boldsymbol{\Psi}' + c_3(\boldsymbol{\Psi}\cdot\boldsymbol{\Psi}')\mathbf{X}\underset{\mathrm{S}}{\otimes}\mathbf{V} + c_3(\mathbf{X}\cdot\boldsymbol{\Psi})\mathbf{V}\underset{\mathrm{S}}{\otimes}\boldsymbol{\Psi} +$$
$$+ \frac{1}{\psi}\left(c_1'(\boldsymbol{\Psi}'\cdot\mathbf{V}) + c_2'(\boldsymbol{\Psi}\cdot\tilde{\mathbf{V}}\boldsymbol{\Psi}') + c_3'(\boldsymbol{\Psi}\cdot\boldsymbol{\Psi}')(\mathbf{V}\cdot\boldsymbol{\Psi})\right)\boldsymbol{\Psi}\underset{\mathrm{S}}{\otimes}\mathbf{X} +$$
$$+ \left(c_3(\boldsymbol{\Psi}'\cdot\mathbf{X}) + \frac{c_3'}{\psi}(\boldsymbol{\Psi}\cdot\mathbf{X})(\boldsymbol{\Psi}\cdot\boldsymbol{\Psi}')\right)\boldsymbol{\Psi}\underset{\mathrm{S}}{\otimes}\mathbf{V}\frac{1}{\psi}c_2'(\mathbf{X}\cdot\boldsymbol{\Psi})\boldsymbol{\Psi}\underset{\mathrm{S}}{\otimes}\tilde{\mathbf{V}}\boldsymbol{\Psi}' \tag{75}$$

$$\dot{\mathbf{C}}_1(\mathbf{X},\mathbf{V},\boldsymbol{\Psi}) = c_1\mathbf{V}\otimes\mathbf{X} - c_2(\tilde{\mathbf{X}}\mathbf{V})\otimes\boldsymbol{\Psi} - c_2(\tilde{\boldsymbol{\Psi}}\mathbf{V})\otimes\mathbf{X} + \left(c_3(\mathbf{X}\cdot\mathbf{V}) + \frac{c_3'}{\psi}(\boldsymbol{\Psi}\cdot\mathbf{X})(\boldsymbol{\Psi}\cdot\mathbf{V})\right)\boldsymbol{\Psi}\otimes\boldsymbol{\Psi} +$$
$$+ c_3(\boldsymbol{\Psi}\cdot\mathbf{V})\mathbf{X}\otimes\boldsymbol{\Psi} + c_3(\boldsymbol{\Psi}\cdot\mathbf{V})\boldsymbol{\Psi}\otimes\mathbf{X} + (c_5(\mathbf{X}\cdot\mathbf{V}) + c_3(\boldsymbol{\Psi}\cdot\mathbf{X})(\boldsymbol{\Psi}\cdot\mathbf{V}))\mathbf{I} + c_5\mathbf{X}\otimes\mathbf{V} +$$
$$+ \frac{c_1'}{\psi}(\boldsymbol{\Psi}\cdot\mathbf{X})\mathbf{V}\otimes\boldsymbol{\Psi} - \frac{c_2'}{\psi}(\boldsymbol{\Psi}\cdot\mathbf{X})(\tilde{\boldsymbol{\Psi}}\mathbf{V})\otimes\boldsymbol{\Psi} + c_2(\boldsymbol{\Psi}\cdot\mathbf{X})\tilde{\mathbf{V}} + c_3(\boldsymbol{\Psi}\cdot\mathbf{X})\boldsymbol{\Psi}\otimes\mathbf{V} \tag{76}$$

The limit processes for the tensors $\mathbf{C}_i, i = 7,\ldots,10$ give

$$\lim_{\boldsymbol{\Psi}\to\mathbf{0}}\mathbf{C}_7(\mathbf{W},\mathbf{V},\boldsymbol{\Psi}) = -\tfrac{1}{3}\mathbf{V}\otimes\mathbf{W} + \tfrac{1}{6}(\mathbf{W}\otimes\mathbf{V} + (\mathbf{W}\cdot\mathbf{V})\mathbf{I}) \tag{77}$$

$$\lim_{\boldsymbol{\Psi}\to\mathbf{0}}\mathbf{C}_8(\mathbf{W},\mathbf{V},\boldsymbol{\Psi}) = -\tfrac{1}{3}\mathbf{V}\otimes\mathbf{W} + \tfrac{1}{6}(\mathbf{W}\otimes\mathbf{V} + (\mathbf{W}\cdot\mathbf{V})\mathbf{I}), \tag{78}$$

$$\lim_{\boldsymbol{\Psi}\to\mathbf{0}}\mathbf{C}_9(\mathbf{X},\mathbf{W},\boldsymbol{\Psi}) = -\tfrac{1}{3}\mathbf{X}\otimes\mathbf{V} + \tfrac{1}{6}((\mathbf{X}\cdot\mathbf{V})\mathbf{I} + \mathbf{V}\otimes\mathbf{X}) \tag{79}$$

$$\lim_{\boldsymbol{\Psi}\to\mathbf{0}}\mathbf{C}_{10}(\mathbf{X},\mathbf{V},\boldsymbol{\Psi}',\boldsymbol{\Psi}) = -\tfrac{1}{12}(\tilde{\mathbf{V}}\boldsymbol{\Psi}'\cdot\mathbf{X})\mathbf{I} - \tfrac{1}{12}\mathbf{X}\underset{\mathrm{S}}{\otimes}\tilde{\mathbf{V}}\boldsymbol{\Psi}' \tag{80}$$

$$\lim_{\boldsymbol{\Psi}\to\mathbf{0}}\dot{\mathbf{C}}_1(\mathbf{X},\mathbf{V},\boldsymbol{\Psi}) = -\tfrac{1}{3}\mathbf{V}\otimes\mathbf{X} + \tfrac{1}{6}((\mathbf{X}\cdot\mathbf{V})\mathbf{I} + \mathbf{X}\otimes\mathbf{V}) \tag{81}$$

REFERENCES

[1] E. Riks. The incremental solution of some basic problems in elastic stability. Technical Report NLR TR 74005 U, National Aerospace Laboratory, The Netherlands, 1974.

[2] E. Riks. An incremental approach to the solution of snapping and buckling problems. *International Journal of Solids and Structures*, 15:529–551, 1979.

[3] P.G. Bergan, G. Horrigmoe, and B. Kråkeland. Solution techniques for nonlinear finite element problems. *International Journal for Numerical Methods in Engineering*, 12:1677–1696, 1978.

[4] W. Wagner and P. Wriggers. A simple method for the calculation of postcritical branches. *Engineering Computation*, 5:103–109, 1988.

[5] J. Huitfeldt. Nonlinear eigenvalue problems - prediction of bifurcation points and branch switching. Technical Report 17, Department of Computer Sciences, Chalmers University of technology, 1991.

[6] J. Huitfeldt and A. Ruhe. A new algorithm for numerical path following applied to an example from hydrodynamic flow. *SIAM Journal on Scientific and Statistical Computing*, 11:1181–1192, 1990.

[7] J.P. Abbot. An efficient algorithm for the determination of certain bifurcation points. *Journal Computational and Applied Mathematics*, 4:19–27, 1987.

[8] J.-M. Battini, C. Pacoste and A. Eriksson. Improved minimal augmentation procedure for the direct computation of critical points. *Computer Methods in Applied Mechanics and Engineering*, 192:2169–2185, 2003.

[9] R. Seydel. Numerical computation of branch points in nonlinear equations. *Numerische Mathematik*, 33:339–352, 1979.

[10] J.P. Keener and H.B. Keller. Perturbed bifurcation theory. *Archive for Rational Mechanics and Analysis*, 50:159–175, 1973.

[11] J.P. Fink and W.C. Rheinboldt. The role of tangent mapping in analyzing bifurcation behaviour. *Zeitschrift für Angewandte Mathematik und Mechanik*, 64(9):407–412, 1984.

[12] B. Werner and A. Spence. The computation of symmetry-breaking bifurcation points. *SIAM Journal on Numerical Analysis*, 21:388–399, 1984.

[13] P. Wriggers, W. Wagner and C. Miehe. A quadratically convergent procedure for the calculation of stability points in finite element analysis. *Computer Methods in Applied Mechanics and Engineering*, 70: 329–347, 1988.

[14] J.P. Keener. Perturbed bifurcation theory at multiple eigenvalues. *Archive for Rational Mechanics and Analysis*, 56:348–366, 1974.

[15] A. Eriksson. Derivatives of tangential stiffness matrices for equilibrium path descriptions. *International Journal for Numerical Methods in Engineering*, 32:1093–1113, 1991.

[16] A. Eriksson. Fold lines for sensitivity analyses in structural instability. *Computer Methods in Applied Mechanics and Engineering*, 114:77–101, 1994.

[17] S. Lopez. Detection of bifurcation points along a curve traced by a continuation method. *International Journal for Numerical Methods in Engineering*, 53:983–1004, 2002.

[18] S. Lopez. Post-critical analysis of structures with a nonlinear pre-buckling state in the presence of imperfections. *Computer Methods in Applied Mechanics and Engineering*, 191:4421–4440, 2002.

[19] A. Magnusson and I. Svensson. Numerical treatment of complete load-deflection curves. *International Journal for Numerical Methods in Engineering*, 41:955–971, 1998.

[20] P. Wriggers and J.C. Simo. A general procedure for the direct computation of turning and bifurcation problems. *International Journal for Numerical Methods in Engineering*, 30:155–176, 1990.

[21] A. Ibrahimbegović and M. Al Mikdad. Quadratically convergent direct calculation of critical points for 3d structures undergoing finite rotations. *Computer Methods in Applied Mechanics and Engineering*, 189:107–120, 2000.

[22] J. Mäkinen. Total Lagrangian Reissner's goemetrically exact beam element without singularities. *International Journal for Numerical Methods in Engineering*, 70:1009–1048, 2007.

[23] J. Mäkinen. Rotation manifold SO(3) and its tangential vectors. *Computational Mechanics*. 42:907–919, 2008.

ANOMALOUS BUCKLING BEHAVIOUR OF TRUSS BEAMS

ALEXIS FEDOROFF and REIJO KOUHIA

Department of Structural Engineering and Building Technology
Helsinki University of Technology, P.O. Box 2100, FI-02015 TKK, Finland

ABSTRACT

A thorough stability analysis of a simple but representative truss beam, modeled as a finite degree of freedom system, is carried out. Depending on the main dimensions of the truss, different buckling modes are possible. One possible buckling mode is characterized by rigid body motion of the compressed member. It will be shown that this buckling mode is not included in the spectrum of the linearized buckling eigenvalue problem. Also the postbuckling behavior is studied in detail.

1 INTRODUCTION

Truss beams are widely used constructive elements due to lightness and high load carrying capacity. Although it is used in very basic building types, such as parking lots, shopping centres and industrial buildings, there seems to be no clear understanding of the structural behaviour or specific regulation in most design codes. Indeed, the design codes for steel construction focus mainly on the dimensioning and design of individual nodes and bars of the truss beam. Typically the designer would calculate resultant forces in each member of the truss using linear theory and compare the obtained effort to the non-linear resistance capacity of the member. In most design codes this non-linear resistance capacity accounts for combined buckling and yielding. The design procedure then assumes that the structure is safe when each compressed member is checked against buckling and each tension member is checked against yield failure.

To ensure stability of the truss against lateral buckling, the designer would restrict lateral movement of the upper chord typically with roof sheeting or purlins. In most situations the lower chord is left free to move laterally. This design choice is based on the assumption that a solid beam does not buckle laterally if the upper chord lateral movement is restricted. However, is this assumption true for a truss beam? In this article, it will be shown with a simple example case that there exists, indeed, a previously unreckoned buckling mode characterized by the rotation and sway of the compressed member as a rigid body while the upper chord undergoes torsion along its axis.

A thorough stability analysis of a simple but representative truss beam, modelled as a finite degree of freedom system, is carried out. Depending on the main dimensions of the truss, different buckling modes are possible. One possible buckling mode is characterized by lateral movement of the lower chord while the compressed vertical member buckles as a rigid body. It will be shown that this buckling mode is not included in the spectrum of the linearized buckling eigenvalue problem. Also the post buckling behaviour is studied in detail.

2 A TRUSS BEAM MODEL

The structure we are about to investigate consists of five members, as per figure 1: the upper chord member (1) and (2), a compressed vertical member (3) and the diagonal tensile members (4) and (5). The application point D of the load F is modeled by a undeformable member (6). Due to the symmetry of the problem with respect to the axis BC we may investigate only half of the structure consisting of members (1), (3) and (4).

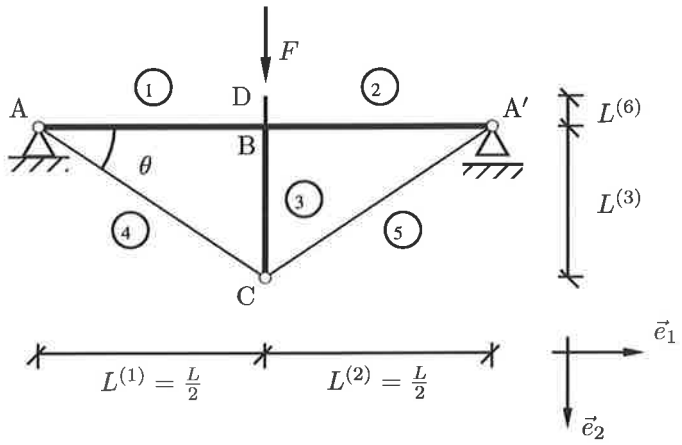

Figure 1: Truss Beam Model

2.1 Model Assumptions

The potential energy functional of the system may be formally written as the sum of internal energies due to each member of the assembly plus the work done by external forces

$$\begin{aligned} \Pi : \mathscr{C}([0, L^{(1)}]) \times ... \times \mathscr{C}([0, L^{(6)}]) \times \mathbb{R} &\longrightarrow \mathbb{R} \\ (\boldsymbol{u}^{(1)}, ..., \boldsymbol{u}^{(6)}, F) &\longmapsto \sum_{e=1}^{6} U^{(e)}(\boldsymbol{u}^{(e)}) - F\,V(\boldsymbol{u}^{(1)}, \ldots, \boldsymbol{u}^{(6)}) \end{aligned}$$

The continuous functions $\boldsymbol{u}^{(e)} : [0, L^{(e)}] \longrightarrow \mathbb{R}^6$ such as $\boldsymbol{u}^{(e)} = (u_1^{(e)}, u_2^{(e)}, u_3^{(e)}, \phi_1^{(e)}, \phi_2^{(e)}, \phi_3^{(e)})$ describe the displacements and rotations for a given member e. The internal energies $U^{(e)} \in \mathscr{L}_2([0, L^{(e)}])$ are square integrable functions on their respective domain. Without a proof, we claim that for small displacements this continuous representation of potential energy can be equated to a discrete representation:

$$\begin{aligned} \Pi : \mathbb{R}^{M+1} &\longrightarrow \mathbb{R} \\ (\boldsymbol{x}, F) &\longmapsto \sum_{e=1}^{6} U^{(e)}(\boldsymbol{x}) - F\,V(\boldsymbol{x}) \end{aligned}$$

Consider the vector $\boldsymbol{x} \in \mathbb{R}^M$, (here $M = 5$) where the meaning of the components is explained in table 1. Assuming linear elastic behaviour, we can then express the internal energy functionals and

Table 1: Discrete state variables.

x_1	$\phi_1^{(1)} := \phi_1^{(1)}(L^{(1)})$	torsion angle of member (1) at point B
x_2	$u_3^{(1)} := u_3^{(1)}(L^{(1)})$	lateral displacement of member (1) at point B
x_3	$u_2^{(1)} := u_2^{(1)}(L^{(1)})$	vertical displacement of member (1) at point B
x_4	$\epsilon_{11}^{(1)} := \partial_1 u_1^{(1)}(L^{(1)})$	axial strain of member (1) at point B
x_5	$\epsilon_{11}^{(3)} := \partial_1 u_1^{(3)}(L^{(3)})$	axial strain of member (3) at point B

Table 2: Stiffness Coefficients

$c_1^{(1)}$	:=	$GI_t^{(1)}/L^{(1)}$	torsional stiffness of member (1)
$k_3^{(1)}$	:=	$3\,EI_{13}^{(1)}/{L^{(1)}}^3$	lateral stiffness of member (1)
$k_2^{(1)}$	:=	$3\,EI_{12}^{(1)}/{L^{(1)}}^3$	vertical stiffness of member (1)
$k_1^{(1)}$	:=	$EA^{(1)}/L^{(1)}$	axial stiffness of member (1)
$k_1^{(3)}$	:=	$EA^{(3)}/L^{(3)}$	axial stiffness of member (3)
$k_1^{(4)}$	:=	$EA^{(4)}/L^{(4)}$	axial stiffness of member (4)

work done by external forces can be expressed as follows:

$$
\begin{aligned}
U^{(1)}(\boldsymbol{x}) &= \frac{1}{2}c_1^{(1)}\ {\phi_1^{(1)}}^2 + \frac{1}{2}k_3^{(1)}\ {u_3^{(1)}}^2 + \frac{1}{2}k_2^{(1)}\ {u_2^{(1)}}^2 + \frac{1}{2}k_1^{(1)}\ \left(\epsilon_{11}^{(1)}\,L^{(1)}\right)^2 \\
U^{(2)}(\boldsymbol{x}) &= U^{(1)}(\boldsymbol{x}) \\
U^{(3)}(\boldsymbol{x}) &= \frac{1}{2}k_1^{(3)}\ \left(\epsilon_{11}^{(3)}\,L^{(3)}\right)^2 \\
U^{(4)}(\boldsymbol{x}) &= \frac{1}{2}k_1^{(4)}\ \left(\epsilon_{11}^{(4)}\,L^{(4)}\right)^2 \\
U^{(5)}(\boldsymbol{x}) &= U^{(4)}(\boldsymbol{x}) \\
U^{(6)}(\boldsymbol{x}) &= 0 \\
V(\boldsymbol{x}) &= L^{(6)}\,(1-\cos\phi_1^{(1)}) + u_2^{(1)}
\end{aligned}
$$

where the constraint equation that expresses the stain in member (4) is defined as follows: (assume $\cos^2\theta = L^{(1)}/L^{(4)}$, $\sin^2\theta = L^{(3)}/L^{(4)}$)

$$
\epsilon_{11}^{(4)} := \cos^2\theta\,\epsilon_{11}^{(1)} + \sin^2\theta\,\epsilon_{11}^{(3)} + \sin\theta\,\cos\theta\,(1+\epsilon_{11}^{(3)})\left(\frac{u_2^{(1)}}{L^{(1)}}\,\cos\phi_1^{(1)} + \frac{u_3^{(1)}}{L^{(1)}}\,\sin\phi_1^{(1)}\right)
$$

dividing the total potential energy functional Π by $2\,c_1^{(1)}$ yields the non dimensional form as follows:

$$
P(\boldsymbol{q},\lambda) = \sum_{t=1}^{5}\frac{1}{2}\,\alpha_t\,q_t^2 + \frac{1}{2}\,\alpha_6\,Q_6^2(\boldsymbol{q}) - \lambda(q_3 + \rho\,R(\boldsymbol{q}))
$$

such as $P := \Pi/(2\,c_1^{(1)})$, $\lambda := F\,L^{(1)}/(2\,c_1^{(1)})$, and where the non dimensional variables are defined as follows:

$$\begin{pmatrix} q_1 \\ q_2 \\ q_3 \\ q_4 \\ q_5 \end{pmatrix} := \begin{pmatrix} \phi_1^{(1)} \\ u_3^{(1)}/L^{(1)} \\ u_2^{(1)}/L^{(1)} \\ \epsilon_{11}^{(1)} \\ \epsilon_{11}^{(3)} \end{pmatrix}$$

the non-dimensional stiffnesses α_i are defined in table 3 and the constraint equations are $Q_6(\boldsymbol{q}) := \cos^2\theta\,q_4 + \sin^2\theta\,q_5 + \sin\theta\,\cos\theta\,(1+q_5)\,(q_3\,\cos q_1 + q_2\,\sin q_1)$ and $R(\boldsymbol{q}) := 1 - \cos q_1$. The non-dimensional eccentricity of load-application point $\rho = L^{(6)}/L^{(1)}$.

Table 3: Non-dimensional stiffness coefficients.

$\alpha_1 :=$	1
$\alpha_2 :=$	$(2\,k_3^{(1)}\,(L^{(1)})^2)/(2\,c_1^{(1)})$
$\alpha_3 :=$	$(2\,k_2^{(1)}\,(L^{(1)})^2)/(2\,c_1^{(1)})$
$\alpha_4 :=$	$(2\,k_1^{(1)}\,(L^{(1)})^2)/(2\,c_1^{(1)})$
$\alpha_5 :=$	$(k_1^{(3)}\,(L^{(3)})^2)/(2\,c_1^{(1)})$
$\alpha_6 :=$	$(2\,k_1^{(4)}\,(L^{(4)})^2)/(2\,c_1^{(1)})$

3 ASYMPTOTIC ANALYSIS

In this section we develop the reduced potential energy taking inspiration from Koiter reduction theory [1, 2]. Although Koiter's works mainly focused on continuous functionals, here we are in presence of a discrete formulation. Hence we can observe some minor differences when comparing to the results obtained by Koiter [3, 4]. Essentially the Koiter's initial post-buckling theory is a kind of a Liapunov-Schmit type reduction technique [5, 6]. Assume $P : \mathbb{R}^{M+1} \to \mathbb{R} : (\boldsymbol{q}, \lambda) \mapsto P(\boldsymbol{q}, \lambda)$ a functional that describes the total potential energy of a discrete system which exhibits pitchfork type symmetric bifurcation behaviour. Additionally we assume that $P(\boldsymbol{q}, \cdot) : \mathbb{R} \to \mathbb{R}$ is linear. The internal energy part of a linear elastic system can always be expressed as a diagonal quadratic form, $U(\boldsymbol{q}) = \sum_{t\geq 1} \frac{1}{2}\,\alpha_t\,Q_t^2(\boldsymbol{q})$ and the work done by external forces as a linear form $\lambda\,V(\boldsymbol{q}) = \lambda\,\sum_{t\geq 1} R_t(\boldsymbol{q})$. We can always find a coordinate system, at least locally, such as $Q_t(\boldsymbol{q}) = q_t$ for $1 \leq t \leq M$, and $R_1(\boldsymbol{q}) = q_{m+1}$ where q_{m+1} is the first non-zero coordinate in the equilibrium set on primary path. We note also $R(\boldsymbol{q}) := \sum_{t\geq 2} R_t(\boldsymbol{q})$. Consider the general equilibrium set $E := \left\{(\boldsymbol{q}, \lambda) \in \mathbb{R}^{M+1} \;:\; P_{\boldsymbol{q}}(\boldsymbol{q}, \lambda) = 0\right\}$ and the equilibrium set on the primary path $E_I := \{(\boldsymbol{q}, \lambda) \in E \;:\; q_i = 0\; for\; 1 \leq i \leq m < M\} \subset E$. With these assumptions we can write a potential energy expression for discrete linear elastic system with distinct primary path:

$$P(\boldsymbol{q}, \lambda) = \sum_{t=1}^{M} \frac{1}{2}\,\alpha_t\,q_t^2 + \sum_{t>M} \frac{1}{2}\,\alpha_6\,Q_6^2(\boldsymbol{q}) - \lambda(q_{m+1} + R(\boldsymbol{q})) \tag{1}$$

We can make a few remarks on the form of the potential energy as expressed in equation (1) and its derivatives. The equilibrium set on the primary path E_I is a 1-manifold in a $\mathbb{R}^{M-m+1}$ space, which implies that m of the M equations $P_{\boldsymbol{q}}(\hat{\boldsymbol{q}}, \hat{\lambda})_i = 0$ have to hold identically. It comes out that the

first derivative is of the form:

$$\hat{P}_{\boldsymbol{q}} = \begin{pmatrix} 0 \\ \hat{P}_{\boldsymbol{q}}\,(m+1..M) \end{pmatrix} \tag{2}$$

Similarly we get from the second derivative a block diagonal matrix form:

$$\hat{P}_{\boldsymbol{qq}} = \begin{pmatrix} \hat{P}_{\boldsymbol{qq}}\,(1..m, 1..m) & 0 \\ 0 & \hat{P}_{\boldsymbol{qq}}\,(m+1..M, m+1..M) \end{pmatrix} \tag{3}$$

These properties propagate of course to higher order derivatives also. Further, since $\hat{P}_{\boldsymbol{qq}}$ is symmetric, it is diagonalizable. Hence $\exists\, \boldsymbol{\Phi} \in \mathbb{R}^{M\times M}$ unitary ($\boldsymbol{\Phi}\,\boldsymbol{\Phi}^T = \boldsymbol{\Phi}^T\,\boldsymbol{\Phi} = \boldsymbol{I}$) such as $\boldsymbol{\Phi}^T\,\hat{P}_{\boldsymbol{qq}}\,\boldsymbol{\Phi} = \mathrm{diag}(0, ..., 0, d_{R+1}, ..., d_M)$ assuming that $\dim \mathrm{Ker}\,\hat{P}_{\boldsymbol{qq}} = R \leq m$. Due to the block matrix shape of $\hat{P}_{\boldsymbol{qq}}$ in equation (3) we get the following form for the unitary matrix $\boldsymbol{\Phi}$:

$$\boldsymbol{\Phi} = \begin{pmatrix} \boldsymbol{\Phi}\,(1..m, 1..m) & 0 \\ 0 & \boldsymbol{\Phi}\,(m+1..M, m+1..M) \end{pmatrix} \tag{4}$$

Considering $\boldsymbol{\phi}_p$ as the p-th column vector of $\boldsymbol{\Phi}$ we get that $\{\boldsymbol{\phi}_1, ..., \boldsymbol{\phi}_M\}$ is a orthonormal basis of $\mathbb{R}^M = \mathrm{Ker}\,\hat{P}_{\boldsymbol{qq}} \oplus \mathrm{Ker}\,\hat{P}_{\boldsymbol{qq}}{}^{\perp}$. Hence $\{\boldsymbol{\phi}_1, ..., \boldsymbol{\phi}_R\}$ would be an orthonormal basis for $\mathrm{Ker}\,\hat{P}_{\boldsymbol{qq}}$ and $\{\boldsymbol{\phi}_{R+1}, ..., \boldsymbol{\phi}_M\}$ for $\mathrm{Ker}\,\hat{P}_{\boldsymbol{qq}}{}^{\perp}$.

Now we seek to expand the potential energy in Taylor series around the critical point $(\hat{\boldsymbol{q}},\, \hat{\lambda}) \in E_I$ defined such as $P_{\boldsymbol{qq}}(\hat{\boldsymbol{q}}, \hat{\lambda})$ is singular. Although it is not generally the case, for simplicity we assume that the geometric multiplicity equals to one. This assumption holds particularly for the system we are investigating. The Taylor's series expansion of the potential energy up to order four is given by equation (5):

$$P(\boldsymbol{q}, \lambda) = \sum_{k=0}^{4} P_k(\Delta\boldsymbol{q}, \hat{\lambda}) + \sum_{k=0}^{3} \Delta\lambda\, \dot{P}_k(\Delta\boldsymbol{q}, \hat{\lambda}) + \mathscr{O}(\|(\Delta\boldsymbol{q}, \Delta\lambda)\|^5) \tag{5}$$

where the $P_k(\Delta\boldsymbol{q}, \hat{\lambda})$ represent the k-th order forms and $\dot{P}_k(\Delta\boldsymbol{q}, \hat{\lambda})$ their derivatives with respect to λ:

$$P_k(\Delta\boldsymbol{q}, \hat{\lambda}) := \frac{1}{k!}\,(\hat{P}_{\boldsymbol{q}...\boldsymbol{q}})_{i_1...i_k}\,\Delta q_{i_1}...\Delta q_{i_k} \tag{6}$$

further we define $P_{(k-l)l}(\boldsymbol{u}, \boldsymbol{v}, \hat{\lambda})$ as $(k-l)$-th order forms in $\boldsymbol{u}$ and l-th order forms in $\boldsymbol{v}$ such as $P_k(\boldsymbol{u}+\boldsymbol{v}, \hat{\lambda}) = \sum_{0\leq l\leq k} P_{(k-l)l}(\boldsymbol{u}, \boldsymbol{v}, \hat{\lambda})$ holds. Since $\Delta\boldsymbol{q} \in \mathbb{R}^M$ it can be uniquely decomposed as $\Delta\boldsymbol{q} = \boldsymbol{u} + \boldsymbol{v}$ such as $\boldsymbol{u} \in \mathrm{Ker}\,\hat{P}_{\boldsymbol{qq}}$ and $\boldsymbol{v} \in \mathrm{Ker}\,\hat{P}_{\boldsymbol{qq}}{}^{\perp}$. Consequently we have the expressions of vectors $\boldsymbol{u}$ and $\boldsymbol{v}$ in their respective basis: $\boldsymbol{u} = \sum_{1\leq p\leq R} a_p\,\boldsymbol{\phi}_p$ and $\boldsymbol{v} = \sum_{R+1\leq p\leq M} b_p\,\boldsymbol{\phi}_p$, where a_p are the amplitudes of each direction of the eigenmode and where b_p are second order amplitudes in directions orthogonal to the eigenmode. Define the coefficients b_p as:

$$b_p := \Delta\lambda \sum_{1\leq s\leq R} a_s\,\xi_{sp} + \sum_{1\leq s,t\leq R} a_s\,a_t\,\eta_{stp} \tag{7}$$

Assume from now on the kernel is one dimensional ($R = 1$), which leads to a simple expression for the coefficients b_p:

$$b_p := \Delta\lambda\,a_1\,\xi_{1p} + a_1^2\,\eta_{11p} \tag{8}$$

Comparing the norms of $\boldsymbol{u}$ and $\boldsymbol{v}$ we can say the following $\|\boldsymbol{v}\| = \mathscr{O}(\left\|(\Delta\lambda\,a_1, a_1^2)\right\|)$, while $\|\boldsymbol{u}\| = \mathscr{O}(|a_1|)$ which is the reason why we call $\boldsymbol{v}$ the second order field. Substituting $\boldsymbol{u}$ and $\boldsymbol{v}$ in the

potential energy Taylor series expansion, equation (5), yields:

$$\begin{aligned} P(\boldsymbol{q},\hat{\lambda}) &= P_0(\boldsymbol{u},\hat{\lambda}) + \\ & P_1(\boldsymbol{u},\hat{\lambda}) + P_1(\boldsymbol{v},\hat{\lambda}) + \\ & P_2(\boldsymbol{u},\hat{\lambda}) + P_{11}(\boldsymbol{u},\boldsymbol{v},\hat{\lambda}) + P_2(\boldsymbol{v},\hat{\lambda}) + \\ & P_3(\boldsymbol{u},\hat{\lambda}) + P_{21}(\boldsymbol{u},\boldsymbol{v},\hat{\lambda}) + \mathscr{O}(\left\|(\Delta\lambda\, a_1, a_1^2)\right\|^5) + \\ & P_4(\boldsymbol{u},\hat{\lambda}) + \mathscr{O}(\left\|(\Delta\lambda\, a_1, a_1^2)\right\|^5) \end{aligned}$$

and

$$\begin{aligned} \Delta\lambda\, \dot{P}(\boldsymbol{q},\hat{\lambda}) &= \Delta\lambda\, \dot{P}_0(\boldsymbol{u},\hat{\lambda}) + \\ & \Delta\lambda\, \dot{P}_1(\boldsymbol{u},\hat{\lambda}) + \Delta\lambda\, \dot{P}_1(\boldsymbol{v},\hat{\lambda}) + \\ & \Delta\lambda\, \dot{P}_2(\boldsymbol{u},\hat{\lambda}) + \Delta\lambda\, \dot{P}_{11}(\boldsymbol{u},\boldsymbol{v},\hat{\lambda}) + \mathscr{O}(\left\|(\Delta\lambda\, a_1, a_1^2)\right\|^5) + \\ & \Delta\lambda\, \dot{P}_3(\boldsymbol{u},\hat{\lambda}) + \mathscr{O}(\left\|(\Delta\lambda\, a_1, a_1^2)\right\|^5) \end{aligned}$$

Now we know from the previous discussion that $P_1(\boldsymbol{u},\hat{\lambda}) = P_1(\boldsymbol{v},\hat{\lambda}) = \dot{P}_1(\boldsymbol{u},\hat{\lambda}) = 0$ as well as $P_2(\boldsymbol{u},\hat{\lambda}) = \boldsymbol{u}^T\, \hat{P}_{\boldsymbol{qq}}\, \boldsymbol{u} = 0$. Likewise $P_{11}(\boldsymbol{u},\boldsymbol{v},\hat{\lambda}) = \boldsymbol{v}^T\, \hat{P}_{\boldsymbol{qq}}\, \boldsymbol{u} = 0$. For symmetry reasons $P_3(\boldsymbol{u},\hat{\lambda}) = 0$, which in turn implies $\dot{P}_3(\boldsymbol{u},\hat{\lambda}) = 0$. Discarding the zero terms we get the following representation for the potential energy:

$$\begin{aligned} P(\boldsymbol{q},\lambda) &= P_0(\boldsymbol{u},\hat{\lambda}) + \Delta\lambda\, \dot{P}_0(\boldsymbol{u},\hat{\lambda}) + \Delta\lambda\, \dot{P}_2(\boldsymbol{u},\hat{\lambda}) + P_4(\boldsymbol{u},\hat{\lambda}) \\ & \Delta\lambda\, \dot{P}_1(\boldsymbol{v},\hat{\lambda}) + \Delta\lambda\, \dot{P}_{11}(\boldsymbol{u},\boldsymbol{v},\hat{\lambda}) + P_{21}(\boldsymbol{u},\boldsymbol{v},\hat{\lambda}) + P_2(\boldsymbol{v},\hat{\lambda}) + \mathscr{O}(\left\|(\Delta\lambda\, a_1, a_1^2)\right\|^5) \end{aligned}$$

We seek now to minimize the functional $F(\boldsymbol{v}) := \Delta\lambda\, \dot{P}_1(\boldsymbol{v},\hat{\lambda}) + \Delta\lambda\, \dot{P}_{11}(\boldsymbol{u},\boldsymbol{v},\hat{\lambda}) + P_{21}(\boldsymbol{u},\boldsymbol{v},\hat{\lambda}) + P_2(\boldsymbol{v},\hat{\lambda})$ by solving the system $\delta F(\boldsymbol{v}) = 0$. Proceeding with the differentiation yields:

$$\Delta\lambda\, \dot{P}_1(\delta\boldsymbol{v},\hat{\lambda}) + \Delta\lambda\, \dot{P}_{11}(\boldsymbol{u},\delta\boldsymbol{v},\hat{\lambda}) + P_{21}(\boldsymbol{u},\delta\boldsymbol{v},\hat{\lambda}) + P_{11}(\boldsymbol{v},\delta\boldsymbol{v},\hat{\lambda}) = 0 \tag{9}$$

Let's substitute in equation (9) the vectors $\boldsymbol{u}$ and $\boldsymbol{v}$ by their component descriptions in the basis $\{\boldsymbol{\phi}_1, ..., \boldsymbol{\phi}_M\}$.

$$\sum_{2\le p\le M} \Big(\Delta\lambda\, \dot{P}_1(\boldsymbol{\phi}_p,\hat{\lambda}) + \Delta\lambda\, a_1\, \dot{P}_{11}(\boldsymbol{\phi}_1,\boldsymbol{\phi}_p,\hat{\lambda}) + a_1^2\, P_{21}(\boldsymbol{\phi}_1,\boldsymbol{\phi}_p,\hat{\lambda}) + \\ + \sum_{2\le q\le M} P_{11}(\boldsymbol{\phi}_p,\boldsymbol{\phi}_q,\hat{\lambda})\, b_q \Big)\, \delta b_p = 0 \tag{10}$$

Equation (10) has to hold $\forall(\delta b_p) \subset \mathbb{R}^{(M-1)}$. Also reminding that $P_{11}(\boldsymbol{\phi}_p,\boldsymbol{\phi}_q,\hat{\lambda}) = d_p\, \delta_{pq}$ and substituting b_q by its expression we get:

$$\begin{aligned} \Delta\lambda \left(\dot{P}_1(\boldsymbol{\phi}_p,\hat{\lambda}) + a_1\, \dot{P}_{11}(\boldsymbol{\phi}_1,\boldsymbol{\phi}_p,\hat{\lambda}) + d_p\, a_1\, \xi_{1p} \right) &+ \\ a_1^2 \left(P_{21}(\boldsymbol{\phi}_1,\boldsymbol{\phi}_p,\hat{\lambda}) + d_p\, \eta_{11p} \right) &= 0 \end{aligned} \tag{11}$$

which has to hold $\forall\Delta\lambda \in \mathbb{R}$. Taking a closer look at the components $\dot{P}_1(\boldsymbol{\phi}_p,\hat{\lambda})$, $\dot{P}_{11}(\boldsymbol{\phi}_1,\boldsymbol{\phi}_p,\hat{\lambda})$ and $P_{21}(\boldsymbol{\phi}_1,\boldsymbol{\phi}_p,\hat{\lambda})$ tells us that

$$\begin{aligned} \dot{P}_1(\boldsymbol{\phi}_p,\hat{\lambda}) &= 0, \qquad 2 \le p \le m \\ \dot{P}_{11}(\boldsymbol{\phi}_1,\boldsymbol{\phi}_p,\hat{\lambda}) &= 0, \quad m+1 \le p \le M \\ P_{21}(\boldsymbol{\phi}_1,\boldsymbol{\phi}_p,\hat{\lambda}) &= 0, \qquad 2 \le p \le m \end{aligned}$$

Taking this information into account yields the following expression for the minimized components $\tilde{b}_p$

$$\tilde{b}_p = \begin{cases} -\Delta\lambda\, a_1 \frac{\dot{P}_{11}(\boldsymbol{\phi}_1,\boldsymbol{\phi}_p,\hat{\lambda})}{P_{11}(\boldsymbol{\phi}_p,\boldsymbol{\phi}_p,\hat{\lambda})} & , \quad 2 \le p \le m \\ -\left(\Delta\lambda \frac{\dot{P}_1(\boldsymbol{\phi}_p,\hat{\lambda})}{P_{11}(\boldsymbol{\phi}_p,\boldsymbol{\phi}_p,\hat{\lambda})} + a_1^2 \frac{P_{21}(\boldsymbol{\phi}_1,\boldsymbol{\phi}_p,\hat{\lambda})}{P_{11}(\boldsymbol{\phi}_p,\boldsymbol{\phi}_p,\hat{\lambda})}\right) & , \quad m+1 \le p \le M \end{cases} \tag{12}$$

Consider any functional, which we want to minimize, consisting of a quadratic and linear part: $F_2(\boldsymbol{v}) + F_1(\boldsymbol{v})$. Let $\tilde{\boldsymbol{v}}$ be the point which minimizes the functional. Taking the first variation and evaluating it at $\boldsymbol{v} = \tilde{\boldsymbol{v}}$ gives $F_{11}(\tilde{\boldsymbol{v}}, \delta\boldsymbol{v}) + F_1(\delta\boldsymbol{v}) = 0$, which holds $\forall \delta\boldsymbol{v}$. In particular it holds for $\delta\boldsymbol{v} = \tilde{\boldsymbol{v}}$, hence $F_{11}(\tilde{\boldsymbol{v}}, \tilde{\boldsymbol{v}}) + F_1(\tilde{\boldsymbol{v}}) = 0$. The latter in turn can be simplified as $2\,F_2(\tilde{\boldsymbol{v}}) + F_1(\tilde{\boldsymbol{v}}) = 0$. Now the original functional at its minimum is expressed as $F_2(\tilde{\boldsymbol{v}}) + F_1(\tilde{\boldsymbol{v}}) = -F_2(\tilde{\boldsymbol{v}})$. Apply this to our case, and express the potential energy functional:

$$P(\boldsymbol{q},\lambda) = P_0(\boldsymbol{u},\hat{\lambda}) + \Delta\lambda\,\dot{P}_0(\boldsymbol{u},\hat{\lambda}) + \Delta\lambda\,\dot{P}_2(\boldsymbol{u},\hat{\lambda}) + P_4(\boldsymbol{u},\hat{\lambda}) - P_2(\tilde{\boldsymbol{v}}) + \mathcal{O}(\left\|(\Delta\lambda\, a_1, a_1^2)\right\|^5)$$

where

$$\begin{aligned} P_2(\tilde{\boldsymbol{v}}) =& \frac{1}{2}\sum_{p=2}^{m} \tilde{b}_p^2\, d_p + \frac{1}{2}\sum_{p=m+1}^{M} \tilde{b}_p^2\, d_p \\ =& \frac{1}{2}\sum_{p=2}^{m} \Delta\lambda^2\, a_1^2 \frac{\dot{P}_{11}(\boldsymbol{\phi}_1,\boldsymbol{\phi}_p,\hat{\lambda})^2}{P_{11}(\boldsymbol{\phi}_p,\boldsymbol{\phi}_p,\hat{\lambda})} + \frac{1}{2}\sum_{p=m+1}^{M} \frac{\left(\Delta\lambda\,\dot{P}_1(\boldsymbol{\phi}_p,\hat{\lambda}) + a_1^2\, P_{21}(\boldsymbol{\phi}_1,\boldsymbol{\phi}_p,\hat{\lambda})\right)^2}{P_{11}(\boldsymbol{\phi}_p,\boldsymbol{\phi}_p,\hat{\lambda})} \end{aligned}$$

Rearranging the equation yields for the potential energy:

$$\begin{aligned} P(\boldsymbol{q},\lambda) \;=\; & P_0(\boldsymbol{u},\hat{\lambda}) + \Delta\lambda\,\dot{P}_0(\boldsymbol{u},\hat{\lambda}) - \Delta\lambda^2\,\frac{1}{2}\sum_{m+1\le p\le M} \frac{\dot{P}_1(\boldsymbol{\phi}_p,\hat{\lambda})^2}{P_{11}(\boldsymbol{\phi}_p,\boldsymbol{\phi}_p,\hat{\lambda})} + \\ & -\Delta\lambda^2\, a_1^2\,\frac{1}{2}\sum_{2\le p\le m} \frac{\dot{P}_{11}(\boldsymbol{\phi}_1,\boldsymbol{\phi}_p,\hat{\lambda})^2}{P_{11}(\boldsymbol{\phi}_p,\boldsymbol{\phi}_p,\hat{\lambda})} + \\ & -\Delta\lambda\, a_1^2 \left(\sum_{m+1\le p\le M} \frac{\dot{P}_1(\boldsymbol{\phi}_p,\hat{\lambda})\, P_{21}(\boldsymbol{\phi}_1,\boldsymbol{\phi}_p,\hat{\lambda})}{P_{11}(\boldsymbol{\phi}_p,\boldsymbol{\phi}_p,\hat{\lambda})} - \dot{P}_2(\boldsymbol{\phi}_1,\hat{\lambda})\right) + \\ & +a_1^4 \left(P_4(\boldsymbol{\phi}_1,\hat{\lambda}) - \frac{1}{2}\sum_{m+1\le p\le M} \frac{P_{21}(\boldsymbol{\phi}_1,\boldsymbol{\phi}_p,\hat{\lambda})^2}{P_{11}(\boldsymbol{\phi}_p,\boldsymbol{\phi}_p,\hat{\lambda})}\right) + \mathcal{O}(\left\|(\Delta\lambda\, a_1, a_1^2)\right\|^5) \end{aligned}$$

Deriving the potential energy with respect to the amplitude yields the reduced equilibrium equation:

$$\begin{aligned} \frac{\mathrm{d}}{\mathrm{d}a_1} P(\boldsymbol{q},\lambda) \;=\; & -a_1 \Bigg\{ \Delta\lambda^2 \sum_{2\le p\le m} \frac{\dot{P}_{11}(\boldsymbol{\phi}_1,\boldsymbol{\phi}_p,\hat{\lambda})^2}{P_{11}(\boldsymbol{\phi}_p,\boldsymbol{\phi}_p,\hat{\lambda})} + \\ & 2\,\Delta\lambda \left(\sum_{m+1\le p\le M} \frac{\dot{P}_1(\boldsymbol{\phi}_p,\hat{\lambda})\, P_{21}(\boldsymbol{\phi}_1,\boldsymbol{\phi}_p,\hat{\lambda})}{P_{11}(\boldsymbol{\phi}_p,\boldsymbol{\phi}_p,\hat{\lambda})} - \dot{P}_2(\boldsymbol{\phi}_1,\hat{\lambda})\right) + \\ & +4\,a_1^2 \left(P_4(\boldsymbol{\phi}_1,\hat{\lambda}) - \frac{1}{2}\sum_{m+1\le p\le M} \frac{P_{21}(\boldsymbol{\phi}_1,\boldsymbol{\phi}_p,\hat{\lambda})^2}{P_{11}(\boldsymbol{\phi}_p,\boldsymbol{\phi}_p,\hat{\lambda})}\right) \Bigg\} + \mathcal{O}(\left\|(\Delta\lambda\, a_1, a_1^2)\right\|^4) \end{aligned}$$

From the equilibrium condition $\frac{\mathrm{d}}{\mathrm{d}a_1} P(\boldsymbol{q}, \lambda) = 0$ we solve the function $\lambda(a_1)$:

$$\lambda(a_1) = \hat{\lambda} + \frac{2\, P_4(\phi_1, \hat{\lambda}) - \sum_{p=m+1}^{M} \frac{P_{21}(\phi_1, \phi_p, \hat{\lambda})^2}{P_{11}(\phi_p, \phi_p, \hat{\lambda})}}{\sum_{p=m+1}^{M} \frac{\dot{P}_1(\phi_p, \hat{\lambda})\, P_{21}(\phi_1, \phi_p, \hat{\lambda})}{P_{11}(\phi_p, \phi_p, \hat{\lambda})} - \dot{P}_2(\phi_1, \hat{\lambda})} a_1^2 + \mathscr{O}(|a_1|^4) \tag{13}$$

3.1 Application to Example Case

Consider the example truss beam defined in section 2. We shall simplify it further by saying that both the upper chord (1) and (3) and the vertical compressed member (3) are axially infinitely stiff, which results in the following constraints: $q_4 = q_5 = 0$. Assume also, for simplicity, that the eccentricity of load application point $\rho = 0$. The potential energy of such a system is given by expression

$$P(\boldsymbol{q}, \lambda) = \frac{1}{2}\alpha_1 q_1^2 + \frac{1}{2}\alpha_2 q_2^2 + \frac{1}{2}\alpha_3 q_3^2 + \frac{1}{2}\alpha_6 Q_6^2(\boldsymbol{q}) - \lambda q_3 \tag{14}$$

where the constraint equation is given by $Q_6(\boldsymbol{q}) := \sin\theta \cos\theta\, (q_3 \cos q_1 + q_2 \sin q_1)$. Application of the equation (13) yields the following result:

$$\lambda(a_1) = \hat{\lambda} + \frac{1}{3}\frac{\alpha_1 (\alpha_3 + \bar{\alpha}_6)}{\hat{\lambda}(\alpha_2 + \bar{\alpha}_6)} \left(3\alpha_3 - 2\alpha_2 + \frac{\alpha_2 \alpha_3}{\bar{\alpha}_6}\right) (\phi_{11}\, a_1)^2 + \mathscr{O}(|a_1|^4) \tag{15}$$

where the critical value of the load parameter is $\hat{\lambda} = \sqrt{\gamma\, \alpha_1 \alpha_2}$ and $\gamma = \frac{(\alpha_3 + \bar{\alpha}_6)^2}{\bar{\alpha}_6 (\alpha_2 + \bar{\alpha}_6)}$. The expression $\bar{\alpha}_6$ has been introduced for convenience and defiend as: $\bar{\alpha}_6 := \sin^2\theta \cos^2\theta\, \alpha_6$. It is worth noting the limit behaviour of the system as $\alpha_6 \to \infty$, which is physically relevant, since usually axial stiffnesses are much larger than flexural or torsional stiffnesses.

$$\lambda(a_1) \xrightarrow[\alpha_6 \to \infty]{} \sqrt{\alpha_1 \alpha_2} + \frac{1}{3}\sqrt{\alpha_1/\alpha_2}\, (3\alpha_3 - 2\alpha_2)\, (\phi_{11}\, a_1)^2 + \mathscr{O}(|a_1|^4) \tag{16}$$

It comes out that we have a finite critical load, and that if the condition $3\alpha_3 - 2\alpha_2 \geq 0$ holds, then we have a stable secondary path in the neighbourhood of the critical point. Assuming that α_2 (lateral flexural stiffness) and α_3 (vertical flexural stiffness) are of same magnitude, which is usually the case, the secondary path is at worst only slightly unstable.

Compare now to another example case, where we restrict lateral sway of the upper chord (point D). We are considering a different model, but it is physically closely related to the previous one. Assume now $\alpha_2 = 0$. The potential energy of this system is given by equation (17)

$$P(\boldsymbol{q}, \lambda) = \frac{1}{2}\alpha_1 q_1^2 + \frac{1}{2}\alpha_3 q_3^2 + \frac{1}{2}\alpha_6 Q_6^2(\boldsymbol{q}) - \lambda q_3 \tag{17}$$

where the constraint equation is given by $Q_6(\boldsymbol{q}) := \sin\theta \cos\theta\, q_3 \cos q_1$. Application of the equation (13) yields the following result:

$$\lambda(a_1) = \hat{\lambda} + \frac{1}{3}\frac{\alpha_1 (\alpha_3 + \bar{\alpha}_6)}{\hat{\lambda}\bar{\alpha}_6} (\alpha_3 - 2\alpha_6)\, (\phi_{11}\, a_1)^2 + \mathscr{O}(|a_1|^4) \tag{18}$$

where the critical value of the load parameter is $\bar{\lambda} = \sqrt{\gamma\, \alpha_1}$ such as $\gamma = \frac{(\alpha_3 + \bar{\alpha}_6)^2}{\bar{\alpha}_6}$. Again, consider the limit behaviour of the system as $\alpha_6 \to \infty$. It comes out that $\hat{\lambda} \xrightarrow[\alpha_6 \to \infty]{} \infty$, and in the

neighbourhood of infinity the expression of λ gives:

$$\lambda(a_1) = \hat{\lambda} + \left(-\frac{2}{3}\hat{\lambda} + \mathscr{O}(\alpha_6^{-1})\right)(\phi_{11}\, a_1)^2 + \mathscr{O}(|a_1|^4) \tag{19}$$

We infer that in case of the laterally restricted system, for large axial stiffnesses of the diagonal members the critical load is large, but on the other hand the postbuckling behaviour is very unstable.

4 NUMERICAL ANALYSIS

The goal is now to find a numeric approximation of the critical load $\hat{\lambda}$ defined previously. One possible strategy is to expand the criticality condition as a Taylor series with respect to the load parameter, and solve the critical load parameter approximation from the polynomial equation given by the truncated series. Usually one truncates starting from the quadratic term. First, we assume that there exists a neighbourhood of $(\boldsymbol{q}^{(0)}, \lambda^{(0)})$, $\mathscr{U}_{(\boldsymbol{q}^{(0)},\lambda^{(0)})}$ such as $(\hat{\boldsymbol{q}}, \hat{\lambda}) \notin \mathscr{U}_{(\boldsymbol{q}^{(0)},\lambda^{(0)})}$ and $P_{\boldsymbol{qq}}(\boldsymbol{q}, \lambda)$ is not singular for $(\boldsymbol{q}, \lambda) \in \mathscr{U}_{(\boldsymbol{q}^{(0)},\lambda^{(0)})}$ Then, by the implicit function theorem we infer that there exists a function $\boldsymbol{q} : \mathscr{U}_{\lambda^{(0)}} \to \mathscr{U}_{\boldsymbol{q}^{(0)}} : \lambda \mapsto \boldsymbol{q}(\lambda)$. Then the criticality condition can be expressed as follows:

$$\hat{P}_{\boldsymbol{qq}}\,\boldsymbol{\phi}_1 = \left(P^{(0)}_{\boldsymbol{qq}} + \Delta\lambda\,\left(P^{(0)}_{\boldsymbol{qqq}}\,\dot{\boldsymbol{q}}^{(0)} + \dot{P}^{(0)}_{\boldsymbol{qq}}\right)\right)\,\boldsymbol{\phi}_1 + \mathscr{O}(\Delta\lambda^2) = 0 \tag{20}$$

where $\Delta\lambda = \hat{\lambda} - \lambda^{(0)}$. The expression of the vector $\dot{\boldsymbol{q}}^{(0)}$ is given by the equilibrium equation at the critical point:

$$\hat{P}_{\boldsymbol{q}} = P^{(0)}_{\boldsymbol{q}} + \Delta\lambda\,\left(P^{(0)}_{\boldsymbol{qq}}\,\dot{\boldsymbol{q}}^{(0)} + \dot{P}^{(0)}_{\boldsymbol{q}}\right) + \mathscr{O}(\Delta\lambda^2) = 0\,,\ \ \forall\Delta\lambda \in \mathbb{R} \tag{21}$$

hence we get the expression $\dot{\boldsymbol{q}}^{(0)} = -\,{P^{(0)}_{\boldsymbol{qq}}}^{-1}\,\dot{P}^{(0)}_{\boldsymbol{q}}$. Since we need that the point $(\boldsymbol{q}^{(0)}, \lambda^{(0)})$ is on the equilibrium path, the only point we know for sure for any system is the origin $(\boldsymbol{q}^{(0)}, \lambda^{(0)}) = (0, 0)$. Now assume that the potential energy is of the form given in equation (1). Then we get the following expressions:

$$\begin{aligned}
\dot{P}^{(0)}_{\boldsymbol{q}} &= -\sum_{i=m+1}^{M}(\delta_{i\,m+1} + R_{,i})\boldsymbol{e}_i \\
P^{(0)}_{\boldsymbol{qq}} &= \sum_{t=1}^{m}\alpha_t \boldsymbol{e}_t \boldsymbol{e}_t^T + \sum_{t\geq M+1}\alpha_t\left(\sum_{i,j=m+1}^{M} Q^{(0)}_{t,i}Q^{(0)}_{t,j}\,\boldsymbol{e}_i\boldsymbol{e}_j^T\right) \\
\dot{\boldsymbol{q}}^{(0)} &= \sum_{i=m+1}^{M}\dot{q}^{(0)}_i \boldsymbol{e}_i \\
\dot{P}^{(0)}_{\boldsymbol{qq}} &= -\rho\left(\sum_{i,j=1}^{m} R_{,ij}\boldsymbol{e}_i\boldsymbol{e}_j^T + \sum_{i,j=m+1}^{M} R_{,ij}\boldsymbol{e}_i\boldsymbol{e}_j^T\right) \\
P^{(0)}_{\boldsymbol{qqq}}\,\dot{\boldsymbol{q}}^{(0)} &= \sum_{t\geq M+1}\alpha_t\Bigg[\sum_{\substack{i,j=1\\ m+1\leq k\leq M}}^{m} Q^{(0)}_{t,ij}Q^{(0)}_{t,k}\dot{q}^{(0)}_k\,\boldsymbol{e}_i\boldsymbol{e}_j^T + \\
&\qquad \sum_{\substack{i,j=m+1\\ m+1\leq k\leq M}}^{M}\left(Q^{(0)}_{t,jk}Q^{(0)}_{t,i} + Q^{(0)}_{t,jk}Q^{(0)}_{t,i} + Q^{(0)}_{t,jk}Q^{(0)}_{t,i}\right)\dot{q}^{(0)}_k\,\boldsymbol{e}_i\boldsymbol{e}_j^T\Bigg]
\end{aligned} \tag{22}$$

We can easily see that our linearized criticality condition $P^{(0)}_{\boldsymbol{qq}} + \Delta\lambda \left(P^{(0)}_{\boldsymbol{qqq}}\, \dot{\boldsymbol{q}}^{(0)} + \dot{P}^{(0)}_{\boldsymbol{qq}} \right)$ is also block diagonal. Actually only the upper left block is relevant if we seek for an approximation of the critical value $\hat{\lambda}$. Introduce the notation: $\boldsymbol{K}^{(0)}_0 := P^{(0)}_{\boldsymbol{qq}}$, $\boldsymbol{K}^{(0)}_1 := P^{(0)}_{\boldsymbol{qqq}}\, \dot{\boldsymbol{q}}^{(0)} + \dot{P}^{(0)}_{\boldsymbol{qq}}$. Solving the equation (23) for $\Delta\lambda$

$$\det \begin{pmatrix} \left(\boldsymbol{K}^{(0)}_0 + \Delta\lambda\, \boldsymbol{K}^{(0)}_1 \right)(1..m, 1..m) & 0 \\ 0 & \left(\boldsymbol{K}^{(0)}_0 + \Delta\lambda\, \boldsymbol{K}^{(0)}_1 \right)(m+1..M, m+1..M) \end{pmatrix} = 0 \quad (23)$$

yields $\det(\left(\boldsymbol{K}^{(0)}_0 + \Delta\lambda\, \boldsymbol{K}^{(0)}_1 \right)(1..m, 1..m)) = 0$ or $\det(\left(\boldsymbol{K}^{(0)}_0 + \Delta\lambda\, \boldsymbol{K}^{(0)}_1 \right)(m+1..M, m+1..M)) = 0$. Assume that $\boldsymbol{K}^{(0)}_1(1..m, 1..m) = 0$, then the equation $\det(\left(\boldsymbol{K}^{(0)}_0 + \Delta\lambda\, \boldsymbol{K}^{(0)}_1 \right)(m+1..M, m+1..M)) = 0$ gives an a result, but this result is not an approximation of $\hat{\lambda}$. Therefore we introduce the following definition: the 1-st order coefficient matrix $\boldsymbol{K}^{(0)}_1$ is degenerated if $\boldsymbol{K}^{(0)}_1(1..m, 1..m) = 0$. When the 1-st order coefficient matrix is degenerated linear approximation can not give accurate numerical approximation of the critical load parameter. In this case one has to solve quadratic approximation of the eigenvalue problem:

$$\hat{P}_{\boldsymbol{qq}}\, \boldsymbol{\phi}_1 = \left(\boldsymbol{K}^{(0)}_0 + \Delta\lambda\, \boldsymbol{K}^{(0)}_1 + \frac{1}{2}\Delta\lambda^2\, \boldsymbol{K}^{(0)}_2 \right) \boldsymbol{\phi}_1 + \mathscr{O}(\Delta\lambda^3) = 0 \quad (24)$$

where $\boldsymbol{K}^{(0)}_2 = \left(P^{(0)}_{\boldsymbol{qqqq}}\, \dot{\boldsymbol{q}}^{(0)} + \dot{P}^{(0)}_{\boldsymbol{qqq}} \right) \dot{\boldsymbol{q}}^{(0)} + P^{(0)}_{\boldsymbol{qqq}}\, \ddot{\boldsymbol{q}}^{(0)} + \ddot{P}^{(0)}_{\boldsymbol{qq}}$

4.1 Application to Example Case

Apply now the previously described numerical scheme to our example case presented in the asymptotic analysis part, where the potential energy is given by:

$$P(\boldsymbol{q}, \lambda) = \frac{1}{2}\alpha_1\, q_1^2 + \frac{1}{2}\alpha_2\, q_2^2 + \frac{1}{2}\alpha_3\, q_3^2 + \frac{1}{2}\alpha_6\, Q_6^2(\boldsymbol{q}) - \lambda\, q_3 \quad (25)$$

Compute the necessary components:

$$\dot{\boldsymbol{q}}^{(0)} = \left(\begin{array}{cc|c} \alpha_1^{-1} & 0 & 0 \\ 0 & \alpha_2^{-1} & 0 \\ \hline 0 & 0 & (\alpha_3 + \bar{\alpha}_6)^{-1} \end{array} \right) \left(\begin{array}{c} 0 \\ 0 \\ \hline -1 \end{array} \right) \Delta\lambda = \left(\begin{array}{c} 0 \\ 0 \\ \hline -(\alpha_3 + \bar{\alpha}_6)^{-1} \end{array} \right) \Delta\lambda \quad (26)$$

$$\boldsymbol{K}^{(0)}_0 = \left(\begin{array}{cc|c} \alpha_1 & 0 & 0 \\ 0 & \alpha_2 & 0 \\ \hline 0 & 0 & (\alpha_3 + \bar{\alpha}_6) \end{array} \right) \quad (27)$$

$$\boldsymbol{K}^{(0)}_1 = -\frac{\bar{\alpha}_6}{\alpha_3 + \bar{\alpha}_6} \left(\begin{array}{cc|c} 0 & 1 & 0 \\ 1 & 0 & 0 \\ \hline 0 & 0 & 0 \end{array} \right) \quad (28)$$

Hence $\det(\left(\boldsymbol{K}^{(0)}_0 + \Delta\lambda\, \boldsymbol{K}^{(0)}_1 \right)(m+1..M, m+1..M)) = \alpha_1\alpha_2 - \Delta\lambda^2\bar{\alpha}_6^2(\alpha_3+\bar{\alpha}_6)^{-2} = 0$ Solving $\Delta\lambda$ yields

$$\Delta\lambda = \frac{\alpha_3 + \bar{\alpha}_6}{\bar{\alpha}_6}\sqrt{\alpha_1\alpha_2} \quad (29)$$

Now apply this scheme to the restricted scheme defined by the portential energy expression:

$$P(\boldsymbol{q}, \lambda) = \frac{1}{2}\alpha_1\, q_1^2 + \frac{1}{2}\alpha_3\, q_3^2 + \frac{1}{2}\alpha_6\, Q_6^2(\boldsymbol{q}) - \lambda\, q_3 \quad (30)$$

Compute the necessary components:

$$\dot{\boldsymbol{q}}^{(0)} = \left(\begin{array}{c|c} \alpha_1^{-1} & 0 \\ \hline 0 & (\alpha_3+\bar{\alpha}_6)^{-1} \end{array}\right)\left(\begin{array}{c} 0 \\ \hline -1 \end{array}\right)\Delta\lambda = \left(\begin{array}{c} 0 \\ \hline -(\alpha_3+\bar{\alpha}_6)^{-1} \end{array}\right)\Delta\lambda \tag{31}$$

$$\boldsymbol{K}_0^{(0)} = \left(\begin{array}{c|c} \alpha_1 & 0 \\ \hline 0 & (\alpha_3+\bar{\alpha}_6) \end{array}\right) \tag{32}$$

$$\boldsymbol{K}_1^{(0)} = -\frac{\bar{\alpha}_6}{\alpha_3+\bar{\alpha}_6}\left(\begin{array}{c|c} 0 & 0 \\ \hline 0 & 0 \end{array}\right) \tag{33}$$

We see that $\boldsymbol{K}_1^{(0)}$ is degenerated and it is not possible to compute $\Delta\lambda$ from the linearized buckling eigenvalue problem.

5 CONCLUSIONS

In this paper we have compared two closely related systems based on a truss beam model: a non-restricted system and a restricted one. Asymptotic analysis showed us that although the critical load for the non-restricted system is less than for the restricted one, the post-buckling path is quite stable. On the other hand, even if the critical load of the restricted system is high, the post-buckling path is very unstable. This instability grows with the critical load. In numerical analysis we pointed out that due to the block diagonal form of the linearized eigenvalue problem, degeneration of the first order coefficient leads to wrong estimate of the critical load. In the particular case of our non-restricted system the first order coefficient is not degenerated, and the linearized eigenvalue problem yields correct estimate of the critical load. However, in the restricted case, the first order coefficient degenerates, and we are unable to get any estimate from the linearized eigenvalue

6 NOTATIONS, DEFINITIONS

$F : \mathbb{R}^N \to \mathbb{R}$, $F_{\boldsymbol{x}\ldots\boldsymbol{x}} \in \mathbb{R}^{N^k}$:	$(F_{\boldsymbol{x}\ldots\boldsymbol{x}})_{i_1,\ldots,i_k} := \partial_1 \ldots \partial_k F$	k-th derivative of F
$F : \mathbb{R}^{(N+1)} \to \mathbb{R}$:	$\dot{F}(\boldsymbol{x},\lambda) := \frac{\partial}{\partial\lambda} F(\boldsymbol{x},\lambda)$	derivative w/r to λ
$F : \mathbb{R}^N \to \mathbb{R}$:	$\hat{F} := F(\hat{\boldsymbol{x}})$	value of F at $\boldsymbol{x} = \hat{\boldsymbol{x}}$
$\boldsymbol{A} \in \mathbb{R}^{m\times n}$:	$\boldsymbol{A}(p..q, r..s)_{ij} = \boldsymbol{A}_{ij}$	
	$p \le i \le q$, $r \le j \le s$	submatrix

REFERENCES

[1] W.T. Koiter. *Over de stabiliteit van het elastisch evenwicht* (in Dutch). PhD thesis, Technische Hogeschool, Delft, 1945. English tranlations: NASA TT F10, 833 (1967) and AFFDL, TR-7025 (1970).

[2] A.M.A. van der Heiden. *W.T. Koiter's Elastic Stability of Solids and Structures*. Cambridge University Press, 2009.

[3] J.M.T. Thompson and G.W. Hunt. *A General Theory of Elastic Stability*. Wiley, London, 1973.

[4] J.M.T. Thompson and G.W. Hunt. *Elastic Instability Phenomena*. Wiley, Chichester, 1984.

[5] M. Golubitsky and D.G. Schaeffer. *Singularities and Groups in Bifurcation Theory*, vol. 1. Springer-Verlag, 1985.

[6] W.J.F. Govaerts. *Numerical Methods for Bifurcations of Dynamic Equilibria*. SIAM, 2000.

DESIGN PROCESS OF LASER CUT INLAY FIXED PARTIAL DENTURE FRAMEWORKS

T. M. R. Alho
Department of Electrical Engineering and Automation
University of Vaasa
P.O.Box 700
FI-65101 Vaasa, FINLAND

ABSTRACT

When it comes to manufacturing dental prostheses, it is probably one of the least automated manufacture processes in the world. This paper presents the design process for laser cut inlay fixed partial denture frameworks. The process includes designing, simulating, manufacturing and mechanical testing. Designing is made using CAD software, simulating is done using FEM simulation software, prototypes are manufactured by laser cutting and mechanical tests using materials testing machine with custom made jaws.

1. INTRODUCTION

When a person loses a tooth, there are number of choices where to choose the best treatment to each situation. Today the usual ways to replace the tooth are implant, removable partial denture (RPD) or inlay fixed partial denture (IFPD). Implant is the most esthetic and durable choice but it is quite expensive, where RPDs are very cheap and attached to mouth using adhesion or mechanical attachment. IFPDs are relatively cheap and when properly manufactured and attached they can last for decades.

Implants are always attached surgically which is very invasive procedure and healing can take a long time. RPDs are attached on the surface of the living teeth and/or palate and no surgical procedures are needed. Attachment of IFPD depends on the location of the missing tooth. If the tooth is missing from the incisor area, the IFPD is attached to the back surfaces of the abutment teeth. When the tooth is missing from posterior area the IFPD's attachment wings are embedded into the neighboring teeth (Fig. 1). [1]

Today the frameworks for IFPDs are either hand made in dental technician laboratory or they are ordered from a company which makes the framework using a milling machine. An experienced dental technician can manufacture up to two frameworks in parallel in 3–5 hours by metal casting, from which at least 2.5 hours are active working. In addition to this, the manufacturing of the crown for the framework can take hours as well.

In the posterior area where the abutment teeth are large enough to allow the attachment wings to be embedded into them, the shape of the frameworks for IFPDs can be quite simple (Fig 2.) and the manufacture process can be automated easily. In the cases where it is possible to use them, with carefully designed shape, cost effective manufacturing method and safe material, the pre-

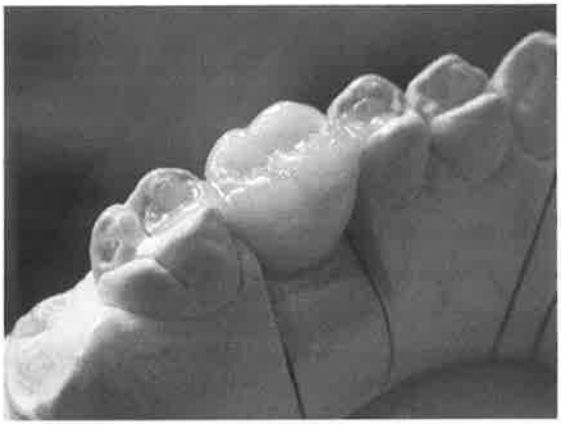

Figure 1. An Inlay Fixed Partial Denture attached to a cast jaw.

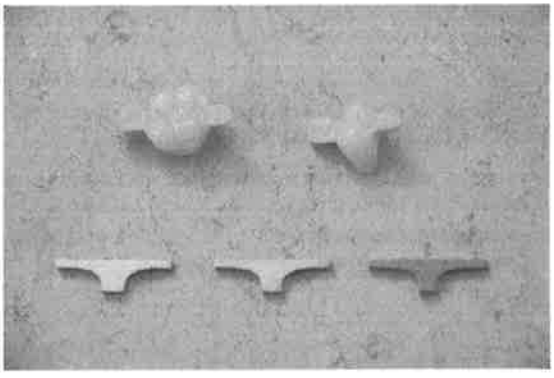

Figure 2. Inlay Fixed Partial Dentures and pre-manufactured frameworks.

manufactured IFPD frameworks can safe hours of dental practitioners work time without scarifying durability of the prosthesis.

Medical grade titanium was selected as the material of the frameworks because of its excellent corrosion resistance and wide acceptance in medical applications. [2][3] Titanium has also proven to be safe material for patients who are allergic to other metals. [4]

2. DESIGNING AND SIMULATIONS

As much of the information about designing an IFPD framework is unwritten knowledge and the design depends so much on the situation where the framework is going to be used, it was vital to have a dentist and a dental technician in the designing process. With the help of the dental practitioners a number of possible framework shapes were designed and the best one taken to further analysis. As seen from Figure 2 the model has a T-like shape and three different size options. The two smaller wings are the attachments wings which are used to attach the prosthesis to the abutment teeth and the center part is to give more attachment surface for the crown. The attachment wings have also a saw-like pattern which is there to give more friction and help to keep the crown attached. (Fig. 3)

The final models of the framework design were drawn using CAD software and the dxf-files were imported directly to the simulation software [5]. The symmetric shape of the frameworks could be used as an advantage by simulating only one half the frameworks (Fig. 3). This enabled to use the freed computing resources to make the simulations more accurate.

Simulations consist of static and time-depended simulations in situations mimicking occlusion (Fig. 4A) and mechanical tests (Fig. 4B) for all size classes. As human occlusion forces can reach up to or over 800 N for healthy young adult males, the acting force in static simulations is constantly 800 N and no transient is considered. [6] In time-depended simulations the acting force is changed between 300 and 500 N in frequency of 1 hertz for 10 seconds to mimic masticatory cycle. In the simulations the force is implemented on 2.5 mm area in the upper right-hand side on top of the model (Fig. 4), this corresponds to a 5 mm wide area in the middle of the framework when the symmetry is taken into account. Table 1 shows the loads implemented on the frameworks when the surface areas are also taken into account.

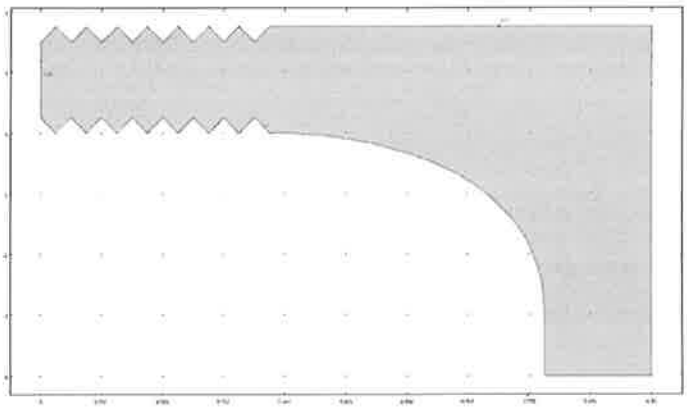

Figure 3. Simulation model of a medium size IFPD framework.

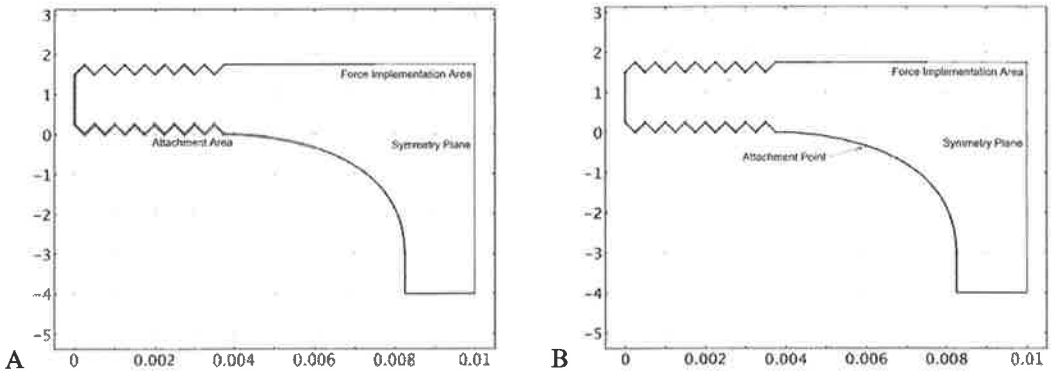

Figure 4. The Boundary conditions in A. occlusion and B. mechanical test simulations.

Table 1. The loads implemented on the frameworks in the FEM simulations.

Simulation type	Value
Static simulations	80 $(-\boldsymbol{e}_y)$ MPa
Time-depended simulations	$\left(40+10\cdot\sin(2\pi t)\right)\left(-\boldsymbol{e}_y\right)$ MPa

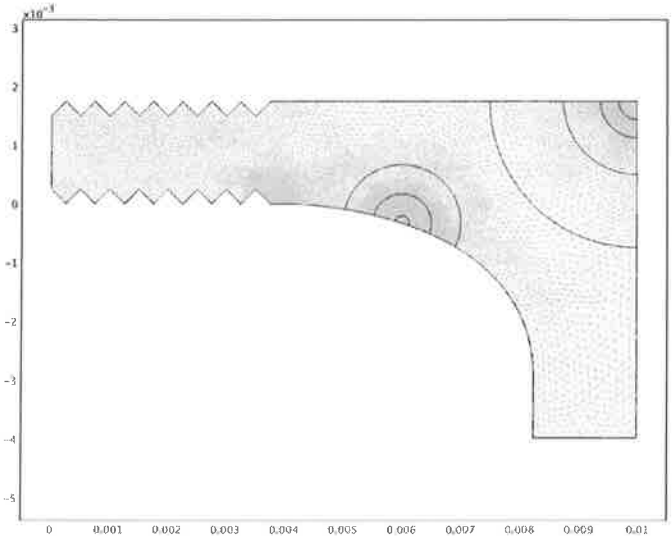

Figure 5. Example of a mesh used in time-depended simulations.

The simulation environment was kept as simple as possible and the abutment teeth in occlusion simulations and materials testing machine jaws in mechanical test simulations were modeled using different kind of boundary conditions. In Figure 4A the framework is attached to the environment using line attachment, this is designed to mimic an immensely hard foundation and strong cement under the wing. While it is not realistic situation and the framework is not able to bend under the acting forces like in real situation, it will raise the stresses concentrated on the interface between the attachment and rest of the framework. This gives more assurances that if the framework withstands these stresses, it will more likely hold in real situation as well.

In mechanical test simulations the framework was attached to the simulation environment from a single point. Numerically this setup is problematic as the stresses at the point and its surroundings are infinite. This effect is minimized by using as dense mesh as possible in the point surroundings so that the polluted area is as small as possible (Fig. 5).

3. PROTOTYPING AND MECHANICAL TESTS

Titanium's reactivity makes it a very demanding material for conventional machining as the wear, cutting temperature and cutting pressure inflicted on conventional tools are much higher than when machining *e.g.* iron. [7][8] As the framework design has very small but important details, like the saw-like pattern on its wings, problematic mechanical tooling is not the best possible solution as the manufacture method.

One of the most flexible ways to cut sheet metal parts is laser cutting. It has many advantages when compared to conventional mechanical tooling, such as there is no mechanical contact between the tool and the object and very small amount of heat is transferred outside of the focus point which reduces deformations. (Fig. 6) As titanium is very reactive metal laser cutting was made in an inert argon gas to prevent the titanium from burning. [9]

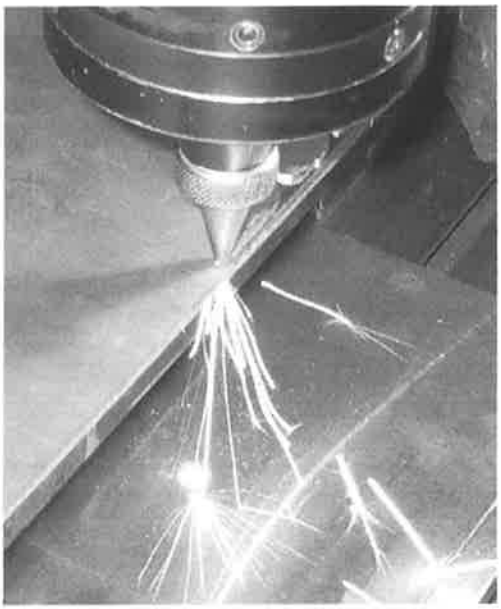

Figure 6. 500 W Nd:YAG pulse laser cutting IFPD framework prototypes.

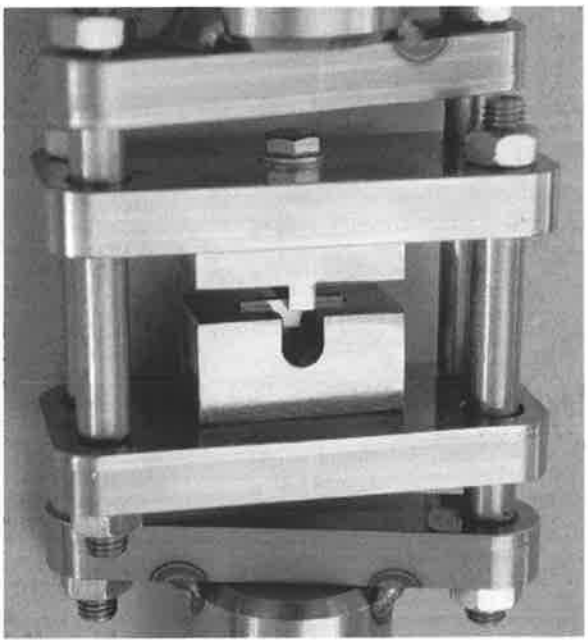

Figure 7. An IFPD framework in the custom-made jaws.

The mechanical tests were conducted using a Lloyd LR10K materials testing machine with custom-made jaws (Fig. 7). The jaws were designed specifically to be used for testing the IFPD frameworks so that the situations correspond as well as possible to the simulations. The frameworks are resting on a steel support with an 8 mm cavity in the middle and the acting force is brought to a 5 mm wide area on top of the framework.

The tests conducted with the testing machine consists of normal bending test where the frameworks are pressed down with ever increasing force and fatigue test where the frameworks are strained using forces changing between two pre-defined values for one hour. The values were set to 300 and 500 N but due to the mechanical properties of the testing machine, in reality the acting forces changed between around 250 and 700 N.

4. RESULTS

4.1 Simulation results

The results of the static simulations are shown in Table 2. As it was expected from the simulation setup the simulated bending values are un-realistically small as the frameworks were not able to bend naturally. This on the other hand causes the stresses inflicted to the frameworks in the simulations to be greater than in reality. Figure 8 shows the von Mises stress graphs of all of the framework classes.

In the figures the maximum von Mises stress value drawn is 920 MPa, which is approximately the yielding stress of titanium. [10] This setting prevents the software from drawing areas that have higher von Mises stress values than that and this way the white area shows the area where the framework theoretically can start yielding. From the size of the white areas and the simulating settings it was concluded with reasonable certainty that the frameworks will not brake in the mechanical tests and gave a good justification to continue with the real mechanical tests.

Figure 9 shows the results from the time-depended simulations. As were the results from the static simulations these values are also un-realistically small due to the simplifications in the simulation model. The good result is that there are no signs of fatigue; the maximum bending value is the same through the simulation. This indicates that in theory the framework can withstand the real fatigue tests.

4.2 Mechanical test results

To ensure the results are reliable, 10 iterations of normal bending tests and 5 iterations of fatigue tests were conducted to each framework size class. In bending tests the testing machine started logging the bending and force values when the jaws reached the framework between them. In fatigue tests the jaws had to be closed manually as well as possible, this inflicts some error in the bending values when the initial empty space is also incorporated into them.

Table 2. Simulation results from static simulations [μm].

Size class	Occlusion simulations	Mechanical test simulations
Small	16.1	26,1
Medium	13.6	20,0
Large	12.4	18,5

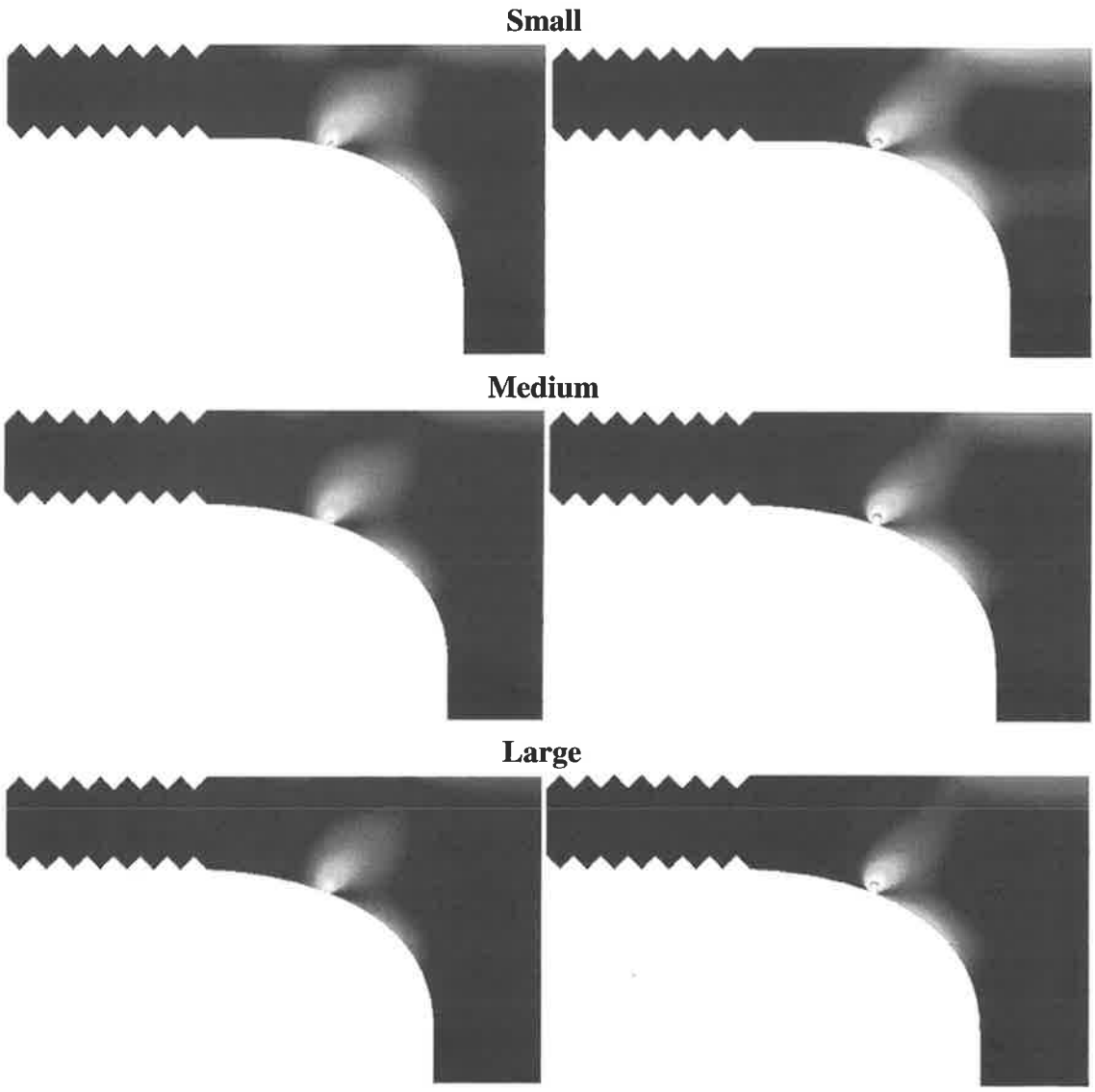

Figure 9. Von Mises stress graphs of all of the frameworks in occlusion and mechanical test simulations respectively.

Figures 10 A, B and C show the results of bending tests for the frameworks. The results show that the frameworks can easily withstand the human occlusion forces without permanent deformation and none of the frameworks broke during the tests.

Figures 11 A, B and C show the results of fatigue test of one of each framework size class. The bending values change between figures radically due to the manual closing of the jaws before tests began but the bending during the tests change only approximately 0.14–0.10 mm. None of the frameworks broke in these tests either.

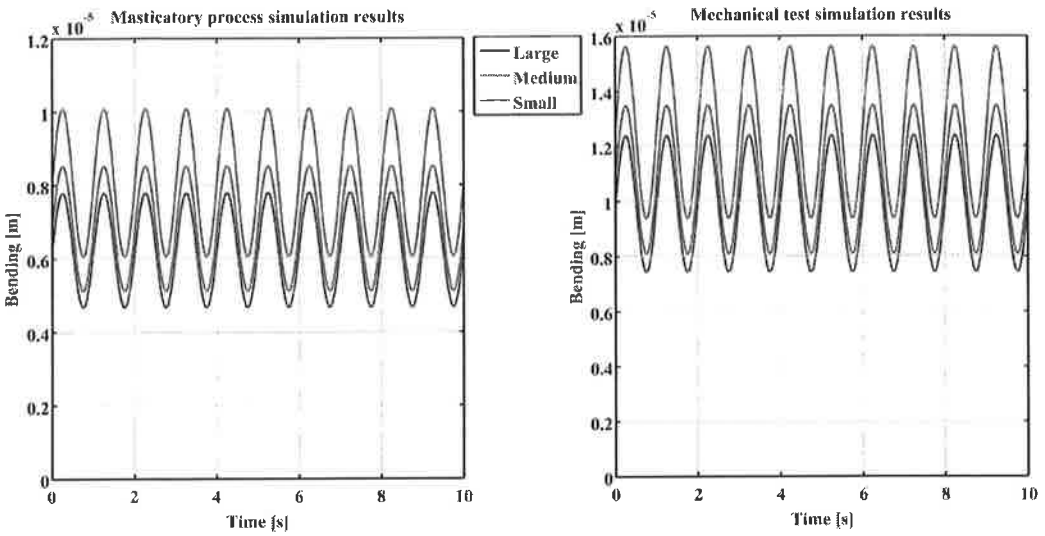

Figure 9. Bending values from time-depended simulations.

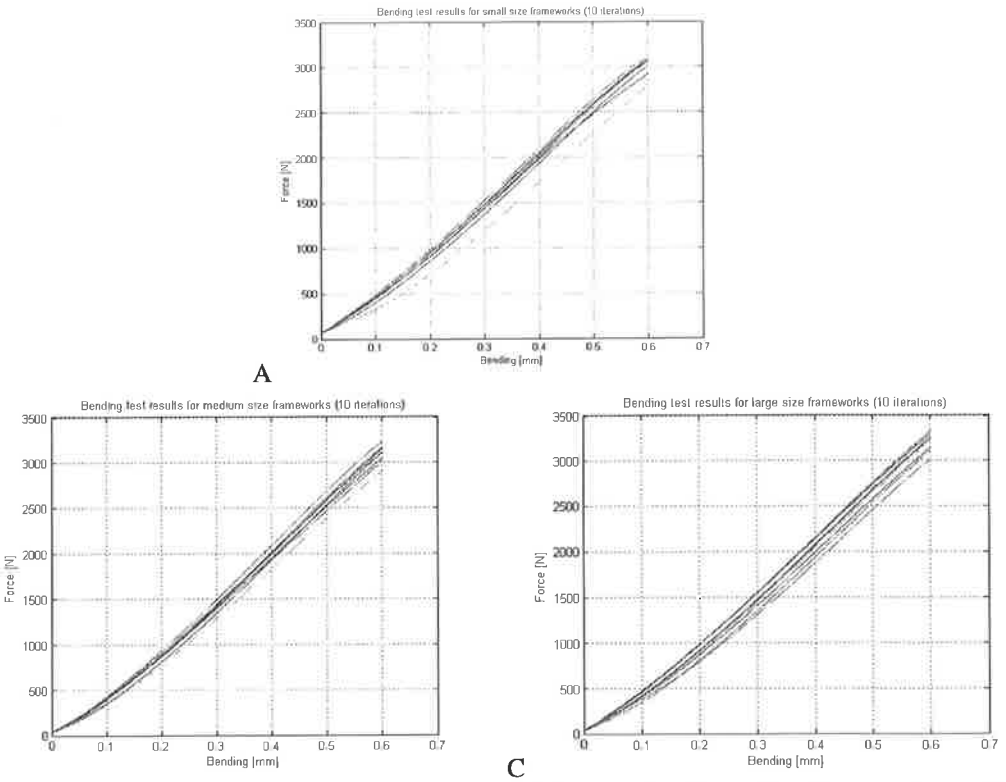

Figure 10. The results of the bending tests for A. small frameworks, B. medium frameworks and C. large frameworks.

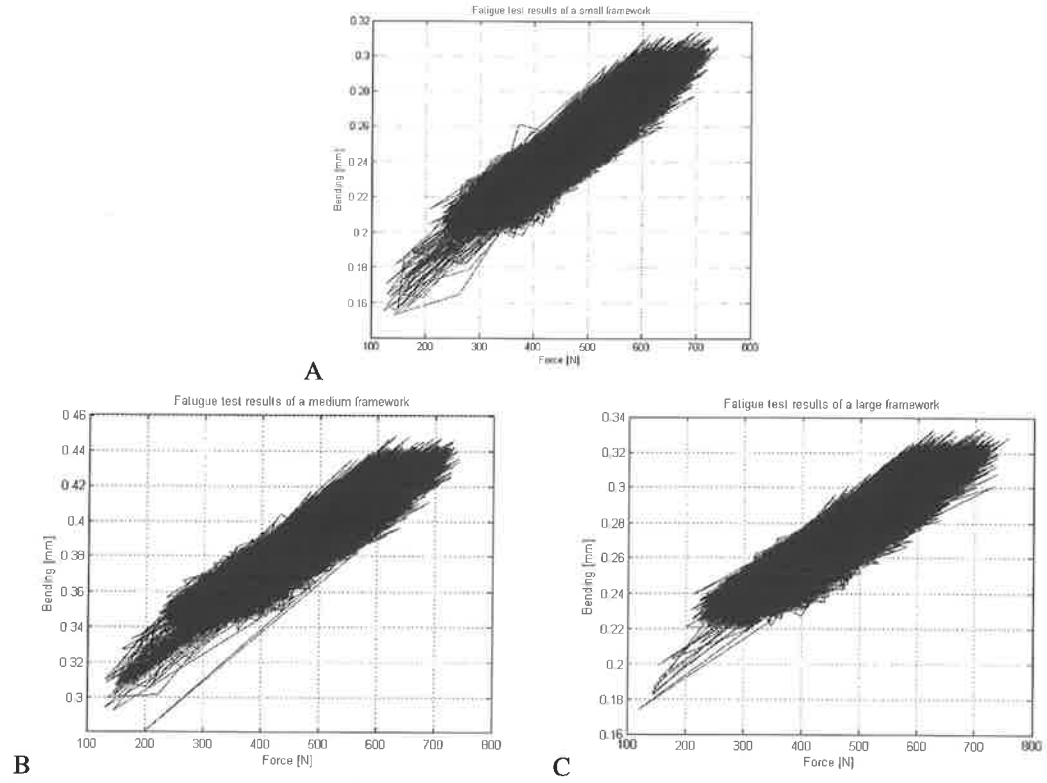

Figure 11. Fatigue test results of example cases.

5. CONCLUSIONS AND FUTURE WORK

When comparing the material, manufacture method, simulation and mechanical test results it can be concluded that the laser cut titanium IFPD frameworks have potential to be part of the dental health care. They will not be able to make any existent IFPD manufacture method obsolete as they can be only used in certain areas in molar and pre-molar areas. In the cases where they can be used they will significantly shorten the IFPD overall manufacture time for the dental practitioner as the framework's manufacture time changes from 3–5 hours to tens of minutes.

Future work includes further optimization of the framework design to minimize the amount of material that has to be removed be the dental practitioner to make the framework to fit in its place. The FEM simulations can also be optimized to include *e.g.* the abutment teeth or the steel support of the testing machine. Development of laser cut framework for incisor area where the attachment of the denture is more demanding will be made possible by 3D-lasers and that will be interesting topic also.

REFERENCES

[1] M. A. Iglesia-Puig, A. Arellano-Cabornero, Inlay fixed partial denture as a conservative approach for restoring posterior missing teeth: A clinical report, Journal of Prosthetic Dentistry, 89, 443–445, 2003.

[2] M. A. Imam, A. C. Fraker, Titanium alloys as implant materials, Medical Applications of Titanium and Its Alloys: The Material and Biological Issues, S. A. Brown, J. E. Lemons (eds.), ASTM, 3–16, 1996.

[3] P. Kovacs, J. A. Davidson, Chemical and electrochemical aspects of the biocompatibility of titanium and its alloys, Medical Applications of Titanium and Its Alloys: The Material and Biological Issues, S. A. Brown, J. E. Lemons (eds.), ASTM, 163–177, 1996.

[4] M. Könönen, J. Rintanen, A. Waltimo, P. Kempainen, Titanium framework removable partial denture used for patient allergic to other metals: A clinical report and literature review, The Journal of Prosthetic Dentistry, 73, 4–7, 1995.

[5] Comsol, CAD Import Module User's Guide, 5, 2007

[6] A. Waltimo, M. Könönen, A novel bite force recorder and maximal isometric bite force values for healthy young adults, Scandinavian Journal of Dental Research, 101, 171–175, 1993.

[7] E. O. Ezugwu, Z. M. Wang, Titanium alloys and their machinability – a review, Journal of Materials Processing Technology, 68, 262-274, 1997.

[8] T. Väisänen, Titaanin koneistaminen, Teknillinen korkeakoulu, Konetekniikan osasto, Konepajatekniikan laboratorio, 2000.

[9] V. Kujanpää, A. Salminen, J. Vihinen, Lasertyöstö, Teknologia teollisuus, 2005.

[10] G. Lûtjering, J. C. Williams, Titanium, Springer, 2007.

ACKNOWLEDGEMENTS

The author gives his gratitude to Ph.D. LDS Jukka Kentala and CDT Timo Nieminen for their insights about dental sciences, D.Sc.(Tech.) Harri Hakula for his help in FEM-analysis and Veslatec Oy for manufacturing the prototypes and custom-made materials testing machine jaws for mechanical tests.

TENSOR'S SYMMETRIZATION ON METRIC SPACES AND THEIR APPLICATIONS IN CONTINUUM MECHANICS

SAMI HOLOPAINEN

Department of Solids Mechanics
Lund University
P. O. Box 118
SWE-22100 LUND, SWEDEN
e-mail: Sami.Holopainen@solid.lth.se

ABSTRACT

The main goal of the present paper is to clear up the determination and the purpose of the duals and transpositions of a general high order tensor. The duals and the transpositions are especially needed for the representation of symmetries. Despite the symmetry is well defined in the literature for bilinear maps, for general multilinear maps or higher order tensors they still remain abstract thinking about applications. To find proper definitions also for them, first the bilinear maps and their dual and transpose are briefly recalled. Then the general higher order tensor is obtained by means of the multilinear extension and represented on the tensor spaces. Finally also their duals and the transpositions are determined. Since a tensor is understood to be an invariant quantity, the usage of absolute and closed-form presentations are preferred. As an application in continuum mechanics, the transpositions of important fourth order tensor are determined.

1. INTRODUCTION

The symmetry of linear maps or tensors are often required in continuum mechanics. For that the corresponding operation, called the symmetrization must also define for the computational implementation. The approach of *tensor analysis on manifolds* are used instead of the classical one, when the clear distinction between the dual and the corresponding primary vector spaces exists, cf. Abraham et al [1], Stumpf and Hoppe [12]. In this presentation the closed-form representations for the transpositions of a tensor of different forms are developed. It is also shown which forms are possible to symmetrize either by means of the dual maps or using the transposed, metric-dependent maps. For that, as a novelty, the explicit expressions for the transposed multilinear maps are also developed.

An important application in continuum mechanics is the fourth order stiffness tensor, which is derived as a second order partial derivative of a potential function with respect to a kinematic tensor. If a kinematic tensor is symmetric, the produced stiffness tensor has two minor symmetries. Then from the existence of a quadratic internal energy rate follows that the stiffness tensor is self-adjoint which property leads to the major symmetry. The tensor having both the major and the minor symmetries is called *supersymmetric tensor.*

In the present paper some novel results are given in that context. For that, as the indispensable part the important double contraction of 4th order tensor with a 2nd order one (4:2) and (2:4) are defined to be consistent with the essential rate relation, the product derivative rule and the chain rule, cf. Itskov [5]. Then some frequently used results are refined such that they are given by means of the duals instead of the transposes. After that, as the main results the explicit expressions for the transpositions of a fourth order tensor are constructed from the second order ones. Consequently the expressions of the transpositions depend on the metric of the metric vector spaces being involved. Then also the difference between the transpositions and the corresponding duals can be clearly identified contrary to the classical approach, cf. Basar and Weichert [2], Van der Giessen [3], Itskov [6], Kintzel [7].

First, in Chapter 2 a brief survey of multilinear (m-linear) algebra is given. There the definition, the existence and the uniqueness of a tensor space and the special decomposable tensor are shortly established. By means of these results tensor is defined as a map between tensor spaces, which are obtained from the cartesian product vector space by means of the unique maps. In Chapter 3 the vector and the dual or covector in addition to their scalar and inner product are recapitulated. Then a general scalar and inner product are defined uniquely by means of the decomposable tensors. To define the tensor's dual and transpose by a convenient way, the general scalar and inner product are split to the two part in Chapter 5. By this, In Chapter 6, the important double contraction is redefined to be consistent with the product derivative rule and the essential rate relation, cf. Itskov [5]. The main results in Chapter 7 compress the derivation of the transpositions of important 4th order tensor on general tensor spaces or on manifolds. There the transpositions of three kinds, namely the major and two minor transpositions are defined. Then e.g. the essential inner power can be properly represented by the double contraction of a fourth order stiffness tensor with second order tensors from the both side denoted by (2:4:2). Consequently the tensor symmetries including the metrics of the ambient space become properly determined. To this context, e.g. the stiffness tensor often include all the three symmetries when it is called supersymmetric tensor.

2. INTRODUCTION, EXISTENCE AND UNIQUENESS OF M-LINEAR FUNCTIONS

The main purpose of this chapter is the introduction of a tensor and a tensor product and verify their existence and uniqueness. The theory of tensor algebra is based on the extension of the classical linear algebra to the multilinear algebra with some restrictions. Since the multilinear algebra is generally not applied to continuum mechanics a brief survey is given in the following, cf. Merris [10], Greub [4]. Roughly speaking, in linear algebra one deals with vectors on vector spaces, but in multilinear algebra one deals with tensors on tensor spaces. A tensor is represented as an object on tensor spaces, which are products of inner-product spaces. The products are the tensor products denoted by $'\otimes'$. Existence of a tensor is verified by the *universal factorization property* (UFP), cf. Merris [10]. The uniqueness of the tensor product follows from the isomorphism included to the maps in UFP. Here, only one- and two-point tensors are considered because they are sufficient in continuum mechanics. A tensor is called a *two-point tensor* if it is defined on two different vector spaces $\mathfrak{V}, \mathfrak{W}$ while a *one-point tensor* is defined either on $\mathfrak{V}$ or on $\mathfrak{W}$.

Let $\mathfrak{V}_1, \mathfrak{V}_2, ..., \mathfrak{V}_m$ and $\mathbb{T}$ be vector spaces. A function $\mathbf{f} : \mathfrak{V}_1 \times \mathfrak{V}_2 \times ... \times \mathfrak{V}_m \to \mathbb{T}$ is m-linear (multilinear) if $\mathbf{f}$ is linear separately in each component of the vector space $\mathfrak{V}_1 \times \mathfrak{V}_2 \times ... \times \mathfrak{V}_m = \{(\mathbf{v}_1, \mathbf{v}_2, ..., \mathbf{v}_i, ..., \mathbf{v}_m) : \mathbf{v}_i \in \mathfrak{V}_i, 1 \leq i \leq m\}$ or

$$\mathbf{f}(\mathbf{v}_1, \mathbf{v}_2, ..., c\mathbf{u}_i + d\mathbf{w}_i, ..., \mathbf{v}_m) = c\mathbf{f}(\mathbf{v}_1, \mathbf{v}_2, ..., \mathbf{u}_i, ..., \mathbf{v}_m) + d\mathbf{f}(\mathbf{v}_1, \mathbf{v}_2, ..., \mathbf{w}_i, ..., \mathbf{v}_m), \quad (1)$$

$\mathbf{v}_i = c\mathbf{u}_i + d\mathbf{w}_i \, 1 \leq i \leq m, c, d \in \mathbb{R}$.

Let $\mathfrak{V}_1, \mathfrak{V}_2, ..., \mathfrak{V}_m$ be vector spaces. A vector space $\mathbb{T}$ and a m-linear function $\mathbf{\Phi} : \mathfrak{V}_1 \times \mathfrak{V}_2 \times ... \times \mathfrak{V}_m \rightarrow \mathbb{T}$ are said to satisfy the *Universal Factorization Property* (UFP) if, for every vector space $\mathbb{S}$, and every m-linear function $\mathbf{f} : \mathfrak{V}_1 \times \mathfrak{V}_2 \times ... \times \mathfrak{V}_m \rightarrow \mathbb{S}$, there exists a linear function

$$\mathbf{h} : \mathbb{T} \rightarrow \mathbb{S} \quad s.t. \quad \mathbf{f} = \mathbf{h} \circ \mathbf{\Phi}. \tag{2}$$

The pair $(\mathbb{T}, \mathbf{\Phi})$, which satisfies UFP is called the *universal pair*.

Figure 1: Commutative diagram

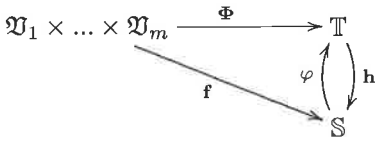

To verify the *existence of universal pair* one has to show that there exist $\mathbb{T}, \mathbf{\Phi}$ and $\mathbf{h}$ such that the diagram in Fig. 1 commutes for each $\mathbf{f}$. I.e. $\varphi = \mathbf{h}^{-1}$ exists, cf. Merris [10], Thm. 5.9.

Suppose the pairs $(\mathbb{S}, \mathbf{f})$ and $(\mathbb{T}, \mathbf{\Phi})$ satisfy the UFP for $\mathfrak{V}_1, \mathfrak{V}_2, ..., \mathfrak{V}_m$. The pairs are *isomorphic* if there exists an invertible linear transformation φ from $\mathbb{S}$ onto $\mathbb{T}$ such that

$$\mathbf{\Phi} = \varphi \circ \mathbf{f}. \tag{3}$$

It follows that the universal pairs $(\mathbb{S}, \mathbf{f})$ and $(\mathbb{T}, \mathbf{\Phi})$ are isomorphic by Eq. (3). Next the tensor product space is defined to be spanned by the decomposable tensor which result is required later for the definition of a tensor, its dual and transpose uniquely.

Let $\mathbf{\Phi} : \mathfrak{V}_1 \times \mathfrak{V}_2 \times ... \times \mathfrak{V}_m \rightarrow \mathbb{T}$ be a m-linear map. If the pair $(\mathbb{T}, \mathbf{\Phi})$ satisfies UFP for $\mathfrak{V}_1, \mathfrak{V}_2, ..., \mathfrak{V}_m$, then a *decomposable tensor*

$$\mathbf{\Phi}(\mathbf{v}_1, \mathbf{v}_2, ..., \mathbf{v}_m) = \mathbf{v}_1 \otimes \mathbf{v}_2 \otimes ... \otimes \mathbf{v}_m \in \mathbb{T} \tag{4}$$

exists, and $\mathbb{T}$ is the tensor product or the tensor product space or simply the tensor space of $\mathfrak{V}_1, \mathfrak{V}_2, ..., \mathfrak{V}_m$, written $\mathbb{T} := \mathfrak{V}_1 \otimes \mathfrak{V}_2 \otimes ... \otimes \mathfrak{V}_m$.

If $(\mathbb{S}, \mathbf{f})$ satisfies UFP then $\mathbb{S}$ is a *model* for the tensor product $\mathbb{T}$, cf. Fig. 1.

(**Associativity**). Suppose $1 \leq k \leq m$. Then $\mathfrak{V}_1 \otimes \mathfrak{V}_2 \otimes ... \otimes \mathfrak{V}_m$ is a model for $(\mathfrak{V}_1 \otimes \mathfrak{V}_2 \otimes ... \otimes \mathfrak{V}_k) \otimes (\mathfrak{V}_{k+1} \otimes \mathfrak{V}_{k+2} \otimes ... \otimes \mathfrak{V}_m)$, where

$$(\mathbf{u}_1 \otimes \mathbf{u}_2 \otimes ... \otimes \mathbf{u}_k) \otimes (\mathbf{w}_1 \otimes \mathbf{w}_2 \otimes ... \otimes \mathbf{w}_{m-k}) = \mathbf{u}_1 \otimes \mathbf{u}_2 \otimes ... \otimes \mathbf{u}_k \otimes \mathbf{w}_1 \otimes \mathbf{w}_2 \otimes ... \otimes \mathbf{w}_{m-k}. \tag{5}$$

Cf. Merris [10], Thm. 5.17.

For the definition and the existence of a tensor and tensor product on different spaces, the definition and the existence for a covector space and a dual tensor space are required. The dual space and consequently the corresponding tensor is determined as a linear map of the original basis on the dual basis being vector space isomorphism. Then it can be also shown that the dual spaces satisfy UFP, when tensors can be defined also on dual spaces. After the definition and the existence of a tensor on (co)vector and a (dual) tensor spaces it is also possible to present more general mixed-form tensor by means of the tensor products on different tensor spaces. There the tensor spaces consist of the tensor products of different vector and covector spaces. A tensor product is unique due to the isomorphism by Eq. (3). The existence of tensors and tensor spaces are verified by UFP. A comprehensive discussion related to tensors of different forms on vector and covector basis is given e.g. in the textbooks by Greub [4], Marsden and Hughes [9].

3. DUAL AND RECIPROCAL BASES ASSOCIATED TO THE SCALAR AND THE INNER PRODUCT

Let $\{\mathbf{G}_A\}$ and $\{\mathbf{g}_A\}$ be the ordered bases of the vector spaces $\mathfrak{V}$ and $\mathfrak{W}$ respectively. On the vector spaces $(\mathfrak{V}, \mathbf{G})$ and $(\mathfrak{W}, \mathbf{g})$ equipped with a metric $\mathbf{G}$ and $\mathbf{g}$, the so called reciprocal bases $\{\mathbf{G}^B\}$ and $\{\mathbf{g}^b\}$ to $\{\mathbf{G}_A\}$ and $\{\mathbf{g}_a\}$ respectively are defined by the inner product as

$$\mathbf{G}_A \cdot \mathbf{G}^B = \delta_A^B, \quad \text{and} \quad \mathbf{g}_a \cdot \mathbf{g}^b = \delta_a^b, \tag{6}$$

where δ_A^B, δ_a^b are *Kronecker delta symbols*. The inner product is defined between objects related to the same space. With the notation $G_{AB} := \mathbf{G}_A \cdot \mathbf{G}_B$, $G^{AB} := \mathbf{G}^A \cdot \mathbf{G}^B$, and analogously for g_{ab} and g^{ab}, one can deduce the linear relations between the reciprocal vector bases and the vector bases as

$$\mathbf{G}^A = G^{AB}\mathbf{G}_B \quad \text{and} \quad \mathbf{g}^a = g^{ab}\mathbf{g}_b. \tag{7}$$

Moreover,

$$\delta_B^A = G^{AC}G_{CB} \quad \text{and} \quad \delta_b^a = g^{ac}g_{cb} \quad \Rightarrow [G^{AB}] = [G_{AB}]^{-1} \quad \text{and} \quad [g^{ab}] = [g_{ab}]^{-1}, \tag{8}$$

where $[\cdot]$ denotes the component matrix of the metric tensor. It then follows that

$$\mathbf{G}_A = G_{AB}\mathbf{G}^B \quad \text{and} \quad \mathbf{g}_a = g_{ab}\mathbf{g}^b \tag{9}$$

and thereby, a vector can be written as $\mathbf{a} = a^A\mathbf{G}_A = a_A\mathbf{G}^A$. The vector's component a^A is related to the resiprocal vector's component a_A by $a^A = G^{AB}a_B$.

The corresponding dual bases $\{\mathfrak{G}^A\}$ and $\{\mathfrak{g}^a\}$ on the dual spaces, $\mathfrak{V}^*, \mathfrak{W}^*$ respectively, are defined as

$$\langle \mathfrak{G}^A, \mathbf{G}_B \rangle_{\mathfrak{V}} = \delta_B^A, \quad \langle \mathfrak{g}^a, \mathbf{g}_b \rangle_{\mathfrak{W}} = \delta_b^a, \tag{10}$$

where the bracket $\langle\ ,\ \rangle$ expresses the dual pairing also called the scalar product. This allow the metric tensors to be defined as $\mathbf{G} = G_{AB}\mathfrak{G}^A \otimes \mathfrak{G}^B \in \mathfrak{V}^* \otimes \mathfrak{V}^*$ and $\mathbf{g} = g_{ab}\mathfrak{g}^a \otimes \mathfrak{g}^b \in \mathfrak{W}^* \otimes \mathfrak{W}^*$.

Let be a linear map represented as a tensor product between a vector $\mathbf{u} \in \mathfrak{W}$ and a covector $\mathfrak{b} \in \mathfrak{V}^*$ as $\mathbf{F} = \mathbf{u} \otimes \mathfrak{b} \in \mathfrak{W} \otimes \mathfrak{V}^*$. The linear mapping $\mathbf{Fa}, \mathbf{a} \in \mathfrak{V}$, is carried out by the scalar product of $\mathfrak{b}, \mathbf{a}$ as $\mathbf{Fa} = (\mathbf{u} \otimes \mathfrak{b})\mathbf{a} = \langle \mathfrak{b}, \mathbf{a} \rangle_{\mathfrak{V}}\mathbf{u} \in \mathfrak{W}$. This results consistently the following identity which relates the *inner product* (or the *dot product induced by the metric* $\mathbf{G}$) and the scalar product as

$$\cdot : \mathfrak{V} \times \mathfrak{V} \to \mathbb{R}, \quad \mathbf{a} \cdot \mathbf{b} := \langle \mathbf{Ga}, \mathbf{b} \rangle_{\mathfrak{V}}, \tag{11}$$

where $\mathbf{a}^\flat := \mathbf{Ga}$ is called the covector associated to $\mathbf{a}$. If the metric space is obvious, $\langle \cdot, \cdot \rangle$ can be used instead of $\langle \cdot, \cdot \rangle_{\mathfrak{V}}$. The relation between the dual and the reciprocal basis is given by

$$\mathfrak{G}^A = \mathbf{G}\mathbf{G}^A =: (\mathbf{G}^A)^\flat \in \mathfrak{V}^* \tag{12}$$

or the dual vector equals to covector associated to $\mathbf{G}^A$. Now, the scalar product can be written as an inner product of two vectors on $\mathfrak{V}$, naturally involving the reciprocal base vectors as

$$\langle \mathfrak{G}^A, \mathbf{G}_B \rangle = \langle \mathbf{G}\mathbf{G}^A, \mathbf{G}_B \rangle = \mathbf{G}^A \cdot \mathbf{G}_B = \delta_B^A. \tag{13}$$

In the case of the tensor algebra on manifolds the application of tensors on vectors is based on the dual pairing, cf. Stumpf and Hoppe [12]. By above results the dual pairing can be written as a

dot product $\langle \mathfrak{b}, \mathbf{a} \rangle_{\mathfrak{V}} = \mathbf{b} \cdot \mathbf{a} \in \mathbb{R}$, where $\mathbf{b}$ is the vector related to the covector $\mathfrak{b}$. Then from Eqs (8)...(12) follows that

$$\mathbf{G}^{-1}\mathfrak{G}^A \cdot \mathbf{G}^{-1} = \mathbf{G}^A \cdot \mathbf{G}^{-1} = G^{AB}\mathbf{G}_B = \mathbf{G}^A, \quad \mathbf{G}^{-1} \cdot \mathbf{G}_A \cdot \mathbf{G}^{-1} = \mathbf{G}_A. \tag{14}$$

I.e. the vector and the reciprocal vector are not affected by the contravariant metric $\mathbf{G}^{-1} =: \mathbf{G}^\sharp$.

The presentation of linear maps $\mathbf{h}$ (cf. Fig. 1) by tensors depends on the specific identification of linear (or vector) spaces $\mathfrak{V}, \mathfrak{W}$ and their dual (vector) space $\mathfrak{V}^*, \mathfrak{W}^*$, cf. Stumpf and Hoppe [12].

Let be an identification of a bilinear map as[1]:

$$\begin{aligned} &Lin(\mathfrak{V}; \mathfrak{W}) : \mathfrak{V} \to \mathfrak{W} \quad \text{or } Lin(\mathfrak{W}^* \times \mathfrak{V}; \mathbb{R}) \doteq Lin(\mathfrak{W}^* \otimes \mathfrak{V}; \mathbb{R}) : \mathfrak{W}^* \times \mathfrak{V} \to \mathbb{R} \\ &\text{s.t.} \quad Lin(\mathfrak{W}^* \times \mathfrak{V}; \mathbb{R}) \cong \mathfrak{W} \otimes \mathfrak{V}^*. \end{aligned} \tag{15}$$

Similarly for multilinear maps[2],

$$\begin{aligned} &Lin(\mathfrak{W}_1^* \times \mathfrak{V}_1 \times \mathfrak{W}_2^* \times \mathfrak{V}_2 \times ... \times \mathfrak{W}_m^* \times \mathfrak{V}_m; \mathbb{R}) \doteq \\ &Lin(\mathfrak{W}_1^* \otimes \mathfrak{V}_1 \otimes \mathfrak{W}_2^* \otimes \mathfrak{V}_2 \otimes ... \otimes \mathfrak{W}_m^* \otimes \mathfrak{V}_m; \mathbb{R}) \cong \\ &\mathfrak{W}_1 \otimes \mathfrak{V}_1^* \otimes \mathfrak{W}_2 \otimes \mathfrak{V}_2^* \otimes ... \otimes \mathfrak{W}_m \otimes \mathfrak{V}_m^*. \end{aligned} \tag{16}$$

Usually in continuum mechanics the identification $\mathfrak{V}_i = \mathfrak{V}$, $\mathfrak{W}_i = \mathfrak{W} \forall\, 1 \le i \le m$ is sufficient. As an illustration, certain type of tensors are expressed next. Now any *second order tensor* (a bold capital letter) and any fourth order tensor (a bold italic capital letter) is defined as a bilinear map and a four-linear map respectively.

A *second order one-point tensor* is given on different basis by Eqs (7) and (12) as

$$\begin{aligned} &\mathbf{C}^\flat = C_{ij}\mathfrak{G}^i \otimes \mathfrak{G}^j = C_{ij}\mathbf{G}\mathbf{G}^i \otimes \mathbf{G}\mathbf{G}^j = C_{ij}G^{ik}G^{jl}\mathbf{G}\mathbf{G}_k \otimes \mathbf{G}_l\mathbf{G} = C^{ij}\mathbf{G}\mathbf{G}_i \otimes \mathbf{G}_j\mathbf{G} = \\ &\mathbf{G}\mathbf{C}^\sharp\mathbf{G} = ... = C_{ij}G^{jl}\mathfrak{G}^i \otimes \mathbf{G}_l\mathbf{G} = C_{i.}^{\ j}\mathfrak{G}^i \otimes \mathbf{G}_j\mathbf{G} = ... = C_{.j}^{\ i}\mathbf{G}\mathbf{G}_i \otimes \mathfrak{G}^j =: \mathbf{G}\mathbf{C}^\natural \quad \text{such that} \\ &\mathbf{C}^\flat = C_{ij}\mathfrak{G}^i \otimes \mathfrak{G}^j \in Lin(\mathfrak{V}; \mathfrak{V}^*),\ \mathbf{C}^\sharp = C^{ij}\mathbf{G}_i \otimes \mathbf{G}_j \in Lin(\mathfrak{V}^*; \mathfrak{V}), \\ &\mathbf{C}^\natural = C_{.j}^{i}\mathbf{G}_i \otimes \mathfrak{G}^j \in Lin(\mathfrak{V}; \mathfrak{V}), \\ &\text{where the components are obtained as } \mathbf{C}^\sharp(\mathfrak{G}^i, \mathfrak{G}^j) = C^{ij} = C_{kl}G^{ik}G^{jl}, ..., C_{.j}^{i} = C_{kj}G^{ki}. \end{aligned} \tag{17}$$

Above the fact $\mathbf{a} \otimes \mathbf{G}\mathbf{b} = (\mathbf{a} \otimes \mathbf{b})\mathbf{G}$ is used. I.e. the relations $\mathbf{C}^\flat = \mathbf{G}\mathbf{C}^\sharp\mathbf{G} = \mathbf{G}\mathbf{C}^\natural \in Lin(\mathfrak{V}; \mathfrak{V}^*)$ hold. If some of the base-(co)vectors are replaced by a base-(co)vectors of a different vector (tangent) space, the produced tensor is called a *second order two-point tensor*, Marsden and Hughes [9].

A fourth order one-point tensor is as

$$\begin{aligned} &\mathcal{C}^\flat = \mathcal{C}_{ijkl}\mathfrak{G}^i \otimes \mathfrak{G}^j \otimes \mathfrak{G}^k \otimes \mathfrak{G}^l = \mathcal{C}_{ijkl}G^{im}\mathbf{G}\mathbf{G}_m \otimes G^{jn}\mathbf{G}\mathbf{G}_n \otimes G^{kp}\mathbf{G}\mathbf{G}_p \otimes G^{lr}\mathbf{G}\mathbf{G}_r \\ &\quad = ... = \mathcal{C}_{.j.l}^{i\ \ k}\mathbf{G}\mathbf{G}_i \otimes \mathfrak{G}^j \otimes \mathbf{G}\mathbf{G}_k \otimes \mathfrak{G}^l \quad \text{s.t,} \\ &\mathcal{C}^\flat = \mathcal{C}_{ijkl}\mathfrak{G}^i \otimes \mathfrak{G}^j \otimes \mathfrak{G}^k \otimes \mathfrak{G}^l \in Lin(\mathfrak{V} \times \mathfrak{V} \times \mathfrak{V} \times \mathfrak{V}; \mathbb{R}), \\ &\mathcal{C}^\sharp = \mathcal{C}^{mnqr}\mathbf{G}_m \otimes \mathbf{G}_n \otimes \mathbf{G}_q \otimes \mathbf{G}_r \in Lin(\mathfrak{V}^* \times \mathfrak{V}^* \times \mathfrak{V}^* \times \mathfrak{V}^*; \mathbb{R}), ..., \\ &\mathcal{C}^\natural = \mathcal{C}_{.j.l}^{i\ \ k}\mathbf{G}_i \otimes \mathfrak{G}^j \otimes \mathbf{G}_k \otimes \mathfrak{G}^l \in Lin(\mathfrak{V} \times \mathfrak{V}^* \times \mathfrak{V} \times \mathfrak{V}^*; \mathbb{R}), \quad \text{where} \\ &\mathcal{C}^{mnqr} := \mathcal{C}_{ijkl}G^{im}G^{jn}G^{qk}G^{rl} \quad \text{etc.} \end{aligned} \tag{18}$$

[1] Below $\doteq$ implies that Fig. commutes.

[2] The first form, ';' is defined via the special scalar products being consistent with the tensor's order, cf. e.g. E.q. (40).

The first one $'\flat'$ is a covariant form, the second one $'\sharp'$ is the contravariant form,..., and the last one $'\natural'$ is called the mixed-variant form. If some of the base-(co)vectors are replaced by the base-(co)vectors of a different vector (tangent) space, the produced tensor is a *fourth order two-point tensor*. As shown by the obtained results, one can not equalize the different forms as in the classical tensor algebra. E.g. $\mathcal{C}^\flat \neq \mathcal{C}^\natural$ etc. Next, the definition of the scalar and the inner product is enlarged to concern higher order tensors. Even though the scalar and the inner product are uniquely defined for m-linear functions, they can completely and uniquely defined also for tensors on tensor spaces by means of the corresponding decomposable tensors based on UFP. That is, because the decomposable tensor spans the corresponding tensor space.

Let $\mathbf{v} := \mathbf{v}_1 \otimes \mathbf{v}_2 \otimes ... \otimes \mathbf{v}_m$ and $\mathfrak{w} := \mathfrak{w}_1 \otimes \mathfrak{w}_2 \otimes ... \otimes \mathfrak{w}_m$ be decomposable tensors on $\mathfrak{V}_1 \otimes \mathfrak{V}_2 \otimes ... \otimes \mathfrak{V}_m$ and $\mathfrak{V}_1^* \otimes \mathfrak{V}_2^* \otimes ... \otimes \mathfrak{V}_m^*$ respectively. The unique scalar product on $\mathfrak{V}_1 \otimes ... \otimes \mathfrak{V}_m$ that satisfies

$$\langle \mathbf{v}, \mathfrak{w} \rangle := \langle \mathbf{v}_1 \otimes \mathbf{v}_2 \otimes ... \otimes \mathbf{v}_m, \mathfrak{w}_1 \otimes \mathfrak{w}_2 \otimes ... \otimes \mathfrak{w}_m \rangle = \prod_{i=1}^{m} \langle \mathbf{v}_i, \mathfrak{w}_i \rangle \in \mathbb{R}, \tag{19}$$

$\mathbf{v}_i \in \mathfrak{V}_i, \mathfrak{w}_i \in \mathfrak{V}_i^*$, $1 \leqslant i \leqslant m$, is called the *induced scalar product*. Let $\mathbf{w} := \mathbf{w}_1 \otimes \mathbf{w}_2 \otimes ... \otimes \mathbf{w}_m \in \mathfrak{V}_1 \otimes \mathfrak{V}_2 \otimes ... \otimes \mathfrak{V}_m$ be the decomposable tensor. The unique inner product,

$$\mathbf{v} \bullet \mathbf{w} := (\mathbf{v}_1 \otimes \mathbf{v}_2 \otimes ... \otimes \mathbf{v}_m) \bullet (\mathbf{w}_1 \otimes \mathbf{w}_2 \otimes ... \otimes \mathbf{w}_m) = \prod_{i=1}^{m} (\mathbf{v}_i \cdot \mathbf{w}_i) \in \mathbb{R}, \tag{20}$$

$\mathbf{w}_i \in \mathfrak{V}_i$, $1 \leqslant i \leqslant m$, is called the *induced inner product.*

The scalar and the inner product are defined between objects related to the same space. As the inner product for two vectors, the generalized inner product for tensors is given by means of the scalar products as

$$\cdot : \mathfrak{V}_1 \times \mathfrak{V}_2 \times ... \times \mathfrak{V}_{2m} \to \mathbb{R}, \quad \mathbf{v} \bullet \mathbf{w} := \langle \tilde{\mathbf{G}} \mathbf{v}, \mathbf{w} \rangle_{\mathfrak{V}}, \tag{21}$$

where $\tilde{\mathbf{G}} := \mathbf{G}_1 \otimes \mathbf{G}_2 \otimes ... \mathbf{G}_m$, $\mathbf{G}_i \in \mathfrak{V}_i^* \otimes \mathfrak{V}_i^*$, $1 \leq i \leq m$ and $\tilde{\mathbf{G}}\mathbf{v} =: \mathbf{v}^\flat$ is called the co-tensor associated to $\mathbf{v}$.

4. THE DUAL AND THE TRANSPOSED MAP

The purpose of that section is to emphasize the difference between the dual and the transpose. The tensor's duals and transpositions are required for the presentation of the tensor symmetries and the corresponding symmetrizations. They must be determined invariantly w.r.t any co-ordinate system. Transpositions are associated to the inner products meanwhile the corresponding duals are used with the scalar products. The symmetric co- or contra- variant tensor field (on topological manifold $\mathcal{M}$) is the co- or contra-variant tensor field of which every value in every point $p \in \mathcal{M}$ is a symmetric tensor. One can also determine the symmetric mixed-variant tensor field and tensor. An important symmetric tensor is the symmetric fourth order stiffness tensor. E.g. its constitutive component or the tangent modulus is developed as the second variation of a (locally convex and piece-wise continuously differentiable) free energy function[3] on general tensor spaces or on the Riemannian manifold. This type of tangent modulus is always symmetric, because the partial derivatives commute for the smooth enough function, cf. Marsden and Hughes [9] (Prop. 1.5, p. 184), Makowski and Stumpf [8].

Instead of the complete symmetry some special symmetry properties are encountered in continuum mechanics. First, for the major-symmetry there are two approaches:

[3] In the case of isothermal deformation process the free energy and the internal energy (often called stored energy function) coincide.

1. The symmetry using the duality or the dual-symmetry for which $T^* = T$ or
2. the symmetry using the transposition or the transposition-symmetry for which $T^T = T$.

The first one is convenient for the co- or contra-variant forms using the scalar products while the second one is suitable for the mixed forms. Indeed, then the members lie on the same space. The symmetry defined as

$$\mathcal{C}^T = \mathcal{C}^* = \mathcal{C}, \quad \mathcal{C} \in Lin \tag{22}$$

holds only when the metric is identity[4]. Indeed, if $\mathcal{C}^T = \mathcal{G}_1^{-1}\mathcal{C}^*\mathcal{G}_2 = \mathcal{C}$ or $\mathcal{G}_1\mathcal{C}\mathcal{G}_2^{-1} = \mathcal{C}^* = \mathcal{C}$, must $\mathcal{G}_1 = \mathcal{G}_2 = \mathcal{I}$ or they are pure identities.

Above, the tensor algebra on topological vector spaces is discussed. Because those spaces are typically induced by manifolds, tensor algebra on manifolds is considered. A manifold as a basic notion of a body seems to offer essential clarifications of the formulations in continuum mechanics, cf. Abraham et al [1], Stumpf and Hoppe [12] and in multibody dynamics, cf. Mäkinen [11]. Then there exist a clear distinction between vectors and covectors and an explicit application of metrics (on Riemannian manifolds). Consequently the symmetry and e.g. the push-forward and the pull-back operations can be clearly defined, cf. Stumpf and Hoppe [12]. Also a tensor as a linear map can be constructed naturally on points of a manifold or on its tangent spaces of the same dimension as manifolds are spanned.

Let $T_{\mathbf{X}}\mathcal{P}_0, T_{\mathbf{x}}\mathcal{P}$ be the tangent spaces on manifold given in embedding space $\mathfrak{V}, \mathfrak{W}$ with the natural base vectors $\{\mathbf{G}_A\}, \{\mathbf{g}_a\}$ respectively. Similarly the corresponding dual bases on the cotangent spaces $T^*_{\mathbf{X}}\mathcal{P}_0, T^*_{\mathbf{x}}\mathcal{P}$ are $\{\mathfrak{G}^A\}, \{\mathfrak{g}^a\}$ respectively. Then the linear tangent map known as the *deformation gradient* is defined locally as a two-point tensor, cf. Stumpf and Hoppe [12],

$$\mathbf{F} := F^a_{.A}\mathbf{g}_a \otimes \mathfrak{G}^A \in Lin(T_{\mathbf{X}}\mathcal{P}_0; T_{\mathbf{x}}\mathcal{P}). \tag{23}$$

The *adjoint* or *dual operator* $\mathbf{F}^* \in Lin(T^*_{\mathbf{x}}\mathcal{P}; T^*_{\mathbf{X}}\mathcal{P}_0)$ of $\mathbf{F}$ is defined by means of the dual pairing as follows

$$\langle \mathbf{F}^*\mathfrak{f}, \mathbf{a}\rangle_{T_{\mathbf{X}}\mathcal{P}_0} = \langle \mathfrak{f}, \mathbf{F}\mathbf{a}\rangle_{T_{\mathbf{x}}\mathcal{P}} \in \mathbb{R} \quad \forall \mathbf{a} \in T_{\mathbf{X}}\mathcal{P}_0, \mathfrak{f} \in T^*_{\mathbf{x}}\mathcal{P}. \tag{24}$$

Since the inner product is defined between the objects associated to the same space, the transposed map becomes essential. The transpose of a two-point tensor $\mathbf{F} \in Lin\big((T_{\mathbf{X}}\mathcal{P}_0, \mathbf{G}); (T_{\mathbf{x}}\mathcal{P}, \mathbf{g})\big)$ is defined by the inner product (11) as

$$\mathbf{F}^T\mathbf{a} \cdot \mathbf{b} = \mathbf{a} \cdot \mathbf{F}\mathbf{b}. \tag{25}$$

Using the inner product (11) and Eq. (24) for the dual (see also Marsden and Hughes [9], prop. 3.4) the transpose by Eq. (25) is evaluated as $\mathbf{F}^T\mathbf{a} \cdot \mathbf{b} := \langle \mathbf{G}\mathbf{F}^T\mathbf{a}, \mathbf{b}\rangle_{\mathfrak{V}} = \langle \mathbf{g}\mathbf{a}, \mathbf{F}\mathbf{b}\rangle_{\mathfrak{W}} = \langle \mathbf{F}^*\mathbf{g}\mathbf{a}, \mathbf{b}\rangle_{\mathfrak{V}}$. I.e.,

$$\mathbf{F}^T = \mathbf{G}^{-1}\mathbf{F}^*\mathbf{g} \in Lin((T_{\mathbf{x}}\mathcal{P}, \mathbf{g}); (T_{\mathbf{X}}\mathcal{P}_0, \mathbf{G})), \quad \mathbf{F} \in Lin((T_{\mathbf{X}}\mathcal{P}_0, \mathbf{G}); (T_{\mathbf{x}}\mathcal{P}, \mathbf{g})) \tag{26}$$

By Eqs (24) and (26) together Eqs (7) and (12) the dual and transposed forms for a linear map are as

$$\mathbf{F}^* = F^a_{.A}\mathfrak{G}^A \otimes \mathbf{g}_a \quad \text{and} \quad \mathbf{F}^T = F^b_{.B}G^{AB}g_{ab}\mathbf{G}_A \otimes \mathfrak{g}^a \tag{27}$$

As for a two-point tensor, the transpose for a one-point tensor can be defined. E.g. for $\mathbf{A} \in Lin(T_{\mathbf{X}}\mathcal{P}_0; T^*_{\mathbf{X}}\mathcal{P}_0)$, cf. Giessen [3],

$$\begin{aligned}\mathbf{A}^T &= \mathbf{G}^{-1}(A_{BA}\mathfrak{G}^A \otimes \mathfrak{G}^B)\mathbf{G}^{-1} = A_{BA}\mathbf{G}^A \otimes \mathbf{G}^B = A_{BA}G^{AC}G^{BD}\mathbf{G}_C \otimes \mathbf{G}_D \\ &=: (\mathbf{A}^T)^{AB}\mathbf{G}_A \otimes \mathbf{G}_B.\end{aligned} \tag{28}$$

[4] This implies to a very special (but usual) Euclidean metric space with an orthonormal co-ordinate system.

Above representation shows that the transpose depends on the metric (tensor) of the metric vector space being involved, but the dual map is defined independently of any metric. For the covariant metric tensor, cf. Stumpf and Hoppe [12], $\mathbf{G} = \mathbf{G}^*$ and thus

$$\mathbf{G}^T = \mathbf{G}^{-1}\mathbf{G}^*\mathbf{G}^{-1} = \mathbf{G}^{-1} =: \mathbf{G}^\sharp \tag{29}$$

holds. Instead, for mixed forms $\mathbf{G}^T = \mathbf{G}$. Further, the inverses are defined by the conditions $\mathbf{F}^{-1}\mathbf{F} = \mathbf{I}$ and $\mathbf{F}\mathbf{F}^{-1} = \mathbf{i}$, where $\mathbf{I}, \mathbf{i}$ are identity tensors. Assuming the inverse exists when the dual of the inverse or the dual-inverse is a linear map,

$$\mathbf{F}^{-*} = F^A_{a.}\mathfrak{g}^a \otimes \mathbf{G}_A, \quad \mathbf{F}^{-1} = F^A_{a.}\mathbf{G}_A \otimes \mathfrak{g}^a. \tag{30}$$

5. EXTENSION TO THE HIGHER ORDER TENSORS

The dual and the transposed map of a general tensor are refined from the scalar or the inner product by Eqs (19) and (20). Based on these definitions, the transpositions of an important fourth order tensor are developed in Chapter 7.

Note: In the following the set of linear mappings between tangent or vector spaces including any component variances is denoted by Lin or Lin_{k}, $\mathrm{k} \in \{2, (3), 4, ...|$ order of a tensor$\}$ if no need for the specialization exists. Similarly the set of invertible or symmetric mappings are denoted by $Inv_k \subset Lin_k$ or $Sym_k \subset Lin_k$ respectively. In addition the usual notations $'\flat', '\natural', '\sharp'$ for covariant, mixed-variant and contravariant forms respectively are used only if necessary, e.g. when the different forms are compared.

Let be $\mathbf{V}$ (e.g. $\mathbf{v}_1 \otimes \mathbf{v}_2 \otimes ... \otimes \mathbf{v}_m$) and $\mathbf{W}$ (e.g. $\mathfrak{w}_1 \otimes \mathfrak{w}_2 \otimes ... \otimes \mathfrak{w}_m$) decomposable tensors. Then the dual map (operator) $\mathcal{C}^*$ of $\mathcal{C} \in Lin_{2m}$ is defined as

$$\langle\langle \mathcal{C}, \mathbf{V}\rangle, \mathbf{W}\rangle = \langle \mathbf{W}, \langle \mathcal{C}, \mathbf{V}\rangle\rangle = \langle\langle \mathbf{W}, \mathcal{C}\rangle, \mathbf{V}\rangle = \langle\langle \mathcal{C}^*, \mathbf{W}\rangle, \mathbf{V}\rangle \in \mathbb{R}. \tag{31}$$

Let be $\mathbf{V}$ and $\mathbf{W}$ decomposable tensors. Then the transposed map $\mathcal{C}^T$ of $\mathcal{C} \in Lin_{2m}$ is defined as

$$\langle \mathcal{C}, \mathbf{V}\rangle \bullet \mathbf{W} = \mathbf{W} \bullet \langle \mathcal{C}, \mathbf{V}\rangle = \langle (\mathbf{W} \bullet \mathcal{C}), \mathbf{V}\rangle = \langle \mathcal{C}^T, \mathbf{W}\rangle \bullet \mathbf{V} \in \mathbb{R}. \tag{32}$$

Using the generalized inner product (21) and Eq. (31) for the dual, the transpose is evaluated according to Eqs (32) and (12) as $\langle \mathcal{C}^T, \mathbf{W}\rangle \bullet \mathbf{V} = \langle\langle \mathcal{G}_1\mathcal{C}^T, \mathbf{W}\rangle, \mathbf{V}\rangle = \langle \mathcal{G}_2\mathbf{W}, \langle \mathcal{C}, \mathbf{V}\rangle\rangle = \langle\langle \mathcal{C}^*\mathcal{G}_2, \mathbf{W}\rangle, \mathbf{V}\rangle$. Thus the transpose of a higher order tensor $\mathcal{C}$ is given as

$$\mathcal{C}^T = \mathcal{G}_1^{-1}\mathcal{C}^*\mathcal{G}_2, \tag{33}$$

where $\mathcal{G}_1, \mathcal{G}_2$ are the tensors of the same order composed of the tensor products of convenient metric tensors. Representations for $\mathcal{G}_1$ and $\mathcal{G}_2$ as linear maps on the whole by tensors depend on the identification of linear spaces $\mathfrak{V}, \mathfrak{W}$ and their dual spaces $\mathfrak{V}^*, \mathfrak{W}^*$. The convenient identification is represented in Chapter 7 being consistent with the inner-product by Eq. (20) and also with the essential rate relation in continuum mechanics including the product derivative rule. I.e this identification leads to the arrangement denoted here by AR. It is consistent with the special dot products, e.g. between 4th and 2nd order tensors denoted by 4:2, 2:4 and 2:4:2, cf. Itskov [6] (specially p. 105, Eq. (5.59)). The idea is concretized in Chapter 6.

6. TENSOR PRODUCTS AND CONTRACTIONS IN CONTINUUM MECHANICS

There are introduced several tensor products and contractions for the different purposes in continuum mechanics. Let $\mathbf{\Phi}_1, \mathbf{\Phi}_2$ be decomposable tensors and $\mathcal{C}_1, \mathcal{C}_1 \in Lin$. Then it follows from

associativity by Eq. (5) and a unique composition '$\circ$' (e.g. scalar or the inner product), that

$$\mathcal{C}_1 \circ \mathbf{\Phi}_1 \otimes \mathcal{C}_2 \circ \mathbf{\Phi}_2 = (\mathcal{C}_1) \otimes (\mathcal{C}_2) \circ (\mathbf{\Phi}_1) \otimes (\mathbf{\Phi}_2) = (\mathcal{C}_1 \otimes \mathcal{C}_2) \circ (\mathbf{\Phi}_1 \otimes \mathbf{\Phi}_2) \tag{34}$$

or $(\mathcal{C}_1) \otimes (\mathcal{C}_2) = \mathcal{C}_1 \otimes \mathcal{C}_2$ since $(\mathbf{\Phi}_1) \otimes (\mathbf{\Phi}_2)$ and $(\mathbf{\Phi}_1 \otimes \mathbf{\Phi}_2)$ span the same tensor space.

Let us now rewrite difficult passages setting $\mathfrak{V}_i = \mathfrak{V}, \quad 1 \leq i \leq n^{(5)}$. *A standard tensor product of tensor* $\mathbf{F} \in Lin(\mathfrak{V} \times ... \times \mathfrak{V} \times \mathfrak{V}^* \times ... \times \mathfrak{V}^*; \mathbb{R})$ and $\mathbf{H} \in Lin(\mathfrak{V} \times ... \times \mathfrak{V} \times \mathfrak{V}^* \times ... \times \mathfrak{V}^*; \mathbb{R})$ on $\mathfrak{V}$ is a tensor $\mathbf{F} \otimes \mathbf{H} \in Lin(\mathfrak{V} \times ... \times \mathfrak{V} \times \mathfrak{V}^* \times ... \times \mathfrak{V}^* \times \mathfrak{V} \times ... \times \mathfrak{V} \times \mathfrak{V}^* \times ... \times \mathfrak{V}^*; \mathbb{R})$,

$$\begin{aligned} &\mathbf{F} \otimes \mathbf{H}(\mathbf{G}_1, ..., \mathbf{G}_k, \mathfrak{G}^1, ..., \mathfrak{G}^l, \mathbf{G}_{k+1}, ..., \mathbf{G}_{k+p}, \mathfrak{G}^{l+1}, ..., \mathfrak{G}^{l+q}) = \\ &\mathbf{F}(\mathbf{G}_1, ..., \mathbf{G}_k, \mathfrak{G}^1, ..., \mathfrak{G}^l)\mathbf{H}(\mathbf{G}_{k+1}, ..., \mathbf{G}_{k+p}, \mathfrak{G}^{l+1}, ..., \mathfrak{G}^{l+q}). \end{aligned} \tag{35}$$

The tensor product satisfies the distributive rule:
$\mathbf{F} \otimes (\mathbf{H} + \mathbf{Q}) = \mathbf{F} \otimes \mathbf{H} + \mathbf{F} \otimes \mathbf{Q}$. By Eq. (35) the tensor product of two second order tensors produces the fourth order tensors as

$$\mathbf{A} \otimes \mathbf{B} := A^i_{.j} \mathbf{G}_i \otimes \mathfrak{G}^j \otimes B^k_{.l} \mathbf{G}_k \otimes \mathfrak{G}^l = A^i_{.j} B^k_{.l} \mathbf{G}_i \otimes \mathfrak{G}^j \otimes \mathbf{G}_k \otimes \mathfrak{G}^l = ... \tag{36}$$

The *double contraction* is a four-linear map $Lin_k \times Lin_l \rightarrow Lin_{k+l-4}$. For two second order tensors it is defined as $Lin_2 \times Lin_2 \rightarrow \mathbb{R}$ as

$$\begin{aligned} &\cdot : \mathfrak{V} \times \mathfrak{W} \times \mathfrak{V}^* \times \mathfrak{W}^* \rightarrow \mathbb{R}, \\ &(\mathfrak{f} \otimes \mathfrak{t}, \mathbf{v} \otimes \mathbf{w}) \mapsto (\mathfrak{f} \otimes \mathfrak{t}) : (\mathbf{v} \otimes \mathbf{w}) := \langle \mathfrak{f}, \mathbf{v} \rangle_{\mathfrak{V}} \cdot \langle \mathfrak{t} \cdot \mathbf{w} \rangle_{\mathfrak{W}} = (\mathfrak{f}_i v^i)(\mathfrak{t}_j w^j) \quad \text{and} \\ &(\mathbf{F}_1, \mathbf{F}_2) \mapsto \mathbf{F}_1 : \mathbf{F}_2 = F_{1,ij} F_2^{kl} \langle \mathfrak{G}^i, \mathbf{G}_k \rangle \cdot \langle \mathfrak{g}^j, \mathbf{g}_l \rangle = (\mathbf{F}_1)_{ij} (\mathbf{F}_2)^{ij} \in \mathbb{R}, \end{aligned} \tag{37}$$

$\mathbf{F}_1 := F_{1,ij} \mathfrak{G}^i \otimes \mathfrak{g}^j \in \mathfrak{V}^* \otimes \mathfrak{W}^*$ and $\mathbf{F}_2 := F_2^{ij} \mathbf{G}_i \otimes \mathbf{g}_j \in \mathfrak{W} \otimes \mathfrak{V}$.

The double contraction is defined consistently with the scalar product by Eq. (20). The double contraction between two 2nd order tensor is as *commutative*: $\mathbf{F}_1 : \mathbf{F}_2 = \mathbf{F}_2 : \mathbf{F}_1$. It satisfies also the *distributive rule*: $\mathbf{A} : (\mathbf{B} + \mathbf{C}) = \mathbf{A} : \mathbf{B} + \mathbf{A} : \mathbf{C}$ and $(\mathbf{A} + \mathbf{B}) : \mathbf{C} = \mathbf{A} : \mathbf{C} + \mathbf{B} : \mathbf{C}$.

The tensor-norm is defined by means of the inner-products according to Eq. (11) and Eq. 37 for the double contraction as

$$||\mathbf{F}|| := F^a_A F^b_B \langle \mathbf{g}\mathbf{g}_a, \mathbf{g}_b \rangle \cdot \langle \mathfrak{G}^A, \mathbf{G}^{-1} \mathfrak{G}^B \rangle = \mathbf{F} : \mathbf{g}\mathbf{F}\mathbf{G}^{-1} = \mathbf{F} : \mathbf{F}^{*T}. \tag{38}$$

I.e. it is a four-linear map, $||\mathbf{F}|| : T^*_{\mathbf{x}} P \times T_{\mathbf{X}} P_0 \times T^*_{\mathbf{x}} P \times T_{\mathbf{X}} P_0 \rightarrow \mathbb{R}$. Note that by Eq. (13) the dual pairings can be written as the corresponding inner products, called the double-dot product involving the reciprocal base vector instead of the dual one.

The double contractions of a fourth order tensor with a second order one (4:2) and (2:4) are redefined to be consistent with the scalar product by Eq. (20), the identification (15) and the differentiation rule such that the chain rule and consequently the essential rate relation $\dot{\mathbf{A}}(\mathbf{B}) = \mathbf{A}_{,\mathbf{B}} : \dot{\mathbf{B}}$ and the product derivative rule are all properly satisfied. Noting $\mathbf{A} : \mathbf{B} = \mathbf{B} : \mathbf{A}$ but $\mathbf{AB} \neq \mathbf{BA}$ in general, the following must hold, cf. Itskov [5],

$$(\mathbf{A} : \mathbf{B})_{,\mathbf{C}} = \mathbf{A} : \mathbf{B}_{,\mathbf{C}} + \mathbf{B} : \mathbf{A}_{,\mathbf{C}}, \quad (\mathbf{AB})_{,\mathbf{C}} = \mathbf{A}_{,\mathbf{C}} \mathbf{B} + \mathbf{A} \mathbf{B}_{,\mathbf{C}} \tag{39}$$

[5] In general, there is not a need to use more than two different spaces in the tensor product in continuum mechanics.

The double contraction between a fourth and a second order tensor is a four-linear map $Lin_4 \times Lin_2 \rightarrow Lin_2$ as

$$\begin{aligned}
&\cdot : (\mathfrak{V}^* \times \mathfrak{W} \times \mathfrak{V}^* \times \mathfrak{W}) \times (\mathfrak{W}^* \times \mathfrak{V}) \rightarrow \mathfrak{V}^* \times \mathfrak{W}, \\
&(\mathbf{a} \otimes \mathfrak{b} \otimes \mathbf{c} \otimes \mathfrak{d}, \mathbf{v} \otimes \mathfrak{w}) \mapsto (\mathbf{a} \otimes \mathfrak{b} \otimes \mathbf{c} \otimes \mathfrak{d}) : (\mathbf{v} \otimes \mathfrak{w}) := \langle \mathfrak{b}, \mathbf{v} \rangle_{\mathfrak{W}} \cdot \langle \mathbf{c} \cdot \mathfrak{w} \rangle_{\mathfrak{V}} \mathbf{a} \otimes \mathfrak{d} \\
&= (\mathfrak{b}_j v^j)(c^k \mathfrak{w}_k) \mathbf{a} \otimes \mathfrak{d} \quad \text{and} \\
&(\mathcal{C}_1, \mathbf{F}_2) \mapsto \mathcal{C}_1 : \mathbf{F}_2 = (\mathcal{C}_1)^{i\ k}_{\cdot j\ \cdot l} (\mathbf{F}_2)^m_{\cdot n} \mathbf{g}_i \langle \mathfrak{G}^j, \mathbf{G}_m \rangle \cdot \langle \mathfrak{g}^n, \mathbf{g}_k \rangle \mathfrak{G}^l = (\mathcal{C}_1)^{i\ k}_{\cdot j\ \cdot l} (\mathbf{F}_2)^j_{\cdot k} \mathbf{g}_i \otimes \mathfrak{G}^l \in Lin(\mathfrak{V}; \mathfrak{W}),
\end{aligned} \tag{40}$$

where $\mathcal{C}_1 := (\mathcal{C}_1)^{i\ k}_{\cdot j\ \cdot l} \mathbf{g}_i \otimes \mathfrak{G}^j \otimes \mathbf{g}_k \otimes \mathfrak{G}^l \in \mathfrak{W} \otimes \mathfrak{V}^* \otimes \mathfrak{W} \otimes \mathfrak{V}^*$ and $\mathbf{F}_2 := F^i_{2.j} \mathbf{G}_i \otimes \mathfrak{g}^j \in \mathfrak{V} \otimes \mathfrak{W}^*$.
The double contraction between two fourth order tensor is a four-linear map $Lin_4 \times Lin_4 \rightarrow Lin_4$,

$$\begin{aligned}
&\cdot : (\mathfrak{V}^* \times \mathfrak{W} \times \mathfrak{V}^* \times \mathfrak{W}) \times (\mathfrak{W}^* \times \mathfrak{V} \times \mathfrak{W}^* \times \mathfrak{V}) \rightarrow \mathfrak{V}^* \times \mathfrak{V} \times \mathfrak{W}^* \times \mathfrak{W}, \\
&(\mathbf{a} \otimes \mathfrak{b} \otimes \mathbf{c} \otimes \mathfrak{d}, \mathbf{e} \otimes \mathfrak{f} \otimes \mathbf{g} \otimes \mathfrak{h}) \mapsto (\mathbf{a} \otimes \mathfrak{b} \otimes \mathbf{c} \otimes \mathfrak{d}) : (\mathbf{e} \otimes \mathfrak{f} \otimes \mathbf{g} \otimes \mathfrak{h}) \\
&:= \langle \mathfrak{b}, \mathbf{e} \rangle_{\mathfrak{W}} \cdot \langle \mathbf{c}, \mathfrak{h} \rangle_{\mathfrak{W}} \mathbf{a} \otimes \mathfrak{f} \otimes \mathbf{g} \otimes \mathfrak{d} = (\mathfrak{b}_j e^j)(c^l \mathfrak{h}_l) \mathbf{a} \otimes \mathfrak{f} \otimes \mathbf{g} \otimes \mathfrak{d} \quad \text{and} \\
&(\mathcal{C}_1, \mathcal{C}_2) \mapsto \mathcal{C}_1 : \mathcal{C}_2 = (\mathcal{C}_1)^{i\ k}_{\cdot j\ \cdot l} (\mathcal{C}_2)^{m\ q}_{\cdot n\ \cdot r} \mathbf{g}_i \langle \mathfrak{G}^j, \mathbf{G}_m \rangle \mathfrak{g}^n \otimes \mathbf{G}_q \langle \mathfrak{g}^r, \mathbf{g}_k \rangle \mathfrak{G}^l \\
&= (\mathcal{C}_1)^{i\ k}_{\cdot j\ \cdot l} (\mathcal{C}_2)^{j\ q}_{\cdot n\ \cdot k} \mathbf{g}_i \otimes \mathfrak{g}^n \otimes \mathbf{G}_q \otimes \mathfrak{G}^l \in Lin(\mathfrak{W}^* \times \mathfrak{W} \times \mathfrak{V}^* \times \mathfrak{V}; \mathbb{R}),
\end{aligned} \tag{41}$$

where $\mathcal{C}_2 := (\mathcal{C}_2)^{i\ k}_{\cdot j\ \cdot l} \mathbf{G}_i \otimes \mathfrak{g}^j \otimes \mathbf{G}_k \otimes \mathfrak{g}^l \in \mathfrak{V} \otimes \mathfrak{W}^* \otimes \mathfrak{V} \otimes \mathfrak{W}^*$. The operations (2:4), (4:2) and (4:4) all fulfill the associative and distributive rules, cf. Itskov [5],

$$(\mathbf{A} : (\mathcal{B} + \mathcal{C})) : \mathbf{D} = \mathbf{A} : ((\mathcal{B} + \mathcal{C}) : \mathbf{D}) = \mathbf{A} : \mathcal{B} : \mathbf{D} + \mathbf{A} : \mathcal{C} : \mathbf{D}, \quad \mathbf{A}, \mathbf{D} \in Lin_2, \mathcal{B}, \mathcal{C} \in Lin_4$$

but they do not obey the commutative rule: $\mathbf{A} : \mathcal{B} \neq \mathcal{B} : \mathbf{A}, \mathcal{A} : \mathcal{B} \neq \mathcal{B} : \mathcal{A}$.

Applying Eq. (40) and noting Eq. (13) the (4:2)- and (2:4)-contraction between $\mathcal{C} \in Lin_4$ or $\mathcal{C}^* \in Lin_4$ and $\mathbf{C} \in Lin_2$ are as

$$\mathcal{C} : \mathbf{C} := \mathcal{C}^{i\ k}_{\cdot j\ \cdot l} \mathbf{G}_i \otimes \mathbf{G}^j \otimes \mathbf{G}_k \otimes \mathfrak{G}^l : C^m_{\cdot n} \mathbf{G}_m \otimes \mathbf{G}^n = \mathcal{C}^{i\ k}_{\cdot j\ \cdot l} C^j_{\cdot k} \mathbf{G}_i \otimes \mathfrak{G}^l \tag{42}$$

$$\mathbf{C} : \mathcal{C}^* = C^m_{\cdot n} \mathbf{G}_m \otimes \mathbf{G}^n : \mathcal{C}^{i\ k}_{\cdot j\ \cdot l} \mathbf{G}^j \otimes \mathbf{G}_i \otimes \mathfrak{G}^l \otimes \mathbf{G}_k = \mathcal{C}^{i\ k}_{\cdot j\ \cdot l} C^j_{\cdot k} \mathbf{G}_i \otimes \mathfrak{G}^l, \tag{43}$$

where $\mathcal{C}^*$ is defined to be the dual map of $\mathcal{C}$, cf. Eq. (31).

7. TRANSPOSITIONS OF FOURTH ORDER TENSORS

Next, the transpositions of fourth order tensors are determined based on Eq. (32). There the general scalar product is replaced by the double contraction according to Eq. (40) and the general inner product by the double-dot product denoted by ':'. Thus, e.g. the double-dot product is evaluated by Eqs (11) and (40) as

$$\begin{aligned}
\mathcal{C} : \mathbf{F} &= \mathcal{C}^{i\ k}_{\cdot j\ \cdot l} (\mathbf{F})^n_{m\cdot} \mathbf{g}_i (\mathfrak{G}^j \cdot \mathfrak{G}^m)(\mathbf{g}_n \cdot \mathbf{g}_k) \mathfrak{g}^l = \mathcal{C}^{i\ k}_{\cdot j\ \cdot l} (\mathbf{F})^n_{m\cdot} \mathbf{g}_i \langle \mathbf{G}^{-1} \mathfrak{G}^j, \mathfrak{G}^m \rangle \langle \mathbf{g}\mathbf{g}_n, \mathbf{g}_k \rangle \mathfrak{g}^l \\
&= \mathcal{C}^{i\ k}_{\cdot j\ \cdot l} (\mathbf{F})^n_{m\cdot} G^{mj} g_{nk} \mathbf{g}_i \otimes \mathfrak{g}^l =: \mathcal{C}^{i\ k}_{\cdot j\ \cdot l} (\mathbf{F})^j_{\cdot k} \mathbf{g}_i \otimes \mathfrak{g}^l.
\end{aligned} \tag{44}$$

Let be $\mathbf{F}_1, \mathbf{F}_2 \in Lin_2, \mathcal{C} \in Lin_4$. Let $(\bullet)^T$, $(\bullet)^t$ and ${}^t(\bullet)$ be the transpositions defined as

$$\begin{aligned}
&\mathbf{F}_1 : \mathcal{C} : \mathbf{F}_2 = \mathbf{F}_2 : \mathcal{C}^T : \mathbf{F}_1 \in \mathbb{R} \quad \text{major transposition of } \mathcal{C}, \\
&\mathbf{F}_1 : \mathcal{C} : \mathbf{F}_2 = \mathbf{F}_1^* : {}^t\mathcal{C} : \mathbf{F}_2 = \mathbf{F}_1 : \mathcal{C}^t : \mathbf{F}_2^* \in \mathbb{R} \quad \text{left and right minor transposition of } \mathcal{C}, \\
&\mathbf{F}_1 : \mathcal{C} : \mathbf{F}_2 = \mathbf{F}_2^* : {}^t(\mathcal{C}^T) : \mathbf{F}_1 = \mathbf{F}_2 : (\mathcal{C}^T)^t : \mathbf{F}_1^* \in \mathbb{R} \quad \text{left and right minor transposition of } \mathcal{C}^T.
\end{aligned} \tag{45}$$

Let be $\mathbf{F}_1, \mathbf{F}_2 \in Lin_2, \mathcal{C} \in Lin_4$. Let $(\bullet)^*$, $(\bullet)^\star$ and ${}^\star(\bullet)$ be the dual operations defined as follows:

$$\begin{aligned}
&\mathbf{F}_1 : \mathcal{C} : \mathbf{F}_2 = \mathbf{F}_2 : \mathcal{C}^* : \mathbf{F}_1 \quad \text{(major) dual of } \mathcal{C},\\
&\mathbf{F}_1 : \mathcal{C} : \mathbf{F}_2 = \mathbf{F}_1^* : {}^\star\mathcal{C} : \mathbf{F}_2 = \mathbf{F}_1 : \mathcal{C}^\star : \mathbf{F}_2^* \quad \text{left and right minor dual of } \mathcal{C} \text{ (star on the left and right)},\\
&\mathbf{F}_1 : \mathcal{C} : \mathbf{F}_2 = \mathbf{F}_2^* : {}^\star(\mathcal{C}^*) : \mathbf{F}_1 = \mathbf{F}_2 : (\mathcal{C}^*)^\star : \mathbf{F}_1^* \quad \text{left and right minor dual of } \mathcal{C}^*
\end{aligned} \tag{46}$$

According to Eqs (45) and (46) the dual and the transpose applied to the tensor products given by Eq. (35) w.r.t the double contraction by Eq. (40) are as

$$(\mathbf{A} \otimes \mathbf{B})^* = \mathbf{A}^* \otimes \mathbf{B}^*, \quad (\mathbf{A} \otimes \mathbf{B})^T = \mathbf{A}^T \otimes \mathbf{B}^T. \tag{47}$$

By Eq. (41), $\mathbf{A} \otimes \mathbf{B} : \mathbf{A}^{-1} \otimes \mathbf{B}^{-1} = \mathcal{I}$ and $\mathbf{A}^{-1} \otimes \mathbf{B}^{-1} : \mathbf{A} \otimes \mathbf{B} = \mathrm{i}, \forall \mathbf{A}, \mathbf{B} \in Lin_2$, where $\mathcal{I}, \mathrm{i}$ are identities. Thus,

$$(\mathbf{A} \otimes \mathbf{B})^{-1} = \mathbf{A}^{-1} \otimes \mathbf{B}^{-1}. \tag{48}$$

According to Eq. (46) the dual and the transpose of the contravariant one-point fourth order tensor are as

$$\begin{aligned}
&\mathcal{C} := \mathcal{C}^{IJKL}\mathbf{G}_I \otimes \mathbf{G}_J \otimes \mathbf{G}_K \otimes \mathbf{G}_L \in Lin(T^*_{\mathbf{X}}P_0 \times T^*_{\mathbf{X}}P_0 \times T^*_{\mathbf{X}}P_0 \times T^*_{\mathbf{X}}P_0; \mathbb{R}) :\\
&\mathcal{C}^* = \mathcal{C}^{IJKL}\mathbf{G}_J \otimes \mathbf{G}_I \otimes \mathbf{G}_L \otimes \mathbf{G}_K = \mathcal{C}^{JILK}\mathbf{G}_I \otimes \mathbf{G}_J \otimes \mathbf{G}_K \otimes \mathbf{G}_L,\\
&\mathcal{C}^\star = \mathcal{C}^{IJKL}\mathbf{G}_I \otimes \mathbf{G}_K \otimes \mathbf{G}_J \otimes \mathbf{G}_L = \mathcal{C}^{IKJL}\mathbf{G}_I \otimes \mathbf{G}_J \otimes \mathbf{G}_K \otimes \mathbf{G}_L,\\
&{}^\star\mathcal{C} = \mathcal{C}^{IJKL}\mathbf{G}_L \otimes \mathbf{G}_J \otimes \mathbf{G}_K \otimes \mathbf{G}_I = \mathcal{C}^{LJKI}\mathbf{G}_I \otimes \mathbf{G}_J \otimes \mathbf{G}_K \otimes \mathbf{G}_L.
\end{aligned} \tag{49}$$

Similarly the transpositions are obtained by Eq. (45). E.g. the major transposition or the transpose of $\mathcal{C} \in Lin(T^*_{\mathbf{x}}P \times T_{\mathbf{X}}P_0 \times T^*_{\mathbf{x}}P \times T_{\mathbf{X}}P_0; \mathbb{R})$ is as

$$\mathcal{C}^T = \mathbf{G}^{-1} \otimes \mathbf{g} : \mathcal{C}^* : \mathbf{g} \otimes \mathbf{G}^{-1} \in Lin(T^*_{\mathbf{X}}P_0 \times T_{\mathbf{x}}P \times T^*_{\mathbf{X}}P_0 \times T_{\mathbf{x}}P; \mathbb{R}). \tag{50}$$

Above result can be verified as follows. Let be $\mathcal{C}_1 = \mathbf{F} \otimes \mathbf{F} \in Lin(T^*_{\mathbf{x}}P \times T_{\mathbf{X}}P_0 \times T^*_{\mathbf{x}}P \times T_{\mathbf{X}}P_0; \mathbb{R})$. Utilizing the transpose of a two-point tensor by Eq. (26) and the dual and the transpose of a higher order tensor by Eq. (47) produce

$$\begin{aligned}
\mathcal{C}_1^* &:= (\mathbf{F} \otimes \mathbf{F})^* = \mathbf{F}^* \otimes \mathbf{F}^* = \mathbf{G}\mathbf{F}^T\mathbf{g}^{-1} \otimes \mathbf{G}\mathbf{F}^T\mathbf{g}^{-1} \quad \text{|| by Eqs. (40) and (12)}\\
&= \mathbf{G} \otimes \mathbf{g}^{-1} : \mathbf{F}^T \otimes \mathbf{F}^T : \mathbf{g}^{-1} \otimes \mathbf{G} \text{ or by Eq. (48)},\\
\mathcal{C}_1^T &:= (\mathbf{F} \otimes \mathbf{F})^T = \mathbf{F}^T \otimes \mathbf{F}^T = \mathbf{G}^{-1} \otimes \mathbf{g} : (\mathbf{F} \otimes \mathbf{F})^* : \mathbf{g} \otimes \mathbf{G}^{-1} = \mathbf{G}^{-1} \otimes \mathbf{g} : \mathcal{C}_1^* : \mathbf{g} \otimes \mathbf{G}^{-1}.
\end{aligned}$$

By Eq. (33) the transpose of $\mathcal{C} \in Lin(T^*_{\mathbf{x}}P \times T_{\mathbf{X}}P_0 \times T^*_{\mathbf{x}}P \times T_{\mathbf{X}}P_0; \mathbb{R})$ can be given as $\mathcal{C}^T = \mathcal{G}_1^{-1} : \mathcal{C}^* : \mathcal{G}_2$, where by Eq. (48) $\mathcal{G}_1 = (\mathbf{G}^{-1} \otimes \mathbf{g})^{-1} = \mathbf{G} \otimes \mathbf{g}^{-1}$ and $\mathcal{G}_2 = \mathbf{g} \otimes \mathbf{G}^{-1}$.

8. CONCLUSIONS

Tensor's symmetries are evaluated using the transpositions or the duals depending on the tensor variance under symmetrization. The transpositions are applied to the mixed-variant forms while the duals are applied to the co- or contra-variant forms. Consequently the symmetrization of the mixed-variant forms is metric-dependent. For that the approach as *tensor algebra on manifolds* is preferred because there a clear distinction between vectors and covectors and consequently between duals and transpositions exist. I.e. their explicit expressions differ. In the literature the transpose of a bilinear map or a second order tensor is well-defined. Instead the transpositions of higher order tensors have been remained as an abstract task. In this paper tensor is defined as a map between tensor

spaces, which are obtained from the cartesian product vector space by means of the unique maps. Then also the duals and the transpositions become well-defined. A tensor, its transpositions and symmetrizations are developed separately and compatibly with the inner products. As an important application in continuum mechanics is a tangential stiffness tensor, which is essential in numerical solution methods. By the given concept it can be developed and symmetrized independently and connected afterwards to different numerical solvers.

REFERENCES

[1] Abraham, R; Marsden, J.E; Ratiu, T. *Manifolds, Tensor Analysis and Applications* Addison-Wesley: New York, 1983.

[2] Basar, Y; Weichert, D. *Nonlinear Continuum Mechanics of Solids.* Springer-Verlag: Berlin, 2000.

[3] Giessen, E; Kollmann, F.G. On mathematical aspects of dual variables in continuum mechanics. Part 1: Mathematical principles. *ZAMM Z. Angew. Math. Mech.* 1996; **76**:447–462.

[4] Greub W.H. *Multilinear Algebra.* Springer-Verlag, Berlin, 1967.

[5] Itskov, M. On the theory of fourth-order tensors and their applications in computational mechanics. *Computer Methods in Applied Mechanics and Engineering* 2000; **189**:419–438.

[6] Itskov, M. *Tensor Algebra and Tensor Analysis for Engineers. With Applications to Continuum Mechanics.* Springer-Verlag, Berlin Heidelberg, 2007.

[7] Kintzel, O. *Modeling of Elasto-plastic Material Behavior and Ductile Micropore Damage of Metallic Materials at Large Deformations.* Shaker-Verlag, Aachen, 2007.

[8] Makowski, J; Stumpf, H. On the 'Symmetry' of Tangent Operators in Nonlinear Mechanics, ZAMM (Z. Angew. Math. Mech). *Applied Mathematics and Mechanics* 1995; **75**(3):189–198.

[9] Marsden, J.E; Hughes, T.J.R. *Mathematical Foundations of Elasticity* Dover: New York, 1993.

[10] Merris, R. *Multilinear Algebra.* Gordon and Breach science publisher: California State University, Hayward, USA. 1997.

[11] Mäkinen, J. *A formulation of flexible multibody Mechanics. Lagrangian Geometrically exact Beam Elements using Constraint Point Manifold Parametrization.* (Research report 2004:3) TTY-Press: Tampere, 2004.

[12] Stumpf, H; Hoppe, U. The application of tensor algebra on manifolds to nonlinear continuum mechanics-invited survey artile, ZAMM (Z. Angew. Math. Mech). *Applied Mathematics and Mechanics* 1997; **77**(5):327–339.

SUORASSA PYÖRÖTANGOSSA ETENEVÄN JÄNNITYSAALLON KOKEELLINEN MITTAUS

M.JOKINEN, A.-J. VUOTIKKA S.-G. SJÖLIND

Teknillisen Mekaniikan Laboratorio

Oulun Yliopisto

PL4200, 90014 OULU

e-mail: marko.jokinen@gbw.fi

TIIVISTELMÄ

Erilaisissa teollisuuden nuohous- ja junttausmenetelmissä on käytössä iskuun perustuvia pitkät perinteet omaavia sovelluksia, jotka ovat saaneet muotonsa käytännössä. Artikkelissa on arvioitu joidenkin edellä mainittujen käytössä olevien sovellutusten tutkimusmahdollisuuksia mittausteknisestä näkökulmasta. Tutkittava ilmiö on pyörötangossa aksiaalisesti etenevä pulssi, joka on saatu aikaan iskemällä tankoa massalla joustavan elementin lävitse. Työssä toteutetut mittaukset tehtiin kuitenkin siten, että heilurityyppisellä vasaralla iskettiin pitkän pyörötangon päähän ilman joustavaa elementtiä. Näin mittaukset ovat toistettavissa. Pyörötangon mittapisteistä mitattiin venymät. Mittauksia tehtiin neljä kierrosta. Pyörötankoa poikkeutettiin linjastaan 0,5 astetta joka kierroksella tarkoituksena saada esiin myös tankoon syntyvät mahdolliset taivutusaallot. Tulokset ovat esitetyt suorasta iskusta ja 1,0 astetta vinosta iskusta. Samalla luotiin pohjaa FEM-laskennalla saatavien tulosten vertailulle.

JOHDANTO

Projektin toteutus alkoi vuonna 2004 Diplomityön muodossa ja sen aiheena oli tutkia voimalaitosteollisuuden jätelämmöntalteenottokattiloissa käytettävän vasaranuohouksen iskua olemassa olevaa tekniikkaa hyödyntäen. Tuolloin näkemys tarvittavista koelaitteista ja mittausmenetelmistä perustui hankittuun kokemukseen ja muutamiin VTT:n tekemiin tutkimusraportteihin.

Ensimmäiset mittaukset tähän projektiin liittyen tehtiin kiihtyvyysantureilla ja lyhyillä iskutangoilla. Tuloksissa päästiin mielestämme melko hyviin tuloksiin aina siihen asti, kunnes huomasimme, että mitattu ilmiö lienee ollut kiihtyvyysanturin kiinnityksen värähtely. Myös mitattavan tangon pituus osoittautui liian lyhyeksi voidaksemme mitata nopeasti etenevän pulssin siten, että se ei heijastu itsensä päälle. Myös heijastukset materiaalin epäjatkuvuuskohdista ja kiihtyvyysantureiden hitsatuista mittapisteistä aiheuttivat ongelmia mittauksissa. Edellä mainittujen epäkohtien havaitseminen mittausten lomassa tuntuu jälkeenpäin melko itsestään selvältä, mutta ne muuttivat moneen kertaan koko projektin luonnetta ja ohjasi sitä samalla kohti pelkistetympiä ja yksinkertaisempia kokeita.

Kiihtyvyysantureilla tehtävät mittaukset tuntuivat aluksi hyvin luonnolliselta valinnalta, koska aiemmat mittaustulokset olivat näin saadut. Niiden kiinnityksestä iskutankoon ei ollut aiempaa kokemusta käytettävissämme. Samoin käytettävissä olevat rajalliset resurssit aiheuttivat ongelmia löytää sopivia antureita.

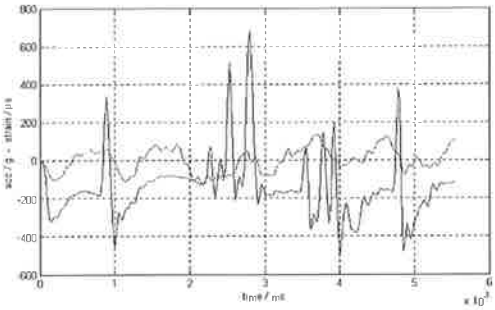

Kuva 1. Ensimmäisiä mittaustuloksia kiihtyvyysantureilla.

Kuvassa 1 tehdyissä alkupään mittauksissa käytettiin keveitä shokki-antureita, jotka liimattiin kiinni. Anturit kuitenkin rikkoutuivat ja kuvassa näkyykin, kuinka toinen anturi irtoaa hetkellisesti alustastaan. Samoin kuvasta voi nähdä kiihtyvyysantureiden kiinnityksen ensimmäisen ominaistaajuuden onnistuneen mittauksen. Edes 40 mm x 40 mm neliö, joka oli noin 15 mm korkea, ei ollut tarpeeksi jäykkä ulokepalkkina, vaan sen alin ominaistaajuus heräsi. Yritimme myös suodattaa heränneen ominaistaajuuden pois, mutta tulokset eivät vakuuttaneet. Vasta noin kolmen vuoden jälkeen päädyttiin mittauksissa käyttämään venymäliuskoja pulssin mittaamiseksi ja niillä alettiinkin saada tuloksia, jotka vastasivat odotuksia.

TEORIAA PITKITTÄIN ETENEVÄSTÄ AALLOSTA

Tarkasteltavissa sovellutuksissa aksiaalisesti etenevä aalto (dilatational wave), jota nimitetään myös pulssiksi, syntyy kahden kappaleen iskiessä toisiaan. Iskun kosketusaika, kappaleiden muoto ja materiaalien ominaisuudet määräävät syntyneen aallon muodon. Syntynyt aalto etenee kappaleen läpi muotonsa säilyttäen ja heijastuu tangon vapaasta päästä vastakkaismerkkisenä.

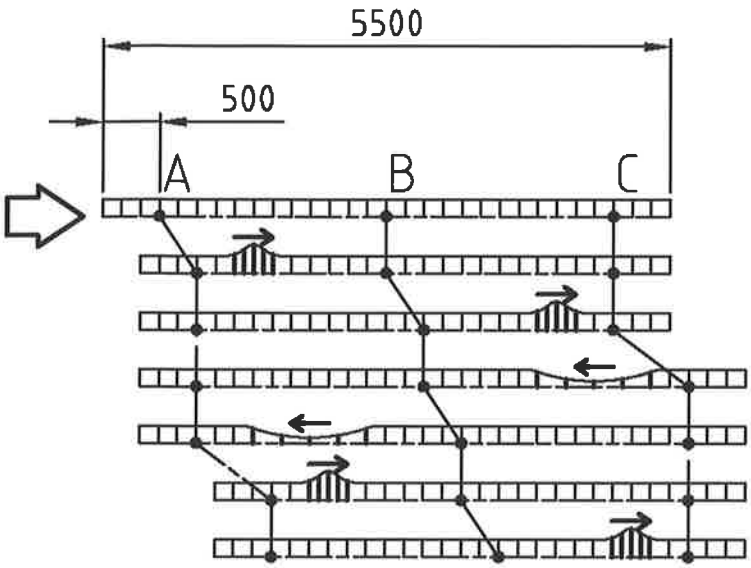

Kuva 2. Aksiaalisesti etenevä aalto tangossa.

Kuvassa 2 on havainnollistettu aallon etenemistä tangossa. Isku osuu tangon vasempaan päähän aiheuttaen siihen siirtymän, jonka kohta A kokee kuvan mukaisesti siirtymänä oikealle. Syntyvä aalto on muodoltaan puristuspulssi, joka etenee teräksessä noin 5100 m/s /2/. Tangon kohta B kokee saman siirtymän tässä tapauksessa oikealle aallon ohittaessa kohdan. Aallon saavuttaessa tangon vapaan pään se vaihtaa merkkiään muuttuen vetopulssiksi ja heijastuu takaisin. Tällöin kohta B kokee vastaavan siirtymän oikealle. Tangon liike muodostuu näiden askeleittain tapahtuvien liikkeiden seurauksena.

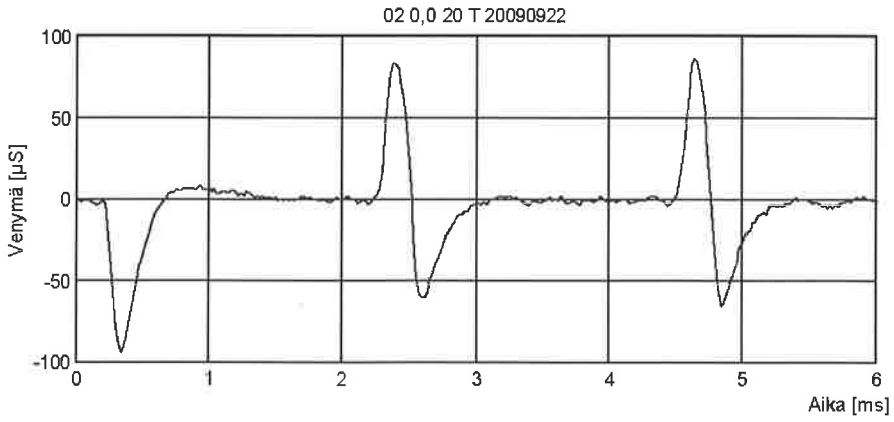

Kuva 3. Kohdan A kokema venymä kuvassa 2.

Tilanteen havainnollistamiseksi on kuvassa 3 esitetty kohdan A kuvassa 2 kokema venymä venymäliuskalla mitattuna. Kohdan A etäisyys tangon päästä on 500 mm tangon kokonaispituuden ollessa 5500 mm. Hetkellä t = 0,3 ms kohta A kokee puristuspulssin maksimin, jonka kokonaiskesto on noin 0,5 ms. Pulssi jatkaa tangon toiseen päähän, josta se heijastuu takaisin

muotonsa säilyttäen, mutta vastakkaismerkkisenä. Hetkellä t = 2,3 ms kohta A alkaa kokea tämän vastakkaismerkkisen palaavan vetopulssin, jonka kesto on siis noin 0,5 ms. Hetkellä t = 2,4 ms käy niin, että pulssi on alkaa heijastua itsensä päälle ja vastakkaismerkkisenä vaimentaa mittaustulosta.

Pulssi etenee materiaalissa kolmiulotteisesti rintamana nopeudella c. Tangossa etenevän aaltorintaman (longitudinal vibrations of rod) voi katsoa etenevän likimääräisesti nopeudella c kaavan yksi mukaisesti /1/.

$$c = \sqrt{\frac{\left(k + \frac{4}{3}\mu\right)}{\rho}} \approx \sqrt{\frac{E}{\rho}} \qquad (1)$$

Jossa k = tilavuudenmuutoskerroin (bulk modulus), μ= leikaus moduuli (Modulus of rigidity), ρ = tiheys ja E = kimmomoduuli. Edellä mainittu nopeus on johdettu alla esitetystä aksiaalisesti etenevän aallon osittaisdifferentiaaliyhtälöstä /2/.

$$EAu'' - \rho A\ddot{u} = 0 \qquad (2)$$

Jonka yleinen ratkaisu on muotoa:

$$u(x,t) = f(x - ct) + g(x + ct) \qquad (3)$$

missä f ja g ovat funktioita, jotka kuvaavat tangossa etenevää aaltoa

Edellä mainittu esittää siis vain puristusaallon etenemisen iskun seurauksena. Sen kokema nopeus on aaltorintaman maksiminopeus. Iskussa syntyy kuitenkin myös taivutusaaltorintama (distortional waves), jonka kokema nopeus on verrannollinen syntyneiden taivutusaaltojen aallonpituuteen ollen kuitenkin pienempi kuin aksiaalisesti etenevän aaltorintaman nopeus, joka on siis vakio. Taivutusaaltoja ei ole kuitenkaan käsitelty tässä tarkemmin, mutta ne tulevat näkyviin mittaustuloksissa.

KOEJÄRJESTELYT

Koejärjestelyitä varten saimme käyttöömme vasaranuohouslaitteen iskutangon, josta oli tarkoitus mitata eri pisteistä kiihtyvyydet ja vähintään yhdestä pisteestä venymät. Siitä siirryimme käyttämään 6 metriä pitkää tankoa, joka tilattiin erikseen mittauksia varten. Lyhyemmälle tangolle rakennettu teline jäi liian lyhyeksi ja se piti muokata sopivaksi pidempää iskutankoa varten.

Tässä artikkelissa esitetyissä mittauksissa on tangon kokonaispituus 5500 millimetriä. Tanko on ripustettu kahdella halkaisijaltaan kuuden millimetrin pyörötangolla, joiden sijoitus näkyy kuvasta 4. Tangon saadessa aksiaalisen liikkeen, se lähtee myös nousemaan tällä kiinnityksellä, joten se ei ole paras mahdollinen.

Iskuvasarana käytettiin vasaranuohouslaitteiston testikäytössä ollutta prototyyppiä, joka asennettiin telineeseen ja linjattiin iskutangon kanssa. Linjaus suoritettiin käyttämällä paperia tangon ja vasaran välissä. Paperista pystyi melko hyvin lukemaan, mille alueelle kosketus on tapahtunut. Itse vasara on painovoimatoiminen heilurivasara ja käytetyissä kokeissa pudotuskulma on 20 astetta kuvan 4 mukaisesti.

Yhden asteen kulmamuutos tehtiin siten, että iskutangon toista tukipistettä siirrettiin sivusuunnassa toisen pysyessä paikalla. Tangon pään koneistus suoraksi aiheutti tässä hieman ongelmia ja näkyy osaltaan pieninä häiriöinä mittaustuloksissa.

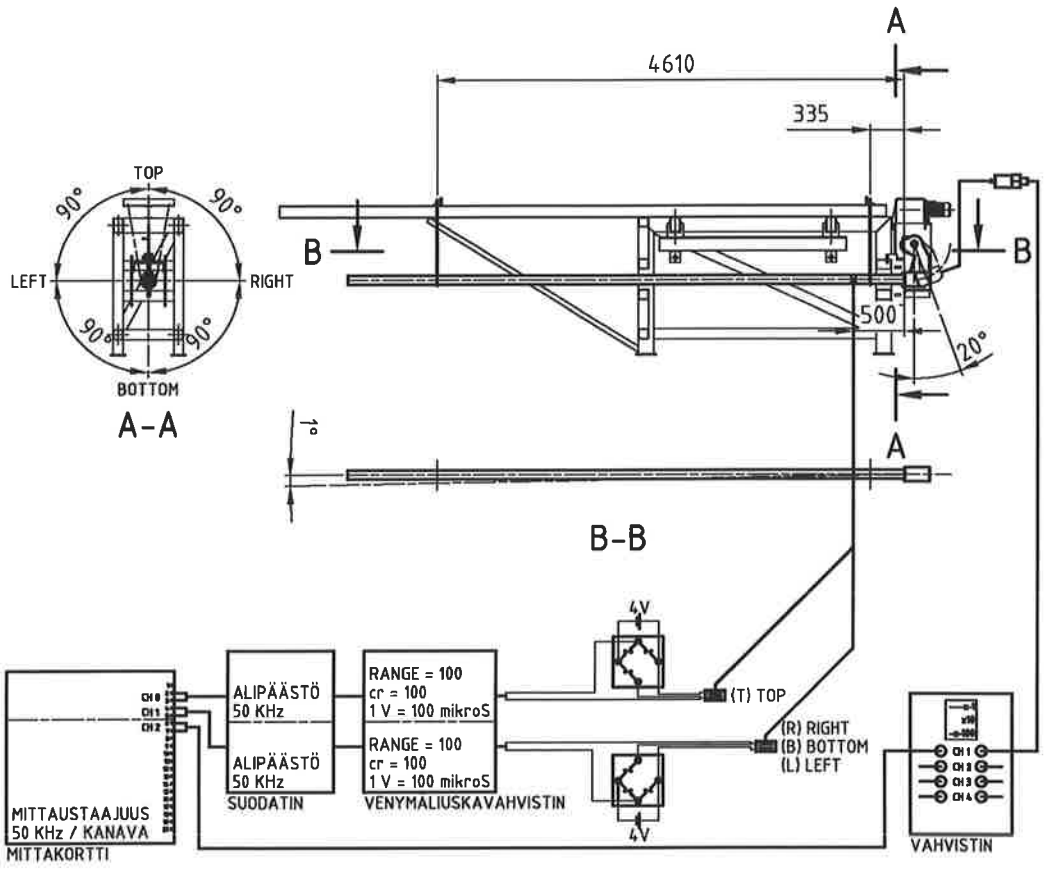

Kuva 4. Mittausjärjestelyt

Kuvassa 4 on esitetty mittalaitteet kaaviollisesti. Venymäliuskat ovat Kyowan KFG-5—120-C1-11L3M3R ja ne sijoitettiin 500 millimetriä tangon päästä 90 asteen välein eri puolille tankoa. Ne nimettiin pulssin etenemissuuntaan siten, että T = Top, R = Right, B = Bottom ja L = Left. Venymäliuskavahvistin on Kyowan CDV-700A. Niiden kanssa sarjaan on liitetty Suodatinvahvistin Kemo VBF8. Suodatuksena on käytetty 50 kHz:n analogista alipäästösuodatinta.

Kiihtyvyysanturi, joka on kierrekiinnityksellä kiinni vasaran takapäässä, on tyypiltään PCB 350A13. Kiihtyvyysanturin signaalia on vahvistettu PCB:n vahvistimella Mod 442B104 kuvan mukaisesti kymmenkertaiseksi. Signaali on analogista aina mittakortille saakka, joka on Computerboards:in valmistama. Sen suurin mittaustaajuus on 330 KHz / käyettyjen kanavien lukumäärä. Mittakorttia on ohjattu DasyLab:n ohjelmalla ja sitä on suodatettu digitaalisesti kaikilla kolmella mitattavalla kanavalla 25 kHz:n alipäästösuodattimella.

Kiihtyvyysanturia on käytetty mittausten triggaamiseen. Koska vinojen iskujen kohdalla mittaustulos vaihteli, tarvittiin triggaamiseen jokin arvo, joka toistuu samanlaisena eri mittauksissa. Kiihtyvyysanturi osoittautui huomattavasti paremmaksi kuin venymistä suoraan triggaamisen. Ongelmia syntyi mm. heränneistä ominaistaajuuksista, heijastuksista, jälki-iskuista ja muista häiriöistä, joille kaikille ei ole löytynyt selitystä.

MITTAUSTEN SUORITUS

Mittauksia suoritettiin tässä tapauksessa yhteensä neljällä eri tangon poikkeutuskulmalla, joista ensimmäinen oli suora isku ja seuraavat 0,5, 1,0 ja 1,5 astetta. Tulokset ovat esitetyt suorasta iskusta ja 1,0 asteen poikkeutuksesta. Koska käytössä oli vain kaksi kanavaa venymäliuskoille, jouduimme tekemään järjestelyjä iskun todentamiselle eri puolille tankoa. Joka iskussa toinen venymäliuskakanava oli T:ssä ja toista vaihdettiin (R, B ja L).

Ensimmäinen mittaus mitattiin T:stä ja R:stä. Se toistettiin kahdesti ja näistä ensimmäisen iskun aikana käytettiin paperia tangon ja vasaran välissä, joka on esitetty myös kuvassa 5 vasemmalla. Seuraava isku oli T ja B, joista myös ensimmäisessä käytettiin paperia, ks. kuva 5 keskellä. Sama toistui kolmannen kerran, jonka jälkeen käännettiin tankoa 0,5 astetta ja mitattiin uusi kierros. Samat toistettiin edelleen 1,0 ja 1,5 asteelle. Yhden liuskan pitäminen koko ajan T:ssä toimi samalla myös indikaattorina iskun osumalle siten, että sen pitäisi olla sama aina kaikkien kuuden mittauksen aikana.

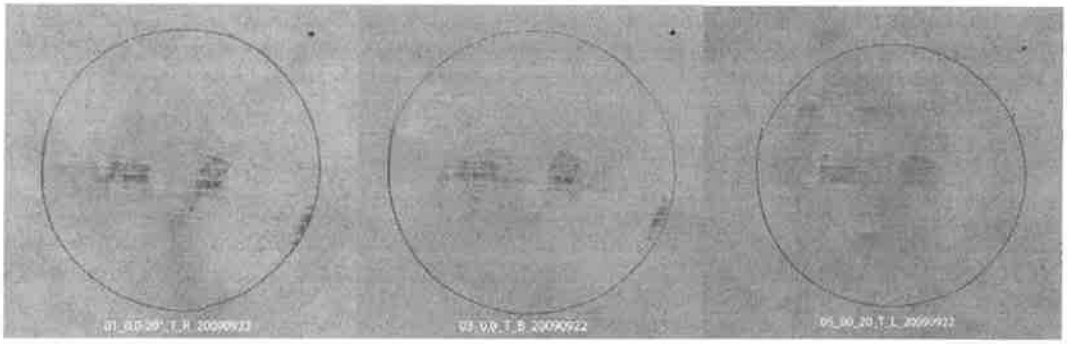

Kuva 5. Suoran iskun osumajälki.

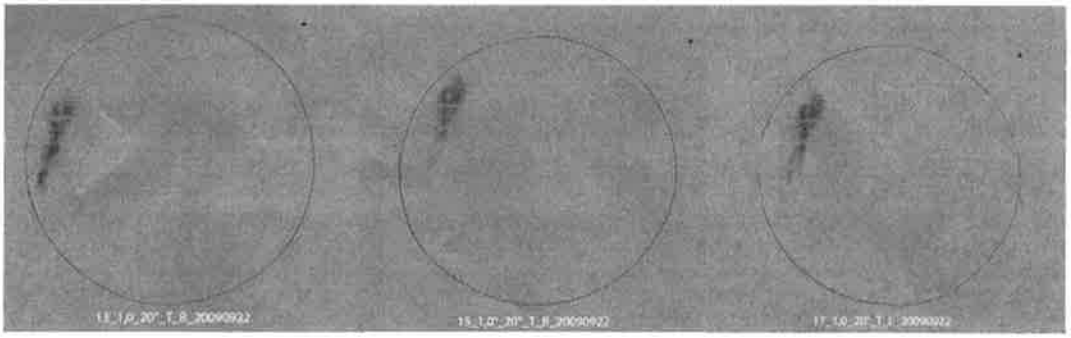

Kuva6. 1,0 Astetta vinon iskun osumajälki.

MITTAUSTULOKSET

Mittaustuloksissa ovat esitetyt suoran osuman (kuva 7) ja 1,0 astetta vinon iskun (kuva 8) mitatut venymät.

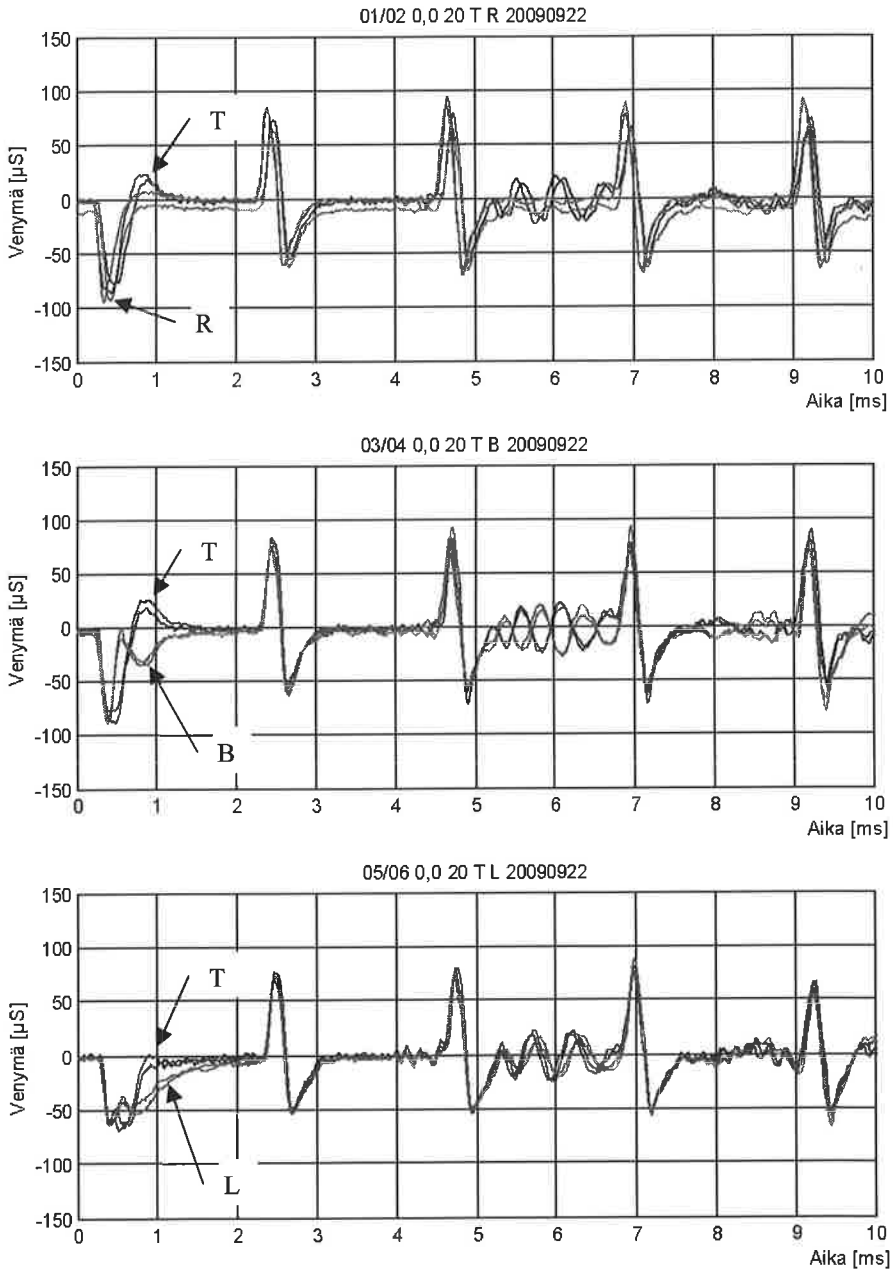

Kuva 7. Mittaustulokset suorassa iskussa.

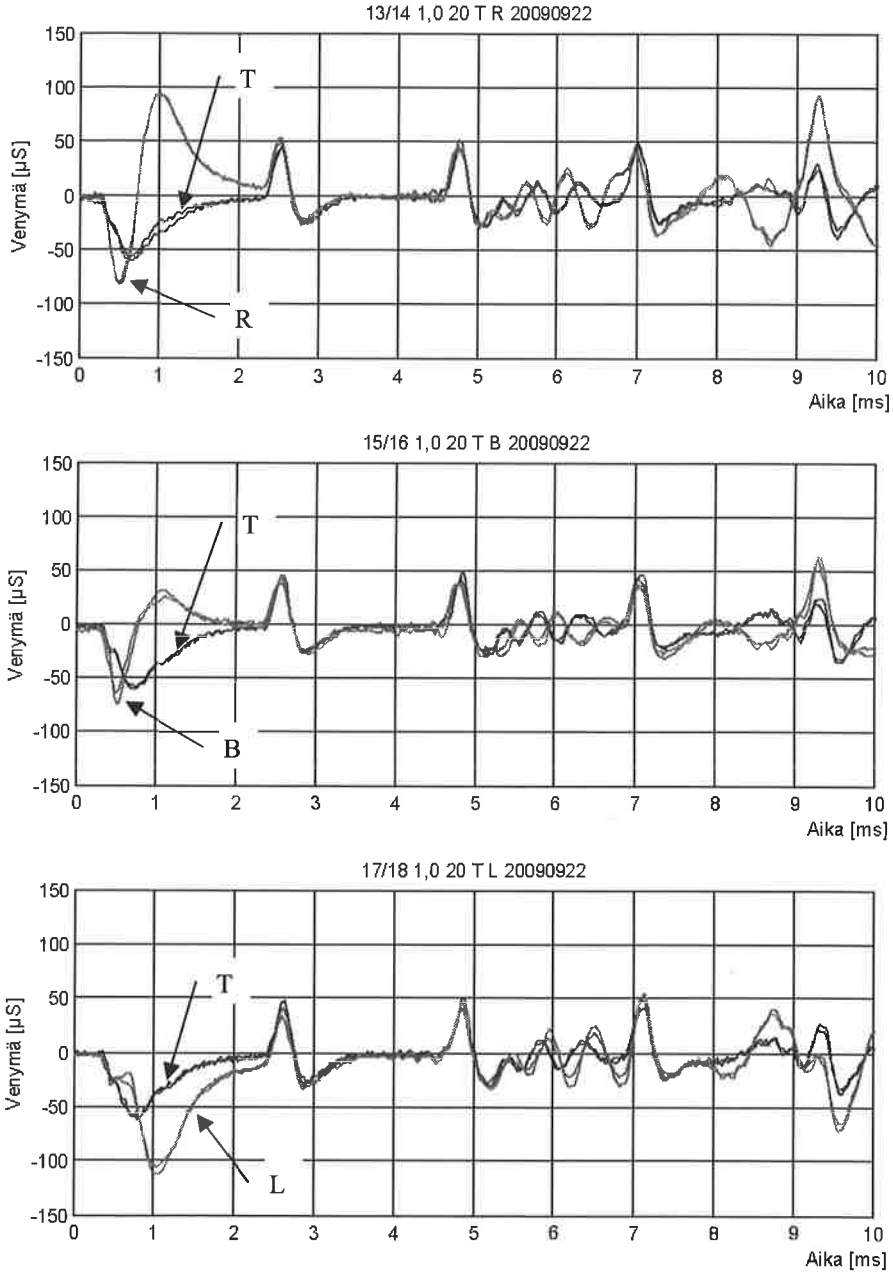

Kuva 8. Mittaustulokset 1,0 astetta vinossa iskussa.

Kuvassa 3 on esitetty mittauksen numero 2 T:stä mitattu pulssi, joka edustaa odotettua tulosta. Maksimi venymät ovat 50 – 100 µS:n luokkaa ja pulssin kesto noin 0,5 millisekuntia.

Kuvassa seitsemän on havaittavissa mittausten hankaluudet iskun kohdistettavuuden suhteen. Vasaran kiertoliike ja tangon roikkuva kiinnitys tekee mittaamisen hyvin herkäksi tangon asemoinnin suhteen. Se näkyy pystysuunnassa syntyneitä taivutusvärähtelyinä. Näiden korjaamiseksi tulisi vasaran liikkeen olla lineaarinen ja tanko voisi olla vaikka rullien päällä.

Tankoa käännettäessä sivusuunnassa taivutusvärähtelyt tulivat melko hyvin näkyviin hitaampana. Ylimpänä kuvassa 8 näkyy varsin selvästi syntynyt vetopulssi heti puristuspulssin perään. Alimpana kuvassa näkyy puristuspulssin maksimi myös hieman hitaampana. Vinoissa mittauksissa tuli esiin tangon pään hieman karkea koneistus.

YHTEENVETO

Mittaustulokset antavat näillä järjestelyillä kuvan aksiaalisesti etenevästä pulssista siinä määrin kuin se tähän projektiin liittyen koettiin tarpeelliseksi. Samalla syntyi ajatuksia mittausjärjestelyiden muuttamisesta. Seuraava iskuvasara pyritään tekemään lineaaritoimiseksi. Iskutangon ripustus vaatii myös hieman ajatustyötä. Mittalaitteita hankittaneen myös uusia ja vaatimuksena on jatkossa, että venymäliuskoilla pystytään mittaamaan ainakin neljältä kanavalta samanaikaisesti. Mittaustaajuudeksi riittää sama kuin jo käytetyissä.

Uusia tutkittavia asioita jatkossa tulevat olemaan mahdollisesti lämpötilan vaikutus, taivutusvärähtelyiden herääminen tankoon sidoksissa olevissa putkissa ja FEM-mallinnuksen hyödyntäminen. Viimeksi mainitusta on tehty jo hieman tutkimusta ja tulokset ovat olleet varsin lupaavia.

VIITTEET

/1/ Kolsky, H. Stress waves in solids. Dover Publications, Inc. 1963. New York.

/2/ Hult, J. Bära brista. Almqvist & Wiksell Förlag AB, 1975. Stockholm.

DEVELOPMENT OF HIGH-SPEED IMAGING AND IMAGE ANALYSIS TECHNIQUES TO MEASURE EXTREMELY FAST MECHANICAL PROCESSES

MARKUS HONKANEN, KALLE MARJANEN, HANNU ELORANTA
Pixact Oy
Hermiankatu 6-8H
33720 Tampere, FINLAND
Hannu.Eloranta@pixact.fi
www.pixact.fi

ABSTRACT

This study presents digital high-speed imaging and image analysis measurements of crack propagation in tempered glass and material deformation in a Hopkinson split bar. Measurements demonstrate the usefulness of novel high-speed imaging techniques. Image analysis provides a plenty of quantitative measurement data as a function of time and location: crack propagation speed, fragment size, shape and orientation and material deformation and displacement field.

1. INTRODUCTION

High-speed imaging combined with advanced image analysis techniques provides a novel measurement tool to analyze extremely fast phenomena and processes. Even if high-speed imaging has been utilized for decades in several branches of engineering and science, the ever increasing performance of the cameras and illumination techniques extends the field of applications continuously. With the state-of-the-art equipment, images can be recorded at the speed of 1 000'000 frames/s with an adequate resolution. Illumination at this high framing rate is typically provided by a pulsed diode laser. This presentation introduces three examples of high-speed imaging combined with image-analysis to produce detailed measurement information from the sequence of images recorded.

The first case presents the analysis of crack propagation in tempered glass. Images of the glass breakup are collected at 100'000 frames/s and the speed of the crack propagation is measured as a function of distance from the fracture origin. Furthermore, it is demonstrated that image analysis can be used to measure the size, shape and orientation of glass fragments created in the breakup.

The second case considers material testing in a Hopkinson split bar that provides a mechanical impulse to the material with a striker. Both compression and tension testing of the material can be performed. Material surface is imaged by a high-speed camera at 20'000 frames/s. The aim of the image analysis is to measure the instantaneous plane displacement fields in the material surface as metric units. High-speed imaging provides better understanding of the material behaviour and of the material failure mechanisms.

2. HIGH-SPEED IMAGING

Imaging very fast phenomena requires special attention on several details. One of the critical issues is the illumination. Without a shutter, 1000 frames/s imaging speed results in an exposure time of 1/1000 s. This is a very short exposure time and a plenty of light is needed to produce good quality images. In this study, two 1000 W halogen lamps and a shutter time of 10 µs are utilized. If the object is moving at high speed, one needs to use the camera shutter to further limit the exposure time or a pulsed light source to freeze the motion. Shutter time down to 1 µs is possible. E.g. *Cavilux* diode lasers can be used for for high-speed imaging applications. *Cavilux HF* laser is capable of producing 500'000 light pulses per second with a light power of 500 W and a duty cycle of 2 %. This is sufficient to overexpose the high-speed images.

Pixact utilizes the *Photron Fastcam-SA1* digital high-speed camera that delivers 5400 frames/s at 1 megapixel resolution and up to 675 000 frames/s at reduced resolution. Camera can record 1.5 s long image sequences at full speed to its 8 GB internal memory. Thanks to camera's endless recording cycle and high storage capacity, a trigger signal to the event is not required. When the studied event has occured, the camera is stopped and the high-speed movie of the previous 1.5 seconds is available in the camera's internal memory. With true 12-bit dynamics and superior light sensitivity this camera is the choice for the most demanding applications. Figure 1 shows the high-speed camera and halogen lamps in the case of crack propagation measurements.

Figure 1.High-speed imaging measurement setup for crack propagation study in tempered glass.

3. CRACK PROPAGATION IN TEMPERED GLASS

Crack propagation in glass is an extremely fast phenomenon that cannot be seen by a human eye. The crack moves at the speed of sound, which is around 1500 m/s in glass. Glass breakup and crack formation are of special interests among tempered glass producers that aim at strong glass products that in the case of a breakage, break safely into small, cubical fragments. - Large, dagger-like fragments must be avoided. Tempered glass is produced by heating it to a critical temperature and then rapidly quenching it. Tempering process aims to create a parabolic stress profile across the thickness of the glass plate, so that the maximal compressive stress on both glass surfaces is obtained. Glass is strong in compression, but weak in tension. Therefore, after tempering, glass holds better against the tensional stresses caused by external loads.

This study measures the speed of the crack propagation via high-speed imaging. A tempered glass plate of 60x60cm^2 size is broken with a sharp prick. Images of the glass breakup are collected at 50'000 and 100'000 frames/s to visualize the crack propagation across the glass plate. Higher frame rate is utilized at smaller field of view, *i.e.* in the case, when the glass is broken in the middle point. Figure 2 shows image frames 8, 9 and 26 of the sequence of crack propagation over a distance of 60 cm. Fracture origin is in the top left corner of the glass plate. 20 images of the crack propagation are obtained until the crack has reached the opposite edge of the plate.

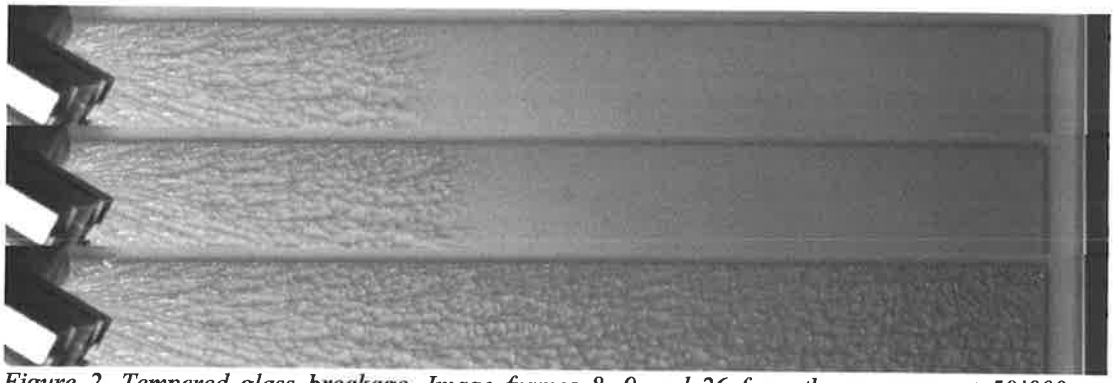

Figure 2. Tempered glass breakage. Image frames 8, 9 and 26 from the sequence at 50'000 frames/s.

A new crack generally propagates in a direction normal to the largest stress component (Gardon, 1980). As the crack grows, stresses normal to it are released, and as it penetrates farther into unbroken glass, the ratio of affected volume to new fracture surface increases, making more strain energy available for crack propagation. The crack is therefore accelerated. Simultaneously, as the unbroken regions on either side of a lengthening crack become larger, residual stresses at the crack tip and parallel to the crack also become larger. Thus, there develops a growing tendency for a new crack to branch off the old one. Formation of the new crack reduces the local strain energy, so that after bifurcation, cracks propagate with a lower velocity than the first crack had just before (Gardon, 1980). These two mechanisms alternate creating fluctuation in the crack propagation speed.

Figure 3 presents the measured crack propagation speed with respect to the distance from the fracture origin. Instantaneous crack propagation speeds are obtained computing the displacement of crack front and knowing the time delay between two images. Four glass plate breakage events are shown here. The fracture origin is varied from the plate middle point to the corner and to the edge of the plate. For all four cases, it can be seen in Figure 3 that the propagation speed fluctuates and the fluctuation increases with increasing distance from the origin. The location of the fracture

origin does not affect crack propagation speed. Mean propagation speed is about 1500 m/s for all cases and all distances from the fracture origin. However, large fragments are observed when the fracture origin is located in the middle of the plate, because in that case the plate bends before breakdown. Glass bending distributes the tensional stresses caused by the impact of the sharp prick to a larger region - similar to a hit by a blunt object.

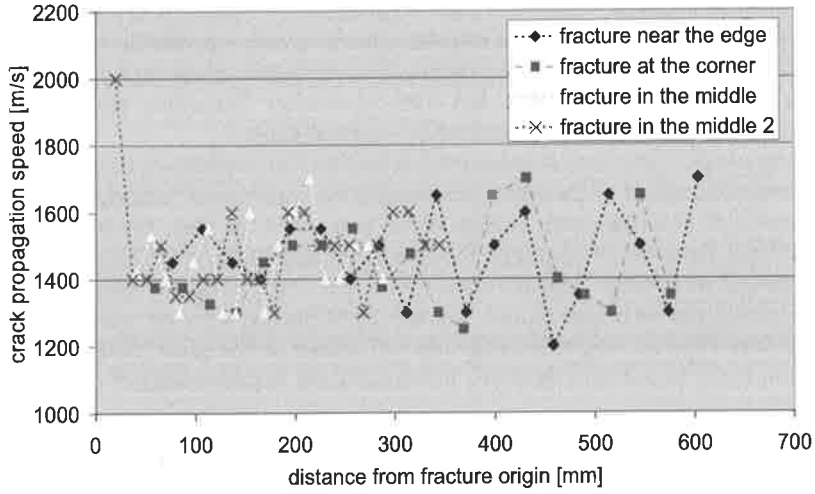

Figure 3. Fracture of tempered glass with a sharp object. Crack propagation speed as a function of the distance from the fracture origin.

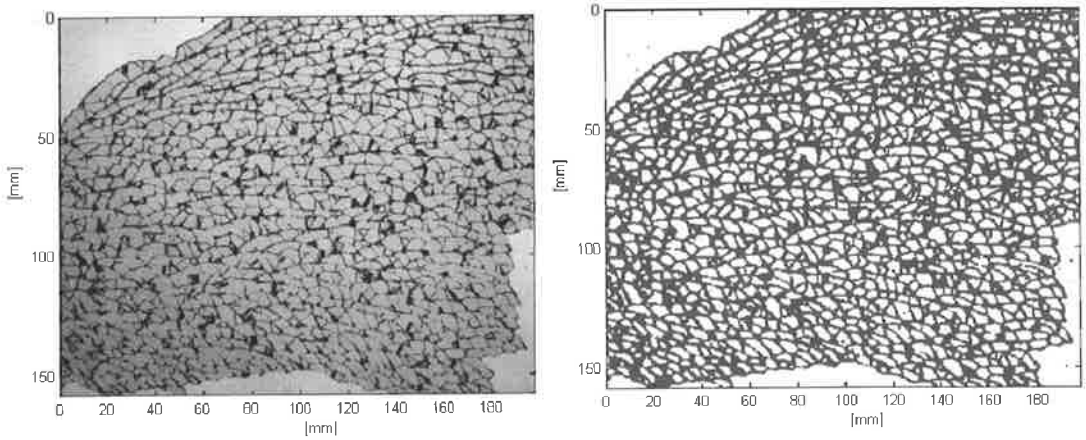

Figure 4. Image of glass fragments and its segmentation result that shows the detected cracks in green.

Image analysis can also be used to measure the size, shape and orientation of glass fragments created in the breakup. The low spatial resolution of image frames in Fig. 2 prevents the detailed fragment analysis, but the analysis is obtained with the images at higher resolution as shown in Figure 4. Crack outlines are detected as the regions of high greyscale gradient. Back-light illumination creates shadows of cracks in contrast to the bright fragment areas. The fragments surrounded by cracks are labelled and their main axes, aspect ratio and orientation are measured by a two-dimensional principal component analysis method. Figure 5 shows the measured length and orientation of the main axis of each fragment as a red line drawn in the middle of the fragment.

Also the size distribution of fragments is shown in Fig. 5. In summary, image analysis enables the detailed, quantitative analysis of fragment number density, size, shape and orientation.

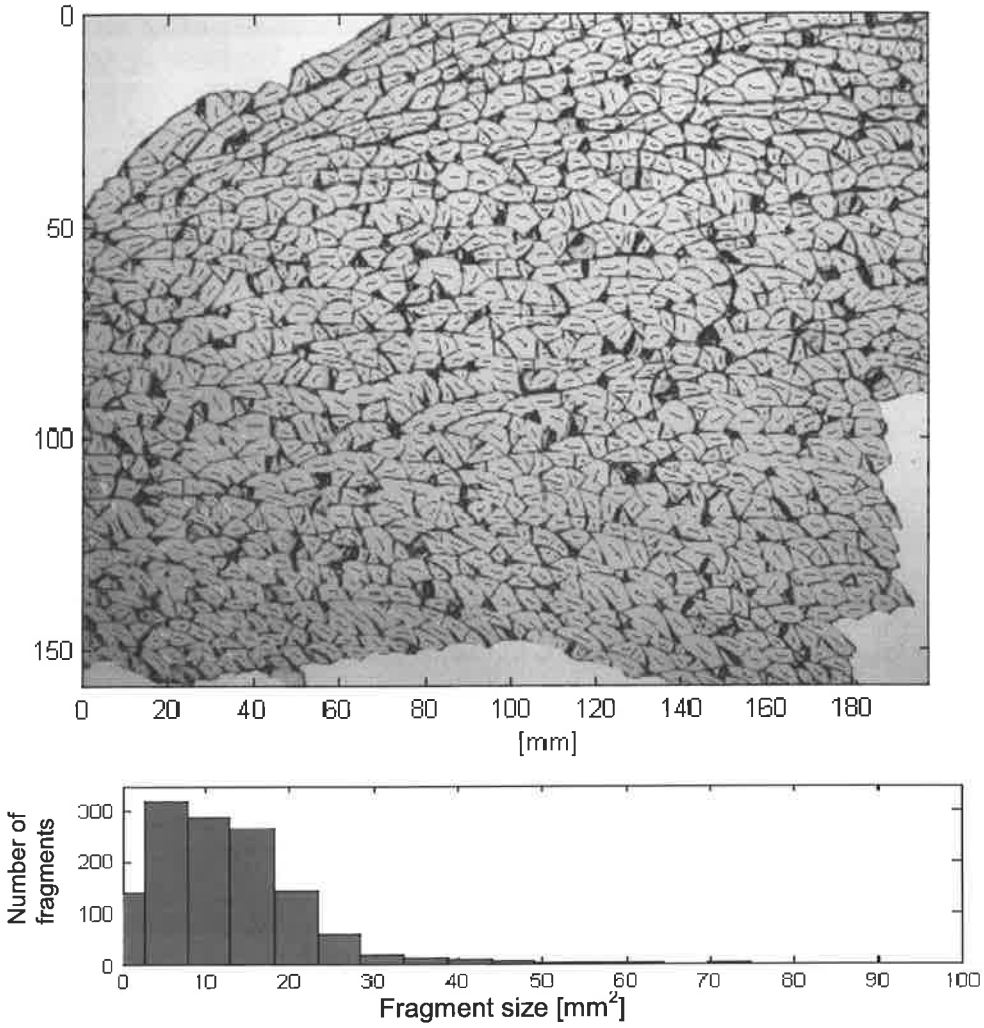

Figure 5. (On top) Image of glass fragments, where the measured length and orientation of the main axis of each fragment are shown with a red line. (On bottom) The measured size distribution of fragments.

4. MATERIAL TESTING IN A HOPKINSON SPLIT BAR

The tests on the Hopkinson Split Bar (*HSB*) provide the stress-strain response of materials at high strain rates. Both compression and tension testing of the material can be performed. A mechanical impulse (wave) is caused by a striker. The stress waves travel through the material and three stress pulses; the incident, the reflected and the transmitted are measured. The waves are measured and the material properties are computed from them. A schematic of the *HSB* test is shown in Figure 6.

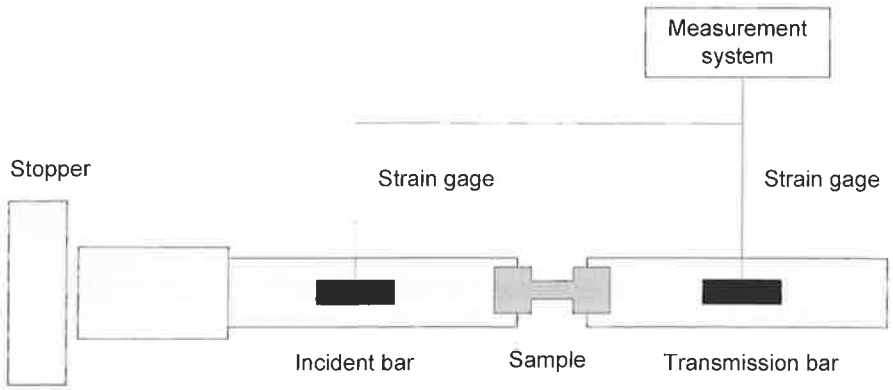

Figure 6. A schematic of the HSB test used in tensile testing.

The *HSB* tests are imaged with a high-speed camera to obtain more information about material properties than from the basic *HSB*. Due to large number of measured points, camera provides better understanding of the material behavior and of the material failure mechanisms. The use of the high-speed camera producing a series of images is necessary, if analysis of the local displacements is desired. An example of the image series obtained from a test is shown in the Fig. 7.

The aim of the image analysis is to measure the local displacements as metric units. The geometric distortions of the camera and the skewed imaging geometry can be corrected before the measurement to ensure the maximum measurement accuracy. The correspondence of the pixel size to the metric units is also established in this process.

The displacement measurement is performed between two sequential images. The displacements are provided as Cartesian or polar coordinates for each imaged point. The displacement computation requires a search for the same points in both images. The result is computed in sub-pixel range thus allowing the measurement of wider scale of displacements, *i.e.* 1:1000.

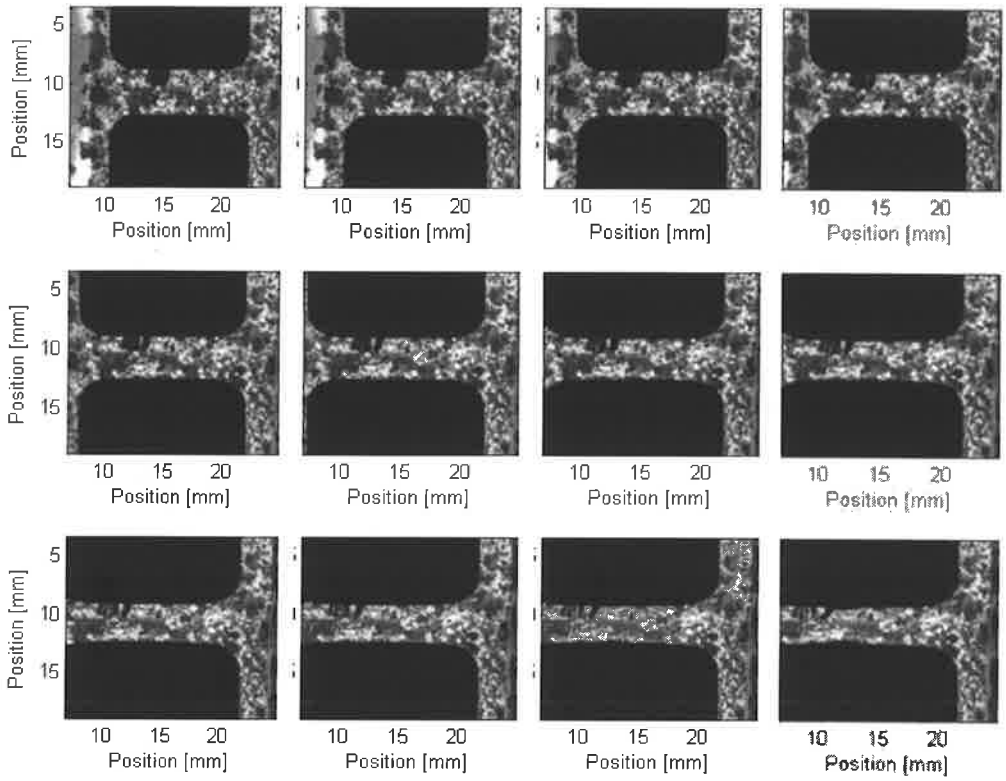

Figure 7. An example of the image series obtained from HSB tension test. The first image is on top-left corner. The last image is on the bottom-right corner. The frame rate is 20 kHz. The change of the shape is clearly visible.

The Cartesian coordinate presentation of the displacement between two images taken at times t_1 and t_2 are for the horizontal direction displacement

$$d_x(o,p) = x_2(o,p) - x_1(o,p)$$

and for the vertical direction displacement

$$d_y(o,p) = y_2(o,p) - y_1(o,p),$$

where (o, p) are the spatial coordinates of image data. The corresponding direction as polar coordinates is

$$\phi(o,p) = \arctan\left(\frac{d_y(o,p)}{d_x(o,p)}\right)$$

and the length of the displacement is

$$r(o,p) = \sqrt{d_x(o,p)^2 + d_y(o,p)^2}\ .$$

An example of an image pair is shown in the Figure 8 and the measured lengths of the displacements are shown in Figure 9. The measured instantaneous displacement field of material surface ease the detection of local irregularities of the material.

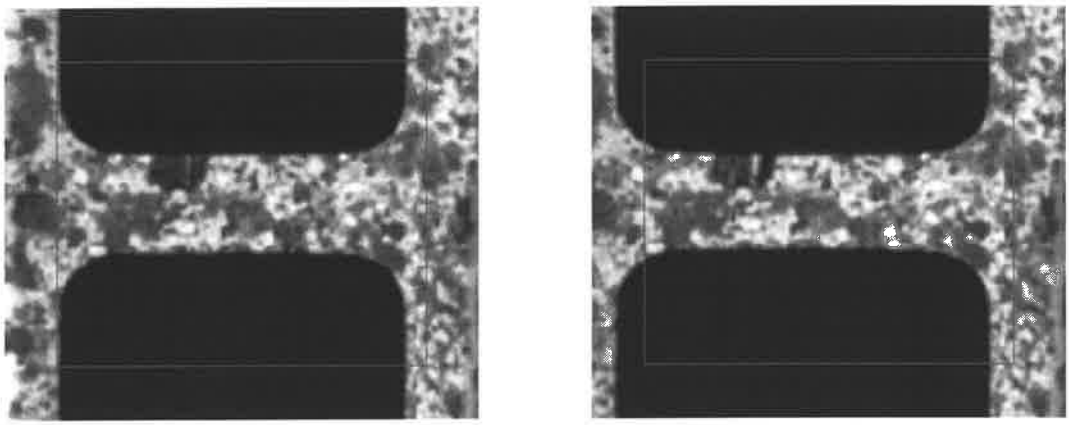

Figure 8. Image pair with different displacements. The measured area is marked with a square.

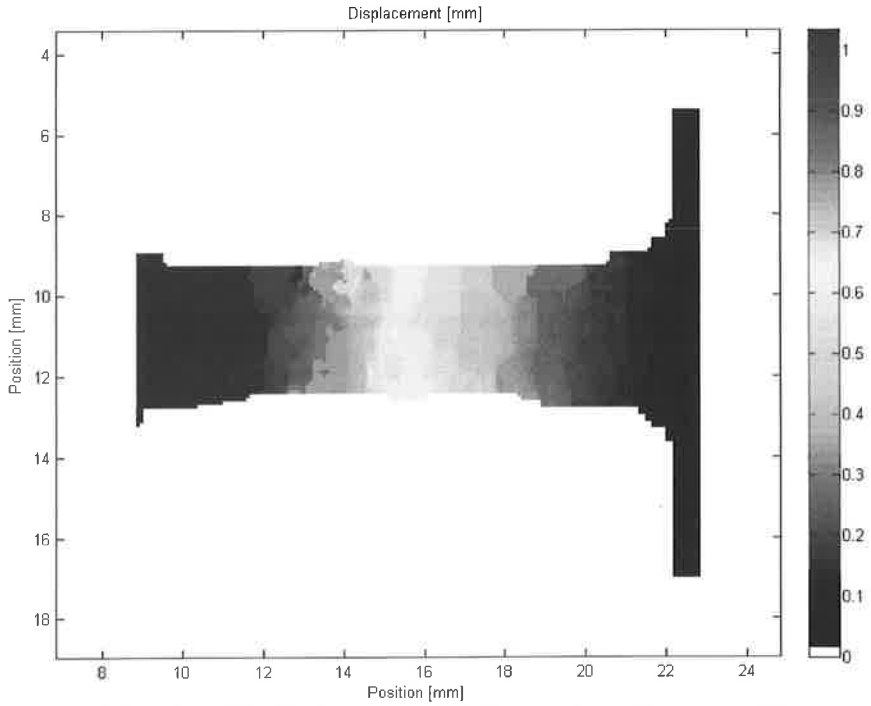

Figure 9. Measured lengths of the displacements. Displacements are in mm and the correspondence to the image colour is expressed by the colour bar.

5. CONCLUSIONS

This paper demonstrated the ability of digital high-speed imaging technique to study extremely fast mechanical processes. High-speed camera can capture the fast events at 100'000 frames/s recording rate with an adequate resolution. Special attention was paid on the image illumination and acquisition parameters. Image analysis provided quantitative information on object properties, velocity and deformation as a function of time and location. Two example cases were presented.

Tempered glass breakup is an extremely fast event. The crack propagation speed of 1500 m/s was measured. The propagation speed fluctuated due to the branching of new cracks causing temporal deceleration that followed with temporal acceleration when the crack propagated farther into a new unbroken region. The measurements showed that the fluctuation of propagation speed increases with increasing distance from the fracture origin. However, the mean propagation speed is constant.

This paper presented image analysis methods to measure fragment size, shape and orientation in a broken glass. Image analysis had crucial role also in the material testing experiments in a Hopkinson split bar. The instantaneous plane displacement fields in the material surface as metric units were measured. High-speed imaging provided better understanding of the material behaviour and of the material failure mechanisms. As a conclusion, digital high-speed imaging and image analysis technique can be exploited in the experiments of large variety of mechanical processes due to its ease of use, extensive versality of image analysis methods and fast image processing possibilities.

ACKNOWLEDGEMENTS

Authors want to thank Jari Rämö for carrying out the HSB tests.

REFERENCES

Gardon R 1980, *Thermal Tempering of Glass*, GLASS SCI. TECHNOL. Vol. 5, Ch. 5, pp. 146-216.

TYKIN AMMUKSEN JA TULIPUTKEN VUOROVAIKUTUKSEN MITTAUSMENETELMÄ

J. TOIVOLA
Mekalyysi Oy
Myllymäentie 5
37960 SOTKIA
juha.toivola@mekalyysi.inet.fi

S. MOILANEN
Patria Land & Armament Oy
PL 18
38201 SASTAMALA
seppo.moilanen@patria.fi

TIIVISTELMÄ

Rotaatiovakavoidun ammuksen johtorenkaan aiheuttama tykin tuliputken rasitus saattaa olla merkittävässä asemassa tuliputken kulumisen ja väsymiskestävyyden suhteen, jos johtorengaskuormitus on selkeästi ruutikaasun painekuormitusta suurempi. Ääritapauksissa suuri johtorengaskuormitus saattaa johtaa ennakoimattomaan tuliputkivaurioon kuten pysyvään putken muodonmuutokseen. Tuliputken ulkopinnan venymämittaukseen sekä kaasun painekuormituksen ja johtorengaskuormituksen superpositioon perustuen on kehitetty yksinkertainen analysointimenetelmä, jolla voidaan arvioida ja luokitella vähintään suhteellisella tasolla johtorengas- ammuskonstruktioiden aiheuttamia tuliputken laukausrasituksia. Artikkelissa esitetään koeammunnoissa tyypillisesti toteutetut mittausjärjestelyt, tuliputken venymämittaustulosten analysointimenetelmä ja sen suhteellinen virhearvio sekä lopuksi joitain mittauksin todettuja johtorengasrasituksiin liittyviä erityispiirteitä.

1. JOHDANTO

Rotaatiovakavoidun tykin ammuksen johtorenkaalla on neljä päätehtävää [1]: a) Varmistaa irtopanoslaukausta käytettäessä ammuksen luotettava latauskiinnittyminen tuliputken ylimenokartioon. b) Antaa hallittu ammuksen aksiaaliliikkeen suuntainen vastusvoima sisäballistisen vaiheen alussa siten, että panosruuti syttyy halutulla tavalla sekä uutta että kulunutta tuliputkea käytettäessä. c) Välittää tuliputken rihlauksen kiertovaikutus ammukselle. d) Tiivistää tuliputken ja ammuksen rajapinta siten, että ruutikaasun ohivuotoa ei esiinny sisäballistisessa vaiheessa. Johtorenkaan ja tuliputken sisäpinnan välinen kontaktipaine, johtorengaspaine, takaa ensisijaisesti tiivistyksen ja on osatekijänä kitkan välityksellä sekä latauskiinnittyvyydessä että sisäballistisessa vaiheessa ammukseen kohdistuvassa aksiaalisuuntaisessa voimassa. Ideaalisessa tapauksessa johtorengaspaine säilyy ammuksen perässä kulloisenkin kaasunpaineen suuruisena, jolloin kaasun ohivirtaus estyy. Kaasun painetasoa merkittävästi suurempi johtorengaspaine on teknisesti hyödytön ja putki- ja ammusrasituksien kannalta haitallinen.

Perinteisesti tuliputken lujuusopillinen mitoitus on perustunut ruutikaasun aiheuttaman painekuormituksen rasituskestävyyteen sekä staattisena kertakuormituksena että toistuvana kuormituksena

väsymisen suhteen tarkasteltuna [7]. Tällöin merkitsevimmiksi tuliputken kuormitustapauksiksi ovat muodostuneet suuren paineen ja ammuksen korkean lähtönopeuden tuottavat laukausyhdistelmät erityisesti tuliputken panoskammion puoleisessa päässä, jossa painekuormitus on suurimmillaan. Joidenkin uusien ammuskonstruktioiden on todettu aiheuttavan suuria tuliputken suupään rasituksia ja tietyillä laukausyhdistelmillä erityisesti matalilla lähtönopeus- ja painetasoilla ammuttaessa [2]. Johtorengaspaineiden on todettu kohoavan tasolle, joka saattaa aiheuttaa putken väsymiskestävyyden suhteen huomioonotettavia rasituksia ja ääritapauksissa jopa ennakoimattomia putkivaurioita; putken ja rihlauksen nopeaa kulumista tai pysyviä putken muodonmuutoksia. Pahimpia putkirasituksia aiheuttavia ammuskonstruktioita ei ole hyväksytty palveluskäyttöön vaan ne palautettu takaisin konstruktiomuutossuunnitteluun ja sen jälkeiseen uudelleen testaukseen [2].

2. MITTAUSKOHDE

Mittauskohteina ovat olleet 155 mm:n, 52 pituuskaliiberinen, JBMoU / ERO (Joint Ballistic Memorandum of Understanding / Extended Range Ordnance) yhteensopiva tuliputki asennettuna koeaselavetille (Kuva 1) sekä 155 mm:n ampumatarvikkeita. Tutkimuksen aikana on koeammuttu ja tuliputken laukausrasituksia mitattu yli 20 erityyppiselle ammus-johtorengasyhdistelmälle (ID1, ID2,...) sekä matalan että korkean lähtönopeuden v_0 ja ruutikaasun paineen p antavilla panoksilla.

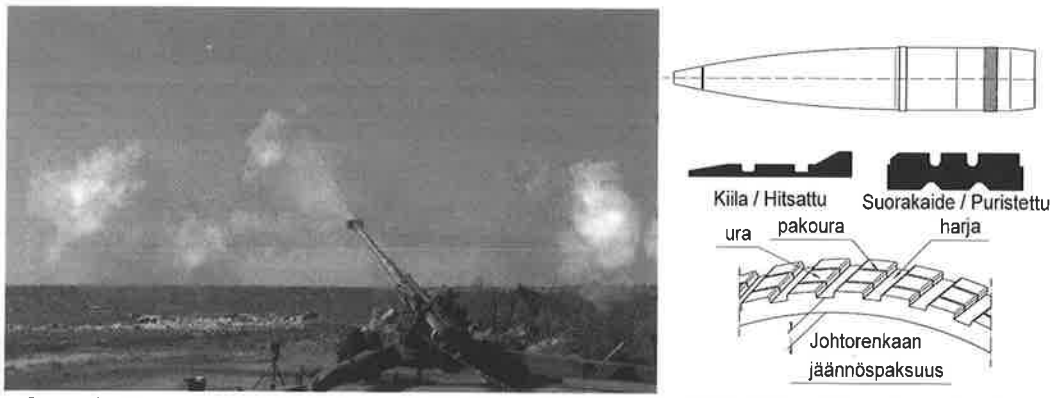

Kuva 1. Patrian 155 GH 52 koease mittausammunnoissa keväällä 2008 sekä periaatepiirrokset ammuksesta, johtorengastyypeistä sekä putken rihlaukseen perustuvat ammutun johtorenkaan muotojen nimitykset.

3. MITTAUSJÄRJESTELYT

Koeammunnoissa tuliputki instrumentointiin 90°:een venymäliuskaruseteilla poikkileikkauksittain. Putken palkkitaivutuksen vaikutus kompensoitiin liimaamalla liuskat putken vastakkaisille puolille ja laskemalla vastakkaisten liuskojen mittaustuloksista keskiarvo. Alkuvaiheessa oli käytössä kolme mittauspoikkileikkausta (A-A, B-B, C-C) putken suupäässä. Myöhemmin saatiin erityisesti mittauskäyttöön modifioitu koease (Kuva 1), joka mahdollisti tuliputken venymämittaukset myös aseen kehdon sisältä, tuliputken luisulieriöiden alueen poikkileikkauksista (D-D, E-E, F-F).

Ruutikaasunpaine (lukkopaine) p_b on mitattu tykin sulkukappaleesta kidepaineanturilla ja tuliputken ulkopinnan aksiaali- ja kehävenymä (ε_x, ε_Θ) mittauspoikkileikkauksittain (Kuva 2). Venymämittauskanavia on ollut 6*2*2= 24 kpl, joten yhteensä putkirasitusten mittaukseen on ollut käytössä 25 kanavaa. Mittaustaajuutena on käytetty tilanteesta, kanavamäärästä ja resursseista riippuen f_c={20, 40, 70, 95} kHz, tavallisimmin keruutaajuus on ollut f_c=40 kHz.

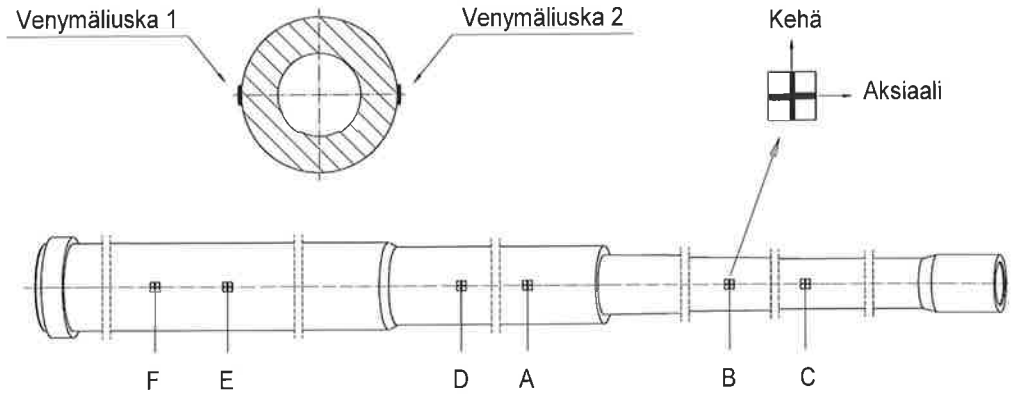

Kuva 2. Poikkileikkauksittain (A-A, B-B,..., F-F) venymäliuskoin instrumentoitu tuliputki.

Ammuksen suunopeus v_0 on mitattu lähtönopeustutkalla. Aseen suuhidastimeen asennettujen, suuhidastimen reiän halkaisijaa pienemmän vapaan aukon omaavien hammastettujen renkaiden avulla on pyritty todentamaan ammuksen normaali käyttäytyminen väliballistisessa vaiheessa. Ammuksen poikkeamat putkilinjalta tai johtorenkaan vaurioituminen putkiaikana aiheuttaisivat iskettymiä suuhidastimen ahtaisiin mittarenkaisiin. Johtorenkaan kuntoa, toimintaa ja ammuksen lennon vakautta on arvioitu laaka-ammunnoissa tutkamittauksen ohella lähtövirhetaulujen läpäisykuvioita mittaamalla sekä evakuoimalla ja tutkimalla pysäytysbunkkerista kaivettua ammusromua normaalien koeammuntatutkimusten tapaan.

Tuliputken sisäpuolinen tähystys, kaliiperimittaus ja ulkohalkaisijoiden mittaukset mittauspoikkileikkauksittain on suoritettu ennen koeammuntaa ja koeammunnan jälkeen sekä laukausten välillä, jos venymämittaustulosten tai jonkun muun syyn perusteella on ollut odotettavissa tuliputkeen syntyneen mittamuutoksia tai muita mittauksin havaittavia vaurioita.

4. TULIPUTKEN VENYMÄDATAN ANALYSOINTIMENETELMÄ

4.1 Vertailupaineen ja johtorengaspaineen laskeminen

Tuliputkeen aiheutuu aksiaalisuuntainen jännitys putken kiihtyvyydestä ja suuhidastimen toiminnasta johtuen. Lisäksi johtorenkaan kohdalla kuormituksen epäjatkuvuudesta johtuen myös johtorengaspaine sekä johtorenkaan kitkavoima aiheuttavat aksiaalisuuntaista jännitystä. Kehänsuuntaisen jännityksen aiheuttaa pääasiassa johtorengaspaine ja ruutikaasun paine. Suppeumavaikutuksen johdosta molemmissa mitatuissa venymäkomponenteissa näkyy sekä aksiaali- että kehänsuuntaiset ilmiöt. Jotta ilmiöiden vaikutukset saataisiin paremmin eroteltua toisistaan erityisesti johtorenkaan aiheuttamaa rasitusta ajatellen, venymäkomponenttien tarkastelun sijasta on parempi tarkastella putken ulkopinnan kehäjännitystä tai siihen suoraan verrannollista suuretta. Putken ulkohalkaisijan muuttumisen vuoksi kehäjännitys ei anna selvää kuvaa johtorenkaan aiheuttamista rasituksista; vertailu eri poikkileikkauksien kesken on hankalaa. Tästä syystä mitatuista tuliputken ulkopinnan venymistä laskettiin vertailupaineeksi nimetty suure

$$p_C = \frac{\omega^2 - 1}{2} \cdot \frac{E}{1-\nu}\left(\varepsilon_\Theta + \nu\varepsilon_x\right), \quad (1)$$

jossa

$$\omega = \frac{D}{d}$$

ja E on putkimateriaalin kimmomoduli, ν on Poisson kerroin, ε_Θ ja ε_x ovat tuliputken mittauspoikkileikkauksen kehä- ja aksiaalivenymä, D on poikkileikkauksen ulkohalkaisija ja d on sisähalkaisija.

Kaava (1) määrittää pitkän, vakioseinämäisen, päistään avoimen ja vapaan (N=0), sisäpuolisella vakiopaineella kuormitetun sylinteriputken paineen ja ulkopinnan venymien välisen riippuvuuden [5, 6]. Vaikka kaavan (1) mukaiset olettamukset eivät täysin toteudu tuliputken rasitustilanteessa, kaavalla laskettu vertailupaine mahdollistaa tuliputken rasituksien vertailun eri mittauskohtien välillä ja palauttaa neljän (tai paremminkin kahden) venymämittauksen datan yhdeksi tulossuureeksi, jonka maksimiarvoa p_{Cp} voidaan verrata ruutikaasun paineeseen ainakin suuruusluokkatasolla. Koska kaavan (1) mukainen vertailupaine on suoraan verrannollinen putken kehäjännitykseen, aksiaaliset ilmiöt eivät vaikuta siihen.

Tuliputken sisäpintaan kohdistuvia ruutikaasun painetta ja johtorengaspainetta approksimoidaan tasan jakaantuneina painekuormituksina kuvan 3 mukaisesti. Kun johtorengas on mittauspisteen kohdalla, voidaan lineaarisessa tapauksessa vertailupaine esittää kuvan 3 tapauksien a) ja b) aiheuttamien vertailupaineiden summana

$$p_{Cp} = p_{Cp,1} + p_{Cp,2}. \quad (2)$$

Lineaarisuudesta johtuen voidaan kirjoittaa

$$p_{Cp,1} = \alpha_1 p_1 \quad (3)$$

$$p_{Cp,2} = \alpha_2 p_2, \quad (4)$$

joissa α_1 ja α_2 voidaan määrittää joko kuvan 3 tapausten a) ja b) analyyttiseen ratkaisuun perustuen tai numeerisella laskennalla. Staattinen ratkaisu on oletettu riittävän tarkaksi. Sijoittamalla lausekkeet (3) ja (4) kaavaan (2) ja ratkaisemalla johtorengaspaine p_2 saadaan

$$p_2 = \alpha_2 \left(p_{Cp} - \frac{p_1}{\alpha_1} \right). \quad (5)$$

Johtorengaspaineen laskemiseen tarvitaan siis vertailupaineen ja ruutikaasun paineen arvot sillä hetkellä, kun johtorengas on mittauspisteen kohdalla kuvan 3 mukaisesti. Kun johtorengaspaine p_2 on selvästi suurempi kuin ruutikaasun paine p_1, vertailupaineeseen aiheutuva piikki johtuu pääosin johtorengaspaineesta, jolloin riittäväksi katsotulla tarkkuudella painearvot voidaan poimia vertailupaineen maksimin kohdalta. Kun johtorengaspaine lähestyy ruutikaasun painetta, laskentamenetelmän tarkkuus vähenee.

4.2 Johtorengaspaineen laskennan virhearviointi

Differentioimalla johtorengaspaineen laskentalauseke (5) puolittain, sieventämällä ja järjestelemällä termejä saadaan johdettua johtorengaspaineen suhteellinen virhearvio

$$\frac{\Delta p_2}{p_2} = \frac{1}{1 - \frac{1}{\alpha_1 \beta}} \frac{\Delta p_{Cp}}{p_{Cp}} - \frac{1}{\alpha_1 \beta - 1} \frac{\Delta p_1}{p_1} + \frac{1}{\alpha_1 \beta - 1} \frac{\Delta \alpha_1}{\alpha_1} + \frac{\Delta \alpha_2}{\alpha_2}, \quad (6)$$

missä $\beta = \frac{p_{Cp}}{p_1}$.

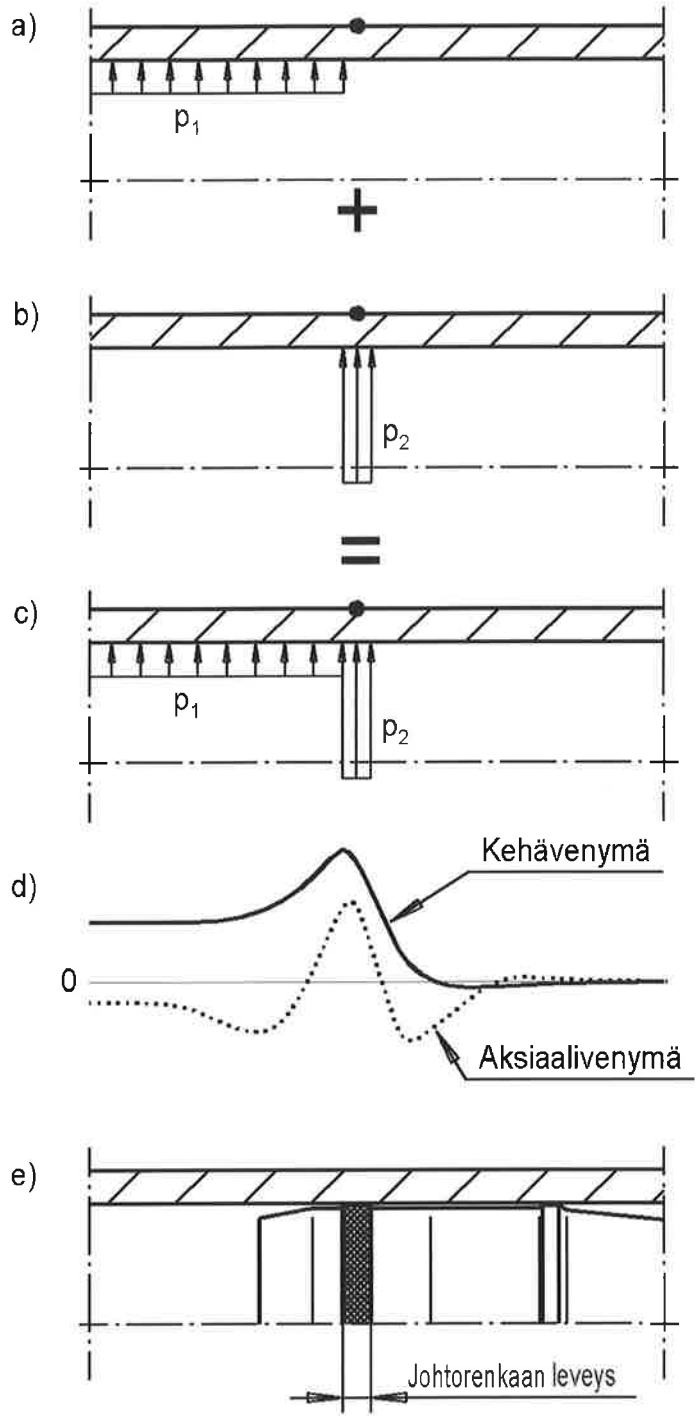

Kuva 3. Kaasun paineen p_1 (a) ja johtorengaspaineen p_2 (b) superpositio porraskuormaksi (c) ja vastaavat putken venymät $\{\varepsilon_\Theta\ \varepsilon_x\}$ (d) sekä ammus ohittamassa mittauskohtaa (e).

Mittauksissa käytetyllä tuliputkella johtorengaspaineen virheen kannalta pahin tilanne esiintyy poikkileikkauksessa, jossa $\alpha_1 = 3{,}5$. Jos tässä tapauksessa painesuhde $\beta = 2$, mikä tarkoittaa sitä, että vertailupaineen maksimiarvo on kaksinkertainen ruutikaasun paineeseen nähden, saadaan virhearvioksi

$$\frac{\Delta p_2}{p_2} = 1.17\frac{\Delta p_{Cp}}{p_{Cp}} - 0.17\frac{\Delta p_1}{p_1} + 0.17\frac{\Delta \alpha_1}{\alpha_1} + \frac{\Delta \alpha_2}{\alpha_2}. \quad (7)$$

Tämä osoittaa, että tällaisessa tapauksessa johtorengaspaineen pääasialliset virhelähteet ovat virheet vertailupaineen maksimiarvossa ja kertoimessa α_2. Ruutikaasun paineen p_1 virheellä on lähes kertaluokkaa pienempi vaikutus.

Rajatapauksessa painesuhde on $\beta = 1$, jolloin vertailupaineessa ei näy piikkiä ammuksen ohittaessa mittauspoikkileikkauksen. Tällöin virhearvio on

$$\frac{\Delta p_2}{p_2} = 1.40\frac{\Delta p_{Cp}}{p_{Cp}} - 0.40\frac{\Delta p_1}{p_1} + 0.40\frac{\Delta \alpha_1}{\alpha_1} + \frac{\Delta \alpha_2}{\alpha_2}. \quad (8)$$

Vertailupaineen piikin pienentyessä johtorengaspaineen laskennassa käytettävien arvojen suhteelliset virheet aiheuttavat suurempia suhteellisia virheitä johtorengaspaineeseen. Johtorengaspaineen laskentamenetelmä menettää siis tarkkuuttaan painesuhteen β pienentyessä. Käytännössä tästä ei ole haittaa, koska tuliputken kestävyyden kannalta ratkaisevassa asemassa ovat suuret johtorengaspaineet.

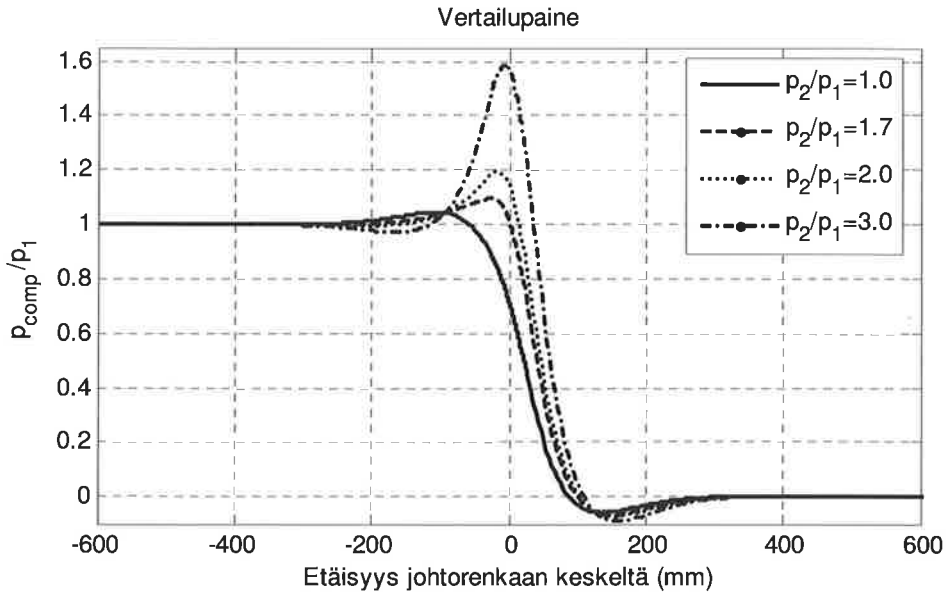

Kuva 4. Staattiseen fe-analyysiin perustuvia vertailupaineen arvoja laskettuna tuliputken ulkopinnan venymistä eräälle tuliputken poikkileikkaukselle.

Johtorengaspaineen laskennassa lähdetään oletuksesta, että vertailupaineen saavuttaessa maksimiarvonsa johtorenkaan keskikohta on mittauspisteen kohdalla. Kertoimet α_1 ja α_2 määritetään tämän perusteella. Kuvassa 4 on esitetty staattisten fe-analyysien tuloksista laskettuja vertailupaineen käyriä. Kuvasta havaitaan, että johtorengaspaineen piikin pienentyessä se samalla siirtyy ammuksen peräpäätä kohden. Kun kertoimet α_1 ja α_2 määritetään venymätuloksista johtorenkaan

keskikohdan kohdalta putken ulkopinnalta, tästä aiheutuu laskettuun johtorengaspaineeseen systemaattinen virhe, jonka suuruutta voidaan arvioida staattisella fe-analyysillä. Tämä virhe eräälle mittauspoikkileikkaukselle on esitetty kuvassa 5. Kuvasta nähdään, että systemaattinen virhe kasvaa painesuhteen β pienentyessä. Koska kyseessä on systemaattinen virhe, se voitaisiin korjata kuvan 5 käyrää vastaavia korjauskäyriä käyttämällä, mutta tähän mennessä tätä ei ole tehty, koska virhe on suurin niissä tapauksissa, joilla on vähiten merkitystä tuliputken kestävyyden kannalta.

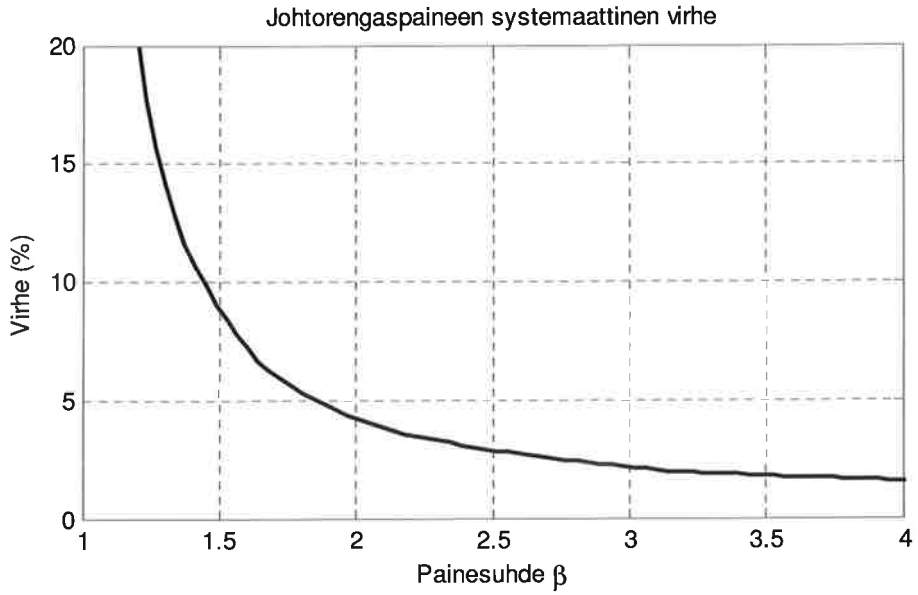

Kuva 5. Staattisiin fe-analyyseihin perustuva systemaattisen virheen arvio eräälle tuliputken poikkileikkaukselle.

4.3 Mittaustuloksien analyyseissä esiin tulleita yksityiskohtia

Ammus kiinnittyy panoskammion ja tuliputken rihlatun osan välillä olevaan loivaan kartioon johtorenkaan puristuessa ja hieman muokkaantuessa ylimenokartion sisäseinämää vasten. Pintojen välinen kitka pidättää ammuksen latausasemassa tuliputken korotuksella ammuttaessa. Ammuksen latautumisesta aiheutuva puristus aiheuttaa venymiä ylimenokartion läheisyydessä oleviin putken mittauspoikkileikkauksiin F-F ja E-E (Kuva 2). Mittausten edetessä havaittiin, että nämä venymät voivat olla niin suuria, että ne vaikuttavat selvästi mittaus- ja laskentatuloksiin. Koska mittauksissa käytettiin tasapainottamattomia venymämittaussiltoja ja tasapainotus hoidettiin laskennallisesti analyysivaiheessa, nämä latausvenymät oli mitattava erikseen ennen jokaista laukausta. Mitatut latausvenymät lisättiin tämän jälkeen laukausmittaustuloksiin. Tasapainotettujen venymämittaussiltojen käyttö ei tule kyseeseen, koska tuliputken lämpenemisen vuoksi tasapainotus olisi tehtävä aina ennen jokaista laukausta, mihin ei ole aikaa kiivaassa koeammuntarytmissä.

Jos laukausyhdistelmä toimii normaalisti, ruutikaasun hetkellinen paine on aina suurin panoskammion perässä (aseen lukossa) ja se pienenee ammuksen perää kohden mentäessä eli $p_b > p_1$. Ruutikaasun paine p_1 ammuksen takana määritettiin lukkopaineen p_b mittaustuloksesta sopivalla käyrän sovituksella vertailupaineen käyrän suhteen. Koska virhearvio osoittaa, että paineen p_1 virheet eivät ole kovin merkityksellisiä, sovitettiin mitattu lukkopaineen käyrä vertailupaineen käyrään visuaalisesti ja paineen p_1 arvo poimittiin tältä sovitekäyrältä. Tarkkuuden kannalta mitään käyrän

sovitusta ei välttämättä edes tarvita, vaan paineen p_1 arvot voitaisiin katsoa suoraan vertailupaine-käyrältä.

5. MITTAUSTULOSESIMERKKEJÄ

Kuvassa 6 on esitetty venymämittaustulokset poikkileikkauksesta D-D sekä mitattu lukkopaine p_b ja venymistä laskettu vertailupaine p_C. Ennen ammuksen ohitusta ($t < 208$ ms) venymissä on nähtävissä rekylöivien osien kiihtyvyydestä aiheutuvaa aksiaalivoimaa vastaavat venymät. Ammuksen tultua ulos tuliputkesta ($t > 217$ ms) tuliputkeen syntyy suuhidastimen toiminnasta aiheutuvaa aksiaalista värähtelyä. Vertailupaineen lauseke (1) kompensoi putken aksiaalirasituksien aiheuttamat venymäheilahtelut ja vertailupaine noudattaa sangen tarkasti lukkopainekäyrän muotoa ja tasoa ollen aluksi ammuksen ohituksen jälkeen hieman sen alapuolella, mutta myöhemmässä vaiheessa vertailupaine kohoaa jonkin verran lukkopainetta korkeammalle tasolle putken lämmetessä kuumien ruutikaasujen huuhdellessa putken sisäpintaa. Vertailupaineen lauseke (1) ei kompensoi putken lämpenemisestä aiheutuvien venymien vaikutusta. Tutkimuksen kannalta mielenkiintoisin hetki on ammuksen johtorenkaan ohitus, johon putken lämpeneminen ei ennätä vaikuttaa.

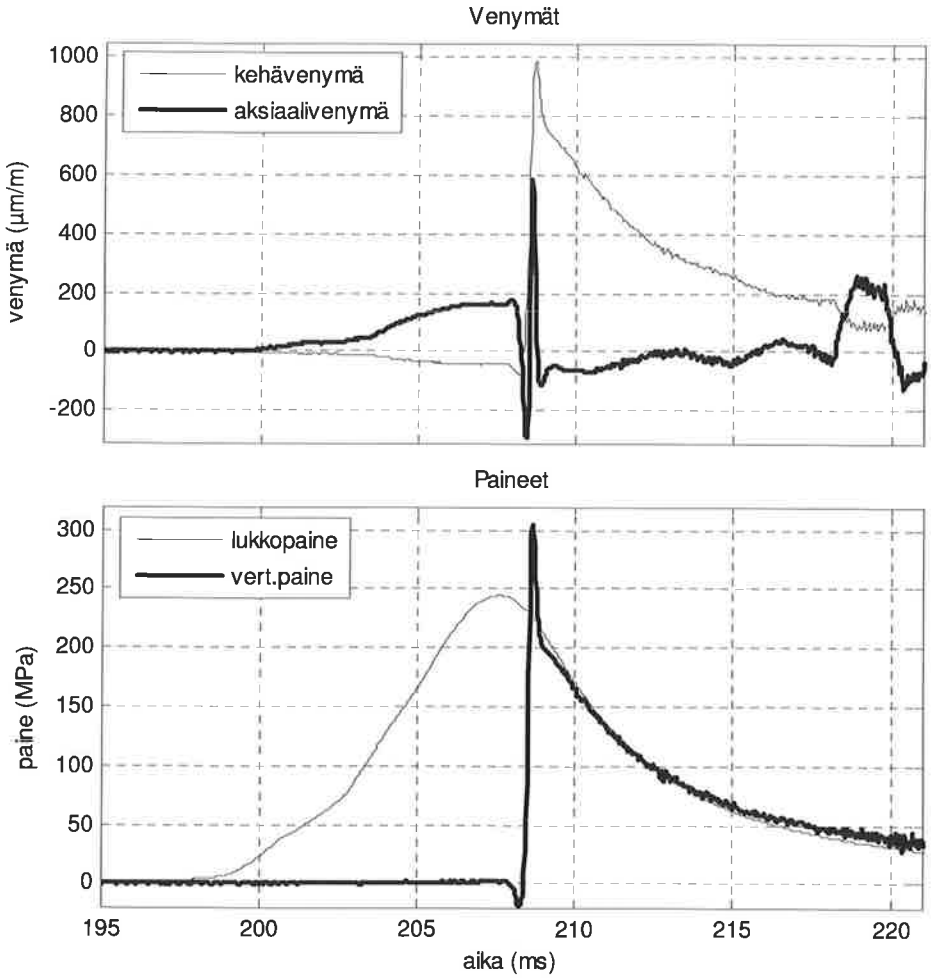

Kuva 6. Tuliputken venymät poikkileikkauksessa D-D yläkuvassa ja vastaava vertailupaine p_C sekä lukkopaine p_b alakuvassa.

Kuvassa 7 on esitetty putken venymistä lasketut vertailupaineet p_C sekä mitattu lukkopaine p_b neljälle eri ammus-johtorengasrakenteelle, kaksi mitattua laukausta kullekin ammustyypille. Ammustyyppi ID2 aiheuttaa selkeät vertailupaineen piikit, muilla ammustyypeillä ei esiinny merkittäviä vertailupaineen piikkejä.

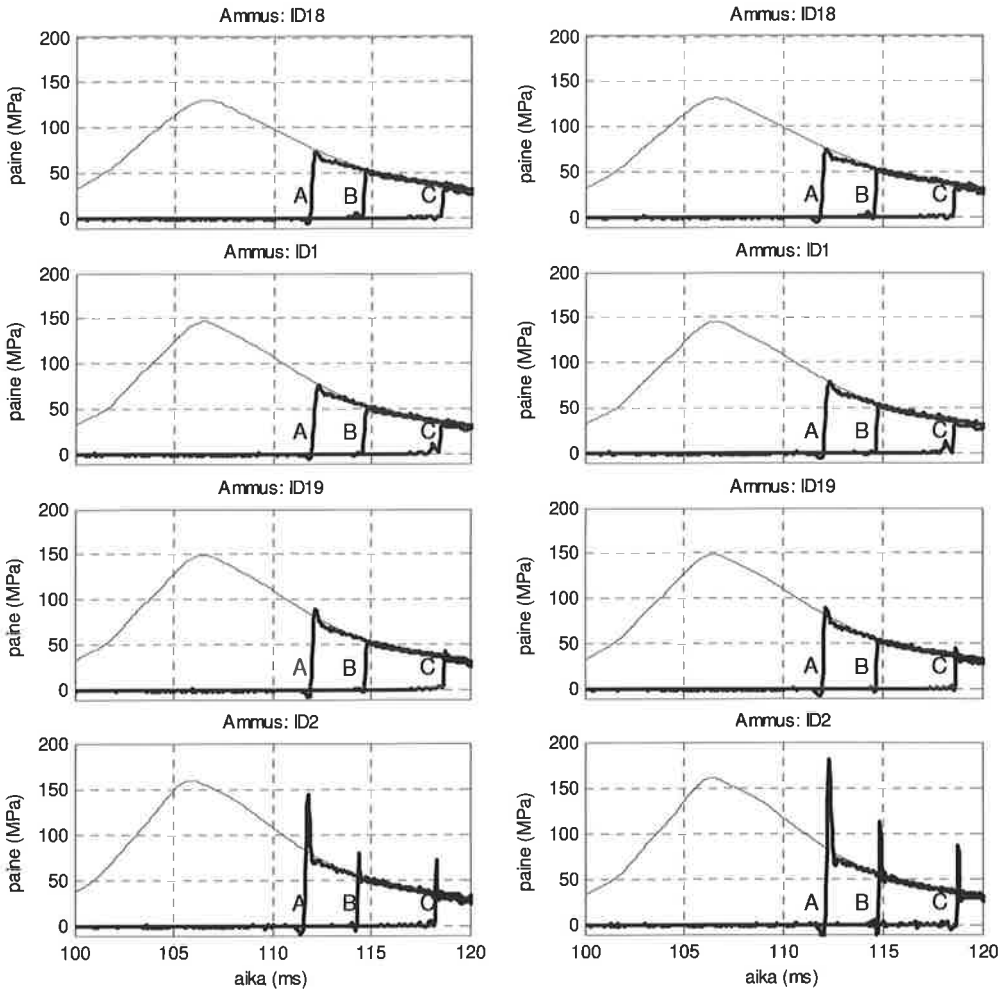

Kuva 7. Lukkopaine ja vertailupaineet putken mittauspoikkileikkauksissa (A-A, B-B, C-C) neljälle ammustyypille. Matalan lähtönopeuden v_o~ +600m/s tuottava panos, tuliputkella ammuttu N~550 laukausta ja mittaustaajuus f_c=20 kHz.

6. MITTAUSTULOKSIIN PERUSTUVIA HAVAINTOJA

Johtorengaspaineen aiheuttamat vertailupaineen piikit olivat suuria matalan lähtönopeuden tuottavilla panoksilla (pienillä panoksilla) ammuttaessa. Varsinkin tuliputken suupään mittauspoikkileikkauksissa (A-A, B-B, C-C) vertailupainepiikkien korkeus kasvoi merkittävästi matalan lähtönopeuden v_o laukauksilla sekä absoluuttiarvoltaan että suhteessa poikkileikkauksen kaasunpaineeseen. Panoskammion (F-F, E-E) läheisyydessä vertailupaineen piikit olivat matalia suhteessa kaasunpaineeseen, mutta absoluuttiset vertailupaineen huippuarvot olivat korkeampia suurilla panoksilla ammuttaessa kuin pienillä panoksilla ammuttaessa. Lähtönopeuden vaikutus vertailupaineen käyriin on esitetty kuvassa (Kuva 8).

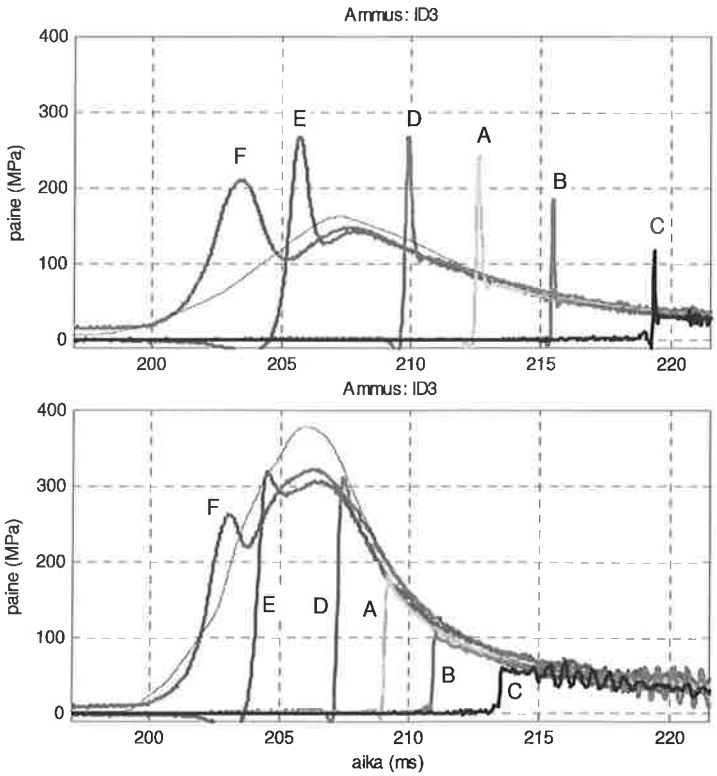

Kuva 8. Matalan lähtönopeuden v_o~ +600 m/s (yläkuva) ja korkean lähtönopeuden v_o~ +900 m/s (alakuva) tuottavan laukausyhdistelmän lukkopaine p_b ja vertailupainekäyrät p_C mittauspoikkileikkauksittain (A,B,…,F). Ammustyyppi ID3, putken laukausmäärä N~180 ls ja mittaustaajuus f_c=40 kHz.

Putken alkupään (F-F, E-E) laukausrasituksessa on kaksi kuormitushuippua, ensin ammuksen ohituksen ja johtorengaspaineen aiheuttama piikki ja myöhemmin ruutikaasun paineen maksimin huippu eli yhden laukauksen väsyttävä vaikutus on "enemmän" kuin pelkkä kaasun paineen kertakuormitus. Matalien paineiden ja lähtönopeuksien laukauksissa johtorenkaan aiheuttamat rasituspiikit ovat putken suupäässä korkeampia kuin suurilla panoksilla ammuttaessa. Tämä on täydellisessä ristiriidassa perinteisen, vain painekuorman huomioivan tuliputken väsymismitoitustavan kanssa.

Tuliputken kuluneisuuden todettiin pienentävän johtorenkaan aiheuttamia tuliputken rasituspiikkejä. Se johtunee putken sisäpintaan muodostuvan lämpösäröverkon sekä pinnan mekaanisen karhenemisen aiheuttamasta johtorenkaan nopeasta kulumisesta putkivaiheen aikana. Kuvassa (Kuva 9) on esitetty mittauspoikkileikkauksen C-C vertailupaineen huipun ja tuliputkella ammutun laukausmäärän N välinen suhde. Vertailupaineen terävät huiput ovat mataloituneet kaasun paineen tasolle jo n. 500 ls:n jälkeen ammustyypillä ID1 ammuttaessa. Saman ilmiön todettiin myös esiintyvän poikkileikkauksissa A-A ja B-B. Kuvan data perustuu vain kolmen eri tuliputken mittaustuloksiin, joten havaintojen tilastollinen luotettavuus on epävarma. Päätelmää kuitenkin tukee viitteessä [2] raportoidut samankaltaiset havainnot kuluneisuuden vaikutuksesta putkirasituksiin. Jos ammuskonstruktio aiheuttaa alun perin suuria putkirasituksia, ne näyttävät säilyvän muita korkeammalla tasolla myös kuluneella putkella ammuttaessa kuten kuvan 7 ammustyypin ID2 vertailupainekäyristä on havaittavissa.

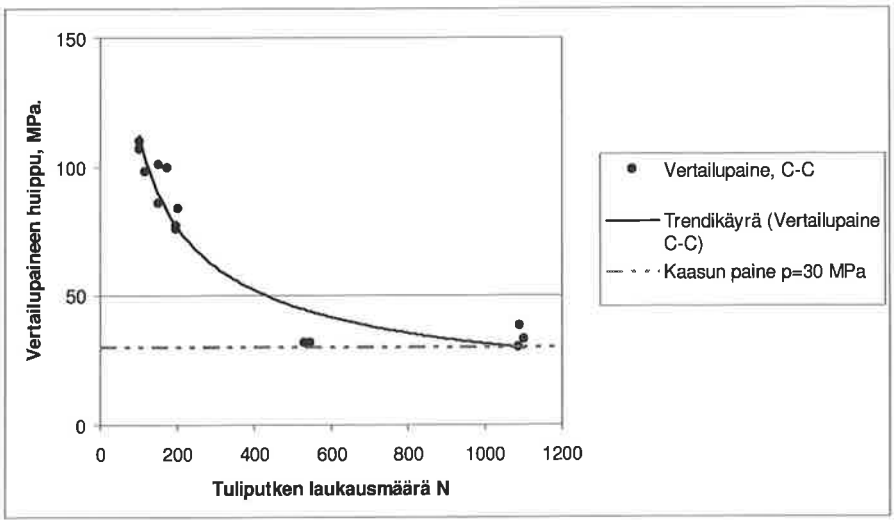

Kuva 9. Vertailupaineen huippuarvo p_{Cp} vs. tuliputken laukausmäärä N putken mittauspoikkileikkauksessa C-C, sovitettu trendikäyrä sekä poikkileikkauksessa esiintyvän ruutikaasun paineen tyypillinen arvo. Matalan paineen ja lähtönopeuden v_o~+600 m/s tuottava panos ja ammustyyppi ID1. HUOM: N~550 ls mittaustuloksissa mittaustaajuus f_c=20 kHz, muissa vähintään f_c=40 kHz.

7. JOHTORENGASRASITUKSIIN VAIKUTTAVAT TEKIJÄT

Mittaustuloksiin ja kirjallisuudessa esitettyihin havaintoihin perustuen voidaan olettaa tuliputkeen kohdistuvien johtorengasrasituksien olevan suurimmillaan mm. seuraavien seikkojen toteutuessa:

1. Tuliputkeen liittyvät:
    a. Kulumaton, uusi tai vähän ammuttu tuliputki
    b. Aamun tai pitkän tulitauon jälkeinen ensimmäinen laukaus putken ollessa likainen.
2. Tuliputken huoltoon ja ylläpitoon liittyvät:
    a. Ampuminen voimakkaasti kuparoituneella putkella. Ilmiö on johtorengas -ammuskonstruktio riippuvainen
    b. Ampuminen likaisella putkella (esim. öljyinen ja/tai karstainen tuliputki). Ilmiön voimakkuus on johtorengas -ammuskonstruktio riippuvainen.
3. Panokseen liittyvät:
    a. Matalan lähtönopeuden ja paineen laukausyhdistelmä tuliputken keskialueen ja etenkin suupään rasituksiin liittyen
    b. Suuren paineen laukausyhdistelmä tuliputken alkupään rasituksiin liittyen.
4. Ammuskuoreen liittyen
    a. Kuoren suuri radiaalinen jäykkyys johtorenkaan kohdalla.
5. Johtorenkaan rakenteeseen liittyen:
    a. Suuri johtorenkaan ulkohalkaisija
    b. Ohut johtorenkaan paksuus
    c. Huono pakourien suunnittelu:
        i. Pienet pakourat
        ii. Pakourien pieni lukumäärä
        iii. Pieni pakourien tilavuus
        iv. Pakourien sijoittelu.
    d. Leveä johtorengas yhdessä c:n osatekijöiden kanssa
    e. Johtorenkaan korkea lujuus yhdessä a,…,d kanssa.

8. PÄÄTELMÄT

Tuliputken venymämittauksin todettiin joidenkin ammuskonstruktioiden aiheuttavan merkittäviä putkirasituksia. Ammuksen ohittaessa mittauspisteen putken ulkopinnan venymistä laskettu vertailupaine oli ääritapauksissa moninkertainen ruutikaasun paineen vaikutukseen nähden. Vertailupaineen huippuarvo antaa mahdollisuuden erilaisten laukausyhdistelmien tuliputkelle aiheuttamien rasitusten arvioimiseen. Laskettujen johtorengaspaineiden avulla voidaan esim. arvioida riskiä tuliputken pysyvien muodonmuutosten syntymiseen sekä todeta johtorenkaan ja/tai ammuksen konstruktiomuutosten vaikutukset johtorengaspaineeseen ja edelleen sekä tuliputkeen että ammukseen kohdistuviin laukausrasituksiin.

KIITOKSET

Kirjoitelman laatijat esittävät kiitokset Maavoimien Materiaalilaitoksen Esikunnan Järjestelmäosastolle tutkimukseen osoitetuista resursseista ja rahoituksesta sekä tulosten ja kirjoitelman julkaisuluvasta. Patria Land & Armament Oy asejärjestelmien testaus- ja evaluointiryhmän toteuttamat mittaukset ovat olleet edellytyksinä tutkimukselle, joten ryhmän koeammunta- ja mittausponnistelut ansaitsevat kirjoittajien lämpimät kiitokset.

VIITELUETTELO

1. Drysdale W.H. & Burns B.P. *Structural Design of Projectiles*. In: Stiefel L. (ed.). Gun Propulsion Technology. AIAA. vol 109. Washington DC. 1988. pp. 133,..., 159.
2. Andrews T.D. *Projectile Driving Band Interactions with Gun Barrels*. In: Gun Tubes 2005 Conference. GT2005. Conference Proceedings. 10 to 13 April 2005. Keble College Oxford. Paper S7/P28. RMCS, Shrivenham. 2005. (Also in: Journal of Pressure Vessel Technology. Vol 128, May 2006. pp. 273,..., 278.)
3. Awitzur, B. *Engraving of Rotating bands – A Modification of Metal-Flow Pattern*. Report ARCLB-TR-83019. Benet Weapons Laboratory. Watervliet, N.Y. 1983. 30 p.
4. Balakin, V.A. *Friction and Wear in Rifled Artillery Gun Barrels*. In: Journal of Soviet Friction and Wear. Vol. 10. No. 3. 1989. pp. 100,..., 106.
5. Flynn, P.D. *Strain-gage Instrumentation for Ammunition Testing*. In: Experimental Mechanics. May 1975. pp. 192,..., 200.
6. Moilanen S. & Tervokoski J. *Raskaan kranaatinheittimen laukauspaineen mittausmenetelmien vertailu*. In: Von Hertzen, R. & Halme, T. (eds). *Proceedings of the IX Finnish Mechanics Days. June 13th and 14th, 2006*. Lappeenranta Univ. of Tech. Dept of Mech. Eng. Report 17. Lappeenranta, 2006. pp. 201,..., 213.
7. Toivola, J. & Moilanen,S. *Aseen tuliputken lujuusteknisen mitoituksen ohjelmointi*. In: Von Hertzen, R. & Halme, T. (eds). *Proceedings of the IX Finnish Mechanics Days. June 13th and 14th, 2006*. Lappeenranta Univ. of Tech. Dept of Mech. Eng. Report 17. Lappeenranta, 2006. pp. 692,..., 698.

SURFACE TENSION PROBLEMS WITH DISTRIBUTED TORQUE

M. REIVINEN[1], E.-M. SALONEN[1], V.P. VASKELAINEN[2]
[1]Department of Structural Engineering and Building Technology
Helsinki University of Technology
P.O.Box 2100, FI-02015 TKK, Finland
e-mail: mika.reivinen@tkk.fi
[2]Department of Communications and Networking
Helsinki University of Technology
P.O.Box 3000, FI-02015 TKK, Finland

ABSTRACT

The present article is an extension of presentation [1]. The problem considered consists again of the determination of the shape of the interface between two material phases. In [1] the emphasis was on the use of the principle of virtual work and on the treatment of a free boundary. In the present work it is assumed contrary to [1] that the surface tension is not a constant but depends in a prescribed way on the orientation of the interface. The non-constancy of the surface tension means that for interface equilibrium certain distributed torque must act on the interface. The virtual work contribution from this loading is presented in some detail. Also, in [1], the pressures in the phases were given but here the volume of one of the phases is fixed and thus the corresponding pressure is originally unknown. The consideration in is restricted to two dimensions.

1. INTRODUCTION

The present article is an extension of presentation [1]. The problem under study consists of the determination of the shape of the interface between two material phases with a non-constant surface tension and a fixed volume for one of the phases. The final purpose is to be able to determine the equilibrium shapes of crystals. In [1] the phases considered were a liquid and a vapor. For continuity of presentation we will follow here the notation of [1] and will thus still speak about the liquid and vapor phases although the physical assumption of an orientation dependent surface tension should actually be related to a solid. As just the mathematical changes needed to extend presentation [1] are now of interest, this approach can be justified.

Let us consider Figure 1 reproduced from [1]. As there, the presentation here is restricted to two dimensions. The basic setting consists of a liquid (l), surrounded by a vapor (v) and resting in equilibrium on a solid surface (s). The task is to determine the position of the interface C between the liquid and the vapor. The shape $\hat{C}$ of the solid surface is considered as given.

In [1] the emphasis was on the use of the principle of virtual work and on the treatment of a free boundary (point b in Figure 1). The so-called Young's equation

$$\sigma \cos\theta = \sigma_{sv} - \sigma_{sl} \tag{1}$$

was assumed to be valid at a free boundary in [1]. The quantities σ, σ_{sv} and σ_{sl} are the surface energy densities or surface tensions of the liquid-vapor, solid-vapor and solid-liquid interfaces, respectively. These quantities are considered as given material parameters and determine at point b the value of the contact angle θ. In a shape determination problem the position of the contact line

where the Young's equation is valid is unknown and forms a part of the problem. Equation (1) will be modified in the present formulation.

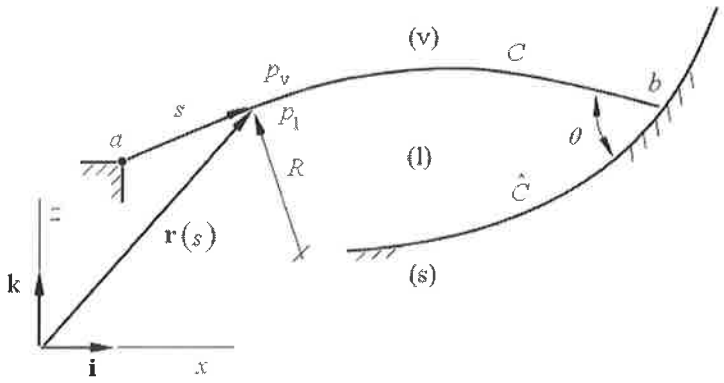

Figure 1 Some notations.

Contrary to [1], now the surface tension σ is not assumed to be a constant but depends in a prescribed way on the orientation of the interface and consequently on position. It is then found that the equilibrium of the interface is not possible without a distributed torque or couple loading m to be described in detail later. In [1], the equilibrium of the interface was expressed as the well-known Laplace equation

$$p_l - p_v = \frac{\sigma}{R}, \tag{2}$$

where p_l and p_v are the pressures in the liquid and vapor, respectively, evaluated at the interface and $1/R$ is the curvature of the interface positive when the center of curvature is on the liquid side. Again, due to the extension with respect to distributed torque, equation (2) will be modified in the present formulation. The contribution of the torque to the virtual work equation will be considered in some detail.

Another extension concerns the pressure inside the liquid. In [1], a constant given pressure was asssumed. However, here the volume or more specifically in two dimensions, the area of the liquid is given. This means that the pressure inside the liquid is originally an unknown and an additional system equation must be generated.

A discrete formulation employing a line segment model is described and applied to a demonstration problem.

2. VIRTUAL WORK

2.1 Virtual work equation

The virtual work equation associated with the liquid-vapor interface is

$$\delta' W \equiv \delta' W^{\text{int}} + \delta' W^{\text{ext}} + \delta' W^{\text{bound}} = 0. \tag{3}$$

In above, the virtual work consists of the virtual work of the internal forces, of the external forces and of the contribution associated with the free boundary. We will repeat shortly the relevant expressions from [1]. The new term due to torque will be considered in some detail in Section 2.3.

2.2 Virtual work of internal forces

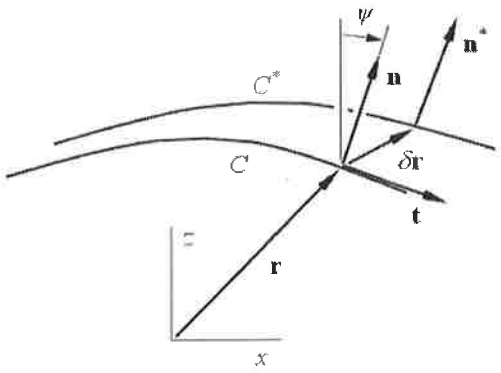

Figure 2 Position vector **r** and virtual movement $\delta\mathbf{r}$.

The arc length s along the interface is used as the curve parameter for the interface curve C (Figure 1). We assume that the interface position is fixed at point a and point b corresponds to the free boundary. Let the position vector to a generic point on the interface curve C be denoted by $\mathbf{r}(s)$ and let the corresponding point on a varied comparison curve C^* be given by $\mathbf{r}(s)+\delta\mathbf{r}(s)$ (Figure 2). $\delta\mathbf{r}$ is called here virtual movement.

The expression for the virtual work of internal forces is

$$\delta' W^{\text{int}} = -\int_s \sigma\,\mathbf{t}\cdot\frac{\mathrm{d}\delta\mathbf{r}}{\mathrm{d}s}\mathrm{d}s\,, \tag{4}$$

where **t** is the unit tangent vector to the interface curve (Figure 2). As σ is here not a constant, it cannot be taken outside the integral sign.

2.3 Virtual work of external forces

The external forces consist here of the pressure difference on the interface and of the distributed torque.

The expression for the virtual work due to the pressure difference is

$$\delta' W^{\text{p}} = \int_s (p_{\text{l}} - p_{\text{v}})\,\mathbf{n}\cdot\delta\mathbf{r}\mathrm{d}s\,, \tag{5}$$

where **n** is the unit normal vector to the interface (Figure 2) and p_{l} and p_{v} are the pressures explained in connection with formula (2). We allow for hydrostatic pressure distribution in the liquid:

$$p_{\text{l}} = p_{\text{l}}^0 - \rho_{\text{l}} g z\,, \tag{6}$$

and in principle also in the vapor:

$$p_{\text{v}} = p_{\text{v}}^0 - \rho_{\text{v}} g z\,. \tag{7}$$

Above, gravity acts in the negative z-axis direction with acceleration g and the densities ρ_{l} and ρ_{v} are assumed to be constants. The pressure p_{v}^0 is given and the pressure p_{l}^0 is initially

unknown due to the fixed liquid area constraint. These pressures correspond to the pressure values at level $z = 0$ (which of course do not need to be actually reached by the phases.)

We will now consider the effect of the distributed torque in some detail and will use such notations that a possible future extension to three dimensions becomes rather straightforward. The vectorial torque is in the present two-dimensional case

$$\mathbf{m} = m\mathbf{j}, \tag{8}$$

where $\mathbf{j}$ is the unit vector in the y-axis direction. The physical unit of m is the same as of σ: N/m. The torque does virtual work on the interface surface angular displacement. From Figure 2, we define a vectorial angular displacement

$$\delta\boldsymbol{\theta} \equiv \mathbf{n}\times\mathbf{n}^* = \mathbf{n}\times(\mathbf{n}+\delta\mathbf{n}) = \mathbf{n}\times\delta\mathbf{n}. \tag{9}$$

Now,

$$\mathbf{n} = \mathbf{t}\times\mathbf{j} = \frac{\mathrm{d}\mathbf{r}}{\mathrm{d}s}\times\mathbf{j} \tag{10}$$

and thus

$$\delta\mathbf{n} = \delta\mathbf{t}\times\mathbf{j} + \mathbf{t}\times\delta\mathbf{j} = \delta\mathbf{t}\times\mathbf{j} = \frac{\mathrm{d}\delta\mathbf{r}}{\mathrm{d}s}\times\mathbf{j}. \tag{11}$$

Further, from (9) and (11):

$$\delta\boldsymbol{\theta} = \mathbf{n}\times\left(\frac{\mathrm{d}\delta\mathbf{r}}{\mathrm{d}s}\times\mathbf{j}\right) = (\mathbf{n}\cdot\mathbf{j})\frac{\mathrm{d}\delta\mathbf{r}}{\mathrm{d}s} - \left(\mathbf{n}\cdot\frac{\mathrm{d}\delta\mathbf{r}}{\mathrm{d}s}\right)\mathbf{j} = -\left(\mathbf{n}\cdot\frac{\mathrm{d}\delta\mathbf{r}}{\mathrm{d}s}\right)\mathbf{j}. \tag{12}$$

Above, the expansion formula for a vector tripleproduct has been used. The virtual work expression from torque is thus

$$\delta' W^{\mathrm{t}} = \int_s \mathbf{m}\cdot\delta\boldsymbol{\theta}\,\mathrm{d}s = -\int_s m\,\mathbf{n}\cdot\frac{\mathrm{d}\delta\mathbf{r}}{\mathrm{d}s}\mathrm{d}s. \tag{13}$$

Adding the terms from the pressure difference and torque, we obtain

$$\delta' W^{\mathrm{ext}} = \delta' W^{\mathrm{p}} + \delta' W^{\mathrm{t}} = \int_s (p_{\mathrm{l}} - p_{\mathrm{v}})\,\mathbf{n}\cdot\delta\mathbf{r}\,\mathrm{d}s - \int_s m\,\mathbf{n}\cdot\frac{\mathrm{d}\delta\mathbf{r}}{\mathrm{d}s}\mathrm{d}s. \tag{14}$$

2.4 VIRTUAL WORK FROM FREE BOUNDARY

The virtual work expression from the free boundary is

$$\delta' W^{\mathrm{bound}} = -\sigma\frac{\hat{\mathbf{n}}\cdot\delta\mathbf{r}}{\sin\theta} + (\sigma_{\mathrm{sv}} - \sigma_{\mathrm{sl}})\frac{\mathbf{n}\cdot\delta\mathbf{r}}{\sin\theta}, \tag{15}$$

where

$$\hat{\mathbf{n}} = -\sin\theta\,\mathbf{t} + \cos\theta\,\mathbf{n} \tag{16}$$

is the unit normal vector to the solid surface directed towards the liquid-vapor side. Of course, the terms in (15) and (16) are to be evaluated at the free boundary.

2.5 Equilibrium equations

Collecting all the terms given above, the virtual work equation (3) obtains the form

$$-\int_s \sigma\,\mathbf{t}\cdot\frac{\mathrm{d}\delta\mathbf{r}}{\mathrm{d}s}\mathrm{d}s+\int_s (p_\mathrm{l}-p_\mathrm{v})\,\mathbf{n}\cdot\delta\mathbf{r}\,\mathrm{d}s-\int_s m\,\mathbf{n}\cdot\frac{\mathrm{d}\delta\mathbf{r}}{\mathrm{d}s}\mathrm{d}s$$
$$-\sigma\frac{\hat{\mathbf{n}}\cdot\delta\mathbf{r}}{\sin\theta}\bigg|_{s=s_\mathrm{b}}+(\sigma_\mathrm{sv}-\sigma_\mathrm{sl})\frac{\mathbf{n}\cdot\delta\mathbf{r}}{\sin\theta}\bigg|_{s=s_\mathrm{b}}=0. \tag{17}$$

Additionally, $\delta\mathbf{r}$ is restrained to vanish at the fixed boundary point a. To deduce the strong forms from the weak form, we have to integrate by parts the first and third term on the left-hand side of (17). We obtain

$$-\int_s \sigma\mathbf{t}\cdot\frac{\mathrm{d}\delta\mathbf{r}}{\mathrm{d}s}\mathrm{d}s=\int_s\frac{\mathrm{d}(\sigma\mathbf{t})}{\mathrm{d}s}\cdot\delta\mathbf{r}\mathrm{d}s-\Big|_{s_\mathrm{a}}^{s_\mathrm{b}}\sigma\mathbf{t}\cdot\delta\mathbf{r}$$
$$=\int_s\frac{\mathrm{d}\sigma}{\mathrm{d}s}\mathbf{t}\cdot\delta\mathbf{r}\mathrm{d}s-\int_s\frac{\sigma}{R}\mathbf{n}\cdot\delta\mathbf{r}\mathrm{d}s-\sigma\mathbf{t}\cdot\delta\mathbf{r}\big|_{s=s_\mathrm{b}}. \tag{18}$$

Frenet formula $\mathrm{d}\mathbf{t}/\mathrm{d}s=-\mathbf{n}/R$ has been applied. Further,

$$-\int_s m\mathbf{n}\cdot\frac{\mathrm{d}\delta\mathbf{r}}{\mathrm{d}s}\mathrm{d}s=\int_s\frac{\mathrm{d}(m\mathbf{n})}{\mathrm{d}s}\cdot\delta\mathbf{r}\mathrm{d}s-\Big|_{s_\mathrm{a}}^{s_\mathrm{b}}m\mathbf{n}\cdot\delta\mathbf{r}$$
$$=\int_s\frac{\mathrm{d}m}{\mathrm{d}s}\mathbf{n}\cdot\delta\mathbf{r}\mathrm{d}s+\int_s\frac{m}{R}\mathbf{t}\cdot\delta\mathbf{r}\mathrm{d}s-m\mathbf{n}\cdot\delta\mathbf{r}\big|_{s=s_\mathrm{b}}. \tag{19}$$

Equation (17) becomes

$$\int_s\left[-\frac{\sigma}{R}+\frac{\mathrm{d}m}{\mathrm{d}s}+p_\mathrm{l}-p_\mathrm{v}\right]\mathbf{n}\cdot\delta\mathbf{r}\mathrm{d}s+\int_s\left(\frac{\mathrm{d}\sigma}{\mathrm{d}s}+\frac{m}{R}\right)\mathbf{t}\cdot\delta\mathbf{r}\mathrm{d}s$$
$$+\left[-\sigma\left(\mathbf{t}+\frac{\hat{\mathbf{n}}}{\sin\theta}\right)+(\sigma_\mathrm{sv}-\sigma_\mathrm{sl})\frac{\mathbf{n}}{\sin\theta}-m\mathbf{n}\right]\cdot\delta\mathbf{r}\big|_{s=s_\mathrm{b}}=0. \tag{20}$$

We get from the integrals the field equations

$$p_\mathrm{l}-p_\mathrm{v}=\frac{\sigma}{R}-\frac{\mathrm{d}m}{\mathrm{d}s},\quad s_\mathrm{a}<s<s_\mathrm{b} \tag{21}$$

and

$$\frac{\mathrm{d}\sigma}{\mathrm{d}s}+\frac{m}{R}=0,\quad s_\mathrm{a}<s<s_\mathrm{b}. \tag{22}$$

Using (16) in the free boundary term in (20) gives

$$\mathbf{t}+\frac{\hat{\mathbf{n}}}{\sin\theta}=\frac{\sin\theta\,\mathbf{t}+\hat{\mathbf{n}}}{\sin\theta}=\frac{\cos\theta\,\mathbf{n}}{\sin\theta}, \tag{23}$$

and the free boundary term becomes

$$\frac{1}{\sin\theta}\left[-\sigma\cos\theta+\sigma_{\mathrm{sv}}-\sigma_{\mathrm{sl}}-m\sin\theta\right]\mathbf{n}\cdot\delta\mathbf{r}\big|_{s=s_{\mathrm{b}}}, \tag{24}$$

and the boundary condition

$$\sigma\cos\theta+m\sin\theta=\sigma_{\mathrm{sv}}-\sigma_{\mathrm{sl}} \tag{25}$$

emerges.

The surface tension σ is assumed to depend on the orientation of the interface or on the angle ψ between the normal $\mathbf{n}$ and the z- axis (Figure 2), $\sigma=\sigma(\psi)$. We have the general relationship

$$\frac{\mathrm{d}(\ )}{\mathrm{d}s}=\frac{\mathrm{d}(\ )}{\mathrm{d}\psi}\frac{\mathrm{d}\psi}{\mathrm{d}s}=\frac{1}{R}\frac{\mathrm{d}(\ )}{\mathrm{d}\psi}. \tag{26}$$

Application of this in equation (22) gives

$$m=-\frac{\mathrm{d}\sigma}{\mathrm{d}\psi}. \tag{27}$$

This important result shows that for equilibrium in the tangential direction, the torque cannot be arbitrary but should be evaluated according to (27).

Using relation (27) in equation (21) gives now

$$p_{\mathrm{l}}-p_{\mathrm{v}}=\frac{\sigma+\mathrm{d}^2\sigma/\mathrm{d}\psi^2}{R} \tag{28}$$

as the final equilibrium equation in the normal direction.

The strong forms: field equation (28) and boundary condition (25) are in accordance with results given for example in Reference [2] by a different approach. This shows that the virtual work formulation of interface shape determination problem is correct.

3. FIXED DROP SIZE

Let the given liquid drop cross-sectional area be A_0. Thus we have the constraint equation

$$A=A_0, \tag{29}$$

where A is evaluated from the positions of the surfaces C and $\hat{C}$.

In detail, application of the divergence theorem gives the well-known formulas

$$A=\oint\!\!\int xn_x\mathrm{d}s, \tag{30}$$

$$A=\oint\!\!\int zn_z\mathrm{d}s. \tag{31}$$

Instead of using either (30) or (31), one can take, say, the average

$$A = \frac{1}{2}\oint (xn_x + zn_z)\,\mathrm{d}s\,. \tag{32}$$

In the discrete formulation, the counterpart of equation (31) is applied.

4. DISCRETE FORMULATION; LINE SEGMENTS

The discrete formulation is quite similar to the one described in [1]. We therefore discuss mainly just the changes due to the non-constancy of the surface tension and due to the fixed area constraint.

The liquid-vapor interface is discretized by two-noded line segments or elements. Figure 3 shows the notations for a generic line segment. The position vector along the segment is given by

$$\mathbf{r} = (1-\xi)\mathbf{r}_1 + \xi\mathbf{r}_2 = \left[(1-\xi)x_1 + \xi x_2\right]\mathbf{i} + \left[(1-\xi)z_1 + \xi z_2\right]\mathbf{j} \tag{33}$$

where instead of the local arc length s the dimensionless coordinate $\xi = s/L$ is used. The length of the segment is

$$L = \sqrt{(x_2 - x_1)^2 + (z_2 - z_1)^2}\,. \tag{34}$$

The generalized coordinates used are (normally) the nodal Cartesian coordinates x_1, z_1, x_2, z_2.

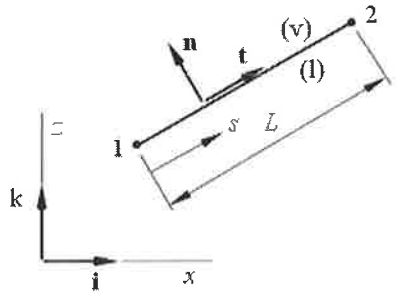

Figure 3 A generic line segment.

From (33) by variation, the virtual movement along the segment is

$$\delta\mathbf{r} = (1-\xi)\delta\mathbf{r}_1 + \xi\delta\mathbf{r}_2 = \left[(1-\xi)\delta x_1 + \xi\delta x_2\right]\mathbf{i} + \left[(1-\xi)\delta z_1 + \xi\delta z_2\right]\mathbf{k}. \tag{35}$$

The virtual work contribution from a generic segment obtains finally the form

$$\delta' W = X_1\delta x_1 + Z_2\delta z_1 + X_2\delta x_2 + Z_2\delta z_2\,, \tag{36}$$

where X_1, Z_1, X_2, Z_2 are the generalized forces. The generalized forces consist similarly as the virtual work from terms corresponding to internal and external forces and to the free boundary.

The unit normal to the segment is given by

$$\mathbf{n} = -\frac{z_2 - z_1}{L}\mathbf{i} + \frac{x_2 - x_1}{L}\mathbf{k}\,. \tag{37}$$

The orientation angle ψ is obtained from

$$\cos\psi = \mathbf{k}\cdot\mathbf{n} = \frac{x_2 - x_1}{L}. \tag{38}$$

As ψ is constant for the segment, the surface tension $\sigma(\psi)$ is also constant in the segment and the generalized forces from the surface tension are thus evaluated with the same formulas as in [1].

The term

$$\frac{\mathrm{d}\delta\mathbf{r}}{\mathrm{d}s} = \frac{\mathrm{d}\delta\mathbf{r}}{\mathrm{d}\xi}\frac{\mathrm{d}\xi}{\mathrm{d}s} = \frac{1}{L}\frac{\mathrm{d}\delta\mathbf{r}}{\mathrm{d}\xi} = \frac{1}{L}\left[\left(-\delta x_1 + \delta x_2\right)\mathbf{i} + \left(-\delta z_1 + \delta z_2\right)\mathbf{k}\right] \tag{39}$$

and

$$\mathbf{n}\cdot\frac{\mathrm{d}\delta\mathbf{r}}{\mathrm{d}s} = \frac{1}{L}\left(\frac{z_2 - z_1}{L}\delta x_1 - \frac{z_2 - z_1}{L}\delta x_2 - \frac{x_2 - x_1}{L}\delta z_1 + \frac{x_2 - x_1}{L}\delta z_2\right). \tag{40}$$

The virtual work contribution from the constant torque

$$m = -\frac{\mathrm{d}\sigma}{\mathrm{d}\psi}(\psi) \tag{41}$$

in the segment is now according to (13)

$$-\int_0^L m\,\mathbf{n}\cdot\frac{\mathrm{d}\delta\mathbf{r}}{\mathrm{d}s}\mathrm{d}s = -L\int_0^1 m\,\mathbf{n}\cdot\frac{\mathrm{d}\delta\mathbf{r}}{\mathrm{d}s}\mathrm{d}\xi = -Lm\,\mathbf{n}\cdot\frac{\mathrm{d}\delta\mathbf{r}}{\mathrm{d}s}$$

$$= m\left(-\frac{z_2 - z_1}{L}\delta x_1 + \frac{z_2 - z_1}{L}\delta x_2 + \frac{x_2 - x_1}{L}\delta z_1 - \frac{x_2 - x_1}{L}\delta z_2\right). \tag{42}$$

The corresponding generalized forces are thus

$$\begin{aligned} X_1^{\mathrm{t}} &= -m\frac{z_2 - z_1}{L}, \quad Z_1^{\mathrm{t}} = m\frac{x_2 - x_1}{L}, \\ X_2^{\mathrm{t}} &= m\frac{z_2 - z_1}{L}, \quad Z_2^{\mathrm{t}} = -m\frac{x_2 - x_1}{L}. \end{aligned} \tag{43}$$

A physical interpretation of these forces is obtained by replacing the total torque mL acting on the segment by two forces of magnitude m acting in opposite directions perpendicular to the segment at the endpoints.

Due to gravity, the pressure intensities can vary here linearly with depth and the pressures on the segment can thus also vary linearly with respect to ξ:

$$\begin{aligned} p_{\mathrm{l}} &= (1-\xi)(p_{\mathrm{l}})_1 + \xi(p_{\mathrm{l}})_2, \\ p_{\mathrm{v}} &= (1-\xi)(p_{\mathrm{v}})_1 + \xi(p_{\mathrm{v}})_2, \end{aligned} \tag{44}$$

where

$$
\begin{aligned}
&(p_l)_1 = p_l^0 - \rho_l g\, z_1, \quad (p_l)_2 = p_l^0 - \rho_l g\, z_2, \\
&(p_v)_1 = p_v^0 - \rho_v g\, z_1, \quad (p_v)_2 = p_v^0 - \rho_v g\, z_2.
\end{aligned}
\tag{45}
$$

Performing the details starting from (5), the generalized forces due to the pressure difference are found to be

$$
\begin{aligned}
X_1^p &= -(z_2 - z_1)\left\{\frac{1}{3}\left[(p_l)_1 - (p_v)_1\right] + \frac{1}{6}\left[(p_l)_2 - (p_v)_2\right]\right\}, \\
Z_1^p &= (x_2 - x_1)\left\{\frac{1}{3}\left[(p_l)_1 - (p_v)_1\right] + \frac{1}{6}\left[(p_l)_2 - (p_v)_2\right]\right\}, \\
X_2^p &= -(z_2 - z_1)\left\{\frac{1}{6}\left[(p_l)_1 - (p_v)_1\right] + \frac{1}{3}\left[(p_l)_2 - (p_v)_2\right]\right\}, \\
Z_2^p &= (x_2 - x_1)\left\{\frac{1}{6}\left[(p_l)_1 - (p_v)_1\right] + \frac{1}{3}\left[(p_l)_2 - (p_v)_2\right]\right\}.
\end{aligned}
\tag{46}
$$

The contribution to the cross-sectional area from the segment is (using expression (31))

$$
\Delta A = \int_0^L n_z z \mathrm{d}s = L \int_0^1 n_z z \,\mathrm{d}\xi . \tag{47}
$$

Integration gives

$$
\Delta A = \frac{1}{2}(x_2 - x_1)(z_1 + z_2). \tag{48}
$$

Of course, this result can also be obtained directly from standard mathematics books.

Because of the simple form of formula (48), the sensitivities of A with respect to the nodal movements discussed in the following chapter could easily be evaluated here also analytically.

5. DISCRETE FORMULATION; SYSTEM EQUATIONS

The geometry of the discrete interface model is fixed by a list consisting of the nodal Cartesian coordinates, say **X**, and of the global node numbers of the segments in the model. The task is to determine that **X** for which the main system equations (equilibrium equations) are satisfied. An additional unknown is the pressure p_l^0 in the liquid phase, which will be denoted from this on for convenience as P. The corresponding additional system equation is the area constraint $A = A_0$. It is to be noted that P appears in the equilibrium equations but not in the constraint equation. As the interface determination problem is strongly non-linear, the solution must be found iteratively.

The generalized coordinates (which might be called also generalized movements) are denoted here q_i They are defined in principle anew for the each current system configuration. Normally, we will employ two movements Δx_k and Δz_k for a generic node k inside the mesh. However, at the free boundary node, only one movement in the solid surface tangent direction is used.

The virtual work for the interface model (with respect to a current configuration) obtains the form

$$
\delta' W = \sum_{i=1}^{N_{\mathrm{dof}}} Q_i\, \delta q_i , \tag{49}
$$

where Q_i is the i:th generalized force corresponding to the i:th movement q_i and N_{dof} the total number of movements. The generalized forces must vanish and the area constraint must be satisfied. Thus, the system equations are

$$\begin{aligned} &Q_i = 0, \quad i = 1,2,\cdots N_{\text{dof}}, \\ &A = A_0. \end{aligned} \tag{50}$$

More specifically, corresponding to a generic node k inside the mesh where the movements Δx_k and Δz_k are used, the corresponding two discrete equilibrium equations in (50) are

$$\begin{aligned} &X_k = 0, \\ &Z_k = 0. \end{aligned} \tag{51}$$

For a given $\bar{\mathbf{X}}$ and $\bar{P}$ — initially guessed or updated — the system equations (50) are naturally usually not satisfied. Let the corresponding values of the left-hand sides in (50) $\bar{Q}_i$ and $\bar{A}$. The movements q_j and the pressure change ΔP needed towards a hopefully better solution are determined from the system

$$\begin{aligned} &\bar{Q}_i + \sum_{j=1}^{N_{\text{dof}}} \frac{\partial Q_i}{\partial q_j} q_j + \frac{\partial Q_i}{\partial P} \Delta P = 0, \quad i = 1,2,\cdots N_{\text{dof}}, \\ &\bar{A} + \sum_{j=1}^{N_{\text{dof}}} \frac{\partial A}{\partial q_j} q_j = A_0. \end{aligned} \tag{52}$$

The derivatives $\partial Q_i / \partial q_j$, $\partial Q_i / \partial P$, $\partial A / \partial q_j$ — often called sensitivities — are evaluated at the current configuration, that is, at all q zero and $P = \bar{P}$. The left-hand sides in (52) are first order Taylor expansion approximation for the generalized forces and the area in a new configuration with finite movements and a finite pressure change. After the solution of the unknowns from (52), new updated values $\bar{Q}_i$ and $\bar{A}$ are obtained. The iteration process consisting of solving (56) repeatedly is continued until the values of $\bar{Q}_i$ and the changes in $\bar{P}$ have hopefully become small enough.

The sensitivities are obtained here similarly as in [1] in an approximative way numerically by applying small given changes $\bar{q}_j$ and $\Delta\bar{P}$.

Quantities $\bar{Q}_i$ and $\bar{A}$ and the sensitivities are assembled from the element contributions in the standard way described in the finite element literature.

To start the calculations, an initial interface geometry must be more or less "guessed". This gives the first $\bar{\mathbf{X}}$ and $\bar{A}$. The first $\bar{P}$ used in evaluating $\bar{\mathbf{X}}$ is estimated using equation (28) in a simplified form as

$$\bar{p}_{\text{l}} - \bar{p}_{\text{v}} = \frac{\bar{\sigma}}{\bar{R}}, \tag{53}$$

where the overbars refer to certain mean values. The radius $\bar{R}$ is taken just as the radius of a circle having area $\bar{A}$. It is to be noted that $\bar{p}_{\text{l}}$ depends on $\bar{P}$ and if gravity is not included, $\bar{p}_{\text{l}} = \bar{P}$.

6. APPLICATIONS

Three applications with given analytical solutions have been considered to get an idea about the accuracy achievable with the discrete method. The solid surface is taken simply as the plane $z = 0$. The effect of gravity is neglected in the vapor ($\rho_v = 0$) so that p_v is a given constant. The surface tensions σ_{sv} and σ_{sl} of the solid-vapor and the solid-liquid interfaces are taken in each application according to two cases: a) $\sigma_{sv} - \sigma_{sl} = 1/\sqrt{2} \cdot \sigma_0$ and b) $\sigma_{sv} - \sigma_{sl} = -1/\sqrt{2} \cdot \sigma_0$. Here, $\sigma_0 = \sigma(0)$, that is, the given value of the surface tension at the "top" of the drop. In the two first applications the surface tension is assumed to be constant ($\sigma = \sigma_0$). Then Young's formula (1) gives the contact angles $\theta = 45°$ and $\theta = 135°$ in cases a) and b), respectively. Also ρ_l and g are given constants. The given volume (cross-sectional area A_0) has been set to two units in each application. The number of line segments for the discrete solution has been just 10.

In the first application the surface tension is assumed to be constant ($\sigma = \sigma_0$ and thus no torque is produced) and the effect of gravity is neglected also in the liquid ($\rho_l = 0$). The analytical solutions for the interface are simply segments of circles. The discrete solutions were very accurate and took well into account the given cross-sectional constraint.

In the second application the surface tension is still assumed to be constant ($\sigma = \sigma_0$ and thus no torque is produced). However, the effect of gravity is included in the liquid phase ($\rho_l \neq 0$). "Semianalytical" solutions for the interface were achieved making use of the Mathematica program. The accuracy of the discrete solutions were rather similar to those shown graphically in Figure 4 for the third application to be described below.

For lack of space we describe just our third application here in more detail. An analytical solution is "manufactured" by assuming that the radius of curvature of interface is of the form

$$R = a + b|\psi|, \tag{54}$$

where a and b are constants. The effect of gravity is neglected also in the liquid ($\rho_l = 0$). The corresponding surface tension is found to be

$$\sigma = (\sigma_0 - a\Delta p)\cos\psi - b\Delta p\,|\sin\psi| + a\Delta p + b\Delta p\,|\psi| \tag{55}$$

and the torque

$$m = (\sigma_0 - a\Delta p)\sin\psi + b\Delta p\cos\psi \cdot \operatorname{sgn}\psi - b\Delta p \operatorname{sgn}\psi\,. \tag{56}$$

The resulting shapes of the interface were obtained again by semianalytical means using the Mathematica program.

The analytical and discrete interface shape solutions are shown in Figure 4.

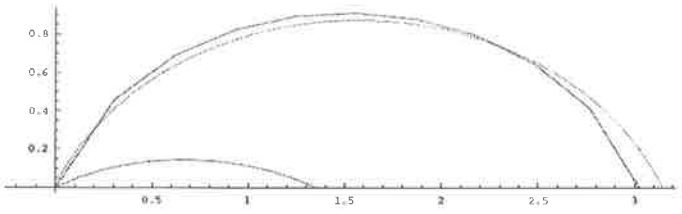

(a)

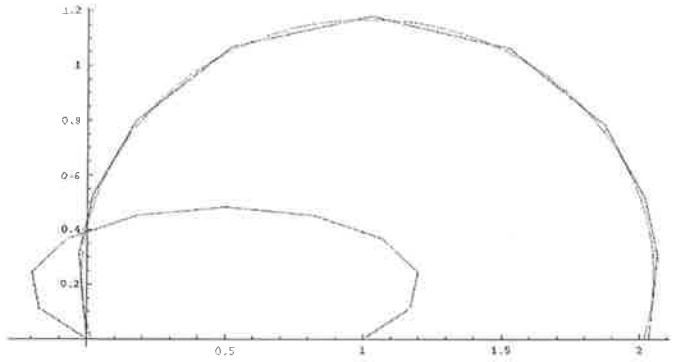

(b)

Figure 4 (a) Analytical, discrete and initial (guessed) interface geometry; case a). **(b)** Analytical, discrete and initial (guessed) interface geometry; case b).

The initial geometries to start the calculations were rather arbitrary and as seen from the figures, very far from the final ones. About 20 iterations were needed to achieve satisfactory convergence. The data used was such that the analytical values for the contact angles were in case a) 64.2° and in case b) 107.8°. It is thus seen that the Young's formula (1) is no more valid and the torque at the contact points changes the contact angles according to equation (25).

7. CONCLUDING REMARKS

The results obtained in this study seem to show that the presented formulation taking into account distributed torque and based on virtual work is correct. Possible future extensions of the formulation are e.g.: proper form of the virtual work principle in three dimensions with distributed torque, a discrete formulation using facet elements.

REFERENCES

1 M. Reivinen E.-M. Salonen. Surface tension problems, virtual work and free boundary. *Proceedings of the IX Finnish Mechanics Days*, Lappeenrannan teknillinen yliopisto, 13.-14. kesäkuuta 2006.

2 P. Nozieres. Shape and growth of crystals, in *Solids far from equilibrium*, Cambridge University Press, edited by C. Godrèche, 1989.

KORVIKELEIKKAUSVOIMASTA

J. PAAVOLA ja E.-M. SALONEN
Teknillinen korkeakoulu,
Rakenne- ja rakennustuotantotekniikan laitos
Rakentajanaukio A, 02150 Espoo

TIIVISTELMÄ

Kirchhoffin laattateoriassa tulee reunaehtojen tarkastelussa tunnetusti esille ns. korvikeleikkausvoiman käsite. Tälle suureelle esitetään kirjallisuudessa usein havainnollistamiseen pyrkivä, fysikaalisluonteinen tulkinta korvaamalla laatan reunalla vaikuttava vääntömomenttijakauma perättäisillä voimapareilla. Aihetta voidaan lähestyä rakenteiden mekaniikan opetuksessa analogisesti yksinkertaisemmassa yhteydessä jo palkkiteoriassa ottamalla ulkoiseen kuormitukseen mukaan jakaantunut momenttikuormitus. Korvikeleikkausvoimalle saadaan virtuaalisen työn periaatetta soveltamalla vaihtoehtoinen, matemaattisluonteinen selitys. Vapaakappalekuvioiden ja virtuaalisen työn periaatteen avulla saatuja tasapainoyhtälöitä vertaillaan. Juuri palkkiteoria onkin opetuksessa ehkä sopivin ensimmäinen aihepiiri, jossa virtuaalisen työn periaatteen käyttöä vaihtoehtona vapaakappalekuvioille on syytä esitellä. Timoshenkon palkkiteorian asemaa korostetaan sopivana peruslähtökohtana eikä vain Euler-Bernoullin teorian tarkennuksena.. Lopuksi osoitetaan tavanomaisen fysikaalisen voimapariajattelun tietty epäjohdonmukaisuus, joka voi osiltaan jopa vaikeuttaa aiheen omaksumista.

JOHDANTO

Lähteessä [1] todetaan laattateorian opetukseen liittyen mm. seuraavaa:

> "The boundary conditions of a free edge in the theory of thin elastic plates are often found by the beginning student to be perplexing and in part artificial. This is not at all surprising. When looking over the nineteenth century literature on the subject, one cannot escape the impression that many of the heroes of elasticity have at times been equally perplexed."

Lähteessä [3] on esitetty s. 170 - 172 samoin klassilliseen laattateoriaan liittyviä melko hämmentäviä huomioita kuten:

> "Nevertheless, puzzling inconsistencies arise from this procedure, as shown in Sec. 5-4."

Jo näiden lainausten perusteella on siis ilmeistä, että laattateorian reunaehtojen ymmärrettävä käsittely opetuksessa vaatii huolellisuutta. Tämän artikkelin tarkoituksena on tarkastella laatan korvikeleikkausvoiman käsitettä osittain samaan tapaan kuin lähteessä [1] ottamalla avuksi palkkiteoria ja siinä jakaantuneen momenttikuormituksen vaikutus.

Kirchhoff-laatan reunalla vaikuttava vääntömomentti käsitellään reunaehtojen yhteydessä tunnetusti siten, että se derivoituna laatan reunaviivakoordinaatin suhteen esiintyy osana leikkausvoimaa. Syntyy ns. korvikeleikkausvoiman käsite; [7, s. 827]. Tämän fysikaalinen selitys

tapahtuu samoin tunnetusti tavallisimmin korvaamalla vääntömomentti paloittain perättäisillä laatan tasoa vastaan kohtisuorassa olevilla vastakkaissuuntaisilla voimilla eli toisin sanoen perättäisillä voimapareilla. Jos näiden voimaparien momentti riippuu paikasta, syntyy efektiivinen lisäleikkausvoima. Edelleen laatan mahdollisiin kulmiin syntyy pistemäisiä pystyvoimia.

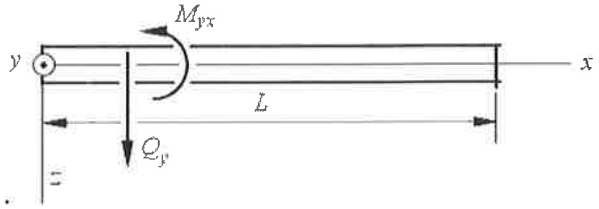

Kuva 1 Laatan reuna.

Kuva 1 esittää y-akselia vastaan kohtisuorassa olevaa x-akselin suuntaista laatan reunapintaa ja siihen vaikuttavaa leikkausvoimaa $Q_y(x)$ ja vääntömomenttia $M_{yx}(x)$. Ne on esitetty kuvassa positiivisina. Korvikeleikkausvoiman lauseke on

$$V_y = Q_y + \frac{\partial M_{yx}}{\partial x} . \tag{1}$$

Palautetaan ensin mieleen lähes kaikissa laattateorian oppikirjoissa esitetty korvike-leikkausvoiman käsitteen tavanomainen fysikaalisluonteinen voimaparien käyttöön perustuva selitys. Alan kirjallisuudessa, esimerkiksi lähteessä [6], tämän voimaparitulkinnan alkuperäisiksi esittäjiksi mainitaan mm. Kelvin ja Tait, v. 1883 [5].

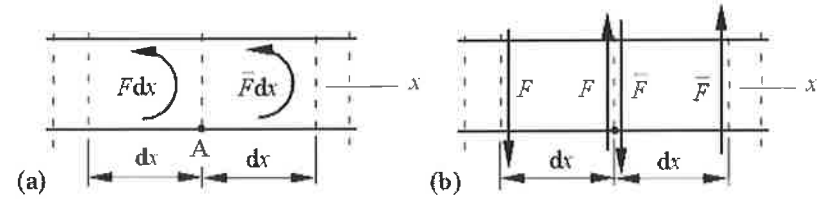

Kuva 2 Laatan reunan kaksi vierekkäistä reuna-alkiota.

Kuvassa 2 (a) on esitetty kaksi vierekkäistä $\mathrm{d}x$–pituista laatan reuna-alkiota, joihin on liitetty vääntömomenttien resultoivat arvot

$$M_{yx}\mathrm{d}x \equiv F\mathrm{d}x \tag{2}$$

ja

$$\left(M_{yx} + \frac{\partial M_{yx}}{\partial x}\mathrm{d}x \right)\mathrm{d}x \equiv \bar{F}\mathrm{d}x . \tag{3}$$

Näiden vaikutus kuvataan nyt voimapareilla, joissa kyseiset voimat F ja $\bar{F}$ vaikuttavat pystysuuntaisina alkioiden reunoilla (kuva 2 (b)). Nähdään, että voimaparien momentit ovat kaavojen (2) ja (3) mukaiset. Resultoiva pystysuuntainen voima pisteessä A on siis

$$\bar{F} - F = M_{yx} + \frac{\partial M_{yx}}{\partial x}\mathrm{d}x - M_{yx} = \frac{\partial M_{yx}}{\partial x}\mathrm{d}x. \tag{4}$$

Kun tämä jaetaan siihen liitetyllä vaikutuspituudella $\mathrm{d}x$, saadaan jakaantunut lisäleikkausvoiman arvo

$$\frac{\partial M_{yx}}{\partial x}. \tag{5}$$

Tämä on juuri vääntömomentista lausekkeen (1) oikealle puolelle tuleva lisätermi.

Vastaavalla voimaparien tarkastelulla havaitaan edelleen, että laatan reunan päissä naapurialkiot puuttuvat ja käsittely johtaa pystysuuntaisiin pistevoimiin $M_{yx}(0)$ ja $-M_{yx}(L)$. Samoin todetaan, että jos vääntömomentin arvossa on jostain syystä hyppäys, hyppäyskohtaan syntyy hyppäyksen suuruinen pystyvoima.

EULER-BERNOULLI-PALKKI

Euler-Bernoulli-palkki on Kirchhoff-laatan yksidimensioinen vastine. Palkkiteoria käsitellään rakenteiden mekaniikan opetuksessa normaalisti ennen laattateoriaa. Korvikeleikkausvoiman käsitteen oleellinen sisältö voidaan tuoda kuitenkin esille jo palkkien yhteydessä sisällyttämällä palkin ulkoiseen kuormitukseen mukaan jakaantuneen momenttikuormituksen osuus. Täten artikkelin jatkossa käsittely koskee pitkälti palkkeja. Saadut tulokset voidaan siirtää analogioiden perusteella lopuksi helposti koskemaan laatan reunaa.

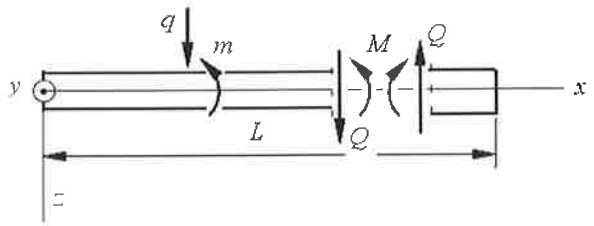

Kuva 3 Suora tasopalkki.

Tarkastellaan kuvan 3 esittämää suoraa tasopalkkia. Palkin ulkoinen kuormitus koostuu jakaantuneesta pystysuuntaisesta kuormituksesta $q(x)$ [N/m] ja momenttikuormituksesta $m(x)$ [Nm/m]. Nämä suureet samoin kuin leikkausvoima $Q(x)$ ja taivutusmomentti $M(x)$ ovat esitetty kuvassa positiivisina. Kuvia 1 ja 3 vertaamalla havaitaan, että laatan suureita Q_y ja M_{yx} vastaavat analogisina (myös fysikaalisten dimensioidensa suhteen) palkin suureet q ja m. Täten laatan tilanne voidaan käsitellä ainakin alustavasti yksinkertaisemmassa yhteydessä palkin avulla.

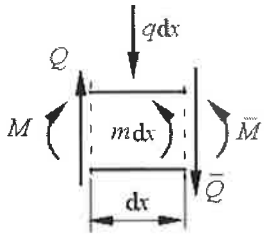

Kuva 4 Palkin pituusalkion vapaakappalekuvio.

Käsittely rajoitetaan pienten siirtymien teoriaan. Tasapainoyhtälöt voidaan siis muodostaa palkin deformoitumattoman alkuaseman suhteen. Palkin pituusalkion vapaakappalekuvion (kuva 4) avulla saadaan pystysuuntainen tasapainoyhtälö (suureiden $\bar{Q}$ ja $\bar{M}$ lausekkeet ovat ilmeiset)

$$\frac{\mathrm{d}Q}{\mathrm{d}x}+q=0\,, \tag{6}$$

ja momenttitasapainoyhtälö

$$\frac{\mathrm{d}M}{\mathrm{d}x}-Q+m=0\,. \tag{7}$$

Eliminoimalla näistä leikkausvoima päädytään edelleen yhtälöön

$$\frac{\mathrm{d}^2M}{\mathrm{d}x^2}+q+\frac{\mathrm{d}m}{\mathrm{d}x}=0\,. \tag{8}$$

Saatu yhtälö osoittaa itse asiassa välittömästi, että momenttikuormituksen derivaatalla $\mathrm{d}m/\mathrm{d}x$ on tässä fysikaalisesti vastaava rooli kuin pystykuormituksella q. Tämä tulos antaa jo erään tulkinnan momenttikuormituksen vaikutustavasta.

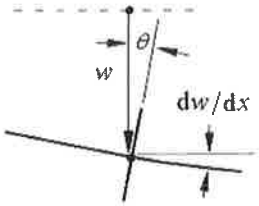

Kuva 5 Euler-Bernoulli palkin akselin taipuma ja poikkileikkauksen kiertymä.

Tarkastellaan aihetta seuraavaksi perusteellisemmin virtuaalisen työn periaatteen kannalta. Euler-Bernoullin palkkiteorian kinematiikan mukaan (kuva 5) palkin pienten siirtymien teorian perusteella poikkileikkauksen kiertymä

$$\theta=\frac{\mathrm{d}w}{\mathrm{d}x}\,, \tag{9}$$

jossa $w(x)$ on palkin akselin taipuma. Toisin sanoen palkin poikkileikkauksen ja akselin kiertymät ovat yhtä suuret. Palkin käyristymä on vastaavasti

$$\kappa=-\frac{\mathrm{d}^2w}{\mathrm{d}x^2}\,. \tag{10}$$

Virtuaalisen työn periaatteen mukainen virtuaalinen työyhtälö on staattisessa tapauksessa yleisesti

$$\delta W^{s}+\delta W^{\mathrm{u}}=0 \tag{11}$$

eli kappaleeseen vaikuttavien sisäisten ja ulkoisten voimien yhteensä tekemä virtuaalinen työ on mielivaltaisessa virtuaalisessa siirtymässä nolla.

Euler-Bernoulli-palkilla sisäisten voimien tekemä virtuaalinen työ on (kinemaattisesti luvallinen virtuaalinen siirtymätila)

$$\delta W^s = -\int_0^L M\delta\kappa \mathrm{d}x = \int_0^L M\frac{\mathrm{d}^2\delta w}{\mathrm{d}x^2}\mathrm{d}x \tag{12}$$

ja vastaavasti ulkoisten voimien tekemä virtuaalinen työ on

$$\delta W^{\mathrm{u}} = \int_0^L (q\delta w - m\delta\theta)\mathrm{d}x + rt = \int_0^L \left(q\delta w - m\frac{\mathrm{d}\delta w}{\mathrm{d}x}\right)\mathrm{d}x + rt\,. \tag{13}$$

Merkintä rt (reunatermit) viittaa palkin päissä $x=0$ ja $x=L$ mahdollisesti vaikuttavien annettujen voimasuureiden tekemään virtuaaliseen työhön. Sen yksityiskohtainen muoto ei ole tässä jatkon kannalta oleellinen.

Kuten lähes aina virtuaalisen työn periaatteen yhteydessä johtopäätösten teossa tarvitaan osittaisintegrointeja. Osittaisintegrointi sovellettuna lausekkeen (13) momenttitermiin antaa

$$-\int_0^L m\frac{\mathrm{d}\delta w}{\mathrm{d}x}\mathrm{d}x = \int_0^L \frac{\mathrm{d}m}{\mathrm{d}x}\delta w\,\mathrm{d}x - m\delta w\big|_{x=L} + m\delta w\big|_{x=0}\,. \tag{14}$$

Tämän yhtälön oikean puolen ilmeinen tulkinta on seuraava: Virtuaalisen työn periaate "näkee" momenttikuormituksen vaikutuksen jakaantuneena pystykuormituksena $\mathrm{d}m/\mathrm{d}x$ ja pystysuuntaisina pistekuormina $m(0)$ ja $-m(L)$ vastaavasti pisteissä $x=0$ ja $x=L$. Tämä tulos selittää siis vaihtoehtoisella tavalla puhtaasti matemaattisesti korvikeleikkausvoiman käsitteen (vastaava manipulaatio voidaan tietenkin tehdä myös laatan reunan yhteydessä). Alan kirjallisuudessa todetaan tähän liittyen Kirchhoffin johtaneen ensimmäisenä nimenomaan variaatiolaskentaa käyttäen laatan oikeat kaksi reunaehtoa [2].

Jos suureen m jakaumassa on epäjatkuvuuksia, täytyy osittaisintegrointi suorittaa paloittain. Olkoon esimerkiksi piste $x=a$ epäjatkuvuuskohta ja olkoon suureen m vasemmanpuoleinen rajaarvo $m^-(a)$ ja oikeanpuoleinen $m^+(a)$. Tällöin

$$\begin{aligned}
&-\int_0^L m\frac{\mathrm{d}\delta w}{\mathrm{d}x}\mathrm{d}x = -\int_0^a m\frac{\mathrm{d}\delta w}{\mathrm{d}x}\mathrm{d}x - \int_a^L m\frac{\mathrm{d}\delta w}{\mathrm{d}x}\mathrm{d}x \\
&= \int_0^a \frac{\mathrm{d}m}{\mathrm{d}x}\delta w\,\mathrm{d}x - m^-(a)\delta w(a) + m\delta w\big|_{x=0} \\
&+ \int_a^L \frac{\mathrm{d}m}{\mathrm{d}x}\delta w\,\mathrm{d}x - m\delta w\big|_{x=L} + m^+(a)\delta w(a) \\
&= \int_0^a \frac{\mathrm{d}m}{\mathrm{d}x}\delta w\,\mathrm{d}x + \int_a^L \frac{\mathrm{d}m}{\mathrm{d}x}\delta w\,\mathrm{d}x + \left(m^+ - m^-\right)\delta w\big|_{x=a} - m\delta w\big|_{x=L} + m\delta w\big|_{x=0}\,.
\end{aligned} \tag{15}$$

Kaavaan (14) verrattuna tulos muuttuu siis pisteessä $x=a$ vaikuttavan pystysuuntaisen voiman $m^+ - m^-$ mukaantulolla. Jälleen saadaan matemaattisesti vastaava tulos kuin fysikaalisella voimapariajattelulla.

Jos vielä lausekkeessa (12) suoritetaan kaksi kertaa osittaisintegrointi ja otetaan huomioon, että δw on mielivaltainen, virtuaalisesta työyhtälöstä (11) voidaan päätellä tasapainoyhtälö (8). Todettakoon, että yhtälöitä (6) ja (7) ei sen sijaan saada tässä virtuaalisen työn periaatteen avulla, jos rajoitutaan kinemaattisesti luvallisiin virtuaalisiin siirtymiin, koska Euler-Bernoulli-palkilla leikkausvoima on rajoitevoimatyyppinen suure eikä se siten esiinny lainkaan lausekkeessa (12).

Vanhemmissa laattateorian oppikirjoissa ei yleensä oteta itse laatan alueella mukaan ulkoisen jakaantuneen momenttikuormituksen osuutta. Kuitenkin tämän osuuden sisällyttäminen tekee teoriasta yhtenäisemmän ja osiltaan vähentää vain reunan yhteydessä esiintyvän korvikeleikkausvoiman "mystiikkaa" (ks. esimerkiksi lähde[4]).

TIMOSHENKO-PALKKI

Timoshenko-palkki on Reissner-Mindlin-laatan yksidimensioinen vastine. Mindlin-laatoilla ei esiinny korvikeleikkausvoimakäsitteen tarvetta. Timoshenko-palkin tarkastelu antaa kuitenkin tässä lisävalaistusta voimapariajattelun sisältöön.

Timoshenko-palkin kinematiikassa palkin akselin taipuma $w(x)$ ja poikkileikkauksen kiertymä $\theta(x)$ ovat toisistaan riippumattomia suureita. Kuvan 5 vastineeksi saadaan kuva 6:

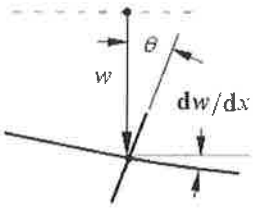

Kuva 6 Timoshenko-palkin akselin taipuma ja poikkileikkauksen kiertymä.

Palkin deformaatioon tulee mukaan liukuma

$$\gamma = \frac{\mathrm{d}w}{\mathrm{d}x} - \theta\,, \tag{16}$$

eikä leikkausvoima Q ole enää rajoitevoimatyyppinen suure. Lisäksi käyristymä (oikeammin tässä kiertymän derivaatta)

$$\kappa = -\frac{\mathrm{d}\theta}{\mathrm{d}x}\,. \tag{17}$$

Timoshenko- palkilla sisäisten voimien tekemä virtuaalinen työ

$$\delta W^{s} = -\int_0^L \left(M\delta\kappa + Q\delta\gamma\right)\mathrm{d}x = \int_0^L \left[M\frac{\mathrm{d}\delta\theta}{\mathrm{d}x} - Q\left(\frac{\mathrm{d}\delta w}{\mathrm{d}x} - \delta\theta\right)\right]\mathrm{d}x \tag{18}$$

ja ulkoisten voimien tekemä virtuaalinen työ

$$\delta W^{\mathrm{u}} = \int_0^L \left(q\delta w - m\delta\theta\right)\mathrm{d}x + rt\,. \tag{19}$$

On jälleen sovellettu kinemaattisesti luvallisia virtuaalisia siirtymiä. Suorittamalla tarvittavat osittaisintegroinnit ja ottamalla huomioon, että δw ja $\delta\theta$ ovat mielivaltaisia virtuaalisesta työyhtälöstä (11) saadaan nyt sekä tasapainoyhtälö (6) että (7).

Tutkitaan seuraavaksi hieman yksityiskohtaisemmin momenttikuormituksen m tekemää virtuaalista työtä. Muodon $m\delta\theta$ käyttö lausekkeessa (19) merkitsee selvästi, että kyseistä voimasuuretta vastaava yleistetty siirtymäsuure on nimenomaan palkin *poikkileikkauksen* kiertymä θ. Mutta miksi juuri näin? Tarkastellaan hetkeksi uudestaan kuvaa 2 (b). Sen voimaparien voimat vaikuttavat laatan pystysuunnassa ja sovellettuina palkkiin siis palkin poikkileikkausten suunnissa. Tämä antaa tulkinnan, että voimasuuretta m vastaava yleistetty siirtymäsuure onkin palkin *akselin* kiertymä $\mathrm{d}w/\mathrm{d}x$. Tämä johtaa esityksen (19) sijasta lausekkeeseen

$$\delta W^{\mathrm{u}} = \int_0^L \left(q\delta w - m\frac{\mathrm{d}\delta w}{\mathrm{d}x}\right)\mathrm{d}x + rt \tag{20}$$

eli uudestaan lausekkeeseen (13). Virtuaalisesta työyhtälöstä saadaan nyt tasapainoyhtälöt

$$\frac{\mathrm{d}Q}{\mathrm{d}x}+q+\frac{\mathrm{d}m}{\mathrm{d}x}=0 \tag{21}$$

ja

$$\frac{\mathrm{d}M}{\mathrm{d}x}-Q=0\,. \tag{22}$$

Nämä poikkeavat kuvan 4 vapaakappalekuvion avulla synnytetyistä tasapainoyhtälöistä (6) ja (7). Voidaan kuitenkin todeta välittömästi, että yhtälöt (21) ja (22) saadaan myös vapaakappalekuvion avulla ottamalla vain käyttöön muoto, jossa momenttina annettu kuormitus m esitetään heti pystykuormituksena $\mathrm{d}m/\mathrm{d}x$. Tällöin täytyy myös ottaa huomioon mahdolliset pistekuormitukset. Siten, jos esimerkiksi arvo $m(L)$ on nollasta eroava, on palkkia analysoitaessa palkin päähän pisteeseen $x=L$ asetettava vaikuttamaan poikittaisvoima $-m(L)$.

On mielenkiintoista todeta ajatuksellinen ero vapaakappalekuvioiden ja virtuaalisen työn periaatteen avulla johdettujen tasapainoyhtälöiden välillä. Kun rajoitutaan pienten siirtymien teorian käyttöön, tasapainoyhtälöt voidaan tunnetusti muodostaa rakenteen deformoitumattomassa asemassa. Täten vapaakappalekuvioihin ei tarvitse liittää mitään kinematiikkaa. Toisaalta Euler-Bernoulli- tai Timoshenko-palkki vaatii käsittelyssä tiettyä kinematiikkaa, jos rajoitutaan kinemaattisesti luvallisiin virtuaalisiin siirtymiin.

Mainittakoon sivuhuomautuksena, että tasapainoyhtälöt (6) ja (7) voidaan tietenkin johtaa myös virtuaalisen työn periaatteen avulla soveltamalla kinemaattisesti luvattomia virtuaalisia siirtymiä. Tällöin tarkasteltava kappale on kuvan 4 palkkialkio ja sille annetaan jäykän kappaleen liikkeen mukainen virtuaalinen siirtymä: pystysuora translaatio ja rotaatio y-akselin suuntaisen akselin ympäri. Sisäisten voimien tekemä virtuaalinen työ häviää tässä sovelluksessa.

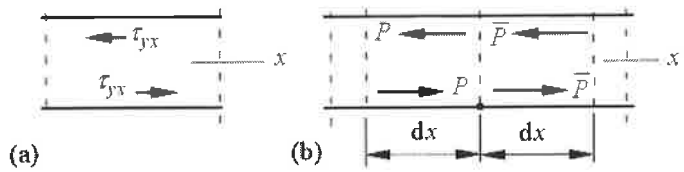

Kuva 7 (a) Leikkausjännitykset . **(b)** Parittaiset voimat.

Palataan vielä laatan reunan tarkasteluun. Kuvaan 2 liittyvä tavanomainen fysikaalinen voimapariajattelu on itse asiassa melko "epäfysikaalinen" ja voi siten olla opetuksellisesti jopa haitallinen. Laatan vääntömomentti M_{yx} kertyy leikkausjännityksistä τ_{yx} (Kuva 7 (a)). Ne vaikuttavat x-akselin suunnassa. Täten niiden vaikutuksen korvaaminen voimapareilla olisi kuvan 2 (b) csityksen sijasta luontevampaa tehdä kuvan 7 (b) tapaan. Tässä siis mm.

$$M_{yx}\mathrm{d}x \equiv Pa\,, \tag{23}$$

jossa a on voimien P vaikutussuorien välinen etäisyys. Nyt on ilmeistä, että kyseiset voimat tekevät virtuaalista työtä nimenomaan laatan normaalin (palkin poikkileikkauksen) virtuaalisen kiertymän suhteen ja siten muoto (19) on tässä myös luontevin. Kuvan 7 (b) avulla ei kuitenkaan enää voida synnyttää korvikeleikkausvoiman käsitettä.

LOPPUHUOMAUTUKSIA

Artikkelissa on ehdotettu, että korvikeleikkausvoiman käsitettä voitaisiin lähestyä opetuksessa jo palkkiteorioiden yhteydessä ja samalla antaa voimapariajattelulle vaihtoehtoinen tulkinta virtuaalisen työn periaatteen avulla.

Lähteessä [1] on esitetty eräs opetuksellinen lähestymistapa selittää korvikeleikkausvoiman käsite käyttäen apuna nimenomaan palkkiteoriaa. Käsittely perustuu kimmoisen palkin siirtymien tarkasteluun Greenin funktion avulla. Artikkelissamme esitetty tapa poikkeaa lähteen [1] sisällöstä ja sitä voidaan pitää yleisempänä, koska otaksumaa kimmoisesta materiaalista ei edes tarvita.

Soveltamalla virtuaalisen työn periaatetta Euler-Bernoulli-palkin kinematiikan mukaisesti momenttikuormitukselle saadaan osittaisintegroinnin jälkeen välittömästi haluttu vaihtoehtoinen tulkinta pystykuormituksena ja mahdollisina pistekuormina. Sen sijaan palkin kahta tavanomaista tasapainoyhtälöä ei vielä saavuteta Euler-Bernoulli-palkin kinematiikan avulla. Siihen tarvitaan Timoshenko-palkin kinematiikkaa. On lisäksi mielenkiintoista, että riippuen momenttikuormituksen valitusta vaikutustavasta päädytään eri tasapainoyhtälöihin, jotka ovat kaikki kuitenkin oikeellisia.

Vapaakappalekuvioiden käyttö tasapainoyhtälöiden johtamisessa on rakenteiden mekaniikan opetuksessa tunnustetusti aivan oleellinen aihepiiri. Pitemmälle menevässä opetuksessa virtuaalisen työn periaatteen sovellukset tulevat taas yhä voimakkaammin esille. Eräänä tärkeänä sovelluksena saadaan mahdollisuus johtaa vaihtoehtoisella tavalla tasapainoyhtälöitä. Palkkiteoria on ehkä juuri oikea aihepiiri esittää rinnakkain vapaakappalekuvioiden ja virtuaalisen työn periaatteen käyttöä.

Palkkiteorian klassilliset oppikirjaesitykset lähtevät usein liikkeelle Euler-Bernoullin palkkiteoriasta ja Timoshenko-palkki käsitellään sitten myöhemmin jonkinlaisena tarkennettuna mallina. Paljon hedelmällisempi lähtökohta on kääntää tämä järjestys ja pitää oikeutetusti Euler-Bernoulli-palkkia Timoshenko-palkin erikoistapauksena. Tällöin tulee mm. korostettua palkin ja myöhemmin laatan ja kuoren "hiusharjamalli"; palkin malli ei ole niinkään palkin yksidimensioinen akseliviiva vaan tämä viiva varustettuna harjaksilla (poikkileikkauksilla). Palkki mm. tarttuu ympäristöönsä päätypoikkileikkauksillaan ja taivutusmomentit tekevät työtä nimenomaan poikkileikkauksiin. Kun Timoshenko-palkilla poikkileikkauksen ja palkin akselin kiertymät poikkeavat toisistaan, hiusharjamalli tulee korostetusti esille.

VIITTEET

[1] J. Dundurs, A pedagogic analogy between beams and free edges in plate theory, *Bull. Mech. Engng Educ.*, Vol. 5, pp. 51-54, 1966.

[2] G. Kirchhoff, *J. Crelle*, vol. 40, 1850.

[3] H. L. Langhaar, *Energy Methods in Applied Mechanics*, Wiley, 1970.

[4] J. Paavola ja E.-M. Salonen, Yksinkertaisten rakennemallien tasapainoyhtälöt - osa II, levy- ja laattarakenteeet, *Rakenteiden Mekaniikka*, Vol. 29, No.1, 1996.

[5] W.Thomson and P. G. Tait, *Treatise on Natural Philosophy*, Clarendon Press, 1867.

[6] S. Timoshenko, S. Woinowsky-Krieger, *Theory of Plates and Shells*, 2nd ed. 1959.

[7] A. Ylinen, *Kimmo-ja lujuusoppi II*, Werner Söderström, 1970.

A PROCEDURE FOR DAMAGE MODELLING OF SHEAR LOADED STRUCTURAL HYBRID INTERFACES

A. OINONEN & G. MARQUIS
Laboratory of Mechanics of Materials
Helsinki University of Technology
P.O.Box 4300
FIN-02015 HUT, Finland
ahti.oinonen@tkk.fi, gary.marquis@tkk.fi

Keywords: Damage analysis, Decohesion, Frictional contact, Hybrid interface

ABSTRACT

Hybrid joints, which combine both mechanical fasteners and adhesive bonding, have been studied experimentally and using the finite element method. Finite element method based simulation involved contact, decohesion and friction. Progressive damage of the adhesive was modelled in terms of a traction-separation law. Experimental data was exploited to find a matching damage law and the corresponding damage equation was set to govern the critical shear mode fracture energy of the bonded interface. The trapezoidal law was found to be able to predict the failure behaviour of the studied interface with a good adaptability.

NOMENCLATURE

d	Damage variable
i	index defining the loading or failure mode I, II or III
k	Number of slip planes
n	Number of fasteners affected by the applied shear loading
r_a	Outer radius of the annular hybrid interface
t_i	Traction stress
t_i^c	Peak value of the traction stress
σ_{33}	Normal stress at the friction interface
τ_1, τ_2	Shear stresses at the contact surface
τ_{cr}	Critical shear stress
τ_{eq}	Equivalent friction stress
ε_i	Nominal strain
δ_i	Relative displacement at the cohesion interface
δ_i^{c1}, δ_i^{c2}	Relative displacements corresponding to the maximum interface traction stress
δ_i^f	Relative displacement corresponding to full interface damage
δ_{eff}	Effective displacement under combined shear and normal displacements across the interface
μ	Static friction coefficient

Δ	Displacement measured between the point of the applied shear loading and corresponding attachment point of the model or specimen
A_i^G	Area under the traction stress vs. relative displacement curve
G^c	Critical total fracture energy
G^i	Fracture energy for a particular mode
K_{ii}	Penalty stiffness
P	Applied shear load
P_f	Preload of the fastener
P_μ	Maximum slip load of the specimen
$\mathbf{t}$	Traction stress vector
$\boldsymbol{\varepsilon}$	Strain vector
$\boldsymbol{\delta}$	Effective displacement vector
$\mathbf{D}$	Damage matrix
$\mathbf{I}$	Identity matrix
$\mathbf{K}$	Constitutive matrix

1 INTRODUCTION

Hybrid joints, which consist of combinations of mechanically fastened and bonded joints, have previously been studied in the context of the light weight aeronautical [1] and composite structures [2]. Weld bonding, which combines spot or laser welding in conjunction with adhesives, is used, for example, to joint thin automotive body structures [3]. This paper represents a finite element method (FEM) based progressive damage modelling procedure for hybrid interfaces. Damage response of a hybrid-joined structural detail is presented as an application. The specific structural detail is a steel annular interface which is epoxy-bonded and clamped with a bolt.

Dragoni and Mauri [4] have performed static testing of torsion loaded annular type hybrid specimens in steel. Their results show that the friction force is linearly dependent on the fastener's clamping load and adhesive bonding provides constant mean shear strength, which is independent on the pretension. Consequently, the modelling principle of this study was based on uncoupled decohesion and frictional behaviour.

Cohesive zone models (CZM) are commonly exploited in damage simulations including both the damage initiation and propagation criteria of adhesive bonded interfaces. Furthermore, the failure is restricted to propagate along the predefined cohesive interface, where zero thickness decohesion elements [5,6] are placed between solid finite elements. Fracture mechanics concepts, such as the fracture energy, are adapted to govern debonding. Thus, the critical interface stress and fracture energy of the adhesive material govern the strength behaviour of the cohesive interface and therefore comprise the basis for material property definition for the FE model calibration. After a specified damage initiation criterion is reached, a damage evolution law begins to govern the degradation process of the interface material. A damage function derived from its corresponding damage evolution criterion, enables incorporation of different damage laws in FEM. Several mathematical models have been suggested for the both damage initiation and evolution criteria; see, e.g., the ABAQUS User's Manual [7]. Perhaps the most commonly used damage evolution models are of the bi-linear [5-7] or exponential type [7]. A trapezoidal damage evolution law [8] is considered to be more suitable for ductile interfaces in comparison to the bi-linear law.

Debonding simulations, even in three dimensional cases, can straightforwardly be performed by FEM. In FEM, the advantages of explicit solution methods over implicit methods are that each time increment is solved relatively quickly and complex contact problems, i.e. sliding contacts and

debonding can be solved more promptly [7]. For the commercial FE program ABAQUS/Explicit, a central difference method is exploited to integrate the equations of motion [7].

In the present study, the combined displacement response of the double lap hybrid joints due to interface slip and damage was numerically investigated by FEM. The adapted three dimensional CZM was based on the trapezoidal traction-separation damage model. In addition, friction between all contacting surfaces was modelled based on the Coulomb's law. Decohesion elements with zero thickness were placed at the bonded interfaces. The applied shear load vs. displacement curves for the structural hybrid joint detail were produced based on computed numerical results and comparing these to the corresponding experimental data. The load vs. local displacement results computed using FEM correlated well with both the initial sliding behaviour and ultimate failure observed in the experimentally tested joints. Even though the structural joints were relatively simple, the instrumentation used was not sensitive to the highly localized nature of the decohesion process and some scatter in the test data was observed.

2 METHODOLOGY AND MODELLING

The combined slip and damage response of the double lap hybrid joints was numerically simulated using ABAQUS/Explicit. Uncoupled decohesion and friction of the hybrid interface was assumed. For simplicity, the constitutive response of the decohesion elements was modelled in terms of the traction-separation law with an uncoupled state between the normal and shear components of the traction vector and separation vector. This traction-separation law was selected based on the experimental data and several trial simulations with alternate damage evolution laws. The FE modelling was performed using ABAQUS/CAE. The damage function derived from the trapezoidal damage evolution law was implemented into the ABAQUS environment.

2.1 Decohesion Model

The adapted CZM was based on the trapezoidal traction vs. separation response [8] for the each mode of loading (i = 1, 2, 3). This model can be illustrated with the help of Fig. 1, where the critical fracture energy for each mode G_i^c is defined as an area integral. The line between points A and B determine the linear-elastic response of the interface. The penalty stiffness parameter K_{ii} determines the slope of the line A-B for the normal and shear deformation across the interface. Decohesion damage initiates when the maximum interface traction stress t_i^c is reached, i.e., point B. At this point, the relative displacement between interfaces, δ_i, is defined as the first critical displacement δ_i^{c1}. As δ_i further increases the traction stress is the constant, t_i^c, until point C which corresponds to the second critical displacement δ_i^{c2}. As loading continues, t_i linearly decreases until full damage has been accumulated at point D and δ_i^f. Displacement beyond δ_i^f corresponds to a zero residual of t_i.

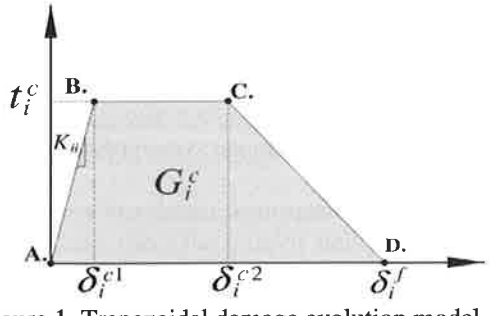

Figure 1. Trapezoidal damage evolution model.

The nominal traction stress vector $\mathbf{t}$ across the surface is related to the nominal strain vector $\boldsymbol{\varepsilon}$ by the elastic constitutive matrix $\mathbf{K}$. Hence, the linear elastic interface behaviour can be written as

$$\begin{Bmatrix} t_1 \\ t_2 \\ t_3 \end{Bmatrix} = \begin{bmatrix} K_{11} & 0 & 0 \\ 0 & K_{22} & 0 \\ 0 & 0 & K_{33} \end{bmatrix} \begin{Bmatrix} \varepsilon_1 \\ \varepsilon_2 \\ \varepsilon_3 \end{Bmatrix}, \tag{1}$$

where the off-diagonal terms of $\mathbf{K}$ are zero due to selected uncoupled behaviour between the normal and shear components of $\mathbf{t}$ and $\boldsymbol{\varepsilon}$. The components of $\mathbf{t}$ are computed by dividing the force components by the initial area at each integration point of the element [7]. The nominal strain components of $\boldsymbol{\varepsilon}$ are equal to the corresponding displacements $\boldsymbol{\delta}$, because the constitutive thickness is appropriately selected equal to one. Therefore, the condition $\boldsymbol{\varepsilon} = \boldsymbol{\delta}$ corresponds to the geometric thickness of zero for the interface layer composed of decohesion finite elements [6]. Damage in the cohesive elements is assumed to initiate based on the quadratic interaction function shown in Eq. (2) [5-7].

$$\left\{\frac{t_1}{t_1^c}\right\}^2 + \left\{\frac{t_2}{t_2^c}\right\}^2 + \left\{\frac{\langle t_3 \rangle}{t_3^c}\right\}^2 = 1 \tag{2}$$

The Macaulay brackets in the third component of Eq. (2) indicate that exclusively compressive normal stressing does contribute to damage initiation. Damage evolution is governed by the damage function $d(\delta_{eff})$ which ranges from zero for the undamaged case to unity for damage corresponding to failure. The effective displacement δ_{eff}, i.e. the highest value of the mixed-mode relative displacement attained by the interface material is obtained from,

$$\delta_{eff} = \|\boldsymbol{\delta}\|, \ \forall \ \delta_3 \in \langle \bullet \rangle . \tag{3}$$

During simulations, the maximum obtained value of δ_{eff} is used to track the accumulation of the damage, i.e. to prevent restoring the interface's condition due to accumulated damage [7].

The degraded stresses are governed by the matrix equation [5,6]

$$\mathbf{t} = (\mathbf{I} - \mathbf{D})\mathbf{K}\boldsymbol{\delta}, \tag{4}$$

where $\mathbf{I}$ is the identity matrix and $\mathbf{D} = d(\delta_{eff})\mathbf{I}$ is the damage matrix. The total critical fracture energy G_i^c for each mode is defined as the work done by the normal or shear tractions corresponding to their relative δ_i. It can be obtained based on the definition of J-integral by Rice [9],

$$G_i^c = \int_{A_i^G} t_i(\delta_i) d\delta_i \,. \tag{5}$$

The trapezoidal damage evolution law is mathematically expressed in Eq. (6).

$$t_i(\delta_i)=\begin{cases}\delta_i K_{ii}, & \delta_i \le \delta_i^{c1}\\ t_i^c, & \delta_i^{c1} < \delta_i \le \delta_i^{c2}\\ t_i^c\left(\dfrac{\delta_i^f-\delta_i}{\delta_i^f-\delta_i^{c2}}\right), & \delta_i^{c2} < \delta_i \le \delta_i^f\\ 0, & \delta_i > \delta_i^f\end{cases} \tag{6}$$

By considering δ_{eff} and substitution Eq. (6) into Eq. (4) and solving for $d(\delta_{eff})$, the corresponding damage function for the trapezoidal damage evolution law can be obtained,

$$d(\delta_{eff})=\begin{cases}0, & \delta_{eff} < \delta_{eff}^{c1}\\ 1-\dfrac{\delta_{eff}^{c1}}{\delta_{eff}}, & \delta_{eff}^{c1} < \delta_{eff} \le \delta_{eff}^{c2}\\ 1-\delta_{eff}^{c1}\left(\dfrac{\delta_{eff}^f-\delta_{eff}}{\delta_{eff}\left(\delta_{eff}^f-\delta_{eff}^{c2}\right)}\right), & \delta_{eff}^{c2} < \delta_{eff} \le \delta_{eff}^f\\ 1, & \delta_{eff} > \delta_{eff}^f\end{cases} \qquad d \in [0,1] \tag{7}$$

Equation (7) reduces to a bi-linear damage evolution law when $\delta_{eff}^{c2} \to \delta_{eff}^{c1}$.

2.2 Material Parameters

Material properties for the cohesive elements assuming a trapezoidal damage evolution model (see Fig. 1) are shown in Table 1. Furthermore, the special condition $K_{33} \to 0$ was set due to hybrid interface involving frictional properties. Based on the selected values in Table 1, the critical fracture energy $G^c \approx 2.25$ N/mm can be computed.

Table 1
Parameters of damage model

δ_{eff}^{c1} [mm]	δ_{eff}^{c2} [mm]	δ_{eff}^{f} [mm]	t_i^c [MPa] $i = 1, 2$	K_{11} [MPa]	K_{22} [MPa]
$1\cdot10^{-5}$	$5\cdot10^{-2}$	$1\cdot10^{-1}$	30	$3\cdot10^{6}$	$3\cdot10^{6}$

The structural joints were fabricated from high strength steel, so typical values for Young's modulus, 210 GPa, Poisson's ratio, 0.3 and density, $7.8\cdot10^3$ kg/m^3 were used.

2.3 FE Model

The three dimensional FE-model involving the plate members, cohesive interface and bolt with the washer is shown in Fig. 2. Symmetry of the structural joint was utilized in the modelling to reduce computational costs. The resulting FE model corresponded to a quarter of a single fastener and the surrounding plate material of the test specimen. The actual specimen is shown in Fig. 3. Eight node linear brick C3D8R solid elements and COH3D8 cohesive elements [7] were used with the ABAQUS/Explicit. The cohesive elements with four integration points had sharing nodes with the neighbouring solid continuum elements.

The specified adhesive application radius r_a (see Fig. 3) was modelled by limiting the cohesive elements to the corresponding annular surface area. Furthermore, a small gap of 0.4 mm between the plates was modelled to exactly correspond to the test specimens. In the test specimens, the gap

was obtained by machining away the surrounding material as a means of precisely controlling the adhesive area. On the symmetry planes, all nodes of the middle plate on the 1-2 plane were fixed in direction 3. For the 1-3 plane, nodes in direction 2 were constrained.

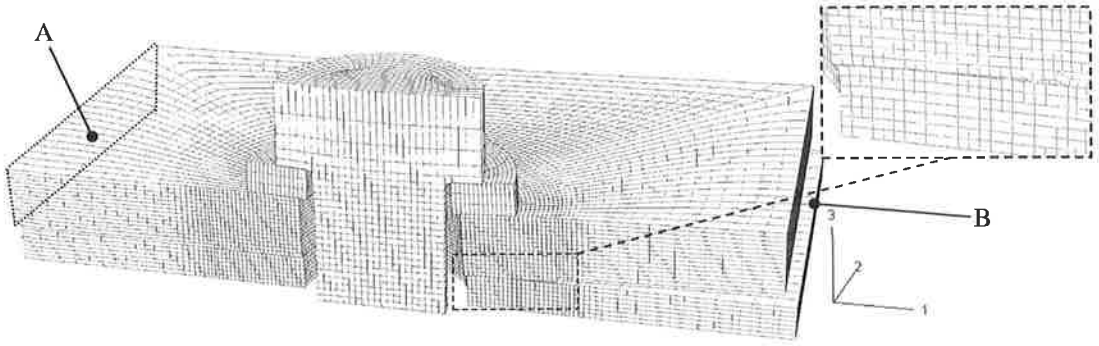

Figure 2. FE model of the structural detail with 0.4 x 0.4 mm mesh, deformation scale factor is 22. In the magnified detail, the annular hybrid interface in the damaged condition is shown. Symmetry was exploited in the modelling; the model shown here corresponds to ⅛ of the respective environment of a real specimen half affected by a shear load.

The failure simulations were performed in two steps. First, the joint was tightened to a specified pretension by constant pressure acting in the negative direction 3 on the fastener's symmetry plane 1-2, see Fig. 2. In the next step, horizontal translational velocity loading condition was applied to generate the desired shear load. This loading was applied along the surface B (see Fig. 2) to the positive direction 1. Surface A was correspondingly constrained in direction 1. The kinematic conditions were applied at a slow rate to minimize oscillatory effects due to inertial forces. A rate of $5 \cdot 10^{-4}$ s was used for clamping and a rate of $5 \cdot 10^{-3}$ s was used to apply the shear load. Additional simulations showed that lower rates did not influence the final results. Two alternate mesh sizes, 0.4 x 0.4 mm and 1.2 x 1.2 mm, were investigated [10].

2.4 Contact Modelling

The contact pairs at the interfaces were modelled by exploiting a kinematic predictor/corrector contact algorithm with the ABAQUS/Explicit. The small sliding tracking approach was chosen, in which a local tangent plane is used for each slave node. The advantage is that it is not necessary to monitor contact along the entire master surface [7]. In the normal direction, the hard contact model [7] was selected. This model assumes that the contacting surfaces can transmit contact pressure only when the nodes of the slave surface are in the contact with the master surface. In the cases involving hybrid interfaces, the material property $K_{33} \rightarrow 0$ does not interfere with this condition.

Isotropic Coulomb friction was modelled along all contacting surfaces. This friction law is based on the assumption that no relative displacements can occur if the equivalent friction stress τ_{eq} computed from

$$\tau_{eq} = \sqrt{\tau_1^2 + \tau_2^2} \tag{8}$$

is less than the corresponding critical shear stress,

$$\tau_{cr} = \mu \sigma_{33}\,, \tag{9}$$

where σ_{33} is the initial normal stress to slip and μ is the static friction coefficient. In Eq. (8) τ_1 and τ_2 are the computed shear stresses at the contact surface.

3 EXPERIMENTAL STUDY

The load vs. displacement response curves were experimentally determined by statically loading the double lap specimens which had eight annular hybrid interfaces. In addition, one corresponding test was performed on a plain specimen without adhesive in order to determine the static friction coefficient μ for FE-modelling. The maximum slip loads P_μ were measured and thus μ can be calculated from

$$\mu = \frac{P_\mu}{knP_f}, \tag{10}$$

where k is the number of slip planes, n is the number of fasteners in the joint affected by the applied shear load P and P_f is the fastener's preload.

Experiments were performed on a 400 kN static capacity servo controlled loading frame. All specimens were loaded incrementally under displacement control. The force and local joint displacements were recorded until the complete failure of the hybrid interface. Tests were stopped after sudden noticeable slip behaviour was observed.

3.1 Specimens

The test specimens shown in Fig. 3a were fabricated from high strength steel with nominal yield strength 960 MPa. Material thickness was 6 mm. Four instrumented M12 bolts were used to control the clamping forces P_f. The testing matrix is presented in Table 2. Contact surfaces with constant values of outer radius r_a for the hybrid interface were manufactured by milling the axisymmetric steps near the fastener positions; see the magnified detail in Fig. 3a. For all specimens, the contacting plate surfaces were treated by a fine shot blasting using aluminium oxide to ensure proper adhesion. Surfaces outside of r_a were protected using thin plastic tape to prevent adhesion outside the contact areas. A two component structural epoxy adhesive DP760 produced by 3M [11] was used for assembling the connections. The standard curing time of the adhesive at room temperature was one week. During the assembly process of the hybrid specimens, adhesive was applied to the contact surfaces of the plate members and the bolts were immediately tightened to the specified P_f. The bolts remained tight during the entire curing process.

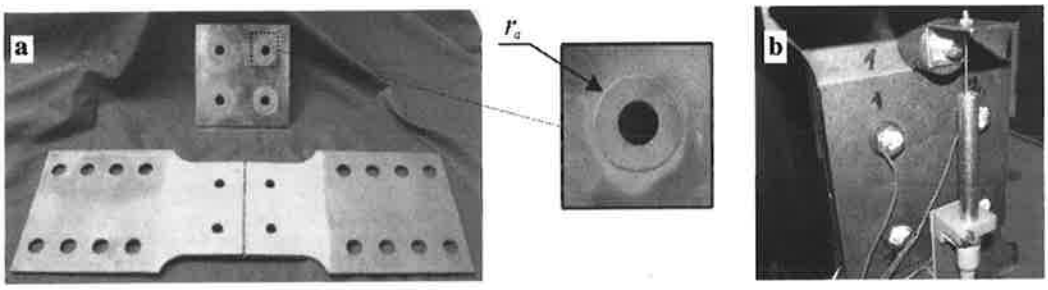

Figure 3. (a) Hybrid specimen before setup with the machining detail and (b) the instrumented specimen attached to a hydraulic testing frame. For bolt through holes, ϕ = 14.5 mm.

Table 2
Matrix for the pilot experiments

Specimen ID	Interface type	P_f [kN]	r_a [mm]
A1	Plain (shot blasted)	50	15.5
B1, B2	Hybrid (shot blasted)	50	15.5

4 RESULTS

4.1 Combined Slip and Damage Response

Based on experimental data from the specimen A1 and the result calculated from Eq. (10), the value 0.41 for the static friction coefficient μ was obtained with $P_\mu \approx 81$ kN.

The computationally obtained applied shear loading P vs. combined slip and damage displacement Δ curves for the studied hybrid connection are shown in Fig. 4 with comparison to the corresponding experimental data. Data for A1 is also shown for reference. During the testing of B1 and B2, sudden slipping occurred at the failure points and it is marked by the arrows pointing downwards.

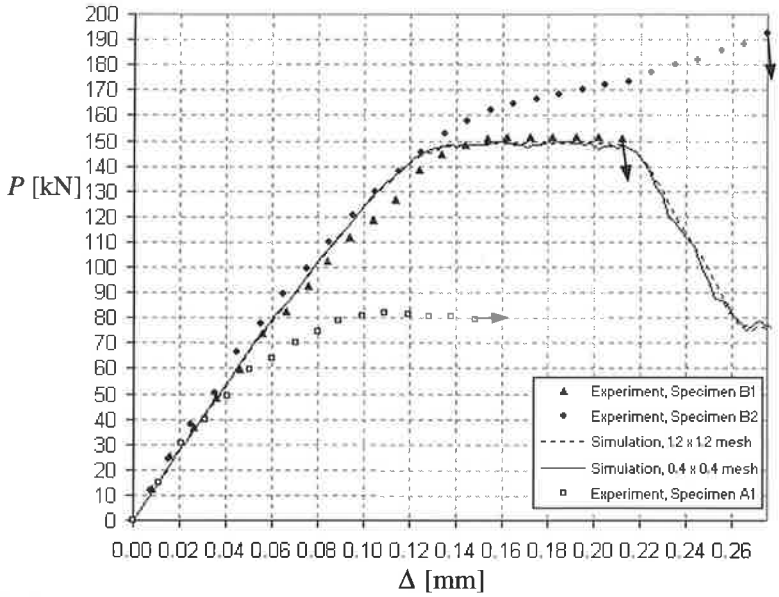

Figure 4. Combined slipping and damage based displacement response of hybrid connections.

From Fig. 4, it can be seen that the displacement response of the hybrid joints is nearly linear with applied load up to $\Delta \approx 0.12$ mm which corresponds to the applied load $P \approx 142$ kN. Ductile behaviour of the hybrid joint is observed for the displacement range of approximately $0.13 < \Delta < 0.21$ mm. This ductile behaviour corresponds to a nearly constant load capacity of about 150 kN for the joint. Final failure occurs at $\Delta \approx 0.26$ mm which indicates the completely damaged state $d(\delta_{eff}) = 1$ for the adhesive bond and the connection is exclusively based on friction when $\Delta > 0.26$ mm. The simulated frictional capacity at $d(\delta_{eff}) = 1$ corresponds to $P \approx 78 \pm 1.5$ kN. This is slightly less than $P_\mu \approx 81$ kN due to Poisson's effect affected P_f in the shear loaded condition. The observable fluctuation is mainly due to induced small vibrations in the simulation runs.

5 DISCUSSION

Computational and experimental methods were exploited to assess the damage behaviour of hybrid interfaces of a structural detail. The selected advanced computational methods and formulations included in ABAQUS 6.8-1 were able to simulate the studied problem with an excellent adaptability. Results were not found to be highly mesh-sensitive for mesh sizes of 0.4 x 0.4 mm and 1.2 x 1.2 mm.

Two experiments were performed for the hybrid specimens. The first specimen did not show hardening behaviour at the ductile area. In contrast, the second experiment did show notable hardening even though both specimens were nominally identical. Hardening may have been due to cohesion of the metal interconnections. Due to the small number of pilot tests, conclusions about structural joint behaviour cannot yet be made. Considerably more experimental data would be needed to implement a fitted damage evolution law, which corresponds to real hybrid interfaces. There is also a need to increase the data collection resolution during testing. With this in mind, a new testing device with a more advanced displacement sensor has been constructed at Helsinki University of Technology. Finally, the more conservative result was adapted as a reference for the numerical assessment. Due to sudden drop in shear load at the final failure points, the possible softening behaviour of the structural adhesive could not be measured. However, as characteristic to the trapezoidal damage evolution law, an assumed softening section was included in the material model.

From the structural applications point of view, the strength effect of the structural adhesive on the service load capacity was investigated. The determined annular interfacial areas can be considered as local attachment points in large scale structures. Thus an advantage of the studied hybrid fastening method is its applicability e.g. for structures, which are subject to optimization [12] and further development in general.

6 CONCLUSIONS

Based on the computed and test results, the following conclusions can be made:

An explicit method can be used to solve multiform contact problems with a very good numerical stability.

Considerably more experimental data would be needed to implement a fitted damage evolution law, which corresponds to real hybrid interfaces.

Notable increase in the static service load capacity can be obtained for hybrid interfaces compared to the same property of corresponding plain connections.

ACKNOWLEDGMENTS

The structural joint tests were partially funded by Ruukki and performed at Lappeenranta University of Technology. The presenting author wishes to thank the Finnish Graduate School in Engineering Mechanics for offering research funding. The authors would also like to thank CSC – IT Center for Science Ltd for providing the ABAQUS 6.8-1 software to be used for the simulations.

REFERENCES

[1] Hart-Smith LJ (1985) Bonded-Bolted Composite Joints. J Aircr 22:993-1000

[2] Kelly G (2005) Load Transfer in Hybrid (Bonded/Bolted) Composite Single-lap Joints. Compos Struct 69:35-43

[3] Fays S (2003) Adhesive Bonding Technology in the Automotive Industry. Adhesion and Interface 4:37-48

[4] Dragoni E, Mauri P (2000) Intrinsic Static Strength of Friction Interfaces Augmented with Anaerobic Adhesives. Int J Adhesion Adhesives 20:315-321

[5] Dávila CG, Camanho PP (2001) Decohesion Elements Using Two and Three-Parameter Mixed-Mode Criteria. Am Helicopter Soc Conf, Williamsburg, VA, Oct 29 - Nov 1

[6] Camanho PP, Dávila CG (2002) Mixed-Mode Decohesion Finite Elements for the Simulation of Delamination in Composite Materials. NASA/TM-2002-211737

[7] ABAQUS Inc. (2008) ABAQUS User's Manual, Version 6.8-1, USA

[8] Tvergaard V, Hutchinson JW (1996) On the Toughness of Ductile Adhesive Joints. J Mech Phys Solids 20:789-800

[9] Rice JR (1968) A Path Independent Integral and the Approximate Analysis of Strain Concentration by Notches and Cracks. J Appl Mech 35:379-386

[10] Turon A, Dávila CG, Camanho, PP, Costa, J (2005) An Engineering Solution for using Coarse Meshes in the Simulation of Delamination with Cohesive Zone Models. NASA/TM-2005-213547

[11] 3M United Kingdom PLC (2001) Scotch-Weld™ EPX™ Epoxy Adhesive DP760 Product Data Sheet

[12] Oinonen A, Tanskanen P, Björk T, Marquis G. (2009) Pattern Optimization of Eccentrically Loaded Multi-fastener Joints. Struct Multidisc Optim (in print, DOI 10.1007/s00158-009-0392-2)

SOME INTERACTIVE MULTIOBJECTIVE OPTIMIZATION METHODS WITH HYBRID IDEAS

KAISA MIETTINEN

Department of Mathematical Information Technology
P.O. Box 35 (Agora)
FI-40014 University of Jyväskylä, FINLAND

E-mail: kaisa.miettinen@jyu.fi

ABSTRACT

Many methods have been developed for multiobjective optimization. Typically, they aim at supporting a decision maker in finding the best compromise solution where several conflicting criteria are optimized at the same time. Because the compromise solutions, so-called Pareto optima, cannot be ordered without additional information, the solution process requires preference information from a decision maker in some for or another, and methods can be classified in four classes based on the role of the decision maker. In this paper, we briefly characterize the different classes and pay most attention to interactive methods. In interactive methods, a solution patterns is formed and repeated several times, and in each iteration further information about the decision maker's preferences is inquired. In this way, the decision maker can learn about the nature of the problem and about the interdependencies among the criteria involved. (S)he can also adjust one's preferences while learning and concentrate on such solutions that seem most promising. We introduce some new interactive hybrid methods for solving nonlinear multiobjective optimization problems. In hybrid methods, ideas of several existing methods and approaches are integrated. The aim is to combine the strengths of the existing methods and, at the same time, avoid their weaknesses. Finally, we consider some computationally demanding real-life problems that have successfully been solved using interactive multiobjective optimization methods.

Keywords: multiple objectives, multiple criteria decision making, interactive methods, applications, hybrid methods

COOPERATION AND COMPETITION IN MULTIDISCIPLINARY SHAPE OPTIMIZATION

JEAN-ANTOINE DÉSIDÉRI

Project-Team Opale
INRIA Sophia Antipolis – Méditerranée
06902 Sophia Antipolis Cedex, FRANCE

E-mail: desideri@sophia.inria.fr

ABSTRACT

The seminar aims at presenting an algorithmic approach to PDE-constrained multidisciplinary shape optimization problems.

In the first part, a number of optimum-shape designs in compressible aerodynamics will be briefly presented. The classical approaches to treat multiobjective optimization problems, their merits and weaknesses will be reviewed. Then, the difficult exercise of an aircraft wing-shape optimization w.r.t. criteria originating from both aerodynamics and structural design will be treated by an approach in which aerodynamics is considered as a preponderant and/or fragile discipline. This prototype problem will serve to support a theoretical construction, valid for disciplines in competition based on a Nash game relying on a split of territory in adequate supplementary subspaces.

In the second part, a result on convex analysis will serve to define a complementary cooperative-optimization phase. As a result, it is proposed to rely on competitive Nash game formulations only at completion of the cooperative phase, when the set of Pareto-stationary points has been reached.

3D DISCRETE NUMERICAL MODELLING OF RIDGE KEEL PUNCH THROUGH TESTS

ARTTU POLOJÄRVI AND JUKKA TUHKURI

Department of Applied Mechanics
Helsinki University of Technology
P. O. Box 4300
02015 TKK, FINLAND
e-mail: arttu.polojarvi@tkk.fi

ABSTRACT

Ridge keel punch through tests were simulated in 3D. In simulations unconsolidated ridge keel was modelled as a rubble pile of loose ice blocks. Combined finite-discrete element method (FEM-DEM) with rigid discrete elements representing ice blocks was used. Simulations were run in full scale. In total 47 simulations were run with various friction coefficients and keel depths. The failure process of simulated rubble piles was analysed and the shear strength of the rubble pile was derived from results. The effect of keel depth and friction on shear strength of the pile was also analysed. The simulation results were compared to laboratory and full-scale punch through tests of unconsolidated ice rubble. Shear strength values achieved from simulations were in range for experimental results. Failure process was observed to be similar to laboratory experiments.

1. INTRODUCTION

Ice ridges are common and important features in Northern seas. Ridge structure can be divided into three main parts. The visible part above the waterline and level ice is called sail. Close to the waterline lies the consolidated layer. Under the consolidated layer lies a rubble pile of ice which can be extensive in size. This part is called the keel. The keel can be consolidated, unconsolidated or a mixture of these.

In a punch through test, a flat indentor is ran down into the ice rubble. From the dimensions of the test set up and measurements during the experiment some material properties for the rubble can be derived. Research has been done on punch through tests in full-scale, laboratory and through modelling. Reviews on both, experimental work and modelling, have been written by Liferov and Bonnemaire [1] and Liferov [2].

Fig. 1a shows a sketch of a full-scale punch through test as conducted by Heinonen and Määttänen [3, 4] and modelled here. In the figure, a circular indentor with diameter d is moved down into ice rubble with thickness h_k measured from the waterline. As only loads caused by the rubble are of interest, a cylindrical plug with height h_{cut} under the indentor is cut through the consolidated layer. Hence, the effective keel thickness becomes $h = h_k + FB - h_{cut}$, where FB is the free board. As one result, the force needed to move the indentor as a function of indentor displacement is achieved. Also in Fig. 1a, a possible shear plane with an angle α from the vertical is presented.

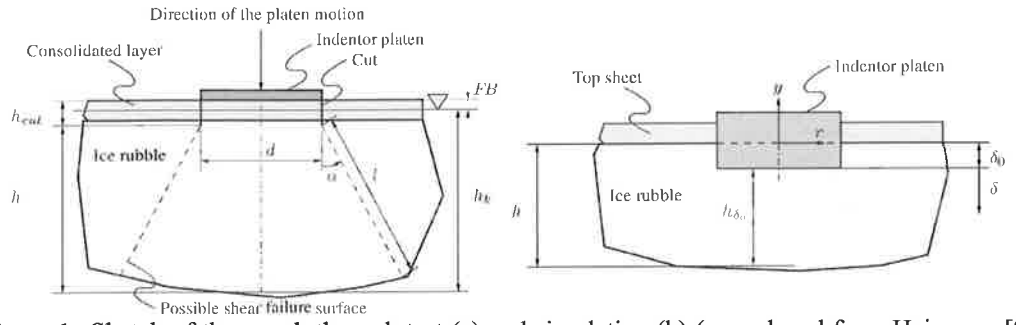

Figure 1: Sketch of the punch through test (a) and simulation (b) (reproduced from Heinonen [9] with modifications): (a) An indentor with diameter d is loading an ice rubble with average keel depths h_k measured from the waterline and h measured from the cut made through the consolidated layer. Depth of the cut is h_{cut}. FB is free board of the ice sheet. α is the angle and l is the slant height of an assumed failure surface. (b) The average keel thickness under the indentor h_{δ_0} in a case with initial indentor displacement δ_0 and indentor displacement δ. See Figure 3a for coordinate axes r and y.

In the presented work, ice rubble is modelled as discontinuous media. Traditional way of modelling discontinuum is the discrete element method (DEM) first introduced by Cundall and Strack [5]. Here, punch through tests of unconsolidated ice rubble were modelled using combined finite-discrete element method (FEM-DEM) [6, 7]. Simulations were run in three dimensions using ice blocks with realistic sizes and shapes. More details of the simulations and results can be found from Polojärvi and Tuhkuri [8].

2. MECHANICS OF THE SIMULATION

In FEM-DEM, the discrete elements are discretized into finite elements. The contact forces are then solved finite element by finite element. The total contact force acting on the discrete element is achieved by superposing the forces acting on its finite elements. In current simulations each of the discrete element representing an ice block was partitioned into six tetrahedron shaped finite elements.

Contact forces were derived using penalty function and potential contact force method [7]. Energy dissipation in collisions was modelled using viscous damping and dynamic Coulomb friction. The deformation of the individual discrete elements was not modelled.

In the potential contact force method, a potential φ with continuous first partial derivatives with respect to spatial coordinates is defined in every point P of each finite element volume Ω. Further, $\varphi = \varphi(P)$ should vanish on finite element boundaries Γ for smooth collision response. Hence, $\varphi(P)$ is defined as follows:

$$\varphi(P) > 0, \qquad P \in \Omega \qquad \wedge \qquad \varphi(P) = 0, \qquad P \in \Gamma. \tag{1}$$

The contact force df_φ applied to an infinitesimal volume element $\mathrm{d}\Omega_o$ penetrating into φ is determined from the gradient of φ as (Figure 2a)

$$\frac{\mathrm{df}_\varphi(P)}{\mathrm{d}\Omega_o} = -s\nabla\varphi(P), \tag{2}$$

where s is a positive constant penalty term arising from the penalty function method. The negative sign is due to repulsive nature of the contact force. The contact force $\mathbf{f}_\varphi$ due to $\varphi(P)$ is determined

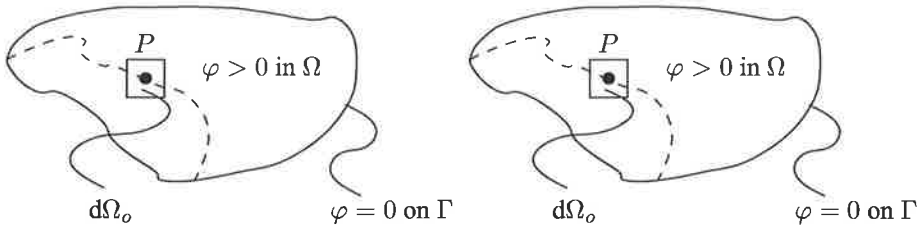

Figure 2: (a) An infinitesimal volume element $d\Omega_o$ at point P penetrating into a finite element with volume Ω and (b) the overlap volume Ω_o of two elements.

by integration over the overlap volume Ω_o of two colliding elements. The integral is reduced into computationally more efficient form by generalized Gauss's theorem

$$\mathbf{f}_\varphi = -s \int_{\Omega_o} \nabla\varphi(P)\, d\Omega = -s \int_{\Gamma_o} \varphi(P)\mathbf{n}\, d\Gamma, \tag{3}$$

where $\mathbf{n}$ is the unit outer normal of Γ_o (Figure 2b). From the previous equation it can be seen that the distributed load acting on overlapping volume elements due to φ becomes reduced into a force acting on a single point on Γ_o.

The inelasticity in collisions is modelled by using viscous damping relative to the rate of change in overlap volume. The viscous component of the normal force $\mathbf{f}_v$ is defined as

$$\mathbf{f}_v = c\Gamma_0 \left(\mathbf{v}_r \cdot \mathbf{n}\right) \mathbf{n}, \tag{4}$$

where $\mathbf{v}_r \cdot \mathbf{n}$ is the normal component of the relative velocity of the contacting discrete elements at the point of application of $\mathbf{f}_\varphi$ and c is the viscous damping constant. The value of c was chosen to make the contacts inelastic: about 80 % of the kinetic energy before collision was dissipated in it.

As no tensile forces between the colliding blocks are allowed, the total contact force $\mathbf{f}_c$ should act on the direction of $-\mathbf{n}$. This is achieved by the following condition:

$$\mathbf{f}_c = \begin{cases} 0, & \text{if } |\mathbf{f}_\varphi| - |\mathbf{f}_v| < 0 \\ \mathbf{f}_\varphi - \mathbf{f}_v & \text{else.} \end{cases} \tag{5}$$

Dissipation due to sliding friction is modelled by using dynamic Coulomb friction. Frictional force $\mathbf{f}_\mu$ is solved from

$$\mathbf{f}_\mu = -\mu|\mathbf{f}_c| \frac{\mathbf{v}_r - \mathbf{v}_r \cdot \mathbf{n}}{|\mathbf{v}_r - \mathbf{v}_r \cdot \mathbf{n}|}, \tag{6}$$

where μ is the friction coefficient and $\mathbf{v}_r - \mathbf{v}_r \cdot \mathbf{n}$ is the tangential component of the relative velocity of contacting blocks at the point of contact.

3. SIMULATIONS

In the simulations, the full scale tests conducted by Heinonen and Määttänen [3] are modelled (see Figure 1a). Table 1 gives the main parameters used in the simulations and Figure 3a shows the coordinate frame. Origin is located at the top of the rubble and y-axis aligns with the center line of the indentor. It was observed that the ice rubble behaviour followed cylindrical symmetry around the indentor, and hence cylindrical coordinates are used. Figure 3b illustrates a typical initial configuration of a simulation.

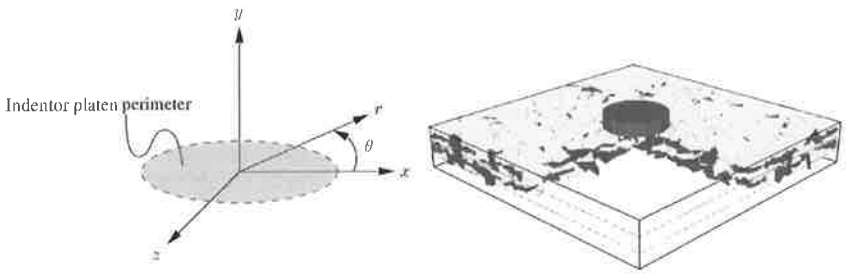

(a) (b)

Figure 3: (a) Cylindrical coordinate frame (r,θ,y) used in the text. Plane $y = 0$ is located at the top of the rubble, y-axis aligns with the center line of the indentor, and x-axis is parallel with one of the pool walls and (b) typical initial configuration of the rubble.

(a) (b)

Figure 4: An illustrative example of a simulation with indentor displacements (a) 400 mm and (b) 800 mm. Blocks are colored with two different colors according to the initial y-coordinate of their centroids.

To generate an ice rubble, blocks with random translational and rotational velocities were released underwater after which the blocks were allowed to float until initial kinetic energy was dissipated. The pool was covered with a discrete element representing the ice sheet on top of the rubble. In simulations with initial indentor displacement δ_0 (see Figure 1b) the indentor had its initial position during the rubble generation phase. Average dimensions for individual ice blocks were chosen after field measurements in the Baltic Sea by Kankaanpää [10] and Heinonen and Määttänen [3, 4] and varied using random number generator. Some simulations were run with homogeneous block sizes for comparison.

In the punch through phase of the simulation, the indentor was moved downwards into the ice rubble as presented in snapshots of Figure 4. The force F applied by the rubble on the indentor was monitored. Contacts between the indentor and blocks and between the pool walls and blocks were frictionless. The pool size was chosen after gauging the force exerted on walls by the rubble to avoid boundaries of the pool to have an effect on measured force values and deformation pattern of the rubble.

4. RESULTS

Force displacement records and maximum force

Typical indentor force-displacement $F(\delta)$-graphs are shown in Figure 5a. In the simulations shown here, the keel thicknesses were approximately same ($h_{\delta_0} = 2.21 \ldots 2.85$ m, see Figure 1b) as in experiment #1/2001 by Heinonen and Määttänen [4] from which $F(\delta)$ is also plotted in the Figure. From the figure it is noticed that initially $F(\delta)$ increases rapidly. Then increase in F is slower until F reaches an approximately constant level. F_{MAX} was defined as the average of F on its approximately constant level. In Figure 5b, F_{MAX} from simulations with various values of μ are plotted against the initial keel depth h_{δ_0} under the indentor (see Figure 1b). In the figure, F_{MAX}

for simulations with homogeneous ice rubble are presented with circled markers.

In addition to simulation results, F_{MAX} from the field experiment #1/2001 by Heinonen and Määttänen [4] is shown in Figure 5b. This experiment provides a good comparison for the simulations, as the experiment was conducted on an unconsolidated keel obtained by first conducting a punch through test, and then conducting another test where the indentor was moved down into the same rubble again. It can be assumed, that after the first punch the freeze bonds were broken and the keel behaved as an unconsolidated rubble.

Also in Figure 5b, the buoyant force F_α of a rubble cone with top diameter d, height h_{δ_0}, slant height l, and bottom diameter defined by angle α (see Figure 1a) is shown for three different values of α. F_α is achieved from

$$F_\alpha = (\rho_w - \rho_i)(1 - \eta_r)V_\alpha g \tag{7}$$

where η_r is the rubble porosity and V_α is the volume of the rubble cone given by

$$V_\alpha = \frac{\pi h_{\delta_0}}{3}\left[\left(\frac{d}{2}\right)^2 + \frac{d}{2}\left(\frac{d}{2} + h_{\delta_0}\tan\alpha\right) + \left(\frac{d}{2} + h_{\delta_0}\tan\alpha\right)^2\right]. \tag{8}$$

Shear strength

A value for rubble shear strength can be obtained by assuming a cylindrical failure surface ($\alpha = 0$, Figure 1a) defined by the perimeter of indentor platen and rubble thickness [11, 9]. If h_{δ_0} is used for rubble thickness, a shear strength τ_{δ_0} is obtained as

$$\tau_{\delta_0} = \frac{F_{MAX}}{\pi d h_{\delta_0}}, \tag{9}$$

where d is the diameter of the indentor (see Figure 1a). Figure 5c shows τ_{δ_0} from simulations and experiment #1/2001 [4]. τ_{δ_0} in the figure is from the same simulations from which F_{MAX} was obtained and shown in Figure 5c. Markers for simulations with homogeneous rubble consisting of

Table 1: Main parameters used in simulations.

	Parameter	Symbol	Unit	Value
General	number of ice blocks			1740 ... 4600
	number of finite elements			10200 ... 27600
Contact	penalty term	s		$1.0 \cdot 10^6 \ldots 1.0 \cdot 10^8$
	damping constant	c	Nsm^{-3}	$5.0 \cdot 10^4 \ldots 8.0 \cdot 10^4$
	time step	Δt	s	$1.0 \cdot 10^{-4} \ldots 2.0 \cdot 10^{-4}$
Ice blocks	length		m	0.3 ... 1.5
	width		m	0.3 ... 1.5
	thickness		m	0.2
	mass density	ρ_i	kgm^{-3}	920
	friction coefficient	μ		0.05 ... 0.6
Water	mass density	ρ_w	kgm^{-3}	1010
Keel	keel depth	h	m	2.1 ... 3.48
	rubble porosity	η_r		0.34 ... 0.51
Indentor	diameter	d	m	4.7
	velocity	$\dot{\delta}$	mms^{-1}	25 ... 50
Pool	length		m	20
	width		m	20

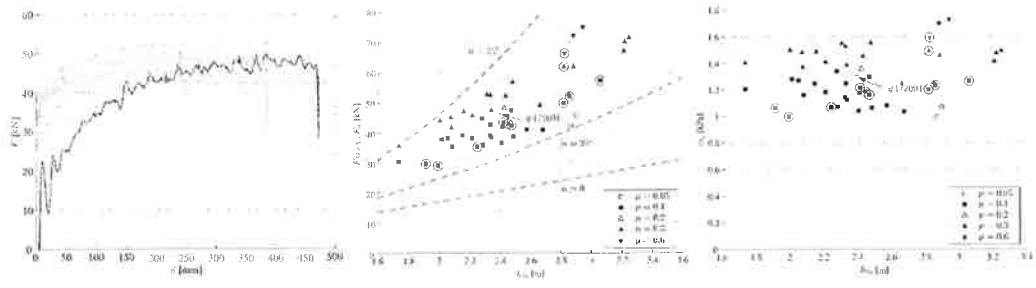

(a) (b) (c)

Figure 5: Force and shear strength values of the rubble: (a) the $F(\delta)$-graph from the full-scale experiment $\#1/2001$ conducted by [4] (black) and simulation runs with similar rubble thicknesses as in the experiment (gray), (b) The maximum force F_{MAX} as a function of h_{δ_0} from simulations and experiment $\#1/2001$. F_α is buoyant force defined by Equation 7 and (c) the shear strength τ_{δ_0} with various values of μ plotted against h_{δ_0} from simulations and experiment $\#1/2001$ using the assumption of cylindrical failure.

equal block sizes are circled in the figure. It is seen that τ_{δ_0} increases with the increase of μ. The average values of τ_{δ_0} for friction coefficients $\mu = 0.1, 0.3$ and 0.6 were $1.17, 1.44$ and 1.67 KPa, respectively.

5. DISCUSSION

Simulations

The sensitivity of the simulations to penalty term value s was done by running fifteen simulation runs with five different initial configurations with penalty term values $1.0 \cdot 10^6$, $1.0 \cdot 10^7$ and $1.0 \cdot 10^8$. It was found out that the τ_{δ_0} values achieved from the simulations increased on average by 7 % when s was increased from $1.0 \cdot 10^6$ to $1.0 \cdot 10^7$. Further, the increase in τ_{δ_0} was 3.5 % when penalty term was increased from $1.0 \cdot 10^7$ to $1.0 \cdot 10^8$.

Shear strength

The shear strength τ_{δ_0} for simulated piles was shown in Figure 5 and the average shear strength for different values of μ in Section 3.2. Using the same definition for rubble shear strength as here (Equation 9), Leppäranta and Hakala [12] reported shear strength values $1.7 \ldots 4$ kPa, Heinonen [9] reported values $1.3 \ldots 18$ kPa, and Croasdale et al. [11] reported values $6 \ldots 12.8$ kPa. The values from simulations are in the low end when compared to experimental data, but this is expected, as no cohesive bonding between ice blocks was modelled. In fact, the effect of the rubble consolidation, i.e. cohesive bonding between the ice blocks, on rubble strength can be estimated by comparing the simulated results with the highest experimental values.

Azarnejad and Brown [13] have used a different definition for rubble shear strength than here. In their terminology, a load-time record consists of an ascending part, peak load F_{MAX}, descending part, and residual load F_R. If inertial effects are ignored, Azarnejad and Brown [13] define shear strength as $\tau = (F_{MAX} - F_R)/A$, where A is area. The residual load F_R is the average load for a period at the end of an experiment when the load remains virtually constant. In the simulations reported here, no such constant residual load following a peak load was observed. If a simulation was continued long enough, the force started to descend after F_{MAX}, but did not level into a constant

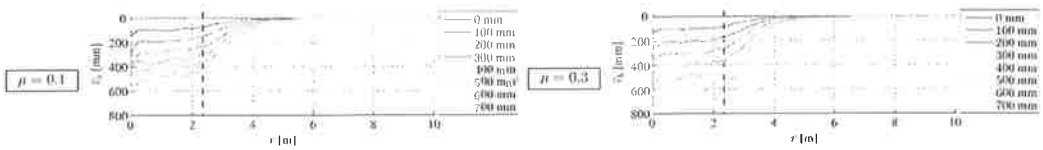

(a) (b)

Figure 6: Average profiles of keel bottom displacements $\bar{v}_b$ with various values of indentor displacement δ (shown in the legend) with (a) $\mu = 0.1$ and (b) $\mu = 0.3$ with same initial configurations. The displacements were averaged from eight simulations for each μ. The perimeter of the indentor is shown with dashed line.

value. Further, if a residual load would still be defined, in all the simulations $F_{MAX} \approx F_R$, and using the definition of Azarnejad and Brown [13] would result into very small or vanishing shear strength.

Failure process

The rubble deformation was studied by analysing the displacements $\bar{v}_b$ of the keel bottom in the negative y-direction. Figure 6 presents average from simulations with 8 different initial configurations for two different friction coefficients, $\mu = 0.1$ and $\mu = 0.3$. The simulations with $\mu = 0.3$ show larger displacement in the bottom of the keel than simulations with $\mu = 0.1$. The same observation can be reached by studying compaction of the rubble, defined here as the ratio $(\bar{v}_b(\delta) - \delta)/h_{\delta_0}$ (see Figure 1b). Figure 7a illustrates the keel compaction for the same simulation data as used in Figure 6. These simulations show that compaction is negligible up to $\delta = 700$ mm when $\mu = 0.3$, but when $\mu = 0.1$, compaction initiates at $\delta \approx 200$ mm. It should be noticed, that in both cases the maximum force F_{MAX} is reached with approximately equal values of δ.

No unique shear plane that could be defined by an angle α (see Figure 1a) was detected in the simulations. Rather, a zone with displacement gradient was observed. However, an approximation for a shear plane angle α_t can be defined by using a threshold value v_t for the displacement $\bar{v}_b$ at a point (r_t, y_t) in the keel bottom. Here the threshold value $v_t = 100$ mm was chosen to be half of the block thickness. It can be observed from the bottom profiles shown in Figure 6 that the condition $\bar{v}_b(r_t, y_t) = v_t$ defines unambiguously a single point, and between that point and the axis $r = 0$, $\bar{v}_b(r_t, y_t) \geq v_t$. The positive direction of α_t is defined in Figure 1a, and hence

$$\alpha_t(\delta) = \arctan\left(\frac{r_t - d/2}{|y_t|}\right), \tag{10}$$

where d is the indentor diameter. Figure 7b shows $\alpha_t(\delta)$-graphs for the same simulation data as used in Figure 7a and Figure 6.

The results shown in Figure 7b are in agreement with visual observations on simulations, where deformation in the keel bottom was seen to initiate close to the center line of the indentor (values $\alpha_t < 0$ when δ is small). With $\delta < 150$ mm, the rate $\partial\alpha_t/\partial\delta$ is large. This corresponds to the observation on the change in the angle defining the zone of the displaced rubble. As δ increases further, $\partial\alpha_t/\partial\delta$ decreases. Angle α_t is increasing slowly as $\delta > 400$ mm corresponding to the approximately constant zone of moving rubble. It is seen from Figure 7b that α_t reaches values of $35 \ldots 45°$. In laboratory scale punch through tests in plane strain conditions, failure angles of approximately $40°$ have been observed [14, 15].

Based on the simulation results described above, in a punch through test three main processes can be identified: (1) a volume of rubble with the shape of an upward opening cone forms under the

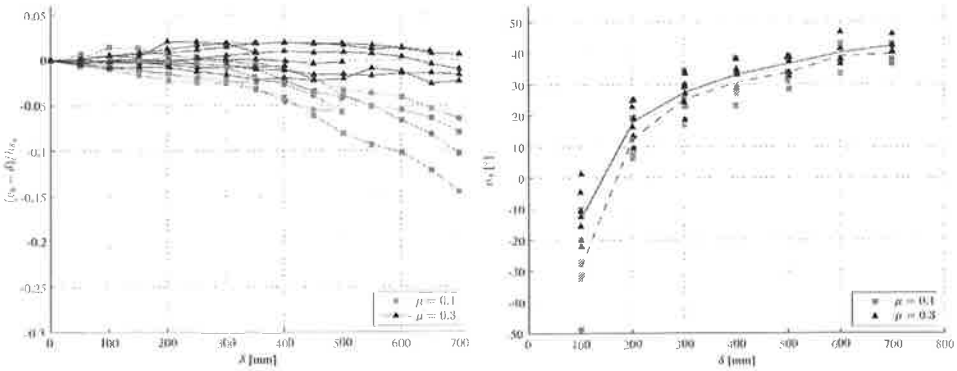

(a) (b)

Figure 7: The failure process of the ice rubble: (a) the compaction and (b) angle α_t as a function of δ. Displacement threshold $v_t = 100$ mm in the rubble bottom was used. The average values of α_t for $\mu = 0.3$ and $\mu = 0.1$ are shown with solid and dashed line, respectively.

indentor, moves with the indentor, and spreads out into a cylindrical plug, (2) ice blocks around this conical / cylindrical core rotate (or shape lock and rotate) causing the zone of displaced rubble to spread horizontally, i.e. the angle α_t defining a downward opening cone containing moving rubble grows, until (3) α_t reaches an approximately constant value and the rubble within the cone defined by α_t moves downwards. Processes (1) and (2) occur at least partly simultaneously.

Simulation results were also compared to laboratory experiments. Azarnejad, Frederking, and Brown [16] and Azarnejad and Brown [13] conducted a series of laboratory punch through tests where they varied the indentor velocity, the time for aging of the ice rubble and ice rubble thickness. In tests with deformation rates $\dot{\delta} < 40$ mms^{-1} they observed a failure process similar with the current simulations: a rectangular, or in some cases trapezoidal, plug of undisturbed ice moved down with the indentor. Around the plug, within a zone of two to three blocks, rotation of ice blocks occurred, but the rubble outside of the zone of rotating blocks remained undisturbed.

6. CONCLUSIONS

Punch through tests of unconsolidated rubble were simulated in 3D. The indentation force values achieved were in the range of full-scale test results for unconsolidated rubble. The simulated failure process was observed to be similar to laboratory experiments.

In simulations, the indentor force F initially increased with displacement δ. After reaching maximum value F_{MAX}, F remained approximately constant. No clear peak force value was observed and it is believed that it is missing from the simulation results because no cohesive forces were modelled.

Following previous studies, the shear strength of the rubble was calculated by assuming cylindrical failure. The values obtained were in the low end when compared to experimental data due to the fact that no cohesive bonds were modelled. Increase in the value of friction coefficient was seen to lead to an increase in shear strength. In addition, the value of friction coefficient was observed to affect the compaction of the rubble.

Failure process of the rubble was analyzed. No unique shear plane was detected. Instead, a shear zone was observed to form during the indentor motion. The location and the shape of the shear zone was not constant during the indentor motion.

References

[1] P. Liferov and B. Bonnemaire. Ice rubble behaviour and strength: Part I. review of testing and interpretation of results. *Cold Regions Science and Technology*, 41(2):135–151, 2005.

[2] P. Liferov. Ice rubble behaviour and strength: Part II. modelling. *Cold Regions Science and Technology*, 41(2):153–163, 2005.

[3] J. Heinonen and M. Määttänen. Ridge loading experiments, field experiments in winter 2000. LOLEIF Progress Report No. 10, TKK, 2000. 40 p.

[4] J. Heinonen and M. Määttänen. Ridge keel mechanical properties - testing. field experiments in winter 2001. STRICE-report, TKK, 2001. 39 p.

[5] P.A. Cundall and O.D.L. Strack. A discrete numerical model for granular assemblies. *Géotechnique.*, 29:47–65, 1979.

[6] A. Munjiza, D.R.J. Owen, and N. Bićanić. A combined finite-discrete element method in transient dynamics of fracturing solids. *Engineering Computations.*, 12:145–174, 1995.

[7] A. Munjiza. *The combined finite-discrete element method.* Chichester, England. John Wiley & Sons Ltd., 2004.

[8] A. Polojärvi and J. Tuhkuri. 3D discrete numerical modelling of punch through tests. *Cold Regions Science and Technology,*, 56(1):18–29, 2009.

[9] J. Heinonen. *Constitutive modeling of ice rubble in first-year ridge keel.* Doctoral Thesis, TKK, 2004. VTT Publications 536. Espoo, Finland, 2004, 142 p, ISSN 1235-0621.

[10] P. Kankaanpää. Distribution, morphology and structure of sea ice pressure ridges in the baltic sea. *Fennia*, (175:2):139–240, 1997. ISSN 0015-0010.

[11] K. R. Croasdale, S. Bruneau, D. Christian, G. Crocker, J. English, M. Metge, and R. Ritch. In-situ measurements of the strength of first-year ice ridge keels. In *Proceedings of the 16th International Conference on Port and Ocean Engineering under Arctic Conditions, POAC'01*, volume 3, pages 1445–1454, Ottawa, Ontario, Canada, 2001.

[12] M. Leppäranta and R. Hakala. The structure and strength of first-year ice ridges in the baltic sea. *Cold Regions Science and Technology*, 20(3):295–311, 1992.

[13] A. Azarnejad and T. G. Brown. Ice rubble behaviour in punch tests. *ASCE Journal of Cold Regions Engineering*, 15(3):135–153, 2001.

[14] A. Jensen, S. Løset, K. V. Høyland, P. Liferov, J. Heinonen, K.-U. Evers, and M. Määttänen. Physical modelling of first-year ice ridges - part II: Mechanical properties. In *Proceedings of the 16th International Conference on Port and Ocean Engineering under Arctic Conditions, POAC'01*, volume 3, pages 1493–1502, Ottawa, Ontario, Canada, 2001.

[15] E. Lemee and T. Brown. Small-scale plane strain punch tests. In *Ice in the Environment: Proc. of the 16th IAHR International Symposium on Ice*, volume 2, pages 1–7, Dunedin, New Zealand, 2002.

[16] A. Azarnejad, R. Frederking, and T. G. Brown. Ice rubble strength from plane strain punch tests. In *Proc. of the 18th Int. Conf. on Onshore Mechanics and Arctic Engineering, OMAE*, pages 1–9, St. Johns, Canada, 1999.

NOVEL MEASUREMENT DEVICE FOR THE INVESTIGATION OF MAGNETOSTRICTION IN ELECTRICAL MACHINERY

K. Fonteyn, , E. Pyhäranta, A. Belahcen, P. Rasilo, A. Arkkio
Department of Electrical Engineering, Unit of Electromechanics
Helsinki University of Technology
P.O.Box 3000
FIN-02015 HUT, FINLAND

ABSTRACT

This paper presents a measurement device for the phenomena of magnetostriction and electromagnetic stress in electrical steel sheets. Accelerometers, sensitive to the vibrations caused by the magnetic flux densities induced in the test device, were placed on the outer boundary. Measurements were conducted under sinusoidal supply at frequencies from 20 Hz to 140 Hz and different amplitudes. Results show that the displacements in the radial direction of the outer boundary tend, for most, to increase with an increasing magnetic flux density.

1. INTRODUCTION

The phenomenon of magnetostriction has been studied extensively since Joule observed the effect in 1842 [1]. Under an applied external magnetic field, some materials present the particularity of changing their shape. Grains in ferromagnetic materials are observed. According to the Weiss theory, these grains are divided into regions having a similar magnetic moment, and called domains. These tend to rearrange themselves when an external magnetic field is applied. The size of the ones with a magnetic moment aligned with the direction of the external magnetic field tends to grow at the expense of the other ones [2]. The resulting variation of size with respect to the initial size of the material is also known as strain. These deformations may be useful in some cases but are often the reason for extra noise in electrical machinery. In order to get better understandings of the phenomenon appearing inside of stator cores of electrical machines, a measurement setup has been designed and built.

Previously, test devices aiming at the same result have been designed. Låftman [3] proposed to study the phenomenon on a stator core only, with the rotor removed. For this reason the device was not only taking the effect of magnetostriction into account, but also, partly the effect of the stesses induced by the leakage fluxes penetrating from one tooth to the other through the air. Later, Belahcen and Cester, considered a device with no air-gap, made of Fe-Si disk sheets, where slots were punched to insert the windings [4-5]. This device had the great advantage of removing mostly the stresses occurring between air and iron; however the design did not produce an equal distribution of the magnetic flux density in the whole device.

2. MEASUREMENT SETUP

The requirement of the device was the ability of achieving a peak magnetic flux density of 1.5 T in the center of the machine when supplied at 50 Hz with a current of 60 A maximum. The calculation of the distribution of the magnetic flux density in the 2D cross-section of the geometry was performed in finite element software, FCSMEK, for solving magnetic problems [6]. The input conditions were according to the previously cited requirements. The test device was wound as a

two-pole machine. The slots were kept as small as possible to avoid the propagation of the deformation due to the fringing of the flux density in the air and copper. Dimensions and data of the device are presented in Table I and Figure 1.

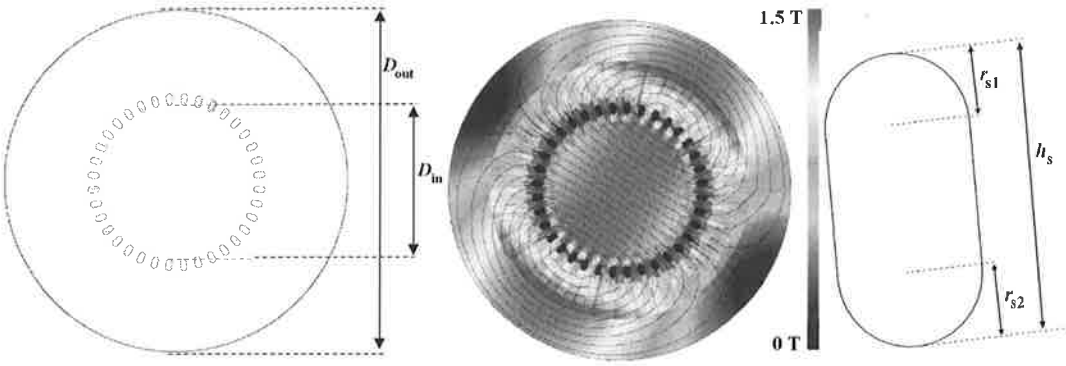

Figure 1 2D-geometry of the test device (left and right pictures) and magnetic flux density distribution (central picture) at a certain time step: the simulation was performed using second order triangular elements at the rated voltage of 280 V.

Table I: Main data of the test device.

Definition	Value
Radius for the shape of the slot, r_{s1}	5.5 mm
Radius for the shape of the slot, r_{s2}	5 mm
Height of a slot, h_s	20 mm
Outer diameter, D_{out}	600 mm
Inner diameter, D_{in}	230 mm
Axial length	100 mm
Number of pole pairs	1
Number of phases	3
Total number of slots	36
Slots per pole per phase	6
Number of parallel wires	4
Parallel paths	1
Weight of the assembled device	260 kg
Depth of a single electrical steel sheet	0.5 mm

For the construction, 199, M400-50A electrical steel sheets with 36 laser cut slots to insert the windings were stacked and welded to form the package. Every sheet was rotated by an angle of 10° with respect to the previous one, so that there is no preferred direction of magnetization in the test device. A total of 5 search coils to acquire the magnetic flux density at different positions of the test device were wound. The test machine was placed on a wooden frame, on a rubber sheet that absorbs the vibration from the structure. The displacements on 8 equally distant points on the external boundary of the device were measured with accelerometers. A reference accelerometer as seen in Figure 2(b) was placed in the middle of the upper part to insure that the obtained results are reflecting the displacements due to magnetostriction and electromagnetic stress in iron. This setup enables to measure the vibrations caused by the properties of the electrical steel sheets when

excited by an external magnetic field. Three ventilators were used to cool down the windings after each set of measurements.

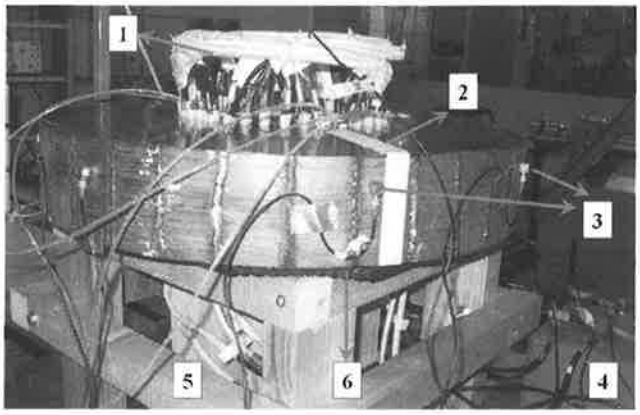

(a) Side view of the device

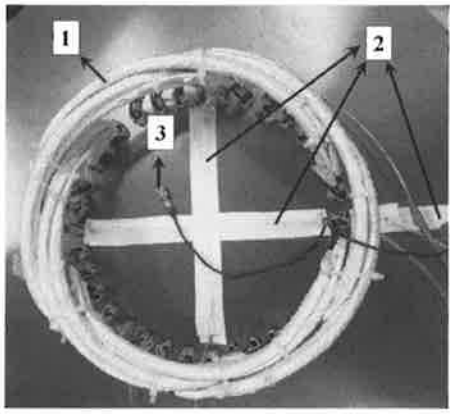

(b) Upper view: positioning of the reference accelerometer and sensing coils

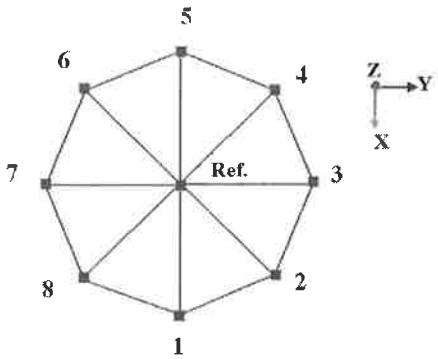

(c) Placement of the accelerometers, schematic view.

Figure 2 Views of the test device. 1. End-windings, 2. Search coils, 3. Accelerometers, 4. Connection to the supply voltage, 5. Wooden support for the device, 6. Rubber isolating sheet.

The device was supplied from a synchronous generator, the phase current and voltage of which were measured by using a multimeter. The synchronous generator was mechanically coupled to a DC motor supplied by a DC generator, itself connected to an asynchronous machine fed by the grid. With this configuration, it was made possible to control the speed of the synchronous machine, and hence, the supply frequency of the test device. The magnetic flux density in the center and in the yoke of the device was measured and stored in a portable PC oscilloscope. The measurement procedure was to keep the amplitude of the magnetic flux density constant for different supply frequencies of the test device. So, the phase voltage was varied accordingly. Low frequencies of less than 20 Hz could not be explored as the synchronous machine lost its stability. The highest measurement frequency was limited to 140 Hz. A general view of the setup is presented in Figure 3.

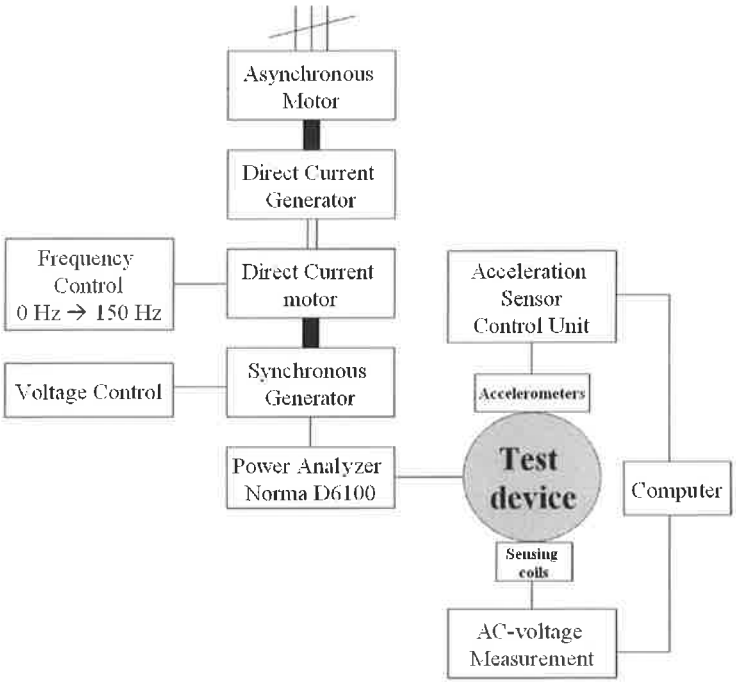

Figure 3 Schematic view of the measurement setup.

3. RESULTS

The frequency and magnetic field dependence of the displacements of the outer boundary of the test device are presented in this paragraph.

First, a frequency analysis of the filtered signals from each of the 8 accelerometers shows the different values of the displacements obtained on the outer boundary for specific supply frequencies. The peak magnetic flux density in the center of the device was kept constant at around 0.7 T and the supply frequency of the feeding voltage was increased from 20 Hz up to 140 Hz.

The results, in Figures 4, 5 and 6 depict the frequency spectrum for RMS values of the magnetic flux densities equal to 0.4 T, 0.8 T, and 1 T. The amplitude of the displacements tends to increase, for most of the cases under an increasing magnetic flux density. Results for higher magnetic flux densities were difficult to perform for under higher supply frequency than 60 Hz. Frequencies higher than 300 Hz are not plotted in the figures as their significance was small. It can be still noticed that the highest amplitude of the displacements is observed for a frequency equal to twice the supply frequency.

Figure 7 presents the different results of the accelerometers obtained for a given supply frequency, here 50 Hz. The first observation is that for all the accelerometers, the general trend is that the peak-to-peak displacements are increasing with an increasing flux density. It is clear from Figure 7 that the displacements can be 2 to 3 times higher for some sensors, but on the average, the obtained peak values of the displacements are acceptable regarding previous research in the field, for instance in [2]. The symmetry of the device should have brought identical signals on all the accelerometers. One major reason is that the outer boundary is not plain, and the accelerometers were attached to the structures by using magnets that covered quite a large unequal surface. As the effect of magnetostriction in iron is very small (typical displacements are in the order of nm), accurate measurements are delicate. For this reason, the average over all the accelerometers has been chosen to depict the general phenomena in Figure 8. As expected, the higher the magnetic flux density, the higher the displacements. In addition, for at 0.4 T, the displacements follow a sinusoidal behavior. However, for higher values, higher frequencies distort the signal.

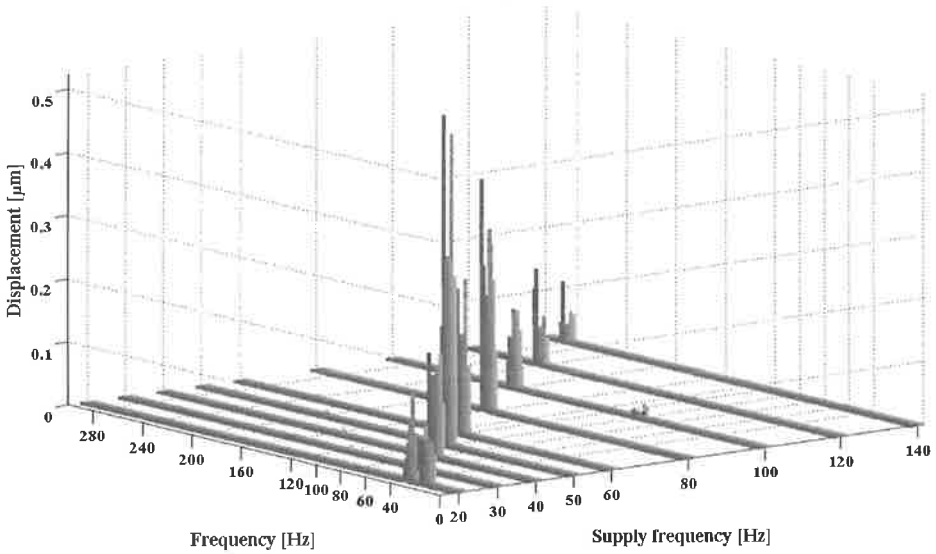

Figure 4 Frequency spectrum as a function of the supply frequency for a constant magnetic flux density in the center of the device of 0.4 T. At each supply frequency, the values obtained from the 8 accelerometers are presented. Displacements in the radial direction.

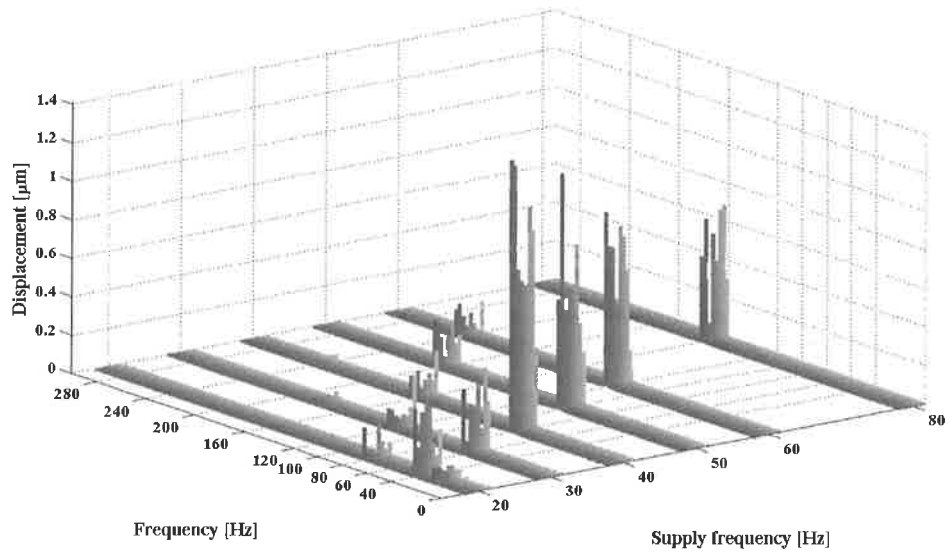

Figure 5 Frequency spectrum as a function of the supply frequency for a constant magnetic flux density in the center of the device of 0.8 T. At each supply frequency, the values obtained from the 8 accelerometers are presented. Displacements in the radial direction.

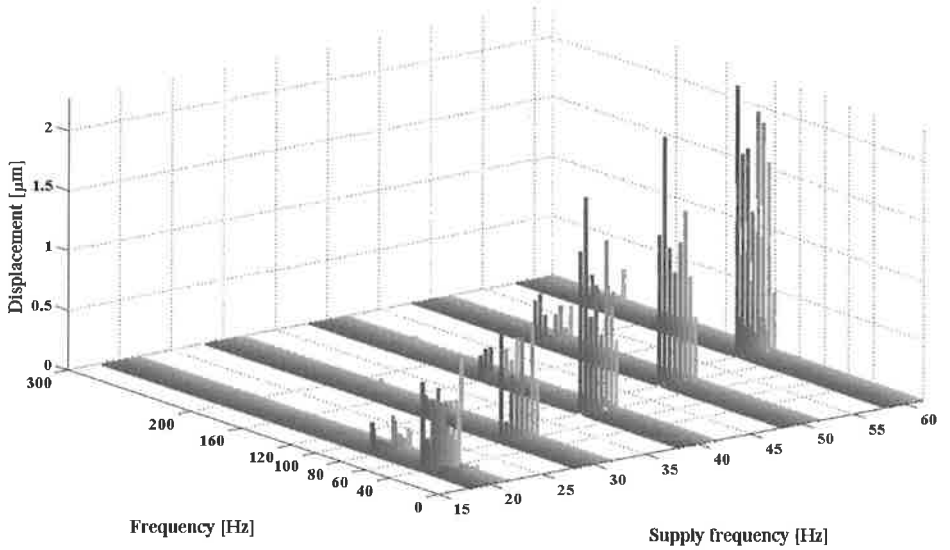

Figure 6 Frequency spectrum as a function of the supply frequency for a constant magnetic flux density in the center of the device of 1 T. At each supply frequency, the values obtained from the 8 accelerometers are presented. Displacements in the radial direction.

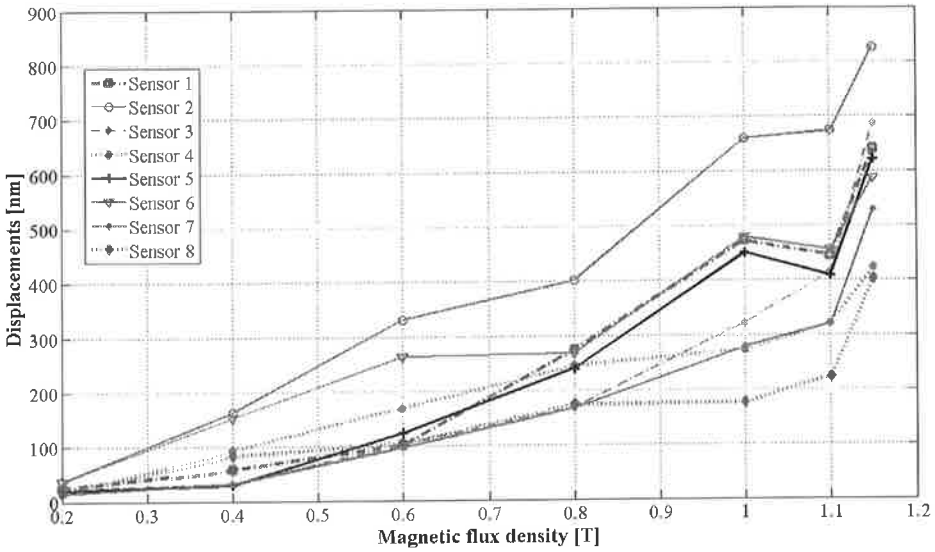

Figure 7 Peak-to-peak displacements obtained from each accelerometer for different RMS values of the magnetic flux density in the center of the device and supply frequency of 50 Hz.

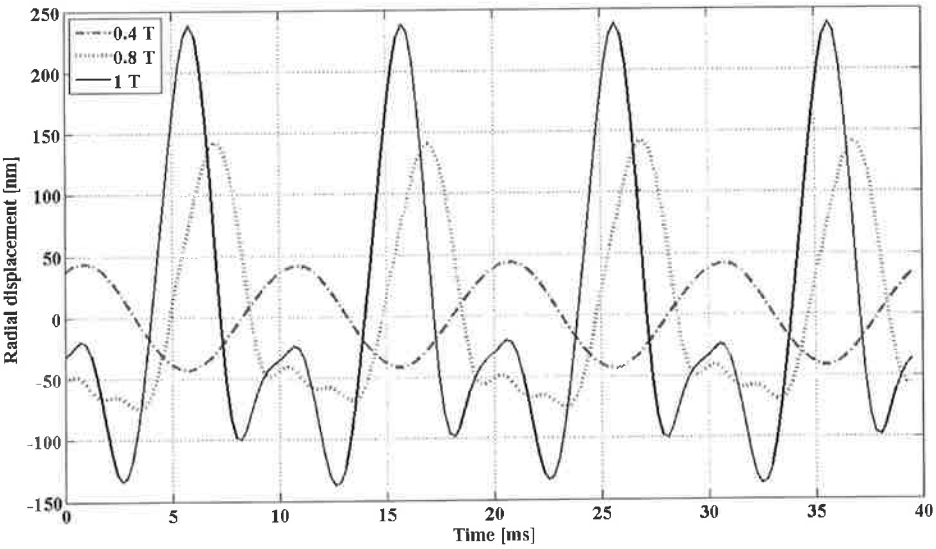

Figure 8 Radial displacement for a supply frequency of 50 Hz. Average over all the accelerometers for 3 RMS values of the magnetic flux density in the center of the test device.

4. CONCLUSION

The presented experimental setup has the merit to account for the phenomenon of magnetostriction and electromagnetic stress tensor inside of the iron only. The design and building procedure of the device has been described. Results from the sensors were analyzed. The difficulty of accurate measurements of magnetostriction is clear The general output of the measurements, taking the average over all the accelerometers to obtain the displacements in the radial direction offers a quantitative value to the magnetostriction effect in iron. The measurements will serve to validate a magneto-mechanical coupled model, presented in [7], and implemented into a finite element code for electrical machinery.

5. REFERENCES

[1] Joule, J.P., 1847, On the effects of magnetism upon the dimensions of iron and steel bars, Philosophical Magazine, Vol. 30, p. 76.

[2] Du Trémolet de Lacheisserie, E., 2003, Magnetostriction – Theory and Applications of Magnetoelasticity, CRC Press.

[3] Låftman, L., 1995. The Contribution to Noise from Magnetostriction and PWM Inverter in an Induction Machine. Doctoral dissertation. Lund Institute of Technology, Sweden.

[4] Belahcen, A., 2004. Magnetoelasticity, Magnetic Forces and Magnetostriction in Electrical Machines. Doctoral dissertation. Helsinki University of Technology, Espoo, Finland.

[5] Cester, P., 2002, Magnetostriction as source of Noise and Vibration. Design, Construction and Measurement on an Experimental Electrical Machine. Master´s thesis, Helsinki University of Technology, Espoo, Finland.

[6] Arkkio, A., 1987. Analysis of Induction Motors Based on the Numerical Solution of the Magnetic Field and Circuit Equations. Doctoral dissertation. Helsinki University of Technology, Espoo, Finland.

[7] Belahcen, A., Fonteyn, K., Hannukainen, A., Kouhia, R., 2008 On numerical modeling of coupled magnetoelastic problem , Proceedings of the 21st Nordic Seminar on Computational Mechanics Trondheim, Kvamsdal T., Mathisen K.M. and Pettersen B. (editors), pp. 203-206.

A POSTERIORI ERROR ESTIMATES FOR THE KIRCHHOFF-LOVE ARCH MODEL

OLLI MALI

Department of Mathematical Information Technology
University of Jyväskylä
P.O. Box 35 (Agora)
FI-40014 University of Jyväskylä, FINLAND
e-mail: olli.mali@jyu.fi

ABSTRACT

In this paper, a posteriori error estimation functionals are derived for the Kirchhoff-Love arch model. They are functionals of the approximate solution, problem data and auxiliary functions. Moreover, they are proven to be guaranteed upper and lower bound for the approximation error and they have no "gap" i.e for some values of auxiliary functions they provide the exact error. The connection between physical laws stating the arch model and error estimates is made transparent.

1. INTRODUCTION

In engineering practise, mechanical models are solved by various approximation methods. It is important to be able to control the approximation error, if any quantitative information is to be obtained from the simulation. Our aim is to provide guaranteed bounds for the approximation error and improve the credibility of the simulation as a whole. The mechanical problem considered is the arch model, which results from the dimensional reduction of the Koiter shell model as presented in the book [4] (for more recent discussion about the model and extension to Lipschitzian arches, see [9]). Error estimates derived in this paper are of similar type as those in [7, 8]. In Section 2, we describe the arch model and decompose classical fourth order equations into two sets of second order equations. These two sets of equations describe fundamental physical laws stating the model. A posteriori error estimates for the arch problem are defined in Section 3 and their main properties are given in Theorem 2. Computations of estimates is briefly discussed. Results are summarized in Section 4 and some future research directions are mentioned.

2. KIRCHHOFF-LOVE ARCH MODEL

We consider a plane arch that has a constant cross section which is small compared to its length. Following [4], the arch and all related functions are presented in the parametrized form. The $\psi : [0, 1] \to \mathbb{R}^2$ is a smooth parametrized non self-intersecting curve of the curvilinear abscissa s that defines the shape of the arch. Displacement vector $u = (u_1, u_2)$ and load vector $f = (f_1, f_2)$ are given on a local basis (a_1, a_2) that varies along the arch, where a_1 is the tangential and a_2 is the normal direction. The angle between the horizontal axis and a_1 is denoted as θ. On both ends of

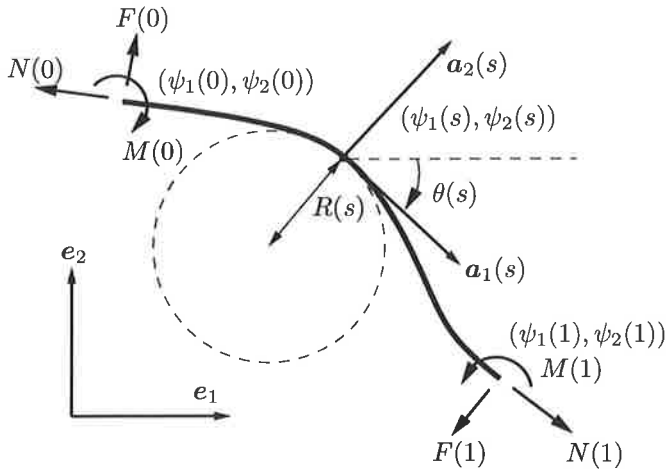

Figure 1: Kirchoff-Love arch

the beam, there are known external loads, normal force N, shear force F, and bending moment M. Mentioned definitions with positive directions of the external loads are depicted in Figure 1.

The function $c : [0,1] \to \mathbb{R}$,

$$c(s) := \frac{1}{R(s)} = \frac{\psi_2''(s)\psi_1'(s) - \psi_1''(s)\psi_2'(s)}{(\psi_1'^2 + \psi_2^2)^{\frac{3}{2}}} \tag{1}$$

is the curvature of the arch. The energy functional of the arch is

$$J(u) = \frac{1}{2}\int_0^1 \{EA(u_1' - cu_2)^2 + EI(cu_1 + u_2')'^2\}\ \mathrm{ds} - \int_0^1 f \cdot u\ \mathrm{ds} - \Big/_0^1 Nu_1 + \Big/_0^1 Fu_2 - \Big/_0^1 Mu_2' \tag{2}$$

where E is the material constant (the Young modulus), A is the area of the cross section and I is the second moment of inertia of the cross section. All these values are strictly positive.

The minimizer of the energy functional is a solution of a following variational problem. Find $u \in V_0$ s. t.

$$a(u, w) = l(w) \quad \forall\, w \in V_0, \tag{3}$$

where

$$a(u,w) = \int_0^1 \begin{bmatrix} EA(u_1' - cu_2) \\ EI(cu_1 + u_2')' \end{bmatrix} \cdot \begin{bmatrix} w_1' - cw_2 \\ (cw_1 + w_2')' \end{bmatrix} \mathrm{ds} \tag{4}$$

and

$$l(w) := \int_0^1 f \cdot w\ \mathrm{ds} + \Big/_0^1 Nu_1 - \Big/_0^1 Fu_2 + \Big/_0^1 Mu_2'. \tag{5}$$

Table 1: Boundary conditions

natural		kinematic	
u_1	(tangential disp.)	N	(tangential stress)
u_2	(normal disp.)	F	(shear force)
u_2'	(rotation)	M	(bending moment)

If u is sufficiently regular, then (3) implies the classical equations,

$$\begin{cases} -(EA(u_1' - cu_2))' - c(EI(cu_1 + u_2')')' &= f_1 \\ -cEA(u_1' - cu_2) + (EI(cu_1 + u_2')')'' &= f_2. \end{cases} \tag{6}$$

The boundary conditions are defined at the end points $s_1 = 0$ and $s_2 = 1$. They are listed on the Table 1. At both ends of the beam, either natural or corresponding kinematic boundary condition has to be defined in order to have a properly defined problem. In this paper, we consider cases where natural boundary conditions are homogeneous. Together with the regularity requirements, natural boundary conditions define the space of admissible displacements,

$$V_0 := \{v \in H^1(0,1) \times H^2(0,1) \mid \text{Natural B.C. are satisfied. }\}. \tag{7}$$

Mentioned assumptions guarantee, that in substitution terms of (5), either the expression containing u is known (by a kinematic boundary condition) or the condition $w \in V_0$ causes it to be zero.

For a straight beam ($c = 0$), the equations (6) are transformed to well-known beam equations (see [10]),

$$-EAu_1'' = f_1 \quad \text{and} \quad (EIu_2'')'' = f_2 \tag{8}$$

We note that (6) can be decomposed into

$$\begin{cases} EA(u_1' - cu_2) &= p_1 \\ EI(cu_1 + u_2')' &= p_2 \end{cases} \tag{9}$$

and

$$\begin{cases} -p_1' - cp_2' &= f_1 \\ -cp_1 + p_2'' &= f_2. \end{cases} \tag{10}$$

These relations are the physical laws governing the beam problem. The equations (9) define the constitutive relation that states the linear dependence between displacement u and tangential stress p_1 and the bending moment p_2. The vector p will be referred as a stress vector. The equation (10) establishes the equilibria between the external load f and the stresses p of the beam. Additionally, at the endpoints of the beam, stresses must coincide with kinematic boundary conditions, i.e.

$$p_1 + cp_2 = N, \quad p_2 = M, \quad \text{and} \quad p_2' = F.$$

Stresses satisfying these relations form the space of admissible stresses

$$Q_0 := \{v \in H^1(0,1) \times H^2(0,1) \mid \text{Kinematic B.C. are satisfied. }\}. \tag{11}$$

The beam is statically determined (or overdetermined) if for $p = 0$, the equations (9) imply $u = 0$. The kernel of the equations (9) consists only of rigid body motions (see [4]), i.e. the displacement is of the form

$$v = \begin{bmatrix} \cos(\theta) & \sin(\theta) \\ -\sin(\theta) & \cos(\theta) \end{bmatrix} \begin{bmatrix} a\psi_2 + b_1 \\ a\psi_1 + b_2 \end{bmatrix}, \tag{12}$$

where a, b_1 and b_2 are constants. Thus the beam is statically determined (or overdetermined) if natural boundary conditions forbid any rigid body motion.

The possible sets of boundary conditions are characterized to three classes:

- *Statically underdetermined* cases, where there are not enough natural boundary conditions to restrict rigid body movement. The problem has no unique solution if no additional constraints are required. These cases are considered non-physical and are neglected in our analysis.
- *Statically determined* cases, where there are three (dimension of the space of rigid body movements) natural boundary conditions that are enough to restrict rigid body movement. Additionally, no initial stresses are possible. In these cases the constitutive equations (10) and the equilibrium equations (10) can be solved separately in a consecutive manner.
- *Statically overdetermined* cases, where there are more than three natural boundary conditions. In these cases the equations (9) and (10) must be solved together as a single fourth order system. This kind of boundary conditions allow initial stresses for the unloaded beam. In other words, the null space of the equation (10) has non zero elements.

The ellipticity of $a : V_0 \times V_0 \to \mathbb{R}$ (and the existence of solution) is proved in the book of Ciarlet [4, Theorem 8.1.2, pp. 433–436]. The proof holds for any statically determined or overdetermined beam. From it follows that the Friedrichs constant C for the arch problem exists.

Theorem 1. *For a statically determined or overdetermined beam, there exists constant C s.t.*

$$\int_0^1 \{w_1^2 + w_2^2\}\ \mathrm{ds} \le C \int_0^1 \{(w_1' - cw_2)^2 + (cw_1 + w_2')'^2\}\ \mathrm{ds} \quad \forall\, w \in V_0.$$

3. A POSTERIORI ERROR ESTIMATES

For detailed approach to the general derivation of a posteriori functional error estimators via variational method see [7, 8]. For a linear elliptic problem the majorant can be derived with the help of integral identities. We will derive a lower bound of the type presented in the book of Mikhlin [6]. First we define the a posteriori error estimators for the problem (3). They are functionals of conforming approximation $v \in V_0$ and some auxiliary functions, error majorant

$$\mathcal{M}_\oplus(v, y, \beta) := \left(1 + \frac{1}{\beta}\right) \frac{C}{\alpha} \int_0^1 \{(f_1 - (y_1' - cy_2'))^2 + (f_2 - (cy_1 + y_2''))^2\}\ \mathrm{ds} +$$

$$+ (1+\beta) \int_0^1 \left\{ \frac{1}{EA}(y_1 - EA(v_1' - cv_2))^2 + \frac{1}{EI}(y_2 - EI(cv_1 + v_2')'^2 \right\}\ \mathrm{ds} \quad (13)$$

and error minorant

$$\mathcal{M}_\ominus(v, w) := -\int_0^1 \begin{bmatrix} EA(w_1' - cw_2 + 2(v_1' - cv_2)) \\ EI((w_2' + cw_1')' + 2(v_2' + cv_1)') \end{bmatrix} \cdot \begin{bmatrix} w_1' - cw_2 \\ (w_2' + cw_1')' \end{bmatrix} \mathrm{ds}$$

$$+ 2 \int_0^1 (f_1 w_1 + f_2 w_2)\ \mathrm{ds}. \quad (14)$$

Note that, the two terms of the error majorant are related to the decomposed form of the classical equations. First part is the error in the equilibrium condition (10) between an arbitrary function representing stresses and the external load. This part guarantees the reliability of the estimate. Second part is the violation of the constitutive relation (9) between the approximation and arbitrary stresses. The quantity

$$\alpha := \min\{EA, EI\}$$

is related only to material properties and geometrical properties of the cross section.

Moreover, majorant and minorant are guaranteed upper and lower bounds and have no "gap", in the sense that for specially selected auxiliary functions, they provide the exact error. These properties are highlighted in the following theorem:

Theorem 2. *Let $u \in V_0$ be the exact solution of the problem* (3)*, $p \in Q_0$ be the respective exact stress vector, and $v \in V_0$ be any conforming approximation, then*

$$\mathcal{M}_{\ominus}(v, w) \leq \| u - v \|^2 \leq \mathcal{M}_{\oplus}(v, \beta, y), \quad \forall\, w \in V_0,\ \beta \in \mathbb{R}_+,\ y \in Q_0 \tag{15}$$

and

$$\mathcal{M}_{\ominus}(v, u - v) = \| u - v \|^2 = \inf_{\beta \in \mathbb{R}_+} \mathcal{M}_{\oplus}(v, \beta, p). \tag{16}$$

Estimates are valid for any conforming approximation. In particular, the Galerkin orthogonality of the approximation is not required. For the application of estimates, the main task is efficient selection of auxiliary functions. They can be selected by solving the following minimization problems:

$$\sup_{w \in V_0^h} \mathcal{M}_{\ominus}(v, w)$$

and

$$\inf_{\beta in \mathbb{R}_+, y \in Q_0^h} \mathcal{M}_{\oplus}(v, \beta, p),$$

where spaces $V_0^h \in V_0$ and $Q_0^h \in Q_0$ are some finite dimensional subspaces. Since expression $\mathcal{M}_{\ominus}$ is concave and quadratic with respect to w, maximizing it leads to a system of linear equations, that can be solved. $\mathcal{M}_{\oplus}$ is quadratic and convex with respect to y and can be minimized in similar manner. To obtain the upper bound, one has to minimize with respect to β (can be done analytically) and y in iterative fashion. This method of solving w and y provides most efficient bounds, but it can be computationally expensive. Since the arch model is one-dimensional, the computational effort is not unfeasible. Other option is to obtain auxiliary stress vector y by postprocessing the approximate solution, see, e.g., [1, 2, 11].

The value of the constant C has to be estimated somehow. Simple alternative is to solve numerically the related eigenvalue problem. Experiments have shown, that even a crude overestimation of this constant does not ruin the error estimate, since if y satisfies the relation (10) well enough, the term multiplying the constant is very small.

Proof of Theorem 2. We prove Theorem 2 in a constructive manner and begin by presenting the derivation of the error majorant. The integral relation required for the derivation is obtained by integration by parts

$$\int_0^1 \begin{bmatrix} w_1' - cw_2 \\ (cw_1 + w_2')' \end{bmatrix} \cdot \begin{bmatrix} y_1 \\ y_2 \end{bmatrix} \mathrm{ds} = \int_0^1 \begin{bmatrix} -y_1' - cy_2' \\ -cy_1 + y_2'' \end{bmatrix} \cdot \begin{bmatrix} w_1 \\ w_2 \end{bmatrix} \mathrm{ds}$$

$$+ \Big/_0^1 w_1 y_1 + \Big/_0^1 (cw_1 + w_2') y_2 - \Big/_0^1 w_2 y_2'. \tag{17}$$

for any $w \in H^1(0,1) \times H^2(0,1)$ and $y \in H^1(0,1) \times H^2(0,1)$.

Next we construct the majorant. Subtracting $a(v,w)$ from (3) and applying (17) yields

$$a(u-v,w) = \int_0^1 f \cdot w \, \mathrm{ds} + \Big/_0^1 Nw_1 - \Big/_0^1 Fw_2 + \Big/_0^1 Mw_2'$$
$$- \int_0^1 \begin{bmatrix} EA(v_1' - cv_2) \\ EI(cv_1 + v_2')' \end{bmatrix} \cdot \begin{bmatrix} w_1' - cw_2 \\ (cw_1 + w_2')' \end{bmatrix} \mathrm{ds} + \int_0^1 \begin{bmatrix} w_1' - cw_2 \\ (cw_1 + w_2')' \end{bmatrix} \cdot \begin{bmatrix} y_1 \\ y_2 \end{bmatrix} \mathrm{ds}$$
$$- \int_0^1 \begin{bmatrix} -y_1' - cy_2' \\ cy_1 + y_2'' \end{bmatrix} \cdot \begin{bmatrix} w_1 \\ w_2 \end{bmatrix} \mathrm{ds} - \Big/_0^1 w_1 y_1 - \Big/_0^1 (cw_1 + w_2')y_2 + \Big/_0^1 w_2 y_2'. \quad (18)$$

We reorganize terms to

$$a(u-v,w) = I_1 + I_2 + I_3 \quad (19)$$

where

$$I_1 = \int_0^1 \begin{bmatrix} f_1 - (y_1' - cy_2') \\ f_2 - (cy_1 + y_2'') \end{bmatrix} \cdot \begin{bmatrix} w_1 \\ w_2 \end{bmatrix} \mathrm{ds},$$

$$I_2 = \int_0^1 \begin{bmatrix} y_1 - EA(v_1' - cv_2) \\ y_2 - EI(cv_1 + v_2')' \end{bmatrix} \cdot \begin{bmatrix} w_1' - cw_2 \\ (cw_1 + w_2')' \end{bmatrix} \mathrm{ds},$$

and

$$I_3 = \Big/_0^1 (N - y_1 - cy_2)w_1 + \Big/_0^1 (-F + y_2')w_2 + \Big/_0^1 (M - y_2)w_2'.$$

After imposing boundary conditions, $w \in V_0$ and $y \in Q_0$, I_3 vanishes. (Another option is to choose $y \in Q$ and obtain a different majorant, where an additional terms representing the violations of kinematic boundary conditions appear.) We estimate remaining terms from above one by one. By the Cauchy-Schwartz inequality,

$$I_1 \quad \leq \quad \left(\int_0^1 (f_1 - (y_1' - cy_2'))^2 + (f_2 - (cy_1 + y_2''))^2 \, \mathrm{ds} \right)^{1/2} \left(\int_0^1 w_1^2 + w_2^2 \, \mathrm{ds} \right)^{1/2}. \quad (20)$$

We apply Theorem 1:

$$I_1 \leq \left(\int_0^1 (f_1 - (y_1' - cy_2'))^2 + (f_2 - (cy_1 + y_2''))^2 \, \mathrm{ds} \right)^{1/2} \times$$
$$\frac{\sqrt{C}}{\sqrt{\alpha}} \left(\int_0^1 EA(w_1' - cw_2)^2 + EI(cw_1 + w_2')'^2 \, \mathrm{ds} \right)^{1/2}. \quad (21)$$

Here $\alpha = \min\{EA, EI\}$, where minimum is taken with respect to the $\| \cdot \|_\infty$-norm.

We apply the Cauchy-Schwartz inequality again:

$$I_2 = \int_0^1 \begin{bmatrix} \frac{1}{\sqrt{EA}}(y_1 - EA(v_1' - cv_2)) \\ \frac{1}{\sqrt{EI}}(y_2 - EI(cv_1 + v_2')') \end{bmatrix} \cdot \begin{bmatrix} \sqrt{EA}(w_1' - cw_2) \\ \sqrt{EI}(cw_1 + w_2')' \end{bmatrix} \mathrm{ds}.$$

$$\leq \left(\int_0^1 \frac{1}{EA}(y_1 - EA(v_1' - cv_2))^2 + \frac{1}{EI}(y_2 - EI(cv_1 + v_2')'^2 \, \mathrm{ds} \right)^{1/2} \times$$

$$\left(\int_0^1 EA(w_1' - cw_2)^2 + EI(cw_1 + w_2')'^2 \, \mathrm{ds} \right)^{1/2}.$$

These estimates have $\| w \|$ as a common multiplier. Apply them to (19) and set $w = u - v$. Then on the left-hand side we obtain $\| u - v \|^2$ and we may divide by $\| u - v \|$ on both sides. Then we arrive at

$$\| u - v \| \leq \frac{\sqrt{C}}{\sqrt{\alpha}} \left(\int_0^1 (f_1 - (y_1' - cy_2'))^2 + (f_2 - (cy_1 + y_2''))^2 \, \mathrm{ds} \right)^{1/2} +$$

$$+ \left(\int_0^1 \frac{1}{EA}(y_1 - EA(v_1' - cv_2))^2 + \frac{1}{EI}(y_2 - EI(cv_1 + v_2')'^2 \, \mathrm{ds} \right)^{1/2}. \quad (22)$$

For computation purposes it is preferable to have quadratic expression. Thus we introduce arbitrary $\beta \in \mathbb{R}_+$ and use the Young inequality to obtain

$$\| u - v \|^2 \leq \left(1 + \frac{1}{\beta}\right) \frac{C}{\alpha} \int_0^1 \{(f_1 - (y_1' - cy_2'))^2 + (f_2 - (cy_1 + y_2''))^2\} \, \mathrm{ds} +$$

$$+ (1 + \beta) \int_0^1 \left\{ \frac{1}{EA}(y_1 - EA(v_1' - cv_2))^2 + \frac{1}{EI}(y_2 - EI(cv_1 + v_2')'^2 \right\} \mathrm{ds}. \quad (23)$$

The right-hand side is the error majorant as defined in (13) If we substitute exact stresses $y := p$ to the majorant, the second part provides the exact error and the first part is zero.

Next, we construct the error minorant. The energy functional (2) can be written as

$$J(u) = \frac{1}{2} a(u, u) - l(u). \quad (24)$$

By the definition of the energy norm and the Galerkin orthogonality,

$$\begin{aligned} \| u - v \|^2 &= a(u - v, u - v) \\ &= a(u, u) - 2a(u, v) + a(v, v) + 2(l(u) - a(u, u)) \\ &= 2\left(\frac{1}{2} a(v, v) - l(v) - \frac{1}{2} a(u, u) + l(u)\right) \\ &= 2(J(v) - J(u)). \end{aligned}$$

The exact solution $u \in V_0$ of the variational problem (3) minimizes the energy functional J (see, for example, [3]). Thus we may estimate from below

$$\begin{aligned} \| u - v \|^2 &= 2(J(v) - J(u)) \geq 2(J(v) - J(v + w)) \\ &= a(w + 2v, w) - 2l(w), \quad \forall w \in V_0. \end{aligned}$$

The exact error is obtained with $w = u - v$. The right-hand side is the general form of a posteriori functional minorant. By substituting definitions (4) and (5), we arrive at (14). □

4. CONCLUSIONS

In this paper, a posteriori functional error estimators were derived for the arch model. The derivation is performed on a functional level, without any assumptions about the applied approximation method. Moreover, estimates do not include any mesh dependent constants. We have proven, that estimates are guaranteed and they have no "gap", i.e. for some auxiliary functions they provide the exact error. Using these functionals, it is possible to control the approximation error of computations dedicated to solve the deformation of arch.

Numerical experiments concerning the arch model are currently in process. In particular, different variants for the computation of y are of practical interest. The derivation of estimates for higher dimensional models such as the the Koiter shell model can be done by similar methods. With help of the estimates derived in this paper, one can analyse the sensitivity of the Kirchhoff-Love arch model with respect to the problem data as in [5].

Acknowledgements. Author wants to thank Prof. S. Repin from the V. A. Steklov Institute of Mathematics for providing the theoretical framework and Prof. P. Neittaanmäki from the University of Jyväskylä for his support.

REFERENCES

[1] M. Ainsworth and J. T. Oden, A Posteriori Error Estimation in Finite Element Analysis, John Wiley and Sons, New York, 2000.

[2] I. Babuška and R. Rodriguez, The problem of the selection of an a posteriori error indicator based on smoothing techniques, Internat. J. Numer. Meth. Engrg., 36:539–567, 1993.

[3] D. Braess, Finite Elements: Theory, Fast Solvers and Applications in Solid Mechanics, Cambridge University Press, Cambrigde, 2001.

[4] P. G. Ciarlet, Finite Element Method for Elliptic Problems, Studies in Mathematics and its Applications, Vol. 4, North-Holland, Amsterdam, 1978.

[5] O. Mali and S. Repin, Estimates of the indeterminacy set for elliptic boundary-value problems with uncertain data, J. Math. Sci. (N.Y.), 150(1):1869–1874, 2008.

[6] S. G. Mikhlin, Variational Methods in Mathematical Physics, Pergamon, Oxford, 1964.

[7] P. Neittaanmäki and S. Repin, Reliable Methods for Computer Simulation, Error Control and A Posteriori Estimates, Elsevier, Amsterdam, 2004.

[8] S. Repin, A posteriori error estimation for variational problems with uniformly convex functionals, Math. Comput. 69:481–500, 2000.

[9] D. Tiba and R. Vodák, A general asymptotic model for Lipschitzian curved rods, Adv. Math. Sci. Appl., 15(1):137–198, 2005.

[10] S. Timoshenko and D. H. Young, Theory of Structures, McGraw-Hill Book Company, Inc., New York, 1945.

[11] O. C. Zienkiewitz and J. Z. Zhu, Adaptive techniques in the finite element method, Comm. Appl. Numer. Methods, 4:197–204, 1988.

A NEW ERROR INDICATOR FOR THE POISSON PROBLEM

I. Anjam[1], O. Mali[2], P. Neittaanmäki[3], and S. Repin[4]

[1]Department of Mathematical Information Technology, University of Jyväskylä, P.O. Box 35 (Agora), FI-40014 University of Jyväskylä, Finland immanuel.anjam@jyu.fi
[2]Department of Mathematical Information Technology, University of Jyväskylä, P.O. Box 35 (Agora), FI-40014 University of Jyväskylä, Finland olli.mali@jyu.fi
[3]Department of Mathematical Information Technology, University of Jyväskylä, P.O. Box 35 (Agora), FI-40014 University of Jyväskylä, Finland pn@mit.jyu.fi
[4]V. A. Steklov Institute of Mathematics in St. Petersburg, Fontanka 27, RU-191024, St. Petersburg, Russia, repin@pdmi.ras.ru

ABSTRACT

In this article, we present a new error indicator for approximate solutions of elliptic problems. The indicator is easily computable, contains no unknown constants and the computation of it admits parallelization. We discuss it with the paradigm of the Poisson problem, however the techniques are easily adaptable to more complicated elliptic problems, for example to linear elasticity.

1. INTRODUCTION

Functional type error estimation technique has proven to be a reliable way to estimate the global error of numerical solutions. The advantages of this approach are that the estimates are valid for any conforming approximation and they contain only global constants. The theory of functional type error estimates is exposed in the books [5, 7]. Also the error bounds for the model problem of this paper can be found in these books. The functional approach can also be used to derive error indicators. In [4], the functional approach is used to derive computable error indicators for approximate solutions of elliptic boundary value problems.

In this paper, we modify some ideas of the functional approach and derive error indicators of a new type. The indicators contain the corresponding numerical solution v, problem data and a auxiliary function $\boldsymbol{y}$, which is to be selected in a suitable way. For this task, we apply two different methods (global and local) and compare their efficiency.

Consider the Poisson equation with the homogenous Dirichlet boundary condition

$$-\Delta u = f \qquad \text{in } \Omega\,, \tag{1}$$

$$u = 0 \qquad \text{on } \partial\Omega\,. \tag{2}$$

Here Ω is a bounded and connected domain in $\mathbb{R}^d$ with Lipschitz boundary $\partial\Omega$, and f belongs to $L_2(\Omega)$.

By V we denote the Sobolev space $\overset{\circ}{H}{}^1(\Omega)$, which is the subspace of $H^1(\Omega)$ functions vanishing on $\partial\Omega$. The generalized solution $u \in \overset{\circ}{H}{}^1(\Omega)$ of (1)-(2) satisfies the relation

$$\int_\Omega \nabla u \cdot \nabla w \, dx = \int_\Omega f w \, dx, \quad \forall w \in V. \tag{3}$$

The goal is to estimate the difference between the exact solution u and a conforming approximation $v \in V$. In this paper, we measure the corresponding error in terms of the energy norm

$$|\!|\!| u - v |\!|\!| := \|\nabla(u - v)\|, \tag{4}$$

where $\|\cdot\|$ denotes the L_2 norm.

2. ERROR MAJORANT AND INDICATOR

Guaranteed error bounds for the problem (1)-(2) are derived by transformations of the integral identity (3), which leads to the following result.

Proposition 1. *Let u be the exact solution and $v \in V$ a numerical solution to the model problem* (1)-(2). *Then*

$$|\!|\!| u - v |\!|\!| \leq M_\oplus(v, \boldsymbol{y}), \qquad \forall \boldsymbol{y} \in H(\mathrm{div}; \Omega),$$

where

$$M_\oplus(v, \boldsymbol{y}) := C_\Omega \|f + \mathrm{div}\, \boldsymbol{y}\| + \|\boldsymbol{y} - \nabla v\|. \tag{5}$$

Here C_Ω is the constant in the Friedrichs inequality and $\boldsymbol{y} \in H(\mathrm{div}; \Omega)$ is a auxiliary function.

This estimate does not contain a gap between the exact error and the estimate (the estimate is *sharp*). This fact is easy to establish by replacing $\boldsymbol{y}$ with the exact function ∇u. The derivation of this upper bound can be found in [5, 7].

The first term of the majorant guarantees the reliability of the estimate. If it is neglected, we obtain the error indicator,

$$I := \|\boldsymbol{y} - \nabla v\|^2, \tag{6}$$

which is no longer a guaranteed upper bound for the error. However, if $\boldsymbol{y}$ is properly chosen, I provides information of the relative error distribution, which is of particular interest for adaptive schemes.

3. CHOOSING THE AUXILIARY FUNCTION $\boldsymbol{y}$

The upper bound (5) and indicator (6) contain the function $\boldsymbol{y} \in H(\mathrm{div}; \Omega)$. The best possible choice of this auxiliary function is of course ∇u. However, this function is unknown, so that a certain procedure for selecting suitable $\boldsymbol{y}$ must be applied. Below we briefly discuss some possible ways. One is based upon global minimization of the upper bound and another (new) exploits a locally based minimization procedure.

3.1. Global minimization

First the upper bound is transformed to a quadratic form by using an algebraic inequality. We obtain

$$M_\oplus \leq (1 + \beta) C_\Omega^2 \|f + \mathrm{div}\, \boldsymbol{y}\|^2 + (1 + \frac{1}{\beta}) \|\boldsymbol{y} - \nabla v\|^2 =: \mathcal{M}_\oplus(v, \boldsymbol{y}, \beta). \tag{7}$$

Then we require that the Gateaux derivative of $\mathcal{M}_\oplus$ is zero:

$$\mathrm{D}(\mathcal{M}_\oplus) = \left\{ \frac{d}{dt} \mathcal{M}_\oplus(v, \boldsymbol{y} + t\boldsymbol{\phi}, \beta) \right\}_{t=0} = \\ = (1+\beta) C_\Omega^2 \int_\Omega (f + \operatorname{div} \boldsymbol{y}) \operatorname{div} \boldsymbol{\phi}\, dx + (1 + \frac{1}{\beta}) \int_\Omega (\boldsymbol{y} - \nabla v) \boldsymbol{\phi}\, dx = 0 \quad (8)$$

for all $\boldsymbol{\phi} \in H(\mathrm{div}; \Omega)$. By rearranging the terms in (8), we arrive at a certain finite dimensional problem for $\boldsymbol{y}$. Since $\boldsymbol{y}$ belongs to the space $H(\mathrm{div}; \Omega)$, a natural choice is to use Raviart-Thomas finite elements to solve this problem (see [3, 6]). The mesh can be the same as was used for the numerical solution v, or a refined mesh. Computation of $\boldsymbol{y}$ on a refined mesh (or higher order elements) improves the approximation of ∇u and more accurate values are obtained for the upper bound.

3.2. Gradient Averaging

A very popular way of approximating the gradient of the exact solution u is to post process the gradient of the numerical solution v (see e.g. [1, 2, 8]).

In this paper, we use linear H^1 elements to compute v, so the gradient ∇v is constant in each element. There are several options on how to average the gradient. A common way is to average the gradient to nodes: for each node, calculate ∇v in each related element and average the values weighted by the areas of respective elements. We denote this procedure by G_N.

Alternatively, it is possible to average the normal components of the gradient to edges by the following procedure: for each edge, calculate the normal components of ∇v in the related elements and average the values weighted by the edge length. It should be noted that the orientation of edge normals must be taken into account. The values obtained in this way are essentially degrees of freedom for the linear Raviart-Thomas finite element. Let us define this procedure more accurately.

Let c_{nl} denote the unknown degree of freedom related to edge e_{nl} with edge length $|e_{nl}|$. Here the subindex letters n and l denote the numbers of the nodes which define the edge. We denote by T_{knl}, T_{nml} the elements related to this edge and by n_{knl}, n_{nml} their respective unit outward normals on the boundary. This setting is visualized in Figure 1. The following equation averages the normal component of ∇v to the edge e_{nl}, when we choose the orientation induced by T_{knl}:

$$c_{nl} = \frac{|e_{nl}| \left(\nabla v|_{T_{knl}} \cdot n_{knl} - \nabla v|_{T_{nml}} \cdot n_{nml} \right)}{2} = \frac{|e_{nl}| \left(\nabla v|_{T_{knl}} + \nabla v|_{T_{nml}} \right) \cdot n_{knl}}{2}. \quad (9)$$

We denote by G_{RT} the procedure, which calculates the values of (9) for all edges in a given mesh. It should be noted that the operator G_{RT} essentially produces functions from linear Raviart-Thomas finite element space.

3.3. Post processing the averaged gradient

In this section, we present a way to post process $\boldsymbol{y}$. Assume that an initial approximation of ∇u has been obtained by the averaging procedure G_{RT} defined in the previous section. We make further post processing of $\boldsymbol{y} = G_{RT}(\nabla u)$ by minimizing the integral

$$\mathcal{J}(\boldsymbol{y}) := \int_\Omega (\operatorname{div} \boldsymbol{y} + f)^2 dx \quad (10)$$

on every pair of neighboring triangles (elements).

Since $\operatorname{div} \boldsymbol{y}$ is constant over T_{knl}, we have

$$\int_{T_{knl}} (\operatorname{div} \boldsymbol{y}) dx = (\operatorname{div} \boldsymbol{y})|_{T_{knl}} |T_{knl}| \,, \tag{11}$$

where $|T_{knl}|$ stands for the area of the element. On the other hand, the Gauss divergence theorem states that

$$\int_{T_{knl}} (\operatorname{div} \boldsymbol{y}) dx = \int_{\partial T_{knl}} (\boldsymbol{y} \cdot n_{knl}) ds = c_{kn} + c_{nl} + c_{lk} \,, \tag{12}$$

where n_{knl} is the unit outward normal of ∂T_{knl} and the degrees of freedom c_{kn}, c_{nl} and c_{lk} are defined by (9). These equations hold for any element.

Let again T_{knl} and T_{nml} be two neighboring elements (see Figure 1). Our goal is to minimize the integral (10) on these two elements. This is done by optimizing the degree of freedom c_{nl} on the shared edge e_{nl}. In the following equations, the new unknown value is denoted by c^*_{nl}.

$$\frac{\partial}{\partial c^*_{nl}} \left(\int_{T_{knl} \cup T_{nml}} (\operatorname{div} \boldsymbol{y} + f)^2 \, dx \right) = 2 \frac{\partial}{\partial c^*_{nl}} (\operatorname{div} \boldsymbol{y})|_{T_{knl}} \left((\operatorname{div} \boldsymbol{y})|_{T_{knl}} |T_{knl}| + \int_{T_{knl}} f \, dx \right) + \\ + 2 \frac{\partial}{\partial c^*_{nl}} (\operatorname{div} \boldsymbol{y})|_{T_{nml}} \left((\operatorname{div} \boldsymbol{y})|_{T_{nml}} |T_{nml}| + \int_{T_{nml}} f \, dx \right) = 0 \,. \tag{13}$$

By (11) and (12), we have

$$\frac{\partial}{\partial c^*_{nl}} \left((\operatorname{div} \boldsymbol{y})|_{T_{knl}} |T_{knl}| \right) = \frac{\partial}{\partial c^*_{nl}} \left(c_{kn} + c^*_{nl} + c_{lk} \right) = 1 \,, \tag{14}$$

$$\frac{\partial}{\partial c^*_{nl}} \left((\operatorname{div} \boldsymbol{y})|_{T_{nml}} |T_{nml}| \right) = \frac{\partial}{\partial c^*_{nl}} \left(c_{nm} + c_{ml} - c^*_{nl} \right) = -1 \,. \tag{15}$$

Hence, (13) yields

$$\frac{1}{|T_{knl}|} \left(c_{kn} + c^*_{nl} + c_{lk} + \int_{T_{knl}} f \, dx \right) - \frac{1}{|T_{nml}|} \left(c_{nm} + c_{ml} - c^*_{nl} + \int_{T_{nml}} f \, dx \right) = 0 \,. \tag{16}$$

By (16) we find c^*_{nl}, which is assigned as the new value for the degree of freedom c_{nl}

$$c^*_{nl} = \frac{-\frac{1}{|T_{knl}|} \left(c_{kn} + c_{lk} + \int_{T_{knl}} f \, dx \right) + \frac{1}{|T_{nml}|} \left(c_{nm} + c_{ml} + \int_{T_{nml}} f \, dx \right)}{\frac{1}{|T_{knl}|} + \frac{1}{|T_{nml}|}} \,. \tag{17}$$

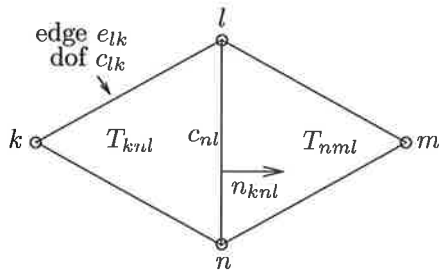

Figure 1: Two neighboring elements T_{knl} and T_{nml} with a common edge.

Table 1: Integral $\mathcal{J}(\boldsymbol{y})$ and efficiency index I_{eff} values with different mesh sizes and $\boldsymbol{y}$ for Example 1 (18).

	82 elems		1342 elems		8562 elems	
function $\boldsymbol{y}$	$\mathcal{J}$	I_{eff}	$\mathcal{J}$	I_{eff}	$\mathcal{J}$	I_{eff}
$G_N(\nabla v)$	3.45e-2	2.46	1.08e-2	4.09	5.57e-3	6.53
$G_{RT}(\nabla v)$	4.74e-2	2.88	6.00e-2	8.35	4.40e-2	16.81
$P^1G_{RT}(\nabla v)$	1.10e-2	2.09	7.39e-3	3.81	5.07e-3	6.60
$P^2G_{RT}(\nabla v)$	5.36e-3	1.87	1.05e-3	2.26	6.54e-4	3.21
$P^5G_{RT}(\nabla v)$	3.84e-3	1.79	2.67e-4	1.80	6.38e-5	1.91
$\boldsymbol{y}_{glo}$	3.62e-3	1.75	2.19e-4	1.72	3.31e-5	1.72

Let us denote by P the operator which calculates the values of (17) for all edges in a given mesh.

It can be proven that the iteration process described possesses *monotonicity* in the sense that the value of $\mathcal{J}(\boldsymbol{y}_k)$ monotonically decreases on each step k. Moreover, it has one other practical attractive property in that it easily admits parallelization.

4. NUMERICAL EXAMPLES

In this section, we test the performance of the error majorant $M_\oplus$ and indicator I with various methods of selecting $\boldsymbol{y}$, which were derived in the previous sections. For the purpose of measuring the performance of the majorant, we define the *efficiency index*

$$I_{eff} = \frac{M_\oplus}{\| u - v \|}.$$

The performance of the error indicator is tested by comparing the error distribution provided by the indicator to the exact error distribution.

To solve the model problem (1)-(2) we use the linear H^1 finite element. For the auxiliary function $\boldsymbol{y}$ we use both the post processing operators G_N, G_{RT}, and P and the global minimization method. For global minimization, we use linear Raviart-Thomas finite elements. In all numerical tests, the auxiliary function $\boldsymbol{y}$ is computed on the same mesh on which the original numerical approximation v was computed.

Example 1. We consider a problem, where

$$\Omega = [0,1]^2, \qquad f = 2(x(1-x) + y(1-y)), \qquad u = x(1-x)y(1-y). \tag{18}$$

Table 1 shows how the integral $\mathcal{J}(\boldsymbol{y})$ and the efficiency indexes I_{eff} for the upper bound $M_\oplus(v, \boldsymbol{y})$ behave with different $\boldsymbol{y}$ and different mesh-sizes. Post processing methods G_N and G_{RT} fail to produce a flux that would satisfy the equilibrium condition, $\operatorname{div} \boldsymbol{y} + f = 0$. For this reason, they do not provide a very accurate upper bound, and the values of I_{eff} are relatively large. By further post processing, the value of the efficiency index can be decreased close to the one obtained by globally solved $\boldsymbol{y}_{glo}$. According to numerical experiments, five iteration rounds are enough independent of the mesh size.

Figure 2 shows how the indicator I performs with different $\boldsymbol{y}$ in the first test example. Those elements, on which the error is greater than the average error, are marked with black color. In the top row, the leftmost picture is the result of using the exact error distribution. Here again $\boldsymbol{y}_{glo}$ denotes the function obtained by global minimization. As expected, global minimization of the upper bound gives good results. The performance of different post

processing methods does not differ drastically. Moreover, further equilibration of $G_{RT}(\nabla v)$ does not significantly improve the error distribution provided by I.

Example 2. The exact solution is unknown, we compute a reference solution calculated in a mesh with 286114 elements. The domain and load are as follows:

$$\Omega = [0,1]^2 \setminus \left([\tfrac{1}{2},1] \times [0,\tfrac{1}{2}]\right) , \qquad f = y^2 \sin(x) + x^2 \sin(y) . \tag{19}$$

Figure 3 contains the results for this test example. The results are similar to those from the previous example.

5. CONCLUSIONS

We conclude that in order to compute an efficient upper bound for the approximation error, the main problem is to obtain well enough equilibrated flux (minimizer of $\mathcal{J}(\boldsymbol{y})$). This task can be done with feasible computational effort using the presented new post processing technique, which admits parallel processing.

For the purpose of obtaining the error distribution, the first examples computed here do not demonstrate any significant difference between the various post processing methods tested. The proposed new post processing technique emphasizes the equilibration of the flux, but the equilibration alone does not guarantee that obtained flux is a good approximation of the true flux.

For full comparison of different post processing methods, additional numerical tests with different problem settings are required. Moreover, there are several possibilities to alter the proposed method. For example, instead of minimizing $\mathcal{J}$, another quantities can be used.

Acknowledgement. This research was supported by the grant N 40234 and N 40277 of the MASI Tekes Technology Programme and grant N 116895 of the Academy of Finland.

REFERENCES

[1] M. Ainsworth and J. T. Oden. A posteriori error estimation in finite element analysis, *Wiley ans Sons, New York*, 2000.

[2] I. Babuška and R. Rodriguez. The problem of the selection of an a posteriori error indicator based on smoothing techniques, *Internat. J. Numer. Meth. Engrg.*, 36: p. 539-567, 1993.

[3] F. Brezzi and M. Fortin. Mixed and hybrid finite element methods, *Springer Series in Computational Mathematics 15*, New York, 1991.

[4] P. Neittaanmäki and S. Repin. Computable Error Indicators for Approximate Solutions of Elliptic Problems, *Computational Methods in Applied Sciences, Springer, Netherlands*, 14: p. 203-218, 2009.

[5] P. Neittaanmäki and S. Repin. Reliable methods for computer simulation. Error control and a posteriori estimates, *Elsevier, Amsterdam*, 2004.

[6] P. A. Raviart and J. M. Thomas. Primal hybrid finite element methods for 2nd order elliptic equations, *Math. Comput.*, 31: p. 391-413, 1977.

[7] S. Repin. A Posteriori Estimates for Partial Differential Equations, *Walter de Gruyter, Berlin*, 2008.

[8] O. C. Zienkiewicz and J. Z. Zhu. A simple error estimator and adaptive procedure for practical engineering analysis, *Internat. J. Numer. Meth. Engrg.*, 24: p. 337-357, 1987.

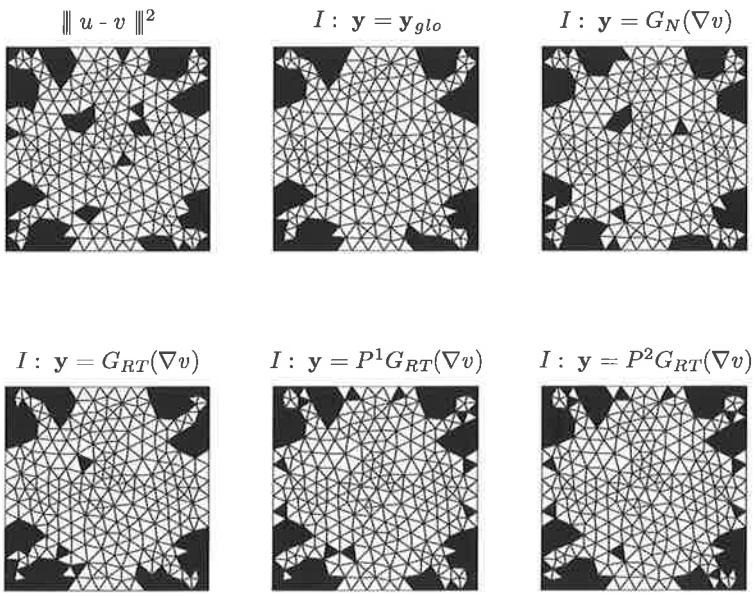

Figure 2: Example 1 (18): Performance of the post processing operator P and the indicator I in a mesh with 502 elements.

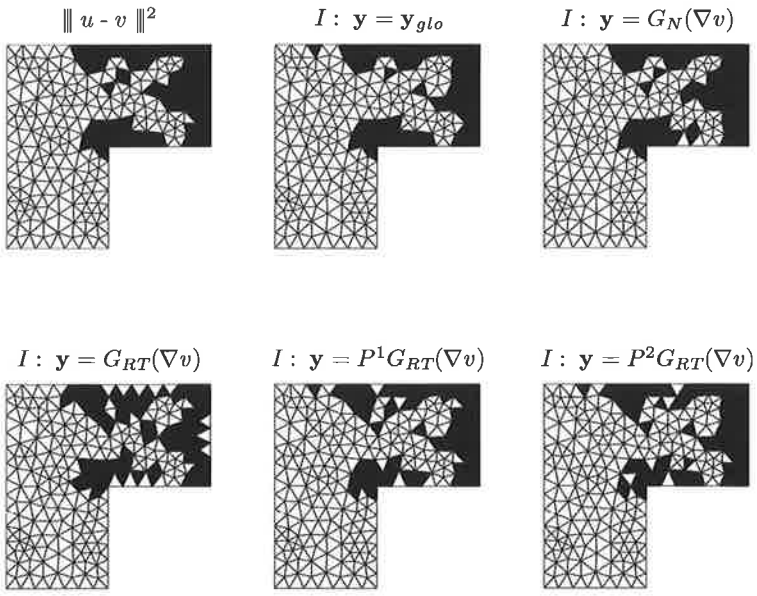

Figure 3: Example 2 (19): Performance of the post processing operator P and the indicator I in a mesh with 382 elements.

'HEALING' AND 'REPAIRING' TECHNIQUES FOR FASTER OPTIMIZATION WITH GENETIC ALGORITHM

J. JELOVICA & A. KLANAC

Marine Technology, Department of Applied Mechanics

Teknillinen korkeakoulu

P.O.Box 5300

FIN-02015 TKK, FINLAND

jasmin.jelovica@tkk.fi; alan.klanac@tkk.fi

ABSTRACT

This paper presents two techniques, the 'healing' and 'repairing' that can reduce optimization time when using genetic algorithm for structural optimization. The techniques can be applied to: (a) quickly find feasible designs from completely infeasible set of alternatives, and (b) to make the best infeasible designs feasible. These procedures are implemented into a genetic algorithm 'VOP'. The performance of the original and the modified version of the algorithm are compared with the widespread genetic algorithm 'NSGA-II' for the weight optimization of a 40 000 DWT chemical tanker midship section. The results show that these procedures can decrease the optimization time by approximately half.

1 INTRODUCTION

Design of modern ships introduces new complex structural solutions that must follow the increasing demand for more reliable and safe products. However, the available time does not follow the increasing complexity of design procedure, thus more advanced support systems are required that can assist designers. Such a system could be based on the optimization process. The intention of this study is to show how to enhance this process with respect to the increase of speed.

Complex ship structures involve large number of variables and even larger number of constraints. Variables are in structural optimization regularly discrete, whether they represent element size, material type, stiffener spacing etc. Constraints are non-linear and non-convex, typically involving yielding and buckling of structural elements. These reasons confine the choice of possible optimization algorithms to those that do not require gradient calculation of constraints and objective functions. Evolutionary algorithms have shown capability to handle such problems and provide sufficient benefits for the structure. One of them is the genetic algorithm (GA). Several applications have shown that GA can be a successful tool for practical problems in ship structural design and optimization, see e.g. Romanoff and Klanac (2007), Ehlers et al. (2007), Klanac and Jelovica (2009), Klanac *et al.* (2009).

Genetic algorithm operates in the design space, by having multiple design alternatives at hand when deciding where to continue the search from generation to generation. This number of available solutions is known as a population size and should grow with the number of considered

variables. Literature suggests using population size in range from 50 to 500; see Deb (2001). This lengthens the optimization time even for the simple engineering problem, since the number of generated and evaluated design alternatives before reaching the optima can be more than several thousands. Clearly, this can be rather costly when optimizing large ship structures, especially if *Finite Element Method* is applied for structural assessment. In any case, optimization should be short, and if it is time-consuming, it is often, for convenience, stopped prematurely, immediately after noticing some improvements in objective values and without attaining their optima. Making relevant conclusions based on such results can be misleading and costly in the later stages.

Optimization in tightly-constrained design space typically involves infeasible designs that do not satisfy all requirements included in the problem. Such designs are considered less valuable than the feasible designs, and are suppressed or completely neglected as for example in NSGA-II (Deb et al. 2002) or ε-MOEA (Deb et al. 2003) genetic algorithms. Here however, a different approach is suggested. Instead of rejection, infeasible design can be *repaired* so that it hopefully yields feasible design, partially maintaining the original's good objective(s) value(s).

The two procedures that form this approach are implemented in a GA called VOP. The original and the modified version of the algorithm are compared with NSGA-II, a recognized genetic algorithm that possesses several advanced features. To demonstrate this comparison, a structure of a 40 000 DWT and 180m long chemical tanker is optimized for the two objectives: minimum of hull steel weight and minimum of duplex steel weight.

The following chapter describes heal and repair techniques and the way how they can be implemented in the GA. Chapter 3 describes the VOP algorithm. Chapter 4 presents the test case that is used for optimization in Chapter 5, where heal and repair procedures are utilized and validated with NSGA-II. The last chapter concludes the paper.

2 HEALING AND REPAIRING FOR FASTER OPTIMIZATION

Diverse set of designs in each generation allows the GA to select better-than-average individuals that will be used for optimization continuation. Infeasible designs are in that sense considered less valuable and completely rejected in the prominent algorithms like NSGA-II or ε-MOEA once the feasible space has been found. But oftentimes those infeasible designs are much better according to objective(s) values(s). In the case where objective(s) depend on the numerous designs variables, for example in the weight optimization of a complex structure, changing few of them would not significantly alter the performance of a design. Then it could be useful to alter such design as little as possible to make it feasible but to retain its objectives.

Various schemes have been reported on how to make infeasible designs feasible. Oftentimes they are based on designer's insights on the physical problem they are dealing with. Certain way is observed how to satisfy a requirement and the designs are composed to fulfill it; see for example Todoroki and Haftka (1998), Liu et al. (2000), Chou et al. (2001), Cheong and Lai (2000). Repair technique is conceived here in a more generic manner. Designs are not improved based on some prior-knowledge specific to a problem at hand, instead they benefit from other solutions present in the current generation. However, there is one condition: a sensitivity of the constraints to variables should be known, $x_l \rightarrow g_j$, so that the variables that caused constraint violation can be identified.

This variable-constraint 'link' should be relatively easy to determine in optimization problem since constraints are always functions of decision variables, $g=g(\mathbf{x})$. At this point, the term 'infeasible' is extended beyond description of a particular design, identifying now a specific constraint that is violated, $g_j < 0$, and associated variable x_l. If a design is infeasible, there exists at least one broken constraint and corresponding infeasible variable. The idea is then to replace that infeasible variable with the variable from different design that does not violate the same constraint.

The proposed approach is divided in two procedures that can be applied in the following cases: (a) to quickly find feasible solutions from completely infeasible population and (b) to make the best infeasible designs feasible, in the presence of feasible designs in the population. The former is named 'heal', and the later 'repair' procedure. Both are described in the sequel.

2.1 Healing

If all designs in the population are infeasible, it does not mean that all of their constraints are too. When a particular constraint is observed, there exist designs in the population which do and do not break it, or even if they all break it, some do it less than the others. To make a design feasible, its infeasible variables are identified and replaced with corresponding feasible variables from a design that is best in objective(s) value(s). Besides 'healing' the design, i.e. turning it into feasible, the intention is to make it competitive objective-wise. There are two interesting categories of designs in the population: those with the smallest overall constraints violation and those with the best objective(s) value(s). The former offers a grater probability to become feasible and requires fewer variables to change. The latter group is tempting since designs with good objective(s) value(s) are the goal of the optimization, but are likely to have more infeasible variables that should be healed.replaced. It would be quite useful to make them feasible and simultaneously not significantly deteriorate their objective value(s). Oftentimes these two features are contrary in structural optimization where weight minimization makes light designs violate many strength constraints, while the feasible ones can in the beginning be quite heavy.

The suggested strategy is to heal N_{CON} of the best designs that violate the least amount of constraints and also N_{OBJ} of the best designs according to objective(s) value(s), starting with the best design in each category. Regardless of the category, every design which undergoes healing process gets its infeasible variables replaced with a feasible value from the best performing design for that variable.

To sort design alternatives according to their constraint violation, the following expression is used:

$$S_{CON}(\boldsymbol{x}) = \sum_{j=1}^{J} \mathrm{H}\left[g_j(\boldsymbol{x})\right] \tag{1}$$

where J is the number of constraints in the problem and $\mathrm{H}[\cdot]$ is a Heaviside operator defined by

$$\mathrm{H}\left[g_j(\boldsymbol{x})\right] = \begin{cases} -g_j(\boldsymbol{x}), \text{if } g_j(\boldsymbol{x}) < 0 \\ 0, \qquad \text{otherwise.} \end{cases} \tag{2}$$

Before using the Equation (1) infeasible constraint values are linearly normalized between 0 and 1.

The performance of the design in the normalized objective space is measured by

$$d_{OBJ}(\boldsymbol{x}) = \left\{ \sum_{m} \left[1 - f_m(\boldsymbol{x})\right]^2 \right\}^{1/2}. \tag{3}$$

The heal procedure is described below:

Step 1: Rank the population according to the smallest overall constraint violation using Eq. (1).
Step 2: Rank the population according to the best objective(s) value(s) using Eq. (3).
Step 3: Determine infeasible variables to the best N_{CON} designs that are ranked based on S_{CON} and the best N_{OBJ} designs based on d_{OBJ}.
Step 4: Starting from the best S_{CON} design, do for each N_{CON}: keep all feasible variables and replace each infeasible with a feasible value from best possible design according to d_{OBJ}.

If there is no feasible value from a particular variable in the population, take the one from the best S_{CON} design.

Step 5: Starting from the best d_{OBJ} design, do for each N_{OBJ} : repeat the action from the *Step 4*.

Population size must remain the same, thus $N_{CON} + N_{OBJ} \leq N$. Beside the designs selected for healing, remaining designs are chosen in a standard way, which can differ depending upon the algorithm where the heal technique is implemented. Remaining part of the population that is not healed is important because it:

- ensures functionality of the GA in case that heal technique has no effect due to improper variables-constraints connection,
- provides diversity in the population if the healing was unable to produce feasible designs, so it can be applied again in the following iteration,
- can be useful for the later stages of the optimization, after finding the feasible design.

Crossing-over two designs can change them radically. Therefore, this operator is disabled when using the heal technique in order to increase the success of producing a feasible design. For the part of the population which is not healed, the crossover is used in a standard way to ensure normal GA process. Mutation operator is used on all designs without any exception as it changes the designs far less than the cross-over and does not present a big threat to their feasibility.

Heal technique is intended to create feasible designs in the first attempt, but even if it is unsuccessful, it should considerably reduce the overall constraint violation of the designs, positioning them close to feasible space. It can be used iteratively until feasible designs are found. Thereafter, it is replaced with the repair procedure.

2.2 Repairing

The repair procedure can be applied after obtaining the variable set that yields the feasible solution. If there are several feasible alternatives, the one with the best objective(s) value(s) is taken as a reference. It can be used as a model to repair the infeasible variables from the infeasible solutions, relying on the same variable-constraint mapping that is used for the healing procedure.

Which designs will be repaired depends upon their performance in objective space that is determined by Eq. (3). Only those infeasible designs that are better in objective(s) value(s) than the reference design will be repaired to make them feasible, simultaneously trying to avoid severe performance deterioration. Obviously there is no point in repairing an infeasible solution which originally performs worse than the reference design. Thus one can apply the repair technique on N_{REP} number of infeasible designs in the population which is automatically reduced if there is not as many better than the reference.

Assuming the existence of infeasible designs in the population which are performing better than the best feasible design, the following repairing technique can be applied to generate improved designs:

Step 1: Rank the population according to the performance of designs in objective(s) space by using Eq. (3).

Step 2: Determine the value of d_{OBJ} for the best feasible design and mark it as a reference design.

Step 3: Check how many infeasible designs are better than the reference design. If there is less than N_{REP} of them, assign that number to $N_{REP,REAL}$, otherwise $N_{REP,REAL} = N_{REP}$.

Step 4: To the best $N_{REP,REAL}$ infeasible solutions identify infeasible variables.

Step 5: Starting with the best infeasible design, do for each $N_{REP,REAL}$: keep all feasible variables and replace the infeasible with the corresponding reference design's variables.

Remaining $N - N_{REP,REAL}$ individuals are selected and processed following the normal procedure of the used optimizer. Variables from those designs that are repaired get mutated, but cross-over is disabled to prevent any possible performance degradation.

Repair technique can be used repeatedly with each new population, if there is at least one feasible solution present. If there is none, the heal technique is re-activated to create it. Healing the designs in such situation is much easier than in the beginning when they are far from the feasible space. Now only few variables are infeasible, so there is far greater chance of correcting them successfully. Healed designs should not differ much in objective(s) value(s) from the original. So throughout the optimization heal and repair strategies are active to aid in more efficient optimization.

3 'VOP' GENETIC ALGORITHM

To implement heal and repair strategies (H&R) a simple GA called VOP is used (Klanac and Jelovica 2007). VOP is a binary coded algorithm consisting of: a) a fitness calculator, b) the weighted roulette wheel selector operating on the basis of computed fitness values, and c) a subroutine executing the single-point cross-over with a probability of p_C and the bit-wise mutation with a probability of p_M. These are standard operators and are, except for the fitness calculator, elaborated in Deb (2001).

VOP's fitness function is defined as:

$$\varphi(\boldsymbol{x},i)=\left(\max_{\boldsymbol{x}\in\mathbf{X}^i}\left[d(\boldsymbol{x},i)\right]-d(\boldsymbol{x},i)\right)^{d(\boldsymbol{x},i)} \tag{4}$$

where the distance $d(\boldsymbol{x},i)$ of a design i from the origin of normalized objective space is obtained as:

$$d(\boldsymbol{x},i)=\left\{\sum_k\left[\bar{f}_k(\boldsymbol{x},i)\right]^2\right\}^{1/2},\forall k\in[1,M+J]. \tag{5}$$

and m is the number of constraints. Normalization of objective f_k for design i is linearly performed using

$$\bar{f}_k(\boldsymbol{x},i)=\frac{f_k-\min\limits_{\forall x\in\mathbf{X}^i}f_k}{\max\limits_{\forall x\in\mathbf{X}^i}f_k-\min\limits_{\forall x\in\mathbf{X}^i}f_k}. \tag{6}$$

4 OPTIMIZATION OF A TANKER STRUCTURE

Optimization will be performed on the 40 000 DWT and 180m long chemical tanker's midship section. Its main frame longitudinal elements are optimized for the smallest allowed scantlings, while keeping the topology of the structure unchanged. The tank's plating is built from duplex steel to resist the aggressive chemicals which are transported and is the only part of the structure with yield strength of 460 MPa. For the remaining structure, 355 MPa steel is used.

4.1 Problem description

Variables considered in the optimization are the plate thicknesses and stiffener sizes. Number of stiffeners per each strake is depicted in Figure 1 together with scantlings of the transversal structure. Considered variable values are discrete, having the step for the plates of 1 mm, a value in general appropriate for early design stage. Plate thicknesses in double bottom and double side

structure are assumed to be available from 8 to 23mm, except of stringers whose range is the same as for longitudinal bulkhead and the deck, 5 to 20mm. Stiffener sizes are taken as standard *holland* profiles.

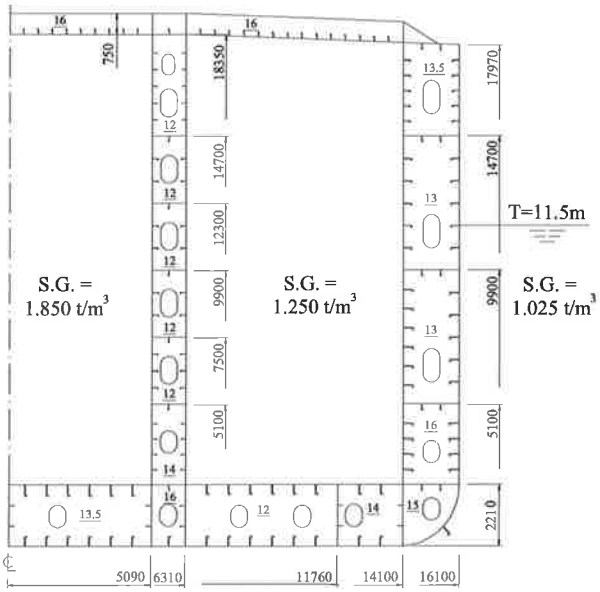

Figure 1. Half of the main frame section of a considered tanker and scantlings of the transverse structures (underlined)

The midship section is assumed to stretch between L/4 and 3L/4 cross-sections, without the change in scantlings. It is subjected to the hull girder loads, the cargo loads and the lateral hydrostatic loads, while ballast tanks are assumed to be empty. Pressure loads are calculated from liquid density indicated in Figure 1. The section is exposed to four critical hull girder loads acting on a section at two positions, L/4 and L/2. For the former, the shear force of 72 960 kN is applied in hogging and -74 880 kN in sagging, while for the later, the total vertical bending moment of 2 933 000 kNm is assumed for hogging and -2 410 000 kNm for sagging.

The response under the hull girder loads is calculated applying the numerical Coupled Beam method of Naar et al. (2004). On top of that is added the response of the panel under the cargo and hydrostatic loads, calculated with uniformly loaded simple beam.

Each strake is checked for eight failure constraints concerning plate yield and buckling, stiffener yield, lateral and torsional buckling, stiffener's web and flange buckling and crossing-over. These criteria are taken from DNV (2005), Hughes (1988) and Hughes et al. (2004). Altogether 376 failure criteria are calculated for each loading condition. They are transformed into adequacies which is a non-linear normalization function between the structural capacity of some structural element j, $a_j(\boldsymbol{x})$, and a loading demand acting on it, $b_j(\boldsymbol{x})$:

$$g_j(\boldsymbol{x}) = \frac{a_j(\boldsymbol{x}) - |b_j(\boldsymbol{x})|}{a_j(\boldsymbol{x}) + |b_j(\boldsymbol{x})|} \tag{7}$$

Two objectives are considered in this study: minimize the total weight of hull steel (abbreviated as f_1) and minimize the total weight of the duplex steel (abbreviated as f_2). Minimizing the hull weight would increase the payload capacity, but reduction in duplex steel would be the most significant for decrease in production costs since the material and labour costs for this steel are tenfold to those of high tensile 355 MPa steel used for the remaining structure.

Both weights are calculated by extending the obtained cross-sectional weight for the whole length of the ship. For the hull steel weight, additional 21.4t each 3.56m is added to account for the weight of the web frames.

5 THE OPTIMIZATION PROCESS

The optimization is carried out with the following parameters: population of 60 design alternatives, crossover probability 0.8 and mutation probability 0.003. Values are set based on the literature (Deb 2001) and previous experiences of the case (Klanac et al. 2008).

Before allowing H&R to operate, a relation between constraints and variables is established: if any of eight constraints from a strake is violated, assume both strake variables to be responsible (plate thickness and stiffener size). This is physically not entirely correct since stiffener-related limitations are not influenced by plate thickness and vice-versa. To satisfy cross-over constraint however it is better to change both variables, so this rule is for simplicity used for all constraints. Changing one part will influence the stress distribution throughout the structure and thus influence all the constraints. Therefore creating a feasible design from the infeasible in the proposed way cannot be guaranteed.

Random initial population is generated that will be used for all the optimization runs. It is completely infeasible, violating from 14 to 31 constraints. This number is actually not that high comparing to total 376 that need to be satisfied for a design to be feasible. Thus their constraints are mostly fulfilled, and those that are not indicate on infeasible variables, following the simple rule for their detection that was set.

5.1 Effects of healing the population

Optimizer starts to operate and determines that the initial population (P-A) is completely infeasible so it activates the healing procedure. Healing is used for 25 designs (41% of population) based on the smallest overall constraint violation, (P-B), 25 based on the best performance, (P-C) and the remaining 10 will be handled as usual with VOP, (P-D). Figure 2 shows the change in number of violated constraints after healing the first generation, according to defined population parts.

Originating from the solutions closest to the x-axis in P-A, first 25 designs from the second generation (P-B) are in average the heaviest designs in that generation as seen in Figure 3 and Figure 4, showing the f_1 and f_2, respectively. Thicker plate or larger stiffener generally cause smaller violation of associated constraints, thus heavier structure is usually less infeasible. That is why designs that are healed based on the smallest constraint violation are heavier (or worse in performance) than those healed based on objectives. The latter are located in P-C in Figure 3 and Figure 4. Table 1 shows that both feasible and infeasible average design in P-B is heavier than in P-C, in both objectives. Figure 3 and Figure 4 visualize also the decrease of feasible solutions in P-C compared to P-B. Contrary to first 25 designs in the healed generation, second 25 originally brake more constraints and are harder to make feasible. Figure 2 and Table 1 confirm this reduced feasibility in P-C. Majority of feasible solutions created using healing is present in the first half of P-B and in the middle and second half of P-C part of the population – those having originally less infeasible variables. Heal technique managed to create totally 18 feasible designs out of 50 attempts (36%), although the remaining designs are also competitive, braking up to four constraints but mainly only one. A qualitative feasible design can arise if those infeasible designs are crossed-over in further stages of optimization.

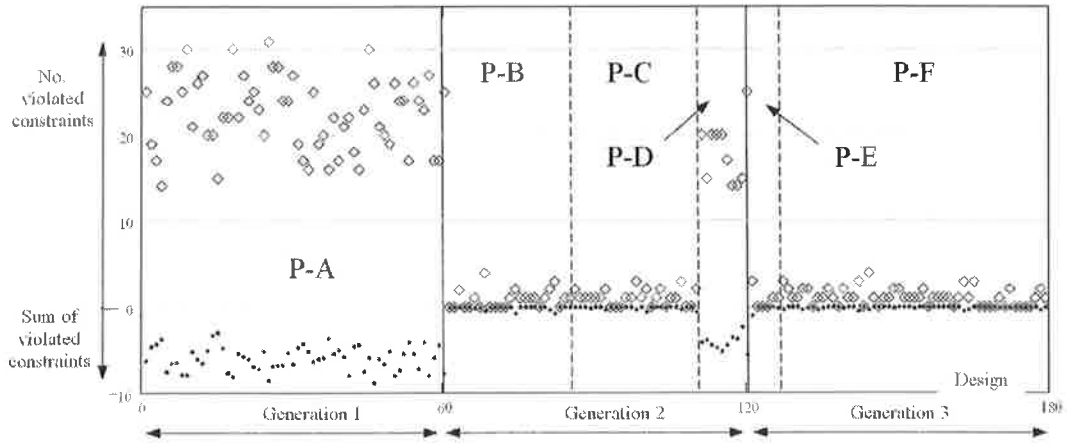

Figure 2. VOP – H&R: Constraint violations of the first 180 designs

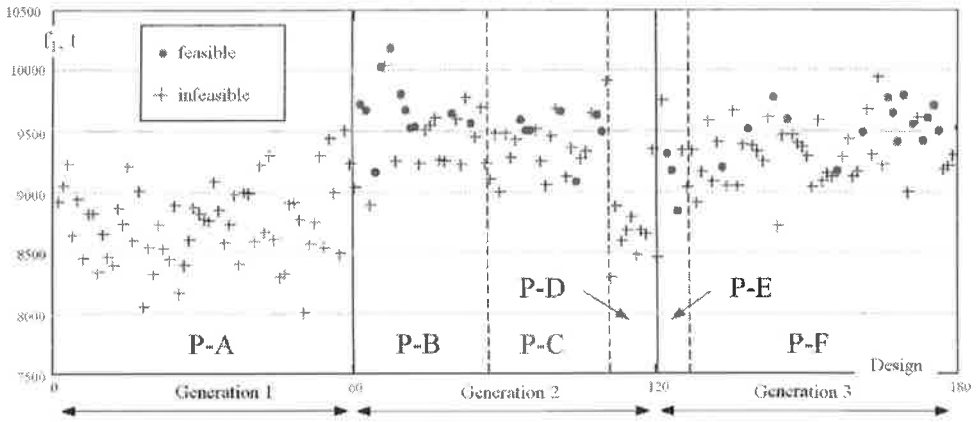

Figure 3. VOP – H&R: Total hull steel weight of the first 180 designs

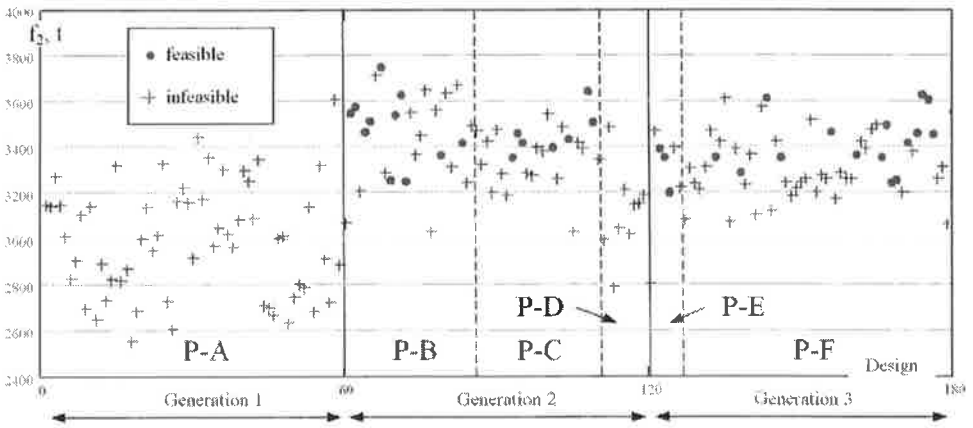

Figure 4. VOP – H&R: Total duplex steel weight of the first 180 designs

Remaining 10 designs for the second generation (P-D) are selected and processed following the normal VOP procedure. They can be seen in Figure 2, Figure 3 and Figure 4. We can see the reduction in number of violated constraints when compared to first generation where they originate

from; see Figure 2. Obviously selection preferred less-infeasible designs having up to 20 broken constraints (and one with 25), which is smaller than the 31 in the initial population.

Table 1. VOP – H&R: Performance of different population parts from the first three generations

Generation		1	2			3	
Population part		P-A	P-B	P-C	P-D	P-E	P-F
Working mode		normal	heal cons	heal objs	normal	repair	normal
Number of designs		60	25	25	10	6	54
Number of feasible designs		0	11	7	0	3	16
Feasible	Avg. hull steel, t	-	9686	9500	-	9113	9550
	Avg. duplex, t	-	3483	3458	-	3317	3431
Infeasible	Avg. hull steel, t	8751	9451	9366	8685	9374	9300
	Avg. duplex, t	2997	3441	3344	3086	3364	3299

Comparing designs in P-D to those in P-B and P-C in Figure 3 and Figure 4 clarifies the reason for not healing the whole second generation – those solutions are much better in objective values. Table 1 shows that average infeasible design from P-D is in fact 800 t lighter in f_1 and 300 t lighter in f_2 than the average design from P-B and P-C. This will provide diversity for the continuation.

5.2 Effects of repairing the population

Continuing with the third generation, infeasible designs from part P-D are repaired since their objective(s) value(s) are better than the best feasible design. The best six of them will undergo repairing (P-E). Six designs or 10% of the population is the maximum amount of individuals that is repaired during the optimization. This will then not interfere much in normal GA operations in case the repair is not effective.

The best feasible solution from the second generation is selected as a 'donor' for repairing. Higher competition among input feasible solutions will yield a better donor design, so it is preferable to have more feasible individuals to choose from. Six designs from the second generation to be repaired in the third are there the best infeasible design, likely from population part P-D. Their infeasible variables are replaced with the feasible ones from the donor design. Repaired designs are presented in P-E in Figure 2, Figure 3 and Figure 4. It can be seen that three of them are repaired successfully while others are almost feasible. The first repaired solution is originally the lightest in the second generation and therefore requires replacing many infeasible variables. After repairing, it stays infeasible and becomes quite heavy. The following three designs are more successful, turning into feasible and importantly, lighter in both objectives than all feasible solutions from the second generation. This is tabulated in Table 1 where it can be seen that the average feasible design in P-E is 4-500 t lighter in f_1 than the average feasible design in P-B and P-C. Weight of duplex steel is some 150 t smaller in the same comparison. These designs will surely be selected in the following generation.

Remaining part of the population from the third generation (P-F) is taken from parts P-B, P-C and P-D and is processed normally. The weight of the resulting designs can be seen in Figure 3 and Figure 4. Clearly among the feasible designs in P-F there are no heavier designs from P-B. Having low fitness, they were not selected for continuation. f_1 of the average feasible design in P-F is 70 t lighter than in combined P-B and P-C population, while the f_2 is reduced by 35 t; see Table 1. Infeasible designs are in P-F also lighter than the ones in P-B and P-C where they originate from. They are not descendants from P-D since designs in P-F violate up to four constraints, much smaller than in P-D.

5.3 Comparing the performance of the algorithms

Optimization with VOP – H&R is continued until generation 350 when the progress became negligible. Starting with the same initial population and using the same parameters, normal VOP and also NSGA-II algorithm was run to compare the results but were both allowed continuing until generation 600. NSGA-II is a widespread multi-objective GA that uses the following concepts: elitism, non-dominated sorting of designs in objective space, crowding-distance operator, binary tournament selection and constraint-domination. Description of these concepts and the algorithm itself can be found in Deb et al. (2002).

Comparison of the optimization progress is tabulated in Table 2. Comparing the objectives in the given generations, clearly VOP - H&R surpasses other two algorithms. This is especially expressed in the beginning since the heal procedure reduced the search for feasible designs to only one generation, for which NSGA-II spend 15 and normal VOP 30 generations. The final design with VOP - H&R is for f_1 better by 90 t and 120 t from VOP and NSGA-II, respectively, while for f_2 by 35 and 100 t in the same algorithm order although the last two algorithms were run almost twice as long.

Table 2. Comparison of optimizers, presenting weight of hull steel (f_1) and weight of duplex steel (f_2) for the best designs of each objective in the given generations

Algorithm	VOP		VOP - H&R		NSGA-II	
Objective	f_1, t	f_2, t	f_1, t	f_2, t	f_1, t	f_2, t
Generation 50	8835	3150	7825	2715	8340	2795
Generation 100	8115	2835	7580	2680	7780	2760
Generation 200	7885	2795	7420	2645	7545	2735
Generation 300	7775	2745	7350	2645	7520	2735
End	7440	2674	7348	2632	7467	2734

5.4 Optimization outcome

Figure 5 presents the best design alternative from the three optimization runs. Its scantlings are not standardized, thus there can be significant differences in plate thicknesses and stiffener sizes from neighboring strakes. This design is compared with design of *minimum rule scantlings* obtained from the calculation of the rules of Bureau Veritas (2006). There is no corrosion addition in any of the presented designs.

In this study high loads are imposed to act on the main frame, requiring that it is not only used in L/2, where it has to deal with maximum vertical bending moment, but also in L/4 and 3L/4 where it is subdue to maximum shear force. Due to this conservative consideration, the minimal rule scantlings design shown in Figure 5, violates 32 constraints, mostly plate and stiffener yielding from the vertical strakes in longitudinal bulkhead, where it does not account for high shear force, but also plate yield in inner bottom. To account for this, plates are in inner bottom and also in bottom strakes for the optimized structuresignificantly thickened, however corresponding stiffeners are reduced guided by weight reduction. The optimized structure also has considerably higher plate thicknesses but also bigger stiffeners in longitudinal bulkhead. This is especially expressed for the lowest strakes, who deal with high cargo pressure. Those plates are the main reason for the increase of the weight of duplex steel, as seen in Table 3. Outer strakes in double side have generally smaller scantlings, while the inner are similar to bottom strakes – thickened plates and reduced stiffeners. Deck scantlings are reduced while the reduction in all stringers is quite significant.

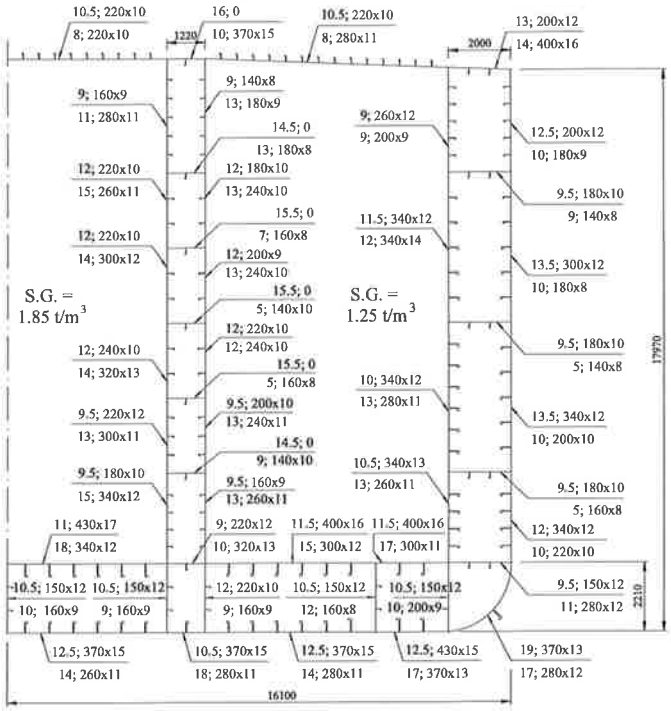

Figure 5. Scantlings of the main-frame members for the design of minimal rule requirements, shown above dimension lines, and for the design xH**, shown below dimension lines

The optimized structure has approached many constraint boundaries, mainly plate yield, plate buckling and stiffener yield from majority of strakes in the main frame, except for stringers in double side and cofferdam but also floors, whose constraint values are generally increased. That design has in total 52 active constraints, as seen in Table 3, where constraint is considered to be active if stress exceeds 3/4 of critical value.

Table 3. Objective's values for the best hull steel design obtained in optimization, compared with design of minimal rule requirements, and also the number of negative and active constraints

	Optimized structure	Min. rule req.
f_1, t	7353	7550
f_2, t	2652	2270
Negative con.	0	32
Active con.	52	18

6 CONCLUSION

The 'healing' and 'repairing' techniques for the genetic algorithm can reduce the number of evaluated designs needed to reach satisfactory optimization solutions. This allows resource and time savings when used in the early design stage. Benefits of these techniques have been shown on example of the main frame of 40 000 DWT chemical tanker. Optimization time was reduced by approximately half when compared to the 'normal' working mode of the algorithm and also when compared to one well-established GA. Crucial detail was to establish proper connection between the constraints and the variables. This was done here in a rather crude manner, however, even with that kind of mapping the results showed clear advantages of using healing and repairing techniques.

In general, it can be assumed that proper sensitivity between variables and constraints ensures the success of creating feasible designs. It also presumably allows capturing the good objective(s) values(s) in the later stages of the optimization when the repair technique is utilized. These assumptions require more thorough investigation.

Objectives used in this study do not form well-developed Pareto frontier, thus the designs are spaced rather condense in the objective space and it is easy to rank them there. The question arises on the proper selection scheme when dealing with large and dense frontier. This is definitely one of the questions to be answered in the following studies.

ACKNOWLEDGMENTS

The authors gratefully acknowledge the support of IMPROVE project, funded by European Union (Contract nr. 031382- FP6 2005 Transport-4), and the Technology Development Centre of Finland – TEKES, including Finnish shipbuilding industry, through the project CONSTRUCT. First author would also like to acknowledge the support of Finnish National Graduate School of Engineering Mechanics.

REFERENCES

Bureau Veritas 2006. *Rules for the classification of steel ships.*

Cheong, F., Lai, R. 2000. *Constraining the Optimization of a Fuzzy Logic Controller Using an Enhanced Genetic Algorithm*, IEEE Trans on Systems, Man, and Cybernetics – part B: Cybernetics, 30(1), p. 31-46.

Chou, H., Premkumar, G., Chu, C.H. 2001. *Genetic algorithms for Communications Network Design – An Empirical Study of the Factors that Influence Performance*, IEEE Trans on Evol Comp, 5(3), p. 236-249.

Deb, K. 2001. *Multi-Objective Optimization Using Evolutionary Algorithms*. Chichester: John Wiley & Sons.

Deb, K., Pratap, A., Agarwal, S., Meyarivan, T. 2002. *A Fast and Elitist Multiobjective Genetic Algorithm* – NSGA-II, IEEE Transactions on Evolutionary Computation. 6/1: 182-197.

Deb, K., Mohan, M., Mishra, S. 2003. *A Fast Multi-objective Evolutionary Algorithm for Finding Well-Spread Pareto-Optimal Solutions*, KanGAL Report Number 2003002

Det Norske Veritas 2005. *Rules for the classification of steel ships*. Høvik.

Ehlers, S., Klanac, A., Tabri, K. 2007. *Increased safety of a tanker and a RO-PAX vessel by implementing a novel sandwich structure.* 4th Int. Conference on Collision and Grounding of Ships. Hamburg:109-115.

Hughes, O.F. 1988. *Ship Structural Design*. Society of Naval Architects and Marine Engineers. New York:Wiley.

Hughes, O.F., Ghosh, B., Chen, Y. 2004. *Improved prediction of Simultaneous local and overall buckling of stiffened panels*. Thinn-Walled Structures, 42: 827-856.

Klanac, A., Jelovica, J. 2009. *Vectorization and Constraint Grouping to Enhance Optimization of Marine Structures.* Marine Structures, 22(2): 225-245.

Klanac, A., Ehlers, S., Jelovica, J. 2009. *Optimization of crashworthy marine structures*. In press by Marine Structures, available online 12 August 2009

Liu, B., Haftka, R.T., Akgün, M.A., Todoroki, A. 2000. *Permutation genetic algorithm for stacking sequence design of composite laminates*, Comp. methods in applied mechanics and engineering, 186, p. 357-372.

Naar, H., Varsta, P., Kujala, P. 2004. *A theory of coupled beams for strength assessment of passenger ships*, Marine Structures, 17(8): 590-611.

Osyczka, A. 2002. *Evolutionary Algorithms for Single and Multicriteria Design Optimization*. New York: Physica-Verlag.

Romanoff, J., Klanac, A. 2007. *Design Optimization of a Steel Sandwich Hoistable Car-Decks Applying Homogenized Plate Theory*. 10th Int. Symp. on Practical Design of Ships and Other Floating Structures – PRADS, Houston.

Todoroki, A., Haftka, R.T. 1998. *Stacking sequence optimization by a genetic algorithm with a new recessive gene like repair strategy*, Composites Part B, Elsevier Science, p. 277-285.

KANTAVIEN RAKENTEIDEN TOPOLOGIAN OPTIMOINNIN FORMULOINNISTA

Kristo Mela, Juhani Koski

Tampereen teknillinen yliopisto – Konstruktiotekniikan laitos
PL 589, 33101 Tampere
e-mail: kristo.mela@tut.fi, juhani.koski@tut.fi

TIIVISTELMÄ

Tässä työssä esitellään topologian optimoinnin tehtävänasetteluja ja tutkitaan niiden ratkaisujen ominaisuuksia. Topologian optimoinnissa minimoidaan useimmiten rakenteen komplianssia siten, että materiaalitilavuudelle on annettu yläraja. Muissa kantavien rakenteiden optimoinnin tehtävätyypeissä minimoidaan tavallisesti rakenteen materiaalitilavuutta jännitys- ja siirtymärajoituksin. Työssä tutkitaan näiden tehtävien ominaisuuksia ja arvioidaan ratkaistujen esimerkkien avulla tehtävänasettelujen tuottamia rakenteita.

1 JOHDANTO

Kantavien rakenteiden optimointi tarjoaa rakennesuunnittelijalle lukuisia työkaluja suunnittelutyön nopeuttamiseksi ja lopputuloksen tehokkuuden parantamiseksi. Perinteisesti optimointimenetelmiä on kehitetty ja sovellettu rakenteiden mitoitusongelmiin, joissa on tyypillisesti määritettävä rakenneosien poikkipintasuureet. Rakenteen optimaalisen muodon ratkaisemista on myös tutkittu laajalti.

Yllä mainituissa tehtävätyypeissä rakenteen osien kytkeytyneisyys, eli topologia, on ennalta määrätty. Tällöin suunnittelija on päättänyt rakenteen topologian, ja optimoinnin avulla selvitetään tälle topologialle parasta mahdollista muotoa ja mitoitusta.

Topologian optimoinnissa laajennetaan muodon optimointia siten, että myös rakenteen topologiaa voidaan muutella. Mitoitustehtävissä topologian muuttuminen tapahtuu rakenneosia (esim. ristikon sauvoja) lisäämällä tai poistamalla. Näin rakennesuunnittelijan ei tarvitse päättää ennakkoon rakenteen topologiaa, jolla on suuri vaikutus mitoitustehtävän optimitulokseen. Topologian optimoinnilla on siten mahdollista löytää edullisia rakenneratkaisuja, jotka ovat suunnittelijan intuition ja kokemuksen ulkopuolella.

Tässä työssä esitellään topologian optimoinnin tyypillisiä tehtävänasetteluja ja tutkitaan ratkaistujen esimerkkien avulla, minkälaisia rakenteita nykyisillä menetelmillä löydetään. Saatuja ratkaisuja arvioidaan suunnittelijan tarpeiden kannalta ja pohditaan tehtävänasettelujen soveltuvuutta käytännön apuvälineeksi.

Työ on jäsennetty siten, että osiossa 2 esitetään käsiteltävät tehtävänasettelut ja osiossa 3 topologian optimoinnissa yleisimmin käytetyt mallit. Osiossa 4 ratkaistaan yksinkertainen suunnitteluongelma eri rakennetyyppejä ja tehtävänasetteluja käyttäen. Saatuja tuloksia analysoidaan osiossa 5.

2 FORMULOINTEJA

Tässä työssä tarkastellut topologian optimoinnin tehtävät kirjoitetaan matemaattisen optimointiteorian yleisessä muodossa, joka on

$$\begin{array}{rl} \min\limits_{\mathbf{x}} & f(\mathbf{x}) \\ \text{siten, että} & g_i(\mathbf{x}) \leq 0, \quad i = 1, \ldots, p \\ & h_j(\mathbf{x}) = 0, \quad j = 1, \ldots, q \\ & \underline{x}_k \leq x_k \leq \overline{x}_k, \quad k = 1, \ldots, n \end{array} \tag{1}$$

Tavallisesti kantavien rakenteiden optimoinnissa kohdefunktio f on rakenteen materiaalitilavuus, joka on useissa suunnitteluongelmissa luonteva kriteeri rakenteen tehokkuudelle.

Optimointitehtävän epäyhtälörajoitukset tulevat suunnittelukoodeista ja standardeista sekä suunnittelijan asettamista valmistukseen tai tuotteen toimintaan liittyvistä lisävaatimuksista, jotka määräävät sallitut arvot rakenteen vasteille. Tavallisesti on huomioitava rakenteen lujuus, jäykkyys ja stabiilisuus, jolloin rajoitusehdot koskevat jännityksiä, siirtymiä ja esimerkiksi nurjahduskuormitusta. Lisäksi dynaamisissa kuormitustapauksissa on usein tarkasteltava rakenteen ominaiskulmataajuuksia tai siirtymävasteita. Analysointiyhtälöt ja mittojen kytkeminen toisiinsa muodostavat tavallisesti tehtävän (1) yhtälörajoitukset. Lisäksi teknisissä sovelluksissa on suunnittelumuuttujilla yleensä ala- ja ylärajat.

Kantavien rakenteiden optimoinnin kirjallisuudessa käsitellään usein tehtäviä, joihin on sisällytetty vain joitakin rajoitusehtoja. Esimerkiksi ristikkorakenteiden optimoinnissa saatetaan huomioida ainoastaan sauvoissa esiintyvät normaalijännitykset siten, että jännityksen suurin sallittu arvo on yhtä suuri veto- ja puristustapauksissa. Tällöin on jätetty nurjahduksen vaikutus sekä mahdolliset solmusiirtymiä koskevat rajoitukset huomiotta. Tällaisissa tehtävänasetteluissa ollaan usein kiinnostuneita valittuihin rajoitusehtoihin liittyvistä ilmiöistä, joiden tutkiminen on helpompaa, kun kaikkia käytännössä vaadittuja rajoitusehtoja ei huomioida. Tämä lähestymistapa on valittu tässäkin työssä. Tarkastelemalla sopivasti laadittuja yksinkertaisia tehtäviä pyritään tuomaan esiin eri formuloinnein saatujen optimirakenteiden välisiä eroja, jotka suunnittelija voi odottaa kohtaavansa mutkikkaampien tehtävien yhteydessä.

2.1 KOMPLIANSSIN MINIMOINTI

Tutkituin topologian optimoinnin tehtävä on komplianssin minimointiongelma siten, että rakenteen materiaalitilavuudelle on annettu yläraja. Kompliansi on rakenteeseen kohdistuvien kuormitusten tekemä työ, jota minimoimalla rakenteesta pyritään saamaan mahdollisimman jäykkä.

Kontinuumiformuloinnissa lähtökohtana on annettu suunnittelualue, jossa tuennat ja kuormitukset tunnetaan. Suunnittelumuuttujana on rakenteen materiaalijakautuma ja tilamuuttujana siirtymäkenttä. Optimointimuuttujien arvot on valittava siten, että tasapainoyhtälöt toteutuvat jokaisessa materiaalipisteessä. Tehtävän numeerista ratkaisua varten suunnittelualue diskretoidaan elementtimenetelmän mukaisesti ja materiaalijakautumaa sekä siirtymiä tarkastellaan elementtitasolla. Näin ääretönulotteinen optimointitehtävä on äärellistetty, ja topologian optimointitehtävä voidaan kirjoittaa muodossa

$$\begin{aligned} \min_{\mathbf{x},\mathbf{u}} \quad & \mathbf{p}^{\mathrm{T}}\mathbf{u} \\ \text{siten, että} \quad & \mathbf{K}(\mathbf{x})\mathbf{u} = \mathbf{p} \\ & V(\mathbf{x}) \leq V_{\max} \\ & \underline{x}_i \leq x_i \leq \overline{x}_i, \quad i = 1, \ldots, n_E \end{aligned} \tag{2}$$

Jokaiseen elementtiin, joita suunnittelualueessa on n_E kappaletta, on liitetty muuttuja x_i. Tämä kertoo, sijoitetaanko elementtiin materiaalia.

Elementtimenetelmän mukaisen diskretoinnin seurauksena saadaan globaali kuormitusvektori $\mathbf{p}$ sekä jäykkyysmatriisi $\mathbf{K}$, jotka riippuvat muuttujista $\mathbf{x}$. Tässä työssä kuormitukset ovat kuitenkin vakioita. Siirtymäkenttäfunktion sijasta elementtien solmusiirtymät, jotka on koottu vektoriin $\mathbf{u}$, ovat lisäksi optimointimuuttujina.

Usein tehtävästä (2) eliminoidaan yhtälörajoitukset ratkaisemalla solmusiirtymät tasapainoyhtälöistä annetuilla muuttujien $\mathbf{x}$ arvoilla esimerkiksi valmisohjelmaa käyttäen. Tällöin solmusiirtymät voidaan kirjoittaa muuttujien $\mathbf{x}$ funktioina, ja tehtävä menee muotoon

$$\begin{aligned} \min_{\mathbf{x}} \quad & \mathbf{p}^{\mathrm{T}}\mathbf{u}(\mathbf{x}) \\ \text{siten, että} \quad & V(\mathbf{x}) \leq V_{\max} \\ & \underline{x}_i \leq x_i \leq \overline{x}_i, \quad i = 1, \ldots, n_E \end{aligned} \tag{3}$$

Formuloinnissa (2) sekä kohdefunktio että rajoitusfunktiot tunnetaan yleensä eksplisiittisesti, ja niiden derivaattojen laskeminen optimointimuuttujien suhteen on suoraviivaista. Toisaalta muuttujia on $q + n_E$ ja rajoitusehtoja $q + 1$ kappaletta, missä q on vapaiden siirtymävapausasteiden lukumäärä. Vastaavasti formuloinnissa (3) on n_E muuttujaa ja yksi rajoitusehto, mutta kohdefunktion ja sen derivaattojen arvojen laskemiseksi on elementtimenetelmän tasapainoyhtälöt ratkaistava luotettavasti kaikilla muuttujien $\mathbf{x}$ arvoilla. Formulointien (2) ja (3) ominaisuuksia on esitetty tarkemmin viitteessä [1].

2.2 JÄNNITYSRAJOITETTU MATERIAALITILAVUUDEN MINIMOINTI

Kantavien rakenteiden optimoinnin yksi yleisimpiä tehtäviä on rakenteen materiaalitilavuuden minimointiongelma. Rajoitusehdot liittyvät tavallisesti rakenteessa esiintyviin siirtymiin tai jännityksiin. Tässä työssä tarkastellaan tehtäviä, joissa huomioidaan vain jännitysrajoitukset. Eri rakennetyypeille jännitysrajoitusehdot ovat erilaisia. Esimerkiksi ristikoissa sauvojen normaalijännitysten on pysyttävä sekä vedossa että puristuksessa suurinta sallittua arvoa pienempänä. Yleisemmissä tapauksissa (levyt, 3D-kappaleet) vaaditaan tyypillisesti, että jonkin myötöhypoteesin mukainen vertailujännitys (esimerkiksi von Mises-jännitys) on rakenteen jokaisessa pisteessä riittävän pieni.

Topologian optimoinnissa jännitysrajoitettua materiaalitilavuuden minimointiongelmaa on käsitelty huomattavasti vähemmän kuin komplianssitehtävää. Topologian optimointitehtävän diskretoitu muoto tuo jännitysrajoitusehtoihin teoreettisia ja laskennallisia haasteita, joihin kirjallisuudessa on pyritty vastaamaan [5, 6].

Yleisessä muodossaan jännitysrajoitettu materiaalitilavuuden minimointiongelma on

$$\begin{aligned} \min_{\mathbf{x},\,\mathbf{u}} \quad & V(\mathbf{x}) \\ \text{siten, että} \quad & \mathbf{K}(\mathbf{x})\mathbf{u} = \mathbf{p} \\ & \underline{\sigma}_i \le \sigma_i(\mathbf{x},\mathbf{u}) \le \overline{\sigma}_i \quad i = 1,\ldots,n_E \\ & \underline{x}_i \le x_i \le \overline{x}_i, \quad i = 1,\ldots,n_E \end{aligned} \tag{4}$$

Nyt jokaisella elementillä on oma jännitysrajoitusehtonsa, joten vaikka tasapainoyhtälöt poistettaisiinkin formuloinnista, on rajoitusehtoja yhtä monta kuin tuntemattomiakin. Tämä lisää tehtävän numeerisen ratkaisemisen haastetta erityisesti kontinuumiformuloinnissa, jossa elementtien lukumäärä voi olla hyvinkin suuri.

Ristikoilla on varauduttava sauvojen veto- ja puristusjännityksiin, jolloin sauvajännityksille annetaan sekä ylä- että alarajat, jotka välttämättä eivät ole yhtä suuret. Jos elementeillä on useampia jännityskomponentteja, jännitys σ_i on usein jokin jännityskomponenteista laskettu vertailujännitys, jolle tyypillisesti annetaan vain yläraja.

Sauvarakenteiden materiaalitilavuuden minimointiongelma voidaan kirjoittaa myös lineaariseksi optimointitehtäväksi (LP), jonka ratkaiseminen on huomattavasti helpompaa kuin yleisemmän tehtävän (4). Tällöin optimointimuuttujina ovat sauvojen poikkipinta-alat ja normaalivoimat. Rajoitusehtoina ovat normaalivoimien avulla kirjoitetut jännitysrajoitukset sekä rakenteen staattisen käypyyden takaavat tasapainoyhtälöt. Formuloinnista on jätetty kinematiikan yhteensopivuusehdot huomiotta, ja tehtävä voidaan kirjoittaa muodossa

$$\begin{aligned} \min_{A_i,\,N_i} \quad & \sum_{i=1}^{n} L_i A_i \\ \text{s.e.} \quad & \mathbf{BN} = \mathbf{F} \\ & \underline{\sigma}_i A_i \le N_i \le \overline{\sigma}_i A_i \quad i = 1,\ldots,n \\ & \underline{A}_i \le A_i \le \overline{A}_i \qquad i = 1,\ldots,n \end{aligned} \tag{5}$$

missä L_i on sauvan i pituus, $\mathbf{N}$ on sauvojen normaalivoimat sisältävä vektori ja $\mathbf{B}$ on tasapainoyhtälöiden kerroinmatriisi. Topologian optimoinnissa asetetaan tavallisesti $\underline{A}_i = 0$. Staattisesti käyvän rakenteen takaamiseksi tarvitaan $p = n - n_R$ lineaarisesti riippumatonta tasapainoyhtälöä, missä n_R on ristikon hyperstaattisuuden kertaluku.

Tehtävän (5) ominaisuudet tunnetaan hyvin [9]. Jos tuloksena saadaan isostaattinen rakenne, toteutuvat yhteensopivuusehdot automaattisesti, ja ratkaisu on myös tehtävän (4) optimi. LP-tehtävän ratkaisu voi myös johtaa mekanismiin, joka toteuttaa tasapainoyhtälöt, mutta on epästabiili. Optimiristikon voi olla myös hyperstaattinen. Tällöin yhteensopivuusehtojen toteutuessa on saatu tehtävän (4) optimaalinen ratkaisu. Usein yhteensopivuusehdot eivät kuitenkaan toteudu, jolloin LP-tehtävällä on saatu tehtävän (4) materiaalitilavuuden alaraja. Todellisen optimin löytämiseksi on ratkaistava epälineaarinen optimointiongelma (4), ja LP-tehtävän ratkaisua voidaan käyttää aloituspisteenä.

3 SUUNNITTELUALUEEN PARAMETRISOINTEJA

3.1 SIMP-MALLI

Edellä esitellyissä topologian optimoinnin tehtävissä (2) ja (4) kuhunkin elementtiin liitettiin suunnittelumuuttuja x_i, joka määrää, laitetaanko elementtiin materiaalia vai ei. Ristikkorakenteissa muuttujiksi x_i voidaan valita sauvojen poikkipinta-alat, mutta muissa tapauksissa muuttujien luonnetta on tarkennettava.

Suunnittelualueeseen sijoitettavan materiaalin jakautuma voidaan parametrisoida elementtitasolla kiinnittämällä muuttujat materiaalin kimmovakioihin. Olkoon $\mathbf{C}$ suunnittelualueeseen sijoitettavan materiaalin kimmomatriisi. Tällöin elementin i laskennallinen kimmomatriisi $\mathbf{C}_i$ on

$$\mathbf{C}_i = x_i \mathbf{C}, \quad x_i \in \{0, 1\} \tag{6}$$

Rakenteen materiaalitilavuus on

$$V(\mathbf{x}) = \sum_{i=1}^{n_E} x_i v_i \tag{7}$$

missä v_i on elementin i tilavuus.

Tämän parametrisoinnin seurauksena saadaan diskreetti optimointitehtävä, jossa muuttujat ovat binäärisiä. Muuttujien lukumäärä on yleensä kuitenkin niin suuri, että tämän tehtävän ratkaiseminen ei ole mielekästä. Tavallisesti topologian optimoinnissa binääriset muuttujat x_i relaksoidaan jatkuviksi välille $[0, 1]$, ja relaksoidun tehtävän ratkaisu pyritään ajamaan kohti diskreetin ongelman ratkaisua.

Tämä idea on saatu puettua yksinkertaiseen muotoon nk. SIMP-mallissa (Solid Isotropic Material with Penalization) [4, 3], joka on eräs topologian optimoinnin suosituimmista menetelmistä. SIMP-mallissa sakotetaan nollasta ja ykkösestä poikkeavia muuttujan arvoja käyttämällä elementin laskennallisena kimmomatriisina matriisia

$$\mathbf{C}_i = x_i^p \mathbf{C}, \quad p > 1 \tag{8}$$

Havaitaan, että muuttujan x_i väliarvoilla elementin laskennalliset kimmovakiot pienenevät jyrkästi elementin laskennalliseen materiaalitilavuuteen (7) nähden. Komplianssia minimoitaessa on siten materiaalin käytön kannalta edullista viedä muuttujat x_i lähelle arvoja 0 ja 1.

Sakotusparametrin p arvon valinnalla on vaikutusta SIMP-mallin mukaisen tehtävän numeeriseen ratkaisemiseen. Tavallisesti käytetään arvoa $p = 3$ tai aloitetaan arvosta $p = 1$ ja kasvatetaan sitä, kun parempaan tulokseen ei enää päästä.

Yhtälöstä (8) seuraa, että tasapainoyhtälöissä esiintyvä jäykkyysmatriisi $\mathbf{K}$ on muotoa

$$\mathbf{K}(\mathbf{x}) = \sum_{i=1}^{n_E} x_i^p \mathbf{K}_i \tag{9}$$

missä $\mathbf{K}_i$ on elementin i jäykkyysmatriisi.

SIMP-mallia käyttäen komplianssin minimointiongelma (3) voidaan kirjoittaa muodossa

$$\begin{aligned} \min_{\mathbf{x}} \quad & c(\mathbf{x}) := \mathbf{p}^{\mathrm{T}} \mathbf{u}(\mathbf{x}) \\ \text{siten, että} \quad & \sum_{i=1}^{n_E} x_i v_i \leq V_{\max} \\ & x_{\min} \leq x_i \leq 1 \end{aligned} \tag{10}$$

missä $x_{\min} > 0$ pieni, esimerkiksi $1 \cdot 10^{-3}$. Näin taataan, että tasapainoyhtälöiden jäykkyysmatriisi (9) pysyy kaikilla muuttujien arvoilla positiivi-definiittinä, mikä varmistaa solmusiirtymien luotettavan määrittämisen.

Tehtävä (10) voidaan ratkaista optimaalisuusehtoihin perustuvalla menetelmällä [3] tai jollakin yleisiin optimointitehtäviin soveltuvalla algoritmilla [11, 8, 9]. Useimmat menetelmät tarvitsevat tehtävän funktioiden gradientteja. Kantavien rakenteiden optimoinnin herkkyysanalyysiä soveltaen voidaan osoittaa, että komplianssin osittaisderivaatta muuttujan x_i suhteen on

$$\frac{\partial c}{\partial x_i} = -\mathbf{u}^{\mathrm{T}} \frac{\partial \mathbf{K}}{\partial x_i} \mathbf{u} = -p x_i^{p-1} \mathbf{u}^{\mathrm{T}} \mathbf{K}_i \mathbf{u} \tag{11}$$

3.2 PERUSRAKENNE

Ristikkorakenteiden topologian optimoinnissa suunnittelualueen parametrisointi tehdään tavallisesti käyttäen niin sanottua perusrakennetta (*ground structure*), joka koostuu useista nivelistä ja niiden välisistä sauvakytkennöistä [9]. Perusrakenteelle ratkaistaan mitoitusongelma, jossa poikkipinta-alojen sallitaan menevän nollaksi, toisin sanoen sauvojen annetaan poistua rakenteesta. Näin rakenteen topologia voi muuttua tavallisen mitoitustehtävän osana.

Koska perusrakenteeseen ei voida lisätä sauvoja optimoinnin aikana, on sen valinta löydettävissä optimitopologian kannalta tärkeässä asemassa. Yleisimmässä tapauksessa perusrakenteessa kaikkien nivelparien välillä on sauva. Tällöin sauvoja on $n = m(m-1)/2$ kappaletta, missä m on nivelten lukumäärä.

4 ULOKEKANNATIN

Tutkitaan seuraavaksi edellä esitettyjä topologian optimoinnin formulointeja kuvan 1 mukaista rakennetta tarkastelemalla. Vasemmasta reunasta jäykästi tuettu suorakaiteen muotoinen suunnittelualue on taso, jonka paksuus $t = 10\,\mathrm{mm}$. Kuormitustapauksia on kaksi kuvien 1a ja 1b mukaisesti. Pistekuormituksien suuruus $F = 100\,\mathrm{kN}$. Kuvassa esiintyvä pituusmitta $L = 1000\,\mathrm{mm}$. Suunnittelualueeseen sijoitettavan isotrooppisen materiaalin kimmomoduuli $E = 200\,\mathrm{GPa}$ ja Poissonin luku $\nu = 0{,}3$.

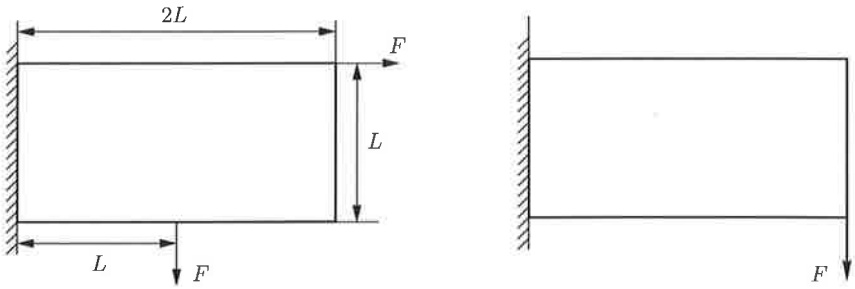

(a) LC 1 (b) LC 2

Kuva 1: Ulokekannatin ja kuormitustapaukset

4.1 LEVYRAKENNE

Diskretoidaan suunnittelualue käyttäen nelisolmuisia nelikulmioelementtejä, jotka ovat tasojännitystilassa. Elementtejä on vaakasuunnassa 80 ja pystysuunnassa 40 kappaletta, jolloin suunnittelumuuttujia on 3200 kappaletta.

Tarkastellaan komplianssin minimointiongelmaa, joka muodostetaan tehtävän (10) mukaisesti. Tehtävä ratkaistaan viitteessä [3] kuvatulla optimaalisuuskriteerien menetelmällä,

jossa haetaan optimaalisuusehdot (KKT-ehdot) toteuttavaa ratkaisua iteratiivisesti käyttäen heuristista sääntöä muuttujien arvojen päivittämiseen.

Suunnittelualueen tilavuus on $V = 2L^2t = 20 \cdot 10^6 \text{mm}^3$. Materiaalitilavuuden yläraja on valittu prosenttiosuus tästä arvosta. Laskennassa käytettiin arvoja $V_{\max} = 0{,}5V$ ja $V_{\max} = 0{,}25V$. Jälkimmäinen materiaalitilavuuden osuus vastaa ristikkorakenteen materiaalitilavuuden minimiä (ks. kohta 4.2.1).

Tarkastellaan aluksi tehtävää, jossa ainoa kuormitustapaus on kuvan 1a mukainen. Kuvaan 2 on piirretty saatu ratkaisu. Tummempi väri kuvaa suurempaa muuttujan x_i arvoa siten, että elementti on musta, kun $x_i = 1$ ja valkoinen, kun $x_i = x_{\min}$.

Kuvasta 2 nähdään, että eri materiaalitilavuuden ylärajaa käyttäen saadaan ratkaisuksi erilaisia topologioita. Lisäksi havaitaan, että materiaalin täyttämän alueen reuna on epäsileä johtuen suunnittelualueen diskretoinnista nelikulmioelementein. Muuttujien x_i väliarvojen sakottamisesta huolimatta numeeriseen ratkaisuun jää elementtejä, joilla $x_{\min} < x_i < 1$. Tällaisten elementtien tulkinta on epäselvää. Kirjallisuudessa ehdotetaan usein, että topologian optimoinnin jälkeen jatketaan muodon optimoinnilla siten, että topologian optimoinnin tuloksesta valitaan rakenteen reuna, johon muodon optimointia sovelletaan [3].

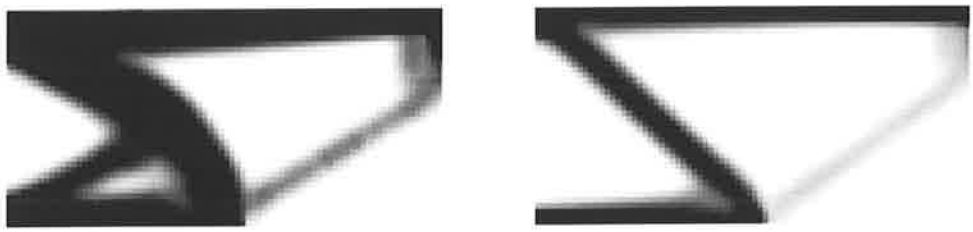

(a) $c_{\min} = 208{,}17\,\text{Nm}$ (b) $c_{\min} = 422{,}58\,\text{Nm}$

Kuva 2: Komplianssin minimointiongelman ratkaisu, kun käytettävissä oleva materiaalitilavuus on (a) 50%, (b) 25% suunnittelualueen tilavuudesta.

Kun kuormitustapauksia on useita, komplianssin minimointiongelmassa on kohdefunktion valintaan kiinnitettävä huomiota. Enää ei ole itsestään selvää, mitä komplianssia pitäisi minimoida. Yleensä kirjallisuudessa minimoidaan eri kuormitustapausten komplianssien painotettua summaa tai suurinta arvoa, jolloin tehtävän kohdefunktio on joko muotoa

$$f(\mathbf{u}_i) = \sum_{i=1}^{n_L} \omega_i \mathbf{p}_i^{\mathrm{T}} \mathbf{u}_i, \quad \omega_i \geq 0 \tag{12}$$

tai

$$f(\mathbf{u}_i) = \max_{i=1,\ldots,n_L} \{\mathbf{p}_i^{\mathrm{T}} \mathbf{u}_i\} \tag{13}$$

missä n_L on kuormitustapausten lukumäärä ja $\mathbf{u}_i$ on kuormitustapaukseen i liittyvä solmusiirtymien vektori.

Kohdefunktiolla (12) tai (13) varustetun usean kuormitustapauksen komplianssin minimointiongelman ratkaisu on monitavoitteisen optimointitehtävän

$$\begin{aligned} \min_{\mathbf{u}_j\ \mathbf{x}} \quad & \mathbf{f} := \{\ \mathbf{p}_1^{\mathrm{T}}\mathbf{u}_1\ \mathbf{p}_2^{\mathrm{T}}\mathbf{u}_2\ \cdots\ \mathbf{p}_{n_L}^{\mathrm{T}}\mathbf{u}_{n_L}\ \} \\ \text{s.e.} \quad & \mathbf{K}(\mathbf{x})\mathbf{u}_j = \mathbf{p}_j \qquad\qquad j = 1, \ldots, n_L \\ & V(\mathbf{x}) \leq V_{\max} \end{aligned} \tag{14}$$

eräs Pareto-optimaalinen piste. Tehtävässä (14) minimoidaan jokaisen kuormitustapauksen komplianssia samanaikaisesti. Tällöin optimiratkaisu on kompromissi eri kuormitustapauksien kesken. Monitavoiteoptimoinnin teoriasta [7] tiedetään, että näitä kompromissiratkaisuja (Pareto-optimeja) on tavallisesti ääretön määrä, joten on mahdollista, että tehtävällä on useita Pareto-optimaalisia topologioita.

Lasketaan kahden kuormitustapauksen komplianssin minimointiongelmalle (14) Pareto-optimaalisia ratkaisuja käyttäen skalarisoitua kohdefunktiota (12). Materiaalitilavuuden ylärajaksi valitaan 45% suunnittelualueen materiaalitilavuudesta. Tämä vastaa osiossa 4.2.1 saatavaa ristikkorakenteen materiaalitilavuuden minimiä.

Kuvassa 3 on kolme Pareto-optimaalista ristikkoa. Kuvan 3a ratkaisussa on kuormitustapauksen 2 osuus kokonaiskomplianssista mitätön. Näin on saatu kuormitustapauksen 1 komplianssin minimi siten, että tasapainoyhtälöt toteutuvat myös kuormitustapauksessa 2. Ratkaisu on lähes identtinen yhden kuormitustapauksen ongelman kanssa. Rakenteen oikeaan reunaan on lisätty ohut pystysuora osa, kytkee kuormitustapauksen 2 rakenteeseen. Vastaavasti kun kuormitustapauksen 1 osuus kokonaiskomplianssista jätetään vähäiseksi (kuva 3b), on rakenne käytännössä optimoitu kuormitustapauksen 2 komplianssin suhteen. Kuormitustapauksen 1 vaakasuora voima kytketään rakenteeseen yläreunassa olevan ohuen osan kautta.

Molempia kuormitustapauksia yhtä paljon painottamalla saadaan kuvan 3c mukainen ratkaisu, joka poikkeaa selvästi kuvien 3a ja 3b ratkaisuista. Nyt tuloksena on selkeä kompromissi kuormitustapausten väliltä.

(a) $\omega_1 = 1, \omega_2 = 0{,}001, c_{\min} = 233{,}79\,\mathrm{Nm}$

(b) $\omega_1 = 0{,}001, \omega_2 = 1, c_{\min} = 458{,}28\,\mathrm{Nm}$

(c) $\omega_1 = 1, \omega_2 = 1, c_{\min} = 852{,}66\,\mathrm{Nm}$

Kuva 3: Kahden kuormitustapauksen komplianssin minimointiongelman ratkaisuja eri painokertoimien yhdistelmillä.

4.2 RISTIKKORAKENNE

Tutkitaan seuraavaksi, minkälaisia optimitopologioita saadaan, kun kuvan 1 suunnittelualueeseen sijoitetaan ristikko. Valitaan perusrakenteeksi kuvan 4 mukainen ristikko, jossa on 12 sauvaa. Kuvissa 4a ja 4b näkyvät myös tarkastellut kuormitustapaukset.

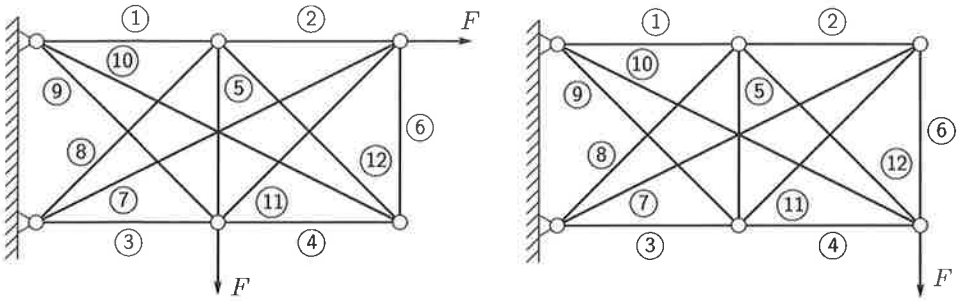

(a) Kuormitustapaus 1 (b) Kuormitustapaus 2

Kuva 4: Perusrakenne ja kuormitustapaukset

4.2.1 Materiaalitilavuuden minimointi

Ratkaistaan ensin materiaalitilavuuden minimointiongelma kummallekin kuormitustapaukselle erikseen. Lähdetään liikkeelle ratkaisemalla lineaarinen tehtävä (5). Jos tuloksena on isostaattinen ristikko, on saatu rakenne myös epälineaarisen tehtävän ratkaisu. Muussa tapauksessa käytetään LP-tehtävän ratkaisua epälineaarisen ongelman (4) aloituspisteenä.

Lineaarista tehtävää varten on kirjoitettava nivelten tasapainoyhtälöitä. Nyt hyperstaattisuuden kertaluku $n_R = 4$, joten tasapainoyhtälöitä tarvitaan yhteensä $p = 12 - 4 = 8$ kappaletta.

Suunnittelualueen poikkipinta-ala $A = Lt = 10000\,\mathrm{mm}^2$. Olkoon suurin sallittu jännitys $\sigma_{\mathrm{sall}} = 0{,}1\,\mathrm{GPa}$. Merkitään $A_0 = A/10$. Tällöin $\sigma_{\mathrm{sall}} = F/A_0$.

Tehtävän numeerisen ratkaisemisen tehostamiseksi skaalataan poikkipinta-alat kertoimella A_0, jolloin saadaan käyttöön dimensiottomat muuttujat $x_i = \frac{A_i}{A_0}$. Vastaavasti LP-formuloinnissa normaalivoimat voidaan skaalata termillä F. Materiaalitilavuuden lauseke puolestaan skaalataan vakiotermillä LA_0.

Saadun LP-tehtävän ratkaisut kummassakin kuormitustapauksessa on piirretty kuvaan 5. Molemmat ristikot ovat isostaattisia, joten ne edustavat myös epälineaarisen optimointitehtävän ratkaisua.

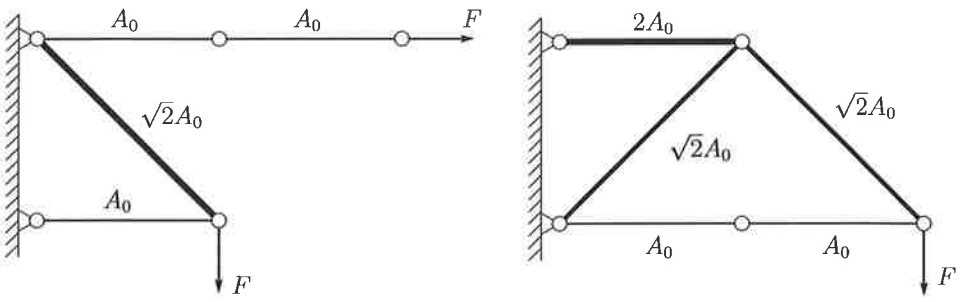

(a) $V_{\min} = 5LA_0$ (b) $V_{\min} = 8LA_0$

Kuva 5: Jännitysrajoitetun materiaalitilavuuden minimointiongelman ratkaisu (a) kuormitustapauksessa 1 ja (b) kuormitustapauksessa 2.

Ristikon kahden kuormitustapauksen materiaalitilavuuden minimointiongelman LP-formuloinnin ratkaisuna on hyperstaattinen rakenne (kuva 6a), jossa yhteensopivuusehdot eivät toteudu. Tätä ratkaisua aloituspisteenä käyttäen saadaan formuloinnin (4) mukaisen

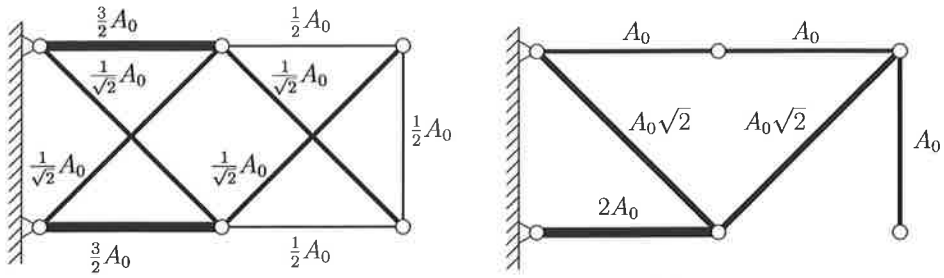

(a) $V_{\min} = 8{,}5LA_0$ (b) $V_{\min} = 9LA_0$

Kuva 6: Kahden kuormitustapauksen materiaalitilavuuden minimointiongelman (a) LP-ratkaisu, jossa yhteensopivuusehdot eivät toteudu, ja (b) formuloinnin (4) mukainen optimi.

tehtävän optimitulokseksi kuvan 6b ristikko, jonka topologia poikkeaa LP-tehtävän tuloksesta selvästi.

4.2.2 Komplianssin minimointi

Voidaan osoittaa, että ristikon komplianssin minimointitehtävä (3) on konveksi, sillä komplianssi on konveksi funktio poikkipinta-alojen suhteen, jos niiden alaraja on positiivinen [10]. Tällöin tiedetään, että tehtävän lokaali minimi on samalla sen globaali minimi, joten useimmilla epälineaarisen optimoinnin ratkaisumenetelmillä globaalisti optimaalinen ristikko on luotettavasti löydettävissä.

Yhden kuormitustapauksen ongelmassa voidaan osoittaa [2], että jos sauvojen normaalijännitysten suurin sallittu arvo on veto- ja puristuspuolella yhtä suuri ($\underline{\sigma} = -\overline{\sigma}$), saadaan komplianssin minimointitehtävän ratkaisuna sama topologia kuin jännitysrajoitettua materiaalitilavuutta minimoiden. Optimitopologiassa sauvojen poikkipinta-alat ovat vakiokertojaa vaille samat tehtävänasettelujen välillä.

Tämän tuloksen mukaiseen ratkaisuun päädytään, kun ratkaistaan yhden kuormitustapauksen komplianssin minimointiongelma. Optimitopologia on sama kuin materiaalitilavuuden minimointiongelmassa, ja sauvojen poikkipinta-alat riippuvat valitusta materiaalitilavuuden ylärajasta. Esimerkiksi kun $V_{\max} = 0{,}5V$, saadaan tehtävän (3) ratkaisuksi kuvan 4a mukainen ristikko, missä poikkipinta-alat ovat kaksi kertaa niin suuret kuin materiaalitilavuuden minimin ($V_{\min} = 0{,}25V$) tuottamassa ristikossa.

Kahden kuormitustapauksen komplianssin minimointiongelma on muodoltaan samanlainen kuin tehtävä (14). Valitaan $V_{\max} = 0{,}45V$, joka vastaa jännitysrajoitetun materiaalitilavuuden minimointiongelman optimaalista materiaalitilavuutta, ja ratkaistaan kaksikriteerisen tehtävän Pareto-optimaaliset pisteet rajoitusmenetelmää [7] käyttäen. Pareto-optimeja vastaavat minimaaliset pisteet on piirretty kuvaan 7. Kriteeri c_i on kuormitustapauksen i komplianssi. Kriteerien minimit (pisteet A ja B) on ratkaistu samaan tapaan kuin levyrakenteelle osiossa 4.1. Piste C on saatu painokertoimilla $\omega_1 = \omega_2 = 1$.

Kuvasta 7 nähdään, että tehtävällä on kolmenlaisia Pareto-optimaalisia ristikoita, joiden edustajat on piirretty kuvaan. Pisteitä A ja B vastaavat ristikot muistuttavat yksittäisten kuormitustapausten optimeja (kuva 5). Toinen kuormitustapaus on huomioitu lisäämällä rakenteeseen hyvin ohuita sauvoja. Sauvojen poikkipinta-alat muuttuvat Pareto-optimista toiseen siirryttäessä, kunnes tullaan alueelle, johon pistettä C vastaava ristikko kuuluu.

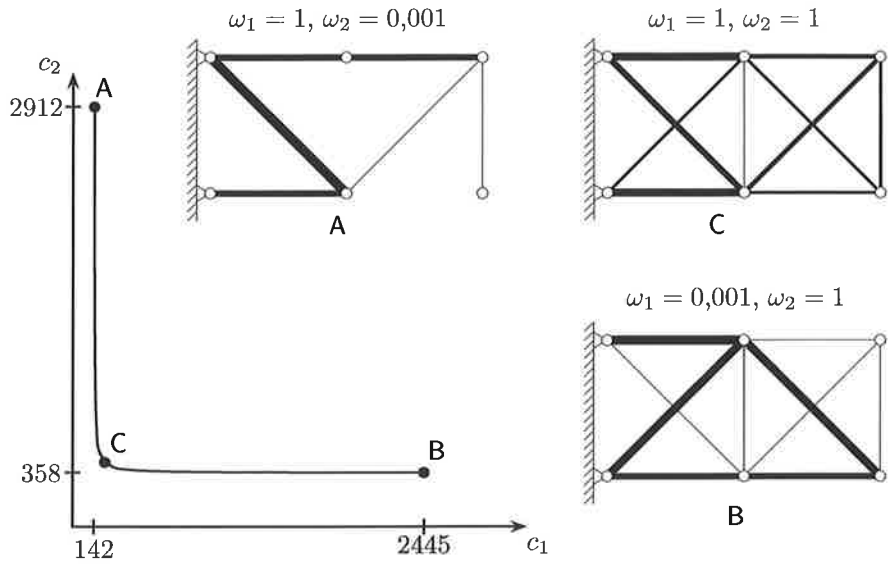

Kuva 7: Minimaaliset pisteet ja kolme Pareto-optimaalista ristikkoa. Kuormitustapausten kompliansit kuvan pisteissä ovat (yksikkönä Nm): A(141,53, 2912,6), B(2445,3, 357,87) ja C(213,10, 427,06).

5 YHTEENVETO

Edellä laskettujen esimerkkien perusteella voidaan tehdä muutamia havaintoja topologian optimointitehtävän asettamisesta ja ratkaisuista.

Materiaalikontinuumiin pohjautuvassa topologian optimoinnissa SIMP-malli on osoittautunut laskennallisesti kelvolliseksi tavaksi selvittää suunnittelualueen materiaalijakautuma. Jos ratkaisuun ei jää elementtejä, joissa $x_{\min} < x_i < 1$, voidaan rakenteen päälinjat nähdä kuvasta helposti. Osion 4.1 levytehtävän ratkaisussa on kuitenkin paljon elementtejä, joissa x_i on lähellä arvoa 0,5. Tällaisten elementtien kohdalla on epäselvää, tulisiko niihin sijoittaa materiaalia vai ei.

Vaikka SIMP-mallilla saataisiinkin ratkaisu, jossa kaikki muuttujat ovat ylä- tai alarajallaan, jää rakenteen reuna epäsileäksi. Tämä seikka voidaan korjata sovittamalla jokin sileä funktio kulkemaan rakenteen reunan muodostavien elementtien kautta. Tällaisen sovitteen yhteys optimaaliseen materiaalijakautumaan vaatii kuitenkin perusteellisempaa tarkastelua.

Levytehtävän topologian optimoinnin tulokset muistuttavat kehärakenteita. Ratkaisuista ei käy ilmi, voitaisiinko liitoskohtiin asettaa niveliä, jolloin rakenteesta tulisi ristikko. Tästä syystä onkin paikallaan suorittaa topologian optimointi eri rakennetyypeillä.

Sekä levy- että ristikkorakenteelle ratkaistiin materiaalitilavuudella rajoitettu kompliansin minimointiongelma. Tällä tehtävällä on laskennallisesti houkuttelevia ominaisuuksia (ristikoilla tehtävä on jopa konveksi), joten se voi soveltua topologian optimoinnin menetelmien numeeriseen testaamiseen. Rakennesuunnittelijan on kuitenkin otettava lähes aina jännitykset huomioon tavalla tai toisella. Koska tehtävässä (2) ei käsitellä jännityksiä mitenkään, ei ole takeita siitä, että saadussa ratkaisussa jännitykset pysyisivät sallituissa rajoissa. Periaatteessa on mahdollista suorittaa muodon optimointi kompliansin minimin tuottaneelle rakenteelle ja varmistua jännitysrajoitusten toteutumisesta. Ei kuitenkaan ole selvää, että samaan topologiaan päädyttäisiin, jos jännitysrajoitusehdot olisivat mukana alusta alkaen.

VIITTEET

[1] J.S. Arora and Q. Wang. Review of formulations for structural and mechanical system optimization. *Structural and Multidisciplinary Optimization*, 30:251–272, 2005.

[2] M. P. Bendsøe, A. Ben-Tal, and J. Zowe. Optimization methods for truss geometry and topology design. *Structural Optimization*, 7:141–159, 1994.

[3] Martin P. Bendsøe and Ole Sigmund. *Topology Optimization: Theory, Methods and Applications*. Springer Verlag, 2003.

[4] M.P. Bensøe. Optimal shape design as a material distribution problem. *Structural Optimization*, 1:193–202, 1989.

[5] Gengdong Cheng and Zheng Jiang. Study on topology optimization with stress constraints. *Engineering Optimization*, 20:129 – 148, 1992.

[6] P. Duysinx and M.P. Bendsøe. Topology optimization of continuum structures with local stress constraints. *International Journal for Numerical Methods in Engineering*, 43:1453 – 1478, 1998.

[7] H. Eschenauer, J. Koski, and A. Osyczka. *Multicriteria Design Optimization, Procedures and Applications*. Springer-Verlag, 1990.

[8] C. Fleury. Conlin: An efficient dual optimizer based on convex approximation concepts. *Structural Optimization*, 1:81–89, 1989.

[9] Uri Kirsch. *Structural Optimization*. Springer Verlag, 1993.

[10] Krister Svanberg. On local and global minima in structural optimization. In E. Atrek et al., editor, *New Directions in Optimum Structural Design*, pages 327–341. John Wiley & Sons, 1984.

[11] Krister Svanberg. The method of moving asymptotes—a new method for structural optimization. *International Journal of Numerical Methods in Engineering*, 24:359—373, 1987.

IS THE LIGHTEST STEEL STRUCTURE ALSO THE MOST ECONOMIC?

M. HEINISUO [1] & J. JALKANEN [2]

1) Tampere University of Technology, Department of Built Environment
P.O. BOX 600, 33101 Tampere, Finland
markku.heinisuo@tut.fi

2) KPM-Engineering Oy
Kalevantie 7 C, 33100 Tampere, Finland
jussi.jalkanen@kpmeng.fi

ABSTRACT

The weight of structure is the traditional minimized objective function in the optimization of building steel skeletons. Manufacturing, painting etc. costs are not considered separately and they are assumed to be directly proportional to the weight of structure. If all the requirements due to clients, authorities and partners in the projects, as well as the recent development in materials and production techniques, among other things, are taken into account, this traditional approach is not necessarily valid anymore today. Moreover, development in computational techniques gives engineers tools to search good solutions more widely than before. This paper demonstrates the use of the most novel information of fabrication costs and the effect of new steel materials for a simplified steel structure. Comparisons are done between weight and cost optimized structures. Particle swarm optimization (PSO) is chosen as the optimization technique. Based on calculated result it can be seen, that the weight optimum is not the cost optimum in the cases considered.

INTRODUCTION

The weight of structure is the traditional minimized objective function in the optimization of building steel skeletons because many contracts in the building projects are based on an estimation of kilograms of steel structures. However, the types of the steel structures have considerable effects to the cost per kilogram of steel. In reference [1] variation between 0,70 – 4,54 Euro/kg in cost of steel structures in completed Finnish projects is shown. In an Australian report of completed steel projects in 1990s the variation was 1,35 – 5,45 $/kg [2].

Companies which buy steel structures frequently, use the typing of steel structures to estimate the costs of steel structures. They use so called unit price groups as a basis for the contracts. Typically steel structures are divided into about ten groups based on the experience of previous projects. A unit price based on kilograms of steel in the group is defined for each group. This way leads to rather relevant solution to both partners of the contract if the amount of steel in groups can be estimated well and if many new solutions are not needed in steel structures.

If we build only similar buildings that we have built many times before, then these kg based cost estimation methods work well. The risks in cost are in the structures which we have not built before. However, buildings are almost always unique. The more complicated a building is, the more complicated it is to estimate the costs of the buildings in advance. Generally in complicated cases or when doing something which has not been done before it would be wise to look where the costs of steel structures are. Is the lightest steel structure also the most economic? The same question arises when developing quite new solutions for building markets.

In *mean* steel project the costs distribution of steel structures is the following [3]:

- Design 13 %,
- Material 38 %,
- Production 27 %,
- Coating 10 %,
- Erection 12 %.

It can be seen, that the material cost is 38 %. Production + coating costs are about the same as the material costs. The material cost may vary in the large scale. In [1] variations between 22 – 56 % are reported.

Important item in steel structures is the grouping of similar parts. This effect is not clearly studied for steel structures. In reference [4] one proposal based on measurements in Japanese factories is given. The result was that neither the lightest (having a lot of different parts) nor the heaviest (having very little amount of different parts) was the cost optimum, but the solution between those. Other important item is the life cycle costs of structures. Some studies dealing with this are available [5] to compare different skeleton solutions: steel, concrete and composite.

There are studies concerning the difference of the final cost between the minimum mass and the minimum cost of structures. According to [6], [7] and [8] it is 0.7 %, 7-26 % or 0 %-8.6 % respectively.

In this study the minimum weight solutions are compared to the cost optimum solutions. The costs functions include materials, production and coating. Design, erection and life cycle costs and grouping effects are not considered. The production cost functions which include costs of all actions needed to fabricate steel structures have been developed recently [6], [9], [10]. To calculate the production costs using these kinds of functions the quantity data can be derived from the product model of steel structures. This is essential, because the amount of this data is enormous. However, very detailed product models including all the features of steel structures are available in practical projects. This is true due to considerable research and development efforts done during the last 20 years. Cost functions are rather complicated and these cost calculations are impossible to perform without computer. In this study the cost functions of [11] are used.

The design variables are connected to the cross-section dimensions, joint feature dimensions and steel grades in this study. In these kinds of sizing optimization problems the shape and the topology of structure remain constant. The feasibility of the solution means that the steel structures fulfill the requirements of the most novel European standards [12] and parts referred in that. The objective function is either the weight of the steel structures or fabrication costs including production and coating.

The example structures are extremely simplified in this study. The idea is to consider the main question of the title. In both example problems there are the finite number of candidate solutions

due to the reason that design variables may have only discrete values. In practical cases it is not possible to check all candidate solutions and pick the best feasible, i.e. use the total enumeration, because there are just too many possibilities. In these kinds of computationally hard discrete structural optimization problems the particle swarm optimization (PSO) algorithm has proven to be suitable [8]. Some general considerations for the heuristic optimization algorithms are given in the text.

COST FUNCTIONS

The fabrication costs include in this case:

- material costs
- production costs based on following activities appearing when fabricating steel skeletons:
    - sawing,
    - drilling,
    - flame cutting,
    - beam welding, automatic submerged arc-welding in this case,
    - fitting welding, manual MAG welding in this case,
    - blasting,
    - painting.

All the costs are calculated based on the duration of each activity needed in the production. The duration of each activity is calculated by summing up the real activity time and time at post-activity and pre-activity. This means that we must simulate the fabrication in the factory. Each activity cost is the combination of the following components:

- labor cost,
- equipment cost of typical machines used in different activities,
- cost of use of the equipment,
- real estate investment cost,
- cost of the use of the real estate,
- cost of the materials,
- energy cost,
- inspection cost.

In Fig. 1 the components of production activity *sawing* and the aggregation of the fabrication costs are demonstrated. The numerical values are calculated using data of Case 2 presented later in this paper. The values are calculated using the cost estimation module implemented into the product modeling software Tekla Structures, which is used worldwide. By these means the costs of any steel structures can be calculated as easily as the kilograms of the structure.

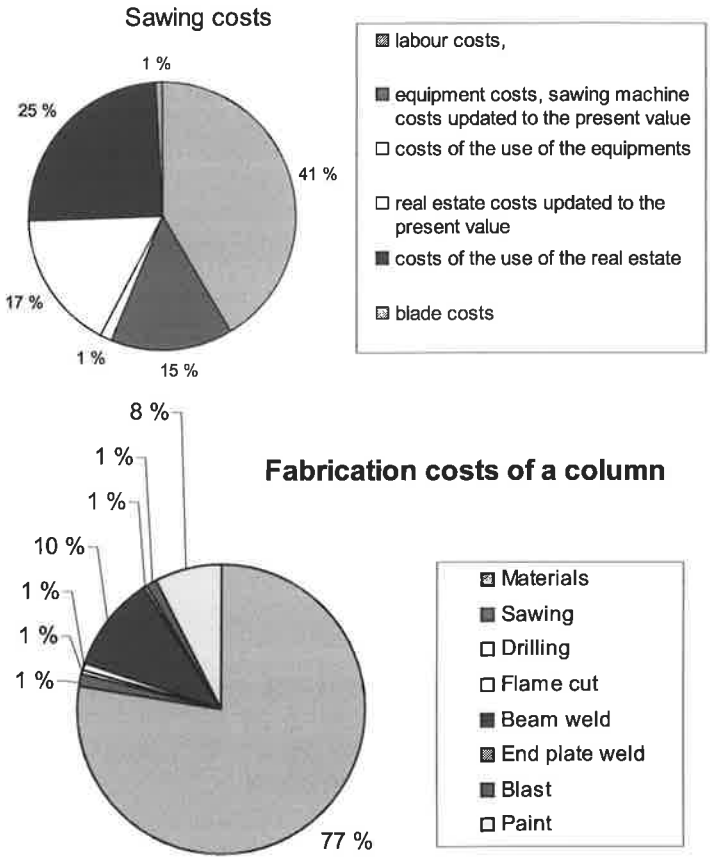

Figure 1. Components of production activity *sawing* and aggregation of fabrication costs for one column (Case 2).

It can be seen that in this case the material cost is dominating because only one joint, the base bolt joint, exists at one column.

PARTICLE SWARM OPTIMIZATION, PSO

Particle swarm optimization was developed by Kennedy et. al. in the mid 1990s [13]. The basic idea of stochastic PSO is to model the social behavior of a swarm (e.g. birds or fishes) in nature. A swarm of particles tries to adapt to its environment by using previous knowledge based on the experience of individual particles and the collective experience of the swarm. It is useful for a single member, and at the same time for the whole swarm, to share information among other members to gain some advantage. PSO belongs to the class of population based optimization methods, like genetic algorithm, because there is the group of solutions instead of a single solution. It can be seen that the group can offer some extra benefit compared to a single individual.

In PSO the new position $\mathbf{x}_{k+1}^{i}$ for particle i depends on the current position $\mathbf{x}_{k}^{i}$ and velocity $\mathbf{v}_{k+1}^{i}$:

$$\mathbf{x}_{k+1}^{i} = \mathbf{x}_{k}^{i} + \mathbf{v}_{k+1}^{i} \tag{1}$$

where the velocity is calculated as follows:

$$\mathbf{v}_{k+1}^{i} = w\mathbf{v}_{k}^{i} + c_1 r_1\left(\mathbf{p}_{k}^{i} - \mathbf{x}_{k}^{i}\right) + c_2 r_2\left(\mathbf{p}_{k}^{g} - \mathbf{x}_{k}^{i}\right). \tag{2}$$

$\mathbf{p}_{k}^{i}$ is the best ever position for particle i and $\mathbf{p}_{k}^{g}$ is the best ever position for the whole swarm. w is so called inertia, r_1 and r_2 are uniform random numbers $r_1, r_2 \in [0,1]$ and c_1 and c_2 are the scaling parameters. The value of w controls how widely the search process is done in the search space. The value of c_1 indicates how much a particle trusts on itself and c_2 how much on the swarm. The idea of the last two terms connected to c_1 and c_2 in the Eq. (2) is to direct the optimization process towards good potential areas in the search space Fig. 2. Usually, $0,8 \le w \le 1,4$ and $c_1 = c_2 = 2$ are selected. The value of w can be changed dynamically so that it is bigger during early iteration rounds and becomes smaller later when it is time to focus on the promising areas.

Basically PSO is an algorithm for continuous unconstrained optimization problems. Discrete design variables can be taken into account simply by rounding each design variable to closest allowed value in Eq. (1) and constraints can be handled by penalizing unfeasible solutions according to the unfeasibility. The standard form of constrained optimization problem:

$$\begin{aligned} &\min f(\mathbf{x}) \\ &g_i(\mathbf{x}) \le 0 \qquad i = 1,\ldots,n \end{aligned} \tag{3}$$

is replaced with a new unconstrained minimization problem in which the object function is:

$$\bar{f}(\mathbf{x}) = f(\mathbf{x})\left[1 + \sum_{g_i(\mathbf{x})>0} R\, g_i(\mathbf{x})\right] \tag{4}$$

and R is the penalty parameter. Penalizing can lead to such situation that solution $\mathbf{p}_{k}^{g}$ is no longer feasible. To avoid this, the best ever found feasible solution in PSO should be kept in memory.

The suitable size of the swarm depends on the amount of design variables so that the more variables the bigger the swarm. Usually the initial swarm is chosen randomly. As a terminating criteria the fixed iteration round amount can be used. Also the best known feasible object function value can be observed and if there is no improvement during last few rounds the optimization is terminated.

In discrete structural optimization the structure has to be analyzed hundreds or thousands of times during the optimization. It is useful to keep the values of the object function and constraints in memory some time after they have been calculated. Before a new analysis the memory is checked and if the solution is not there, the values of the object function and the constraints are calculated. It is typical for heuristic methods that later in the optimization process most of the needed values of the object function and constraints have already been calculated.

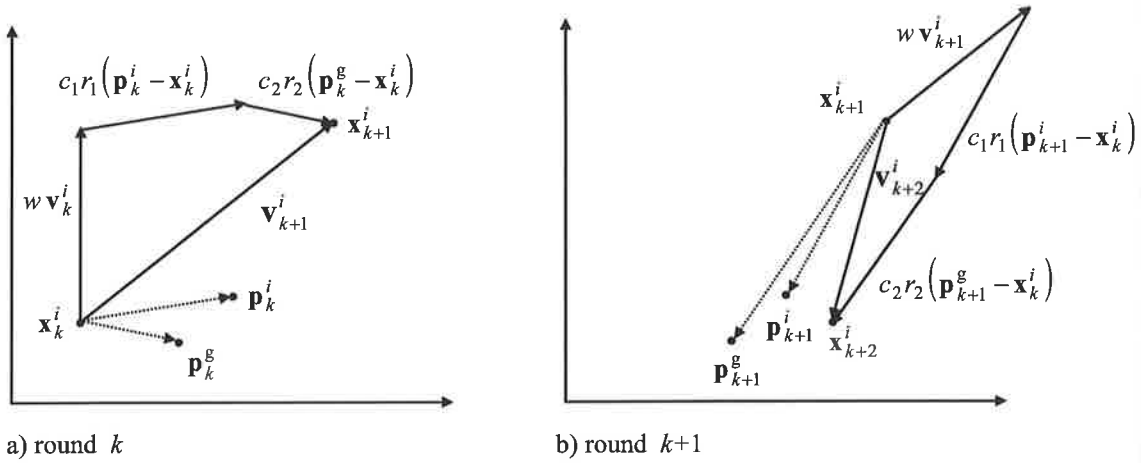

Figure 2. a) Step from point $\mathbf{x}_k^i$ to $\mathbf{x}_{k+1}^i$ and b) from point $\mathbf{x}_{k+1}^i$ to $\mathbf{x}_{k+2}^i$ in PSO. Inertia term (e.g. $w\mathbf{v}_k^i$) widen the optimization process and terms connected to $\mathbf{p}_k^g$ and $\mathbf{p}_k^i$ direct the search towards known good solutions.

HEURISTIC OPTIMIZATION ALGORITHMS

Heuristic means a deduction which does not fulfill all strict logical requirements but still often leads to a correct or a good answer. This means a stochastic or deterministic optimization algorithm which usually works but does not necessarily produce the optimum and may sometimes fail badly. The selection of heuristic optimization algorithms is large and there are also several different combinations. In many versions the idea is taken from nature like the evolution or the behavior of a swarm. The wide applicability and the ability to solve, at least approximately, computationally hard discrete and mixed-integer problems have made heuristic algorithms popular in structural optimization.

There are several common features between heuristic optimization algorithms even thought their backgrounds are different (Table 1). Some of the characteristics can be though as clear benefits and some unfortunate drawbacks from practitioner's point of view. The main reason that makes heuristic algorithms tempting is that they are rather simple and very flexible and still suitable for a variety of hard discrete or combinatorial optimization problems. The major limitation is the big number of objective and constraint function evaluations which means that structural analysis has to be done typically several hundred or thousand times during the optimization.

Table 1. The common advantages and disadvantages of heuristic optimization algorithms.

Advantages:	Disadvantages:
• Simple idea and implementation. • Very flexible. • Suitable for computationally hard discrete problems. • No need for sensitivity analysis. • The ability to avoid weak local optima. • Easy to use parallel processing. • Rapid improvement at the early iteration rounds. • Analysis tools can be "blackbox"-type.	• A lot of function evaluations (FEM-analysis) needed. • The quality of result unknown. • A lot of algorithms and many parameters connected to them. • No sensitivity information available. • How to deal with constraints? • Stochastic algorithms demand several optimization runs. • The similar way to solve easy and hard problems (e.g. linear-nonlinear, convex-nonconvex).

CASE 1

Consider first the minimum weight versus the minimum cost solution when the costs include only the material price of steel and the coating costs. This case has been recently considered in [14] for extremely expensive coating of steel structures: fire protection paint varying between 20 – 60 $/m^2 depending on the fire resistance requirements (R30/R60). It was found, that for R30 the cost without any fire protection, using heavier steel profile, was only about 5 % more expensive than to use the fire protection paint. If the life cycle costs are taken into account in this case the result may be different.

Consider next a not so expensive coating case. Search the optimum beam profile where the bending moment resistance is 500 kNm and the shear force resistance is 300 kN. The compressed flange is supported at every 2 m. The shape of the beam profile is symmetric welded I. The steel material is S355 and the unit price of the steel material is 1 Euro/kg. The ultimate limit state requirements are from [12]. Only restriction is that no local instability is allowed. The serviceability limit state is not considered because pre-chamfer is frequently used to eliminate the deflections for welded beams. The equations of the constraints and solution details using PSO are given in [15]. The variables are the dimensions (height, width, thicknesses of flanges and web) of the beam. The thicknesses should be in the ranges which are available in stocks. The width and the height are varying between 50 – 1000 mm with 5 mm steps.

Figure 3 illustrates the results. It can be seen, that the minimum weight solution means the same beam profile than the minimum cost solution if the coating costs are below about 4 Euro/m^2. Typically the painting costs are above this and then the height and the width of the beam are changing from the minimum weight solution as shown in Fig 3. E.g. the height of the beam is changing from above 700 mm to below 600 mm in the range of the painting costs (0-16 Euro/m^2) of the figure. Fig. 3 also shows the cost variation if the beam is made of S690 grade material. The unit cost for steel material in this case is taken from [16].

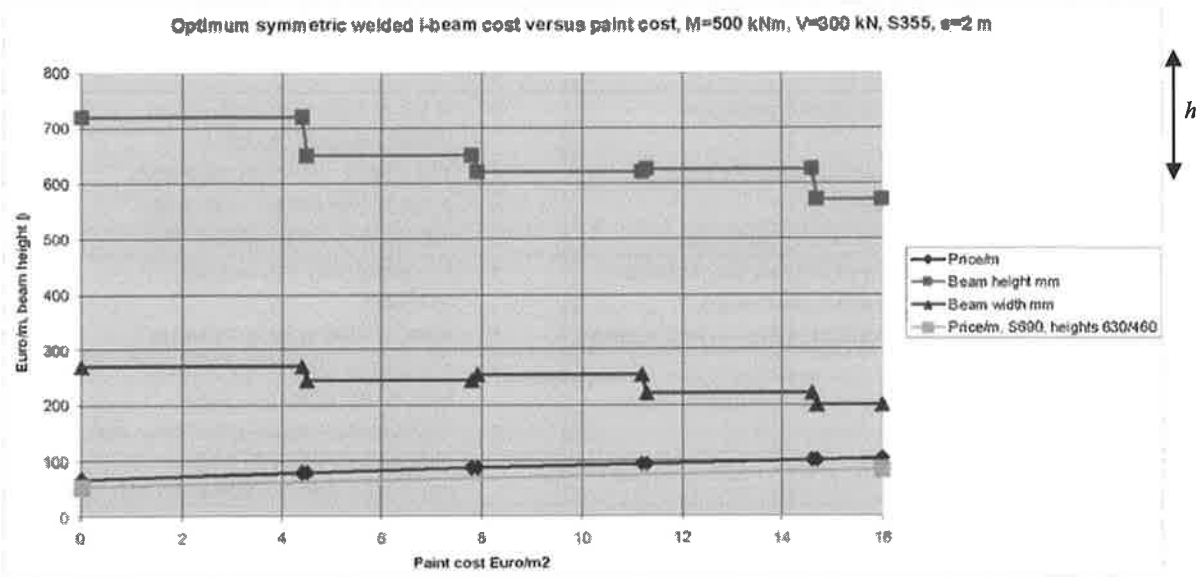

Figure 3. Effect of painting costs to the optimum shape of I-profile in bending and shear.

Perhaps the most important life cycle costs of steel structures are the possible preparations of coatings. This case has been considered in [17]. The re-use of steel products can be taken into account in the life cycle costs, too.

CASE 2

Consider next the optimum column design including all the fabrication costs described above. The structure is extremely simple including the welded symmetric I-profile and the base bolt joint at the bottom. At the top is a hinge joint and its fabrication costs are not taken into account. The details of this case have been presented in [18], [19]. The column considered is shown in Fig. 4. Constraints include the resistance checks for bending and axial force including flexural buckling around both main axes of the member cross-section, and the resistance check of the joint. The rotational stiffness around both axes of the base bolt joint is taken into account when calculating the buckling lengths of the column.

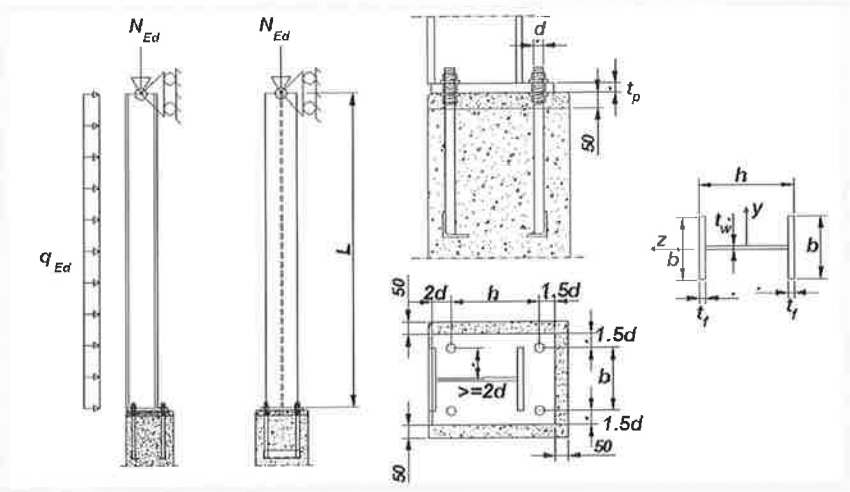

Figure 4. Column considered.

In this case the PSO was used ten times for the original problem which included over 900 Million candidate solutions. Since PSO is a stochastic algorithm one optimization run is not enough and several runs are needed in order to receive reliable results. Then the design space was reduced around the best PSO solution and the final solution was found using exhaustive search in this reduced design space (called "exact" in the next table). This technique seems to be very efficient for the solution of this type of problems.

The solution for one column span length and for one loading case is presented in Table 2.

Table 2: Results of the optimization $L = 8$ m, $N_{Ed} = 2000$ kN, $q_{Ed} = 10$ kN/m.

Case	d (mm)	t_p (mm)	h (mm)	b (mm)	t_f (mm)	t_w (mm)	f_y (MPa)	W (kg)	Cost (Euro)	Utility Column	Utility Joint
Min W (PSO)	24	40	270	280	15	8	420	700	1495	1.00	0.50
Min W (Exact)	20	30	275	280	15	8	420	689	1455	1.00	0.71
Min Cost (PSO)	16	40	325	330	15	8	235	826	1316	1.00	0.95
Min Cost (Exact)	16	35	325	330	15	8	235	820	1309	1.00	0.95

It can be seen, that the minimum cost solution is quite different to the minimum weight (W) solution in this case. Fig. 1 demonstrates the components of sawing costs and the aggregation of the fabrication costs for the optimum cost solution in this case. It can be seen, that in this case the material cost are dominating, because only the fabrication costs of the base bolt joint are taken into account in cost calculations. Regardless of that, the cost optimum solution is quite different to the weight optimum solution in this case.

CONCLUSIONS

It has been shown for extremely simplified structures that only when unrealistic small fabrication cost (coating costs below 4 Euro/m2) for steel structures are used the minimum weight solution is the same as the minimum cost solution. When the fabrication costs are taken into account using the most novel results from that research field and allowing the use of different steel grades the minimum weight solution is different to the minimum cost solution, using the input data of this study. In Case 2 the difference in costs between the minimum weight and the minimum cost solution was 11 %.

These results give an idea to search for new good solutions using new steel grades such as high strength, fire and weather resistant steels. The design, transportation, erection and life cycle costs should be in the cost functions in the future to minimize the risks in new solutions. When integrating search of good solutions to the product modeling techniques, brand new solutions may be found for steel structures. This means, that we should simulate the entire steel building process. Now we simulate only the activities in the factory in cost functions. Simulating the entire steel building process enables us to look for new solutions by taking into account e.g. automatisation in factories and in sites. The described optimizations can be done already at the preliminary stages if the product models are used in the project. Huge potential can be seen in this field in the future.

If the cost calculations can be done by practicing engineers as easily as the weight calculations, then there is no sense to use the weight as the criteria to make decisions of the final structures. Using reliable information of the costs for the structures the economical risks can be reduced at all stages of the building projects. In a pilot project completed recently in TUT the fabrication cost calculations used in this study were implemented into the most widely used (in Finland, and rather widely used globally) product modeling software. The result was that cost calculations can be done easily for many kinds of steel structures (product model ensures the generic forms of structures) by taking into account the costs of activities needed to fabricate steel structures. Forthcoming papers illustrate these efforts. Next we should implement mathematical optimization routines to that. We are approaching the situation where we do not need to think whether the weight optimum is also the cost optimum.

REFERENCES

[1] Salokangas J., Teräsrakentamisen kustannukset, TRY, *Teräsrakenteiden pääsuunnittelijan ja vastaavan teräsrakennetyönjohtajan kurssi*, Hämeenlinna, 13.12.2005 (in Finnish).

[2] Cordell Building Information Services, Cordell Building Cost Guide, Commercial Industrial, Vol 26 No 1, 1996, *Rawlinsons, Australian Construction Handbook*, The Rawlinson Group (ed), 1996.

[3] Evers H.G.A., Maatje IR.F., Cost based engineering and production of steel constructions, 1999.

[4] Sawada K., Shimizu H., Matsuo A., Sasaki T., Yasui T., Namba A., A simple function to estimate fabrication time for steel building rigid frames, in International Conference Proceedings: *Design, Fabrication and Economy of Welded Structures* (Eds. Jarmai K., Farkas J.), Horwood Publishing Limited, UK, 2008, pp. 135-141.

[5] Grierson D. E., Khajehpour S., Multi-Criteria Conceptual Design of Office Buildings Using Adaptive Search, *Artificial Intelligence in Engineering, Information Technology for Design, Manufacturing, Mainetance, and Monitoring*, Borkowski A. (Ed), Wydawnictwa Naukowo Techniczne, Warszawa, 1999.

[6] Pavlovčič L., Kranjc A., Beg D., Cost function analysis in the structural optimization of steel frames, *Structural and Multidisciplinary Optimization* 28, 2004, pp. 286-295.

[7] Sarma K., Adeli H., Cost optimization of steel structures. *Engineering optimization* 32, 2000, pp. 777-802.

[8] Jalkanen J., *Tubular Truss Optimization Using Heuristic Algorithms*, Dissertation, Tampere University of Technology, 2007.

[9] Farkas J., Jarmai K., Economic Design of Metal Structures, Millpress, Rotterdam, 2003.

[10] Klansek U., Kravanja S., Cost estimation, optimization and competitiveness of different composite floor systems - Part 1: Self-manufacturing cost estimation of composite and steel structures, *Journal of Constructional Steel Research* 62, 2006, pp. 434-448.

[11] Haapio J., Feature based fabrication cost estimation of steel structures, Tampere University of Technology (in preparation), 2010.

[12] EN 1993-1-1. Eurocode 3: *Design of steel structures*, Part 1-1: General rules and rules for buildings, CEN, Brussels, 2005.

[13] Kennedy J. and Eberhart R., Particle Swarm Optimization, Proceedings of the *IEEE International Conference on Neural Networks*, Perth, Australia, 1995.

[14] Jarmai K., Optimization of a steel frame for fire resistance with and without protection, in International Conference Proceedings: *Design, Fabrication and Economy of Welded Structures* (Eds. Jarmai K., Farkas J.), Horwood Publishing Limited, UK, 2008, pp. 79-88.

[15] Heinisuo M., Saikkonen M., Haapio J., Miles J., Welded steel beam design using particle swarm analysis, Proceedings of *14th EG-ICE Workshop*, Maribor, 2007.

[16] Johansson B., Buckling resistance of structures of high strength steel, in Use and Application of High-Performance Steel for Steel Structures, *Structural Engineering Documents* 8, IABSE, 2005.

[17] Sarma K. C., Adeli H., Life-cycle cost optimization of steel structures, *International Journal for Numerical Methods in Engineering*, 55, 2002, pp. 1451-1462

[18] Heinisuo M., Laine V., Saikkonen M., From 7D design to 8D design of steel structures, Proceedings of *15th EG-ICE Workshop*, Berlin, 2007.

[19] Heinisuo M., Laine V., Lehtimäki E., Enlargement of the component method into 3D, Proceedings of *Nordic Steel Construction Conference*, Malmö, 2009.

PUURAKENTEIDEN OPTIMOINTI

J. JALKANEN [1] & J. LÄNSILUOTO [2]

1) KPM-Engineering Oy
Kalevantie 7 C, 33100 Tampere
jussi.jalkanen@kpmeng.fi

2) Metsäliitto Osuuskunta, Puutuoteteollisuus
Tuulikuja 2, 02100 Espoo
jaakko.lansiluoto@finnforest.com

TIIVISTELMÄ

Tässä artikkelissa käsitellään kantavien rakenteiden optimoinnin soveltamista liima- ja kertopuisten runkorakenteiden suunnittelussa. Matemaattisen optimointiteorian käyttäminen entistä kilpailukykyisempien rakenteiden löytämiseksi on luonnollinen jatke niiden tietokoneavusteiselle rakenneanalyysille. Sen sijaan, että tyydyttäisiin olemassa olevien rakennevaihtoehtojen keskinäiseen vertailuun, optimointialgoritmien avulla voidaan etsiä uusia entistä parempia konstruktioita, jotka muuten jäisivät löytymättä. Minimoitavaksi kohdefunktioksi on valittu rakenteeseen kuluvan puun tilavuus, joka on suoraan verrannollinen hintaan. Optimoidun rakenteen käyttökelpoisuudesta huolehtivien rajoitusehtojen pohjana on yleiseurooppalainen Eurokoodi 5, Puurakenteiden suunnittelu. Artikkelin esimerkit käsittelevät tyypillisiä puurakenteiden käytännön suunnittelutyössä vastaantulevia rakenteita.

JOHDANTO

Kantavien rakenteiden mitoitusmenetelmien kehittyessä tarkemmiksi on rakenteista voitu suunnitella samalla materiaalin kulutukseltaan edullisempia. Rakenneanalyysin kehittyessä rasitukset voidaan laskea tarkemmin ja kokeellisen tutkimustiedon lisääntyessä poikkileikkauksen/sauvan kestävyys osataan määrittää varmemmin. Puurakenteiden kohdalla tapahtuneesta kehityksestä hyvänä esimerkkinä on varsin pitkälle edennyt naulalevyristikoiden suunnittelu. Mitoitusmenetelmien kehittäminen ei voi kuitenkaan loputtomasti tarjota keinoja rakenteen kilpailukyvyn parantamiseen. Tällöin seuraavaksi luonnolliseksi askeleeksi muodostuu kantavien rakenteiden optimointi (structural optimization). Kehittyneet mitoitusmenetelmät yhdistettynä optimointiin pystyvät yhdessä tarjoamaan parhaan lopputuloksen.

Optimointiteoriaa ei ole sovellettu puurakenteiden suunnittelussa vielä kovinkaan paljon verrattuna teräsrakenteisiin. Teräsrakenteiden optimointi on ollut kiinnostuksen kohteena jo pidemmän aikaa ja aiheesta löytyy runsaasti kirjallisuutta ja tutkimuksia, esimerkiksi [2] ja [4]. Syynä puurakenteiden vaatimattomampaan optimointitutkimukseen lienee niiden valmistuksen ja tutkimuksen volyymi suhteessa teräsrakenteisiin. Periaatteessa puurakenteiden optimoinnissa ei ole kuitenkaan kyse mistään sen vaikeammasta kuin teräsrakenteiden optimoinnissakaan.

Melko usein jonkin asian tai rakenteen parantelua intuitioon, kokemukseen tai kokeiluihin perustuen kuulee sanottavan optimoinniksi ja näin saatua lopputulosta väitettävän optimoiduksi. Tällaisessa prosessissa ei kuitenkaan ole kyse optimoinnista, vaan tavallisesta tuotekehityksestä. Tässä esityksessä optimoinnilla tarkoitetaan matemaattisen optimointiteorian soveltamista yksikäsitteisesti asetetun rakenteiden mitoitusongelman ratkaisemiseen parhaalla mahdollisella tavalla.

PUURAKENTEET

Puurakenteiden kilpailukyvyn pääasialliset tekijät ovat betonirakenteisiin nähden keveys sekä teräsrakenteisiin nähden hyvät ja ennustettavissa olevat palo-ominaisuudet. Täysin uusiutuvana, hiiltä sitovana ja valmistuksessa vähän luonnonvaroja kuluttavana puu on ympäristörasitukseltaan ylivoimainen kilpaileviin rakennusmateriaaleihin nähden. Ympäristötekijöiden kasvanut painoarvo lisää puurakenteiden saamaa huomiota ja kiinnostusta puurakentamiseen. Tämä on hyvä asia kansantalouden kannalta, sillä puurakenteiden raaka-aine saadaan kotimaasta.

Monissa sovelluksissa puiset rakenneratkaisut ovat hyvin kustannustehokkaita. Esimerkkeinä voidaan mainita naulalevyristikot tai erilaiset hallirakennukset. Nykyaikaiset suuret puurakenteet toteutetaan käyttämällä teollisesti liimattuja puutuotteita, kuten Kerto®-puuta tai liimapuuta (kuva 1).

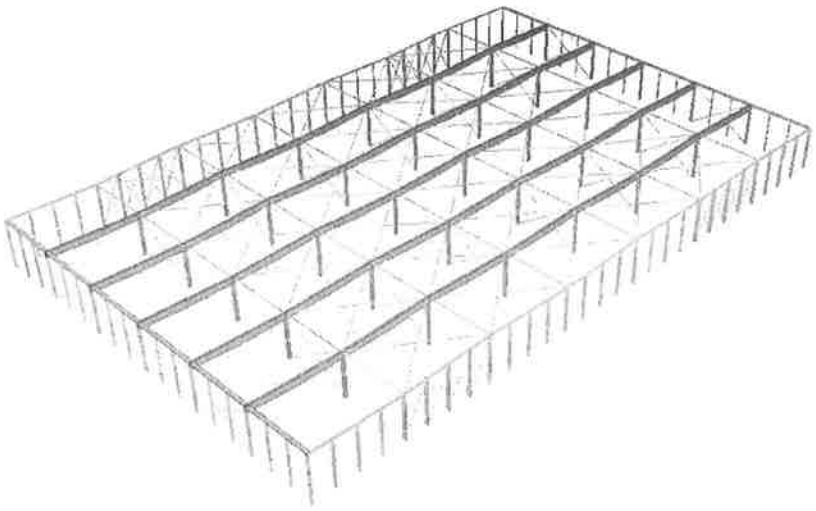

Kuva 1. Hallirakennuksen liimapuurunko. Palkit ovat alapuolelta kuperia mahapalkkeja ja katto toteutetaan puisilla kattoelementeillä.

Suomesta puurakennekomponentteja viedään kaikkialle maailmaan. Pääasiallinen vientikohde on Eurooppa, mutta vientiä suuntautuu myös mm. Yhdysvaltoihin, Venäjälle ja Japaniin. Vientikohteissa tulee usein huomioida Suomessa tarpeettomia kuormituksia, kuten esimerkiksi maanjäristys. Oikein toteutettuna puurakenteiden liitosten kyky sitoa energiaa plastisoitumalla tekee puusta hyvän rakennusmateriaalin myös maanjäristysalueille.

Tulevaisuuden suunta puurakenteiden kehityksessä on siirtyminen yhä suurempiin ja vaativampiin liimatuista osista koottuihin rakenteisiin. Myös puun ja muiden materiaalien liittorakenteet tarjoavat mielenkiintoisia mahdollisuuksia. Tällaisissa rakenteissa voidaan hyödyntää kunkin

materiaalin hyviä ominaisuuksia sellaisen lopputuloksen saamiseksi, johon mikään materiaali ei yksinään pysty.

KANTAVIEN RAKENTEIDEN OPTIMOINTI

Kantavien rakenteiden optimoinnilla tarkoitetaan hyvien lujuusopillisten rakennevaihtoehtojen systemaattista hakua optimoinnin tarjoamia keinoja hyväksikäyttäen. Tavoitteena on löytää sellaisia ratkaisuja, jotka perinteisellä suunnittelijan kokemukseen ja intuitioon perustuvalla menetelmällä olisivat muuten jääneet löytymättä. Erilaisten numeeristen ratkaisumenetelmien lisäksi on sovellusten kannalta ensiarvoisen tärkeää osata muodostaa optimointimalli järkevästi. Edellytykset optimointiongelman formuloinnin onnistumisessa ovat sitä paremmat mitä paremmin suunnittelija tuntee sovelluskohteensa.

Kantavien rakenteiden optimoinnissa voidaan erottaa kolme luonteeltaan toisistaan poikkeavaa tehtävätyyppiä: mitoituksen, muodon ja topologian optimointi. Mitoitustehtävässä ongelmana on valita rakenteen poikkileikkausmitoille sellaiset arvot, että rakenteesta tulisi optimaalinen. Rakenteen tyyppi ja geometria ovat jo lyöty lukkoon ja tehtävänä on vain mitoittaa osat parhaalla mahdollisella tavalla. Esimerkiksi naulalevyristikolla tämä tarkoittaa ristikon kapuloiden kokojen valitsemista parhaalla mahdollisella tavalla (kuva 2a).

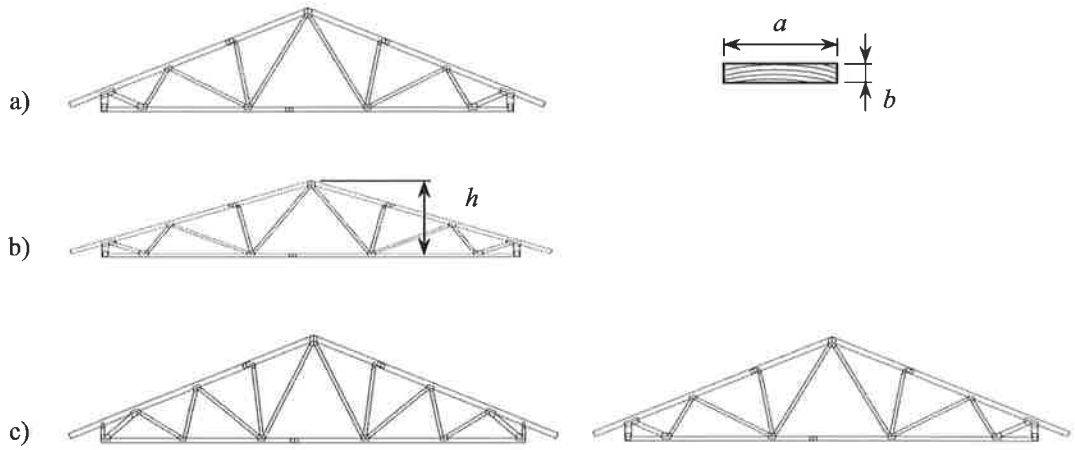

Kuva 2. Naulalevyristikon optimointi, kun kyseessä on a) mitoitustehtävä, b) muodon optimointi ja c) topologian optimointi.

Muodon optimoinnissa on puolestaan ideana muutella optimoitavan rakenteen muotoa. Pyritään siis valitsemaan sellainen muoto, että esimerkiksi materiaalin kulutus minimoituu ja rakenne vielä kestää. Muodon optimointi yhdistetään usein mitoitustehtävän kanssa, jolloin naulalevyristikolla muuteltaisiin kapuloiden koon lisäksi samanaikaisesti myös vaikkapa ristikon korkeutta (kuva 2b). Topologian optimoinnissa on kyse astetta pidemmälle viedystä optimoitavan kappaleen geometrian muuttelemisesta kuin muodon optimoinnissa. Nyt tarkoituksena on löytää paras mahdollinen ratkaisu vaikuttamalla mukaan tulevien rakenneosien määrään, tyyppiin ja sijoitteluun. Naulalevyristikolla voidaan valita optimiratkaisuun mukaan vain osa alun perin mahdollisista uumasauvoista eli muutella ristikon sauvoittelua (kuva 2c). Topologian optimointi yhdistetään usein muodon optimoinnin ja mitoitustehtävän kanssa.

Optimointiongelman muodostamiseksi täytyy matemaattisesti määritellä suunnittelumuuttujista riippuva kohdefunktio, jonka lukuarvo ilmaisee minimoitavana tai maksimoitavana olevan suureen arvon. Tehtävässä voidaan lisäksi asettaa suunnittelumuuttujista riippuvia lisäehtoja, jotka täytyy pukea rajoitusyhtälöiksi ja rajoitusepäyhtälöiksi. Optimointiongelman ratkaiseminen tarkoittaa sellaisten arvojen määrittämistä suunnittelumuuttujille jossakin annetussa joukossa, että kohdefunktio saa pienimmän tai suurimman mahdollisen arvon niin, että rajoitusehdot toteutuvat. Jos kohdefunktio ja rajoitusehtofunktiot ovat suunnittelumuuttujien suhteen lineaarisia, on optimointiongelma lineaarinen. Tavallisesti kantavien rakenteiden optimoinnissa päädytään kuitenkin epälineaariseen tehtävään, missä yleensä ainakin rajoitusehtofunktiot ovat epälineaarisia. Epälineaarinen optimointiongelma on pääsääntöisesti hankalampi ratkaista kuin lineaarinen tehtävä.

Optimointiongelmat voidaan jakaa suunnittelumuuttujien tyypin perusteella jatkuviin ja diskreetteihin ongelmiin sekä sekalukutehtäviin. Jatkuvassa optimointiongelmassa kukin suunnittelumuuttujista voi saada mitä tahansa arvoja joltakin sallitulta väliltä. Diskreetissä ongelmassa kaikki suunnittelumuuttujat voivat saada pelkästään joitakin tiettyjä arvoja, eivätkä mitään arvoa näiden välistä. Sekalukutehtävä on puolestaan näiden kahden edellisen yhdistelmä eli se sisältää sekä jatkuvia että diskreettejä muuttujia. Suunnittelumuuttujiin perustuva optimointiongelmien jaottelu on oleellista, koska sekalukutehtävät ja diskreetit ongelmat ovat usein huomattavasti työläämpiä ratkaista kuin pelkkiä jatkuvia muuttujia sisältävät ongelmat.

Puurakenteilla optimointiongelman luonnolliseksi kohdefunktioksi valikoituu edulliseen lopputulokseen pyrittäessä rakenteen massa tai materiaalitilavuus. Rakennustekniikan sovelluksissa on ensiarvoisen tärkeää, että suunniteltu kuormia kantava rakenne täyttää kulloisenkin suunnittelunormin vaatimukset. Eurokoodi 5 [10] ja vastaava suomalainen suunnitteluohje [9] tarjoavat selvät säännöt puurakenteiden mitoitukseen ja niiden perusteella voidaan muodostaa optimointiongelman rajoitusehdot. Koska puurakenteiden poikkileikkaukset ovat useimmiten suorakaiteen muotoisia, mitoitustehtävässä suunnittelumuuttujiksi voidaan ottaa kapuloiden korkeus ja leveys. Puutavaran kokovalikoiman ollessa standardisoitu, muodostuu usein ainakin osa suunnittelumuuttujista diskreeteiksi.

Kantavien rakenteiden optimoinnin perusteisiin tutustuminen onnistuu oppikirjojen [1], [3] ja [5] avulla. Puurakenteiden suunnittelua eurokoodin pohjalta on käsitelty puolestaan esimerkiksi kirjoissa [6] ja [7].

LIIMAPUISEN HARJAPALKIN OPTIMOINTI

Ensimmäinen esimerkki käsittelee kuvan 3 nosturilla (nostokyky 1 tonni) varustetun liimapuisen harjapalkin tilavuuden minimointia. Ideana on valita suunnittelumuuttujina toimivien poikkileikkausmittojen h_1 (korkeus tuella), h_{ap} (korkeus harjalla) ja b (leveys) arvot niin, että kuluvan liimapuun (GL32c) määrä minimoituu ja asetetut rajoitusehdot toteutuvat. Rajoitusehdot, joiden pohjana on Eurokoodi 5, huolehtivat siitä, että palkin maksimi taivutusjännitys ei ylitä suurinta sallittua arvoa, harjan poikittaiset vetojännitykset leikkausjännitys huomioiden eivät kasva liian suuriksi, tuella ei tapahdu leikkautumista, palkki ei kiepahda yläreunan poikittaistukien välillä (2,5 metrin välein) ja palkin kokonais- ja lopputaipuma pysyvät sallituissa rajoissa. Taivutusjännityksen yhteydessä tulee tarkistaa erikseen harja sekä muut palkin osuudet. Tukipainetta ei tarvitse tarkistaa, koska tuella käytetään liimatankoja ja teräslevyvahvistusta. Esimerkki on otettu Puuinfon kokonaista hallirakennusta koskevista Eurokoodi 5:n esimerkkilaskelmista [8].

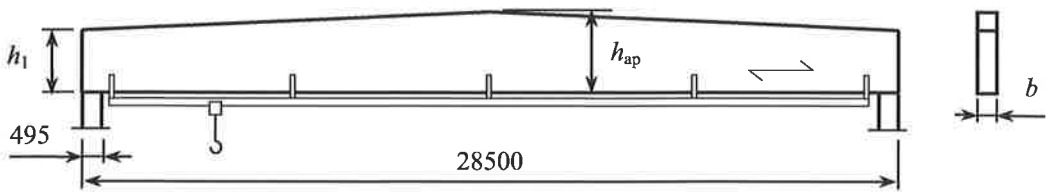

Kuva 3. Liimapuinen nosturilla varustettu harjapalkki.

Matemaattisesti esitettynä optimointiongelma on muotoa

$$\min \quad V(\mathbf{x}) \tag{1}$$

$$g_{\mathrm{m},\alpha}(\mathbf{x}) = \frac{\sigma_{\mathrm{m},\alpha,\mathrm{d}}(\mathbf{x})}{k_{\mathrm{m},\alpha}(\mathbf{x}) f_{\mathrm{m,d}}} - 1 \leq 0 \tag{2a}$$

$$g_{\mathrm{m}}(\mathbf{x}) = \frac{\sigma_{\mathrm{m,d}}(\mathbf{x})}{k_{\mathrm{r}} f_{\mathrm{m,d}}} - 1 \leq 0 \tag{2b}$$

$$g_{\mathrm{t,90}}(\mathbf{x}) = \frac{\sigma_{\mathrm{t,90,d}}(\mathbf{x})}{k_{\mathrm{dis}} k_{\mathrm{vol}}(\mathbf{x}) f_{\mathrm{t,90,d}}} - 1 \leq 0 \tag{2c}$$

$$g_{\mathrm{v,t,90}}(\mathbf{x}) = \frac{\tau_{\mathrm{d}}(\mathbf{x})}{f_{\mathrm{v,d}}} + \frac{\sigma_{\mathrm{t,90,d}}(\mathbf{x})}{k_{\mathrm{dis}} k_{\mathrm{vol}}(\mathbf{x}) f_{\mathrm{t,90,d}}} - 1 \leq 0 \tag{2d}$$

$$g_{\mathrm{v}}(\mathbf{x}) = \frac{\tau_{\mathrm{d}}(\mathbf{x})}{f_{\mathrm{v,d}}} - 1 \leq 0 \tag{2e}$$

$$g_{\mathrm{crit},\alpha}(\mathbf{x}) = \frac{\sigma_{\mathrm{m},\alpha,\mathrm{d}}(\mathbf{x})}{k_{\mathrm{crit}}(\mathbf{x}) f_{\mathrm{m,d}}} - 1 \leq 0 \tag{2f}$$

$$g_{\mathrm{w,fin}}(\mathbf{x}) = \frac{w_{\mathrm{fin}}(\mathbf{x})}{L_0 / 200} - 1 \leq 0 \tag{2g}$$

$$g_{\mathrm{w,fin,net}}(\mathbf{x}) = \frac{w_{\mathrm{fin,net}}(\mathbf{x})}{L_0 / 300} - 1 \leq 0 \tag{2h}$$

$$\mathbf{x}^{\min} \leq \mathbf{x} \leq \mathbf{x}^{\max}$$

$$\mathbf{x} = \begin{bmatrix} h_{\mathrm{l}} & h_{\mathrm{ap}} & b \end{bmatrix}^{\mathrm{T}}$$

Edellä $\sigma_{\mathrm{m},\alpha,\mathrm{d}}(\mathbf{x})$ tarkoittaa palkin suurinta taivutusjännitystä pulpettiosuuksilla. $\sigma_{\mathrm{m,d}}(\mathbf{x})$ on harjan taivutusjännitys, jossa on huomioitu harjapalkin geometrian vaikutus. $\sigma_{\mathrm{t,90,d}}(\mathbf{x})$ tarkoittaa poikittaista vetojännitystä harjalla ja $\tau_{\mathrm{d}}(\mathbf{x})$ leikkausjännitystä tuella tai harjalla. $w_{\mathrm{fin}}(\mathbf{x})$ on puolestaan palkin kokonaistaipuma ja $w_{\mathrm{fin,net}}(\mathbf{x})$ lopputaipuma, missä on huomioitu esikorotus $w_{\mathrm{c}} = 50$ mm. Harjapalkin geometriasta johtuva kerroin $k_{\mathrm{m},\alpha}(\mathbf{x})$ pienentää liimapuun taivutuslujuutta $f_{\mathrm{m,d}}$. Harjapalkilla on kerroin k_{r} = 1,0. Poikittaista vetolujuutta $f_{\mathrm{t,90,d}}$ muokataan harjaosan tilavuudesta riippuvalla kertoimella $k_{\mathrm{vol}}(\mathbf{x})$ ja jännitysten jakautumisen huomioivalla

kertoimella k_{dis}=1,4. f_v on liimapuun leikkauslujuus ja $k_{crit}(\mathbf{x})$ kerroin, jolla pienennetään taivutuslujuutta $f_{m,d}$ kiepahduskestävyyttä tarkistettaessa. Jotta saataisiin mitoitusarvot lujuuksille, tulee ominaisarvoja (Taulukko 1) kertoa aika- ja käyttöluokasta riippuvalla kertoimella k_{mod} ja jakaa materiaalin osavarmuusluvulla γ_M = 1,2. L_0 = 28005 mm on palkin jänneväli. Suunnittelumuuttujien ala- ja ylärajat voidaan valita vapaasti paitsi, että palkin pienin mahdollinen leveys on b^{min} = 180 mm, jotta tuen liitoksen harjaterästangot mahtuvat poikkileikkaukseen.

Taulukko 1. Liimapuun GL32c ominaislujuudet sekä kimmomoduli, [9].

taivutuslujuus $f_{m,k}$ [N/mm^2]	leikkauslujuus $f_{v,k}$ [N/mm^2]	vetolujuus poikittain syysuuntaan $f_{t,90,k}$ [N/mm^2]	kimmomoduli $E_{0,05}$ [N/mm^2]
32,0	3,2	0,45	11100

Kuormitusyhdistelmiä on liimapuurunkoiselle hallille alkuperäisessä lähteessä [8] kaikkiaan 33 kpl. Harjapalkin tapauksessa rajoitusehtoja ei tarkisteta kuitenkaan joka kuormitusyhdistelmällä, vaan laskelmat tehdään vain niille yhdistelmille, jotka on havaittu palkin kannalta mitoittaviksi. Rajoitusehtojen (2a), (2b), (2c), (2e) ja (2f) tulee toteutua tasaisella lumikuormalla 15,84 kN/m, katon ja palkin omapainolla 5,4 kN/m sekä nosturin omapainolla 1,15 kN, joka vaikuttaa keskellä palkkia. Aikaluokka on tällöin keskipitkä (k_{mod} = 0,8). Rajoitusehdon (2d) tulee toteutua kuormitusyhdistelmällä, joka muuten sama kuin edellinen, mutta toisella lappeella on vain puolikas lumikuorma. Tämän takia rajoitusehdoissa (2c) ja (2d) poikittainen vetojännitys $\sigma_{t,90,d}(\mathbf{x})$ ei ole sama molemmissa. Taipumarajoitukset (2g) ja (2h) tarkistetaan kuormitusyhdistelmällä, missä huomioidaan tasainen lumikuorma, palkin omapaino ja nosturin omapaino sekä nosturin taakkakuorma. Aikaluokka on lyhytaikainen (virumaluku k_{def} = 0,6).

Harjapalkin optimointiongelma on suunnittelumuuttujiltaan jatkuva, epälineaarinen ja rajoitettu optimointiongelma. Kyseessä on mitoitustehtävä, koska suunnittelumuuttujat liittyvät palkin poikkileikkauksen dimensioihin. Tehtävä on ratkaistu käyttäen Matlabin optimointi toolboxia, missä algoritmina on toistettu kvadraattinen optimointi (sequential quadratic programming, SQP). Tarvittavat kohde- ja rajoitusehtofunktioiden derivaatat suunnittelumuuttujien suhteen lasketaan differenssimenetelmällä. Optimoinnissa saadut tulokset on esitetty oheisessa taulukossa 2 ja kohdefunktion kehitys iteraatiokierrosten funktiona kuvassa 4. Alkuarvauksena optimoinnissa on ollut lähteessä [8] käytetyt mitat h_1 = 1310 mm, h_{ap} = 2200 mm ja b = 240 mm, jolloin palkin tilavuudeksi tulee 12004 litraa.

Taulukko 2. Optimoinnin tulos ja alkuarvausta vastaavat ratkaisu.

	Alkuarvaus [8]	Optimoinnin tulos
Tilavuus [l]	12004	11569
Pään korkeus h_1 [mm]	1310	1231
Harjan korkeus h_{ap} [mm]	2200	2382
Leveys b [mm]	240	225
Käyttöasteet:		
- taivutus	93%	97%
- taivutus harjalla	79%	75%
- poikittainen veto harjalla	73%	92%
- poikittainen veto ja leikkaus harjalla	73%	90%
- leikkaus tuella	77%	86%
- kiepahdus	96%	100%
- kokonaistaipuma	91%	100%
- lopputaipuma	84%	96%

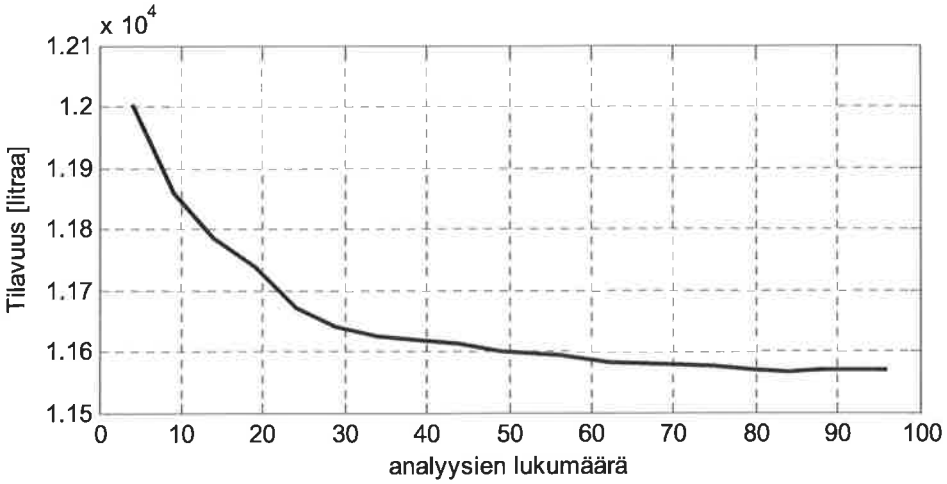

Kuva 4. Kohdefunktion (tilavuus) kehitys optimoinnissa kuluneiden analyysien funktiona.

Saatujen tulosten perusteella nähdään, että harjapalkin tilavuutta onnistuttiin pienentämään 435 litraa, jolloin optimoitu palkki on 3,6 % kevyempi kuin alkuperäinen suunnitelma. Palkin keventyessä käyttöasteet luonnollisesti kasvavat lukuun ottamatta harjan taivutusjännitystä. Vaikka palkin keventyminen prosenteissa ei tunnu kovinkaan suurelta, täytyy muistaa, että alkuarvaus oli jo varsin hyvä ja käyttöasteet korkeita.

KERTOPUISEN A-KEHÄN OPTIMOINTI

Toinen esimerkkitehtävä käsittelee kuvan 5 mukaisen kertopuusta (Kerto-S) valmistetun kattokannattajan optimointia. Tarkastellun A-kehän yläpaarre muodostuu kahdesta rinnakkaisesta palkista, joiden välissä on alapaarre. Vertikaali on kaksiosainen. Eri osat liittyvät toisiinsa harjalla erillisen puisen liitoslevyn välityksellä. Kaikki rakenteen liitokset ovat puhtaasti puuosien välisiä tappivaarnaliitoksia, joissa ei käytetä teräslevyjä. Kehän jänneväli on 22 metriä.

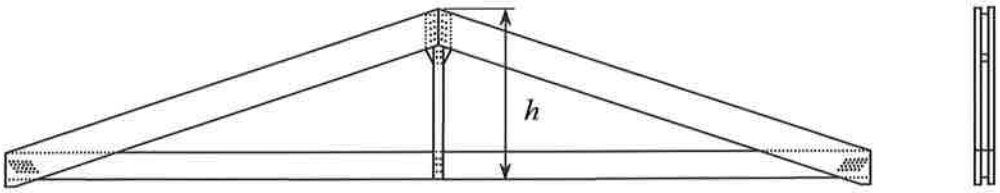

Kuva 5. Kertopuinen A-kehä, jossa liitokset on toteutettu tappivaarnoin ilman teräslevyjä.

Tehtävänä on valita suunnittelumuuttujina toimivat kehän korkeus h sekä kuvassa 6 esitetyt paarteiden ja vertikaalin poikkileikkausten korkeudet (h_{yp}, h_{ap}, h_{ver}) ja leveydet (b_{yp}, b_{ap}, b_{ver}) niin, että rakenteen tilavuus minimoituu ja asetetut rajoitusehdot toteutuvat. Kyseessä on siis yhdistetty mitoitustehtävä ja muodon optimointi. Rajoitusehdot huolehtivat rakenteen kestävyyden säilymisestä ja ne muodostuvat Eurokoodi 5:n [10] ja sen suomalaisen sovellusohjeen [9] perusteella. Rajoitusehdoissa ei yksinkertaisuuden vuoksi huomioida liitos- tai palomitoitusta, eikä myöskään taipumarajoja.

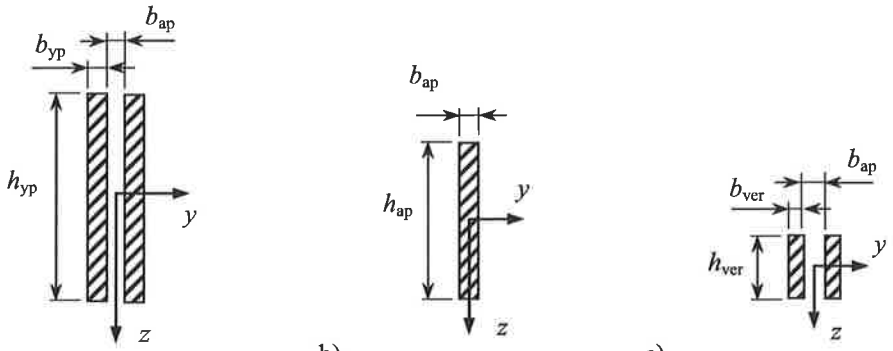

Kuva 6. A-kehän a) yläparteen, b) alapaarteen ja c) vertikaalin poikkileikkauksiin liittyvät suunnittelumuuttujat.

A-kehän laskentamallissa ala- ja yläpaarteet sekä vertikaali on mallinnettu useammalla tasopalkkielementillä niin, että kehän eri osat liittyvät liitoksissa nivelellisesti toisiinsa. Nivelten ajatellaan sijaitsevan liitinryhmien keskiöissä, vaikkakin liitinten tarkat paikat ja siten nivelen sijainti määräytyvät vasta statiikan ratkaisun jälkeen liitosmitoituksessa. Kehän vaakasuuntaiset siirtymät on estetty vain toisen pään tuella. Yläpaarre on tuettu yläreunastaan poikittaissuunnassa kattoelementin leveyden välein (2,5 m).

Taulukko 3. Kerto-S:n ominaislujuudet sekä kimmomoduli, [5].

taivutuslujuus $f_{m,k}$ [N/mm^2] [1)]	leikkauslujuus $f_{v,k}$ [N/mm^2]	vetolujuus $f_{t,k}$ [N/mm^2] [1)]	puristuslujuus $f_{c,k}$ [N/mm^2]	kimmomoduli $E_{0,05}$ [N/mm^2]
44,0	4,1	35,0	35,0	11600

1) Kokovaikutuseksponentti $s = 0{,}12$ ottaa huomioon palkin koon vaikutuksen taivutus- ja vetolujuuteen.

Kuormitusyhdistelmäksi on valittu sellainen, jonka on yleensä todettu olevan mitoituksen kannalta rajoittavin. Tämä koostuu tasaisesta lumikuormasta (tässä tapauksessa 2,2 kN/m^2) sekä yläpaarteen omasta painosta 0,6 kN/m^2 ja alapaarteen omasta painosta 0,2 kN/m^2. Näiden lisäksi huomioidaan A-kehän oma paino. Kuormitusleveys on 6,6 metriä, aikaluokka keskipitkä ($k_{\mathrm{mod}} = 0{,}8$) ja materiaalin osavarmuusluku $\gamma_M = 1{,}2$. Kuormituksen seurauksena yläpaarteeseen syntyy puristusta ja alapaarteeseen sekä vertikaaliin vetoa.

Matemaattisesti esitettynä optimointiongelma on muotoa

$$\min \quad V(\mathbf{x}) \tag{3}$$

$$g_{\mathrm{m,c}}^{\mathrm{yp}}(\mathbf{x}) = \left(\frac{\sigma_{\mathrm{c,0,d}}^{\mathrm{yp}}(\mathbf{x})}{f_{\mathrm{c,0,d}}}\right)^2 + \frac{\sigma_{\mathrm{m,d}}^{\mathrm{yp}}(\mathbf{x})}{f_{\mathrm{m,d}}} - 1 \le 0 \tag{4a}$$

$$g_{\mathrm{v}}^{\mathrm{yp}}(\mathbf{x}) = \frac{\tau_{\mathrm{d}}^{\mathrm{yp}}(\mathbf{x})}{f_{\mathrm{v,d}}} - 1 \le 0 \tag{4b}$$

$$g_{\mathrm{crit,y}}^{\mathrm{yp}}(\mathbf{x}) = \frac{\sigma_{\mathrm{c,0,d}}^{\mathrm{yp}}(\mathbf{x})}{k_{\mathrm{c,y}}(\mathbf{x}) f_{\mathrm{c,0,d}}} + \frac{\sigma_{\mathrm{m,d}}(\mathbf{x})}{f_{\mathrm{m,d}}} - 1 \le 0 \tag{4c}$$

$$g_{\mathrm{crit,z}}^{\mathrm{yp}}(\mathbf{x}) = \frac{\sigma_{\mathrm{c,0,d}}^{\mathrm{yp}}(\mathbf{x})}{k_{\mathrm{c,z}}(\mathbf{x}) f_{\mathrm{c,0,d}}} + k_{\mathrm{m}} \frac{\sigma_{\mathrm{m,d}}(\mathbf{x})}{f_{\mathrm{m,d}}} - 1 \le 0 \tag{4d}$$

$$g_{\mathrm{crit,m,c}}^{\mathrm{yp}}(\mathbf{x}) = \left(\frac{\sigma_{\mathrm{m,d}}(\mathbf{x})}{k_{\mathrm{crit}}(\mathbf{x}) f_{\mathrm{m,d}}}\right)^2 + \frac{\sigma_{\mathrm{c,0,d}}^{\mathrm{yp}}(\mathbf{x})}{k_{\mathrm{c,z}}(\mathbf{x}) f_{\mathrm{c,0,d}}} - 1 \le 0 \tag{4e}$$

$$g_{\mathrm{v}}^{\mathrm{ap}}(\mathbf{x}) = \frac{\tau_{\mathrm{d}}^{\mathrm{ap}}(\mathbf{x})}{f_{\mathrm{v,d}}} - 1 \le 0 \tag{4f}$$

$$g_{\mathrm{m,t}}^{\mathrm{ap}}(\mathbf{x}) = \frac{\sigma_{\mathrm{t,0,d}}^{\mathrm{ap}}(\mathbf{x})}{f_{\mathrm{t,0,d}}} + \frac{\sigma_{\mathrm{m,d}}(\mathbf{x})}{f_{\mathrm{m,d}}} - 1 \le 0 \tag{4g}$$

$$g_{\mathrm{t}}^{\mathrm{ver}}(\mathbf{x}) = \frac{\sigma_{\mathrm{t,0,d}}^{\mathrm{ver}}(\mathbf{x})}{f_{\mathrm{t,0,d}}} - 1 \le 0 \tag{4h}$$

$$\mathbf{x}^{\min} \le \mathbf{x} \le \mathbf{x}^{\max}$$

$$\mathbf{x} = \left[h \quad h_{\mathrm{yp}} \quad b_{\mathrm{yp}} \quad h_{\mathrm{ap}} \quad b_{\mathrm{ap}} \quad h_{\mathrm{ver}} \quad b_{\mathrm{ver}} \right]^{\mathrm{T}}$$

Yläpaarteen rajoitusehdot (4a) – (4e) liittyvät taivutuksen ja puristuksen yhteisvaikutukseen, leikkautumiseen, nurjahdukseen sekä kiepahduksen ja puristuksen yhteisvaikutukseen. Alapaarteen rajoitusehdot (4f) ja (4g) liittyvät leikkautumiseen sekä taivutuksen ja vedon

yhteisvaikutukseen. Vertikaalissa ei ole taivutusta tai leikkausta ja ainoa rajoitusehto (4h) liittyy vetoon. Rajoitusehtojen tulee toteutua kaikissa ylä- ja alapaarteen sekä vertikaalin poikkileikkauksissa. Tukipainetta tuella ei huomioida.

Saatavilla ole Kerto-S palkkien valikoima rajoittuu vain tiettyihin kokoihin, jotka on esitetty taulukossa 4. Tästä syystä poikkileikkauksiin liittyvät suunnittelumuuttujat ovat diskreettejä. A-kehän korkeus h on periaatteessa jatkuva ja voisi saada mitä tahansa arvoja ala- ja ylärajansa välistä. Tässä työssä se on kuitenkin valittava 2 ja 5 metrin välistä niin, käytettävissä olevat mitat ovat kymmenen senttimetrin välein (2,0 m, 2,1 m, 2,2 m jne.).

Taulukko 4. Kerto-S palkkien kokovalikoima.

	korkeus [mm]								
paksuus [mm]	200	260	300	360	400	450	500	600	900
27	•								
33	•	•							
39	•	•	•						
45	•	•	•	•					
51	•	•	•	•	•				
57	•	•	•	•	•	•			
63	•	•	•	•	•	•	•		
75	•	•	•	•	•	•	•	•	•

A-kehän optimointiongelma on ratkaistu käyttäen tabuhakua (tabu search, TS) ja Matlab-ohjelmaa. Tabuhaku on perusidealtaan suhteellisen yksinkertainen heuristinen optimointimenetelmä. Se sopii hyvin varsinkin diskreettejä suunnittelumuuttujia sisältävien laskennallisesti työläiden optimointiongelmien likimääräiseen ratkaisemiseen. Vaikka tabuhaku ei pystykään takaamaan globaalin optimin löytymistä, voidaan usein parantaa siihen asti parasta tiedettyä ratkaisua. Monissa käytännön sovelluksissa ei olla kiinnostuneita kaikkein parhaimmasta ratkaisusta, vaan sitä lähellä oleva kohtuullisella laskentatyöllä saatava ratkaisu on houkuttelevampi vaihtoehto. Tabuhaun tarvitsemana alkuarvauksena on käytetty mittoja $h = 3600$ mm, $h_{yp} = 900$ mm, $b_{yp} = 75$ mm, $h_{ap} = 600$ mm, $b_{ap} = 75$ mm, $h_{ver} = 260$ mm ja $b_{ver} = 45$ mm. Optimoinnissa saadut tulokset on esitetty oheisessa taulukossa 5 ja kohdefunktion kehitys FEM-analyysien funktiona kuvassa 7.

Taulukko 5. Optimoinnin lopputulos ja alkuarvausta vastaavat ratkaisu.

	Alkuarvaus	Optimoinnin tulos
Tilavuus [l]	4199	3944
A-kehän korkeus h [mm]	3600	3100
Yläpaarteen korkeus h_{yp} [mm]	900	900
" leveys b_{yp} [mm]	75	75
Alapaarteen korkeus h_{ap} [mm]	600	500
" leveys b_{ap} [mm]	75	75
Vertikaalin korkeus h_{ver} [mm]	260	200
" leveys b_{ver} [mm]	45	27
Käyttöasteet:		
- leikkaus yläpaarteella	60%	60%
- taivutus ja puristus yläpaarteella	63%	63%
- nurjahdus pois tasosta yläpaarteella	59%	61%
- nurjahdus tasossa yläpaarteella	79%	80%
- kiepahdus ja puristus yläpaarteella	98%	98%
- leikkaus alapaarteella	60%	60%
- taivutus ja veto alapaarteella	72%	99%
- veto vertikaalilla	5%	9%

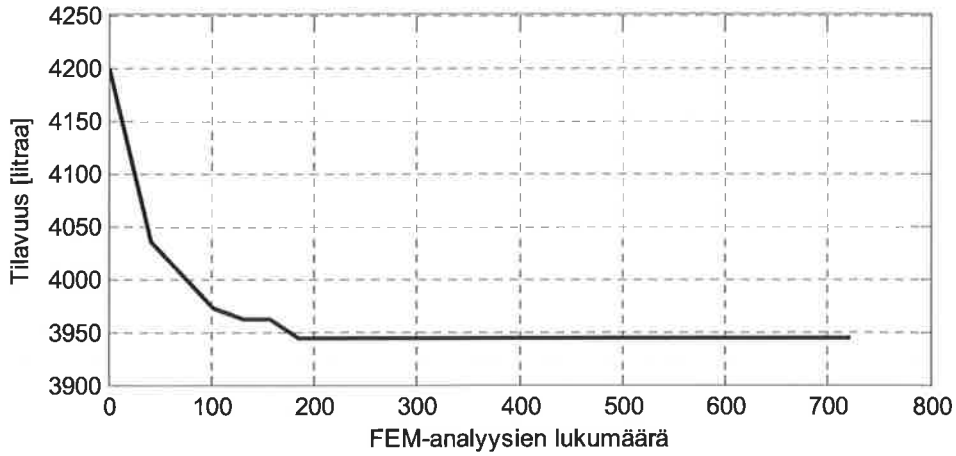

Kuva 7. Kohdefunktion (tilavuus) kehitys optimoinnissa kuluneiden FEM-analyysien funktiona.

A-kehän tilavuus pieneni 255 litraa eli optimoitu rakenne on 6% kevyempi kuin alkuarvaus. Käyttöasteet eivät nousseet merkittävästi muulta osin kuin alapaarteen taivutuksen ja vedon sekä vertikaalin vedon kohdalla.

YHTEENVETO

Optimointi on luonnollinen jatke rakenteiden tietokoneavusteiselle analysoinnille. Suunnittelijan ei kannata tyytyä muutaman vaihtoehdon keskinäiseen vertailuun laskelmien perusteella, vaan on paljon järkevämpää pistää tietokone hakemaan optimoinnin avulla uusia entistä parempia ratkaisuja. Annetusta alkuarvauksesta liikkeelle lähteviä optimointialgoritmeja, kuten esimerkkitehtävien SQP ja TS, voidaan käyttää kätevästi suunnittelijan valitseman ratkaisun parantamiseen. Rakenteen lopullisten mittojen valitseminen optimaalisesti hoituu automaattisesti, eikä suunnittelijan tarvitse käyttää aikaa erilaisiin kokeiluihin.

Puurakenteiden optimoinnin merkitys tulee tulevaisuudessa kasvamaan, koska se tarjoaa selkeän keinon saavuttaa etua totuttuihin suunnittelumenetelmiin nähden. Yksittäisen kattokannattajan optimoinnin sijasta voidaan keskittyä esimerkiksi kokonaisen hallin rungon optimointiin. Rungon kehien lukumäärän ottaminen suunnittelumuuttujaksi (eli siirtyminen topologian optimointiin) mahdollistaa huomattavasti suuremman materiaalin säästön kuin yksittäisten kehien mitoituksen ja muodon optimointi. Luonnollisesti samalla tehtävän koko kasvaa ja ratkaisun haku vaikeutuu. Tietokoneiden kasvava laskentakapasiteetti ja kehittyvät optimointialgoritmit mahdollistavat kuitenkin vaativampien ongelmien ratkaisemisen edelleen kohtuullisessa ajassa.

Pitkälle kehittyneet laskentamenetelmät eivät poista sitä tosiasiaa, että optimoinnin soveltamisessa käytännön ongelmaan tarvitaan kulloisenkin sovellusalan ymmärrystä. Optimointimallin muodostaminen vaikuttaa pitkälle mahdollisuuksiin onnistua menestyksellisesti mallin ratkaisemisessa. Tällaisten päätösten tekemiseen tarvitaan hyvää puurakenteiden ja peruslujuusopin tuntemusta.

LÄHTEET

[1] Christensen, P. & Klarbring, A. 2008. *An Introduction to Structural Optimization*. Springer-Verlag.

[2] Farkas, J. & Jármai, K. 2008. *Design and Optimization of Metal Structures*. Horwood Publishing.

[3] Haftka, R. & Gürdal, Z. 1992. *Elements of Structural Optimization*. Kluwer.

[4] Jalkanen, J. 2007. *Tubular Truss Optimization Using Heuristic Algorithms*. Väitöskirja, TTY.

[5] Kirsch, U. 1993. *Structural Optimization*. Springer-Verlag.

[6] McKenzie, W. & Zhang, B. 2007. *Design of Structural Timber to Eurocode 5*. Palgrave Macmillan.

[7] Porteous, J. & Karmani, A. 2007. *Structural Timber Design to Eurocode 5*. Blackwell Publishing.

[8] Puuinfo. 2008. *EC 5 Sovelluslaskelmat. Hallirakennus.*

[9] RIL 205-1-2007. 2007. *Puurakenteiden suunnitteluohje.*

[10] SFS-EN 1995-1-1 + AC. 2004. *Eurokoodi 5. Puurakenteiden suunnittelu. Osa 1-1: Yleiset säännöt ja rakennuksia koskevat säännöt.*

STABILITY ANALYSIS OF ROTATING NIPPED ROLLS WITH MEMORY

Anssi Karttunen
Lappeenranta University of Technology
P.O. Box 20, FI-53851 Lappeenranta, Finland
e-mail: anssi.karttunen@lut.fi

Raimo von Hertzen
Lappeenranta University of Technology
P.O. Box 20, FI-53851 Lappeenranta, Finland
e-mail: rhertzen@lut.fi

ABSTRACT

As a result of increased speeds and loads in rotatory machines, the dynamic instability of viscoelastically covered nipped rolls has also increased. This instability results in high vibration levels and deformation of the roll surfaces, limiting the operating speed of many machines. In this work, a dynamic model of a nipped two-roll system with a recovering polymer cover is developed, and the stability of the system is studied. The polymer cover is described by using the rheological standard model of viscoelastic material. The stability analysis is performed using Laplace-transform techniques. The calculated results display instability regions and various surface patterns on the roll cover.

INTRODUCTION

There exists a wide variety of rotatory systems in which two or more rolls are rotating in contact with each other. In the nip, that is, within the contact area between the rolls, the peripheral surfaces of the rolls deform to an out-of-round shape mainly elastically, and possibly also viscoelastically and plastically, depending on the surface materials and loading conditions. In addition, the deformations are influenced significantly by different environmental factors, such as temperature. Removal of the surface material may also occur in the form of wear, grinding and cutting. The surface deformations recover, for the most part, instantly outside the nip, but what remains after one revolution period (two-roll system), is fed back into the nip. This time-delayed feedback causes self-excited vibrations in the roll system, which can lead to the formation of a periodic polygonal deformation pattern on the roll surfaces. The wave-like surface pattern may grow gradually and this can be observed as severe unstable vibration of the rotatory system during operation. This sort of vibration ultimately results in defective products in numerous industrial processes involving nipped rolls and makes the continuous operation of production machines impossible. The aim of this study is to investigate unstable vibrations in a two-roll system in which a polymer cover and its viscoelastic memory is the source of the vibrations.

The self-excited vibrations of rotating nipped rolls with time-delayed feedback loads have been a subject of considerable interest recently. Sueoka *et al.* have investigated the pattern formation phenomenon of a polymer cover in two-roll systems both experimentally and theoretically [1, 2]. The viscoelastic properties of the polymer have been included in the analytical lumped-mass models with a simple three-parameter element possessing one time constant to describe the relaxation process of the polymer outside the nip. The experimental and computational results are shown to be in good agreement. Sowa *et al.* have used similar models to create a method to be applied to the structural design process of roll systems with polymer covers to prevent the pattern formation and unstable vibrations [3]. By modifying the model presented in Ref. [1], Jorkama and von Hertzen applied it successfully to the process of paper winding [4, 5]. In these winding configurations, a wound paper roll with an increasing diameter acts as the viscoelastic part. Delayed roll systems with viscoelastic memory and grinding effects have been comprehensively studied also by Yuan [6]. Järvenpää and Yuan have extended the study of polymer cover-induced roll vibrations with new approaches, which include the use of multibody dynamics and finite element method [7], and a contact mechanical model [8]. Extensive experimental studies concentrating on the mechanical behavior of polymer covers in rolling contact and the effect of environmental factors therein have been conducted by Vuoristo [9]. Valuable experimental data has also been given by Chinn [10].

In this paper, an analytical lumped-mass model is developed to study the formation of polygonal deformation patterns on a polymer covered roll, and the unstable vibrations induced by it, in a two-roll system. The viscoelastic properties of the cover will be taken into account by the use of the Standard Linear Solid model (SLS). Thus, the viscoelastic memory effect and the relaxation of the deformations will be modelled in a new way. The dynamic equations of motion of the system constitute a set of linear delay differential equations. For the stability analysis, the equations are transformed to the Laplace domain. The stability and complex eigenmodes of the system and deformation patterns of the polymer cover are then investigated numerically.

THEORY

The model of the studied system is shown in Fig. 1. The system has two rolls and a polymer cover.

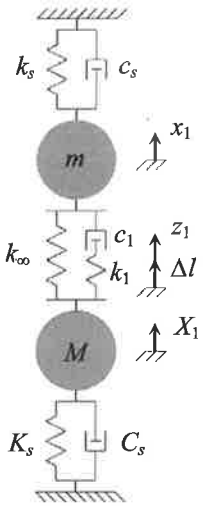

Figure 1. Model for a two-roll system with a polymer cover attached to the upper roll. The rolls are modelled as rigid bodies and the cover by an SLS element.

The rolls have masses m and M, and the polymer cover is modelled as massless. The vertical displacement coordinates for the upper and lower roll are x_1 and X_1, respectively. The roll supports are modelled by springs and viscous dashpots with stiffness and viscous damping coefficients k_s and c_s for the upper roll, and K_s and C_s for the lower roll, respectively. The parameters for the SLS element are k_∞, k_1 and c_1, where the latter two form a Maxwell element. The coordinate z_1 determines the movement of the spring's end plate in the damper of the Maxwell element. The variable Δl describes the residual deformation, that is, the deviation of the upper roll from circular shape, just before re-entering the nip.

The equations of motion of the system are

$$\begin{bmatrix} m & 0 & 0 \\ 0 & 0 & 0 \\ 0 & 0 & M \end{bmatrix} \begin{Bmatrix} \ddot{x}_1 \\ \ddot{z}_1 \\ \ddot{X}_1 \end{Bmatrix} + \begin{bmatrix} c_s + c_1 & -c_1 & 0 \\ -c_1 & c_1 & 0 \\ 0 & 0 & C_s \end{bmatrix} \begin{Bmatrix} \dot{x}_1 \\ \dot{z}_1 \\ \dot{X}_1 \end{Bmatrix} + \begin{bmatrix} k_s + k_\infty & 0 & -k_\infty \\ 0 & k_1 & -k_1 \\ -k_\infty & -k_1 & k_1 + k_\infty + K_s \end{bmatrix} \begin{Bmatrix} x_1 \\ z_1 \\ X_1 \end{Bmatrix} = \begin{Bmatrix} k_1 \Delta l \\ 0 \\ -k_1 \Delta l \end{Bmatrix}, \quad (1)$$

where the residual deformation, bringing about a time delay into the system, is included as

$$\Delta l(t) = \sum_{k=1}^{N} \underbrace{e^{kAT}}_{a^k} \left[x_1(t - kT) - z_1(t - kT) \right]. \quad (2)$$

Here N is the total number of revolution periods at time t, T is the revolution period of the upper roll, $a = e^{AT}$ is the decay factor for one revolution, and the recovery coefficient for the viscoelastic deformation is

$$A = -\frac{k_\infty}{k_\infty + k_1} \frac{1}{\tau_1}, \quad (3)$$

where $\tau_1 = c_1 / k_1$ is the relaxation time of the polymer cover. The driving force is exerted to both rolls in the nip as an impact via the spring of the Maxwell element, the damper being momentarily stiff due to the lack of time to react when entering the nip. When the initial conditions are set to zero, the Laplace transform of Eq. (1) can be written as

$$\begin{bmatrix} ms^2 + (c_s + c_1)s + k_s + k_\infty - k_1\alpha & -c_1 s + k_1\alpha & -k_\infty \\ -c_1 s & c_1 s + k_1 & -k_1 \\ -k_\infty + k_1\alpha & -k_1(1+\alpha) & Ms^2 + C_s s + k_1 + k_\infty + K_s \end{bmatrix} \begin{Bmatrix} \hat{x}_1 \\ \hat{z}_1 \\ \hat{X}_1 \end{Bmatrix} = 0, \quad (4)$$

where

$$\alpha = \sum_{k=1}^{N} a^k e^{-ksT}. \quad (5)$$

The characteristic equation of the system is

$$\det \mathbf{A} = 0, \quad (6)$$

where **A** is the multiplication matrix of Eq. (4). The complex valued roots $s_i = \alpha_i + j\beta_i$ can be solved from Eq. (6). The system is stable if the real parts of all the roots are negative. On the other hand, the system is unstable if even one of the real parts is positive. Due to the complex exponential function of Eq. (5), the characteristic equation has an infinite number of roots. The roots of interest are those *polygonal roots*, which correspond to the actual deformation patterns of the polymer cover and follow the equation

$$\mathrm{Im}[s_i] = 2\pi N_i f, \tag{7}$$

where N_i is the polygonal number and f is the revolution frequency of the upper roll. The polygonal number gives essential information on the surface pattern, which is evidently related to the vibration frequency of the system. By substituting the solved polygonal roots back to Eq. (4) the system's complex eigenmodes corresponding to each polygonal root can be calculated. Moreover, the roll system's (relative) vibration amplitudes and phase angles can be solved from the complex eigenmodes by equations

$$|\hat{x}| = \sqrt{\mathrm{Re}[\hat{x}]^2 + \mathrm{Im}[\hat{x}]^2} \quad \text{and} \quad \arg(\hat{x}) = \arctan\frac{\mathrm{Im}[\hat{x}]}{\mathrm{Re}[\hat{x}]} \quad \left(\hat{x} = \hat{x}_1, \hat{z}_1, \hat{X}_1\right). \tag{8), (9}$$

Furthermore, it is possible to generate eigensolutions for the system of the form

$$\begin{Bmatrix} x_1 \\ z_1 \\ X_1 \end{Bmatrix}_i (t) = \begin{Bmatrix} \hat{x}_1 \\ \hat{z}_1 \\ \hat{X}_1 \end{Bmatrix}_i e^{s_i t} \quad \text{or} \quad \mathbf{x}_i(t) = \hat{\mathbf{x}}_i e^{s_i t}, \tag{10}$$

where s_i is a complex valued root of the characteristic equation and $\hat{\mathbf{x}}_i$ is the corresponding eigenmode. Based on the Maxwell element's equilibrium of forces, the relation

$$(\hat{x}_1 - \hat{z}_1)_i = \frac{1}{\sqrt{(1+\alpha_i\tau_1)^2 + \beta_i^2\tau_1^2}} (\hat{x}_1 - \hat{X}_1)_i \, e^{-j\phi_i} \tag{11}$$

for the i^{th} eigenmode can now be written between the viscous displacement $(x_1 - z_1)_i$ and the cover thickness $(x_1 - X_1)_i$ (nip gap). Of particular interest is the phase shift between these two, which is

$$\tan\phi_i = \frac{\beta_i\tau_1}{1+\alpha_i\tau_1}. \tag{12}$$

It can also be easily shown that for the i^{th} eigenmode the phasor of the residual deformation is

$$\Delta\hat{l}_i = \sum_{k=1}^{N} a^k e^{-ks_iT} (\hat{x}_1 - \hat{z}_1)_i. \tag{13}$$

Therefore, the amplitude and phase angle of the residual deformation can also be calculated. By removing the memory effect from the system ($T \to \infty$), the characteristic equation becomes a polynome, because Eq. (5) rearranges as $\alpha = 0$. One can calculate the modal damping coefficients and the undamped eigenfrequencies from the complex valued roots of this characteristic equation from the equations [11]

$$\zeta_i = -\frac{\mathrm{Re}[s_i]}{\sqrt{\mathrm{Re}[s_i]^2 + \mathrm{Im}[s_i]^2}} \quad \text{and} \quad f_{n,i} = \frac{\sqrt{\mathrm{Re}[s_i]^2 + \mathrm{Im}[s_i]^2}}{2\pi}. \tag{14), (15}$$

Alternatively, the undamped (angular) eigenfrequencies can be calculated by using the equation

$$\det\left(\begin{bmatrix} k_s + k_\infty + k_1 & -k_\infty - k_1 \\ -k_\infty - k_1 & k_1 + k_\infty + K_s \end{bmatrix} - \omega^2 \begin{bmatrix} m & 0 \\ 0 & M \end{bmatrix}\right) = 0, \tag{16}$$

which corresponds to the limit $c_1 \to \infty$. Eq. (16) is often used in simple analysis.

In this work, the roots of the characteristic equation are solved by using Müller's method. This iterative method is based on the secant method, but uses quadratic interpolation instead of linear. In addition, Müller's method requires no derivatives and can handle complex valued roots as well, if the given starting values are complex and the computations use complex arithmetic. All calculations are performed by using MATLAB 7.7.

RESULTS AND DISCUSSION

In the numerical analysis, a simulation case was studied with parameter values acquired from a real industrial machine. The relaxation time of the polymer was set to $\tau_1 = 1$ ms. In a more detailed scenario, the recovery of the polymer would be determined by a relaxation spectrum spanning over a large scale of relaxation times. This would require the generalization of the SLS model in Fig. 1 by increasing the number of Maxwell elements. However, it has been shown that a single viscoelastic element, which reacts rapidly to the system dynamics, is enough to model the behavior of the viscoelastic roll cover adequately, if the element's recovery is retarded [1]. In the case of the model presented in this paper, the relaxation coefficient A, Eq. (3), was divided by 1000 to account for that part of the relaxation spectrum, which was not included in the SLS model of the cover. The roots of the characteristic equation were solved with $N = 1$. In the results, the notation s_i is used for the polygonal roots, where i refers to the root's polygonal number (nearest integer) at the revolution frequency $f = 1$ Hz. The polygonal number is calculated from Eq. (7).

Given by Eq. (14), the modal damping coefficients of the system are $\zeta_1 = 0.027$ and $\zeta_2 = 0.038$. Therefore, the damping of the system is subcritical. When calculated from Eq. (15), the undamped eigenfrequencies of the system are $f_{n,1} = 36.68$ Hz and $f_{n,2} = 184.36$ Hz. The corresponding values calculated from Eq. (16) are 36.69 Hz and 188.89 Hz. The difference is explained by the fact that Eq. (15) takes into account the polymer cover dynamics and shows the changes in the eigenfrequencies, when the relaxation time τ_1 is altered by changing the value of c_1. When calculated from Eq. (15), a decrease in the value of τ_1 lowers the eigenfrequencies. Eq. (16), on the other hand, gives always the same values regardless of the value of τ_1. With high values of τ_1, the eigenfrequencies given by Eq. (15) approach those of Eq. (16).

The relationship between the polygonal numbers, upper roll's revolution frequency $f = \omega / 2\pi$ and the undamped eigenfrequencies from Eq. (15) for $i = 9$ and 10 is shown in Fig. 2.

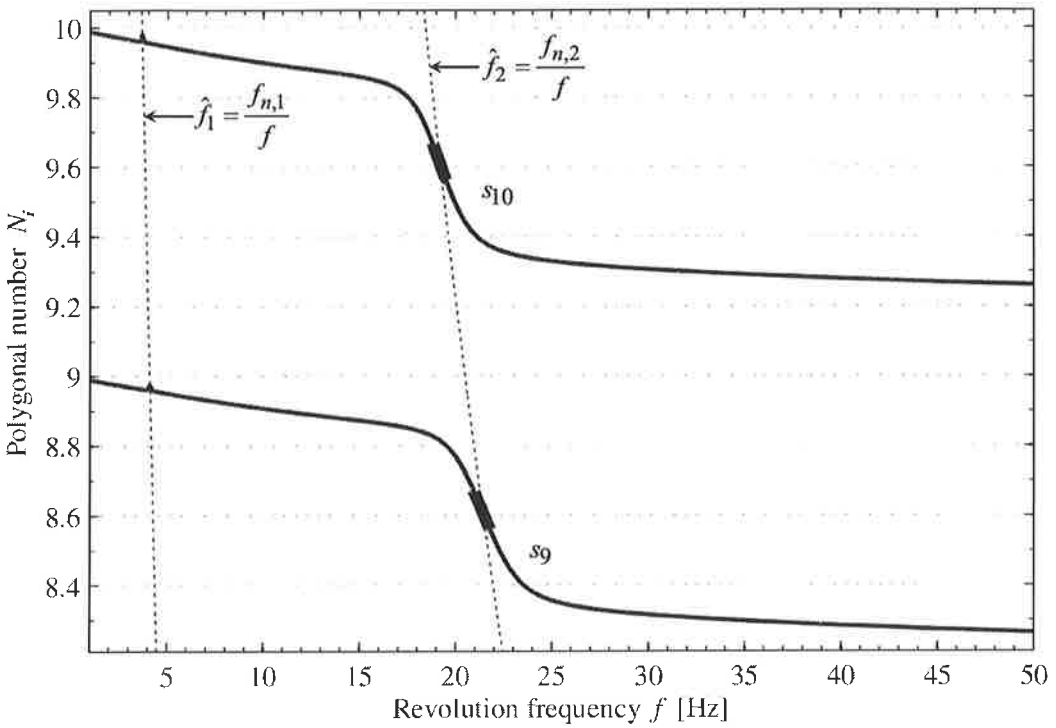

Fig. 2. Polygonal numbers of the polygonal roots s_9 and s_{10} shown as a function of the upper roll's revolution frequency. Unstable regions ($\alpha_i > 0$) are marked with thicker lines.

At low revolution frequencies the polygonal numbers of the roots are close to an integer. When the roots are in the area of influence of the lower eigenfrequency, a small rise can be seen in their polygonal numbers, nevertheless the roots stay stable. After the roots have passed the lower eigenfrequency and approach the higher, their polygonal numbers exhibit a steady decrease. In the vicinity of the higher eigenfrequency, a drastic fall can be observed in the polygonal numbers and due to the resonance of the second eigenmode the system also becomes unstable. In the second complex eigenmode the vibration phases of the rolls are nearly opposite, which causes large deformations on the covered roll surface able to synchronize with the second eigenmode. After the roots are no longer influenced significantly by the higher eigenfrequency and the revolution frequency continues to grow, the polygonal numbers of the roots exhibit a steady decrease again approaching asymptotically a constant value.

It should be noted that a stationary surface pattern on the polymer cover has only full wave-like periods on the peripheral surface of the roll, in other words, the stationary polygonal number (wavenumber) is an integer. The polygonal numbers with changing values in Fig. 2 are related to the fact that, when observed from aside, it would seem that the surface pattern was moving constantly on the peripheral surface of the roll. The movement was discovered experimentally in [1]. The current model is formulated so that on every revolution period the new deformations are superposed on the existing polymer cover and the sum of all contributions from preceding periods is the total deformation, yet all the deformations recover all the time. To give a more illustrative view – it can be presumed that the cover is attached to the roll only in the nip and is actually fed as an infinitely long undeformed thread to the nip. The deformations are gathered along the thread to assemble the force term, which drives the roll system. In conclusion, the use of the summing in Eq. (2) is a consequence from the one-dimensionality of the model and bares close resemblance to

the Boltzmann superposition principle [12]. To capture the complex pattern movement phenomenon in a precise manner, a more detailed two-dimensional contact model would have to be constructed.

As it was calculated, Eq. (16) gave higher eigenfrequencies than Eq. (15), which corresponds to a complete complex eigenmode analysis. Because Eq. (16) is nevertheless more commonly used for the sake of simplicity, it is often stated that the polygonal deformation and unstable vibrations take place at a clearly lower frequency than the eigenfrequency (resonance frequency) predicts. Moreover, on the basis of this interpretation, it is often deduced that there exists a separate pattern formation frequency, which, however, seems not to be the case as has been shown above.

Fig 3. shows the real parts of several polygonal roots. The figure clearly presents separate instability regions. Even though the general solution of the system is the sum of all possible solutions formed from Eq. (10), the general behavior of the roll system can be investigated satisfactorily on the basis of individual roots, since only one root is unstable at a time. There is an instability threshold at f = 9.3 Hz, when the system becomes unstable for the first time, in this case because of the root s_{20}. The real parts are near their maximum values when the corresponding polygonal numbers of the roots cross the higher eigenfrequency (see Fig. 2). As the revolution frequency grows, the roots get more unstable and the instability regions widen. The bigger the real part of a root is, the faster the polygonal deformation pattern grows on the roll surface. It has been verified by several authors that the unstable and stable regions alter as the revolution frequency (speed) of the covered roll grows. Refs. [1-3, 6-8] show such computational results with various models and [1, 10] include experimental verifications.

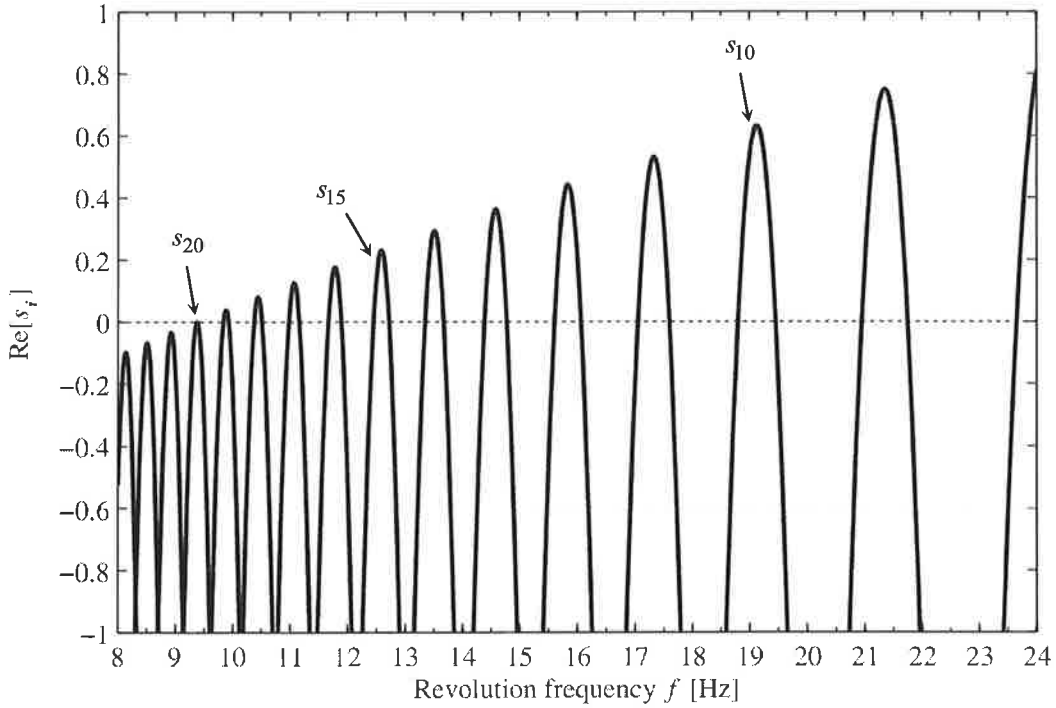

Fig. 3. Real parts of polygonal roots shown as a function of the revolution frequency of the upper roll. If Re[s_i] > 0, the roll system is unstable. Note the altering of the stable and unstable regions.

In Fig. 4, the relative phase angles $\arg(\hat{x}_1)$ and $\arg(\hat{X}_1)$, calculated from Eq. (9) with the root s_{10} and $\hat{z}_1 = 1$, are presented. Also, the phase difference of the rolls $\arg(\hat{x}_1) - \arg(\hat{X}_1)$, the phase shift $\arg(\hat{x}_1 - \hat{X}_1) - \arg(\hat{x}_1 - \hat{z}_1)$ between the nip gap and the viscous displacement of the Maxwell element, and the phase angle of the residual deformation $\Delta\hat{l}$ are shown in the figure. The residual deformation (memory effect) of the viscoelastic polymer cover drives the system constantly into a mode where the rolls are in opposite phases. In the vicinity of the lower eigenfrequency, the rolls strive for the same phase angle, a situation which corresponds to the first complex eigenmode. Above the lower eigenfrequency, the rolls are driven to opposite phases again. The root in question, s_{10}, is unstable between $f = 18.8 - 19.5$ Hz. The root's polygonal number intercepts with the higher eigenfrequency at $f = 19.2$ Hz (Fig. 2). If calculated from Eq. (12), the viscous displacement is 49 degrees behind the nip gap in phase, which is in unison with the plotted phase shift in Fig. 4. At $f = 19.2$ Hz the phase shift between the rolls and the residual deformation (driving force) is approximately ± 90 degrees. As the revolution frequency continues to grow the phase shift between the viscous displacement and the nip gap approaches $\pi/2$.

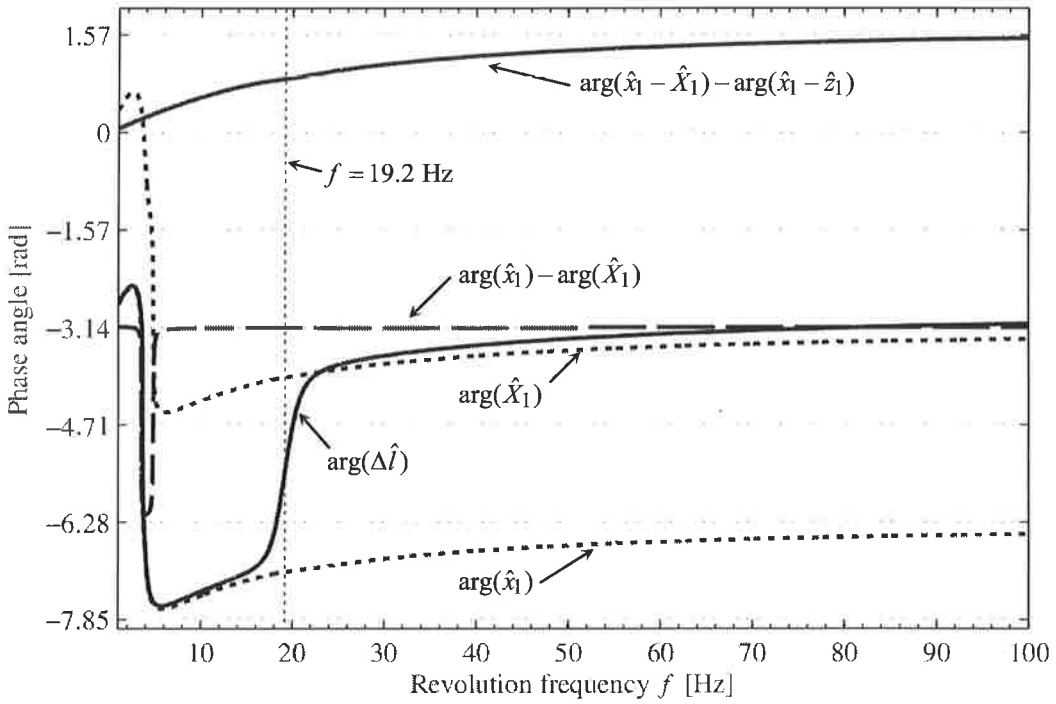

Fig 4. Relative phase angles and their relations in the case of the root s_{10} and $\hat{z}_1 = 1$. The phase of the residual deformation $\Delta\hat{l}$ calculated from Eq. (13) is also shown.

CONCLUSIONS

The viscoelastic memory effect of a polymer roll cover and the unstable vibrations induced by it were investigated analytically, by stability analysis, in a two-roll system. The memory introduces a time delay into the roll system, thus the equations of motion of the system constitute a set of delay differential equations. The results of numerical computations show separate instability regions of the system, which emerge in the vicinity of an eigenfrequency. Only one eigensolution of the system is unstable at a time, therefore comprehensive conclusions of the behavior of the roll

system can be drawn based only on stability analysis. It was also shown that the values of the undamped eigenfrequencies of the system may vary depending on the used calculation method, thus care ought to be taken when interpreting the results in relation to the eigenfrequencies. It should also be noted that the roll system may seem to act as if it was driven by a harmonic force, although the force caused by the memory effect cannot be considered as completely harmonic. When studying the subject further, a more detailed modelling of the mechanical properties of the polymer cover is of great importance. Notably, the way how several Maxwell element's would interact in the model is of interest. With sufficient knowledge of the phenomena presented in this paper, measures can be taken to eliminate the formation of the polygonal deformation pattern on a roll cover.

REFERENCES

[1] Sueoka, A., Ryu, T., Kondou, T., Tsuda, Y., Katayama, K., Takasaki, K., Yamaguchi, M., Hirooka, H., 'Polygonal deformation of roll-covering rubber', *JSME International Journal*, Series C, **39**(1), pp. 1-10, 1996.

[2] Sueoka, A., Ryu, T., Yoshikawa, M., Kondou, T., Tsuda, Y., 'Pattern formation generated in a winder system of textile machine', *JSME International Journal*, Series C, **41**(3), pp. 630-638, 1998.

[3] Sowa, N., Kondou, T., Mori, H., Choi, M.S., 'Method of preventing unstable vibration caused by time delays in contact rotating systems (Application of new stability analysis)', *JSME International Journal*, Series C, **49**(4), pp. 973-982, 2006.

[4] Jorkama, M. and von Hertzen, R., 'Delay phenomena in roll vibrations', *VIII Finnish Mechanics Days*, pp. 111-121, 2003, (ed.) Råback, P., Santaoja, K. & Stenberg, R.

[5] Jorkama, M. and von Hertzen, R., 'Two-drum winder stability analysis', *Pulp & Paper Canada*, **108**(5), pp. 35-37, 2007.

[6] Yuan L.H., 'Analysis of Delay Phenomena in Roll Dynamics', *Doctoral Dissertation*, Tampere University of Technology, Publication **397**, 2002.

[7] Järvenpää, V.M. and Yuan, L.H., 'Numerical Modeling of Paper Machine Roll Contact with Regenerative Out-Of-Roundness Excitation', *IUTAM Symposium on multiscale problems in multibody system contacts*, Springer, pp. 55-64, 2007, (ed.) Eberhard P.

[8] Yuan L.H. and Järvenpää V.M., 'Nonlinear Vibrations in a Covered Roll System with Viscoelastic Contact', *Journal of Communication of Nonlinear Science and Numerical Simulation*, **14**(7), pp. 3170-3178, 2009.

[9] Vuoristo, T., 'Effect of Strain Rate on the Deformation Behavior of Dual Phase Steels and Particle Reinforced Polymer Composites', *Doctoral Dissertation*, Tampere University of Technology, Publication **488**, 2004.

[10] Chinn, F., 'Dynamic instability of poly covered press rolls', *Pulp & Paper Canada*, **100**(1), pp. 11-14, 1999.

[11] Inman, D.J., *Engineering Vibration*, Prentice-Hall Inc., 2001.

[12] Ward, I.M., *Mechanical Properties of Solid Polymers*, John Wiley & Sons Ltd, 1971.

UNSTABLE VIBRATIONS OF ROTATING NIPPED ROLLS WITH MEMORY

Raimo von Hertzen
Lappeenranta University of Technology
P.O. Box 20, FI-53851 Lappeenranta, Finland
e-mail: rhertzen@lut.fi

Anssi Karttunen
Lappeenranta University of Technology
P.O. Box 20, FI-53851 Lappeenranta, Finland
e-mail: anssi.karttunen@lut.fi

ABSTRACT

Dynamic instability of viscoelastically covered rolls generates harmful vibrations in various industrial machines so that continuous operation of the machines is no longer possible. Of primary interest is the origin of the vibrations and design of suitable speed profiles and roll cover polymers, which could hinder the onset of the vibrations. In this paper, a two-roll model with a polymer cover is presented. The dynamic equations of motion of the system constitute a set of delay differential equations, which are solved numerically. The onset of unstable vibrations and the related surface patterns of the cover are studied.

INTRODUCTION

Many industrial applications involve cylindrical rolls which are rotating in contact with each other. Within the contact area between the rolls, called nip hereafter, the peripheral surfaces of the rolls deform elastically and lose their roundness temporarily. Viscoelastic and plastic deformations are also possible, depending on the loading conditions and surface materials of the rolls. In addition, the deformations are influenced considerably by a variety of environmental factors such as temperature and moisture, for example. Material may also be removed from the roll surfaces because of wear, grinding and cutting. The surface deformations recover instantly outside the nip, for the most part, but the residual deformations, which still exist after one revolution period (two-roll system), are fed back into the nip. This time-delayed feedback causes self-excited vibration in the roll system, which can lead to the formation of a periodic polygonal pattern on the roll surfaces. The wave-like surface pattern may grow gradually and the growth can be monitored as unstable vibration of the rotatory system during operation. This type of vibration becomes more powerful in time and is the cause for defective products and production breaks in many industrial processes involving nipped rolls. The aim of this study is to investigate unstable vibrations in a two-roll system in which the viscoelastic memory of a polymer roll cover acts as the source of vibrations.

The unstable vibrations of rotating nipped rolls with time-delayed feedback loads have recently been studied by several authors. Sueoka *et al.* have investigated the unstable vibrations caused by the pattern formation phenomenon of a polymer cover in two-roll systems both experimentally and theoretically [1, 2]. The polymer's viscoelastic properties have been included in the analytical lumped-mass models with a simple three-parameter element possessing one time constant to describe the relaxation process of the polymer outside the nip. The experimental and computational results show unstable vibrations at certain rolling speeds and deformation patterns which travel on the peripheral surface of the covered roll. Sowa *et al.* have used similar models to provide a method to prevent the pattern formation and unstable vibrations in roll systems with polymer covers [3]. Jorkama and von Hertzen succeeded in modifying the model of Ref. [1] and applied it to the process of paper winding [4, 5]. A wound paper roll with an increasing diameter acts as the viscoelastic part and causes unstable vibrations in these winding systems. Delayed roll systems with viscoelastic memory and grinding effects have been comprehensively studied also by Yuan [6]. Järvenpää and Yuan have investigated the polymer cover-induced roll vibrations with time domain simulations by using multibody dynamics [7] and a contact mechanical model [8]. Hermanski has also studied the pattern formation phenomenon by simulations in time domain [9]. Extensive experimental studies concentrating on the mechanical behavior of polymer covers in rolling contact and the effect of environmental factors therein have been conducted by Vuoristo [10]. Useful experimental data on roll vibrations has also been given by Chinn [11].

In this work, an analytical lumped-mass model is developed for a two-roll system with a polymer roll cover to study the formation of polygonal deformation patterns on the covered roll and the unstable vibrations induced by it. The viscoelastic properties of the cover will be modelled by the Standard Linear Solid model (SLS). The dynamic equations of motion of the system constitute a set of linear delay differential equations. The equations are solved numerically and the deformation of the polymer cover and the unstable vibrations of the system are then studied.

THEORY

The model of the studied system consisting of two rolls and a polymer cover is shown in Fig. 1.

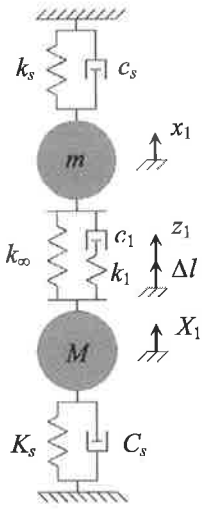

Figure 1. Model for a two-roll system with a polymer cover attached to the upper roll.

The rolls have masses m and M, and the polymer cover is modelled as massless. The vertical displacement coordinates for the upper and lower roll are x_1 and X_1, respectively. The roll supports are modelled by springs and viscous dashpots with stiffness and viscous damping coefficients k_s and c_s for the upper roll, and K_s and C_s for the lower roll, respectively. The SLS element has parameters k_∞, k_1 and c_1, where the latter two form a Maxwell element. The coordinate z_1 determines the movement of the spring's end plate in the damper of the Maxwell element. The variable Δl, bringing a time delay into the system, describes the residual deformation, in other words, the deviation of the upper roll from circular shape, just before entering the nip.

The equations of motion of the system are

$$\mathbf{M}\ddot{\mathbf{X}}(t)+\mathbf{C}\dot{\mathbf{X}}(t)+\mathbf{K}\,\mathbf{X}(t)=\mathcal{K}\sum_{k=1}^{N}a_k(t)\,\mathbf{X}(t-T_k(t))\,, \tag{1}$$

where the vector for the displacement coordinates is

$$\mathbf{X}=\{x_1,z_1,X_1\}^{\mathrm{T}}\,, \tag{2}$$

the mass, damping and stiffness matrices are

$$\mathbf{M}=\begin{bmatrix} m & 0 & 0\\ 0 & 0 & 0\\ 0 & 0 & M\end{bmatrix},\quad \mathbf{C}=\begin{bmatrix} c_s+c_1 & -c_1 & 0\\ -c_1 & c_1 & 0\\ 0 & 0 & C_s\end{bmatrix},\quad \mathbf{K}=\begin{bmatrix} k_s+k_\infty & 0 & -k_\infty\\ 0 & k_1 & -k_1\\ -k_\infty & -k_1 & k_1+k_\infty+K_s\end{bmatrix}, \tag{3), (4), (5)}$$

and the stiffness matrix related to the viscous displacement of the Maxwell element is

$$\mathcal{K}=k_1\begin{bmatrix} 1 & -1 & 0\\ 0 & 0 & 0\\ -1 & 1 & 0\end{bmatrix}. \tag{6}$$

In addition, N is the total number of revolution periods at time t, $a_k(t)=e^{AT_k(t)}$ the decay factor for the viscoelastic deformation, and T_k determines the time used for k revolution periods preceding the time t. For example, $T_1(t)$ is the time used for the previous period and $T_2(t)$ the time for the last two periods preceding the time t. The recovery coefficient for the viscoelastic deformation is

$$A=-\frac{k_\infty}{k_\infty+k_1}\frac{1}{\tau_1}, \tag{7}$$

where $\tau_1=c_1/k_1$ is the relaxation time of the polymer cover.

For the numerical analysis, a change of variables is performed in Eq. (1) by changing the time variable t to the revolution angle θ of the upper roll. This results in

$$\omega^2(\theta)\mathbf{M}\,\mathbf{X}''(\theta)+\left(\alpha(\theta)\mathbf{M}+\omega(\theta)\mathbf{C}\right)\mathbf{X}'(\theta)+\mathbf{K}\,\mathbf{X}(\theta)=\mathcal{K}\sum_{k=1}^{N}a_k(\theta)\;\mathbf{X}(\theta-2\pi k)\,. \tag{8}$$

Here $a_k(\theta) \equiv e^{AT_k(t(\theta))}$ and $\mathbf{X}(\theta) \equiv \mathbf{X}(t(\theta))$ and the prime stands for differentiation with respect to the revolution angle θ. In the special case when the angular acceleration vanishes ($\alpha = 0$), the angular revolution frequency ω is constant, and Eq. (8) rearranges as

$$\omega^2 \mathbf{M}\,\mathbf{X}''(\theta) + \omega \mathbf{C}\,\mathbf{X}'(\theta) + \mathbf{K}\,\mathbf{X}(\theta) = \mathcal{K} \sum_{k=1}^{N} a_k \mathbf{X}(\theta - 2\pi k), \tag{9}$$

where $a_k = e^{kAT}$ and $T = 2\pi / \omega$.

For numerical integration Eqs. (8) and (9) are transformed into state space presentation. The equations are integrated by using MATLAB 7.7 and its *ode45* solver. After every integration step the solver calls for its own output function, and the results are transferred therein and saved as vectors. The results can be read from the computer memory during the integration to create the time delay terms for the computations. The procedure is an adaptation of the method of steps [12]. Other ode-solvers may be used as well, since the principles of the output functions are the same for most solvers in MATLAB. Therefore, if the differential equations are stiff because of the parameters of the system, *ode23s* can be used. Alternatively, the well-known solvers for delay differential equations, *dde23* and *ddesd*, could be used, but these are not optimized for the studied case and, thus, lack the speed of *ode45* combined with the method of steps. To investigate the results in the frequency domain, the Fast Fourier Transform (FFT) is used.

RESULTS AND DISCUSSION

A simulation case was studied with parameter values acquired from a real industrial machine. The relaxation time of the polymer was set to $\tau_1 = 1$ ms. In a more detailed scenario, the recovery of the polymer would be determined by a relaxation spectrum spanning over a large scale of relaxation times. This would require the generalization of the SLS model in Fig. 1 by increasing the number of Maxwell elements. However, it has been shown that a single viscoelastic element, which reacts rapidly to the system dynamics, is enough to model the behavior of the viscoelastic roll cover adequately, if the element's recovery is retarded [1]. In the case of the model presented in this paper, the relaxation coefficient A, Eq. (7), was divided by 1000 to account for that part of the relaxation spectrum, which was not included in the SLS model of the cover. The equations were integrated with $N = 1$.

Fig. 2 shows results which were integrated from Eq. (9) with a constant revolution frequency $f =$ 19.2 Hz of the upper roll. The used initial condition was $X_1(0) = -0.001$ m with all other initial conditions set to zero. Fig. 2a indicates that the system is unstable at the revolution frequency in question. The vibration amplitudes of the rolls grow exponentially, the small picture shows the steady-state response of the system during one revolution period. It can be seen that the rolls are in opposite phases. In Fig. 2b FFT has been performed on the data of the displacement coordinate x_1 in Fig 2a. The figure shows the power spectrum (squared amplitude in [dB]) of the upper roll. The power spectrum of the signal represents the contribution of every frequency of the spectrum to the power of the overall signal. The peak value appears at the frequency 184.4 Hz, in [13] it was shown that this corresponds to the resonance frequency of the second complex eigenmode of the system. By dividing the peak frequency by the revolution frequency, we get 184.4 Hz / 19.2 Hz = 9.6. This is the polygonal number (wave-number) of the wave-like deformation pattern of the covered roll and verifies the results and conclusions made of the general behavior of the system on the basis of the stability analysis in [13]. The transient vibrations of the rolls during the first three revolution periods of the upper roll are shown in Fig. 2c. The phase shift between the nip gap and

the viscous displacement of the Maxwell element can be seen in Fig. 2d. If approximated from the figure, the shift is about 50 degrees, which corresponds to the result in [13].

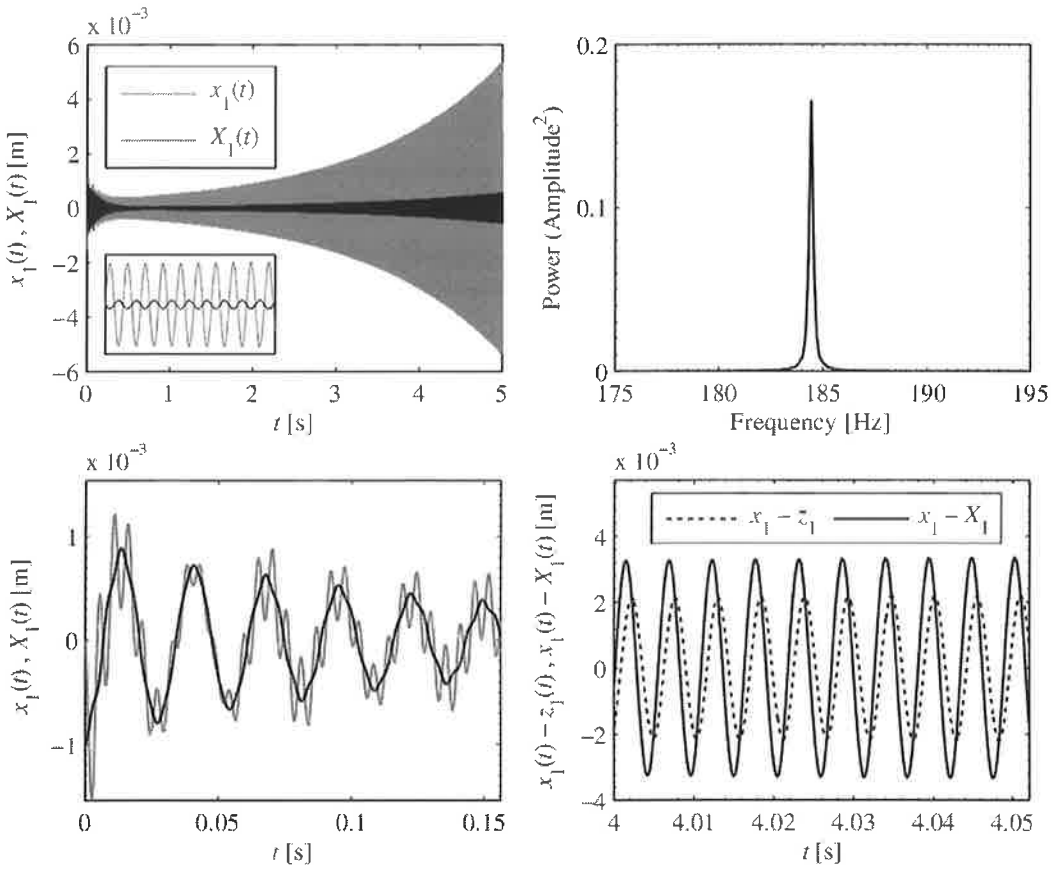

Fig. 2 a) Self-excited responses of the rolls for f = 19.2 Hz, b) Vibration power spectrum of the response of x_1, c) Transient vibrations of the roll responses, d) Responses of the nip gap and the viscous displacement of the Maxwell element during one revolution period. Note the phase shift between the two.

Fig. 3 shows an integration result calculated from Eq. (8) using a constant angular acceleration of 0.5 rad/s^2 of the upper roll to model a speed-up ramp. The initial condition was $X_1(0)$ = -0.1 m with all other initial conditions set to zero. The transient vibrations in the beginning of the simulation with large amplitudes have been left out from the figure. Separate instability regions of the system can be seen in the figure. As the revolution frequency of the upper roll grows, these regions widen and the system gets clearly more unstable. When accelerating real industrial machines to certain speeds, the unstable zones may cause problems. At some point the instability regions may be too wide and unstable to cross.

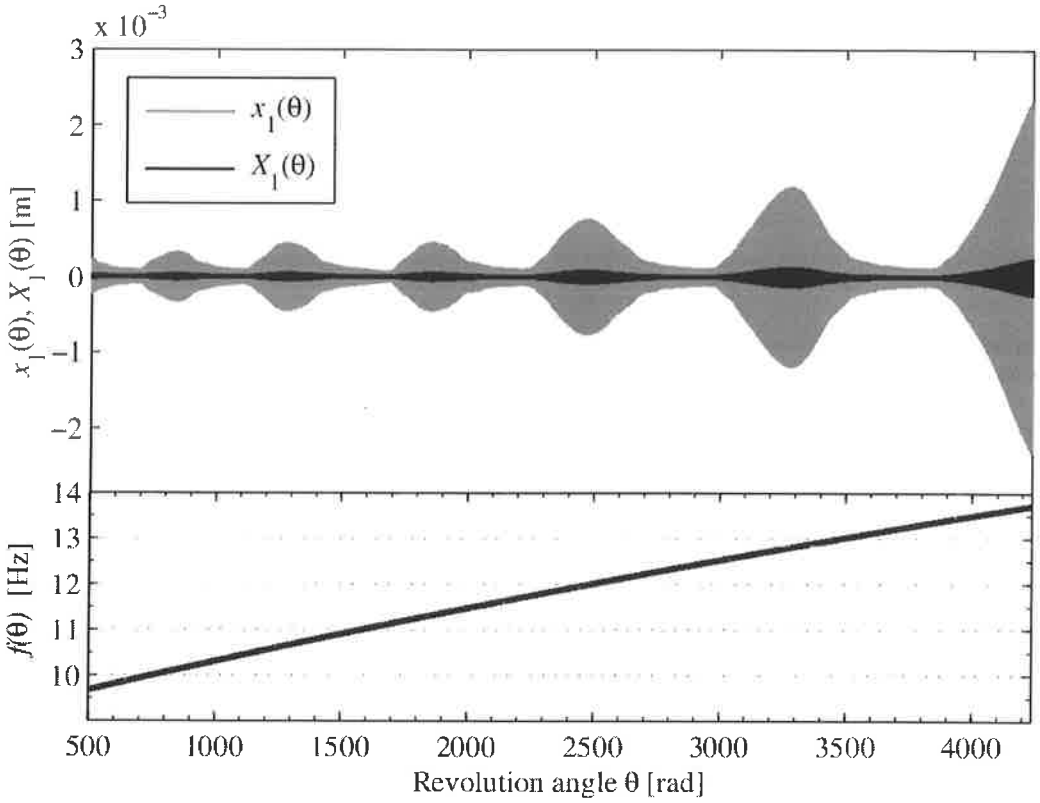

Fig 3. Computed result for a roll system with a constant angular acceleration $\alpha = 0.5$ rad/s^2 of the upper roll. The upper figure shows the self-excited responses of the rolls and the lower figure the growing revolution frequency of the upper roll as a function of its revolution angle.

Fig. 4 shows a waterfall plot combined from the power spectras formed from the responses of the upper roll at constant revolution frequencies $f = 9, 9.05, \ldots, 15$ Hz. Every individual spectrum has been calculated as in Fig. 2b. The waterfall plot also shows that there are separate instability regions in the system. Several authors have verified that the unstable and stable regions alter as the revolution frequency (speed) of the covered roll grows. Refs. [1-3, 6-8] show such computational results with various models and [1, 10] include experimental verifications.

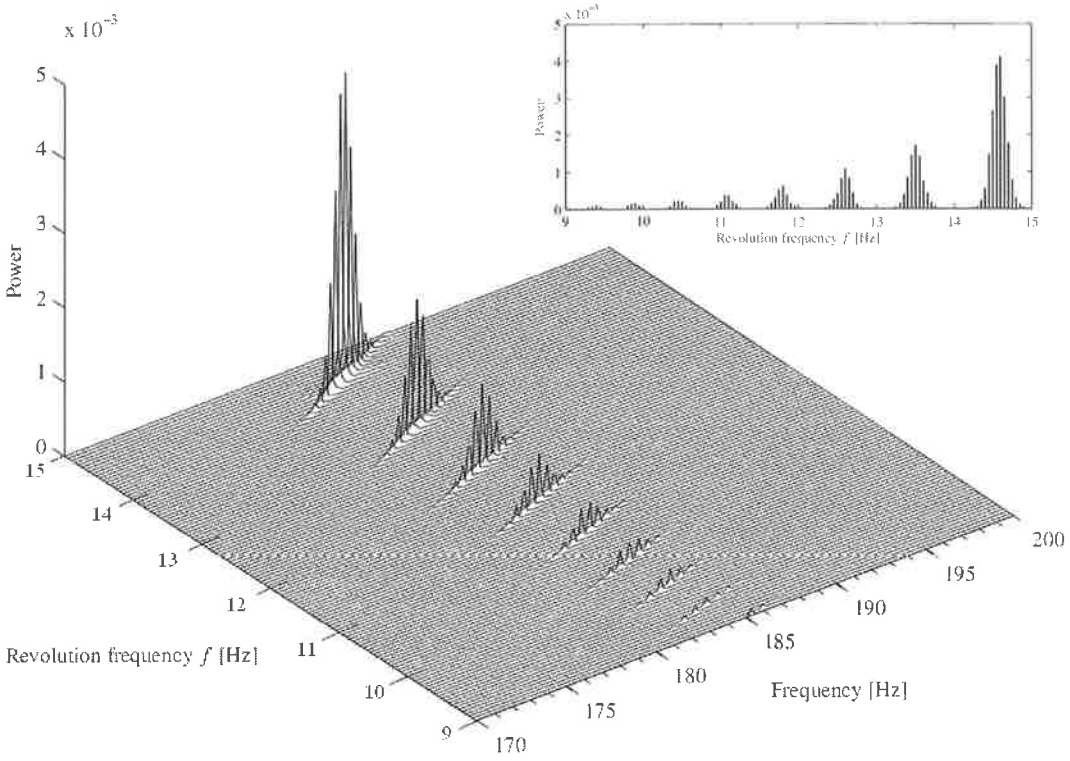

Fig. 4. Waterfall plot formed from separate power spectras. The projection in the smaller figure shows the stable zones between the unstable ones.

CONCLUSIONS

The viscoelastic memory effect of a polymer roll cover and the unstable vibrations induced by it were investigated numerically in a two-roll system. The memory introduces a time delay into the roll system and, therefore, the equations of motion of the system constitute a set of linear delay differential equations. The results of the numerical computations display separate instability regions of the system. It can be deduced, based on the results of this paper and Ref. [13], that the unstable zones emerge in the area of influence of the higher eigenfrequency of the system. It should also be noted that the roll system may seem to act as if it was driven by a harmonic force, although the force caused by the memory effect cannot be considered as completely harmonic. When studying the subject further, a more detailed modelling of the mechanical properties of the polymer cover is of great importance. Notably, the way how several Maxwell element's would interact in the model is of interest. In addition, by including the bearings of the rolls in the model, more useful information could be gained to further stimulate the design of damping mechanisms for nipped roll systems with polymer covers.

REFERENCES

[1] Sueoka, A., Ryu, T., Kondou, T., Tsuda, Y., Katayama, K., Takasaki, K., Yamaguchi, M., Hirooka, H., 'Polygonal deformation of roll-covering rubber', *JSME International Journal*, Series C, **39**(1), pp. 1-10, 1996.

[2] Sueoka, A., Ryu, T., Yoshikawa, M., Kondou, T., Tsuda, Y., 'Pattern formation generated in a winder system of textile machine', *JSME International Journal*, Series C, **41**(3), pp. 630-638, 1998.

[3] Sowa, N., Kondou, T., Mori, H., Choi, M.S., 'Method of preventing unstable vibration caused by time delays in contact rotating systems (Application of new stability analysis)', *JSME International Journal*, Series C, **49**(4), pp. 973-982, 2006.

[4] Jorkama, M. and von Hertzen, R., 'Delay phenomena in roll vibrations', *VIII Finnish Mechanics Days*, pp. 111-121, 2003, (ed.) Råback, P., Santaoja, K. & Stenberg, R.

[5] Jorkama, M. and von Hertzen, R., 'Two-drum winder stability analysis', *Pulp & Paper Canada*, **108**(5), pp. 35-37, 2007.

[6] Yuan L.H., 'Analysis of Delay Phenomena in Roll Dynamics', *Doctoral Dissertation*, Tampere University of Technology, Publication **397**, 2002.

[7] Järvenpää, V.M. and Yuan, L.H., 'Numerical Modeling of Paper Machine Roll Contact with Regenerative Out-Of-Roundness Excitation', *IUTAM Symposium on multiscale problems in multibody system contacts*, Springer, pp. 55-64, 2007, (ed.) Eberhard P.

[8] Yuan L.H. and Järvenpää V.M., 'Nonlinear Vibrations in a Covered Roll System with Viscoelastic Contact', *Journal of Communication of Nonlinear Science and Numerical Simulation*, **14**(7), pp. 3170-3178, 2009.

[9] Hermanski, M., 'Barringbildung am Glättkalander einer Papiermaschine', *Das Papier*, **49**(6), pp. 344-347, 1995.

[10] Vuoristo, T., 'Effect of Strain Rate on the Deformation Behavior of Dual Phase Steels and Particle Reinforced Polymer Composites', *Doctoral Dissertation*, Tampere University of technology, Publication **488**, 2004.

[11] Chinn, F., 'Dynamic instability of poly covered press rolls', *Pulp & Paper Canada*, **100**(1), pp. 11-14, 1999.

[12] Driver, R.D., '*Ordinary and Delay Differential Equations*', Springer-Verlag, 1977.

[13] Karttunen A.T. and von Hertzen, R., 'Stability Analysis of Rotating Nipped Rolls', *X Finnish Mechanics Days*, Jyväskylä 3.-4. December 2009.

NOPEUDESTA RIIPPUVIEN HITAUSVOIMATERMIEN VAIKUTUS PALKKILASKENTAAN

Jari MÄKINEN, Heikki MARJAMÄKI & Sami PAJUNEN
Konstruktiotekniikan laitos
Tampereen teknillinen yliopisto
PL 589, 33101 TAMPERE

TIIVISTELMÄ

Geometrisesti tarkkaa palkkimallia käytetään yleisesti epälineaarisessa dynamiikassa, missä siirtymät ja kiertymät ovat suuria. Tässä palkkimallissa solmusiirtymät ja -kiertymät kuvataan suoraan inertiaalisen referenssikoordinaatiston avulla, eikä palkin suhteellista siirtymää johonkin palkin mukana liikkuvaan vertailukoordinaatistoon tarvita, toisin kuin epäinertiaalisissa (co-rotational) palkkimalleissa. Geometrisesti tarkan palkkimallin yhtenä etuna on yksinkertaisempi hitausvoimavektorin rakenne verrattuna epäinertiaalisiin palkkimalleihin. Yksinkertaisimmillaan tasoelementin, jossa solmut sijaitsevat palkin neutraaliakselilla, hitausvoimavektori on muotoa massamatriisi kertaa kiihtyvyysvektori, eikä muita termejä ole. Jos solmut eivät sijaitse tasopalkin neutraaliakselilla (offset-elementti), hitausvoimavektoriin tulee myös nopeudesta riippuvia termejä. Samoin avaruustapauksessa (3D) näin on asian laita.

Tässä esityksessä tutkitaan nopeudesta riippuvien hitausvoimatermien vaikutusta laskentatapauksiin. Esimerkkinä tarkastellaan Reissnerin palkkimallin mukaista geometrisesti tarkkaa palkkimallia ja tästä palkkimallista johdettuja elementtejä. Tavallisesti elementtimalleissa lasketaan kaikki hitausvoimatermit, myös nopeudesta riippuvat, mutta nopeudesta riippuvat tangenttimatriisit jätetään laskematta. Tavallisesti ajatellaan, että näiden tangenttimatriisien vaikutus laskentaan on vähäinen. Lisäksi nämä tangenttimatriisit ovat rakenteeltaan varsin mutkikkaita ja siten laskennallisesti työläitä ja sen lisäksi vielä epäsymmetrisiä, mikä rikkoisi muutoin symmetrisen laskentarakenteen. Tutkimuksessa pyritään selvittämään, milloin nopeudesta riippuvat tangenttimatriisit olisi syytä ottaa laskennassa mukaan, ja milloin nämä termit voidaan huoletta jättää laskematta.

1 VIRTUAALISEN TYÖN PERIAATE

Mekaniikan tehtävissä ratkaistavana on tavallisesti ulkoisten kuormitusten vaikutuksesta muotoaan muuttava kappalesysteemi. Perustuntemattomana on tällöin yleensä kappalesysteemin siirtymäkenttä. Tällöin usein käytetty menetelmä tehtävän formuloinnissa on virtuaalisen työn periaate. Virtuaalisen työn periaatteen

$$\delta W = \delta W_{\text{ext}} - \delta W_{\text{int}} - \delta W_{\text{acc}} = 0 \tag{1}$$

termit koostuvat ulkoisten voimien tekemästä virtuaalisesta työstä δW_{ext}, sisäisten voimien virtuaalisesta työstä δW_{int} ja hitausvoimien δW_{acc} virtuaalisesta työstä, missä miinus merkki on valittu siten, että sisäisten voimien ja hitausvoimien tekemä työ on vastakkaismerkkinen ulkoisten voimien tekemään virtuaaliseen työhön nähden.

Virtuaalisen työn periaate (1) voidaan kirjoittaa vektoreiden pistetulon avulla seuraavasti

$$\delta W = \delta\mathbf{u}\bullet\left(\mathbf{F}_{\mathrm{u,ext}}(t) - \mathbf{F}_{\mathrm{u,int}}(t) - \mathbf{M}_{\mathrm{u}}\ddot{\mathbf{u}}\right) = 0 \qquad \forall\delta\mathbf{u}$$

missä $\delta\mathbf{u}$ on kinemaattisesti käypä virtuaalinen siirtymä, $\mathbf{F}_{\mathrm{u,ext}}$ on ulkoinen voimavektori (kuormitusvektori), $\mathbf{F}_{\mathrm{u,int}}$ on sisäinen voimavektori ja $\mathbf{M}_{\mathrm{u}}\ddot{\mathbf{u}}$ on hitausvoimavektori, ts. massamatriisi kertaa kiihtyvyysvektori. Tässä esityksessä käytetään tätä hitausvoimien merkintää.

Kun elementtimenetelmän mukainen diskretointi, interpolointi ja linearisointi on tehty, saadaan virtuaalisen työn periaatetta soveltamalla johdettua elementtien sisäiset solmuvoimat sekä tangenttioperaattorit, kuten jäykkyys- ja massamatriisit. Kinemaattiset rajoitteet voidaan hoitaa helposti upottamalla, erityisesti, mikäli ne ovat holonomisia eli yhtälötyyppisiä siirtymärajoituksia.

2 VAPAUSASTEMITTAUSJÄRJESTELMÄN MUUTTAMINEN

Kinemaattiset rajoitteet ja vapausastemittausjärjestelmän muuttaminen voidaan hoitaa seuraavaksi esitettävää orjuutustekniikkaa ("isäntä-orja") käyttäen. Perusajatus orjuutustekniikassa on esittää orjasiirtymät, jotka edustavat orjaelementin siirtymämuuttujia isäntäsiirtymien avulla [1] ja [2]. Isäntäsiirtymät ovat vapausasteita, jotka syntyvät mallinnettaessa erilaisia kinemaattisia kytkentöjä, kuten joustava translaatioliitos, jonka vapausaste kuvaa liitettyjen elementtien asemaa toisiinsa nähden mitattuna elementin keskiviiva pitkin.

Olkoon $\mathbf{f}$ derivoituva kuvaus kahden kytketyn siirtymämittausjärjestelmän $\mathbf{u}$ ja $\mathbf{v}$ välillä:

$$\mathbf{u} = \mathbf{f}(\mathbf{v}) \tag{2}$$

missä $\mathbf{u}$ on orjasiirtymävektori ja $\mathbf{v}$ vastaava isäntäsiirtymävektori. Tällöin orjasiirtymän $\mathbf{u}$ ja isäntäsiirtymän $\mathbf{v}$ välinen linearisoitu yhteys saadaan

$$\delta\mathbf{u} = D_{\mathrm{v}}\mathbf{f}(\mathbf{v})\bullet\,\delta\mathbf{v} = \mathbf{B}(\mathbf{v})\bullet\delta\mathbf{v} \tag{3}$$

missä D_{v} viittaa derivointiin isäntäsiirtymien $\mathbf{v}$ suhteen. Yhtälö (3) määrittelee kinemaattisen matriisin $\mathbf{B}(\mathbf{v})$ jonka avulla voidaan määrittää orjasiirtymien variaatiot $\delta\mathbf{u}$ kun isäntäsiirtymien variaatiot $\delta\mathbf{v}$ tunnetaan. Oletetaan vielä, että kinemaattisen matriisin $\mathbf{B}$ ranki on täysi.

Koska molemmissa mittausjärjestelmissä tehty virtuaalinen työ tulee olla yhtä suuri, on vastaavien voimamittausten välillä on yhteys

$$\delta W = \delta\mathbf{u}\bullet\mathbf{F}_{\mathrm{u}} = \delta\mathbf{v}\bullet\mathbf{F}_{\mathrm{v}} \tag{4}$$

ja vastaavien voimamittausten $\mathbf{F}_{\mathrm{v}}$ ja $\mathbf{F}_{\mathrm{u}}$ välinen yhteys saadaan sijoittamalla yhteys (3) yhtälöön (4)

$$\mathbf{F}_{\mathrm{v}} = \mathbf{B}^{\mathrm{T}}\mathbf{F}_{\mathrm{u}} \tag{5}$$

Edellä oleva yhtälö on erityisen tärkeä yhteys isäntä-orja tekniikkaa käytettäessä. Jäykkyysmatriisi mittausjärjestelmässä $\mathbf{v}$ saadaan linearisoimalla voimamittausten välinen yhteys (5) pisteessä $\mathbf{v}_0$ tai vastaavassa orja-pisteessä $\mathbf{u}_0 = \mathbf{f}(\mathbf{v}_0)$ suuntaan $\Delta\mathbf{v}$ käyttäen mittausjärjestelmään $\mathbf{u}$ kuuluvia voimia:

$$\begin{aligned}\mathit{Lin}(\mathbf{F}_{\mathrm{v}};\Delta\mathbf{v}) &= \mathbf{B}^{\mathrm{T}}\mathbf{F}_{\mathrm{u}_0} + \mathbf{B}^{\mathrm{T}}D_{\mathrm{v}}(\mathbf{F}_{\mathrm{u}})\bullet\Delta\mathbf{v} + D_{\mathrm{v}}(\mathbf{B}^{\mathrm{T}}\overline{\mathbf{F}}_{\mathrm{u}})\bullet\Delta\mathbf{v} \\ &= \mathbf{F}_{\mathrm{v}_0} + \mathbf{B}^{\mathrm{T}}\mathbf{K}_{\mathrm{u}}\mathbf{B}\bullet\Delta\mathbf{v} + \mathbf{K}_{\mathrm{g}}(\mathbf{F}_{\mathrm{u}})\bullet\Delta\mathbf{v}\end{aligned} \tag{6}$$

Viiva orja-mittauksen $\mathbf{F}_u$ päällä tarkoittaa, että voimaa pidetään vakiona derivoitaessa jälkimmäistä termiä, eli derivointi kohdistuu kinemaattiseen kytkentään. Yhtälöä (6) pidämme määritelmänä materiaaliselle jäykkyysmatriisille, jonka lauseke nähdään toisesta termistä sekä geometriselle jäykkyysmatriisille $\mathbf{K}_g$, jonka lauseke saadaan jälkimmäisestä termistä. Massamatriisin $\mathbf{M}$ ja nopeudesta riippuvien hitausvoimanvektorin $\mathbf{F}_{cent}$ määritykseen tarvitaan hitausvoimien tekemää virtuaalista työtä

$$\delta W_{acc} = \delta \mathbf{u} \bullet (\mathbf{M}_u \ddot{\mathbf{u}}) \tag{7}$$

Derivoimalla yhtälö (2) ajan suhteen, saadaan yhteys mittausjärjestelmien nopeuksien ja kiihtyvyyksien välille

$$\begin{aligned} \dot{\mathbf{u}} &= D_v \mathbf{f}(\mathbf{v}) \bullet \dot{\mathbf{v}} = \mathbf{B}\,\dot{\mathbf{v}} \\ \ddot{\mathbf{u}} &= \mathbf{B}\,\ddot{\mathbf{v}} + \dot{\mathbf{B}}\,\dot{\mathbf{v}} \end{aligned} \tag{8}$$

Sijoittamalla yhtälö (8) yhtälöön (7) saadaan hitausvoimien virtuaalinen työ mittausjärjestelmässä $\mathbf{v}$

$$\begin{aligned} \delta W_{acc} &= \delta \mathbf{v} \bullet \mathbf{B}^T \mathbf{M}_u (\mathbf{B}\,\ddot{\mathbf{v}} + \dot{\mathbf{B}}\,\dot{\mathbf{v}}) \\ &= \delta \mathbf{v} \bullet \left(\mathbf{B}^T \mathbf{M}_u \mathbf{B}\,\ddot{\mathbf{v}} + \mathbf{B}^T \mathbf{M}_u \dot{\mathbf{B}}\,\dot{\mathbf{v}} \right) \end{aligned} \tag{9}$$

Massamatriisi ja hitausvoimien aiheuttama solmuvoimavektori isäntämittausjärjestelmässä $\mathbf{v}$ saadaan orjamittausjärjestelmän $\mathbf{u}$ vastaavien suureiden avulla

$$\begin{aligned} \mathbf{M}_v &= \mathbf{B}^T \mathbf{M}_u \mathbf{B} \\ \mathbf{F}_{v,cent} &= \mathbf{B}^T \mathbf{M}_u \dot{\mathbf{B}}\,\dot{\mathbf{v}} \end{aligned} \tag{10}$$

missä $\mathbf{M}_v$ on isäntäelementin jäykkyysmatriisi ja $\mathbf{F}_{v,cent}$ isäntäelementin nopeudesta riippuva hitausvoimavektori. On syytä huomata, että mikäli kinemaattinen matriisi $\mathbf{B}$ muuttuu siirtymien $\mathbf{v}$ funktiona, niin myös massamatriisi muuttuu siirtymien funktiona.

Hitausvoimavektorin tangenttimatriisien johdossa tarvitaan orjakiihtyvyysvektorin $\ddot{\mathbf{u}}$ derivaattoja isäntänopeus- ja isäntäkiihtyvyysvektorin suhteen. Nämä derivaatat ovat

$$\frac{\partial \ddot{\mathbf{u}}}{\partial \mathbf{v}} = \frac{\partial \ddot{\mathbf{f}}(\mathbf{v})}{\partial \mathbf{v}} = \frac{d^2}{dt^2} \frac{\partial \mathbf{f}(\mathbf{v})}{\partial \mathbf{v}} = \frac{d^2 \mathbf{B}}{dt^2} = \ddot{\mathbf{B}} \tag{11}$$

jossa on käytetty derivoinnin vaihtosääntöä, sekä

$$\begin{aligned} \ddot{\mathbf{u}} &= D_{vv} \mathbf{f}(\mathbf{v}) : \dot{\mathbf{v}} \otimes \dot{\mathbf{v}} + D_v \mathbf{f}(\mathbf{v}) \ddot{\mathbf{v}} \\ \frac{\partial \ddot{\mathbf{u}}}{\partial \ddot{\mathbf{v}}} &= 2 D_{vv} \mathbf{f}(\mathbf{v}) \bullet \dot{\mathbf{v}} = 2 D_v \mathbf{f}(\mathbf{v}) = 2\dot{\mathbf{B}} \end{aligned} \tag{12}$$

missä on käytetty ketjusääntöä. Tällöin hitausvoiman tangenttimatriiseiksi saadaan

$$\begin{aligned} \mathbf{K}_{v,acc} &= \frac{\partial \mathbf{B}^T \mathbf{M}_u \ddot{\mathbf{u}}}{\partial \mathbf{v}} = \mathbf{B}^T \mathbf{M}_u \frac{\partial \ddot{\mathbf{u}}}{\partial \mathbf{v}} + \frac{\partial \mathbf{B}^T \overline{\mathbf{M}_u \ddot{\mathbf{u}}}}{\partial \mathbf{v}} = \mathbf{B}^T \mathbf{M}_u \ddot{\mathbf{B}} + \mathbf{K}_g (\mathbf{M}_u \ddot{\mathbf{u}}) \\ \mathbf{C}_{v,acc} &= \frac{\partial \mathbf{B}^T \mathbf{M}_u \ddot{\mathbf{u}}}{\partial \dot{\mathbf{v}}} = \mathbf{B}^T \mathbf{M}_u \frac{\partial \ddot{\mathbf{u}}}{\partial \dot{\mathbf{v}}} = 2 \mathbf{B}^T \mathbf{M}_u \dot{\mathbf{B}} \end{aligned} \tag{13}$$

jossa $\mathbf{K}_{v,acc}$ on hitausvoimien jäykkyysmatriisi ja $\mathbf{C}_{v,acc}$ vaimennusmatriisi isäntämittausjärjestelmässä **v**. Jäykkyysmatriisi $\mathbf{K}_{v,acc}$ riippuu kiihtyvyyksistä ja $\ddot{\mathbf{B}}$ kautta myös nopeuksista, vaimennusmatriisi $\mathbf{C}_{v,acc}$ riippuu nopeuksista mutta ei kiihtyvyyksistä. Molemmat matriisit riippuvat yleisessä tapauksessa myös siirtymistä. $\mathbf{K}_g$ on isäntä-orjakytkennästä johtuva geometrinen jäykkyysmatriisi.

3 EPÄLINEAARINEN TASOPALKKIELEMENTTI

Epälineaarisissa palkkielementeissä käytetään tässä työssä Reissnerin kinemaattisesti tarkkaa palkkiteoriaa, missä siirtymäkenttä mitataan kiinteään koordinaatistoon nähden.

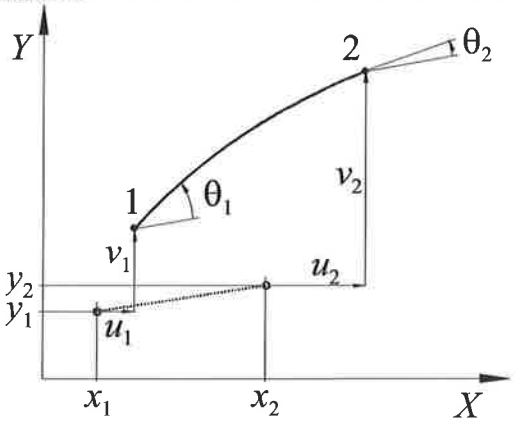

Kuva 1. Tasopalkkielementin alkuasema (katkoviiva) ja siirtynyt tila (yhtenäinen viiva)

Kiinteätä koordinaatistoa käyttäen saadaan yksinkertaisempi muoto palkin kineettiselle energialle [3]. Tällä palkkielementillä on yksinkertaiset muotofunktiot, koska siirtymä- ja rotaatiovapausasteet ovat toisistaan riippumattomia. Tämä ominaisuus helpottaa muun muassa translaatioliitosten mallinnusta antaen sisäisten solmuvoimien vektorille ja tangentiaaliselle jäykkyysmatriisille verrattain yksinkertaiset lausekkeet. Lisäksi elementti ottaa huomioon leikkausmuodonmuutoksen, joka voi olla merkittävä korkeaprofiilisilla palkkirakenteilla.

Palkkielementti perustuu suurten venymien teoriaan, katso [4] ja [5] ja sillä on kolme solmuvapausastetta, kaksi siirtymävapausastetta ja yksi rotaatiovapausaste. Yksinkertaisuuden vuoksi tässä työssä rajoittaudutaan vain palkkielementtiin, jolla on kaksi solmua ja lineaariset muotofunktiot. Palkin sisäinen solmuvoimavektori on

$$\mathbf{q}_{\text{int}} = \int_{L_0} \mathbf{B}^{\mathrm{T}} \mathbf{S}\, dL_0 \tag{14}$$

missä kinemaattinen matriisi **B** on

$$\mathbf{B} = \begin{bmatrix} cN_1' & sN_1' & \gamma N_1 & cN_2' & sN_2' & \gamma N_2 \\ -sN_1' & cN_1' & -N_1 & -sN_2' & cN_2' & -N_2 \\ 0 & 0 & N_1' & 0 & 0 & N_2' \end{bmatrix}$$

$$c = \cos\theta, s = \sin\theta \tag{15}$$

$$(\bullet)' = \frac{d}{dL_0}$$

ja poikkileikkauksen jännitysresultanttivektorilla **S** tarkoitetaan vektoria

$$\mathbf{S} = \begin{bmatrix} N \\ Q \\ M \end{bmatrix} = \begin{bmatrix} EA & 0 & 0 \\ 0 & GA_s & 0 \\ 0 & 0 & EI \end{bmatrix} \begin{bmatrix} \varepsilon \\ \gamma \\ \kappa \end{bmatrix} = \mathbf{D}_2 \boldsymbol{\varepsilon} \tag{16}$$

missä ε on aksiaalinen venymä, γ on liukuma ja κ on kimmoviivan kaarevuus. Ne määritellään kaavoilla

$$\boldsymbol{\varepsilon} = \begin{bmatrix} \varepsilon \\ \gamma \\ \kappa \end{bmatrix} = \begin{bmatrix} (X'+u')\cos\theta + (Y'+v')\sin\theta - 1 \\ (Y'+v')\cos\theta - (X'+u')\sin\theta \\ \varphi' \end{bmatrix} \tag{17}$$

missä u ja v ovat siirtymät X- ja Y- suuntiin. Kulma $\theta = \theta_{in} + \varphi$ missä θ_{in} on elementin kulma X-akselin suhteen alkutilassa ja φ on rotaatio alkutilasta mitattuna, katso kuva 2. Palkin kimmomatriisi $\mathbf{D}_2$ yhtälössä (16) koostuu aksiaalijäykkyydestä EA, leikkausjäykkyydestä GA_s ja taivutusjäykkyydestä EI.

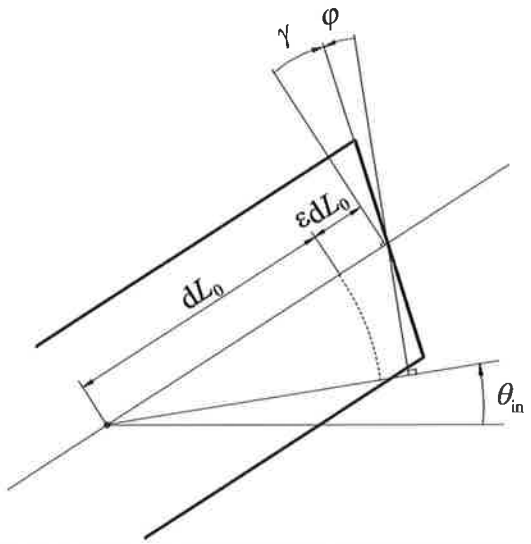

Kuva 2. Palkkielementin poikkileikkauksen deformoituminen

Palkkielementin tangentiaalinen jäykkyysmatriisi saadaan linearisoimalla sisäisten solmuvoimien vektori suuntaan $\Delta\mathbf{u}$:

$$\mathbf{k}_t = \int_{L_0} \mathbf{B}^T \mathbf{D}_2 \mathbf{B}\, dL_0 + \int_{L_0} D_u (\mathbf{B}^T \bar{\mathbf{S}})\, dL_0 \tag{18}$$

Jäykkyysmatriisin lauseke suljetussa muodossa yksityiskohtaisina johtoineen löytyy esimerkiksi lähteestä [4].

Olettaen taas, että palkkielementti on tasapaksu ja homogeeninen, sen massamatriisi saadaan käyttäen yhtälöä (9)

$$\mathbf{M} = \frac{m}{6}\begin{bmatrix} 2 & 0 & 0 & 1 & 0 & 0 \\ 0 & 2 & 0 & 0 & 1 & 0 \\ 0 & 0 & 2i^2 & 0 & 0 & i^2 \\ 1 & 0 & 0 & 2 & 0 & 0 \\ 0 & 1 & 0 & 0 & 2 & 0 \\ 0 & 0 & i^2 & 0 & 0 & 2i^2 \end{bmatrix} \tag{19}$$

missä m on palkin kokonaismassa ja i on palkin poikkileikkauksen neliösäde.

4 OFFSET-PALKKIELEMENTTI

Offset-palkkielementtejä voidaan käyttää esimerkiksi mallinnettaessa palkkirakennetta, jossa on rotaationivel, joka ei sijaitse palkin pintakeskiössä. Ensinnäkin laskentamallin vapausasteiden määrä vähenee nopeuttaen näin systeemiyhtälöiden ratkaisuaikaa ja toisaalta laskentamallissa ei tarvita topologisia muutoksia elementtiverkossa, vaikka rotaationiveliä siirretään palkin keskilinjasta sivuun. Offset-elementillä tarkoitetaan tässä elementtiä, jossa solmut eivät sijaitse palkin neutraaliakselilla. Kuvassa 3 tällainen elementti on esitetty isäntä- ja orjavapausasteineen. Alaindeksit m (master) viittaavat solmuihin, joiden siirtymät **v** ovat mukana laskentamallissa ja alaindeksi s (slave) viittaavat kuviteltuihin solmuihin elementin neutraaliakselilla. Kuviteltujen solmujen siirtymät on koottu vektoriin **u**. Siirtymien **u** ja **v** välillä oletetaan olevan jäykkä kytkentä.

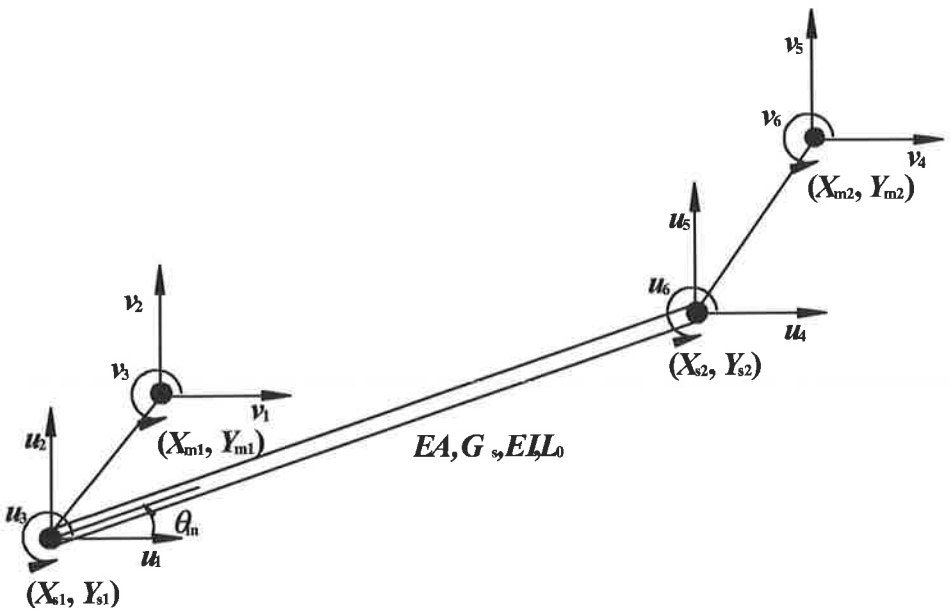

Kuva 3. Offset palkkielementti ja sen vapausasteet isäntä- ja orja-mittausjärjestelmässä

Ensimmäisen solmun isäntä- ja orjasolmun siirtymien ja virtuaalisten siirtymien välillä on kinemaattinen yhteys

$$\begin{aligned} \mathbf{x}_{s1} &= \mathbf{x}_{m1} + \mathbf{R}(v_3)\mathbf{X}_{s1/m1} \\ \delta\mathbf{x}_{s1} &= \delta\mathbf{x}_{m1} + \delta\mathbf{R}(v_3)\mathbf{X}_{s1/m1} \end{aligned} \tag{20}$$

missä $\mathbf{X}_{s1/m1}$ on offset-vektori elementin siirtymättömässä tilassa, joka saadaan $\mathbf{X}_{s1/m1} = \mathbf{X}_{s1} - \mathbf{X}_{m1}$. Rotaatiomatriisi $\mathbf{R}$ ja sen variaatio saadaan

$$\begin{aligned} \mathbf{R} &= \begin{bmatrix} \cos v_3 & -\sin v_3 \\ \sin v_3 & \cos v_3 \end{bmatrix} \\ \delta\mathbf{R} &= \begin{bmatrix} -\sin v_3 & -\cos v_3 \\ \cos v_3 & -\sin v_3 \end{bmatrix} \delta v_3 \end{aligned} \tag{21}$$

Vastaavat yhteydet ovat voimassa myös toiselle solmulle. Yhdistämällä alku- ja loppusolmun siirtymien väliset yhteydet ja lisäämällä rotaatiovapausasteet saadaan kinemaattinen matriisi $\mathbf{B}$ isäntä- ja orjasolmusiirtymien välillä

$$\mathbf{B} = \begin{bmatrix} 1 & 0 & -X_{s1/m1}\sin v_3 - Y_{s1/m1}\cos v_3 & 0 & 0 & 0 \\ 0 & 1 & X_{s1/m1}\cos v_3 - Y_{s1/m1}\sin v_3 & 0 & 0 & 0 \\ 0 & 0 & 1 & 0 & 0 & 0 \\ 0 & 0 & 0 & 1 & 0 & -X_{s2/m2}\sin v_6 - Y_{s2/m2}\cos v_6 \\ 0 & 0 & 0 & 0 & 1 & X_{s2/m2}\cos v_6 - Y_{s2/m2}\sin v_6 \\ 0 & 0 & 0 & 0 & 0 & 1 \end{bmatrix} \tag{22}$$

missä $X_{s1/m1}$ ja $Y_{s1/m1}$ ovat vektorin $\mathbf{X}_{s1/m1}$ komponentteja. Geometrisen jäykkyysmatriisin muodostamista varten tarvitaan yhtälöä

$$\mathbf{K}_g := D_v(\mathbf{B}^T\overline{\mathbf{F}}) = \begin{bmatrix} 0 & 0 & 0 & 0 & 0 & 0 \\ 0 & 0 & 0 & 0 & 0 & 0 \\ 0 & 0 & F_2B_{13} - F_1B_{23} & 0 & 0 & 0 \\ 0 & 0 & 0 & 0 & 0 & 0 \\ 0 & 0 & 0 & 0 & 0 & 0 \\ 0 & 0 & 0 & 0 & 0 & F_5B_{46} - F_4B_{56} \end{bmatrix} \tag{23}$$

missä F_i termit viittaavat orjaelementin sisäisten solmuvoimien vektorin komponentteihin ja termit B_{ij} kinemaattisen matriisin $\mathbf{B}$ alkioihin. Elementin sisäisten solmuvoimien vektori saadaan yhtälöä (5) käyttäen ja tangentiaalinen jäykkyysmatriisi yhtälöstä (6). Massamatriisi ja hitausvoimien vektori saadaan yhtälöstä (10).

Nopeudesta riippuvien tangenttimatriisien (13) laskennassa tarvitaan offsetin kinemaattisen matriisin (22) aikaderivaattoja. Nämä aikaderivaatat ovat

$$\dot{\mathbf{B}} = \begin{bmatrix} 0 & 0 & -X_{s1/m1}\dot{v}_3\cos v_3 + Y_{s1/m1}\dot{v}_3\sin v_3 & 0 & 0 & 0 \\ 0 & 0 & -X_{s1/m1}\dot{v}_3\sin v_3 - Y_{s1/m1}\dot{v}_3\cos v_3 & 0 & 0 & 0 \\ 0 & 0 & 0 & 0 & 0 & 0 \\ 0 & 0 & 0 & 0 & 0 & -X_{s2/m2}\dot{v}_6\cos v_6 + Y_{s2/m2}\dot{v}_6\sin v_6 \\ 0 & 0 & 0 & 0 & 0 & -X_{s2/m2}\dot{v}_6\sin v_6 - Y_{s2/m2}\dot{v}_6\cos v_6 \\ 0 & 0 & 0 & 0 & 0 & 0 \end{bmatrix} \tag{24}$$

ja

$$\ddot{\mathbf{B}} = \begin{bmatrix} 0 & 0 & a\cos v_3 + b\sin v_3 & 0 & 0 & 0 \\ 0 & 0 & a\sin v_3 - b\cos v_3 & 0 & 0 & 0 \\ 0 & 0 & 0 & 0 & 0 & 0 \\ 0 & 0 & 0 & 0 & 0 & c\cos v_6 + d\sin v_6 \\ 0 & 0 & 0 & 0 & 0 & c\sin v_6 - d\cos v_6 \\ 0 & 0 & 0 & 0 & 0 & 0 \end{bmatrix}$$

$$a := Y_{s1/m1}\dot{v}_3^2 - X_{s1/m1}\ddot{v}_3,\ b := Y_{s1/m1}\ddot{v}_3 + X_{s1/m1}\dot{v}_3^2 \tag{25}$$

$$c := Y_{s2/m2}\dot{v}_6^2 - X_{s2/m2}\ddot{v}_6,\ d := Y_{s2/m2}\ddot{v}_6 + X_{s2/m2}\dot{v}_6^2$$

Nähdään, että kinemaattisen matriisin toisessa aikaderivaatassa $\ddot{\mathbf{B}}$ esiintyy sekä kulmakiihtyvyystermejä että kulmanopeuksien neliöistä riippuvia termejä.

5 LASKENTAESIMERKKI

Tarkastellaan kuvan 4 mukaista puomia, joka on nivelöity vasemmasta päästään 0,5 m sivuun neutraaliakseliltaan. Niveleen kohdistuu ajan mukana kasvava momenttikuormitus, jonka kuvaaja on esitetty kuvassa. Momenttikuormituksen lauseke on

$$M(t) = \begin{cases} M_0 t & t \le 1 \\ M_0 t^6 & t > 1 \end{cases} \tag{26}$$

Puomiosuus on mallinnettu neljällä tasopalkkielementillä, joista ensimmäisen elementin alkusolmu on edellä mainitun etäisyyden päässä puomin neutraaliakselista y-suuntaan. Tämän solmun siirtymät x- ja y- suuntaan ovat estetty.

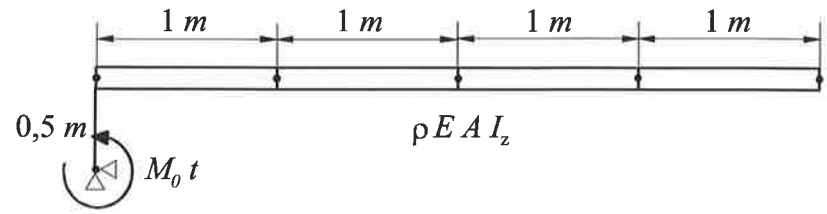

Kuva 4. Sivusta nivelöidyn puomin neljän elementin laskentamalli

Edellä esitetty laskentamalli ohjelmoitiin MATLAB- ohjelmistolla ja tehtävän aikaintegrointi suoritettiin Newmarkin implisiittisellä aikaintegrointimenetelmällä [6]. Jotta laskenta konvergoituisi paremmin, niin laskentamalliin lisättiin rakenteellista vaimennusta. Laskennan lähtöarvot ovat koottuna taulukossa 1.

Taulukko 1. Laskentamallin lähtöarvot

Suure	Symboli	Arvo	Yksikkö
Elementtien lukumäärä	n_{ele}	4	kpl
Palkin tiheys	ρ	7850	kg/m^3
Kimmomoduuli	E	207	GPa
Poikkipinta-ala	A	1900	mm^2
Neliömomentti	I_z	3,756 10^6	mm^4
Elementin pituus	L	1,00	m
Rayleighin vaimennus	α	0,1	
Rayleighin vaimennus	β	0	
Newmarkin vaimennus	α	0,001	
Konvergointitoleranssi	ε	0,001	
Kiertomomentti	M_0	2000	kNm

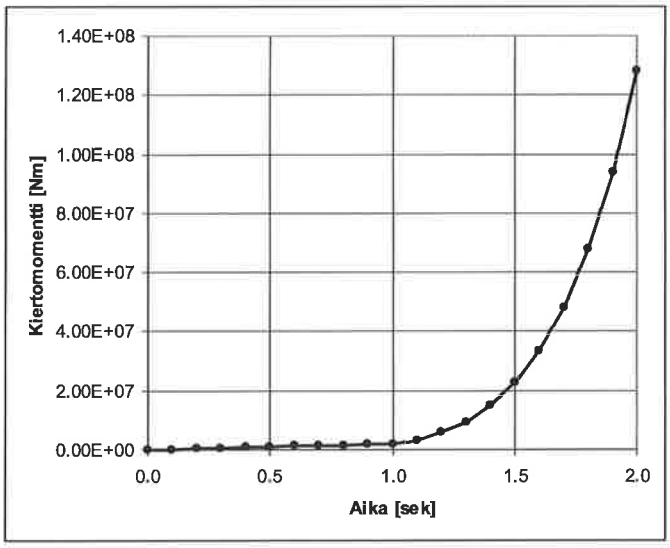

Kuva 5. Laskentamallin alkusolmuun vaikuttava kiertomomentti

Laskennan aika-askeleeksi valittiin ensin 0,001 sekuntia. Laskenta suoritettiin sekä käyttämällä hitausvoimista aiheutuvaa jäykkyys- ja vaimennusmatriisia, että jättämällä nämä termit pois laskennasta. Laskentaa jatkettiin kunnes tehtävä ei enää konvergoitunut. Laskennat tulokset ovat taulukossa 2.

Taulukko 2. Laskentatulokset aika-askeleella 0,001 sekuntia

Tulokset	Hitaustermit mukana	Ilman hitaus-termejä
Askelten lukumäärä	442	442
Iteraatioiden lukumäärä	1762	2250
Suurin pyörimisnopeus	3762	3762

Taulukossa 3 on esitetty vastaavat tulokset aika-askeleella 0,0001 sekuntia.

Taulukko 3. Laskentatulokset aika-askeleella 0,0001 sekuntia

Tulokset	Hitaustermit mukana	Ilman hitaus-termejä
Askelten lukumäärä	19971	19971
Iteraatioiden lukumäärä	59945	94379
Suurin pyörimisnopeus	17724	17724

Kuvassa on esitettynä hitausvoimista aiheutuvien termien suhteellista osuutta tangentiaaliseen jäykkyysmatriisiin käytännön koneenrakennuksen pyörimisnopeuksilla.

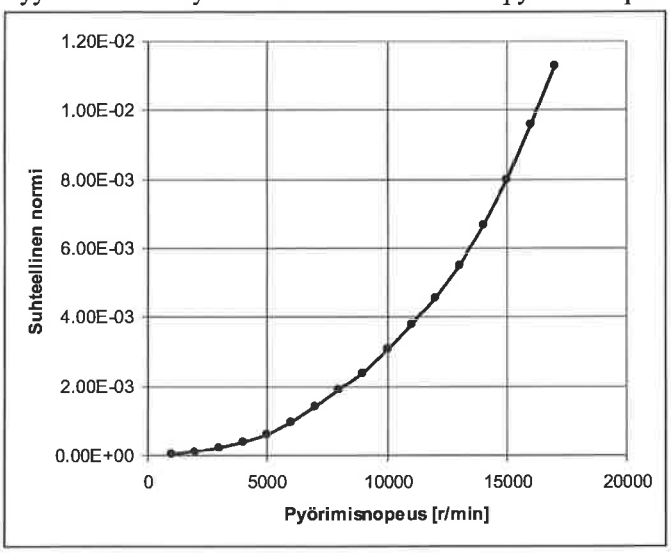

Kuva 6. Hitausvoimista aiheutuvan jäykkyysmatriisin suhteellinen normi eri pyörimisnopeuksilla

YHTEENVETO

Tässä artikkelissa on tutkittu nopeudesta riippuvien hitausvoimatermien vaikutusta epälineaarisen dynamiikan palkkilaskentaan käytännön koneenrakennuksen pyörimisnopeuksilla. Tehtävässä vain offset-palkki aiheuttaa näitä nopeudesta riippuvia hitausvoimatermejä. Laskentaesimerkillä on osoitettu, että hitausvoimatermien vaikutus on melko vähäinen tangenttimatriiseihin. Iteroinnin suppenevuus on kuitenkin parempi, kun nämä termit otetaan huomioon. Vaikka esimerkissä on tarkasteltu tasotapausta, tulokset ovat yleistettävissä myös avaruustapaukseen.

Nopeudesta riippuvat tangenttimatriisit rikkovat muutoin symmetrisen laskentarakenteen. Luonnollisesti voitaisiin käyttää myös tangenttimatriisien symmetristä osuutta. Mikäli offsetin suhteellinen osuus on suurempi kuin laskentaesimerkissä, nopeudesta riippuvat tangenttimatriisit ovat luonnollisesti määräävämpiä.

LÄHDEVIITTEET

[1] Jelenic, G., Crisfield, M.A. (1996), "Non-linear 'master-slave' relationship for joints in 3-D beams with large rotations", Comput. Methods Appl. Mech. Engrg; 135:211-228.

[2] Crisfield, M.A. (1997), "Non-linear Finite Element Analysis of Solids and Structures", Vol. 2: Advanced Topics, J. Wiley & Sons, New York, 494 pp.

[3] Behdinan, K., Stylianou, M.C., Tabarrok,B. (1998), "Co-rotational dynamic analysis of flexible beams", Computer Methods Appl. Mech. Engrg; 154:151-161.

[4] Simo, J.C., Vu-Quoc, L. (1986), "On the dynamic of flexible beams under large overall motions - The plane case: Part I and II", ASME Journal of Applied Mechanics; 53:849-863.

[5] Simo, J.C., Vu-Quoc, L. (1987), "The role of non-linear theories in transient dynamic analysis of flexible structures", J. Sound and Vibration; 119(3):487-508.

[6] Géradin M & Cardona A, (2001), "Flexible Multibody Dynamics, A Finite Element Approach", John Wiley & Sons, 327 pp.

SUORASSA PYÖRÖTANGOSSA ETENEVÄN JÄNNITYSAALLON ANALYSOINTI FEM:LLÄ

A.-J. VUOTIKKA, M. JOKINEN, S.-G. SJÖLIND

Teknillisen Mekaniikan Laboratorio
Oulun Yliopisto
PL 4200, 90014 OULU
e-mail: Antti-Jussi.Vuotikka@oulu.fi

TIIVISTELMÄ

Tavoitteena on tutkia elementtimenetelmällä iskun aiheuttamaa pitkittäistä jännitysaaltoa ja sen muuttumista taivutusaalloiksi. Tutkittavana rakenteena on suora pyörähdyssymmetrinen teräksinen iskutanko, jonka päähän isketään mekaanisella iskurilla. Jännitysaaltoja analysoidaan ja verrataan vastaavaan kokeellisesti mitatun rakenteen tuloksiin. Iskut tehdään suoralla iskulla sekä iskulla, jossa vasaran ja tangon välinen kulma on yksi aste. Tutkimuksessa käytetyksi ohjelmistoksi valitaan ABAQUS-ohjelmisto, jolla tutkittava rakenne mallinnetaan ja analysoidaan.

JOHDANTO

Analyyttisten menetelmien kehittäminen on alkanut jo 1800-luvun puolella. Teoriaa on kehitetty intensiivisesti /6/, mutta jopa sylinterimäisen äärellisen kappaleen analyyttinen ratkaisu on erittäin monimutkainen. Tämän takia numeeristen menetelmien käyttö tällaisissa ongelmissa on hyvin houkuttelevaa.

Elastodynaamisten ongelmien analysointia voidaan tehdä kahden erilaisen FEM:n avulla /1/, /6/. Toinen on implisiittinen FEM ja toinen on eksplisiittinen FEM. Jälkimmäistä menetelmää käytetään yleensä, kun analysoidaan nopeita dynaamisia tapahtumia ja aallon etenemistä. Jotta aaltorintama voidaan selvittää FEM:llä, pitää Courant-ehto toteuttaa. Tämä tarkoittaa käytännössä sitä, että aaltorintama saa edetä korkeintaan yhden elementin pituuden aika-askeleen aikana. Tällöin askel on hyvin lyhyt ja siten implisiittistä FEM:ä käytettäessä laskennasta tulee hyvin raskasta. Eksplisiittisen menetelmän heikkoutena on stabiilin aika-askeleen lyhyys, mutta sen laskenta on huomattavan yksinkertaista. Tällöin laskenta etenee nopeasti, jolloin Courant-ehto ei vaikuta oleellisesti laskentaan.

Aallonetenemisilmiötä voidaan hyödyntää mahdollisesti mm. paalujen junttaamisessa käytettävissä laitteistoissa, voimalaitosten erilaisissa iskuun perustuvissa nuohousjärjestelmissä. Ilmiö on huomioitava useissa tilanteissa, joissa tapahtuu äkillisiä iskuja, kuten esimerkiksi ydinvoimaloiden reaktoreiden shutoff-tangoissa /7/ tai muissa turvalaitteissa /4/.

TEORIAA

Tutkitaan sylinterimäistä kappaletta, jonka paksuus on paljon pituutta pienempi. Tällaisissa rakenteissa esiintyy kolme erityyppistä värähtelyä. Ne on luokiteltu pitkittäis-, vääntö- ja taivutusvärähtelyyn (*longitudinal, torsional ja lateral vibrations*). Näille värähtelyille on esitetty teoreettisia esityksiä jo viime vuosisadan alkupuolella, joista tähän on koottu perusteet lähteistä /3/ ja /5/. Jätetään tässä tutkimatta tangon vääntövärähtely, koska sen vaikutus tutkittavassa tapauksessa on mitätön.

Iskettäessä tangon päähän täysin suoralla ja keskitetyllä iskulla rakenteeseen muodostuu puhdas pitkittäisvärähtelytapaus. Oletetaan, että tangon jokainen poikkileikkaustaso pysyy tasona liikkeen aikana ja jännitys poikkileikkaustasolla on yhtenäinen. Tangon poikkileikkaus ja materiaaliominaisuudet oletetaan vakioiksi koko tangon pituudelta. Tällöin saadaan muodostettua liikeyhtälö

$$w_{,xx} = \frac{1}{c_b} w_{,tt} , \tag{1}$$

kun tankoon ei kohdistu aksiaalikuormia iskun jälkeen. Yhtälölle voidaan esittää ratkaisu muodossa

$$w = g(x + c_b t) + f(x - c_b t) , \tag{2}$$

missä f ja g ovat funktioita, jotka kuvaavat tangossa etenevää aaltoa. c_b on äänennopeus materiaalissa, jolle voidaan esittää kaava

$$c_b = \sqrt{\frac{E}{\rho}} , \tag{3}$$

missä E on materiaalin kimmokerroin ja ρ tiheys. Kuten kaavasta (3) huomataan, aallon etenemisnopeus on riippumaton sen taajuudesta, jolloin se kulkee tangossa ilman dispersiota. Kun tällainen aalto saavuttaa tangon vapaan pään, se heijastuu takaisin eri merkkisenä. Samalla tangon pää siirtyy eteenpäin nykäyksittäin. Tangon siirtymä pulssin vaikutuksesta on esitetty kuvassa 1, kun rakenne oletetaan vapaasti tuetuksi.

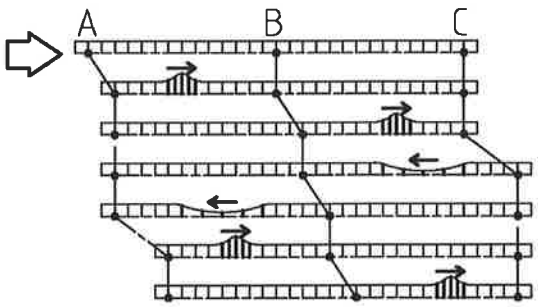

Kuva 1. Iskun aiheuttaman pituusaallon eteneminen tangossa.

Edellinen on vain approksimaatio, sillä siinä oletetaan poikkipintojen pysyvän tasoina jännitysaallon edetessä ja jännitys pysyy samanlaisena jokaisessa tasossa. Pituussuuntaiset

venymät aiheuttavat kuitenkin venymiä myös tangon poikkileikkauspinnalla Poissonin vaikutuksen vuoksi. Tällä on merkitystä, kun aallonpituus on samaa kokoluokkaa kuin tangon paksuus eli pienillä aallonpituuksilla ilmenee dispersiota. Myös tangon sisäinen kitka vaikuttaa aallon muotoon kuluttamalla koko ajan sen energiaa, jolloin aallon amplitudi pienenee vähitellen.

Jos isku tangon päähän ei ole keskeinen, pituussuuntainen aalto lähtee etenemään tangon pinnassa aiheuttaen samalla taivutusta tangossa. Tämä herättää sauvan taivutusvärähtelyn. Taivutusvärähtelyä voidaan kuvata Bernoulli-Eulerin palkkiteorian mukaan seuraavalla differentiaaliyhtälöllä, kun kappaleeseen ei kohdistu ulkoisia kuormituksia ja taivutusmomentteja

$$w_{,xxxx} + \frac{1}{r^2 c_b^2} w_{,tt} = 0 \quad , \tag{4}$$

missä $r^2 = I/A$ on poikkileikkauksen pyörähdyssäde. Edellisen yhtälön ratkaisu voidaan esittää muodossa

$$w(x,t) = A_0 e^{ik(x - c_\varphi t)} \quad , \tag{5}$$

missä $k = \omega/c_\varphi$ on aaltoluku, c_φ on vaihenopeus ja A_0 on vakioamplitudi. Ratkaisemalla yhtälö (4) saadaan vaihenopeuden ja materiaalin äänennopeuden välille yhteys

$$c_\varphi = krc_b \quad , \tag{6}$$

josta nähdään, että taivutusaallon taajuus vaikuttaa sen etenemisnopeuteen. Jos alkuperäinen aalto koostuu usean eri taajuuden aaltokomponenteista, edetessään kappaleessa sen muoto muuttuu eri komponenttien liikkuessa eri etenemisnopeudella. Ainoa aaltomuoto, joka voi edetä muotoaan muuttamatta dispersoivassa rakenteessa, on aalto, joka sisältää vain yhden taajuuden. Eri taajuuksista koostuvan aallon kuljettaman energian nopeus voidaan esittää kaavalla

$$c_g = c_\varphi + k\frac{dc_\varphi}{dk} = 2c_\varphi \quad . \tag{7}$$

Tämän mukaan aaltoryhmän nopeus on kaksinkertainen verrattuna vaihenopeuteen Bernoulli-Eulerin teorian mukaisessa tapauksessa. Kun aallonpituus pienenee, molemmat aallonnopeudet kasvavat kohti ääretöntä, mikä ei ole fysikaalisesti mahdollista. Tästä ongelmasta päästään eroon vaihtamalla Bernoulli-Eulerin oletukset Timoshenkon teorian mukaisiksi. Tällöin yhtälö (4) korvataan yhtälöparilla

$$\begin{cases} \rho A w_{,tt} - \kappa G A(w_{,xx} - \psi_{,x}) = 0 \\ \rho I \psi_{,tt} - EI\psi_{,xx} - \kappa G A(w_{,x} - \psi) = 0 \end{cases} \quad , \tag{8}$$

missä κ on Timoshenkon leikkauskerroin, G on leikkausmoduli, A on tangon poikkipinta-ala ja ψ on puhtaan taivutuksen aiheuttama poikkileikkauksen kallistuskulma. Ratkaisemalla yhtälöt saadaan vaihenopeudelle ja ryhmänopeudelle uudet yhtälöt, jotka lähestyvät aallonpituuden pienentyessä raja-arvoa. Timoshenkon malli kuvaa riittävän tarkasti fysikaalista ongelmaa. /2/

MALLINNUS

Mallinnettavana rakenteena on 5.5m pitkä pyörötanko, jonka paksuus on 90mm. Materiaali on terästä, jolla $E = 210\text{GPa}$, $\nu = 0.3$ ja $\rho = 7800\text{kg/m}^3$. Tangon päähän isketään mittauksissa heilurityyppisellä vasaralla, mutta analyysissä isku tehdään lineaaritoimisella vasaralla. Lineaaritoimisen vasaran pituus on sama kuin todellisessa vasarassa ja paksuus on valittu siten, että vasaroiden massat täsmäävät. Vasaran materiaaliparametrit ovat samat kuin tangolla, ja sille määritellään alkunopeuskenttä, joka on 0.65m/s. Alkunopeus on laskettu energian säilymislauseen perusteella.

Vasara ja tanko on verkotettu C3D8I-elementillä. Tangossa elementtien lukumäärä on pituussuunnassa 550 ja poikkisuunnassa on 10 elementtiä. Vasarassa on käytetty harvempaa verkkoa. Verkosta pyrittiin tekemään mahdollisimman säännöllinen, jotta elementeissä olisi mahdollisimman pienet alkuvääristymät. Vasaran ja tangon iskupinnoille asetettiin kitkaton yleinen kontakti (*general contact*) ja niiden välillä ei sallita tunkeumaa. Massan skaalausalgoritmeja ei ole käytetty stabiilin aikainkrementin kasvattamiseksi, ja bulkki viskositeetti -parametrit ovat pidetty oletusarvoissaan.

Analyysin kestoajaksi valittiin 4ms, jolloin analyysissä saadaan näkyviin myös ensimmäinen tangon päästä heijastunut pitkittäisaalto. Venymäaallot on mitattu 500mm:n päästä iskukohdasta kolmesta kohdasta, jotka ovat iskusuunnasta katsottuna tangon yläpinta (T), vasen (L) ja oikea (R) reuna.

TULOKSET

Suoran iskun mittaustulokset ja analyysistä saadut tulokset on esitetty kuvissa 2. Niistä nähdään, että iskun pituus on aika tarkasti samanpituinen, mutta intensiteetti on hieman suurempi kuin mitatuissa tuloksissa. Tämä voi johtua siitä, että heilurivasaralla ei voi saada aikaiseksi täysin puhdasta pituuspulssia, vaan osa energiasta menee aina taivutusvärähtelyyn. Tätä tukee se, että mittauksissa jokaisesta pisteestä pitäisi tulla samanlainen käyrä, mutta kuten kuvista nähdään, ne eivät ole samanlaisia. Äänen nopeus on laskennallisesti hieman suurempi kuin se todellisuudessa on, sillä palkin päästä heijastunut laskettu vetopulssi saapuu hieman ennen mitattua vetopulssia.

Vinon iskun mittaustulokset ja analyysistä saadut tulokset on esitetty kuvissa 3. Kuten edellisissäkin kuvissa näissä on nähtävissä aallon etenemisnopeuden ero. Intensiteetin puolesta laskennalliset ja mitatut tulokset vastaavat toisiaan paremmin kuin edellisissä kuvissa. Tämän perusteella halutunlainen vino isku on helpompi tehdä kuin täysin suora isku.

Tangon keskeltä ja molemmista päistä on valittu solmut sekä yksi vasaran solmu, joista on esitetty siirtymät kuvassa 4. Kuvan perusteella kontakti vasaran ja tangon välillä kestää noin 2ms. Kun ensimmäinen vetopulssi saapuu iskupäähän, tanko ja vasara erkanevat. Analyysin perusteella vasara luovuttaa koko liike-energiansa tangolle, sillä se jää paikalleen iskun jälkeen.

Kuvista 5 nähdään pituussuuntaisen venymäaallon eteneminen tangon poikkileikkauksessa. Venymäaalto on muodostettu suoralla iskulla. Kuvat ovat ajan hetkiltä 15μs ja 75μs. Pituussuuntainen aaltorintama etenee tasaisesti koko poikkileikkauksessa. Hitaammilla aalloilla on nähtävissä nopeampaa etenemistä tangon pinnalla kuin keskustassa.

Vinossa iskussa pituusaalto lähtee etenemään ensin tangon toisella reunalla, mutta 75μs:n kohdalla se on levittäytynyt jo koko poikkipinnalle. Samalla tankoon alkaa muodostua selvä taivutustila. Vinon iskun tulokset on esitetty kuvissa 6.

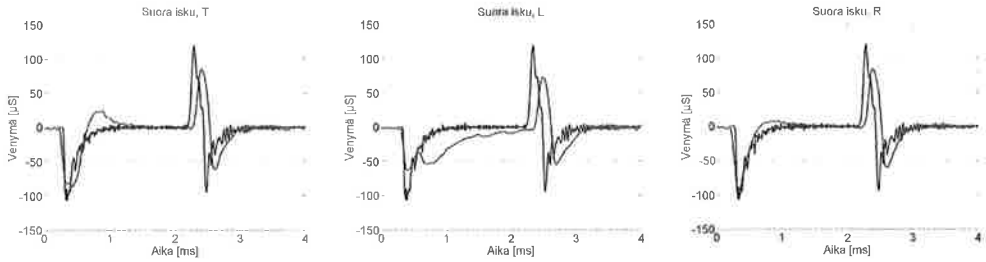

Kuva 2. Tangon venymäpulssi mittauspisteissä T, L ja R. Sileämpi käyrä on mittaustulos ja rosoisempi käyrä on laskennallinen tulos.

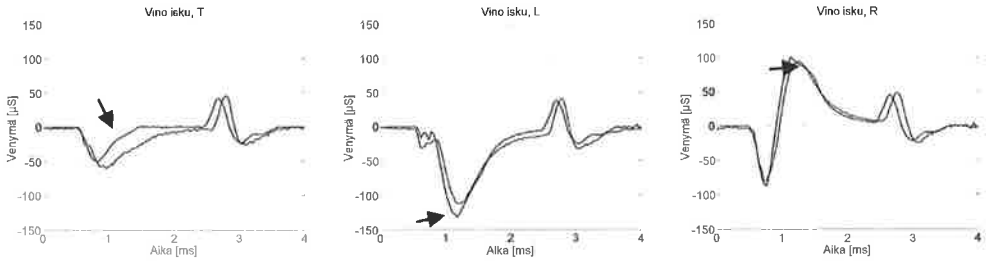

Kuva 3. Tangon venymäpulssi vinon iskun jälkeen mittauspisteissä T, L ja R. Laskennallinen tulos on osoitettu nuolella.

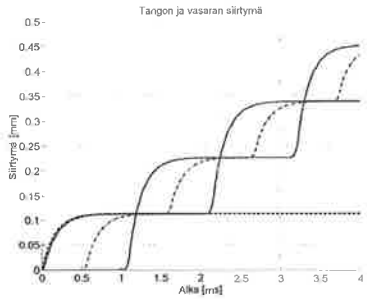

Kuva 4. Kuvassa on tangon siirtymät kolmessa eri pisteessä ja vasaran siirtymät yhdestä pisteestä. Yhtenäinen viiva kuvaa tangon päiden siirtymää ja pistekatkoviiva tangon keskikohdan siirtymää. Vasaran siirtymä on kuvattu katkoviivalla.

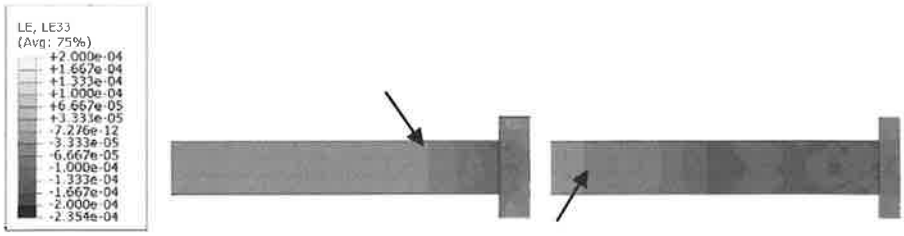

Kuva 5. Kuvissa on esitetty pituussuuntaisen pulssin eteneminen suoran iskun jälkeen ajan hetkillä 0.015ms ja 0.075ms. Nuolet osoittavat aaltorintaman etenemisen.

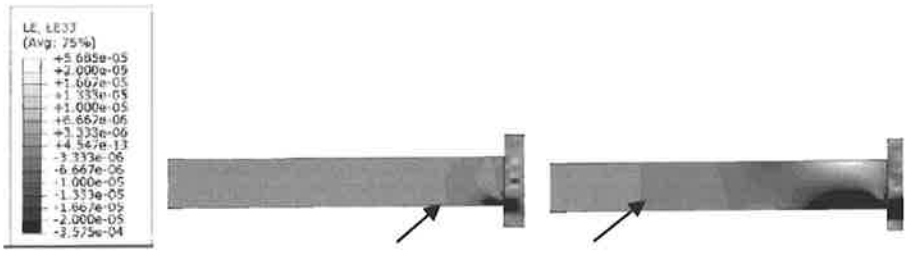

Kuva 6. Kuvissa on esitetty pituussuuntaisen pulssin eteneminen vinon iskun jälkeen ajan hetkillä 0.015ms ja 0.075ms. Nuolet osoittavat aaltorintaman etenemisen.

YHTEENVETO

Analyysistä saadut tulokset vastaavat hyvin mitattuja tuloksia. Suurimpana virhelähteenä ovat iskun tuottamistavan erot. Mittauksissa käytetty heilurivasara ei käytännössä voi olla niin hyvin asemoitu, jotta se antaisi vastaavan iskun kuin lineaarinen vasara, vaikka ideaalitapauksessa voitaisiin näin ajatella olevan. Toinen virhelähde voi olla energian säilymislausekkeen avulla laskettu vasaran alkunopeus. Koska kuvissa 2 ja 3 intensiteetti on FEM:llä saaduissa tuloksissa suurempi, alkunopeus voi olla liian suuri.

Jatkossa seuraavia FE-analyysin tavoitteita ovat iskupulssin muodon muokkaaminen käytettäessä joustavia elementtejä iskutangon ja vasaran välissä. Kiinnostavia asioita ovat myös lämpötilan ja tankoon liitettyjen osien vaikutus pulssin etenemiseen.

Lähdeluettelo

1. ABAQUS. (2009). *Analysis User Manual.* Providence, RI: Dassault Systèmes.
2. Bhaskar, A. (2009). Elastic waves in Timoshenko beams: the 'lost and found' of an eigenmode. *Proceedings of the Royal Society A* , 239-255.
3. Kolsky, H. (1963). *Stress waves in solids.* New York: Dover publications Inc.
4. M. Grujicic, B. P. (2009). A simple ballistic material model for soda-lime glass. *International Journal of Impact Engineering* , 36, 386–401.
5. Magrab, E. (1963). *Vibrations of elastic structural members.* Alphen aan den Rijn: Sijthoff&Noordhoff.
6. Puckett, A. (2000). *Fidelity of a Finite Element Model for Longitudinal Wave Propagation in Thick Cylindrical Wave Guides.* Los Alamos National Laboratory: Master thesis.
7. R. Rajendran, K. P. (2009). Axial impact studies on steel tubes and zircaloy rod. *Experimental Techniques* , Vol33, No1, 17-22.

BAYESILÄINEN LÄHESTYMISTAPA VÄRÄHTELYPERUSTEISEEN RAKENTEIDEN KUNNONVALVONTAAN

Antti Huhtala

Matematiikan ja systeemianalyysin laitos
Teknillinen korkeakoulu
PL 1100
FIN-02015 TKK
e-mail: ahhuhtal@math.tkk.fi

TIIVISTELMÄ

Rakenteen värähtelymoodit muuttuvat vaurion vaikutuksesta. Tämä muutos on riippuvainen sekä vaurion suuruudesta että sen sijainnista. Käyttämällä rakenteen mallia ja tietoa siitä miten vaurio muuttaa tuota mallia, on mahdollista estimoida vaurio moodiparametrien mitattujen muutosten perusteella. Tämä tehtävä on käänteisongelma ja siten huonosti asetettu, joten suora ratkaisu ei onnistu. Tässä artikkelissa tutkitaan tehtävän regularisointia käyttämällä Bayesiläistä tilastotiedettä.

JOHDANTO

Älykäs rakenteiden kunnonvalvonta on ollut aktiivisen tutkimuksen aiheena viimeisen 20 vuoden ajan [1, 2]. Monet esitetyistä menetelmistä ovat perustuneet tietoon siitä, että rakenteen moodiparametrit muuttuvat sen vaurioituessa. Tämä muutos riippuu sekä vaurion suuruudesta että sen sijainnista [2].

Näistä menetelmistä ne jotka pyrkivät myös paikallistamaan vaurion, sen läsnäolon havaitsemisen lisäksi, perustuvat yleensä rakenteen malliin ja oletukseen siitä miten vaurio muuttaa tätä mallia. Mallista saatuja simuloituja moodiparametreja verrataan todellisesta rakenteesta mitattuihin moodiparametreihin. Tämän jälkeen etsitään mallille vauriotila, joka minimoi eron simuloitujen ja mitattujen moodiparametrien välillä. Tästä muodostuva tehtävä on huonosti asetettu käänteisongelma. Ratkaisun löytämistä varten tehtävää on regularisoitava tavalla tai toisella.

Koska todellisessa tilanteessa mittavirheet ja mallinnusvirheet ovat aina läsnä, käytetty lähestymistapa on tilastollinen. Käyttämällä Bayesiläistä tilastotiedettä voidaan johtaa rakenteen vaurion posteriorijakauma, joka ilmaisee mikä on vaurion todennäköisyysjakauma kun moodiparametreille on saatu tietty mittaustulos. Lopuksi tästä jakaumasta valitaan edustajaksi suurimman uskottavuuden estimaatti.

VAURION TUNNISTAMISESTA

Rakenteen moodit

Lineaarisen rakenteen vapaa vaimentamaton värähtely on diskretoitavissa muotoon

$$\boldsymbol{M}\ddot{\boldsymbol{U}}(t) + \boldsymbol{K}\boldsymbol{U}(t) = \boldsymbol{0}, \tag{1}$$

jossa $\boldsymbol{M}, \boldsymbol{K} \in \mathbb{R}^{n\times n}$ ovat massamatriisi ja jäykkyysmatriisi. $\boldsymbol{U}(t)$ on vektori, joka sisältää diskreetin siirtymäkentän vapausasteet ajasta riippuvina.

Ratkaistaan yleistetty ominaisarvotehtävä

$$\boldsymbol{K}\boldsymbol{X} = \boldsymbol{M}\boldsymbol{X}\boldsymbol{\Lambda}. \tag{2}$$

Tästä saadaan ominaisarvot sisältävä diagonaalimatriisi $\boldsymbol{\Lambda}$ ja vastaavat ominaisvektorit sarakkeinaan sisältävä matriisi $\boldsymbol{X}$. Ominaisvektorit on normalisoitu siten, että

$$\boldsymbol{X}^T\boldsymbol{M}\boldsymbol{X} = \boldsymbol{I}. \tag{3}$$

Yhtälöistä (2) ja (3) seuraa, että

$$\boldsymbol{X}^T\boldsymbol{K}\boldsymbol{X} = \boldsymbol{X}^T\boldsymbol{M}\boldsymbol{X}\boldsymbol{\Lambda} = \boldsymbol{\Lambda}. \tag{4}$$

Koska matriisi $\boldsymbol{M}$ on symmetrinen ja positiividefiniitti ja $\boldsymbol{K}$ on symmetrinen, ominaisvektorit muodostavat täyden kannan ja siten $\boldsymbol{X}$ on kääntyvä. On siis mahdollista ottaa muuttujanvaihto muotoa

$$\boldsymbol{U}(t) = \boldsymbol{X}\boldsymbol{\eta}(t). \tag{5}$$

Sijoitus yhtälöön (1) antaa

$$\boldsymbol{M}\boldsymbol{X}\ddot{\boldsymbol{\eta}}(t) + \boldsymbol{K}\boldsymbol{X}\boldsymbol{\eta}(\boldsymbol{t}) = 0. \tag{6}$$

Kertomalla tämä vasemmalta matriisilla $\boldsymbol{X}^T$ ja käyttämällä yhtälöjä (3) ja (4) saadaan

$$\ddot{\boldsymbol{\eta}}(t) + \boldsymbol{\Lambda}\boldsymbol{\eta}(t) = \boldsymbol{0}. \tag{7}$$

Koska $\boldsymbol{\Lambda}$ on diagonaalinen, yhtälö (7) esittää itse asiassa n:ää riippumatonta harmonista oskillaattoria, joiden oskillaatiotaajuudet ovat ominaisarvojen neliöjuuria. Merkitään näitä taajuuksia $\omega_i = \sqrt{\lambda_i}$.

Ratkaisu yhtälöön (1) on siis

$$\boldsymbol{U}(t) = \boldsymbol{X}\boldsymbol{\eta}(t) = \sum_{i=1}^{n} \boldsymbol{x_i}\eta_i(t), \tag{8}$$

joka on riippumattomien värähtelymoodien $\boldsymbol{x_i}\eta_i(t)$ lineaarikombinaatio. Tästä nähdään, että ominaisvektorit $\boldsymbol{x_i}$ ovat siirtymäkentän moodimuotojen vapausasteet.

Jos yhtälöön (1) lisätään pieni määrä viskoottista vaimennusta, taajuudet ja moodimuodot muuttuvat vain hyvin pienen määrän tässä ratkaistuista. Kevyt vaimennus voidaan siis usein jättää huomiotta.

Mittausmalli

Rakennetta tarkkailaan useilla antureilla. Niiden tuottamien mittausten käyttämiseksi tarvitaan malli, joka yhdistää rakenteen käyttäytymisen anturien mittatuloksiin.

Mikä tahansa lineaarinen funktionaali diskretoidulla siirtymäkentällä voidaan esittää sisätulona siirtymäkentän vapausasteiden kanssa. Olettaen, että anturit voidaan mallintaa siirtymäkentän lineaarisina funktionaaleina, niiden mittaustulokset voidaan esittää muodossa

$$\boldsymbol{Y}(t) = \boldsymbol{H}\boldsymbol{U}(t) = \sum_{i=1}^{n} \boldsymbol{H}\boldsymbol{x_i}\eta_i(t). \tag{9}$$

On olemassa menetelmiä, jotka ratkaisevat esitetynkaltaisesta aikadatasta esimerkiksi m kappaletta mooditaajuuksia ω_i ja vastaavia havaintojen moodimuotoja $\boldsymbol{H}\boldsymbol{x_i}$ [3]. Tämä aikadatatunnistus tehdään todellisesta rakenteesta kerätylle datalle. Mallista vastaavat suureet saadaan suoraan ominaisarvotehtävästä ja operoimalla havaintomatriisilla $\boldsymbol{H}$ ominaisvektoreihin $\boldsymbol{x_i}$. Määritellään mittaustulosvektori

$$\boldsymbol{m} = \begin{pmatrix} \omega_1 \\ \boldsymbol{H}\boldsymbol{x_1} \\ \vdots \\ \omega_m \\ \boldsymbol{H}\boldsymbol{x_m} \end{pmatrix}. \tag{10}$$

Vauriomalli

Vaurio voidaan mallintaa rakenteen paikallisen jäykkyyden vähenemisenä [4]. Rakenteen massan voidaan olettaa pysyvän oleellisesti samana [1, 2, 4]. Diskretoidussa mallissa tämä tarkoittaa muutosta jäykkyysmatriisissa $\boldsymbol{K}$, mutta ei muutosta massamatriisissa $\boldsymbol{M}$.

Olettaen jäykkyyden menetyksen olevan vakio kussakin diskretoidun mallin elementissä, jäykkyysmatriisin muutos $\boldsymbol{\Delta K}$ voidaan esittää yksinkertaisesti muodossa

$$\boldsymbol{\Delta K} = -\sum_{i=1}^{N} d_i \boldsymbol{K_i^e}, \tag{11}$$

jossa matriisit $\boldsymbol{K_i^e}$ ovat elementtikohtaiset jäykkyysmatriisit. Parametrit $d_i \in [0, 1]$ ovat elementtikohtaiset vaurioparametrit, jotka määrittävät jäykkyyden menetyksen määrän. Parametrin arvo 0 tarkoittaa vauriotonta tilaa ja arvo 1 täydellistä jäykkyyden menetystä.

Suora tehtävä

Vaurion tunnistus on käänteisongelma, jonka ratkaisemista varten on ensin tunnettava suora tehtävä. Tässä tapauksessa suora tehtävä yhdistää vauriomallin ja mittausmallin. Sen ratkaisu on ennuste vaurioituneen rakenteen moodiparametreista, kun vauriotila tunnetaan. Oletetaan tehtävä ratkaistuksi ja esitetään se muodossa

$$\boldsymbol{m} = \boldsymbol{f}(\boldsymbol{d}), \tag{12}$$

jossa $\boldsymbol{d}$ on elementtikohtaiset vaurioparametrit sisältävä vektori ja $\boldsymbol{m}$ on vauriotilaan $\boldsymbol{d}$ liittyvä mittaustulosvektori, kuten määriteltiin yhtälössä (10).

Tilastollinen inverssi

Todellisuudessa mittaukset poikkeavat suoran tehtävän ratkaisusta. Tämä johtuu mittausvirheistä ja mallinnusvirheistä. Nämä ilmiöt otetaan huomioon lisäämällä virhetermi suoran tehtävän ratkaisuun. Bayesiläisessä tilastotieteessä kaikki muuttujat ovat satunnaismuuttujia (merkitään isoilla kirjaimilla). Tällöin mittaustuloksen, vauriotilan ja virhetermin välinen yhteys on esitettävissä muodossa

$$\boldsymbol{M} = \boldsymbol{f}(\boldsymbol{D}) + \boldsymbol{E}. \tag{13}$$

Olettaen, että $\boldsymbol{E}$ on moniulotteisesti normaalijakautunut kovarianssilla $\boldsymbol{\Sigma}$ ja odotusarvolla $\epsilon_{\boldsymbol{M}}$, sillä on todennäköisyysjakauma

$$p(\boldsymbol{E} = \epsilon) = C \exp\left(-\frac{1}{2}(\epsilon - \epsilon_{\boldsymbol{m}})^T \boldsymbol{\Sigma}^{-1}(\epsilon - \epsilon_{\boldsymbol{m}})\right). \tag{14}$$

Satunnaismuuttujan $\boldsymbol{E}$ tilastollisuus on mahdollista estimoida toistomittauksista, olettaen että todellisen rakenteen vauriotila tunnetaan. Tämä on helpointa tehdä kun rakenne on vielä vaurioitumaton.

Olettaen, että $\boldsymbol{E}$ on riippumaton $\boldsymbol{D}$:stä, joka tarkoittaa että $\boldsymbol{E}$:n jakauma säilyy samana riippumatta vauriotilasta, ehdollinen todennäköisyystiheys havaita mittaustulos $\boldsymbol{m}$ vauriotilan ollessa $\boldsymbol{d}$ on

$$p(\boldsymbol{M} = \boldsymbol{m} | \boldsymbol{D} = \boldsymbol{d}) = p(\boldsymbol{E} = \boldsymbol{m} - \boldsymbol{f}(\boldsymbol{d})). \tag{15}$$

Käyttämällä Bayesin kaavaa, posteriorijakauma on

$$p(\boldsymbol{D} = \boldsymbol{d} | \boldsymbol{M} = \boldsymbol{m}) = \frac{p(\boldsymbol{M} = \boldsymbol{m} | \boldsymbol{D} = \boldsymbol{d}) p(\boldsymbol{D} = \boldsymbol{d})}{p(\boldsymbol{M} = \boldsymbol{m})}. \tag{16}$$

Tämä on ehdollinen todennäköisyystiheys vauriotilalle $\boldsymbol{d}$, kun mittaustuloksen tiedetään olevan $\boldsymbol{m}$. Jakauma $p(\boldsymbol{D} = \boldsymbol{d})$ on priorijakauma, johon on sisällytetty kaikki ennen mittausta $\boldsymbol{m}$ tunnettu tieto vauriotilasta.

Posteriorijakaumaa voidaan pitää tehtävän ratkaisuna, mutta sen esittäminen ja siten myös hahmottaminen on vaikeaa. Siksi on usein hyödyllistä esittää jokin posteriorijakauman piste-estimaatti. Eräs yleisesti käytetty piste-estimaatti on ns. maximum a posteriori -estimaatti, joka on yksinkertaisesti posteriorijakauman moodi, eli

$$\boldsymbol{d}_{MAP} = \underset{\boldsymbol{d}}{\operatorname{argmax}} \frac{p(\boldsymbol{M} = \boldsymbol{m} | \boldsymbol{D} = \boldsymbol{d}) p(\boldsymbol{D} = \boldsymbol{d})}{p(\boldsymbol{M} = \boldsymbol{m})}. \tag{17}$$

Koska mittaustulos $\boldsymbol{m}$ on määrätty, $p(\boldsymbol{M} = \boldsymbol{m})$ on vakio ja toimii ainoastaan jakauman normalisointiparametrina. Se ei siis vaikuta MAP-estimaattiin ja estimaatti voidaan yksinkertaistaa muotoon

$$\boldsymbol{d}_{MAP} = \underset{\boldsymbol{d}}{\operatorname{argmax}}\, p(\boldsymbol{M} = \boldsymbol{m} | \boldsymbol{D} = \boldsymbol{d}) p(\boldsymbol{D} = \boldsymbol{d}). \tag{18}$$

TULOKSET

Teräksistä ulokepalkkia, joka on 1400 millimetriä pitkä (x-suunta), 60 millimetriä leveä (y-suunta) ja 5 millimetriä paksu (z-suunta) mitattiin 7 kiihtyvyysanturilla z-suuntaan. Värähtelyn aikaansaamiseksi palkkia napautettiin kumivasaralla. Palkin ollessa ehjä tehtiin ensin joukko mittauksia. Tämän jälkeen palkkiin sahattiin rautasahalla 20mm lovi y-suuntaan, jossa suunnassa palkki on suhteellisen epäherkkä vauriolle, koska värähtely tapahtuu z-suunnassa. Mittaukset toistettiin vaurioituneella palkilla. Kuuden alimman moodin taajuudet ja muodot tunnistettiin molemmissa tapauksissa.

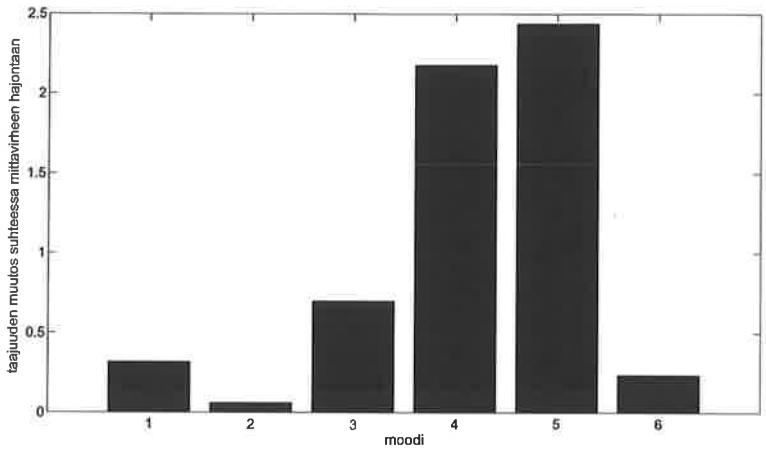

Kuva 1: Ehjän ja vaurioituneen palkin mooditaajuuksien ero suhteutettuna mittavirheeseen. Moodit 4 ja 5 ovat muuttuneet merkittävästi.

Suhteellisen hajonnan keskiarvo oli taajuuksille noin 0,05% kun taas moodimuotojen komponenteille se oli 0,97%.

Kuva 1 esittää ehjän ja vaurioituneen palkin mooditaajuuksien eron suhteutettuna mittavirheeseen. Moodeissa 4 ja 5 nähdään merkittävä muutos. Ero ehjän ja vaurioituneen rakenteen välillä on siis tilastollisesti merkitsevä, joten mittaustarkkuus on riittävä. Merkittäviä muutoksia nähdään myös moodimuotojen yhteydessä.

Palkki mallinnettiin Euler-Bernoulli -palkkimallilla käyttäen elementtimenetelmää, jossa palkin pituus jaettiin 50:een keskenään samankokoiseen elementtiin. Mallissa käytettiin materiaalille kimmokerrointa 210 GPa ja tiheyttä 7860 $\mathrm{kg/m^3}$. Simuloitujen moodiparametrien ja mitattujen parametrien keskiarvon välinen ero otettiin virhetermin $\boldsymbol{E}$ odotusarvoksi. Virhetermin kovarianssi estimoitiin mitattujen parametrien otoskovarianssina.

Priorijakauma valittiin siten, että vaurioparametrit d_i ovat riippumattomia ja samoin jakautuneita. Koska suurimman osan palkista tiedettiin olevan vaurioitumaton, priorijakauman tuli antaa matala todennäköisyys suurelle vauriolle ja korkea todennäköisyys matalalle vaurioparametrin arvolle. Lisäksi vaurioparametrin arvot yli yhden ja alle nollan tuli olla kiellettyjä. Tähän tarkoitukseen valittiin jakauma, joka käyttäytyy kuten $\mathcal{N}(0, \sigma^2)$-normaalijakauma, kun $d_i \in [0, 1]$ ja on nolla muuten. Priorijakaumassa on siten yksi vapaa parametri σ.

Kuva 2 esittää MAP-estimaatin vaurioparametreille d_i. Suurimman piikin sijainti vastaa sahatun loven sijaintia, mikä osoittaa menetelmän toimivan tässä tilanteessa. Estimaatti ei ole herkkä priorijakauman parametrille, kuvassa näkyvä piikki erottuu selkeänä laajalla parametrialueella. Kuvan estimaatti on laskettu parametrin arvolla $\sigma^2 = \frac{1}{2}$.

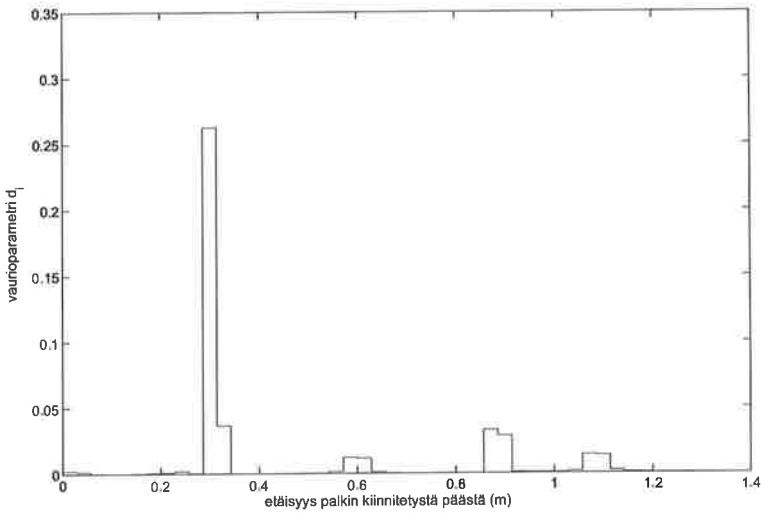

Kuva 2: MAP-estimaatti ulokepalkin vauriolle. Korkein piikki vastaa todellisen vaurion sijaintia.

JOHTOPÄÄTÖKSET

Tässä artikkelissa on esitetty vauriontunnistusmenetelmä, joka ottaa huomioon mittavirheen ja tietynlaisen mallinnusvirheen. Sen on osoitettu tuottavan hyvän lokalisaation vauriolle yksinkertaisessa rakenteessa käytettäessä todellista mittadataa.

Tämä tutkimus on osa ISMO-projektia, joka on Teknillisen korkeakoulun MIDE-tutkimusohjelman älykkään rakenteiden kunnonvalvonnan projekti.

VIITTEET

[1] A. D. Dimarogonas, Vibration of cracked structures: A state of the art review, Engineering Fracture Mechanics, **55**, 831–857, 1996.

[2] O. S. Salawu, Detection of structural damage through changes in frequency: a review, Engineering Structures, **19**, 718–723, 1997.

[3] L. Mevel, A. Beneviste, M. Basseville and M. Goursat, Blind subspace-based eigenstructure identification under nonstationary excitation using moving sensors. IEEE Transactions of Signal Processing, **50**, 41–48, 2002.

[4] D. A. Castello, L. T. Stutz and F. A. Rochinha, A structural defect identification approach based on a continuum damage model, Computers & Structures, **80**, 417–436, 2002.

DYNAMIC RESPONSE AND CHARACTERISTICS OF SPECTRUM IN A CONTACT VIBRATION MODEL WITH RANDOM INPUT

L. Yuan, V. Järvenpää, P. Salmenperä, J. Miettinen, E. Keskinen

Department of Mechanics and Design
Tampere University of Technology
P.O. Box 589, 33101 Tampere, Finland
E-mail: lihong.yuan@tut.fi

ABSTRACT

A pilot roll station has been studied and the contact vibration problem of a roll nip system is addressed in this work.The Hertzian contact deformation constitutes a nonlinear spring coupling masses of rolls. The dynamic vibrations of the system are excited by retard effect and random input. The random sources input to the nip are generated from the paper web and the roughness surface owing to the deformation of the polymer roll cover, which are expressed as power spectra with the special characteristics of retard effect. The multi-scale method is implemented to yield theoretical solutions. The effects from the parameters of interest in rolling contact are discovered.

1. INTRODUCTION

Roll nips are used for finishing the surface of processing paper and extensively exist in large scale paper machines of modern paper manufacturing industry. One nip unit consists of two rolls rotating with contact.

The traditional hard-nip machine calenders, in which a paper web is calendered to a uniform thickness, causes the variations in paper surface properties [1, 2].In supercalenders, the nip is typically formed by one hard metal roll and one soft roll coated with polymer layer, so-called soft-nip. The soft cover may distribute the contact pressure in the nip and produce a paper with more constant density rather than constant caliper of the paper. However, the polymer material has such strong viscoelastic characters that can considerably affect the contact stresses. As the result a regenerative vibration condition evidently originates from the polymer cover due to its finite viscoelastic recovery time. A pilot roll station with soft-nip has been studied and the contact vibration problem of a roll nip system is addressed in this work.

The interesting works on dynamic modeling of rolling contact intrigue us. For example, Nayak [3] in earlier 1972 presented a rolling contact dynamic model with two elastic bodies solving by harmonic balance method. Much later in 1997, using the same model as Nayak, Narayana and Sekar[4] solved its equation by Fourier-Galerkin-Newton Method and obtained the bifurcation structure of contact vibrations. Gray and Johnson [5] investigated the response of the rolling elastic bodies through the theory and techniques of random vibration. They claimed that contact load and damping are significant parameters. Turner [6] studied nonlinear vibrations with cantilever-Hertzian contact boundary conditions in a beam application. In recent researches, the dynamic

contact force has been analyzed and might be nonlinear from the contact stiffness [7-8]. But it is still needed to discovery more for the aspect that the contact force can be applied into a dynamic model. Such kind of contact vibrations has attracted more attentions.

We have studied on the time delay dynamic system whereas some tests and observations on a nip installation have been done and analyzed [9]. To model and predict the vibration motion of the nip system, formulating of the contact force based on the contact theory is needed to explore the soft-nip contact mechanics.

The Hertzian contact deformation constitutes a nonlinear spring coupling masses of rolls. The dynamic vibrations of the system are excited by retard effect and random roughness surface owing to the deformation of the polymer cover. The normal contact force is difficult directly to measure. However, the simplest observation of the response of the system can be made by attaching an accelerometer to the end of the roll to measure the acceleration of the roll mass. The random sources input to the nip are including the paper web and the roughness of the polymer roll surface, which are expressed as power spectra with the special characteristics of retard effect.

As refer to the stability of time delay system is more complex and interesting especially when it involves nonlinear elements. The analysis of the Hopf bifurcation in different models can be carried out by using analytical methods like multi-scale, harmonic and Floquet theory [10-14]. From the perturbation theory [15], the multi-scale method in this work will be executed for analyzing the mathematical model to obtain the normal form and the amplitude of the limit cycle of the motion.

Based on the model of contact vibrations of the nip, the theoretical result is achieved by the multi-scale method and the bifurcation diagram is plotted. Specifically, in the numerical simulations the random input has been embedded into the model. Many cases have been carried out. First in time history the comparisons between cases without and with random signals are illustrated. Secondly the comparisons also are given by spectrum. In both time and frequency domain, it indicates the stability characteristics of time delay systems. . The effects from random excitation in rolling contact are observed.

2. MATHEMATICAL MODEL

To establish the mathematical model of the rolling nip system (see figure 1), the normal contact force between the rigid roll and the polymer covered roll should be formulated at first. The static normal force over the contact area can be computed by the integration of the distribution function of the normal contact pressure between two roll's contact [16]. It is expressed as

$$P=\frac{E}{R\cdot s}\left[\frac{2}{3}+\beta\xi^{2}(1+e^{-\frac{2}{\xi}})+\beta\xi^{-3}(-1+e^{-\frac{2}{\xi}})\right]a^{3} \tag{1}$$

The maximum depth of the penetration of the roll δ in the dynamical model should be related to the dynamic displacements x_1, x_2 and expressed like

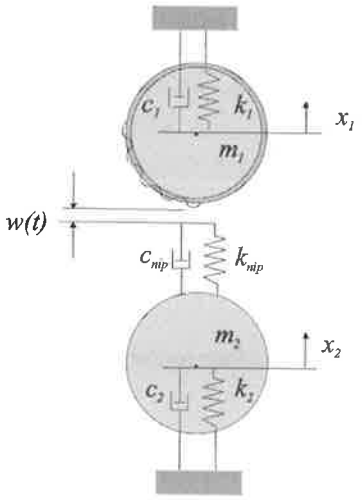

Figure 1. Two metal rolls in contact, one with s smooth, one with a polymer deformed surface.

$$\delta = \delta_0 + x_1 - x_2 \tag{2}$$

where δ_0 is the nominal penetration in the contact region.

Then, the nonlinear relation between the width of the contact a and dynamical displacements x_1 and x_2 [17] is written as

$$a^3(t) = (2R\delta_0(1 + \frac{x_1}{\delta_0} - \frac{x_2}{\delta_0}))^{3/2} \tag{3}$$

The governing equations of the motion of the rolling system in figure 1 are expressed as a two-degree model

$$\ddot{x}_1 + 2\zeta_1\dot{x}_1 + {p_1}^2 x_1 = -N(x_1, x_{1\tau}, x_2, x_{2\tau}, t)/m_1 \tag{4}$$

$$\ddot{x}_2 + 2\zeta_2\dot{x}_2 + {p_2}^2 x_2 = N(x_1, x_{1\tau}, x_2, x_{2\tau}, t)/m_2 \tag{5}$$

where $2\zeta_i = c_i/m_i$, ${p_i}^2 = k_i/m_i$, and i =1,2.

Considering the time delay effect in formula (1& 3), the entire dynamic contact force N including the nip damping in the contact is

$$\begin{aligned} N(x_1, x_{1\tau}, x_2, x_{2\tau}, t) &= P_{dynamic} + h \cdot c_{nip} \cdot \dot{\delta}(t) + w(t) \\ &= h \cdot F_{\Phi} \cdot \left[a^3(t) - \gamma_e a^3(t-\tau)\right] + h \cdot c_{nip} \cdot \dot{\delta}(t) + w(t) \end{aligned} \tag{6}$$

where $w(t)$ is a general zero-mean random excitation.

3. THEORETICL ANALYSIS BY PERTURBATION

The perturbation analysis can be performed into the delay type equations using the method of multiple scales [15]. In this method, a fast time-scale $T_0 = t$ and a slow time-scale $T_1 = \varepsilon^2 t$ are introduced.

We seek a second-order expansion for the equations (4 and 5) in the form

$$x_i = \varepsilon x_{i0}(T_0, T_1) + \varepsilon^2 x_{i1}(T_0, T_1) + \varepsilon^3 x_{i2}(T_0, T_1) + \mathrm{O}(\varepsilon^4)\ ,\ i=1,\ 2. \tag{7}$$

Then we perturb the contact parameter (relevant to the effective thickness of the polymer layer), let

$$h = h_c + \varepsilon^2 h_1 \tag{8}$$

where h_c is the reciprocal of thickness value s at the stability boundary.

It is convention to introduce the polar transformation A_1

$$A_1 = \frac{1}{2}\alpha e^{i\delta} \tag{9}$$

Analogously, the polar transformation A_2 can be also introduced but for the sake of abbreviation we dropped it.

Substituting the equation (9) into the equation (4-5) and separating the real and imaginary parts, we obtain the normal form corresponding to x_1

$$\alpha' = g_1 h_1 \alpha + g_2 \alpha^3 + w_1 \tag{10}$$

$$\delta' = g_3 h_1 + g_4 \alpha^2 + w_2 \tag{11}$$

where w_1 and w_2 represent the responses generated from the random excitation, meanwhile the other parameters are illustrated at the appendix.

To the approximation, the deterministic steady-state response is given by

$$x_1 = \alpha \cos(\omega t + \delta) + \ldots \tag{12}$$

When $w_1 = w_2 = 0$, the steady-state values can obtained. They correspond to $\alpha' = 0$ and $\delta' = 0$.Hence it yields the expression of determining the constant amplitude of the limit cycles

$$\alpha = \sqrt{\frac{g_1}{g_2}(h_c - h)} \tag{13}$$

The effect of the random input will be illustrated in the following numerical results.

4. NUMERACAL RESULTS

The bifurcation diagram presenting the amplitude of the limit cycle vs. the bifurcation parameter from the equation (13) can be depicted in Figures 2 to 3. As mentioned (6), the layer thickness is $s = 1/h$. Here the value $s_c = 1mm$ is with respect to h_c on the Hopf bifurcation. In Figure 2, the values of the time delays are $\tau = 0.2160s$ (rolling speed 480m/min) and $0.2116s$ (490m/min), $0.2033s$ (510m/min), respectively. When the rolling speed is 490m/min, the amplitude is lower than the two others owing to the characteristics of the stability lobe of time delay system. Similarly in Figure 3, the values of the time delays are $\tau = 0.2033s$ (510m/min) and $0.1994s$ (520m/min), $0.1920s$ (540m/min), respectively. And the amplitude in 520m/min case is lower than the two others as well. Thus in the rolling speed range of from 480 to 520 m/min, there are jumps from the stable to the unstable alternatively.

With experimental experiences, the dynamic response shows different behaviors when drives speed up and down. The system addressed above shows soft spring type in nonlinear model. As we know from the nonlinear theory, speed-up operation will have low amplitudes of the responses whereas speed-down have higher amplitudes. Here only the speed-down cases are obtained in numerically.

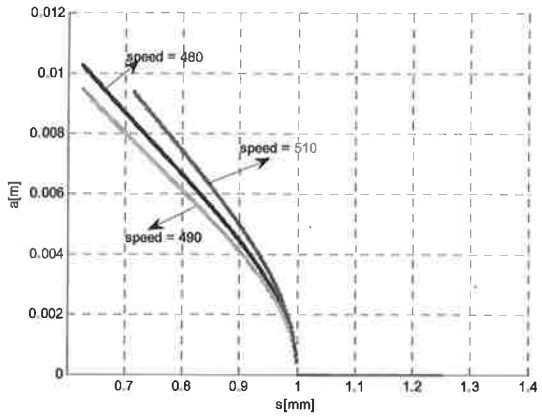

Figure 2. Bifurcation diagram when rotational speed 480,490,510m/min.

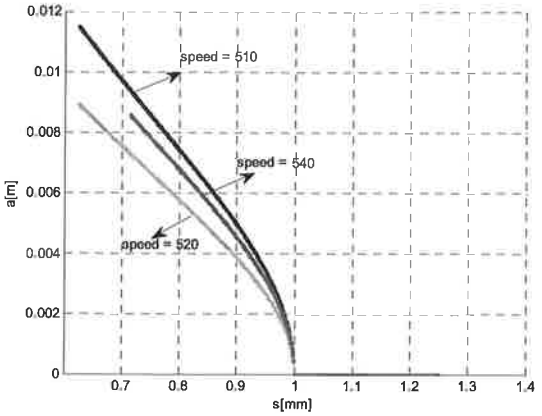

Figure 3. Bifurcation diagram when rotational speed 510,520,540m/min.

The numerical solutions are carried out by the Matlab simulink environment. In figure 4, the embedded Matlab function block is solving equations (4-5) in time domain. The displacement results in time history are obtained in figure 5-12.

Some observations are given as following. The stability characteristics should be verified numerical results. Here only the displacement x_1 of the polymer covered roll are most concerned. From figure 5 to 8, the displacement x_1 responses in time domain are illustrated. Totally, there are five cases in different speeds (480, 490, 510, 520, 540 m/min). But the difference is that the cases in left side pictures do not take account in random inputs and analogously the ones in right side do. Both types with and without random input, the displacement amplitudes at the rolling speeds 490 and 520 m/min are much smaller than the others. The stability characteristics are consistent with the bifurcation plots in Figure3 and 4. Moreover, the random inputs cause the displacement curves with more irregular envelopes. This kind of effects depends on the amplitude of random input.

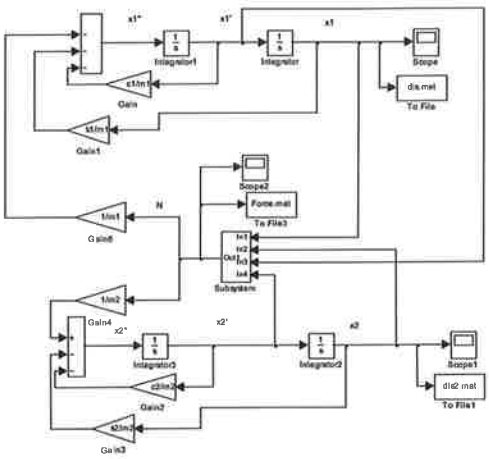

Figure 4. The Simulink model.

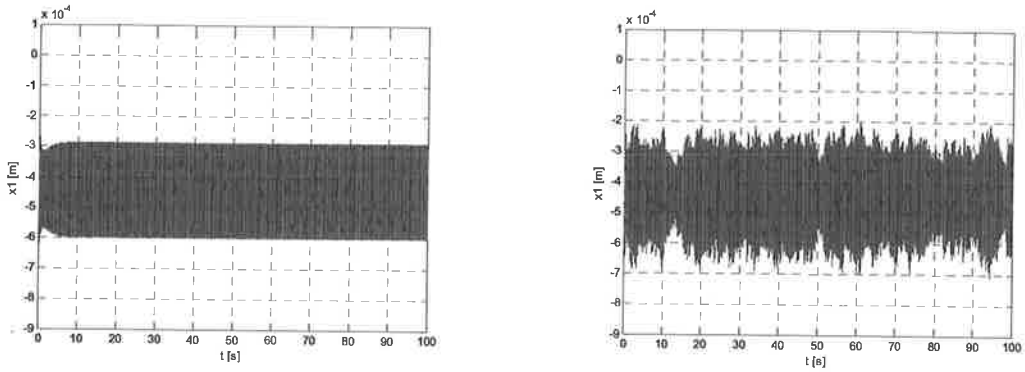

Figure 5. Time domain response without and with random input in 480 m/min.

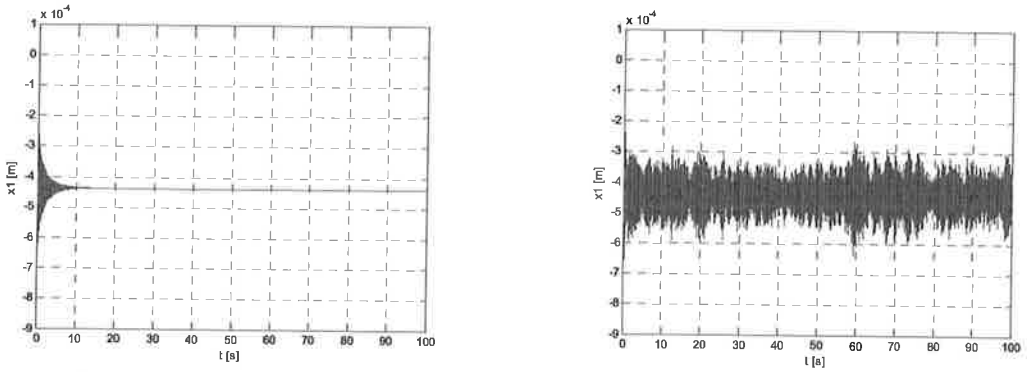

Figure 6. Time domain response with random input in 490 m/min.

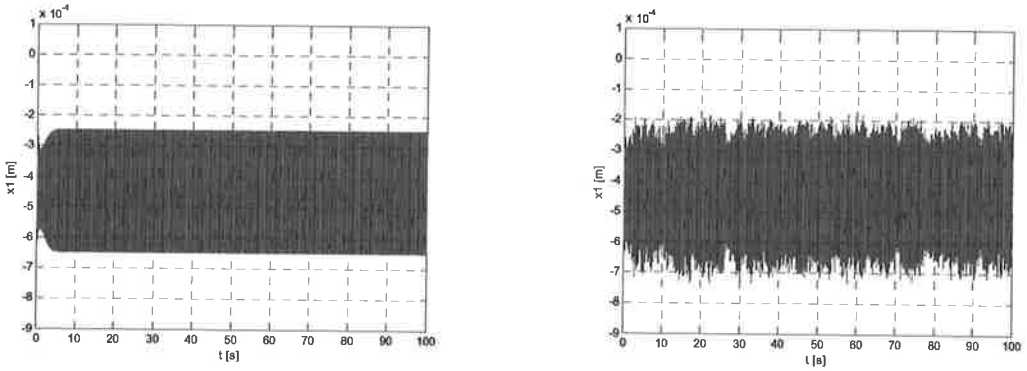

Figure 7. Time domain response without and with random input in 510 m/min.

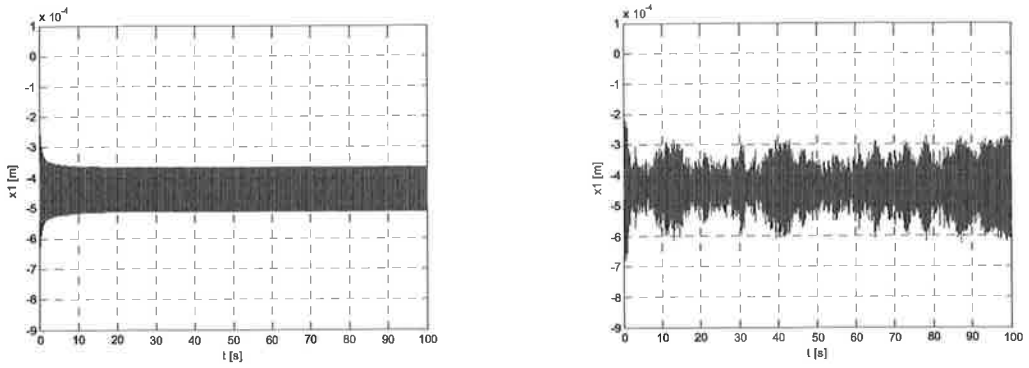

Figure 8. Time domain response without and with random input in 520 m/min.

For more clearly, we can see in the spectral plots corresponding to the above rolling speeds in frequency domain [17]. From figure 9 to 12, similarly the cases in left side pictures do not take account in random inputs and the ones in right side do. Firstly, the lower natural frequencies are found around 35Hz and 122Hz. Secondly, the satellite peaks appear near the natural frequencies which indicate the time delay effect. Finally, the random inputs cause the spectral curves with much more irregular peaks.

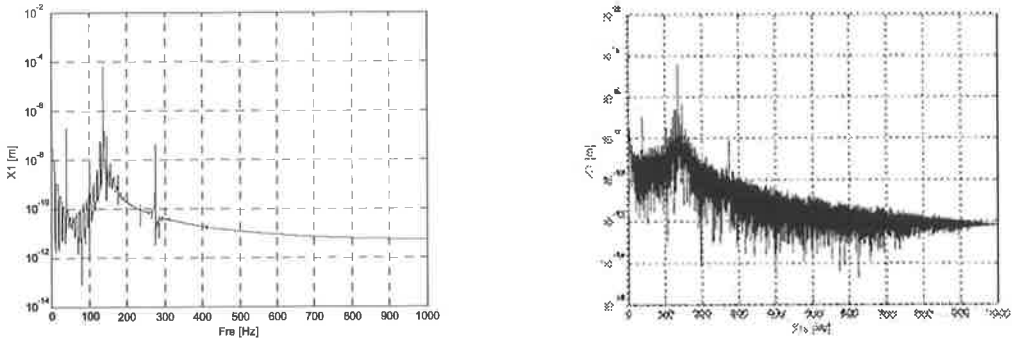

Figure 9. The spectral response without and with at rolling speed 480m/min.

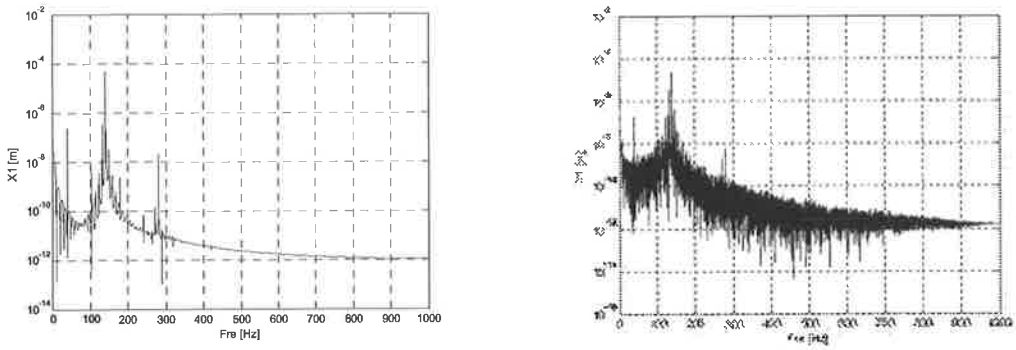

Figure 10. The spectral response without and with at rolling speed 490m/min.

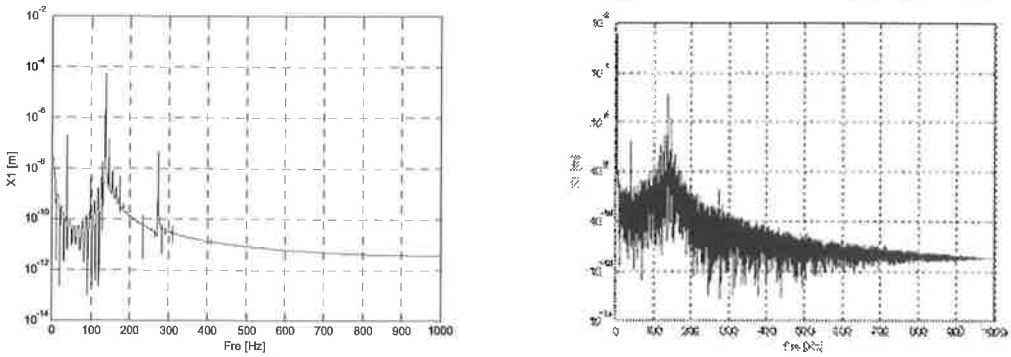

Figure 11. The spectral response without and with at rolling speed 510m/min.

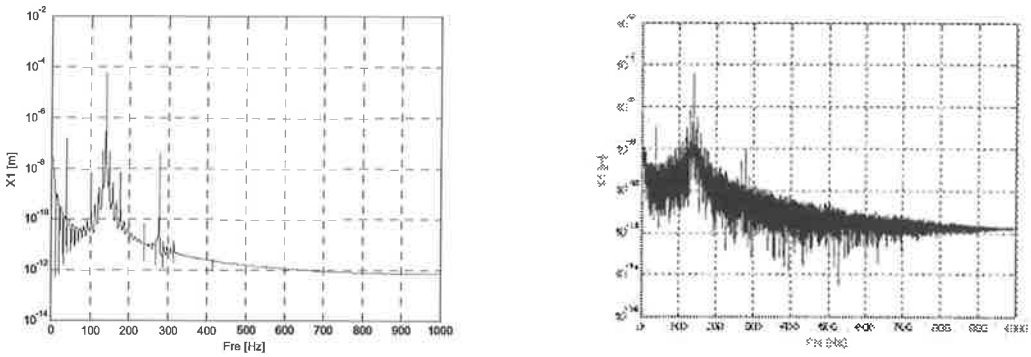

Figure 12. The spectral response without and with at rolling speed 520m/min.

5. CONCLUSIONS

The dynamic model of a roll nip system has been established in nonlinear and time delay differential equations with the random input consideration. The nonlinear normal form of the equations of motion is obtained by the multi-scale method. Thereby the bifurcation diagrams are obtained. The time history responses are consistent with the bifurcation diagrams. Both at the same rolling speeds indicate the same characteristics of the time delay system jumping from the stable to unstable alternatively. The random excitations do give influence to the responses illustrated numerically both in displacement and spectrum plots. However, the theoretical analysis results could be extended into the case with random terms in the next work.

ACKNOWLEDGMENT

The Research is funded by the Academy of Finland.

REFERENCES

[1] G.A. Smook, Handbook for Pulp & Paper Technologists, Angus Wilde Publications Inc., 1992.
[2] D.R. Roisum, The Mechanics of Rollers, Pappi press 1996.
[3] P. Ranganath Nayak, Contact Vibrations, Journal of Sound and Vibration (1972) 22(3) 297-322.
[4] S. Narayanan & P. Sekar, A Frequency Domain Based Numeric-Analytical Method for Non-Linear Dynamical Systems, Journal of Sound and Vibration (1998) 211(3), 409-424.
[5] G.G. Gray & K. L. Johnson, The Dynamic Response of Elastic Bodies in Rolling Contact to Random Roughness of Their Surfaces, Journal of Sound and Vibration (1972) 22(3), 323-342.
[6] J. A. Turner, Non-Linear Vibrations of a Beam with Cantilever-Hertzian Contact boundary Conditions, Journal of Sound and Vibrations 275 (2004) 177-191.
[7] K. Zaki, S. Noah, K.R. Rajagopal & A. R. Srinivasa, Effect of Nonlinear Stiffness on the Motion of a Flexible Pendulum, Nonlinear Dynamics 27:1-18, 2002, Kluwer Academic Publisher.
[8] J-E Oh, Y-G Joe & K.Shin, Analysis of Out-Of-Plane Motion of a Disc Brake System Using a Two-Degree-Of-Freedom Model with Contact Stiffness, Proc. IMechE Vol. 219 Part D: J. Automobile Engineering, 2005.
[9] V.M. Järvenpää , V. Järvinen, P. Salmenperä, L. Yuan, Experimental Analysis of Non-Linear Roll Contact , Society for Experimental Mechanics, Inc., IMAC-XXV conference, February 15-18, 2007, Florida USA.
[10] F.C. Moon, Dynamics and Chaos in Manufacturing Processes, John Wiley &Sons, Inc., 1998.
[11] G. Stepan, Retarded Dynamical Systems: Stability and Characteristic Functions, John Wiley & Sons, Inc., 1989.
[12] T. Kalmar-Nagy, G. Stepen, F.C. Moon, Subcritical Hopf Bifurcation in the Delay Equation Model for Machine Tool Vibrations, Nonlinear Dynamics, 26, 121-142,2 001, Kluwer Academic Publishers.
[13] B. Balachandran, Nonlinear Dynamics of Milling Processes, Phil. Trans. R. Soc. Lond A (2001), 359, 793-819.
[14] E. Stone, S. A. Campbell, Stability and Bifurcation Analysis of a Nonlinear DDE Model for Drilling, J. Nonlinear Sci. Vol. 14:pp. 27-57 (2004), Springer-Verlag New York, LLC.
[15] A.H. Nayfeh and S.J. Serhan, Response Statistics of Non-linear Systems to Combined Deterministic and Random Excitations, Int. J. Non-Linear Mechanics, Vol.25, No. 5,pp 493-509, 1990, Pergamon Press plc.
[16] K.L. Johnson, Contact Mechanics, Cambridge Univ. Press, 2003.
[17] L.Yuan, V.M. Järvenpää, Nonlinear vibrations in a covered roll system with viscoelastic contact, Journal of Communications in Nonlinear Science and Numerical Simulation, July 2009, Volume 14, issue 7, Elsever Science Ltd..
[18] Albert S. Kobayashi, Handbook on Experimental Mechanics, VCH Publishers, Inc., 1993.

APPENDIX

Parameters used in the normal form (formulas 10-11):

$$\phi_1=\frac{\Delta_2\Gamma_3+\Delta_3\Gamma_1}{\Delta_1\Gamma_1-\Delta_2\Gamma_2},\ \phi_2=\frac{\Delta_5\Gamma_6+\Delta_6\Gamma_4}{\Delta_4\Gamma_4-\Delta_5\Gamma_5},\ \phi_3=\frac{\Delta_8\Gamma_9+\Delta_9\Gamma_7}{\Delta_7\Gamma_7-\Delta_8\Gamma_8},\ \theta_1=\frac{\Delta_3\Gamma_2+\Delta_1\Gamma_3}{\Delta_1\Gamma_1-\Delta_2\Gamma_2},\ \theta_2=\frac{\Delta_6\Gamma_5+\Delta_4\Gamma_6}{\Delta_4\Gamma_4-\Delta_5\Gamma_5},$$

$$\theta_3=\frac{\Delta_9\Gamma_8+\Delta_7\Gamma_9}{\Delta_7\Gamma_7-\Delta_8\Gamma_8},$$

$$\Delta_1=-4\omega_c^2+4\zeta_1 i\omega_c+p_1^2+\frac{3}{2}Fh_c(1-\gamma_e e^{-2i\omega_c\tau})+2i\omega_c h_c c_n,$$

$$\Delta_2=\frac{3}{2}Fh_c(1-\gamma_e e^{-2i\omega_c\tau})+2i\omega_c h_c c_n$$

$$\Delta_3=-\frac{3}{8}Fh_c(1-\gamma_e e^{-2i\omega_c\tau}),\ \Delta_4=-4\omega_c^2-4\zeta_1 i\omega_c+p_1^2+\frac{3}{2}Fh_c(1-\gamma_e e^{2i\omega_c\tau})-2i\omega_c h_c c_n$$

$$\Delta_5=\frac{3}{2}Fh_c(1-\gamma_e e^{2i\omega_c\tau})-2i\omega_c h_c c_n,\ \Delta_6=-\frac{3}{8}Fh_c(1-\gamma_e e^{2i\omega_c\tau}),\ \Delta_7=p_1^2+\frac{3}{2}Fh_c(1-\gamma_e)$$

$$\Delta_8=\frac{3}{2}Fh_c(1-\gamma_e),\ \Delta_9=\frac{3}{4\delta_0}Fh_c(1-\gamma_e)$$

$$\Gamma_1=-4\omega_c^2+4\zeta_2 i\omega_c+p_2^2+\frac{3}{2}Fh_c(1-\gamma_e e^{-2i\omega_c\tau})+2i\omega_c h_c c_n,$$

$$\Gamma_2=\frac{3}{2}Fh_c(1-\gamma_e e^{-2i\omega_c\tau})+2i\omega_c h_c c_n$$

$$\Gamma_3=\frac{3}{8}Fh_c(1-\gamma_e e^{-2i\omega_c\tau}),\ \Gamma_4=-4\omega_c^2-4\zeta_2 i\omega_c+p_2^2-\frac{3}{2}Fh_c(1-\gamma_e e^{2i\omega_c\tau})-2i\omega_c h_c c_n$$

$$\Gamma_5=\frac{3}{2}Fh_c(1-\gamma_e e^{2i\omega_c\tau})-2i\omega_c h_c c_n,\ \Gamma_6=\frac{3}{8}Fh_c(1-\gamma_e e^{2i\omega_c\tau}),\ \Gamma_7=p_2^2+\frac{3}{2}Fh_c(1-\gamma_e),$$

$$\Gamma_8=\frac{3}{2}Fh_c(1-\gamma_e),\ \Gamma_9=-\frac{3}{4\delta_0}Fh_c(1-\gamma_e)$$

$$a_3=h_c F(1-h_b)^3\cdot\left(\frac{3}{128\delta_0^2}-\frac{1}{32\delta_0}(\phi_3-\theta_3+\phi_1-\theta_1)\right)$$

$$g_1=\frac{g_3-F\frac{3}{4}(1-h_b)}{\zeta_1+\frac{1}{2}c_n h_c(1-h_b)},\ g_2=\frac{g_4+a_{3r}(1-\gamma_e\cos\omega_c\tau)-a_{3i}\gamma_e\sin\omega_c\tau}{\zeta_1+\frac{1}{2}c_n h_c(1-h_b)}$$

$$g_3=\frac{\omega_c F\frac{3}{4}(1-h_b)-(\zeta_1+\frac{1}{2}c_n h_c(1-h_b))\frac{1}{2}c_n h_1\omega_c(1-h_b)}{\omega_c^2-\omega_c a_{3i}\gamma_e\sin\omega_c\tau+(\zeta_1+\frac{1}{2}c_n h_c(1-h_b))\frac{1}{2}c_n h_c(1-h_b)}$$

$$g_4=\{\omega_c a_{3i}\gamma_e\sin\omega_c\tau-\omega_c a_{3r}(1-\gamma_e\cos\omega_c\tau)+(\zeta_1+\frac{1}{2}c_n h_c(1-h_b))\cdot$$

$$(a_{3r}\gamma_e\sin\omega_c\tau+a_{3i}(1-\gamma_e\cos\omega_c\tau))\}/\{\omega_c^2-\omega_c a_{3i}\gamma_e\sin\omega_c\tau+(\zeta_1+\frac{1}{2}c_n h_c(1-h_b))\frac{1}{2}c_n h_c(1-h_b)\}$$

USE OF A BALANCING FACTOR IN VENTILATION DUCT SYSTEM FLOW ANALYSES

E.-M. SALONEN[1] and R. HOLOPAINEN[2]
[1] Helsinki University of Technology, Department of Structural Engineering and Building Technology, P.O. Box 2100, FI-02015 TKK, Finland
e-mail: eero-matti.salonen@tkk.fi
[2] Finnish Institute of Occupational Health, Good Environmental Theme, Arinatie 3 A, FIN-00370 Helsinki, Finland

ABSTRACT

A modification step that can be applied on the flow rates during the iterative solution of the nonlinear system equations for ventilation duct system flows is described. Macroscopic mechanical energy balance equation is formed for the duct system as a whole. The nonconverged flow rates do not in general satisfy this equation. Based on the resulting unbalance, the value of a dimensionless quantity β, called balancing factor, is determined. In the converged case the value of the balancing factor is 1. The current value of the balancing factor differing from 1 gives an indication of the accuracy of the current solution. The modification step, called balancing step, consists of multiplying the current flow rates by β. The balancing factor can also be used to obtain a reasonable initial flow rate distribution to start the calculations.

1. INTRODUCTION

The basic original unknowns in ventilation duct system flow analyses may be considered to be the flow rates in the channel sections and the static pressures at the channel section ends. The most usual way to solve the unknowns seems to consist — at least when just one static pressure value is associated with a junction — of approaches where the flow rates are eliminated by expressing them in terms of the static pressures using the Bernoulli equations. Then the system equations having only the static pressures as unknowns are generated using the continuity equations for the junctions. The pressures are solved from this set.

We will use in this article an alternative way, where the original unknowns are kept in the system equations without any eliminations. The total number of unknowns in the system equations becomes thus $3\times n_e$ where n_e is the number of channel sections in the system. We call this approach PQ-formulation. This terminology stems from the symbols for the unknowns (pressures with symbol p and flow rates with symbol Q). The system equations in the PQ-formulation are the Bernoulli equations for the channel sections, the inlet and outlet pressure jump equations at the inlet and outlet nodes, the continuity equations at the junctions and the pressure jump equations at the junctions. The price is the rather large number of unknowns but as an advantage the formulation is found to become very straightforward. The main features of the PQ-formulation have been introduced shortly in [1] and in more detail in reports [2] and [3].

The system equations in ventilation duct system flow analysis are nonlinear and (1): iterative solution methods must thus be used. The Picard method is applied here. Additionally, (2): a reasonably (guessed) initial flow rate distribution must normally be used to start a successful

converging solution process. The present article puts emphasis on the use of a dimensionless quantity — called balancing factor or β-factor — applied in connection with themes (1) and (2) to help in achieving a solution.

2. BASIC EQUATIONS

2.1 Some nomenclature

The equations used in duct system flow analyses can be based (except for the pressure jump equations at the junctions) on the principle of conservation of mass and on the principle of balance of mechanical energy in macroscopic forms. These are recalled very shortly in this chapter. Constant density steady flow is assumed. However, before discussing the two principles a simple schematic demonstration example duct system case depicted in Figure 1 is considered to introduce some nomenclature and notation.

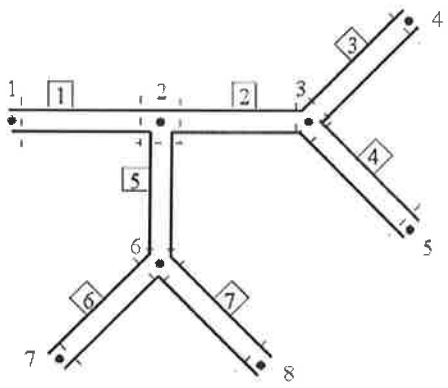

Figure 1 A schematic duct system.

The duct channel sections and nodes — the latter represented by solid dots in the figure — in a duct system are numbered separately. This numbering system resembles that used in the finite element method. In fact, the channel sections can be considered here as kind of finite elements joining nodal points. There are seven channel sections and eight nodes in the example system. For extra clarity, the channel section numbers are surrounded by boxes. Certain representative cross-sections at the channel section ends — dashed lines in the figure — are imagined separating the channel parts from the junction parts and from the inlet and outlet parts. The nodes where three (or more) channel sections meet are called junctions; here nodes 2, 3, 6. Correspondingly, nodes 1, 4, 5, 7, 8 are inlet or outlet (flow) nodes depending on effect of possible fans and on the effect of given static pressure values in the surroundings. The 14 dashed cross-sections mean 14 unknown static pressure values and the 7 channel section mean 7 unknown flow rates.

The 21 system equations corresponding to the 21 unknown quantities described above are obtained as follows. For each channel section a Bernoulli equation can be written down (together 7 equations). The so-called Bernoulli equation is in fact a special form of the energy equation to be described below. The Bernoulli equations are nonlinear in the flow rates. At inlet and outlet nodes, pressure jump equations are written down (together 5 equations). These equations can also be considered as special kind Bernoulli equations. Further, continuity equations for the flow rates can be set up at the junction nodes (together 3 equations). The static pressures get jumps in their values from cross-section to cross-section around a junction. Additional equations are generated to represent these jumps. These equations will be called also pressure jump equations. These equations are also nonlinear in the flow rates. In the present example, where three channel sections join at a junction, two additional pressure jump equations are needed for each junction (together 6

equations). In conclusion, considering the present example case, the PQ-formulation contains thus 21 unknowns and the same number of equations.

2.2 Conservation of mass

Under the assumptions of steady constant density flow the principle of conservation of mass obtains the well-known simple form

$$\int_S v_n \mathrm{d}S = 0 . \tag{1}$$

This is written for a fixed control volume surface S and v_n is the normal component of the flow velocity vector at the control surface. Equation (1) says that the net outflow through the closed control volume surface is zero. Equation (1) is often called as the (macroscopic) continuity equation.

2.3 Balance of mechanical energy

In the present article the principle of mechanical energy balance has an important role so this theme is considered here in some detail. The principle of the mechanical energy balance can be stated as follows: the rate of change of the kinetic energy of a body equals the power of the external and internal forces acting on the body, or with obvious notation:

$$\frac{\mathrm{D}K}{\mathrm{D}t} = P_{\mathrm{ext}} + P_{\mathrm{int}} \tag{2}$$

This is roughly the way the principle is expressed in general mechanics texts; e.g. [4]. The names used for the principle vary in the literature: law of kinetic energy, work-energy principle, etc. We will call the principle here as mechanical energy principle and (2) shortly as energy equation. It should be noticed that (2) applies for a closed body; in the terminology of thermodynamics, for a closed system. This is also indicated by the left-hand side of (2) containing the substantial derivative symbol. It should perhaps be stressed — especially in teaching the subject — that (2) is not the energy equation corresponding to the first law of thermodynamics. In fact, (2) is obtained just by manipulations from the local momentum equations. Reference [5] contains a thorough treatment and some specialized application formulas associated with the principle of mechanical energy balance in fluid mechanics

Under the assumptions of steady constant density Newtonian fluid flow and neglecting the effect of gravity the mechanical energy principle obtains finally the form (a rather detailed derivation is given in [2])

$$-\int_S \left(\frac{1}{2}\rho v_i v_i\right) v_n \, \mathrm{d}S - \int_S p v_n \mathrm{d}S + P^\tau = D . \tag{3}$$

Here, ρ is the density, v_i the velocity vector, p the (static) pressure. The term

$$P^\tau = \int_S t_i^\tau v_i \mathrm{d}S \tag{4}$$

is the power of the so-called deviatoric (or viscous) traction vector t_i^τ acting on the control surface. For instance, if the control surface cuts a rotating shaft, term (4) has an effect. The term

$$D = \int_V 2\mu d_{ij} d_{ij} \mathrm{d}V , \tag{5}$$

where μ the viscosity and d_{ij} is the deformation rate tensor. D is called dissipation rate (or shortly dissipation) and it is seen to be a non-negative quantity. Dissipation means irreversible transformation of mechanical energy into internal energy.

2.4 Standard control volume

In the applications to follow, we will consider a standard type control volume from which the governing duct equations are obtained as special cases. An example case of the standard control volume type to be employed is sketched in Figure 2. To simplify the representation the figure may be considered actually as a plane section of a control volume. The control surface S of the control volume V has certain plane openings — called here *plane ports*. Further, some plane openings may not be part of the closed control surface. Instead, an opening may be "blown" out to specific separate more or less spherical control surface part called here *spherical port*.

The actual detailed shapes of the spherical ports are of no importance. Spherical ports will be needed in dealing with the inlet and outlet openings of a ductwork. The plane ports are numbered from 1 to n_{p} and the spherical port from 1 to n_{s}. There are three openings in the present example control volume and two plane ports and one spherical port.

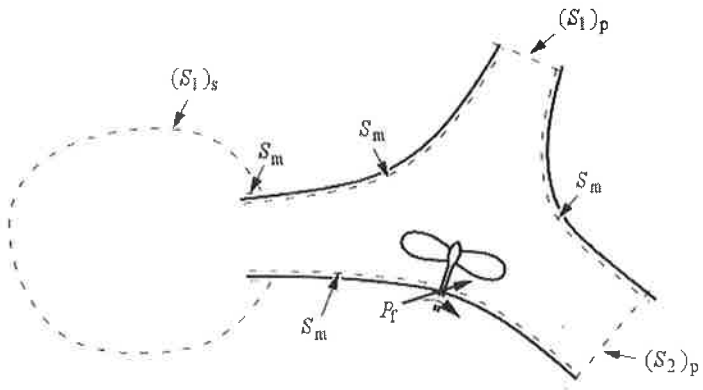

Figure 2 A control volume.

The rest of the control surface is denoted S_{m} (mantle surface), on which the velocity vector is assumed to vanish: $\mathbf{v} = \mathbf{0}$. This follows by letting the surface part S_{m} to coincide in the applications with solid duct surfaces. The thick continuous lines in Figure 2 represent here duct walls and the surface part S_{m} coincides with it. To be more exact, a symbolic fan and its shaft are also shown in Figure 2. The fan shaft cross-section does not properly belong to S_{m}. However, on it the normal velocity v_n is assumed to vanish.

As no flow takes place through the mantle surface S_{m}, the continuity equation (1) can be expressed here simply as

$$\sum_{k=1}^{n_{\mathrm{p}}} \left(Q_k\right)_{\mathrm{p}} + \sum_{k=1}^{n_{\mathrm{s}}} \left(Q_k\right)_{\mathrm{s}} = 0, \tag{6}$$

where the symbol Q refers to (volume) flow rate through a port.

The spherical control surface parts are selected specifically to be used around the inlet and outlet openings of a duct system. The kinetic energy flux terms in (3) are dropped on these parts.

The reasoning behind this is that if the control surface is taken to be relatively far from the actual inlet or outlet opening the pressure and velocity fields are no more strongly affected by the duct flow itself. Due to this, the quadratic terms corresponding to the kinetic energy can be neglected in the energy equation. Of course, when applying mass balance through the control surface, the velocities itself cannot be neglected. Further, the surrounding pressure on the spherical control surface part is assumed to be constant and the effect of viscous stresses is neglected. (In [2], the effect of gravity and the assumption of a hydrostatic surrounding pressure are considered.) Based on the above considerations the energy equation (3) applied on the type of standard control volume discussed above can finally be presented as

$$-\sum_{k=1}^{n_p}\left[\langle p_k\rangle+\frac{1}{2}\rho\langle v_k\rangle^2\right](Q_k)_p-\sum_{k=1}^{n_s}p_k\left(Q_k\right)_s+P_f=D. \tag{7}$$

D is here the dissipation rate taking place inside the whole control volume including the volumes inside the spherical ports. The angular bracket notation refers as in [5] to the cross-sectional mean value. It may be noticed that it has not been considered necessary to equip the pressures and velocities with a subscript p or s as the meaning can be seen from the context.

2.5 System equations

The nature of the system equations for a duct system flow was described shortly in Section 2.1. For lack of space we do not write down all the kind of system equations. Just as an example the so-called (engineering) Bernoulli equation is described in connection with a generic channel section e having nodes i and j (Figure 3).

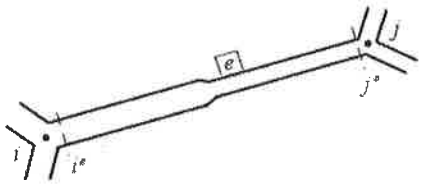

Figure 3 Channel section e and nodes i and j.

Applying continuity equation (6) for a control volume bounded by two plane ports (two arbitrary cross-sections) and the duct wall of type S_m it is found immediately the well-known result that the flow rate along the channel section is constant with respect to position. This flow rate is denoted Q^e.

Applying then the energy equation (7) gives finally a Bernoulli equation

$$p_i^e-p_j^e-\bar{K}_{ij}^e Q^e=0, \tag{8}$$

with the short-hand notation

$$\bar{K}_{ij}^e=\left\{\frac{1}{2}\rho\left[\frac{1}{\left(A_j^e\right)^2}-\frac{1}{\left(A_i^e\right)^2}\right]\operatorname{sgn}\left(\bar{Q}^e\right)+\operatorname{sgn}(j-i)k^e\right\}\left|\bar{Q}^e\right|. \tag{9}$$

A symbol equipped with an overbar means that under the present solution step this quantity is assumed to be known from an earlier step or from an initial guess. The flow rate appears in the

Bernoulli equation actually roughly in the second power. The apparently linear form (8) is obtained by manipulations to be used in the Picard method. The quantities A_i^e and A_j^e are the cross-sectional areas at the cross-sections i^e and j^e. The coefficient k^e appears in the formula

$$\Delta p_{\mathrm{tpl}}^e = k^e \left(Q^e\right)^2 \tag{10}$$

giving the so-called total pressure loss $\Delta p_{\mathrm{tpl}}^e$ as a function of the flow rate. The coefficient depends for instance on the Reynolds number and must actually be also updated during the calculations. Equation (8) is written for a channel section without a fan. With a fan the equation gets more complicated.

3. BALANCING FACTOR

3.1 Energy equation for the whole duct system

The balancing factor idea is based on applying the energy equation on whole duct systems. A special case of the standard control volume concept of Section 2:4 is taken here to be according to Figure 4. It describes a schematic illustrative duct system with one inlet and two outlets. The inlets are numbered in the general case with indices $k = 1, 2, \cdots n_{\mathrm{i}}$ and the outlets with $k = 1, 2, \cdots n_{\mathrm{o}}$, where n_{i} and n_{o} are the total number of inlets and outlets, respectively. We consider a control volume as follows. The main part S_{m} of the control volume surface coincides with the duct channel walls and if needed, with small wall surface areas near the openings. The control volume is closed around the inlets and outlets with more or less spherical type surface parts, denoted $(S_{\mathrm{i}})_k$, $k = 1, 2, \cdots n_{\mathrm{i}}$ and $(S_{\mathrm{o}})_k$, $k = 1, 2, \cdots n_{\mathrm{o}}$. These parts are extended relatively far from the actual duct openings. For simplicity of presentation, no indexing for the inlet and the outlets is employed in the figure. Again, the viscous stresses are neglected and additionally, the corresponding pressures, denoted $(p_{\mathrm{i}})_k$ and $(p_{\mathrm{o}})_k$, are assumed to be constants on the surfaces.

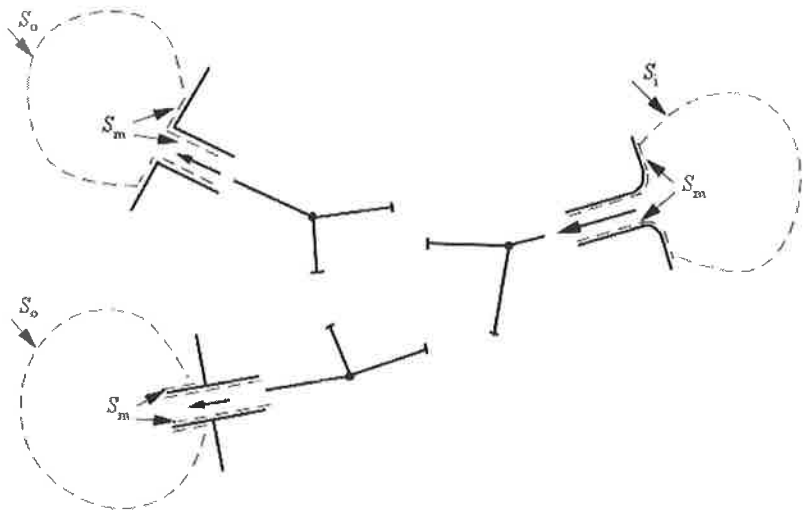

Figure 4 Schematic duct system and a control volume.

On the 'wetted' part of the control surface S_m the fluid velocity (and the normal velocity) vanishes due to the no-slip condition. However, we assume that surface S_m may be penetrated by fan shaft axes and this produces the net driving power P_f. Thus here $P^\tau = P_f$. All the ports in the energy equation (7) are here spherical so the kinetic energy flux terms are neglected and we obtain the form Based on the above assumptions, energy equation (7) obtains first the form

$$-\sum_{k=1}^{n_i}(p_i)_k\left[(Q_i)_k\right]_s-\sum_{k=1}^{n_o}(p_o)_k\left[(Q_o)_k\right]_s+P_f=D. \tag{11}$$

D is the dissipation rate inside the whole control volume. From mass balance applied for the control volumes and taking the flow directions into account, we obtain

$$\left[(Q_i)_k\right]_s=-\left|(Q_i)_k\right|,\quad \left[(Q_o)_k\right]_s=\left|(Q_o)_k\right|. \tag{12}$$

The quantities on the right-hand side inside the absolute signs are the flow rates through the corresponding plane ports. These can be finally associated with the corresponding channel section flow rates using the appropriate input data. We obtain an energy equation for the whole duct system:

$$P=D \tag{13}$$

where

$$P\equiv\sum_k(p_i)_k\left|(Q_i)_k\right|-\sum_k(p_o)_k\left|(Q_o)_k\right|+P_f. \tag{14}$$

Equation (13) is the main result to be used in Section 3.3 to produce the β-factor. The content of the equation is: the total "driving power" P in the system equals the total dissipation D in the system. The detailed expression for the driving power of a fan is given in [2].

To apply the energy equation (13) we need also the expression for the dissipation. The total dissipation rate can be written as

$$D=\sum_e D^e+\sum_i(D_i)_i+\sum_i(D_o)_i+\sum_i(D_c)_i+\sum_i(D_d)_i \tag{15}$$

where the first sum is over the channel sections, the second over the inlet nodes, the third over the outlet nodes, the fourth over the converging flow junctions and the fifth over the diverging flow junctions. The detailed expressions are given in [2]. As an example, for channel sections,

$$D^e=k^e\left|Q^e\right|^3. \tag{16}$$

3.2 Balancing factor; theory

It is found that the driving power is mainly linear in the flow rates. However, quite strikingly, the total dissipation rate is found to be of third power in the flow rates. (Strictly speaking, we then have to consider coefficient k^e in (16) not to depend on the flow rate magnitude.) These observations give an idea for a possible correction or balancing step during the system equation solution manipulations.

We write the energy equation (13) now as

$$P(\mathbf{Q}) = D(\mathbf{Q}) . \tag{17}$$

The vector argument $\mathbf{Q}$ means symbolically the list consisting of flow rates Q^e, $e = 1, 2, \cdots, n_e$. The notation introduced into (17) emphasizes that P and D depend on the flow rate distribution in the duct system.

Let the preliminary flow rates achieved at some stage of the iterations be $\tilde{Q}^e$, $e = 1, 2, \cdots, n_e$. They do not in general satisfy (17). We now assume that the exact (or more correct) solution is of the form

$$Q^e = \beta \tilde{Q}^e, \quad e = 1, 2, \cdots, n_e \tag{18}$$

or $\mathbf{Q} = \beta \tilde{\mathbf{Q}}$, where β is a dimensionless positive constant to be determined. That is, we assume that by scaling the preliminary values by the factor β we can reach the exact solution. Of course, this cannot in general be true but it can in any case be made use of in steering the solution in some sense into a correct direction. We substitute $\mathbf{Q} = \beta \tilde{\mathbf{Q}}$ into the energy equation (17). This gives $P(\beta \tilde{\mathbf{Q}}) = D(\beta \tilde{\mathbf{Q}})$ or approximately $\beta P(\tilde{\mathbf{Q}}) = \beta^3 D(\tilde{\mathbf{Q}})$. This last form is based on the power exponent properties described above. We obtain thus

$$\beta = \frac{\sqrt{P(\tilde{\mathbf{Q}})}}{\sqrt{D(\tilde{\mathbf{Q}})}} . \tag{19}$$

This is the required formula for the β- factor and the reason for the name "balancing factor" is now obvious. The balancing step (18) can be applied using the value (19) for each updated flow rate distribution before continuing the solution manipulations. Clearly, for the iterations to proceed correctly, β- factor should finally approach the value 1. Further, the deviations in the value of β from the value 1 during the iterations give some overall information about the current solution accuracy.

Additionally, the balancing step can also be applied to obtain a reasonable initial flow rate distribution as will be explained in Section 4.5.

4 ANALYSIS DETAILS

4.1 System equations

As described already in Chapter 1, the governing system equations in the PQ-formulation consist of the Bernoulli equations for the channel sections, of the pressure jump equations at the inlets and outlets, of the continuity equations at the junctions, and of the pressure jump equations at the junctions. A MATLAB program was developed to generate and to solve the system equations.

The nonlinear system equations (the continuity equations are as an exception linear) are written as an apparently linear system

$$\bar{\mathbf{A}}\,\bar{\mathbf{x}} = \mathbf{b} , \tag{20}$$

Here, $\bar{\mathbf{A}}$ is the system coefficient matrix, $\mathbf{b}$ the right-hand side column vector and $\bar{\mathbf{x}}$ the column vector of unknowns (flow rates and static pressures). The overbar notation in (20) refers to the fact that $\bar{\mathbf{A}}$ depends on the current flow rate values used to generate them. A detailed description of

the structure $\bar{\mathbf{A}}$ is given in [3]. The iteration process consists of solving the linear system at each solution phase always directly. This corresponds to the so-called linear theory method described in [6]. In the mathematical literature, this kind of approach to solve non-linear equations in general is called usually the Picard method, e.g. [7].

4.2 Stopping criterion

The decision on the convergence of solution in the program is based on following the changes in the values of the flow rates from consecutive solutions. We use the norm

$$\| \mathbf{Q} \| = \sqrt{\frac{1}{n_e}\left[\left(Q^1\right)^2 + \left(Q^2\right)^2 + \cdots + \left(Q^{n_e}\right)^2 \right]} \tag{21}$$

to evaluate the magnitude of the system flow rate. From two consecutive solutions the relative change

$$e = \frac{\| \bar{\mathbf{Q}} - \bar{\mathbf{Q}}_{\text{old}} \|}{\| \bar{\mathbf{Q}} \|} \tag{22}$$

is evaluated. Here the subscript "old" refers to the flow rates from the previous solution (used to update the system equations) and the values without the subscript to the flow rates obtained by the final new solution. The new flow rate solution from the system equations is not usually employed directly as such but first modified by applying the relaxation and balancing steps described below. The iteration is stopped if

$$e < \delta, \tag{23}$$

where δ is a small positive number. In the program the default value $\delta = 0.001$ is used.

4.3 Relaxation step

In Reference [7] a standard underrelaxation or damping type step to avoid oscillations is also explained. In our case this step can be presented as

$$\bar{Q}^e_{\text{rel}} = (1-\alpha)\,\bar{Q}^e_{\text{sol}} + \alpha\,\bar{Q}^e_{\text{old}}, \quad e = 1, 2, \cdots, n_c \tag{24}$$

where α $(0 \le \alpha \le 1)$ is a relaxation or damping factor. Subscript "old" has the meaning explained above in Section 4.2. Subscript "sol" refers to the flow rates obtained from the solution of the updated system equations and subscript "rel" refers to the relaxed or damped values appearing on the left-hand side of (24). The value $\alpha = 0$ means that the new solution values are used as such without any damping and the value $\alpha = 1$ means total damping so that the old solution is obtained.

4.4 Balancing step

Finally, the modification proposed by the authors consists of the balancing step using the β-factor. Thus, after applying the relaxation formula (24), the value of the corresponding β-factor is evaluated from (19) using the values $\bar{Q}^e_{\text{rel}}$. After that, the formula

$$\bar{Q}^e = \beta\,\bar{Q}^e_{\text{rel}}, \quad e = 1, 2, \cdots, n_e \tag{25}$$

is employed. This is the balancing step. The left-hand sides $\bar{Q}^e$ in (25) are the final new values to be used in (22) and in the convergence test (23). If the test is not passed, the values $\bar{Q}^e$ become the values $\bar{Q}^e_{\text{old}}$ to be used in updating the system equations in the next iteration round. The effect of using the balancing step is reported in connection with the example case in Chapter 5.

An alternative possibility to that described above is to apply the balancing step first and the relaxation step next. Our conclusion from numerical tests is that this possibility demands usually more iterations than the one described above.

4.5 Starting values

Some initial (guessed) flow rates must be given to the program to start the calculations. The pressures need not to have any initial values as they appear in the PQ-formulation linearly. Of course, the better initial flow rate distribution guessed using, say some engineering judgment, the better possibility for achieving convergence is to be expected and this probably with a small number of iterations.

To obtain an initial flow rate distribution, the duct system is analyzed first in a strongly simplified setting. Laminar flow is assumed and the losses at the inlets and outlets and at the junctions are neglected. Just one pressure value is associated with a junction. The system equations consist of kind of linear Bernoulli equations for the channel sections and from the continuity equations for the junctions. The unknowns are the flow rates in the channel sections and the static pressures at the junctions. This system is directly linear and needs to be solved thus only once. This very first solution is then corrected (or scaled) by evaluating the corresponding β- factor and by applying the balancing step. In this way at least the continuity equations at the junction are satisfied. We will call the initial solution obtained in this way as *refined* initial guess.

However, the initial guess does not necessarily have to satisfy the continuity equations. One very simple possibility — called here *crude* guess — is just to give some flow rates of constant magnitude in the assumed correct flow directions. With the crude initial guess the continuity equations are clearly violated. In Chapter 5 the effect of the two guesses on the number of necessary iterations are also shown.

5. EXAMPLE RESULTS

We will give some results from a simple example case. The duct geometry is according to Figure 1. The lengths of the channel sections are $L = 5\,\text{m}$. The ducts are round and have constant diameters $d = 0.2\,\text{m}$ .The driving power is due to an overpressure 100 Pa at the inlet node 1. Then the nodes 4, 5, 7 and 8 are found to become outlets. The density and the dynamic viscosity of air are taken to be $\rho = 1.2044\,\text{kg m}^{-3}$ and $\mu = 0.000\,0185\,\text{N s m}^{-2}$. The roughness factor for the ducts is fixed to $\varepsilon = 0.000\,15\,\text{m}$. The inlet loss coefficient for the inlet is 0.5 and the outlet loss coefficient for the outlets 1.0. The junction coefficients are evaluated according to the graphs in Reference [8].

The initial guessed flow rates and the final ("exact") converged flow rates are given in Table 1. In the crude guess just flow rates of magnitude $1\,\text{m}^3\text{s}^{-1}$ are used. In is seen that with the refined guess (and naturally with the final flow rates) the continuity equations at junctions 2, 3 and 6 are satisfied (see Figure 1). The very initial flow rates obtained by the laminar flow assumption were so large that the balancing factor value needed to scale the flow was just $\beta = 0.0129$.

Table 1 Initial and final flow rates.

	crude guess	refined guess	final
$Q^1\ \left(\mathrm{m^3 s^{-1}}\right)$	1	0.3120	0.2915
Q^2	1	0.1560	0.2504
Q^3, Q^4	1	0.0780	0.1252
Q^5	1	0.1560	0.0411
Q^6, Q^7	1	0.0780	0.0206

The number of iterations needed to achieve condition (23) is recorded in Table 2. The calculations have been performed with the values 0, 0.1, 0.2, 0.3, 0.4, 0.5, 0.6, 0.7, 0.8, 0.9 of α and without and with the balancing step and further both for the crude and the refined initial guesses.

Table 2 Number of iteration steps.

α	0	0.1	0.2	0.3	0.4	0.5	0.6	0.7	0.8	0.9
Balancing step not included, crude guess	92	24	11	9	10	13	16	22	32	59
Balancing step included, crude guess	20	13	9	8	8	10	13	16	23	39
Balancing step not included, refined guess	76	22	12	7	5	5	7	10	14	24
Balancing step included, refined guess	29	16	10	7	4	5	7	10	14	24

The static pressures at the channel section ends are (Pa)

$$p_1^1 = 22.3,\quad p_2^1 = -5.0,\quad p_2^2 = 9.1,\quad p_3^2 = -11.3,\quad p_3^3 = 5.6,\quad p_4^3 = 0,$$
$$p_3^4 = 5.6,\quad p_5^4 = 0,\quad p_2^5 = 0.5,\quad p_6^5 = -0.2,\quad p_6^6 = 0.2,\quad p_7^6 = 0,$$
$$p_6^7 = 0.2,\quad p_8^7 = 0.$$

The development of β with the iterations is as follows (crude initial guess and $\alpha = 0.4$)

$$\beta_0 = 0.1232,\quad \beta_1 = 0.3002,\quad \beta_2 = 0.7540,\quad \beta_3 = 0.9569, \beta_4 = 0.9860,$$
$$\beta_5 = 0.9949,\quad \beta_6 = 0.9981,\quad \beta_7 = 0.9993,\quad \beta_8 = 0.9997.$$

The subscripts refer to the iteration number. Subscript 0 refers to the initial guess.

It may be mentioned that that the PQ-formulation seems to be rather efficient in general. For instance, the calculation time for a duct system with 1001 channel sections treated in [3] was just 1.5 s. Nine iteration steps were needed.

6. CONCLUSIONS

The balancing factor β described in this article can be used to accelerate somewhat the solutions towards convergence. Further, the balancing factor can be applied to obtain reasonable initial guesses for the flow rates to start the computations.

The main conclusion from the example results and from similar calculations is that when the PQ-formulation is used, the application of the relaxation step is very important for decreasing the number of necessary iterations and on the average, the value $\alpha \approx 0.4$ gives the best results. However, near this value the balancing step seems to have small influence. Perhaps more importantly, the values of β during the iterations give important information about the solution development. As finally β must be (close to) 1, this gives an extra check for the applier about convergence to a correct solution.

As expected, the initial flow rate guess has clearly an effect on the number of necessary iterations. However, no convergence difficulties were met even with the crude guess.

The balancing factor concept can probably be used also to profit in some alternative duct flow formulations than in the PQ-formulation. Further, suitably modified, the balancing factor could perhaps be employed also in multi-zone airflow analyses.

When a fan is driving the flow, the energy equation $P = D$ has some similarity with the equations used in fan selection, e.g. [9]. There the fan pressure-volume curve and the duct system curve are demanded to intersect at a proper place. However, the equalities concern pressures and not power quantities. The use of the energy equation could offer an alternative approach.

REFERENCES

1. Salonen E-M and Holopainen R (2008). A PQ-Formulation for Ventilation Duct System Flow Analyses, *International Journal of Ventilation*. **7**, (3), pp251-265.
2. Salonen E-M and Holopainen R (2009). A PQ-Formulation for Ventilation Duct System Flow Analyses; Theory, *TKK Structural Engineering and Building Technology Publications, TKK-R-BE1*.
3. Holopainen R and Salonen E-M (2009). A PQ-Formulation for Ventilation Duct System Flow Analyses; Applications, *TKK Structural Engineering and Building Technology Publications, TKK-R-BE2*.
4. Langhaar HL (1989). *Energy Methods in Applied Mechanics*, KriegerA.
5. Bird RB, Stewart WE, Lightfoot EN (2002). *Transport Phenomena*, 2nd ed., Wiley.
6. Jeppson RW (1976). *Analysis of Flow in Pipe Networks*, Ann Arbor Science.
7. Reddy JN and Gartling DK (2001). *The Finite Element Method in Heat Transfer and Fluid Dynamics*, 2nd ed., CRC Press.
8. Miller DS (1990). *Internal Flow Systems*, 2nd ed. BHRA, The Fluid Engineering Centre.
9. ASHRAE (2001). *ASHRAE Handbook*, Chapter 34, Duct Design.

TURBULENSSIMALLIEN VERTAILU 3D-ASKELVIRTAUKSEN MALLINNUKSESSA

A. KARVINEN JA H. AHLSTEDT

Energia- ja prosessitekniikan laitos
Tamperen teknillinen yliopisto
PL 589, 33101 TAMPERE

TIIVISTELMÄ

Eri turbulenssimallien – k-ε-malli sekä LRR, QI, SSG, SMC-ω ja BSL Reynoldsin jännitys -mallit – soveltuvuutta voimakkaasti kaareutuvan irtoavan virtauksen laskentaan on tutkittu kolmiulotteisen taaksepäin suuntautuvan askelvirtauksen tapauksessa käytten kaupallista virtauslaskentaohjelmistoa. Reynoldsin jännitys -mallien tulokset ovat parempia kuin k-ε-mallin.

1 JOHDANTO

Askelvirtauksella tarkoitetaan tilannetta, jossa vakiopoikkileikkauksinen kanava laajenee äkillisesti kuvan 1 mukaisesti. Askelvirtaus on teoreettisesti mielenkiintoinen, koska virtaukseen muodostuu irtoamisalue siten, että virtaus irtoaa askeleen särmästä ja kiinnittyy takaisin noin matkan 5–7h päässä askeleesta, missä h on askeleen korkeus. Irtoava virtaus on haasteellinen turbulentin virtauksen simulointimenetelmille. Askelvirtauksessa irtoamiskohta tunnetaan tarkasti, mutta eri turbulentin virtauksen mallinnusmenetelmät ennustavat kiinnittymisen eri kohtiin – usein varsin kauas oikeasta kohdasta. Simuloidun kiinnittymiskohdan oikeellisuutta pidetään usein laskentamenetelmän hyvyyden mittarina.

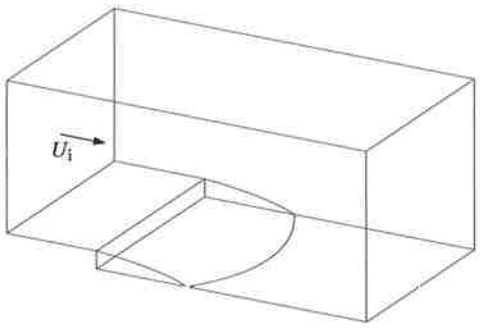

Kuva 1: Askelvirtaus neliökanavassa.

Virtauksen irtoamisen lisäksi askelvirtaus on teoreettisesti mielenkiintoinen siksi, että virtaus on irtoamiskuplan alueella voimakkaasti kaareutunut, mistä johtuen turbulenssi on voimakkaasti epäisotrooppista.

Edellä mainittujen seikkojen takia askelvirtausta on käytetty usein turbulenssimallien vertailussa; esimerkiksi Thangam ja Speziale [1] ovat tutkineet kaksiyhtälömallien käyttäytymistä[1] askelvirtauksen laskennassa. Launder [2] on tutkinut Reynoldsin jännitys -mallia askelvirtauksen tapauksessa. Suoraa simulointia (DNS) on käytetty mm. lähteissä [3] ja [4]. Askelvirtauksen virtauskenttää on mitattu mm. lähteissä [5], [6], [7], [8], [9], [10] ja [11], joista viimeistä on käytetty tämän työn vertailukohtana. Kattavampi katsaus askelvirtauksen tutkimukseen löytyy lähteestä [12].

Askelvirtauskanava voi olla leveydeltään joko ääretön tai äärellinen. Näistä ensimmäiseen muodostuu kaksiulotteinen (2D) keskiarvovirtauskenttä, kun taas jälkimmäiseen muodostuu sivuseinien vaikutuksesta kolmiulotteinen (3D) edellistä monimutkaisempi virtauskenttä. Usein viitatun lähteen [13] mukaan askelvirtaus voidaan olettaa kaksiulotteiseksi, mikäli kanavan leveys on vähintään kymmenen kertaa askeleen korkeus. Tällöin sivuseinien vaikutus on mitätön tarkasteltaessa virtaussuureita kanavan symmetriatasolla. Suuri osa kirjallisuudesta löytyvästä tutkimuksesta koskee 2D-tilannetta, vaikka irtoava virtaus on käytännön sovelluksissa lähes aina kolmiulotteinen. Tässä työssä onkin haluttu tutkia turbulenssin mallintamista 3D-tapauksessa.

2 VIRTAUSTA HALLITSEVAT YHTÄLÖT JA NIIDEN RATKAISU

Tässä työssä virtaus on oletettu kokoonpuristumattomaksi, jolloin virtausta hallitsevat Reynolds-keskiarvotetut Navier-Stokesin yhtälöt ovat

$$\nabla \cdot \boldsymbol{U} = 0 \tag{1}$$

ja

$$\nabla \cdot (\boldsymbol{U} \otimes \boldsymbol{U}) = \nabla \cdot \left(-\frac{p}{\rho} I + \nu(\nabla \boldsymbol{U} + (\nabla \boldsymbol{U})^T) - \overline{\boldsymbol{u} \otimes \boldsymbol{u}} \right), \tag{2}$$

missä $\boldsymbol{U}$ on aikakeskiarvotettu nopeusvektori, p on aikakeskiarvotettu paine, ρ on tiheys, ν on kinemaattinen viskositeetti ($\nu = \mu/\rho$, missä μ on dynaaminen viskositeetti) ja yläviiva tarkoittaa aikakeskiarvotusta. Merkintä $\otimes$ tarkoittaa tensorituloa. Reynoldsin jännitykset $-\overline{\boldsymbol{u} \otimes \boldsymbol{u}}$ ilmaisevat turbulenssin vaikutusta ja ne täytyy mallintaa, jotta yhtälöt (1) ja (2) sulkeutuisivat.

2.1 k-ε-malli

k-ε-mallissa käytetään Boussinesq'n pyörreviskositeettimallia [14], missä Reynoldsin jännitykset, $-\overline{\boldsymbol{u} \otimes \boldsymbol{u}}$, approksimoidaan kaavalla

$$-\overline{\boldsymbol{u} \otimes \boldsymbol{u}} = -\frac{2}{3} k I - \frac{2}{3} \nu_t \nabla \cdot \boldsymbol{U} I + \nu_t (\nabla \boldsymbol{U} + (\nabla \boldsymbol{U})^T), \tag{3}$$

missä k on turbulenssin kineettinen energia ja ν_t on turbulentti eli pyörreviskositeetti. Näin saadaan liikemääräyhtälöksi

$$\nabla \cdot (\boldsymbol{U} \otimes \boldsymbol{U}) = -\frac{1}{\rho} \nabla p' + \nabla \cdot \left(\nu_{\text{eff}} \left(\nabla \boldsymbol{U} + (\nabla \boldsymbol{U})^T \right) \right), \tag{4}$$

missä $\nu_{\text{eff}} = \nu + \nu_t$ on tehollinen virkositeetti ja modifioitu paine $p' = p + 2\rho k/3$.

k-ε-mallissa oletetaan, että turbulentti viskositeetti on yhteydessä turbulenssin kineettiseen energiaan ja sen dissipaatioon, ε:

$$\nu_t = C_\mu \frac{k^2}{\varepsilon}. \tag{5}$$

[1] Turbulenssimalli, jossa on kaksi siirtoyhtälöä turbulenssisuureille, esimerkiksi k-ε-malli.

Turbulenssin kineettinen energia ja sen dissipaatio lasketaan omista yhtälöistään [15]:

$$\nabla \cdot (\boldsymbol{U}k) = \nabla \cdot \left[\left(\nu + \frac{\nu_t}{\sigma_k} \right) \nabla k \right] + P_k - \varepsilon \tag{6}$$

ja

$$\nabla \cdot (\boldsymbol{U}\varepsilon) = \nabla \cdot \left[\left(\nu + \frac{\nu_t}{\sigma_\varepsilon} \right) \nabla \varepsilon \right] + \frac{\varepsilon}{k}(C_{\varepsilon 1} P_k - C_{\varepsilon 2}\varepsilon). \tag{7}$$

Turbulenssin kineettisen energian tuotto

$$P_k = \nu_t \nabla \boldsymbol{U} \cdot (\nabla \boldsymbol{U} + (\nabla \boldsymbol{U})^T). \tag{8}$$

k-ε-mallissa käytetään vakioille seuraavia kokeellisesti määritettyjä arvoja [16]:

$$C_\mu = 0{,}09;\ C_{\varepsilon 1} = 1{,}44;\ C_{\varepsilon 2} = 1{,}92;\ \sigma_k = 1{,}0;\ \sigma_\varepsilon = 1{,}3.$$

k-ε-mallin suurin heikkous on siihen sisältyvä Boussinesq'n pyörreviskositeettimalli, joka olettaa Reynoldsin jännitysten olevan suoraan verrannollisia venymänopeuksiin. Tämä ei kuitenkaan päde mm. voimakkaasti kaareutuvalle virtaukselle.

2.2 LRR, QI ja SSG Reynoldsin jännitys -mallit

Reynoldsin jännitys -malleissa (Reynolds Stress Model, RSM) edellä mainitusta ongelmasta on päästy eroon mallintamalla kaikki Reynoldsin jännitykset erikseen.

LRR (Launder Reece Rodi), QI (Quasi-Isotropic) ja SSG (Speziale Sarkar Gatski) Reynoldsin jännitysmalleissa [17, 18] Reynoldsin jännitysten siirtoyhtälö on

$$\nabla \cdot (\boldsymbol{U} \otimes \overline{\boldsymbol{u} \otimes \boldsymbol{u}}) = \boldsymbol{P} + \boldsymbol{\phi} + \nabla \cdot \left[\left(\nu + \frac{2}{3} c_s \frac{k^2}{\varepsilon} \right) \nabla \overline{\boldsymbol{u} \otimes \boldsymbol{u}} \right] - \frac{2}{3} I\varepsilon, \tag{9}$$

missä $\boldsymbol{P}$ on jännitystuottotermi:

$$\boldsymbol{P} = -\overline{\boldsymbol{u} \otimes \boldsymbol{u}}(\nabla \boldsymbol{U})^T - (\nabla \boldsymbol{U})\overline{\boldsymbol{u} \otimes \boldsymbol{u}}. \tag{10}$$

Painevenymänopeustensori $\boldsymbol{\phi}$ lasketaan kaavasta:

$$\begin{aligned} \boldsymbol{\phi} = \varepsilon \left[C_{s1}\boldsymbol{a} + C_{s2} \left(\boldsymbol{a}\boldsymbol{a} - \frac{1}{3}\boldsymbol{a} \cdot \boldsymbol{a} I \right) \right] - C_{r1} P \boldsymbol{a} + C_{r2} k \boldsymbol{S} - C_{r3} k \boldsymbol{S} \sqrt{\boldsymbol{a} \cdot \boldsymbol{a}} + \\ C_{r4} k \left(\boldsymbol{a}\boldsymbol{S}^T + \boldsymbol{S}\boldsymbol{a}^T - \frac{2}{3}\boldsymbol{a} \cdot \boldsymbol{S} I \right) + C_{r5} k \left(\boldsymbol{a}\boldsymbol{W}^T + \boldsymbol{W}\boldsymbol{a}^T \right), \end{aligned} \tag{11}$$

missä $\boldsymbol{a}$ on Reynoldsin jännitysten anisotrooppinen osuus:

$$\boldsymbol{a} = \frac{\overline{\boldsymbol{u} \otimes \boldsymbol{u}}}{k} - \frac{2}{3} I, \tag{12}$$

$\boldsymbol{S}$ on venymänopeustensori:

$$\boldsymbol{S} = \frac{1}{2} \left(\nabla \boldsymbol{U} + (\nabla \boldsymbol{U})^T \right) \tag{13}$$

ja $\boldsymbol{W}$ on pyörteisyystensori:

$$\boldsymbol{W} = \frac{1}{2} \left(\nabla \boldsymbol{U} - (\nabla \boldsymbol{U})^T \right). \tag{14}$$

Reynoldsin jännitysten yhtälössä esiintyvä turbulenssin kineettisen energian dissipaatio lasketaan samasta yhtälöstä kuin k-ε-mallin tapauksessa eli yhtälöstä (7).

LRR, QI ja SSG Reynoldsin jännitys -mallit eroavat toisistaan painevenymänopeustermin osalta, mikä näkyy eroina mallien vakioissa. Vakiot on esitetty taulukossa 1.

Taulukko 1: Vakiot.

	c_s	$C_{\varepsilon 1}$	$C_{\varepsilon 2}$	C_{s1}	C_{s2}	C_{r1}	C_{r2}	C_{r3}	C_{r4}	C_{r5}
LRR	0,22	1,45	1,9	1,8	0,0	0,0	0,8	0,0	0,6	0,6
QI	0,22	1,45	1,9	1,8	0,0	0,0	0,8	0,0	0,6	0,6
SSG	0,22	1,45	1,83	1,7	−1,05	0,9	0,8	0,65	0,625	0,2

2.3 SMC-ω ja BSL Reynoldsin jännitys -mallit

SMC-ω (Second Moment Closure) ja BSL (BaSeLine) jännitysmalleissa [19] Reynoldsin jännitysten siirtoyhtälö on

$$\nabla \cdot (\boldsymbol{U} \otimes \overline{\boldsymbol{u} \otimes \boldsymbol{u}}) = -\boldsymbol{P} - \boldsymbol{\phi} + \nabla \cdot \left[\left(\nu + \frac{\nu_t}{\sigma^*} \right) \nabla \overline{\boldsymbol{u} \otimes \boldsymbol{u}} \right] + \frac{2}{3} I \beta' \omega k. \tag{15}$$

SMC-ω Reynoldsin jännitys -malli käyttää ominaisdissipaation yhtälönä yhtälöä

$$\nabla \cdot (\boldsymbol{U}\omega) = \nabla \cdot \left[\left(\nu + \frac{\nu_t}{\sigma} \right) \nabla \omega \right] + \alpha \frac{\omega}{k} P_k - \beta \omega^2. \tag{16}$$

Mallissa käytetään vakioille seuraavia arvoja:

$$\sigma = 2;\ \sigma^* = 2;\ \alpha = 5/9;\ \beta = 0{,}075.$$

BSL Reynoldsin jännitys -mallin ω-yhtälö on

$$\nabla \cdot (\boldsymbol{U}\omega) = \nabla \cdot \left[\left(\nu + \frac{\nu_t}{\sigma_3} \right) \nabla \omega \right] + \alpha_3 \frac{\omega}{k} P_k - \beta_3 \omega^2 + (1 - F_1) \frac{2}{\sigma_3 \omega} \nabla k \nabla \omega, \tag{17}$$

missä esimerkiksi vakio α_3 lasketaan kaavalla

$$\alpha_3 = F \alpha_1 + (1 - F) \alpha_2. \tag{18}$$

Sekoitusfunktio $F = \tanh(\arg^4)$, missä

$$\arg = \min \left[\max \left(\frac{\sqrt{k}}{\beta' \omega y}, \frac{500\nu}{y^2 \omega} \right), \frac{4\rho k}{\mathrm{CD}_{k\omega} \sigma_{k-\varepsilon} y^2} \right], \tag{19}$$

missä

$$\mathrm{CD}_{k\omega} = \max \left(2\rho \frac{1}{\sigma_{k-\varepsilon} \omega} \nabla k \nabla \omega, 10^{-10} \right).$$

Mallissa käytetään vakioille seuraavia arvoja:

$$\alpha_1 = 0{,}553;\ \alpha_2 = 0{,}44;\ \beta_1 = 0{,}075;\ \beta_2 = 0{,}0828;\ \sigma_1 = 2;\ \sigma_2 = 0{,}856.$$

Sekä SMC-ω että BSL Reynoldsin jännitys -mallissa käytettävä painevenymänopeustensori $\boldsymbol{\phi}$ saadaan kaavasta

$$\boldsymbol{\phi} = \beta' C_1 \omega \left(\overline{\boldsymbol{u} \otimes \boldsymbol{u}} + \frac{2}{3} k I \right) - \hat{\alpha} \left(\boldsymbol{P} - \frac{2}{3} P I \right) - \hat{\beta} \left(\boldsymbol{D} - \frac{2}{3} P I \right) - \hat{\gamma} k \left(\boldsymbol{S} - \frac{1}{3} \mathrm{trace}(\boldsymbol{S}) I \right), \tag{20}$$

missä $P = \mathrm{trace}(\boldsymbol{P})/2$ ja

$$\boldsymbol{D} = \overline{\boldsymbol{u} \otimes \boldsymbol{u}} (\nabla \boldsymbol{U}) + (\nabla \boldsymbol{U})^T \overline{\boldsymbol{u} \otimes \boldsymbol{u}}. \tag{21}$$

Vakioille käytetään seuraavia arvoja:

$$\beta' = 0{,}09;\ \hat{\alpha} = (8 + C_2)/11;\ \hat{\beta} = (8C_2 - 2)/11;\ \hat{\gamma} = (60C_2 - 4)/55;\ C_1 = 1{,}8;\ C_2 = 0{,}52.$$

2.4 Seinän lähialueen laskenta

Turbulenssimalleissa jotka perustuvat ω-yhtälöön, käytetään ns. automaattista seinämäkäsittelyä. Muiden mallien yhteydessä seinämäkäsittely tehdään ns. skaalautuvilla seinämäfunktioilla.

2.4.1 Skaalautuvat seinämäfunktiot

Skaalautuvia seinämäfunktioita käytettäessä leikkausjännitys seinällä

$$\tau_{\mathrm{w}} = \rho u^* u_\tau, \tag{22}$$

missä dimensioton nopeus

$$u^* = C_\mu^{1/4} k^{1/2} \tag{23}$$

ja leikkausnopeus

$$u_\tau = \frac{U_t}{\frac{1}{\kappa}\ln(y^*) + C}, \tag{24}$$

missä κ ja C ovat vakioita. Dimensiotonta etäisyyttä y^* laskettaessa käytetään rajoitinta, joka estää arvon ottamisen liian läheltä seinää:

$$y^* = \max\left[(u^* \Delta y)/\nu; 11{,}06\right], \tag{25}$$

missä Δy on etäisyys seinältä. Etäisyytenä seinästä käytetään arvoa $\Delta y = \Delta n/4$, missä Δn on ensimmäisen ja toisen hilapisteen välinen etäisyys.

2.4.2 Automaattinen seinämäkäsittely

ω-yhtälöön perustuvissa turbulenssimalleissa käytetään tässä työssä ns. automaattista seinämäkäsittelyä, jossa virtauskenttä ratkaistaan seinälle asti, mikäli laskentaverkko on riittävän tiheä.

Liikemääräyhtälössä oleva vuo kirjoitetaan muotoon

$$F_U = -u_\tau u^*, \tag{26}$$

missä

$$u_\tau = \sqrt{\nu \left| \frac{\Delta U}{\Delta y} \right|} \tag{27}$$

ja

$$u^* = \max\left(\sqrt{a_1 k}, u_\tau\right). \tag{28}$$

Kineettisen energian yhtälössä oleva vuo pidetään keinotekoisesti nollana:

$$F_k = 0. \tag{29}$$

Ominaisdissipaation yhtälössä ω:lle on annettu algebrallinen muoto

$$\omega = \omega_s \sqrt{1 + \left(\frac{\omega_\ell}{\omega_s}\right)^2}, \tag{30}$$

joka on sekoitus logaritmisen alueen analyyttisen muodon (dimensioton etäisyys $y^+ = u_\tau y/\nu$)

$$\omega_\ell = \frac{u^*}{a_1 \kappa y} = \frac{1}{a_1 \kappa \nu} \frac{u^{*2}}{y^+} \tag{31}$$

ja laminaarin alakerroksen analyyttisen muodon

$$\omega_s = \frac{6\nu}{\beta(\Delta y)^2} \tag{32}$$

välillä.

2.5 Yhtälöiden numeerinen ratkaisu

Kaikki laskennat on tehty käyttäen kaupallista kontrollitilavuusmenetelmään perustuvaa ohjelmaa Ansys CFX 5.7.1 [19]. Kaikkien termien paikkadiskretointi on tehty käyttäen toista kertalukua olevaa keskeisdifferenssiä lukuun ottamatta konvektiotermejä, joiden diskretointiin on käytetty menetelmää, jota kutsutaan nimellä "High Resolution Scheme". Menetelmässä ensimmäisen kertaluvun ylävirtakaavalla saatuun tulokseen lisätään korjaus ("Numerical Advection Correction"), joka vähentää numeerista diffuusiota. Painenopeuskytkentä on tehty käyttäen perinteistä SIMPLE-menetelmää [20].

Ansys CFX käyttää kytkettyä ratkaisijaa, jossa kaikki hydrodynaamisia suureita (nopeuskomponentit ja paine) hallitsevat yhtälöt ratkaistaan yhtenä yhtälöryhmänä. Muita suureita (mm. turbulenssisuureet) hallitsevat yhtälöt ratkaistaan erikseen hydrodynaamisten suureiden ratkaisun jälkeen. Ansys CFX:n laskenta tehdään aina ajasta riippuvana – myös stationäärisissä tilanteissa kuten tässä työssä.

3 LASKENTA-ALUE JA -VERKKO

Edellä esiteltyjä turbulenssimalleja on verrattu kuvan 1 kolmiulotteisessa askelvirtauksessa. Sisääntulovirtauksen poikkileikkauksen yli laskettu aikakeskiarvonopeuden keskiarvo on U_i.

Laskenta-alueen geometria ja mitat sekä reunaehdot on esitetty kuvassa 2. Mittauksissa [11] on varmistuttu siitä, että sisäänvirtaus on täysin kehittynyt kanavavirtaus askeleen kohdalla, joten laskennassa sisäänvirtausreunaehdot on annettu riittävän kaukana askeleesta. Reunaehdoista aikakeskiarvonopeus on sama kuin mittauksissa, hydraulinen halkaisija on laskettu kanavan mitoista ja turbulenssin intensiteetti, I, on laskettu käyttäen kaavaa $I = 0{,}16\mathrm{Re}_D^{-1/8}$. Virtauksen hydrauliseen halkaisijaan perustuva Reynoldsin luku on $\mathrm{Re}_D \approx 51\,600$ askeleen korkeuteen perustuvan Reynoldsin luvun ollessa $\mathrm{Re}_h \approx 11\,000$.

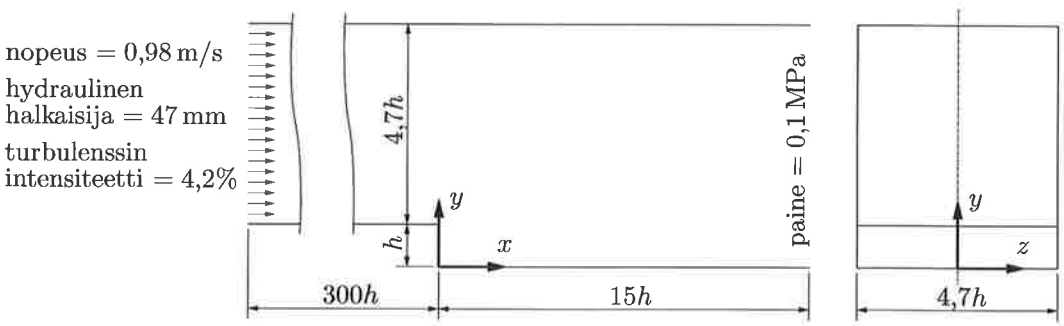

Kuva 2: Laskenta-alue ($h = 10\,\mathrm{mm}$), reunaehdot ja koordinaatisto.

Virtausaineena on vesi, jonka tiheydelle ja dynaamiselle viskositeetille on käytetty laskentaohjelman oletusarvoja eli $\rho = 997{,}0\,\mathrm{kg/m^3}$ ja $\mu = 0{,}8899 \times 10^{-3}\,\mathrm{kg/ms}$.

Laskentaan on käytetty kuvassa 3 esitettyä noin 1,7 miljoonaa kontrollitilavuutta sisältävää laskentaverkkoa. Virtaustilanteen symmetria on käytetty hyväksi ja kanavasta on laskettu vain puolet. Laskentaverkkoa on tihennetty seiniä kohti siten, että rajakerroksissa ensimmäisen kontrollitilavuuden korkeus on 0,04 mm. Mittauksissa leikkausnopeudeksi on saatu $u_\tau = 0{,}051\,\mathrm{m/s}$. Tällöin saadaan ensimmäisen kontrollitilavuuden dimensiottoman etäisyyden arvioksi $y^+ = 1$. Laskentaverkkoriippumattomuutta on tarkasteltu lähteessä [21].

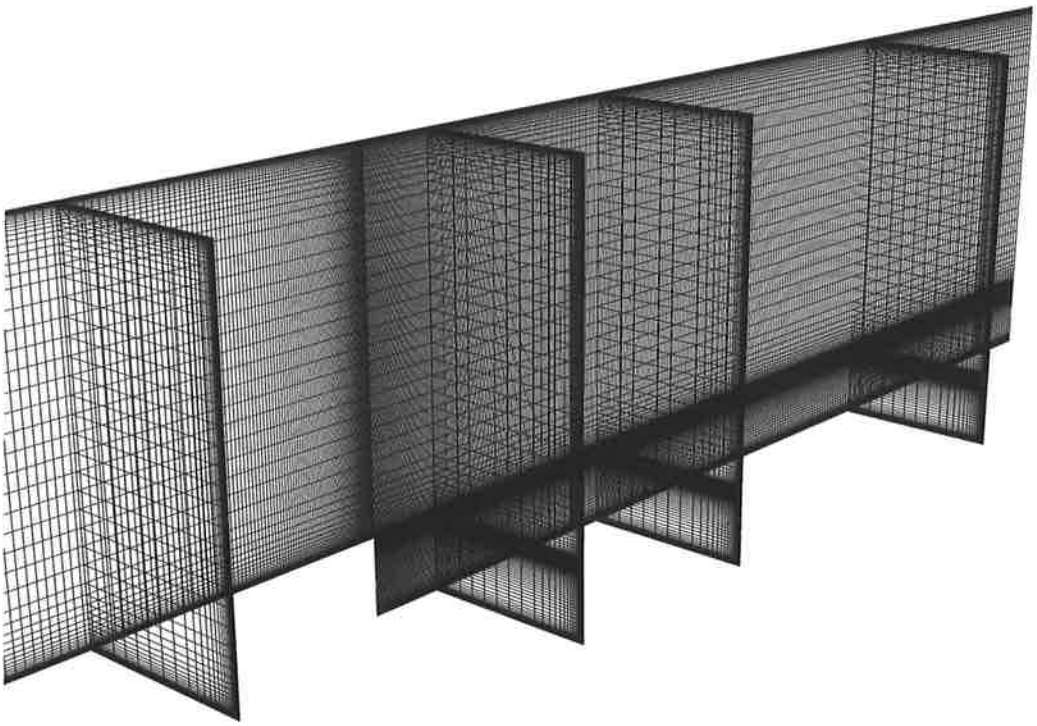

Kuva 3: Laskentaverkko tasoilla $x/h = -4$, $x/h = 1$, $x/h = 4$, $x/h = 10$ ja symmetriatasolla. Jäljempänä esitetyt tulokset on esitetty näiden tasojen leikkaussuorilla.

4 TULOKSET

Kuvassa 4 on esitetty suoralta $x = -5h$, $y = 1{,}1h$ lähteviä virtaviivoja käytettäessä k-ε-mallia. Lasketun puolen tulokset on kuvassa peilattu myös symmetriatason toiselle puolelle. Virtaviivoista näkyy selvästi tilanteen kolmiulotteisuus, eli kuinka askeleen yläpinnalta lähtevät virtaviivat supistuva askeleen alavirran puolella lähelle symmetriatasoa. Kuvasta näkyy myös kuinka irtoamiskupla on symmetriatasolla pidempi kuin sivuseinien läheisyydessä.

Laskettu sinsäänvirtausnopeusprofiili on selvästi tulppamaisempi kaikilla käytetyillä turbulenssimalleilla kuin mitattu profiili (kuva 5). Sama tulppamaisuus jatkuu myös askeleen jälkeen irtaomiskuplan yläpuolella. k-ε-mallin antamien nopeusprofiilien maksimikohdat ovat takaisinvirtausalueella liian lähellä seinää lähellä askelta, kohdalla $x/h = 1$. Reynoldsin jännitys -mallien tulokset ovat varsin lähellä toisiaan ja mittauksia lukuun ottamatta SSG Reynoldsin jännitys -mallia, jonka takaisinvirtaus on voimakkaampi. SSG RSM:n ennustama nopeus lähellä seinää kohdalla $x/h = 10$ on selvästi muita malleja pienempi. Kyseinen

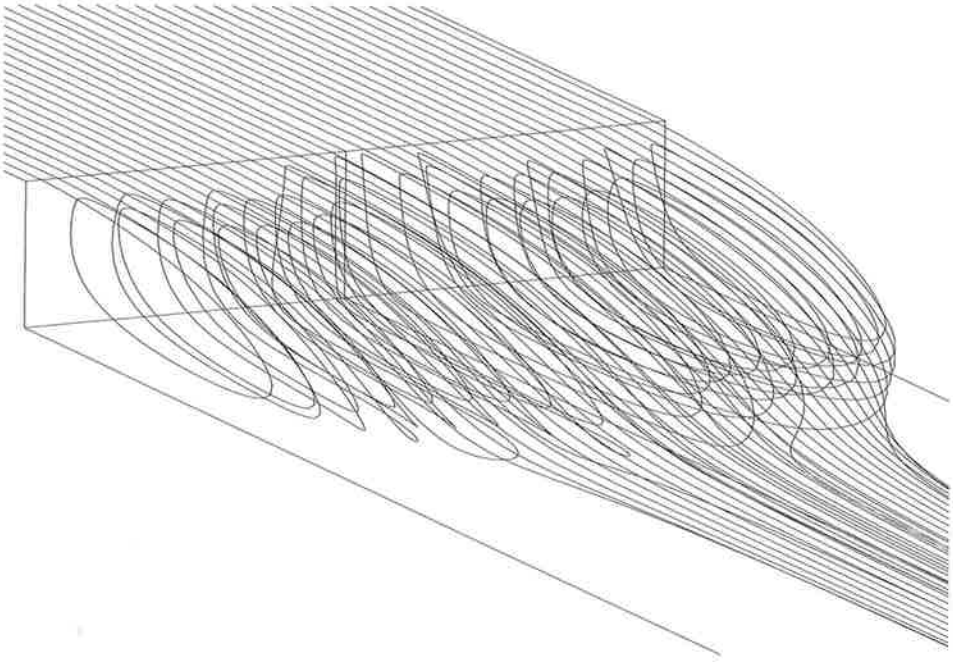

Kuva 4: Suoralta $x = -5h$, $y = 1{,}1h$ lähteviä virtaviivoja käytettäessä k-ε-mallia.

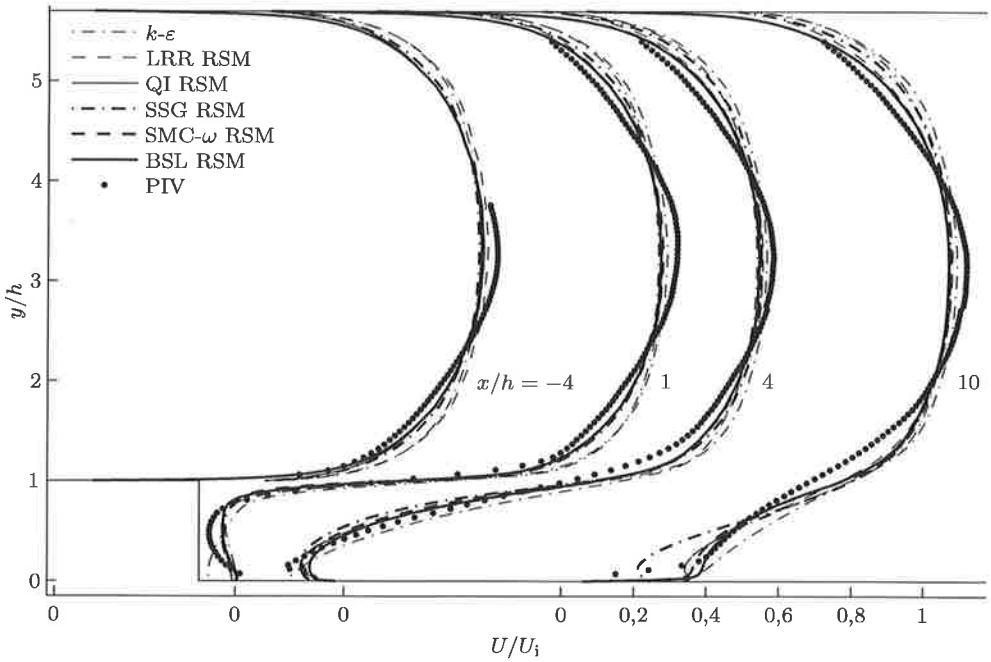

Kuva 5: x-akselin suuntainen aikakeskiarvonopeus.

malli näyttääkin ennustavan irtoamiskuplan pidemmäksi kuin muut mallit.

Reynoldsin normaali- ja leikkausjännitysten osalta tulokset on esitetty kuvissa 6, 7 ja 8. Kohdalla $x/h = 1$ lasketut x-akselin suuntaiset Reynoldsin normaalijännitykset ovat selvästi mitattuja pienemmät ollen kaikilla malleilla vain noin puolet mitatuista arvoista. Irtoamiskuplan jälkeen, kohdalla $x/h = 10$, laskettujen Reynoldsin jännitysten maksimikohta on liian lähellä seinää. Lisäksi kohdalla $x/h = 4$ näkyy SSG Reynoldsin jännitys -mallin tuloksissa selvä poikkeama mittaustuloksista. Testattujen turbulenssimallien erot näkyvät selvimmin pystysuuntaisessa Reynoldsin normaalijännityksessä ja Reynoldsin leikkausjännityksessä irtoamiskuplan alueella molempien maksimiarvojen ollessa k-ε-mallia käytettäessä yli kaksinkertaiset verrattuna mittauksiin. Tämä johtuu kaksiyhtälömallin kyvyttömyydestä ottaa oikein huomioon turbulenssin anisotropia. Kaikki tässä työssä käytetyt Reynoldsin jännitys -mallit SSG-mallia lukuun ottamatta ennustavat arvot lähes oikein. SSG-mallin tuloksissa näkyy sama anomalia kuin vaakasuuntaisissa normaalijännityksissä; kyseinen malli ennustaa pystysuuntaisen Reynoldsin normaalijännityksen ja Reynoldsin leikkausjännityksen liian pieniksi.

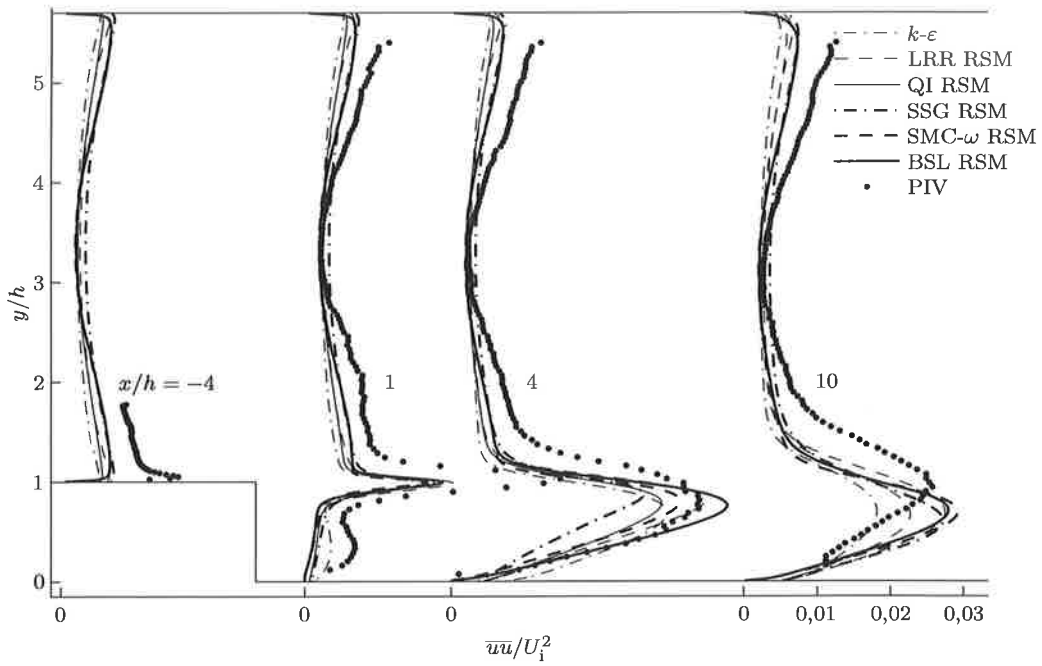

Kuva 6: x-akselin suuntainen Reynoldsin normaalijännitys.

Kuten johdannossa mainittiin, käytetään askelvirtauksen irtoamiskuplan kiinnittymiskohdan etäisyyttä askeleesta usein turbulenssimallin hyvyyden mittarina. Taulukossa 2 on esitetty kiinnittymiskohtien etäisyydet symmetriatasolla kaikilla lasketuilla turbulenssimalleilla. Laskentatulosten osalta kiinnittymiskohta on tässä määritelty leikkausjännityksen suunnan muuttumiskohtana symmetriatasolla. Mittausartikkelissa [11] kiinnittymiskohta on määritelty hieman toisin, mutta mittaustulos on mittaustarkkuuden rajoissa sama $5{,}3h$ määriteltiinpä kiinnittymiskohta kummalla tavalla hyvänsä.

Kiinnittymiskohdan osalta k-ε-malli antaa – yhdessä QI RSM:n kanssa – parhaat tulokset. Tätä voidaan kuitenkin pitää osittain sattumana, koska irtoamiskuplan virtauskentän

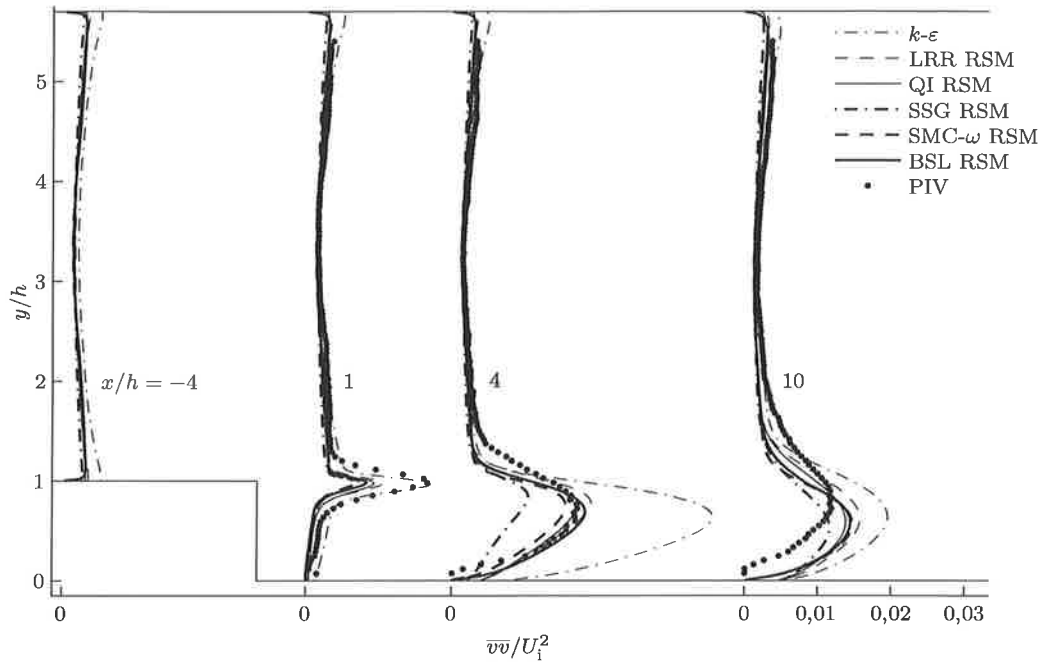

Kuva 7: y-akselin suuntainen Reynoldsin normaalijännitys.

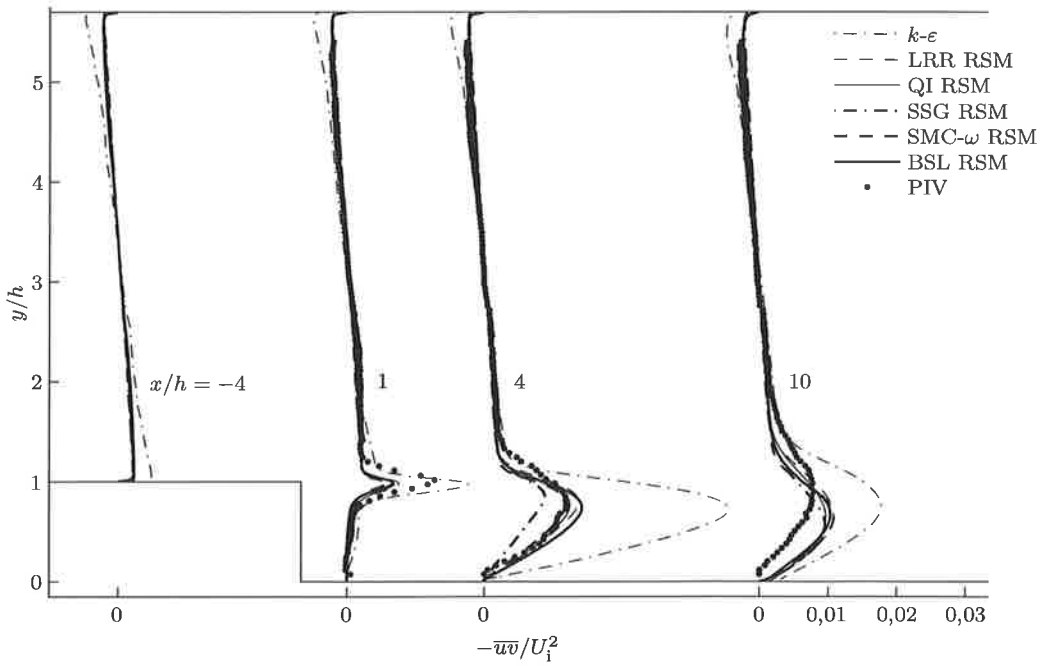

Kuva 8: Reynoldsin leikkausjännitys.

Taulukko 2: Kiinnittymiskohtien etäisyydet askeleesta symmetriatasolla.

Malli	Etäisyys
k-ε	$5{,}40h$
LRR RSM	$6{,}50h$
QI RSM	$5{,}10h$
SSG RSM	$6{,}55h$
SMC-ω RSM	$6{,}25h$
BSL RSM	$5{,}70h$
PIV[11]	$5{,}3h$

tuloksista – varsinkin Reynoldsin jännitysten osalta – voidaan päätellä k-ε-mallin toimivan väärin. Tämä johtuu kaksiyhtälömallien kyvyttömyydestä mallintaa kaareutuvaa virtauskenttää ja siinä ilmenevää epäisotrooppista turbulenssia oikein. SSG RSM:n tulokset poikkeavat kiinnittymiskohdankin osalta muiden Reynoldsin jännitys -mallien tuloksista. Tämä johtuu kyseisen mallin liian pienistä Reynoldsin jännityksistä, mikä pidentää irtoamiskuplaa.

5 JOHTOPÄÄTÖKSET

Jo pelkän neliökanavan simulointi antaa mittauksista eroavia tuloksia kaikkien turbulenssimallien antaman nopeusprofiilin ollessa liian tulppamainen. Testattujen turbulenssimallien erot näkyvät selvimmin pystysuuntaisessa Reynoldsin normaalijännityksessä ja Reynoldsin leikkausjännityksessä irtoamiskuplan alueella molempien maksimiarvojen ollessa k-ε-mallia käytettäessä yli kaksinkertaiset verrattuna mittauksiin kaikkien tässä työssä käytettyjen Reynoldsin jännitys -mallien – SSG-mallia lukuun ottamatta – ennustaessa arvot lähes oikein. k-ε-malli ennustaa tästä huolimatta askelvirtaukseen syntyvän irtoamiskuplan kiinnittymiskohdan parhaiten. Reynoldsin jännitys -mallien tulokset ovat lähellä mittaustuloksia ja toisiaan lukuun ottamatta SSG Reynoldsin jännitys -mallia, jonka tuloksissa on epäfysikaalista anomaliaa.

Irtoavan ja voimakkaasti kaareutuvan virtauksen mallintaminen vaatii selvästi Reynoldsin jännitysten oikeaa mallintamista ja kaksiyhtälömalleihin sisältyvästä Reynoldsin jännitysten ja venymänopuksien lineaarisesta korrelaatiosta luopumista.

VIITTEET

[1] S. Thangam ja C. G. Speziale. *Turbulent separated flow past a backward-facing step: A critical evaluation of two-equation turbulence models.* Raportti ICASE Report 91-23, Institute for Computer Applications in Science and Engineering, NASA Langley Research Center, Hampton, Virginia, 1991.

[2] B. E. Launder. *Second-moment closure: Present... and future?.* International Journal of Heat and Fluid Flow, **10**, 282-300 (1989).

[3] H. Le, P. Moin ja J. Kim. *Direct numerical simulation of turbulent flow over a backward-facing step.* Journal of Fluids Mechanics, **330**, 349-374 (1997).

[4] H.-J. Kaltenbach ja G. Janke. *Direct numerical simulation of flow separation behind a swept, rearward-facing step at* $Re_H = 3000$. Physics of Fluids, **12**, 2320-2337 (2000).

[5] D. M. Driver ja H. L. Seegmiller. *Features of a reattaching turbulent shear layer in divergent channel flow.* AIAA Journal, **23**, 163-171 (1985).

[6] E. W. Adams ja J. P. Johnston. *Effects of the separating shear layer on the reattachment flow structure part 1: Pressure and turbulence quantities*. Experiments in Fluids, **6**, 400-408 (1988).

[7] E. W. Adams ja J. P. Johnston. *Effects of the separating shear layer on the reattachment flow structure part 2: Reattachment length and wall shear stress*. Experiments in Fluids, **6**, 493-499 (1988).

[8] J. G. Berbee ja J. L. Ellzey. *The effect of aspect ratio on the flow over a rearward-facing step*. Experiments in Fluids, **7**, 447-452 (1989).

[9] S. Jovic ja D. M. Driver. *Backward-facing step measurements at low Reynolds number, $Re_h = 5000$*. Raportti TM-108807, NASA, Moffett Field, California, 1994.

[10] S. Jovic. *An experimental study of a separated/reattached flow behind a backward-facing step. $Re_h = 37{,}000$*. Raportti TM-110384, NASA, Moffett Field, California, 1996.

[11] M. Piirto, A. Karvinen, H. Ahlstedt, P. Saarenrinne ja R. Karvinen. *PIV measurements in square backward-facing step*. Jounal of Fluids Engineering, **129**, 984-990 (2007).

[12] J. K. Eaton ja J. P. Johnston. *A review of research on subsonic turbulent flow reattachment*. AIAA Journal, **19**, 1093-1100 (1981).

[13] V. de Brederode ja P. Bradshaw. *Three-dimensional flow in nominally two-dimensional separation bubbles*. Raportti Aero Report 72-19, Imperical College of Science and Technology, 1972.

[14] J. O. Hinze. *Turbulence*. McGraw-Hill, New York, 1975.

[15] W. P. Jones ja B. E. Launder. *The prediction of laminarization with a two-equation model of turbulence*. International Journal of Heat and Mass Transfer, **15**, 301-314 (1972).

[16] B. E. Launder ja B. I. Sharma. *Application of the energy dissipation model of turbulence to the calculation of flow near a spinning disc*. Letters in Heat and Mass Transfer, **1**, 131-138 (1974).

[17] B. E. Launder, G. J. Reece ja W. Rodi. *Progress in the development of a Reynolds-stress turbulence closure*. Journal of Fluid Mechanics, **68**, 537-566 (1975).

[18] C. G. Speziale, S. Sarkar ja T. B. Gatski. *Modelling the pressure-strain correlation of turbulence: An invariant dynamical system approach*. Journal of Fluid Mechanics, **277**, 245-272 (1991).

[19] Ansys Inc. *CFX 5.7.1 Manual*, 2004.

[20] S. V. Patankar. *Numerical Heat Transfer and Fluid Flow*. Hemisphere, Washington D.C., 1980.

[21] A. Karvinen ja H. Ahlstedt. *Turbulenssimallit askelvirtauksen mallinnuksessa*. Raportti 185, Tamperen teknillinen yliopisto, Energia- ja prosessitekniikan laitos, 2006.

MODEL REDUCTION OF STEADY FLUID-STRUCTURE INTERACTION PROBLEMS WITH FREE-FORM DEFORMATIONS AND REDUCED BASIS METHODS

T. LASSILA[1], G. ROZZA[2]

[1]Institute of Mathematics
Helsinki University of Technology
P.O. Box 1100, FI-02015 TKK, Finland
e-mail: toni.lassila@tkk.fi

[2]Modelling and Scientific Computing
Institute of Analysis and Scientific Computing
École Fédérale Polytechnique de Lausanne
Station 8, EPFL, CH-1015 Lausanne, Switzerland
e-mail: gianluigi.rozza@epfl.ch

ABSTRACT

We propose a two-fold approach to model reduction of fluid-structure interaction. The state equations for the fluid are solved with reduced basis methods. These are model reduction methods for parametric partial differential equations using well-chosen snapshot solutions in order to build a set of global basis functions. The other reduction is in terms of the geometric complexity of the moving fluid-structure interface. We use free-form deformations to parameterize the perturbation of the flow channel at rest configuration. As a computational example we consider a steady fluid-structure interaction problem: an incompressible Stokes flow in a channel that has a flexible wall.

1 INTRODUCTION

Many problems in fields such as aerodynamic and cardiovascular modelling can be expressed as fluid-structure interaction (FSI) problems. The mathematical modelling of such coupled problems consists of four main parts: solution of the fluid equations given the current fluid geometry, solution of the structural displacements given the normal stresses exerted by the fluid, fulfillment of coupling constraints to achieve force balance across the interface, and transport of the fluid-structure interface

Even when both the fluid and structure equations are independently linear, the geometric variability of the fluid-structure interface can cause a significant nonlinearity in the coupled system. Solution methods for fluid-structure interaction problems are iterative in nature and involve the repeated solution of the fluid and structure equations in many different configurations.

A modal reduction of the structural equations was adopted in [11] to reduce the complexity of an FSI problem involving pulsatile flow in a channel, but no reduction to the complexity of solving the fluid equations was made. Another work by the same author is

[10], where the steady problem was parameterized using shape functions for the boundary trace of the pressure obtained from an assumption of near-Poiseuille flow profile. The strong coupling of normal stresses on the interface was treated in the reduced space obtained by considering only the leading structural eigenmodes, and solved as a least-squares optimization problem.

Another approach are the Reduced Basis (RB) methods, which work on parametric partial (and ordinary) differential equations. They are based on a greedy sampling algorithm that chooses snapshot solutions of the parametric PDE at different parameter values for constructing a global approximation basis. For an introduction, see [13] and [19]. The reduction of steady incompressible Stokes flow (without FSI) in an arterial bypass configuration by parameterization with piecewise affine maps was considered in [20]. The same problem parameterized with nonaffine maps was considered in [18] for Stokes equations and in [14] for Navier-Stokes equations. We also mention the reduced basis element method proposed for Stokes flows in [8] that aims to reduce flow computations in complex flow networks with multiple branches and junctions. A posteriori error estimation for Navier-Stokes equations solved by reduced basis methods is considered in [2, 23]

2 PROBLEM OF STEADY STOKES FLOW IN A FLEXIBLE CHANNEL

Let $\Omega_0 \subset \mathbb{R}^2$ be a bounded domain with piecewise smooth boundary that represents the fluid domain at rest configuration (without deformations induced by the fluid flow). We denote the flexible part of the boundary as $\Sigma_0 \subset \partial\Omega_0$. To simplify things, we assume the geometry displayed in Fig. 1 – a straight 2-d tube, where the displacement of the flexible part of the upper wall is described with a C^2 function $\eta : [a, b] \to \mathbb{R}$ with $\eta(a) = \eta(b) = \eta'(a) = \eta'(b) = 0$. The tube is at rest configuration when $\eta \equiv 0$. We denote by $\Omega(\eta)$ the deformed domain. In this domain we have the incompressible steady Stokes problem to find $\boldsymbol{u} \in H^1(\Omega(\eta)) \times H^1(\Omega(\eta))$ and $p \in L^2(\Omega(\eta))$ s.t.

$$\begin{cases} -\nu \triangle \boldsymbol{u} + \nabla p = \boldsymbol{f}^F, & \text{in } \Omega(\eta) \\ \nabla \cdot \boldsymbol{u} = 0, & \text{in } \Omega(\eta) \\ \boldsymbol{u} = \boldsymbol{u}_0 \text{ on } \partial\Omega(\eta) \setminus \Sigma(\eta), \quad \boldsymbol{u} = \boldsymbol{0} & \text{on } \Sigma(\eta) \end{cases} \tag{1}$$

where ν is the viscosity, and $\boldsymbol{f}^F$ is the volume force acting on the fluid. The Dirichlet data are assumed to satisfy a conservation principle

$$\int_{\partial\Omega(\eta)} \boldsymbol{u}_0 \cdot \boldsymbol{n} \, d\Gamma = 0, \tag{2}$$

which together with the incompressibility condition implies volume conservation of the fluid.

Following [22], after a suitable assumption of small structural displacement the flexible section of the wall is modelled using a 1-d elliptic equation ("elastic membrane") to find the displacement $\eta \in H_0^1(\Sigma_0)$ s.t.

$$\int_{\Sigma_0} K(\boldsymbol{x}) \eta' \phi' \, d\Gamma = \int_{\Sigma_0} \tau(\boldsymbol{u}, p) \phi \, d\Gamma, \quad \forall \, \phi \in H^1(\Sigma_0) \tag{3}$$

where $\tau(\boldsymbol{u}, p)$ is the normal traction on the interface imposed by the fluid

$$\tau(\boldsymbol{u}, p) = \left[p\boldsymbol{n} - \nu \left(\nabla \boldsymbol{u} + \nabla \boldsymbol{u}^T \right) \cdot \boldsymbol{n} \right]^T \begin{bmatrix} 0 \\ 1 \end{bmatrix} \tag{4}$$

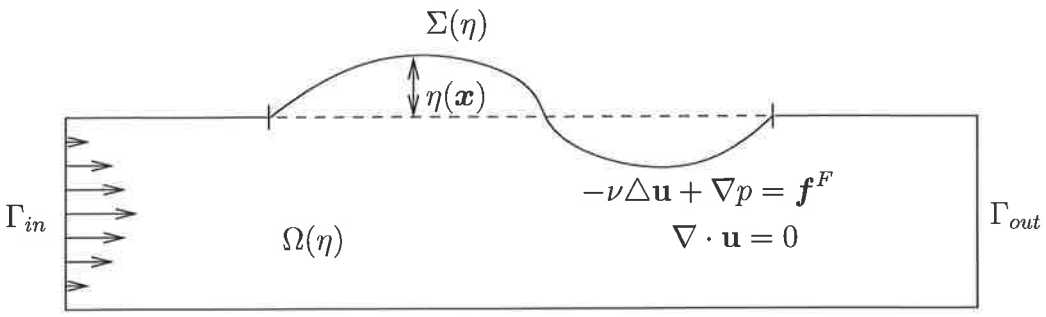

Figure 1: Stokes flow in a channel with a flexible wall section

obtained from the solution $(\boldsymbol{u}, p)$ of the fluid equation (1), and $K(\boldsymbol{x}) \geq K_0 > 0$ is the spring constant of the wall to displacements in the normal direction. It was shown in [10] that the incompressibility and conservation condition (2) together mean that the stress on the interface is a function of boundary trace of the pressure alone, $\tau = p|_{\Sigma(\eta)}$. It also follows that the boundary trace of pressure fulfills a zero-average property

$$\int_{\Sigma(\eta)} p \, d\Gamma = 0, \tag{5}$$

which fixes the pressure uniquely.

The coupled fluid-structure problem can be considered to be of the form

$$\begin{bmatrix} -\nu\triangle & \nabla & 0 \\ \text{div} & 0 & 0 \\ 0 & 0 & -K\triangle \end{bmatrix} \begin{bmatrix} \boldsymbol{u} \\ p \\ \eta \end{bmatrix} = \begin{bmatrix} \boldsymbol{f}^F \\ 0 \\ \tau(p) \end{bmatrix}. \tag{6}$$

Because the fluid domain depends on the domain defined by the function η, this is in fact a nonlinear free-boundary problem. Existence of solutions for the more general case of Navier-Stokes equations for the fluid and linear elasticity equations for the solid was shown in [5].

3 PARAMETERIZATION WITH FREE-FORM DEFORMATIONS

To reduce the complexity of the free-boundary problem (6) we introduce a parameterization of the fluid domain, $\Omega(\boldsymbol{\mu})$, where the parameters $\boldsymbol{\mu} \in \mathcal{D}$ belong in some low-dimensional parameter space. The problem (6) is then solved (approximately) in the space of the parameters instead of directly working with the mesh points of the discretized fluid domain. One option to construct $\Omega(\boldsymbol{\mu})$ would be to use a family of parametric curves, such as B-splines, to directly parameterize the displacement function η. We prefer to use *free-form deformations* [7, 21].

Free-form deformations are a technique of obtaining small, parametric deformations of an arbitrary reference domain $\Omega_0 \subset \mathbb{R}^d$ for $d = 2, 3$. First we map the reference domain to a subset of the unit square with a continuous invertible map $\Psi : \Omega_0 \to [0,1] \times [0,1]$ and then embed it in a regular grid of control points $\boldsymbol{P}^0_{\ell,m}$ where $\ell = 0, \ldots, L$ and $m = 0, \ldots, M$ so that

$$\boldsymbol{P}^0_{\ell,m} = \begin{bmatrix} \ell/L \\ m/M \end{bmatrix}. \tag{7}$$

The parameterization is obtained by allowing the control points to move and then using a spline basis to construct a smooth deformation map as a function of the positions of the

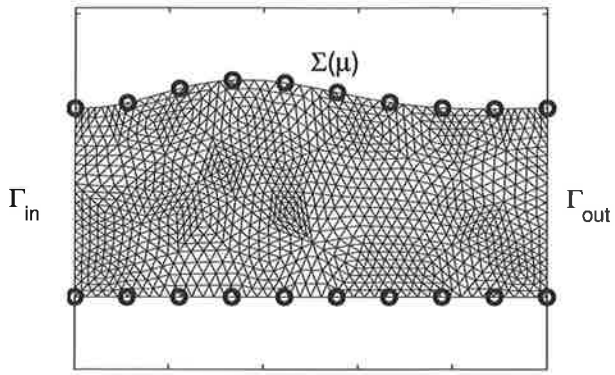

Figure 2: Free-form deformation of the flexible channel with six parameters.

control points. The perturbed control points are given by a set of $(L+1)(M+1)$ parameter vectors $\boldsymbol{\mu}_{\ell,m}$. For each $\boldsymbol{\mu}$ a parametric domain map $T : D_0 \to D(\boldsymbol{\mu})$ is defined as

$$T(\boldsymbol{x};\boldsymbol{\mu}) = \Psi^{-1}\left(\sum_{\ell=0}^{L}\sum_{m=0}^{M} b_{\ell,m}^{L,M}(\Psi(\boldsymbol{x}))\left(\boldsymbol{P}_{\ell,m} + \boldsymbol{\mu}_{\ell,m}\right)\right), \tag{8}$$

where

$$b_{\ell,m}^{L,M}(s,t) = \binom{L}{\ell}\binom{M}{m}(1-s)^{(L-\ell)}s^{\ell}(1-t)^{(M-m)}t^{m}$$

are tensor products of the 1-d Bernstein basis polynomials

$$b_{\ell}^{L}(s) = \binom{L}{\ell}(1-s)^{(L-\ell)}s^{\ell}, \quad b_{m}^{M}(t) = \binom{M}{m}(1-t)^{(M-m)}t^{m}$$

defined on the unit square with local variables $(s,t) \in [0,1] \times [0,1]$. It is typical that only some of the control points are allowed to move freely, we do not use the full parameterization but only a few of the most relevant shape parameters. To parameterize the flow channel we use a 10×2 grid of control points. Six control points in the top row are moving in the x_2-direction, resulting in a smooth parameterized deformation of the channel with 6 real parameters. The result when applied on a sample computational mesh is shown in Fig. 3.

After the parametric domain $\Omega(\boldsymbol{\mu})$ is obtained as the image of a fixed reference domain Ω_0 under a differentiable and invertible map $T : \Omega_0 \times \mathcal{D} \to \Omega(\boldsymbol{\mu})$, we proceed to transform the PDE on a parametric domain to a parametric PDE on the fixed reference domain. Denoting by $J_T := \nabla_{\boldsymbol{x}} T$ the Jacobian matrix of T we define the parametric transformation tensors for the viscous term

$$\nu_T := J_T^{-T} J_T^{-1} \det(J_T) \tag{9}$$

and the pressure-divergence term

$$\chi_T := J_T^{-1} \det(J_T) \tag{10}$$

respectively and obtain the weak form of the *parametric Stokes equations* on a fixed reference

domain: find $\boldsymbol{u} \in H^1(\Omega_0) \times H^1(\Omega_0) \times \mathcal{D}$ and $p \in L^2(\Omega_0) \times \mathcal{D}$ s.t.

$$\begin{cases} \displaystyle\int_{\Omega_0} \left(\nu \frac{\partial u_k}{\partial x_i} [\nu_T]_{i,j} \frac{\partial v_k}{\partial x_j} + p\, [\chi_T]_{k,j} \frac{\partial v_k}{\partial x_j} \right) d\Omega_0 = \int_{\Omega_0} \det(J_T) [f^F]_k \, d\Omega_0, \\ \qquad\qquad \forall\, \boldsymbol{v} \in H_0^1(\Omega_0) \times H_0^1(\Omega_0) \\ \displaystyle\int_{\Omega_0} q\, [\chi_T]_{k,j} \frac{\partial u_k}{\partial x_j} \, d\Omega_0 = 0, \\ \qquad\qquad \forall\, q \in L^2(\Omega_0) \end{cases} \tag{11}$$

with summation understood over the indices $i = 1, 2$ and $j = 1, 2$.

4 PARAMETRIC FLUID-STRUCTURE COUPLING ALGORITHM

We can alternatively formulate the fluid-structure problem (6) as a calculus of variations problem to find $\eta \in C_0^2([a, b])$ the minimizer of

$$\min_{\eta} \quad \tfrac{1}{2} \int_{\Sigma_0} |K \triangle \eta + \tau(\boldsymbol{u}, p)|^2 \, d\Gamma, \tag{12}$$

$$\text{s.t.} \quad \begin{cases} -\nu \triangle \boldsymbol{u} + \nabla p = \boldsymbol{f}^F & \text{in } \Omega(\eta) \\ \nabla \cdot \boldsymbol{u} = 0 & \text{in } \Omega(\eta) \\ \displaystyle\int_{\Sigma(\eta)} p \, d\Gamma = 0 \end{cases}$$

If a solution of (6) exists then it is also a minimizer of (12). Problem (12) in the parametric form given by (11) is still valid: find $\boldsymbol{\mu} \in \mathcal{D}$ s.t.

$$\min_{\boldsymbol{\mu}} \quad \tfrac{1}{2} \int_{\Sigma_0} |K \triangle \eta + \tau(\boldsymbol{u}, p)|^2 \, d\Gamma, \tag{13}$$

$$\text{s.t.} \quad \begin{cases} -\nu \triangle \boldsymbol{u} + \nabla p = \boldsymbol{f}^F & \text{in } \Omega(\boldsymbol{\mu}) \\ \nabla \cdot \boldsymbol{u} = 0 & \text{in } \Omega(\boldsymbol{\mu}) \\ \displaystyle\int_{\Sigma(\boldsymbol{\mu})} p \, d\Gamma = 0 \end{cases}$$

but this time we expect that the optimal value of the functional is $J^* > 0$ and the coupling of stresses on the interface between fluid and structure is only achieved in a least-squares sense. The "goodness of fit" depends on the dimension of the parameter space $\mathcal{D}$. We call this the *strong parametric coupling* approach.

It should be noted that we perform a reduction by parameterizing the displacement η of the fluid-structure interface. In [10] the traction τ (which corresponds to the boundary trace of the pressure in this case) was instead parameterized. This alternative approach allowed the author to solve directly a parametric minimization problem of the form (13). Instead, we must consider the minimization problem

$$\min_{\boldsymbol{\mu}} \quad \tfrac{1}{2} \int_{\Sigma_0} |\eta(\boldsymbol{\mu}) - \hat{\eta}|^2 \, d\Gamma, \tag{14}$$

$$\text{s.t.} \quad \begin{cases} -\nu \triangle \boldsymbol{u} + \nabla p = \boldsymbol{f}^F & \text{in } \Omega(\boldsymbol{\mu}) \\ \nabla \cdot \boldsymbol{u} = 0 & \text{in } \Omega(\boldsymbol{\mu}) \\ K \triangle \hat{\eta} + \tau(\boldsymbol{u}, p) = 0 & \text{on } \Sigma(\boldsymbol{\mu}) \\ \displaystyle\int_{\Sigma(\boldsymbol{\mu})} p \, d\Gamma = 0 \end{cases}$$

where $\hat{\eta}$ is an assumed displacement obtained from solving the wall equation for a given traction obtained from the solution of the fluid equations. The reason for this is that, in order to reduce the complexity of the fluid equations, we must be able to transfer the parametric dependence to the Stokes equations. This can be done more easily by parameterizing the displacement rather than the boundary trace of the pressure.

A computational algorithm for the solution of (14) is detailed in Algorithm 1.

Algorithm 1 Strong parametric coupling of fluid and structure

Require: initial guess $\boldsymbol{\mu}^0$

1: Let $k = 0$.
2: **repeat**
3: Solve the reduced fluid equations for $(\boldsymbol{u}^k, p^k)$ in $\Omega(\boldsymbol{\mu}^k)$.
4: Compute assumed traction $\hat{\tau} = p^k|_{\Sigma(\boldsymbol{\mu})}$ from pressure p satisfying (5).
5: Solve the minimization problem

$$\boldsymbol{\mu}^{k+1} := \underset{\boldsymbol{\mu}\in\mathcal{D}}{\operatorname{argmin}} \quad \frac{1}{2}\int_{\Sigma_0} |\eta(\boldsymbol{\mu}) - \hat{\eta}|^2 \, d\Gamma$$

where $\eta(\boldsymbol{\mu})$ is the displacement of the interface given by the parameterization of the geometry and the *assumed displacement* $\hat{\eta} \in H_0^1(\Sigma_0)$ is the solution of

$$\int_{\Sigma_0} K\hat{\eta}'\beta' \, d\Gamma = \int_{\Sigma_0} \hat{\tau}\beta \, d\Gamma \quad \forall\, \beta \in H^1(\Sigma_0)$$

6: Set $k := k + 1$.
7: **until** stopping criteria is met

5 REDUCED BASIS APPROXIMATION OF THE STOKES PROBLEM

The computational efficiency of solving the least squares problem with PDE-constraints (14) hinges on the efficient solution of the fluid equations on the parametric domain $\Omega(\boldsymbol{\mu})$. We present briefly the general approach to reduced basis approximations for the steady Stokes problem. For more details see [17], [18], and [20].

We denote by $\mathcal{Y} := H^1(\Omega_0)\times H^1(\Omega_0)$ the velocity space, $\mathcal{Q} := L^2(\Omega_0)$ the pressure space, and the continuous parametric bilinear forms $\mathcal{A} : \mathcal{Y}\times\mathcal{Y}\times\mathcal{D} \to \mathbb{R}$ and $\mathcal{B} : \mathcal{Q}\times\mathcal{Y}\times\mathcal{D} \to \mathbb{R}$. The weak form (11) of the parametric Stokes equations for velocity and pressure can be written: given any $\boldsymbol{\mu} \in \mathcal{D}$, find $\boldsymbol{u}(\boldsymbol{\mu}) \in \mathcal{Y}$ and $p(\boldsymbol{\mu}) \in \mathcal{Q}$ s.t.

$$\begin{aligned} \mathcal{A}(\boldsymbol{u}, \boldsymbol{v}; \boldsymbol{\mu}) + \mathcal{B}(p, \boldsymbol{v}; \boldsymbol{\mu}) &= \langle \boldsymbol{F}(\boldsymbol{\mu}), \boldsymbol{v}\rangle_{\mathcal{Y}} \qquad \text{for all } \boldsymbol{v} \in \mathcal{Y} \\ \mathcal{B}(q, \boldsymbol{u}(\boldsymbol{\mu})) &= \langle G(\boldsymbol{\mu}), q\rangle_{\mathcal{Q}} \qquad \text{for all } q \in \mathcal{Q}, \end{aligned} \tag{15}$$

where $\boldsymbol{F}(\boldsymbol{\mu}) \in \mathcal{Y}' \times \mathcal{D}$ and $G(\boldsymbol{\mu}) \in \mathcal{Q}' \times \mathcal{D}$ are continuous parametric linear forms. The inhomogeneous Dirichlet condition is treated by introducing an extension of the boundary data $\tilde{\boldsymbol{u}}_0 \in H^1(\Omega_0)$ and looking for a solution $\tilde{\boldsymbol{u}} \in H_0^1(\Omega_0) \times H_0^1(\Omega_0) \times \mathcal{D}$ to (15) with a modified right-hand side $\langle \tilde{\boldsymbol{F}}(\boldsymbol{\mu}), \boldsymbol{v}\rangle_{\mathcal{Y}} := \langle \boldsymbol{F}(\boldsymbol{\mu}), \boldsymbol{v}\rangle_{\mathcal{Y}} - \langle \mathcal{A}(\boldsymbol{\mu})\tilde{\boldsymbol{u}}_0, \boldsymbol{v}\rangle_{\mathcal{Y}}$. The solution is then recovered as $\boldsymbol{u}(\boldsymbol{\mu}) = \tilde{\boldsymbol{u}}(\boldsymbol{\mu}) + \mathcal{A}(\boldsymbol{\mu})\tilde{\boldsymbol{u}}_0$.

Define $\alpha(\boldsymbol{\mu})$ the parameter-dependent coercivity constant of the problem as

$$\alpha(\boldsymbol{\mu}) := \inf_{\boldsymbol{v}\in\mathcal{Y}} \frac{\mathcal{A}(\boldsymbol{v}, \boldsymbol{v}; \boldsymbol{\mu})}{||\boldsymbol{v}||_{\mathcal{Y}}^2}, \tag{16}$$

and $\beta(\boldsymbol{\mu})$ the parameter-dependent inf-sup constant of the problem as

$$\beta(\boldsymbol{\mu}) := \inf_{q \in \mathcal{Q}} \sup_{\boldsymbol{v} \in \mathcal{Y}} \frac{\mathcal{B}(q, \boldsymbol{v}; \boldsymbol{\mu})}{||q||_{\mathcal{Q}} ||\boldsymbol{v}||_{\mathcal{Y}}}. \tag{17}$$

A necessary condition known as the Ladyzhenskaya-Babuška-Brezzi condition for problem (15) to have a unique solution is that $\alpha(\boldsymbol{\mu}) \geq \alpha_0 > 0$ and $\beta(\boldsymbol{\mu}) \geq \beta_0 > 0$. We assume in what follows that the coercivity constant is always positive and concentrate on the inf-sup constant.

From here on we forego any interest in the infinite-dimensional problem and assume instead that both $\mathcal{Y}$ and $\mathcal{Q}$ are replaced by strictly finite-dimensional spaces $\mathcal{Y}_h$ and $\mathcal{Q}_h$. More concretely, we consider only the finite-dimensional problem obtained by discretization of the partial differential equations using the finite element method. The discretized model problem

$$\begin{aligned} \mathcal{A}(\boldsymbol{u}_h, \boldsymbol{v}_h; \boldsymbol{\mu}) + \mathcal{B}(p_h, \boldsymbol{v}_h; \boldsymbol{\mu}) &= \langle \boldsymbol{F}_h(\boldsymbol{\mu}), \boldsymbol{v}_h \rangle_{\mathcal{Y}_h} \qquad \text{for all } \boldsymbol{v}_h \in \mathcal{Y}_h \\ \mathcal{B}(q_h, \boldsymbol{u}_h; \boldsymbol{\mu}) &= \langle G_h(\boldsymbol{\mu}), q_h \rangle_{\mathcal{Q}_h} \qquad \text{for all } q_h \in \mathcal{Q}_h, \end{aligned} \tag{18}$$

involves a similar inf-sup condition to guarantee the existence of a unique velocity-pressure pair satisfying (18):

$$\beta_h(\boldsymbol{\mu}) = \inf_{q_h \in \mathcal{Q}_h} \sup_{\boldsymbol{v}_h \in \mathcal{Y}_h} \frac{\mathcal{B}(q_h, \boldsymbol{v}_h; \boldsymbol{\mu})}{||q_h||_{\mathcal{Q}} ||\boldsymbol{v}_h||_{\mathcal{Y}}} \geq \beta_0 > 0. \tag{19}$$

In the case of the steady Stokes problem we employ the $\mathbb{P}^2 - \mathbb{P}^1$ Taylor-Hood elements [4, 15] that satisfy the condition (19) without the necessity of adding extra stabilizing terms.

The reduced basis method seeks an approximation of the finite element solution to (18). The first step is to construct a set of global basis functions. Let $\boldsymbol{\mu}^1, \ldots, \boldsymbol{\mu}^N$ be a set of snapshot parameter values chosen according to some rule. We denote by $\boldsymbol{u}(\boldsymbol{\mu}^n)$ and $p(\boldsymbol{\mu}^n)$ the corresponding snapshot solutions for the velocity and pressure. The snapshot solutions are obtained as solutions of a stable finite element formulation of (18). The reduced basis velocity space is then defined as

$$\text{span}(u(\boldsymbol{\mu}^1), \ldots, u(\boldsymbol{\mu}^N)) =: \mathcal{Y}_N \subset \mathcal{Y}_h, \tag{20}$$

and the reduced basis pressure space as

$$\text{span}(p(\boldsymbol{\mu}^1), \ldots, p(\boldsymbol{\mu}^N)) =: \mathcal{Q}_N \subset \mathcal{Q}_h. \tag{21}$$

We define the *reduced basis Galerkin* problem: for any $\boldsymbol{\mu} \in \mathcal{D}$ find $u_N \in \mathcal{Y}_N$ and $p_N \in \mathcal{Q}_N$ such that

$$\begin{aligned} \mathcal{A}(u_N(\boldsymbol{\mu}), v; \boldsymbol{\mu}) + \mathcal{B}(p_N(\boldsymbol{\mu}), v; \boldsymbol{\mu}) &= \langle \boldsymbol{F}_h(\boldsymbol{\mu}), v \rangle \qquad \text{for all } v \in \mathcal{Y}_N \\ \mathcal{B}(q, u_N(\boldsymbol{\mu}); \boldsymbol{\mu}) &= \langle G_h(\boldsymbol{\mu}), q \rangle \qquad \text{for all } q \in \mathcal{Q}_N. \end{aligned} \tag{22}$$

Then $(\boldsymbol{u}_N(\boldsymbol{\mu}), p_N(\boldsymbol{\mu}))$ is a reduced basis approximation for $(\boldsymbol{u}_h(\boldsymbol{\mu}), p_h(\boldsymbol{\mu}))$ the solution of (18). To represent and solve these equations in matrix form, an orthonormal basis is constructed for $\mathcal{Y}_N$ and $\mathcal{Q}_N$ to guarantee algebraic stability as $N \to \infty$ [20].

Provided that the dimension N is chosen to be much smaller than the dimension of the finite element spaces, this system is inexpensive to solve. If the dependence of the bilinear forms on the parameters is smooth and the snapshot parameter values $\boldsymbol{\mu}_n$ are properly chosen, we find that choosing a moderately small N permits rapid convergence towards the

finite element solution, provided that . For details on how to choose the snapshots with the help of a greedy algorithm that controls the residual a posteriori approximation error, we refer to existing works on reduced basis methods [6, 13, 19].

A key issue in the reduced basis approximation of the Stokes problem is approximation stability. We remark that use of inf-sup-stable finite elements for the snapshot computation does not necessarily result in a stable reduced basis approximation when the basis functions are orthonormalized, as was observed in [20]. On the other hand, the orthonormalization is vital for the algebraic stability of the reduced basis approximation. Thus there is a need to extend the concept of inf-sup constants into the reduced basis formulation. This is typically done by defining the so-called supremizers in velocity space and enriching the reduced basis velocity space $\mathcal{Y}_N$ accordingly. Following [20] we define the inner supremizer operator $T^{\boldsymbol{\mu}} : \mathcal{Q}_h \to \mathcal{Y}_h$ as the solution of the elliptic problem

$$\langle T^{\boldsymbol{\mu}} q, \boldsymbol{v} \rangle_{\mathcal{Y}} = \mathcal{B}(q, \boldsymbol{v}; \boldsymbol{\mu}) \quad \text{for all } \boldsymbol{v}_h \in \mathcal{Y}_h. \tag{23}$$

After the pressure approximation space $\mathcal{Q}_N$ and velocity approximation space $\mathcal{Y}_N$ have been constructed we add all the velocity supremizers, i.e. velocity fields of the form $T^{\boldsymbol{\mu}}(p(\boldsymbol{\mu}^n))$, to the velocity space:

$$\tilde{\mathcal{Y}}_N := \mathcal{Y}_N \cup \text{span}\left[T^{\boldsymbol{\mu}}(p(\boldsymbol{\mu}^1)), \ldots, T^{\boldsymbol{\mu}}(p(\boldsymbol{\mu}^N))\right], \tag{24}$$

where $\tilde{\mathcal{Y}}_N$ is a stabilized reduced velocity space. Then

$$\tilde{\beta}_N(\boldsymbol{\mu}) := \inf_{q \in \mathcal{Q}_N} \sup_{\boldsymbol{v} \in \tilde{\mathcal{Y}}_N} \frac{\mathcal{B}(q, \boldsymbol{v}; \boldsymbol{\mu})}{\|q\|_{\mathcal{Q}_N} \|\boldsymbol{v}\|_{\tilde{\mathcal{Y}}_N}} \geq \beta_h(\boldsymbol{\mu}) \geq \beta_0 > 0. \tag{25}$$

As a consequence of this approach to stabilization the dimension of the velocity approximation space grows to $2N$, where N is the original dimension of velocity and pressure approximation spaces respectively.

The computational benefits of the reduced basis method rely on the assumption that the parametric bilinear forms are affinely parameterized:

$$\mathcal{A}(\boldsymbol{u}, \boldsymbol{v}; \boldsymbol{\mu}) = \sum_{m=1}^{M_a} \Theta_a^m(\boldsymbol{\mu}) \mathcal{A}^m(\boldsymbol{u}, \boldsymbol{v}), \quad \mathcal{B}(p, \boldsymbol{v}; \boldsymbol{\mu}) = \sum_{m=1}^{M_b} \Theta_b^m(\boldsymbol{\mu}) \mathcal{B}^m(p, \boldsymbol{v}) \tag{26}$$

for some parameter-independent continuous bilinear forms $\mathcal{A}^m$ and $\mathcal{B}^m$, and parametric coefficient functions Θ_a^m and Θ_b^m that can be readily evaluated. Then the finite element equations (18) split into

$$\begin{aligned} \sum_{m=1}^{M_a} \Theta_a^m(\boldsymbol{\mu}) \mathcal{A}^m(\boldsymbol{u}_N(\boldsymbol{\mu}), \boldsymbol{v}) + \sum_{m=1}^{M_b} \Theta_b^m(\boldsymbol{\mu}) \mathcal{B}^m(p_N(\boldsymbol{\mu}), \boldsymbol{v}) &= \langle \boldsymbol{F}_h(\boldsymbol{\mu}), \boldsymbol{v} \rangle \qquad \text{for all } \boldsymbol{v} \in \mathcal{Y}_h \\ \sum_{m=1}^{M_b} \Theta_b^m(\boldsymbol{\mu}) \mathcal{B}^m(q, \boldsymbol{u}_N(\boldsymbol{\mu})) &= \langle G_h(\boldsymbol{\mu}), q \rangle \qquad \text{for all } q \in \mathcal{Q}_h, \end{aligned} \tag{27}$$

and the reduced basis equations (22) respectively into

$$\begin{aligned} \sum_{m=1}^{M_a} \Theta_a^m(\boldsymbol{\mu}) \mathcal{A}^m(\boldsymbol{u}_N(\boldsymbol{\mu}), \boldsymbol{v}) + \sum_{m=1}^{M_b} \Theta_b^m(\boldsymbol{\mu}) \mathcal{B}^m(p_N(\boldsymbol{\mu}), \boldsymbol{v}) &= \langle \boldsymbol{F}_h(\boldsymbol{\mu}), \boldsymbol{v} \rangle \qquad \text{for all } \boldsymbol{v} \in \mathcal{Y}_N \\ \sum_{m=1}^{M_b} \Theta_b^m(\boldsymbol{\mu}) \mathcal{B}^m(q, \boldsymbol{u}_N(\boldsymbol{\mu})) &= \langle G_h(\boldsymbol{\mu}), q \rangle \qquad \text{for all } q \in \mathcal{Q}_N. \end{aligned} \tag{28}$$

Once bases $\{\boldsymbol{\xi}_n^v\}_{n=1}^{2N}$ and $\{\xi_n^p\}_{n=1}^{N}$ for the reduced basis spaces $\tilde{\mathcal{Y}}_N$ and $\mathcal{Q}_N$ respectively have been constructed, the reduced system matrices

$$\begin{aligned}[A^m]_{k,\ell} &:= \mathcal{A}^m(\boldsymbol{\xi}_k^v, \boldsymbol{\xi}_\ell^v), \quad 1 \le k, \ell \le 2N; \\ [B^m]_{k,\ell} &:= \mathcal{B}^m(\boldsymbol{\xi}_k^v, \xi_\ell^p), \quad 1 \le k \le 2N, \quad 1 \le \ell \le N,\end{aligned} \tag{29}$$

are independent of the parameters $\boldsymbol{\mu}$, and can be precomputed and stored. This is the parameter-independent *offline stage*. In the *online stage*, for any $\boldsymbol{\mu} \in \mathcal{D}$ we assemble and solve the $3N \times 3N$ system for the reduced velocity $\boldsymbol{u}_N \in \mathbb{R}^{2N \times 1}$ and reduced pressure $\boldsymbol{p}_N \in \mathbb{R}^{N \times 1}$ s.t.

$$\begin{aligned}\left(\sum_{m=1}^{M_a} \Theta_a^m(\boldsymbol{\mu}) A^m\right) \boldsymbol{u}_N + \left(\sum_{m=1}^{M_b} \Theta_b^m(\boldsymbol{\mu}) B^m\right) \boldsymbol{p}_N &= \boldsymbol{F}(\boldsymbol{\mu}) \\ \sum_{m=1}^{M_b} \Theta_b^m(\boldsymbol{\mu}) [B^m]^T \boldsymbol{u}_N &= \boldsymbol{G}(\boldsymbol{\mu}).\end{aligned} \tag{30}$$

In the case of pure Dirichlet boundary conditions we have

$$\boldsymbol{F}(\boldsymbol{\mu}) = \boldsymbol{f}^F - \sum_{m=1}^{M_a} \Theta_a^m(\boldsymbol{\mu}) A^m \tilde{\boldsymbol{u}}_0 \tag{31}$$

where the inhomogeneous Dirichlet condition has been treated by lifting the solution of the homogeneous equation into the space with proper boundary conditions. Therefore also the computation of the right-hand side splits affinely in terms of parametric dependence. The assembly and solution of the reduced system can be done independent (and thus very efficiently) of the dimensions of the finite element spaces for the velocity $\mathcal{Y}_h$ and pressure $\mathcal{Q}_h$ respectively. While the offline stage is more expensive compared to solving the finite element problem, if the parametric PDE is evaluated for sufficiently many $\boldsymbol{\mu}$ (typically the cutoff point is between 100-500 PDE evaluations), the inexpensive online stage negates the preliminary costs involved in setting up the reduced basis matrices.

In our case the viscous transformation tensor ν_T obtained by free-form deformations does not satisfy the affine parameterization assumption (26). This difficulty is handled by using the Empirical Interpolation Method (EIM) [1, 9, 18], which approximates the nonaffinely parameterized tensor with a suitable affinely parameterized one by replacing each term of the viscous transformation tensor with an approximate expansion

$$[\nu_T]_{i,j} = \sum_{m=1}^{M_{i,j}} \vartheta_m^{i,j}(\boldsymbol{\mu}) \zeta_m^{i,j}(\boldsymbol{x}) + \varepsilon^{i,j}(\boldsymbol{x}, \boldsymbol{\mu}), \tag{32}$$

where the error terms are chosen to be under some tolerance, $||\varepsilon^{i,j}(\cdot, \boldsymbol{\mu})||_{L^\infty} < \varepsilon_{tol}^{EIM}$ for all $\boldsymbol{\mu} \in \mathcal{D}$. For this problem we use $\varepsilon_{tol}^{EIM} = 1\text{e-}5$, which is satisfied with $M_{i,j} \le 22$ for $i, j = 1, 2$. The affine decomposition (26) is then recovered. The tolerance should be chosen small enough so that the introduced additional error term does not dominate the error reduced basis approximation [12, 18]. For an a posteriori error estimate of reduced basis approximation for the Stokes problem we refer at the moment to [16].

6 NUMERICAL EXPERIMENTS

Because an analytical solution for the fluid-structure problem described in Sect. 2 is not obtainable, we verified our (finite element) computations by comparing them to results

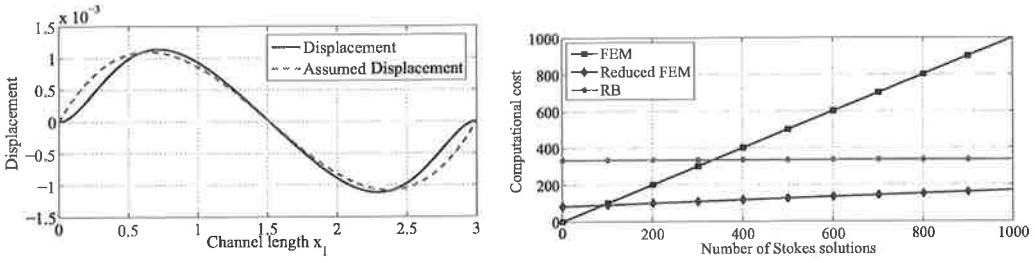

(a) Displacement η and assumed displacement $\hat{\eta}$ at end of coupling Algorithm 1 for (14)

(b) Computational costs of FEM, reduced FEM, and reduced basis approach as number of parametric PDE solutions increases

Figure 3: Result of the fluid-structure algorithm and a comparison of computational costs

presented in [10] for the same test case and parameter values, except with a second-order wall law. For a flexible channel with length 3 cm and half-width 0.5 cm we imposed a Poiseuille flow profile at both the inflow and outflow

$$\boldsymbol{u}_0(\boldsymbol{x}) = v_0 \begin{bmatrix} 1 - 4x_2^2 \\ 0 \end{bmatrix}. \tag{33}$$

The numerical values for the physical parameters were chosen according to [3] so that the inflow velocity was $v_0 = 30$ cm/s and the blood viscosity $\nu = 0.035$ g/cm·s. The volume force on the fluid $\boldsymbol{f}^F$ was taken to be zero. The spring constant was $K = 62.5$ g/s^2. From the initial guess $\boldsymbol{\mu} = \mathbf{0}$ the least-squares optimization algorithm for the strong parametric coupling took 287 iteration steps (Stokes evaluation + solution of least-squares problem for the coupling) until the stopping criteria $||\boldsymbol{\mu}^{k+1} - \boldsymbol{\mu}^k|| <$ 1e-5 was fulfilled. The final value of the cost functional was $J =$ 5e-8. The obtained displacement η of the fluid-structure interface versus the assumed displacement $\hat{\eta}$ are shown in Fig. 3(a).

Once the full FEM solution was verified to be correct, we performed the model reduction of the Stokes problem. We consider two levels of model reduction. In the first level, the problem is parameterized with free-form deformations following Sect. 3 , the transformation tensors are affinely decomposed with the empirical interpolation as in (32), and the parametric decomposition (27) of the system matrices is precomputed. Then we can either:

1. Assemble and solve the full FEM Stokes-problem from (27) using the precomputed system matrices for each $\boldsymbol{\mu}$. The only reduction is in terms of the parameterized geometry. We call this *reduced FEM*.

2. Perform the full reduced basis offline stage and construct the reduced system matrices in (28), then solve the reduced basis system for each $\boldsymbol{\mu}$. Reduction is both in terms of the parameterized geometry and the PDEs. This is the *reduced basis* approach.

The computational costs are compared in Fig. 3(b). The costs are scaled so that the cost of one full FEM solution equals 1. The full FEM incurs no starting overhead, but scales poorly as the number of PDE solutions increases. The reduced FEM has moderate starting cost (empirical interpolation + matrix assembly) and scales fairly well. The full reduced basis approach is costly in terms of the offline stage, but solving the PDE is almost free, resulting in extremely good scalability when thousands of parametric PDE evaluations are desired. For the steady FSI problem we don't need thousands of PDE evaluations, so that reduced FEM would seem the best option in terms of total computational cost for this problem. For the unsteady case we anticipate a need for many more PDE solutions during time-stepping

so that the added scalability of the full reduced basis becomes significant. This is future work to be considered.

7 CONCLUSIONS

A model reduction technique for steady fluid-structure interaction problem of Stokes flow in a flexible 2-d channel was proposed. A geometric reduction was performed using free-form deformations to reduce the free-boundary problem to a low-dimensional parameter space. Reduced basis methods were then used to reduced the complexity of the resulting parametric PDEs.

A least-squares parametric coupling formulation between the fluid and structure was given. The approximate balance of stresses across the interface was formulated using the parameterized displacement of the interface and solved using nonlinear programming techniques. A low-dimensional parameterization with six parameters coming from a free-form deformation technique was enough to obtain approximate coupling.

Computational costs between the full FEM, a geometrically reduced FEM, and the full reduced basis approach were compared. It was observed that the reduced FEM without the overhead of the reduced basis reduction was the computationally most attractive choice, but that for unsteady or nonlinear problems there could be a need for the better scalability of reduced basis methods as the number of PDE evaluations increases.

REFERENCES

[1] M. Barrault, Y. Maday, N.C. Nguyen, and A.T. Patera. An 'empirical interpolation' method: application to efficient reduced-basis discretization of partial differential equations. *C. R. Math. Acad. Sci. Paris*, 339(9):667 – 672, 2004.

[2] S. Deparis. Reduced basis error bound computation of parameter-dependent Navier–Stokes equations by the natural norm approach. *SIAM J. Num. Anal.*, 46(4):2039–2067, 2008.

[3] L. Formaggia, J.-F. Gerbeau, F. Nobile, and F. Quarteroni. On the coupling of 3D and 1D Navier-Stokes equations for flow problems in compliant vessels. *Comput. Methods Appl. Mech. Engrg.*, 191(6-7):561–582, 2001.

[4] V. Girault and P.-A. Raviart. *Finite element methods for Navier-Stokes equations: Theory and algorithms.* Springer-Verlag Berlin and New York, 1986.

[5] C. Grandmont. Existence for a three-dimensional steady state fluid-structure interaction problem. *J. Math. Fluid Mech.*, 4:76–94, 2002.

[6] M.A. Grepl and A.T. Patera. A posteriori error bounds for reduced-basis approximations of parametrized parabolic partial differential equations. *ESAIM Math. Modelling Numer. Anal.*, 39(1):157–181, 2005.

[7] T. Lassila and G. Rozza. Parametric free-form shape design with PDE models and reduced basis method. *Comput. Methods Appl. Mech. Engrg.*, 2009. Under review.

[8] A.E. Løvgren, Y. Maday, and E.M. Rønquist. A reduced basis element method for the steady Stokes problem. *ESAIM Math. Modelling Numer. Anal.*, 40(3):529–552, 2006.

[9] Y. Maday, N.C. Nguyen, A.T. Patera, and G.S.H. Pau. A general multipurpose interpolation procedure: the magic points. *Commun. Pure Appl. Anal.*, 8(1), 2009.

[10] C.M. Murea. The BFGS algorithm for a nonlinear least squares problem arising from blood flow in arteries. *Comput. Math. Appl.*, 49:171–186, 2005.

[11] C.M. Murea. Numerical simulation of a pulsatile flow through a flexible channel. *ESAIM Math. Modelling Numer. Anal.*, 40(6):1101–1125, 2006.

[12] N.C. Nguyen. A posteriori error estimation and basis adaptivity for reduced-basis approximation of nonaffine-parametrized linear elliptic partial differential equations. *J. Comp. Phys.*, 227:983–1006, 2007.

[13] A.T. Patera and G. Rozza. *Reduced Basis Approximation and A Posteriori Error Estimation for Parametrized Partial Differential Equation.* Version 1.0, Copyright MIT 2006, to appear in (tentative rubric) MIT Pappalardo Graduate Monographs in Mechanical Engineering, 2009.

[14] A. Quarteroni and G. Rozza. Numerical solution of parametrized Navier-Stokes equations by reduced basis methods. *Numer. Methods Partial Differential Equations*, 23(4):923–948, 2007.

[15] A. Quarteroni and A. Valli. *Numerical Approximation of Partial Differential Equations (1st Ed.).* Springer-Verlag, Berlin-Heidelberg, 1994.

[16] D.V. Rovas. *Reduced-basis output bound methods for parametrized partial differential equations.* PhD thesis, Massachusetts Institute of Technology, 2003.

[17] G. Rozza. *Shape design by optimal flow control and reduced basis techniques: applications to bypass configurations in haemodynamics.* PhD thesis, École Polytechnique Fédérale de Lausanne, 2005.

[18] G. Rozza. Reduced basis methods for Stokes equations in domains with non-affine parameter dependence. *Comput. Vis. Sci.*, 12(1):23–35, 2009.

[19] G. Rozza, D.B.P. Huynh, and A.T. Patera. Reduced basis approximation and a posteriori error estimation for affinely parametrized elliptic coercive partial differential equations. *Arch. Comput. Methods Engrg.*, 15:229–275, 2008.

[20] G. Rozza and K. Veroy. On the stability of Reduced Basis methods for Stokes Equations in parametrized domains. *Comput. Methods Appl. Mech. Engrg.*, 196(7):1244–1260, 2007.

[21] T.W. Sederberg and S.R. Parry. Free-form deformation of solid geometric models. *Comput. Graph.*, 20(4), 1986.

[22] K.G. van der Zee, E.H. van Brummelen, and R. de Borst. Goal-oriented error estimation for Stokes flow interacting with a flexible channel. *Int. J. Numer. Meth. Fluids*, 56:1551–1557, 2008.

[23] K. Veroy and A.T. Patera. Certified real-time solution of the parametrized steady incompressible Navier-Stokes equations: rigorous reduced-basis a posteriori error bounds. *Int. J. Numer. Meth. Fluids*, 47(8-9):773–788, 2005.

More reliable simulation results with Fluid-Structure Interaction

Sami Pajunen[a], Jani Ojala[b], Eero Immonen[b]

[a] *Department of Mechanics and Design, Tampere University of Technology, sami.pajunen@tut.fi*
[b] *Process Flow Ltd Oy, jani.ojala@processflow.fi, eero.immonen@processflow.fi*

Abstract
In many engineering applications, processes and structures cannot be analysed in isolation of their operating environments, because they affect the environment and vice versa. In order to describe such complex effects accurately and robustly, one has to perform a coupled analysis of the relevant phenomena. Modern fluid-structure interaction (FSI) simulations facilitate accurate numerical analyses of the vastly complex couplings between fluid flows and motion of solid structures. FSI simulations are gaining widespread attention as a tool to meet the ever increasing reliability and accuracy requirements imposed on design efforts. Indeed, the rapid evolution of parallel computing has enabled researchers and engineers alike to robustly solve such FSI problems that were previously considered too difficult. Additional momentum on the popularity of FSI simulations is given by the possibility to seamlessly combine in-house codes to commercial ones. In this paper, some theoretical aspects of different FSI coupling methods and practical issues related to FSI simulations are discussed. An FSI simulation of a *water hammer* is presented.

1. INTRODUCTION

A fluid-structure interaction (FSI) problem refers to such a coupled system, where fluid flow induces motion of solid structures and, conversely, structural displacements affect the fluid flow. Fluid-structure interaction is nowadays one of the most popular topics in a more general class of coupled field problems commonly called *multiphysics*. During the 1980s and the 1990s some successful FSI methods were presented (e.g. acoustic applications), but it was not until the present decade that the number of FSI applications increased dramatically. This is especially true in industrial engineering applications, but the trend is also seen in theoretical research. The development of software and algorithms, as well as the decreasing cost of high-performance computers, enables analysts today to tackle such highly complex FSI problems as wing flutter in aeroplanes, oscillation of long-span bridges, turbomachinery, parachutes, fluid conveying pipes and tanks, blood flow and biomedical heart valves. Usually FSI problems are transient, which adds a degree of complexity to their solution.

The first step in the FSI analysis history was to analyse both the fluid flow with rigid structure and the structural problem with constant fluid tractions separately and afterwards transfer traction and displacement data between the separate solvers and optionally rerun the analyses with updated interface data. This intuitive strategy would be useful, if the fluid and structure physics were only weakly coupled. For example, large structural displacements would cause this solution strategy to fail. Consequently, more advanced strategies have been presented after this simple approach and nowadays much more accurate and robust methods are available for a large class of FSI problems.

One of the major topics in FSI is the choice whether to use monolithic or partitioned FSI solvers. Monolithic method (sometimes called also as direct method or fully implicit scheme) [1] means, that both the fluid and structural equations are solved simultaneously in the same system of equations. On the other hand, partitioned method (sometimes called as iterative method or staggered method) [2-8] means that fluid and structural problems are solved with separate solvers and the interaction equations are handled outside these applications with a third-party solver. The partitioned approach has the major advantage, that the commercial CFD solvers and FEM solvers can be adopted for fluid and structural problems, respectively. The interface solver can be either in-house application or commercial code [9].

In this paper, various FSI-solution strategies are discussed in Chapter 2. The governing equations of fluid, structure and especially the interface are given in Chapter 3 and their solution procedures are discussed in chapter 4. Chapter 5 contains a presentation of a loosely-coupled FSI application, namely a water hammer. Chapter 6 highlights some aspects of the use of commercial ANSYS package in FSI problem handling. Finally, Chapter 7 contains some conclusions.

2. FSI SOLVER STRATEGIES

Partitioned method means, as mentioned before, that the fluid and structural problems are solved separately. If real engineering applications including complex turbulence and boundary layer characteristics are considered, this means usually that the fluid problem is solved using the control volume method discretised using Arbitrary Lagragian–Eulerin (ALE) formulation that enables the flow equations solution in moving domain. On the other hand, the structural problem is inevitably solved using the finite element method. Partitioned method also enables the use of commercial FEM- and CFD-solvers as black-box routines.

Partitioned method is called *loosely-coupled* [2-4] if the solvers only change data after converged time-steps. Usually this means, that the fluid solver sends fluid tractions of the common interface to the structural solver, and the structural solver sends interface displacements to the fluid solver. After data transfer, both solvers proceed to the next time-step. If either solver uses smaller time-steps, sub-cycling is possible in this scheme. As can be easily seen, loosely-coupled strategy violates equilibrium equations, because in the interface the tractions and the displacements taken from distinct solvers might be incompatible and they are not iterated to equilibrium state. When loosely-coupled partitioned method is used, one has to examine the results carefully, and make judgements if the physical nature of the interaction is weak enough for the use of loosely-coupled algorithm. However, this argumentation is not fully true, because in [4] an second-order accurate algorithm is derived for loosely-coupled analysis.

When the loosely-coupled partitioned method is augmented with some interface iterations to ensure equilibrium at the end of each time-step, the method is called *strongly-coupled* [5-8] partitioned method. According to its name, the method is suitable for FSI-problems, in which the physics between fluid and structural fields are strongly coupled. Physically strong coupling appears e.g. when the structural displacements (being small or large) affect the flow field remarkably. The strongly-coupled method uses different algorithms to iterate the nonlinear interface equations to the equilibrium state. Indeed, it would be desirable to use the traditional Newton-Raphson iteration scheme but when commercial "black box" solvers are used, the needed jacobians from fluid and structural solvers are not available. Hence, other methods must be used. Depending on the interface problem definition, different strategies are available for the interface residual equation problem. One efficient, but rather simple method is the interface-block-quasi-Newton method with two least-squares reduced-order models (IBQN-LS), that calculate approximate jacobians of the flow and structural solvers [10]. Another useful method, called

interface-quasi-Newton with inverse jacobian from least-squares model (IQN-ILS) calculates approximation of the inverse of the jacobians [5]. The Newton-iteration method in which the interaction-based off-diagonal blocks are solved using finite difference approximations is presented e.g. in [11]. Slightly different method, based on fixed-point iteration and dynamic relaxations, called Aitken's method is presented in [12].

The *monolithic method* differs from the partitioned solution strategy remarkably due to the fact, that fluid and structural equations are collected to the same system of equations, and solved as one. This strategy has some pros and cons. The system of equations is by no means easy to solve, and the solution may be very time-consuming. Additionally, the use of the best commercial FEM- or CFD-solvers is impossible with monolithic approach. One of the advantages of the method is however that all the mathematical analyses derived for coupled systems is available in monolithic method giving it sound theoretical basis. However, the applications of the monolithic method seem to be rather simple mainly because the method does not take into account different nature of the fluid and structural equations, and it requires the same time step size for both the fluid and structure equations.

3. GOVERNING EQUATIONS OF FSI

In what follows, Ω_f and Ω_s denote the fluid and structural domains, respectively, while their boundaries are Γ_f and Γ_s. The common interface boundary between fluid and structural fields is denoted by Γ_{fs}. The subscripts *f*, *s* and *fs* are used to denote fluid and structure, respectively.

3.1 Structural equations

The principle of virtual displacements can be written as

$$\int_{\Omega_s} \boldsymbol{\sigma}_s^{\mathrm{T}} \delta\boldsymbol{\varepsilon}_s \mathrm{d}\Omega_s - \int_{\Omega_s} \mathbf{b}_s^{\mathrm{T}} \delta\mathbf{u}_s \mathrm{d}\Omega_s - \int_{\Gamma_s} \mathbf{t}_s^{\mathrm{T}} \delta\mathbf{u}_s \mathrm{d}\Gamma_s = 0 \tag{1}$$

in which $\boldsymbol{\sigma}_s$ is the stress tensor and $\delta\boldsymbol{\varepsilon}_s$ is the associated work conjugate virtual strain field, $\delta\mathbf{u}_s$ contains the kinematically feasible virtual displacements. Body forces acting on domain Ω_s are represented by $\mathbf{b}_s$ and tractions on boundary Γ_s are denoted by $\mathbf{t}_s$. Using D'Alembert formalism and discretising (1) using the standard finite element method procedure will lead us to nonlinear ordinary differential equation system

$$\mathbf{r}(\mathbf{u}_s) - \mathbf{p}(\mathbf{u}_s, t) + \mathbf{M}\ddot{\mathbf{u}}_s = \mathbf{0} \tag{2}$$

in which $\mathbf{p}$ is external load vector, $\mathbf{r}$ contains internal resistance forces, $\mathbf{M}$ is the so called mass matrix and $\ddot{\mathbf{u}}$ contains nodal point accelerations. The discretised equation (2) is solved usually using implicit Newmark integration method augmented with possibly required Newton-Raphson iterations within the time-steps. Also explicit integration methods are used if the problem contains impacts or other rapid phenomena. Equation (2) can be rewritten in implicit form as

$$\mathbf{R}_s(\mathbf{u}_s, t) = \mathbf{0} \tag{3}$$

in which $\mathbf{R}_s$ is residual operator.

3.2 Fluid equations

The equations governing velocity and pressure of fluid flow are mass conservation and momentum conservation equations. In general form, the mass conservation equation reads in

$$\frac{\partial \rho_f}{\partial t} + \nabla \cdot (\rho_f \mathbf{v}_f) = S \tag{4}$$

in which ρ_f is the fluid density, $\mathbf{v}_f$ is fluid velocity and S contains source terms. The momentum conservation equations can be written as

$$\frac{\partial (\rho_f \mathbf{v}_f)}{\partial t} + \nabla \cdot (\rho_f \mathbf{v}_f \mathbf{v}_f) - \nabla \cdot \boldsymbol{\sigma}_f = \mathbf{b}_f \tag{5}$$

in which $\boldsymbol{\sigma}_f$ is the stress tensor, and $\mathbf{b}_f$ contains all the body forces. In (5) the stress is

$$\boldsymbol{\sigma}_f = \mu \left(\nabla \mathbf{v}_f + (\nabla \mathbf{v}_f)^T \right) - p\mathbf{I} \tag{6}$$

where μ is molecular viscosity, p is static pressure and $\mathbf{I}$ is unit tensor. When the fluid flow equations are used in FSI context, it is inevitable, that the equations must be solved in mesh, that is moving with time. Thus, equation (5) has to be written using the arbitrary Lagrangian-Eulerian (ALE) formulation as

$$\frac{\partial (\rho_f \mathbf{v}_f)}{\partial t} + \nabla \cdot (\rho_f (\mathbf{v}_f - \mathbf{v}_m) \mathbf{v}_f) - \nabla \cdot \boldsymbol{\sigma}_f = \mathbf{b}_f \tag{7}$$

in which $\mathbf{v}_m$ is the velocity of the moving mesh. The flow equations (4) and (7) are usually discretised and solved using the finite control volume method. Finally, the flow field equations can be expressed concisely using an implicit residual formulation as

$$\mathbf{R}_f (\mathbf{v}_f, p, t) = \mathbf{0} \tag{8}$$

3.3 Interaction equations

When partitioned methods are used, the interface compatibility must be ensured with separate interaction equations. At the common interface boundary Γ_{fs} between the fluid and structure domains, the FSI problem contains two unknowns, namely stresses and displacements. The equilibrium equations at the interface Γ_{fs} can be thus stated as [13]

$$\mathbf{v}_f = \frac{\mathrm{d}\mathbf{u}_s}{\mathrm{d}t} \tag{9}$$

$$\mathbf{n}_f \cdot \boldsymbol{\sigma}_f = \mathbf{n}_s \cdot \boldsymbol{\sigma}_s \tag{10}$$

The former equation (9) states, that the kinematics are consistent at the boundary (no-slip condition is assumed here). Equation (10) is the equilibrium condition at the interface, where $\mathbf{n}_f$ and $\mathbf{n}_s$ are the unit normal vectors of fluid and structural domains, respectively.

The usual Dirichlet-Neumann method is used for manipulating these interface conditions [5]. Meaning that, the fluid problem is solved using given interface displacements and the interface stresses are considered in the structural solver. After this interaction equation handling strategy is defined, the residual equations of the structure (3) and flow (8) can be rewritten formally as

$$\mathbf{R} = \begin{bmatrix} \mathbf{R}_s\left(\mathbf{u}_s, \boldsymbol{\sigma}_{fs}(\mathbf{v}_f, p)\right) \\ \mathbf{R}_f\left(\mathbf{v}_f, p, \mathbf{u}_{fs}(\mathbf{u}_s)\right) \end{bmatrix} = \mathbf{0} \tag{11}$$

When the structural equations are solved with a given interface stresses, the outcoming interface displacements can be represented by a function F_s, say

$$\mathbf{u}_{fs} = F_s\left(\boldsymbol{\sigma}_{fs}\right) \tag{12}$$

Similarly, the stresses at the interface are solved using the fluid solver. This can be written as

$$\boldsymbol{\sigma}_{fs} = F_f\left(\mathbf{u}_{fs}\right) \tag{13}$$

Writing the interface displacements with the aid of functions F_s and F_f results in

$$\mathbf{u}_{fs} = F_s \circ F_f\left(\mathbf{u}_{fs}\right) \tag{14}$$

The equation (14) is the interface residual equation, that can be rewritten as

$$\mathbf{R}_{fs} = \mathbf{u}_{fs} - F_s \circ F_f\left(\mathbf{u}_{fs}\right) = \mathbf{0} \tag{15}$$

4. FSI SOLUTION STRATEGIES

4.1. Monolithic method

Fluid and structural equations are solved simultaneously in the monolithic scheme. This means, that within a time-step, the nonlinear system of equations (11) can be linearised and solved with the standard Newton-Raphson iteration as

$$\begin{bmatrix} \dfrac{\partial \mathbf{R}_s}{\partial \mathbf{u}_s} & \dfrac{\partial \mathbf{R}_s}{\partial \mathbf{q}_f} \\ \dfrac{\partial \mathbf{R}_f}{\partial \mathbf{u}_s} & \dfrac{\partial \mathbf{R}_f}{\partial \mathbf{q}_f} \end{bmatrix} \begin{bmatrix} \Delta \mathbf{u}_s \\ \Delta \mathbf{q}_f \end{bmatrix} = - \begin{bmatrix} \mathbf{R}_s \\ \mathbf{R}_f \end{bmatrix} \tag{16}$$

$$\begin{bmatrix} \mathbf{u}_s \\ \mathbf{q}_f \end{bmatrix}^{i+1} = \begin{bmatrix} \mathbf{u}_s \\ \mathbf{q}_f \end{bmatrix}^{i} + \begin{bmatrix} \Delta \mathbf{u}_s \\ \Delta \mathbf{q}_f \end{bmatrix} \tag{17}$$

in which the superscript denotes the iteration cycle number and fluid velocity and pressure are collected to vector $\mathbf{q}$ so that $\mathbf{q}_f = \begin{bmatrix} \mathbf{v}_f^T & p \end{bmatrix}^T$. Note, that the off-diagonal terms in (16) ensure that the fluid-structure interaction is taken into account properly. Due to nature of system matrix in (16) preconditioning must be used for efficient solution of the system.

4.2. Partitioned method with loose coupling

Assume, that the partitioned solution is arranged so that, the structure solver step is taken before the fluid solver step (opposite assumption would naturally lead to the same conclusion). At the end of time step k+1, say, the interface displacements and stresses are then according to (12) and (13)

$$\mathbf{u}_{fs}^{k+1} = F_s\left(\boldsymbol{\sigma}_{fs}^{k}\right) \tag{18}$$

$$\boldsymbol{\sigma}_{\mathrm{fs}}^{\mathrm{k+1}} = F_{\mathrm{f}}\left(\mathbf{u}_{\mathrm{fs}}^{\mathrm{k+1}}\right) \tag{19}$$

It follows from (18) and (19), that

$$F_{\mathrm{s}} \circ F_{\mathrm{f}}\left(\mathbf{u}_{\mathrm{fs}}^{\mathrm{k+1}}\right) = \mathbf{u}_{\mathrm{fs}}^{\mathrm{k+2}} \tag{20}$$

On the other hand, the interface residual equation (15) requires, that

$$F_{\mathrm{s}} \circ F_{\mathrm{f}}\left(\mathbf{u}_{\mathrm{fs}}^{\mathrm{k+1}}\right) = \mathbf{u}_{\mathrm{fs}}^{\mathrm{k+1}} \tag{21}$$

Hence, there is a contradiction between (20) and (21) and the loosely coupled method does not fulfil the interface equation (15). The error is due to the explicit and non-iterative nature of the loosely coupled method. As mentioned in introduction, a second-order loosely-coupled method is presented in [4] meaning that the above equations (18)-(21) is the simplest, but no means the only way to describe a loosely-coupled strategy.

4.3. Partitioned method with strong coupling

As mentioned before, several strategies are presented to solve the interface residual equation (15). The key issue in the solution process is that the exact jacobians of the flow and structural solvers are not available, because partitioned method is usually equipped with black-box commercial solvers. In what follows, the IQN-ILS method presented in [5] is concisely revisited. First, the Newton-Raphson iteration is applied to the interface equation (15) as

$$\mathbf{u}_{\mathrm{fs}}^{\mathrm{i+1}} = \mathbf{u}_{\mathrm{fs}}^{\mathrm{i}} + \Delta\mathbf{u}_{\mathrm{fs}} \tag{22}$$

$$\Rightarrow \mathbf{u}_{\mathrm{fs}}^{\mathrm{i+1}} = \mathbf{u}_{\mathrm{fs}}^{\mathrm{i}} + \left[\left.\frac{\partial \mathbf{R}_{fs}}{\partial \mathbf{u}_{\mathrm{fs}}}\right|_{\mathbf{u}_{\mathrm{fs}}^{\mathrm{i}}}\right]^{-1}\left(-\mathbf{R}_{\mathrm{fs}}^{\mathrm{i}}\right) \tag{23}$$

When the residual equation (15) is solved iteratively, the following notation can be used

$$\mathbf{R}_{\mathrm{fs}}^{\mathrm{i}} = \mathbf{u}_{\mathrm{fs}}^{\mathrm{i}} - F_{\mathrm{s}} \circ F_{\mathrm{f}}\left(\mathbf{u}_{\mathrm{fs}}^{\mathrm{i}}\right) = \mathbf{u}_{\mathrm{fs}}^{\mathrm{i}} - \tilde{\mathbf{u}}_{\mathrm{fs}}^{\mathrm{i+1}} \tag{24}$$

The differences between the vectors $\tilde{\mathbf{u}}_{\mathrm{fs}}^{\mathrm{i+1}}$ and $\mathbf{R}_{\mathrm{fs}}^{\mathrm{i}}$ form all previous iterations during the current time step are stored to matrices $\mathbf{V}^{i}$ and $\mathbf{W}^{i}$ as

$$\mathbf{V}^{i} = \left[\mathbf{R}_{\mathrm{fs}}^{\mathrm{i-1}} - \mathbf{R}_{\mathrm{fs}}^{\mathrm{i}} \quad \mathbf{R}_{\mathrm{fs}}^{\mathrm{i-2}} - \mathbf{R}_{\mathrm{fs}}^{\mathrm{i}} \quad \ldots \quad \mathbf{R}_{\mathrm{fs}}^{0} - \mathbf{R}_{\mathrm{fs}}^{\mathrm{i}}\right] =: \left[\Delta\mathbf{R}_{\mathrm{fs}}^{\mathrm{i-1}} \quad \Delta\mathbf{R}_{\mathrm{fs}}^{\mathrm{i-2}} \quad \ldots \quad \Delta\mathbf{R}_{\mathrm{fs}}^{0}\right] \tag{25}$$

$$\mathbf{W}^{i} = \left[\tilde{\mathbf{u}}_{\mathrm{fs}}^{\mathrm{i}} - \tilde{\mathbf{u}}_{\mathrm{fs}}^{\mathrm{i+1}} \quad \tilde{\mathbf{u}}_{\mathrm{fs}}^{\mathrm{i-1}} - \tilde{\mathbf{u}}_{\mathrm{fs}}^{\mathrm{i+1}} \quad \ldots \quad \tilde{\mathbf{u}}_{\mathrm{fs}}^{1} - \tilde{\mathbf{u}}_{\mathrm{fs}}^{\mathrm{i+1}}\right] =: \left[\Delta\tilde{\mathbf{u}}_{\mathrm{fs}}^{\mathrm{i}} \quad \Delta\tilde{\mathbf{u}}_{\mathrm{fs}}^{\mathrm{i-1}} \quad \ldots \quad \Delta\tilde{\mathbf{u}}_{\mathrm{fs}}^{1}\right] \tag{26}$$

Finally we want, that at the end of iteration loop, the residual vector equals to zero vector, meaning, that the difference between the desired residual vector (zero-vector) and the current residual vector is

$$\Delta\mathbf{R}_{\mathrm{fs}} = \mathbf{0} - \mathbf{R}_{\mathrm{fs}}^{\mathrm{i}} \tag{27}$$

This difference can be approximated as a linear combination of the known values as

$$\Delta\mathbf{R}_{\mathrm{fs}} \approx \mathbf{V}^{\mathrm{i}}\mathbf{c}^{\mathrm{i}} \tag{28}$$

in which the vector $\mathbf{c}^{\mathrm{i}}$ contains the decomposition coefficients. The decomposition is overdetermined (number of unknowns is usually much less that the number of equations), so that a

least-squares solution in order to determine the coefficients in $\mathbf{c}^i$ is used. First the matrix $\mathbf{V}$ is rewritten using QR-decomposition as

$$\mathbf{V}^i = \bar{\mathbf{Q}}^i \bar{\mathbf{R}}^i \tag{29}$$

in which $\bar{\mathbf{Q}}^i$ is orthogonal and $\bar{\mathbf{R}}^i$ is upper triangular matrix. The coefficients are solved from the triangular equation

$$\bar{\mathbf{R}}^i \mathbf{c}^i = \left(\bar{\mathbf{Q}}^i\right)^T \left(-\mathbf{R}_{fs}^i\right) \tag{30}$$

Similarly, the displacement difference $\Delta\tilde{\mathbf{u}}_{fs}$ corresponding to $\Delta\mathbf{R}_{fs}$ is expressed as a linear combination of previous differences as

$$\Delta\mathbf{u}_{fs} \approx \mathbf{W}^i \mathbf{c}^i \tag{31}$$

From differentiation of (24) it follows that

$$\Delta\mathbf{R}_{fs} = \Delta\mathbf{u}_{fs} - \Delta\tilde{\mathbf{u}}_{fs} \tag{32}$$

Substituting (32) into (31) gives the equation from which the iterative displacement $\Delta\mathbf{u}_{fs}$ can be calculated as

$$\Delta\mathbf{u}_{fs} = \mathbf{W}^i \mathbf{c}^i - \Delta\mathbf{R}_{fs} \tag{33}$$

Note, that this equation replaces (23) in which inverse of the exact jacobian is required.

4.4 Other solution aspects

Both in monolithic and partitioned solution methods the so called added-mass effect might cause difficulties to solvers as discussed in [14]. Added-mass effect becomes important usually when fluid to solid density ratio is high, e.g. biomedical applications in which the fluid is usually blood, is an example about high added mass effect. In such applications, generally speaking, loosely-coupled algorithms will diverge, strongly-coupled algorithms might have convergence difficulties and monolithic algorithms seem to have the best convergence.

Another important topic in partitioned solvers, especially in industrial applications, is the fluid solver re-meshing capability. In many applications, there are fluid regions containing very dense boundary layer mesh at the moving solid boundary. When the solid is moved during FSI-simulation, the fluid solvers re-meshing algorithm should be able to maintain good mesh quality. Even for the best commercial CFD-packages, this seems to be a true problem.

5. Example 1 - Water hammer

Abrupt pressure spikes in water-filled tubes – so-called *water hammers* – are abundant in industrial applications. A water hammer can result from a sudden change of valve status (open to closed or vice versa). One sound approach towards damping the peak pressure levels in such cases is to use tubes with *flexible wall segments*: In the event of a water hammer, the flexible wall regions deform and help absorb the energy carried by the pressure pulses. For example, Larox Oyj has taken this approach in order to eliminate pressure spikes in the Ceramec® filters.

In this section we study deformations of a rigid-flexible tube section in the event of a water hammer via a transient FSI simulation. In our simulation, the idealized cylindrical water-filled tube consists of a flexible rubber-made region between two rigid wall regions, as depicted below.

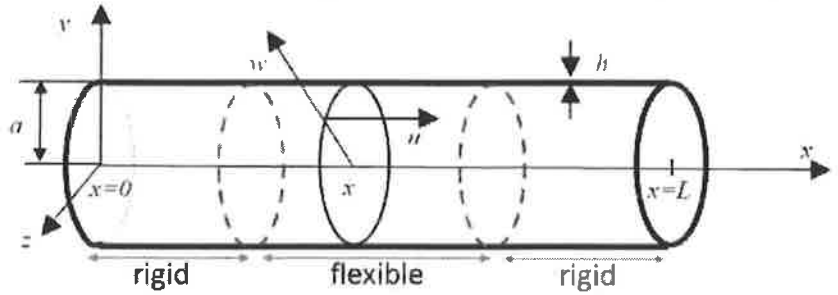

Figure 1. Overall construction of the tube section

A 300 kPa pressure pulse activated at $x = 0$ and $t = 0$ propagates at the speed of sound in the water within the tube and causes oscillating pressure spikes due to slight compressibility of the water. Peak pressure levels are monitored at $x = L$ as a function of time. Outside of the tube is set at atmospheric pressure.

A mathematical model for the deformations of the flexible tube region as a result of pressure difference p is presented in [15]. With the notation of Figure 1 above, the partial differential equations governing the transverse (w) and axial (u) motion of the flexible region are:

$$\begin{bmatrix} \frac{\partial^2}{\partial x^2} - \frac{\partial^2}{c_L^2 \partial t^2} & \frac{\nu}{a}\frac{\partial}{\partial x} \\ \frac{\nu}{a}\frac{\partial}{\partial x} & \frac{1-\nu^2}{E}\frac{T}{A}\frac{\partial^2}{\partial x^2} - \frac{1}{a^2} - \frac{\partial^2}{c_L^2 \partial t^2} \end{bmatrix} \begin{bmatrix} u \\ w \end{bmatrix} = \begin{bmatrix} 0 \\ -\frac{p}{\rho c_L^2 h} \end{bmatrix} \tag{34}$$

Here ν denotes the Poisson ratio, E denotes the Young's modulus for the flexible tube, T denotes the axial tension of the flexible tube, the longitudinal wave speed in the flexible section $c_L = \sqrt{E/\rho(1-\nu^2)}$ and, finally, $A = 2\pi ah$ in the notation of Figure 1. We impose Dirichlet (zero-deflection) conditions at the transition boundaries from flexible to rigid tube regions.

In order to simplify the analysis, we study *transverse* deflections – the parameter w above – only. This allows us to carry out the simulations on the following axis-symmetric 2D geometry:

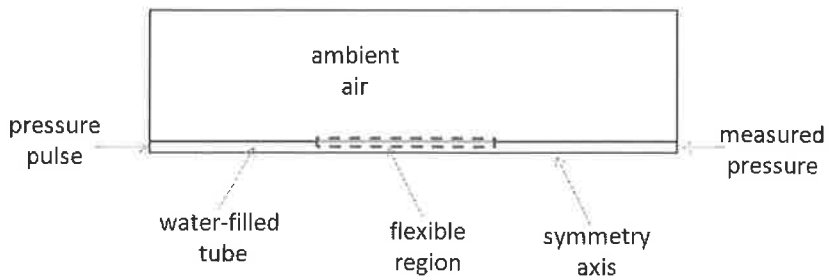

Figure 2. Computational geometry for FSI simulation

The FSI simulations were carried out using a commercial solver (ANSYS Fluent), with a proprietary UDF code taking care of deformation of the computational grid in accordance with the

above linear equations of motion. The solution strategy is loosely coupled: The CFD solver independently resolves the pressure difference p, and, based on this p, the UDF independently resolves the deformations w, which affect the fluid volume and pressure on subsequent time steps.

From the application point of view, an important question is this: What flexible material is the most effective at damping pressure pulses? As the peak pressure level reaches above 500 kPa for fully rigid walls (see figure 3), this question merits considerable attention.

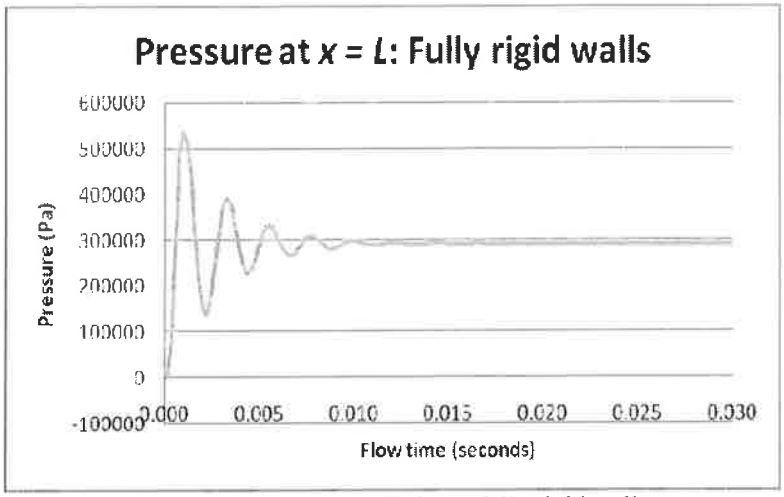

Figure 3. Pressure oscillation – fully rigid walls

In figure 4, we display the time evolution of pressure levels for certain fictive values $E_1 < E_2 < E_3$ of elastic modulus of the flexible tube section. Clearly, the more flexible the tube is, the more the peak pressure level is damped.

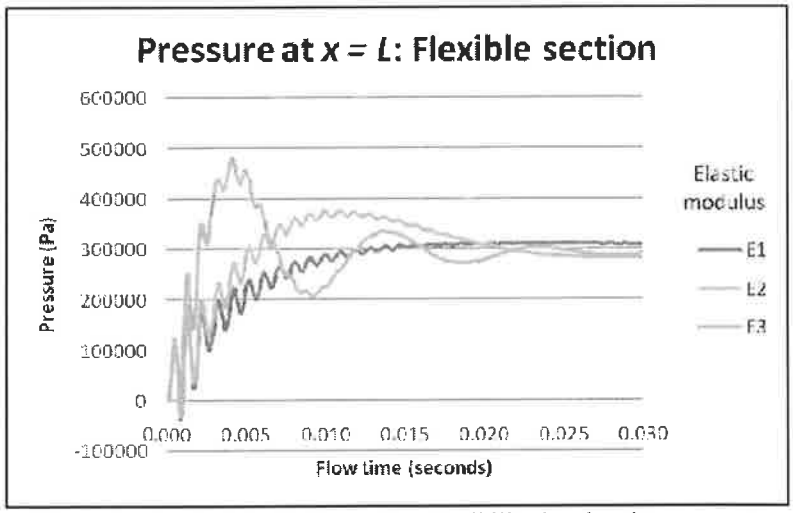

Figure 4. Pressure oscillation – tube flexibility is taken into account

It is clear that accurate conclusions regarding the peak pressure levels can only be made using nonlinear constitutive equations. Moreover, the constant Rayleigh type viscous damping model, which is assumed for the flexible tube section, may not be sufficiently realistic in practice.

However, this FSI model has been successfully used to evaluate the performance of a given flexible material in an industrial process (Larox Oyj). In particular, it facilitated an understanding of the relative importance of the several different material parameters that affect the peak pressure levels.

6. Example 2 – FSI capabilities of ANSYS

Setting up an FSI-analysis in commercial software, like ANSYS, is very straightforward and easy-to-use. Coupling ANSYS Mechanical and ANSYS CFX in ANSYS Workbench enables one-way or two-way FSI-analysis in one unified interface thus reducing possible errors while setting up the analysis. In addition such interface provides effective and robust data handling and management from engineering simulation point of the view. A general picture of ANSYS Workbench is shown in figure 5 where two-way coupled FSI-analysis has been defined. In addition all simulation models may be driven by parameters, thus enabling optimization or design-of-experiment (DOE) analysis. ANSYS FSI simulation can be either transient or steady-state. An example of a transient FSI-analysis of sloshing water in a tank is depicted in figure 6.

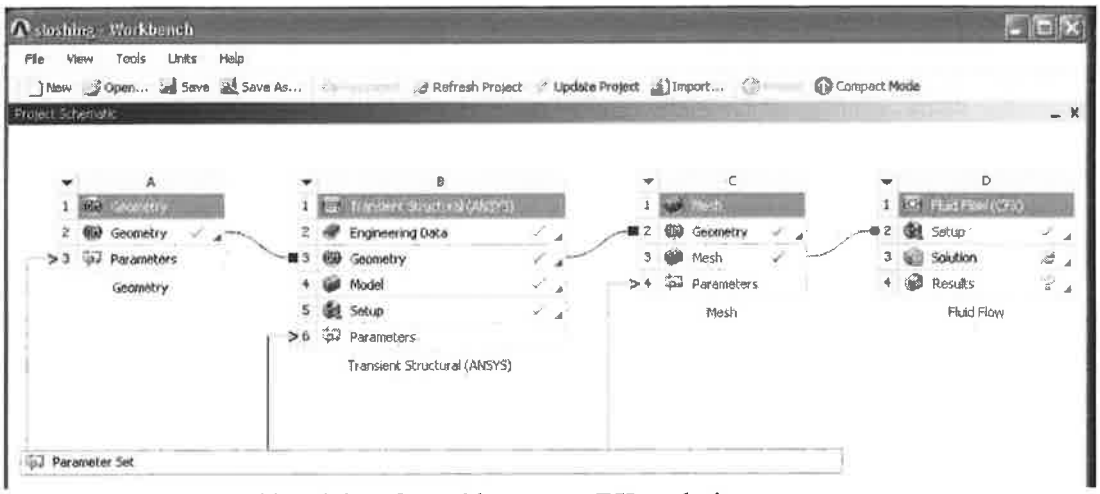

Figure 5. ANSYS Workbench interface with two-way FSI-analysis set up

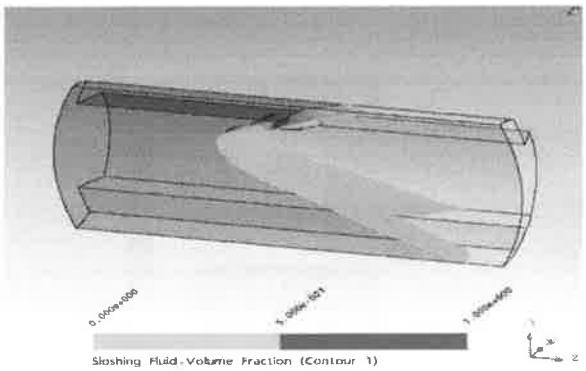

Figure 6. Water sloshing in a container

Using FSI-analysis in engineering simulation with commercial codes also enables more reliable results, since less approximations and guesses are needed for e.g. boundary conditions definition. Consider, for instance, transient exhaust pipe thermal-stress analysis where thermal fatigue is of interest. By using FSI-analysis one can easily define the boundary conditions for stress analysis more accurately by calculating convection coefficients with CFD-analysis and then solving consequent stress analysis.

Some concerns are, however, involved with FSI-analysis. Firstly, the analysis time is usually much longer compared with the corresponding uncoupled analysis. This is especially the case with two-way coupled simulation where in many cases CFD-analysis is the most painful one. There is not much one can do in order to reduce the analysis time in such case. Secondly, large deformations may considerably complicate the CFD-analysis, since the mesh experiences severe distortion and must be remeshed during the analysis. This may lead to remeshing problems or convergence problems. In ANSYS it is possible either smooth the deformed mesh or, if the deformations are large, remesh the whole fluid domain. Thirdly, setting up FSI-analysis may need significant competence in both structural mechanics and fluid dynamics. Understanding both sides of computational physics can be challenging, thus limiting the usability of FSI-technology.

The FSI-analysis can be executed in two ways in ANSYS. Field solvers can be grouped together for simultaneous execution during each stagger iteration. When grouped this way, all field solvers collect their respective loads from the other field solvers, and then all proceed to solve their physics fields simultaneously. Field solvers that are not grouped together for simultaneous execution are executed sequentially during each stagger iteration. In this case, each field solver collects its respective loads from the other field solvers and proceeds to solve its physics fields.

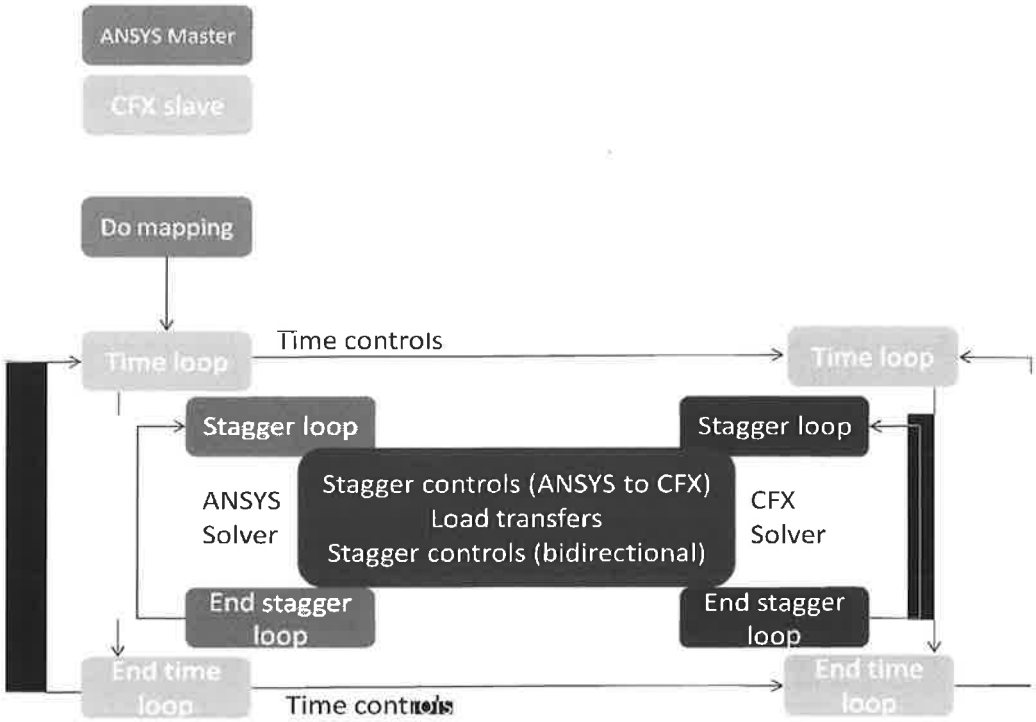

Figure 7. General overview of ANSYS FSI-solution process [16]

7. CONCLUSIONS

In the paper, some basic methods for defining and solving the governing equations of general FSI-simulation are presented. The equations are given in rather implicit form for monolithic and partitioned solution strategies whereas the detailed handling of the equations is not discussed. An application of water pressure pulse damping in a flexible tube is presented in more detail.

REFERENCES

[1] Hübner B., Walhorn E., Dinkler D., A monolithic approach to fluid-structure interaction using space-time finite elements. *Computer methods in applied mechanics and engineering* 2004; **193**: 2087-2104.

[2] Felippa C., Park K., Staggered transient analysis procedures for coupled-field mechanical systems: formulation. *Computer methods in applied mechanics and engineering* 1980; **24**: 61-111.

[3] Lohner R., Yang C., Cebral J., Baum J., Luo H., Pelessone D., Charman C., Fluid-structure interaction using a loose coupling algorithm and adaptive unstructured grids. *AIAA* paper No. 95-2259, 1995.

[4] Farhat C., van de Zee K., Geuzaine P., Provably second-order time-accurate loosely coupled solution algorithms for transient nonlinear computational aeroelasticity. *Computer methods in applied mechanics and engineering* 2006; **195**: 1973-2001.

[5] Degroote J., Bathe K.-J., Vierendeels J., Performance of a new partitioned procedure versus a monolithic procedure in fluid-structure interaction. *Computers & Structures* 2009; **87**: 793-801.

[6] Degroote J., Haelterman R., Annerel S., Coupling techniques for partitioned fluid-structure interaction simulations with black-box solvers. Proceedings of 10th MpCCI user forum, February 17th and 18th 2009: 82-91.

[7] Kalro V., Tezduyar T., A parallel 3D computational method for fluid-structure interactions in parachute systems. *Computer methods in applied mechanics and engineering* 2000; **190**: 321-332.

[8] Le Tallec P., Mouro J., Fluid structure interaction with large structural displacements. *Computer methods in applied mechanics and engineering* 2001; **190**: 3039-3067.

[9] MpCCI 3.1.0. Manual, 2009. http://www.mpcci.de/mpcci_manuals.html

[10] Vierendeels J., Lanoye L., Degroote J., Verdonck P., Implicit coupling of partitioned fluid-structure interaction problems with reduced order models. *Computers & Structures* 2007; **85**: 970-976.

[11] Matthies H., Steindorf J., Partitioned strong-coupling algorithms for fluid-structure interaction. *Computers & Structures* 2003; **81**: 805-812.

[12] Küttler U., Wall W., Fixed-point fluid-structure interaction solvers with dynamic relaxation. *Computational Mechanics* 2008; **43**: 61-72.

[13] Bathe K-J., Zhang H., Finite element developments for general fluid flows with structural interactions. *International journal for Numerical Methods in Engineering* 2004; **60**: 213-232.

[14] Idelsohn S., Del Pin F., Rossi R., Oñate E., Fluid-structure interaction problems with strong added-mass effect. International Journal for Numerical Methods in Engineering 2009; DOI: 10.1002/nme.2659

[15] Gautier F., Gilbert J., Dalmont J.-P., Picó Vila R., Wave propagation in a fluid filled rubber tube: Theoretical and experimental results for Korteweg's wave. Acta Acustica united with Acustica 2007; **93** (3): 333-344.

[16] ANSYS Release 12 documentation.

DISPERSION ANALYSIS OF A STRAIN-RATE DEPENDENT DUCTILE-TO-BRITTLE TRANSITION MODEL

HARM ASKES[1], JUHA HARTIKAINEN[2], KARI KOLARI[3], and REIJO KOUHIA[2]

[1] The University of Sheffield, Department of Civil and Structural Engineering Mappin Street, Sheffield, S1 3JD, UK
[2] Helsinki University of Technology, Structural Mechanics, P.O. Box 2100, FIN-02015 TKK
[3] VTT Technical Research Center of Finland, P.O. Box 1000, FIN-02044 VTT

ABSTRACT

Most materials exhibit rate-dependent inelastic behaviour. Increasing strain-rate usually increases the yield stress thus enlarging the elastic range. However, the ductility is gradually lost, and for some materials there exists a rather sharp transition strain-rate after which the material behaviour is completely brittle.

In this paper, a dispersion analysis of a simple phenomenological constitutive model for ductile-to-brittle transition of rate-dependent solids is presented. The model is based on consistent thermodynamic formulation using proper expressions for the Helmholtz free energy and the dissipation potential. In the model, the dissipation potential is additively split into damage and visco-plastic parts and the transition behaviour is obtained using a stress dependent damage potential.

1 INTRODUCTION

A large number of engineering materials, such as metals, polymers, concrete, soils and rock, can show reduction in the load carrying capacity accompanied by increasing localised deformations after the ultimate load is reached. If this phenomenon is considered as material property, it will lead to a negative slope of the stress-strain diagram, which is known as strain softening.

A demerit pertaining to strain-softening models for classical continua is that they result in problems which are not well-posed in general. The field equations of motion lose hyperbolicity and become elliptic as soon as strain softening occurs. The domain is split into an elliptic part, in which the waves are not able to propagate, and into a hyperbolic part with propagating waves. In static and quasi-static problems, localisation of deformation is usually understood as a synonym to the loss of ellipticity of the underlying rate-boundary value problem. When such problems are solved numerically, the solution of the localisation zone of zero thickness can result in mesh sensitivity. A simple remedy is to include viscous effects in the plastic model as proposed in [1]. Other improvements, e.g. [2, 3, 4, 5], are also possible. However, they usually involve additional field unknowns which make numerical computations more time-consuming. Also, the physical interpretation of the additional boundary conditions can be ambiguous.

In this study, a phenomenological model, which is capable of describing the strain-rate dependent ductile-to-brittle transition, is analysed. The ductile behaviour is considered as a viscoplastic feature, whereas the strain softening behaviour, after reaching the transition strain-rate, is dealt with

a continuum damage model. A dispersion analysis of the linearized equations of motion is carried out.

2 TRANSITION MODEL

The constitutive equations to model the ductile-to-brittle transition due to increasing strain-rate, are derived using a thermodynamic formulation, in which the material behaviour is described completely through the Helmholz free energy and the dissipation potential in terms of the variables of state and dissipation and considering that the Clausius-Duhem inequality is satisfied [6]. Detailed derivation of the model can be found in ref. [7]. The particular choice presented in ref. [7] can be described in a uniaxial case by the following constitutive equations, relating the stress σ, the elastic and inelastic strains, ϵ^{e}, ϵ^{i}, and the integrity or continuity, β as

$$\sigma = \beta E \epsilon^{\mathrm{e}} = \beta E \left(\epsilon - \epsilon^{\mathrm{i}}\right), \tag{1}$$

$$\frac{\mathrm{d}\epsilon^{\mathrm{i}}}{\mathrm{d}t} = \left[\frac{\varphi_{\mathrm{d}}}{(t_{\mathrm{vp}}^{\mathrm{ps}}\eta)^n \beta\sigma_{\mathrm{r}}}\left(\frac{|\sigma|}{\beta\sigma_{\mathrm{r}}}\right)^{np-1} + \frac{1}{t_{\mathrm{vp}}^{\mathrm{ps}}\beta}\left(\frac{|\sigma|}{\beta\sigma_{\mathrm{r}}}\right)^{p}\right] \operatorname{sign}\left(\frac{\mathrm{d}\epsilon}{\mathrm{d}t}\right), \tag{2}$$

$$\frac{\mathrm{d}\beta}{\mathrm{d}t} = -\frac{\varphi_{\mathrm{tr}}}{t_{\mathrm{d}}\beta}\left(\frac{Y}{Y_{\mathrm{r}}}\right)^{r}, \tag{3}$$

where the damage and transition parts of the dissipation potential are

$$\varphi_{\mathrm{d}} = \frac{1}{r+1}\frac{Y_{\mathrm{r}}}{t_{\mathrm{d}}\beta}\left(\frac{Y}{Y_{\mathrm{r}}}\right)^{r+1}, \tag{4}$$

$$\varphi_{\mathrm{tr}} = \frac{1}{pn}\left[\frac{1}{t_{\mathrm{vp}}^{\mathrm{ps}}\eta}\left(\frac{|\sigma|}{\beta\sigma_{\mathrm{r}}}\right)^{p}\right]^{n}. \tag{5}$$

The thermodynamic force Y, conjugate to the integrity flux is expressed as

$$Y = \frac{1}{2}E(\epsilon^{\mathrm{e}})^2 = \frac{1}{2E}\left(\frac{\sigma}{\beta}\right)^2. \tag{6}$$

The integrity β is related to the familiar damage parameter D by

$$\beta = 1 - D. \tag{7}$$

Parameters t_{d} and r, concern the damage evolution, the transition strain rate η and the exponent n the transition phase, and parameters $t_{\mathrm{vp}}^{\mathrm{ps}}$ and p the viscous behaviour. In addition E is the Young's modulus. The reference values σ_{r} and Y_{r} are arbitrary and here the following value for Y_{r} is chosen

$$Y_{\mathrm{r}} = \frac{\sigma_{\mathrm{r}}^2}{2E} = \frac{1}{2}E\epsilon_{\mathrm{r}}^2, \quad \text{where} \quad \epsilon_{\mathrm{r}} = \frac{\sigma_{\mathrm{r}}}{E}. \tag{8}$$

The transition function, φ_{tr}, deals with the change in the mode of deformation when the strain-rate $\mathrm{d}\epsilon^{\mathrm{i}}/\mathrm{d}t$ increases. In the viscous part, an overstress type of viscoplasticity [8, 9, 10] and the principle of strain equivalence [11, 12] are applied. The "pseudo"-relaxation time $t_{\mathrm{vp}}^{\mathrm{ps}}$ is related to the true relaxation time t_{vp} as

$$t_{\mathrm{vp}} = \epsilon_{\mathrm{r}} t_{\mathrm{vp}}^{\mathrm{ps}}. \tag{9}$$

The exponents $r, p \geq 0$ and $n \geq 1$ are dimensionless.

3 DISPERSION ANALYSIS

3.1 Non-dimensional form

Dispersion is the observation that harmonic waves, with a different wave length or frequency, propagate with different velocities. The ability to transform the shape of waves seems a necessary condition for continua to capture localisation phenomena. In a classical strain-softening solid, the waves are not dispersive, which means that the continuum is not able to transform propagating waves into stationary localisation waves [4]. In the dispersion analysis, a single linear harmonic wave is considered and the displacement field u for an infinitely long 1-D continuum has the form

$$u(x,t) = A\exp\left[i(kx - \omega t)\right], \tag{10}$$

in which k is the wave number and ω is the angular frequency.

The equation of motion for a uniform bar is

$$\rho\frac{\mathrm{d}^2u}{\mathrm{d}t^2} - \frac{\mathrm{d}\sigma}{\mathrm{d}x} = 0, \tag{11}$$

where ρ is the mass density of the material. For the dispersion analysis, the equations (11) and (1)-(3) are written in a non-dimensional form by defining the following non-dimensional quantities:

$$\tau = t/t_{\mathrm{e}}, \quad t_{\mathrm{e}} = L/c_{\mathrm{e}}, \quad \text{where} \quad c_{\mathrm{e}} = \sqrt{E/\rho}, \tag{12}$$

$$\xi = x/L, \quad \bar{u} = u/L, \quad s = \sigma/\sigma_{\mathrm{r}}, \tag{13}$$

where L is a typical characteristic length of the bar, and c_{e} is the speed of an elastic wave. In addition, it is convenient to define the relative strain

$$e = \epsilon/\epsilon_{\mathrm{r}}. \tag{14}$$

The following non-dimensional times are also used

$$\tau_{\mathrm{vp}} = t_{\mathrm{vp}}/t_{\mathrm{e}}, \quad \tau_{\mathrm{vp}}^{\mathrm{ps}} = t_{\mathrm{vp}}^{\mathrm{ps}}/t_{\mathrm{e}}, \quad \tau_{\mathrm{d}} = t_{\mathrm{d}}/t_{\mathrm{e}}. \tag{15}$$

Using the non-dimensional quantities, the equation of motion (11) takes the form

$$\ddot{\bar{u}} - \epsilon_{\mathrm{r}}s' = 0, \quad \text{where} \quad \ddot{\bar{u}} = \frac{\mathrm{d}^2\bar{u}}{\mathrm{d}\tau^2} \quad \text{and} \quad s' = \frac{\mathrm{d}s}{\mathrm{d}\xi}. \tag{16}$$

In the sequel, the superimposed dot represents the derivative w.r.t. the non-dimensional time τ and the prime the derivative w.r.t. the non-dimensional spatial coordinate ξ. If needed, the superimposed circle will denote the derivative w.r.t. real time, i.e.

$$\overset{\circ}{\epsilon} = \frac{\mathrm{d}\epsilon}{\mathrm{d}t}. \tag{17}$$

The constitutive equations (1)-(3) take the form

$$s = {\epsilon_{\mathrm{r}}}^{-1}\beta\epsilon^{\mathrm{e}}, \tag{18}$$

$$\dot{\epsilon}^{\mathrm{i}} = f(\beta, s), \tag{19}$$

$$\dot{\beta} = g(\beta, s) \quad \text{or} \quad \dot{\beta} = \tilde{g}(\beta, \epsilon^{\mathrm{e}}), \tag{20}$$

and the non-dimensional form of the wave is

$$\bar{u}(\xi,\tau) = \bar{A}\exp[i(\bar{k}\xi - \bar{\omega}\tau)]. \tag{21}$$

3.2 Viscous case

In the absense of damage the constitutive equations (1)-(3) reduce to

$$\dot{s} = {\epsilon_{\mathrm{r}}}^{-1}(\dot{\epsilon} - \dot{\epsilon}^{\mathrm{i}}), \tag{22}$$

$$\dot{\epsilon}^{\mathrm{i}} = \frac{1}{\tau_{\mathrm{vp}}^{\mathrm{ps}}} s^p. \tag{23}$$

In the equation of motion (16), the divergence of the stress at an arbitrary stress state s_* is

$$\dot{s}' = {\epsilon_{\mathrm{r}}}^{-1}\dot{\epsilon}' - \frac{p}{\epsilon_{\mathrm{r}}\tau_{\mathrm{vp}}^{\mathrm{ps}}} s_*^{p-1}s' = \epsilon_{\mathrm{r}}\dot{\epsilon} - as', \quad \text{where} \quad a = \frac{p}{\tau_{\mathrm{vp}}} s_*^{p-1}. \tag{24}$$

Taking time derivative of the equation of motion (16) and substituting the kinematical relation $\epsilon = \bar{u}'$ into the constitutive equations will result in the partial differential equation

$$\dddot{\bar{u}} - \dot{\bar{u}}'' + a\ddot{\bar{u}} = 0. \tag{25}$$

Substituting the waveform (21) into the equation (25) gives

$$i\bar{\omega}(\bar{\omega}^2 - \bar{k}^2) - a\bar{\omega}^2 = 0. \tag{26}$$

This equation can only be satisfied if the wavenumber is complex, i.e. $\bar{k} = \bar{k}_{\mathrm{r}} + \bar{\alpha}i$, which means that the harmonic wave is attenuated exponentially when traversing through the bar as

$$\bar{u}(\xi, \tau) = \bar{A}\exp(-\bar{\alpha}\xi)\exp[i(\bar{k}_{\mathrm{r}}\xi - \bar{\omega}\tau)]. \tag{27}$$

This will result in the dispersion relation

$$i\bar{\omega}(\bar{\omega}^2 - \bar{k}_{\mathrm{r}}^2 + \bar{\alpha}^2) + 2\bar{\omega}\bar{\alpha}\bar{k}_{\mathrm{r}} - a\bar{\omega}^2 = 0, \tag{28}$$

which has a solution

$$\bar{\omega} = \frac{\bar{k}_{\mathrm{r}}}{\sqrt{1 + \frac{1}{4}(a/\bar{k}_{\mathrm{r}})^2}}, \tag{29}$$

$$\bar{\alpha} = \frac{a}{\sqrt{2}\sqrt{1 + \sqrt{1 + (a/\bar{\omega})^2}}}. \tag{30}$$

The group and phase velocities c_{R} and c, respectively, are defined as

$$c_{\mathrm{R}} = \frac{\mathrm{d}\omega}{\mathrm{d}k_{\mathrm{r}}} = c_{\mathrm{e}}\frac{\mathrm{d}\bar{\omega}}{\mathrm{d}\bar{k}_{\mathrm{r}}} \quad \text{and} \quad c = \frac{\omega}{k_{\mathrm{r}}} = c_{\mathrm{e}}\frac{\bar{\omega}}{\bar{k}_{\mathrm{r}}}, \tag{31}$$

Notice that the group velocity is now larger than the phase velocity, a situation which is referred to as anomalous disperison ([13], p. 218).

The phase and group velocities and the damping coefficient as a function of the wavenumber k_{r} are shown in fig. 1 with different relative relaxation times and values of the exponent p at state $\sigma = \sigma_{\mathrm{r}}$. It can be seen that the waves are dispersive and the long waves are slowed down while the short waves are damped. Notice that the damping factor $\bar{\alpha}$ has the limit

$$\lim_{\bar{\omega}\to\infty} \bar{\alpha} = \tfrac{1}{2}a = \frac{p}{2\tau_{\mathrm{vp}}} s_*^{p-1}. \tag{32}$$

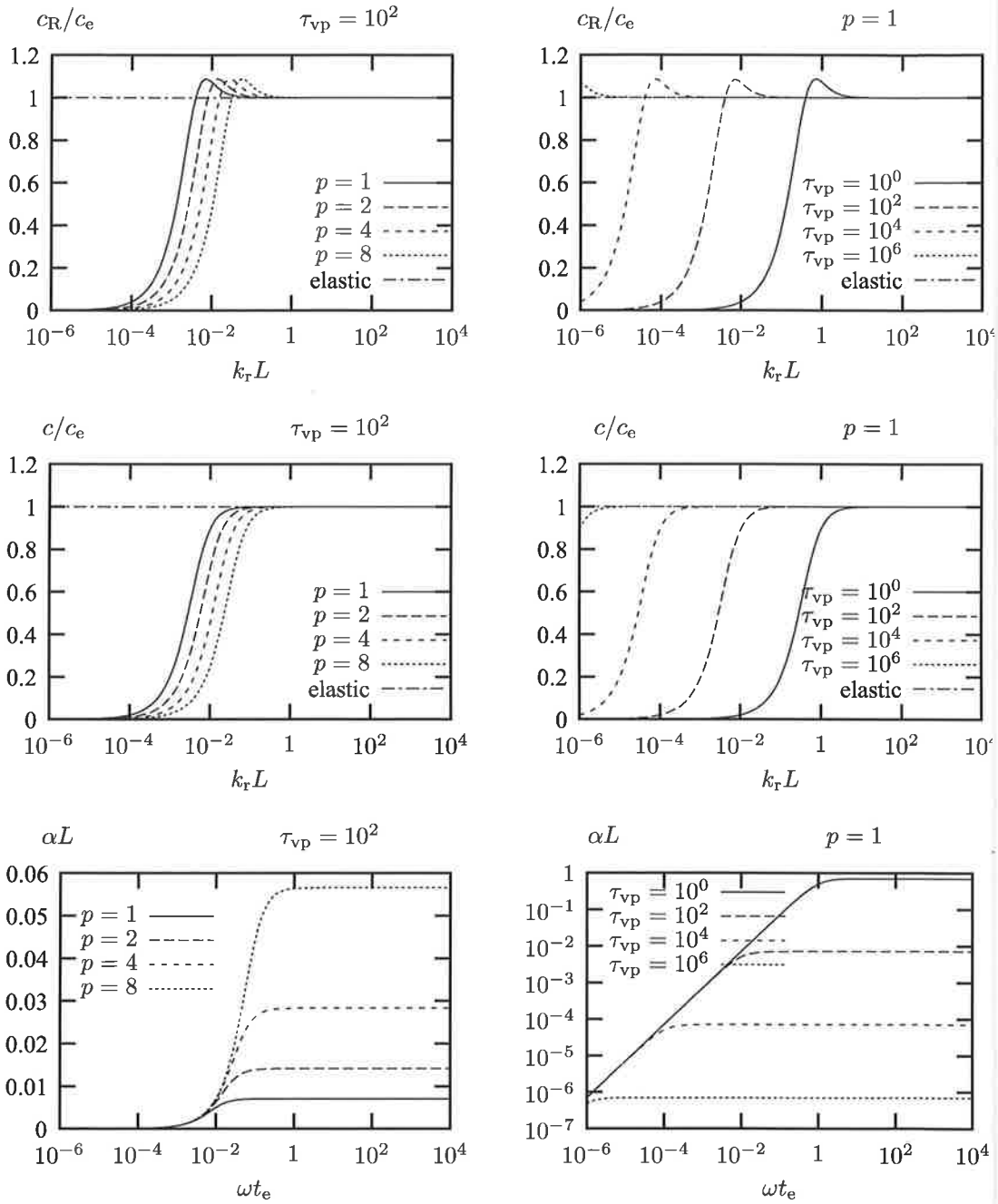

Figure 1: Viscous bar; group and phase velocity as a function of wavenumber and damping as a function of angular frequency.

3.3 Elasticity with damage

In the absense of viscous component the constitutive equations (1)-(3) reduce to

$$s = {\epsilon_\mathrm{r}}^{-1}\beta\epsilon = \beta e, \tag{33}$$

$$\dot{\beta} = -\frac{1}{\tau_\mathrm{d}}\beta^{-2r-1}s^{2r}, \tag{34}$$

and the non-dimensional equation of motion, linearized at state β_*, s_* is

$$\ddot{\bar{u}} - \epsilon_\mathrm{r} s' = \ddot{\bar{u}} - \epsilon_\mathrm{r}(\beta_*\dot{e}' + e_*\beta') = 0. \tag{35}$$

Divergence of the integrity rate is

$$\dot{\beta}' = g_1\beta' + g_2 s' = g_1\beta' + g_2{\epsilon_\mathrm{r}}^{-1}\ddot{\bar{u}}, \tag{36}$$

where

$$g_1 = \frac{2r+1}{\tau_\mathrm{d}}\beta_*^{-2r-2}s_*^{2r} \quad \text{and} \quad g_2 = -\frac{2r}{\tau_\mathrm{d}}\beta_*^{-2r-1}s_*^{2r-1}. \tag{37}$$

The elimination of β' results in

$$\dddot{\bar{u}} - h_0\dot{\bar{u}}'' - h_1\ddot{\bar{u}} + h_2\bar{u}'' = 0, \tag{38}$$

where

$$h_0 = \beta_*, \tag{39}$$

$$h_1 = g_1 + s_*\beta_*^{-1}g_2 = {\tau_\mathrm{d}}^{-1}\beta_*^{-2r-2}s_*^{2r}, \tag{40}$$

$$h_2 = \beta_* g_1 = (2r+1){\tau_\mathrm{d}}^{-1}\beta_*^{-2r-2}s_*^{2r}. \tag{41}$$

Substituting the expression for damped harmonic wave (27) into (38), yields

$$i\left[\bar{\omega}^3 - h_0\bar{\omega}(\bar{k}_\mathrm{r}^2 - \bar{\alpha}^2) - 2h_2\bar{k}_\mathrm{r}\bar{\alpha}\right] + 2h_0\bar{\omega}\bar{k}_\mathrm{r}\bar{\alpha} + h_1\bar{\omega}^2 - h_2(\bar{k}_\mathrm{r}^2 - \bar{\alpha}^2) = 0. \tag{42}$$

Since both the real and imaginary part of this expression has to vanish, it will result in two equations from which the wavenumber $\bar{k}_\mathrm{r}$ and the damping coefficient $\bar{\alpha}$ can be solved. After manipulations, resulting equations are

$$\bar{k}_\mathrm{r}^{\,4} - a_1\bar{k}_\mathrm{r}^2 - a_0^2\bar{\omega}^2 = 0, \quad \bar{\alpha} = a_0\bar{\omega}/\bar{k}_\mathrm{r}, \tag{43}$$

where

$$a_0 = \frac{(h_2 - h_0h_1)\bar{\omega}^2}{2(h_0^2\bar{\omega}^2 + h_2^2)}, \qquad h_2 - h_0h_1 = \frac{2r}{\tau_\mathrm{d}\beta_*}\left(\frac{s_*}{\beta_*}\right)^{2r}, \tag{44}$$

$$a_1 = h_0^{-1}(\bar{\omega}^2 - 2h_2a_0). \tag{45}$$

Clearly the term a_0 is positive, but the sign of the term a_1 depends on the state. Thus, the solution of (43) can be written as

$$\bar{k}_\mathrm{r}^2 = \tfrac{1}{2}|a_1|\left(\sqrt{1 + 4(a_0/a_1)^2} + \mathrm{sign}(a_1)\right). \tag{46}$$

The limit for the damping factor $\bar{\alpha}$ is

$$\lim_{\bar{\omega}\to\infty}\bar{\alpha} = \frac{h_2 - h_0h_1}{2h_0^2} = \frac{r}{\tau_\mathrm{d}\beta_*^3}\left(\frac{s_*}{\beta_*}\right)^{2r}. \tag{47}$$

The phase and group velocity as a function of the wavenumber at three instantaneous states are shown in fig. 2 for a constant strain rate loading case, the solution of which is:

$$\beta = \sqrt{1 - \frac{2}{2r+1}\frac{\epsilon_{\mathrm{r}}}{\overset{\circ}{\epsilon}_0 t_{\mathrm{d}}} e^{2r+1}}, \tag{48}$$

and $\overset{\circ}{\epsilon}_0$ is the constant loading rate. In the figure, the following value is used $\overset{\circ}{\epsilon}_0 t_{\mathrm{d}} = 10^{-2}$. The three states shown are (a) 19 % below the peak load ($e_* = 1.0, \beta_* = 0.9944, s_* = 0.9944$), (b) at the peak load ($e_* = 1.364, \beta_* = 0.9045, s_* = 1.234$) and (c) a softening region ($e_* = 1.5, \beta_* = 0.757, s_* = 1.135$). The damping coefficient at these three stages is shown in fig. 4. It can be seen that the elastic damaging bar exhibits normal dispersion, i.e. $c_{\mathrm{R}} < c$.

At the peak load, the effect of parameter variations on the phase velocity is shown in fig.3 and on the damping coefficient in fig. 4 on the right-hand-side. The peak value of stress and the corresponding integrity value are

$$s_* = s_{\mathrm{peak}} = \left(\frac{2r+1}{2r+3}\right)^{\frac{2r+3}{4r+2}} \left(\frac{\overset{\circ}{\epsilon}_0 t_{\mathrm{d}}}{\epsilon_{\mathrm{r}}}\right)^{\frac{1}{2r+1}}, \quad \beta_* = \sqrt{\frac{2r+1}{2r+3}}. \tag{49}$$

3.4 Full model

The constitutive equations (1)-(3) reduce to

$$s = {\epsilon_{\mathrm{r}}}^{-1} \beta \epsilon^{\mathrm{e}} = \beta e^{\mathrm{e}}, \tag{50}$$

$$\dot{e}^{\mathrm{i}} = f(\beta, s) = \gamma_1 \beta^{-np-2r-3} s^{np+2r+1} + \gamma_2 \beta^{-p-1} s^p, \tag{51}$$

$$\dot{\beta} = g(\beta, s) = \gamma_3 \beta^{-np-2r-1} s^{pn+2r}, \tag{52}$$

where

$$\gamma_1 = \left[2(r+1)\tau_{\mathrm{d}}(t_{\mathrm{vp}}^{\mathrm{ps}}\eta)^n\right]^{-1}, \quad \gamma_2 = \tau_{\mathrm{vp}}^{-1} \quad \text{and} \quad \gamma_3 = -[pn\tau_{\mathrm{d}}(t_{\mathrm{vp}}^{\mathrm{ps}}\eta)^n]^{-1}. \tag{53}$$

Divergence of the inelastic strain rate and the integrity rate, linearized at state (β_*, s_*) can be represented as

$$\dot{e}^{\mathrm{i}\prime} = \frac{\partial f}{\partial \beta}|_* \beta' + \frac{\partial f}{\partial s}|_* s' = f_1 \beta' + f_2 s' = f_1 \beta' + f_2 \epsilon_{\mathrm{r}}^{-1} \ddot{u}, \tag{54}$$

$$\dot{\beta}' = \frac{\partial g}{\partial \beta}|_* \beta' + \frac{\partial g}{\partial s}|_* s' = g_1 \beta' + g_2 s' = g_1 \beta' + g_2 \epsilon_{\mathrm{r}}^{-1} \ddot{u}. \tag{55}$$

Eliminating β' will finally result in the equation

$$\dddot{u} - h_0 \ddot{u}'' - h_1 \dddot{u} + h_2 \dot{u}'' - h_3 \ddot{u} = 0, \tag{56}$$

where

$$h_0 = \beta_*, \tag{57}$$

$$h_1 = g_1 + (s_*/\beta_*) g_2 - \beta_* f_2, \tag{58}$$

$$h_2 = \beta_* g_1, \tag{59}$$

$$h_3 = \beta_* (g_1 f_2 - f_1 g_2). \tag{60}$$

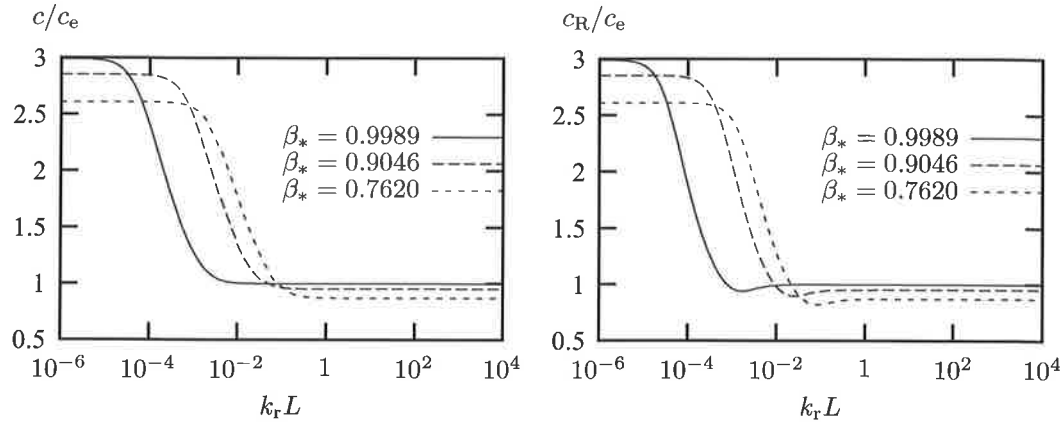

Figure 2: Elastic damaging bar; phase and group velocity as a function of wavenumber at different stages of the loading.

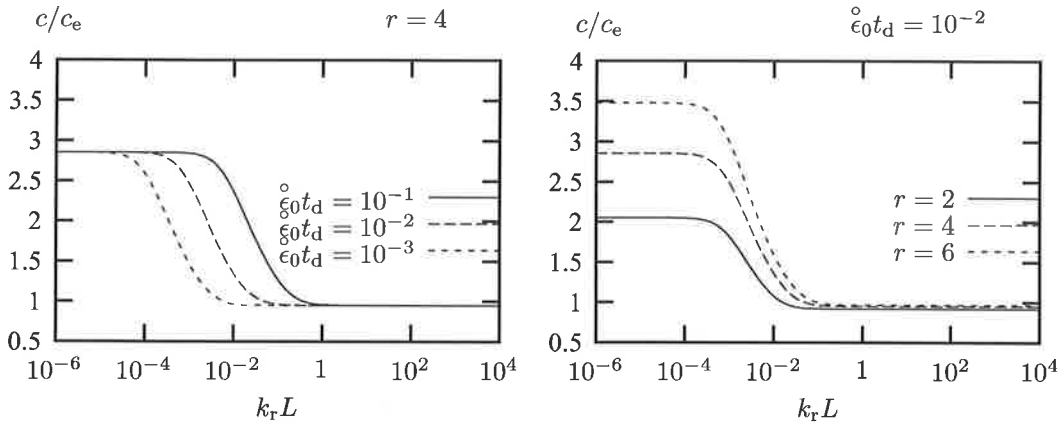

Figure 3: Elastic damaging bar; phase velocity as a function of wavenumber at the peak load with changing parameters.

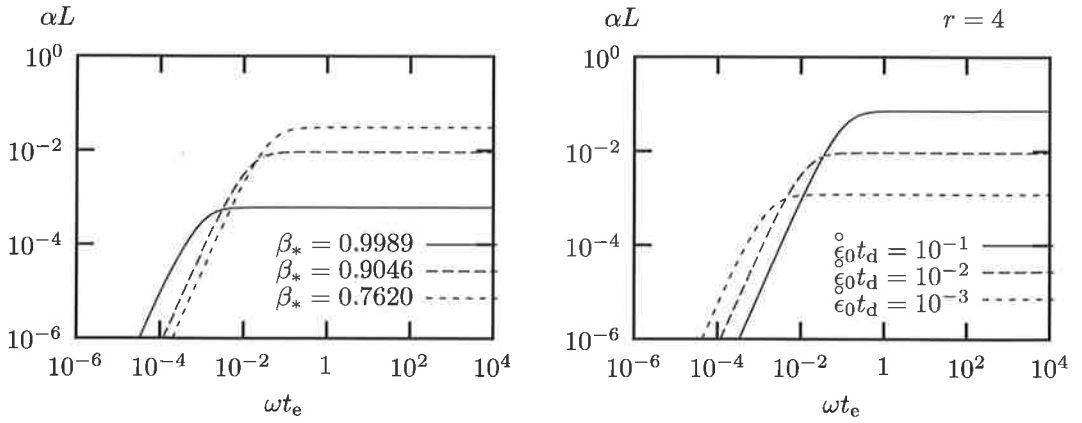

Figure 4: Elastic damaging bar; damping coefficient as a function of frequency at different stages of the loading: (l.h.s.) and with different values of the t_d-parameter at the peak load.

Table 1: Full transition model, the seven stages considered.

	1	2	3	4	5	6	7
e	0.100	0.400	0.700	0.900	1.100	1.500	2.500
s	0.100	0.400	0.697	0.888	1.067	1.110	0.718
β	1.000	1.000	1.000	1.000	0.999	0.913	0.612

The wavenumber $\bar{k}_{\mathrm{r}}$ and the damping coefficient $\bar{\alpha}$ can be solved from equations (43). In the full transition model, the coefficients in (43) have the forms

$$a_0 = \frac{(h_2 - h_0 h_1)\bar{\omega}^2 + h_2 h_3}{2(h_0^2\bar{\omega}^2 + h_2^2)}, \tag{61}$$

$$a_1 = h_0^{-1}(\bar{\omega}^2 - 2h_2 a_0 + h_3). \tag{62}$$

The behaviour of the coefficient a_0 for the full transition model (61) is different in comparison to the pure damage model (44). For the damage model a_0 is a positive, monotonously increasing function with the frequency attaining the zero value at vanishing frequency. In the full transition model, a_0 can have either positive or negative values. The limit values of a_0 are

$$a_{0,0} = \lim_{\bar{\omega}\to 0} a_0(\bar{\omega}) = \tfrac{1}{2}h_2^{-1}h_3 = \tfrac{1}{2}(f_2 - g_1^{-1}f_1 g_2), \tag{63}$$

$$a_{0,\infty} = \lim_{\bar{\omega}\to\infty} a_0(\bar{\omega}) = \tfrac{1}{2}h_0^{-1}(h_0^{-1}h_2 - h_1) = \tfrac{1}{2}(f_2 - \beta_*^{-2}s_* g_2) > 0. \tag{64}$$

The value of $a_{0,0}$ can be negative, which means that there exist a critical frequency $\bar{\omega}_{\mathrm{c}}$ when a_0 is zero, which gives zero value also for the wavenumber $\bar{k}_{\mathrm{r}}$, since it turns out that the coefficient a_1 is also negative. The special case of vanishing $\bar{k}_{\mathrm{r}}$ results the following form for the motion

$$\bar{u}(\xi,\tau) = \bar{A}\exp(-\bar{\alpha}\xi)\exp(-i\bar{\omega}_{\mathrm{c}}\tau), \tag{65}$$

which indicates a spatially varying but non-propagating disturbance.

In fig. 5, the stress-strain and integrity-strain curves are shown for a constant strain rate loading. The material parameters are those given in ref. [7], i.e. Young's modulus $E = 40$ GPa, Poisson's ratio $\nu = 0.3$, reference stress $\sigma_{\mathrm{r}} = 20$ MPa, the viscoplastic pseudo relaxation time $t_{\mathrm{vp}}^{\mathrm{ps}} = 1000$ s and characteristic time for damage evolution $t_{\mathrm{d}} = 1$ s and the transition strain rate $\eta = 10^{-3}$ s^{-1}. All the exponents p, r and n have the value of 4. The loading strain-rate is ten times the transition strain rate.

The dispersion relation, phase velocity as and damping factor are presented in figs. 6-7 at the seven different stages indicated in fig. 5. The corresponding values of strain, stress and continuity are given in Table 1. The evolution of the critical frequency as a function of strain for different loading rates is shown in fig.8.

4 DISCUSSION AND CONCLUDING REMARKS

A dispersion analysis for a phenomenological constitutive model describing the ductile-to-brittle transition due to increased strain-rate is presented. Depending on the loading rate, the behaviour resembles either the behaviour of a viscous solid or an elastic-damaging solid. At strain-rates smaller

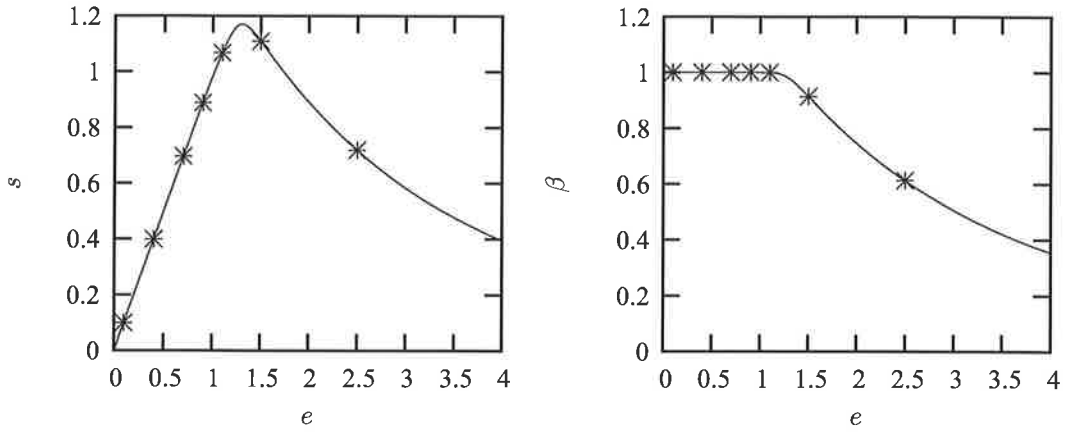

Figure 5: Stress-strain and integrity-strain curves. The seven considered stages are marked.

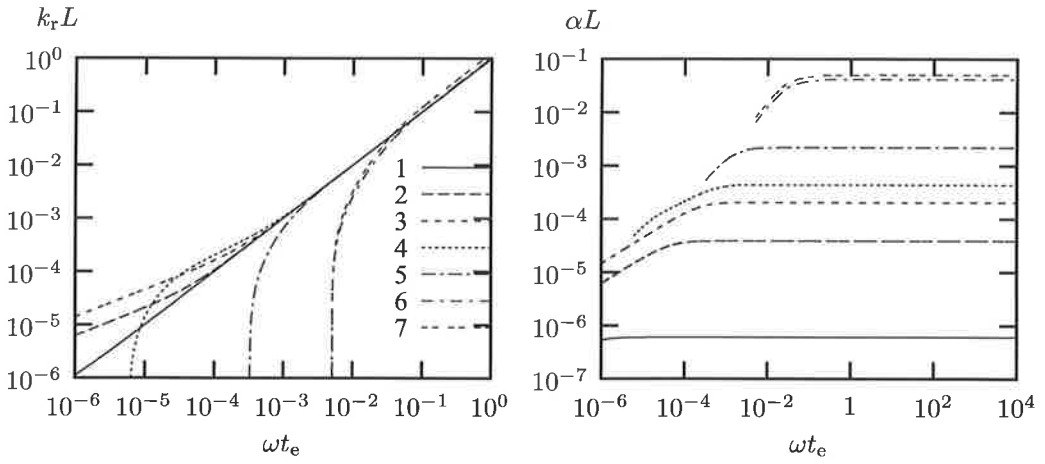

Figure 6: Full transition model; dispersion relation and the damping coefficient α as a function of frequency at different stages of the loading.

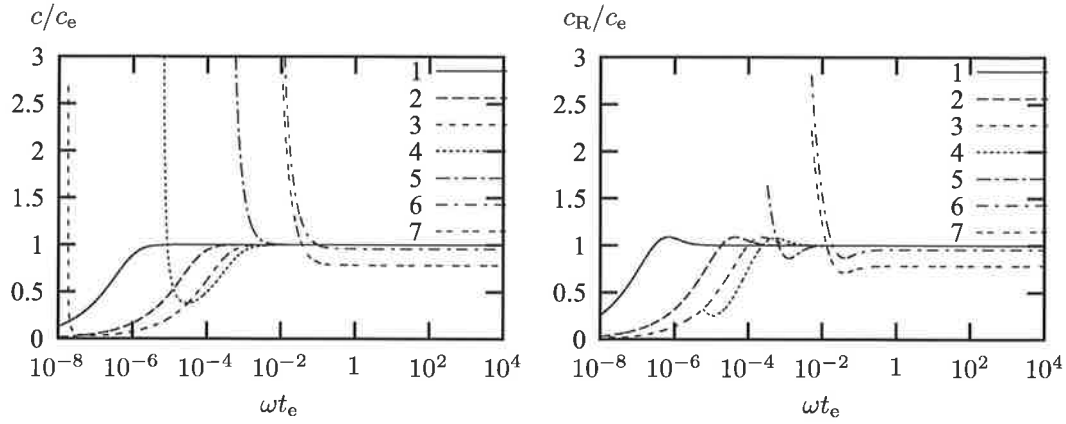

Figure 7: Full transition model; phase and group velocity c as a function of frequency at different load points.

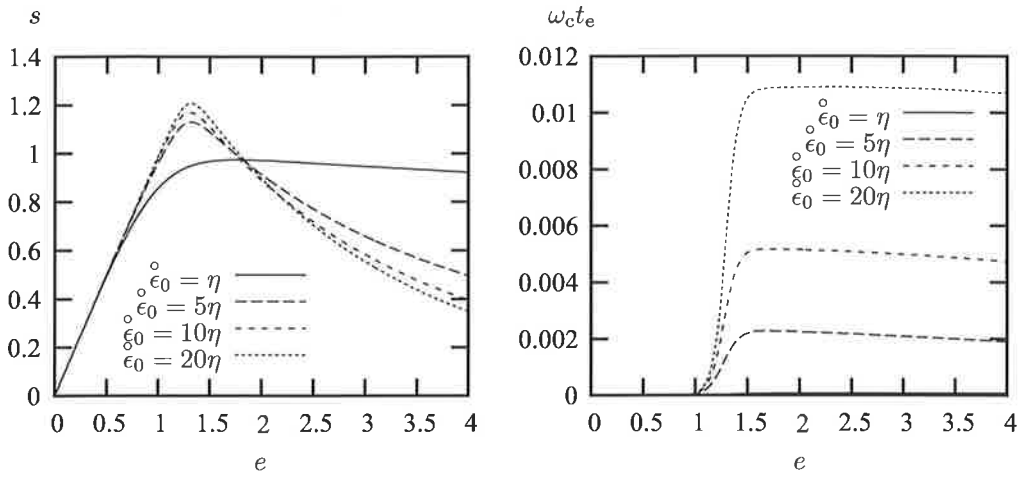

Figure 8: Stress-strain relation using different loading rate (l.h.s.) and evolution of the cut-off frequency with these loading rates (r.h.s.).

than the transition strain rate the behaviour is like in viscous solid; the phase- and group velocity approach the elastic wave speed at high frequences and vanish in the low frequency range. The dispersion is in such case of anomalous type. This is also true for higher strain-rates at the beginning of a loading process. For strain-rates higher than the transition strain-rate and states in the softening range, the behaviour is like elastic-damaging solid and the dispersion is of normal type. However, a rapidly growing critical frequency emerges near the maximum stress. At the intermediate states just before the peak load the dispersion is either anomalous or normal depending on the frequency (wavelength). As expected, the model is not able to slow down the high frequency components on the softening range. To obtain a model with such behaviour a higher-order continuum model is required [2].

At frequences higher than the critical frequency, the dispersion resembles a strain-softening viscoplastic solid. It is well known that viscosity introduces the material length scale in the model. An approximation to the width of the material length scale is (linearized from eq. (6.42) in Ref. [5]) $l_{\mathrm{mat}} \approx c_{\mathrm{s}} t_{\mathrm{vp}}^{\mathrm{ps}} \sigma_{\mathrm{r}} / (\frac{3}{4} G - h)$, where G is the shear modulus and $c_{\mathrm{s}} = \sqrt{G/\rho}$ is the elastic shear wave velocity and $-h$ is the softening modulus ($p = 1$). It should be mentioned that for softening viscoplastic solid, the width of the localisation zone could be dictated by the size of an imperfection. In a quasi-static loading the width of the localisation zone growns with increasing strain rate and enlarging material parameter p [14]. For the transition model for which the softening behaviour is due to the damage evolution, the situation might be different and is under investigation.

ACKNOWLEDGMENTS

This research has been supported in part by the Academy of Finland, decision number 121778.

REFERENCES

[1] A. Needleman. Material rate dependence and mesh sensitivity in localization problems, *Comp. Meth. Appl. Mech. Engng.*, **67**, 69–85 (1988).

[2] H. Askes, A.V. Metrikine. Higher-order continua derived from discrete media: continualisation aspects and boundary conditions. *Int. J. Solids Struct.* **42**(1), 187–202 (2005).

[3] A.C. Eringen. *Microcontinuum Field Theories, I. Foundations and Solids*, Springer, New-York, 1999.

[4] L.J. Sluys. *Wawe propagation, localisation and dispersion in softening solids*, PhD thesis, Department of Civil Engineering, Delft University of Technology, 1992.

[5] W. Wang. *Stationary and propagative instabilities in metals – a computational point of view*, PhD thesis, Department of Civil Engineering, Delft University of Technology, 1997.

[6] M. Frémond. *Non-Smooth Thermomechanics*, Springer, Berlin, 2002.

[7] S. Fortino, J. Hartikainen, K. Kolari, R. Kouhia and T. Manninen. A constitutive model for strain-rate dependent ductile-to-brittle transition. *The IX Finnish Mechanics Days*, 13-14.6.2006, Lappeenranta, Finland R. von Hertzen and T. Halme (eds.), pp. 652–662.

[8] P. Perzyna. Fundamental problems in viscoplasticity, *Advances in Applied Mechanics*, **9**, 243–377 (1966).

[9] G. Duvaut and L.J. Lions. *Inequalities in Mechanics and Physics*, Springer, Berlin, 1972.

[10] M. Ristinmaa and N.S. Ottosen. Consequences of dynamic yield surface in viscoplasticity, *Int. J. Solids Structures*, **37**, 4601–4622 (2000).

[11] J. Lemaitre, J.-L. Chaboche. *Mechanics of Solid Materials*, Cambridge University Press, 1990.

[12] J. Lemaitre. *A Course on Damage Mechanics*, Springer-Verlag, Berlin, 1992.

[13] J.D. Achenbach. *Wave propagation in elastic solids*. North-Holland series in applied mathematics and mechanics, Vol 16, 1973.

[14] K. Kolari, R. Kouhia and T. Kärnä. On viscoplastic regularization of strain softening solids. *The VIII Finnish Mechanics Days*, 12-13.6.2003, Espoo, Finland P. Råback, K. Santaoja and R. Stenberg (eds.), pp. 489–496.

VISKOPLASTIS-VAURIOMEKAANINEN MATERIAALIMALLI KIVEN RIKKOUTUMISEN MALLINNUKSEEN KALLIONPORAUKSESSA

TIMO SAKSALA
Konstruktiotekniikka
Tampereen teknillinen yliopisto
PL 589 FIN-33101, TAMPERE

TIIVISTELMÄ

Tutkimuksessa esitetään vauriomekaniikkaan ja viskoplastisuusteoriaan perustuva materiaalimalli sekä elementtimenetelmään perustuva proseduuri kiven ja nastan välisen vuorovaikutuksen mallinnukseen iskevässä kallionporauksessa. Materiaalimallissa hauraan vauriotumisen osoittaa yhdistetty Rankine-Drucker-Prager-myötöfunktio. Kiven sitkeää käyttäytymistä kuvaa parabolinen niin sanottu cap-malli, joka sovitetaan sileästi Drucker-Prager-kartioon. Vetotiloissa kiven jäykkyyden ja lujuuden menetystä mallinnetaan isotrooppisella vauriomallilla, ja puristustiloissa pehmenemistä (lujuuden menetystä) hallitsee viskoplastinen pehmenemislaki. Kiven materiaalinen heterogeenisuus mallinnetaan mesoskooppisella tasolla tilastollisesti Weibull-jakaumaa käyttäen menetelmällä, jossa kiven puristus- ja vetolujuus ovat tilastollisia muuttujia. Diskretoidut liikeyhtälöt ratkaistaan eksplisiittisellä aikaintegraattorilla. Porakruunu mallinnetaan jäykkänä kappaleena idealisoimalla se pisteeksi. Nastan ja kiven välinen vuorovaikutus mallinnetaan kontaktimekaniikan keinoin. Kehitettyä menetelmää testataan numeerisin esimerkein materiaalipisteen ja laboratorionäytteen tasolla kolmiaksiaalisessa puristuskokeessa. Lopuksi kiven ja nastan vuorovaikutusta simuloidaan yhden nastan tapauksessa.

JOHDANTO

Kiven rikkoutumisen numeerinen mallinnus on tärkeä ongelma kalliomekaniikassa. Erityisesti kallionporauslaitteita valmistavat yritykset ovat kiinnostuneita porakruunun kiveen aiheuttaman vaurion numeerisesta simuloinnista. Tärkein ongelma on porakruunun nastan ja kiven välisen vuorovaikutuksen mallinnus. Tämä ongelma on monimutkaisuutensa (säröjen suuri määrä ja vauriotyyppien erilaisuus) vuoksi analyyttisten menetelmien ulottumattomissa, joten numeerisen mallinnuksen merkitys on tietotekniikan aikakaudella korostunut. Ongelman ratkaisuun on staattisessa tapauksessa sovellettu elementtimenetelmää [1] ja dynaamisessa tapauksessa elementtimenetelmää [2] ja diskreettien elementtien menetelmää [3] (tässä vain yksi tutkimus kustakin tapauksesta on esimerkiksi mainittu).

Menetelmät ovat enimmäkseen keskittyneet syntyvän jännitystilakentän ratkaisemiseen tai jonkin yksityiskohdan, kuten sivuttaissäröjen kasvun, mallintamiseen. Ne ovat myös usein olleet liian yksinkertaistavia siten, että esimerkiksi ongelman transientti luonne on jätetty huomiotta (kvasistaattinen mallinnus [1]). Lisäksi kuormitusnopeuden vaikutus materiaalin käyttäytymiseen on oletettu merkityksettömäksi [1-3] tai kiven mahdollinen sitkeä käyttäytyminen triaksiaalisessa jännitystilassa porakruunun nastan alla on oletettu merkityksettömäksi [2, 3].

Tässä tutkimuksessa esitetään vauriomekaniikkaan ja viskoplastisuusteoriaan perustuva konstitutiivinen malli, joka periaatteessa kykenee mallintamaan kaikkia dynaamisessa kiven ja nastan vuorovaikutuksessa esiintyviä ilmiöitä. Erityisesti, koska menetelmä perustuu viskoplastisuusteoriaan, se kykenee mallintamaan materiaalin kuormitusnopeudesta riippuvaa dynaamista lujittumista. Viskoplastisuus tarjoaa dynaamisessa kuormituksessa deformaation lokalisaatiorajoittimen, jolloin kenttäongelma säilyy hyvinasetettuna (well-posed).

Kehitetty konstitutiivinen malli, joka implementoidaan elementtimenetelmän avulla, on esitetty lähteessä [4]. Porakruunu oletetaan jäykäksi kappaleeksi, jolloin se voidaan idealisoida pisteeksi. Nastan ja kiven välinen vuorovaikutus mallinnetaan kontaktimekaniikan keinoin. Kontaktireunaehdot käsitellään eksplisiittisen aikaintegroinnin kanssa yhteensopivalla Lagrangen kertojien menetelmän modifikaatiolla. Kenttäyhtälöt ratkaistaan eksplisiittisellä modifioidulla Eulerin aikaintegraattorilla. Äärellisen elementtimallin reunoilla jännitysaaltojen heijastuminen estetään asettamalla reunoille viskoosiin vaimennukseen perustuva heijastamaton reunaehto. Menetelmää testataan materiaalipisteen ja laboratorionäytteen tasolla kolmiaksiaalisessa puristuskokeessa. Lopuksi kiven ja nastan vuorovaikutusta simuloidaan yhden nastan tapauksessa.

KIVEN KONSTITUTIIVINEN MALLI

Viskoplastisuusformulointi

Kiven materiaalimallin viskoplastisen osan formulointiin valitaan Wangin [5] konsistentti viskoplastinen malli, joka tuo kuormitusnopeudesta riippuvuuden mukaan perinteiseen plastisuusteoriaan. Sen perusyhtälöt ovat

$$\begin{aligned} f_{\mathrm{vp}} &= f(\boldsymbol{\sigma}, \kappa, \dot{\kappa}) \\ \dot{\boldsymbol{\varepsilon}}^{\mathrm{vp}} &= \dot{\lambda}\frac{\partial g_{\mathrm{vp}}}{\partial \boldsymbol{\sigma}} \\ f_{\mathrm{vp}} &\le 0, \quad \dot{\lambda} \ge 0, \quad \dot{\lambda} f_{\mathrm{vp}} = 0 \end{aligned} \tag{1}$$

jossa f_{vp} on myötöfunktio, $\boldsymbol{\sigma}$ on jännitystensori, κ ja $\dot{\kappa}$ ovat sisäinen muuttuja ja sen muutosnopeus, g_{vp} on viskoplastinen potentiaali, $\dot{\lambda}$ on viskoplastinen inkrementti ja $\dot{\boldsymbol{\varepsilon}}^{\mathrm{vp}}$ on viskoplastinen venymäinkrementti. Venymä jaetaan klassisen teorian mukaisesti elastiseen ja viskoplastiseen osaan: $\dot{\boldsymbol{\varepsilon}} = \dot{\boldsymbol{\varepsilon}}^{\mathrm{e}} + \dot{\boldsymbol{\varepsilon}}^{\mathrm{vp}}$. Suurin ero perinteiseen plastisuusteoriaan on, että myötöfunktion määrittelemä myötöpinta voi kutistua ja laajentua sen alkuperäiseen asemaan nähden kuormitusnopeudesta riippuen.

Tämän tutkimuksen tarkoituksiin myötöfunktioksi valitaan modifioidusta Rankine-kriteeristä (MR), Drucker-Prager-myötöfunktiosta (DP) sekä parabolisesta cap-funktiosta muodostuva pinta (ks. kuva 1), jotka pääjännitysavaruudessa saavat muodon [4]

$$\begin{aligned} f_{\mathrm{DP}}(\boldsymbol{\sigma}, \kappa_{\mathrm{DP}}, \dot{\kappa}_{\mathrm{DP}}) &= \sqrt{J_2} + \alpha_{\mathrm{DP}} I_1 - k_{\mathrm{DP}} c(\kappa_{\mathrm{DP}}, \dot{\kappa}_{\mathrm{DP}}) \\ f_{\mathrm{MR}}(\boldsymbol{\sigma}, \kappa_{\mathrm{MR}}, \dot{\kappa}_{\mathrm{MR}}) &= \sqrt{\textstyle\sum_{i=1}^{3} \langle \sigma_i \rangle^2} - f_{\mathrm{t}}(\kappa_{\mathrm{MR}}, \dot{\kappa}_{\mathrm{MR}}) \\ f_{\mathrm{Cap}}(\boldsymbol{\sigma}, c, p_{\mathrm{P}}) &= \sqrt{J_2} - C_1(c, p_{\mathrm{P}}) I_1^2 - C_2(c, p_{\mathrm{P}}) I_1 - C_3(c, p_{\mathrm{P}}) \end{aligned} \tag{2}$$

missä $I_1 = \mathrm{tr}(\boldsymbol{\sigma})$ ja $J_2 = \mathrm{dev}(\boldsymbol{\sigma}) : \mathrm{dev}(\boldsymbol{\sigma})$ (deviaattori), σ_i on pääjännitys, c ja f_t ovat koheesio ja vetolujuus, κ_{MR} ja κ_{DP} ovat sisäinen muuttuja vedossa ja puristuksessa vastaavasti, ja p_{P} on paine, joka yhdessä parametrien C_i kanssa määrittelee cap-funktion aseman. Lisäksi kaavoissa (2)

esiintyy DP-parametrit, jotka lausutaan kitkakulman φ avulla siten, että sovitetaan kiven puristuslujuus:

$$\alpha_{\mathrm{DP}} = \frac{2\sin\varphi}{\sqrt{3}(3-\sin\varphi)}, \quad k_{\mathrm{DP}} = \frac{6\cos\varphi}{\sqrt{3}(3-\sin\varphi)} \tag{3}$$

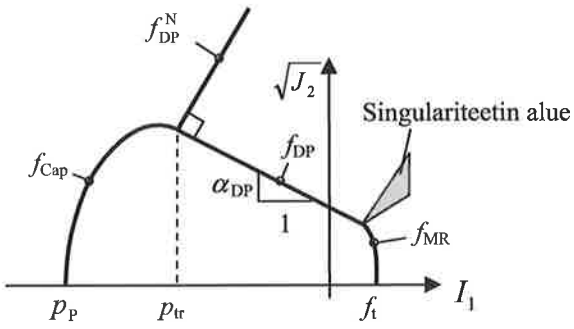

Kuva 1. DP-MR-myötöpinta I_1-$\sqrt{J_2}$ -avaruudessa

Yleisesti ottaen sisäinen muuttuja riippuu plastisesta inkrementistä relaation $\dot{\kappa} = \dot{\lambda} q(\boldsymbol{\sigma}, \kappa)$ mukaisesti, jossa q on relaation välittävä funktio. Tässä q valitaan ykköseksi vetotilassa. Siten vetotilassa plastinen inkrementti ja sisäinen muuttuja voidaan samaistaa: $\lambda_{\mathrm{MR}} = \kappa_{\mathrm{RM}}$. Puristustiloissa määritellään $q_{\mathrm{DP}}(\boldsymbol{\sigma}) = \sqrt{\frac{2}{3}\partial_{\boldsymbol{\sigma}} g_{\mathrm{DP}}(\boldsymbol{\sigma})^{\mathrm{T}} \partial_{\boldsymbol{\sigma}} g_{\mathrm{DP}}(\boldsymbol{\sigma})}$, jossa $\partial_{\boldsymbol{\sigma}}$ tarkoittaa derivaattaa jännityksen suhteen. Nyt lineaariseksi oletettu pehmenemis/lujittumislaki voidaan kirjoitaa muotoon

$$\begin{aligned} c &= c_0 + h_{\mathrm{DP}}\lambda_{\mathrm{DP}} + s_{\mathrm{DP}}\dot{\lambda}_{\mathrm{DP}} \\ f_{\mathrm{t}} &= f_{\mathrm{t0}} + h_{\mathrm{MR}}\lambda_{\mathrm{MR}} + s_{\mathrm{MR}}\dot{\lambda}_{\mathrm{MR}} \end{aligned} \tag{4}$$

jossa c_0 ja f_{t0} ovat koheesion ja vetolujuuden alkuarvot ja jossa on käytetty merkintöjä $h_{\mathrm{DP}} = h_{\mathrm{c}} q_{\mathrm{DP}}(\boldsymbol{\sigma}), s_{\mathrm{DP}} = s_{\mathrm{c}} q_{\mathrm{DP}}(\boldsymbol{\sigma})$, jossa h_{c} ja s_{c} ovat pehmenemis- ja viskositettimoduli. Tässä tutkimuksessa nämä ja vastaavat modulit vetopuolella (merkitään h_{t}, s_{t}) oletetaan vakioiksi materiaalidatan puutteen takia. Yleisesti viskositeettimoduli riippuu kuormitusnopeudesta, joten lineaarisella mallilla (4) ei välttämättä saada realistisia tuloksia. Vakioksi olettaminen kuitenkin säilyttää mallin lineaarisena, jolloin esimerkiksi DP-viskoplastisuustehtävälle löytyy analyyttinen ratkaisu 3D tapauksessa (DP-myötöpinta on suora Haigh-Westergaard-avaruudessa, kuten kuvasta 1 näkyy).

Kiven dilataatiokäyttäytymisen huomioimiseksi puristuskokeessa valitaan tyypillinen viskoplastinen potentiaali $g_{\mathrm{DP}}(\boldsymbol{\sigma}) = \sqrt{J_2} + \beta_{\mathrm{DP}} I_1$ jossa β_{DP} on dilataatioparametri, joka määritellään kuten kaavassa (3), jossa kitkakulma dilataatiokulmalla ψ.

Cap-mallin parametrit ja lujittumislaki

Cap-mallille valitaan geomateriaaleille tyypillisesti käytetty lujittumislaki (hardening law)

$$p_{\mathrm{P}}(\varepsilon_V^{\mathrm{p}}) = \frac{1}{D}\ln(1+\frac{\varepsilon_V^{\mathrm{p}}}{W}) + p_{\mathrm{P0}} \tag{5}$$

jossa $\varepsilon_V^{\mathrm{p}}$ on hydrostaattinen plastinen venymä ja W ja D ovat parametrejä, joiden fysikaalinen merkitys on volumetrinen (plastinen) maksimivenymä, ja muutosnopeus, jolla materiaalin kompaktoituminen (compaction) tapahtuu. Tämän tutkimuksen tarkoituksiin lakia (5) modifioidaan siten, että vain puristus-tyyppinen hydrostaattinen plastinen venymä huomioidaan.

Transitiopaineen p_{tr} oletetaan yleensä liikkuvan jossakin suhteessa paineeseen p_{P} nähden. Tässä sen oletetaan liikkuvan siten, että paraabeli f_{Cap} (ks. kuva 1) säilyttää muotonsa: $p_{\mathrm{tr}} = p_{\mathrm{P}}(\varepsilon_V^{\mathrm{p}})p_{\mathrm{tr0}} / p_{\mathrm{P0}} = p_{\mathrm{P}}(\varepsilon_V^{\mathrm{p}})k_{\mathrm{p}}$, jossa $p_{\mathrm{tr0}}, p_{\mathrm{P0}}$ ovat paineiden $p_{\mathrm{tr}}, p_{\mathrm{P}}$ alkuarvot ja k_{p} on niiden (vakio)suhde.

Jännitysintegrointi ja aktiivisen pinnan määrittely

Jännitysten integrointia (stress return mapping) varten tarvitaan menetelmä aktiivisen pinnan tai prosessin määritykseen. Tätä varten konstruoidaan pääjännitysavaruuteen apupinta, joka Haigh-Westergaard-avaruudessa (ks. kuva 1) on DP-suoran normaali [4]:

$$f_{\mathrm{DP}}^{\mathrm{N}} = \sqrt{J_2} - \alpha_{\mathrm{DP}}^{-1} I_1 - \kappa_{\mathrm{DP}}^{\mathrm{N}}\ , \quad \kappa_{\mathrm{DP}}^{\mathrm{N}} = p_{\mathrm{tr}}(\alpha_{\mathrm{DP}} + \alpha_{\mathrm{DP}}^{-1}) + k_{\mathrm{DP}} c(\lambda_{\mathrm{DP}}, \dot{\lambda}_{\mathrm{DP}}) \tag{6}$$

Nyt aktiivisen prosessin määritys tapahtuu taulukossa 1 esitetyn algoritmin avulla, jossa myötökriteerien arvot on laskettu trial-tilan eli jännityksen $\boldsymbol{\sigma}_{\mathrm{trial}} = \mathbf{E}(\boldsymbol{\varepsilon}_t - \boldsymbol{\varepsilon}_{t-\Delta t}^{\mathrm{vp}})$ avulla.

Taulukko 1. Aktiivisen prosessin määritysalgoritmi [4].

1. $f_{\mathrm{DP}}^{\mathrm{N}} > 0$

   If $f_{\mathrm{Cap}}^{\mathrm{trial}} > 0 \rightarrow$ Cap - plastisuusprosessi

   Else $\rightarrow$ elastinen prosessi

2. $f_{\mathrm{DP}}^{\mathrm{N}} \leq 0$

   If $I_1^{\mathrm{trial}} < p_{\mathrm{tr}}$ & $f_{\mathrm{Cap}}^{\mathrm{trial}} > 0 \rightarrow$ Cap - plastisuusprosessi

   Elseif $f_{\mathrm{DP}}^{\mathrm{trial}} > 0$ & $f_{\mathrm{MR}}^{\mathrm{trial}} > 0 \rightarrow$ MR - DP viskoplastinen prosessi

   Elseif $f_{\mathrm{DP}}^{\mathrm{trial}} > 0$ & $f_{\mathrm{MR}}^{\mathrm{trial}} \leq 0 \rightarrow$ DP viskoplastinen prosessi

   Elseif $f_{\mathrm{DP}}^{\mathrm{trial}} \leq 0$ & $f_{\mathrm{MR}}^{\mathrm{trial}} > 0 \rightarrow$ MR viskoplastinen prosessi

   Else $\rightarrow$ elastinen prosessi

Taulukossa 1 MR-DP viskoplastinen prosessi, jota kuvassa 1 edustaa harmaa kolmio, vaatii erityiskäsittelyä, koska siinä myötöpinnan gradientti ei ole yksikäsitteinen. Tässä yhteydessä käytetään Koiterin sääntöön perustuvaa tekniikkaa, joka on esitetty esimerkiksi lähteessä [6]. Varsinainen jännitysten integrointi, jonka yksityiskohdat sivuutetaan, suoritetaan standardimenetelmin, joita on käsitelty esimerkiksi lähteissä [5, 6]. Koska malli on DP-prosessin ja lujittumis-/pehmenemislain osalta lineaarinen, antaa standardi jännityksen palautusalgoritmi (stress return mapping) tarkan ratkaisun kahdella askeleella, kun s_{c} on vakio. Jos $s_{\mathrm{c}} = 0$, analyyttinen ratkaisu saadaan yhdellä askeleella. MR- ja cap-prosessi vaativat epälineaarisina muutaman askeleen supetakseen kohtuullisen pieneen toleranssiin.

Mallin kalibrointi puristustiloissa

Esitettävässä mallissa siis viskoplastinen pehmenemislaki (4) säätelee lujuuden menetystä (strenght degradation) puristustiloissa silloin, kun cap-malli ei ole aktiivinen. Cap-mallin aktivoituminen riippuu kolmiaksiaalisen jännitystilan sivuttaispaineen suuudesta. Monien kivilajien tyypillisiä piirteitä kolmiaksiaalisessa puristuskokeessa ovat, että sivuttaispaineen noustessa jännityshuippu (peak stress) nousee, lujuuden degradaatio vähenee, jolloin jäännösjännitys (residual stress) nousee, jännitys-venymäkäyrän huippujännityksen jälkeinen osa loivenee ja lopulta jollakin sivuttaispaineen arvolla esiintyy siirtyminen hauraasta (pehmenevästä) käyttäytymisestä sitkeään (lujittuvaan). Lisäksi huippujännitystä edeltää yleensä selvä epälineaarisesti lujittuva osa. Nämä piirteet näkyvät kuvien 3a ja 4c kokeellisista käyristä.

Tässä tutkimuksessaa seurataan lähteessä [8] tehtyä oletusta tyypillisen laboratorionäytteen vasteen yksinkertaistamiseksi materiaalipisteen tasolla seuraavasti: elastis-hauras yksiaksiaalisessa tapauksessa, elastis-lineaarisesti pehmenevä pienillä ja kohtuullisilla sivuttaispaineen arvoilla ja elastis-ideaaliplastinen hauras-sitkeä-siirtymäpaineen ja sitä korkeampien sivuttaispaineiden arvoilla. Tässä esitettävässä mallissa cap-plastisuusprosessi aktivoituu, kun hauras-sitkeä-siirtymäpaine saavutetaan.

Lähteissä [7, 8] ehdotetaan kokeisiin perustuva materiaaliparametri, niinsanottu degradaatioindeksi (degradation index), joka kuvaa huippujännityksen jälkeistä kiven lujuuden ja jäykkyyden (stiffness) degradaatiota kolmiaksiaalisessa puristuskokeessa. Degradaatioindeksi saa arvoja välillä 0 ja 1 vastaten elastis-plastista vastetta (hauras-sitkeä-siirtymäpaine) ja elastis-haurasta vastetta (yksiaksiaalinen tapaus). Yksiaksiaalinen (maksimi)degradaatio on siten puristuslujuuden ja jäännöslujuuden erotus $\delta\sigma_u = \sigma_c - \sigma_{du}$. Matemaattisesti degradaatioindeksi määritellään jännitysten avulla suhteeksi $r_d = (\sigma - \sigma_d)/(\sigma - \sigma_{dh}) = \delta\sigma / \delta\sigma_h$. Tässä aktuaalisen jännityksen ja sitä vastaavan jäännösjännityksen erotus $\delta\sigma = \sigma - \sigma_d$ on aktuaalinen degradaatio ja aktuaalisen jännityksen ja sitä vastaavan hypoteettisen jäännösjännityksen erotus $\delta\sigma_h = \sigma - \sigma_{dh}$ on hypoteettinen degradaatio. Tämä on se degradaatio, joka esiintyisi, jos yleinen (aktuaalinen) degradaatio olisi suoraan verrannollinen yksiaksiaaliseen degradaatioon.

Kokeellisesti mitattuihin sivuttaispaineesta σ_{con} riippuviin degradaatioindeksin arvoihin on lähteessä [7] sovitettu eksponentiaalinen käyrä

$$r_d(\sigma_{con}) = \exp(-n_d \sigma_{con}) \tag{7}$$

jossa n_d on kivilajista riippuva vakio, joka esimerkiksi Tennesseen marmorille on 0.075. Degradaatioindeksiä käytetään nyt koheesion nyky- ja jäännösarvon sekä pehmenemismodulin laskentaan [4]:

$$\begin{aligned} c_t &= \max(c_{res}, c_0 + h_{DP}\lambda_{DP} + s_{DP}\dot{\lambda}_{DP}) \\ c_{res} &= (1 - r_d(\sigma_{con}))c_0 \\ h_c(\sigma_{conf}) &= h_{c0} \cdot r_d(\sigma_{con}) \end{aligned} \tag{8}$$

jossa h_{c0} pehmenemismodulin alkuarvo. Näiden määrittelyjen mukaan mallin vaste on puristuksessa lineaarisesti kimmoinen puristuslujuuteen asti, jonka jälkeen lineaarisesti pehmenevä osuus jatkuu, kunnes jäännöslujuus saavutetaan. Pehmenemismoduli pienenee eksponentiaalisesti sivuttaispaineen funktiona.

Vaurioformulointi

Isotrooppisen vauriomallin perusoletus on, että mikrosäröt ja muut viat ovat orientaatioltaan satunnaisia, jolloin niiden vaikutus kimmomodulin pienentymiseen on kaikissa suunnissa sama. Tämä ei yleisesti pidä paikkansa, mutta valitaan yksinkertaisuutensa vuoksi tämän tutkimuksen tarkoituksiin. Vauriomalli vastaa tässä siis jäykkyyden ja lujuuden degradaatiosta vetotiloissa. Vaurionkehityslaiksi valitaan tyypillinen kokeiden perusteella muotoiltu eksponenttilaki

$$\omega_t = g_t(\varepsilon_{\mathrm{eqvt}}^{\mathrm{vp}}) = 1-\left(1-A_t+A_t\exp\left(-\beta_t\varepsilon_{\mathrm{eqvt}}^{\mathrm{vp}}\right)\right) \tag{9}$$

jossa A_t ja β_t ovat parametreja jotka säätelevät vaurionkasvun nopeutta ja sen maksimiarvoa. Lisäksi $\Delta\varepsilon_i^{\mathrm{vp}}$ on kumulatiivinen equivalentti viskoplastinen venymä, joka toimii siten myös vaurion historiamuuttujana. Sen inkrementti lasketaan kaavalla $\Delta\varepsilon_{\mathrm{eqvt}}^{\mathrm{vp}} = \sqrt{\sum_{i=1}^{3}\langle\Delta\varepsilon_i^{\mathrm{vp}}\rangle^2}$, jossa on käytetty McAuley-sulkeita ja $\Delta\varepsilon_i^{\mathrm{vp}}$ on viskoplastinen päävenymä. Koska vaurio riippuu viskoplastisesta venymästä, se riippuu siten myös kuormitusnopeudesta. Edelleen tästä riippuvuudesta seuraa, että vaurioituminen tapahtuu vain, kun MR-kriteeriä rikotaan.

Vaurion deaktivointi ja aktivointi syklisessä kuormituksessa

Vaurion unilateraalinen luonne eli jäykkyyden palautus vaurioparametrin deaktivoinnilla siirryttäessä vetotilasta puristustilaan käsitellään tässä tutkimuksessa operoimalla vaurioparametrilla vain jännityksen positiiviseen osaan. Tällöin nominaalin ja efektiivisen jännityksen välinen yhteys pääavaruudessa on

$$\boldsymbol{\sigma} = (1-\omega_t)\overline{\boldsymbol{\sigma}}_+ + \overline{\boldsymbol{\sigma}}_- \quad (\overline{\boldsymbol{\sigma}} = \overline{\boldsymbol{\sigma}}_+ + \overline{\boldsymbol{\sigma}}_-) \tag{10}$$

jossa $\overline{\boldsymbol{\sigma}}_+ = \max(\overline{\boldsymbol{\sigma}},0)$ ja $\overline{\boldsymbol{\sigma}}_- = \min(\overline{\boldsymbol{\sigma}},0)$ ovat efektiivisen pääjännityksen positiivinen ja negatiivinen osa. Voidaan osoittaa, että tämä määrittely säilyttää mallin termodynaamisesti konsistenttina [4].

Vaurion ja viskoplastisuuden kytkentä

Vauriomallin ja (visko)plastisuusteorian kytkentä vaikuttaa mallin parametrien vaatimuksiin ja implementointiin. Lähteessä [9] on tutkittu nominaaliseen ja efektiiviseen jännitykseen perustuvien formulaatioiden vaikutuksia mallin parametreille. Efektiiviseen jännitykseen perustuva formulaatio ei aseta mallin parametreille lisävaatimuksia termodynamiikan kannalta, kun taas nominaaliseen jännitykseen perustuvassa formulaatiossa plastisuusmallin on oltava voimakkaasti lujittuva. Lisäksi efektiiviseen jännitykseen perustuva formulaatio tarjoaa luonnollisen tavan erottaa plastisoituminen ja vaurioituminen omiksi osatehtävikseen siten, että ensin ratkaistaan standardimenetelmin plastisuustehtävä eli integroidaan efektiivinen jännitys. Tämän jälkeen päivitetään vauriomuuttuja ω_t ja lasketaan nominaalinen jännitys kaavasta (10). Koska jännitysintegrointi suoritetaan pääavaruudessa, niin nominaalisen jännityksen laskun jälkeen täytyy vielä laskea jännitys referenssikoordinaatistossa.

PORAKRUUNUN KONTAKTIN MALLINNUS

Porakruunu oletetaan jäykäksi, jolloin sen nastat voidaan idealisoida pisteiksi. Tällöin nastan geometrian voi määrittää kontaktireunaehtojen avulla antamalla nastan pinnan etäisyydet kiven pinnan kontaktisolmuihin (b_{1i} kuvassa 2). TkT M. Keskinivan (Sandvik Mining and Construction Oy) kirjoittajalle ehdottama menetelmä porankruunun nastan ja kiven välisen vuorovaikutuksen simulointiin on esitetty kuvassa 2.

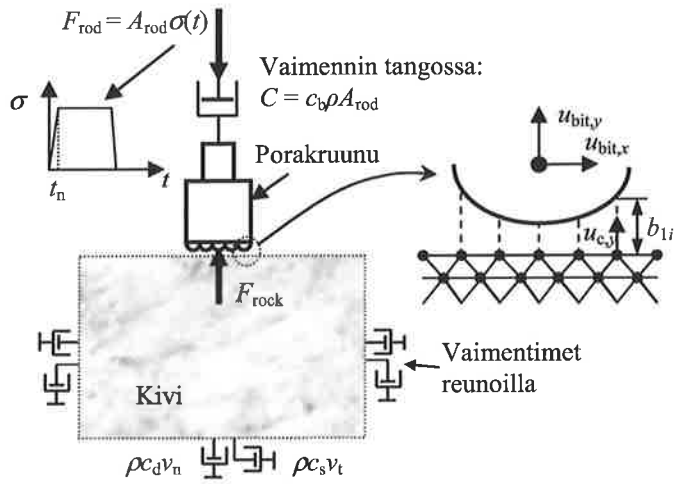

Kuva 2. Laskennallinen malli iskevän porauksen simulointiin.

Kuvassa 2 kiven reunoille ja porakruunua kuvaavaan pisteeseen asetetut jännitysaaltojen heijastuksia estävät viskoosit vaimentimet (dashpot) simuloivat kiven tapauksessa puoliääretöntä kalliota ja porakangen tapauksessa pitkää porakankea. Viskoosit vaimentimet, joiden teoria on esitetty alun perin lähteessä [10], ovat suorituskyvyltään heikohkoja, joten niiden käyttö vaatii 2D- ja 3D-tapauksissa suurehkoa elementtiverkkoa. Niiden implementointi (käsitellään materiaalisen vaimennusmatriisin tavoin) on kuitenkin vaivatonta verrattuna edistyneempiin menetelmiin (kuten PML-menetelmät), että niitä kannattaa käyttää insinöörisovelluksissa.

Porakruunun nastan y-suuntaisen vapausasteen $u_{\mathrm{bit},y}$ liikeyhtälö on

$$m_{\mathrm{bit}}\ddot{u}_{\mathrm{bit},y} + c_{\mathrm{b}}\rho A_{\mathrm{rod}}\dot{u}_{\mathrm{bit},y} = -2A_{\mathrm{rod}}\sigma(t) - F_{\mathrm{rock}} \tag{11}$$

jossa F_{rock} on kontaktivoima, A_{rod} on kangen pinta-ala, ρ on sauvan materiaalin tiheys, m_{bit} on kruunun (laskennallinen) massa ja $\sigma(t)$ on jännityspulssi, joka kuvaa iskumännän törmäyksessä synnyttämää ja porakangessa nopeudella c_{b} etenevää puristusaaltoa. Nastan liikeyhtälö lisätään kiven vapausasteiden liikeyhtälöihin, jotka ratkaistaan eksplisiittisellä aikaintegraattorilla.

Aikaintegrointi ja kontaktireunaehtojen käsittely

Eksplisiittisistä menetelmistä valitaan modifioitu Eulerin menetelmä [11], jolle vasteet lasketaan kaavoilla

$$\ddot{\mathbf{u}}^{t} = \mathbf{M}^{-1}\left(\mathbf{f}_{\mathrm{ext}}{}^{t} - \mathbf{C}\dot{\mathbf{u}}^{t} - \mathbf{f}_{\mathrm{int}}{}^{t}\right), \quad \dot{\mathbf{u}}^{t+\Delta t} = \dot{\mathbf{u}}^{t} + \Delta t\ddot{\mathbf{u}}^{t}, \quad \mathbf{u}^{t+\Delta t} = \mathbf{u}^{t} + \Delta t\dot{\mathbf{u}}^{t+\Delta t}. \tag{12}$$

Menetelmä on toista kertalukua tarkka, kuten keskeisdifferenssimenetelmä. Tämän menetelmän etu on, että nopeus saadaan laskettua ennen siirtymää. Tätä nopeutta tarvitaan heijastamattoman reunaehdon yhteydessä. Kontaktireunaehdot, jotka ovat muotoa $u_{\mathrm{c},y} - u_{\mathrm{bit},y} = b_i$ (ks. kuva 2), käsitellään modifioidulla Lagrangen kertoimien menetelmällä. Menetelmän mukaiset liike- ja rajoiteyhtälöt kontaktiongelmalle ovat [12]

$$\mathbf{M}\ddot{\mathbf{u}}^{t} + \mathbf{C}\dot{\mathbf{u}} + \mathbf{f}_{\mathrm{int}} = \mathbf{f}_{\mathrm{ext}}^{t} - \mathbf{G}^{\mathrm{T}}\boldsymbol{\lambda}^{t} \quad \& \quad \mathbf{G}\mathbf{u}^{t+\Delta t} - \mathbf{b} = \mathbf{0}, \tag{13}$$

jossa $\mathbf{C} = \mathbf{C}_{qp} + \mathbf{C}_{qs}$ on dilataatio- ja leikkausaaltoon liittyvä vaimennusmatriisi, $\mathbf{G}$ sisältää kontaktipintojen normaalit ja $\boldsymbol{\lambda}$ on Lagrangen kertoimien vektori, jonka fysikaalinen tulkinta on kontaktivoimavektori. Lisäksi $\mathbf{f}_{ext}$ on ulkoisten voimien vektori, joita tässä edustaa vain jännityspulssi $\sigma(t)$. Kun nämä yhdistetään kaavojen (12) kanssa, saadaan

$$\begin{aligned} \ddot{\mathbf{u}}^t &= \tilde{\ddot{\mathbf{u}}}^t - \mathbf{M}^{-1}\mathbf{G}^{\mathrm{T}}\boldsymbol{\lambda}^t & \tilde{\ddot{\mathbf{u}}}^t &= \mathbf{M}^{-1}\left(\mathbf{f}_{\mathrm{ext}}^t - \mathbf{C}\dot{\mathbf{u}}^t - \mathbf{f}_{\mathrm{int}}^t\right) \\ \dot{\mathbf{u}}^{t+\Delta t} &= \dot{\mathbf{u}}^t + \Delta t\ddot{\mathbf{u}}^t \quad \text{, missä} & \tilde{\mathbf{u}}^{t+\Delta t} &= \mathbf{u}^t + \Delta t\dot{\mathbf{u}}^t + \Delta t^2\tilde{\ddot{\mathbf{u}}}^t \\ \mathbf{u}^{t+\Delta t} &= \mathbf{u}^t + \Delta t\dot{\mathbf{u}}^t + \Delta t^2\ddot{\mathbf{u}}^t & \boldsymbol{\lambda}^t &= \left(\Delta t^2\mathbf{G}\mathbf{M}^{-1}\mathbf{G}^{\mathrm{T}}\right)^{-1}\left(\mathbf{G}\tilde{\mathbf{u}}^{t+\Delta t} - \mathbf{b}\right) \end{aligned} \tag{14}$$

Menetelmä (14) on eräänlainen ennustaja-korjaaja-menetelmä, jossa ensin oletetaan, että kontakteja ei ole (suureet, joiden symbolin päällä on aaltoviiva) ja tämän lasketaan kontaktivoimat saadun tunkeuman perusteella. Kiihtyvyys korjataan vähentämällä kontaktivoimien vaikutus.

Kiven lujuuksien tilastollinen mallintaminen

Kiven veto- ja puristuslujuus, f_t, f_c, oletetaan Weibull-jakautuneeksi. Tämän jakauman 3-parametrinen kertymäfunktio on

$$\Pr(x) = 1 - \exp\left(-\left((x - x_u)/x_0\right)^{m_w}\right) \tag{15}$$

Kaavan (15) skaalausparametri m_w on lähteessä [13] tulkittu materiaalin homogeenisuusindeksiksi siten, että mitä suurempi m_w, sitä homogeenisempaa on materiaali. Parametri x_0 on Weibull-jakauman odotusarvo: kun $m_w \to \infty$, niin Pr(x) $\to x_0$. Parametri x_u siirtää jakauman kuvaajaa vertikaalisuunnassa, eli sen avulla säädetään kertymäfunktion käänteisfunktion minimiarvo. Materiaaliparametrin spatiaalisesti heterogeeninen jakauma tuotetaan ratkaisemalla kullekin elementille kyseisen materiaaliparametrin arvo x kaavasta (15), kun kertymäfunktion arvona Pr(x) on tasajakaumasta otettu satunnaisluku väliltä [0,1].

Tämän menetelmän käytöstä seuraa, että kalibrointi materiaalipisteen tasolla ei riitä, vaan myös laboratorionäytetasolla täytyy kalibroida Weibull-jakauman parametrien avulla. Tämän tutkimuksen simulaatioissa käytetään Tennesseen marmorille seuraavia arvoja: vetojuluudelle x_0 = 13 MPa, x_u = 6 MPa ja m_w = 3 sekä puristuslujuudelle x_0 = 130 MPa, x_u = 60 MPa ja m_w = 3. Molemmille lujuuksille käytetään samaa parametrin m_w arvoa, mutta omaa satunnaisdataa. Siten veto- ja puristuslujuuden suhde ei ole vakio vaan myös Weibull-jakautunut.

NUMEERISET ESIMERKIT

Testit materiaalipisteen tasolla

Aluksi esitettyä konstitutiivista mallia testataan materiaalipisteen tasolla käyttäen yhtä 8-solmuista solidielementtiä ja yhden Gaussin pisteen numeerista integrointia. Kivilajeiksi valitaan kolmiaksiaalista puristuskoetta varten Carraran marmori ja Salemin kalkkikivi sekä kuormitusnopeuden vaikutuksen testiin Bukit Timan graniitti. Muissa testeissä malli kalibroidaan Tennesseen marmorille, koska kirjallisuudesta sille löytynyt kokeellinen data on matalilla sivuttaispaineen arvoilla täydellisempi. Muita testejä materiaalipisteen tasolla ovat yksiaksiaalinen puristus eri kuormitusnopeuden arvoilla Bukit Timan graniitille ja mallin antama vaste syklisessä kuormituksessa. Vedossa malli asetetaan ideaaliplastiseksi (h_t = 0), koska vauriomalli säätelee pehmenemistä. Kaikki tulokset on esitetty kuvassa 3. Sivuttaispaine otetaan huomioon ratkaisemalla statiikan ongelmasta sen aiheuttama siirtymä alkuehdoksi ja käsittelemällä siirtymäpainetta ulkoisena kuormana totuttuun tapaan.

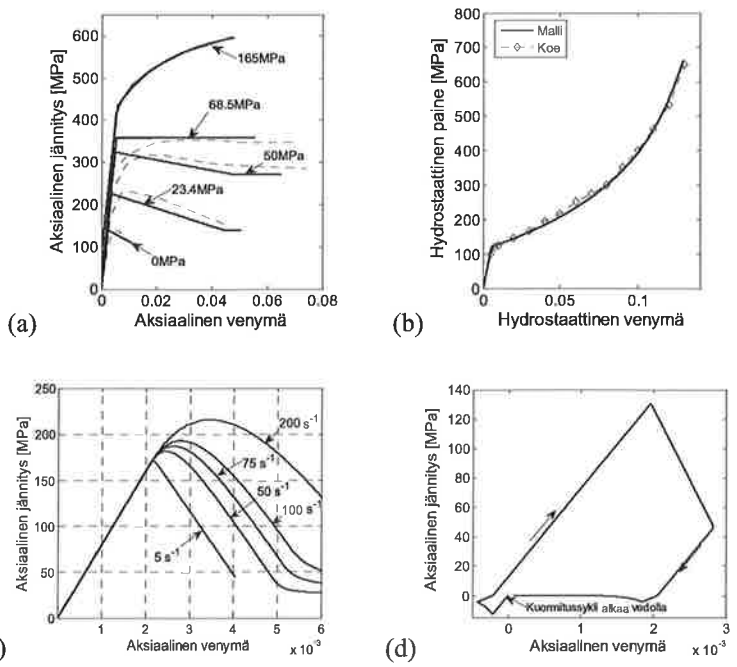

Kuva 3. Kiven materiaalimallin vaste materiaalipisteen tasolla: vaste kolmiaksiaalisessa puristuskokeessa Carraran marmorille (kokeelliset käyrät lähteestä [14]) (a), vaste hydrostaattisessa kokeessa Salemin kalkkikivelle (kokeellinen käyrä lähteestä [15]) (b), vaste aksiaalisessa puristuksessa useilla kuormitusnopeuksilla (Bukit Timan graniitti) (c) ja vaste aksiaalisessa kuormituksen vaihtoja sisältävässä testissä (Tennesseen marmori) (d).

Tuloksista (kuva 3a) nähdään, että tulokset vastaavat huippujännityksen ja jäännösjännityksen osalta kohtalaisen hyvin kokeellisia tuloksia hauras-sitkeä-siirtymäpaineen (68.5 MPa) alapuolella. Tämän paineen yläpuolella, kun cap-plastisuusprosessi on aktiivinen, vaste yhtyy "silmänormilla" tarkasteltuna täysin kokeelliseen tulokseen. Myös hydrostaattisen kokeen ja cap-mallin ennustama vaste yhtyvät erinomaisella tarkkuudella (kuva 3b). Malli ei luonnollisesti materiaalipisteen tasolla testattuna tuota oletustensa vuoksi huippujännitystä edeltävää epälineaarisuutta, joka nähdään kokeellisissa tuloksissa korostuvana sivuttaispaineen kasvaessa.

Bukit Timan graniitin huippujännitykset kuormitusnopeuden funktiona ovat noin 175 MPa (50 s^{-1}), 205 MPa (75 s^{-1}), 235 MPa (97 s^{-1}) [16], joten kuvan 3c arvoihin vertaamalla nähdään, että vakioviskositeettimodulilla malli ei tuota realistisia tuloksia ainakaan kyseiselle kivilajille.

Kuvasta 3d nähdään mallin vaste syklisessä kuormituksessa. Vetopuolella vaste on eksponentiaalisesti pehmenevä ja sekä vaurioitumista että pysyviä muodonmuutoksia syntyy. Puristuspuolella vaste on lineaarisesti pehmenevä ja vain pysyviä muodonmuutoksia esiintyy. Tultaessa uudelleen vetokuormitukselle kuormanlisäys tapahtuu alentuneella kimmomodulin arvolla ja pehmeneminen alkaa edellisellä kierroksella saavutetun jäännöslujuuden tasolta.

Testit rakenteen tasolla: kolmiaksiaalinen puristuskoe Tennesseen marmorille

Seuraavaksi mallia testataan laboratorionäytteen tasolla kolmiaksiaalisessa puristuskokeessa. Laskentamalli, sen reunaehdot, elementtiverkko ja kokeelliset jännitys-venymäkäyrät Tennesseen marmorille on esitetty kuvassa 4.

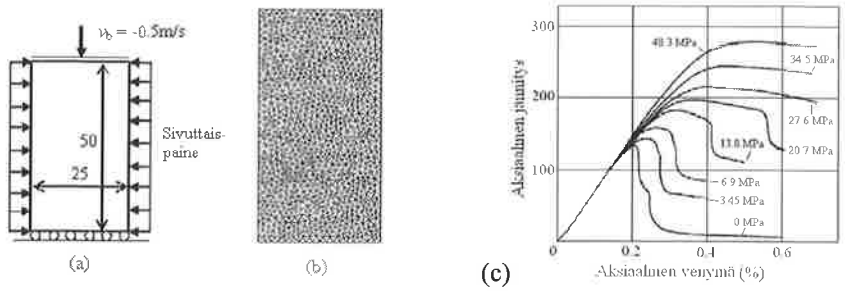

Kuva 4. Laskentamalli (a), elementtiverkko (2028 CST elementtiä) (b) ja kokeelliset jännitys-venymäkäyrät Tennesseen marmorille (lähteestä [7]) (c).

Tehtävää simuloidaan tasovenymätilassa pakottamalla mallin yläreunan solmuille vakionopeusreunaehto. Materiaaliparametrit ja muu data ovat seuraavat: E = 60 GPa, f_c = 130 MPa, f_t = 13 MPa, ν = 0.2, φ = 30°, ψ = 5°, ρ = 2600 kg/m^3, h_t = 0, α_t = 0.98, β_t = 5000, n_d = 0.075, h_{c0} = 10 GPa, $s_t = s_c$ = 0.01MPa·s, $p_{tr0} = 2.9f_c, p_{P0} = 8f_c, D$ = 0.001, W = 0.0433, $\Delta t = 1.1\times10^{-7}$ s. Tulokset esitetään vauriomuuttujan ω_t ja kumulatiivisen viskoplastisen venymän jakaumina kuvassa 5 (jälkimmäisen inkrementti lasketaan kaavalla $\Delta\varepsilon^{vp}_{eqvc} = \sqrt{\frac{2}{3}\Delta\boldsymbol{\varepsilon}^{vp}\cdot\Delta\boldsymbol{\varepsilon}^{vp}}$).

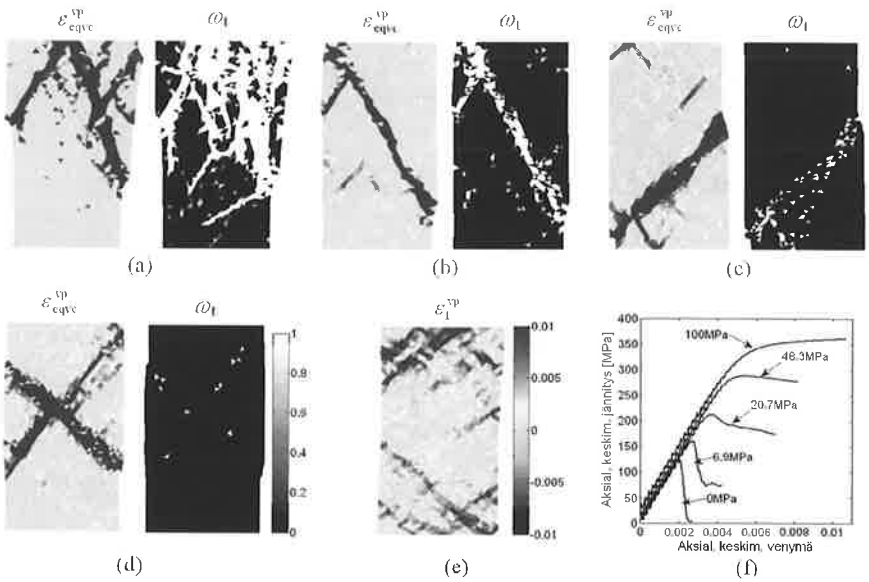

Kuva 5. Viskoplastisen ekvivalenten venymän ja vaurion jakaumat sivuttaispaineen arvoilla: 0 (a), 6.9 (b) 20.7 (c), 48.3 (d), 100 MPa (e) ja vastaavat keskimääräiset jännitys-venymäkäyrät (f).

Yksiaksiaalisessa tapauksessa (kuva 5a) vaurioituminen lokalisoituu useiksi lähes aksiaalisiksi vetotyyppisiksi säröiksi. Tämä vauriokuvio (axial splitting mode) havaitaan tyypillisesti myös kokeissa. Sivuttaispaineen kasvaessa aksiaalinen vauriomuoto korvautuu yksittäisellä leikkaustasolla (shear band), jonka kulma ja paksuus kasvavat sivuttaispaineen funktiona (kuvat 5b, c). Sivuttaispaineen kasvaessa vetovaurion määrä pienenee huomattavasti. Jännitys-venymäkäyristä, jotka yhtyvät kokeellisiin tuloksiin kohtalaisella tarkkuudella, nähdään, että

lujuuksien tilastollinen mallintaminen tuottaa huippujännitystä edeltävän epälineaarisuuden laboratorionäytteen tasolla, vaikka sitä ei materiaalipisteen tasolla mallinnettu.

Testit rakenteen tasolla: nastan ja kiven välinen vuorovaikutus

Viimeiseksi simuloidaan porakruunun nastan ja kiven välistä vuorovaikutusta tasovenymätilassa kuvassa 2 esitetyllä menetelmällä. Valitaan 10 mm leveä tylppä nasta. Jännityspulssin parametrit asetetaan seuraavasti: σ_A = 1500 MPa, t_{rise} = 1×10^{-5} s ja t_{dur} = 3×10^{-5} s, jossa parametrit ovat amplitudi, nousuaika ja kestoaika. Aika-askel on Δt = 5.92×10^{-8} s. Tulokset vaurion ja viskoplastisen päävenymän jakaumille eri ajanhetkillä on esitetty kuvassa 6.

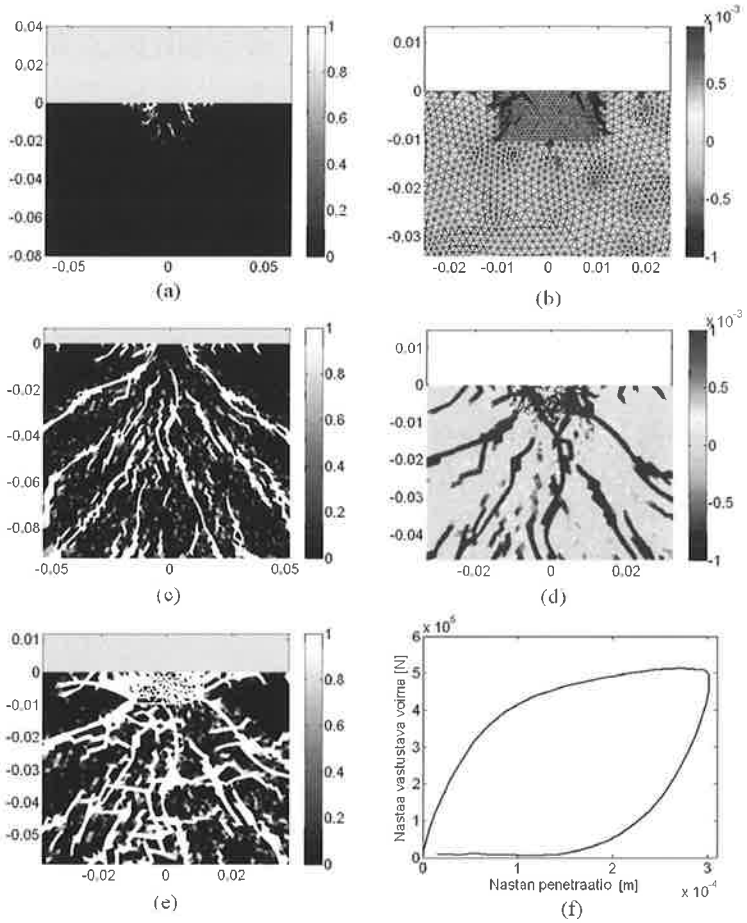

Kuva 6. Nastan ja kiven vuorovaikutuksen simulointitulokset: ω_t (a) ja ε_{vpl} (b) ajanhetkellä t = 1.18×10^{-5} s, ω_t (c) ja ε_{vpl} (d) ajanhekellä t = 4.74×10^{-5} s, ω_t (e) ajanhetkellä t = 6.8×10^{-5} s ja nastan penetraatio-voimakuvaaja (f).

Kuvista 6a, b nähdään, että kuormituksen alkuvaiheessa muodostuu Hertsin kartiosärö, joka ei ole symmetrinen eikä säännöllinen kiven lujuuksien heterogeenisuuden vuoksi. Kun maksimipenetraatio (0.3 mm) on saavutettu, vetovauriojakauman säröt muodostavat alaspäin avautuvan viuhkamaisen kuvion (kuva 6c). Leikkaustyyppinen vaurioituminen eli DP-viskoplastisuusprosessin aiheuttama myötöpehmeneminen (jota kuvassa 6d edustaa punainen väri, jonka kohdalla kuvassa 6c ei ole vauriota) on rajoittunut lähelle nastaa. Kuvasta 6d (sininen väri) nähdään myös, että cap-lujittumisprosessi on aktivoitunut nastan alla olevissa elementeissä.

Kuormanpoistovaiheessa, kun nasta vetäytyy, tapahtuu huomattavaa vetotyyppistä vaurioitumista, kuten kuvasta 6e nähdään. Nämä nastaan nähden teoreettisesti samankeskiset vetosäröt syvemmällä kivessä (consentric tensile cracks) ja pintaan ulottuvat "lohkeilusäröt" (spall cracks) aiheutuvat nopean kuormanpoiston aiheuttamasta vetoaallosta, joka etenee kiven suutaan.

YHTEENVETO JA PÄÄTELMÄT

Tässä tutkimuksessa esitettiin menetelmä kiven rikkoutumisen simulointiin iskevässä kallionporauksessa. Viskoplastisuuteen ja vauriomekaniikkaan perustuva konstitutiivinen malli kykenee kuvaamaan tarkasteltavassa ongelmassa esiintyvät fysikaaliset ilmiöt ja tuottaa standardimateriaalitesteissä kokeita vastaavia tuloksia hyvällä tarkkuudella. Kallionporauksen simulointiin esitetty menetelmä tuo uutuutena kuormitusnopeudesta ja sivuttaispaineesta riippuvuuden yhdistettynä tilastollisesti heterogeeniseen lujuuksien mallinnukseen.

LÄHDELUETTELO

[1] H.Y. Liu. Numerical Modelling of the Rock Fragmentation Process by Mechanical Tools, Väitöskirja. Luleå University of Technology, 2004.

[2] T. Saksala. Damage-Plastic Model for Numerical Simulation of Rock Fracture in Dynamic Loading. In *Proceedings of the Sixth International Conference on Engineering Computational Technology*, Topping BHV (editor), Civil-Comp Press, Stirling, United Kingdom, paper 163, 2008.

[3] H.P. Rossmanith, R.P. Knasmillner, A. Daehnke, L. Mishnaevsky Jr. Wave propagation, damage evolution, and dynamic fracture extension. Part I: Percussion drilling. *Materials Science*, Vol. 32 350-358, 1996.

[4] T. Saksala. (Hyväksytty julkaistavaksi) Damage-viscoplastic consistency model with a parabolic cap for rocks with brittle and ductile behaviour under low-velocity impact loading, *International Journal for Numerical and Analytical Methods in Geomechanics*.

[5] W.M. Wang, L.J. Sluys, R. De Borst. Viscoplasticity for instabilities due to strain softening and strain-rate softening, *International Journal for Numerical Methods in Engineering*, Vol. 40, 3839-3864, 1997.

[6] J.C. Simo, T.J.R. Hughes, Computational Inelasticity, Springer, 1998.

[7] Z. Fang, J.P. Harrison, A mechanical degradation index for rock. *International Journal of Rock Mechanics and Mining Sciences*, Vol. 38, 1193-1199, 2001.

[8] Z. Fang, J.P. Harrison, Development of a local degradation approach to the modelling of brittle fracture in heterogeneous rocks. *International Journal of Rock Mechanics and Mining Sciences*, Vol. 39, 443-457, 2002.

[9] P. Grassl, M. Jirásek, Damage-Plastic model for concrete failure, *International Journal of Solids and Structures*, Vol. 43, 7166-7196, 2006.

[10] J. Lysmer and R. L. Kuhlemeyer. Finite dynamic model for infinite media. *Journal of Engineering Mechanics Division*, ASCE, Vol. 95, 377-392, 1969.

[11] G.D. Hahn. A Modified Euler Method for dynamical analyses. *International Journal for Numerical Methods in Engineering*. Vol. 32, 943-955, 1991.

[12] N.J. Carpenter et al.. Lagrange Constraints for Transient Finite Element Surface Contact. *International Journal for Numerical Methods in Engineering*. Vol. 32. 103 – 128, 1991.

[13] C.A. Tang. Numerical Simulation of Progressive Rock Failure and Associated Seismicity. *Int. J. Rock Mech. Min. Sci.*, Vol. 34, 249-261, 1997.

[14] J.C. Jaeger, N.G.W. Cook, Fundamentals of Rock Mechanics, Chapman and Hall 1971.

[15] V.A. Lubarda, S. Mastilovic, J. Knap, Brittle-Ductile Transition in Porous Rocks by Cap Model, *Journal of Engineering Mechanics*, Vol. 122, 633-642, 1996.

[16] Y. Zhai, G. Ma, J. Zhao, C. Hu, Dynamic failure analysis on granite under uniaxial impact compressive load, *Front. Archit. Civ. Eng. China*, Vol. 2, 253-260, 2008.

QUANTIFICATION OF GEOMETRICAL IRREGULARITY OF WOOD

JOHANNA SJÖLUND AND JOUNI FREUND

Department of Applied Mechanics
Helsinki University of Technology
P. O. Box 4300
FIN-02015 Espoo, FINLAND
e-mail: johanna.sjolund@tkk.fi

ABSTRACT

A simple way to quantify and model the geometrical irregularity of a material sample is presented. In particular, the model should reproduce the geometrical features having strong effect on heterogeneity of the stress field. Effects of sample size and scale are discussed by using examples with known statistics of irregularity.

1. INTRODUCTION

Wood can be taken to be composed of thin-walled, long cells having roughly hexagonal cross sections. Cells form growth rings with differences in density, cell wall thickness, cell wall configuration and cell number per unit volume. In addition, the cell structure contains geometrical features on various scales (Fig. 1). As mechanical properties of wood depend strongly on the geometrical details, they should be accounted for in material description of wood. This raises the question of how to describe the geometry so that the modelled material has similar geometrical characteristic to a wood sample. Knowing this, one may study the effect of cell structure geometry statistics on strength by a model, and reduce the need for expensive physical experiments.

According to review [1], most micromechanical models of wood are based on a regular honeycomb, where a hexagonal cell is repeated [2, 3]. Some of the models take into account the variation of the growth ring [4]. A few references consider the different geometrical features of wood by tracing the scanned image cell by cell [5, 6, 7]. However, to our knowledge, modelling the statistics of regularity to generate cellular material samples for finite element analysis has not been considered.

The aim is to discuss a way to quantify the geometrical irregularity of a sample of honeycomb material so that modelled material is similar to the sample in geometrical characteristics. Then one may generate a sample of specimen, use a micromechanical model, finite element method, and statistical analysis of results to improve the understanding on the effect of geometric details on e.g. strength of the material in the macroscopic sense. In particular, the model should reproduce the geometrical features having strong effect on heterogeneity of the stress field.

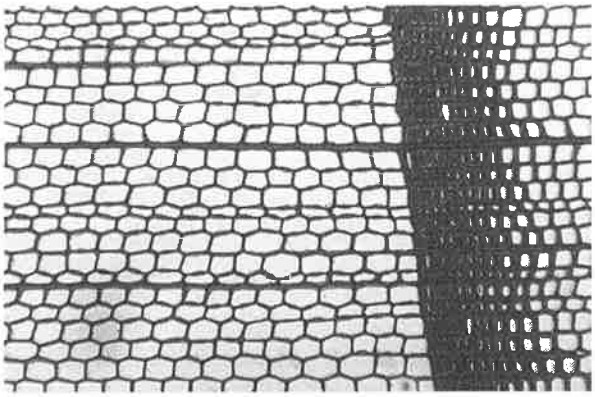

Figure 1: Softwood cell structure showing also the growth ring [8].

2. REGULARITY OF A TEXTURE

A regular texture (Fig. 2) has a wallpaper-like, congruent appearance so that it can be generated by simple mappings, translation, rotation, reflection, from a structural unit or a set of them. In this context, regularity is a measure of simplicity of description. Roughly speaking, the simpler the description is the more regular the texture is. Then, a highly regular structure has lots of symmetry and the set of structural units of the texture is small. A near-regular texture (Fig. 2) is taken here as the outcome of a distortion in shape, size i.e. it is taken anything excess to the shape preserving mapping in a wallpaper making. For an irregular texture (Fig. 2) no structural unit smaller than the whole sample can be found which could be mapped to form the whole sample.

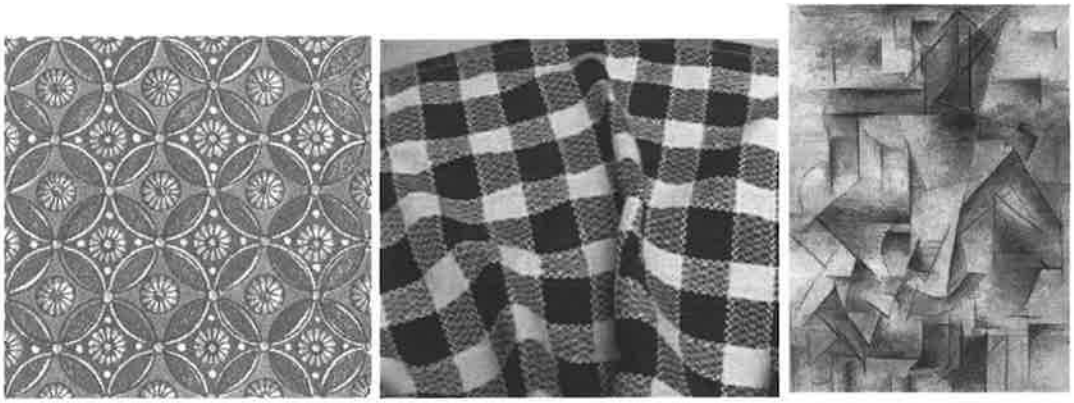

Figure 2: Examples of textures. Shown from left to right a regular [9], a near-regular [10] and an irregular [11] texture.

3. HONEYCOMB MAPPING

Emphasis of this study is placed on a hexagonal texture that can be generated from a triangular structural unit by iteration on honeycomb mapping. Honeycomb mapping in its general form is

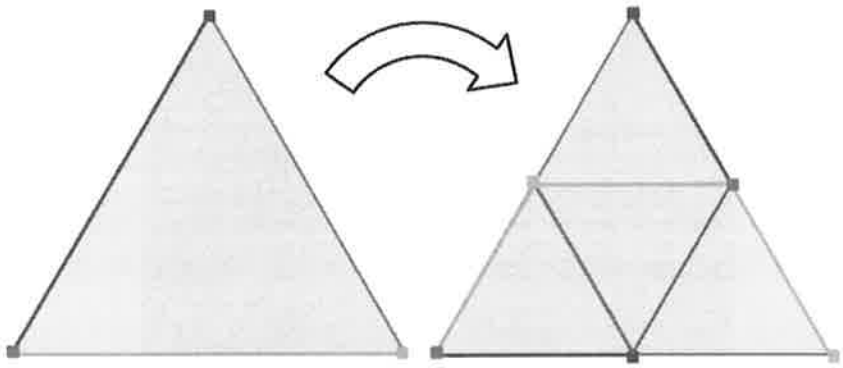

Figure 3: General mapping.

shown in Fig. 3. The structural unit consists of a triangle, three edges and three points having different colors. For a hexagonal honeycomb, two of the edges and points are marked with the same color. Fig. 4 is obtained by iteration on the mapping of Fig. 3. On each application, a honeycomb structure of smaller hexagon size is generated inside the triangle. The number of iterations will be called the level or scale l of the structure. If the level of the starting point is zero and the size of the triangle is H, the size of the hexagon is given by $h/H = 2^{-l}$. The outcome of levels 1, 2, 3, 4 are shown in Fig. 4. More detailed describtion on the subject can be found in [12].

Scale of near-regularity is important in analysis of variation in shape and size. Highest level is determined by the lenght of the cell wall h, as the smallest geometrical features are of that scale. Lowest level is more difficult to determine. For example if the analysis should also include growth ring, the cell wall lenght h of the lowest level should be of the same order as the growth ring width.

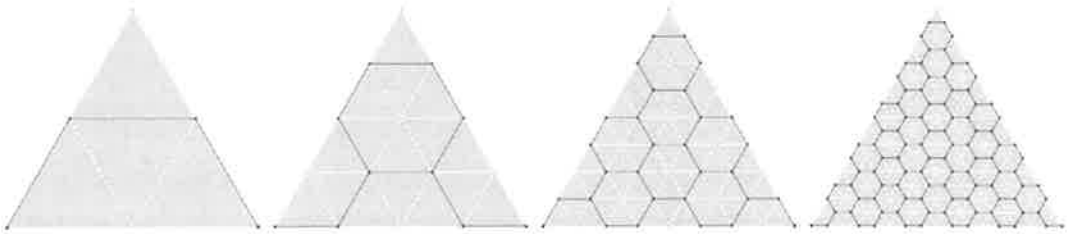

Figure 4: Honeycomb material in four scales. Size h/H of the sample from left to right 1/2, 1/4, 1/8 and 1/16, where h is the size of the cell wall and H is the sample size.

4. ANALYSIS OF NEAR-REGULARITY

Regularity in shape and size are just particular choices and one may well consider regularity in any other attribute like color or a combination in them. Honeycomb on the left of Fig. 5 is clearly a highly regular texture as it can generated from a triangle having one black and two white edges of the same length. Texture in the middle of Fig. 5 is less regular than the honeycomb on the left. A near-regular texture on the right of Fig. 5 is obtained by using a statistical distortion in shape. Growth rings, cell cross-sections etc. of wood belong roughly to this class of textures. Near-

regularity on properties like cell-wall thickness, stiffness etc. play also an important role in studies on strength.

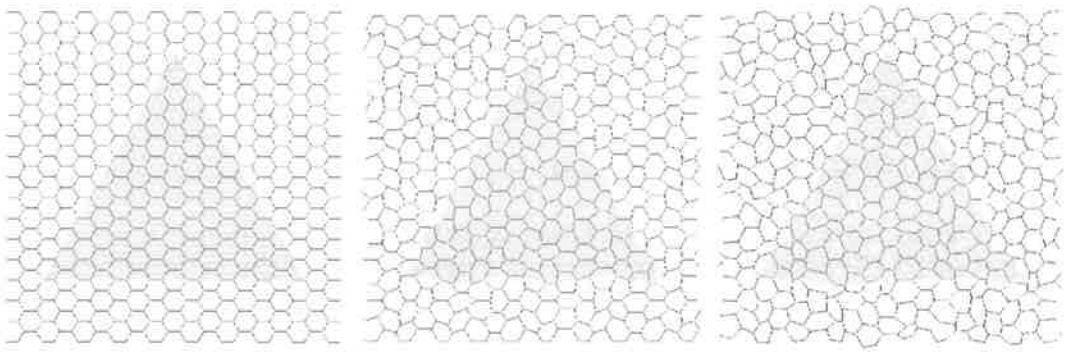

Figure 5: Examples of regular (on the left and in the middle) and near-regular (on the right) textures. The triangular sample is shown in gray.

The aim of texture analysis is to quantify the statistical distortion of a near-regular honeycomb when material properties are in one-to-one correspondence with colors, line thickness or any attribute to a texture. With this information, obtained within confidence depending on the relative size of the sample h/H, one may generate finite-element representations of near-regular textures.

Quantification of near-regularity is based on comparison of the actual and reference geometries. When analysing the distortion on level l, the reference geometry is chosen to be the honeycomb structure of level $l-1$. This gives information about near-regularity on various scales. To be precise, offsets $\Delta\vec{x}_i$ (Fig. 6) are used to form the experimental cumulative distribution function

$$cdf(a) = |\{a_i \in \Sigma : a_i < a\}| \,/\, |\Sigma| \tag{1}$$

in which a stands for Δx_i or Δy_i and $|a|$ denotes the size of set a.

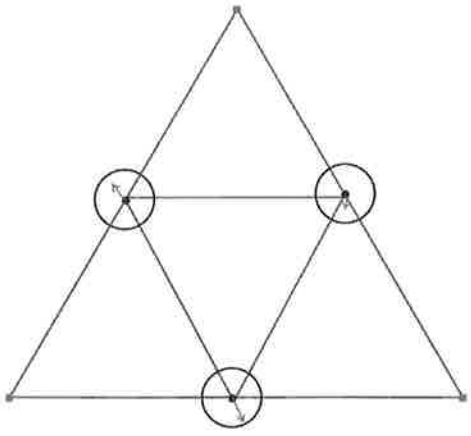

Figure 6: Offsets $\Delta\vec{x}_i$ are marked by the arrows. The circles show the largest possible value for offset distribution.

The corner points seen in Fig. 6 can be used to form flattening of the cells as seen in the growth ring. Moving the corner points does not change the statistics of the offsets $\Delta\vec{x}_i$, as the reference geometry and sample geometry do not move in relation to each other.

Different types of statistics can tell something about the mechanism causing the geometrical features. If different mechanisms cause the irregularities on different levels the resulting distribution is normal. Analysis indicate also what scale the features are.

5. FINDING AND APPLYING STATISTICS

Two examples of material, generated using known statistics of irregularity, are used to discuss the effect of sample size and scale of irregularity on the outcome of the analysis. A sample, to which known statistics has been applied, is generated, from which a triangular sample is chosen to be analysed as in Fig. 5. The analysis gives the statistics of offsets or cumulative distribution functions seperately for each scale and x and y coordinates. The coordinates are treated seperately, not in pairs. The statistics can be used to regenerate a sample which can be compared to the original one. A sample can be analysed without knowing the statistics and the sample regenerated no matter what the statistics or distribution is.

In the first example, uniform distribution was introduced on two scales. The sample, statistics and the sample generated from the statistics are shown in Fig. 7 and Fig. 8. Statistics clearly shows that the near-regularity has scales corresponding to levels 3 and 4. For all other levels are the statistics of near-regularity is negligible. The blue line in Fig. 7 is not straight as the level 3 distortion affecs the lenght of the cell walls and also the statistics of higher levels. Generated sample has same type of geometrical features as the original sample.

In the second example uniform distribution was again introduced on two scales. The difference from the previous example is that now the irregularity is introduced already at level two and it is larger. The sample, statistics and the sample generated from the statistics are seen in Fig. 9 and Fig. 10. As seen in Fig. 9, the geometrical features are again same for the original and generated sample. This example shows that scales do need to be accounted for in order to generate the correct geometry.

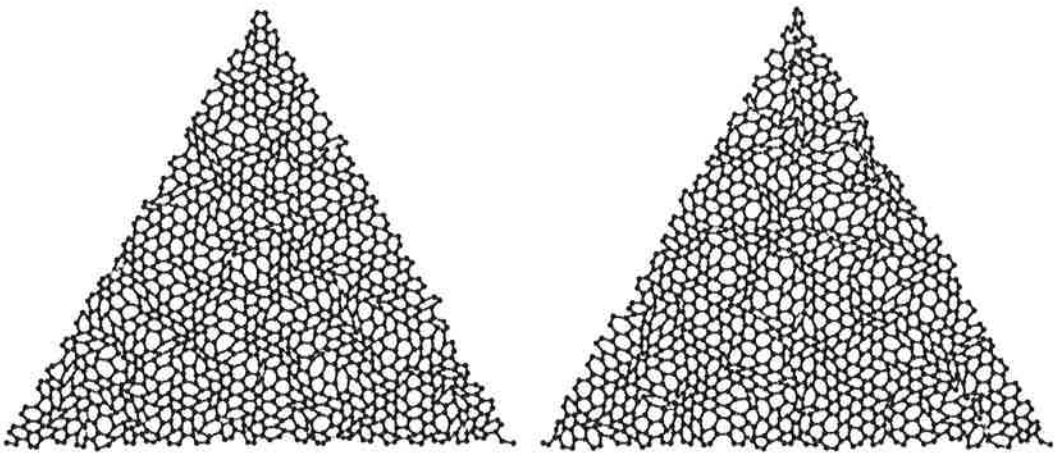

Figure 7: Sample and the generated sample generated using statistics.

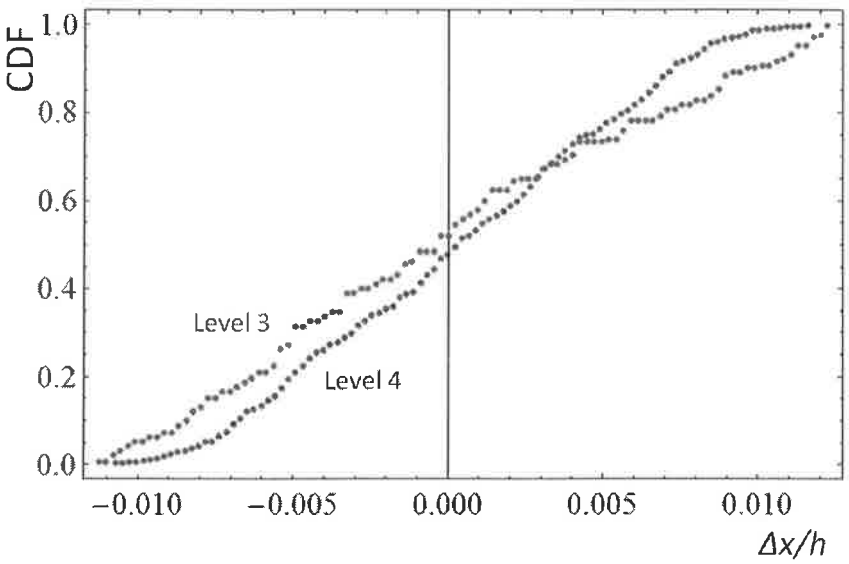

Figure 8: Cumulative distribution function of the offset on two levels, red is for level 3 and blue for level 4.

6. CONCLUSIONS

Finding the statistics on geometrical irregularities of the sample has been discussed. Repeating the analysis multiple times shows how much the statistics change during the analysis and what effect it has on the geometry. If the statistics change notably not all features are analysed and repeated correctly. Including different scales correctly collects features of different scales so that they are also correctly generated. Samples with known statistics were used to get information about the effect of sample size needed to analyse the sample and still capture important geometrical features.

The statistical data from the analysis can be, when dealing with real-life samples, replaced with the corresponding distribution. This reduces the possible deviations due to the quality of the figure or analysis and results in a more correct geometry. Near-regularity of other attributes, such as color or cell size, can also be analysed in the same way.

This work is part of Virtual Wood task of E-wood, Energy Efficient Wood Processing and Machining, -project. To aim of the task is to predict strength statistics of wood by virtual experiments on a micromechanical model.

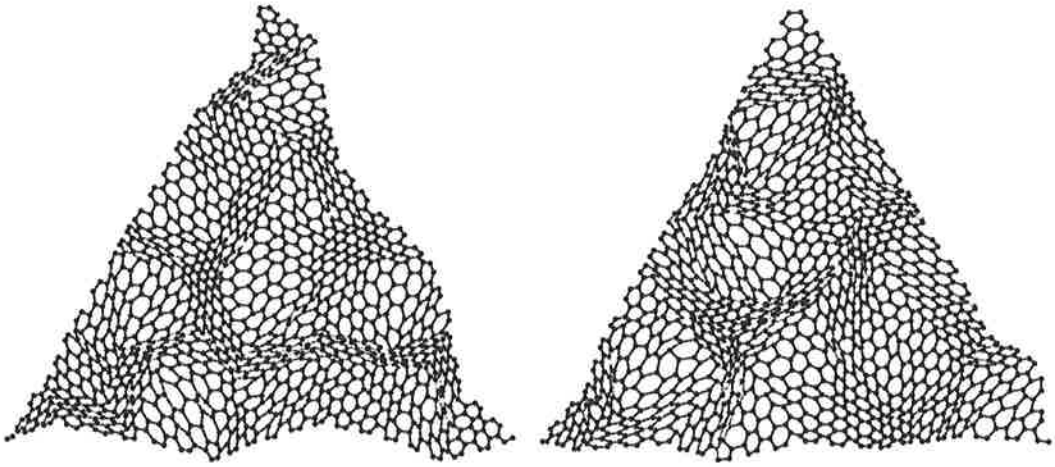

Figure 9: Sample and the generated sample generated using statistics.

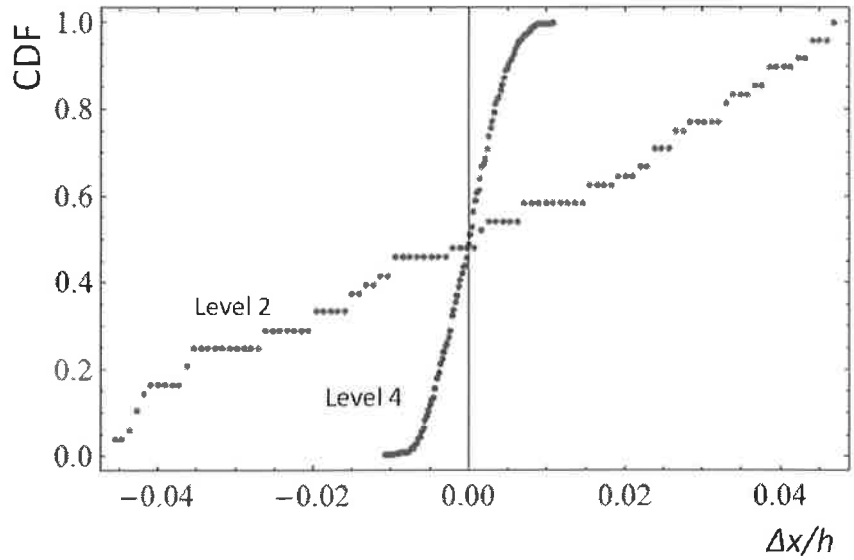

Figure 10: Cumulative distribution function of the offset on two levels, red is for level 2 and blue for level 4.

REFERENCES

[1] L. Mishnaevsky Jr. and H. Qing, Micromechanical modelling of mechanical behaviour and strenght of wood: State-of-the-art review, Comp. Mater. Sci., **44**, 363–370, 2008.

[2] l. J. Gibson and M. F. Ashby, Cellular solids: Structure and properties, Pergamon Press, Oxford, Second edition 1988.

[3] U. Watanabe, M. Fujita, and M. Norimoto, Transverse Young's Moduli and Cell Shapes in Coniferous Early Wood, Holzforschung, **56**, 1–6, 2002.

[4] F. K. Wittel, G. Dill-Langer, and B. H. Kroplin, Modeling of damage evolution in soft-wood perpendicular to grain by means of discrete element approach, Comput. Mater. Sci, **32**, 594–603, 2005.

[5] K. Persson, Micromechanical modelling of wood and fibre properties, Doctoral thesis, Lund University, 1997.

[6] S. Holmberg, K. Persson, and H. Petersson, Nonlinear mechanical behaviour and analysis of wood and fibre materials, Comput. Struct., **72**, 459–480, 1999.

[7] E. Kahle and J. Woodhouse, The influence of cell geometry on the elasticity of softwood, J. Mater. Sci, **29**, 1250–1259, 1994.

[8] http://www.steve.gb.com/images/science/softwood_rings.jpg

[9] http://en.wikipedia.org/wiki/File:Wallpaper_group-p4m-5.jpg

[10] W. Lin and Y. Liu, IEEE Trans. Pattern Analysis and Machine Intelligence, **29**, 777–792, 2007.

[11] Pablo Picasso, The guitar player, 1910.

[12] J. Freund, mesh generation of honeycomb material, these proceedings.

ON THE EFFECTS OF BENDING RIGIDITY ON THE STABILITY OF AN AXIALLY MOVING ORTHOTROPIC PLATE

JUHA JERONEN[1]*, NIKOLAY BANICHUK[2], PEKKA NEITTAANMÄKI[1], TERO TUOVINEN[1]

[1]Department of Mathematical Information Technology, University of Jyväskylä, P. O. Box 35, FIN-40014 Jyväskylä, FINLAND
[2]Institute for Problems in Mechanics RAS, prosp. Vernadskogo 101, block 1, Moscow 119526, Russian Federation
*Corresponding author, e-mail: juha.jeronen@jyu.fi

ABSTRACT

In this paper, we consider the effect of bending rigidity on the stability of a rectangular, axially moving orthotropic thin elastic plate. The problem is investigated in a vacuum formulation, i.e., there is no surrounding fluid. A fully analytical approach is used. It is found that with pinned-free boundary conditions, the space of elastic problem parameters splits into two regions, in one of which the bending forces are guaranteed to have a stabilizing character, whereas in the other region this property is lost. Thus, in this other region the bending forces may either stabilize or destabilize the system, depending on the particular shape of the transverse deformation. This result differs from the isotropic case, where the bending forces always have a stabilizing effect. The result has implications, from a basic research perspective, on the range of applicability of linear small deformation theory to orthotropic plates.

1. INTRODUCTION

The motivation for this study comes from the papermaking process. As is well known, the mechanical behaviour of paper under a non-failure condition is adequately described by the model of an elastic orthotropic plate. The rigidity coefficients for the plate model have been estimated in e.g. [1], [2], [3] and [4].

There are numerous studies on the loss of stability of moving elastic webs based on one-dimensional models. These studies are devoted to various aspects of free and forced vibrations, including the nature of wave propagation in moving media, and the effects of axial motion on the frequency spectrum and eigenfunctions. The studies include e.g. [5], [6], [7], [8], [9], [10], [11], [12], [13], [14], and [15].

Two-dimensional studies have also been performed. In [16], an axially moving membrane was studied in a 2D formulation, predicting the equilibrium displacement and stress distributions under transverse loading. Later, the same authors predicted the wrinkling instability and the corresponding

wrinkled shape of a web with small flexural stiffness [17]. The stability and vibration characteristics of an axially moving plate were investigated in [18]. The loss of stability was studied with application of dynamic and static approaches and Wickert's [15] approach to derive the equation of motion for the plate in matrix form and to use the Galerkin method. It was shown by means of numerical analysis that, for all cases dynamic instability (flutter) is realised when the frequency is zero and the critical velocity coincides with the corresponding velocity obtained from static analysis. In [19], the out-of-plane vibration of an axially moving membrane was investigated. Also here, it was found by numerical analysis, that for a membrane with a no-friction boundary condition in the lateral direction along the rollers, the membrane remains dynamically stable until the critical speed, at which statical instability occurs.

The two-dimensional problem of instability analysis of an axially moving elastic plate was formulated and investigated analytically in [20] in the context of the isotropic model. In particular, it was proved that the loss of stability is realized for some critical velocity in a divergence mode. It was also observed that the transverse deflection localizes near the free edges. This was noted to correspond to the eigenfunctions of stationary plates under in-plane compressive load (see e.g. [21]), and the results matched the above mentioned results of [18] and [19] for moving plates and membranes.

This paper concentrates on the effect of the bending forces in the orthotropic model. The work is an extension of the above cited [20], presenting some of the details that are encountered in the orthotropic case.

It should be noted that when applied to the particular context of paper production, the present study still ignores some potentially important effects. First, damping effects resulting from the viscoelastic nature of paper are neglected. The introduction of damping is mainly expected to change the postdivergence behaviour [13], which is not discussed here. Secondly, the interaction between the travelling web and the surrounding air is known to influence the critical velocity [22] [23] and the dynamical response [24]. These effects, which are not directly related to the bending forces discussed here, are ignored by the in-vacuum model used in the present study.

2. GOVERNING EQUATIONS

Consider a thin, elastic orthotropic plate of constant thickness h travelling with a constant velocity V_0 in the x direction between two rollers located at $x = 0$ and $x = \ell$ in a Cartesian coordinate system (see Figure 1). We assume that the "1" axis of the orthotropic material is aligned with the x direction, while the "2" axis is aligned with the y direction. The plate is subjected to homogeneous tension, acting in the x direction. The sides of the plate $x = 0$, $-b \leq y \leq b$ and $x = \ell$, $-b \leq y \leq b$ are simply supported, and the sides $y = -b$, $0 \leq x \leq \ell$ and $y = b$, $0 \leq x \leq \ell$ are free of tractions. The transverse displacement of the travelling plate is described by the deflection function w, which depends on the coordinates x, y and time t. The differential equation for small transverse vibrations has the form

$$m\left(\frac{\partial^2 w}{\partial t^2} + 2V_0\frac{\partial^2 w}{\partial x \partial t} + V_0^2\frac{\partial^2 w}{\partial x^2}\right) = T_{xx}\frac{\partial^2 w}{\partial x^2} + 2T_{xy}\frac{\partial^2 w}{\partial x \partial y} + T_{yy}\frac{\partial^2 w}{\partial y^2} - \mathcal{L}(w)\,, \qquad (1)$$

where the bending operator is

$$\mathcal{L}(w) = D_1\frac{\partial^4 w}{\partial x^4} + 2D_3\frac{\partial^4 w}{\partial x^2 \partial y^2} + D_2\frac{\partial^4 w}{\partial y^4}\,, \qquad (2)$$

where D_1, D_2 and D_3 are the bending rigidities.

Here m is the mass per unit area of the middle surface of the plate, and T_{xx}, T_{xy} and T_{yy} are in-plane tensions. We assume that the deflection function w and its partial derivatives are small, and

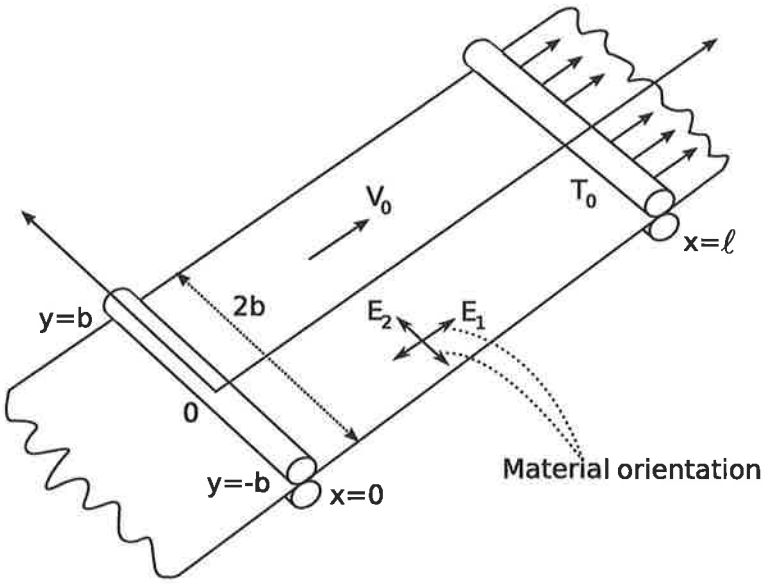

Figure 1: Axially moving elastic orthotropic plate, simply supported at $x = 0$ and $x = \ell$.

that they satisfy the boundary conditions corresponding to simply supported boundaries at $x = 0$, $-b \leq y \leq b$ and $x = \ell$, $-b \leq y \leq b$, and free boundaries at $-b \leq y \leq b$, $0 \leq x \leq \ell$. We have

$$(w)_{x=0,\ell} = 0, \qquad \left(\frac{\partial^2 w}{\partial x^2}\right)_{x=0,\ell} = 0, \qquad -b \leq y \leq b \tag{3}$$

$$\left(\frac{\partial^2 w}{\partial y^2} + \beta_1 \frac{\partial^2 w}{\partial x^2}\right)_{y=\pm b} = 0, \qquad 0 \leq x \leq \ell \tag{4}$$

$$\left(\frac{\partial^3 w}{\partial y^3} + \beta_2 \frac{\partial^3 w}{\partial x^2 \partial y}\right)_{y=\pm b} = 0, \qquad 0 \leq x \leq \ell \tag{5}$$

where β_1 and β_2 are mechanical parameters defined below. Since we assume homogeneous tension on the simply supported boundaries, it follows that for the tension inside the domain we have

$$T_{xx,} = T_0 \qquad T_{yy} = T_{xy} = 0, \qquad (x, y) \in \Omega\,, \tag{6}$$

where $\Omega \equiv [0, \ell] \times [-b, b]$.

For the bending rigidities in (2), we have the expressions (see e.g. [25], p. 365)

$$\begin{aligned} D_1 &= \frac{E_1 h^3}{12\,(1 - \nu_{12}\nu_{21})} \\ D_2 &= \frac{E_2 h^3}{12\,(1 - \nu_{12}\nu_{21})} \\ D_3 &= \frac{h^3}{12}\left(\frac{\nu_{12} E_2}{(1 - \nu_{12}\nu_{21})} + 2\,G_{12}\right)\,, \end{aligned} \tag{7}$$

where E_1 (respectively E_2) is the Young modulus in the x (respectively y) direction, ν_{12} (ν_{21}) is the Poisson ratio in the xy plane when the stretching is applied in the x (y) direction, and G_{12} is the shear modulus in the xy plane.

The mechanical parameters in the boundary conditions (4)–(5) are given by

$$\begin{aligned} \beta_1 &= \nu_{12} \\ \beta_2 &= \nu_{12} + \frac{4\,G_{12}}{E_2}\,(1 - \nu_{12}\nu_{21}) \ , \end{aligned} \tag{8}$$

where ν_{12}, G_{12}, E_2 and ν_{21} are as defined above.

It is possible to eliminate G_{12} from the list of independent physical parameters by using the formula due to M. T. Huber,

$$G_{12} = \frac{\sqrt{E_1 E_2}}{2\left(1 + \sqrt{\nu_{12}\nu_{21}}\right)} \ , \tag{9}$$

which applies geometric averages of the other material parameters to estimate G_{12}. In the case of paper materials, the values obtained agree with the range of G_{12} observed in experiments. Thus, in this work we have used the estimation (9).

In the following, we will assume that the bending rigidity $D_1 \neq 0$. Making this assumption, we may work in a nondimensional system where we set $\tilde{D}_j \equiv D_j/D_1$ with $j = 1, 2, 3$. After applying (9), we obtain the following:

$$\tilde{D}_1 = 1 \tag{10}$$

$$\tilde{D}_2 = \hat{E}^2 \tag{11}$$

$$\tilde{D}_3 = \hat{E}^2\nu_{12} + \hat{E}(1 - \hat{\nu}) \tag{12}$$

$$\beta_1 = \nu_{12} \tag{13}$$

$$\beta_2 = \nu_{12} + 2\frac{1 - \hat{\nu}}{\hat{E}} \ . \tag{14}$$

We thus have three independent material parameters, i.e., ν_{12} and the following two combinations,

$$\hat{E} \equiv \sqrt{E_2/E_1} \quad \text{and} \tag{15}$$

$$\hat{\nu} \equiv \sqrt{\nu_{12}\nu_{21}} \ . \tag{16}$$

The parametrization (10)–(16) will be used below.

3. CRITICAL INSTABILITY MODE

We will only briefly run through the main ideas that are needed to frame the current discussion, to be presented in the next section. Most of the analysis will be skipped. The basic outline is the same as in the isotropic case, explained in detail in [20].

It can be shown that the loss of stability for the system (1), (3)–(5) occurs in a statical form. This is done by considering time-harmonic solutions [26]

$$w(x, y, t) \equiv W(x, y)e^{st} \ , \tag{17}$$

where s is a complex eigenfrequency. If s is pure imaginary, the plate performs harmonic vibrations of small amplitude and its motion can be considered stable. If, for some values of the problem parameters, the real part of s becomes positive, the transverse vibrations grow exponentially and consequently the behaviour of the plate is unstable.

By inserting (17) into (1), multiplying by $W(x,y)$ and integrating over the domain (to establish a variational form), and then proving that certain terms vanish, it can be shown that for the complex eigenfrequency s, we have the relation

$$-s^2 = \frac{\left(\frac{T_0}{m} - V_0^2\right)\int_\Omega \left(\frac{\partial W}{\partial x}\right)^2 \mathrm{d}\Omega + \frac{D_1}{m}\int_\Omega W\mathcal{L}(W)\,\mathrm{d}\Omega}{\int_\Omega W^2\,\mathrm{d}\Omega}\,, \tag{18}$$

where the bending rigidities contained in the bending operator $\mathcal{L}$ have been replaced with the nondimensional ones (10)–(12), hence the D_1 outside the integral.

The first integral in the numerator, and the one in the denominator, are obviously real and positive for nontrivial real-valued functions $W \not\equiv 0$. Thus, the interesting question is to estimate the bending integral, i.e. the one that contains the bending operator $\mathcal{L}(W)$.

Let us first consider the case where the bending integral is real and nonnegative. We have that $s^2 < 0$ for $V_0^2 < T_0/m$, i.e. until the velocity reaches the divergence velocity of a membrane in vacuum. At that point the first term in the numerator becomes zero, and as V_0 is further increased, it becomes negative. Finally, at some value $V_0 = V_0^{\mathrm{div}}$ the first term balances out the second one, and s becomes zero. (For an ideal membrane, the bending term vanishes and this value is obviously $V_0 = \sqrt{T_0/m}$ as expected [27].)

The point where the numerator vanishes corresponds to a (nontrivial) steady-state solution of (1), (3)–(5), which represents a buckling (divergence) type of instability. If V_0 is still increased from this critical value, $s^2 > 0$ and the displacement function of the plate grows exponentially with time. Note that s will always pass through the origin in the complex plane before its real part becomes nonzero. Thus, the critical mode of instability of the system (1), (3)–(5) is a statical one.

If the bending integral is allowed to be negative, then the stability of the system ($s^2 < 0$) at $V_0 = 0$ depends on the material parameters. Because linear theory is only valid up to the first instability, this in turn determines whether small deformation theory is applicable. This limit can be found numerically by solving the steady-state problem (which corresponds to $s = 0$) repeatedly while e.g. increasing $\hat{E}$ and looking for the point where $V_0^{\mathrm{div}} \to 0$.

For the rest of this paper, we will concentrate on the question of when the bending integral is positive definite, i.e. the conditions under which it can be guaranteed to be positive regardless of W.

4. EFFECT OF THE BENDING TERM ON THE ELASTIC STABILITY

As was shown in detail in [20], in the isotropic case it is possible to use Green's second identity (see e.g. [28], p. 628) with $u = W$ and $v = \triangle W$ to estimate the bending integral. Specifically, in the isotropic case the bending operator $\mathcal{L}(W) \equiv \triangle^2 W \equiv \triangle(\triangle W)$, and Green's second identity produces

$$\int_\Omega W\triangle^2 W\,\mathrm{d}\Omega = \int_\Omega (\triangle W)^2\,\mathrm{d}\Omega + \int_\Gamma (W\frac{\partial}{\partial \mathbf{n}}(\triangle W) - \triangle W\frac{\partial}{\partial \mathbf{n}}(W))\,\mathrm{d}\Gamma\,, \tag{19}$$

where $\triangle$ denotes the Laplacian, Γ is the boundary of the domain Ω and $\mathbf{n}$ is the outer unit normal. From (19) it is seen that if the contour integral vanishes, the remaining term on the right-hand side and thus the whole expression is nonnegative for all real-valued functions W.

On the simply supported boundaries, the integrand of the boundary term is identically zero. Furthermore, by using our particular geometry and the boundary conditions (4)–(5), it can be shown that

on the boundaries free of tractions, the integrand (accounting for the direction of the outer normal) is antisymmetric with respect to the x axis, and thus the contour integral indeed vanishes.

The same argument does not directly apply to the orthotropic case, because the orthotropic bending operator $\mathcal{L}$ contains weighting factors and thus Green's second identity must be modified to account for this. Below, we first do this, then show that the contour integral vanishes as before, and finally estimate the sign of the first term in terms of the problem parameters.

We introduce the notation

$$\nabla_\alpha u \equiv (\alpha_1 \frac{\partial u}{\partial x_1}, \ldots, \alpha_n \frac{\partial u}{\partial x_n}) \tag{20}$$

$$\triangle_\alpha u \equiv \sum_{i=1}^{n} \alpha_i \frac{\partial^2 u}{\partial x_i^2} \,, \tag{21}$$

where the α_i are arbitrary complex constants. We replace $u \leftarrow u$ and $v \leftarrow \alpha_i \frac{\partial v}{\partial x_i}$ in the integration by parts formula for an n-dimensional domain ([28], p. 628) and sum over n, obtaining

$$\int_\Omega (\nabla u \cdot \nabla_\alpha v + u \triangle_\alpha v)\, \mathrm{d}\Omega = \int_\Gamma u\, \mathbf{n} \cdot \nabla_\alpha v \, d\Gamma \,. \tag{22}$$

Note that the first term on the left can be written equivalently $\nabla_\alpha u \cdot \nabla v$, because the inner product is not affected by the choice of which of the vectors the weights are assigned to. We write another copy of (22) with u and v switched and subtract it from the original, obtaining

$$\int_\Omega (\nabla u \cdot \nabla_\alpha v - \nabla v \cdot \nabla_\alpha u + u \triangle_\alpha v - v \triangle_\alpha u)\, \mathrm{d}\Omega = \int_\Gamma (u\, \mathbf{n} \cdot \nabla_\alpha v - v\, \mathbf{n} \cdot \nabla_\alpha u)\, \mathrm{d}\Gamma \,. \tag{23}$$

We see that the first two terms on the left-hand side cancel, and we obtain the modified Green's second identity for the weighted derivative operators (20)–(21):

$$\int_\Omega (u \triangle_\alpha v - v \triangle_\alpha u)\, \mathrm{d}\Omega = \int_\Gamma (u\, \mathbf{n} \cdot \nabla_\alpha v - v\, \mathbf{n} \cdot \nabla_\alpha u)\, \mathrm{d}\Gamma \,. \tag{24}$$

By choosing $u = W$ and $v = \triangle_\gamma W$, with arbitrary complex weights γ_i independent of α_i, it follows from (24) that

$$\int_\Omega (W \mathcal{L}(W) - (\triangle_\gamma W)(\triangle_\alpha W))\, \mathrm{d}\Omega = \int_\Gamma (W\, \mathbf{n} \cdot \nabla_\alpha (\triangle_\gamma W) - (\triangle_\gamma W)\, \mathbf{n} \cdot \nabla_\alpha W)\, \mathrm{d}\Gamma \,, \tag{25}$$

where

$$\mathcal{L}(W) \equiv \triangle_\alpha (\triangle_\gamma W) \,. \tag{26}$$

That is, we can use the modified Green's second identity (24) to estimate the bending integral, if we write the orthotropic bending operator (2) as the combination of two weighted Laplace operators. Since the bending operator is two-dimensional and the weights are constants, we obtain by comparing (2) and (26) that

$$\begin{aligned} \mathcal{L}(W) &= \alpha_1 \gamma_1 \frac{\partial^4 W}{\partial x^4} + (\alpha_1 \gamma_2 + \alpha_2 \gamma_1) \frac{\partial^4 W}{\partial x^2 \partial y^2} + \alpha_2 \gamma_2 \frac{\partial^4 W}{\partial y^4} \\ &\equiv \tilde{D}_1 \frac{\partial^4 W}{\partial x^4} + 2\tilde{D}_3 \frac{\partial^4 W}{\partial x^2 \partial y^2} + \tilde{D}_2 \frac{\partial^4 W}{\partial y^4} \,, \end{aligned} \tag{27}$$

i.e. $\alpha_1\gamma_1 = \tilde{D}_1$, $\alpha_1\gamma_2 + \alpha_2\gamma_1 = 2\tilde{D}_3$ and $\alpha_2\gamma_2 = \tilde{D}_2$. Since we have three equations in four unknowns, and it does not matter which solution we pick, let us fix $\alpha_1 = 1$. Then, from the first equation we have $\gamma_1 = \tilde{D}_1 = 1$. This leaves us with two equations in two unknowns, for which the solution is

$$\alpha_2 = \tilde{D}_3 \left(1 \mp \sqrt{1 - \tilde{D}_2/\tilde{D}_3^2}\right) \tag{28}$$

$$\gamma_2 = \tilde{D}_3 \left(1 \pm \sqrt{1 - \tilde{D}_2/\tilde{D}_3^2}\right) , \tag{29}$$

where the upper and lower signs correspond to each other. We see that regardless of the sign of the quantity under the square root, the coefficients of (27) are real and positive, as expected.

Let us now estimate $\int_\Omega W\mathcal{L}(W)\,\mathrm{d}\Omega$ by using (25). The contour integral can be written as

$$I \equiv \int_\Gamma (W\,\mathbf{n}\cdot\nabla_\alpha(\triangle_\gamma W) - (\triangle_\gamma W)\,\mathbf{n}\cdot\nabla_\alpha W)\,\mathrm{d}\Gamma \equiv I_- + I_r + I_+ + I_\ell \ , \tag{30}$$

where the contour of integration is taken in the counterclockwise direction, and the subscripts refer to the lower, right, upper and left edges of the domain. On the left ($x = 0$) and right ($x = \ell$) edges, the simply supported boundary conditions (3) declare that $W = 0$ and $\partial^2 W/\partial x^2 = 0$. Because the first condition implies that W is a constant on these edges, and because the edges are aligned with the y axis, we have also $\partial^2 W/\partial y^2 = 0$ on these same edges. Thus, on these edges, the first term of the integrand in the contour integral vanishes because $W = 0$. Then, because $\partial^2 W/\partial x^2 = \partial^2 W/\partial y^2 = 0$, both components of the weighted Laplacian $\triangle_\gamma W$ in the second term are zero, and thus the second term vanishes. Therefore, $I_\ell = I_r = 0$, and we are left with

$$I = I_- + I_+ \ . \tag{31}$$

As in the isotropic analysis, we expand I_- and I_+ with the particulars of our geometry applied:

$$\begin{aligned} I_- &= -\int_0^\ell \left(W\alpha_2\frac{\partial}{\partial y}(\triangle_\gamma W) - (\triangle_\gamma W)\alpha_2\frac{\partial W}{\partial y}\right)_{y=-b} \mathrm{d}x \\ &= -\alpha_2\int_0^\ell \left(W\frac{\partial}{\partial y}(\triangle_\gamma W) - (\triangle_\gamma W)\frac{\partial W}{\partial y}\right)_{y=-b} \mathrm{d}x \\ I_+ &= -\int_0^\ell \left(W\alpha_2\frac{\partial}{\partial y}(\triangle_\gamma W) - (\triangle_\gamma W)\alpha_2\frac{\partial W}{\partial y}\right)_{y=+b} \mathrm{d}x \\ &= -\alpha_2\int_0^\ell \left(W\frac{\partial}{\partial y}(\triangle_\gamma W) - (\triangle_\gamma W)\frac{\partial W}{\partial y}\right)_{y=+b} \mathrm{d}x \ . \end{aligned}$$

We combine these into one integral by using (31):

$$I = -\alpha_2\int_0^\ell (Q_{y=+b} + Q_{y=-b})\,\mathrm{d}x \ , \tag{32}$$

where

$$Q \equiv W\frac{\partial}{\partial y}(\triangle_\gamma W) - (\triangle_\gamma W)\frac{\partial W}{\partial y} \ . \tag{33}$$

Note that our simple geometry made it possible to extract the common factor α_2, and to combine I_- and I_+.

In (32), Q is evaluated on the free boundaries. Recall the free boundary conditions (4)–(5). By using (4), we can evaluate the term

$$\begin{aligned}(\triangle_\gamma W)_{y=\pm b} &\equiv \gamma_1 \frac{\partial^2 W}{\partial x^2}|_{y=\pm b} + \gamma_2 \frac{\partial^2 W}{\partial y^2}|_{y=\pm b} \\ &= \gamma_1 \left(-\frac{1}{\beta_1} \frac{\partial^2 W}{\partial y^2}|_{y=\pm b} \right) + \gamma_2 \frac{\partial^2 W}{\partial y^2}|_{y=\pm b} \\ &= \left(\gamma_2 - \frac{\gamma_1}{\beta_1} \right) \frac{\partial^2 W}{\partial y^2}|_{y=\pm b} \,. \end{aligned} \tag{34}$$

Similarly, by (5) we have

$$\begin{aligned}(\frac{\partial(\triangle_\gamma W)}{\partial y})_{y=\pm b} &\equiv \gamma_1 \frac{\partial}{\partial y} \left(\frac{\partial^2 W}{\partial x^2} \right) |_{y=\pm b} + \gamma_2 \frac{\partial}{\partial y} \left(\frac{\partial^2 W}{\partial y^2} \right) |_{y=\pm b} \\ &= \gamma_1 \left(-\frac{1}{\beta_2} \frac{\partial^3 W}{\partial y^3}|_{y=\pm b} \right) + \gamma_2 \frac{\partial^3 W}{\partial y^3}|_{y=\pm b} \\ &= \left(\gamma_2 - \frac{\gamma_1}{\beta_2} \right) \frac{\partial^3 W}{\partial y^3}|_{y=\pm b} \,. \end{aligned} \tag{35}$$

Now, by (33) and (34)–(35) we have

$$Q|_{y=\pm b} = \left(W \cdot \left[\gamma_2 - \frac{\gamma_1}{\beta_2} \right] \frac{\partial^3 W}{\partial y^3} - \left[\gamma_2 - \frac{\gamma_1}{\beta_1} \right] \frac{\partial^2 W}{\partial y^2} \frac{\partial W}{\partial y} \right) |_{y=\pm b} \,.$$

From considerations a priori, we know that W is either symmetric or antisymmetric with respect to the x axis. Noting that parity (symmetric or antisymmetric) flips once by each differentiation in the direction perpendicular to the symmetry axis, we conclude that Q is always antisymmetric with respect to the x axis. Therefore, the integrand of (32) vanishes identically everywhere, and thus also the contour integral (30) vanishes.

Consequently, we are left with

$$\int_\Omega W \mathcal{L}(W) \, \mathrm{d}\Omega = \int_\Omega (\triangle_\gamma W)(\triangle_\alpha W) \, \mathrm{d}\Omega \,. \tag{36}$$

The integrand on the right-hand side is, writing explicitly,

$$\begin{aligned}&(\triangle_\gamma W)(\triangle_\alpha W) = \\ &\qquad \gamma_1 \alpha_1 \left(\frac{\partial^2 W}{\partial x^2} \right)^2 + (\gamma_1 \alpha_2 + \gamma_2 \alpha_1) \left(\frac{\partial^2 W}{\partial x^2} \right) \left(\frac{\partial^2 W}{\partial y^2} \right) + \gamma_2 \alpha_2 \left(\frac{\partial^2 W}{\partial y^2} \right)^2 \,. \end{aligned} \tag{37}$$

This expression is not a square due to the cross term of indeterminate size. However, if

$$D_3 \leq \min(D_1, D_2) \,, \tag{38}$$

then the cross term is at most as large (in magnitude) as in a full square, and thus the integrand is nonnegative at each point regardless of the choice of W. The inequality (38) thus represents the condition for the positive definiteness of the bending integral. Note that this property in turn implies the guaranteed stabilizing nature of the bending forces.

On the other hand, if (38) is not fulfilled, i.e. if

$$D_3 > \min(D_1, D_2) \,, \tag{39}$$

then we can split the sum (37) as a full square, plus a positive term, plus a term of indeterminate sign. The last term can be written as

$$R(W) \equiv [(\gamma_1\alpha_2 + \gamma_2\alpha_1) - 2\,\min(\gamma_1\alpha_1, \gamma_2\alpha_2)] \left(\frac{\partial^2 W}{\partial x^2}\right)\left(\frac{\partial^2 W}{\partial y^2}\right) , \tag{40}$$

where the coefficient is always positive in the case (39) and thus the sign of $R(W)$ only depends on the curvatures of W.

By solving the steady-state eigenvalue problem corresponding to (1), (3)–(5), the signs of the curvatures are known to be linked to the parity of W with respect to the x axis. If W is symmetric with respect to this axis (as it turns out is the case with the critical mode), the curvatures in x and y will have opposite signs, and thus $\int_\Omega R(W)\,\mathrm{d}\Omega < 0$. If W is antisymmetric (which can occur with higher modes), we first note that $\partial^2 W/\partial x^2$ is not affected (we still have the same solution with respect to x_1). Then, by the antisymmetricity property, we have that $\partial^2 W(x,y)/\partial y^2 = -\partial^2 W(x,-y)/\partial y^2$. Thus, in the antisymmetric case $\int_\Omega R(W)\,\mathrm{d}\Omega = 0$.

From these two considerations, we conclude that if our solution is symmetric and the condition (38) is not fulfilled, we may have $\int_\Omega R(W)\,\mathrm{d}\Omega < 0$, and thus, once it balances out the positive terms, the bending integral may eventually become negative.

To finish the analysis, we determine the parameter ranges where the condition (38) holds, i.e. where the bending forces are guaranteed to have a stabilizing effect. In the nondimensional system (10)–(16), the condition becomes

$$\tilde{D}_3 \leq \min(1, \tilde{D}_2) , \tag{41}$$

which further expands to

$$\hat{E}^2\nu_{12} + \hat{E}(1-\hat{\nu}) \leq \min(1, \hat{E}^2) . \tag{42}$$

We investigate both possibilities on the right-hand side. First, if $\hat{E} \leq 1$, then (42) reduces to

$$\hat{E} \leq \hat{\nu}/\nu_{12} . \tag{43}$$

This can be written, in terms of the original material parameters, as

$$\frac{E_2}{E_1} \leq \frac{\nu_{21}}{\nu_{12}} , \tag{44}$$

which we note is the case for at least some practically interesting materials (e.g. all isotropic materials, and dry paper with the fibers along the machine direction). In the other case, if $\hat{E} > 1$, we have from (42) the condition

$$\hat{E} \leq \frac{\sqrt{(1-\hat{\nu})^2 + 4\nu_{12}} - (1-\hat{\nu})}{2\nu_{12}} , \tag{45}$$

which can be used to numerically evaluate the limiting value of $\hat{E}$ for any given ν_{12} and $\hat{\nu}$.

It is important to notice that the conditions (43) and (45), and thus (38), are sufficient conditions guaranteeing $\int_\Omega (\triangle_\gamma W)(\triangle_\alpha W)\,\mathrm{d}\Omega \geq 0$ and thus, by (36), also the positive definiteness of the bending integral. However, they are not necessary conditions; we can have $\int_\Omega (\triangle_\gamma W)(\triangle_\alpha W)\,\mathrm{d}\Omega \geq 0$ even if (38) is violated, and in practice, we may expect there to be such a parameter range as $\hat{E}$ is increased beyond the point where the condition (38) is first violated. Eventually, if $\hat{E}$ is further increased, it is possible that the bending integral becomes negative and starts having a destabilizing effect, but this behavior depends on the displacement function W.

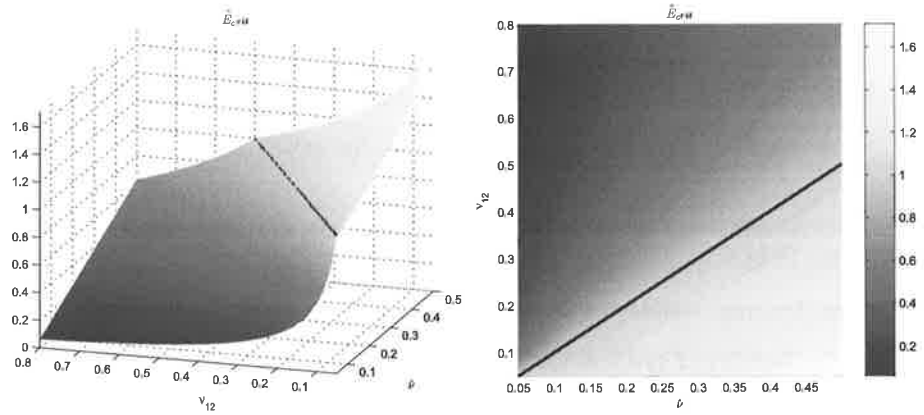

Figure 2: Parameter range where the condition (38) holds; the condition is fulfilled if $0 < \hat{E} \leq \hat{E}_{\text{crit}}$. The bold black line represents the case of isotropic material, on both sides of which $\hat{E}_{\text{crit}}$ has a different expression.

Figure 2 illustrates the range where the condition (38) holds. The part of the 3D space below the plotted surface consists of the union of the regions $\{\hat{E} \leq 1\} \cap \{\hat{E} \leq \hat{\nu}/\nu_{12}\}$ and $\{\hat{E} > 1\} \cap \{\hat{E} \leq \left[\sqrt{(1-\hat{\nu})^2 + 4\nu_{12}} - (1-\hat{\nu})\right]/2\nu_{12}\}$. Whenever a point, specified by a given triplet of parameters, is below (or exactly at) the surface in the figure, then the condition (38) is fulfilled. We especially see that it indeed holds for isotropic material ($\nu_{12} = \hat{\nu}$, $\hat{E} = 1$; from the figure, $\hat{E}_{\text{crit}} = 1$) and dry paper ($E_1 = 8$ GPa, $E_2 = 0.8$ GPa, $\nu_{12} = 0.8$, $\nu_{21} = 0.2$; from which we have $\hat{\nu} = 0.4$ and $\hat{E} = \sqrt{0.8/8} \approx 0.3162$; from the figure, $\hat{E}_{\text{crit}} = 0.5$).

5. CONCLUSIONS

The effect of bending rigidity on the stability of a rectangular, axially travelling thin orthotropic elastic plate was considered. It was found that for a certain range of elastic material parameters, the bending forces are guaranteed to have a stabilizing effect, as is familiar from the isotropic case. However, outside this range the guaranteed stabilization property is lost, and there may exist another range for these parameters in which the forces have a destabilizing character. Explicit expressions were given for the parameter range which guarantees stabilizing behavior, in the case where the shear modulus is estimated by using Huber's formula. Finally, it was calculated that at least for some materials of practical interest, the bending forces are guaranteed to have a stabilizing effect.

REFERENCES

[1] L. Göttsching and H. L. Baumgarten. Triaxial deformation of paper under tensile load. In *The Fundamental Properties of Paper Related to Its Uses, Vol. 1*, pages 227–252. Technical Division of the British Paper and Board Industry Federation, 1976.

[2] J. L. Thorpe. Paper as an orthotropic thin plate. *TAPPI-Journal*, 64(3):119–121, 1981.

[3] J. Skowronski and A. A. Robertson. A phenomenological study of the tensile deformation properties of paper. *Journal of Pulp and Paper Sciences*, 11(1):J21–J28, 1985.

[4] Y. B. Seo. Determination of in-plane shear properties by an off-axis tension method and laser speckle photography. *Journal of Pulp and Paper Sciences*, 25(9):321–325, 1999.

[5] F. R. Archibald and A. G. Emslie. The vibration of a string having a uniform motion along its length. *ASME Journal of Applied Mechanics*, 25:347–348, 1958.

[6] W. L. Miranker. The wave equation in a medium in motion. *IBM J. R&D*, 4:36–42, 1960.

[7] R. D. Swope and W. F. Ames. Vibrations of a moving threadline. *J. Franklin Inst.*, 275:36–55, 1963.

[8] C. D. Mote. Divergence buckling of an edge-loaded axially moving band. *Int. J. Mech. Sci.*, 10:281–195, 1968.

[9] C. D. Mote. Dynamic stability of axially moving materials. *Shock Vib. Dig.*, 4(4):2–11, 1972.

[10] C. D. Mote. Stability of systems transporting accelerating axially moving materials. *ASME Journal of Dynamic Systems, Measurement, and Control*, pages 96–98, 1975.

[11] A. Simpson. Transverse modes and frequencies of beams translating between fixed end supports. *J. Mech. Eng. Sci.*, 15:159–164, 1973.

[12] A. G. Ulsoy and C. D. Mote. Analysis of bandsaw vibration. *Wood Science*, 13:1–10, 1980.

[13] C. D. Mote and A. G. Ulsoy. Vibration of wide band saw blades. *ASME Journal of Engineering for Industry*, 104:71–78, 1982.

[14] S. Chonan. Steady state response of an axially moving strip subjected to a stationary lateral load. *J. Sound Vib.*, 107:155–165, 1986.

[15] J. A. Wickert and C. D. Mote. Classical vibration analysis of axially moving continua. *J. Appl. Mech.*, 57:738–744, 1990.

[16] C. C. Lin and C. D. Mote. Equilibrium displacement and stress distribution in a two-dimensional, axially moving web under transverse loading. *ASME Journal of Applied Mechanics*, 62:772–779, 1995.

[17] C. C. Lin and C. D. Mote. Eigenvalue solutions predicting the wrinkling of rectangular webs under non-linearly distributed edge loading. *Journal of Sound and Vibration*, 197(2):179–189, 1996.

[18] C. C. Lin. Stability and vibration characteristics of axially moving plates. *Int. J. Solids Structures*, 34(24):3179–3190, 1997.

[19] Changho Shin, Jintai Chung, and Wonsuk Kim. Dynamic characteristics of the out-of-plane vibration for an axially moving membrane. *Journal of Sound and Vibration,*, 286(4-5):1019–1031, 9/22 2005.

[20] N. Banichuk, J. Jeronen, P. Neittaanmäki, and T. Tuovinen. On the instability of an axially moving elastic plate. *Int. J. Solids Struct*, 2009. doi:10.1016/j.ijsolstr.2009.09.020.

[21] D. J. Gorman. *Free Vibration Analysis of Rectangular Plates*. Elsevier North Holland, Inc., 1982.

[22] A. Pramila. Sheet flutter and the interaction between sheet and air. *TAPPI-Journal*, 69(7):70–74, 1986.

[23] T. Frondelius, H. Koivurova, and A. Pramila. Interaction of an axially moving band and surrounding fluid by boundary layer theory. *Journal of Fluids and Structures*, 22(8):1047–1056, 2006.

[24] A. Kulachenko, P. Gradin, and H. Koivurova. Modelling the dynamical behaviour of a paper web. part ii. *Computers & Structures*, 85:148–157, 2007.

[25] S. P. Timoshenko and S. Woinowsky-Krieger. *Theory of plates and shells*. New York : Tokyo : McGraw-Hill, 2nd edition, 1959.

[26] V. V. Bolotin. *Nonconservative Problems of the Theory of Elastic Stability*. Pergamon Press, New York, 1963.

[27] Y. B. Chang and P. M. Moretti. Interaction of fluttering webs with surrounding air. *TAPPI journal*, 1991.

[28] L. C. Evans. *Partial Differential Equations*. American Mathematical Society, 1998.

DEFECT DISTRIBUTION AND FATIGUE

Roger Rabb
Research & Development
Wärtsilä Finland Oy
P. O. Box 244
FI-65101 Vaasa, FINLAND

ABSTRACT

The reason for most engine component failures is fatigue. Usually a defect in the form of an inclusion can be found at the initiation point. The extreme value theory can be used to predict the defect size in some material domain if only the distribution of the maximum defect in some reference domain is known. The Gumbel distribution has been found to model these defect distributions well. Fracture mechanics is used to relate the defect to a corresponding fatigue strength. More than a year ago a Finnish strategic research project called FATE-DEFEX was started to examine these questions. The benefits of mastering defect distributions are many. Also failure investigations in the field will be facilitated. Moreover, it will help steelmakers to improve their products and to create better product quality instructions.

FRAMING THE PROBLEM

If dynamic loads acting on an engine part cause a stress amplitude exceeding or close to the fatigue limit, a fatigue failure will probably be the result. Usually, when the fracture surfaces of such engine parts or test specimens are examined, a defect in the form of an inclusion or even a void (pore), see Fig.1c, can be found at the initiation point of the fatigue crack. Sometimes these defects can be so small that they can be hard to detect, and sometimes fatigue cracks can even initiate from badly orientated slip bands of a material grain. However, the fatigue limit of most materials is determined by the maximum defect size in the highly stressed material volume. This fact has been repeatedly proven from the results of examinations of fatigue failures in the field. Mathematically, this means that the use of the extreme value theory is obvious when the likely maximum defects size in some material domain has to be predicted.

Traditionally the fatigue limit is determined with fatigue tests on specimens of a certain size. As an example, the results given by Rabb /1/ of the staircase tests on plain and notched specimens shown in Figs. 1, 2 and 3 are used. A typical defect at the crack initiation point in the fatigue tests of plain specimens was the void shown in Fig. 1c. These specimens were machined from pieces cut from a big cylinder head in nodular cast iron grade 500-7/ISO 1083. A defect at the surface tends to be more prone to initiate a growing fatigue crack than an interior defect. This is partly explained by the higher stress intensity factor caused by the surface defect than by an interior defect of comparable size. But also the stress concentration in a nominally plain specimen, as the one in Fig. 1a, will promote initiation at the surface. In the test illustrated in Fig. 2 all cracks initiated at the surface or very close to it. This will not always be the case. When the size of the specimen grows, the probability to find a much bigger internal defects grows and initiation at an internal defect will take over. However, it is important to notice that real engine components will almost always have a sharp notch which will force the crack to initiate from the surface.

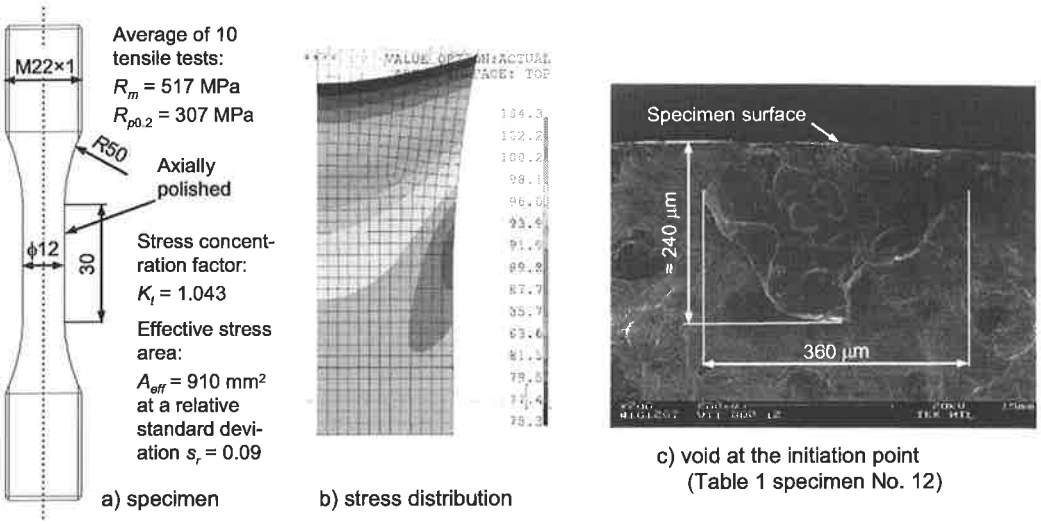

Figure 1. Test specimens of nodular cast iron grade 500-7/ISO 1083 in staircase tests in fully reversed tension compression (stress ratio R = -1) and with stress ratio R = 0.

Defect characterization

It is obvious that it would be tempting to base the fatigue analysis on the use of the actual defect distribution within the material. Many advantages could be possible in this way. For instance, it would encourage the use of fracture mechanics in engineering. The modern trend is to use fracture mechanics more and more – mostly for crack propagation analyses. However, with increasing knowledge of the short crack threshold stress intensity factor, the possibility to use it also as an aid in fatigue analyses is steadily increasing. Failure analyses and the creation of quality instructions would benefit greatly from a possibility to make accurate analyses based on known defect distributions. To be able to do this, the mastering of the threshold stress intensity factor is needed. Also a good knowledge of the defect distribution in the given material and the facility to predict the likely maximum defect in the interesting material domain are needed. The maximum defect size will determine the actual fatigue limit.

The effective use of defect distributions will require some seemingly easy and trivial problems to be solved. For instance, how should, considering the irregular shape of the defects, a meaningful effective size of them be defined? Already in the tests shown in Figs. 1 and 2 on nodular cast iron three different types of defects at the initiation point were found. These types are illustrated in Figs. 1 and 2 as the following, a) the void or pore illustrated in Fig. 1c, b) the nodule cluster shown in Fig. 2b and c) the graphite precipitate shown in Fig. 2c. Moreover, a third complicating factor with defects in the form of inclusions is the friction forces between the defect and the base material. One of the pioneers in this field Y. Murakami /2/ uses the square root of the defect area as the effective defect size in his investigations of bearing steels. This method seems mostly to give fairly good results.

There are also some questions to examine before the most appropriate mathematical distribution can be chosen. It is quite obvious that defects of different types follow their own distribution. Should these distributions be treated separately in the analyses, or is it possible to describe their superposed action with only one distribution? A distinction must be made between the parent distribution in the material and the distribution of extreme values from a collection of samples. The choice of the correct extreme value theory could be influenced by the parent distribution.

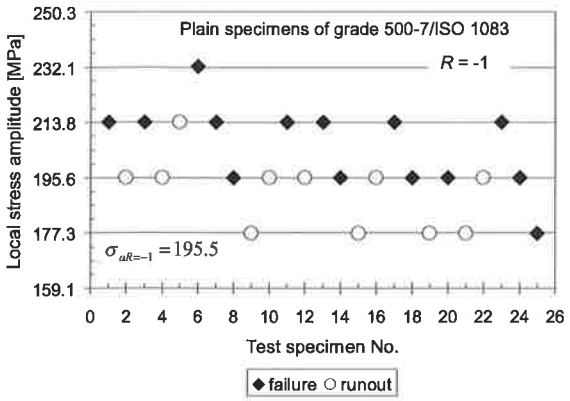

a) Outcome of the staircase test. Cutoff limit 10 million cycles

Nodular cast iron grade 500-7/ISO 1083 with tensile strength R_m = 517 MPa and yield strength $R_{p0.2}$ = 307 MPa.

Maximum likelihood evaluation of the sample fatigue limit from the results of the staircase test gave the following result:

$\sigma_{aR=-1}$ = 195.5 MPa sample fatigue limit

s = 17.6 MPa sample standard deviation

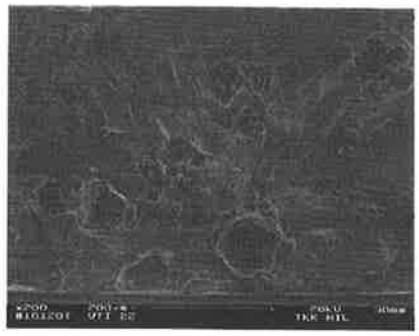

b) nodule cluster

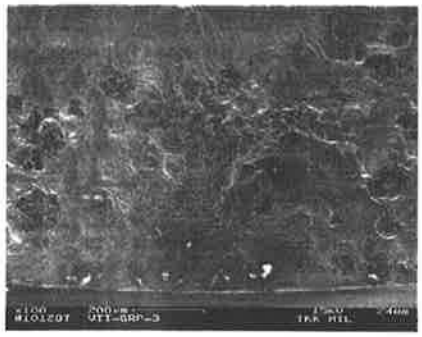

c) graphite precipitate

Figure 2. Outcome of a staircase test on plain specimens and two typical crack initiation sites.

Extrapolation and the theory of the weakest link (TWL)

Extreme value theory has long been used to predict floods and storms over a time interval. As an example, Germanische Lloyd's /3/ rules for wind turbines states that "...The reference wind speed defined as the 10-minutes mean of the extreme wind speed with a recurrence period of 50 years at a height of 10 m, is given for the wind zones in Table...". The fatigue limit and fatigue life of some component is determined by the maximum defect at the critical point and, consequently, fatigue is in fact an extreme value problem.

The traditional fatigue analysis is based upon the tested fatigue limit of specimens with a certain effective stress area. The theory of the weakest link is used to calculate the statistical size factor. This factor is used to change the fatigue limit of the specimen to the corresponding value of the actual component. The number of links is calculated as the ratio of the effective stress areas or stress volumes of the actual component and the reference test specimen. This is illustrated in Fig. 3 with the results of a staircase test on notched specimens. The same material as for the case in Figs. 1 and 2 was used in these notched specimens.

For the theory of the weakest link to give correct predictions of the statistical size factor, the number of links must be defined as the ratio of the larger stress area to the smaller, i.e., the number of links has to be greater or equal to one. The theory of the weakest link is a well established theory. As an example, it has been applied by Rabb et al. /4/ with success on a fretting test with pads and specimens of quenched and tempered steel and with a number of links of about 40 000.

A very important issue when defect distributions are used to predict the statistical size factor is how this extrapolation should be done. Traditionally the so called return period has been used in

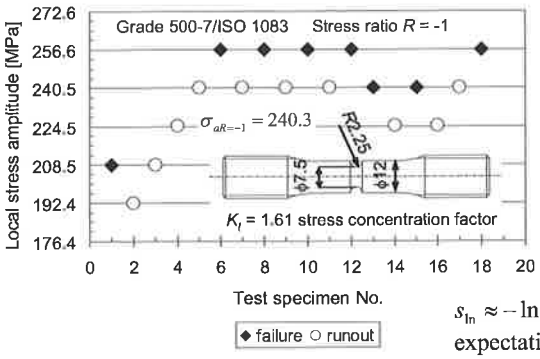

Using tested relative standard deviation $s_r = 0.09$

$A_{eff} = \sum \frac{\ln R_i}{\ln 0.5} \cdot A_i = 21.8\,\text{mm}^2$ effective stress area

$n = \frac{910}{21.8} = 41.7$ number of links related to the plain specimen

$R'' = 0.5 \Rightarrow R = 0.9835 \Rightarrow \lambda = -2.14$

According to TWL the fatigue limit of the notched specimen must be reduced to reliability 98.35 % to give the expectation for the plain specimen, i.e. using lognormal

$s_{\ln} \approx -\ln(1 - s_r) = 0.0943 \Rightarrow K_{size} = e^{-\lambda \cdot s_{\ln}} = 1.224$

expectation $\sigma_{aR=-1,plain} = 240.3 / 1.224 = 196.3 \approx 195.5$ observed

Figure 3. Use of the theory of the weakest link (TWL) gives quite accurate predictions of the statistical size factor.

connection with the extreme value theory, but this measure has at least to be modified when it is used to extrapolate or predict the median defect size in some material volume. The suggested procedure will be shown below.

Clean steels and fatigue survival with material imperfections (FATE-DEFEX)

A big strategic 3-years research project called FATE-DEFEX to investigate these issues was started from the beginning of year 2008. This project is largely financed by TEKES, a Finnish organization directing government money for research. The scope and participants of this project is sketched in Fig. 4.

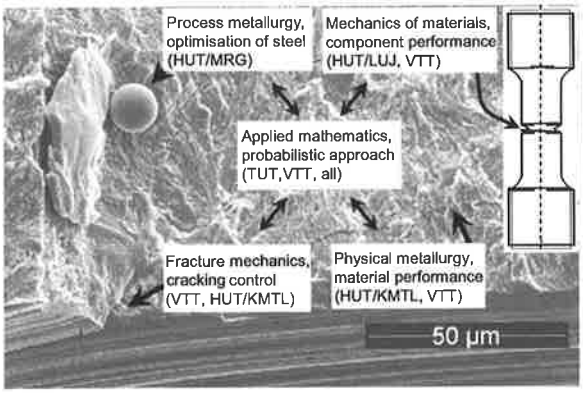

Outline of FATE-DEFEX research volume 12.12.2007/JS		
Specification of tasks		
Task	**keuro**	**Responsible**
Probabilistic approach	60	TUT MSc-thesis (2)
Extreme value distributions	90	VTT expert
Inclusions	180	HUT expert
Fatigue model: Murakami, incl.+H2	220	HUT (PhD-thesis; Japan)
Fatigue assessment, UHCF	60	HUT (MSc-thesis 2)
Murakami model extension to HCF+LCF	50	VTT expert (Japan)
Synthesis, dissemination	120	VTT expert
UHCF notch/gradient fatigue	15	HUT (lab.)
UHCF axial fatigue (defects)	170	VTT (lab.)
Co-ordination	50	VTT expert
Costs	**1015**	**TOTAL**

Abbreviations: TUT Tampere University of Technology
HUT Helsinki University of Technology
VTT Technical Research Centre of Finland

Figure 4. Research project Clean Steels and Fatigue Survival with Material Imperfections (FATE-DEFEX).

GUMBEL DISTRIBUTION – A USEFUL EXTREME VALUE DISTRIBUTION

The choice of the best suited extreme value distribution function has to be carefully considered. There exist many different possibilities, a part of which can be found in e.g. Coles' /5/ text book on extreme value theory. As long as the defect distributions in different materials are badly examined and known, it is better to use a distribution which is as simple as possible and not to complicate the statistical treatment with a too difficult distribution with many hardly testable variables. When more experiences have been collected, it is possible to judge if another distri-

bution function would provide any benefits. Although quite many different extreme value distribution functions have been tried in project FATE-DEFEX, the focus will here be on the Gumbel distribution function. This contains only two parameters that need to be tested, and it is easy to fit to test data by using the maximum likelihood method. However, some comparisons to the somewhat more complicated generalized extreme value theory (GEV) will be made. This distribution contains a third parameter, the shape parameter, which often can be difficult to evaluate from the test results.

The Gumbel density and distribution functions are as follows:

$$f(a)=\frac{1}{\sigma}\cdot e^{\frac{a-\mu}{\sigma}}\cdot e^{-e^{\frac{a-\mu}{\sigma}}} \qquad \text{density function} \qquad (1)$$

$$G(a)=P(\text{defect size}\le a)=e^{-e^{\frac{a-\mu}{\sigma}}} \qquad \text{distribution function} \qquad (2)$$

where
- a defect size
- P probability
- μ location parameter ($G(\mu)=1/e=0.367$)
- σ scale parameter
- e base of natural logarithm, i.e., Napier's number 2.7183...

The mean value and standard deviation for the Gumbel distribution are as follows:

$$s=\frac{\pi\cdot\sigma}{\sqrt{6}} \qquad \text{standard deviation} \qquad (3)$$

$$\bar{\mu}=\mu+\gamma\cdot\sigma \qquad \text{mean value} \qquad (4)$$

where

$$\gamma=-\int_0^1 \ln\left(\ln\frac{1}{x}\right)dx=0.57721.... \qquad (5)$$

The absolute standard deviation is constant, but it will be shown below that the relative standard deviation will change in the extrapolation.

Maximum likelihood evaluation of the parameters

Because of the shape of the density function, it is obvious that, if there is a sequence of tested extreme values a_i (i = 1,...,n), the best fit of the density function is when the following equation has its maximum value. This is the essence of the maximum likelihood method.

$$L(\mu,\sigma)=\prod_{i=1}^{n} f(a_i;\mu,\sigma)=\frac{1}{\sigma}\cdot\prod_{1=1}^{n} e^{\frac{a_i-\mu}{\sigma}}\cdot e^{-e^{\frac{a_i-\mu}{\sigma}}} \qquad (6)$$

By taking the logarithm of both sides of Eq. (6), a more convenient form, the log-likelihood form, to handle can be obtained. In connection with the Gumbel distribution, a still more convenient way to fit the density function in a maximum likelihood sense is to use the method of least squares. To do this a ranking of the observed defects from the smallest to the biggest has first to be done, i.e.

$$a_1\le a_2\le\ldots\le a_n \qquad \text{ranking of the defects} \qquad (7)$$

After the ranking, the empirical distribution function is constructed in the following way. The empirical distribution function is an approximation of the correct one in Eq. (2)

$$F_i = \frac{i}{n+1} \qquad i = 1,2,...,n \tag{8}$$

A linearization of the distribution function is obtained by taking the natural logarithm two times of Eq. (2). The value of the double logarithm is called the reduced variate.

$$y = -\ln(-\ln P) \qquad \text{reduced variate} \tag{9}$$

$$\Rightarrow$$

$$a = \mu + \sigma \cdot y \qquad \text{i.e., the defect size is linearly related to the reduced variate} \tag{10}$$

The following expression has to be minimized to find the parameters in the distribution function:

$$F(a) = \sum_{i=1}^{n} [a_i - (\mu + \sigma \cdot y_i)]^2 \tag{11}$$

By derivating Eq. (11) with regard to the location parameter μ and scale parameter σ and putting the derivatives equal to zero, two equations are obtained to solve them:

$$\sigma = \frac{n \cdot D - A \cdot B}{n \cdot C - B^2} \tag{12}$$

$$\mu = \frac{A - B \cdot \sigma}{n} \tag{13}$$

where $$A = \sum_{i=1}^{n} a_i \tag{14}$$

$$B = \sum_{i=1}^{n} y_i \qquad \text{with} \qquad y_i = -\ln(-\ln F_i) \tag{15}$$

$$C = \sum_{i=1}^{n} y_i^2 \quad \text{and} \quad D = \sum_{i=1}^{n} y_i \cdot a_i \tag{16} \quad (17)$$

Extrapolation

The parameters of the Gumbel distribution function derived as shown in the previous chapter are related to specimens, like the one shown in Fig. 1, or to some other control area. In the FATE-DEFEX project, standardized mirror-polished control areas with the dimension 5×5 mm are scanned. Every defect exceeding 5 µm can be found in this way. To obtain the extreme value distribution of such control areas, the maximum defect of about 50 control areas are recorded and treated in the way described above.

The real purpose of using extreme value theory is, however, to get a tool to predict the likely median defect size in a different area than the control area. To get an image of how this extrapolation can be done, it is thought at the moment that this area is bigger than the control area, i.e., the area ratio (number of links) is as follows:

$$n = \frac{A_{eff}}{A_{control}} \tag{18}$$

When floods and storms are predicted, the concept return period T ($T = n$) is normally used. The relation between probability of non-exceedance and return period is in such cases defined as $P = (T\text{-}1)/T$. The extreme value corresponding to this probability is expected to be exceeded on average once every T years.

In the FATE-DEFEX project, it has been found more suitable to extrapolate the likely median value of the defect in a slightly different way. This defect size can be calculated with Eq. (10) using the following probability of non-exceedance which also will work for $n < 1$:

$$P = \frac{n}{n+1} \tag{19}$$

Another way to extrapolate is an analogy to the theory of the weakest link. If $P_{a\max}$ is the probability of nonexceedance, i.e., $a \le a_{\max}$ for one control area, then if there are n pieces, the probability of non-exceedance $P_{a\max\text{-}n}$ will be much less or as follows:

$$P_{a\max-n} = P_{a\max}^{n} = \left\{\exp\left[-\exp\left(-\frac{a_{\max}-\mu}{\sigma}\right)\right]\right\}^{n} \tag{20}$$

To have a total probability of non-exceedance of 50 % for a system consisting of n control areas, the corresponding probability of the single control area must be taken at

$$P_{a\max} = \sqrt[n]{P_{a\max-n}} = \sqrt[n]{0.5} \tag{21}$$

As with the theory of the weakest link, to get meaningful results now, the area ratio has to be bigger than one. By taking the double logarithm of Eq. (20) the following interesting form is obtained:

$$\ln\left(-\ln P_{a\max-n}\right) = -\frac{a_{\max}}{\sigma} + \left(\frac{\mu}{\sigma} + \ln n\right) \tag{22}$$

This means that the extrapolated mean defect size $\overline{\mu}_n$ is

$$\overline{\mu}_n = \mu + \sigma \cdot (\gamma + \ln n) \qquad \text{mean value for } n \text{ control areas} \tag{23}$$

And hence, although the absolute standard deviation according to Eq. (3) will not change, the relative value s_r will change due to the increase of the mean value, i.e.

$$s_r = \frac{s}{\overline{\mu}_n} = \frac{\pi}{\sqrt{6}\cdot\left(\frac{\mu}{\sigma} + \gamma + \ln n\right)} \tag{24}$$

Application of the theory to the two staircase tests on nodular cast iron

The application of the theory given above will now be illustrated on the staircase tests on nodular cast iron illustrated in Figs. 1, 2 and 3. The fracture surfaces of the broken plain specimens of these tests were examined with an electrone microscope to find the defect at the crack initiation point. The observed defects are listed in Table 1. The obtained defect distribution is of course a little biased towards too big defects because the defects in the runouts were not examined. The defects in the runouts should also have been examined by increasing their load level until failure occurred and by examining their fracture surfaces. Regrettably, the area of the observed defects was not measured. Only the peripheral width, radial height, and distance to the surface were measured. The area of these defects is for this reason calculated assuming an elliptical shape. However, when the effective surface crack depth is calculated, a semi-elliptical crack with axis ratio a/c = 0.7 is

Table 1. Defects at the crack initiation point of the failed plain specimens of nodular cast iron.

Specimen No.	Defect size Width 2c × height 2a [μm]	Distance to surface [μm]	Defect area $A = \pi ac$ [μm²]	Effective crack depth [μm] $a_{eff} = \sqrt{\frac{2 \cdot 0.7 \cdot A}{\pi}}$	Description
1	890×1020	220	712980	564	Large shrinkage pore near the surface
2	370×320	0	92990	204	Shrinkage pore at the surface
3	480×560	70	211120	307	Large graphite precipitate
4	290×380	0	86550	196	Shrinkage pores near the surface
5	320×230	0	57810	161	Graphite precipitate at the surface
6	380×390	0	116400	228	Shrinkage pore at the surface
7	350×580	0	159440	267	Shrinkage pore at the surface
8	650×560	0	285880	357	Shrinkage pore at the surface
9	340×690	0	184250	287	Shrinkage pore at the surface
10	290×380	0	86550	196	Graphite nodule cluster at the surface
11	330×340	0	88120	198	Shrinkage pore at the surface
12	360×240	0	67860	174	Shrinkage pore at the surface
13	330×310	0	80350	189	Shrinkage pore at the surface
14	400×680	110	213630	309	Shrinkage pore near the surface
15	310×260	0	63300	168	Probably a nodule cluster
16	430×760	0	256670	338	Shrinkage pores at the surface
17	190×220	110	32830	121	Two close shrinkage pores
18	580×630	0	286980	358	Shrinkage pore at the surface
19	750×500	0	294520	362	Shrinkage pore at the surface
20	260×290	0	59220	162	Shrinkage pore at the surface
21	230×300	0	54190	155	Two shrinkage pores at the surface
22	310×230	0	56000	158	Probably a nodule cluster at the surface
23	440×820	0	283370	355	Shrinkage pores at and near the surface
24	650×430	0	219520	313	Shrinkage pore at the surface
25	1540×260	0	314470	374	Large shrinkage pore at the surface
26	570×280	0	125350	236	Shrinkage pore at the surface
27	270×250	0	53010	154	Graphite precipitate at the surface
28	460×330	0	119220	230	Nodule cluster at the surface
29	250×200	0	39270	132	Shrinkage pore at the surface
30	230×310	0	56000	158	Shrinkage pore at the surface

assumed. This axis ratio gives the maximum stress intensity factor at the bottom of the crack. The following mean defect size and standard deviation are obtained from the values in Table 1:

$$a_{mean} = \frac{1}{n} \cdot \sum_{i=1}^{n=30} a_{eff,i} = 247 \ \mu m \quad \text{and} \quad s = \left[\frac{1}{n-1} \cdot \sum_{i=1}^{n=30} \left(a_{eff,i} - a_{mean} \right)^2 \right]^{1/2} = 100 \ \mu m$$

The maximum likelihood fit of the Gumbel and GEV distribution functions to the values in Table 1 is shown in Fig. 5. Moreover, the extrapolation to the effective stress area of the notched specimen in Fig. 3 is sketched. It is surprising to see how much the fits of the Gumbel function with the methods of least square and with the log-likelihood differ. However, in this case the fit with the method of least squares provides better predictions. It seems like the GEV distribution could be more suitable in the upper tail, but at the lower tail it gives altogether too big a median defect size. As will be shown later, the predicted median defect size 87.9 μm in the notch is in fairly good agreement with the tested statistical size factor. The location parameter 201.0 μm and scale parameter 85.8 μm for the defect distribution from the plain specimens indicate that the mean value and standard deviation will be in good agreement with the approximate values calculated

directly from the values in Table 1, i.e. using Eqs. (3) and (4) as follows:

$$a_{mean} = 201 + 0.5772 \cdot 85.8 = 250.5 \ \mu m \quad \text{and} \quad s = \frac{\pi \cdot 85.8}{\sqrt{6}} = 110.0 \ \mu m$$

The 95 % confidence interval for the Gumbel distribution function in Fig. 5 is calculated with an equation given in the American standard ASTM E 2283 – 03. The standard does not explain how this equation has been derived, and it is a bit unclear how these limits should be interpreted and used.

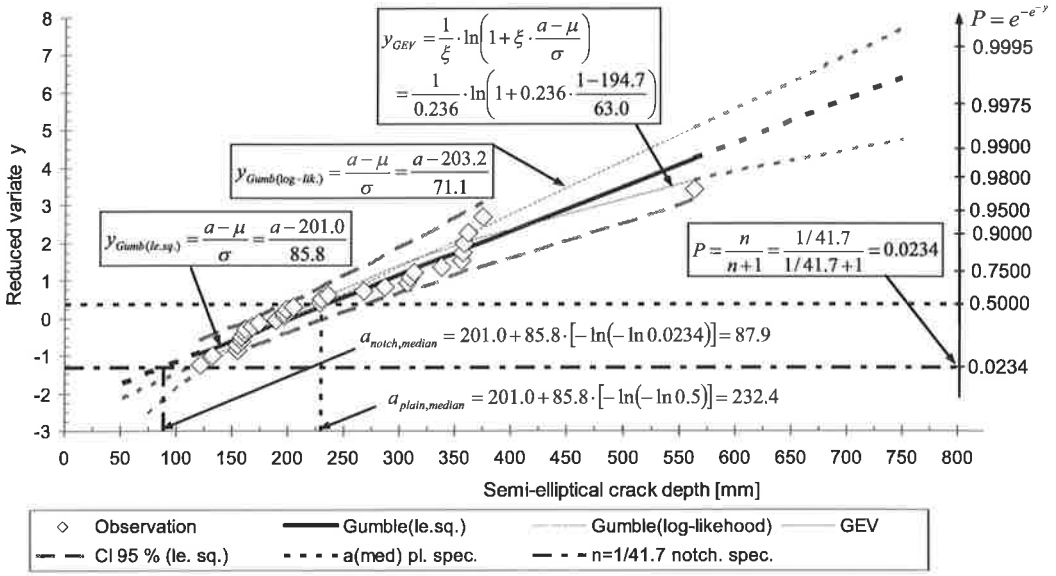

Figure 5. Gumbel and GEV distribution functions fitted to the defects found at the crack initiation point of the broken plain specimens in staircase tests on nodular cast iron.

RELATION BETWEEN DEFECT SIZE AND FATIGUE LIMIT

The effective use of the likely maximum defect size in some material domain presupposes that the corresponding fatigue limit can be estimated. This requires good knowledge of the threshold of the short crack stress intensity factor. Much research is going on nowadays in this field, and it has already been decided in the connection with the FATE-DEFEX project to investigate in a separate project both the long crack and short crack thresholds and crack growth parameters. A promising approach could be to use for instance the Kitagawa-Takahashi /6/ diagram modified in the short crack regime as El Haddad et al. /7/ suggest. Because these tests have not yet been conducted, the values given by the material data base of AFGROW /8/ and also by Janssen et al. /9/ are used to get an idea of the threshold stress intensity factor for nodular cast iron. This factor is chosen corresponding to a stress ratio of $R = \sigma_{min}/\sigma_{max} = 0$ to avoid the tricky question of crack closure as far as possible. The fatigue limit at this stress ratio of the plain specimen in Fig. 1 was also tested and is $\sigma_{aR=0} = 127.4$ MPa. The crack closure effect is assumed to act in the same way on both the effective stress range and the effective stress intensity factor as shown in Fig. 6.

The material data base of AFGROW contains only one nodular cast iron, i.e., A536 Grd 80-55-06 with the following static strength properties: tensile strength $R_m = 552$ MPa and yield strength $R_{p0.2} = 400$ MPa. This material has thus somewhat higher static strength than the material used in the fatigue tests described above. The range of the stress intensity factor threshold given by AFGROW

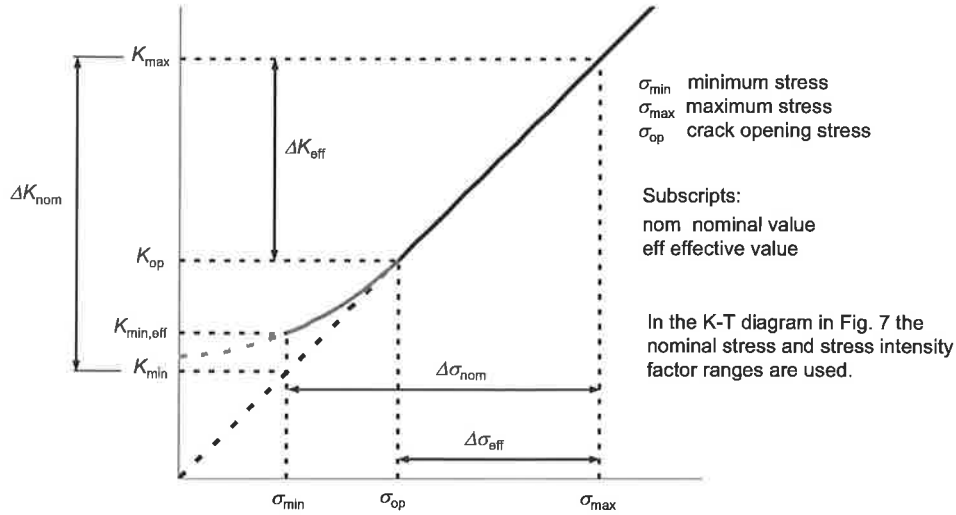

Figure 6. Interpretation of nominal and effective stress range and corresponding range of the stress intensity factor.

is remarkably high, i.e., $\Delta K_{th,R=0} \approx 8.8$ MN/m$^{3/2}$. Janssen et al. give a considerably lower value of $\Delta K_{th,R=0} = 6.2$ MN/m$^{3/2}$ for some not specified nodular cast iron type with a much higher fatigue limit of $2 \cdot \sigma_{aR=0} = 320$ MPa than the actual 2·127.4 MPa. The value given by AFGROW seems therefore to suit to the test data better and is therefore used in the construction of the Kitagawa-Takahashi (K-T) diagram. The relation between the stress range at start of crack propagation and range of threshold stress intensity factor is as follows:

$$\Delta\sigma = \frac{\Delta K_{th}}{C_g \cdot \sqrt{\pi \cdot a}} \qquad \text{for long cracks} \qquad (25)$$

$$\Delta\sigma = \frac{\Delta K_{th}}{C_g \cdot \sqrt{\pi \cdot (a + a_0)}} \qquad \text{El Haddad et al. modification for short cracks} \qquad (26)$$

where
- a crack length
- a_0 intrinsic crack length
- C_g geometry factor (≈ 0.817 for a semi-elliptical surface crack according to Janssen et al. /9/)

The K-T diagram constructed with these values is shown in Fig. 7. The modified curve fits very well to test data when the intrinsic crack length is chosen to 336.5 µm. Usually the intrinsic crack length is chosen to correspond to the crack length where the linear extension of the curve crosses the horizontal line for the stress range at the fatigue limit. This value would be 569 µm and thus a little bigger than the chosen. However, with the chosen intrinsic crack length, it is seen that the modified curve gives the correct tested fatigue limit 127.4 MPa at the tested median defect size 232.4 µm. Moreover, the lines corresponding to the tested standard deviations on both fatigue limit and defect size cross at nearly exactly the right points. This excellent agreement gives confidence that it is possible to calculate also the expected standard deviation of the fatigue limit from the known defect distribution. For the fatigue limit a relative standard deviation of 10 % has now been used because a more careful examination of the fatigue tests has shown that it is closer to 10 % than to the 9 % mentioned before.

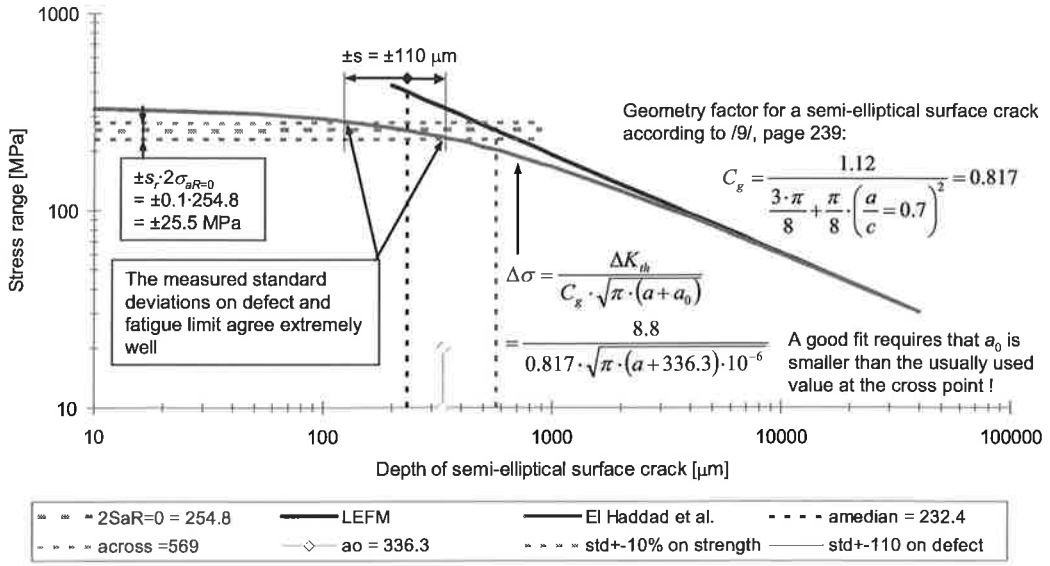

Figure 7. Comparison of tested average defect size and fatigue limit in a modified K-T diagram.

DISCUSSION

The results already gained in project FATE-DEFEX have proved that it is possible to develop methods to calculate the expected fatigue limit and its scatter from the knowledge of the maximum defect distribution in some control areas of the material. This is very promising because the use of defect distributions offer some advantages compared with the use of only the tested fatigue strength. These advantages are

1. A better understanding of the fatigue phenomenon
2. Introduces fracture mechanics as a normal tool to handle both the crack initiation and the propagation stages
3. Facilitate the creation of quality instructions where allowable defect sizes can be stipulated at different places
4. Failure examinations can be made more exact
5. For steel suppliers it will be a help in their striving to create clean steels

However, much work has still to be done before these methods can be taken into regular use and at the present moment they can only serve as a good complement to the normal fatigue analysis. More comprehensive data bases over defect distributions of different materials have to be created. Exact knowledge of the short crack behaviour must be established. It may also be necessary to use a method which combine separately the different distributions which have been found for different inclusions types. This is illustrated in Fig. 8 from tests of control areas of quenched and tempered steel 34CRNiMo6 in project FATE-DEFEX. In fact the log-likelihood form of Eq. (6) has been used to create Fig. 8. The differences in the parameter values obtained with various methods of fitting the distribution functions must also carefully be considered.

It seems also clear that to collect information of the maximum defect distribution by looking for the defect at the crack initiation point of the specimens in a fatigue test will give more trustful data than to examine the polished surfaces of small control samples. In this way, a much bigger domain can be examined, and it is obvious that it is the worst defect that has caused the initiation. It is also worth to remember that to investigate material anisotropy, specimens and control samples should be taken both perpendicularly and parallel to the grain flow.

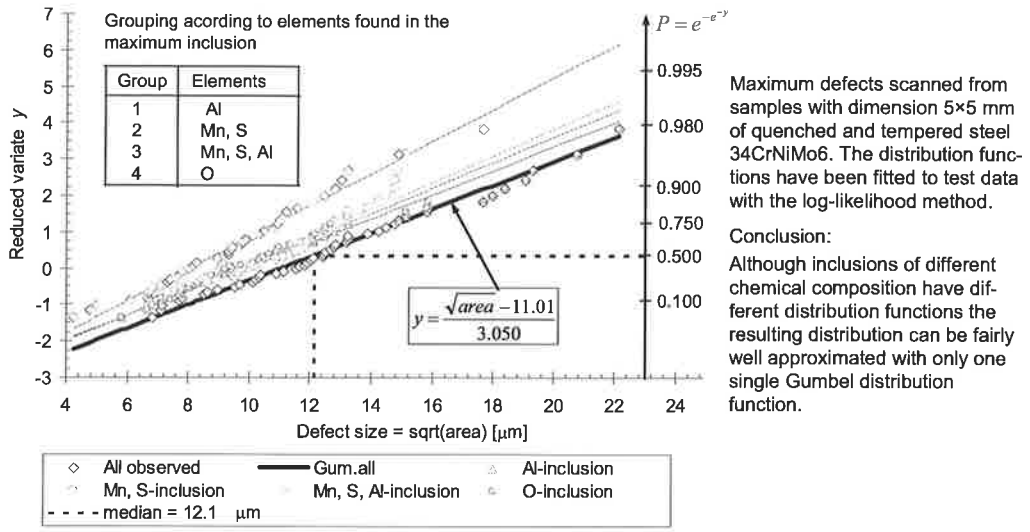

Maximum defects scanned from samples with dimension 5×5 mm of quenched and tempered steel 34CrNiMo6. The distribution functions have been fitted to test data with the log-likelihood method.

Conclusion:

Although inclusions of different chemical composition have different distribution functions the resulting distribution can be fairly well approximated with only one single Gumbel distribution function.

Figure 8. Defect distributions found in FATE-DEFEX from samples with control area 5×5 mm grouped according to inclusion analysis. Data from reference /10/.

REFERENCES

/1/ B. R. Rabb. Fatigue Testing and Its Statistical Evaluation Into Design Rules. Tampere University of Technology Publications 253. Dissertation April 1999.

/2/ Y. Murakami. Metal Fatigue: Effects Of Small Defects and Nonmetallic Inclusions. Elsevier Science Ltd. 2002.

/3/ Germanischer Lloyd. IV Rules and Guidelines. Industrial Services. Guideline For the Certification Of Wind Turbines. 1 General Conditions for Approval. Edition 2003 with Supplement 2004.

/4/ R. Rabb, P. Hautala and A. Lehtovaara. Fretting Fatigue In Diesel Engineering. Proceedings from the CIMAC Congress 2007 in Vienna.

/5/ S. Coles. An Introduction To Statistical Modeling Of Extreme Values. Springer-Verlag London Limited 2001.

/6/ H. Kitagawa and S. Takahashi. Applicability Of Fracture Mechanics To Very Small Cracks Or the Cracks In the Early Stage. 2nd International Conference on Mechanical Behaviour of Materials, Boston, Mass., Aug. 1976, pp. 627-630.

/7/ M. H. El Haddad, K. N. Smith and T. H. Topper. Fatigue Crack Propagation Of Short Cracks. Transactions of ASME. Vol. 101, January 1979.

/8/ AFGROW. Afgrow Users Guide and Technical Manual. James A. Harter, June 2004. http://www.afgrow.net

/9/ M. Janssen, J. Zuidema and R. J. H. Wanhill. Fracture Mechanics. Second edition. Delft University Press 2002.

/10/ Hanna-Kaisa Hurme. Teräksen Tilastollinen Rakenneanalyysi. Master Thesis. Tampere University of Technology 06.05.2009.

EFFECT OF GEOMETRICAL FEATURES AND SCALE ON FAILURE INITIATION OF WOOD LIKE CELLULAR MATERIAL

ALP KARAKOÇ and JOUNI FREUND

Department of Applied Mechanics
Helsinki University of Technology,
P.O.Box 4300
FIN-02015 HUT, FINLAND
email: alp.karakoc@tkk.fi

ABSTRACT

The scale and irregularity effects on strength of a honeycomb material are discussed. The results of a virtual experiment, based on a micromechanical model and the use of Abaqus® Standard and Mathematica® software packages, indicate that strength decreases in scale and irregularity.

1. INTRODUCTION

Wood is a cellular material which has anisotropic and heterogeneous nature at different structural levels, which has been the center of interest due to wide applicability as an engineering material. Especially, understanding of wood at cell level and integrating this knowledge on different scales give more precise material description. The reason is that wood deformation and fracture can be clearly explained in terms of cell wall peeling and breaking at cellular level.

The material data for wood is strongly influenced by the type of species and the growth conditions of the trees. This indicates that the material behaviours at higher structural levels are strongly influenced by lower levels. Thus, in order to provide realistic material descriptions, wood must be analyzed starting from-micro-to-macro levels [1]. For this purpose, statistical strength approach is appropriate inside each sample and between different samples which are classified based on structural levels (in other words, different scales), etc. By mimicking the cellular composition as depicted in Figure 1, each sample is defined based on diverse properties which can be density, cell wall cross-section and configuration, i.e. rectangle, hexagon, etc., cell number per unit volume and loading condition.

Hence, the aim is to discuss the effect of geometrical features of cellular structure and size of the specimen on statistics of failure initiation load by using micromechanical modeling. A square sample of wood like material, consisting of hexagonal cells with thin walls, modeled as slender beams, is considered. The material inside the cells is taken to be soft compared to the walls and the walls almost inextensible. Bending moment on a wall is taken to be critical for failure. As the length-to-thickness ratio of tracheids is usually very large, variation of quantities in the plane perpendicular to the long direction of tracheids, is taken to be decisive.

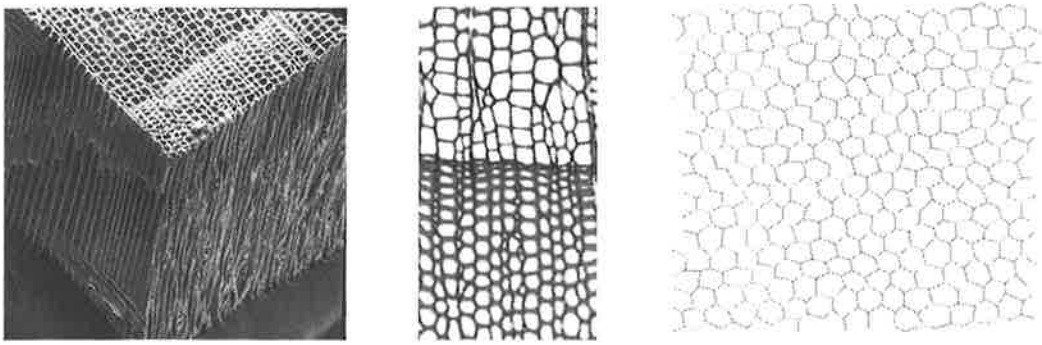

(a) (b) (c)

Figure 1: (a) Tracheids of a softwood species [2] ; (b) yellow pine cross-section [3] and (c) rectangular micro-model composed of irregular hexagonal cells.

2. MICROMECHANICAL MODEL

As the length to thickness ratio of wood-cells is large, the effect of heterogeneity on strength can be studied by using a 2D model. In a simple micromechanical model, the walls of the cells are taken as beams with some statistics on thickness, Young's modulus, length, and strength.

2.1. Material element

The material element is a $H \times H$ square having a honeycomb structure (Figure 2). The cell size of the regular structure is denoted by h. Regularity of the honeycomb structure is described by a one-parameter model, in which $\alpha = 0$ corresponds to a regular structure and a value $\alpha > 0$, a random deviation in shape and size taken from the uniform distribution as illustrated in Figure 2. To be precise, the vertex points are given random offsets of magnitude αh. The geometrical parameters of interest are the relative size of the hexagonal cells H / h and irregularity α.

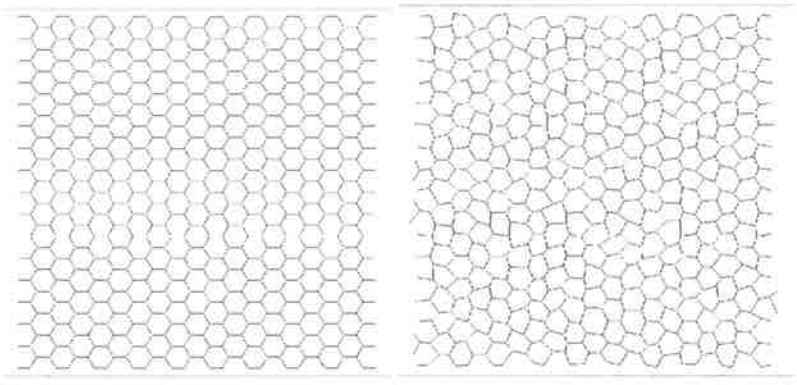

Figure 2: Regular ($\alpha = 0$, left) and irregular ($\alpha = 0.1$, right) honeycomb in a square $H / h = 28$.

In the laboratory $XY-$coordinate system, the domain occupied by the specimen is $\Omega = [0, H] \times [0, H]$.

2.2. Beam equations

In the micromechanical model, the walls of the cells (Figure 2) are modelled as elastic Timoshenko beams in order to provide applicability in a wider range, i.e., from slender to thick beams. The material inside the cells is taken to be soft compared to that of the walls. The differential equations of an elastic Timoshenko plane beam model in xy-coordinate system are

$$EAu'' + f_x = 0\,, \tag{1}$$

$$GA(v'' - \psi') + f_y = 0\,, \tag{2}$$

$$EI\psi'' + GA(v' - \psi) = 0\,, \tag{3}$$

in which EA, GA, EI are the constant material parameters of the problem and f_x, f_y are the components of the external forces. Above u, v, ψ are the displacement components in the directions of the x-axis and y-axis and rotation component in the direction of the z-axis. The x-axis of the material coordinate system is assumed to coincide with the neutral axis of the beam.

The constitutive equations for the normal force and shear forces, and the bending moment are $N = EAu'$, $Q = GA(v' - \psi)$ and $M = EI\psi'$, respectively. Solutions to equations (1), (2), (3) for the beams of Figure 2 are connected by continuity conditions concerning displacement and rotations at the vertex points and the equilibrium equations of the vertex point.

2.3. Failure criterion

Failure mechanisms of a cellular structure depend highly on the material details. In wood, separation of the cells and cell-wall breaking are common. Identification and modelling of the likely mechanisms are one of the challenges of a virtual experiment design. Here, the material is assumed to fail when the bending moment in a beam exceeds its limit value M_{cr}.

Let us denote the maximal absolute values of the bending moments of the beams of Figure 2 by $M_i \quad i \in \{1, 2, \ldots, n\}$ (n is the number of the beams). Then the failure initiation occurs when

$$\max_{i\in\{1,2\ldots n\}} M_i = M_{cr} \tag{4}$$

and the beam of failure initiation is the maximize of the bending moment in the structure. Assuming that the loading of the specimen of Figure 2 depends on parameter f, the external force acting on the beams is proportional to f, and that the solution to equations (1), (2), (3) is known for the parameter value $\bar{f}$, the critical value of the loading parameter f_{cr} making the first beam to fail, is given by

$$f_{\mathrm{cr}} = \bar{f}\frac{M_{\mathrm{cr}}}{\max_{i\in\{1,2\ldots n\}} M_i} \tag{5}$$

in which the overbar in $\bar{M}_i$ means a value obtained with $\bar{f}$. Therefore, under linearity assumption, it is enough to solve the problem with some value of the loading $\bar{f}$. In what follows, the loading parameter f represents a constant macroscopic stress acting on the material element of Figure 2 multiplied by the thickness of the material element.

3. VIRTUAL EXPERIMENT ON STRENGTH

A virtual experiment on strength is designed similar to a physical one: in order to study population characteristics –such as strength of a heterogeneous honeycomb material–, experiment is repeated on a random sample, and the strength statistics is estimated from the results of the sample. In the design here, the aim is to study the effect of geometrical parameters on strength statistics.

The independent variables of the experiment are scale H/h and irregularity α. The dependent variable is the dimensionless loading parameter $f_{cr}h^2/M_{cr}$ of the failure initiation. Material parameters of the model are assumed to satisfy condition $EI/EAh^2 \ll 1$ and $EI/GAh^2 \ll 1$ so that the bending effect in (1), (2), (3) is significant. Above, quantities h and M_{cr} are used for the dimensionless representation.

3.1 Strength test

Figure 3 illustrates a strength experiment with somewhat different combinations of the independent variables H/h and α. The actual specimen size is chosen to somewhat larger than the measuring domain. The critical bending moment M_{cr} is taken to be very large compared to that of the red beams so that these elements never fail. Otherwise the material properties of the blue and red beams are the same. This is quite essential as the constant loading acting on the edges tend to cause artifacts in the bending moment near the edges and thereby failure initiation whose location is not evenly distributed in the measuring domain. The zero traction condition seems not to be an exception in the rule.

In practice, the blue elements are just excluded from the set of beams in equation (5). Also, one of the vertices is given the zero displacement and rotation to make the solution to (1), (2), (3) unique. The external loading of Figure 3 acting on the specimen is taken into account in equations (1) and (2) of the beams on the edge: The components of the loading in the directions of the beam coordinate system are $f_x = f\cos\gamma$ and $f_y = f\sin\gamma$ in which angle γ defines the orientation of the beam.

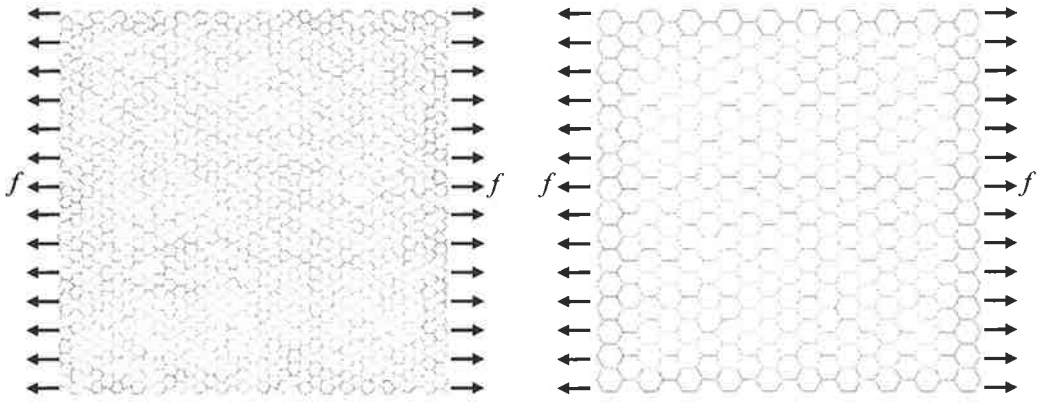

Figure 3: Specimen of the strength test: (left) $H/h = 56$ and $\alpha = 0.13$; (right) $H/h = 28$ and $\alpha = 0$.

Virtual strength tests are performed with Abaqus® Standard and Mathematica® software packages. Mathematica is used as the pre- and post-processor and Abaqus to solve the beam equations on the honeycomb structure.

3.2. Sample

The effect of geometrical parameters on strength is studied by taking a $n=100$ sample from populations having fixed values of the geometrical parameters H/h and α. Calculations are repeated on all combinations of the parameters $\alpha \in \{0, 0.03, 0.05, 0.07, 0.1, 0.13, 0.15, 0.2\}$ and $H/h \in \{28,56,112\}$. In total, 2400 experiments are conducted. Total computational time for the entire process is around 14~16 hours.

4. RESULTS

For each fixed combination of the geometrical parameters, the virtual experiment gives a set $F=\{f_1, f_2, \ldots f_n\}$ $(n=100)$ of critical values f_{cr} of the loading. This data is used to generate the experimental cumulative distribution function of failure

$$\mathrm{cdf}(f_{cr}) = \frac{\left|\{f \in F : f \le f_{cr}\}\right|}{|F|} \tag{6}$$

in which $|\ |$ denotes the size of a set. The cumulative distribution function gives the probability with which a specimen fails under loading f_{cr}. Alternatively, one may think that (6) gives an estimate for the proportion of the specimen of the population failing before f_{cr}. The experimental cumulative distribution functions are shown in Figure 4 and Figure 5.

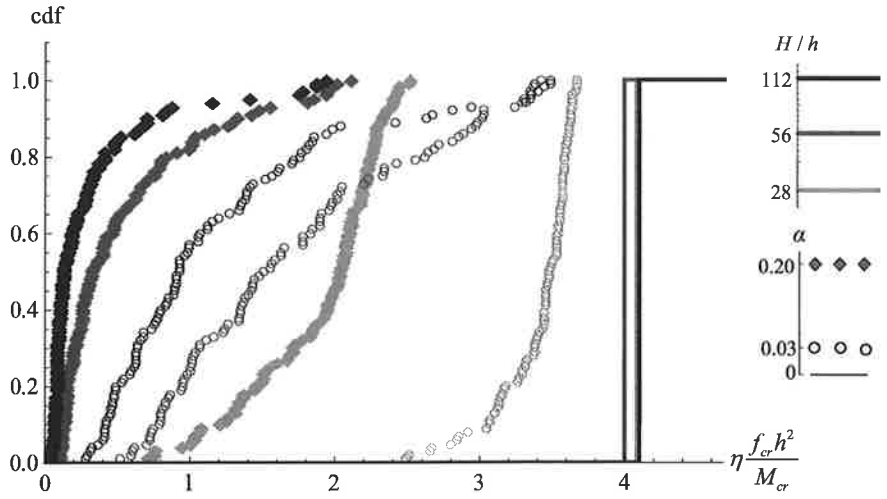

Figure 4: Experimental cumulative distribution functions of failure initiation for scales $H/h \in \{28, 56, 112\}$ and irregularities $\alpha \in \{0, 0.03, 0.2\}$. For convenient representation, η is used as a coefficient

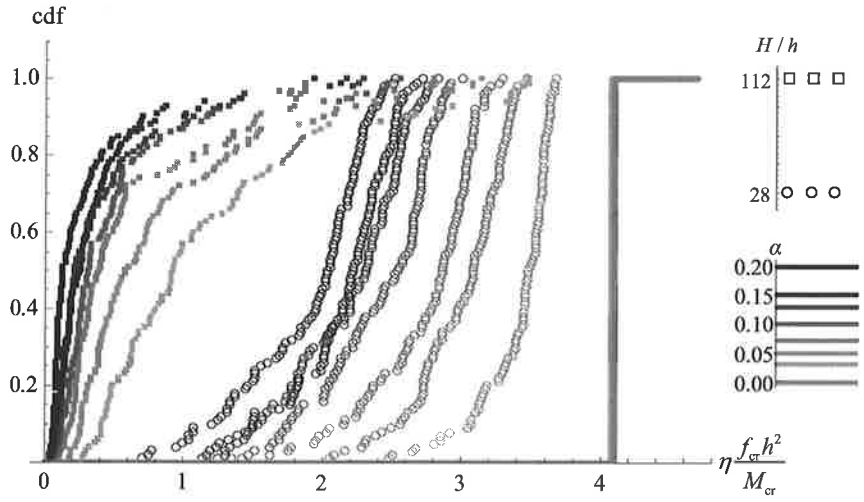

Figure 5: Experimental cumulative distribution functions of failure initiation for scales $H/h \in \{28, 112\}$ and irregularities $\alpha \in \{0, 0.03, 0.05, 0.07, 0.1, 0.13, 0.15, 0.2\}$. For convenient representation, η is used as a coefficient

The solid lines of the figures correspond to regular structures $\alpha = 0$. The strength of a regular honeycomb structure does not depend on H/h and the cumulative distribution function corresponds to a deterministic material behaviour. Strength clearly decreases in irregularity and even a small geometrical imperfection ($\alpha = 0.03$) may induce a large reduction in strength [4]. Furthermore, the material behaviour depends on the scale H/h so that strength decreases in scale. This is understandable as a large specimen is more likely to contain severe imperfections than a small one and strength criterion, based on the failure initiation, is sensitive to that [5]. The cumulative distribution function approaches deterministic material behaviour, when $H/h \to \infty$ for $\alpha > 0$ because possibility of imperfection existence increases. The strength at this "homogeneous material" limit is, however, much lower than that for $\alpha = 0$.

5. CONCLUDING REMARKS

According to the virtual experiment of this study, strength of the honeycomb material decreases in scale and irregularity. The conclusion relies, however, on the simplified strength definition and failure mechanism of the model. A virtual experiment, aiming at a quantitative prediction, should take into account all the likely failure mechanisms. The strength criterion should also be based on the capacity of the material element to sustain the loading, not the failure initiation.

This work is part of the Virtual Wood task of E-wood – Energy Efficient Wood Processing and Machining – project. The aim of the task is to predict the strength statistics of wood by virtual experiments on a micromechanical model.

REFERENCES

[1] K. Persson, Modelling of wood properties by a micromechanical approach. Report TVSM-3020, University of Lund, Lund, 1997.

[2] http://www.steve.gb.com/images/science/softwood.jpg (Checked: Sept, 2009).

[3] http://micro.magnet.fsu.edu/trees/pages/yellowpine.html (Checked: Sept, 2009) .

[4] L. Mishnaevsky, H. Qing, Micromechanical modeling of mechanical behavior and strength of wood: State-of-the-art-review, Computational Materials Science, 44, 363-370, 2008.

[5] M.R. Gurvich, Strength/size effect for anisotropic brittle materials under a random stress state, Composites Science and Technology, 59, 1701-1711, 1999.